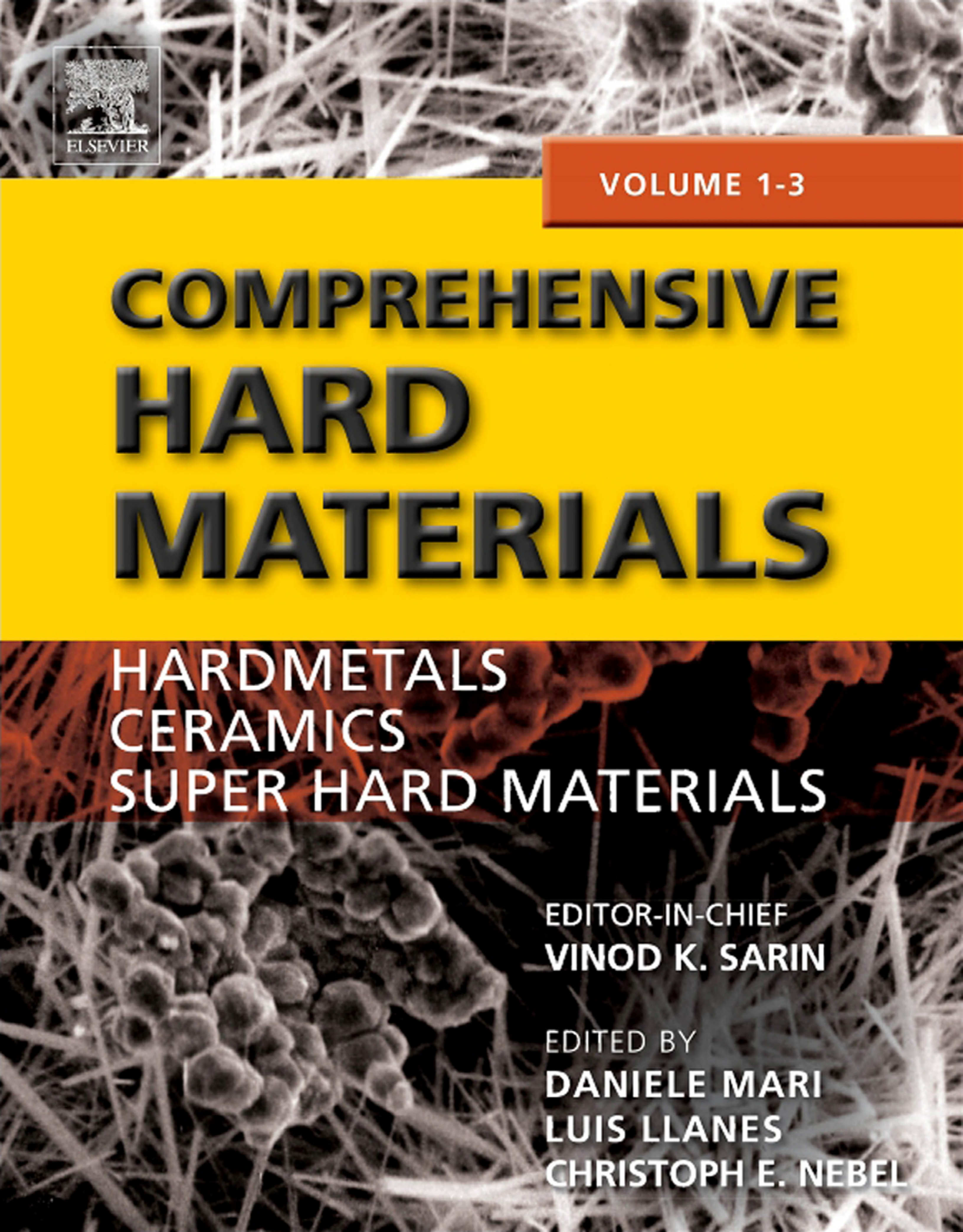

VOLUME 1-3

COMPREHENSIVE HARD MATERIALS

HARDMETALS
CERAMICS
SUPER HARD MATERIALS

EDITOR-IN-CHIEF
VINOD K. SARIN

EDITED BY
DANIELE MARI
LUIS LLANES
CHRISTOPH E. NEBEL

COMPREHENSIVE HARD MATERIALS

VOLUME 2

CERAMICS

This page intentionally left blank

COMPREHENSIVE HARD MATERIALS

VOLUME 2

CERAMICS

EDITOR-IN-CHIEF

VINOD K. SARIN

College of Engineering, Boston University

Boston, MA, USA

EDITED BY

LUIS LLANES

Departament de Ciència dels Materials i Enginyeria Metal·lúrgica

Universitat Politècnica de Catalunya · Barcelona Tech

Barcelona, Spain

DANIELE MARI

Laboratoire de Physique de la Matière Complexe

Ecole Polytechnique Fédérale de Lausanne, Lausanne, Switzerland

ELSEVIER

AMSTERDAM • WALTHAM • HEIDELBERG • LONDON • NEW YORK • OXFORD
PARIS • SAN DIEGO • SAN FRANCISCO • SINGAPORE • SYDNEY • TOKYO

Elsevier
The Boulevard, Langford Lane, Kidlington, Oxford OX5 1GB, UK
225 Wyman Street, Waltham, MA 02451, USA

© 2014 Elsevier Ltd. All rights reserved.

No part of this publication may be reproduced, stored in a retrieval system or transmitted in any form or by any means electronic, mechanical, photocopying, recording or otherwise without the prior written permission of the publisher.

Permissions may be sought directly from Elsevier's Science & Technology Rights Department in Oxford, UK: phone (+44) (0) 1865 843830; fax (+44) (0) 1865 853333; email: permissions@elsevier.com. Alternatively you can submit your request online by visiting the Elsevier web site at http://elsevier.com/ locate/permissions, and selecting Obtaining permission to use Elsevier material.

Notice
No responsibility is assumed by the publisher for any injury and/or damage to persons or property as a matter of products liability, negligence or otherwise, or from any use or operation of any methods, products, instructions or ideas contained in the material herein. Because of rapid advances in the medical sciences, in particular, independent verification of diagnoses and drug dosages should be made.

British Library Cataloguing in Publication Data
A catalogue record for this book is available from the British Library

Library of Congress Cataloging in Publication Data
A catalog record for this book is available from the Library of Congress

Volume 1 ISBN: 978-0-444-63385-9
Volume 2 ISBN: 978-0-444-63384-2
Volume 3 ISBN: 978-0-444-63383-5
SET ISBN: 978-0-08-096527-7

For information on all Elsevier publications
visit our website at www.store.elsevier.com

Printed and bound in UK
14 15 16 17 10 9 8 7 6 5 4 3 2 1

ELSEVIER
Book Aid
International
Working together
to grow libraries in
developing countries
www.elsevier.com • www.bookaid.org

CONTENTS

Volume 1 – Hardmetals

Section I Introduction to Hardmetals

Section II Classes of Materials

Section III Synthesis and Processing

Section IV Mechanical Properties

Section V Applications

Volume 2 - Ceramics

Section I Introduction

Section II Synthesis and Processing

Section III Microstructure and Properties

Section IV Coatings and Applications

Volume 3 - Super Hard Materials

Section I Theory

Section II Materials: Growth, Properties and Applications: Carbon-Based DLC

Section III Nano— and Poly—Diamond

Section IV Single Crystalline Diamond

Section V Selected Properties of Diamond and Applications

Section VI Other Carbon Phases

Section VII III-V Based and Novel Materials

PREFACE

Comprehensive Hard Materials, first reference work of its types, is intended to merge together the myriad facets of this class of materials in a three volume series that reflect the abundance of established and novel uses across industry, from tribology to electronics and from transportation to energy. The range, growth, and innovations of the hard/superhard materials field has become commonplace within materials science as is evident from the vibrant growth of research across and within hardmetals (cemented carbides), ceramics, and superhard materials. Furthermore, the global nature of material science is also reflected by this work and contributors have been drawn from a panorama of global research hubs, with many chapters addressing the specific resource and application challenges within basic research, development, and emergent industrial markets. It is in the true spirit of collaboration across the range of these otherwise hermetically sealed areas of research that this work has been conceived and built. The reader will find original articles covering many relatively unexamined but converging research spaces and the content fully examines the various relationships that focus on fundamentals, properties, characterization, and applications of such materials. It was the objective of the editorial team to assemble a work that would provide strategic insights into hard/superhard materials.

The first volume is devoted to hardmetals, generally known as cemented carbides in the US. This class of materials is composed of unique combinations of carbides and nitrides of transition metals ranging from the fourth to the sixth group of the periodic table and ferrous metals such as Co, Ni, Fe. Since the discovery of WC–Co by Schröter in 1922, they have epitomized a century of industrial applications mainly as cutting tools and wear resistant parts. Probably, without them many challenging enterprises in the field of rock drilling, mechanics or just wire manufacture would not have been possible. Starting from a historical viewpoint the volume contains detailed aspects of manufacturing, composition/structure/properties, and applications. The aim was to define the state of the art in hardmetal manufacturing together with a thorough illustration of the most recent progress obtained by scientific research.

Volume 2 is devoted to hard ceramics—a unique group of materials with a long-standing technical success history but subjected to permanent scientific and technological evolution. Representative ceramics within this subgroup of hard materials are alumina, silicon nitride, silicon carbide, their composites, in the form of bulk material and coatings. Also included are transition metal nitrides, carbides, borides, oxides, and mullite-based environmental barrier coatings. The intention was not only to project the substantial progress achieved in this field, but also to illustrate how scientific research findings are continuously transferred into industrial and technological advances. The overall aim of this volume was to present a critical review of established knowledge and recent advances of hard ceramics covering both their materials science and engineering aspects.

Volume 3 is devoted to superhard materials—materials resistant to a change of shape under applied force, and with a Vickers hardness value exceeding 40 GPa. The strongest of these are composed out of boron, carbon, nitrogen, and oxygen, and can be classified into two categories: intrinsic compounds and extrinsic compounds. The intrinsic group includes diamond as hardest material, cubic boron nitride (c-BN), carbon nitrides and ternary compounds such as B–N–C. Extrinsic materials are those that show super hardness determined by microstructure rather than composition, such as nanocrystalline diamond. These materials are of great interest in many industrial applications such as abrasives, polishing and cutting tools, wear-resistant, and protective coatings. Furthermore, diamond is emerging as an attractive material for new device applications in the field of power electronics, room temperature quantum computing, biosensing, biointerfaces, microelectromechanical systems, color centers and high energy radiation, and particle detectors to name a few. The aim of volume 3 was to present all the critical areas related to superhard materials with an emphasis on recently achieved progress in research, development, and applications.

The Elsevier publication team, especially Paul Prasad Chandramohan, has worked tirelessly to make this publication possible and available in two formats:

- An online version via the Science Direct platform that will guarantee easy worldwide distribution.
- A hard copy version that will be made available based on orders received.

This dual concept readily lends itself to maintaining this reference work current via additions and modifications. Elsevier (Donna de Weerd-Wilson) has discussed this concept with the editors and is in the process of moving on it in the near future.

The idea for this multivolume major reference work originated through discussions at the International Conferences on the Science of Hard Materials. From the outset, David Sleeman and Graham Nisbet (Elsevier) identified not only an overwhelming qualitative demand for extensive, international, innovative, methodologically sound coverage of the subject matter, but also keen interest in a quantitative form as well. Given this encouragement the volume editors Daniele Mari, Luis Miguel Llanes, Christoph E. Nebel, numerous expert contributors and reviewers are responsible for the creation of this definitive publication to encompass the full breadth and considerable depth of the hard/superhard materials field. The editors, contributors, and publishers invested 5 years of time and effort culminating in this, *Comprehensive Hard Materials*, and we are proud to present it to our colleagues and the community it is intended to serve.

Vinod K. Sarin
Boston University
Boston, MA 02215
USA

EDITOR-IN-CHIEF

Prof. Sarin graduated from MIT (Boston, MA) with an Sc.D in material science. He then joined Sandvik's Coromant Research Center, Stockholm, Sweden. Four years later he came back to the US, joined Adamas Carbide and then GTE, where he started an R&D group on hardmetals and ceramics, and was promoted to senior research scientist (Fellow) at GTE. After nearly 20 years of industrial experience he joined academia (Boston University) as professor in the College of Engineering. He has been the recipient of several technical, achievement, and industrial awards, invited distinguished scientist at the Max Planck Institute (Germany), University of Linkoping (Sweden), Visiting Professor, University of Lund (Sweden), Visiting Scholar/Professor Universitat Politècnica de Catalunya (Spain), and a global industrial R&D consultant. He singly or jointly holds over 80 patents, has edited several books, has authored or coauthored several chapters, and over a hundred technical publications. He is a member of the editorial board of several journals, and has chaired several technical sessions and organized several conferences on hard materials.

This page intentionally left blank

VOLUME EDITORS

Daniele Mari graduated in physics in 1986, and in 1991 obtained his PhD at the Federal Institute of Technology (EPFL) in Lausanne, Switzerland, with a study on high temperature properties of hardmetals. From 1992 to 1993, he continues his research at the Massachusetts Institute of Technology working in the field of shape memory alloys. In 1993, he joins the company Amysa Yverdon SA (Switzerland) as director of R&D and creates Advanced Composite & Microwave Engineering with activities in the fields of the electromagnetic heating and materials. In 2004, he returns to academia at EPFL with a research group specialized in mechanical spectroscopy. He is the co-author of more than 70 scientific papers and is presently deputy director of the physics section at EPFL. He is a member of the Editorial Board of the International Journal of Refractory Metals and Hard Materials. He has been co-chairman of the last two International Conferences on the Science of Hard Materials (ICSHM).

Luis Llanes is a full professor and current chairman in the Department of Materials Science and Metallurgical Engineering, as well as board member of the Research Center of Nanoengineering in the Technical University of Catalonia (UPC). He graduated in materials engineering from Simon Bolivar University and received his PhD degree in 1992 from the University of Pennsylvania. He carries out his research activities within the Structural Integrity, Micromechanics and Reliability of Engineering Materials (CIEFMA) group at UPC. His research interests include mechanical integrity and damage assessment of structural materials, particularly hardmetals, advanced ceramics, stainless steels, and hard coatings. He is the co-author of more than 70 papers published in top journals in these fields. In addition, he has a track record of technology transfer and consultancy with hard materials industries. He is member of the Editorial Board of the International Journal of Refractory Metals and Hard Materials as well as of the Steering Committee of the European Hard Materials Group within the European Powder Metallurgy Association. He has been co-chairman of the last three ICSHM.

Chrsitoph E. Nebel graduated in electrical engineering at the University of Stuttgart where he also got his PhD in 1989. He became a postdoc at the Xerox Research Center, Palo Alto, USA between 1990 and 1992 funded by the Alexander v. Humboldt Foundation, Germany. He joined the team of Martin Stutzmann at the Walter Schottky Institute of the Technical University Munich in 1993 where he habilitated in 1998. In 2004, he joined the Diamond Research Center of the National Institute of Advanced Industrial Science and Technology, Japan, where he was leading the "Bio-Functionalized Device Team". In 2008, he went back to Germany to become head of the Micro- and Nano-Sensor Department of the Fraunhofer-Institute for Applied Solid State Physics in Freiburg.

LIST OF CONTRIBUTORS

Jocelyn Achard
Laboratoire des Sciences des Procédés et des Matériaux (LSPM), UPR3407 CNRS, Université Paris 13, France; Laboratoire d'Excellence Sciences and Engineering for Advanced Materials and devices (SEAM), Villetaneuse, France

Igor Aharonovich
School of Physics and Advanced Materials, University of Technology Sydney, Ultimo, New South Wales, Australia

Marc Anglada
Departament de Ciència dels Materials i Enginyeria Metal·lúrgica, Universitat Politècnica de Catalunya · Barcelona Tech, Barcelona, Spain

Thomas Babinec
Departments of Electrical Engineering and Applied Physics, Stanford University, CA, USA

Soumendra N. Basu
Division of Materials Science and Engineering, Department of Mechanical Engineering, Boston University, Boston, MA, USA

Bikramjit Basu
Materials Research Center, Indian Institute of Science, Bangalore, India

Carmen Baudín
Instituto de Cerámica y Vidrio, CSIC, Madrid, Spain

I. Bello
Center of Super-Diamond and Advanced Films (COSDAF), and Department of Physics and Materials Sciences, City University of Hong Kong, Tat Chee Avenue, Hong Kong SAR, P.R. China

Eleni Berdermann
GSI Helmholtzzentrum für Schwerionenforschung GmbH, Darmstadt, Germany

Raul Bermejo
Institut für Struktur- und Funktionskeramik, Montanuniversität Leoben, Leoben, Austria

Vladimir Blank
Technological Institute for Superhard and Novel Carbon Materials, Moscow, Russia

Vadim Brazkin
Institute for High Pressure Physics, Russian Academy of Sciences, Troitsk, Moscow, Russia

Ovidiu Brinza
Laboratoire des Sciences des Procédés et des Matériaux (LSPM), UPR3407 CNRS, Université Paris 13, France; Laboratoire d'Excellence Sciences and Engineering for Advanced Materials and devices (SEAM), Villetaneuse, France

Y.M. Chong
Center of Super-Diamond and Advanced Films (COSDAF), and Department of Physics and Materials Sciences, City University of Hong Kong, Tat Chee Avenue, Hong Kong SAR, P.R. China

Marvin L. Cohen
Department of Physics, University of California at Berkeley, Berkeley, CA, USA; Materials Sciences Division, Lawrence Berkeley National Laboratory, Berkeley, CA, USA

Christoph Czettl
CERATIZIT Austria GmbH, Reutte, Austria

Robert Danzer
Institut für Struktur- und Funktionskeramik, Montanuniversität Leoben, Leoben, Austria

Goffredo de Portu
National Research Council of Italy (CNR), Chemical Science & Materials Technology Department, Institute of Science and Technology for Ceramics (ISTEC), Faenza, Italy

Nadira Derkaoui
Laboratoire des Sciences des Procédés et des Matériaux (LSPM), UPR3407 CNRS, Université Paris 13, France; Laboratoire d'Excellence Sciences and Engineering for Advanced Materials and devices (SEAM), Villetaneuse, France

Eric F. Drake
Rice University, Houston, Texas, USA

Yasuaki Einaga
Department of Chemistry, Keio University, Yokohama, Japan

Peter Ettmayer
Vienna University of Technology, Institue of Chemical Technologies and Analytics, Vienna, Austria

Z. Zak Fang
Department of Metallurgical Engineering, University of Utah, Salt Lake City, UT, USA

Gilbert Fantozzi
INSA de Lyon, MATEIS (UMR CNRS 5510), Villeurbanne, France

S.A. Firstov
Department of Physics of Strength and Plasticity of Materials, Frantsevich Institute for Problems of Materials Science, Kiev, Ukraine

Rainer Gadow
University of Stuttgart, Institute for Manufacturing Technology of Ceramic Components and Composites, Stuttgart, Germany

A.J. Gant
National Physical Laboratory, Teddington, Middlesex, TW, UK

Mark G. Gee
National Physical Laboratory, Teddington, Middlesex, TW, UK

Randall M. German
Department of Mechanical Engineering, College of Engineering, San Diego State University, San Diego, CA, USA

Alix Gicquel
Laboratoire des Sciences des Procédés et des Matériaux (LSPM), UPR3407 CNRS, Université Paris 13, France; Laboratoire d'Excellence Sciences and Engineering for Advanced Materials and devices (SEAM), Villetaneuse, France

Brahma Raju Golla
Engineering Ceramics Research Group, Korea Institute of Materials Science, Changwon, Gyeongnam, Korea

Stefano Guicciardi
National Research Council of Italy (CNR), Chemical Science & Materials Technology Department, Institute of Science and Technology for Ceramics (ISTEC), Faenza, Italy

Stuart Hampshire
Materials and Surface Science Institute, University of Limerick, Limerick, Ireland

Khaled Hassouni
Laboratoire des Sciences des Procédés et des Matériaux (LSPM), UPR3407 CNRS, Université Paris 13, France; Laboratoire d'Excellence Sciences and Engineering for Advanced Materials and devices (SEAM), Villetaneuse, France

Bin He
Center of Super-Diamond and Advanced Films (COSDAF), and Department of Physics and Materials Sciences, City University of Hong Kong, Tat Chee Avenue, Hong Kong SAR, P.R. China

Mathias Herrmann
Fraunhofer-Institut für Keramische Technologien und Systeme IKTS, (www.ikts.fraunhofer.de) Dresden, Germany

Jonathan Hird
Schlumberger Gould Research, Cambridge, United Kingdom

Tetsuo Irifune
Geodynamics Research Center, Ehime University, Matsuyama, Japan; Earth-Life Scinece Institute, Tokyo Institute of Technology, Tokyo, Japan

Thomas J. Jewett
Global Tungsten and Powders Corporation, Towanda, Pennsylvania, USA

Emilio Jiménez-Piqué
Departament de Ciència dels Materials i Enginyeria Metal·lúrgica, Universitat Politècnica de Catalunya · Barcelona Tech, Barcelona, Spain

Shinhoo Kang
Department of Materials Science and Engineering, Seoul National University, Gwanak-ku, Seoul, Korea

Hiromitsu Kato
Energy Technology Research Institute, AIST, Japan

Frank Kern
University of Stuttgart, Institute for Manufacturing Technology of Ceramic Components and Composites, Stuttgart, Germany

Hagen Klemm
Fraunhofer-Institut für Keramische Technologien und Systeme IKTS, (www.ikts.fraunhofer.de) Dresden, Germany

Hans Kolaska
Fachverband für Pulvermetallurgie e.V., Hagen, Germany

Igor Konyashin
Element Six Hard Materials, Element Six GmbH, Städeweg, Burghaun, Germany

Mark C. Koopman
Department of Metallurgical Engineering, University of Utah, Salt Lake City, UT, USA

Aaron D. Krawitz
University of Missouri, Columbia, Missouri, USA

Jochen Kriegesmann
Department of Materials Technology, Glass and Ceramics, University of Applied Sciences Koblenz, Höhr-Grenzhausen, Germany

Anke Krueger
Institute for Organic Chemistry, Julius-Maximiliaus University würzburg, Am Hubland, 97074 Würzburg, Germany

Boris Kulnitskiy
Technological Institute for Superhard and Novel Carbon Materials, Moscow, Russia

Sabine Lay
Grenoble Institute of Technology, Saint-Martin d'Hères, France

Shuit-Tong Lee
Center of Super-Diamond and Advanced Films (COSDAF), and Department of Physics and Materials Sciences, City University of Hong Kong, Tat Chee Avenue, Hong Kong SAR, P.R. China

Luis Llanes
Departament de Ciència dels Materials i Enginyeria Metal·lúrgica, Universitat Politècnica de Catalunya · Barcelona Tech, Barcelona, Spain

Kian Ping Loh
Department of Chemistry, National University of Singapore, Singapore

Guillaume Lombardi
Laboratoire des Sciences des Procédés et des Matériaux (LSPM), UPR3407 CNRS, Université Paris 13, France; Laboratoire d'Excellence Sciences and Engineering for Advanced Materials and devices (SEAM), Villetaneuse, France

John E. Lowther
School of Physics and DST/NRF Centre of Excellence in Strong Materials, University of the Witwatersrand, Johannesburg, South Africa

Andriy O. Lyakhov
Department of Geosciences, Stony Brook University, Stony Brook, NY, USA

Alexander Lyapin
Institute for High Pressure Physics, Russian Academy of Sciences, Troitsk, Moscow, Russia

Daniele Mari
Laboratoire de Physique de la Matière Complexe, Ecole Polytechnique Fédérale Lausanne, Lausanne, Switzerland

Julián Martínez-Fernández
Dpto. Física de la Materia Condensada—ICMS, Universidad de Sevilla—CSIC, Sevilla, Spain

Pankaj K. Mehrotra
Kennametal Inc., Latrobe, PA, USA

Jan Meijer
Nuclear Solid State Physics, University Leipzig, Leipzig, Saxony, Germany

Lutz-Michael Berger
Fraunhofer Institute IWS, Dresden, Germany

Armelle Michau
Laboratoire des Sciences des Procédés et des Matériaux (LSPM), UPR3407 CNRS, Université Paris 13, France; Laboratoire d'Excellence Sciences and Engineering for Advanced Materials and devices (SEAM), Villetaneuse, France

Claude Michotte
CERATIZIT Luxembourg S. à. r. l., Route de Holzem, Mamer, Luxembourg

K.P. Mingard
National Physical Laboratory, Teddington, Middlesex, TW, UK

Rosa M. Miranda
UNIDEMI, Departamento de Engenharia Mecânica e Industrial, Faculdade de Ciências e Tecnologia, Universidade Nova de Lisboa, Caparica, Portugal

Pilar Miranzo
Institute of Ceramics and Glass, CSIC. Kelsen, 5, Madrid, Spain

Jean-Michel Missiaen
Grenoble Institute of Technology, Saint-Martin d'Hères, France

Christian Mitterer
Department of Physical Metallurgy and Materials Testing, Montanuniversität Leoben, Leoben, Austria

Michael Moseler
Fraunhofer Institute for Mechanics of Materials IWM, Freiburg, Germany

Christoph E. Nebel
Fraunhofer-Institute for Applied Solid State Physics, Freiburg, Germany

Steffen Nowotny
Fraunhofer Institut IWS, Dresden, Germany

Artem R. Oganov
Department of Geosciences, Center for Materials by Design, Institute for Advanced Computational Science, Stony Brook University, Stony Brook, NY, USA; Moscow Institute of Physics and Technology, Dolgoprudny city, Moscow Region, Russian Federation; Northwestern Polytechnical University, Xi'an, China

Hugo M. Ortner
Darmstadt University of Technology, Department of Material Sciences: Materials Characterization, Darmstadt, Germany

Maria Isabel Osendi
Institute of Ceramics and Glass, CSIC. Kelsen, 5, Madrid, Spain

Lars Pastewka
Fraunhofer Institute for Mechanics of Materials IWM, Freiburg, Germany

Arvid Eric Pasto
Retired from Sparks, NV, USA

Sébastien Pezzagna
Nuclear Solid State Physics, University Leipzig, Leipzig, Saxony, Germany

S.S. Ponomarev
Department of Physics of Strength and Plasticity of Materials, Frantsevich Institute for Problems of Materials Science, Kiev, Ukraine

Michail Popov
Technological Institute for Superhard and Novel Carbon Materials, Moscow, Russia

Leo Prakash
Kyocera Unimerco Tooling A/S, Sunds, Denmark

Joaquin Ramírez-Rico
Dpto. Física de la Materia Condensada—ICMS, Universidad de Sevilla—CSIC, Sevilla, Spain

Pascal Reynaud
INSA de Lyon, MATEIS (UMR CNRS 5510), Villeurbanne, France

John Robertson
Department of Engineering, Cambridge University, Cambridge, UK

B. Roebuck
National Physical Laboratory, TW, UK

Gregory S. Rohrer
Department of Materials Science and Engineering, Carnegie Mellon University, Pittsburgh, PA, USA

Catherine Rond
Laboratoire des Sciences des Procédés et des Matériaux (LSPM), UPR3407 CNRS, Université Paris 13, France; Laboratoire d'Excellence Sciences and Engineering for Advanced Materials and devices (SEAM), Villetaneuse, France

Malika Saâdaoui
LERSIM Ecole Mohammadia d'Ingénieurs, Université Mohamed V Agdal, Rabat, Morocco

Vinod K. Sarin
Division of Materials Science and Engineering, Department of Mechanical Engineering, Boston University, Boston, MA, USA

Uwe Schleinkofer
CERATIZIT Austria GmbH, Reutte, Austria

Matthias Schreck
Universität Augsburg, Institut für Physik, Augsburg, Germany

Alex V. Shatov
8 Parkside Drive, Jamesburg, NJ, USA

Olga A. Shenderova
International Technology Center, Raleigh, NC, USA; Adámas Nanotechnologies, NC, USA

François Silva
Laboratoire des Sciences des Procédés et des Matériaux (LSPM), UPR3407 CNRS, Université Paris 13, France; Laboratoire d'Excellence Sciences and Engineering for Advanced Materials and devices (SEAM), Villetaneuse, France

Raj P. Singh Gaur
Global Tungsten and Powders Corporation, Towanda, Pennsylvania, USA

Vladimir L. Solozhenko
LSPM–CNRS, Université Paris 13, Villetaneuse, France

Jörg Spatzier
Fraunhofer Institut IWS, Dresden, Germany

Hitoshi Sumiya
Electronics Materials R&D Laboratories, Sumitomo Electric Industries Ltd, Itami, Japan

Alexandre Tallaire
Laboratoire des Sciences des Procédés et des Matériaux (LSPM), UPR3407 CNRS, Université Paris 13, France; Laboratoire d'Excellence Sciences and Engineering for Advanced Materials and devices (SEAM), Villetaneuse, France

Takashi Taniguchi
Advanced Key Technology Division, National Institute for Materials Science, Tsukuba, Ibaraki, Japan

Shi Wun Tong
Department of Chemistry, National University of Singapore, Singapore

Yadir Torres
Universidad de Sevilla, Department of Mechanical and Materials Engineering—ETSI, Sevilla, Spain

Vladimir Turkevich
Synthesis and Sintering of Superhard Materials at High Pressures and High Temperatures, Institute for Superhard Materials of the Ukrainian National Academy of Sciences, Kiev, Ukraine

Hongtao Wang
Kennametal Inc., Rogers, AR, USA

Maxime Wartel
Laboratoire des Sciences des Procédés et des Matériaux (LSPM), UPR3407 CNRS, Université Paris 13, France; Laboratoire d'Excellence Sciences and Engineering for Advanced Materials and devices (SEAM), Villetaneuse, France

Dow Whitney
Retired from Department of Materials Science and Engineering at the University of Florida, Gainesville, Florida, USA

Christoph Wild
Diamond Materials GmbH, Freiburg, Germany

Thomas A. Wolfe
Global Tungsten and Powders Corporation, Towanda, Pennsylvania, USA

Eckhard Wörner
Diamond Materials GmbH, Freiburg, Germany

Wenjun J. Zhang
Center of Super-Diamond and Advanced Films (COSDAF), and Department of Physics and Materials Sciences, City University of Hong Kong, Tat Chee Avenue, Hong Kong SAR, P.R. China

Qiang Zhu
Department of Geosciences, Stony Brook University, Stony Brook, NY, USA

This page intentionally left blank

SECTION I

INTRODUCTION

This page intentionally left blank

2.01 Fundamental Aspects of Hard Ceramics

Stuart Hampshire, Materials and Surface Science Institute, University of Limerick, Limerick, Ireland

© 2014 Elsevier Ltd. All rights reserved.

Nomenclature

Al_2O_3 Alumina, aluminium oxide which in α-Al_2O_3 adopts a hexagonal structure but also exists as other structural modifications, notably γ-alumina which adopts the cubic spinel structure

B_4C Boron Carbide

BN Boron Nitride, which exists as both cubic (with pseudo-diamond crystal structure) and hexagonal (with pseudo-graphite crystal structure) forms

HfB_2 Hafnium Diboride

LiF Lithium Fluoride

$MoSi_2$ Molybdenum Disilicide

NbC Niobium Carbide

SiC Silicon Carbide, which exists as many different structural polytypes. The basic forms are β-SiC which adopts a cubic zinc blende (3C) structure and α-SiC which is hexagonal (6H).

Si_3N_4 Silicon Nitride, which has three confirmed crystallographic modifications, α and β, both hexagonal, and a high pressure produced cubic spinel phase, γ-Si_3N_4. Silicon nitride is also a general term for a family of ceramics which are named according to their fabrication or sintering process:

RBSN Reaction Bonded Silicon Nitride, formed by nitriding silicon powder compacts in the temperature range 1100–1450 °C. The final material contains 15–25% porosity.

SSN Dense Sintered (or Pressureless Sintered) Silicon Nitride, formed by sintering a silicon nitride powder compact containing densification additives (e.g. Y_2O_3 + Al_2O_3) under 0.1MPa N_2 atmosphere at 1750–1900 °C. The process involves Liquid Phase Sintering.

HPSN Hot-Pressed Silicon Nitride, formed by sintering a silicon nitride powder compact containing densification additives (e.g. Y_2O_3 + Al_2O_3) under an applied pressure in a graphite die heated by induction at 1750–1900 °C. The process involves Liquid Phase Sintering aided by the applied pressure.

HIPSN Hot-Isostatically Pressed Silicon Nitride, formed by sintering a silicon nitride powder compact containing densification additives (e.g. Y_2O_3 + Al_2O_3) under a gas pressure applied through an impermeable vitreous membrane to encapsulate the compact. The final process involves Liquid Phase Sintering.

GPSSN Gas Pressure Sintered Silicon Nitride, formed by sintering a silicon nitride powder compact containing densification additives (e.g. Y_2O_3 + Al_2O_3) under a gas pressure (MPa). The process involves Liquid Phase Sintering.

SRBSN Sintered Reaction Bonded Silicon Nitride, formed by nitriding a silicon powder compact containing densification additives (e.g. Y_2O_3 + Al_2O_3) in the temperature range 1100–1450 °C, followed by pressureless sintering under 0.1MPa N_2 atmosphere at 1750–1900 °C. The final process involves Liquid Phase Sintering.

SiAlONs Solid solutions of Al and O in the silicon nitride structure. β′-SiAlON is formed when O^{2-} replaces N^{3-} in the β-Si_6N_8 structure while, at the same time, Si^{4+} is replaced by Al^{3+} to maintain charge neutrality. α-sialons (α′) contain Al^{3+} and O^{2-} and are based on the α-$Si_{12}N_{16}$ unit cell with accommodation of other ions, M = Li^{+}, Ca^{2+}, Y^{3+} or other rare earth lanthanide ions (Ln^{3+}), in two interstitial sites in the unit cell.

SiO_2 Silica, silicon dioxide

TaB_2 Tantalum Diboride

TaC Tantalum Carbide

TaN Tantalum Nitride

TiB_2 Titanium Diboride

TiC Titanium Carbide

TiO_2 Titania, titanium dioxide

WC Tungsten Carbide, usually liquid phase sintered with cobalt (WC-Co) to give a Cermet (ceramic-metal) composite.

ZrB_2 Zirconium Diboride, sometimes used in a composite ceramic with SiC (ZrB_2–SiC).

2.01.1 Introduction

Ceramics are inorganic, nonmetallic materials that are produced from minerals or synthetic particulate materials that are formed into a green shape. Consolidation is typically achieved via a high-temperature process to reduce porosity and densify and strengthen the compact. Traditional ceramics include pottery and whitewares as well as industrial products such as clay ware, building materials, refractories, abrasives and cements. Advanced ceramics are generally pure oxides or nonoxides (nitrides, carbides, borides, etc.) or composites of these materials. They include materials that have been developed with designed microstructures for (1) structural applications (hard ceramics), making use of their mechanical, tribological or high-temperature properties for cutting and drilling tools, bearings, seals, dies, engine components and coatings on other materials to improve corrosion resistance or thermal stability and (2) functional applications, such as electronic, dielectric or magnetic components, biomedical implants or devices, filters, membranes or catalyst supports.

Ceramics are hard, brittle, strong in compression, weaker in tension, wear resistant, can withstand high temperatures (1200–1700 °C), and have good resistance to chemical corrosion. These properties are, as with other materials, highly dependent on their structure, both at the atomic level (crystal structure) and on the micro- and macrostructural levels. These in turn are crucially dependent on the overall chemical composition and the material fabrication conditions which need to be carefully controlled in order to optimize the desired properties. Since ceramics are manufactured for use in wear-resistant applications and possess high hardness, most parts have to be formed as near-net shape as possible by compacting powders into a body which is then sintered at high temperatures. During sintering the body shrinks, the grains bond together and a dense material is produced.

2.01.2 Structure and Property Relationships

Ceramics are made up of metallic and nonmetallic elements, the atoms of which are held together by chemical bonds that can be covalent and/or ionic. The type of bonding and the atomic arrangements (crystal structure)

Table 1 Young's modulus and melting point of some engineering ceramics

Ceramic	*Young's modulus (GPa)*	*Melting point (°C)*
Titania TiO_2	230	1605
Silica SiO_2 (fused)	72	1715
Chromic oxide Cr_2O_3	270	1990
Alumina Al_2O_3	390	2050
Silicon nitride Si_3N_4	310	1910 (sublimates)
Boron nitride c-BN	~400	2970 (sublimates)
Tantalum nitride TaN	–	3090 (sublimates)
Silicon carbide SiC	410	2500
Boron carbide B_4C	470	2750
Tungsten carbide WC	650	2850
Titanium carbide TiC	460	3120
Niobium carbide NbC	370	3500
Tantalum carbide TaC	530	3850
Titanium diboride TiB_2	–	3230
Tantalum diboride TaB_2	680	3000
Hafnium diboride HfB_2	–	3250

have a strong influence on mechanical properties including elastic modulus and hardness. For high elastic modulus, the bond strength between atoms and stiffness of the bond must be high. Some values for Young's modulus of some engineering ceramics are given in **Table 1** along with their melting or decomposition temperatures, which also require high bond strengths. Ceramics have much higher melting points than other materials, the lowest in the range 1600–1700 °C, which is still higher than iron and steels.

2.01.2.1 Bonding

The types of bonds present in ceramics are ionic, covalent or a combination of the two. Pauling (1948) proposed a relationship between the "ionic character" of a bond and the difference in electronegativities of the two elements. Electronegativity is the tendency of an atom to attract electrons toward itself. **Table 2(a)** shows the electronegativity values for elements in the first two rows of the periodic table. The greater the difference between electronegativity values, the more ionic character the bond will possess. Conversely, the smaller the differences in electronegativity values the more "covalent character" the bond will possess. **Table 2(b)** compares the differences in electronegativity values between elements for different compounds and the approximate fraction of ionic or covalent character of the bonds. If the electronegativity difference is less than ~1.7, the bond is more covalent with atoms sharing the bonding electrons. Thus, boron carbide, silicon carbide and silicon nitride (Si_3N_4) have more covalent bonding whereas alumina has a higher proportion of ionic character.

Table 2(a) Electronegativity values for elements in the first two rows of the Periodic table

I	*II*	*III*	*IV*	*V*	*VI*	*VII*
Li	Be	B	C	N	O	F
0.98	1.57	2.04	2.55	3.04	3.44	3.98
Na	Mg	Al	Si	P	S	Cl
0.93	1.31	1.61	1.90	2.19	2.58	3.16

Table 2(b) Electronegativity differences and percentage of ionic/covalent character of the bonds for representative ceramic materials

Compound	*LiF*	*Al_2O_3*	*SiO_2*	*Si_3N_4*	*SiC*	*B_4C*	*C (Diamond)*
Electronegativity difference	3.0	1.83	1.54	1.14	0.65	0.51	0
% ionic character	90	63	50	30	11	6	0
% covalent character	10	37	50	70	89	94	100

2.01.2.2 Crystal Structure

The type of bonding and the relative sizes of atoms, as well as balance of electrostatic charges, all have an influence on the actual arrangement of atoms in ceramic crystal structures. In covalent crystals, the bond is directional and the atoms have small coordination numbers (≤ 4). For example, SiC exists in many polymorphic forms called *polytypes* where the coordination between Si and C is always tetrahedral and the structures differ only in the sequence of identical layers of Si atoms coordinated to four C atoms. β-SiC adopts the cubic zinc blende structure shown in **Figure 1(a)**, in which the Si atoms are arranged in a face-centered cubic or cubic close-packed type of lattice and the C atoms occupy half of the tetrahedral sites in the cube with each atom surrounded by four atoms of the other element (Fisher & Barnes, 1990; Pandey & Krishna, 1975). Using Ramsdell (1947) notation, which specifies the total number of stacking layers within a cubic (C), hexagonal (H) or rhombohedral (R) unit cell, β-SiC can be classified as 3C-SiC in which there are three Si–C bilayers with stacking sequence ABCABC. The other common polymorphs have a hexagonal structure, related to the wurtzite crystal structure shown in **Figure 1(b)** and, for historical reasons, are collectively referred to as α-SiC (Pandey & Krishna, 1975). The difference between them is in the stacking planes of the Si–C bilayers along the *c*-axis. The wurtzite structure is 2H-SiC with stacking sequence AB–AB–A, 4H-SiC has a stacking sequence of ABCB-A, and 6H-SiC has a stacking sequence of ABCACB-A (Ching et al., 2006).

Si_3N_4 has three confirmed crystallographic modifications, α and β (Hardie & Jack, 1957), both hexagonal, and a high pressure produced cubic spinel phase, γ-Si_3N_4 (Zerr et al., 1999). In α- and β-Si_3N_4, all Si atoms are tetrahedrally bonded to N and all N atoms are in an approximate planer configuration. Octahedral bonding of Si to N is very rare and apparently only forms at high temperatures and pressures. The bonding leads to a framework of SiN_4 tetrahedra (slightly distorted) joined by sharing nitrogen corners so that each nitrogen is common to three tetrahedra. The β-structure is composed of puckered rings of alternating Si and N atoms which can be considered as layers with a stacking sequence ABAB as shown in **Figure 2(a)** (Hampshire, Park, Thompson, & Jack, 1978) and forming long continuous channels in the *c*-direction. The *c*-dimension of the α-Si_3N_4 structure is approximately twice that of β, where the layers of atoms in β are linked along the [001] direction in the sequence ABAB, the α-structure has the sequence ABCDABCD. The CD layer, shown in **Figure 2(b)** (Hampshire et al., 1978), is similar to the AB layer except that it is rotated by180° on the *c*-axis. The long continuous channels in the *c*-direction of β are therefore closed off to form two large interstices. In γ-Si_3N_4, Si occupies both the tetrahedral A site and the octahedral B site in the spinel structure (Zerr et al., 1999).

In alumina, the oxygen atoms form an almost close-packed hexagonal arrangement with aluminum atoms occupying two-thirds of the octahedral sites (coordination of six) within the structure (Ishizawa, Miyata, Minato, Marumo, & Iwai, 1980). Alumina also exists as other structural modifications, notably γ-alumina that adopts the cubic spinel structure (Lee, Cheng, Heine, & Klinowski, 1997).

Boron-containing compounds have much more complex structures involving "clusters" of B atoms (Yakel, 1975). In B_4C, a central C–B–C chain is coordinated to a number of B_{12} structural units making up a rhombohedral unit cell.

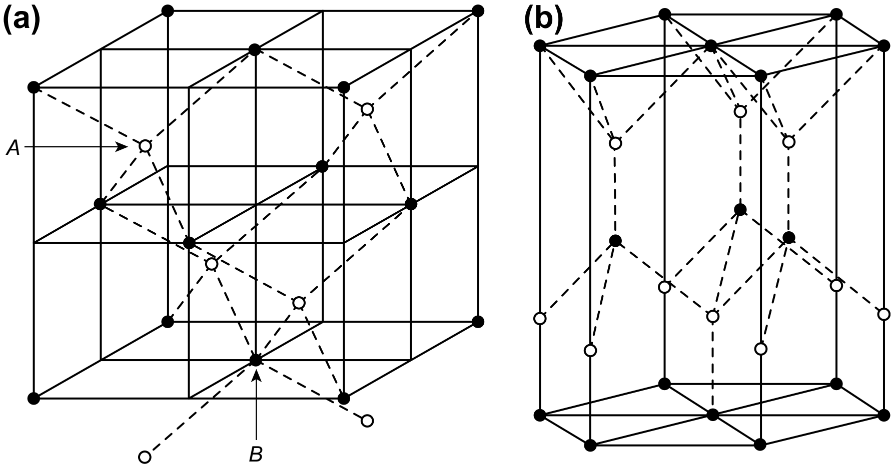

Figure 1 (a) Cubic zinc blende (3C) structure adopted by β-SiC. (b) Hexagonal wurtzite (2H) structure similar to α-SiC (6H).

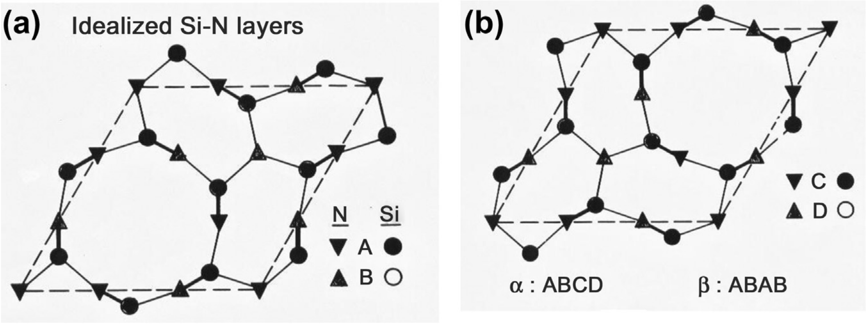

Figure 2 Silicon nitride crystal structure showing (a) ABAB layers of β-silicon nitride and (b) ABCD layers of α-silicon nitride. Hampshire et al. (1978).

While the intrinsic properties of a material are dependent on chemistry, bonding and crystal structure, the major properties of ceramics, particularly strength and fracture resistance are much more influenced by microstructure.

The type of microstructure obtained for a ceramic depends on a number of factors:

- Shape, size, and size distribution of initial powder particles
- Various steps used for shaping
- Conditions used for thermal treatment (temperature, time, atmosphere, pressure, etc.)
- Mechanisms of densification
- Chemical reactions or crystal-phase transitions.

2.01.3 Processing and Fabrication of Ceramics

2.01.3.1 Shaping and Forming

2.01.3.1.1 Basic Ceramic Forming Processes

Most ceramic forming processes prior to firing may be classified into three types (Heinrich, 2004):

1. Casting, including slip casting and tape casting.
2. Plastic forming including extrusion and injection molding.
3. Pressing including die pressing and isostatic pressing.

In these processes, the initial starting powders are prepared by suspending in aqueous or organic solvents. In the case of casting, these suspensions are directly processed into a final thin-walled complex shape with a uniform thickness using a suitable porous mold. A slip is prepared by ball milling appropriate powders with binders, plasticizers or deflocculants in water or an organic solvent. The liquid from the slip is absorbed into the mold by capillary action depositing a layer of the ceramic powder on the internal wall of the mold. Higher green densities can be achieved using pressure casting.

Plastic forming requires partly dewatered or higher viscosity feeds. Injection molding is suitable for high-volume processing of complex-shaped parts and precision components with a high level of reproducibility since it is a near-net shape technique. The powder has to be mixed with the appropriate polymer vehicle which becomes fluid during the injection process. The disadvantage is that the polymer has to be burned out before sintering.

In pressing, almost completely dry free-flowing granules produced by spray drying are used. Die pressing, which involves the uniaxial compaction of this type of granulated powder in a metal die, is by far the most frequently used forming process for advanced ceramics. Isostatic pressing involves the shaping of powder compacts in a flexible container subject to either a pressurized liquid, the wet-bag process, or a compressed gas, the dry-bag process. Both methods allow a uniform compaction to form a green body with homogeneous density that retains the general shape of the flexible container and the profile of any internal tooling.

2.01.3.1.2 Near-Net-Shape Processes

In addition to slip casting and injection molding, other near-net-shape forming methods have been developed, based on the principles of colloid science, in order to produce complex-shaped components and these include the following.

2.01.3.1.2.1 Direct Coagulation Casting (DCC)

This process (Graule, Baader, & Gauckler, 1994) allows consolidation of high solids content ceramic slurries into uniform, defect-free powder compacts by coagulation. If a polar liquid is used as the liquid vehicle, the viscosity of the ceramic suspension at a given solids loading depends on the particle surface charge, usually described by the zeta potential. This can be greatly influenced by changing the pH of the suspension. In general, the viscosity is maximum in the pH range close to the isoelectric point (IEP) of a given system. If a chemical reaction occurs within the suspension, such as the enzymatic decomposition of urea, then the pH value of the aqueous suspension can be shifted closer to the IEP, which causes coagulation and setting of the highly loaded ceramic suspension.

2.01.3.1.2.2 Hydrolysis-Assisted Solidification

This is a similar process to DCC (Kosmac, Novak, & Sajko, 1997) using an added powder that undergoes hydrolysis which results in a shift of pH toward the IEP with an increase in viscosity which can be exploited for solidifying a cast or molded ceramic green body in a way similar to that in the DCC process.

2.01.3.1.2.3 Gel Casting

This process (Omatete, Janney, & Strehlow, 1991) uses concentrated ceramic powder slurry in a solution of organic monomers, which is poured into a mold and gelled by in situ polymerization to form a green ceramic body. The monomer solution provides a low-viscosity vehicle to transport the fluid slurry into the mold and the polymer gel holds the ceramic powder in the desired shape. Vinyl monomers are used and, because they undergo a free-radical chain polymerization reaction, the setting is very rapid. Drying is then carried out to remove the solvent (water) followed by burnout of the polymer and firing of the ceramic.

2.01.3.1.2.4 Colloidal-Based Methodologies

Colloidal-based methodologies for ceramics fabrication (Lewis, 2000) enable control over the structural evolution within the ceramic suspension leading to much improved homogeneity. This requires careful control of the different stages of ceramics fabrication, especially powder synthesis, suspension preparation and rheology, consolidation into the desired component shape and removal of the solvent phase (drying) to produce the final microstructure during firing that gives optimal performance.

2.01.3.1.2.5 Solid Freeform Fabrication

Solid freeform fabrication describes a series of moldless manufacturing methods (Halloran, 1999) that incorporate the use of computer-aided design (CAD) to create a 3D computer model of the desired part. This model is then separated into thin layers and a computer-controlled device is used to build the component up by sequential deposition, layer by layer. These methods are outlined below.

2.01.3.1.2.5.1 Direct Inkjet Printing

Inkjet printing is a noncontact dot matrix printing method (Derby, 2011) where droplets of ink are ejected from a printhead nozzle directly to a specified position on a substrate.

2.01.3.1.2.5.2 Three-Dimensional Printing (TDP) or 3-DP

This process is under development for flexible production of prototype parts and components directly from a CAD model. Three-dimensional printing or 3-DP takes a relatively long time to form a ceramic green body and has limitations when processing ceramic particles <1 μm diameter.

2.01.3.1.2.5.3 Fused Deposition of Ceramics

This process uses ceramic–polymer feedstock that are extruded into thin filaments and used as feed material for fabrication of three-dimensional green ceramic objects (Agarwala, Bandyopadhyay, van Weeren, Safari, & Danforth, 1996) using a commercial fused depositional modeling (FDM)™ system. The polymer or wax acts as a carrier and binder for the ceramic particles as the material flows out of the heated extruder head. The green ceramic object thus created is then subjected to conventional binder removal and sintering processes, to produce fully dense ceramic components.

2.01.3.1.2.5.4 Stereolithography

Stereolithography involves dispersion of a concentrated suspension of ceramic particles within a photopolymerizable liquid solution. The ceramic suspension is photocured, layer by layer, converting the solution to a polymer binder and forming a net-shape ceramic green body (Griffith & Halloran, 1996) without the need for molds. Binder burnout is then required before sintering.

2.01.3.2 Thermal Treatment of Ceramics—Sintering

The term *sintering* is used to refer to the process that consolidates powder compacts into strong and usually dense polycrystalline materials via heating. When an aggregate of particles is assembled into a shape, they do not fill space and the maximum packing density is usually <60% of full density, that is >40% porosity. Many changes occur during sintering. The compact usually shrinks and the particles change shape with average grain size increasing.

Sintering is possible only if the atoms can diffuse to form the necks that effectively bond the particles together. The transport of matter can occur in the vapor phase, in the liquid phase, by diffusion in the solid state, or through the viscous flow of a glass. Most mechanisms are activated thermally because the action of temperature is necessary to overcome the potential barrier between the initial state of higher energy (compacted powder) and the final state of lower energy (consolidated material).

The driving force for sintering is the reduction in surface energy within the compact and therefore one prime requirement is a high surface area powder or one with a fine particle size. German (1996) states "With particles there is an inherent driving force for mass flow, and the smaller the particle size, the greater the driving force." The reduction in total interfacial energy occurs via densification and also coarsening or grain growth. If γ is the specific surface or interfacial energy and A is the total surface or interfacial area within a powder compact, then the total interfacial energy of the compact is γA. The reduction in this total energy can be expressed by (Kang, 2005) the following equation:

$$\Delta(\gamma A) = \Delta\gamma A + \gamma\Delta A \tag{1}$$

The change in interfacial energy, $\Delta\gamma$, is due to densification and the change in interfacial area, ΔA occurs because of grain coarsening. $\Delta\gamma$ is related to replacement of solid/vapor interfaces or surfaces by solid/solid interfaces. The overall change in total interfacial energy occurs through densification and grain growth (coarsening) as shown schematically in **Figure 3** (Kang, 2005).

It is only when the temperature is sufficiently high in the range 0.5–0.8 Tm (where Tm is the melting point in Kelvin) that sintering occurs at a practical rate. The mechanisms by which the important atom movements occur determine the final densification and microstructural features of the ceramic.

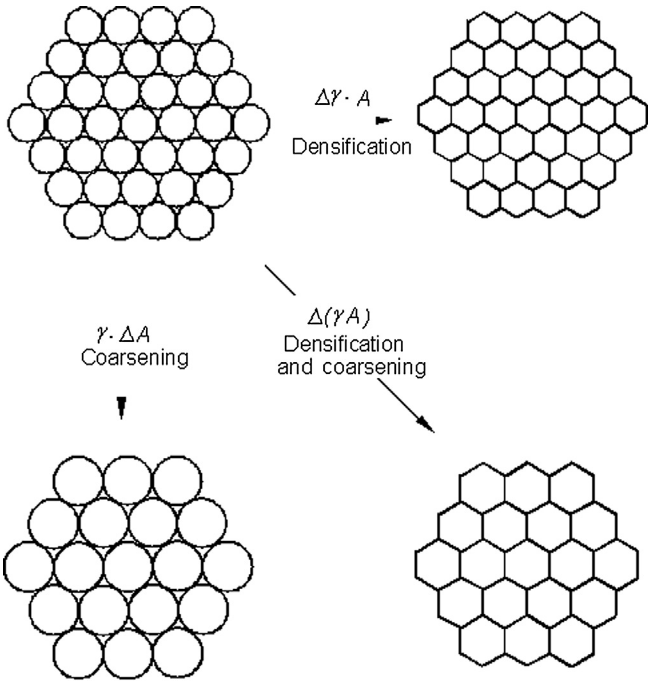

Figure 3 Basic phenomena (densification and grain coarsening) occurring under the driving force for sintering, $\Delta(\gamma A)$. Kang (2005), by kind permission.

2.01.3.2.1 Solid-State Sintering

Densification and strengthening during sintering in the solid state relies wholly on diffusion of atoms with no formation of liquid. Three stages have been identified:

1. *Initial stage*, during which necks begin to form at the contact points between adjacent particles. Neck formation is driven by the energy gradient resulting from the different curvatures of the particles and the necks.
2. *Intermediate stage*, during which the growing necks merge to form grains within a polycrystalline body with an interconnecting cylindrical pore network (density ranging from 70% to 93% theoretical) forming along the grain boundaries (GBs). At the end of this stage, the pore surfaces are smoother and pores become isolated from each other.
3. *Final stage*, during which isolated pores gradually reduce in volume and grain growth becomes significant.

Figure 4 shows the schematic curve of densification of a powder compact with time during the three stages of sintering.

There are a number of material transport mechanisms that may operate during solid-state sintering of a polycrystalline ceramic and these are shown schematically in Figure 5 and are classified below.

2.01.3.2.1.1 Surface Transport Processes

Surface transport processes, which change the pore shape but not the pore volume and lead to strengthening but no shrinkage or densification, include the following:

1. *Surface diffusion*, D_s, which involves the diffusion of atoms along surfaces where the source is a particle surface and the sink is a neck. It only occurs to a depth of approximately one to two atomic distances (0.3–0.5 nm) (Rahaman, 2003). This type of diffusion is initiated at lower temperatures due to its lower activation energy and is usually the dominant mass-transport mechanism during the early stages of neck

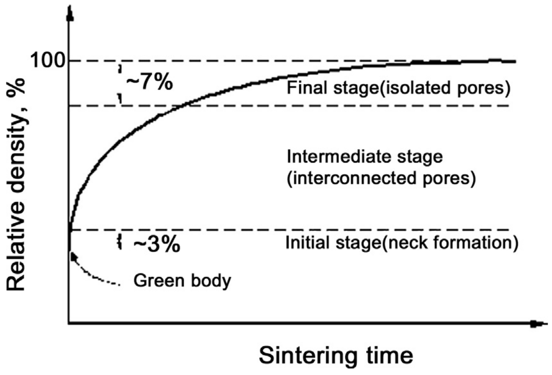

Figure 4 Schematic curve of densification of a powder compact with time during the three stages of sintering. Kang (2005), by kind permission.

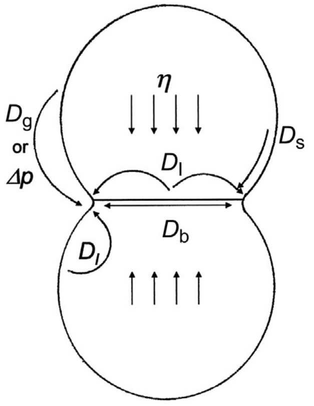

Figure 5 Material transport paths during sintering. Kang (2005), by kind permission.

growth, as the compact is heated up to the sintering temperature. It becomes less dominant as neck formation between particles increases.

2. *Vapor transport*, D_g, which allows the material to be transported from one source surface to another sink surface by evaporation of atoms and condensation at another site, through the pore network. This can also take place because of vapor pressure difference Δp.
3. *Lattice diffusion*, D_l, which allows the material to be transported from a particle surface to the neck area by diffusion through the bulk lattice with no increase in densification of the material.

2.01.3.2.1.2 Bulk Transport Processes

Bulk transport processes, associated with GBs or the crystal lattices, allow movement of material so that particle centers approach each other, resulting in shrinkage, reductions in pore volume and densification and include the following:

1. *GB diffusion*, D_b, which allows the atoms from the GB to be transported along the GB to a neck region or pore surface, driven by the high level of disorientation of the atoms along the GB. Even though GBs are quite narrow, they are very active transport paths.
2. *Bulk lattice diffusion*, D_l, which allows the atoms from the GB to be transported from the GB through the lattice to a neck or pore surface and so the boundary acts as a site for vacancy annihilation.
3. *Plastic flow*, η, which is only active where the initial dislocation density is very high and therefore is not usually operative in ceramics. *Viscous flow*, η, may operate in ceramics where a viscous liquid phase is formed. This will be considered under Section 2.01.3.2.2.

2.01.3.2.1.3 Densification Kinetics

Kuczynski (1949) analyzed the rate of growth of the neck during the initial stage for various mechanisms of transport of material into the neck from the particle surface and Herring (1951) included the effects of particle size. For all mechanisms, a general relationship follows:

$$(x/r)^n = K_1 t/r^m \tag{2}$$

where r is the particle radius, x is the radius of the interparticle contact area, t is the time and n, m and K_1 are constants. Plots of log (x/r) versus log t or log r should result in linear plots with slopes of n or m.

During the second intermediate stage, depending on the mechanism of material transport, shrinkage may occur according to

$$\Delta L/L_o = K_2 t^{\gamma} \tag{3}$$

where ΔL is the change in length, L_o is the original length, t is the time and γ and K_2 are constants. A plot of $\Delta L/L_o$ versus log t should be linear with slope γ. The mechanism of material transport is then deduced from the slope as follows:

	n	m	y
Surface diffusion, D_s	7	4	No shrinkage
Evaporation/condensation, D_g	3	2	No shrinkage
Volume (bulk) diffusion, D_l	5	3	0.4/0.5
Grain boundary diffusion, D_b	5	3	0.3/0.33
Viscous/plastic flow, η	2	1	1

During the intermediate stage, when relative density is in the range 0.85–0.93, porosity P is decreasing in volume but pores are still interconnected. If no grain growth occurs, then

$$\Delta P/P_o = K_3 t \tag{4}$$

where ΔP is the change in volume fraction porosity, P_o is the original volume fraction porosity, t is time and γ and K_2 are constants. If grain growth occurs according to

$$D^3 - D_o^3 = K_4 t \tag{5}$$

where D is the grain size after time t and D_o is the original grain size, then

$$\Delta P/P_o = K_5 \log t \tag{6}$$

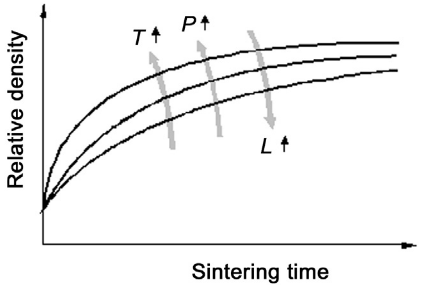

Figure 6 Effect of sintering parameters (*T*, temperature; *P*, pressure; *L*, particle size) on densification. Kang (2005), by kind permission.

More than one of the above matter transport mechanisms may operate at the same time. For example, a compact may increase density by a diffusion process but at the same time, an evaporation/condensation process may round pores. A shrinkage measurement (isothermally with time) would reveal only matter transport by diffusion whereas vapor or surface diffusion would decrease the driving force for all material transport and would thus decrease the rate of shrinkage.

The activation energies for surface, GB and lattice diffusivity increase in that order (Barsoum, 2002). Thus the type of matter transport mechanism is highly dependent on the sintering temperature. Particle size, packing, degree of agglomeration, presence of impurities, sintering atmosphere, etc. can affect the mechanism of sintering, the extent of pore/GB interactions (Brook, 1969) and whether densification or coarsening occurs. **Figure 6** shows schematic curves of relative density versus time and the effects of temperature, pressure and particle size (Kang, 2005).

2.01.3.2.1.3.1 Fast Firing

Fast firing (Harmer & Brook, 1981) was proposed as a sintering method in order to enhance densification and suppress grain growth and involved heating a powder compact at much higher heating rates than in conventional sintering. This has the effect of attaining higher temperatures very rapidly where the activation energy for densification, Q_ρ, is higher than Q_g, the activation energy for grain growth. The ratio of densification rate to grain growth rate increases with increasing temperature above an intermediate temperature T_{int}, but below this temperature, grain growth will be faster than densification as shown in **Figure 7**. Fast firing thus allows a powder compact to reach temperatures above T_{int} very quickly thus minimizing grain coarsening during heating.

2.01.3.2.2 Liquid-Phase Sintering

Liquid-phase sintering is a more complex process than solid-state sintering and involves the partial melting of one or more components and therefore takes place at a temperature above the solidus for the particular composition. Changes in temperature result in changes in the nature of both the solid and the liquid phases. The parameters which control densification include grain size and shape, pore size and shape, liquid volume and viscosity, solubility of the solid, wetting of the solid by the liquid, phase distribution and phase-boundary energies.

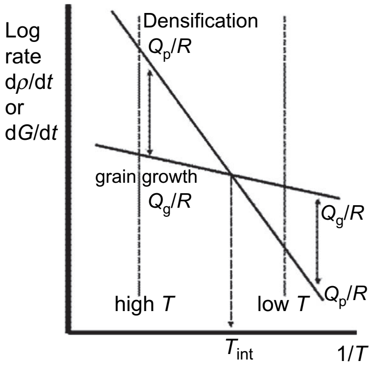

Figure 7 Densification rate or grain growth rate as a function of temperature. Adapted from Harmer and Brook (1981).

When one of the components melts or liquid is formed as a result of some reaction between components, an initial rapid densification occurs by the movement of solid particles from their initial positions to a higher degree of packing. A number of different parameters can influence the mobility of particles including surface and interfacial energies.

2.01.3.2.2.1 Surface and Interfacial Forces

Whenever dissimilar phases are brought into contact at surfaces, equilibrium between the surface energies involved will have a considerable bearing on the way in which phases will be distributed. The effects on microstructure have been reviewed by Smith (1948).

Considering a drop of liquid resting on the surface of a solid phase (**Figure 8(a)**), the system will reach equilibrium such that

$$\gamma_{\mathrm{SL}} - \gamma_{\mathrm{SL}} = \gamma_{\mathrm{LV}} \cos\theta \qquad (7)$$

where γ is the surface energy of the respective interfaces (SV, solid/vapor; SL, solid/liquid; LV, liquid/vapor). If $\theta < 90°$, then the liquid wets the solid. If $\theta = 0°$, the liquid will spread along the solid surface but complete wetting cannot occur if

$$\gamma_{\mathrm{LV}} > \gamma_{\mathrm{SV}}.$$

If the liquid is surrounded by the solid as in a pore, the conditions are slightly different because spreading generates only new liquid–solid interfaces but no new liquid–vapor interfaces. A wetting liquid will always tend to rise up a capillary or be drawn into a pore, even if it would not spread on a free surface.

Where the liquid phase is in contact with a solid GB as in **Figure 8(b)**, penetration of the liquid between the grains will be dependent on the surface energies involved. At equilibrium,

$$\gamma_{\mathrm{GB}} = 2\gamma_{\mathrm{SL}}\cos(\phi/2) \qquad (8)$$

where ϕ is the dihedral angle. In the case of complete wetting, the liquid phase can penetrate along the GBs and separate the grains.

Jackson, Ford, and White (1963) showed that increasing the dihedral angle and the degree of solid–solid contact between grains tends to increase the resistance to shrinkage and densification. This occurs mainly during the initial rapid formation of the liquid phase when any grain-to-grain contact inhibits the ability of the particles to rearrange within the liquid phase.

2.01.3.2.2.2 Mechanisms of Densification

Kingery (1958) discussed the effect of surface energy and suggested that densification is due to an effective pressure acting on the compact from capillary forces. Kingery (1959) developed the theoretical relationships for

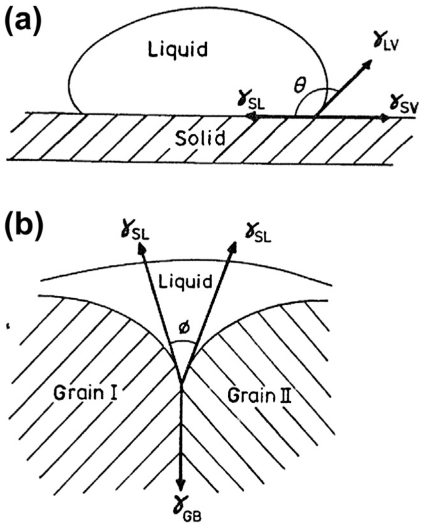

Figure 8 (a) Liquid drop on solid showing contact angle, θ. (b) Liquid penetration along GB depends on dihedral angle, ϕ.

densification during three distinct stages described as (1) the rearrangement stage, (2) the solution-precipitation stage and (3) the coalescence stage.

In the ideal case envisaged by Kingery, capillary forces draw the liquid that is first formed to the points of contact between grains at a rate that is determined by the surface tension and viscosity of the liquid. Particle rearrangement thus occurs by viscous flow and shrinkage, $\Delta L/L_o$, is given by

$$\Delta L/L_o = K_6 t^{1+\gamma} \tag{9}$$

where t is the time and K_6 is a constant. Kingery suggested that γ is some small fraction, typically ~0.3. However, the normal form of a sintering curve does not follow such a relationship and γ, in fact, must be a small negative fraction.

The proportion of complete densification that can be achieved through a rearrangement process with spherical particles depends on the volume fraction of liquid present and Kingery's relationship is shown in **Figure 9(a)**. The shrinkage may also depend on particle shape and size distribution, the solubility of the solid in the liquid and interfacial energies.

The second stage involves atom transport in the liquid by solution, diffusion and reprecipitation. The first detailed investigation of the process (Price, Smithells, & Williams, 1938) concluded that a process of grain growth by solution and reprecipitation occurs. For very small crystals, the interfacial tensions between the crystals and their saturated solution are greater than that for large crystals. The surface tension, γ, is related to the solubility, S, of a small particle of radius, r, by the equation (Ostwald, 1900)

$$\gamma = \frac{RT\rho r}{2M} \log \frac{S}{S_o} \tag{10}$$

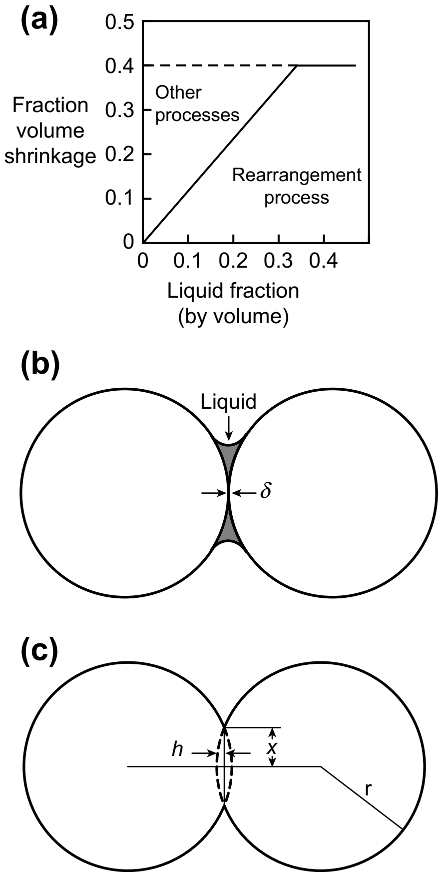

Figure 9 Kingery's model for liquid-phase sintering (Kingery, 1959): (a) fractional shrinkage due to rearrangement process, (b) spherical particles held together by liquid capillary pressure, and (c) particles approach due to solution at the contact area for solution into the liquid phase.

where M is the molecular weight of the solid and S_o is the normal solubility. Consequently, small particles are more soluble than large ones.

Kingery's hypothesis states that the solubility at the contact points between particles becomes larger than at other parts of the surface because of the compressive stresses generated by the hydrostatic pressure from the presence of pores at the particle junctions. The situation is shown schematically in **Figure 9(b) and (c)** for spherical particles. After rearrangement, the particles of radius r are separated by a thin film of liquid, of thickness δ, but held together by liquid capillary pressure as in **Figure 9(b)**. The contact points tend to dissolve such that the centers of spheres approach each other by a distance h, as in **Figure 9(c)**, and a circular contact area of radius x develops. The shrinkage equation developed is

$$h/r \equiv \Delta V/V_o = K_7 t^{1/n} \tag{11}$$

The value of K_7 and n are dependent on the rate-controlling process. Where the rate-controlling process is diffusion through the liquid phase, $n = 3$ for spherical particles and $n = 5$ for prismatic particles. Where the rate-controlling process is the interfacial reaction resulting in solution into the liquid phase (or precipitation from it), $n = 2$ for spherical particles and $n = 3$ for prismatic particles. A plot of log shrinkage versus log time should be linear with slope $1/n$. This model is more commonly referred to as Contact Flattening. Kingery, Niki, and Narashiman (1961) showed that shrinkage data for a MgO–kaolin ceramic and for a WC–Co hardmetal plotted in this way were in good agreement with the equations developed.

Kingery's model assumes (1) an appreciable amount of liquid, (2) an appreciable solubility of the solid in the liquid, and (3) a complete wetting of the solid by the liquid. The last assumption is not always fulfilled for many systems of interest in ceramic technology. White (1970) has argued that Kingery's suggestion that the change in grain shape is due to transport of material along the liquid film between the grains is not correct if the dihedral angle is greater than zero. He suggested that a more probable mechanism would be that of Herring (1951) for neck growth between single-crystal particles with a GB between them and having their surfaces intersecting at the equilibrium dihedral angle. Under these conditions, the tendency of the system to minimize its surface energy causes neck growth and a reduction in center-to-center distance. White suggested that in the presence of a liquid phase the surface energy of the grains is replaced by a much lower interfacial energy but the capillary pressure exerted by pores supplements this.

Gessinger, Fischmeister, and Lukas (1973) indicated that shrinkage with a partially wetting liquid approximately follows Kingery's kinetics with deviations in the exponent $1/n$ being so small that they cannot be demonstrated experimentally. It should also be noted that for spherical particles with diffusion as the rate-controlling process, Eqn (11) differs from Eqn (3), which is based on Coble's (1958, 1961) equation for GB diffusion (solid-state sintering), only by a numerical constant assuming that the diffusion constants are the same. Later modifications of Kingery's model have been proposed taking into account grain growth (Mortensen, 1997; Svoboda, Riedel, & Gaebel, 1996).

The third stage of sintering involves a reduction in the densification rate which may be caused by a number of different processes. Lenel (1948) ascribes the termination of the solution-precipitation stage to a coalescence process, in which grains grow together preventing further transport of liquid phase. Kingery et al. (1961) have observed the trapping of gases in closed pores and the resulting pressure acts against the capillary pressure normally causing shrinkage. If the dihedral angle is zero, densification ends after the second stage since the grains are separated by liquid. An alternative model of pore filling for densification and shrinkage during the final stage of liquid-phase sintering was proposed by Kang, Kim, and Yoon (1991). Densification occurs by the liquid filling of pores during grain growth, which results in an instantaneous drop of liquid pressure in the compact and causes gradual accommodation of grain shape. A final microstructural homogenization occurs around filled pores.

In ceramics technology, liquid-phase sintering is now recognized as the densification process for fine-grained covalent substances such as Si_3N_4 and silicon carbide which under normal conditions may be considered unsinterable. For these ceramics, dense materials can be achieved with the use of sintering additives which form liquids (Section 2.01.6).

2.01.3.2.3 Reaction Sintering

Some advanced ceramics are produced by reaction sintering processes (Di Rupo, Anseau, & Brook, 1979) in which the solid phase precipitates from an intermediary liquid phase that is formed during compaction. When the size of the precursor powder particles is <100 nm, other sintering mechanisms come into prominence such as GB slip, dislocation motion, grain straining and viscous flow at GBs. With nanosized powders, then the driving force for sintering is greater with enhanced kinetics due to higher surface curvatures. As a result, densification of nanopowders may occur at temperatures well below those of micron-sized powders. Thus, small final grain sizes can be achieved although the process must be carefully controlled to avoid unwanted grain growth.

2.01.3.2.4 Microwave Sintering

Microwave sintering allows reductions in both sintering temperature and time since there is direct coupling of the microwaves with electric dipoles within the ceramic body and this also allows control of grain growth (Binner & Vaidhyanathan, 2008). This is thought to be due to the higher heating rates which bring the ceramic up to the sintering temperature more rapidly so avoiding the lower temperature region where the rate of grain growth is higher than the rate of densification.

2.01.3.2.5 Pressure-Assisted Sintering

Densification of ceramics can be achieved more effectively using pressure-assisted forming techniques that combine external pressure with temperature in order to enhance the final density. These include hot pressing, hot isostatic pressing (HIP), sinter forging, hot extrusion and gas pressure sintering (GPS).

Hot pressing, which involves application of a uniaxial pressure through a simple shaped die, only produces simple shaped components, which require subsequent diamond machining to final tolerances. For any particular material, the use of applied pressure at the sintering temperature increases the densification rate and the ability to reach near-theoretical density in a reasonable time. It is generally considered that several simultaneous mechanisms contribute to densification during hot-pressing. As well as diffusion enhanced by the applied pressure, grain-boundary sliding and plastic flow have some effect. With a liquid phase present, the applied pressure is thought to be merely additive to the capillary pressure (Kingery, Woulbroun, & Charvat, 1963).

2.01.3.2.5.1 Hot Isostatic Pressing

HIP combines high temperature and a gas pressure, which is uniformly applied to the powders in all directions, usually through an impermeable membrane to encapsulate the powder compact. An almost fully densified body with no open porosity can be hot-isostatically pressed directly without the encapsulation.

2.01.3.2.5.2 Spark Plasma Sintering

Spark plasma sintering (Nygren & Shen, 2003), also known as field-assisted sintering technique, uses an electrical current (direct current (DC), pulsed DC, or alternate current) which is passed through a conducting pressure die (graphite) and, if the material has reasonable electrical conductivity, through the ceramic itself. The die therefore acts as a heat source, so the sample is heated both internally and externally. The technique allows very rapid heating and cooling rates, very short holding times and results in densification at much lower sintering temperatures, usually a few hundred degrees lower than for conventional sintering.

2.01.3.2.5.3 Plasma Pressure Compaction ($P^2C^®$)

A specialized technique known as plasma pressure compaction ($P^2C^®$) (Ghosh, Subhash, Radhakrishnan, & Sudarshan, 2008) has been used for highly covalent ultra-high-temperature ceramics such as zirconium diboride and ZrB_2–SiC composites. The method involves localized resistive heating (i.e. Joule heating) of a powder compact through the application of a low-voltage/high-ampere DC. Bonding of powder particles is accomplished in two stages:

1. An in-situ elimination of surface oxide and contaminants due to application of a pulsed DC voltage.
2. Sintering of the purified powder through Joule heating due to application of a continuous DC voltage at a high current density ($>4000\ \mathrm{A\ cm^{-2}}$).

Rapid densification over a period of 2–10 min is facilitated through microwelding and plastic-yielding mechanisms due to the applied external pressure (<100 MPa). This results in a dense microstructure with minimum grain growth.

2.01.3.3 Finishing Processes

Following sintering and related processes, the actual final size and shape of ceramics need to be brought within certain tolerances. Surfaces of these sintered ceramics may also contain defects that become strength-limiting flaws in service if not removed.

Therefore, abrasive machining is usually undertaken at this stage of the process to produce the desired shape, size, finish, and strength and must be carried out so that material is removed in a controlled way with minimal microscopic damage and possible microcrack formation. Most hard ceramics have to be machined after firing and the close tolerances required mean that expensive precision grinding is the only viable technique using polycrystalline diamond or cubic boron nitride cutting tools. As the machining costs for hard ceramics are very high, optimization of fabrication processes for near-net shape forming are increasingly employed to reduce the amount of material to be removed. Control of sintering parameters also allows reductions in deformities during firing and minimization of shrinkage during densification. Diamond-machined components using grinding tools have typical tolerances of $\sim 20\ \mu m$. Tolerances of $<20\ \mu m$ can be achieved by using loose abrasive powders as in lapping or polishing.

2.01.4 Microstructure

Properties are the consequence not only of the chemistry and crystallography but also of the microstructure, which describes the arrangement of grains, pores and possibly intergranular phases. Mastering the microstructure is an essential criterion to control of properties. Despite the many different types of ceramics, their microstructures have a number of common features. One or more crystalline phases may be present along with pores and the microstructure may also contain an associated vitreous or glassy phase. A wide range of grain shapes and sizes is observed, generally in the range from 0.1 to 100 μm. Porosity may be fine or coarse, open or closed.

GBs have a particularly profound effect on the structure-sensitive properties of ceramics such as mechanical behavior. In pure single-phase materials, GBs are simply surfaces separating individual crystallites and can be regarded as thin regions of atomic disarray where the density of atoms is slightly lower than normal. GBs can thus act as sources of and sinks for structural defects such as point defects and dislocations and as sites for pores. In impure materials, impurities and second phases are localized at GBs.

Microstructural defects may come from starting powders, for example, needle-shaped grains in Si_3N_4 raw materials or strong alumina agglomerates which will be difficult to split into primary crystals (Cambier, 2011). **Figure 10** shows a pressed alumina ceramic with a flaw resulting from an original granule that was too strong and did not deform easily during pressing.

Microstructure can be controlled by optimization of the fabrication process through careful choice of raw materials, selection of the appropriate shaping technology and optimization of the temperature–time schedule during sintering. In addition, the thermal treatment can be modified, particularly using pressure-assisted methods such as hot pressing, HIP, postsintering HIP treatments where the driving force includes an extra parameter related to external pressure $(2\gamma/r + P_{ext})$.

Controlled rate sintering (Palmour & Johnson, 1967, p. 779) allows optimization of grain size and pore elimination because the densification rate constant at relative densities >0.75 favors GB diffusion, D_B, rather

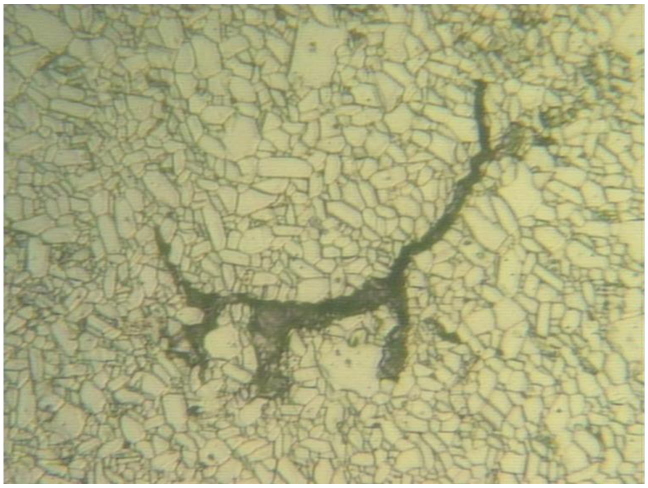

Figure 10 Flaw in pressed alumina resulting from original strong granule. Cambier (2011), by kind permission. *(For color version of this figure, the reader is referred to the online version of this book.)*

than surface diffusion, D_S. Fast firing also favors D_l and D_B over short periods of time at high temperatures leading to smaller grain sizes.

2.01.4.1 Grain Boundary Structure and Modification

Structurally, GBs can be categorized (Kang, 2012) as (1) rough, that is atomically disordered and macroscopically rounded, and (2) faceted, atomically ordered and macroscopically straight or zig-zagged (Lee, Chung, & Kang, 2000). The structural transition between rough and faceted boundaries can be induced by changing the temperature, oxygen partial pressure or by adding dopants. Kang (2012) outlines recent theories of normal ("stationary") and abnormal (or non-normal) grain growth and how impurities or solute segregation, uneven distributions of impurities or second phases at GBs, presence of second phase particles and GB faceting affect this.

2.01.4.1.1 Addition of Dopant Elements to Modify Grain Boundary Energy

Dopants can be introduced to modify GB energy. When the concentration of the dopant is greater than the solubility limit in the major component, then segregation occurs at GBs. GB mobility is slowed by segregated dopant ions. Concentration of maximum dopant increases with surface to volume ratio of the grain, i.e. it is higher for nanosize grains. Above a given concentration, a new (dopant-rich) phase precipitates. Precipitation occurs at lower dopant concentrations as grain size increases.

Recent work (Dillon, Tang, Carter, & Harmer, 2007; Harmer, 2008) has shown how ceramics may contain multiple different GB phases (complexions) that are chemically induced by certain additives. These interface complexions have some characteristic equilibrium feature such as (1) a characteristic solute profile, (2) a crystallographic reconstruction, (3) a common disorder parameter, (4) an interfacial film width, and so on. Thermodynamics predict that their stability is dependent on temperature, chemistry, and crystallography. The intergranular films in Si_3N_4 and silicon carbide are examples of GB complexions (Section 2.01.6.1.2).

Six distinctly different GB complexions may exist in alumina in order of increasing GB mobility: (1) submonolayer adsorption, (2) the clean "intrinsic" boundary, (3) bilayer adsorption, (4) multilayer adsorption, (5) a nonwetting intergranular film (IGF), and (6) a wetting intergranular film. Each GB complexion has its own associated characteristic average GB mobility (absent significant second-phase drag effects), and there is a trend of increasing mobility with increasing disorder within the core of the GB. The coexistence of any two or more complexions within a microstructure is the condition for abnormal grain growth.

Harmer (2008) describes how transitions between these complexions occur and at which GBs they are most likely to occur. The number of complexion transitions that occur increases linearly with grain size (GB excess concentration), and exponentially with temperature. Both the distribution of chemical elements and the distribution of GB energies, due to anisotropy, are important in predicting which GBs undergo a complexion transition. The results indicate that low-energy GBs are least likely and high-energy GBs are most likely to undergo a disordering complexion transition. The highest temperature at which no abnormal grains will form will be defined by the energy of the highest energy GB.

2.01.4.1.2 Addition of Small Particles at Grain Boundaries

If insoluble particles are dispersed in a ceramic matrix, grain growth will be slowed down (or even stopped). Inclusions will exert blocking forces opposed to GB mobility, resulting in so-called "pinning" of GBs as shown

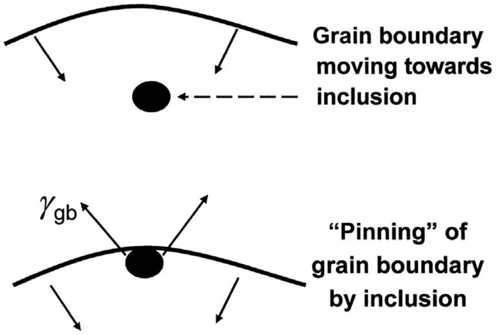

Figure 11 Schematic illustration of effect of inclusion on GB mobility.

in **Figure 11**. The blocking force is equal to the GB migration force for a given grain size d (Zener equation; see also Manohar, Ferry, & Chandra, 1998):

$$d_{\max} = \alpha 2r_i/f_i \tag{12}$$

where r_i is the inclusion particle radius and f_i is the volume fraction of inclusions. The Zener equation was first reported by Smith (1948) and since then has been modified based on analytical models and experimental evidence. Equation (12) demonstrates that grain growth will depend on the inclusion size, which must be lower than the desired grain size, and on inclusion content. If the inclusions are slightly soluble in the matrix then Ostwald ripening may occur leading to a decrease in number of small particles and growth of larger ones.

2.01.5 Mechanical Properties

Although ceramics are hard, wear-resistant materials that retain a reasonable degree of their mechanical properties even at high temperatures, they are very brittle and undergo very little plastic deformation under mechanical stress. Some background to this aspect of the behavior of ceramics is given in the following sections.

2.01.5.1 Strength and Fracture Resistance

Theoretical tensile strength of a material with elastic modulus, E, and interatomic spacing, r_o, is given by the following relationship developed by Orowan (1949):

$$\sigma_{th} = (E\gamma_o/r_o)^{1/2} \tag{13}$$

Therefore, high strength is associated with high thermodynamic surface energy, γ_o, high elastic modulus or stiffness, E, and small lattice spacing, r_o, all usually found in elements, or compounds from elements, in the first and second rows of the periodic table exhibiting predominantly covalent bonding (**Table 2**). Thus, the strongest ceramics are expected to be the oxides, carbides, nitrides, borides of silicon and aluminum and some other metals. Typical values of these parameters for ceramics are

- Thermodynamic surface energy, $\gamma_o = 1\ \mathrm{J\ m^{-2}}$
- Stiffness (elastic modulus), $E = 300$ GPa
- Lattice spacing, $r_o = 3 \times 10^{-10}$ m.

Therefore, theoretical strength, $\sigma_{th} \cong 30$ GPa, i.e. $E/10$. In practice, actual fracture strengths of ceramics are of the order of $E/1000$ although some fibers or whiskers may have strengths closer to $E/10$. The explanation for the large difference lies in the stress concentrating effects of cracks and flaws in brittle materials such as ceramics, first outlined by Griffith (1921):

$$\sigma_f = \left(2E\gamma_f/\pi c\right)^{1/2} \tag{14}$$

where γ_f is the fracture surface energy, E is the elastic modulus and c is the size of a "critical" crack or flaw to cause fracture of the material.

Consideration of the Griffith's relationship explains why a set of ceramic samples from the same batch will fail over a range of applied stresses because fracture strength will depend on the types and sizes of critical surface flaws and defects present on each component. Thus, it is necessary to test a large number of samples in order to obtain a reliable assessment of the behavior of the ceramic. The failures will usually follow a relationship based on a statistical distribution (Weibull, 1951) where probability of failure $P_f = 1 - P_s$, and P_s is the probability of survival given by

$$P_s = 1 - P_f = \exp[-\{(\sigma - \sigma_c)/\sigma_o\}^m (V/V_o)] \tag{15}$$

where σ is the applied stress to cause failure, σ_c is the critical value of stress below which the sample is not expected to fail, usually set as zero, m is the Weibull modulus, V is the volume under consideration, and σ_o and V_o are "normalizing" constants. The Weibull modulus defines the width of the probability distribution. If m is large (>10–20), the distribution is narrow showing a small spread of failure strengths and this would be classed as a "reliable" material, whereas if m is small (<10), the distribution is wide with a large variation in strengths and therefore this would be an "unreliable" material.

Taking logs of both sides of relationship (15) gives

$$\ln\left(1-P_{\rm f}\right) = -(V/V_{\rm o})\{(\sigma-\sigma_{\rm c})/\sigma_{\rm o}\}^{m} \tag{16}$$

Taking logs again gives

$$\ln\{-\ln\left(1-P_{\rm f}\right)\} = \ln(V/V_{\rm o}) + m\ln\{(\sigma-\sigma_{\rm c})/\sigma_{\rm o}\} \tag{17}$$

Thus, assuming that $\sigma_{\rm c} = 0$, plotting $\ln\{-\ln(1-P_{\rm f})\}$ versus $\ln \sigma$ should give a straight line with gradient m, the Weibull modulus. A more extensive overview of the brittle fracture and stochastic failure of ceramics from a probabilistic fracture mechanics approach is given by Danzer and Bermejo (2014) in this volume (see Chapter 2.09).

The fracture surface energy, $\gamma_{\rm f}$, and elastic modulus, E, are combined in the expression for the critical stress intensity factor $K_{\rm Ic}$, otherwise known as *fracture toughness*:

$$K_{\rm Ic} = \left(2E_{\gamma{\rm f}}\right)^{1/2} \tag{18}$$

As brittle materials, such as ceramics, have very little ductility, the values for $K_{\rm Ic}$ are generally low (2–10 MPa m$^{1/2}$). Most advanced ceramics have fracture toughness values <10 MPa m$^{1/2}$ (e.g. Fantozzi & Saâdaoui, 2013). The failure of ceramic materials is controlled on the one hand by processing defects (such as porosity, impurities, and microcracking) and on the other by the microstructure (Davidge, 1979), so there are two approaches which can be taken when selecting a material for structural applications:

1. Select a material that is so strong that the fracture strength is never reached in service.
2. Select a material with superior fracture toughness.

The first of these relies on reducing c, the size of the critical flaw in the Griffith equation, and requires a careful approach to processing, that is, what is termed "flaw-minimal fabrication". The second approach relies on increasing $\gamma_{\rm f}$ in the Griffith equation and is referred to as "microstructural engineering" (Becher, 1991).

The microstructure depends on the composition and crystal structure of the solid phases as well as the presence of pores, microcracks and impurity phases. Grain size, grain size distribution, and volume fraction of pores are all important parameters to be controlled. The aim of microstructural engineering is to achieve a microstructure that results in high hardness and fracture toughness. Toughening creates microstructures that impart sufficient fracture resistance that the strength becomes much less sensitive to flaw size so that small levels of processing and post-processing damage can be tolerated.

The fracture toughness in ceramics can be improved by various mechanisms (Becher, 1991), such as in situ toughening (growth of platelets or whiskers within the microstructure), transformation toughening (transformation of tetragonal zirconia grains into the lower density monoclinic phase at the crack tip, thus generating crack closure forces), crack deflection, crack bridging (filament or fiber toughening), or microcrack toughening.

2.01.5.2 Time Dependence of Strength

Many ceramic materials undergo a progressive weakening with time. Failure occurs under static loads lower than those that cause fracture during "normal" short-term tests. This phenomenon, which is known as *static fatigue*, suggests that the defect population is evolving with time with the occurrence of "subcritical" crack growth (SCCG) in which smaller flaws eventually grow to become "critical" [see Griffith's Eqn (14)]. This SCCG is a function of applied stress intensity $K_{\rm I}$ and environmental conditions. Oxides tend to be more susceptible than nonoxides as water molecules can attack the bonds at the crack tips causing a stress-corrosion effect leading to extension of the cracks. The relationship between crack velocity v and applied stress intensity factor $K_{\rm I}$ is given by (Davidge, 1979; Fett & Munz, 1985):

$$v = \alpha K_{\rm I}^{n} \tag{19}$$

It has been shown (Davidge, 1979) that the relationship between the applied stress σ and the expected time to failure $t_{\rm f}$ is

$$t_{\rm f}\sigma^{n} = \text{constant} \tag{20}$$

Data from these v–K tests can be combined with Weibull probability data to give strength–probability–time diagrams (Davidge, McLaren, & Tappin, 1974). The Weibull distribution as a function of time taking into account the effects of SCCG has also been derived (Danzer & Bermejo, 2013; Danzer, Lube, Supancic, & Damani, 2008; Fantozzi & Saâdaoui, 2013) which allows calculation of times to failure for design purposes.

By proof testing at a higher proof stress σ_p, it is possible to remove before service any individual samples from a batch that are not up to specification. To do this, it is necessary to determine the ideal proof test conditions. The proof test will have the effect of growing the cracks in the survivors so effectively weakening them. However, for a given ratio of proof stress to applied stress (σ_p/σ_a), the minimum time to failure t_{fmin} is proportional to σ_a^{-2}. Thus, a plot of log t_{fmin} versus log σ_a gives a straight line of slope −2. When failure probability data is superimposed on these data, it results in a proof test failure diagram from which, knowing the lifetime expected of components under a particular applied stress, the proof stress can be determined and the test carried out (Fuller & Wiederhorn, 1980).

2.01.5.3 Hardness

Hardness is, in effect, the resistance of a material to deformation, scratching or erosion but is defined as resistance to surface indentation or penetration by an applied mechanical load. Therefore, hardness is not necessarily a bulk property and is therefore not necessarily related to the strength, but relates to the ability of the material to withstand penetration of the surface through a combination of brittle fracture and plastic flow. The hardness of ceramics is measured using the Knoop and Vickers indentation methods that involve the application of a load via a geometrically defined indenter. Vickers uses a square pyramid diamond while in the Knoop technique, an elongated diamond pyramid is used.

Under known loading conditions, the size of the indentation is related to the hardness of the material so the hardness value quoted for any material is a function of the type of test conducted and the loading conditions. The general relation for hardness number H is given by (Smith & Sandland, 1922)

$$H = P/A \tag{21}$$

where P is the applied load and A is the representative area of the residual indent.

Generally, the lower the load applied, the higher the hardness values. Typically in a Vickers Hardness test, the notation HV10 or HV20 relates to the applied load in kg (in this case 10 or 20 kgf respectively). It is difficult to convert values from one hardness method to that of another so making comparison difficult. Other factors that need to be taken into account when interpreting hardness data for ceramic materials are the amount of porosity in the surface, the grain size and the effects of GB phases. This is particularly important where the size of the indent is small and the same order of magnitude as microstructural features. Variations in hardness values arise also depending on the particular laboratory and the observer, and errors of up to 15% are common. Some typical hardness values for ceramic materials are given in **Table 3**.

Whatever the shape of the indenter, the hardness number may increase or decrease with load; it may be independent of load or it may show a complex variation with load changes, depending on the material. This hardness–load dependence is known as the Indentation Size Effect.

Studies on the Vickers hardness of several brittle ceramics show hardness–load curves which exhibit a distinct transition to a plateau of constant hardness level. This involves a relationship between hardness (H), Young's modulus (E), and fracture toughness (K_{Ic}). Using these parameters, a brittleness index B used in designing with ceramics (Lawn & Marshall, 1979) was proposed that is derived from deformation and fracture energy ratios as follows:

$$B = HE/K_{\mathrm{Ic}}^2 \tag{22}$$

Table 3 Comparison of hardness values for "hard" ceramics

Ceramic	*Knoop hardness (GPa)*
Alumina Al_2O_3	15–18
Silicon nitride, Si_3N_4	20–22
Tungsten carbide, WC–Co	18–22
Titanium carbide, TiC	28
Silicon carbide, SiC	24–28
Boron carbide, B_4C	32

Besides toughness and hardness, there are several mechanical properties of ceramic materials which are relevant to their applications, including wear resistance, hot hardness, creep resistance, tribochemical stability, and thermal expansion coefficient. Wear behavior of ceramic materials is complex and is dependent upon many variables, of which hardness is an important variable but not the only significant one (De Portu & Guicciardi, 2013). For example, in many wear environments, such as the erosive wear behavior of oxide engineering ceramics, it is the ratio of fracture toughness to hardness (related to brittleness index) which is found to be significant in determining wear behavior. Chemical changes, especially corrosion and oxidation, also influence wear behavior, especially at high temperatures which may be operating at the surface of the materials under consideration.

2.01.6 Some Examples of Hard Ceramics

2.01.6.1 Silicon Nitride

A comprehensive review of Si_3N_4 ceramics is given by Riley (2000). A further review of processing of Si_3N_4 is given by Pasto (2014) in this volume (see Chapter 2.03). Silicon nitride is a term that is used to describe a family of materials based on Si_3N_4 but fabricated using different methods which give their names to the type of Si_3N_4 (Hampshire, 1993).

2.01.6.1.1 Reaction-Bonded Silicon Nitride

Si_3N_4 as a ceramic was first developed in the 1950s for use as thermocouple tubes, crucibles for molten metals and also rocket nozzles (Collins & Gerby, 1955). This type of material was formed by nitriding silicon powder compacts in the temperature range 1100–1450 °C and was later termed reaction-bonded silicon nitride (RBSN) (Parr, Martin, & May, 1960). One advantage is that little or no shrinkage occurs during the nitriding process. However, considerable internal rearrangement occurs as the Si_3N_4 grows within the pre-existing pores of the powder compact. Thus, the original dimensions of the silicon compact remain almost unchanged (linear shrinkage $<0.1\%$) during nitriding, allowing complex shapes to be machined to final size either before nitriding or after an initial nitridation to impart strength. Often, a prereaction annealing step under argon at 1100 °C is included, which results in slight neck formation between particles as a result of surface diffusion and strengthens the silicon compact for the machining process. On completion of the nitriding process, the close dimensional tolerances are maintained and the product requires very little subsequent machining. The reaction bonding process is thus suitable for economic mass production. A major obstacle to the use of RBSN for engineering applications is its limited mechanical strength (~200–250 MPa) as a result of the presence of 15–25% microporosity.

2.01.6.1.2 Dense Silicon Nitride

For an intrinsically high-strength, high-hardness material such as Si_3N_4, the high-energy covalent chemical bonds giving rise to these properties are a disadvantage in fabrication. Self-diffusivity in Si_3N_4 is quite low and species only become sufficiently mobile for sintering at temperatures where the decomposition of Si_3N_4 commences (>1850 °C). Thus, alternative approaches were developed by the use of densification additives to create the conditions for liquid-phase sintering either with or without applied pressure to assist the process. Magnesia was used as the densification additive in the first commercial development of hot-pressed silicon nitride (HPSN), and it is now known that this helped to form a sintering liquid at the hot-pressing temperature. The initial predominant α-Si_3N_4 powder was observed to transform to the β modification during the hot-pressing process and this was thought to be responsible for the development of high strengths (Coe, Lumby, & Pawson, 1972). The subsequent use of yttria as a densifying aid for HPSN (Gazza, 1975) also resulted in the formation of secondary phases at the Si_3N_4 GBs some of which resulted in degradation of high-temperature properties.

Currently, pressureless sintering of Si_3N_4 is carried out at 1750–1900 °C under a nitrogen atmosphere (0.1–10 MPa). Without pressure, dissociation of Si_3N_4 becomes a problem at high temperatures. During pressureless sintering at temperatures much above 1700 °C, Terwilliger and Lange (1975) showed that density starts to decrease at longer times as a result of increasing weight losses. The use of so-called *powder beds*, where the component to be sintered is surrounded by a mixture of powder of its own composition and inert boron nitride, has proved successful in reducing volatilization (Riley, 2000). This creates local gas equilibrium immediately adjacent to the Si_3N_4 compact, thus minimizing volatilization. An alternative is to increase the nitrogen pressure to higher levels (10 MPa) as in GPS. Densities of ~99% of the theoretical value are routinely achieved with bend strengths of up to 1000 MPa.

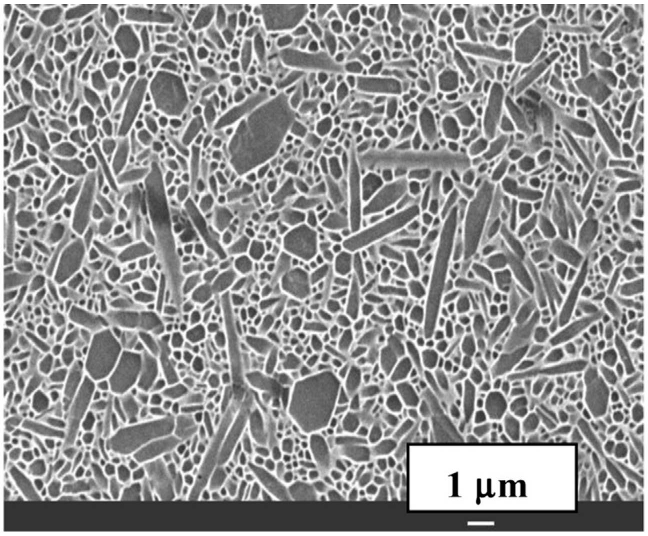

Figure 12 Scanning electron micrograph of silicon nitride (6 wt.% $Y_2O_3 + 2$ wt.% Al_2O_3) showing dark β-Si_3N_4 grains and bright YSiAlON glass.

The use of mixed oxide additives, such as alumina and yttria, or various rare earth oxides allows the development of specific microstructures by modifying the chemistry of the GB phase which has a significant effect on the grain size and aspect ratios of the β-Si_3N_4 grains. The microstructural development results from the fact that the additives (alumina and yttria) combine with the silica layer which is present on the surface of Si_3N_4 powder particles to provide a liquid phase to densify the ceramics by rearrangement of the α-Si_3N_4 particles followed by solution–diffusion–reprecipitation (Hampshire, 1994, 2009). The α-Si_3N_4 dissolves in the liquid and is precipitated as β-Si_3N_4 which grows in the longitudinal direction as prismatic hexagonal rod-like crystals that eventually impinge on each other forming an interlocked microstructure. The liquid cools as an intergranular phase, usually a glass, according to the following:

$$\alpha{-}Si_3N_4 + SiO_2 + M_xO_y \rightarrow \beta{-}Si_3N_4 + M{-}Si{-}O{-}N \text{ phase} \tag{23}$$

A typical scanning electron micrograph of Si_3N_4 sintered with 6 wt.% yttria and 2 wt.% alumina is shown in **Figure 12** in which can be seen high aspect ratio hexagonal rod-like β-Si_3N_4 grains surrounded by an intergranular oxynitride glass (Hampshire & Pomeroy, 2012).

A systematic study of pressureless sintering kinetics for Si_3N_4 ceramics (Hampshire & Jack, 1981) applied the Kingery liquid-phase sintering model in which three stages are identified, as shown schematically by the log shrinkage–log time plot of **Figure 13**. The stages are:

1. *Particle Rearrangement* following formation of the initial liquid phase, where the rate and the extent of shrinkage depend on both the volume and viscosity of the liquid; this is also the incubation period for the α → β transformation;
2. *Solution-diffusion-reprecipitation*, where, according to Kingery, shrinkage is given by:

$$\Delta V/V_0 \; \alpha \; t^{1/n} \tag{24}$$

where t is time and $n = 3$ if solution into or precipitation from the liquid is rate controlling, as was found in the case of MgO as additive, and $n = 5$ if diffusion through the liquid is rate-controlling, as was found for the Y_2O_3 additive, where diffusion through a more viscous oxynitride liquid is much slower and densification without pressure proves difficult; the α → β transformation begins in this stage and is more rapid for Y_2O_3;

3. *Coalescence* or final elimination of closed porosity during which the liquid acts to further grow the elongated β grains but this critically depends on GB glass chemistry; final density is greater than 95% of the theoretical value and normally >99%.

The types and amounts of additives used for sintering determine the nature and quantity of the resulting GB phase. The term “GB engineering” was coined (Gazza, 1975) and this aimed to understand the structure of the GBs in Si_3N_4 based materials and the reactions occurring at them during sintering in order to achieve significant

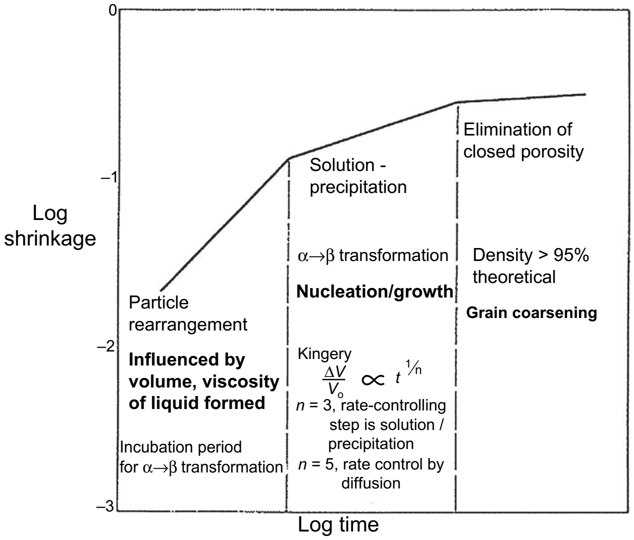

Figure 13 Schematic log shrinkage–log time plot showing three stages of liquid phase sintering of silicon nitride ceramics according to model of Kingery (1959).

advances in materials properties. Clarke and Thomas (1977) subsequently found that the amorphous phase extended and formed thin films between most grains. A typical transmission electron micrograph of a glass triple point and the thin intergranular oxynitride film between Si_3N_4 grains is shown in **Figure 14** (Hampshire & Pomeroy, 2012). The thickness of the IGF is very sensitive to the type of oxide additive used and its concentration and film thickness (in the range 0.5–1.5 nm) depends strongly on chemical composition but not on the amount of glass present (Wang, Pan, Hoffmann, Cannon, & Rühle, 1996).

It has been shown that nitrogen increases Tg, viscosities, elastic moduli and microhardness of oxynitride glasses (Becher et al., 2011; Hampshire, 2008). These property changes can be compared with known effects of GB glass chemistry in Si_3N_4 ceramics where significant improvements in fracture resistance of Si_3N_4 can be achieved by tailoring the intergranular glass chemistry (Becher et al., 2010; Hampshire & Pomeroy, 2012). The impact of various rare-earth and related additive elements (RE = Lu, Sc, Yb, Y, Sm, La) on grain growth anisotropy and mechanical properties of Si_3N_4 ceramics has been studied (Becher et al., 2006). In this case, an RE-Si-Mg-O-N glass matrix is formed and with increasing ionic radius of the RE, grain anisotropy increases and ceramics with equivalent grain sizes and morphologies exhibit increasing toughness with increasing ion size of the RE^{3+}, reflecting an increasingly intergranular crack mode. A first-principles model, the differential binding energy (DBE), was developed to characterize the competition between RE and Si as they migrate to the β-Si_3N_4 grain surfaces. The theory predicts that La should have the strongest and Lu the weakest preferential segregation to the grain surfaces and this was confirmed by unique atomic-resolution images obtained by aberration-corrected Z-contrast scanning transmission electron microscopy (STEM) (Shibata et al., 2004).

The viscosity of these glassy phases decreases with increasing temperature, which can lead to GB sliding and cavitation when the ceramic is subjected to stress at elevated temperatures and thus these oxynitride glassy

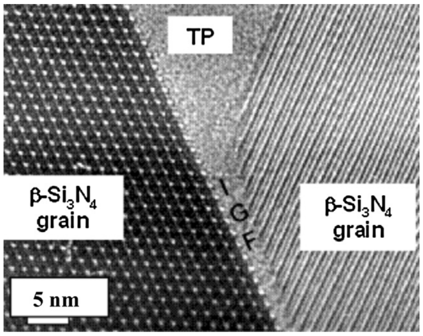

Figure 14 TEM micrograph of silicon nitride showing two β-Si_3N_4 grains, a triple point (TP) glass pocket and intergranular glass film (IGF).

phases control many high-temperature properties such as creep (Wiederhorn, Krause, Lofaj, & Täffner, 2005) and high-temperature strength as well as oxidation resistance.

One significant milestone in improvements of properties through reductions in GB phases was the discovery of the "SiAlONs" (Jack, 1975).

2.01.6.1.3 SiAlONs

SiAlONs are solid solutions based on the Si_3N_4 structure. β′-SiAlON is formed when oxygen replaces nitrogen in the β-Si_6N_8 structure while, at the same time, silicon is replaced by aluminum to maintain charge neutrality (Oyama & Kamigaito, 1971; Jack & Wilson, 1972). The solid solution composition is:

$$Si_{6-z}Al_zO_zN_{8-z}$$

retaining the 6:8 metal:non-metal ratio of β-Si_6N_8, with z values in the range 0–4.2. The single-phase β′-sialon still requires a sintering additive such as Y_2O_3 in order to densify the ceramic (Ekstrøm & Nygren, 1992). Microstructures are similar to β-Si_3N_4 with elongated hexagonal grains of β′-sialon but a reduced amount of intergranular glass phase.

α-sialons (α′) are based on the α-$Si_{12}N_{16}$ unit cell with general composition (Hampshire et al., 1978):

$$M_xSi_{12-(m+n)}Al_{(m+n)}O_nN_{(16-n)}$$

In α′-SiAlON, partial replacement of Si^{4+} by Al^{3+} occurs if, at the same time, charge compensation is effected by the accommodation of other ions, $M = Li^+$, Ca^{2+}, Y^{3+} or other rare earth lanthanide ions (Ln^{3+}), in the two interstitial sites (x) in the unit cell. x (<2) is determined by the valence (v) of the M^{v+} ion. The structural principle is similar to that in the formation of the "stuffed" quartz derivatives in which $A1^{3+}$ replaces Si^{4+} and valency charge balance is maintained by "stuffing" Li^+ or Mg^{2+} into the interstitial sites. As with β′, Y_2O_3 is used as a densification aid but also provides Y^{3+} ions for stabilization of α′. Other oxides are also used for sintering (Mandal, 1999).

Unlike Si_3N_4, where β-Si_3N_4 is the main stable phase after sintering, the two SiAlON phases, α′ and β′ can coexist depending on the sintering additives used. Therefore, there are more variables to be used as design parameters for SiAlON ceramics and the amount of α′-SiAlON can be varied from 0 to 100% continuously and the type and amount of intergranular phase can also be modified by using mixed additives (Mandal, Oberacker, Hoffmann, & Thompson, 2000). These are usually combinations of CaO and two rare earth lanthanide oxides which allow more easier densification but on subsequent heat treatment, the final properties of the SiAlON ceramics can be tailored so that when high hardness is needed, α′-SiAlON content is increased and when higher toughness is required, then additive chemistry is changed to give predominantly β′-SiAlON. These ceramics are already available as cutting tools or refractories and are being developed as wear parts.

2.01.6.2 Silicon Carbide

Silicon carbide has excellent high-temperature strength, good oxidation and thermal shock resistance, high hardness, and low specific weight. Because of its strong covalent bonding character, however, SiC proved difficult to densify without sintering additives and external pressure. In order to obtain dense SiC ceramics by conventional sintering techniques, different sintering additives were investigated. Prochazka (1975) found that β-SiC powders could be sintered to high densities at very high temperatures of ~2100 °C by using additions of both boron and carbon (see also Cao et al., 1996). Coppola, Hawler, and McMurtry (1978) demonstrated that α-SiC powders are sinterable under similar conditions. Several authors (Lee & Kim, 1994; She & Ueno, 1999) have shown that both α- and β-SiC powders can be densified at lower temperatures of 1850–2000 °C with the addition of Al_2O_3 and Y_2O_3 which involves liquid-phase-sintering. Omori and Takei (1982) showed that oxide additives, including a wide variety of rare-earth oxides, usually in combination with alumina and/or boron compounds, promote densification of SiC via liquid phase sintering. Sigl and Kleebe (1993) used an yttrium–aluminium garnet (YAG: $3Y_2O_3.5Al_2O_3$) powder as the densification additive and showed that Ostwald ripening by solution and re-precipitation controls the sintering mechanism. Lee and Kim (1994) densified SiC ceramics by pressureless sintering of both α- and β-SiC powders using Y_2O_3 and Al_2O_3 additives. With α-SiC, the microstructure consisted of equiaxed SiC grains, whereas with β-SiC, a plate-like grain structure resulted from the grain growth associated with the β → α-SiC phase transformation during sintering. As grain size increased for the sintered SiC from α-SiC powder, fracture toughness increased slightly whereas for the sintered SiC from β-SiC powder, fracture toughness increased significantly which was attributed to crack bridging and crack deflection by the plate-like β-SiC grains. A detailed review on processing of silicon carbides is given in a companion paper of this book by Kriegesmann (2013).

2.01.6.3 Borides

Transition metal borides are widely recognized as an attractive class of materials for a broad range of mechanical applications in abrasive, erosive, corrosive and high-temperature environments, owing to their high melting points and hardness, thermodynamic stability and excellent electrical conductivity. Most studies (Anisimov, Iavnovskii, Gubanov, & Kurmaev, 1986) have focused on the borides of Ti, Zr and Hf for application as cutting tools, for molten metals processing or as sharp components of new generation space vehicles in ultrahigh-temperature environments. The densification of ZrB_2 powder is achieved using hot-pressing and generally requires very high temperatures, 2100 °C or above and moderate pressure (20–30 MPa), because of the covalent character of the bonding and its low volume and GB diffusion rates. Sciti, Silvestroni, Medri, and Guicciardi (2011) studied pressureless sintering as an in situ toughening method for ZrB_2–SiC composite ceramics with addition of Si_3N_4 or $MoSi_2$ at temperatures of 2100–2150 °C that induced SiC anisotropic growth from particles to platelets, within a ZrB_2 matrix, which consisted of more equiaxed rounded grains. The method has promise in terms of producing near-net shaped or large-sized components using atmospheric process sintering with the possibility of increasing the volume of the reinforcing phase.

2.01.7 Summary

Ceramics used as hard materials that are typically oxides or nonoxides (nitrides, carbides, borides, etc.) and their composites that have engineered microstructure to obtain unique properties. Although ceramics are brittle and weak in tension, they are wear resistant and can withstand high temperatures and have good resistance to chemical corrosion. These properties are, as with other materials, highly dependent on their structure, both at the atomic level (crystal structure) and on the micro- and macro-structural levels.

Hard ceramics are produced from synthetic particulate materials which are formed into a shape. To obtain these desirable microstructures techniques that allow near net shaping, consolidated by a high-temperature sintering process to reduce porosity, densify and strengthen the material are used. However, ceramics are brittle materials with low fracture resistance, due to the stress concentrating effects of surface cracks and flaws. Fracture strength depends on the types and sizes of "critical" defects present on each component and follows a relationship based on the Weibull statistical distribution. Ceramics undergo a progressive weakening with time due to SCCG in which smaller flaws eventually grow to become "critical". Special processes have been developed for hard ceramics in order to optimize the microstructures and, hence, the mechanical properties.

References

Agarwala, M. K., Bandyopadhyay, A., van Weeren, R., Safari, A., & Danforth, S. C. (1996). FDC, rapid fabrication of structural components (fused deposition of ceramics). *American Ceramic Society Bulletin, 75*(11), 60–65.

Anisimov, V. I., Iavnovskii, A. L., Gubanov, V. A., & Kurmaev, E. Z. (1986). Electronic structure of the cubic monoborides of Ti, Zr and Hf and some ternary boron-containing compounds. *Journal of Structural Chemistry, 27*(1), 1–6.

Barsoum, M. W. (2002). *Fundamentals of ceramics*. Oxford: Taylor and Francis.

Becher, P. F. (1991). Microstructural design of toughened ceramics. *Journal of the American Ceramic Society, 74*(2), 255–269.

Becher, P. F., Hampshire, S., Pomeroy, M. J., Hoffmann, M. J., Lance, M., & Satet, R. (2011). An overview of the structure and properties of silicon-based oxynitride glasses. *International Journal of Applied Glass Science, 2*(1), 63–83.

Becher, P. F., Painter, G. S., Shibata, N., Satet, R. L., Hoffmann, M. J., & Pennycook, S. J. (2006). Influence of additives on anisotropic grain growth in silicon nitride ceramics. *Materials Science and Engineering A, 422*, 85–91.

Becher, P. F., Shibata, N., Painter, G. S., Averill, F., van Benthem, K., Lin, H.-T., et al. (2010). Observations on the influence of secondary Me oxide additives (Me = Si, Al, Mg) on the microstructural evolution and mechanical behavior of silicon nitride ceramics containing RE_2O_3 (RE = La, Gd, Lu). *Journal of the American Ceramic Society, 93*(2), 570–580.

Binner, J., & Vaidhyanathan, B. (2008). Processing of bulk nanostructured ceramics. *Journal of the European Ceramic Society, 28*(7), 1329–1339.

Brook, R. J. (1969). Pore-grain boundary interactions and grain growth. *Journal of the American Ceramic Society, 52*, 56–57.

Cambier, F. (2011). Ceramics: black magic or exact science. *Stuijts Award plenary lecture, 12th European Ceramic Society conference (ECerS XII), Stockholm, June.*

Cao, J. J., MoberlyChan, W. J., De Jonghe, L. C., Gilbert, C. J., & Ritchie, R. O. (1996). In situ toughened silicon carbide with Al-B-C additions. *Journal of the American Ceramic Society, 79*(2), 461–469.

Ching, W. Y., Xu, Y.-N., Rulis, P., & Ouyang, L. (2006). The electronic structure and spectroscopic properties of 3C, 2H, 4H, 6H, 15R and 21R polymorphs of SiC. *Materials Science and Engineering A, 422*, 147–156.

Clarke, D. R., & Thomas, G. (1977). Grain boundary phases in a hot-pressed MgO fluxed silicon nitride. *Journal of the American Ceramic Society, 60*(11–12), 491–495.

Coble, R. L. (1958). Initial sintering of alumina and hematite. *Journal of the American Ceramic Society, 41*, 55–62.

Coble, R. L. (1961). Sintering of crystalline solids. I. Intermediate and final state diffusion models. *Journal of Applied Physics, 32*(5), 787–792.

Coe, R. F., Lumby, R. J., & Pawson, M. F. (1972). Some properties and applications of hot-pressed silicon nitride. In P. Popper (Ed.), *Special ceramics 5* (pp. 361–376). Stoke-on-Trent: British Ceramic Research Association.

Collins, J. F., & Gerby, R. W. (1955). New refractory uses for silicon nitride reported. *Journal of Metals, 7*, 612–615.

Coppola, J. A., Hawler, H. A., & McMurtry, C. H. (1978). US Patent 4 123 286.

Danzer, R., & Bermejo, R. (2014). Mechanical characterisation of ceramics: Designing with brittle materials. In V. K. Sarin, Luis Llanes & Daniele Mari (Eds.), *Comprehensive Hard Materials, Volume 2: Ceramics*. Oxford, UK: Elsevier Ltd.

Danzer, R., Lube, T., Supancic, P., & Damani, R. (2008). Fracture of advanced ceramics. *Advanced Engineering Materials, 10*, 275–298.

Davidge, R. W. (1979). *Mechanical characterisation of ceramics*. Cambridge: Cambridge University Press.

Davidge, R. W., McLaren, J. R., & Tappin, G. (1974). Strength-probability-time relationships (SPT) in ceramics. *Journal of Materials Science, 8*, 1699–1705.

De Portu, G., & Guicciardi, S. (2014). Wear of hard ceramics. In V. K. Sarin, Luis Llanes & Daniele Mari (Eds.), *Comprehensive Hard Materials, Volume 2: Ceramics*. Oxford, UK: Elsevier Ltd.

Derby, B. (2011). Inkjet printing ceramics: from drops to solid. *Journal of the European Ceramic Society, 31*(14), 2534–2550.

Di Rupo, E., Anseau, M. R., & Brook, R. J. (1979). Reaction sintering: correlation between densification and reaction. *Journal of Materials Science, 14*, 2924–2928.

Dillon, S. J., Tang, M., Carter, W. C., & Harmer, M. P. (2007). Complexion: a new concept for kinetic engineering in materials science. *Acta Materialia, 55*, 6208–6218.

Ekstrøm, T., & Nygren, M. (1992). SiAlON ceramics. *Journal of the American Ceramic Society, 75*(2), 259–276.

Fantozzi, G., & Saâdaoui, M. (2014). Toughness, fatigue and thermal shock of ceramics: Microstructural effects. In V. K. Sarin, Luis Llanes & Daniele Mari (Eds.), *Comprehensive Hard Materials, Volume 2: Ceramics*. Oxford, UK: Elsevier Ltd.

Fett, T., & Munz, D. (1985). Determination of v-K curves by a modified evaluation of lifetime measurements in static bending tests. *Journal of the American Ceramic Society, 68*, C213–C215.

Fisher, G. R., & Barnes, P. (1990). Toward a unified view of polytypism in silicon carbide. *Philosophical Magazine, 61*(2), 217–236.

Fuller, E. R., Jr., & Wiederhorn, S. M. (1980). Proof testing of ceramics: part I experimental. *Journal of Materials Science, 15*, 2275–2281 (See also: Fuller Jr., E. R., Wiederhorn, S. M., Ritter Jr., J. E., & Oates, P. B. (1980). Proof testing of ceramics: part 2 theory. *Journal of Materials Science*, 15, 2282–2295).

Gazza, G. E. (1975). Effect of yttria additions on hot-pressed Si_3N_4. *American Ceramic Society Bulletin, 54*, 778–781.

German, R. M. (1996). *Sintering theory and practice*. Weinheim: Wiley-VCH Verlag.

Gessinger, G. H., Fischmeister, H. F., & Lukas, H. L. (1973). A model for second-stage liquid-phase sintering with a partially wetting liquid. *Acta Metallurgia, 21*, 715–724.

Ghosh, D., Subhash, G., Radhakrishnan, R., & Sudarshan, T. S. (2008). Scratch-induced microplasticity and microcracking in zirconium diboride–silicon carbide composite. *Acta Materialia, 56*, 3011–3022.

Graule, T. J., Baader, F. H., & Gauckler, L. J. (1994). Shaping of ceramic green compacts direct from suspensions by enzyme catalyzed reactions. *Ceramic Forum International, 71*(6), 317–323.

Griffith, A. A. (1921). The phenomena of rupture and flow in solids. *Philosophical Transactions of the Royal Society of London, Series A, 221*, 163–198.

Griffith, M. L., & Halloran, J. W. (1996). Freeform fabrication of ceramics via stereolithography. *Journal of the American Ceramic Society, 79*(10), 2601–2608.

Halloran, J. W. (1999). Freeform fabrication of ceramics. *British Ceramic Proceedings, 59*, 17–28.

Hampshire, S. (1993). Nitride ceramics. In M.Swain (Series Ed.) & R. W. Cahn, P. Haasen, & E. J. Kramer (Vol. Eds.), *Structure and properties of ceramics: Vol. 11. Materials science and technology – a comprehensive treatment* (pp. 121–171). Weinheim: VCH Verlagsgesellschaft.

Hampshire, S. (1994). The role of additives in the pressureless sintering of nitrogen ceramics for engine applications. *Metals Forum, 7*(3), 162–170.

Hampshire, S. (2008). Oxynitride glasses. *Journal of the European Ceramic Society, 28*, 1475–1483.

Hampshire, S. (2009). Silicon nitride ceramics. In B. Ralph, & P. Xiao (Eds.), *Materials science forum: Vol. 606. Advances in ceramic materials* (pp. 27–41). Zurich: Trans Tech Publications.

Hampshire, S., & Jack, K. H. (1981). The kinetics of densification and phase transformation in nitrogen ceramics. *Proceedings of the British Ceramic Society, 31*, 37–49.

Hampshire, S., Park, H. K., Thompson, D. P., & Jack, K. H. (1978). α'-sialon ceramics. *Nature, 274*, 880–882.

Hampshire, S., & Pomeroy, M. J. (2012). Grain boundary glasses in silicon nitride: a review of chemistry, properties and crystallisation. *Journal of the European Ceramic Society, 32*, 1925–1932.

Hardie, D., & Jack, K. H. (1957). Crystal structures of silicon nitride. *Nature, 180*, 332–333.

Harmer, M. P. (2008). Demystifying the role of sintering additives with “complexion”. *Journal of the European Ceramic Society, 28*, 1485–1493.

Harmer, M. P., & Brook, R. J. (1981). Fast firing – microstructural benefits. *Transactions & Journal of the British Ceramic Society, 80*, 147–149.

Heinrich, J. G. (2004). *Introduction to the principles of ceramic forming*. Baden-Baden: Göller Verlag (CD-ROM).

Herring, C. (1951). Surface tension as a motivation for sintering. In W. E. Kington (Ed.), *The physics of powder metallurgy* (pp. 143–179). New York: McGraw-Hill.

Ishizawa, N., Miyata, T., Minato, I., Marumo, F., & Iwai, S. (1980). A structural investigation of α-Al_2O_3 at 2170 K. *Acta Crystallographica, B36*, 228–230.

Jack, K. H. (1975). Review: SiAlONs and related nitrogen ceramics. *Journal of Materials Science, 11*, 1135–1158.

Jack, K. H., & Wilson, W. I. (1972). Ceramics based on the Si-Al-O-N and related systems. *Nature Physical Sciences, 238*(80), 28–29.

Jackson, B., Ford, W. F., & White, J. (1963). The influence of Cr_2O_3 and Fe_2O_3 on the wetting of periclase grains by liquid silicate. *Transactions & Journal of the British Ceramic Society, 62*, 577–601.

Kang, S.-J. L. (2005). *Sintering, densification, grain growth and microstructure*. Oxford: Elsevier Butterworth-Heinemann.

Kang, S.-J. L. (2012). Sintering (Chapter 6). In R. Riedel, & I.-W. Chen (Eds.), *Synthesis and processing: Vol. 3. Ceramics science and technology* (pp. 143–169). Weinheim: Wiley-VCH Verlag GmbH & Co. KGaA.

Kang, S.-J. L., Kim, K.-H., & Yoon, D. N. (1991). Densification and shrinkage during liquid phase sintering. *Journal of the American Ceramic Society, 74*, 425–427.

Kingery, W. D. (1958). In W. D. Kingery (Ed.), *Ceramic fabrication processes* (pp. 131–143). Cambridge, MA: MIT Press (New York: J. Wiley & Sons).

Kingery, W. D. (1959). Sintering in the presence of a liquid phase. *Journal of Applied Physics, 30*, 301–306.

Kingery, W. D., Niki, E., & Narashiman, M. D. (1961). Sintering of oxide and carbide-metal compositions in presence of a liquid phase. *Journal of the American Ceramic Society, 44*, 29–35.

Kingery, W. D., Woulbroun, J. M., & Charvat, F. R. (1963). Effects of applied pressure on densification during sintering in the presence of a liquid phase. *Journal of the American Ceramic Society, 46*, 391–395.

Kosmac, T., Novak, S., & Sajko, M. (1997). Hydrolysis-assisted solidification (HAS): a new setting concept for ceramic net-shaping. *Journal of the European Ceramic Society, 17*, 427–432.

Kriegesmann, J. (2014). Processing of silicon carbide based ceramics. In V. K. Sarin, Luis Llanes & Daniele Mari (Eds.), *Comprehensive Hard Materials, Volume 2: Ceramics*. Oxford, UK: Elsevier Ltd.

Kuczynski, G. C. (1949). Self-diffusion in sintering of metallic particles. *Journal of Metals, 1*, 169–178.

Lawn, B. R., & Marshall, D. B. (1979). Hardness, toughness, and brittleness: an indentation analysis. *Journal of the American Ceramic Society, 62*, 347–350.

Lee, B.-K., Chung, S.-Y., & Kang, S.-J. L. (2000). Grain boundary faceting and abnormal grain growth in Ba Ti O_3. *Acta Materialia, 48*, 1575–1580.

Lee, M.-H., Cheng, C.-F., Heine, V., & Klinowski, J. (1997). Distribution of tetrahedral and octahedral A1 sites in gamma alumina. *Chemical Physics Letters, 265*, 673–676.

Lee, S. K., & Kim, C. H. (1994). Effects of α-SiC vs. β-SiC starting powders on microstructure and fracture toughness of SiC sintered with Al_2O_3-Y_2O_3 additives. *Journal of the American Ceramic Society, 77*, 1655–1658.

Lenel, F. V. (1948). Sintering in the presence of a liquid phase. *Transactions of the American Institute of Mining Engineers, 175*, 878–896.

Lewis, J. A. (2000). Colloidal processing of ceramics. *Journal of the American Ceramic Society, 83*(10), 2341–2359.

Mandal, H. (1999). New developments in α-SiAlON ceramics. *Journal of the European Ceramic Society, 19*, 2349–2357.

Mandal, H., Oberacker, R., Hoffmann, M. J., & Thompson, D. P. (2000). α-SiAlON ceramics densified with mixed oxide sintering additives. *Materials Science Forum, 325–326*, 207–212.

Manohar, P. A., Ferry, M., & Chandra, T. (1998). Five decades of the Zener equation. *ISIJ International, 38*(9), 913–924.

Mortensen, A. (1997). Kinetics of densification by solution-precipitation. *Acta Materialia, 45*, 749–758.

Nygren, M., & Shen, Z. (2003). On the preparation of bio-, nano- and structural ceramics and composites by spark plasma sintering. *Solid State Sciences, 5*, 125–131.

Omatete, O. O., Janney, M. A., & Strehlow, R. A. (1991). Gelcasting – a new ceramic forming process. *American Ceramic Society Bulletin, 70*(10), 1641–1649.

Omori, M., & Takei, H. (1982). Pressureless sintering of SiC. *Journal of the American Ceramic Society, 65*(6), C92.

Orowan, E. (1949). Fracture and strength of solids. *Reports of Progress in Physics, 12*, 185–232.

Ostwald, W. (1900). Über die vermeintliche isomerie des roten und gelben quecksilberoxyds und die oberflächenspannung fester körper. *Zeitschrift fur Physikalische Chemie, 34*, 495–503.

Oyama, Y., & Kamigaito, O. (1971). Solid solubility of some oxides in Si_3N_4. *Japanese Journal of Applied Physics, 10*, 1637–1642.

Palmour, H., III, & Johnson, D. R. (1967). *Sintering and related phenomena*. New York: Gordon & Breach Publishers.

Pandey, D., & Krishna, P. (1975). Influence of stacking faults on the growth of polytype structures, II. Silicon carbide polytypes. *Philosophical Magazine, 31*(5), 1133–1148.

Parr, N. L., Martin, G. F., & May, E. R. W. (1960). Preparation, microstructure and mechanical properties of silicon nitride. In P. Popper (Ed.), *Special ceramics 1* (pp. 102–135). London: Heywood.

Pasto, A. (2014). Synthesis and processing of silicon nitride ceramics. In V. K. Sarin, Luis Llanes & Daniele Mari (Eds.), *Comprehensive Hard Materials, Volume 2: Ceramics*. Oxford, UK: Elsevier Ltd.

Pauling, L. (1948). *The nature of the chemical bond*. Ithaca, NY: Cornell University Press.

Price, G. H. S., Smithells, C. J., & Williams, S. V. (1938). Sintered alloys. Part I – copper-nickel-tungsten alloys sintered with a liquid phase present. *Journal of the Institute of Metals, 6*, 239–264.

Prochazka, S. (1975). Sintering of silicon carbide. In J. J. Burke, A. E. Gorum, & R. M. Katz (Eds.), *Ceramics for high performance applications* (pp. 7–13). Chestnut Hill, OH: Brook Hill Publishing Co.

Rahaman, M. N. (2003). *Ceramic processing and sintering* (2nd ed.). Boca Raton, FL: CRC Press – Taylor and Francis.

Ramsdell, L. S. (1947). Studies on silicon carbide. *American Mineralogist, 32*, 64–82.

Riley, F. L. (2000). Silicon nitride and related materials. *Journal of the American Ceramic Society, 83*, 245–265.

Sciti, D., Silvestroni, L., Medri, V., & Guicciardi, S. (2011). Pressureless sintered in situ toughened ZrB_2–SiC platelets ceramics. *Journal of the European Ceramic Society, 31*, 2145–2153.

She, J. H., & Ueno, K. (1999). Effect of additive content on liquid-phase sintering of silicon carbide ceramics. *Materials Research Bulletin, 34*(10/11), 1629–1636.

Shibata, N., Pennycook, S. J., Gosnell, T. R., Painter, G. S., Shelton, W. A., & Becher, P. F. (2004). Observation of rare earth segregation in silicon nitride ceramics at sub-nanometer dimensions. *Nature, 428*, 730–733.

Sigl, L. S., & Kleebe, H.-J. (1993). Core/rim structure of liquid-phase-sintered silicon carbide. *Journal of the American Ceramic Society, 76*, 773–776.

Smith, C. S. (1948). Grains, phases and interfaces – an interpretation of microstructure. *Transactions of the American Institute of Mining Engineers, 175*, 15–51.

Smith, R. L., & Sandland, G. E. (1922). An accurate method of determining the hardness of metals, with particular reference to those of a high degree of hardness. *Proceedings of the Institution of Mechanical Engineers, 1*, 623–641.

Svoboda, J., Riedel, H., & Gaebel, R. (1996). A model for liquid phase sintering. *Acta Materialia, 44*, 3215–3226.

Terwilliger, G. R., & Lange, F. F. (1975). Pressureless sintering of silicon nitride. *Journal of Materials Science, 10*, 1169–1174.

Wang, C. M., Pan, W. Q., Hoffmann, M. J., Cannon, R. M., & Rühle, M. (1996). Grain boundary films in rare-earth-glass-based silicon nitride. *Journal of the American Ceramic Society, 79*(3), 788–792.

Weibull, W. (1951). A statistical distribution function of wide applicability. *Journal of Applied Mechanics, 18*, 293–298.

White, J. (1970). Magnesia based refractories (Chapter 2). In A. M. Alper (Ed.), *High temperature oxides Part I: Magnesia, lime and chrome refractories*. New York & London: Academic Press.

Wiederhorn, S. M., Krause, R. F., Jr., Lofaj, F., & Täffner, U. (2005). Creep behavior of improved high temperature silicon nitride. *Key Engineering Materials, 287*, 381–392.

Yakel, H. L. (1975). The crystal structure of a boron-rich boron carbide. *Acta Crystallographica, B31*, 1797–1806.

Zerr, A., Miehe, G., Serghiou, G., Schwarz, M., Kroke, E., Riedel, R., et al. (1999). Synthesis of cubic silicon nitride. *Nature, 400*, 340–342.

SECTION II

SYNTHESIS AND PROCESSING

2.02 Processing of Alumina and Corresponding Composites

2.03 Synthesis/Processing of Silicon Nitride Ceramics

2.04 Processing of Silicon Carbide-Based Ceramics

2.05 Spark Plasma Sintering of Nanoceramic Composites

2.06 Advanced Manufacturing of Hard Ceramics

2.07 Joining Methods for Hard Ceramics

This page intentionally left blank

2.02 Processing of Alumina and Corresponding Composites

Carmen Baudín, Instituto de Cerámica y Vidrio, CSIC, Madrid, Spain

© 2014 Elsevier Ltd. All rights reserved.

Glossary

Alumina materials Family of ceramics whose principal constituent is aluminium oxide (Al_2O_3), known as alumina in the ceramic sector.

http://dx.doi.org/10.1016/B978-0-08-096527-7.00021-0

2.02.1 Introduction

Alumina materials are a family of ceramics whose principal constituent is aluminium oxide (Al_2O_3), known as alumina in the ceramic sector. On a weight basis, these materials have the largest share of the ceramics' world market.

Alumina is the ceramic material most extensively studied, both from a theoretical and practical stand points. There exist several reviews about alumina materials—properties, production, and uses (Briggs, 2007; Doremus, 2008; Dörre & Hübner, 1984; Gitzen, 1970; Hart, 1990; Kingery, 1984; McColm, 1990; Riley, 2009)—on which this chapter relies to summarize the basic aspects of traditional alumina materials. This chapter tries to add to the previous publications by dealing with new developments and trends that were just proposed as possibilities in some of these reviews.

In Table 1, the main commercial applications of alumina materials and the properties required for the envisaged application are summarized.

As a single crystal (sapphire), alumina is prized as gemstone (sapphire or ruby, depending on the impurities) and for special applications such as watch bearings. Moreover, some high-grade glass substitutes are made of single-crystal alumina (artificial sapphire). The first commercial application as ceramic material is described in a German patent from 1907 (Riley, 2009). In coarse, polycrystalline form, alumina is the major constituent of high-grade shaped and unshaped refractory materials. Porous sintered aluminas are used as catalyst supports for chemical processes. In the form of powder and grids, alumina is used as a grinding and abrasive media. In the form of whiskers and fibers, alumina is used for low–thermal mass furnace insulation and metal reinforcement. Last but not the least, a wide range of wear-resistant and electrically insulating components are constituted by alumina-based materials with micrometer grain size.

Structural applications of alumina at room temperature are based on the combination of hardness, wear resistance, and corrosion resistance that alumina ceramics provide. Room temperature applications include wear parts in medical engineering (total prostheses for hip joints), in process plants (pump components and valve faces, lining of pipework), and in mechanical engineering (bearings and valves). Alumina pieces of different shapes and sizes are currently used as textile guides. The main disadvantage of alumina in room temperature applications is its brittleness that leads to a lack of reliability of the pieces in use. In fact, even though fine-grained and dense aluminas with high strength are available, they still present relatively low Weibull modulus; thus, a number of monolithic and layered alumina-based composites have been developed and are still under development, seeking reliability.

Alumina also presents high refractoriness, that is, high melting point (2050 °C; McColm, 1990) and retention of structural integrity at a high temperature. In particular, it experiences practically no deformation

Table 1 Commercial applications of alumina materials and the related properties

	Applications	*Primary property*	*Other properties*
Single crystal	Gemstones	Aesthetics	Mechanical stability at room temperature
	Glass substitutes	Translucency/transparency	Hardness and stiffness up to 1000 °C
	Special applications (e.g., watch bearings)	Hardness and stiffness	
Grains	Abrasives	Hardness	
	Aggregates for unshaped refractories	Chemical inertness at high temperatures	Hardness and stiffness at high temperature
Shaped: polycrystalline	Shaped refractories		
	Medical engineering (e.g., total prostheses for hip joints)	Biocompatibility	Wear resistance at room temperature
	Mechanical engineering (e.g., bearings and valves)	Wear resistance at room temperature	Chemical inertness at room temperature
	Process plants (e.g., pump components and valve faces, lining of pipework)		
	Cutting tools	Wear resistance up to 1200 °C	Hardness and stiffness at high temperature chemical inertness

under compressive loads at temperatures up to 1200 °C, above which sapphire can deform by dislocation motion (Kronenberg, 1957; Lagerlof, Heuer, Castaing, Rivière, & Mitchell, 1994; Scott & Orr, 1983; Snow & Heuer, 1973). Only under extremely high hydrostatic stresses, which prevent crack propagation, plasticity may be extended at low temperatures such as 200 °C; deformation is further enhanced in hydrogen atmosphere (Korinek & Castaing, 2003). Due to its high refractoriness, one of the most successful applications of alumina is in cutting tools for high-speed machining of metals. Applications of alumina bodies as components for engines are limited by its low thermal shock resistance.

In this chapter, fine-grained ($\leq 30\ \mu m$), wear-resistant aluminas and alumina-matrix composites are addressed. Such materials also dominate the engineering ceramics market. As a term of comparison, alumina shipments (372×10^6 €) constituted more than half from the total shipments of structural ceramics in the Japanese market in 2003 (715×10^6 €) (Okada, 2008). Commercial aluminas for high-responsibility applications such as hip parts for arthroplasty or cutting tools have typical grain sizes under 5 μm. First, the processing methods to optimize the microstructure of single-phase and fine-grained materials are addressed. Second, the development of special microstructures in single-phase as well as in composite systems is described. Table 2 summarizes the advanced structural aluminas with special microstructures and alumina-based composites that are described in this chapter together with their applications.

The optimization of the microstructure of single-phase materials and the development of alumina-based composites have been the research subjects since the general use of aluminas in the 1930s. The example of three of the most performance-demanding applications allows summarizing the main processing developments of alumina materials.

Alumina-based cutting tools have experienced a huge development since their commercial introduction in the early 1950s. Initially, major applications of alumina tools were the high-speed machining of cast iron. Later, processing improvement as well as the development of composites allowed new uses as machining of relatively harder and stronger steels quite effectively and economically and also intermittent cutting at reasonably high speeds, feeds, and depths of cut. Main developments have been reduced grain sizes and porosity and the development of composites, specially alumina–zirconia (ZrO_2), alumina–TiC, and alumina–SiC_w silicon carbide whiskers.

Alumina implant technology has been improving since the 1970s, focusing on the grain size refining, density increase, and significant reduction in the level of inclusions. Also, alumina-matrix composites, in particular, alumina–zirconia (ZrO_2), have been proposed.

Evolution from the translucent aluminas used in high-pressure sodium vapor lamp tubes to the transparent ones with promising applications as windows, armor, and bulbs of high-pressure metal halide lamps is being done by reducing the grain size to the submicrometric scale together with further density increase.

Table 2 Advanced structural aluminas with special microstructures and alumina-based composites and their applications

	Microstructure size	*Status*	*Secondary phase*	*Application/envisaged properties*
Textured aluminas		Under development	Remaining glass in some cases	Flaw tolerance
Monolithic composites	Micrometric	Commercial	ZrO_2	Implants
			TiC	Cutting tools
			SiC_w	
		Under development	SiC_w	Electrical
			Al_2TiO_5	Thermal shock and wear
Nanocomposites	Micro-nanometric	Under development	ZrO_2	Implants
	Nano-nanometric		SiC	Wear
			$FeAl_2O_4$	
			Al_2SiO_5	
			CNTs	
Laminates	Mili-micro–nanometric	Under development	ZrO_2	Strengthening and/or flaw tolerance
			Al_2SiO_5	Flaw tolerance
			$CaAl_{12}O_{19}$	

In summary, for single-phase aluminas, in general, microstructures with submicrometer grain sizes for obtaining components with improved hardness (Krell, 1995), wear resistance (Goh, Lim, Rahman, & Lim, 1997; Krell, 1996), strength (Krell & Blank, 1996), or optical performance (Apetz & van Bruggen, 2003) are required. When dealing with composites, processing procedures that allow the homogeneous mixing of phases with different compositions, sizes, and even shapes together with the sintering of the mixture to full density are major issues.

2.02.1.1 Single-Crystal Aluminium Oxide

2.02.1.1.1 Crystalline Structure

The pure form of aluminium oxide exists only in one crystalline form, α-Al_2O_3, throughout the whole temperature range up to the melting point, even though the confusing nomenclature β and γ-Al_2O_3 would suggest the existence of different polymorphs. The crystalline structure of α-Al_2O_3 is described in several sources (e.g., Brook, 1991): Hexagonal structure, D_{3a}^{6} space group, and two Al_2O_3 units per unit cell. Slip occurs on $\{0001\}<11\text{–}20>$ systems. The mean aluminium–oxygen distance is 192 pm. The single-crystal density is 3990 kg m^{-3} (Powder X-ray diffraction file ASTM42-1468). Aluminium oxide is ionic, constituted by Al^{3+} and O^{2-}; however, its bonds have some covalent character (Sousa, Illas, & Pacchioni, 1993). β-Al_2O_3 is a ternary oxide with general composition Na_2 0.11 Al_2O_3, and γ-Al_2O_3 describes a group of phases with the cubic form of a defect spinel that are produced by dehydration of gelatinous $Al(OH)_3$, giving Al_2O_3 with impurity protons.

All non-cubic materials present anisotropy in properties at the crystalline level, such as thermal expansion that is increased in ionic oxides due to partial polarization. On average, simple image of the structures of ionic oxides is a series of close-packed layers of O^{2-} ions generating cubic or hexagonal symmetry, with the cations localized at octahedral or tetrahedral interstices in the close-packed layers. The real structure is not so symmetrical as polarization is produced when the small cations with large charges occupy the interstices. Then, a series of unequal M^{n+}–O^{2-} distances are generated. In the case of aluminium oxide, three O^{2-} are closer to each Al^{3+} than the other three and the final structure is formed by highly distorted AlO^6 octahedra. These distorted octahedra and the overall hexagonal symmetry lead to anisotropy in the properties at the crystalline level.

2.02.1.1.2 Mechanical and Elastic Properties

The single crystals of aluminium oxide might present extremely high strengths due to the strong aluminium–oxygen bonds. Room temperature bending strengths of 400–700 MPa and tensile strengths of 500 MPa, depending on orientation and the surface perfection, are common (Brook, 1991; Riley, 2009). Moreover, values up to 7 GPa have been reported for flame-polished artificial sapphire rods (Brook, 1991; Watchman & Maxwell, 1959), which are increased up to 11 GPa for thin filaments. Recent data obtained using cantilever beams (10–30 μm long, width and depth 2–5 μm) machined by Focused Ion Beam (FIB) and tested in a nanoindenter range from 10 to 13 GPa for monocrystals. Strengths of polycrystals tested in the same way are about 5 GPa, failure is intergranular and usually initiates at the grain boundary. Carbon has been demonstrated to strengthen the grain boundaries of alumina, changing the fracture mode to transgranular. Then, strengths of polycrystals doped with 0.01% C are almost double than those obtained for pure alumina (about 8 GPa) (Yahya & Todd, in press).

Such strength values are of the order of theoretical strength for aluminium oxide (31 GPa; Riley, 2009). Aluminium oxide also presents high Young's modulus ($\approx$520 GPa; Brook, 1991) and hardness. Sapphire presents a hardness of 9 in the Mohs scale (nonlinear, 1: talc, 10: diamond) and Vickers hardness up to 30 GPa, depending on the orientation (Ryshkewitch & Richerson, 1985). However, the fracture energy and fracture toughness of alumina single crystals in the rhombohedral plane, which is the preferred cleavage plane, are relatively low, as reviewed by Iwasa and Bradt (1984). A value of $\gamma_f \cong 6\ J\ m^{-2}$ for alumina monocrystals at room temperature and a fracture toughness of about 2.4 MPa $m^{1/2}$ have been reported (Wiederhorn, 1969; Wiederhorn, Hockey, & Roberts, 1973). Most of the work on the development of alumina materials has been devoted to take advantage of the desired properties of the single crystals while increasing toughness. For such purpose, another property of the single crystal, the thermal expansion anisotropy, has been exploited, as described below.

2.02.1.1.3 Thermal Expansion Anisotropy

α-Al_2O_3 presents a relatively low crystalline average thermal expansion coefficient ($\alpha \approx 8.7 \times 10^{-6}\ K^{-1}$ between 25 and 1000 °C; Taylor, 1984a). However, there is a perceptible larger thermal expansion coefficient parallel to the c-axis ($\alpha \approx 9.2 \times 10^{-6}$ K^{-1} and 8.4×10^{-6} K^{-1} between 25 and 1000 °C, in the parallel and perpendicular directions, respectively; Taylor, 1984a). This thermal expansion anisotropy is responsible for the development of stresses in alumina materials when cooling from the sintering temperature, as described by different authors (e.g., Blendell & Coble, 1982).

The stress level depends on the particular relative orientation of the grain boundaries. For grain sizes above a critical one, these stresses can lead to fracture. However, for the small grain sized (<30 μm) structural aluminas, the developed stresses remain as residual stresses in the sintered materials and are partially responsible for the dependence of properties such as hardness, fracture toughness, and strength on grain size because they add to the externally applied stresses (Bueno & Baudín, 2006a; Bueno, Berger, Moreno, & Baudín, 2008; Mussler, Swain, & Claussen, 1982; Rice, Freiman, & Becher, 1981). Impurity phases, often glassy at grain boundaries, add further to these variations due to the thermal expansion mismatch between these phases and alumina, which also depend on the particular orientation of the grain boundary.

The residual stresses created in single-phase polycrystalline aluminium oxide and in composites as a result of its constrained anisotropic thermal contraction can be measured with the technique of piezospectroscopy using the fluorescence from trace Cr^{3+} impurities (Ma & Clarke, 1994). Over the range of grain sizes from 2 to 16 μm, the residual stresses exhibit a dependence on grain size consistent with the prediction of the Evans–Clarke model of thermal stress relaxation by grain boundary diffusion.

The hardness of Al_2O_3 increases from grain sizes of 5 μm down to 0.5 μm because of an increasing limitation microplastic deformation by movement of dislocations and twins (Krell, 1995, 1996). In addition, large-grain materials tend to present grain boundary microcracking under localized loads with associated hardness lowering; a decrease from 20 to 17 GPa for an increase in average grain size from ≈1 to ≈5.5 μm has been reported (Bueno & Baudin, 2006a). On the contrary, the adequate manipulation of the crystalline thermal expansion anisotropy can lead to increased toughness due to crack deflection, crack branching, and microcracking during the fracture process, acting as toughening mechanisms. A number of alumina-matrix composites have been developed on the basis of thermal expansion mismatch of the second phase with alumina to increase toughness.

2.02.1.2 Thermodynamic Stability of Aluminium Oxide

As stated by Brewer (1953) in his exhaustive revision, from a thermodynamic stand point, α-Al_2O_3 is one of the most stable of the metal oxides. This fact is clearly demonstrated by the large negative Gibbs energy of formation from the metal, ΔG_T, according to:

$$2\text{Al} + 1.5\text{O}_2(\text{g}) \rightarrow \text{Al}_2\text{O}_3 \tag{1}$$

Whose values range from −1590 to −945 kJ mol^{-1} from $T = 273$ to 2273 K (calculations using the program Outokumpu, 1993). This high thermodynamic stability is responsible for the absence of natural deposits of free metal.

Dissociation of Al_2O_3 to suboxides, Al_2O and AlO, has been reported to take place at high temperature and low oxygen partial pressures (Brewer, 1953; Brewer & Searcy, 1951) according to the following.

$$\text{Al}_2\text{O}_3(\text{c}) \rightarrow 2\text{AlO}(\text{g}) + 2\text{O}_2(\text{g}) \tag{2}$$

$$\text{Al}_2\text{O}_3(\text{c}) \rightarrow \text{Al}_2\text{O}(\text{g}) + \text{O}_2(\text{g}) \tag{3}$$

However, both reactions present a negative Gibbs energy and the corresponding equilibrium constants are extremely low (e.g., at 1773 K, $K = 2.76 \times 10^{-30}$ and 4.56×10^{-24} for Reactions (2) and (3), respectively; calculations using the program Outokumpu, 1993). Therefore, alumina experiences extremely low weight losses in vacuum, even at high temperatures (e.g., $\approx 10^{-6}$ to 10^{-5} kg/m·s in the temperature interval of 1973–2273 K; Harper, 2001).

Even though the fusion temperature of alumina is very high, liquids can be formed at lower temperatures due to impurities that originate at low invariant points. Some examples of liquid-forming temperatures (Levin, Robbins, & McMurde, 1964) are those corresponding to the systems Al_2O_3–SiO_2 (1590 °C: mullite–tridymite), Al_2O_3–SiO_2–CaO (1170 °C: pseudowollastonite–tridymite–anorthite), Al_2O_3–MgO–SiO_2 (1355 °C: protoensteatite–cordierite–tridymite), Al_2O_3–SiO_2–K_2O (689 °C: quartz-potash feldpart-$K_2Si_4O_9$, 990 °C: leucite–mullite–cristobalite), and Al_2O_3–SiO_2–Na_2O (720 °C: quartz-albite-anorthite). Some of these impurities can be used as sintering aids to increase the final density and/or reduce the sintering temperature.

However, they remain at the grain boundaries in the sintered material, often in glass form, and are detrimental for the high temperature strength and creep resistance of the material.

2.02.2 Production of Alumina

Aluminium is the third most common element in the Earth's crust (≈ 8 wt%), after oxygen and silicon, with enough economically available reserves to supply at least another 300 years of current demand (International Aluminium Institute, 2011).

However, because of its chemical reactivity, it is mostly found in its oxidized form (approximately 250 different minerals exist) and almost never occurs in the elemental state. The natural, pure, anhydrous aluminium oxide is a rare mineral called corundum. Even rarer is the single-crystal form, sapphire, which is usually slightly colored due to metallic impurities (Ni and Mg give yellow and Ti gives blue), and ruby, which contains a small amount of Cr (≈ 1 wt%).

The most prominent group of aluminium-containing minerals are the aluminosilicates, and the products of their weathering, the clays. With regard to aluminium production, it is the aluminium hydroxides that represent the most important compounds. Pure, anhydrous alumina forms two hydrates: $Al_2O_3{\cdot}H_2O$ ($AlO(OH)$) and $Al_2O_3{:}3H_2O$ ($Al(OH)_3$). Each of these compounds has two crystalline forms, α and γ, and a specific name (diaspore: α-$Al_2O_3{\cdot}H_2O$, bohemite: γ-$Al_2O_3{\cdot}H_2O$, bayerite: α-$Al_2O_3{:}3H_2O$, and gibbsite or hydrargillite: γ-$Al_2O_3{:}3H_2O$).

Small particle size (≈ 1 μm or less) and high-purity (>99.5%) aluminium oxide powders are required for the production of high strength and hard alumina ceramics used in commercial applications. Most alumina grades were originally manufactured from mineral sources. For structural applications of responsibility, especially involving high temperature, extremely high-purity aluminium oxide is needed. In particular, liquid-forming agents such as SiO_2, Na_2O, CaO, etc., should be avoided. The most significant step in terms of raw materials has been the development of chemical routes to fabricate new powders.

2.02.2.1 Industrial Processes

The raw material for aluminium and alumina is bauxite (named after Les Baux-en-Provence in France), a mixture of the oxide hydrates and clays (aluminosilicates) with impurity oxides such as SiO_2 and TiO_2 and small amounts (ppm) of the strategic compound Ga_2O_3 and iron oxides that occur as a weathering product of low iron and silica bedrock in tropical climatic conditions. The most common mineral constituent of bauxite is gibbsite. A description of bauxite mineralogy can be found in a number of textbooks (e.g., Wells, 1984), and summaries are found in several revisions (Doremus, 1984). Evolution of gibbsite with temperature has been recently studied by neutron thermodiffractometry (Rivas Mercury, Pena, de Aza, Sheptyakov, & Turrillas, 2006). Deposits of bauxite exist around the world, the largest bauxite deposits being found in Guinea, Australia, Brazil, and Jamaica.

Purification of bauxite to fabricate aluminium, and to a lesser extent, alumina, is done by the Bayer process. Two to three tonnes of bauxite are required to produce a tonne of alumina and 4–6 tonnes of bauxite for the production of 1 tonne of aluminium metal (International Aluminium Institute, 2011). **Figure 1(a)** shows the geographical share of alumina production by weight in 2011 recognized by the International Aluminium Institute. Most of the alumina is used for the production of aluminium and a small part goes to the ceramic industry (**Figure 1(b)**).

The Bayer process starts by dissolving crushed bauxite in sodium hydroxide under pressure at 300 °C to form a supersaturated solution of sodium aluminate at normal conditions of pressure and temperature. The insoluble oxides are then removed and the hydrated aluminium oxide is precipitated as gibbsite by seeding, more frequently, or as metastable bayerite by reduction of pH by carbon dioxide. The precipitated low-temperature forms, γ-alumina, are then washed and subsequently dehydrated at 1000–1200 °C to fully convert into the stable α-alumina phase. This material is named "calcined alumina" and typically contains 0.1–0.5 wt% of sodium oxide and calcium oxide. Calcinations at intermediate temperatures give mixtures of α-Al_2O_3 and transition aluminas; these powders are usually called "reactive aluminas". The coarse aggregates made of large alumina single crystals for the refractory industry (fused alumina) are obtained by fusing this alumina powder and crushing the obtained material. Also, it can be graded to be used for grinding and abrasives.

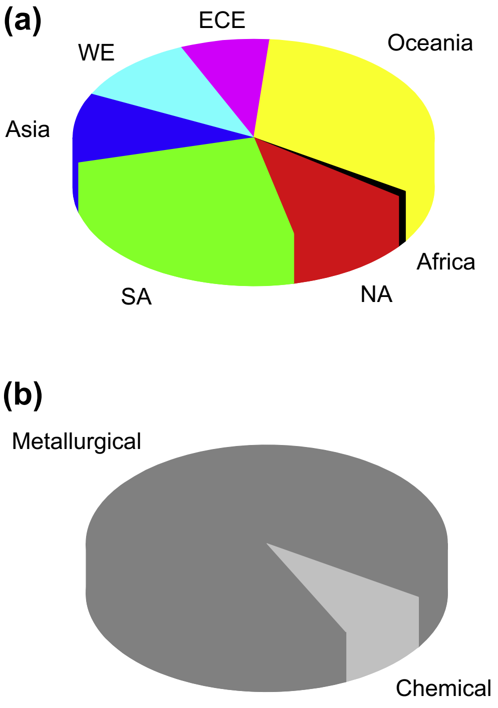

Figure 1 Alumina production by weight in 2011, recognized by the International Aluminium Institute (2011). (a) Geographical share. WE, West Europe; ECE, East and Central Europe; NA and SA, North and South America. (b) Metallurgical (Al production) and chemical (Al_2O_3 production) share.

The calcined agglomerates have sizes up to ≈100 μm, even though the sizes of the primary crystals can be smaller than 1 μm. The powders required for the fabrication of high-performing ceramics are much smaller (≈μm); thus, a major objective of the calcination step is to obtain soft agglomerates in order to avoid intensive milling as much as possible. Then, the calcined agglomerates can be milled down to get uniform sized and small particles. The other main characteristic of the calcined aluminas is the presence of up to 0.5 wt% NaO_2 as mentioned above. Low soda–calcined aluminas are considered when the NaO_2 is lower than 0.05 wt%. Typical specifications of calcined aluminas can be found elsewhere (Riley, 2009).

2.02.2.2 High-Purity Alumina Powders

Since the late 1980s, new processes to obtain high-purity powders have been developed. The high-purity alumina is most commonly fabricated by decomposition of aluminium-containing salts such as ammonium aluminium sulphate ($(NH_4)2SO_4^{\cdot}Al_2(SO_4)_3^{\cdot}12H_2O$) or aluminium hydroxides in air. The obtained alumina is then converted into alumina by heating at temperatures over 1000 °C. This calcination process promotes not only the transformation from transition aluminas to α-alumina but also the growth of the α-alumina particles and the formation of hard agglomerates. Since the early uses of alumina, different ways have been proposed to reduce the temperature of treatment in order to limit the formation of agglomerates. Additions of metal oxides (Messing, Shelleman, & McArdle, 1988; Xue & Chen, 1992), α-alumina seeds (Kumagai & Messing, 1985; Messing et al., 1988; Rajendran, 1994; Wakao & Hibino, 1962; Yoshizawa & Saito, 1996; Yoshizawa, Hirao, & Kanzaki, 2004a, 2004b), liquid-phase formers (Shelleman & Messing, 1988), and different organic and nonorganic compounds (Rajendran, 1994; Wu, Zhang, Pezzotti, & Guo, 2002; Xue & Chen, 1992) as well as high-energy ball milling (Tonejc et al., 1994; Wang, Suryanarayana, & An, 2005) have proven to be effective in reducing the α-alumina transformation temperature. The hydrolysis of aluminium alkoxide has also been proposed to obtain high-purity alumina (Fujiwara, Tamura, Maki, Azuma, & Takeuchi, 2007). All these processes are relatively expensive and produce only small quantities of alumina; thus, the fabricated powders are used only for specific applications.

More recently, a huge effort is being devoted to fabricate not only high-purity alumina but also extremely fine-grained alumina (≈100 nm). In this sense, direct processing of the nanosized and high-specific surface transition aluminas to fabricate the bulk material has been proposed, as discussed below in Section 2.02.4.5.1.

2.02.3 Alumina Materials

In general, commercial alumina materials are considered as those with more than 75 wt% of alumina, with the balance presenting a broad spectrum of compositions. High-purity (>99.7 wt%) materials are available at high densities, and dependent on the dopant (MgO, Y_2O_3) can be translucent with zero porosity; principal applications are as machine tool tips, crucibles, and high-pressure sodium vapor lamp tubes. Grades around 99 wt%, usually doped with MgO, SiO_2, and CaO, are used for mechanical components and high-temperature tubing. Sometimes, small amounts (1–2 wt%) of Cr_2O_3 are added to high-purity alumina materials in order to increase hardness and wear resistance (Bradt, 1967; Ghate, Smith, Kim, Hasselman, & Kane, 1975). The large Cr^{3+} ions replace the smaller Al^{3+} ions in the crystalline lattice, creating a compressive lattice strain that would reduce the tendency to grain boundary microcracking. Low-purity (93–99 wt%) materials with the same general dopants are also used for room temperature applications such as pumps because of their high acid resistance.

In the last decades, a series of alumina-based composites (75–93 Al_2O_3 wt% ZrO_2, TiC, SiC_w as secondary phases) designed to present high strength and toughness have been developed and are extensively used for tool tips, mechanical mills, textile guides, and erosion protection sheaths (Whitney, 1994). Exhaustive description of the properties and uses of ceramic cutting tools for metal machining can be found elsewhere (Kumar, Durai, & Sornakumar, 2006; Mandal, Doloi, & Mondal, 2011; Whitney, 1994).

Initially used only for metal machining, alumina tools are nowadays used for cutting and machining of nonmetal materials, even in the domestic environment. Recently, tools made of submicrometric alumina particles have been proposed for milling wood-based materials not easily workable (Gogolewski, Klimke, Krell, & Beer, 2009).

A relatively new application of fine-grained and dense alumina materials is in total hip arthroplasty, where they are increasingly used since their introduction in the 1970s (Hannouche, Zaoui, Zadegan, Sedel, & Nizard, 2011; Huet, Sakona, & Kurtz, 2011). Alumina implant technology has been improving by focusing on grain size refining, density increase, and significant reduction in the level of inclusions (Hannouche et al., 2011; Huet et al., 2011; Insley, Turner, Fisher, & Streicher, 2002; Tateiwa et al., 2008; Zywiel, Sayeed, Johnson, Schmalzried, & Mont, 2011). Also, alumina-matrix composites, in particular, alumina–zirconia (ZrO_2), have been proposed (Insley et al., 2002; Piconi & Maccauro, 1999).

Compared with the systems formed by metallic components coupled with ultra-high–molecular weight polyethylene, ceramic bearings have the advantage of exhibiting a higher wear resistance (Huet et al., 2011; Tateiwa et al., 2008) that reduces the possibility of damage due to debris associated with metals and polyethylene (Cuckler, Bearcroft, & Asgian, 1995; Lancaster, Dowson, Isaac, & Fisher, 1997). Obviously, catastrophic failure associated with brittle fracture is the main disadvantage of alumina parts. This failure can occur at stress intensities lower than those corresponding to material toughness due to subcritical crack growth processes (de Aza, Chevalier, Fantozzi, Schehl, & Torrecillas, 2002). Even though the actual fracture risk is relatively low—approximately 1.4 per 1000 alumina balls used in the United States, according to a survey from the 1990s (Hannouche et al., 2011)—more reliable microstructures are being continuously investigated. In particular, average grain sizes have been reduced down to less than 1.8 μm and densities have been risen up to 3980 kg m^{-3} by implementation of improved processing techniques such as hot isostatic-pressing (HIP) and powder quality (Garino, 2005; Huet et al., 2011). The latest development was the introduction of alumina–zirconia (ZrO_2) composites (Insley et al., 2002; Piconi & Maccauro, 1999), which are currently produced by several international ceramic producers. However, they have a relatively short clinical history (Huet et al., 2011). Commercial alumina–zirconia femoral balls (CeramTec Inc., Lauf, Germany) present strengths more than twice those of single-phase materials. In dentistry, glass-infiltrated alumina is being applied as cores or implants in all-ceramic restorations (Yin, Song, Song, Huang, & Li, 2006).

Pore-free aluminas are desired for reliable and durable high-responsibility applications such as for hip prostheses, as described above. In general, pore-free ceramics are increasingly being a research subject due to their promising optical, mechanical, and electrical properties (Messing & Stevenson, 2008; Wei, 2009). In particular, full-density aluminas change from translucent for microsized grains to transparent when density is extremely increased (>99.99% of theoretical) and grain size is decreased down to below 100 nm. Transparent aluminas have promising applications as windows, armor, and bulbs of high-pressure metal halide lamps.

The development of high-purity and dense alumina materials has led to their use in the production of advanced materials (Okada, 2008). Nowadays, they are the common constituents of the parts that support silicon wafers in the vacuum chamber where the etching of semiconductors is done and in the welding nozzles for the manufacture of steel parts for automobiles, whose tips can reach up to 600 °C. Alumina is adequate for these applications due to its excellent performance in corrosive (reactive gases) and plasma environments.

2.02.4 Fabrication of Alumina Materials

One of the consequences of the high melting point of ceramics is that they are generally fabricated from powders and not from fused mixtures. The general processing schedule (Figure 2) includes the processing of the powders before the thermal treatment to reach a shaped powder form, usually named "green body", and the thermal treatment. The word "sintering" is used to describe the phenomenon that occurs during the thermal treatment. Due to the high cost of machining hard materials such as alumina, near–net shape methods are being developed. Also, green bodies with sufficient strength as to be green machined are fabricated by optimization of the shaping methods. Green machining after isostatic-pressing is used routinely to fabricate insulators. The extreme geometrical requirements for hip and knee implants require intermediate and final machining and final polishing and two- or three-stage sintering.

When the powder compact is heated to a suitable temperature at which the mass transport mechanisms are operative, the porous compact shrinks as a result of the initial misfit of the particles. Apart from shrinkage, grain growth occurs during the process. In some cases, reaction between the constituents occurs, which might aid or impede shrinkage. This latter process is fundamental when the in situ formation of second phases is aimed. The packing structure of the green body determines the development of the microstructure during sintering. In order to get high-quality materials, the control of the shape-forming processes is of prime importance. In order to avoid defects in the green state, dispersal approaches have to be applied to the powders to bring them into the state that allows the use of the different shaping methods available.

The sintering of submicronic and high-purity (99.5%) aluminium oxide powders to near-full density (99% of theoretical) was first reported in 1956 (Cahoon & Cristensen, 1956). Nowadays, for fabricating high-performing alumina materials, the new corundum powders with submicrometric particle sizes (average diameters ≈0.2–0.6 μm) and high purity (>99.7%) commercially available since the late 1980s are used. Also, the use of new nanosized (<50 nm) powders to obtain materials with new properties is under investigation. In principle, the small size together with the increased particle curvature would increase the driving force for solid-state sintering, reducing the required temperature and consequently limiting the grain growth. However, fine

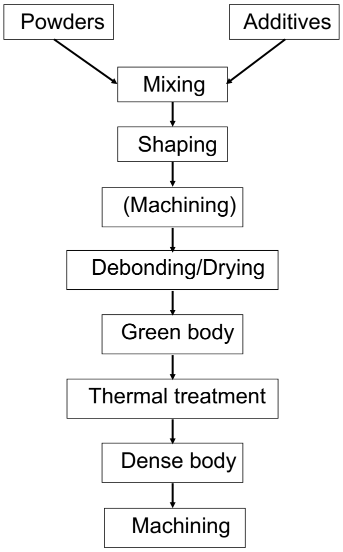

Figure 2 Basic flowchart for the fabrication of ceramic components. Shaping methods used for alumina ceramics are summarized in **Table 3**.

particles present larger tendency to agglomerate. Agglomeration hinders a locally homogeneous densification as explained first by Lange (Lange, 1984) and confirmed later on for finer raw materials (Xue & Chen, 1990). Therefore, the agglomerates in the green body evolve toward differential sintered areas constituted by large particles or particle assemblies surrounded by low-density zones. In order to get real profit of the submicrometric powders, the relationships between sintering temperature, sintered density, and grain size as a function of spatial homogeneity and interfaces have to be known and handled.

Most alumina-matrix composites are fabricated by powder processing and sintering methods of the same kind as those for single-phase alumina materials. However, each processing step presents specific problems due to the different characteristics that present the matrix and the reinforcing phase (size, shape, specific surface area, composition, density). First, it is necessary to prepare the homogeneous mixture of the matrix and the reinforcing phase and consolidate it. Second, adequate thermal treatment has to be selected in order to reach a high-density matrix, even though the reinforcing phase can act as shrinkage inhibitor. And third, the interface between the matrix and the reinforcement has to be controlled to allow the action of the reinforcement mechanisms.

2.02.4.1 Powder Processing and Shaping

Shaping can be defined as the processing step in which a system constituted by isolated particles is transformed into a consolidated body with specific shape, size, and microstructure. The selection of one or another shaping procedure is based on the required characteristics of the sintered form—shape and size—of the material microstructure—grain size and shape, dispersion of secondary phases, and density—on the number of pieces to be produced and its necessary reliability, and on environmental and economical aspects. The most expensive stage of the fabrication of pieces of hard materials such as alumina is final machining; thus, great effort is devoted to the development of shaping procedures to avoid machining.

The powder processing and shaping technology of alumina materials started on the basis of that of clay ceramics (Gitzen, 1970). Therefore, shaping methods were taken directly from those used for clays, which presented some problems due to the lack of plasticity of the available alumina powders. Most of the further developments of the traditional forming methods—slip-casting, dry and semidry cold-pressing, isostatic-pressing, extrusion, etc.—as well as new forming processes such as hot-pressing (HP) have been developed using alumina as the principal agent.

Due to the lack of plasticity of advanced ceramic powders, organic additives (binders, plasticizers, and lubricants) are usually added to provide plasticity during forming and green strength of the formed product. Starting materials for forming are powder, additives, and solvents, and the three main material states for forming are granules, masses, and slurries. In Table 3, the main ceramic cold-forming (shaping) methods used to fabricate alumina parts that are discussed in which follows are summarized. In general, they are classified on the basis of the degree of moisture in the starting material.

Table 3 Shaping methods used to fabricate alumina materials classified by the degree of moisture (those which are not specifically discussed in the text is indicated in italic.)

Dry	*Plastic (semi-dry and wet)*	*Direct slurry shaping*
Cold pressing: Uniaxial Biaxial Isostatic Hot pressing, hot isostatic pressing	Extrusion Injection moulding Others: pressure moulding	Filtration: Slip casting Pressure casting Vacuum casting Deposition/evaporation: Tape casting Centrifugal casting *Others: electrophoretic deposition, screen printing, dip coating* Polymerization/gelation: Gel-casting *Others: freeze casting, rapid prototyping, floculation/coagulation*

The powder processing before consolidation is of prime importance to avoid defects in the sintered material. Major heterogeneities in the powders are soft and hard agglomerates, organic and inorganic inclusions, and large grains. Moreover, more than one phase have to be homogeneously mixed when considering composites. Mixing difficulty is increased when particles of different shape are considered as occurs in the alumina–SiC_w composites used for cutting tools. Even when the desired homogeneity is reached during mixing, mass segregation during shaping can lead to heterogeneities in the green body in multiphase ceramics. Most heterogeneities can be eliminated by manipulating and controlling interparticle forces as practiced in colloid science (Lange, 1989, 2001). Repulsive interparticle forces are used to break apart weak agglomerates, fractionate inclusions greater than a given size, and mix different fractionated powders. Moreover, colloidal technology can be combined with milling procedures. Once fractioned and mixed, the interparticle forces can be made attractive to form a network that prevents mass segregation.

2.02.4.1.1 Cold-Pressing Methods

Pressing technologies involve the compaction of the powder by applying either a rigid (axial-pressing) or flexible (isostatic-pressing) pressure. For specific shapes such as tubes or insulators, part of the mold used for isostatic-pressing can be rigid. Fundamentals of pressing are discussed by Hofmann et al. (Hoffman, Scharrer, Czerch, Fruhauf, & Burck, 1962). These authors identified the Coulomb force between the moisture ions adsorbed on the surface of the ceramic particles as the main cause for the cohesion in the green body. As the saturation degree is very low (0.01–0.5), the required applied pressures are high ($\approx$50–200 MPa). The degree of moisture in the starting material may change from less than 7% (dry-pressing) to 15–20% (semidry and wet). Axial-pressing can involve the application of pressure on one direction (uniaxial) or two directions (biaxial). Wall friction during axial-pressing is the major source of density variation in the pressed body (Allen, 1961). When isostatic-pressing is used, pressure is applied equally through the whole mass and the density gradients characteristics of uniaxial-pressing are avoided. However, axial-pressing is the most used at industrial level when it is possible to reach the required shape due to the easiness of automation and the high production speed. High-purity ($\geq$98.5%) alumina dense (>95%) parts such as tap seals with smaller height than diameter are routinely fabricated by uniaxial-pressing. Isostatic-pressing is used for shapes that cannot be obtained by uniaxial-pressing or for added value products that require high density and isotropic green bodies. Molds for axial-pressing are usually made of steel and for isostatic-pressing they are made of elastomeres, silicone, and polyurethanes. The latter have better properties but are more difficult to synthesize.

In order to improve the flowing of the fine powders during pressing, they are usually granulated before compaction. Otherwise, the specific volume of nonagglomerated particles in or beyond the micrometer range is so large that on compaction, the decrease in volume is excessive, causing extensive elastic relaxation (and associated cracking) on removing the load. The granules are most often produced by colloidal dispersion techniques followed by spray drying ceramic powder slurries containing additions of organic materials to act as binders, usually polymers, and have to fulfill several requirements in order to avoid defects in the sintered body (see, e.g., Eckhard & Nebelung, 2011; Lange & Metcalf, 1983; Nakamura, Tanaka, Kato, & Uematsu, 2009). They have to be large (>50 μm) and strong enough for handling but soft enough to be destroyed by compaction to avoid relicts of the granules in the green body that will evolve to defects by differential sintering. In addition, they have to uniformly deform to fill interagglomerate void space during pressing (Frey & Halloran, 1984; Lin & Lin, 2008). It is necessary to avoid the movement of the binders toward the surface of the slurry droplets, in the stream of hot air during the spray drying process, because it would produce binder segregation at the surface of the granules after the liquid evaporates. In order to reduce segregation, binders that bond strongly on the powder surface should be used. In the case of alumina powders, strong chemical bonding has been proved with binders containing functional groups of the polyacrylic type (Tanaka, Pin, & Uematsu, 2006).

For optimized powder conditioning before isostatic-pressing and sintering schedules, materials with densities higher than 98% of theoretical and grain sizes of about 1–5 μm can be fabricated from undoped alumina powders of about 0.5 μm average particle size.

2.02.4.1.2 Extrusion and Injection Molding

Higher moisture contents increase the plasticity of the powder, and plastic-forming methods such as extrusion, pressure molding, or injection molding can be used. Pressure molding is mainly used for tableware. In these cases, the starting material deforms at relatively low pressures (1–20 MPa) due to the high saturation degree (>0.9).

Extrusion is adequate when long pieces of constant transversal section, such as tubes, cylinders, or tiles, are required. However, it is scarcely used for advanced materials because the noncompressible powders used require additives, which make difficult the dimensional control and require special treatments to eliminate. Extrusion is mainly used in clay systems that confer plasticity to the shaped material.

Injection moulding is a special case because the solid is saturated by a fused polymer that solidifies due to the temperature change in the mould after injection. Due to the high viscosity (≥ 103 Pa·s) of the mixtures, which are prepared by colloidal techniques, it is necessary to apply high pressures (10–150 MPa) at temperatures of about 120–200 °C. The shaped piece has to be subjected to a treatment to eliminate organics, usually done by a slow thermal treatment, which increases the price. An attractive characteristic of this method, broadly used to fabricate textile guides, is that a wide spectrum of near–net-shaped complicated shapes can be fabricated, limiting machining in the sintered state. Due to the high viscosity of the mixtures and the high organic content (20–50 vol%), this procedure usually leads to defect formation, so it is not generally used for advanced ceramics. However, in order to take profit of its advantages, developments are being done to incorporate it into their standard fabrication methods (Mannschatz, Höhn, & Moritz, 2010). In fact, some companies are already offering high-purity sintered alumina (≥ 99.8) pieces green shaped using injection moulding (e.g., http://www.adamoutechnicalceramics.com/news/8/57/Adamou-featured-in-Powder-Injection-Moulding-International).

By using low–molecular weight thermoplastic polymers, it is possible to decrease the applied pressure (down to ≈ 0.3–0.3 MPa) significantly. This relatively new process is called "low pressure injection moulding" (Mangels, 1994; Novak, Vidovic, Sajko, & Kosmac, 1997; Rak & Hamburg, 1995). The low viscosity required for this method limits the acceptable solid contents of the slurries (max 65 vol%), which leads to a significant shrinkage during sintering and the possibility of low-density defects (Mangels, 1994).

2.02.4.1.3 Direct Slurry Consolidation Methods

Colloidal technology is used to produce the slurries used for spray drying and injection molding. However, a major issue for exploiting the advantages of the colloidal approach is the direct shaping of green bodies from the slurry without addition of the large amounts of forming additives. Direct slurry consolidation includes a variety of procedures in which the applied pressures are very low (for filtration, $P < 1$ MPa) or zero. Main problem of the direct slurry consolidation methods is that homogenization and pouring introduces air into the slurry, forming "bubbles", whose complete elimination is difficult. Therefore, relatively large spherical pores might be formed in the green compact, which cannot be eliminated by solid-state sintering, as shown in **Figure 3**, where the fracture surfaces of green (**Figure 3(a)**) and sintered (**Figure 3(b)**) bodies show the evolution of one of these bubbles after sintering.

Slip-casting and tape-casting are the two conventional slurry consolidation methods. During slip-casting, the slurry is poured into a permeable mould, which allows the fabrication of complex-shaped pieces. High-density (>98% of theoretical) alumina materials can be fabricated from high-purity (>99.9%), undoped powders of about 0.5 μm average grain size, with grain sizes dependent on the sintering temperature (e.g., ≈ 3–5 μm for temperatures ranging between 1450 and 1550 °C; Bueno et al., 2008; Sánchez Herencia, Moreno, & Baudín, 2000). The homogeneous dispersion of 5 vol% zirconia stabilized with 3 mol% Y_2O_3 (YTZP) allows keeping the grain size smaller than ≈ 2 μm (Ruiz-Hervías, Bruno, Gurauskis, Sánchez-Herencia, & Baudín, 2006). The main limitation derives from the low kinetics of the filtering process that limits the allowable thicknesses of the shaped pieces. There have been different techniques proposed to accelerate the process such as performing the filtration under vacuum or microwaves, centrifugation, or application of a pressure (<1 MPa) that has to be high (>5 MPa) when fine-grained powders such as those used for advanced aluminas are considered (Yu & Lange, 2010; Zhang & Lange, 2006). From an industrial point of view, slip-casting is used for the fabrication of thin-walled complex pieces in short series such as a wide spectrum of laboratory ware. To avoid excessive shrinkage during fluid removal and densification, slurries containing the highest possible fraction of particles are needed, which requires the careful manipulation of particle interaction to maintain the stability of the slurry (Cesarano, Aksay, & Bleier, 1988; Lewis, 2000; Sigmund, Bell, & Bergstrom, 2000).

Tape-casting (Shanefield & Mistier, 1974; Shanefield, Morzenti, & Mistier, 1974; Williams, 1976) is generally used when substrates with high microstructural and thickness control and good surface finish are needed. This process involves the deposition of the slurry on a substrate where consolidation occurs due to the evaporation of the liquid medium. The thickness of the deposited tape is controlled by a blade. The obtained tape has to be flexible to be manipulated, so special additives, binders, and plasticizers, which have to be eliminated by the thermal treatment, have to be added (Moreno, 1992a, 1992b). Tape-casting is limited to the fabrication of relatively thin (≈ 25–400 μm) tapes. Thicker tapes and bulk pieces can be fabricated by stacking cast tapes and

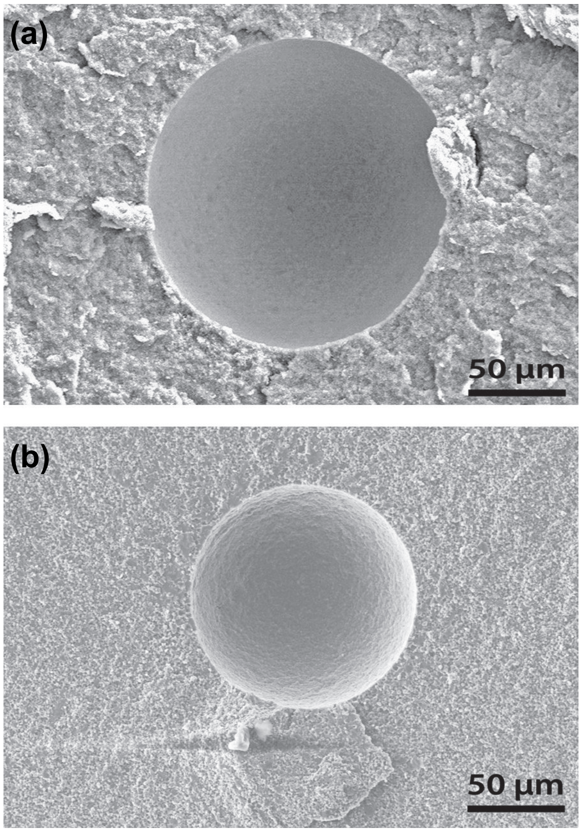

Figure 3 Characteristic defects formed in bodies shaped directly from the slurries. Scanning electron microscopy of fracture surfaces. (a) Spherical pore in the green body formed as a result of an air bubble in the slurry. (b) Spherical pore in the sintered material formed as a consequence of the evolution during sintering of a spherical pore in the green body.

sintering (Gurauskis, Sánchez-Herencia, & Baudín, 2006; Lambrinou et al., 2007), with microstructural characteristics similar to those of bulk pieces obtained by slip-casting (Ruiz-Hervías et al., 2006). Relatively porous ($\approx$90–92% of theoretical density) alumina ($\geq$96% purity) substrates designed to sustain thermal gradients are fabricated by tape-casting.

Centrifugal-casting is a particle consolidation process in which particles in a colloidal suspension settle under centrifugal acceleration (Chang, Lange, Pearson, & Pollinger, 1994; Huisman, Graule, & Gauckler, 1995). When compared with other colloidal-forming methods, it has the advantage of producing massive ceramic objects combined with a reduced risk of stress gradients in the formed part because stresses during the centrifugal forming process act on every volume element. During sedimentation, the particles move in the direction of gravity, whereas the liquid flows in the opposite direction. This means that the total volume of liquid in the dispersion does not have to be transported through the sedimented powder, leaving defects such as filtration channels as in the case of slip-casting and pressure filtration. The drawback of this technology, however, is that particle size separation might occur due to differential settling during the consolidation stage. In order to avoid this problem, consolidation of the system in the flocculated state or in the coagulated state or the use of highly concentrated slurries was proposed. Centrifugal-casting is limited for relatively thin-walled shapes.

A lot of effort is being put in the study of processes that transform a high solid content (>50 vol%) flowable slurry into a firm body without liquid phase removal. This solid body retains the structure of the stable suspension. This transformation can be done by manipulation of the electrical characteristics of the particles (the electrical double layer) or by changing the pH or the additive concentration, as occurs in the process of direct coagulation (Prabhakaran, Raghunath, & Melkeri, 2008). Another possibility is the addition of chemical species that polymerize under controlled conditions. The most usually investigated methods are the addition of catalysts that produce the polymerization of monomers added to the suspension (gel-casting).

A recent review about the gel-casting method has been published by Yang and coworkers (Yang, Yu, & Huang, 2011). The typical route of the gel-casting process is preparing suspensions with high solid loading and low viscosity and then solidifying the suspension cast in a pore-free mold. The generic principle is that monomers react to form polymers and create a three-dimensional network that freezes the suspended particles in the desired shape. The ceramic particles together bonded by the strong gel develop sufficient strength to support their own weight, and thus, the green body can be handled without shape distortion. In principle, gel-casting would allow the fabrication of high-quality complex-shaped parts (Omatete & Janney, 1991; Omatete, Janney, & Strelow, 1991; Tari, 2003; Young, Omatete, Janney, & Menchhofer, 1991). Moreover, as direct constant volume consolidation technique, it has the potential to maintain in the green state the high degree of homogeneity achieved in the slurry (Tari, 2003). The process was first developed by Omatete, Janey, and coworkers in the early 1990s and applied for alumina shaping (Omatete & Janney, 1991; Omatete et al., 1991; Young et al., 1991). The monomer solution was done with water and acrylamide which is a neurotoxin. This fact limited the generalization of the process. A lot of efforts are being directed toward the use of new nontoxic monomers (Bednarek, Szafran, & Mizerski, 2010; Falkowski, Bednarek, Danelska, Mizerski, & Szafran, 2010; Kokabi, Babaluo, & Barati, 2006; Tallon, Jach, & Moreno, 2007).

Another route of gel-casting that includes the use of temperature and environmentally friendly chemicals is the thermal gelling of hot water solutions of natural polymers such as agarose, agar, and carrageenans (Millán, Nieto, Baudín, & Moreno, 2002; Millán, Nieto, & Moreno, 2002; Millán, Nieto, Moreno, & Baudín, 2002; Santacruz, Baudin, Moreno, & Nieto, 2004). These polysaccharides are low-viscosity fluids at temperatures about 60–90 °C, and when cooled in a mould at temperatures lower than their Tg (35–45 °C), these are converted into a high-resistance gel.

In general, the green bodies obtained by gel-casting are strong enough even to be machined (Millán et al., 2002). However, some disadvantages of the processes prevent their extensive utilization by manufacturers. Besides the toxicity of the gel-cast materials, there are some limitations in the obtainable density of the gel-cast body because its green density is directly related to the solid loading of the slurry; thus, to attain dense packing, extremely high–solid loading slurries would be needed (Saeed, Hossein, & Jan, 2010). As mentioned above, for highly concentrated slurries, the range and magnitude of the interparticle forces become very important in controlling the rheological response (Cesarano et al., 1988; Lewis, 2000; Sigmund et al., 2000) and slurries with lower flowability are formed. As no external force is applied in gel-casting, slurry with sufficient flowability for self-filling up of the mold under gravity is needed. Therefore, there is a trade-off between slurry flowability and green density when using gel-casting as a shaping method. In addition, defects can be formed in the sintered compacts due to the memory effect in the ceramic process. This fact is shown in **Figure 4**, where a low-density zone in the green compact with the structure of the gel formed by a network of elongated units (**Figure 4(a)**) transforms into a low-density zone with elongated pores in the sintered body (**Figure 4(b)**).

Optimized gel-casting and thermal treatment (pressureless sintering, ≈1250 °C for 2 h plus HIP at ≈1200 °C for 15 h) of submicron-sized (≈200 nm), high-purity (99.99%) alumina and alumina with 300 ppm of MgO has allowed the fabrication of fine-grained (≈0.5–0.6 μm) and high-density (≈99.99% of theoretical) aluminas, with strengths of about 600–630 MPa, highly performant for cutting processes (Gogolewski et al., 2009).

As it can be concluded from the above discussion, powder processing prior to shaping is a main issue in ceramic processing. In general, well-dispersed and stable suspensions with high solid loading and reasonably low viscosity to allow the shaping are needed to start with. In this sense, the effect of the parameters that determine the slurry rheology has been deeply investigated, particularly in alumina suspensions. The effect of particle size, solid loading, and surface chemistry has been studied, especially for submicron-sized powders. The key effect of particle size distribution (Smith & Haber, 1992; Tari, Ferreira, & Lyckfeldt, 1998) has been demonstrated as well as the necessity of reaching stability by means of additives (Cesarano & Aksay, 1988; Cesarano et al., 1988; Hidber, Graule, & Gauckler, 1996; Hidber, Graule, & Gauckler, 1997; McAfee & Nettleship, 2006; Tari et al., 1998) and of adaption of the slurry characteristics to the specific shaping method. A review on colloidal processing methods for advanced ceramics was published by Sigmund and coworkers (Sigmund et al., 2000).

The main point of direct slurry consolidation is that wet shaping processes (slip-casting, gel-casting, etc.) provide the freedom for particles to find the position of their own, improving the particle coordination in the green body. Contrarily, on dry-pressing, the external force can never arrive on an individual particle in the body to shift it into an optimum position between its neighbors. This fact is made evident in **Figure 5**, in which the

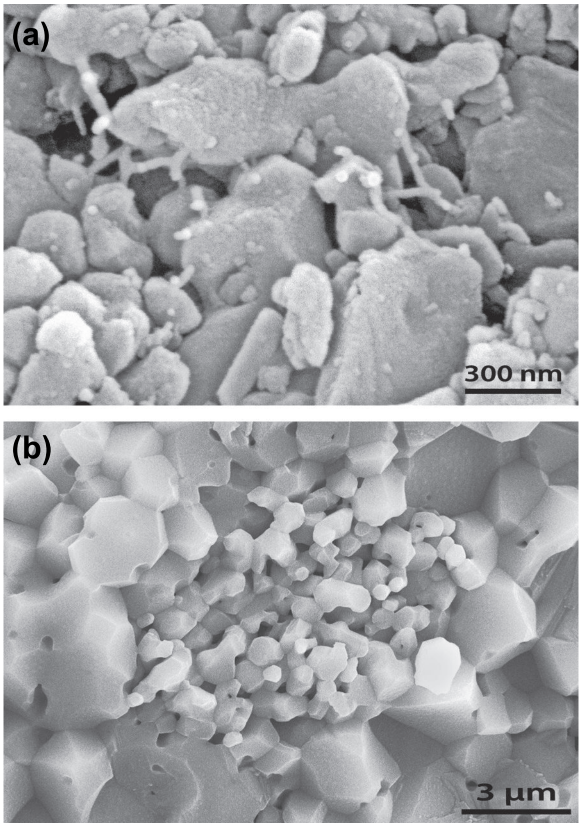

Figure 4 Fracture surfaces of alumina bodies fabricated by gel-casting using aqueous agarosa solution, showing the formation of defects due to the memory effect in the ceramic process. Scanning electron microscopy. (a) Green body. Detail of a low-density zone, where the structure of the gel formed from the solution is observed. The structure is constituted by a network of elongated units. (b) Sintered body. Low-density zone with elongated pores.

characteristics of cold isostatic–pressed (CIP) and slip-cast alumina bodies fabricated from the same undoped starting powders are shown. The pore size distribution (Figure 5(a)) is centered in a smaller value and much closer for the green compact shaped by slip-casting than for the one shaped by CIP, revealing the higher particle coordination and homogeneity of the microstructure. Consequently, the microstructural development at high temperature is also more homogeneous for the slip-cast material (Figure 5(b)), which shows practically no pore trapping associated with exaggerated grain growth, clearly observed in the CIP material (Figure 5(c)).

2.02.4.2 Sintering Processes and Microstructures

The sintering of dense bodies from relatively pure (>99 wt%) alumina powders has received more attention than any other single oxide system. In fact, it was considered as a model system for the analysis of conventional sintering of ceramics and the effect of additives and of the sintering of ceramics under pressure.

Diffusion of the aluminium and oxygen ions is slow at temperatures below 1000 °C. However, both ions diffuse at higher temperatures (>1300 °C), allowing the solid-state sintering of alumina materials, which is the most used process to fabricate alumina parts. In general, it is agreed that diffusion of both aluminium and oxygen occurs by a vacancy mechanism. However, suitable doping is needed for oxygen diffusion. Basic parameters for solid-state alumina sintering were already known in the early 1960s (Coble, 1961, 1962; Coble, Song, Brook, Hendwerker, & Dynys, 1984; Phillips & Shiue, 1984; Shaw & Brook, 1986; Vasilos & Spriggs, 1963). Several articles reviewing early knowledge on alumina sintering can be found in the book edited by Kingery (Kingery, 1984). The contributions to two *International Conferences on Science and Technology of Alumina* are published in two special issues of the *Journal of the American Ceramic Society* (Elsässer, Heuer, Rühle, & Wiederhorn, 2003; French & Heuer, 1994), being the first of the issues dedicated to R.L. Coble, one of the greatest researchers in alumina, who set up the basis for the understanding of the sintering of alumina materials

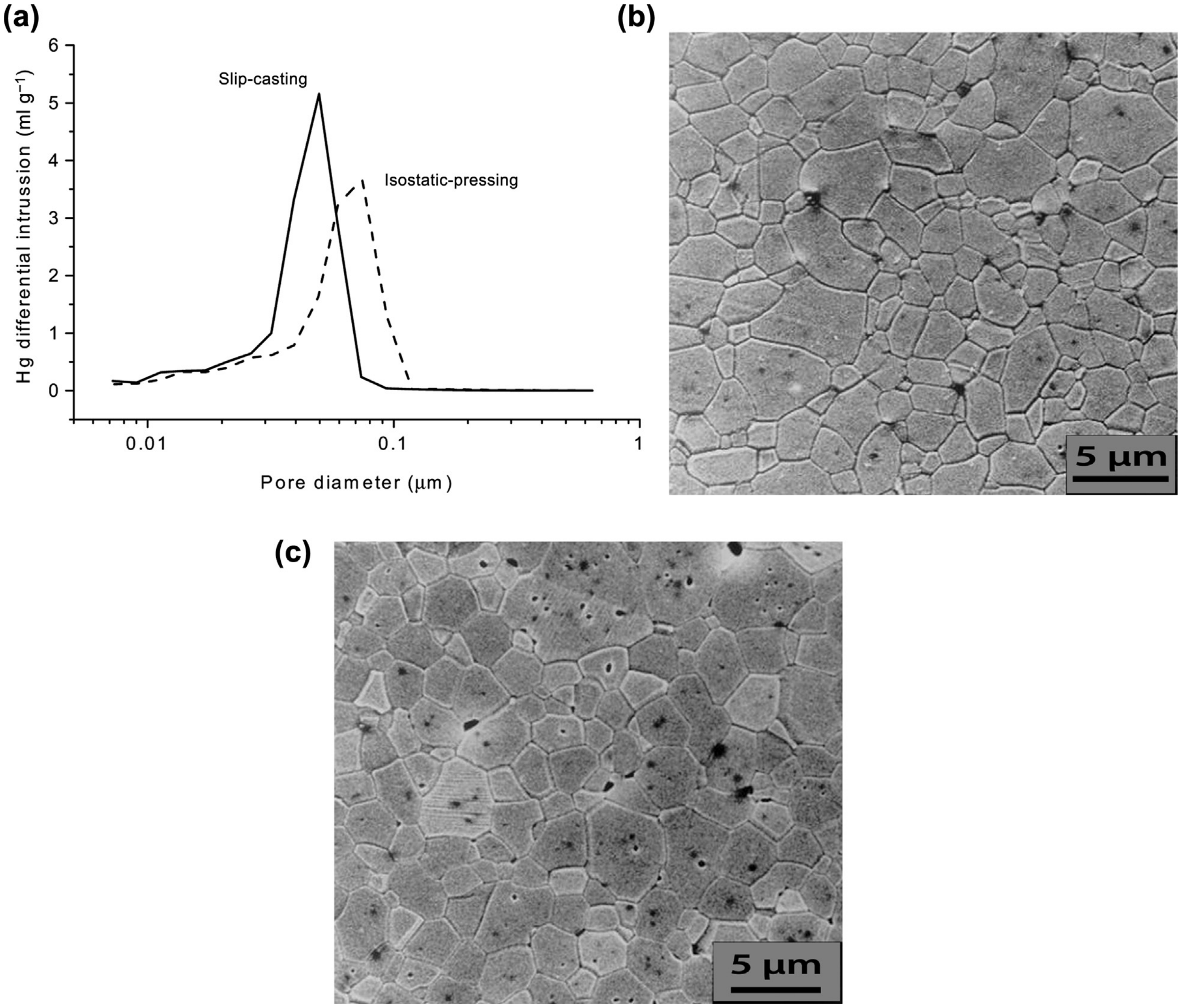

Figure 5 Effect of shaping method on the microstructural development of alumina green bodies from a powder with initial average grain size of 0.5 μm, without MgO addition. Sintering schedule: 1500 °C during 1 h, 5 °C/min heating and cooling rates. (a) Pore size distributions of the green bodies. (b) Microstructure of the sintered slip-cast material. (c) Microstructure of the sintered cold isostatic–pressed material. Exaggerated grain growth associated with pore trapping.

(Handwerker, Cannon, & French, 1994). The issue from 2003 is especially devoted to the advancements on diffusion and grain growth.

Two main processes occur during solid-state sintering: shrinkage (or densification) and coarsening. Surface diffusion, grain boundary diffusion, and lattice (or volume) diffusion are the main mechanisms for material transfer. Only the last two lead to shrinkage, whereas surface diffusion increases the interparticle contacts and decreases the surface curvature, eliminating smaller grains and reducing the sintering activity. Some additives can decrease the temperature needed for these processes to take place.

In Figure 6, the effect of surface diffusion at low temperatures in the microstructural evolution of alumina–titania (TiO_2) mixtures is observed (Uribe, 2001; Uribe & Baudín, 2000). Surface diffusion leads to the smoothing of the surfaces and the formation of necks between the particles. As a consequence, the specific surface area of the green body decreases and the mean pore diameter increases without changes in compact density.

Nowadays, it is generally agreed that densification in pure and relatively fine ($\approx$0.5–1 μm) alumina powders at moderate to high temperature is controlled by lattice diffusion of the Al^{3+} cations, with an activation energy $Q = 580$ kJ/mol (Rahaman, 2008). However, some works, dealing mainly with fine-grained powders, find sintering parameters compatible with grain boundary diffusion, which reveals the difficulty of performing

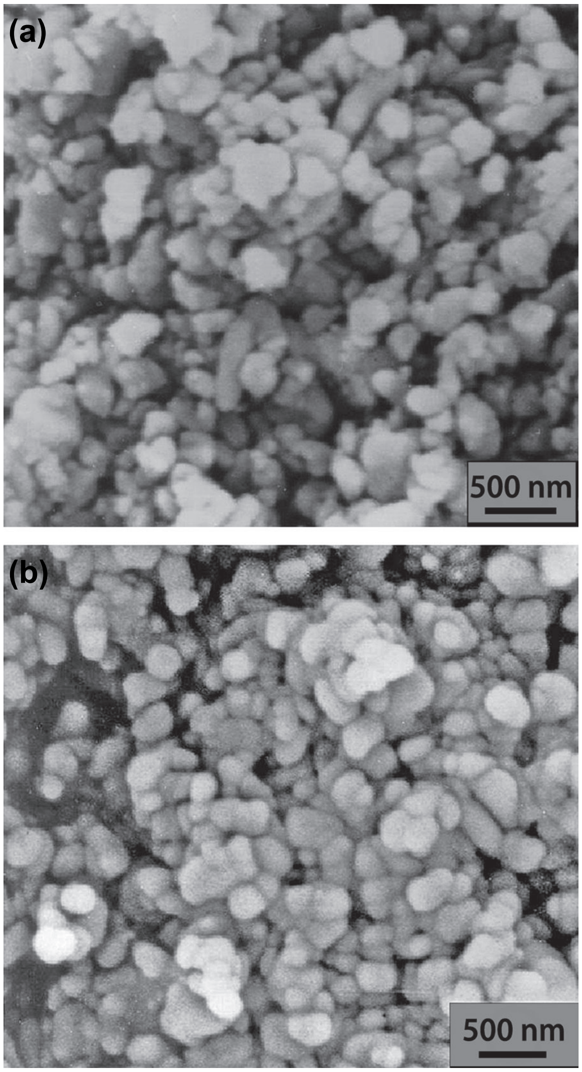

Figure 6 Evolution of the microstructure of an alumina–titania green compact during thermal treatment at low temperatures. Fracture surfaces observed by scanning electron microscopy. Relative density is the same for both stages (64%), and zero linear contraction was detected in a dynamic sintering experiment using a heating rate of 10 °C/min. (a) Green body. Average pore size (nm): 45 ± 1; specific surface area ($\times 10^3$ m^2/kg): 10.0 ± 0.5. (b) Body heated at 1050 °C for 0 h, heating and cooling rates 10 °C/min. Average pore size (nm): 68 ± 1; specific surface area ($\times 10^3$ m^2/kg): 6.0 ± 0.5.

accurate sintering tests with adequate green compacts (Bernard-Granger, Guizard, & Addad, 2007). Moreover, sintering of nanoparticles presents specific characteristics. In general, coarsening is the result of different processes taking place simultaneously. However, results indicate that in alumina, coarsening is dominated by surface diffusion, with activation energies in the range of 230–280 kJ/mol. In fact, in most ceramics, grain growth is controlled by drag of the attached porosity, the pores moving by surface diffusion of atoms (Harmer & Brook, 1981).

In the most idealized form of solid-state sintering, the powder compact is constituted by individual crystal grains that remain solid throughout the process. Atom movement leads to the reduction of the surface energy of the porous compacts, which is the driving force for sintering.

Basically, solid-state sintering is modeled in three following stages.

1. Initial: The individual particles are bonded together by the growth of necks between the particles and a grain boundary forms at the junction of the two particles.
2. Intermediate: Characterized by interconnected networks of particles and pores.
3. Final: The structure consists of space-filling polyhedra and isolated pores.

Real green compacts consist of assemblages of powder particles that are generally irregularly shaped and consist of a distribution of (or crystal) sizes. In some compacts, tens to thousands of individual crystals are grouped together into agglomerates in which the packed density is higher than the average density for the compacts (50–60% depending on the powder characteristics and the shaping method). The pore spaces formed among the imperfectly fitting particles typically have a bimodal or multimodal size distribution. Therefore, different simultaneous processes take place during sintering, which can lead to heterogeneous microstructural development (Dynys & Halloran, 1984; Nettleship & McAfee, 2003; Zheng & Reed, 1988). Kinetic field diagrams can be used to identify mechanisms interacting with shrinkage in order to establish improved temperature cycles for alumina sintering (Raether & Schulze, 2009).

2.02.4.2.1 Sintering without Pressure

In the conventional sintering process, the green body is subjected to the thermal treatment in the absence of other effects. Since the early 1960s, existing technology permits fabrication of dense alumina pieces by pressureless sintering with MgO (Coble, 1961, 1962; Phillips & Shiue, 1984; Shaw & Brook, 1986) or liquid-forming additives such as $CaSiO_3$ or SiO_2 (Phillips & Shiue, 1984).

Pure alumina is susceptible of exaggerated grain growth of a fraction of grains and associated pore detachment during pressureless sintering. As a consequence, wide distributions of grain sizes and isolated pores trapped within the largest grains might be present in the microstructure. The addition of small amounts ($\approx$0.5 wt%) of MgO allows the control of alumina grain growth and MgO-doped alumina can undergo normal grain growth to large sizes (>20 μm) without pore trapping inside the grains. The effect of MgO is clearly observed in **Figure 7** (Uribe, 2001; Uribe & Baudín, 2000) in which a comparison between an undoped and a doped material both green-processed and sintered in the same way is done. In the material without MgO addition (**Figure 7(a)**), the characteristic intragranular porosity evidencing exaggerated grain growth is observed, while no intragranular pores are present in the MgO-doped material (**Figure 7(b)**). There have been different and, even contradictory, explanations for the mechanisms of MgO controlling the grain growth of alumina (Bennison & Harmer, 1990; Gavrilov, Bennison, Mikeska, & Levi-Setti, 2003; Handwerker, Morris, & Coble, 1989). Nowadays, it is generally accepted that MgO-doped alumina sinters in the solid state.

$CaSiO_3$- and SiO_2-doped materials undergo liquid-phase sintering, which enhances anisotropic grain growth (Gavrilov et al., 2003; Rödel & Glaeser, 1990; Song & Coble, 1990). $CaSiO_3$-doped alumina is susceptible of exaggerated growth as undoped alumina. Small amounts of titania (TiO_2) can be used as an agent for alumina sintering enhancement and grain growth (Bueno & Baudín, 2006b; Chi, Gu, Wang, & Wang, 2003; Powers & Glaeser, 1997). Alumina grains experience elongated growth with calcium additions above the solubility limit, whose specific amount depends on sintering temperature and powder grain size (Altay & Gülgün, 2003; Jung & Baik, 2003; Sánchez Herencia et al., 2000).

Further aid for compact densification during sintering is the use of hydrogen or water-rich atmosphere to enhance the diffusion of the gas trapped in the closed pores during the final stages of sintering (Coble, 1962).

Sintered, high-purity, polycrystalline alumina is white to pale cream in color (due to trace metallic contamination) and is opaque, except as a very thin section. This opacity results from a very small amount of residual porosity. Translucent aluminas are prepared by solid-state sintering of cold-pressed submicrometer powders under controlled atmosphere and with the addition of small amounts of MgO ($\approx$0.5 wt%) (Brook, 1991). These materials with in-line transmissions ranging from $\approx$4 to 5% for grain sizes $\approx$ 60–100 μm (e.g., Tokoname, Oda, & Yamamoto, 1980) up to $\approx$15–20% for grain sizes $\approx$200 μm (Krell, Blank, Ma, Hutzler, & Nebelung, 2003) are widely used in high-pressure sodium vapor lamps because of their sufficient high temperature strength and resistance against attack by the sodium vapor. Optimized forms of cold-pressed alumina materials with controlled fine grains (<4 μm) might have strengths up to 500 MPa and are used as cutting tools (Whitney, 1994).

Based on the rate equations for densification and grain growth, a thermal treatment schedule that included fast firing up to a temperature higher than that necessary for densification using a conventional sintering treatment and a short stage ($\approx$min) at that temperature was proposed in the early 1980s (Harmer & Brook, 1981). For this method to be adequate, the activation energy for densification has to be higher than that for grain growth, as occurs in alumina. This hypothesis was confirmed with alumina doped with $\approx$200 ppm of MgO. Fast firing at 1850 °C during 10 min led to a dense and fine-grained alumina material.

A different procedure, initially proposed by Chen and Wang to obtain fully dense Y_2O_3 (Chen & Wang, 2000), includes a high-temperature short step, to reach an intermediate density, followed by a long

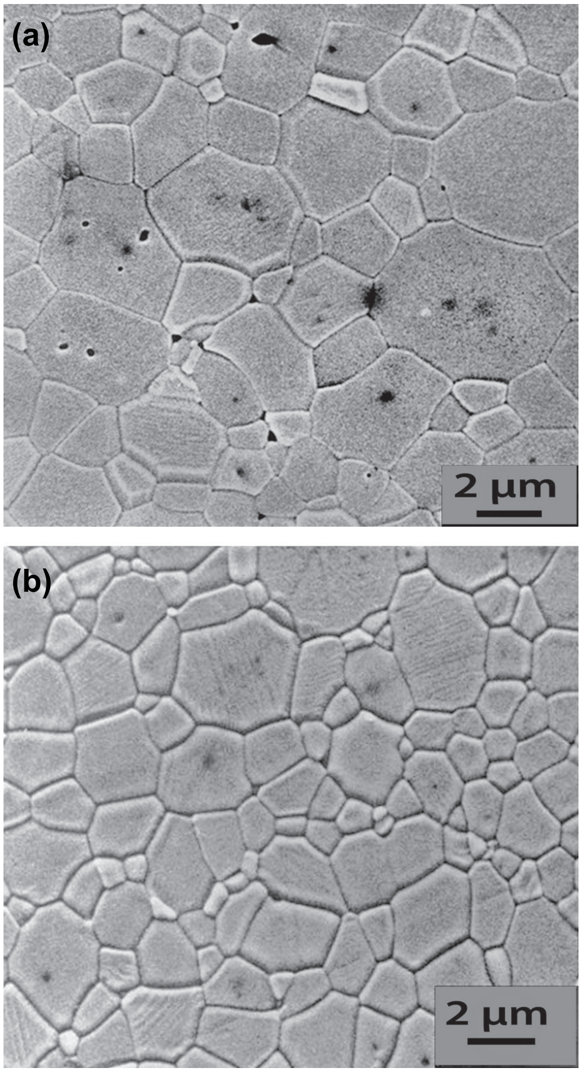

Figure 7 Effect of MgO in the microstructural development of alumina green bodies from a high-purity (99.9%) alumina powder with initial average grain size of 0.4 μm. Sintering schedule: 1500 °C during 1 h, 5 °C/min heating and cooling rates. Green compacts shaped by cold isostatic–pressing. (a) No MgO addition. Exaggerated grain growth associated with pore trapping. (b) 0.5 wt% of MgO. Normal grain growth with no pore trapping.

low-temperature step, to complete densification without grain growth. In order for this process to be adequate, the activation energy for densification should be lower than that for grain growth, which is not true for alumina. As described above, shrinkage of alumina occurs by lattice diffusion with higher activation energy than that for grain growth, which is dominated by surface diffusion. However, as already discussed, in compacts with extremely small particles (≈100–200 nm), the contribution of surface might be much more important than in the conventional (≈0.5–1 μm) ones. In fact, some authors have reported rather encouraging results in this respect (Bodisova, Sajgalik, Galusek, & Svancarek, 2007). Even though no significant improvement in density was obtained, the grain size was maintained under 1 μm, about 60% lower than that obtained for conventionally sintered alumina of the same density (≈98.8% of theoretical).

2.02.4.2.2 Pressure-Assisted Sintering

The application of a pressure during the thermal treatment allows reaching higher densities in shorter times and using lower temperatures while the microstructure retains small grain sizes.

When applying a pressure during sintering, shrinkage is accelerated by enhanced pressure generated at the contacts between the grains by the external pressure. However, there is no acceleration of the grain growth because there is no increase in pressure gradient across the grain boundary (Coble & Ellis, 1963). Since the early 1960s, existing technology permits fabrication of dense pieces by HP of undoped powders (Phillips & Shiue, 1984; Vasilos & Spriggs, 1963).

Comstock (Norton Company, 1952) described a method to obtain high-density alumina bodies by HP fine (98% of the particles under 2.5 μm and 50% under 1 μm) and high-purity (99%) alumina powder mixed with magnesium oxide (0.4 wt%) and cobalt oxide (0.9 wt%) additions. The reported temperatures (≈1650–1800 °C) were rather high as compared to those used nowadays, whereas the used pressures (≈24 kPa) were very low.

Pressure-assisted sintering of alumina is usually done uniaxially (usually named HP), by applying the pressure directly to the powder using a graphite die. However, special shapes cannot be fabricated by uniaxial pressing such as femoral heads for which isostatically applied pressure is necessary.

During HIP, an encapsulated starting powder or a pre-molded or pre-sintered shape with closed porosity is simultaneously subjected to both high temperature and high isostatic pressure using a gas as pressure transmitting medium. In principle, HIP materials would be fully isotropic because pressure is distributed isotropically.

In the ceramics field, initially, HIP was used as a reaction bonding method for non-oxide ceramics and the gas used was nitrogen. About 20 years ago, the HIP was introduced to manufacture alumina parts from nonencapsulated, presintered bodies. Helium, and later, argon due to cost reasons, substituted nitrogen to HIP oxide ceramics. Further research and development activity are focused on the application of O_2-HIPing and HIPing using and argon–oxygen gas mixture as pressure medium, which improves material properties as compared to those of materials processed in inert atmosphere (Bocanegra-Bernal, 2004).

Originally, HP and HIP were only used for high–added value components because they were rather expensive techniques limited to small-scale production. Nowadays, alumina-based cutting tool inserts are routinely fabricated using high-temperature pressing at reasonable prices (Whitney, 1994). Nearly full-density alumina materials with small and uniform grain size (≈0.5 μm) can be fabricated by HP (35–70 MPa) at 1200–1400 °C during very short times (≈min). Fluxing additives can be added to further accelerate densification. The implementation of improved processing of the raw materials, reducing inclusions, and the use of HIP have increased the density of hip femoral heads to 3.98 g cm^{-3} while reducing the average grain size to less than 1.8 μm (Huet et al., 2011; Kirchner et al., 1973). High-purity (≥99.5%) alumina femoral heads with near-zero porosity are fabricated by two- or three-step sintering including HIP of presintered and machined bodies sometimes followed by a final thermal treatment.

As previously discussed, high heating rates, applied pressures, and strain rates enhance the densification process while avoiding grain growth. Spark plasma sintering (SPS), or better named electrical field–assisted sintering, combines these processing parameters and is mainly useful for the efficient densification of nanosized ceramics. SPS is a uniaxial HP technique where extremely high heating rates (≈500–600 °C min^{-1}) are achieved by the application of a pulsed electrical current to a graphite die that contains the powder. Applied pressures are relatively low (≈100 MPa). The main advantage of SPS is that the particle-specific surfaces are preserved during sintering, contrary to the pressureless sintering. Therefore, under the applied load, the compact may benefit of the low-temperature mass transport mechanisms provided by the nanoparticle surfaces and interfaces. The short time at low temperature limits the surface diffusion–controlled grain growth. The local temperature gradients at interparticle contacts during high heating rate can be about 3–10 times higher than in low heating rate cycles.

SPS has been successfully applied for the densification of single-phase (Aman, Garnier, & Djurado, 2011; Gao, Hong, & Torre, 2000; Mishra, Risbud, & Mukherjee, 1998; Risbud et al., 1995; Shen, Johnsson, Zhao, & Nygren, 2002; Yao et al., 2011) and composite (Kim, Hiraga, Morita, & Yoshida, 2007; Zhan, Kuntz, Wan, Garay, & Mukherjee, 2002) alumina ceramics with submicrometric grain sizes. For instance, alumina materials with densities higher than 99.5% of theoretical and grain sizes of ≈290 nm to 3.2 μm have been fabricated with a high-purity (99.99%) starting powder (≈150 nm average grain size) using temperatures in the range of 1175–1400 °C and holding times of 6–10 min (Yao et al., 2011). An in-depth study (Aman et al., 2011) of SPS of high-purity (99.99%) α-alumina fine (≈170 nm) powders has demonstrated that for pressures around 80 MPa, relatively low heating rates (≈300 °C min^{-1}) are much favorable to achieve near-full density with fine-grained size at low sintering temperatures (≈1100 °C). The preforming of the green compacts as well as the SPS parameters have to be carefully selected as a function of the processed material to avoid differential sintering effects and attain full-density bodies (Aman, Garnier, & Djurado, 2009; Aman, Garnier, & Djurado, 2010; Jayaseelan, Ueno, Ohji, & Kanzaki, 2004; Mishra et al., 1998).

There are other special heating procedures under investigation and with specific application in the field of nanoceramics, such as microwave sintering. This method has been successfully used to sinter nanopowders of transitional aluminas to get dense and nanosized α-alumina bodies (Freim, Mckittrick, Katz, & Sickafus, 1994).

2.02.4.3 Textured Aluminas

Textured aluminas have received much attention because anisotropic growth and orientation of the grains can improve the material behavior by magnifying the anisotropic properties of the α-Al_2O_3 single crystal. Due to the anisotropic grain growth, related to the rhombohedral crystal structure with close-packed oxygen planes perpendicular to the c-axis, a variety of suitable processing methods have been proposed to reach preferred orientation in the bulk material. The highly textured microstructures drastically reduce the residual stresses developed during cooling from the sintering temperature associated with thermal expansion anisotropy. The degree of mechanical behavior improvement changes from one paper to another and no clear toughening has been identified, even though it is generally observed that the textured microstructure inhibits crack propagation in the through-thickness direction.

Textured aluminas are fabricated by a variety of processing methods, including high-temperature deformation (Ma & Bowman, 1991; Yoshizawa et al., 2004a, 2004b; Yoshizawa, Toriyama, & Kanzaki, 2001), application of a strong magnetic field during shaping using different methods as slip-casting (Suzuki, Sakka, & Kitazawa, 2001; Zhang, Vleugels, & Van der Biest, 2010) or electrophoretic deposition (EPD) (Uchikoshi, Suzuki, Okuyama, & Sakka, 2004), tape-casting (Hall, Swinnea, & Kovar, 2001), and templated grain growth (Carisey, Laugierwerth, & Brandon, 1995; Carisey, Levin, & Brandon, 1995; Seabaugh, Kerscht, & Messing, 1997; Suvaci & Messing, 2000).

It has been recognized that the templated grain growth processes are the most effective. In these processes, template particles are uniformly distributed through a fine powder and the templates are aligned during forming, by either tape-casting or uniaxial-pressing. While sintering proceeds, the oriented template grains grow preferentially by consuming the fine and nonoriented matrix grains. The final microstructure consists of grains with an orientation distribution that is determined by the initial placement and alignment of the template particles. Figure 8 shows examples of textured microstructural development of alumina obtained by template grain growth (Pavlacka & Messing, 2010); the plate-like alumina grains are oriented. Template particles have to be larger than those of the matrix (preferably at least 10 times larger) because the size difference is the driving force for preferred growth (Suvaci & Messing, 2000) and should have a large aspect ratio because most forming processes use shear stresses for template alignment. During sintering, the template particles act as rigid inclusions, impeding shrinkage; thus, sintering aids such as liquid-forming additives have to be added. For instance, full densification has been reached with mixtures of CaO and SiO_2 (Pavlacka & Messing, 2010; Seabaugh et al., 1997). Major problem of this approach is that a residual glassy phase remains at the grain boundaries of the sintered material. Improvements in processing, including higher aspect ratio templates and increased template loading, have permitted a significant reduction in the proportion of liquid-forming dopant and, consequently, the remaining glass in the sintered material (Pavlacka & Messing, 2010).

2.02.4.4 Reaction-Bonded Alumina

Reaction-bonded aluminium oxide (RBAO) was introduced by Claussen and coworkers (Claussen, Wu, & Holz, 1994; Holz, Wu, Scheppokat, & Claussen, 1994) in the 1990s as a means to fabricate alumina and alumina–zirconia-based composites, and this was further developed by other authors (a review can be found in Watson, Chan, Harmer, & Caram, 2005). This process presents advantages such as high green strength, tailorable shrinkage, and high final density. RBAO has three main steps: powder preparation, shape forming, and reaction bonding. Precursor powders typically contain 30–80 vol% of aluminium, 0–20 vol% ZrO_2, and the remainder is Al_2O_3. The mixture of powders is wet-milled down to 1–2 μm, dried, and sieved. Afterward, any powder-shaping technique can be used to prepare the porous pre-form, generally cold uniaxial– or isostatic-pressing. The green compact is then treated in oxidizing atmosphere to oxidize the aluminium. Important parameters controlling the RBAO process are Al content, particle size, and green density. Successful fabrication of high-strength bodies requires fine and homogeneous powders. Low milling intensity does not lead to the required particle fineness, whereas overmilling causes extensive oxidation and hydrolyzation of Al. Oxidation of Al during milling is enhanced by ZrO_2 additions. As Al should be mainly oxidized by solid/gas reaction, the size

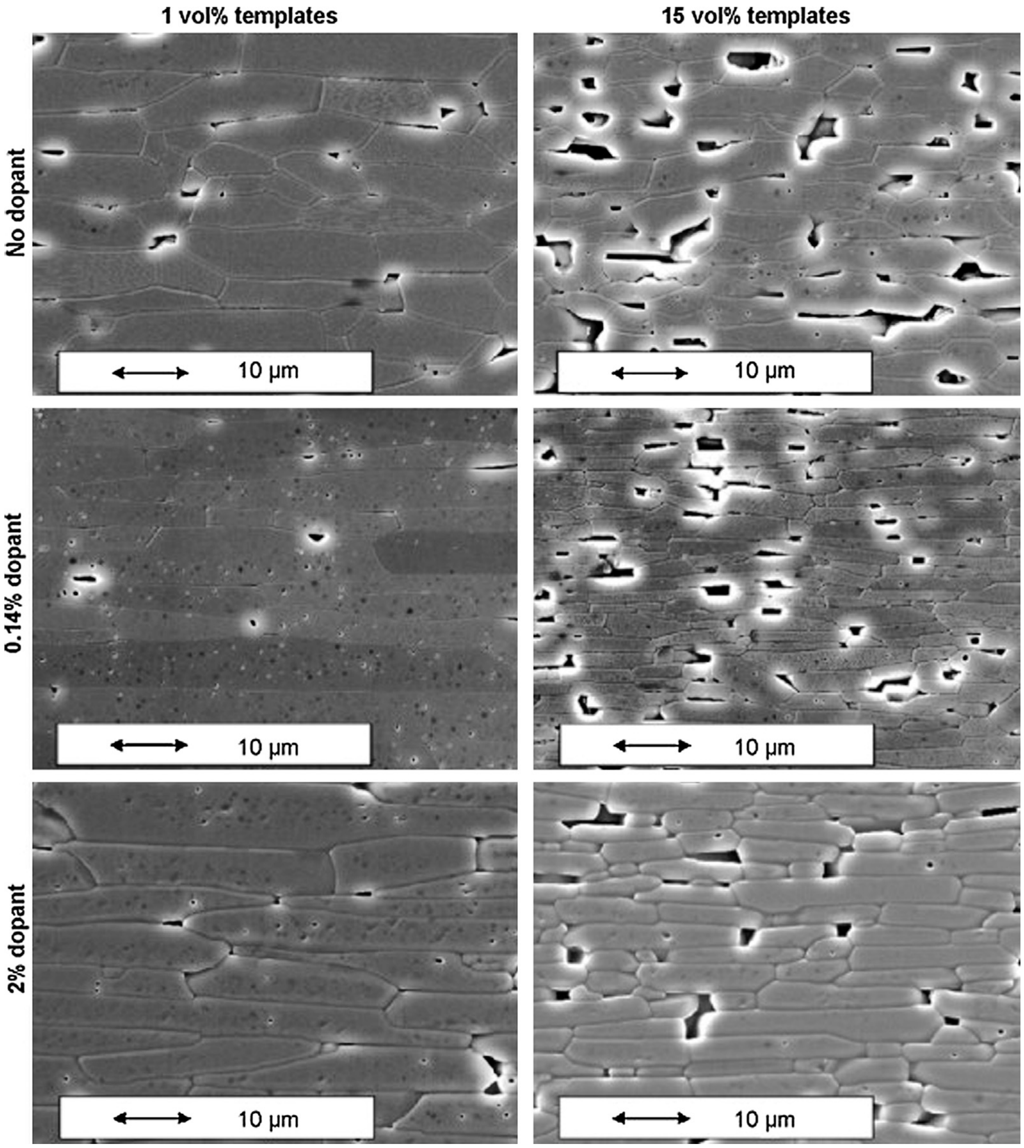

Figure 8 SEM micrographs showing the microstructures of textured aluminas fabricated using different dopant ($SiO_2 + CaO$) concentrations and template loadings. Pavlacka and Messing (2010).

of the fabricated parts is limited. This process has also been used for template growth processing as described before.

2.02.4.5 Aluminas with Submicronic Grain Sizes

2.02.4.5.1 Processing of Nanoparticles

Nanostructured materials, in which the particles of at least one of the constituent phases have nanometric sizes, have attractive new properties linked to the high density of grain boundaries and interfaces that result from the nanoscaled structure. These expected new properties together with the potential of nanoparticles to fabricate submicron-sized sintered materials has led to the extensive study of the processing of nanoparticles to form green bodies and the sintering procedures.

In principle, ceramic nanopowders would permit the use of low sintering temperatures, thus keeping small grain sizes in the sintered body (Chaim, Levin, Shlayer, & Estournes, 2008). As discussed before, main issue for adequate sintering is to start with a high density and homogeneous green body, which is not evident when dealing with nanoparticles due to their high–specific surface areas. Forming methods for very fine powders have been oriented for some years toward colloidal processing, which has been proved more adequate than pressing or sol–gel methods to fabricate ceramic pieces. In the case of alumina, most work has been done on transition aluminas. Bowen and Carry (2002) published a comprehensive review on colloidal processing of nanoparticles, where most issues about the processing of transition aluminas are discussed. For transitional alumina systems, the control of the transformation into the stable phase avoiding explosive grain growth was demonstrated to be the most difficult step toward fully dense, nanograined ceramics. On the contrary, encouraging results for stable crystalline forms were reported by these authors in their review paper.

Much of the posterior research on the processing of nanoparticles did not give the successful results predicted by Bowen and Carry. The preparation of high solid content, stable and low-viscosity slurries of nanoparticles to be the starting point for shaping is not so evident. The small size and large specific surface areas of nanoparticles result in very high–viscosity suspensions for solid contents often lower than 20 wt% (Lu & Kessler, 2006; Tseng & Wu, 2002). Therefore, although some authors have reported suspensions up to 50 vol% of solids and relatively low viscosities (Studart, Amstad, Antoni, & Gauckler, 2006), the more usual low values of solid contents admissible are not enough to obtain ceramic pieces with high green densities. Special sintering procedures such as SPS are then required for densification (Shen et al., 2002; Zhan et al., 2002).

More recent works (Azar et al., 2008) devoted to the fabrication of nanosized alumina investigated the effect of the shaping method (slip-casting or pressing) on particle packing and its consequent effects on the phase transformations and the sintering behavior of a transition alumina powder constituted by a mixture of δ- and γ-alumina. Electrostatic dispersion was used to prepare the slips. Slip-cast bodies, with homogeneous distribution of porosity, limited the formation α-Al_2O_3 with hard agglomeration or vermicular morphology and allowed sintering without pore trapping. However, maximum attained density was 98% of theoretical and temperatures as high as 1700 °C had to be applied with associated grain growth.

By also using electrostatic dispersion to prepare the slips, Franks and coworkers have studied the effect of particle size (11, 44, 190, and 600 nm) on both processability (rheological behavior) and microstructure (density and grain size) of the sintered materials using slip-casting (Tallon, Limacher, & Franks, 2010). Additionally, they have performed a careful study on the ζ potentials of the alumina particles as a function of particle size, volume fraction, and electrolyte concentration, keeping the viscosity of the suspensions at constant (Jailani, Franks, & Healy, 2008). From these works, it has been concluded that the electrical double-layer approach is not successful in producing low-viscosity, high-volume, fraction-stable suspensions of nanoparticles and associated high-density sintered materials. These results suggested the necessity of developing new dispersants for high-volume-fraction nanoparticle suspensions based on steric repulsion, thus opening new possibilities for the processing of nanoparticles.

2.02.4.5.2 Processing of Submicronic Powders

The need of real nanostructures for improving the mechanical performance of ceramics is limited to very special conditions, and most technical advances require controlled and dense submicrometer microstructures rather than nanostructures. Even though the hardness of Al_2O_3 increases from grain sizes of 5 μm down to 0.5 μm (Section 2.02.1.2), in the submicrometer range, this favorable influence of grain size decreases because of a growing (and counteracting) influence of the network of grain boundaries. In fact, nanomaterials exhibit a decreasing resistance to microplasticity. Consequently, in order to maintain the desirable high hardness of alumina, grain size should be kept over 100 nm.

To obtain a dense microstructure with submicrometer grain size, the process must start with powders of still smaller particle size, but it is not obliged to work with nanoparticles. A very interesting and relatively new approach is to work with particles in the range of 100–300 nm, instead of dealing with nanoparticles. As occurs, when larger particle sizes are being considered, main point to reach homogeneous and dense microstructures is to avoid agglomerates in the green body as they locally hinder homogeneous densification. In this sense, it is better to work with coarser powders with lesser tendency to agglomerate (≈200 nm) than with finer ones (≈40–60 nm). Once agglomeration is avoided, optimum sinterability for particle sizes in the range of 150–200 nm is associated with adequate particle coordination in the green body. This is later characterized by the following features of the pore size distribution, as given by Krell and Klimke (2006): (1) absence of "larger" pores (>0.5 of the average particle size), (2) narrow width of the main body of the pore size distribution (a steep slope at the center of the distribution), and (3) close particle spacing (a small average pore size close to 1/5 particle size).

As proposed and reviewed by Krell (Krell, Blank, Ma, Hutzler, & Nebelung, 2003; Krell & Klimke, 2006), a number of different approaches like dry- (preferentially cold isostatic) pressing and various wet-shaping methods followed by pressureless sintering have turned out applicable not only for obtaining small samples with submicrometer microstructures but also for providing larger sintered corundum components with grain sizes of 0.5–0.6 μm at relative densities >99.5%. These materials present high hardness (≈20 GPa) and sufficient strength (650–850 MPa in 3-point bending and 550–650 MPa in 4-point bending) (Krell et al., 2003) to be used in high-responsibility applications.

Furthermore, the use of submicronic powders (≈200 nm) and the substitution of dry iso-pressing by a colloidal pressing approach to improve the particle coordination of green bodies can lead to a decrease in the sintering temperature by 200–250 °C (Yu & Lange, 2010), with the associated decrease in grain growth. Similar conclusions were found by Franks and coworkers in one of the works referred above (Tallon et al., 2010). These authors found that particles with sizes ranging from 100 to 300 nm were adequate for slurries with low viscosity and high volume fraction of solids, to produce slip-cast green bodies of sufficiently high green density to reach ful density (99% of theoretical) and homogeneous microstructures once sintered. These results were much better than those obtained with smaller particles (11, 44 nm). In addition, they found that particles larger than about 300–500 nm can produce low-viscosity suspensions and high–green density bodies, but they do not have sufficient specific surface area to drive successful densification.

For some specific applications, pore-free ceramics with grain sizes in the nanometer range will be required. Such materials promise to have unprecedented optical, mechanical, and electrical properties for use in lasers, health care, and electrical devices. In principle, full density to over 99.9999% of theoretical and grain size refinement below 100 nm will change the dominant light-scattering mechanism in alumina, allowing the material to become transparent. However, to reach such microstructure, it would be needed to start from nanosized powders that tend to agglomerate and experience very large shrinkage during sintering, and even the smallest defect would have to be avoided during the green processing (Messing & Stevenson, 2008).

Nevertheless, in-line transmissions much higher than the maximum (15–20%) for sintered, coarse-grained (≈200 μm) corundum (Section 2.02.4.1) have been reported for aluminas with grain sizes ≤1 μm and densities >99.9% of theoretical. Decreasing the grain size and the residual porosity of high-purity alumina down to 0.27 μm and 0.03%, respectively, by controlling the SPS parameters allows reaching in-line transmission of

Figure 9 High-transmittance aluminas fabricated from high-purity (99.99%), submicronic ($d_{50} = 0.2$ μm) powders by aqueous colloidal processing. Courtesy of Mata-Osoro et al. (2012). (1) Sintering at 1400 °C for 2 h in vacuum followed by HIP. (2) Sintered at 1500 °C for 2 h in vacuum followed by HIP. (3) Sintered at 1350 °C for 50 h in vacuum. (4) Sintered at 1600 °C for 50 h in vacuum.

47% (Kim et al., 2007). Aman and coworkers have studied the influence of the green state and the SPS parameters in translucency of alumina (Aman et al., 2009) and reached values of in-line transmission ≈40% for high-density (>99.97% of theoretical) materials with grains of about 1 μm. For the same specimen thickness (0.8–1 mm), in-line transmissions in the range of 50–79% depending on grain size (0.34–0.50 μm) and surface preparation have been reported by Krell et al. for slip-cast and hot-pressed or gel-cast, pressureless, sintered and hot-pressed high-purity alumina of 150 nm starting size (Krell et al., 2003; Krell et al., 2003; Krell, Hutzler, & Klimke, 2009). Alternatively to SPS, vacuum sintering followed by post-HIP has been used to reach aluminas with high transmittance, as shown in Figure 9 (Mata-Osoro, Moya, & Pecharromán, 2012).

In addition to high transmittance, all these materials present high strength and hardness; thus, alumina has promising applications as windows, transparent armor, and bulbs of high-pressure metal halide lamps.

2.02.5 Fabrication of Alumina-Matrix Composites

2.02.5.1 Alumina-Oxide Composites

2.02.5.1.1 Alumina–Zirconia Micro and Nanocomposites

The alumina–zirconia system is by far one of the most investigated and promising system for ceramic composites. The most studied compositions are constituted by alumina Y_2O_3—stabilized zirconia (3 mol% of Y_2O_3, 3YTZP). A large number of studies have demonstrated their improved mechanical behavior (Casellas, Rafols, Llanes, & Anglada, 1999; Cesari, Esposito, Furgiuele, Maletta, & Tucci, 2006; Chevalier, Grandjean, Kuntz, & Pezzotti, 2009; Choi & Bansal, 2005; Magnani & Brillante, 2005; Tuan, Chen, Wang, Cheng, & Kuo, 2002) and thermal properties (Bansal & Zhu, 2005) compared with those of monophase alumina. These materials combine the outstanding properties of alumina, i.e., hardness, chemical inertness, and wear resistance, with improved fracture resistance. Therefore, they could be used extensively in machining and cutting applications (Mandal et al., 2011; Smuk, Szutkowska, & Walter, 2003) as well as in fabricating biomedical implants (Chevalier et al., 2009; Insley et al., 2002; Piconi & Maccauro, 1999; Rahaman, Yao, Sonny Bal, Garino, & Ries, 2007). Transformation of the small (<0.5 μm), stabilized, tetragonal zirconia to monoclinic in the stress field of the propagating crack is assumed to be the main toughening mechanism in most of the works. However, no evidence of transformation in the crack propagation zone of fracture surfaces of indentation strength specimens has been found (Baudín, Gurauskis, Sánchez-Herencia, & Orera, 2009). In fact, optimum behavior is reached with scale reduction of the microstructure, which hinders transformation. The compressive residual stresses developed in the alumina matrix due to thermal expansion mismatch between 3YTZP and alumina together with the refinement of the alumina microstructure due to the presence of zirconia can be partially responsible for the improved strength of these composites. Moreover, transformation occurs due to shear under the indent, which might improve the wear behavior. Composites with fine-grained alumina matrices (≤3 μm) containing 5–50 vol% of fine-grained 3YTZP ($d_{V50} \approx 0.3$–0.4 μm) have been reported. In general, colloidal mixing of the powders followed by spray drying and pressing, slip-casting, or stacking of tape cast layers by pressing have been used to shape these kind of composites. The green bodies are thermally treated by pressureless sintering, followed by HIP for high-responsibility parts.

There also exists zirconia-toughened alumina (ZTA) composites in which zirconia is not stabilized. Best properties are expected from micro-nano composites in which nano-zirconia particles are embedded in a micron-sized alumina matrix due to improved slow crack growth resistance and stability (de Aza, Chevalier, Fantozzi, Schehl, & Torrecillas, 2002).

To reach the maximum performance of ZTA, investigations have been focused on the severe control of the initial powder characteristics, such as particle size and shape and homogeneity of the phase mixture, to reach controlled final grain size and morphology. In particular, special routes different from the simple powder mixing are needed, which include specific steps for powder synthesis before fabrication of the ceramic body. Several methods have been proposed to prepare intimate mixtures of alumina–zirconia nanopowders, including chemical vapor synthesis (Srdic, Winterer, Miehe, & Hahn, 1999), thermal decomposition of mixed salts (Chandradass, Yoon, Bae, 2008a, 2008b; Kikkawa, Kijima, Hirota, & Yamaguchi, 2002), calcination of an emulsion precursor (Chandradass & Bae, 2009), sol–gel (Jayaseelan, Nishikawa, Awaji, & Gnanam, 1998; Sarkar, Adak, & Mitra, 2007; Sarkar, Mohapatra, Ray, Bhattacharyya, Adak, & Mitra, 2007; Srdic & Radonjic, 1997), solution combustion synthesis (Biamino, Fino, Pavese, & Badini, 2006), and hydrothermal synthesis (Chandradass et al., 2008a, 2008b). Hydrothermal synthesis seems to be one of the most adequate methods for nanopowder production but it lacks efficiency. In order to improve its kinetics, microwave heating has been proposed and successfully used for the synthesis of different nanopowders, as described elsewhere (Prete, Rizzuti, Esposito, Tucci, & Leonelli, 2011).

A specific approach to reach micro-nanocomposites is to cover alumina grains by a zirconia precursor. After thermal treatments, zirconia nanocrystals strongly bonded to the alumina surface are developed. Initially, zirconium alkoxide was used as the precursor (Schehl, Diaz, & Torrecillas, 2002). This route has been simplified by working in aqueous medium with inorganic zirconium salts (Naglieri, Joly-Pottuz, Chevalier, Lombardi, & Montanaro, 2010; Palmero, Naglieri, Chevalier, Fantozzi, & Montanaro, 2009). Adequate thermal treatments of the powders followed by colloidal powder processing and shaping have permitted to fabricate alumina–zirconia composites with high reliability (Chevalier et al., 2011; Naglieri et al., 2010). The same procedure has been used to fabricate bi- and tri-phase composites in the system alumina–$Y_3Al_5O_{12}$–ZrO_2 system with homogeneous and fine microstructures (Palmero et al., 2012).

2.02.5.1.2 Alumina–Aluminium Titanate

Alumina (Al_2O_3)–aluminium titanate (Al_2TiO_5) is one of the most versatile systems in terms of mechanical performance due to the wide range of different microstructures and behaviors resulting from the extreme stresses that can be developed during cooling from the sintering temperature.

Aluminium titanate presents large crystalline thermal expansion anisotropy ($\alpha_{a25-1000\ ^\circ C} = 10.9 \times 10^{-6}\ ^\circ C^{-1}$, $\alpha_{b25-1000\ ^\circ C} = 20.5 \times 10^{-6}\ ^\circ C^{-1}$, $\alpha_{c25-1000\ ^\circ C} = -2.7 \times 10^{-6}\ ^\circ C^{-1}$; Taylor, 1984b). Therefore, stresses are originated by the thermal expansion mismatch between aluminium titanate and alumina as well as between grains of each phase with different orientations and can be very different depending on the particular orientation between grains. Moreover, cracking of the material might take place depending on the grain sizes.

Starting from alumina and aluminium titanate powders, different flaw-tolerant microstructures have been processed. Duplex and partially microcracked microstructures have been fabricated using wet ball milling in organic fluid, spray-drying, and uniaxial-pressing followed by isostatic-pressing and sintering (Padture, Bennison, & Chan, 1993). Drying of aqueous-stable slurries, crushing the cake, and uniaxial-pressing followed by isostatic-pressing and sintering were used to fabricate homogeneous microstructures with aluminium titanate grain sizes up to 14 μm. For constant aluminium titanate content (20 vol%), the degree of cracking of the microstructure depended on the aluminium titanate grain size that was tailored by the time period at the maximum sintering temperature (Runyan & Bennison, 1991). Alumina–aluminium titanate microcracked composites with aluminium titanate amounts up to 20 vol% were fabricated using extrusion as shaping method. Stable slurries of mixtures of alumina and aluminium titanate, which was obtained by sol–gel method, were extruded using boehmite gel as a binder, dried, and sintered (Ananthakumar & Warrier, 2001). A strict control, of the initial particle size, green processing by attrition milling in organic medium and pressing allowed to reach homogeneous and uncracked microstructures with improved toughness and unchanged strength (Uribe & Baudín, 2003).

A more attractive way to fabricate alumina–aluminium titanate composites in terms of energy saving is by the reaction sintering of alumina and titania (TiO_2) mixtures. Most resultant microstructures obtained by this method display low as-fired densities, abnormal grain growth, and even unreacted titania particles (Bartolome, Requena, Moya, Li, & Guiu, 1996; Bartolome, Requena, Moya, Li, & Guiu, 1997) due to the special characteristics of the alumina–titania reaction process. Completely reacted, homogeneous uncracked, and dense alumina–aluminium titanate (up to 10 vol%) composites were prepared by strict control of the rheology of aqueous suspensions, slip-casting, and sintering (Bueno, Moreno, & Baudín, 2004).

2.02.5.2 Alumina–Non-oxide Composites

2.02.5.2.1 Alumina-TiC

Commercially available cutting tool materials belonging to the group of carboxide ceramics consist of alumina with additions of 30–34 vol% titanium carbide and/or titanium nitride (Whitney, 1994). The dispersion of these hard particles increases the hardness at temperatures up to 800 °C. Fracture toughness is improved due to crack deflection and bowing by these non -penetrable particles. In addition, thermal conductivity is increased and thermal expansion is lowered, improving the thermal shock resistance of the matrix (El Hakim, Abad, Abdelhameed, Shalaby, & Veldhuis, 2011). Alumina and TiC powders of high purity and fine size (<1 μm) are used to fabricate these composites. The homogeneous mixing of the ceramic powders together with the binder is done by dry- or wet-milling, followed by drying when necessary. As the presence of a compound with high bond energy as TiC hinders densification during the thermal treatment, relatively low densities are obtained by pressureless sintering (e.g., Cutler, Hurford, & Virkar, 1989). Therefore, the simultaneous application of pressure and temperature is required to reach full density (Burden, Hong, Rue, & Stromborg, 1988). Originally, graphite dies were used to treat the pieces at temperatures of 1600–1750 °C under pressures of 200–300 bar. HIP methods were introduced to work at pressures up to 200 MPa by using inert gas media (N_2 or Ar; Bocanegra-Bernal, 2004). HIP requires the piece to be hermetically sealed or pre-sintered to 94% minimum density and completely closed porosity to prevent penetration of the gas. Alternative methods to this procedure with two different sintering steps, pressureless sintering and HIP, are being investigated. For instance, microwave-induced combustion synthesis followed by pressureless sintering at 1900 °C has been proposed (Kitiwan & Duangduen, 2007); however, the performance of the produced inserts is still significantly lower than that of the commercial ones.

2.02.5.2.2 Alumina-SiC Whiskers

The reinforcement of alumina with single-crystal silicon carbide whiskers is one of the most recent developments for alumina ceramics accepted by the industry. Two toughening mechanisms that drastically increase the matrix fracture toughness ($\approx$2.5 times) act in these composites: crack deflection and whisker pull out (Becher & Wei, 1984; Homeny & Vaughn, 1990). The surface chemistry of the whiskers has a major impact on the fracture toughness of the composites because it determines the characteristics of the interfacial matrix–whisker bonding and, consequently, the interactions of the crack with the microstructure. The presence of silicon oxicarbides and free carbon is associated with better performance (Homeny, Vaughn, & Ferber, 1990). As occurs for alumina–TiC composites, thermal conductivity is increased and thermal expansion is decreased with the corresponding increase in the thermal shock resistance.

Alumina–SiC_w composites might contain up to about 45 vol% whiskers, which are a mixture of the α- and β-phases of SiC. Whiskers are monocrystals that range from 0.05 to 1 μm in diameter and from 5 to 125 μm in length. Therefore, mixing of the submicronic alumina powder matrix with this second phase of high aspect ratio is one of the main concerns of their processing. In fact, main defects in these composites are whisker clusters and associated large pores, or whisker-deficient sites composed mainly by matrix, both due to insufficient dispersion of the mixture during powder processing (Shalek, Petrovic, Hurley, & Gac, 1986).

Once mixing is reached, the shaping procedure is fundamental to avoid segregation of particles during consolidation. Initially, processes such as slip-casting or low-speed centrifugal-casting of stable slurries followed by conventional sintering in flowing nitrogen was proposed (Sacks, Lee, & Rojas, 1988); however, maximum attained densities were extremely low (e.g., $\approx$92% for just 5 vol% whiskers). Nowadays, stable slurries are obtained and granules with the homogeneous and uniform packing structure are formed by spray-drying. In order to optimize the sintering behavior, direct contact between the whiskers in the granules has to be avoided.

Alumina–SiC_w composites present an even increased difficulty of sintering with a high bond energy second phase (described for alumina–TiC composites) due to the shape of the whiskers. Therefore, HP (Becher & Wei, 1984; Homeny & Vaughn, 1990; Shalek et al., 1986) or HIP (Bocanegra-Bernal, 2004) is required for whisker loadings from 10 to 40 vol%. Hot uniaxial-pressing is highly adequate to fabricate cutting tools as it generally results in very high–density (<2% porosity) small ($\approx$2 cm) parts. This process leads to whisker orientation in direction perpendicular to the applied pressure, even for randomly oriented whiskers in the green body (Wei & Becher, 1985). As a consequence, most whisker-reinforced cutting tools have anisotropic properties.

Recently, the application as a microwave absorber has sparked renewed scientific interest and research on the Al_2O_3–SiC_w composites due to their electrical response (Bertram & Gerhardt, 2011). For microwave applications, a relatively large number of sizeable ceramic rods ($\sim$30 cm long and 8–14 mm wide) are needed and the mechanical requirements are much lower than required in the case of cutting tools. Therefore, extrusion followed by pressureless sintering has been proposed as the adequate processing route (Bertram, Gerhardt, & Schultz, 2011).

2.02.6 Fabrication of Alumina-Based Laminates

In the last decades, new strategies fundamentally different from the conventional "flaw elimination" approach of monolithic ceramics have emerged, which are directed to achieve "flaw tolerance". Advances in processing technology have made it possible to produce structures in which the layered architecture combining materials with different properties leads to a laminate with mechanical behavior superior than that of the individual constituents. Large effort has been devoted to the fabrication of alumina-based laminates in order to combine

Table 4 Colloidal shaping methods for alumina-based laminates and associated ranges of layer widths

Shaping method	*Layer widths (μm)*
Tape-casting	100–500
Slip-casting	200–1000
Centrifugal-casting	10–100
Dip coating	1–10
Electrophoretic deposition	1–100

the desirable properties of alumina, particularly hardness and chemical inertness, with high strength and/or flaw tolerance. There are several reviews about design, properties, and processing of ceramic laminates (Bueno & Baudín, 2007b; Chan, 1997; Clegg, 1998; Sánchez-Herencia, 2007).

One large group of ceramic laminates is designed on the basis of the development of residual stresses between the layers during cooling from the sintering temperature. A number of different alumina–zirconia laminates have been designed on this basis. Major limit for them is the degradation of the mechanical behavior when the temperature of use goes up to that of stress relaxation. As a consequence, residual stresses free-layered materials combining high stiffness external layers with weak interfaces or flaw tolerant internal layers have also been developed. Alumina–aluminium titanate, alumina–calcium hexaluminate, and alumina–alumina laminates have been designed using this approach. Depending on the specific structure, high strength and/or flaw tolerance can be obtained, once the adequate sequence of layers of controlled thickness and composition is assured.

As it is described in the following, colloidal processing routes involving the direct shaping of slurries are the most routes used to fabricate alumina-based multilayer ceramics (Tables 3 and 4). In a much lesser extent, dry-pressing has also been used. Alumina–calcium hexaluminate (An, Chan, Padture, & Lawn, 1996) and alumina–zirconia laminates (Wang & Hu, 1996) have been fabricated from green structures shaped by pressing.

When tape-casting followed by stacking the green cast tapes is used, the adequate sequence of tapes for the desired structure has to be stacked before sintering. Suitable methods are cold-pressing, when aqueous slurries are used (Bueno, Moreno, & Baudín, 2005; Gurauskis, Sánchez-Herencia, & Baudín, 2007; Sánchez-Herencia, Gurauskis, & Baudín, 2006) and warm-pressing, for organic slurries (Davis, Kristoffersson, Carlstrom, & Clegg, 2000; de Portu, Micele, & Pezzotti, 2006; Lambrinou et al., 2007; Ma, Wanga, Weng, & Tan, 2004; Mawdsley, Kovar, & Halloran, 2000; Russo, Harmer, Chan, & Miller, 1992; Toschi et al., 2003).

Other techniques imply the direct sequential shaping of stable slurries with specific compositions to form the layers. Sequential centrifugal-casting (Moon, Bowman, Trumble, & Rödel, 2001; Sbaizero & Lucchini, 1996), sequential slip-casting (Bermejo, Baudín, Moreno, Llanes, & Sánchez-Herencia, 2007; Bermejo, Sánchez-Herencia, Llanes, & Baudín, 2007; Bueno & Baudín, 2007a; Bueno & Baudín, 2009; Rao, Rödel, & Lange, 2001; Rao, Sanchez-Herencia, Beltz, McMeeking, & Lange, 1999), and EPD (Ferrari, Bartret, & Baudín, 2009; Ferrari, González, Moreno, & Baudín, 2006; Sarkar, Prakash, Wang, & Nicholson, 1994) have been widely used.

In all cases, the thicknesses of the layers are adjusted by controlling the specific processing parameter associated with each technique (e.g., casting time for slip-casting or blades gap for tape-casting). A broad spectrum of layer thicknesses can be obtained by the adequate selection of the specific shaping technique, as summarized in Table 4. The lower limit for tape-casting is ≈25–100 μm and the higher limit is ≈400 μm; thicker layers can be obtained by stacking layers of the same composition together. Typical slip-casting thicknesses are ≈100–400 μm, and by centrifugal-casting, it is possible to go down to 10 μm. Combination of techniques such as dip coating slip-cast tapes in binder-containing slurries (Nicolaidis, Gurauskis, Baudín, Moreno, & Sánchez-Herencia, 2008) or deposit layers by electrophoresis on presintered slip-cast tapes (Ferrari et al., 2009; Ferrari et al., 2006) and further lamination and sintering allow the fabrication of structures with layers of extremely different sizes. The range of layer widths that can be obtained by EPD is very broad (≈1–10^2 μm; Ferrari, Sanchez-Herencia, & Moreno, 1998a, 1998b), and it is possible to locate very thin-layered structures between the load bearing thicker layers that constitute the laminate (Ferrari et al., 2009; Ferrari et al., 2006).

As the final material is obtained by sintering a green laminate structure, the heat treatment has to be suitable for the compatible sintering of layers with different compositions and/or microstructures. Symmetric laminates are preferred to avoid curvature during sintering. In general, no reaction between the layers is desired, so

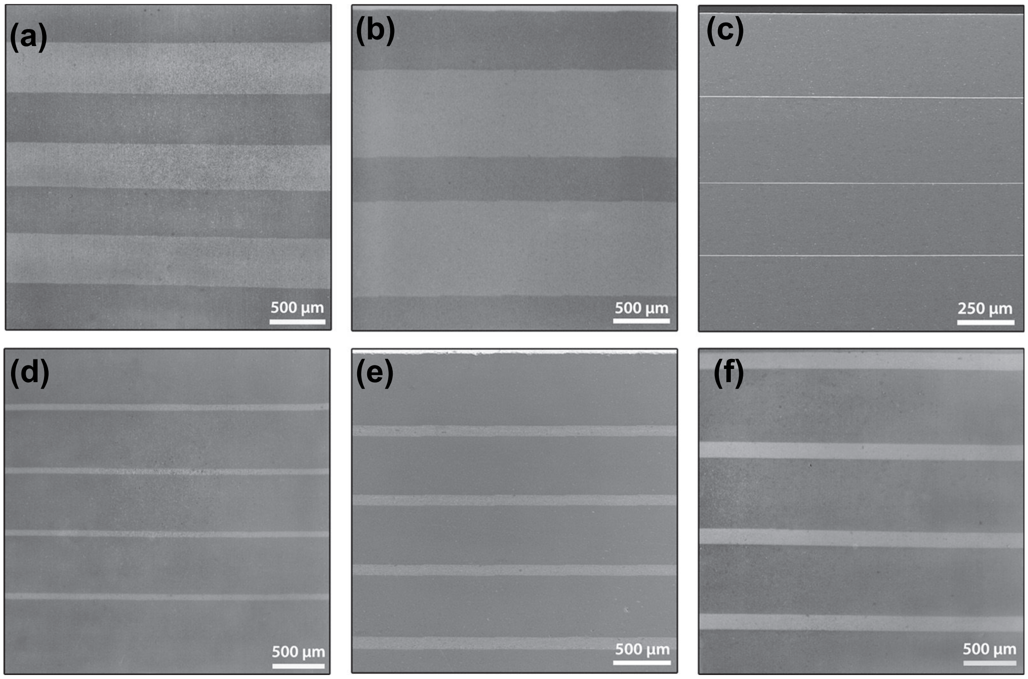

Figure 10 Capability of direct shaping of aqueous slurries methods to fabricate ceramic laminates. Examples of alumina–zirconia laminates. Different layer thicknesses can be obtained as a function of the method. Layers containing the maximum amounts of alumina appear darker. (a) and (b) Stacking pre-sintered cast tapes of two different compositions ($Al_2O_3 + 5$ vol% YTZP and $Al_2O_3 + 40$ vol% YTZP) at room temperature with low pressures. (a) Dip coating of pre-sintered cast tapes ($Al_2O_3 + 5$ vol% YTZP) in binder-containing slurries (pure ZrO_2), stacking at room temperature with low pressures and sintering (Nicolaidis et al., 2008). (d), (e), and (f) Sequential slip-casting. Bermejo, Baudín, et al. (2007), Bermejo, Sánchez-Herencia, et al. (2007).

laminates are designed with thermodynamically compatible layers to avoid reaction and inter-diffusion of the constituents. This latter process can deliberately be used as it has been done in the alumina–titania system to introduce extreme microstructural differences between contiguous alumina layers (Bueno & Baudín, 2006b). To reach admissible density and grain size in the different layers, minor second phases can act as grain growth inhibitors, as in alumina–3YTZ laminates, where 5 vol% of YTZP avoided alumina grain growth at 1550 °C (Bermejo, Baudín, et al., 2007; Gurauskis et al., 2007).

A special kind of laminates with flaw-tolerant internal layers are those with internal porous layers of the same composition as that of the external ones. They have been fabricated by pilling up tapes casted from slurries with the same alumina powders and with porosity introduced into the internal interlayer by adding starch particles to the slurry (Davis et al., 2000; Ma et al., 2004).

In Figure 10, several examples of alumina–zirconia laminates demonstrate the capability of different direct shaping of aqueous slurries methods to build up ceramic laminates. Stacking pre-sintered tapes at room temperature and low pressures allows the fabrication of different sequences and thicknesses of the layers depending on the number of tapes and the composition that are stacked together (Figures 8(a) and 8(b); Gurauskis et al., 2007; Sánchez-Herencia et al., 2006). These tapes can be previously dipped in binder-containing ceramic slurries prior to stacking in order to obtain very thin layers between the tapes (Figure 8(c); Nicolaidis et al., 2008). Sequential slip-casting is extremely versatile in terms of layer thickness (Figures 8(d), 8(e) and 8(f); Bermejo, Baudín, et al., 2007; Bermejo, Sánchez-Herencia, et al., 2007).

2.02.7 Fabrication of Alumina Nanocomposites

2.02.7.1 Alumina–SiC

Since the seminal work by Niihara (1991), the recognition of the appealing mechanical, physical, and tribological properties of bulk nanocomposites, defined by the grain size of at least one of the constituent microstructural phases being smaller than 100 nm or finer, has generated considerable recent research activity.

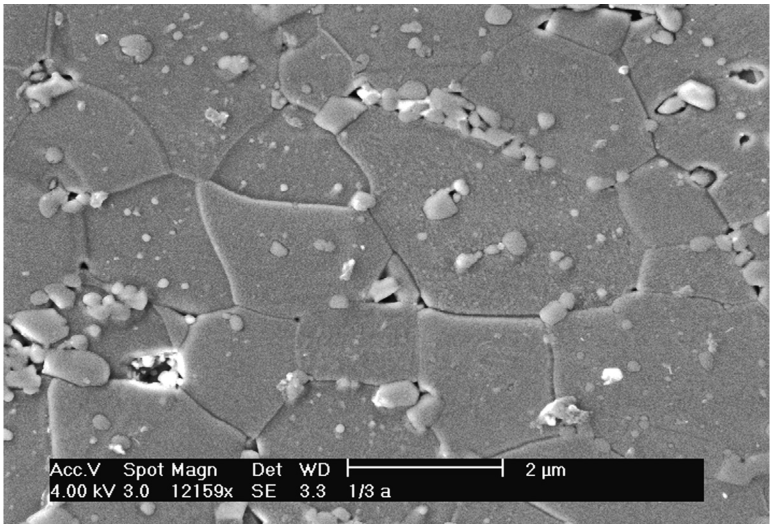

Figure 11 SEM micrograph showing the characteristic microstructure of an alumina–SiC nanocomposite (Winn & Todd, 1999). Nanometric and submicrometric grains of SiC appear clearer than the micrometric alumina matrix.

A major challenge in this research field is concerned with processing, in particular, dispersion of the fine second phase and restriction of grain growth during sintering. In this regard, novel processing techniques have been developed with the aim of fabricating bulk ceramic nanomaterials. Once more, most of the work has been done on alumina-matrix composites. Reviews on processing and properties of alumina–SiC composites can be found elsewhere (Mukhopadhyay & Basu, 2007; Sternitzke, 1997).

Most work on alumina-based nanocomposites has been done in the system alumina–SiC. Figure 11 shows a typical microstructure of such kind of materials, with alumina grain sizes in the range of micrometers and nanometric SiC grains located inside the alumina grains and at grain boundaries (Winn & Todd, 1999).

Original works by Niihara's group give little processing detail while reporting the use of ethanol, toluene, and acetone. A later detailed study on processing with nonaqueous media found methanol to be a suitable dispersing medium (Stearns, Zhao, & Harmer, 1992; Zhao et al., 1993). Other groups have used methanol (O'Sullivan et al., 1995, 1996) or ethanol (Jeong, Nakahira, & Niihara, 1999) as the medium. Nonpolar organic molecules, hexane and toluene, are not a suitable dispersing medium for alumina–SiC mixtures (Stearns et al., 1992; Timms & Ponton, 2002).

Aqueous processing has been widely used to fabricate these composites. Different additives and ultrasonic dispersion (Borsa, Jones, Brook, & Todd, 1997; Walker, Borsa, Todd, Davidge, & Brook, 1994), attrition milling (Cock, Shapiro, Todd, & Roberts, 2005; Kumar, Baron, & Hampshire, 1999; Limpichaipanit & Todd, 2009), or ball milling (Timms & Ponton, 2002) have been used in the mixing stage in which polyethyleneglycol was added as a binder. The main drawback associated with aqueous processing is the occurrence of hard agglomerates and segregation on slow drying of the slurry, so different rapid drying methods have been investigated. Freeze-drying was found to avoid the formation of hard agglomerates (Walker et al., 1994) and has been successfully used later (Cock et al., 2005; Limpichaipanit & Todd, 2009). It has also been found that pH adjustment can be used to induce flocculation of the slurry, preventing segregation and agglomeration of the silicon carbide particles (Borsa et al., 1997; Walker et al., 1994). Pressure filtration has also been proposed as a means to maintain the same quality of dispersion as that of the slurry in the mixed dried powder (Timms, Ponton, & Strangwood, 2002).

As discussed before for Al_2O_3–SiC_w composites (Section 2.02.4.2.2), the incorporation of the high bond energy second phases such as the SiC nanoparticles severely inhibits sintering (Mukhopadhya & Basu, 2007; Mukhopadhyay & Todd, 2011; Sternitzke, 1997).

More than 99% of theoretical density materials with 5 vol% SiC have been reported by Timms et al. (Timms et al., 2002) after pressureless sintering at 1900 °C. Anya and Roberts (1997) claimed still higher density (>99.6% of theoretical) after sintering in flowing nitrogen at 1700–1775 °C for amounts of SiC up to 15 vol%. However, in general, pressureless sintering is only possible with low volume fractions of SiC and impure alumina powders (Baron, Kumar, Le Gonidec, & Hampshire, 2002) or through the use of sintering aids (Cock et al., 2005; Kumar et al., 1999).

The most used solution is to use pressure-assisted sintering techniques, such as HP and SPS (Borsa et al., 1997; Limpichaipanit & Todd, 2009; Mukhopadhyay & Basu, 2007; Sternitzke, 1997; Zhao et al., 1993).

Jeong et al. (Jeong et al., 1999) proposed the use of sintering additives and pressureless sintering followed by HIP to circumvent the limitations—shape, size, anisotropy—of HP. However, such expensive two-step process has not been generally accepted.

2.02.7.2 In situ-Formed Nanocomposites

As occurs with alumina–zirconia composites, when less refractory, oxide nanoparticles are incorporated into the powder mixture, pressureless sintering is feasible but the particles tend to coarsen beyond the nanosized regime and adhere to the grain boundaries. In order to avoid both the inhibition of sintering by refractory non-oxide second phases and the coarsening of oxide phases, the fabrication of ceramic nanocomposites in situ by solid-state reaction has been proposed as a means to overcome the sintering and coarsening limitations to make nanocomposites. Solid-state reaction involves not only reaction between incompatible phases during sintering but also solid-state precipitation. In general, it is necessary to start from a nanosized second phase that would react with the matrix particles during sintering process. Al_2O_3–$FeAl_2O_4$ nanocomposites, with improved wear resistance as compared to that of single-phase alumina with similar grain sizes, have been produced by solid-state precipitation during the aging of Al_2O_3–10 wt% Fe_2O_3 solid solutions in reducing atmosphere (Mukhopadhyay & Todd, 2010a; Mukhopadhyay & Todd, 2011). The microstructure of the materials was further improved by doping with 250 ppm Y_2O_3 (Mukhopadhyay & Todd, 2010b, 2011). Reaction sintering method has been successfully applied to fabricate alumina–mullite nanocomposites (Burgos-Montes, Moreno, & Baudín, 2010) from mixtures of microsized alumina and colloidal silica.

2.02.7.3 Alumina–Carbon Nanotubes

Since their discovery by Iijima (1991), carbon nanotubes (CNTs) have been considered as potential reinforcements of ceramics due to their excellent mechanical characteristics such as high Young's modulus and tensile strength (Padture, 2009; Popov, 2004; Ruoff & Lorents, 1995). There are two main challenges in the processing of CNTs as fillers: the homogeneous dispersion of CNTs in the matrix and the interfacial bonding between matrix and CNTs. Figure 12 shows the microstructure of a series of alumina–CNTs compared to that of single-phase alumina processed in a similar way (Zhang, Fahrenholtz, Hilmas, & Yadlowsky, 2010). Well-dispersed, independent CNTs as well as CNTs clusters are located at the grain boundaries of the alumina matrix. The presence of CNTs limits matrix grain growth. The presence of clusters is due to the fact that nanotubes are difficult to process as they have unfavorable geometrical characteristics for colloidal processing. Consequently, they tend to agglomerate due to their strong Van der Waals interactions. Mixing with the alumina matrix is difficult and the agglomerates of CNTs act as critical defects in the composites (Lee, Mo, Park, & Ho, 2011). Moreover, sintering presents the same kind of problems as alumina–SiC_w composites but still enhanced difficulty. First works on CNT-reinforced ceramics dealt with alumina matrix composites (Laurent, Peigney, Dumortier, & Rousset, 1998; Peigney, Laurent, Dumortier, & Rousset, 1998) and since then effort is being dedicated to the fabrication of alumina–CNT composites by different green-forming processes before the sintering step, usually by HP or SPS. Physical mixing has been conducted under wet conditions to disperse CNTs into alumina powder, followed by ultrasonication and ball-milling (Ahmad, Pan, & Shi, 2006; Fan, Zhao, Wu, Xu, & Song, 2006; Zhan, Kuntz, Wan, & Mukherjee, 2003; Zhang et al., 2010). Chemical treatments for surface modification have been performed on CNTs to obtain better uniformity of dispersion during colloidal processing (Estili et al., 2008; Poorteman, Traianidis, Bister, & Cambier, 2009; Sun, Gao, & Jin, 2005; Sun, Gao, & Li, 2002; Unwin et al., 2010). The in situ growth of CNTs using chemical vapor decomposition onto alumina particles has been demonstrated to be adequate to avoid CNTs agglomerates in the composites (An, You, & Lim, 2003; Zhang et al., 2009).

In order to improve the poor interfacial bonding between the CNTs and alumina matrix after densification, some methods have been proposed to reach intimate contacts between them. The sol–gel method has been used to improve the poor interfacial bonding; however, the mechanical properties were not increased to the expected level (Mo, Cha, Kim, Lee, & Hong, 2005). The optimization of the interfacial interactions of the alumina matrix and the CNTs in the green state, referred to as molecular-level mixing, has allowed to reach a significant

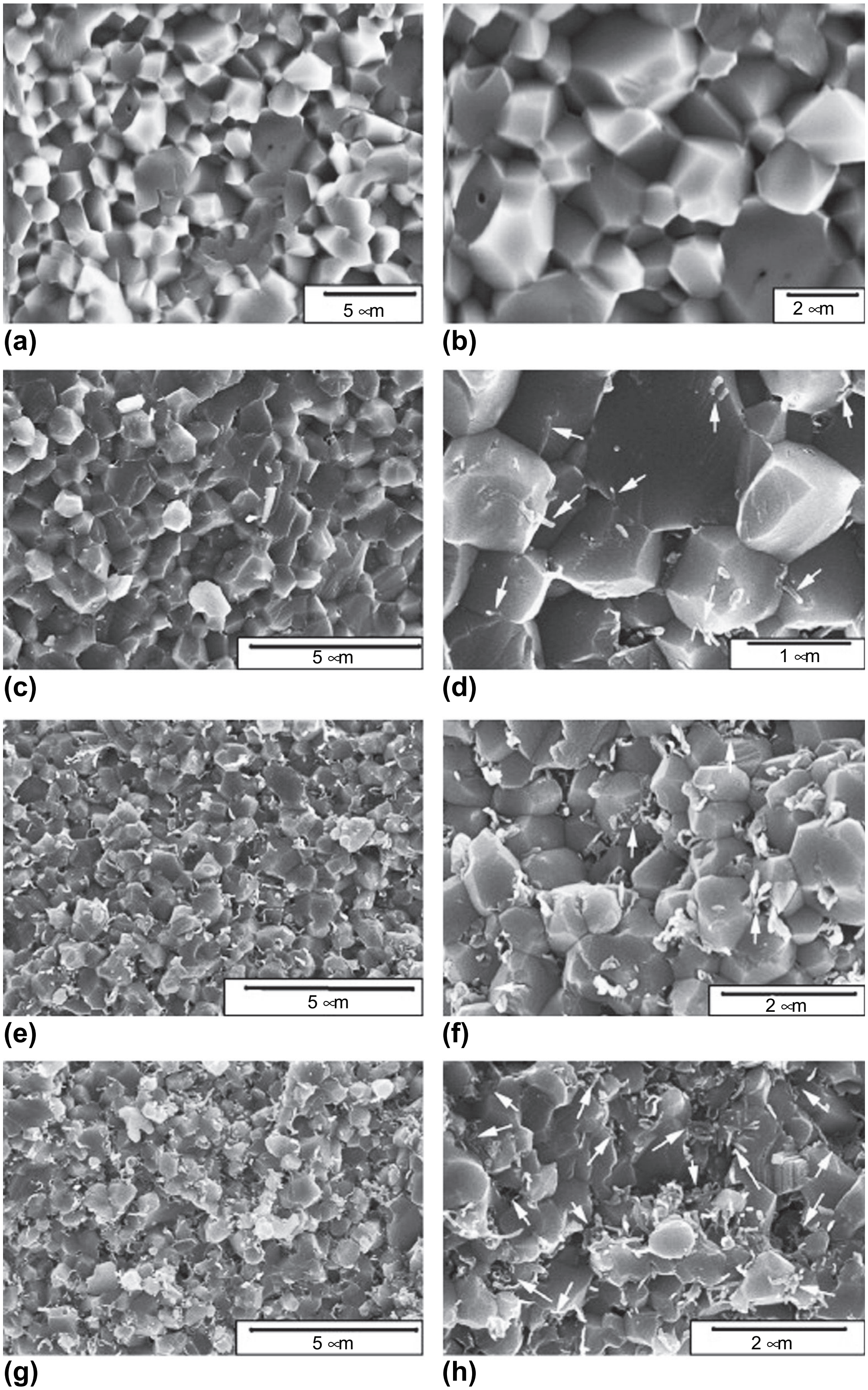

Figure 12 Microstructures of nominally pure Al_2O_3 and composites containing 1, 3, and 5 vol% CNTs sintered at 1500 °C for 2 h. Arrows in images (c) and (d) indicate individual CNTs, while arrows in images (f) and (h) indicate CNT clusters. (a) and (b) Pure Al_2O_3. (c) and (d) 1 vol% CNT–Al_2O_3. (e) and (f) 3 vol% CNT–Al_2O_3. (g) and (h) 5 vol% CNT–Al_2O_3. Zhang et al. (2010).

improvement in the alumina matrix CNTs bonding in the sintered state (Cha, Kim, Arshad, Mo, & Hong, 2005; Cha, Kim, Lee, Mo, & Hong, 2005; Lee et al., 2011).

Some of these methods have had some successful results for relatively small specimens; however, scaling is still difficult. Therefore, till date, there are no reports of defect free high-density pieces to be commercialized. In the same way as CNTs, boron nitride nanotubes/alumina composites are being investigated. Fabrication of dried mixtures by HP has been reported (Wang et al., 2011).

2.02.8 Concluding Remarks

As it has been described through this chapter, alumina is the ceramic material most extensively used for structural applications due to combination of hardness, wear resistance, and corrosion resistance. In general, very fine–grained microstructures are required for single-phase aluminas with improved hardness, wear resistance, or optical performance. The main disadvantage of alumina is brittleness that leads to a lack of reliability of the pieces in use. Thus, a number of monolithic and layered alumina-based composites have been developed and are still under development-seeking reliability.

Most alumina grades were originally manufactured from mineral sources. Nowadays, small particle size ($\approx 1\ \mu m$ or less) and high-purity (>99.5%) aluminium oxide powders are used for the production of high-strength and hardness alumina ceramics used in commercial applications. More recently, a huge effort is being devoted to fabricate not only high-purity alumina materials but also extremely fine-grained (≈ 100 nm) alumina materials for which the direct processing of nanosized powders is under investigation. Most technical advances require controlled and dense submicrometer microstructures more than nanostructures; therefore, optimization of processing of submicrometric powders is a main objective.

For alumina-based composites, processing procedures that allow the homogeneous mixing of phases with different compositions, sizes, and even shapes together with the sintering of the mixture or the layered structure to full density are major issues. In particular, for alumina-based nanocomposites, the inhibition of sintering by second phases and the coarsening of alumina grains have to be avoided. The fabrication of ceramic nanocomposites in situ by solid-state reaction is being investigated as a means to overcome these sintering and coarsening limitations.

In order to maximize the benefits of the new alumina-based microstructures being developed, the simplification of the processing routes, avoiding two-step sintering and machining, as examples, will be sought. Also, advances in processing technology will have to imply the use of environmentally friendly powder processing and shaping methods.

Acknowledgments

Project MAT2010-17753 (Spain). The author thank coworkers Prof. R. Moreno, Dr M.I. Nieto, Dr B. Ferrari, Dr A.J. Sánchez-Herencia, Dr M. Santacruz, Dr S. Bueno, Dr R. Bermejo, Dr J. Gurauskis, and Dr R. Uribe; and Prof. P. Pena and Dr M.A. Rodriguez, for helpful discussions.

References

Ahmad, K., Pan, W., & Shi, S. L. (2006). Electrical conductivity and dielectric properties of multiwalled carbon nanotube and alumina composites. *Applied Physical Letters, 89*, 133122.

Allen, W. C. (1961). Dimensional control of ceramic materials. *American Ceramic Society Bulletin, 40*, 383–389.

Altay, A., & Gülgün, M. A. (2003). Microstructural evolution of calcium-doped α-alumina. *Journal of the American Ceramic Society, 86*, 623–629.

Aman, Y., Garnier, V., & Djurado, E. (2009). Influence of green state processes on the sintering behavior and the subsequent optical properties of spark plasma sintered alumina. *Journal of the European Ceramic Society, 29*, 3363–3370.

Aman, Y., Garnier, V., & Djurado, E. (2010). A screening design approach for the understanding of spark plasma sintering parameters: a case of translucent polycrystalline undoped alumina. *International Journal of Applied Ceramic Technology, 7*, 574–586.

Aman, Y., Garnier, V., & Djurado, E. (2011). Spark plasma sintering kinetics of pure α-alumina. *Journal of the American Ceramic Society, 94*, 2825–2833.

An, L., Chan, H. M., Padture, N. P., & Lawn, B. R. (1996). Damage-resistant alumina-based layer composites. *Journal of Materials Research, 11*, 204–210.

An, J. W., You, D. H., & Lim, D. S. (2003). Tribological properties of hot-pressed alumina-CNT composites. *Wear, 255*, 677–681.

Ananthakumar, S., & Warrier, K. G. K. (2001). Extrusion characteristics of alumina–aluminium titanate composite using boehmite as a reactive binder. *Journal of the European Ceramic Society, 21*, 71–78.

Anya, C. C., & Roberts, S. G. (1997). Pressureless sintering and elastic constants of Al_2O_3/SiC nanocomposites. *Journal of the European Ceramic Society, 17*, 565–573.

Apetz, R., & van Bruggen, M. P. B. (2003). Transparent alumina: a light-scattering model. *Journal of the American Ceramic Society, 86*, 480–486.

Azar, M., Palmero, P., Lombardi, M., Garnier, V., Montanaro, L., Fantozzi, G., et al. (2008). Effect of initial particle packing on the sintering of nanostructured transition alumina. *Journal of the European Ceramic Society, 28*, 1121–1128.

Bansal, N. P., & Zhu, D. (2005). Thermal conductivity of zirconia–alumina composites. *Ceramics International, 31*, 911–916.

Baron, B., Kumar, C. S., Le Gonidec, G., & Hampshire, S. (2002). Comparison of different alumina powders for the aqueous processing and pressureless sintering of Al_2O_3–SiC nanocomposites. *Journal of the European Ceramic Society, 22*, 1543–1552.

Bartolome, J., Requena, J., Moya, J. S., Li, M., & Guiu, F. (1996). Cyclic fatigue crack growth resistance of Al_2O_3–Al_2TiO_5 composites. *Acta Materialia, 44*, 1361–1370.

Bartolome, J., Requena, J., Moya, J. S., Li, M., & Guiu, F. (1997). Cyclic fatigue of Al_2O_3–Al_2TiO_5 composites in direct push–pull. *Fatigue Fracture of Engineering Materials and Structures, 20*, 789–798.

Baudín, C., Gurauskis, J., Sánchez-Herencia, A. J., & Orera, V. M. (2009). Indentation damage and residual stress field in alumina-Y_2O_3-stabilized zirconia composites. *Journal of the American Ceramic Society, 92*, 152–160.

Becher, P. F., & Wei, G. C. (1984). Toughening behavior in SiC-whisker-reinforced alumina. *Journal of the American Ceramic Society, 63*, C-267–C-269.

Bednarek, P., Szafran, M., & Mizerski, T. (2010). Saccharides derivatives in shaping of ceramic powders. New monomers and dispersants. *Advances in Science and Technology, 62*, 169–174.

Bennison, S. J., & Harmer, M. P. (1990). A history of the role of MgO in the sintering of α-alumina. In C. A. Hanwerker, & J. E. Blendell (Eds.), *Ceramic transactions: Vol. 7. Sintering of advanced ceramics* (pp. 13–49). Ohio, USA: The American Ceramic Society.

Bermejo, R., Baudín, C., Moreno, R., Llanes, L., & Sánchez-Herencia, A. J. (2007). Processing optimisation and fracture behaviour of layered ceramic composites with highly compressive layers. *Composites Science and Technology, 67*, 1930–1938.

Bermejo, R., Sánchez-Herencia, A. J., Llanes, L., & Baudín, C. (2007). High temperature mechanical behaviour of flaw tolerant alumina–zirconia multilayered ceramics. *Acta Materialia, 55*, 4891–4901.

Bernard-Granger, G., Guizard, C., & Addad, A. (2007). Sintering of ultrapure α-alumina powder; I. Densification, grain growth and sintering path. *Journal of Materials Science, 42*, 6316–6324.

Bertram, B. D., & Gerhardt, R. A. (2011). Properties and applications of ceramic composites containing silicon carbide whiskers. In R. A. Gerhardt (Ed.), *Properties and applications of silicon carbide* (pp. 197–230). Rijeka, Croatia: Tech Open Access Publications.

Bertram, B. D., Gerhardt, R. A., & Schultz, J. W. (2011). Extruded and pressureless-sintered Al_2O_3–SiC composite rods: fabrication, structure, electrical behavior, and elastic modulus. *Journal of the American Ceramic Society, 94*, 4391–4398.

Biamino, S., Fino, P., Pavese, M., & Badini, C. (2006). Alumina–zirconia–yttria nanocomposites prepared by solution combustion synthesis. *Ceramics International, 32*, 509–513.

Blendell, J. E., & Coble, R. L. (1982). Measurement of stress due to thermal expansion anisotropy in Al_2O_3. *Journal of the American Ceramic Society, 65*, 174–178.

Bocanegra-Bernal, M. H. (2004). Review. Hot isostatic pressing (HIP) technology and its applications to metals and ceramics. *Journal of Materials Science, 39*, 6399–6420.

Bodisova, K., Sajgalik, P., Galusek, D., & Svancarek, P. (2007). Two-stage sintering of alumina with submicrometer grain size. *Journal of the American Ceramic Society, 90*, 330–332.

Borsa, C. E., Jones, N. M. R., Brook, R. J., & Todd, R. I. (1997). Influence of processing on the microstructural development and flexure strength of Al_2O_3/SiC nanocomposites. *Journal of the European Ceramic Society, 17*, 865–872.

Bowen, P., & Carry, C. (2002). From powders to sintered pieces: forming, transformations and sintering of nanostructured ceramic oxides. *Powder Technology, 128*, 248–255.

Bradt, R. C. (1967). Cr_2O_3 solid solution hardening of Al_2O_3. *Journal of the American Ceramic Society, 50*, 54–55.

Brewer, L. (1953). The thermodynamic properties of the oxides and their vaporization processes. *Chemical Reviews, 52*, 1–75.

Brewer, L., & Searcy, A. W. (1951). The gaseous species of the Al–Al_2O_3 system. *Journal of the American Chemical Society, 73*, 5308–5314.

Briggs, J. (2007). *Engineering ceramics in Europe and the USA*. Worcester, UK: Menwith Wood.

Brook (Ed.), (1991). *Concise encyclopedia of advanced ceramic materials*. Oxford, GB: Pergamon Press.

Bueno, S., & Baudin, C. (2006a). Instrumented Vickers microindentation of alumina-based materials. *Journal of Material Research, 21*, 161–173.

Bueno, S., & Baudín, C. (2006b). In situ developed laminates with large microstructural differences between layers of similar composition. *Journal of Materials Science, 21*, 3695–3700.

Bueno, S., & Baudín, C. (2007a). Layered materials with high strength and flaw tolerance based on alumina and aluminium titanate. *Journal of the European Ceramic Society, 27*, 1455–1462.

Bueno, S., & Baudín, C. (2007b). Flaw tolerant ceramic laminates with negligible residual stresses between layers. *Key Engineering Materials, 333*, 17–26 (Switzerland: Tans Tech Publications).

Bueno, S., & Baudín, C. (2009). Design and processing of a ceramic laminate with high toughness and strong interfaces. *Composites Part A, 40*, 137–143.

Bueno, S., Berger, M. H., Moreno, R., & Baudín, C. (2008). Fracture behaviour of microcrack free alumina–aluminium titanate ceramics with second phase nanoparticles at alumina grain boundaries. *Journal of the European Ceramic Society, 28*, 1961–1971.

Bueno, S., Moreno, R., & Baudín, C. (2004). Reaction sintered Al_2O_3/Al_2TiO_5 microcrack-free composites obtained by colloidal filtration. *Journal of the European Ceramic Society, 24*, 2785–2791.

Bueno, S., Moreno, R., & Baudín, C. (2005). Design and processing of Al_2O_3–Al_2TiO_5 layered structures. *Journal of the European Ceramic Society, 25*, 847–856.

Burden, S. J., Hong, J., Rue, J. W., & Stromborg, C. L. (1988). Comparison of hot-isostatically-pressed and uniaxially hot-pressed alumina–titanium carbide cutting tools. *American Ceramic Society Bulletin, 67*, 1003–1006.

Burgos-Montes, O., Moreno, R., & Baudín, C. (2010). Effect of mullite additions on the fracture mode of alumina. *Journal of the European Ceramic Society, 30*, 857–863.

Cahoon, H. P., & Cristensen, C. J. (1956). Sintering and grain-growth of alpha-alumina. *Journal of the American Ceramic Society, 39*, 337–344.

Carisey, T., Laugierwerth, A., & Brandon, D. (1995). Control of texture in Al_2O_3 by gel-casting. *Journal of the European Ceramic Society, 15*, 1–8.

Carisey, T., Levin, I., & Brandon, D. G. (1995). Microstructure and mechanical properties of textured Al_2O_3. *Journal of the European Ceramic Society, 15*, 283–289.

Casellas, D., Rafols, I., Llanes, L., & Anglada, M. (1999). Fracture toughness of zirconia–alumina composites. *International Journal of Refractory Metals and Hard Materials, 17*, 11–20.

Cesarano, J., & Aksay, I. A. (1988). Processsing of highly concentrated aqueous α-alumina suspensions stabilized by polyelectrolytes. *Journal of the American Ceramic Society, 71*, 1062–1067.

Cesarano, J., Aksay, I. A., & Bleier, A. (1988). Stability of aqueous α-alumina suspensions with poly(methacrylic acid) polyelectrolyte. *Journal of the American Ceramic Society, 71*, 250–255.

Cesari, F., Esposito, L., Furgiuele, F. M., Maletta, C., & Tucci, A. (2006). Fracture toughness of alumina–zirconia composites. *Ceramics International, 32*, 249–255.

Cha, S. I., Kim, K. T., Arshad, S. N., Mo, C. B., & Hong, S. H. (2005). Extraordinary strengthening effect of carbon nanotubes in metal-matrix nanocomposites processed by molecular-level mixing. *Advanced Materials, 17*, 1377–1381.

Cha, S. I., Kim, K. T., Lee, K. H., Mo, C. B., & Hong, S. H. (2005). Strengthening and toughening of carbon nanotube reinforced alumina nanocomposite fabricated by molecular level mixing process. *Scripta Materalia, 53*, 793–797.

Chaim, R., Levin, M., Shlayer, A., & Estournes, C. (2008). Sintering and densification of nanocrystalline ceramic oxide powders: a review. *Advances in Applied Ceramics, 107*, 159–168.

Chan, H. M. (1997). Layered ceramics: processing and mechanical behavior. *Annual Review of Materials Science, 27*, 249–282.

Chandradass, J., & Bae, D.-S. (2009). Nano α-Al_2O_3-t-ZrO_2 composite powders by calcining an emulsion precursor at 1100 °C. *Journal of Alloys and Compounds, 469*, L10–L12.

Chandradass, J., Yoon, J. H., & Bae, D.-S. (2008a). Low temperature synthesis and characterization of zirconia doped alumina nanopowder by hydrothermal process. *Materials and Manufacturing Processes, 23*, 138–142.

Chandradass, J., Yoon, J. H., & Bae, D.-S. (2008b). Synthesis and characterization of zirconia doped alumina nanopowder by citrate–nitrate process. *Materials Science and Engineering A, 473*, 360–364.

Chang, J. C., Lange, F. F., Pearson, D. S., & Pollinger, J. P. (1994). Pressure sensitivity for particle packing of aqueous Al_2O_3 slurries vs interparticle potential. *Journal of the American Ceramic Society, 77*, 1357–1360.

Chen, I. W., & Wang, X. H. (2000). Sintering nanocrystalline ceramics without final-stage grain growth. *Nature, 404*, 168–169.

Chevalier, J., Grandjean, S., Kuntz, M., & Pezzotti, G. (2009). On the kinetics and impact of tetragonal to monoclinic transformation in an alumina/zirconia composite for arthroplasty applications. *Biomaterials, 30*, 5279–5282.

Chevalier, J., Taddei, P., Gremillard, L., Deville, S., Fantozzi, G., Bartolome, J. F., et al. (2011). Reliability assessment in advanced nanocomposite materials for orthopaedic applications. *Journal of the Mechanical Behavior of Biomedical Materials, 4*, 303–314.

Chi, M., Gu, H., Wang, X., & Wang, P. (2003). Evidence of bilevel solubility in the bimodal microstructure of TiO_2-doped alumina. *Journal of the American Ceramic Society, 86*, 1953–1955.

Choi, S. R., & Bansal, N. P. (2005). Mechanical behavior of zirconia/alumina composites. *Ceramics International, 31*, 39–46.

Claussen, N., Wu, S. X., & Holz, D. (1994). Reaction bonding of aluminum-oxide (RBAO) composites – processing, reaction-mechanisms and properties. *Journal of the European Ceramic Society, 14*, 97–109.

Clegg, W. J. (1998). Design of ceramic laminates for structural applications. *Materials Science and Technology, 14*, 483–495.

Coble, R. L. (1961). Sintering crystalline solids: II experimental test of diffusion models in powder compacts. *Journal of Applied Physics, 32*, 793–799.

Coble, R. L. (1962). Sintering of alumina: effect of atmospheres. *Journal of the American Ceramic Society, 45*, 123–128.

Coble, R. L., & Ellis, J. S. (1963). Hot-pressing alumina: mechanisms of material transport. *Journal of the American Ceramic Society, 46*, 438–441.

Coble, R. L., Song, H., Brook, R. J., Hendwerker, C. A., & Dynys, J. M. (1984). In W. D. Kingery (Ed.), *Structure and properties of MgO and Al_2O_3 ceramics* (pp. 839–852). Ohio, USA: The American Ceramic Society.

Cock, A. M., Shapiro, I. P., Todd, R. I., & Roberts, S. G. (2005). Effects of yttrium on the sintering and microstructure of alumina–silicon carbide nanocomposites. *Journal of the American Ceramic Society, 88*, 2354–2361.

Cuckler, J. M., Bearcroft, J., & Asgian, C. M. (1995). Femoral head technologies to reduce polyethylene wear in total hip arthroplasty. *Clinical Arthoplasty, 317*, 57–63.

Cutler, R. A., Hurford, A. C., & Virkar, A. V. (1989). Pressureless-sintered Al_2O_3–TiC composites. *International Journal of Refractory Metals and Hard Materials, 6*, 114–120.

de Aza, A. H., Chevalier, J., Fantozzi, G., Schehl, M., & Torrecillas, R. (2002). Crack growth resistance of alumina, zirconia and zirconia toughened alumina ceramics for joint prostheses. *Biomaterials, 23*, 937–945.

de Portu, G., Micele, L., & Pezzotti, G. (2006). Laminated ceramic structures from oxide systems. *Composites Part B-Engineering, 37*, 556–567.

Davis, J. B., Kristoffersson, A., Carlstrom, E., & Clegg, W. J. (2000). Fabrication and crack deflection in ceramic laminates with porous interlayers. *Journal of the American Ceramic Society, 83*, 2369–2374.

Doremus, R. H. (1984). Alumina–silica system. Chap. 2. In N. P. Cheremisinoff (Ed.), *Synthesis and properties: Vol. 1. Handbook of ceramics and composites* (pp. 23–34). New York, USA: Marcel Dekker.

Doremus, R. H. (2008). Alumina. In J. F. Shackelford, & R. H. Doremus (Eds.), *Ceramic and glass materials structure, properties and processing*. USA: Springer.

Dörre, E., & Hübner, H. (1984). *Alumina. Processing, properties and applications*. Berlin, Germany: Springer-Verlag.

Dynys, F. W., & Halloran, J. W. (1984). Influence of aggregates on sintering. *Journal of the American Ceramic Society, 67*, 596–601.

Eckhard, S., & Nebelung, M. (2011). Investigations of the correlation between granule structure and deformation behavior. *Powder Technology, 206*, 79–87.

El Hakim, M. A., Abad, M. D., Abdelhameed, M. M., Shalaby, M. A., & Veldhuis, S. C. (2011). Wear behavior of some cutting tool materials in hard turning of HSS. *Tribology International, 44*, 1174–1181.

Elsässer, C., Heuer, A. H., Rühle, M., & Wiederhorn, S. M. (Eds.), (2003). *Special topical issue: Alumina. Journal of the American Ceramic Society*, *86*(4).

Estili, M., Kawasaki, A., Sakamoto, H., Mekuchi, Y., Kuno, M., & Tsukada, T. (2008). The homogeneous dispersion of surfactantless, slightly disordered, crystalline, multiwalled carbon nanotubes in α-alumina ceramics for structural reinforcement. *Acta Materialia, 56*, 4070–4079.

Falkowski, P., Bednarek, P., Danelska, A., Mizerski, T., & Szafran, M. (2010). Application of monosaccharides derivatives in colloidal processing of aluminum oxide. *Journal of the European Ceramic Society, 30*, 2805–2811.

Fan, J. P., Zhao, D. Q., Wu, M. S., Xu, Z. N., & Song, J. (2006). Preparation and microstructure of multi-wall carbon nanotubes-toughened Al_2O_3 composite. *Journal of the American Ceramic Society, 89*, 750–753.

Ferrari, B., Bartret, A., & Baudín, C. (2009). Sandwich materials formed by thick alumina tapes and thin layered alumina–aluminium titanate structures shaped by EPD. *Journal of the European Ceramic Society, 29*, 1083–1092.

Ferrari, B., González, S., Moreno, R., & Baudín, C. (2006). Multilayer coatings with improved reliability produced by aqueous electrophoretic deposition. *Journal of the European Ceramic Society, 26*, 27–36.

Ferrari, B., Sanchez-Herencia, A. J., & Moreno, R. (1998a). Aqueous electrophoretic deposition of Al_2O_3/ZrO_2 layered ceramics. *Materials Letters, 35*, 370–374.

Ferrari, B., Sanchez-Herencia, A. J., & Moreno, R. (1998b). Electrophoretic forming of Al_2O_3/Y-TZP layered ceramics from aqueous suspensions. *Materials Research Bulletin, 33*, 487–499.

Freim, J., Mckittrick, J., Katz, J., & Sickafus, K. (1994). Phase transformation and densification behavior of microwave sintered γ-AL_2O_3. In M. F. Iskander, R. J. Lauf, & W. H. Sutton (Eds.), *Materials research society symposium proceedings: Vol. 347. Microwave processing of materials IV* (pp. 525–530).

French, R. H., & Heuer, A. H. (Eds.), (1994). *Science of alumina. Journal of the American Ceramic Society*, *77*(2).

Frey, R., & Halloran, J. W. (1984). Compaction behavior of spray-dried alumina. *Journal of the American Ceramic Society, 67*, 199–203.

Fujiwara, S., Tamura, Y., Maki, H., Azuma, N., & Takeuchi, Y. (2007). *Development of new high-purity alumina. Sumitomo Kagaku 2007-I*, 1–10.

Gao, L., Hong, J. S., & Torre, S. D. D. L. (2000). Bending strength and microstructure of Al_2O_3 ceramics densified by spark plasma sintering. *Journal of the European Ceramic Society, 20*, 2149–2152.

Garino, J. P. (2005). Ceramic component fracture: trends and recommendations with modern components based on improved reporting methods. In A. James, & M. D. D'Antonio (Eds.), *Ceramics in orthopaedics: Bioceramics and alternative bearings in joint arthroplasty* (pp. 157–168). Germany: Springer.

Gavrilov, K. L., Bennison, S. J., Mikeska, K. R., & Levi-Setti, R. (2003). Role of magnesia and silica in alumina microstructure evolution. *Journal of Materials Science, 38*, 3965–3972.

Ghate, B. B., Smith, W. C., Kim, C. H., Hasselman, D. P. H., & Kane, G. E. (1975). Effect of chromia alloying on machining performance of alumina cutting tools. *American Ceramic Society Bulletin, 54*, 210–215.

Gitzen, W. H. (1970). *Alumina as a ceramic material.* In *American ceramic society special publication no 4.* Ohio, USA: The American Ceramic Society.

Gogolewski, P., Klimke, J., Krell, A., & Beer, P. (2009). Al_2O_3 tools towards effective machining of wood-based materials. *Journal of Materials Processing Technology, 209*, 2231–2236.

Goh, G. K. L., Lim, L. C., Rahman, M., & Lim, S. C. (1997). Effect of grain size on wear behaviour of alumina cutting tools. *Wear, 206*, 24–32.

Gurauskis, J., Sánchez-Herencia, A. J., & Baudín, C. (2006). Al_2O_3/Y-TZP and Y-TZP materials fabricated by stacking layers obtained by aqueous tape casting. *Journal of the European Ceramic Society, 26*, 1489–1496.

Gurauskis, J., Sánchez-Herencia, A. J., & Baudín, C. (2007). Alumina–zirconia layered ceramics fabricated by stacking water processed green ceramic tapes. *Journal of the European Ceramic Society, 27*, 1389–1394.

Hall, P. W., Swinnea, J. S., & Kovar, D. (2001). Fracture resistance of highly textured alumina. *Journal of the American Ceramic Society, 84*, 1514–1520.

Handwerker, C. A., Cannon, R. M., & French, R. H. (1994). Robert L. Coble: a retrospective. *Journal of the American Ceramic Society, 77*, 293–297.

Handwerker, C. A., Morris, P. A., & Coble, R. L. (1989). Effects of chemical inhomogeneities on grain growth and microstructure in Al_2O_3. *Journal of the American Ceramic Society, 72*, 130–136.

Hannouche, D., Zaoui, A., Zadegan, F., Sedel, L., & Nizard, R. (2011). Thirty years of experience with alumina-on-alumina bearings in total hip arthroplasty. *International Orthopaedics, 35*, 207–213.

Harmer, M. P., & Brook, R. J. (1981). Fast firing – microstructural benefits. *Transactions and Journal of the British Ceramic Society, 80*, 147–148.

Harper, C. A. (Ed.), (2001). *Handbook of ceramic, glasses and diamonds.* New York, USA: McGraw-Hill.

Hart, L. D. (Ed.), (1990). *Alumina chemicals: Science and technology handbook.* USA: The American Ceramic Society.

Hidber, P. C., Graule, T. J., & Gauckler, L. J. (1996). Citric acid-a dispersant for aqueous alumina suspensions. *Journal of the American Ceramic Society, 79*, 1857–1867.

Hidber, P. C., Graule, T. J., & Gauckler, L. J. (1997). Influence of the dispersant structure on properties of electrostatically stabilized aqueous alumina suspensions. *Journal of the European Ceramic Society, 17*, 239–249.

Hoffman, U., Scharrer, E., Czerch, W., Fruhauf, K., & Burck, W. (1962). Fundamentals of dry pressing and the causes of compacting of the dry body. *Berichte der Deutschen Keramischen Gesellschaft, 39*, 125–130.

Holz, D., Wu, S. X., Scheppokat, S., & Claussen, N. (1994). Effect of processing parameters on phase and microstructure evolution in RBAO ceramics. *Journal of the American Ceramic Society, 77*, 2509–2517.

Homeny, J., & Vaughn, W. L. (1990). *R*-curve behavior in a silicon-carbide whisker alumina matrix composite. *Journal of the American Ceramic Society, 73*, 2060–2062.

Homeny, J., Vaughn, W. L., & Ferber, M. K. (1990). Silicon–carbide whisker alumina matrix composites – effect of whisker surface-treatment on fracture-toughness. *Journal of the American Ceramic Society, 73*, 394–402.

Huet, R., Sakona, A., & Kurtz, S. M. (2011). Strength and reliability of alumina ceramic femoral heads: review of design, testing, and retrieval analysis. *Journal of the Mechanical Behavior of Biomedical Materials, 4*, 476–483.

Huisman, W., Graule, T., & Gauckler, L. J. (1995). Alumina of high reliability by centrifugal casting. *Journal of the European Ceramic Society, 15*, 811–821.

Iijima, S. (1991). Helical microtubules of graphitic carbon. *Nature, 354*, 56–58.

Insley, G., Turner, I., Fisher, J., & Streicher, R. (2002). In-vitro testing and validation of zirconia toughened alumina (ZTA). In J. P. Garino, & G. Willmann (Eds.), *Bioceramics in joint arthroplasty. 7th International Biolox Symposium* (pp. 26–31). Germany: Thieme.

International Aluminium Institute. (2011). http://www.world-aluminium.org/Statistics.

Iwasa, M., & Bradt, R. C. (1984). Fracture toughness of single-crystal alumina. In W. D. Kingery (Ed.), *Structure and properties of MgO and Al_2O_3 ceramics* (pp. 767–779). Ohio, USA: The American Ceramic Society.

Jailani, S., Franks, G. V., & Healy, T. W. (2008). ζ potential of nanoparticle suspensions: effect of electrolyte concentration, particle size, and volume fraction. *Journal of the American Ceramic Society, 91*, 1141–1147.

Jayaseelan, D., Nishikawa, T., Awaji, H., & Gnanam, F. D. (1998). Pressureless sintering of sol–gel derived alumina–zirconia composites. *Materials Science and Engineering A, A256*, 265–270.

Jayaseelan, D. D., Ueno, S., Ohji, T., & Kanzaki, S. (2004). Differential sintering by improper selection of sintering parameters during pulse electric current sintering. *Journal of the American Ceramic Society, 87*, 159–161.

Jeong, Y. K., Nakahira, A., & Niihara, K. (1999). Effects of additives on microstructure and properties of alumina–silicon carbide nanocomposites. *Journal of the American Ceramic Society, 82*, 3609–3612.

Jung, J., & Baik, S. (2003). Abnormal grain growth of alumina: CaO effect. *Journal of the American Ceramic Society, 86*, 644–649.

Kikkawa, S., Kijima, A., Hirota, K., & Yamaguchi, O. (2002). Soft solution preparation methods in a ZrO_2–Al_2O_3 binary system. *Solid State Ionics, 151*, 359–364.

Kim, B. N., Hiraga, K., Morita, K., & Yoshida, H. (2007). Spark plasma sintering of transparent alumina. *Scripta Materialia, 57*, 607–610.

Kingery, W. D. (Ed.), (1984). *Structure and properties of MgO and Al_2O_3 ceramics*. Ohio, USA: The American Ceramic Society.

Kirchner, H. P., Gruver, R. M., & Walker, R. E. (1973). Strengthening of hot-pressed alumina by quenching. *Journal of the American Ceramic Society, 56*, 17–21.

Kitiwan, M., & Duangduen, A. (2007). Preparation of Al_2O_3–TiC composites and their cutting performance. *Journal of Solid Mechanics and Materials Engineering, 1*, 938–946.

Kokabi, M., Babaluo, A. A., & Barati, A. (2006). Gelation process in low-toxic gelcasting systems. *Journal of the European Ceramic Society, 26*, 3083–3090.

Korinek, S. L., & Castaing, J. (2003). Slip and twinning in polycrystalline alumina (α-Al_2O_3) deformed under hydrostatic pressure between 600 and 1000 °C. *Journal of the American Ceramic Society, 86*, 566–573.

Krell, A. (1995). Grain size dependence of hardness in dense submicrometer alumina. *Journal of the American Ceramic Society, 78*, 1118–1120.

Krell, A. (1996). Improved hardness and hierarchic influences on wear in submicron sintered alumina. *Materials Science and Engineering A, 209*, 156–163.

Krell, A., & Blank, P. (1996). The influence of shaping method on the grain size dependence of strength. *Journal of the European Ceramic Society, 16*, 1189–1200.

Krell, A., Blank, P., Ma, H. W., Hutzler, T., & Nebelung, M. (2003). Processing of high-density submicrometer Al_2O_3 for new applications. *Journal of the American Ceramic Society, 86*, 546–553.

Krell, A., Blank, P., Ma, H., Hutzler, T., Van Bruggen, M., & Apetz, R. (2003). Transparent sintered corundum with high hardness and strength. *Journal of the American Ceramic Society, 86*, 12–18.

Krell, A., Hutzler, T., & Klimke, J. (2009). Transmission physics and consequences for materials selection, manufacturing, and applications. *Journal of the European Ceramic Society, 29*, 207–221.

Krell, A., & Klimke, J. (2006). Effects of the homogeneity of particle coordination on solid-state sintering of transparent alumina. *Journal of the American Ceramic Society, 89*, 1985–1992.

Kronenberg, M. L. (1957). Plastic deformation of single crystals of sapphire: basal slip and twining. *Acta Metallurgica, 5*, 507–529.

Kumagai, M., & Messing, G. L. (1985). Controlled transformation and sintering of a boehmite sol–gel by α-alumina seeding. *Journal of the American Ceramic Society, 68*, 500–505.

Kumar, C. S., Baron, B., & Hampshire, S. (1999). Effect of Y_2O_3 on pressureless sintering and erosive wear resistance of Al_2O_3–5 vol% SiC nanocomposites. *British Ceramic Proceedings, 60*, 395–396.

Kumar, A. S., Durai, A. R., & Sornakumar, T. (2006). Wear behaviour of alumina based ceramic cutting tools on machining steels. *Tribology International, 39*, 191–197.

Lagerlof, K. P. D., Heuer, A. H., Castaing, J., Rivière, J. P., & Mitchell, T. E. (1994). Slip and twinning in sapphire (α-Al_2O_3). *Journal of the American Ceramic Society, 77*, 385–397.

Lambrinou, K., Lauwagie, T., Chalvet, F., de Portu, G., Tassini, N., Patsias, S., et al. (2007). Elastic properties and damping behaviour of alumina–alumina/zirconia laminates. *Journal of the European Ceramic Society, 27*, 1307–1311.

Lancaster, J. G., Dowson, D., Isaac, G. H., & Fisher, J. (1997). The wear of ultra-high molecular weight polyethylene sliding on metallic and ceramic counterfaces representative of current femoral surfaces in joint replacement. *Proceedings of the Institution of Mechanical Engineers H, 211*, 17–24.

Lange, F. F. (1984). Sinterability of agglomerated powders. *Journal of the American Ceramic Society, 67*, 83–89.

Lange, F. F. (1989). Powder processing science and technology for increased reliability. *Journal of the American Ceramic Society, 72*, 3–15.

Lange, F. F. (2001). Shape forming of ceramic powders by manipulating the interparticle pair potential. *Chemical Engineering and Science, 56*, 3011–3020.

Lange, F. F., & Metcalf, M. (1983). Processing-related fracture origins: ii, agglomerate motion and cracklike internal surfaces caused by differential sintering. *Journal of the American Ceramic Society, 66*, 398–406.

Laurent, Ch., Peigney, A., Dumortier, O., & Rousset, A. (1998). Carbon nanotubes–Fe–alumina nanocomposites. Part II: microstructure and mechanical properties of the hot-pressed composites. *Journal of the European Ceramic Society, 18*, 2005–2013.

Lee, K., Mo, C. B., Park, S. B., & Ho, S. H. (2011). Mechanical and electrical properties of multiwalled CNT-alumina nanocomposites prepared by a sequential two-step processing of ultrasonic spray pyrolysis and spark plasma sintering. *Journal of the American Ceramic Society, 94*, 3774–3779.

Levin, E. M., Robbins, C. R., & McMurde, H. F. (Eds.), (1964). *Phase diagrams for ceramists*. Ohio, USA: The American Ceramic Society.

Lewis, J. A. (2000). Colloidal processing of ceramics. *Journal of the American Ceramic Society, 83*, 2341–2359.

Limpichaipanit, A., & Todd, R. I. (2009). The relationship between microstructure, fracture and abrasive wear in Al_2O_3/SiC nanocomposites and micro-composites containing 5 and 10% SiC. *Journal of the European Ceramic Society, 29*, 2841–2848.

Lin, C. S., & Lin, S. T. (2008). Effects of granule size and distribution on the cold isostatic pressed alumina. *Journal of Materials Processing Technology, 201*, 657–661.

Lu, K., & Kessler, C. (2006). Colloidal dispersion and rheology study of nanoparticles. *Journal of Materials Science, 41*, 5613–5618.

Ma, Y., & Bowman, K. (1991). Texture in hot-pressed or forged alumina. *Journal of the American Ceramic Society, 74*, 2941–2944.

Ma, Q., & Clarke, D. R. (1994). Piezospectroscopic determination of residual stresses in polycrystalline alumina. *Journal of the American Ceramic Society, 77*, 298–302.

Ma, J., Wanga, H., Weng, L., & Tan, G. E. B. (2004). Effect of porous interlayers on crack deflection in ceramic laminates. *Journal of the European Ceramic Society, 24*, 825–831.

Magnani, G., & Brillante, A. (2005). Effect of the composition and sintering process on mechanical properties and residual stresses in zirconia–alumina composites. *Journal of the European Ceramic Society, 25*, 3383–3392.

Mandal, N., Doloi, B., & Mondal, B. (2011). Development of flank wear prediction model of zirconia toughened alumina (ZTA) cutting tool using response surface methodology. *International Journal of Refractory Metals and Hard Materials, 29*, 273–280.

Mangels, J. A. (1994). Low-pressure injection molding. *American Ceramic Society Bulletin, 73*, 37–41.

Mannschatz, A., Höhn, S., & Moritz, T. (2010). Powder-binder separation in injection moulded green parts. *Journal of the European Ceramic Society, 30*, 2827–2832.

Mata-Osoro, G., Moya, J. S., & Pecharromán, J. C. (2012). Transparent alumina by vacuum sintering. *Journal of the European Ceramic Society*.

Mawdsley, J. R., Kovar, D., & Halloran, J. W. (2000). Fracture behavior of alumina/monazite multilayer laminates. *Journal of the American Ceramic Society, 83*, 802–808.

McAfee, R. J., & Nettleship, I. (2006). Effect of slip dispersion on microstructure evolution during isothermal sintering of cast alumina. *Journal of the American Ceramic Society, 89*, 1273–1279.

McColm, I. J. (1990). *Ceramic hardness*. New York, USA: Plenum Press.

Messing, G. L., Shelleman, R. A., & McArdle, J. L. (1988). Controlled chemical nucleation of alpha alumina transformation. In D. Taylor (Ed.), *Science of ceramics* (Vol. 14; pp. 101–106). Stoke-on-Trent, GB: The Institute of Ceramics.

Messing, G. L., & Stevenson, A. J. (2008). Toward pore-free ceramics. *Science, 322*, 383–384.

Millán, A. J., Nieto, M. I., Baudín, C., & Moreno, R. (2002). Thermogelling polysaccharides for aqueous gelcasting, part II: influence of gelling additives on rheological properties and gel casting of alumina. *Journal of the European Ceramic Society, 22*, 2217–2222.

Millán, A. J., Nieto, M. I., & Moreno, R. (2002). Thermogelling polysaccharides for aqueous gelcasting, part II: a comparative study of gelling additives. *Journal of the European Ceramic Society, 22*, 2209–2215.

Millán, A. J., Nieto, M. I., Moreno, R., & Baudín, C. (2002). Thermogelling polysaccharides for aqueous gelcasting. Part III: mechanical and microstructural characterization of green alumina bodies. *Journal of the European Ceramic Society, 22*, 2223–2230.

Mishra, R. S., Risbud, S. H., & Mukherjee, A. K. (1998). Influence of initial crystal structure and electrical pulsing on densification of nanocrystalline alumina powder. *Journal of Materials Research, 13*, 86–89.

Mo, C. B., Cha, S. I., Kim, K. T., Lee, K. H., & Hong, S. H. (2005). Fabrication of carbon nanotube reinforced alumina matrix nanocomposite by sol–gel process. *Materials Science and Engineering A, 395*, 124–128.

Moon, R. J., Bowman, K. J., Trumble, K. P., & Rödel, J. (2001). Fracture resistance curve behavior of multilayered alumina–zirconia composites produced by centrifugation. *Acta Materialia, 49*, 995–1003.

Moreno, R. (1992a). The role of slip additives in tape-casting technology: part I-solvents and dispersants. *American Ceramic Society Bulletin, 71*, 1521–1531.

Moreno, R. (1992b). The role of slip additives in tape-casting technology: part II-binders and plasticizers. *American Ceramic Society Bulletin, 71*, 1647–1657.

Mukhopadhyay, A., & Basu, B. (2007). Consolidation–microstructure–property relationships in bulk nanoceramics and ceramic nanocomposites: a review. *International Materials Reviews, 52*, 257–288.

Mukhopadhyay, A., & Todd, R. I. (2010a). Microstructure and mechanical properties of Al_2O_3 matrix nanocomposites developed via solid state precipitation. *Journal of the European Ceramic Society, 30*, 1359–1372.

Mukhopadhyay, A., & Todd, R. I. (2010b). Effect of yttria doping on the microstructure and mechanical properties of Al_2O_3–$FeAl_2O_4$ nanocomposites developed via solid state precipitation. *Journal of the European Ceramic Society, 30*, 2905–2915.

Mukhopadhyay, A., & Todd, R. I. (2011). Relationship between microstructure and abrasive wear resistance of Al_2O_3–$FeAl_2O_4$ nanocomposites produced via solid-state precipitation. *Journal of the European Ceramic Society, 31*, 339–350.

Mussler, B., Swain, M. V., & Claussen, N. (1982). Dependence of fracture toughness of alumina on grain size and test technique. *Journal of the American Ceramic Society, 65*, 566–572.

Naglieri, V., Joly-Pottuz, L., Chevalier, J., Lombardi, M., & Montanaro, L. (2010). Follow-up of zirconia crystallization on a surface modified alumina powder. *Journal of the European Ceramic Society, 30*, 3377–3387.

Nakamura, S., Tanaka, S., Kato, Z., & Uematsu, K. (2009). Strength-processing defects relationship based on micrographic analysis and fracture mechanics in alumina ceramics. *Journal of the American Ceramic Society, 92*, 688–693.

Nettleship, I., & McAfee, R. (2003). Microstructural pathways for the densification of slip cast alumina. *Materials Science and Engineering, A352*, 287–293.

Nicolaidis, I., Gurauskis, J., Baudín, C., Moreno, R., & Sánchez-Herencia, A. J. (2008). Forming of ceramic laminates comprising thin layers of a few particles. *Journal of the American Ceramic Society, 91*, 2124–2129.

Niihara, K. (1991). New design concept of structural ceramics–ceramic nanocomposites. *Journal of the Ceramic Society of Japan, 99*, 974–982.

Novak, S., Vidovic, K., Sajko, M., & Kosmac, T. (1997). Surface modification of alumina powder for LPIM. *Journal of the European Ceramic Society, 17*, 217–224.

Okada, A. (2008). Automotive and industrial applications of structural ceramics in Japan. *Journal of the European Ceramic Society, 28*, 1097–1104.

Omatete, O. O., & Janney, M. A. (1991). *Method for molding ceramic powders using a water-based gelcasting*. US Patent No: 5028362.

Omatete, O. O., Janney, M. A., & Strelow, R. A. (1991). Gelcasting—a new ceramic forming process. *American Ceramic Society Bulletin, 70*, 1641–1649.

O'Sullivan, D., Poorteman, M., Descamps, P., Cambier, F., Leriche, A., & Thierry, B. (1995). Optimisation of alumina—silicon carbide dispersions and the fabrication of nanocomposite ceramic materials. *Key Engineering Materials, 99–100*, 247–256. Switzerland: Tans Tech Publications.

O'Sullivan, D., Poorteman, M., Thierry, B., Descamps, P., Leriche, A., & Cambier, F. (1996). Comparison of properties of alumina silicon carbide nano-composites processed in aqueous and organic media. *Silicates Industriels, 61*, 235–241.

Outokumpu Research Oy, Pori, Finland Outokumpu HSC Chemistry for Windows Version 1.10., 1993.

Padture, N. P. (2009). Multifunctional composites of ceramics and single-walled carbon nanotubes. *Advanced Materials, 21*, 1767–1770.

Padture, N. P., Bennison, S. J., & Chan, H. M. (1993). Flaw-tolerance and crack-resistance properties of alumina–aluminium titanate composites with tailored microstructures. *Journal of the European Ceramic Society, 76*, 2312–2320.

Palmero, P., Naglieri, V., Chevalier, J., Fantozzi, G., & Montanaro, L. (2009). Alumina based nanocomposites obtained by doping with inorganic salt solution: application to immiscible and reactive system. *Journal of the European Ceramic Society, 29*, 59–66.

Palmero, P., Sola, A., Naglieri, V., Bellucci, D., Lombardi, M., & Cannillo, V. (2012). Elaboration and mechanical characterization of multi-phase alumina-based ultra-fine composites. *Journal of Materials Science, 47*, 1077–1084.

Pavlacka, R. J., & Messing, G. L. (2010). Processing and mechanical response of highly textured Al_2O_3. *Journal of the European Ceramic Society, 30*, 2917–2925.

Peigney, A., Laurent, Ch., Dumortier, O., & Rousset, A. (1998). Carbon nanotubes–Fe–alumina nanocomposites. Part I: influence of the Fe content on the synthesis of powders. *Journal of the European Ceramic Society, 18*, 1995–2004.

Phillips, D. S., & Shiue, Y. R. (1984). Grain-boundary microstructures in alumina ceramics. In W. D. Kingery (Ed.), *Structure and properties of MgO and* Al_2O_3 *ceramics* (pp. 357–367). Ohio, USA: The American Ceramic Society.

Piconi, C., & Maccauro, G. (1999). Zirconia as a ceramic biomaterial, a review. *Biomaterials, 20*, 1–25.

Poorteman, M., Traianidis, M., Bister, G., & Cambier, F. (2009). Colloidal processing, hot pressing and characterisation of electroconductive MWCNT-alumina composites with compositions near the percolation threshold. *Journal of the European Ceramic Society, 29*, 669–675.

Popov, V. N. (2004). Carbon nanotubes: properties and application. *Materials Science and Engineering R-Reports, 43*, 61–102.

Powers, J. D., & Glaeser, A. M. (1997). Titanium effects on sintering and grain boundary mobility of alumina. *Ceramic Engineering and Science Proceedings, 18*, 617–622.

Prabhakaran, O. J. O., Raghunath, K. S., & Melkeri, A. (2008). Novel coagulation method for direct coagulation casting of aqueous alumina slurries prepared using poly(acrylate) dispersant. *Journal of the American Ceramic Society, 91*, 615–619.

Prete, F., Rizzuti, A., Esposito, L., Tucci, A., & Leonelli, C. (2011). Highly homogeneous Al_2O_3–ZrO_2 nanopowder via microwave-assisted hydro- and solvothermal synthesis. *Journal of the American Ceramic Society, 94*, 3587–3590.

Raether, F., & Schulze, H. P. (2009). Investigation of sintering mechanisms of alumina using kinetic field and master sintering diagrams. *Journal of the European Ceramic Society, 29*, 2225–2234.

Rahaman, M. N. (2008). *Sintering of ceramics*. Forida, USA: CRC Press.

Rahaman, M. N., Yao, A., Sonny Bal, B., Garino, J. P., & Ries, M. D. (2007). Ceramics for prosthetic hip and knee joint replacement. *Journal of the American Ceramic Society, 90*, 956–988.

Rajendran, S. (1994). Production of ultrafine alpha alumina powders and fabrication of fine grained strong ceramics. *Journal of Materials Science, 29*, 5664–5672.

Rak, Z. S., & Hamburg, F. W. (1995). Manufacturing of alumina products by low and high pressure injection moulding. *Ceramica Acta, 7*, 5–13.

Rao, M. P., Rödel, J., & Lange, F. F. (2001). Residual stress induced *R*-curves in laminar ceramics that exhibit a threshold strength. *Journal of the American Ceramic Society, 84*, 2722–2724.

Rao, M. P., Sanchez-Herencia, A. J., Beltz, G. E., McMeeking, R. M., & Lange, F. F. (1999). Laminar ceramics that exhibit a threshold strength. *Science, 286*, 102–105.

Rice, R. W., Freiman, S. W., & Becher, P. F. (1981). Grain-size dependence of fracture energy in ceramics: I, experiment. *Journal of the American Ceramic Society, 64*, 345–350.

Risbud, S. H., Shan, C. H., Mukherjee, A. K., Kim, M. J., Bow, J. S., & Holl, R. A. (1995). Retention of nanostructure in aluminum-oxide by very rapid sintering at 1150 °C. *Journal of Materials Research, 10*, 237–239.

Riley, F. L. (2009). *Structural ceramics. Fundamentals and case studies*. Cambridge, UK: Cambridge University Press.

Rivas Mercury, J. M., Pena, P., de Aza, A. H., Sheptyakov, D., & Turrillas, X. (2006). On the decomposition of synthetic gibbsite studied by neutron thermodiffractometry. *Journal of the American Ceramic Society, 89*, 3728–3733.

Rödel, J., & Glaeser, A. M. (1990). Anisotropy of grain growth in alumina. *Journal of the American Ceramic Society, 73*, 3292–3301.

Ruiz-Hervías, J., Bruno, G., Gurauskis, J., Sánchez-Herencia, A. J., & Baudín, C. (2006). Neutron diffraction investigation for possible anisotropy within monolithic Al_2O_3/Y-TZP composites fabricated by stacking cast tapes. *Scripta Materialia, 54*, 1133–1137.

Runyan, J. L., & Bennison, S. J. (1991). Fabrication of flaw-tolerant aluminum-titanate-reinforced alumina. *Journal of the European Ceramic Society, 7*, 93–99.

Ruoff, R. S., & Lorents, D. C. (1995). Mechanical and thermal properties of carbon nanotubes. *Carbon, 33*, 925–930.

Russo, C. J., Harmer, M. P., Chan, H. M., & Miller, G. A. (1992). Design of a laminated ceramic composite for improved strength and toughness. *Journal of the American Ceramic Society, 75*, 3396–3400.

Ryshkewitch, E., & Richerson, D. W. (1985). *Oxide ceramics: Physical chemistry and technology* (2nd ed.). Florida, USA: Academic Press.

Sacks, M. D., Lee, H. W., & Rojas, O. E. (1988). Suspension processing of Al_2O_3/SiC whisker composites. *Journal of the American Ceramic Society, 71*, 370–379.

Saeed, M., Hossein, P. M., & Jan, M. (2010). Centrifugal gel casting: a combined process for the consolidation of homogenous and reliable ceramics. *Journal of the American Ceramic Society, 93*, 413–419.

Sánchez-Herencia, A. J. (2007). Water based colloidal processing of ceramic laminates. *Key Engineering Materials, 333*, 39–48. Switzerland: Tans Tech Publications.

Sánchez-Herencia, A. J., Gurauskis, J., & Baudín, C. (2006). Processing of Al_2O_3/Y-TZP laminates from water based cast tapes. *Composites Part B, 37*, 499–505.

Sánchez Herencia, A. J., Moreno, R., & Baudín, C. (2000). Fracture behavior of alumina–calcium hexaluminate composites obtained by colloidal processing. *Journal of the European Ceramic Society, 20*, 2575–2583.

Santacruz, I., Baudin, C., Moreno, R., & Nieto, M. I. (2004). Improved green strength of ceramics through aqueous gelcasting. *Advanced Engineering Materials, 6*, 672–676.

Sarkar, D., Adak, S., & Mitra, N. K. (2007). Preparation and characterization of an Al_2O_3–ZrO_2 nanocomposite, part I: powder synthesis and transformation behavior during fracture. *Composites Part A, 38*, 124–131.

Sarkar, D., Mohapatra, D., Ray, S., Bhattacharyya, S., Adak, S., & Mitra, N. (2007). Nanostructured Al_2O_3–ZrO_2 composite synthesized by sol–gel technique: powder processing and microstructure. *Journal of Materials Science, 42*, 1847–1855.

Sarkar, P., Prakash, O., Wang, G., & Nicholson, P. S. (1994). Micro-laminate ceramic/ceramic composites (YSZ/Al_2O_3) by electrophoretic deposition. *Ceramics Engineering and Science Proceedings, 15*, 1019–1027.

Sbaizero, O., & Lucchini, E. (1996). Influence of residual stresses on the mechanical properties of a layered ceramic composite. *Journal of the European Ceramic Society, 16*, 813–818.

Schehl, M., Diaz, J. A., & Torrecillas, R. (2002). Alumina nanocomposites from powder–alkoxide mixtures. *Acta Materialia, 50*, 1125–1139.

Scott, W. D., & Orr, K. K. (1983). Rhombohedral twinning in alumina. *Journal of the American Ceramic Society, 66*, 27–32.

Seabaugh, M., Kerscht, I., & Messing, G. (1997). Texture development by templated grain growth in liquid-phase-sintered α-alumina. *Journal of the American Ceramic Society, 80*, 1181–1188.

Shalek, P. D., Petrovic, J. J., Hurley, G. F., & Gac, F. D. (1986). Hot-pressed SiC whisker/Si, N, matrix composites. *American Ceramic Society Bulletin, 65*, 351–356.

Shanefield, D. J., & Mistier, R. E. (1974). Fine-grained alumina substrates: I. The manufacturing process. *American Ceramic Society Bulletin, 53*, 416–420.

Shanefield, D. J., Morzenti, P. T., & Mistier, R. E. (1974). Fine-grained alumina substrates: II. Properties. *American Ceramic Society Bulletin, 53*, 564–568.

Shaw, N. J., & Brook, R. J. (1986). Structure and grain coarsening during the sintering of alumina. *Journal of the American Ceramic Society, 69*, 107–110.

Shelleman, R. A., & Messing, G. L. (1988). Liquid-phase-assisted transformation of seeded γ-alumina. *Journal of the American Ceramic Society, 71*, 317–322.

Shen, Z., Johnsson, M., Zhao, Z., & Nygren, M. (2002). Spark plasma sintering of alumina. *Journal of the American Ceramic Society, 85*, 1921–1927.

Sigmund, W. M., Bell, N. S., & Bergstrom, L. (2000). Novel powder-processing methods for advanced ceramics. *Journal of the American Ceramic Society, 83*, 1557–1574.

Smith, P. A., & Haber, R. A. (1992). Reformulation of an aqueous alumina slip based on modification of particle-size distribution and particle packing. *Journal of the American Ceramic Society, 75*, 290–294.

Smuk, B., Szutkowska, M., & Walter, J. (2003). Alumina ceramics with partially stabilized zirconia for cutting tools. *Journal of Materials Processing Technology, 133*, 195–198.

Snow, D., & Heuer, A. H. (1973). Slip systems in α-Al_2O_3. *Journal of the American Ceramic Society, 56*, 153–157.

Song, H., & Coble, R. L. (1990). Origin and growth kinetics of platelike abnormal grains in liquid-phase-sintered alumina. *Journal of the American Ceramic Society, 73*, 2077–2085.

Sousa, C., Illas, F., & Pacchioni, G. (1993). Can corundum be described as an ionic oxide. *Journal of Chemical Physics, 99*, 6818–6823.

Srdic, V. V., & Radonjic, L. (1997). Transformation toughening in sol–gel-derived alumina–zirconia composites. *Journal of the American Ceramic Society, 80*, 2056–2060.

Srdic, V. V., Winterer, M., Miehe, G., & Hahn, H. (1999). Different zirconia alumina nanopowders by modification of chemical vapor synthesis. *Nanostructured Materials, 12*, 95–100.

Stearns, L. C., Zhao, J., & Harmer, M. P. (1992). Processing and microstructure development in Al_2O_3–SiC 'nanocomposites'. *Journal of the European Ceramic Society, 10*, 473–477.

Sternitzke, M. (1997). Review: structural ceramic nanocomposites. *Journal of the European Ceramic Society, 17*, 1061–1082.

Studart, A. R., Amstad, E., Antoni, M., & Gauckler, L. J. (2006). Rheology of concentrated suspensions containing weakly attractive alumina nanoparticles. *Journal of the American Ceramic Society, 89*, 418–425.

Sun, J., Gao, L., & Jin, X. H. (2005). Reinforcement of alumina matrix with multi-walled carbon nanotubes. *Ceramics International, 31*, 893–896.

Sun, J., Gao, L., & Li, W. (2002). Colloidal processing of carbon nanotube/alumina composites. *Chemistry of Materials, 14*, 5169–5172.

Suvaci, E., & Messing, G. L. (2000). Critical factors in the templated grain growth of textured reaction-bonded alumina. *Journal of the American Ceramic Society, 89*, 2041–2048.

Suzuki, T., Sakka, Y., & Kitazawa, K. (2001). Orientation amplification of alumina by colloidal filtration in a strong magnetic field and sintering. *Advanced Engineering Materials, 3*, 490–492.

Tallon, C., Jach, D., & Moreno, R. (2007). Gelcasting performance of alumina aqueous suspensions with glycerol monoacrylate: a new low toxicity acrylic monomer. *Journal of the American Ceramic Society, 90*, 1386–1393.

Tallon, C., Limacher, M., & Franks, G. V. (2010). Effect of particle size on the shaping of ceramics by slip casting. *Journal of the European Ceramic Society, 30*, 2819–2826.

Tanaka, S., Pin, C. C., & Uematsu, K. (2006). Effect of organic binder segregation on sintered strength of dry-pressed alumina. *Journal of the American Ceramic Society, 89*, 1903–1907.

Tari, G. (2003). Gelcasting ceramics: a review. *American Ceramic Society Bulletin, 82*, 43–46.

Tari, G., Ferreira, J. M. F., & Lyckfeldt, O. (1998). Influence of the stabilizing mechanism and solid loading on slip casting of alumina. *Journal of the European Ceramic Society, 18*, 479–486.

Tateiwa, T., Clarke, I. C., Williams, P. A., Garino, J., Manaka, M., Shishido, T., et al. (2008). Ceramic total hip arthroplasty in the United States: safety and risk issues revisited. *The American Journal of Orthopedics, 37*, E26–E31.

Taylor, D. (1984a). Thermal expansion data: III. Sesquioxides, M_2O_3 with the corundum and the A-, B- and C-M_2O_3. *British Ceramic Transactions and Journal, 83*, 92–98.

Taylor, D. (1984b). Thermal expansion data. XI. Complex oxides, A_2BO_5, and the garnets. *British Ceramic Transactions and Journal, 86*, 1–6.

Timms, L. A., & Ponton, C. B. (2002). Processing of Al_2O_3/SiC nanocomposites—part 1: aqueous colloidal processing. *Journal of the European Ceramic Society, 22*, 1553–1567.

Timms, L. A., Ponton, C. B., & Strangwood, M. (2002). Processing of Al_2O_3/SiC nanocomposites—part 2: green body formation and sintering. *Journal of the European Ceramic Society, 22*, 1569–1586.

Tonejc, A., Stubiæar, M., Tonejc, A. M., Kosanoviæ, K., Subotiæ, B., & Smit, I. (1994). Transformation of γ-AlOOH (boehmite) and $Al(OH)_3$ (gibbsite) to α-Al_2O_3 (corundum) induced by high energy ball milling. *Journal of Materials Science Letters, 13*, 519–520.

Tokoname, M. K., Oda, I., & Yamamoto, N. (1980). *Transparent polycrystalline alumina and high pressure vapor discharge lamp*. US Patent No: 4182972.

Toschi, F., Melandri, C., Pinasco, P., Roncari, E., Guicciardi, S., & de Portu, G. (2003). Influence of residual stresses on the wear behavior of alumina/alumina–zirconia laminated composites. *Journal of the American Ceramic Society, 86*, 1547–1553.

Tseng, W. J., & Wu, C. H. (2002). Aggregation, rheology and electrophoretic packing structure of aqueous Al_2O_3 nanoparticles suspensions. *Acta Materialia, 50*, 3757–3766.

Tuan, W. H., Chen, R. Z., Wang, T. C., Cheng, C. H., & Kuo, P. S. (2002). Mechanical properties of Al_2O_3–ZrO_2 composites. *Journal of the European Ceramic Society, 22*, 2827–2833.

Uchikoshi, T., Suzuki, T., Okuyama, H., & Sakka, Y. (2004). Fabrication of textured alumina by electrophoretic deposition in a strong magnetic field. *Journal of Materials Science, 39*, 861–865.

Unwin, A. M., Cao, H., Chen, H., Zhao, H., Kennedy, A., & Zhu, Y. Q. (2010). Multi-walled carbon nanotubes reinforced Al_2O_3 nanocomposites: mechanical properties and interfacial investigations. *Composites Science and Technology, 70*, 1199–1206.

Uribe, R. (2001). *Desarrollo de materials estructurales de alumina-titanato de aluminio con alta resistencia al choque térmico* (Ph.D. thesis). Universidad Autónoma de Madrid.

Uribe, R., & Baudín, C. (2000). *Procesamiento de materiales estructurales de alúmina-titanato de aluminio. XL Congreso de la Sociedad Española de Cerámica y Vidrio*. Onda, Spain.

Uribe, R., & Baudín, C. (2003). Influence of a dispersion of aluminum titanate particles of controlled size on the thermal shock resistance of alumina. *Journal of the American Ceramic Society, 86*, 846–850.

Vasilos, T., & Spriggs, R. M. (1963). Pressure sintering: mechanisms and microstructures for alumina and magnesia. *Journal of the American Ceramic Society, 46*, 493–496.

Wakao, Y., & Hibino, T. (1962). Effect of metallic oxides on α-transformation of alumina. *Nagoya Kogyo Gijutsu Shikennjyo Hokoku, 11*, 588–595.

Walker, C. N., Borsa, C. E., Todd, R. I., Davidge, R. W., & Brook, R. J. (1994). Fabrication, characterisation and properties of alumina matrix nanocomposites. *British Ceramic Proceedings, 53*, 249–264.

Wang, W.-L., Bi, J.-Q., Sun, K.-N., Du, M., Long, N.-N., & Ba, Y.-J. (2011). Fabrication of alumina ceramic reinforced with boron nitride nanotubes with improved mechanical properties. *Journal of the American Ceramic Society, 94*, 3636–3640.

Wang, H., & Hu, X. (1996). Surface properties of ceramic laminates fabricated by die pressing. *Journal of the American Ceramic Society, 79*, 553–556.

Wang, Y., Suryanarayana, C., & An, L. (2005). Phase transformation in nanometersized γ-alumina by mechanical milling. *Journal of the American Ceramic Society, 88*, 780–783.

Watchman, J. B., Jr., & Maxwell, L. H. (1959). Strength of single crystal sapphire and ruby as a function of temperature and orientation. *Journal of the American Ceramic Society, 42*, 432–453.

Watson, M. J., Chan, H. M., Harmer, M. P., & Caram, H. S. (2005). Feedback-controlled firing of reaction-bonded aluminum oxide. *Journal of the American Ceramic Society, 88*, 3380–3387.

Wei, G. C. (2009). Transparent ceramics for lighting. *Journal of the European Ceramic Society, 29*, 237–244.

Wei, G. C., & Becher, P. F. (1985). Development of SiC-whisker-reinforced ceramics. *American Ceramic Society Bulletin, 64*, 298–304.

Wells, A. F. (1984). *Structural inorganic chemistry*. Oxford, GB: Oxford University Press.

Whitney, E. D. (Ed.), (1994). *Ceramic cutting tools. Materials, development and performance*. Florida, USA: Noyes Publications.

Wiederhorn, S. M. (1969). Fracture of sapphire. *Journal of the American Ceramic Society, 52*, 485–491.

Wiederhorn, S. M., Hockey, B. J., & Roberts, D. E. (1973). Effect of temperature on the fracture of sapphire. *Philosophical Magazine, 28*, 783–796.

Williams, J. C. (1976). Doctor-blade process. In F. Y. Y. Wang (Ed.), *Ceramic fabrication processes: Vol. 9. Treatise on materials science and technology*. New York, USA: Academic Press.

Winn, A. J., & Todd, R. I. (1999). Microstructural requirements for alumina-SiC nanocomposites. *British Ceramic Proceedings, 59*, 153–164.

Wu, Y., Zhang, Y., Pezzotti, G., & Guo, J. (2002). Influence of AlF_3 and ZnF_2 on the phase transformation of gamma to alpha alumina. *Materials Letters, 52*, 366–369.

Xue, L. A., & Chen, I.-W. (1990). Deformation and grain growth of low-temperature-sintered high-purity alumina. *Journal of the American Ceramic Society, 73*, 3518–3521.

Xue, L. A., & Chen, I.-W. (1992). Influence of additives on γ- to-α transformation of alumina. *Journal of Materials Science Letters, 11*, 443–445.

Yahya, & Todd., (in press) submitted to *Journal of the European ceramic Society*.

Yang, J., Yu, J., & Huang, Y. (2011). Recent developments in gelcasting of ceramics. *Journal of the European Ceramic Society, 31*, 2569–2591.

Yao, W., Liu, J., Holland, T. B., Huang, L., Xiong, Y., Schoenung, M., et al. (2011). Grain size dependence of fracture toughness for fine grained alumina. *Scripta Materialia, 65*, 143–146.

Yin, L., Song, X. F., Song, Y. L., Huang, T., & Li, J. (2006). An overview of in vitro abrasive finishing & CAD/CAM of bioceramics in restorative dentistry. *International Journal of Machine Tools and Manufacture, 46*, 1013–1026.

Yoshizawa, Y., Hirao, K., & Kanzaki, S. (2004a). Fabrication of low cost fine-grained alumina powders by seeding for high performance sintered bodies. *Journal of the European Ceramic Society, 24*, 325–330.

Yoshizawa, Y., Hirao, K., & Kanzaki, S. (2004b). Mechanical properties of textured alumina made by high-temperature deformation. *Journal of the American Ceramic Society, 87*, 2147–2149.

Yoshizawa, Y., & Saito, F. (1996). Formation of α-Al_2O_3 from $Al(OH)_3$ in the presence of seed particles and its sinterability. *Journal of the Ceramic Society of Japan, 104*, 867–871.

Yoshizawa, Y., Toriyama, M., & Kanzaki, S. (2001). Fabrication of textured alumina by high-temperature deformation. *Journal of the American Ceramic Society, 84*, 1392–1394.

Young, A. C., Omatete, O. O., Janney, M. A., & Menchhofer, P. A. (1991). Gelcasting of alumina. *Journal of the American Ceramic Society, 74*, 612–618.

Yu, B. C., & Lange, F. F. (2010). Shape forming alumina slurries via Colloidal IsoPressing. *Journal of the European Ceramic Society, 30*, 2795–2803.

Zhan, G. D., Kuntz, J., Wan, J., Garay, J., & Mukherjee, A. K. (2002). Alumina-based nanocomposites consolidated by spark plasma sintering. *Scripta Materialia, 47*, 737–741.

Zhan, G. D., Kuntz, J. D., Wan, J., & Mukherjee, A. K. (2003). Single-wall carbon nanotubes as attractive toughening agents in alumina-based nanocomposites. *Nature Materials, 2*, 38–42.

Zhang, S. C., Fahrenholtz, W. G., Hilmas, G. E., & Yadlowsky, E. J. (2010). Pressureless sintering of carbon nanotube-Al_2O_3 composites. *Journal of the European Ceramic Society, 30*, 1373–1380.

Zhang, T., Kumari, L., Du, G. H., Li, W. Z., Wang, Q. W., Balani, K., et al. (2009). Mechanical properties of carbon nanotube-alumina nanocomposites synthesized by chemical vapor deposition and spark plasma sintering. *Composites Part A, 40*, 86–93.

Zhang, Z., & Lange, F. F. (2006). Investigation on strain recovery during microfabrication by colloidal isopressing. *Journal of the American Ceramic Society, 89*, 2348–2351.

Zhang, L., Vleugels, J., & Van der Biest, O. (2010). Slip casting of alumina suspensions in a strong magnetic field. *Journal of the American Ceramic Society, 93*, 3148–3152.

Zhao, J., Stearns, L. C., Harmer, M. P., Chan, H. M., Miller, G. A., & Cook, R. F. (1993). Mechanical behavior of alumina–silicon carbide nanocomposites. *Journal of the American Ceramic Society, 76*, 503–510.

Zheng, J., & Reed, J. S. (1988). Effects of particle packing characteristics on solid-state sintering. *Journal of the American Ceramic Society, 72*, 810–817.

Zywiel, M. G., Sayeed, S. A., Johnson, A. J., Schmalzried, T. P., & Mont, M. A. (2011). Review: state of the art in hard-on-hard bearings: how did we get here and what have we achieved? *Expert Review of Medical Devices, 8*, 187–207.

2.03 Synthesis/Processing of Silicon Nitride Ceramics

Arvid Eric Pasto, Retired from Sparks, NV, USA

© 2014 Elsevier Ltd. All rights reserved.

2.03.1 Overview of Silicon Nitride Ceramics

2.03.1.1 Introduction to the Family of Materials

Silicon nitride is a fairly simple material at first glance, consisting of three silicon atoms and four nitrogen atoms, as Si_3N_4. It can in fact be made in just this composition by simply heating a silicon metal powder in a nitrogen atmosphere. The resulting material has, however, much residual porosity, resulting in low toughness and strength, as well as poor oxidation resistance. If one adds to the silicon powder an accessory oxide, such as yttrium, an entirely different type of silicon nitride develops: the density, microstructure, toughness, strength, oxidation resistance, and a host of other properties are improved. Most of this chapter will deal with the latter type of silicon nitride, so-called sintered silicon nitride (SSN), even though sintering is not the only way to densify it. The silicon nitride composition can be a basis for composites as well, utilizing particulates, whiskers, or fibers. Silicon nitrides prepared for thin-film applications such as electronics, by techniques such as chemical vapor deposition (CVD), physical vapor deposition (PVD), and others, will not be discussed.

Arguably Petzow and Hermann, consisting of 121 pages and including 658 references, wrote the most complete review of silicon nitrides in 2002. This review covers phase equilibria, crystal structures, powders, processing, microstructural development, properties and behaviors, applications, and it even touches on composites (Petzow & Herrmann, 2002). A more recent review of the fabrication of dense silicon nitride ceramics was published in 2009 (Bochanegra-Bernal & Matovic, 2009).

Books on silicon nitride are also available, many of which are published proceedings of major conferences on the subject. The 1993 Boston Conference of the Materials Research Society called “Silicon Nitride Ceramics—Scientific and Technological Advances,” and the international conferences on materials for heat engine applications are good examples (Bunk & Hausner, 1986, 1280 pp.; Chen, Becher, Mitomo, Petzow, & Yen, 1993; Tennery, 1989, 1559 pp.).

2.03.1.2 History of Development

The first patent on silicon nitride, interestingly enough, was as “manure”. That is, it was thought that silicon would combine with nitrogen, which could then be spread on the ground as a fertilizer, releasing nitrogen to plants as it decayed naturally. Much later, largely due to efforts in England, it was determined that silicon nitride could be a possible structural material, possessing high strength, along with good creep and oxidation resistance, thereby making it potentially useful for gas turbine engines and other applications where elevated temperature resistance was required. See reaction-bonded silicon nitride (RBSN) in the following sections. **Figure 1** depicts the hot isostatically pressed (HIPed) silicon nitride turbine components.

These initial findings launched a major worldwide series of efforts in numerous countries (England, Japan, the US, Germany, etc.) throughout the 1970s and into the 1990s, sponsored by government agencies involved in energy and/or defense work. Because of rapid advances made across the globe, the technology grew rapidly, and potential applications by the score were evaluated. While the primary thrust was high-temperature application in turbine engines, the materials' promised high strength at high temperatures, excellent oxidation resistance, relatively good toughness (for a ceramic), high hardness, low thermal expansion coefficient, and other properties and behaviors made it an excellent candidate for internal combustion (piston) engines as well (**Figure 2**) (Worthen & Pasto, 1988).

It also appeared to be an ideal material for high-speed missile applications, for jet engine exhaust protection, possibly for coal gasification or liquefaction environments, and on and on. The onset of work on composites

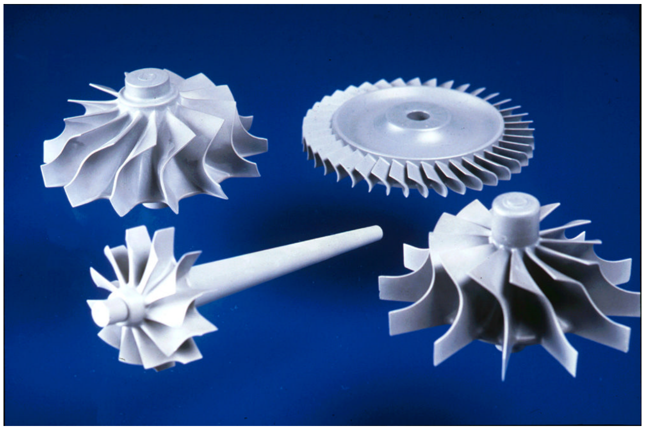

Figure 1 HIPed silicon nitride turbine components. Clockwise from top left: radial-flow turbine engine rotor, axial-flow turbine engine rotor, counter-rotating radial-flow turbine engine rotor, and turbocharger rotor (before final machining). Photo courtesy of GTE Laboratories Incorporated.

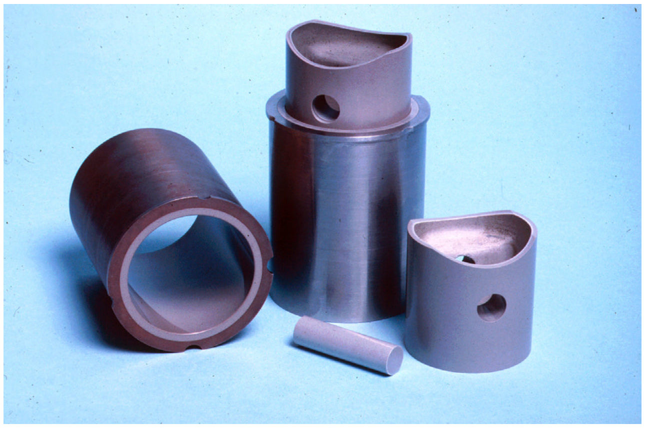

Figure 2 Sintered silicon nitride piston(s), cylinder liners inside metallic cylinders, and silicon nitride wrist pin. The high stability of silicon nitride and its low thermal expansion coefficient would allow maintenance of such close tolerances that a ringless piston design was being developed here. Photo courtesy of GTE Laboratories Incorporated.

added yet another set of applications, including high toughness, high hardness, and high-temperature chemical attack resistance areas such as cutting and milling tools. Fiber toughening of silicon nitride increased the potential range of application even further, to include larger structures such as jet or turbine engine combustors.

With the demise of the major funding program in the United States (run by the Department of Energy) in the early 2000s, work on silicon nitride structural ceramics in the US slowed dramatically, and in the rest of the world as well. It was realized that although tremendous progress had been made in improving all the critical properties and behaviors (strength, creep and oxidation resistance, etc.), these materials were still not reliable and inexpensive enough to justify their use in, for example, gas turbine engines for automotive usage. Programmatic attention in the US shifted to lightening up vehicles, and use of electrical or hydrogen-powered propulsion systems. Nonetheless, huge amounts of excellent information on every technology involved in silicon nitride (and other ceramics such as silicon carbide) from powders through composition development into fabrication technologies and application development were made available as government reports and papers published in the open literature.

2.03.1.3 Strength of Brittle Materials, Including Silicon Nitride

The strength of any given ceramic component depends on many variables. The three major ones are (1) the material's inherent toughness (typically specified as K_{Ic}), (2) the type and size distribution of failure-inducing "flaws" which have been incorporated into the component during processing or finishing (or even during handling and installation), and (3) the distribution of stress throughout the component in operation. The strength of a material (its stress at failure, s_{f}) can be related to the toughness and the size and severity of the failure-inducing flaws by the relationship

$$s_{\mathrm{f}} = \frac{K_{\mathrm{Ic}}}{Y(\pi a_{\mathrm{c}})^{1/2}}$$

where a_{c} is the size of the flaw. Y is a dimensionless constant that depends on the crack configuration and geometry, and may also depend on the stress distribution. Many test specimens must be prepared and fractured in order to obtain a good representation of the flaw size and type distributions since brittle materials fail in a stochastic fashion. Weibull statistics are typically utilized in order to characterize a ceramic's mechanical behavior.

Even though it is difficult to prepare ceramic tensile test specimens, these are extremely useful in determining which fatal flaws are present and in what frequency, since this type of test places a large volume of material under constant stress.

Thus, for a high-reliability component, one ordinarily looks for a silicon nitride with good toughness, which is processed in such a fashion as to produce few defects, and which yields a resultant high average strength, but, more importantly, a high Weibull modulus.

A detailed description of the strength and reliability of ceramics is treated in depth in another chapter of this series (Chapter 2.09).

2.03.2 Types of Silicon Nitride

There are many means to prepare a silicon nitride component, and with these different techniques come different properties and behaviors. The fabrication technique utilized has lent its name to the material, and there is quite a litany of abbreviations derived therefrom.

2.03.2.1 Monolithics

2.03.2.1.1 RBSN and Offshoots

For instance, if one begins by forming a rough component shape from silicon powder, then nitrides that shape, one gets what is called reaction-bonded silicon nitride or RBSN. RBSN is, then, basically pure silicon and nitrogen combined. However, it was found early on that adding a catalyst such as Fe would increase the rate and extent of the reaction, so there may be impurities deliberately added (or they may be there from the original powders). Recently research and development efforts have included investigation of other metal catalysts, including the rare earths (Pavarajarn, Wongthavorn, & Praserthdam, 2007). This type of silicon nitride has relatively low strength, toughness, and oxidation resistance, primarily because it has residual porosity (up to ca 15%) and the microstructure has not developed the toughening high-aspect-ratio silicon nitride crystals that are required. Its major virtues were its strength retention to elevated temperatures, and the lack of major dimensional changes on densification (nitridation). A variant of this process is called sintered reaction-bonded silicon nitride (SRBSN), wherein a sintering aid such as yttrium oxide is added to the silicon powder prior to shaping. Upon heating in nitrogen, silicon nitride is formed, and a liquid as well, from the reaction between the silicon and nitrogen with the oxygen and cation (e.g. Y) in the sintering aid. The liquid causes shrinkage and pore reduction, and allows development of a tougher crystal structure. Reduction of pore volume also increases oxidation resistance. This additional densification, however, introduces shrinkage and dimensional changes. A paper from 1960 gives an excellent summary of RBSN development up to that time (Parr, Martin, & May, 1960).

Efforts to further develop the SRBSN process have been continuing, with a number of papers being published between 2006 and the present. Zhu, Zhou, Hirao, and Lences (2006) found improved thermal conductivity in SRBSN through control of the purity of the initial powders, and maintaining low levels of oxygen and aluminum. The same team of authors then studied the sintering additives, including yttria and magnesia, as well as magnesium silicon nitride, again attempting to increase the thermal conductivity. They found that MgO and $MgSiN_2$ were equally effective (Zhu, Zhou, Hirao, & Lences, 2007). Zhu, Sakka, Zhou, and Hirao (2007) have further studied SRBSN, looking at the effects of addition of, for example, Li_2O, along with yttria and magnesium silicon nitride.

Müller, Bauer, and Knitter (2009), Müller, Rögner, Okolo, Bauer, and Knitter (2010), and Müller, Bauer, Knitter, and Rögner (2010) have also investigated SRBSN recently, evaluating the reaction-bonding process itself, the densification behavior, and the resultant mechanical behavior and properties. They utilized a low-pressure injection-molding process to fabricate small components, and found the strength to be limited by the presence of secondary phases at the surface of bending-test specimens, and that these phases must be avoided to obtain good mechanical reliability.

Schematic diagrams of the processing of RBSN and SRBSN components are presented in **Figures 3** and **4**.

2.03.2.1.2 SSN/HPSN/HIPSN

The second major family of silicon nitrides is the hot-pressed silicon nitride(HPSN)/sintered silicon nitride (SSN)/hot isostatically pressed silicon nitride (HIPSN) series. In all of these, a densification aid, chosen from among any number of oxides, is added to silicon nitride powder. These additions started initially with MgO but rapidly progressed to yttrium oxide and then all of the rare earths, as well as mixtures of oxides (Cinibulk, Thomas, & Johnson, 1992). A huge amount of research was required on the development of the phase equilibria amongst these cation–oxygen–nitrogen–silicon pseudoquaternary compounds in order to truly understand what was happening. Many compounds new to the ceramic world were discovered, including a series of yttrium–silicon–oxygen–nitrogen compounds and their analogs among the rare earths.

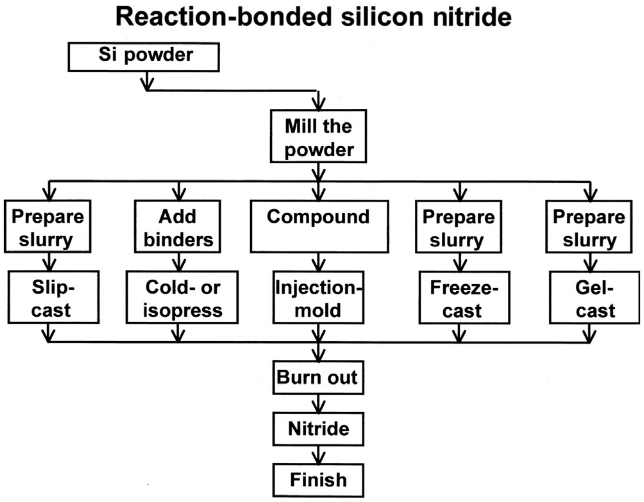

Figure 3 Schematic flow diagram for the processing of reaction-bonded silicon nitride components.

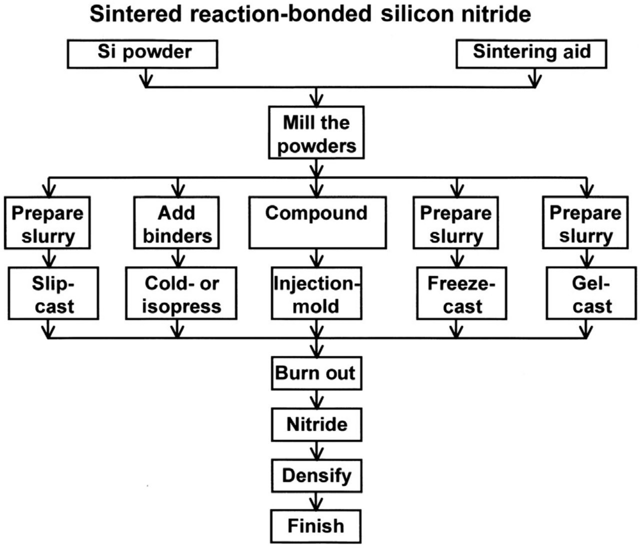

Figure 4 Schematic flow diagram for the processing of sintered reaction-bonded silicon nitride components.

Elucidation of the mechanism(s) of densification and microstructural development required a huge effort among many investigators. It was quickly determined that a liquid-phase sintering mechanism was occurring, with reaction between the silicon, oxygen, nitrogen, and other cations from additive oxides resulting in a viscous liquid at elevated temperatures. Hampshire and Jack (1981) studied the kinetics and mechanisms. Tsuge and Nishida (1978) showed how yttria and alumina additions to Si_3N_4 resulted in high-strength materials if the glassy grain boundary phase could be at least partially crystallized. Studies of the grain boundary, and other accessory phases, also required expenditure of much effort, and this continues to this day (Bonnell, Tien, & Ruhle, 1987; Cinibulk, Thomas, & Johnson, 1990; Shibata et al., 2004; Yang, Ohji, & Niihara, 2000; Ziegler, Idrobo, Cinibulk, Browning, & Ritchie, 2004).

Studies on the properties, especially the strength both at low temperatures and at elevated temperatures, resulted in a great deal of investigation into microstructures. Hirao et al. showed how to generate high-toughness and -strength silicon nitrides by controlling grain size and shape during processing, while others studied not only the microstructure but also the influence of the sintering aid and its resultant phase distribution (Becher et al., 1998; Hirao, Ohashi, Brito, & Kanzaki, 1995; Kleebe, Pezzotti, & Ziegler, 1999; Sajgalik, Dusza, & Hoffmann, 1995; Shen, Zhao, Peng, & Nygren, 2002; Sun et al., 1998).

Hot pressing is actually quite a simple process, involving pouring a mixture of silicon nitride powder and a densification aid into a graphite or boron nitride (BN)-lined mold and heating it while applying pressure to two punches. The atmosphere is typically vacuum or nitrogen. The pressure from the punches assists the driving force for pore closure, and a nearly 100% dense product can be attained. The uniaxial nature of this process causes the silicon nitride grains within the compact to grow in the direction normal to the pressure, with the result being that there exists a differential strength and toughness along the directions normal to versus parallel to the pressing direction.

HIPing obviates this problem of differential properties in varying direction, by applying a uniform pressure all around the component. Of course, this process cannot be utilized until the internal pores in the structure are closed, so one can either do a sinter-HIP process, where sintering is performed until closed porosity is attained, or one can utilize an enclosed HIP process, wherein the burned-out component is encapsulated in a metal container prior to heating/pressurization. A Swedish company named ASEA developed and patented a process called glass-encapsulated HIPing, and it or a variant of it was widely utilized in the 1980–2000 timeframe by various manufacturers (Adlerborn, Burnström, Hermansson, & Larker, 1987; Westman & Larker, 1999).

A schematic process flow diagram for the preparation of sintered or an HIPed silicon nitride component is presented in Figure 5. Note that sintering can be accomplished via simple furnace heating, but a large effort was made in the 1980s–1990s, and it has continued onward, to develop microwave heating (Sreekumar & Earl, 2009; Sreekumar & Traver, 2010). However, in retrospect it appears that little economic impact ever resulted

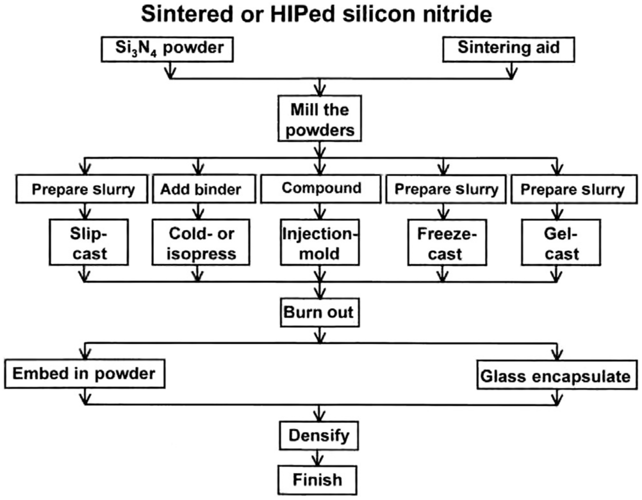

Figure 5 Schematic process flow diagram for the preparation of sintered or HIPed silicon nitride ceramic components.

from this effort. More recently, a process called "spark plasma sintering" has been in vogue, and, as with microwave sintering, it appears to have some benefits (Peng, Shen, & Nygren, 2005).

2.03.2.1.3 Chemically Derived

In the 1980s, a number of papers appeared in the literature concerning the preparation of silicon nitride ceramics via chemical processes: that is, a chemical compound containing a backbone of Si instead of C, and with accessory nitrogen atoms (typically a polysilazane), was prepared and pyrolized. This process was very appealing, but had a number of problems. Most of the molecules had carbon and hydrogen attached, and it was difficult to totally eliminate the carbon, so that a carbonitride compound was the result. The pyrolysis process also incorporated a huge weight loss and resultant shrinkage, so that making a shape and then maintaining it during heating was extremely difficult, if not improbable. Despite all the R&D to date, no structural ceramic product ever made it to the mass market from this approach. It is useful for the preparation of thin films, however, where the gas evolution and three-dimensional shrinkage can be accommodated by the thin dimension (Dixmier, Bellissent, Bahloul, & Goursat, 1994; Kroll, 2005; Schwab & Page, 1995).

2.03.2.1.4 SiAlONs

In the early days of silicon nitride development, it was discovered that the silicon nitride lattice could accommodate a certain amount of Al substitution for Si, if it was counterbalanced by the charge-balancing amount of O for N (Hampshire, Park, Thompson, & Jack, 1978). The resulting material exhibited a slightly expanded lattice compared to pure Si_3N_4, and could be fabricated into shapes with the same types and amounts of sintering aids as for SSN. As for pure silicon nitride, there exist both the alpha and the beta phase. However, alpha Si_3N_4 tends to dissolve in the liquid phase present during sintering and precipitate as the beta phase, whereas in SiAlONs, one can retain either or both phases in the final product. A recent review of silicon nitride and sialon ceramics by Hampshire describes these materials and their phase relations and behaviors in depth (Hampshire, 2009).

2.03.2.2 Composites

The potential for, and application of, ceramic composites based on silicon nitride was reviewed in 1987 (Buljan & Sarin, 1987). The following paragraphs elucidate the main points and update the work described.

2.03.2.2.1 Particulate

Much of the structural materials research in the 1980s involved composite theory, with researchers attempting to understand the principles of strength and toughness, including the main topic of fracture (crack origination, crack propagation, slow crack growth at high temperatures, etc.). At the same time, experimenters were adding any number of different materials to silicon nitride bodies in an attempt to strengthen and/or toughen (or harden) them. SiC was an obvious choice since it also had an Si basis and was known to exhibit a high hardness. TiC and others were also evaluated. Particulates had the advantage over whiskers and fibers of being readily incorporated into a body without having to worry about any preferred orientation affects. That is, composite additions with a high aspect ratio would tend to orient themselves during processing, whereas the more equidimensional particulates would not. On the other hand, one had to be concerned with maintaining the particulate additions equally well dispersed throughout the product: great differences in particle size, or worse, density could cause the particulate and the silicon nitride to separate during forming.

Because of the potential health problems that could be caused by the processing of ceramic or metal whiskers (next section), efforts on particulate-toughened silicon nitride focused on less problematic, but still highly anisotropic materials, such as microfibrils (not as small and inhalable as whiskers) and nanomaterials, include nanotubes. The potential adverse health effects of nanomaterials are as yet not fully explored, allowing materials processing research and development to proceed apace. Carbon nanotube production processes have been ramped up to such a level that they could possibly be economically feasible as additions to silicon nitride, and efforts have been made to develop such ceramics (Balázsi et al., 2005).

Microfibrils, or short fibers, have been introduced into Si_3N_4 ceramics, including chopped carbon fibers (Herzog, Woetting, & Vogt, 2007). These authors investigated use of a novel preceramic chemical as a precursor to the silicon nitride (RBSN), and studied the composite's strength properties.

2.03.2.2.2 Whisker

In the 1980s, silicon carbide whiskers were made available at a relatively low cost, as a byproduct of the pyrolysis of, for example, rice hulls. Additional research determined the mechanism for the formation of these whiskers, and several processes arose by which one could make very pure, high-aspect ratio whiskers in large quantities. These became the basis for the aluminum oxide–SiC whisker cutting tools, sold by the Greenleaf, for instance. However, the apparent health problems caused by the asbestos fiber scare put the use of whiskers into great doubt, and the whisker technology basically disappeared (Das Chowdhury, Carpenter, & Braue, 1992).

2.03.2.2.3 Fiber

Fiber composite technology, typically involving the wrapping of a mandrel with fibers, such as graphite or amorphous carbon, and then infiltration by a chemical precursor to a ceramic, was well known by the time silicon nitride ceramics became a hot topic. Researchers experimented with use of carbon fibers, then with the more recently available SiC fibers (and/or silicon carbide/nitride mixed fibers) as a basis for composites. Newer work has even evaluated silica fibers. Infiltration was performed with either liquid- or gas-phase precursors to the silicon nitride matrix. These were called ceramic matrix composites (CMCs). Enormous strides were made in understanding the nature of toughening, vis-à-vis the amount of bonding between the fiber and the matrix (Hyuga, Jones, Hirao, & Yamauchi, 2004; Lundberg, Pompe, Carlsson, & Goursat, 1990; Qi, Zhang, & Hu, 2007; Saigal et al., 1993).

For turbine engine application, overcoating processes and compositions were developed, to protect the fiber–matrix bond interaction and to prevent complete oxidation of the structure (Ramasamy, Tewari, Lee, Bhatt, & Fox, 2010).

2.03.3 Powders and Their Processing

Silicon powders for RBSN and its offshoots have been around for many years. Quality silicon nitride powders for the SSN family were not readily available until the 1980s, when a large number of companies (Starck in Germany, Ube in Japan, others) stepped in to fill the need. High purity in the starting material is always required for those applications requiring the highest temperature strength and creep- and oxidation resistance. For other applications at less rigorous conditions, cheaper, typically less-pure powders are also available.

Silicon nitride powder and its densification aid(s) are typically mixed and ground in a mill of some sort (e.g. attritor mill), often with a compaction aid (stearate) if it is to be pressed and sintered. For hot pressing, no compaction aid is needed. It the fabrication process is to be a fluid-based casting process, such as slip casting, freeze casting, or gel casting, the powders have to be well dispersed in the fluid. For economic purposes, the fluid is typically water, but various organic media have also been utilized. In the latter case, to keep costs under control, the fluid is recaptured, if possible, and purified for reuse. For casting processes, called "colloidal processing," the powders are typically milled within the liquid which is the casting vehicle. To prevent contamination of the powders, silicon nitride milling balls have been developed by some companies. Others utilize oxide-based milling media, e.g. aluminum oxide, and allow for the added Al_2O_3 as part of the composition.

2.03.4 Shape Making

There are several means available to fabricate a silicon nitride shape. It is important to understand that the chosen technique may well cause the component to exhibit very different properties as compared to one fabricated using a different process. This is largely due to the incorporation into the component of different types of manufacturing defects, which strongly influence strength, for instance (Natansohn & Pasto, 1991; Pasto, Neil, & Quackenbush, 1984). A particularly difficult problem with silicon nitride materials is the reaction that occurs at elevated temperatures (e.g. during densification) between the Si_3N_4 and any Fe, which may be present, from grinding or compounding or injection molding processes. The propensity to form a range of Fe silicides during this reaction leaves large metallic Fe–Si chunks in the matrix, as well as high-pressure gaseous nitrogen bubbles, which act as strength limiters (Pasto, 1984).

The simplest way to make a shape is to pour the powder(s) and a binder into a die and uniaxially press it. This technique, of course, limits one to simple flat shapes. Another technique for simple shapes is isostatic pressing, which typically leaves the component with less of an internal density gradient. This may be done via either what is called dry-bag or wet-bag pressing, depending on whether the bagged component is placed into a wet (hydraulic) or gaseous (nitrogen or other) environment for pressure application. Hot pressing has the same shape limitation. Two major problems exist with cold-pressing operations: (1) the silicon nitride powder must be extremely finely divided and well mixed with the sintering additives to provide for sintering reactivity, and (2) it must be granulated in such a way that the extremely fine powder(s) do not separate from each other, and the granules flow easily into the die/mold. Typically, a process called *spray drying* has been utilized: the powders are milled in an aqueous (or other) fluid and then sprayed into a heated chamber. The spray droplets form approximately spherical granules, in which the sintering additives are contained, hopefully homogeneously. However, sometimes the movement of the liquid phase from the center of the droplet to the surface preferentially drags along with it some of the sintering additive. This effect may have deleterious ramifications on the development of structural flaws during the pressing and densification steps. A better means may be to perform "freeze granulation" (Lyckfeldt, Rundgren, & Sjostedt, 2004), wherein binder/additive surface migration is limited.

To generate more unique shapes, one must resort to slip casting, pressure casting, freeze casting, tape casting, gel casting, or injection molding. These are typically classified as "colloidal processes" since the silicon nitride and sintering aid powders must be dispersed into some fluid matrix, however viscous it may be. Excellent reviews of colloidal processing of silicon nitride were presented in 1998 and 2003 (Laarz, Muerk, & Bergstrom, 2003; Lange, 1998). A final means to obtain intricate shapes is isostatic pressing and green machining. This requires use of a binder with great strength if the machining is performed in the green state, or, alternatively, the blank can have the binder burned out and one can perform some presintering to strengthen the material.

In slip casting, the silicon nitride and densification aid powders are dispersed into a liquid, typically water, milled, and then poured into a porous mold. The liquid escapes via capillary processes into the porous mold, leaving the binder and powders behind. One may apply external hydrostatic pressure to speed up the process, as in pressure casting. Some outstanding work was performed at Saint Gobain Corporation in Massachusetts in the late 1980s–early 1990s, in pursuit of a technique to provide complex silicon nitride shapes with extremely high strength. They ultimately developed a colloidal processing scheme that yielded tensile strengths of >1 GPa in ASTM Type A tensile rod tests. The process avoided contact of the slurry with metallic fabrication components as much as possible, recognizing the deleterious effects generated by the reactions between silicon nitride and the metals at HIPing temperatures (Pujari et al., 1995).

Slip casting of silicon nitride has been accomplished utilizing a variety of dispersants, and in one case using polyethyelenimine (Zhu, Uchikoshi, & Sakka, 2007), it was performed under a strong magnetic field, so as to align the silicon nitride powder crystallites in a preferred orientation. In another case, the dispersant utilized was ammonium polyacrylate, and significant improvement in densified material properties was determined when the slip was made using alumina- and yttria-coated silicon nitride powder particles as compared to dispersing all three components separately in the milling process (Albano & Garrido, 2004). A process to generate porous silicon nitride via slip casting, along with a pore-forming agent, was developed in 2009, utilizing yet another dispersant (carboxymethyl cellulose) (Wang, Yang, Gao, Yu, & Li, 2009).

Alternatively, one may add chemicals to the slip, which inhibit growth of large ice crystals, and then pour the slip into a mold and freeze the suspension. From there, it is vacuum freeze-dried. After drying and binder burnout, sintering and or sinter-HIPing is then applied to densify the product. An alternative to the slip-casting approach is to perform an injection molding operation using the aqueous-based suspension. This process was patented by the Ceramics Process Systems Corporation [i.e. Forming of Complex High Performance Ceramic and Metallic Shapes (U. S. Patent 5047181)].

Tape casting involves mixing the powders with additives which allow a thick continuous film to be laid upon a moving plastic or other organic sheet, so that the suspension forms a flat, uniform thickness sheet. After drying, the sheet may be cut into basically two-dimensional shapes and utilized as-is, or further manipulated. One concept involves stacking of the tapes (Bitterlich & Heinrich, 2005), with use of an Si-based polymer intermediate between the layers to help bond them together. The current author developed a silicon nitride tape-casting technology in the 1980s, from which square cross-section shapes were cut from the sheet. These sections were hole-punched or drilled, then stacked one upon the other and dried and fired. This process led to such potential components as gas burners, where the holes in the stacks were arranged to allow passage of air and fuel from a manifold to finer sized holes at the combustion side. Stacking pieces of either different composition or different density tape atop one another led to a controllable shrinkage difference, with a resulting predictable warpage and shape contour (unpublished work).

A variant developed at the Oak Ridge National Laboratory, called *gel casting*, utilizes a monomer dissolved in water as the vehicle in which the milling occurs. In gel casting, the silicon nitride and densification aid powders are milled in water or some other fluid that also contains several percentage of a monomer. The milled suspension is poured into a nonporous container, unlike slip casting, and the container set into an oven to cause polymerization of the monomer. This process leaves the silicon nitride and densification aid powder particles trapped in a web-like matrix of the polymer, from which the water can be readily removed by simple heating. This results in no shrinkage as the polymer cage stays intact as the water leaves. Further heating causes the polymer to decompose and leave through the existing pores, and densification ensues (Omatete, Janney, & Nunn, 1997). This process has a unique advantage over such slip casting, wherein the suspending fluid moves outward from the component being cast toward the mold, often rearranging the particles of the silicon nitride and the additive(s) and leaving density gradients which become flaws after densification. Similarly, in the injection molding process, the green part must be burned out, wherein the injection molding binder moves outward, again rearranging the particles and causing density gradients. The gel casting process effectively immobilizes all of the particles during the low-temperature heat-treatment step, which causes polymerization. Then, while the particles are entrapped within the now-solidified polymer matrix, the fluid can be extracted without particle motion. Then the polymer matrix is vaporized during another heat-treatment step, without the formation of any liquid phase to cause particle motion. Since the Oak Ridge work, gel casting has been further developed (Yu, Wang, Zeng, & Zhang, 2008; Yang, Yu, & Huang, 2011).

In injection molding, the milled powders are intensively compounded into a viscous carrier vehicle, either a thermosetting binder, which hardens (polymerizes) upon heating, or a thermoplastic binder, which becomes less viscous upon heating. For silicon nitride, the thermosetting type binders prove impractical, as they tend to leave residual carbon behind upon pyrolysis, while the thermoplastic binders allow relatively easy fabrication into intricate shapes via the injection-molding machine. The major problem with this latter technique is that the binder has to be reheated after removal of the component from the injection-molding machine, and it is difficult to accomplish this uniformly throughout a large component of varying cross-section. The binder burnout step can lead to density gradients in the burned-out part, which will lead to shrinkage variations during densification, and components that are not of the expected shape (Bandyopadhyay & French, 1993). Much more research into injection molding binders and their burnout processes could be very helpful as the injection molding (IM) process allows generation of extremely complicated shapes in one simple forming step.

To overcome all the above difficulties in shape making, some have resorted to use of a simple fabrication technique, wherein they fabricate by uniaxial pressing or slip- or gel-casting a basic shape. Given a strong and resilient binder, they then perform a green machining process to develop the final shape before densification. Components with very thin areas, such as radial inflow turbine wheels, must be approached extremely carefully and slowly to prevent damage, which impacts cost.

2.03.5 Densification

Given the porous compact left after binder burnout from the shape-making step, the next-to-final phase of component manufacture is densification. As mentioned, for simple shapes, hot pressing can be utilized, as can any of the other techniques. For complex shapes, sintering or HIPing is required. Sintering typically requires higher temperatures than HIPing, since it has no added pressure effect, so that control of the silicon nitride decomposition reaction Si_3N_4 to Si (m) plus N_2 (gas) is necessary. This can be accomplished by immersing the component in a powder bed of similar composition, but with an additive to prevent the bed from sintering (e.g. BN), as well as sintering under an overpressure of N_2.

HIPing in the enclosed environment of a can or glass encapsulation will prevent the decomposition reaction, but it is always wise to utilize a N_2 atmosphere.

Densification of these types of silicon nitrides occurs through liquid-phase sintering, wherein the oxygen present on the surface of the silicon nitride powders and in the oxide additives reacts with the silicon and other cations to form a multicomponent liquid, which dissolves the solids. The initial alpha-phase silicon nitride reprecipitates as beta phase, typically growing long needle-shaped crystals, which impart toughness and thus strength to the materials. The remnant liquid, containing leftover Si and the other cations and oxygen, will typically form crystals of other phases, and then there will be a glassy grain boundary phase surrounding most or all of the crystals. This phase typically is responsible for the strength drop-off and onset of creep at elevated temperatures. Composition must be tightly controlled in these ceramics to prevent poor mechanical and oxidation behavior due to the presence of unfavorable phases in the final product. These effects were discussed earlier.

2.03.6 Finishing

Any component of densified silicon nitride ceramic that requires specific dimensional control will require some sort of final finish machining. Because of its hardness, diamond or cubic BN tools are necessary. These will remove any geometric nonuniformity, as well as remove any compositional inhomogeneities arising from reactions that may have occurred at the surface during densification (reaction with the HIP glass encapsulant, with the powder bed during sintering, etc.). However, grinding with abrasive tools can also impart damage to the component, and it can be particularly severe depending on the type of grinding and the direction of the grind marks vis-à-vis the principal stress that the component will endure in service. Often, it is wise to further process the component after grinding, to, for example, remove residual stresses imparted during grinding, to heal surface cracks, etc. Sometimes a simple heating in a slightly oxidative environment will suffice. Alternatively, one can heat the material surface via laser or infrared heat source, to heal surface cracks (Harrer, Danzer, & Morrell, 2012; Sun, Malshe, Jiang, & McCluskey, 2006).

It is also well known that during the oxidation process, whether performed via heating or electrical processing, the sintering aid cations (e.g. Y) in the silicon nitride will preferentially accumulate in the surface oxide. This causes a surface depletion of sintering aid cation underneath the oxidized surface, which may lead to a type of "surface toughening" effect, once the oxide scale is removed.

Other means of machining have also been utilized for structural ceramics, as reviewed by Samant and Dahotre (2009). These authors describe mechanical machining, chemical machining, electrical machining, radiation machining, and hybrid techniques, and compare and contrast their relative advantages and disadvantages.

Sometimes, for specific applications such as machine tooling, a final overcoating may be applied. These can be TiN, TiC, Ti(C,N) or others depending on intended service. For additional oxidation resistance, coating systems for CMCs have been developed to improve their lifetimes.

2.03.7 Effects on Properties and Behavior

Silicon nitrides are desirable ceramics for several reasons: high strength to elevated temperatures, oxidation- and creep resistance, good toughness, etc. These properties and/or behaviors can all be strongly influenced by the processing methodologies chosen, as already mentioned in Section 2.03.4. It is critical for successful application that the potential makers and users of these materials comprehend that reality. Tramp impurities deriving from the raw powders or introduced in the processing, and/or unresolved agglomerates, will have ramifications on strength, while the overall composition (amount and type of sintering aid(s)) will greatly affect the strength, toughness, and creep- and oxidation resistance. Strength in brittle materials like ceramics is generally a direct function of the toughness parameter, and inversely proportional to the type and severity of incorporated defects (Section 2.03.1.3). Thus, means to increase the inherent toughness (growing longer, more intertwined silicon nitride phase grains; incorporation of particulate or whisker toughening agents) can increase the strength, if done properly. A recent paper reviews the many means of increasing the strength of silicon nitride and SiAlON ceramics via controlled processing, including postprocessing steps such as hot working the densified ceramic (Zhu & Sakka, 2008). Similarly, improving the powders, binders, and processing steps so as to minimize the size and number of defects incorporated in the final ceramic component will pay off (Neil, Pasto, & Bowen, 1988).

Most components will have undergone some sort of final finishing steps to ensure correct dimensional control, and these operations will influence properties and behavior (Buljan, Neil, Pasto, Smith, & Zilberstein, 1986).

The following paragraph will detail many of the strength-limiting defects, which can compromise the great strength and toughness of silicon nitride components.

Firstly, agglomerates in powders that are not broken down to the individual crystallite size may sinter at a different rate than the rest of the powder matrix, and open up a crack-like defect, which may not "heal," but instead will cause failure (**Figure 6**). Second, during powder processing, or perhaps even in the initial handling of the incoming powders, or worse, arising from cleaning of the processing equipment, hairs or fibers from brushes or cleaning cloths may become entrapped. These will cause elongated "pores" during burnout and densification, and can be serious failure-inducing defects (**Figure 7**). Third, grinding of powders utilizing metallic components, or compounding with injection-molding waxes, or even during the injection-molding process may introduce iron-bearing particles, which will react with the ceramic during densification and lead to failure (**Figure 8**). Additionally, due to incomplete mixing of the sintering additive with the silicon nitride, additive-rich regions may spawn silicon nitride crystals of exaggerated length, and these may become failure sources (**Figure 9**). The need to burn out binders from the casting or molding process may lead to shrinkage cracks in components, which will certainly be extremely deleterious (**Figure 10**). Finally, mechanical grinding of the surfaces of the produced components can lead to surface cracks and improperly oriented stress gradients, and these can cause premature failure (**Figure 11**).

Obviously, paying strict attention to the handling and processing of the raw ceramic powders can pay benefits to the resultant properties and behavior of the components produced. Shaping and finishing must also be controlled. However, one should ensure that no deleterious flaws have been left in the components, if economically and technically feasible. Therefore, one may either perform selected nondestructive examination, such as of the highly stressed areas, or in fact perform proof-testing, wherein the component is subjected to some fraction of its (predicted) in-service stress levels (Cotter, Koeningsberg, Pasto, & Bowen, 1988; Lange, 1989).

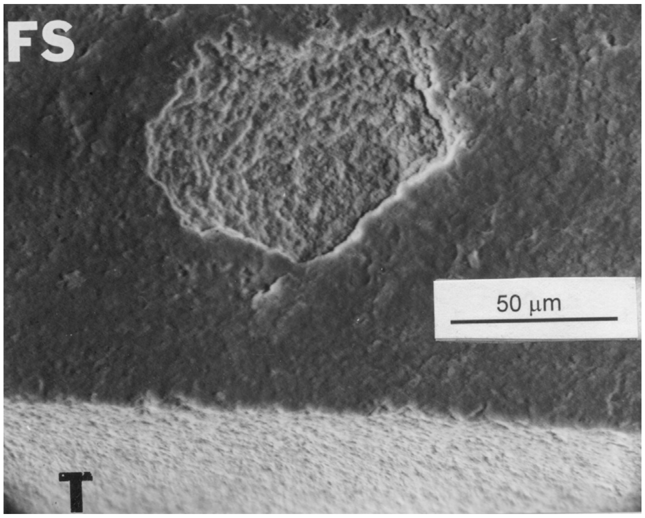

Figure 6 Porous spot in a bend-test specimen of Norton NC-350. It was likely an interagglomerate defect. Photo courtesy of George Quinn, NIST.

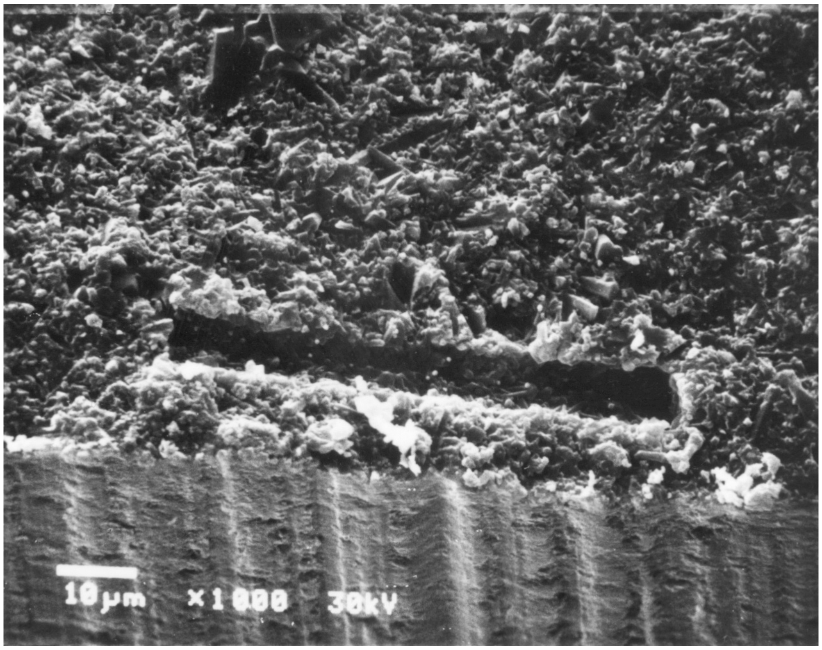

Figure 7 Defect near the surface of a GTE AY6 silicon nitride bend-test specimen. It was likely a fiber that was included in the powders or the processing equipment. Photo courtesy of George Quinn, NIST.

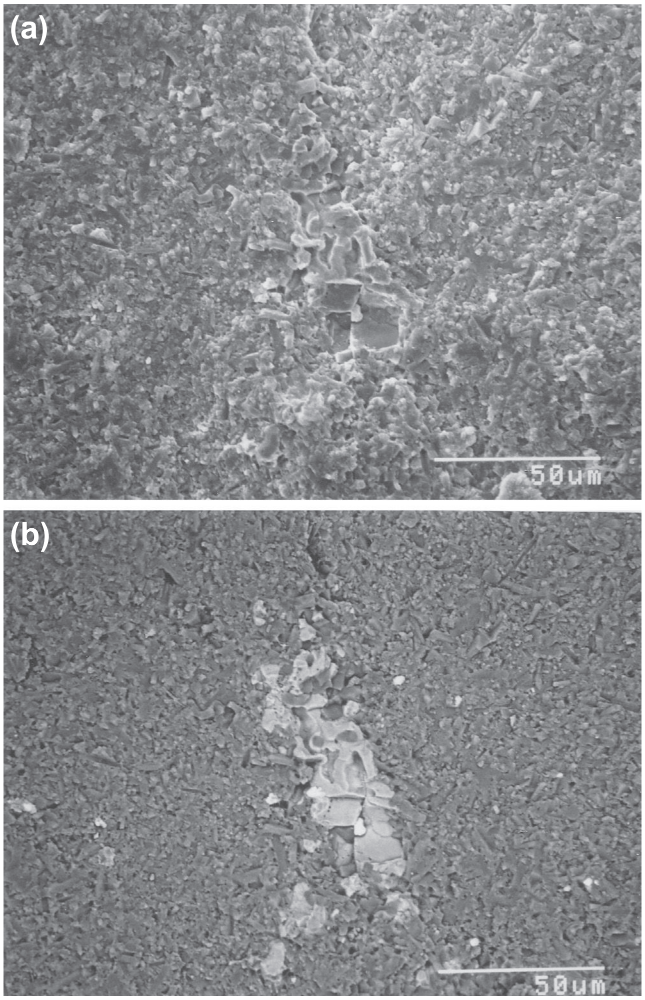

Figure 8 Scanning electron micrographs of a failure-inducing defect in Ceradyne Ceralloy 147 SRBSN. (a) Secondary electron image. (b) Backscattered electron image showing high-electron-density material present (Fe). Photo courtesy of George Quinn, NIST.

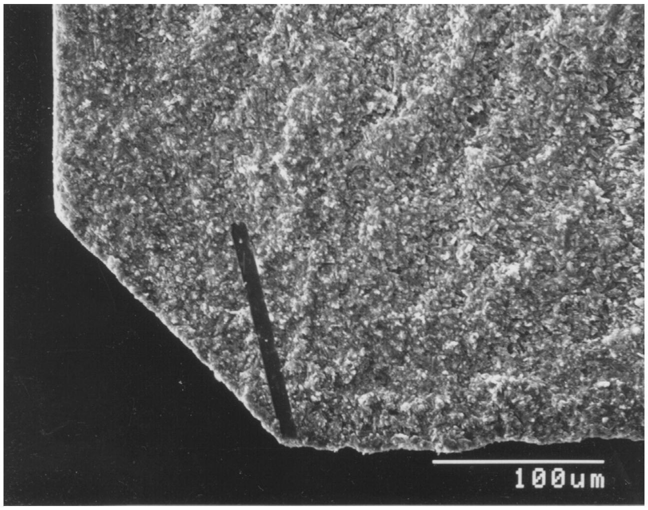

Figure 9 Scanning electron micrograph of a failure-inducing large grain defect in Kyocera AS-800 SSN. Photo courtesy of George Quinn, NIST.

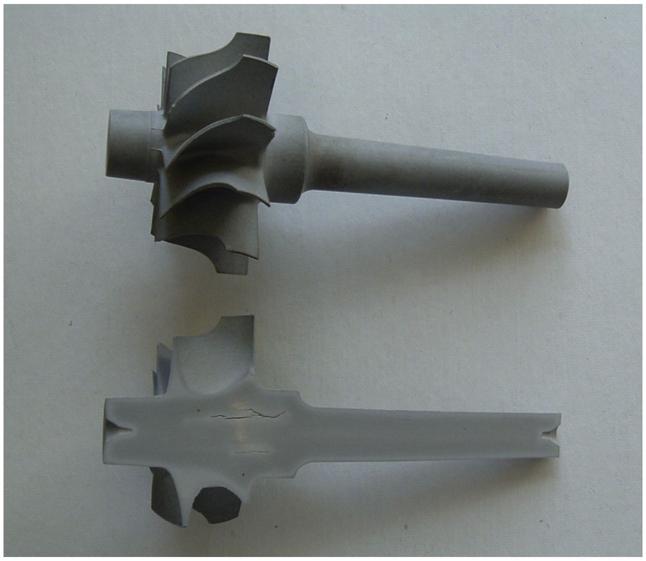

Figure 10 Sectioned silicon nitride turbocharger rotor illustrating interior shrinkage cracks, and “white spot” defects. Photo courtesy of George Quinn, NIST.

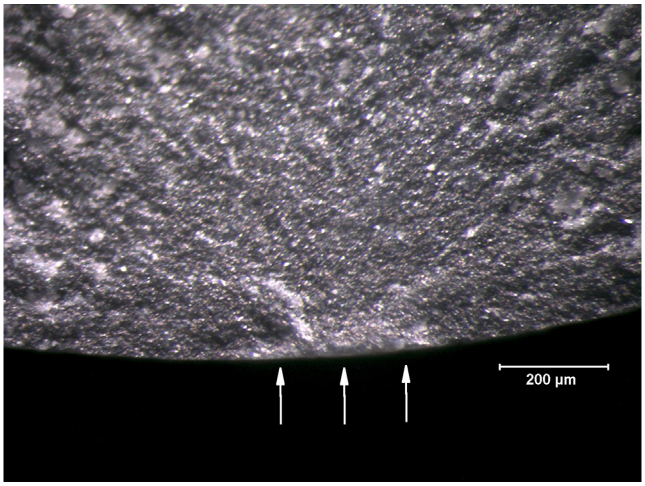

Figure 11 Scanning electron micrograph of a machining defect on the surface of a Ceradyne SRBSN tensile test specimen. Photo courtesy of George Quinn, NIST.

2.03.8 Summary and Suggested Further Research

Silicon nitrides of several various types, prepared via several different fabrication techniques, have been used for many different structural purposes. For the ultimate in high strength, elimination of internal defects has favored use of the HIPing process, with compositions containing various rare-earth oxide additives. For less demanding applications, SSNs may be used, again with a variety of sintering additives. For applications demanding the ultimate in low cost, RBSN and perhaps SRBSN can be applied. For high toughness, composites appear to be the most effective route, although these have processing challenges (especially difficulty in shape making) and extra costs. All silicon nitrides, which require a final finishing step or series of steps, are possibly subject to additional sources of strength-limiting flaws.

Consequently, an extremely useful service for the potential user of silicon nitride would be the preparation of a series of charts listing the advantages and limitations of the various types of silicon nitride (RBSN, SSN, HPSN, etc.) and the various means of fabrication (slip casting, gel casting, etc.), as a function of strength (room temperature and elevated temperature), oxidation- and creep resistance, and cost-effectiveness. Enough data now exist for most of the above parameters, perhaps except for cost (which can be modeled) to prepare such an engineering aid.

Additional research would be useful in developing a computer model (a "tool") to be used by potential application developers, which could use the output of the first suggestion, above.

The present author, for example, evaluated room- and elevated-temperature strength of SSNs in the 1980s, prepared with a "standard" composition, for a number of silicon nitride powders of varying cost. The results were sometimes surprising: the cheaper powders did NOT always yield lower strengths. Consequently, one could make informed decisions about strength versus cost. What was missing in this research, for time and funding reasons, was derivation of the actual reasons for the differences in strength due to the powder source or type. That is, useful research could be performed to truly define which parameters control strength: impurity level (if so, which one(s) and at what levels?), phase content (alpha versus beta), and other parameters (surface area, crystallite shape, state of agglomeration, etc.).

References

Adlerborn, J., Burnström, M., Hermansson, L., & Larker, H. T. (1987). Development of high-temperature high strength silicon nitride by glass-encapsulated hot isostatic pressing. *Materials and Design, 8*(4), 229–232.

Albano, M. P., & Garrido, L. B. (2004). Improvement in the colloidal processing of concentrated silicon nitride slips with ammonium polyacrylate by an yttria-alumina surface coating. *Colloids and Surfaces A: Physicochemical and Engineering Aspects, 248*(1–3), 1–8.

Balázsi, Cs., Shen, Z., Kónya, Z., Kaszlovsky, Zs., Wéber, F., Vértesy, Z., et al. (2005). Processing of carbon nanotube reinforced silicon nitride composites by spark plasma sintering. *Composites Science and Technology, 65*(5), 727–733.

Bandyopadhyay, G., & French, K. W. (1993). Injection-molded ceramics: critical aspects of the binder removal process and component fabrication. *Journal of the European Ceramic Society, 11*(1), 23–34.

Becher, P. F., Sun, E. Y., Plucknett, K. P., Alexander, K. B., Hsueh, C.-H., Lin, H.-T., et al. (1998). Microstructural design of silicon nitride with improved fracture toughness: I, effects of grain size and shape. *Journal of the American Ceramic Society, 81*(11), 2821–2830.

Bitterlich, B., & Heinrich, J. G. (2005). Processing, microstructure, and properties of laminated silicon nitride stacks. *Journal of the American Ceramic Society, 88*(10), 2713–2721.

Bochanegra-Bernal, M. H., & Matovic, B. (2009). Dense and near-net-shape fabrication of Si_3N_4 ceramics. *Materials Science and Engineering A, 500*, 130–149.

Bonnell, D. A., Tien, T.-Y., & Ruhle, M. (1987). Controlled crystallization of the amorphous phase in silicon nitride ceramics. *Journal of the American Ceramic Society, 70*(7), 460–465.

Buljan, S. T., & Sarin, V. K. (1987). Silicon nitride-based composites. *Composites, 18*(2), 99–106.

Buljan, S. T., Neil, J. T., Pasto, A. E., Smith, J. T., & Zilberstein, G. (1986). Silicon nitride ceramics and composites: a view of reliability enhancement. In S. Hampshire (Ed.), *Non-oxide technical and engineering ceramics* (pp. 409–431). London and New York: Elsevier Applied Science.

Bunk, W., & Hausner, H. (1986). *Ceramic materials and components for engines* (Second international symposium). Deutsche Keramische Gesellschaft e.v., D-5340 Bad Honnel, pp. 1280.

Chen, I.-W., Becher, P. F., Mitomo, M., Petzow, G., & Yen, T.-S. (1993). *Silicon nitride ceramics – scientific and technical advances.* In *Materials research society symposium proceedings* (Vol. 287). Pittsburgh, PA: Materials Research Society.

Cinibulk, M. K., Thomas, G., & Johnson, S. M. (1990). Grain-boundary-phase crystallization and strength of silicon nitride sintered with a YSiAlON glass. *Journal of the American Ceramic Society, 73*(6), 1606–1612.

Cinibulk, M. K., Thomas, G., & Johnson, S. M. (1992). Oxidation behavior of rare-earth disilicate-silicon nitride ceramics. *Journal of the American Ceramic Society, 75*(8), 2044–2049.

Cotter, D. J., Koenigsberg, W. D., Pasto, A. E., & Bowen, L. J. (1988). Predicting failure stress of silicon nitride ceramics using microfocus radiography. *Journal of the American Ceramic Society, 71*(11), C460–C461.

Das Chowdhury, K., Carpenter, R. W., & Braue, W. (1992). A comparative high-resolution study of interface chemistry in silicon-nitride-based ceramic matrix composites reinforced with silicon carbide whiskers. *Ultramicroscopy, 40*, 229–239.

Dixmier, J., Bellissent, R., Bahloul, D., & Goursat, P. (1994). Neutron diffraction study of the amorphous phase structure in silicon carbonitride ceramics obtained by pyrolysis of a polyvinylsilazane. *Journal of the European Ceramic Society, 13*, 293–298.

Hampshire, S. (2009). Silicon nitride ceramics. *Materials Science Forum, 606*, 27–41.

Hampshire, S., & Jack, K. H. (1981). The kinetics of densification and phase transformation of nitrogen ceramics. *Proceedings of the British Ceramic Society, 31*, 37–49.

Hampshire, S., Park, H. K., Thompson, D. P., & Jack, K. H. (1978). α'-Sialon ceramics. *Nature, 274*, 880–882.

Harrer, W., Danzer, R., & Morrell, R. (2012). Influence of surface defects on the biaxial strength of a silicon nitride ceramic-increase of strength by crack healing. *Journal of the European Ceramic Society, 32*(1), 27–35.

Herzog, A., Woetting, G., & Vogt, U. F. (2007). Short-fibre-reinforced reaction-bonded silicon nitride (RBSN) by precursor route: processing and properties. *Journal of the European Ceramic Society, 27*(12), 3561–3572.

Hirao, K., Ohashi, M., Brito, M. E., & Kanzaki, S. (1995). Processing strategy for producing highly anisotropic silicon nitride. *Journal of the American Ceramic Society, 78*(6), 1687–1690.

Hyuga, H., Jones, M. I., Hirao, K., & Yamauchi, Y. (2004). Influence of carbon fibre content on the processing and tribological properties of silicon nitride/carbon composites. *Journal of the European Ceramic Society, 24*, 877–885.

Kleebe, H.-J., Pezzotti, G., & Ziegler, G. (1999). Microstructure and fracture toughness of Si_3N_4 ceramics: combined roles of grain morphology and secondary phase chemistry. *Journal of the American Ceramic Society, 82*(7), 1857–1867.

Kroll, P. (2005). Modelling polymer-derived ceramics. *Journal of the European Ceramic Society, 25*, 163–174.

Laarz, E., Muerck, A., & Bergstrom, L. (2003). Colloidal processing of silicon nitride. *Ceramic Transactions, 142*, 3–34.

Lange, F. F. (1989). Powder processing science and technology for increased reliability. *Journal of the American Ceramic Society, 72*(1), 3–15.

Lange, F. F. (1998). Colloidal processing of powder for reliable ceramics. *Current Opinion in Solid State and Materials Science, 3*(5), 496–500.

Lundberg, R., Pompe, R., Carlsson, R., & Goursat, P. (1990). Fibre reinforced silicon nitride composites. *Composites Science and Technology, 37*, 165–176.

Lyckfeldt, O., Rundgren, K., & Sjostedt, M. (2004). Freeze granulation for the processing of silicon nitride ceramics. *Key Engineering Materials, 264–268*(I), 281–284.

Müller, M., Bauer, W., & Knitter, R. (2009). Processing of micro-components made of sintered reaction-bonded silicon nitride (SRBSN), part 1: factors influencing the reaction-bonding process. *Ceramics International, 35*(7), 2577–2585.

Müller, M., Bauer, W., Knitter, R., & Rögner, J. (2010). Processing of complex-shaped micro parts by reaction-bonding and sintering of silicon nitride. *Ceramic Engineering and Science Proceedings, 31*(8), 213–222.

Müller, M., Rögner, J., Okolo, B., Bauer, W., & Knitter, R. (2010). Processing of micro-components made of sintered reaction-bonded silicon nitride (SRBSN), part 2: sintering behavior and micro-mechanical properties. *Ceramics International, 36*(2), 707–717.

Natansohn, S., & Pasto, A. E. (1991). *Improved processing methods for silicon nitride ceramics*. ASME paper 91-GT-316. New York, NY: American Society of Mechanical Engineers.

Neil, J. T., Pasto, A. E., & Bowen, L. J. (1988). Improving the reliability of silicon nitride: a case study. *Advanced Ceramic Materials, 3*(3), 225–230.

Omatete, O. O., Janney, M. A., & Nunn, S. D. (1997). Gelcasting: from laboratory development toward industrial production. *Journal of the European Ceramic Society, 17*(2–3), 401–413.

Parr, N. L., Martin, G. F., & May, E. R. W. (1960). Preparation, microstructure, and mechanical properties of silicon nitride. In P. Popper (Ed.), *Special ceramics* (pp. 102–135). London: Heywood.

Pasto, A. E. (1984). Causes and effects of Fe-bearing inclusions in sintered Si_3N_4. *Journal of the American Ceramic Society, 67*(9), C-178–C-180.

Pasto, A. E., Neil, J. T., & Quackenbush, C. L. (1984). Microstructural effects influencing strength of sintered silicon nitride. In L. L. Hench, & D. L. Ullrich (Eds.), *Ultrastructure processing of ceramics, glasses, and composites* (pp. 476–489). Wiley-Interscience.

Pavarajarn, V., Vongthavorn, T., & Praserthdam, P. (2007). Enhancement of direct nitridation of silicon by common metals in silicon nitride processing. *Ceramics International, 33*(4), 675–680.

Peng, H., Shen, Z., & Nygren, M. (2005). SPS processing and superplastic deformation of silicon nitride based ceramics. *Key Engineering Materials, 287*, 146–155.

Petzow, G., & Herrmann, M. (2002). Silicon nitride ceramics. In M. Jansen (Ed.), *High performance non-oxide ceramics II* (pp. 50–171). Berlin and NY: Springer.

Pujari, V. K., Tracey, D. M., Foley, M. R., Paille, N. I., Pelletier, P. J., sales, L. C., et al. (1995). Reliable ceramics for advanced heat engines. *Bulletin of the American Ceramic Society, 74*(4), 86–90.

Qi, G., Zhang, C., & Hu, H. (2007). High strength three-dimensional silica fiber reinforced silicon nitride-based composites via polyhydridomethylsilzane pyrolysis. *Ceramics International, 33*, 891–894.

Ramasamy, S., Tewari, S. N., Lee, K. N., Bhatt, R. T., & Fox, D. S. (2010). Slurry-based multilayer environmental barrier coatings for silicon carbide and silicon nitride ceramics-II. Oxidation resistance. *Surface and Coatings Technology, 205*, 266–270.

Saigal, A., Kupperman, D. S., Singh, J. P., Singh, D., Richardson, J., & Bhatt, R. T. (1993). Thermal residual strains and stresses in silicon carbide-fiber-reinforced silicon nitride composites. *Composites Engineering, 3*(11), 1075–1086.

Sajgalik, P., Dusza, J., & Hoffmann, M. J. (1995). Relationship between microstructure, toughening mechanism, and fracture toughness of reinforced silicon nitride ceramics. *Journal of the American Ceramic Society, 78*(10), 2619–2624.

Samant, A. N., & Dahotre, N. B. (2009). Laser machining of structural ceramics – a review. *Journal of the European Ceramic Society, 29*, 969–993.

Schwab, S. T., & Page, R. A. (1995). Nanostructure of polymer-derived silicon nitride. *Materials Science and Engineering A, 204*, 201–204.

Shen, Z., Zhao, Z., Peng, H., & Nygren, M. (2002). Formation of tough interlocking microstructures in silicon nitride ceramics by dynamic ripening. *Nature, 417*, 266–269.

Shibata, N., Pennycook, S. J., Gosnell, T. R., Painter, G. S., Shelton, W. A., & Becher, P. F. (2004). Observation of rare-earth segregation in silicon nitride ceramics at subnanometre dimensions. *Nature, 428*, 730–733.

Sreekumar, C., & Earl, D. A. (2009). Mechanical properties of 2.45 GHz microwave sintered Si_3N_4-Y_2O_3-MgO-ZrO_2 system. *Journal of the European Ceramic Society, 29*, 2037–2043.

Sreekumar, C., & Traver, H. K. (2010). Microwave sintering of beta-sialon-ZrO_2 composites. *Materials and Design, 31*, 3041–3046.

Sun, L., Malshe, A. P., Jiang, W., & McCluskey, W. (2006). Effects of CO_2 laser surface processing on fracture behavior of silicon nitride ceramic. *Journal of Engineering Materials and Technology, Transactions of the ASME, 128*(3), 460–467.

Sun, E. Y., Becher, P. F., Plucknett, K. P., Hsueh, C.-H., Alexander, K. B., Waters, S. B., et al. (1998). Microstructural design of silicon nitride with improved fracture toughness: II, effects of yttria and alumina additives. *Journal of the American Ceramic Society, 81*(11), 2831–2840.

Tennery, V. J. (1989). *Ceramic materials and components for engines* (Third international symposium). Worthington, OH: The American Ceramic Society.

Tsuge, S., & Nishida, K. (1978). High strength hot-pressed Si_3N_4 with concurrent Y_2O_3 and Al_2O_3 additions. *Bulletin of the American Ceramic Society, 57*, 424–426 and 431.

Wang, H.-R., Yang, J.-F., Liu, J.-Q., Yu, F.-L., & Li, Y. (2009). Processing, microstructure and mechanical properties of porous silicon nitride by a slip casting method using petroleum coke as a pore former. *Journal of Ceramic Processing Research, 10*(6), 823–826.

Westman, A.-K., & Larker, H. T. (1999). Interaction of encapsulation glass and silicon nitride ceramic during HIPing. *Journal of the European Ceramic Society, 19*, 2739–2746.

Worthen, R. P., & Pasto, A. E. (1988). *Ceramic engine components*. SAE technical paper series 88150. Warrendale, PA: SAE-The Engineering Society for Advancing Mobility-Land, Sea, Air, and Space.

Yang, J.-F., Ohji, T., & Niihara, K. (2000). Influence of yttria-alumina content on sintering behavior and microstructure of silicon nitride ceramics. *Journal of the American Ceramic Society, 83*(80), 2094–2096.

Yang, J., Yu, J., & Huang, Y. (2011). Recent developments in gelcasting of ceramics. *Journal of the European Ceramic Society, 31*, 2569–2591.

Yu, J., Wang, H., Zeng, H., & Zhang, J. (2008). Effects of monomer content on physical properties of silicon nitride ceramic green body prepared by gelcasting. *Ceramics International, 35*, 1039–1044.

Zhu, X., & Sakka, Y. (2008). Textured silicon nitride: processing and anisotropic properties. *Science and Technology of Advanced Materials, 9*(3).

Zhu, X., Sakka, Y., Zhou, Y., & Hirao, K. (2007). Processing and properties of sintered reaction-bonded silicon nitride with Y_2O_3-$MgSiN_2$: effects of Si powder and Li_2O addition. *Acta Materialia, 55*(16), 5581–5591.

Zhu, X., Uchikoshi, T., & Sakka, Y. (2007). Aqueous processing of textured silicon nitride ceramics by slip casting in a strong magnetic field. *Materials Science Forum, 534-6*(Part 2), 1009–1012.

Zhu, X., Zhou, Y., Hirao, K., & Lences, Z. (2006). Processing and thermal conductivity of sintered reaction-bonded silicon nitride. I: effect of Si powder characteristics. *Journal of the American Ceramic Society, 89*(11), 3331–3339.

Zhu, X., Zhou, Y., Hirao, K., & Lences, Z. (2007). Processing and thermal conductivity of sintered reaction-bonded silicon nitride. *Journal of the American Ceramic Society, 90*(6), 1684–1692.

Ziegler, A., Idrobo, J. C., Cinibulk, M. K., Kisielowski, C., Browning, N. D., & Ritchie, R. O. (2004). Interface structure and atomic bonding characteristic in silicon nitride ceramics. *Science Magazine, 306*(5702), 1768–1770.

2.04 Processing of Silicon Carbide-Based Ceramics

Jochen Kriegesmann, Department of Materials Technology, Glass and Ceramics, University of Applied Sciences Koblenz, Höhr-Grenzhausen, Germany

© 2014 Elsevier Ltd. All rights reserved.

http://dx.doi.org/10.1016/B978-0-08-096527-7.00023-4

2.04.1 Introduction

Silicon carbide (SiC) is a covalently bonded compound. Notable properties as a result of this strong bonding include high hardness, thermal conductivity, Young's modulus and electrical conductivity (the latter is quite relevant due to its semiconducting behavior) together with relatively low thermal extension. Furthermore, much stronger bonded compounds like diamond (C), cubic boron nitride (CBN) or boron carbide (B_4C) can be applied only at relatively low temperatures in oxygen-rich atmospheres since they are either structurally unstable or high-temperature exposure alter their properties as a consequence of their poor oxidation resistance. Basically SiC is—like all non-oxides—not really oxidation resistant. However to a large extent, since an oxidation-induced amorphous silica (SiO_2) layer adheres on the SiC surface, the material gets passivated against further oxidation. Table 1 compares the SiC and diamond in terms of hardness, density, thermal stability (according to their crystallographic data), stability of crystal structure, and oxidation products.

The compound SiC has substantial potential as a base material for diverse applications, which involve machining demands, tribological stresses, chemically aggressive media, high temperatures and/or severe thermal shocks. These applications command fully dense SiC-based ceramics. This claim is not easily realized since the consolidation of SiC-based ceramics is not at all trivial since—like all other covalently bonded compounds—SiC is not very reactive. Manufacturing challenges and prospective applications have resulted in diverse processing approaches of SiC-based ceramics especially in recent years.

Table 2 lists both traditional and proposed applications for SiC-based ceramics in terms of its potential attributes. It is noteworthy that none of the referred applications can be satisfied with a single attribute, but on the other hand, none of the applications requires whole set.

The focus of this chapter is to review the processing stages of polycrystalline SiC-based materials. In recent years, the fabrication of bulk SiC single has been of considerable importance especially for electronic applications (Lely, 1955, 1958; Tairov & Tsvetkov, 1981). The processing of these single crystals is not treated in this chapter. The reader, who is interested in bulk SiC single crystals, may refer to the book edited by Feng (2010).

2.04.2 Phase Relations and Crystal Structure

SiC is the only stable compound in binary Si–C system (Figure 1). SiC does not have a congruent melting point, but decomposes peritectically into graphite and a silicon-rich melt in a closed system under atmospheric pressure at 2830 °C. In an open system the decomposition already starts at 2300 °C associated with gaseous silicon. At 1430 °C a degenerated eutectic exists for 0.02 atomic% C (Kleykamp & Schumacher, 1993).

All SiC crystal structures to a large extent resemble the diamond lattice. Thus both covalent solids—diamond and SiC—show the same atomic coordination number of four due to the sp^3-hybridization containing four equivalent orbitals. This implies that for the binary compound SiC, the Si atoms show tetrahedral surroundings of C atoms or vice versa. The building unit of SiC crystals is a silicon–carbon bilayer, in which the Si atoms are arranged in a two-dimensional hexagonal close-pack pattern and the C atoms are directly on the top of the Si atoms. The three-dimensional lattices are built up through stacking the bilayers along their normal direction, in which the C atoms (or the Si atoms) occupy halves of all possible tetrahedral sites between the stacks.

Since in a single-layered close-pack lattice the adjacent layers are dislocated one-third of an atomic diameter from each other, three different stack positions of layers exist in such a lattice named A, B and C, respectively (Figure 2). It can be expected that the close-pack bilayers of the SiC lattice act in the same way. Thus in SiC crystals we expect three different stack positions as well.

Table 1 Comparison between diamond and SiC

Compound	*Diamond*	*SiC*
Interatomic distance (pm)	154	190
Theoretical density (kg m^{-3})	3520	3125
Hardness HV (MPa)	100	35
Stability of crystal structures (up to °C)	1000	1900
Oxidation product	CO, CO_2 (gases)	SiO_2 (amorphous solid)
Thermal stability (up to °C)	1000	2000

Table 2 Some SiC parts for diverse applications in terms of the attributes provided by SiC

SiC parts	*Mechanical*	*Tribological*	*Thermal*	*Thermal shock*	*Chemical*	*Electrical*
Aircraft rotor	●	●	●	●		
Ball valve	●	●		●	●	
Brake disc		●		●		
Burner pipe	●	●	●	●		
Convertor brick			●	●		
Crucible			●	●	●	
Friction bearing	●	●		●		
Grinding ball	●	●				
Grinding tool	●	●				
Heat exchanger			●	●		
Heating element			●	●		●
Heat shield			●	●	●	
Kiln furniture			●	●		
Particulate filter	●		●	●		●
Protection sleeve		●			●	
Rocket nozzle			●	●		
Seal ring		●		●	●	

● Potential attributes for the listed applications

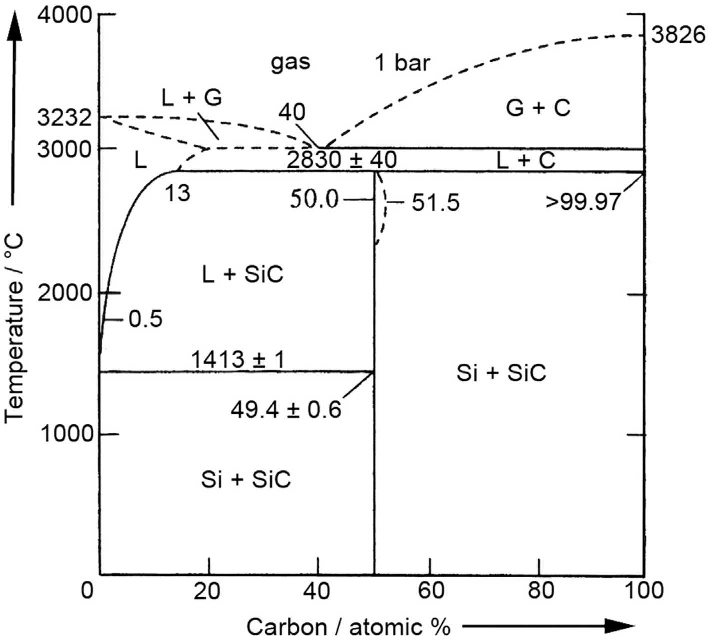

Figure 1 Binary system silicon–carbon. Reproduced with kind permission of the Deutsche Bunsen-Gesellschaft für Physikalische Chemie e.V.

Although only three different stacking positions in SiC are possible, multiple combinations of stack sequence alternatives are liable. Consequently the crystal structure of SiC exhibits a large number of different one-dimensional ordering sequences without any deviation from stoichiometry; more than 200 different versions are known (Jepps & Page, 1993). Since these structural variants only vary in stacking sequence, they all have the same theoretical density of 3214 kg m^{-3}. In this respect the structural variants of SiC differ from the crystal modifications of most other compounds. This is the reason that the term "polytype" is used for a stack sequence alternative. The two-dimensional polymorphism in SiC—usually referred to as polytypism—can be represented by various periodic hexagonal Si–C bilayer structures along the *c*-axis. Figure 3 shows the structural pattern of the most common polytypes of SiC, where large and small circles represent Si and C atoms, respectively

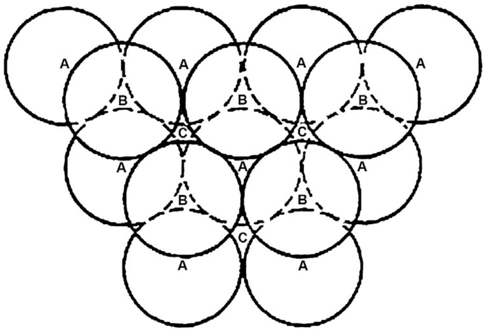

Figure 2 Possible positions of atoms in a single-layered close-pack lattice.

(Tairov & Vodakov, 1977). The polytypes are specified by the Ramsdell notation through the total number of layers contained in a unit cell and then add the letter H, C or R to denote the overall lattice type being hexagonal, cubic and rhombohedral, respectively (Ramsdell, 1947). Thus 3C is a *cubic polytype* containing the stacking sequence ABC, 4H and 6H are *hexagonal polytypes* containing the ABCB and ABCACB sequence, respectively, and 15R is a *rhombohedral polytype* containing the ABCACBCABACABCB sequence. The cubic polytype (3C-SiC) is the only one formed at relatively low temperatures, whereas most of the others (except the scarcely found 2H-SiC) are generated at elevated temperatures (Knippenberg, 1963). As a consequence, 3C-SiC is usually denoted by β-SiC, whereas the hexagonal and the rhombohedral polytypes are collectively referred to as α-SiC, though this is not strictly correct from a crystallographic point of view (Figure 3).

2.04.3 SiC Raw Materials Production

Although natural SiC with the mineral name Moissanite exists (Moissan, 1904), raw SiC is synthesized since there are no commercially recoverable deposits anywhere in the world. Some small- and large-scale synthesis concepts are described in the next section. Normally ceramics are consolidated through a sintering process. If highly densified materials are required, the corresponding raw materials batch should contain—besides special sintering aids—a fine-grained base powder. This especially applies to a nonreactive, covalent bonded compound like SiC. For special applications like refractories or grinding tools, the SiC particles may also be coarse grained. Thus SiC synthesis includes grinding and screening, which is also treated in the next section.

Generally SiC-based ceramics are extremely brittle if the SiC crystals within the ceramics are fairly equiaxial. However, the brittleness can be reduced if the grains are elongated or at least exhibit a large aspect ratio. Thus, the toughness of the ceramics might be improved through reinforcement using flattened or elongated particles like platelets, whiskers or fibers. The synthesis of SiC particles offering large aspect ratios is discussed below too.

2.04.3.1 SiC Synthesis, Grinding and Classification of SiC Powders

2.04.3.1.1 Acheson Process

To date large-scale production of SiC is based upon the historic Acheson process, which was applied for patent more than a century ago (Acheson, 1893). The inventor Edward Goodrich Acheson can be regarded as the first prominent pioneer of SiC-based ceramics. In his process, a mixture of pure quartz sand ($>99.5\%$ SiO_2) and petrol coke poor in ashes ($<0.2\%$ ashes) is heated up to about 2500 °C in a batch resistance furnace to generate SiC according to the overall reaction,

$$SiO_2 + 3C \leftrightarrow SiC + 2CO \tag{1}$$

The grain sizes of the two starting components are comparatively coarse (up to 10 mm) with a narrow size distribution for a loose packing density in order to let CO leave the charge.

Because the process involves many partial reactions, the actual kinetics is much more complicated than the carbothermal reduction of silica shown in Eqn (1). There are two different design versions of Acheson

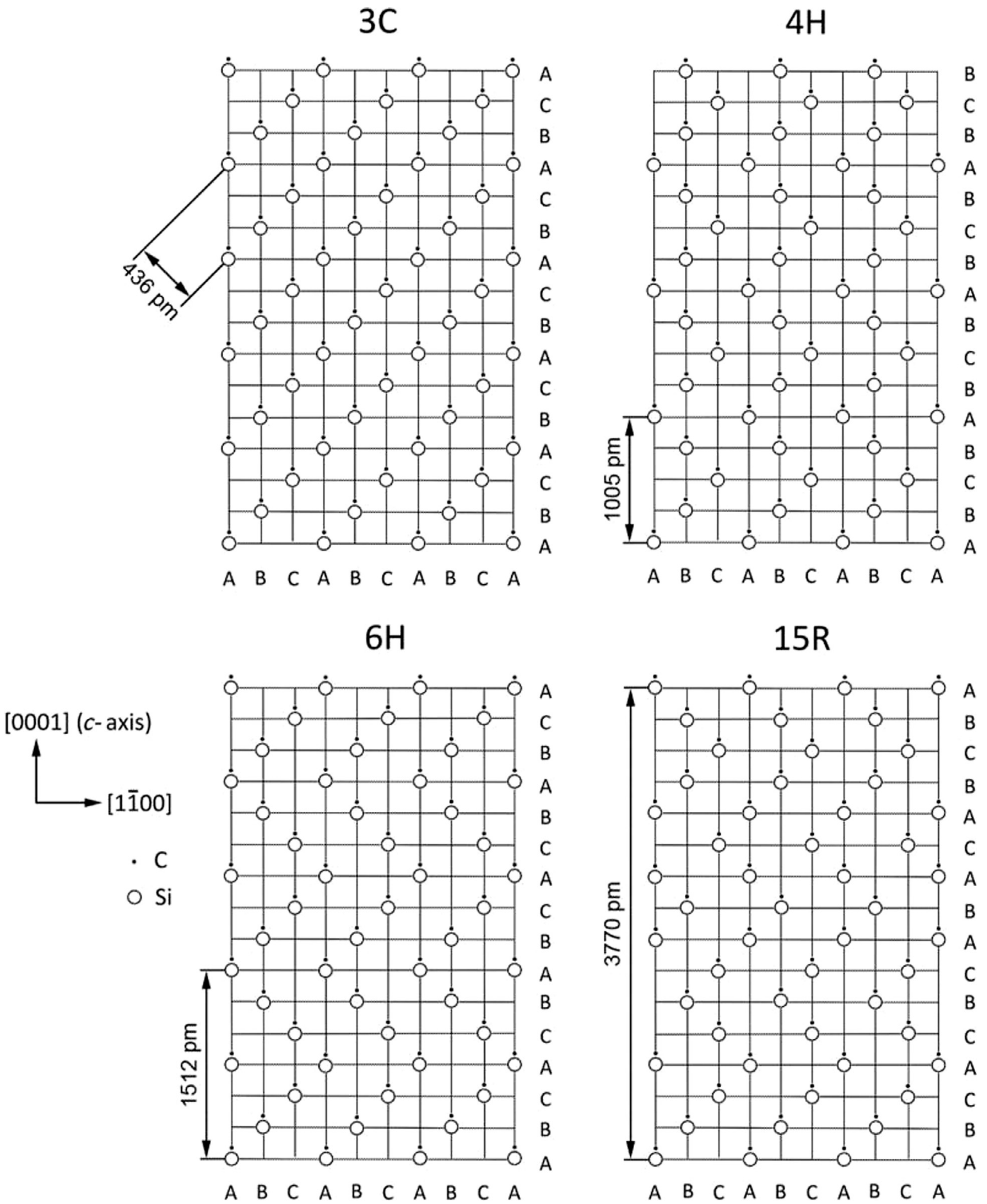

Figure 3 Stacking sequence of Si–C bilayers forming different polytypes seen from $[11\bar{2}0]$. Tairov, Y. M, Vodakov, Y. A. (1977). Group IV materials (mainly SiC). In J. I. Pankove (Ed.) *Topics of applied physics*, Vol. 17, Electroluminescence. Berlin, Heidelberg, New York: Springer-Verlag, pp. 31–61, with permission from Springer Science + Business Media.

furnace today. The ordinary design resembles the old Acheson patent application to a large extent, whereas the ESK-type construction has got some useful technical changes, and some of them are explained below. The ordinary Acheson furnaces are lined up side-by-side in a long hall. A typical Acheson furnace has a rectangular cross-section with a length of about 25 m, a width of 4 m and a height of 4 m, with partly movable narrow sidewalls. The carbon electrodes for the current feed-through are installed in the center of refractory furnace heads. For efficient electrical installation, a single transformer is simultaneously connected to several furnaces in such a way that one furnace is in an operating state while the others are cooling down, dismounted or being newly fed.

SiC develops as a solid cylindrical ingot around the graphite resistance core, which is usually called the "roll". In the center, where the maximum temperature (2500 °C) is reached, the crystal growth is quite considerable. According to the temperature drop, the crystal sizes are scaled down with increasing distances from the core.

After the power is turned off, the furnace cools down for several days. Thereafter the sidewalls are removed and the cylinder is excavated from the nonconverted component mixture. The cylinder contains not only the primary resistance core but also an additional graphite internal ring originated from the dissociation of SiC. After removing the graphite the inner part of the cylinder contains coarse α-SiC crystals whereas in the outer part finer SiC crystals of mainly β-type are dominant. The SiC crude material is carefully crushed, classified, sometimes ground again and optionally chemically treated in order to obtain the specific properties based on application.

The conventional design of the Acheson process has disadvantages. First is the fact that the reaction gases, which consist essentially of CO but also of H_2S, cannot be captured completely and are lost for an energy gain. The second drawback derives from the problem that these gases pollute the environment. These disadvantages can be reduced through the modified ESK version of the Acheson process (Figure 4) (Benecke, Korsten, Petersen,

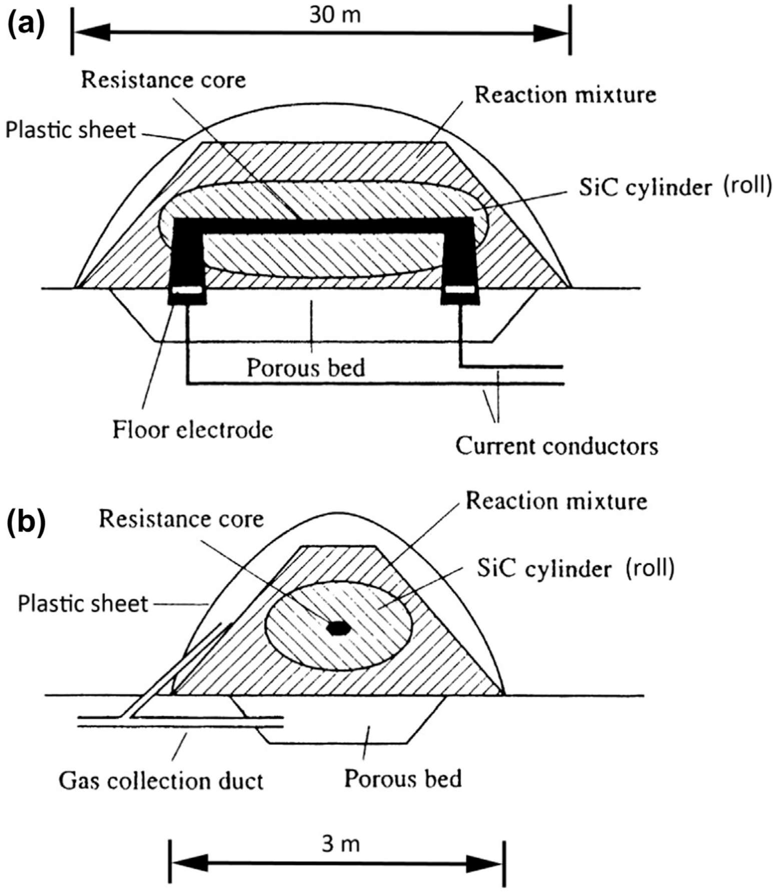

Figure 4 Principle of SiC synthesis according to the ESK process: (a) longitudinal and (b) transverse sections. From ESK SiC GmbH, Frechen, Germany.

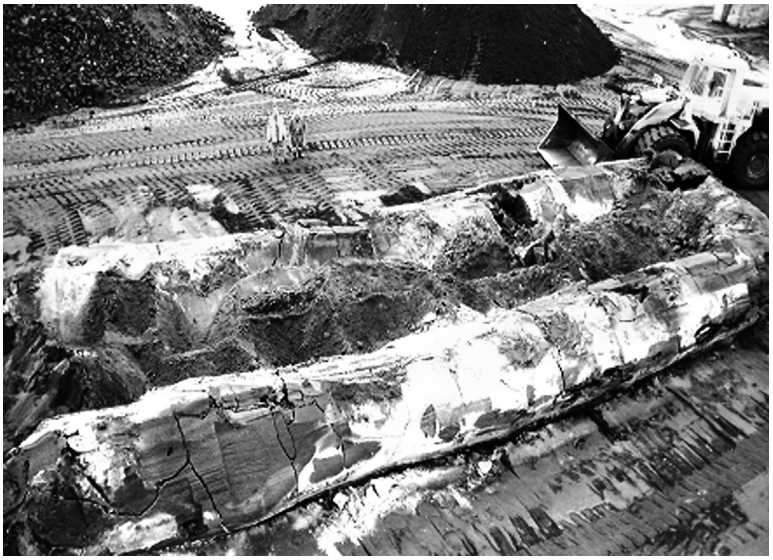

Figure 5 U-shaped SiC roll. From ESK SiC GmbH, Frechen, Germany.

& Wiebke, 1976; Wiebke, Korndörfer, Korsten, Benecke, & Petersen, 1976). Only the resistance core is still horizontally located. The current is supplied via floor electrodes to the resistance core. The complete furnace unit is located outdoors. The bulk mixture of sand and coke is covered with a huge plastic sheet. The reaction gases are collected under the sheet, which will be blown up. CO will be exhausted partly through the porous bed of the floor directly underneath the sheet. The gases will be desulfurized and finally combusted in a power station to be transferred to electrical energy. The latter contributes to the electric power that is necessary for the synthesis of SiC.

The reaction time of the ESK process takes about a whole week. Another week is needed to cool the batch down through water spraying. The SiC roll is uncovered from the unreacted part of the batch. The length of the SiC roll is usually 60 m and the weight is about 300 tons. Because of space saving, the roll is generally U-shaped (Petersen & Korsten, 1979) as shown in Figure 5.

After cooling, the roll is broken into pieces and classified. Classification is necessary since only near the core pure large α-SiC crystals form. The outer area contains a lower grade (90–95% purity) fine-grained β-SiC which is recycled again for the next run or applied as a dopent for the iron and steel metallurgy.

The subsequent preparation route depends upon the application. Targeted grain characteristics are defined: color (green/black), shape (compact/splintery), mean-size and size distribution. In all cases, the route includes fracturing, ball milling, attrition milling, sieving, screening and elutriating. Grain sizes and their distributions for abrasives are defined in Europe according to the Fédération Européenne des Fabricants de Produits Abrasifs standard. Commercial SiC powders vary in terms of color between green and black. The purest commercial SiC grade (99.5% purity) has a light green color and the crystals are translucent. The usage of very pure quartz sand as a starting material is necessary to obtain such a pure grade. The sand for the ordinary nontransparent black grade with purity of only 98.5% contains some impurities, especially aluminum. The black color is due to the presence of elementary carbon. For some applications the SiC powders are further purified. Adherent impurities like elementary silicon, metals (in particular iron), metal compounds, graphite and silica can be removed chemically.

Even today, Acheson process variants represent the main source of SiC raw material for all applications; it should be noted that there are a few drawbacks concerning the synthesis of SiC using these routes. First, extremely high temperatures (above 2300 °C) are necessary for a complete reaction. Such high temperatures give rise to exaggerated grain growth. Furthermore, the large crystals are sintered together. Thus lumps of SiC have to be ground through elaborated milling and purification steps. Hence, roughly speaking the route via the Acheson process for the requirement of fine SiC powders is usually involved with the input of excess energy in two respects, first the thermal excess energy for the formation of large crystals during carbothermal synthesis and second the mechanical excess energy for the pulverization of the large crystals after cooling down. Another drawback can be derived from the batch process itself that implies a distinct temperature gradient within the accumulation during the firing cycle, resulting in a property gradient.

Hence, through the years many intensive attempts have been made to overcome these drawbacks while maintaining the advantageous carbothermal reduction of silica. Most approaches target lowering of the temperature level in order to reduce the grain size, which mostly leads to β-SiC. It should be noted that in some cases β-SiC powders as a starting material for some ceramics could cause some problems during the sintering process, as it will be shown below.

2.04.3.1.2 Sugar Solution Method

In a method developed by General Electric Company (Prener, 1963), first a silica gel in a sugar solution is generated through hydrolysis of $SiCl_4$. Subsequently the gel is dehydrated at 300 °C in order to decompose the sugar and to achieve a thorough mixture of silica and amorphous carbon. Finally the mixture is heated in argon at 1800 °C to generate β-SiC powder. This fine powder was first provided for the semiconductor and pigment industry. Later this method was modified for the production of submicron β-SiC powders (Prochazka, 1972; Schwetz & Lipp, 1978) through the usage of combination of either tetraethyl silicate/sugar or pyrogenic silica/sugar, which could be produced at lower temperatures.

2.04.3.1.3 Pyrolysis of Rice Hulls

Fine β-SiC powders with grain sizes around 0.1 μm (without grinding) is possible if rice hulls are pyrolyzed between 1290 and 1600 °C (Lee & Cutler, 1975). Rice hulls contain both cellulose, which may provide carbon for the SiC synthesis, and amorphous silica. Hence the corresponding SiC production can be regarded as a carbothermal synthesis as well. The reaction temperature is extremely low since on the one hand, both components are homogeneously mixed and on the other hand, the uniformly distributed iron acts as catalyst.

2.04.3.1.4 Fluidized Bed Technique

A continuous production of mainly β-SiC powder was developed by the Superia Graphite Company (Goldberger & Reed, 1984, 1985; Goldberger, 1985). The synthesis of SiC occurs using an electrically heated fluidized bed technique at temperatures between 1500 and 1600 °C. The discharged fractions have grain sizes smaller than 3 mm, which are polycrystalline and contain elementary carbon. The material can easily be ground and the elementary carbon removed.

2.04.3.1.5 Rotary Furnace Process

Fine β-SiC powder is continuously produced through carbothermal reduction of silica in a rotary furnace at temperatures between 1600 and 1700 °C (van Dijen & Metselaar, 1989; Wei, 1983). The rotary tube consists of graphite.

2.04.3.1.6 Elementary Synthesis

A quite different approach is the elementary synthesis of SiC according to the reaction:

$$\mathrm{Si}_{(\mathrm{l,g})} + \mathrm{C}_{(\mathrm{s})} \leftrightarrow \mathrm{SiC}_{(\mathrm{s})} \tag{2}$$

Prochazka (1972) generated β-SiC with a specific surface area of 7 $m^2\,g^{-1}$ in the temperature range between 1500 and 1600 °C through this method. For his investigations he used extremely pure silicon and carbon as starting materials. He tried to apply this powder for sintering experiments, but the sintering activity of the generated powder proved to be only moderate. He attributed this low activity to the presence elementary silicon, which inhibits sintering.

2.04.3.1.7 Vapor-Phase Synthesis

The preparation of very fine powders without using grinding techniques can be successfully achieved by the vapor-phase synthesis techniques: chemical vapor deposition (CVD) or physical vapor deposition (PVD). In principle, β-SiC powders with spherical uniform particles can be obtained using both routes. CVD uses chemical reactions of metals, metalloids or the corresponding compounds, whereas PVD uses evaporation–condensation of solids with similar compositions. The usage of CVD technique is more popular since its production rate as a rule is higher than PVD. Additionally, because in the former often the reactants have high purities or may be purified easily, the powders generated from the gas phase generally exhibit low-impurity concentrations. Sometimes it is even possible to integrate a little quantity of sintering aids into the batch (Chen, Goto, & Hirai, 1996) which are then homogeneously distributed. Another advantage of CVD is derived from short reaction times. On the other hand, it should be noted that there are a few severe problems concerning the use of vapor-phase synthesis techniques. For instance, it is difficult to complete the reaction among the starting components, thus the products often contain unreacted fractions. It can also be supposed that the transference from a laboratory scale fabrication to large-scale production takes a long development time. This may be the reason that large-scale production of vapor-phase synthesis techniques for SiC powders does not exist so far.

The CVD technique (Section 2.04.4.3) for the synthesis of SiC powders includes several variations depending on the source for chemical reactions: heated tube furnace (Suyama & Yamaguchi, 1991), d.c. arc plasma (Baumgartner & Rossing, 1989), high-frequency plasma (Stroke, 1981) or laser (Cannon, Danforth, Flint, Haggerty, & Marra, 1982; Suyama, Marra, Haggerty, & Bowen, 1985). Either one or two precursor gases, with hydrogen as the carrier one, are commonly used for the deposition, for instance:

$$CH_3SiCl_{3(g)} \overset{H_2}{\Rightarrow} SiC_{(s)} + 3HCl_{(g)} \tag{3}$$

$$SiCl_{4(g)} + CH_{4(g)} \overset{H_2}{\Rightarrow} SiC_{(s)} + 4HCl_{(g)} \tag{4}$$

As a summary, all mentioned SiC synthesis versions are compiled in Figure 6. As noted above, both Acheson variants mainly produce α-SiC, whereas all others generate β-SiC. Though presently there exist two continuously running SiC synthesis processes (fluidized bed technique and the rotary furnace method), large-scale production has only been realized through the two batched Acheson techniques.

2.04.3.2 Whiskers, Platelets and Fibers of SiC

The brittleness of ceramic materials is often a big problem in respect of their use in structural applications. Monolithic SiC materials are inherently brittle ceramics. Hence in the last decades one of the most important domains in ceramic research programs has been toughening of ceramic materials, and this is particularly true for

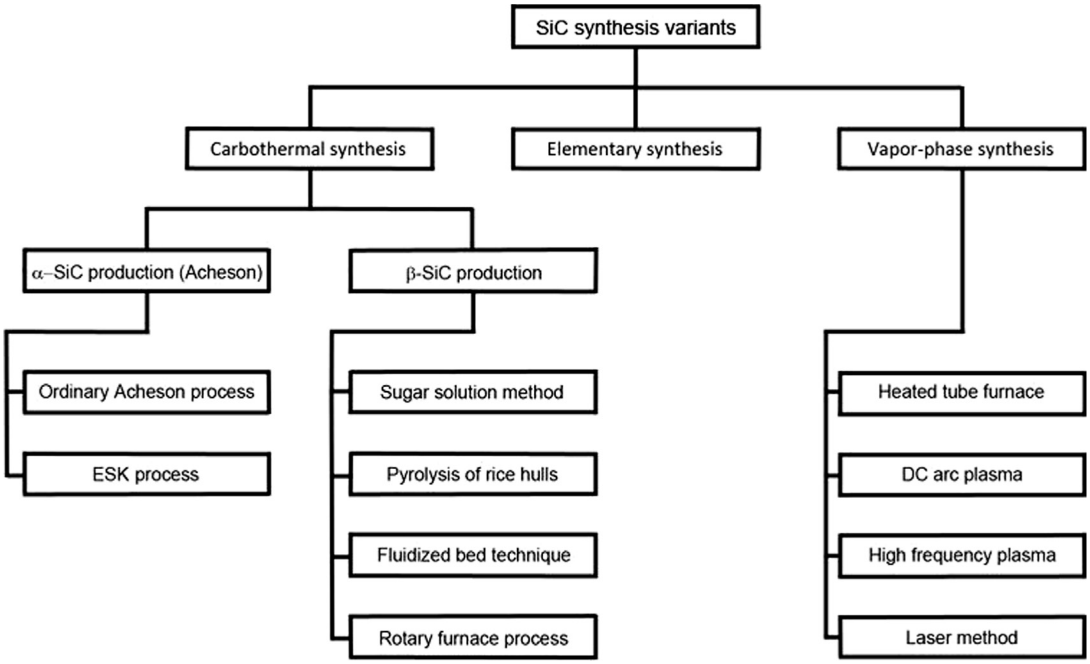

Figure 6 SiC synthesis variants.

high-strength SiC ceramics. One successful approach has been the ex situ incorporation of particles exhibiting large aspect ratios like whiskers, platelets and fibers into ceramic microstructures. The basic idea of this development has been the potentiality that mechanisms which absorb energy are generated through the reinforcement of those elongated or flattened particles into a matrix with isotropic microstructure. The increase of crack growth resistance as it extends is achieved through energy dissipation processes like deflection, branching and bridging of microcracks as well as delamination and pull-out effects. All these mechanisms have positive effects on crack propagation resistance and damage tolerance of the ceramic composites. The attributes of SiC-type nonisometric particles are both high-specific Young's modulus (i.e. ratio between stiffness and density) and good high-temperature properties. It should be noted that these particles have been not only used as reinforcing components for SiC-based ceramics or other ceramics but also successfully incorporated into metals.

2.04.3.2.1 SiC Whiskers

Initially the research projects had been focused on the capabilities of reinforcement through SiC whiskers, which are monocrystalline trichoid short fibers with diameters of 0.1–5 μm, lengths of 5–100 μm; and thus, aspect ratios ranging between 20 and 100, respectively (Figure 7). The Young's modulus and the tensile strength values reach high levels, up to 580 and 16 GPa, respectively. But the main reason for the early interest in those reinforcing components had been the idea of being able to handle them by using simple conventional powder preparation techniques. However, a severe health risk was later identified through medical investigations, especially if the diameter of the whiskers is smaller than 3 μm. Thus both the preparation and the subsequent treatment of the whiskers require in most cases strict safety-related measures.

SiC whiskers can be fabricated using three methods (Shaffer, 1994):

- Vapor–solid (VS) reaction
- Evaporation–condensation or vapor condensation (VC)
- Vapor–liquid–solid (VLS) reaction.

The most cost-efficient and therefore the prevalent method of producing SiC whiskers is based on the carbothermal reduction of silica. The maximum reaction temperature range for the synthesis of these VS-β-SiC whiskers varies between 1500 and 1700 °C. There are a few processing versions, which vary in the raw materials or in the kind of catalyst. It should be mentioned that in nearly any case, a catalyst must be used otherwise only globular particulates but no whiskers would be generated. The only known exception is the formation of β-SiC whiskers through the pyrolysis of rice hulls under reduced pressure of N_2 (Raju & Verma, 1997). The porous cellular structure of the rice hulls seem to act favorably for whisker growth.

If loosely packed, SiC powders are evaporated at temperatures above 2200 °C at low gas pressures, α-SiC whiskers are generated during the cooling down period. The formation mechanism of this whisker generation,

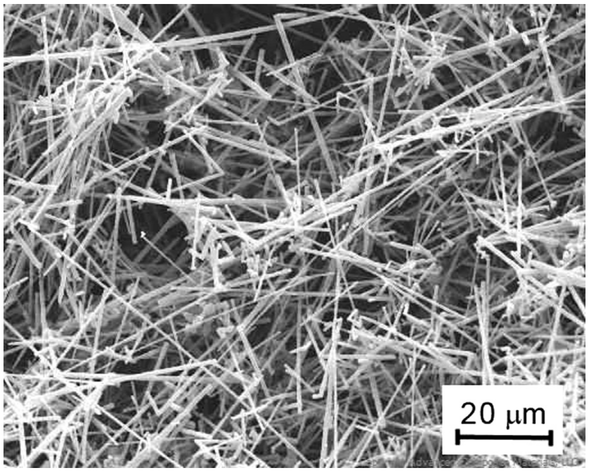

Figure 7 β-SiC whiskers. This photo is kindly released by Advanced Composite Materials, SC, USA.

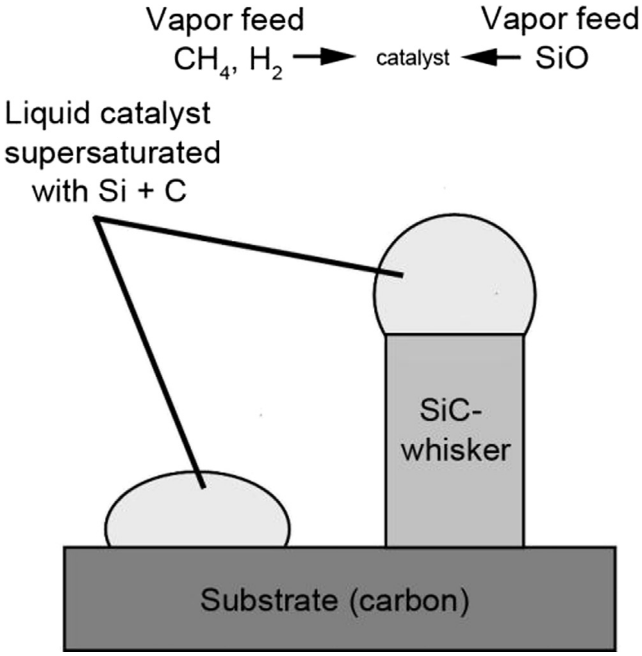

Figure 8 Schematic illustration of SiC whisker growth through the VLS mechanism.

which is referred to as VC method, seems to resemble the mechanisms of both the introductorily mentioned bulk SiC single crystals and the below treated recrystallized SiC (RSiC) which are also generated through an evaporation–condensation process.

VLS method is a mechanism for the growth of whiskers from CVD. Generally the growth rate of a crystal through direct adsorption of a gas phase on a solid surface is comparatively low. Through VLS this problem is avoided by placing a catalytic liquid alloy phase being able to adsorb vapor to supersaturation levels on the surface of a substrate. Thus crystal growth occurs from the nucleated seed at the liquid–solid interface. The VLS mechanism was first proposed to explain the growth of silicon whiskers in the gas phase in the presence of a liquid gold droplet located upon a silicon substrate (Wagner & Ellis, 1964). For the generation of SiC whiskers, molten transition metals and iron alloys fulfill the requirement of catalyst (Milewski, Gac, Petrovic, & Skaggs, 1985; Shyne & Milewski, 1971). Figure 8 illustrates the VLS growth of β-SiC whiskers. First metal microparticulates (usually iron) are distributed on the carbon surface of the substrates. At about 1400 °C the solid particulate melts and forms liquid catalyst droplets. Both carbon and silicon from vapor feeds, $CH_4 + H_2$ and SiO, are dissolved in the liquid catalyst, which soon will be supersaturated. Solid SiC crystallizes at the liquid–graphite interface. Further dissolution of the gas species in the liquid catalyst induces the whisker to grow. The droplet stays on top of the growing whisker surface during the whole process. It should be mentioned that surprisingly VLS technique has not reached large-scale production yet, though VLS whiskers are longer than VS whiskers and offer diameters (4–6 μm) which are presently not regarded to be harmful to health.

2.04.3.2.2 SiC Platelets

SiC platelets are—like whiskers—monocrystals with improved but reverse aspect ratios, thus they are flat and compact (Figure 9). Because of the enhanced aspect ratios platelets offer similar possibilities concerning ex situ toughening of materials. However, they are less expensive and nontoxic. Their aspect ratio is less, only between 4 and 15, which means that generally their toughening effects are lower compared to those caused by the whiskers. The diameter of the platelets ranges from 5 to 100 μm and their thickness from 1 to 5 μm. The crystal structure of the SiC platelets is always noncubic.

SiC platelets are industrially fabricated at temperatures between 1600 and 2100 °C in inert gas using low-cost raw materials like silica, carbon or fine β-SiC powders (Boecker, Chwastiak, Frechette, & Lau, 1989). The crystal habit depends on some doping elements (Kristler-De Coppi & Richarz, 1986; Meier, Hamminger, & Nold,

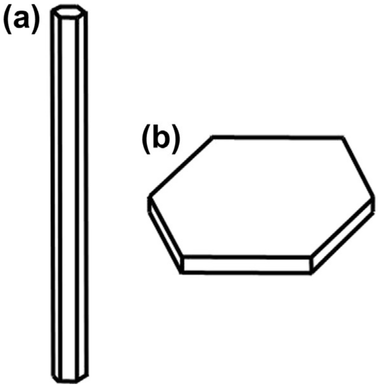

Figure 9 (a) Whiskers and (b) platelets.

1990). Al in SiC platelets increases crystal growth toward the *c*-axis and inhibits it perpendicular to the *c*-axis, whereas B accelerates growth perpendicular to the *c*-axis.

It should be noted that SiC platelets not only improve toughness but also increase the strength, thermal shock and wear resistance of SiC-based ceramics. SiC platelets are used as reinforcement materials for ceramics, metals and plastics.

2.04.3.2.3 SiC Fibers

Ceramic fibers are axially elongated cylindrical shapes exhibiting diameters between 1 and 100 μm (sometimes even longer), which are filamentously formed. They might be amorphous, single- or polycrystalline, and are marketed as continuous, chopped or staple fibers in accordance with the respective production method. Most of the fibers have diameters <6 μm, thus it is not sure whether they are completely safe from a health viewpoint.

The chopped fibers and the staple ones are assembled either as shaped mats or as felts, whereas the single filaments of the continuous fibers are further processed into bundles of 300 up to 2000 filaments containing also two-dimensional or even three-dimensional fabrics.

Because of their small volumes, ceramic fibers have low defect frequency and hence excellent physical properties like high tensile strengths (up to values higher than 2 GPa), high Young's moduli (some larger than 400 GPa) and low densities (below 4000 kg m^{-3}). They resist elevated temperatures to a certain level and are chemically stable. Thin fibers can be processed into textiles.

There are two major types of continuous SiC fibers (DiCarlo & Yun, 2005) on the market. The first type is achieved through CVD coating of β-SiC on either tungsten (W) or carbon (C) filaments of about 40 μm thickness. The filaments act as hot substrates during the heterogeneous nucleation. Those CVD-SiC fibers generally are very thick (typically 100–160 μm in diameter) and rigid (DeBolt, Krukonis, & Wawner, 1974). The surfaces of the SiC/W are bumpy and nodular, thus those fibers are sensitive to self-abrasion which reduces the tensile strength of the fibers significantly. More important is the fact that prolonged exposure to elevated temperature may cause a severe degradation of the fiber strength, probably due to detrimental tungsten core reaction (Kim & Mai, 1998). The tungsten core was later replaced by a carbon core, which is usually coated with a thin (about 1 μm) layer of pyrolytic carbon before deposition of SiC in order to reduce the reaction between the carbon core and SiC. In fiber-reinforced ceramics it is often necessary to lower the stress at the interface fiber/matrix to allow the energy absorbing pullout of the fibers during fracture. Therefore a thin layer of carbon is deposited upon the surface of the CVD-SiC fibers for these applications. Additionally carbon helps to reduce the extreme surface sensitivity of the fibers. The CVD-SiC fibers are marketed by the enterprise Specialty Materials, Inc. (formerly Textron) with the trade name of "SCS-fibers".

Already in the 1970s Yajima and his coworkers (Hayashi, Omori, & Yajima, 1978; Yajima, Hayashi, & Omori, 1975, 1977; Yajima, Hayashi, Omori, & Okamura, 1976; Yajima, Okamura, Hayashi, & Omori, 1976; Yajima, Hasegawa, Hayashi, & Limura, 1978) showed that it was possible to fabricate thin (from 8 to 30 μm) β-SiC fibers via melt spinning, curing and pyrolysis of polycarbosilanes (PCS) without a central core. The production line was built up by the Japanese enterprise Nippon Carbon Ltd, and has been running since 1979 (Ishikawa, 1991). The corresponding product was called Nicalon™, which contained about 10% oxygen. The actual

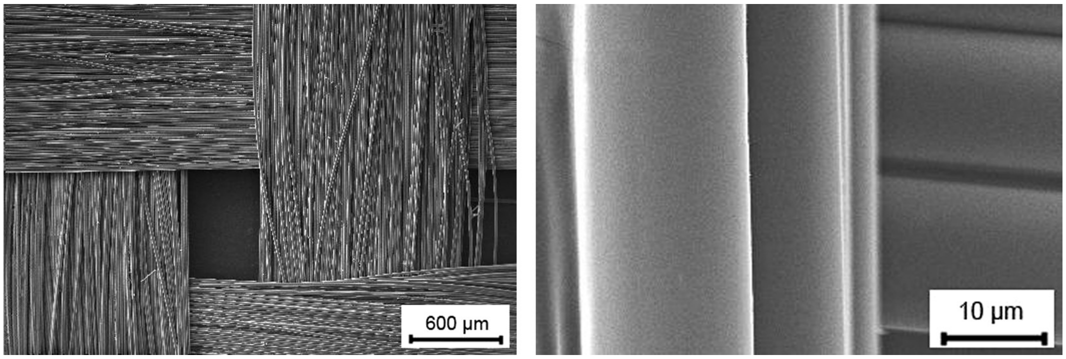

Figure 10 Hi-Nicalon™ S fiber fabric. The copyright of these images is held by the author of this article.

chemical composition of the Nicalon fiber is $Si_{0.58}C_{0.35}O_{0.11}$. Only 40–50% of the silicon atoms are surrounded by carbon atoms like in ordinary SiC. Six percent of the silicon atoms are bound to oxygen like in silica and the rest is bound to both oxygen and carbon. The oxygen and carbon impurities are responsible for the relatively poor thermal stability and the drop of tensile strength at elevated temperatures. A modified process via a PCS titanium alkoxide polymer of the Japanese enterprise Ube Industries resulted in an amorphous Si–Ti–C–O fiber with the tradename Tyranno fiber. The further development aimed at more pure materials from polymer precursors. Nippon Carbon marketed the fiber type Hi-Nicalon in 1993 and Hi-Nicalon S in 1998 with 0.5 and 0.1% oxygen, respectively. These grades have got a much better thermal stability than the predecessor. It could be proved, for example, that Hi-Nicalon S fibers sustain 1900 °C in argon without change. At 1950 °C, however, they start to become unstable (Kriegesmann & Schumacher 2004a, 2004b). Figure 10 shows two SEM photos of a Hi-Nicalon S fiber fabric with two different magnifications. Another approach of SiC fibers with low oxygen content was achieved by the US enterprise Dow Chemical Company with the fiber named Sylramic. In the meantime the marketing activities of Sylramic fibers have been transferred by the US enterprise ATK COI Ceramics Inc.

The characteristics of some selected continuous SiC fibers are listed in Table 3.

Finally an interesting approach of fiber development should be mentioned. It contains only Si and C atoms to some extent. It was introduced in the market by the German enterprise Bayer AG in the 1990s, and corresponds to an amorphous Si–B–C–N fiber synthesized through pyrolysis of a polyborosilazan polymer (Baldus, Passing, Sporn, & Thierauf, 1995). The fiber with the stoichiometrical composition of roughly $SiBN_3C$ remains amorphous up to temperatures higher than 1800 °C. Its oxidation resistance is even better than the one of those pure SiC fibers described above.

2.04.4 Silicon Carbide-Based Ceramics

As already mentioned in the introduction of this article many processing approaches have been developed for silicon-based ceramics in the past. The complex variety of different processing methods of SiC-containing

Table 3 Characteristics of some continuous SiC fibers (manufacturer information)

Trade name	*Manufacturer*	*Composition*	*Diameter (μm)*	*Tensile strength (GPa)*	*Young's modulus (GPa)*
SCS-6	Textron	SiC/C	150	3.92	406
Nicalon™ NL	Nippon Carbon	Si(C, O)	14	3.0	220
Hi-Nicalon™ S	Nippon Carbon	SiC	12	2 .45	390
Hi-Nicalon™	Nippon Carbon	SiC	14	3.02	273
Tyranno	Ube Industries	Si, Ti, C, O	8	2.7	206
Tyranno SA	Ube Industries	>99% SiC	8	3.0	290
Sylramic	Dow Chemical	>99% SiC, 0.5% O	10	3.0	400

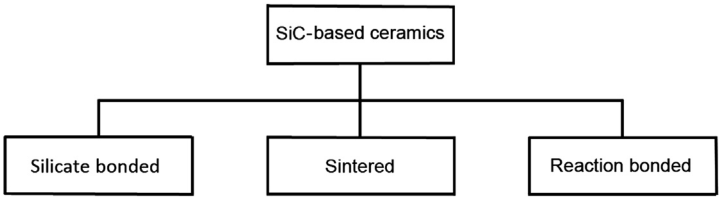

Figure 11 Different groups of silicon carbide-based ceramics.

ceramics should be systemized for a better understanding of their technologies. The consolidation is the processing step where the microstructure of a ceramic is completed. Hence through the consolidation step a ceramic material is actually generated. The respective consolidation mechanism is most important for the properties and thus for the application profile of the corresponding material. This statement particularly applies to SiC ceramics (Kriegesmann, 2005a). If one classifies the SiC-based ceramics according to their fundamental consolidation mechanisms, three different groups can be distinguished as shown in Figure 11.

Silicate bonded SiC ceramics refer to porous ceramics with relatively coarse particles bonded by a large amount of amorphous silicate matrix. The processing occurs via a sintering process in air, which may be compared with sintering process of traditional ceramics. The main sintering effect is the contact formation of a silicate melt with the SiC grains. Thus shrinkage is low or not existent.

The second group comprises either dense or porous SiC ceramics without or at most low-impurity contents. They are sintered in protective atmospheres like argon and/or vacuum, and utilize solid-state, liquid-phase or vapor-phase (evaporation–condensation) mechanisms (Kriegesmann, 2005a). The sintering process may also be pressure assisted through axial hot pressing (HP) or hot isostatic pressing (HIP).

In general sintering means high-temperature consolidation of a bulk material through surface or interface reactions and atomic transport phenomena (diffusion). Thus sintering is a physical–chemical process occurring within the material and should not be confused with firing, a technological step occurring within a kiln which may only cause sintering. The sintering reactions are only atomic site changes and thus "one-component reactions" (Kriegesmann, 2005b) in contrast to normal chemical reactions, which can be regarded as "two-components reactions".

It was discovered in the 1970s that the consolidation of ceramics can also be achieved through normal chemical reactions (Moulson, 1979). This special consolidation has been called "reaction bonding". SiC-based ceramics can also be consolidated through reaction bonding. Some of them are consolidated by reaction action alone, whereas for others the reaction bonding is combined with the infiltration of liquids. Both types of related materials can be referred to as the third group of silicon-based ceramics.

In the subsequent subsections, the processing phenomena of the three groups are described and the corresponding ceramics are characterized.

2.04.4.1 Silicate Bonded Silicon Carbide-Based Ceramics

The most striking properties of the compound SiC are its high hardness and its high thermal stability. Therefore it is not astonishing that the first attempts to develop SiC-based ceramics were focused on SiC grinding tools and refractories more than 100 years ago. Because of the already mentioned nonreactivity of covalently bonded compounds, it was not strived for achieving a self-bonding of the SiC particles. Rather, it was preferred to interconnect the particles via an aluminosilicate bond which could be compared best with the well-known microstructural conditions in traditional clay ceramics. The attempts of creating ceramics, in which the SiC grains were consolidated via a so-called ceramic bond, were successful since the surfaces of the SiC grains can be easily wetted by aluminosilicate melts.

2.04.4.1.1 Silicon Carbide Grinding Tools

The first SiC-based class of materials treated here, the grinding tools, belongs only partially to ceramics. All grinding tools are open-pored in order to be able to capture swarf. The higher the open porosity the better is the grinding yield, but the rougher will be the ground surface. The grinding tools consist of abrasive grains embedded in a binder phase matrix. Each abrasive grain can be regarded as an undefined cutting edge; thus, a

Figure 12 SiC grinding tool for hip joints. This photo was kindly transmitted from Tyrolit Schleifmittelwerke Swarovski K.G., Schwaz, Austria.

multiple cutting edge tool is formed through the surface abrasive grains interconnected by the matrix. In grinding tools with ceramic bond the abrasive particles like diamond, CBN, corundum (α-Al_2O_3) or SiC are interconnected by a vitreous or a glass–ceramic matrix and thus silicate bonded. It should be mentioned that grinding tools can also have resin, sintered metal, galvanic and rubber bonds, but those tools cannot be regarded as ceramics and hence they are not treated here.

Diamond and CBN are the hardest compounds of all and thus the corresponding ceramic bonded grinding tools constitute a quite special and expensive category of materials. On the other hand, the cheaper corundum and SiC grinding tools are often compared with each other. SiC is harder abrasive than the corundum grinding tools, but the latter have a larger market share, particularly because the range of different qualities is wider for corundum grinding tools. Without previous testing, it is difficult to predict which grinding material fits best for a specific assignment. However, there is a trend of using corundum grinding tools for machining of steel, whereas SiC tools are applied for more brittle materials like glass, ceramics, gray iron and nonferrous metals. Figure 12 shows a tool for grinding alumina ball for hip joints.

Since the process engineering for the manufacture of ceramic bonded SiC grinding tools will be treated below together with the refractory bricks, only some aspects concerning the recipe are covered here. For the production of SiC grinding tools both the green and the black SiC raw material powder grades are used. The SiC particles of more expensive green grade exhibit higher hardness but lower toughness than the SiC particles of the cheaper black grade. It should be taken into account that each SiC raw material particle is coated by a thin silica layer because of previous oxidation. Thus the components of the binding system for the SiC grains should be composed in such a way that the silica layer of SiC particles can be wetted through the components and interconnect with them through mutual dissolution processes. Since those processes are highly temperature-dependent, the binding systems should exhibit a high thermal stability. In order to avoid shortening the firing temperature range, which is advantageous for the production process, the recipes of binding systems should not contain valence and coordination number changes. Thus the batches of the binding systems should not include transition elements like iron or boron. Whereas the binding systems for corundum grinding tools are indicated as vitreous by the tool manufacturers, the binding systems for SiC grinding tools are considered to be porcelain-like. For this reason binder batches contain clay components like kaolin or bentonite.

Too high firing temperatures might lead to the risk of foaming, which originates from the oxidation reaction of SiC:

$$2SiC + 4O_2 \leftrightarrow 2SiO_2 + 2CO_2 \quad (\text{at temperatures} < 1100\,^\circ\text{C}) \tag{5}$$

$$2SiC + 3O_2 \leftrightarrow 2SiO_2 + 2CO \quad (\text{at tempetatures} > 1100\,^\circ\text{C}) \tag{6}$$

and the fact that the viscosity of binding composition will be reduced at higher temperatures. If the viscosity is lower, oxygen can diffuse easier through the binder phase to the binder/SiC interface. Through oxygen attack on SiC according to Eqns (5) and (6) gaseous components CO and CO_2 are released, respectively, which have got relatively high vapor pressure and hence high space requirements. The above-mentioned porcelain-like binding system with high thermal stability turns out to be advantageous in order to avoid the foaming as well. At lower temperatures the binder system is still porous so that gases can escape. The risk of foaming is the reason that the SiC grinding tools are more porous compared to some relatively dense corundum grinding tools (Frank, 1998).

The raw material composition for the binding system consists of plastic materials (kaolin, clay, and bentonite), fluxes (feldspar, nepheline syenite, and frit) and additives (quartz sand and soda). The raw materials composition should be constituted such that in the sintered ceramic tool the mismatch between thermal expansion coefficients of the SiC grains ($4.5 \times 10^{-6}\,K^{-1}$) and the binder phase should be low. It had been discovered that the strength of a grinding tool ceramic is strongly dependent on the match between the thermal expansion coefficients of the abrasive grains (here SiC particles) and the aluminosilicate matrix (Kriegesmann, Rasch, & Büchler, 2002). Normally the thermal expansion coefficient of the binding phase is higher than that of the SiC if the above-mentioned fluxes are used. The coefficient can be reduced by replacing feldspar or nepheline syenite with lithium-containing minerals like spodumen or petalite.

The firing is conducted using oxidizing atmospheres (usually air). The maximum firing temperature varies between 1100 and 1350 °C. The microstructural changes during the sintering process are principally comparable with those occurring during the sintering of refractory silicate bonded SiC bricks, even though the firing temperature of the latter materials are generally higher. The SiC refractory bricks are treated in the next section.

The hardness of the grinding tool, i.e. the measure for the ultimate power of aluminosilicate matrix to resist cracking, is an important property according to the grinding experts (Frank, 1998). However, the specifications are not defined precisely and the measuring methods differ between the grinding tool suppliers. Some use destructive and others nondestructive measuring techniques. The destructive techniques are based on the sandblasting principle regularly. The nondestructive method seems to prevail more and more. Sonic methods allow measuring the resonance frequency, from which the Young's modulus can be calculated. Many grinding tool suppliers believe that the Young's modulus is the best measure of hardness. This seems to be reasonable since if we suppose that grinding tool materials (like all brittle materials) have nearly the same breaking strain (0.1%), then the strength of the grinding tool material should linearly depend on its Young's modulus (Kriegesmann, Glagovsky, Moskovenko, & Schmid, 1993).

Figure 13 shows the fracture surface of an SiC grinding tool. The fracture mode is mainly intergranular (Section 2.04.4.2). Practical application has shown that this is advantageous for grinding since the grains break

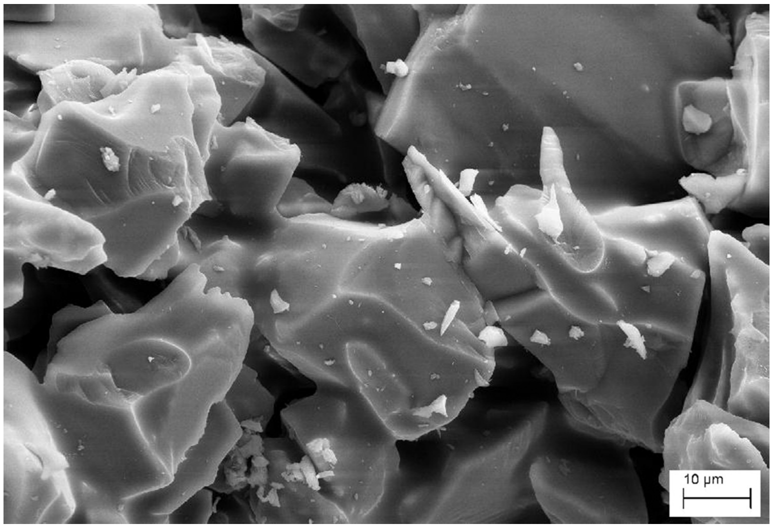

Figure 13 SEM image of a typical fracture surface of an SiC grinding tool. This photo was kindly transmitted from Tyrolit Schleifmittelwerke Swarovski K.G., Schwaz, Austria.

off. This means that SiC grains break off as a whole and thus the corresponding grinding tool remains sharp for the further use.

2.04.4.1.2 Silicon Carbide Refractory Bricks

Refractory bricks should also be porous but for reasons different from those indicated for grinding tools. Pores decrease the crack propagation rate during thermal stressing. Thus porosity improves the thermal shock resistance of ceramics. The open porosity and the pore sizes should, however, be small because otherwise gases or melts can easily penetrate into the brick during the thermal application in practice and thus attack or even destroy its microstructure. Additionally it should be noted that the bending strength and the thermal conductivity of a ceramic increase with decreasing porosity. The microstructure should be designed in such a way to ensure volume stability at high temperature exposure; a porous refractory brick which is shrinking during its sintering process also tends toward shrinking during the application, since sintering and application temperatures of refractory bricks are in the same range. Firing shrinkage can be suppressed by using so-called tiered grain size distributions in the raw material batch. The single grain fraction itself should have a narrow grain size distribution and should be only slightly overlapped by the prior finer and the next coarser fraction, respectively. In this way the overall configuration of particles provides a multimodal grain size distribution. These kinds of distributions give rise to high densifications during the shape-forming step since the finer grains fit into the gaps formed by the coarser ones. The subsequent sintering step is not affected by shrinkage if the coarsest grain size fraction of the distribution is coarse enough. Hence, getting back to SiC-based refractory bricks (Wecht, 1977), the particle sizes of the multimodal grain size distribution of SiC particles should reach from the millimeter down to the micrometer range. Since the SiC grains are less rounded (often called "compact") but rather splintery, the proper grain size distribution cannot be calculated properly. A practical empirical approach of multimodal grain size distribution, however, had been established a long time ago (Litzow, 1930), which is still up to date even for many other refractory recipes. Though the green SiC powder grade seems to be better than the black one because of its higher purity, in practice, this difference implies minor effects on the properties of the SiC-based ceramics. Thus in most cases the black grade has been favored because of its lower price.

The SiC content of refractory silicate bonded SiC bricks ranges from 40 to 90 wt.%. For the silicate bond the recipe contains mostly the so-called refractory clays with a high alumina content (up to 42 wt.%), which usually consist of fire clays, which are imperfectly structured kaolinites. It should be noticed that the clay not only is responsible for the interconnection of SiC grains but also increases the plasticity of the raw material composition. If the SiC content is high, the plasticity of raw material mixture is too poor for the shape-forming technique of pressing. In this case bentonite can be added (not more than 1 wt.%) to improve the plasticity. If the SiC content is low, some of the clay content may be replaced by grog (also called chamotte) in order to reduce plasticity. These recipes may also contain organic polymers as binders like polyacrylates, polyvinyl alcohols or polyvinyl acetates. For achieving better refractoriness, natural highly alumina-containing minerals like sillimanite or artificial additives like fused alumina may replace clays.

The firing is conducted using oxidizing atmospheres (air with added oxygen). The maximum firing temperatures vary between 1350 and 1500 °C according to the composition. They are higher regularly than the maximum firing temperatures applied for SiC grinding tools. The reason is the higher thermal stability that is required for a refractory material.

As mentioned above, the microstructural changes in silicate bonded SiC bricks during the sintering process are in principle comparable with changes occurring in silicate bonded SiC grinding tools, even though the corresponding reaction temperatures may be shifted a bit to higher temperature ranges. At about 1000 °C first silicate melt droplets may occur depending on the alkaline impurity content in raw material mixture. Mullite ($3\ Al_2O_3 \cdot 2\ SiO_2$) is formed between 1200 and 1400 °C. If mullite originates directly from the clay minerals via solid-state reactions, the shape of the crystals is spherical (primary mullite). On the other hand, if the mullite is formed via solution of clay relicts (e.g. meta kaolinite, $Al_2O_3 \cdot 2\ SiO_2$) in the liquid phase followed by reprecipitation, the shapes of the crystals are needle-like (secondary mullite). The mullite/glass phase ratio in the interparticle space affects the properties of silicate bonded SiC brick notably. Thus it can be expected that a higher ratio provides better refractoriness, strength, creep resistance and thermal shock resistance for the brick (Eckert, Kara, & Kerber, 1994). Particular problems might arise from cristobalite, which usually is generated through crystallization of the early oxidized surface of the SiC particles due to the oxygen-rich atmosphere of the firing stage. The phase transformation of cristobalite at 240 °C causes a tremendous volume change, thus in a long run the corresponding brick might be destroyed through periodic temperature cycling in the practice.

The processing principles for the production of silicate bonded SiC bricks and for the production of corresponding grinding wheels resemble each other widely. Thus the processing of those two SiC-based ceramic groups should be treated together.

The compound conditioning depends on the kind of shape-forming techniques. If the shape forming is implemented through slip casting, the different SiC particle fractions and ceramic binder components should be wet stirred (15–30% water) in a counter flow mixer for 1/2 and 6 h depending on the grain size distribution. The resulting slurry is cast in a porous plaster mold, dried after demolding first in indoor air later in drying chambers. The mixture may contain components, which increase the thixotropy of the slurry, like magnesia (Frank, 1998), in order to reduce the water content of the slurry; the casting of thixotropic slurries requires a vibrational motion of the molds. Through slip casting technique it is possible to fabricate homogeneous parts, but the variation of the slip composition, especially if the recipe contains gas-forming substances (see below) is limited. Furthermore the slip casting technique is time-consuming and thus is only used for producing complex parts.

The standard shape-forming method for silicate bonded SiC-based ceramics is the uniaxial pressing technique, for which a dry formable material mass is needed. The components of the mass are mixed in a compulsory mixer. Apart from SiC particles and the above-mentioned inorganic binder constituents, they contain pulverulent temporary binders like dextrin, urea resin, phenolic resin, wax or their aqueous solutions and water. Sometimes it is necessary to increase the pore sizes. In this case the components contain the so-called pore formers, which could be artificial granulated sublimating substances like naphthalene as well as natural opening substances like coke or nutshells.

The uniaxial pressing is carried out in hydraulic, friction, toggle, excentric and vibratory presses. The highest green densities can be achieved with the latter technique because of superposition of static and dynamic loads. A press mold should consist of either hardened tool-steel or cemented carbide because of extreme abrasion of the SiC grains. The contact pressure per unit area ranges from 500 to 4000 MPa. The so-called hand mold-shaped bodies are compressed with vibratory pneumatic hammers.

The moisture of the shaped bodies range from 2 to 4% for pressed, from 5 to 8% for hand mold and up to 20% for cast bodies, respectively (Wecht, 1977). Too rapid drying may induce overpressure in the pores, which may cause bursting of the bodies. Thus the drying of the shaped bodies should be proceeded with caution. Large bodies have to be dried through warm air drying (up to 50 °C) first. Smaller bodies can be put also directly into drying chambers with temperatures of 110 °C. A thorough drying process is needed for the silicate bonded SiC-based ceramics because of the risk of “black cores”, given by residual moisture promoting the decomposition of SiC (see below).

The firing is conducted in gas- or oil-heated continuous tunnel kilns or in intermittent shuttle and hood kilns. During the heat-up stage the residual moisture should be expelled completely and both the organic polymers and the gas-forming substances have to be burned out. It should be noted that at this stage an oxidizing atmosphere is necessary in order to prevent the formation of free carbon, which can cause the “black cores”.

Simply shaped bricks and small grinding tools (with diameters of up to 300 mm) can be left unmachined. However, larger cutting tools and those for special applications, such as threaded and profiled disks, need thorough final machining.

Figure 14 shows the course of the processing procedure for the silicate bonded SiC grinding tools and refractory bricks. The final machining is displayed with dotted lines since it is only necessary for some special applications. The course of processing of the silicate bonded SiC-based ceramics is largely comparable to the processing of many traditional ceramics, which is understandable, since the manufacturing routes the silicate bonded SiC-based ceramics had been developed out of the knowledge of the processing of traditional ceramics.

The uses of silicate bonded SiC bricks are too multifaceted (Wecht, 1977) to be treated in this survey. Nevertheless the demand of the silicate bonded SiC bricks has slowed down tremendously before 2010. Generally it can be stated that the loss of significance is attributed to the fact that lots of new SiC-based ceramics have been developed in the meantime, thus for some applications the bricks were replaced by new materials. Particularly worth mentioning are the SiC-containing “unshaped refractory materials” (Krebs, 2008). The roots of this new material class derive from the procedure of repairing damaged parts of firing assemblies. First it had been demonstrated that it is possible to repair damaged parts on location in such a

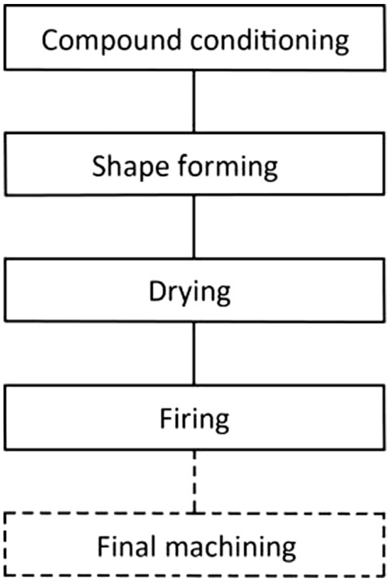

Figure 14 Flow sheet of the processing routes for the most silicate bonded SiC-based ceramics.

manner that a dry mixture of the main components and binders is transported to the installation position, where water or other liquids are added in order to achieve moldability, followed by reshaping; the consolidation is reached by heating up the repaired parts to application temperature. This procedure had proved beneficial compared with the brick technology, since one firing step could be omitted. Thus later this idea not only was restricted to repairs only but also was extended to the construction and fabrication of voluminous linings of furnace assemblies. It has also the advantage that the constructions of refractory lining for the industrial furnaces are jointless since joins are often sources for corrosive attack. Another advantage is that a technical simplification can be achieved since the refractory supplier only has to deliver loose mixtures or at most slurries (castables) and the user himself performs the shaping, the setting and the consolidation. The shaping may be performed by ramming, casting, gunning and injecting. The setting can be conducted via manifold bonding mechanisms like hydraulic, ceramic, chemical and/or organic interconnection. The consolidation, however, occurs during the high-temperature application, where in most cases a ceramic bond is formed (not necessarily a silicate bond). The unshaped refractory materials have soon conquered the market. This trend was not only observed for SiC-containing unshaped materials alone of course, it has also applied for a larger sector of refractory materials. If the unshaped materials contain SiC, usually their content is small, definitely smaller than 30%. Because of the low SiC content, the SiC-containing unshaped refractory materials cannot be regarded as real SiC-based ceramics, and thus this subject should not be covered here any further.

2.04.4.1.3 Silicon Carbide-Based Foam Filters

This subsection shall be completed with a silicate bonded SiC-based foam filter, a refractory which is different from the treated SiC-based bricks concerning both process sequence and application.

Ceramic foam filters (Figure 15) are used for the foundry technology in order to remove inclusions from molten metals, which otherwise would affect the quality of the metal cast parts regarding surface finish, strength and hardness. Such inclusions might be for instance slag residues, refractory parts and other nonmetallic particles. Additionally the filters improve the filling of the mold during the casting process. The molten metal has a turbulent flow characteristic during the pour. Due to the three-dimensional pore structure of the ceramic foam filter, the turbulent flow is converted into a laminar one. This calm flow results in an improved mold filling and less erosion of the sand molds.

There are foam filters based on alumina, zirconia and SiC depending on the metal melt that has to be filtered. SiC-based filters show a thermal stability up to 1470 °C and have been proven useful for copper and bronze alloys as well as cast iron, including alloyed variants.

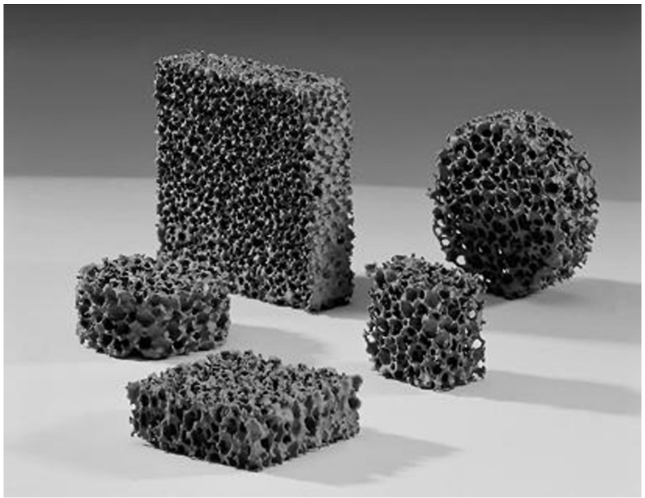

Figure 15 SiC-based foam filters. This photo was kindly transmitted from Drache Umwelttechnik GmbH, Diez, Germany.

The raw material composition of SiC-based foam filters is comparable to the corresponding composition of the silicate bonded refractory bricks. The first processing step is generation of slurry which, in spite of low water content, exhibits low viscosity through addition of a small amount of bentonite within the batch. Open-pored polyurethane foam is then immersed in the slurry. Effective wetting by the latter results in a foam coated with the raw material composition. After drying in air-recycling dryers at about 110 °C, the coated foam is fired in those kilns mentioned above. The oxidizing atmosphere first burns out the polyurethane foam completely, leaving a hollow network of the ceramic composition behind which will sinter to rigid skeleton in the further course of firing. It should be noted that the change of temperature should be low during the decomposition stage of the polyurethane because otherwise the skeleton can be destroyed through gas evolution. The maximum sintering temperature ranges from 1350 to 1450 °C. Figure 16 shows the secondary (artificial) pore structure of an SiC-based foam filter. It should be kept in mind that bars of the skeleton are hollow so that these ceramics have a primary and secondary pore structure.

Figure 17 shows the course of the processing procedure for the SiC-based foam filter. The firing step consists actually of two stages: decomposition of polyurethane and sintering.

In this subsection the processing of such SiC-based ceramics should have been described, which possess a silicate bond between the SiC grains. Three material groups have been selected, which meet the required

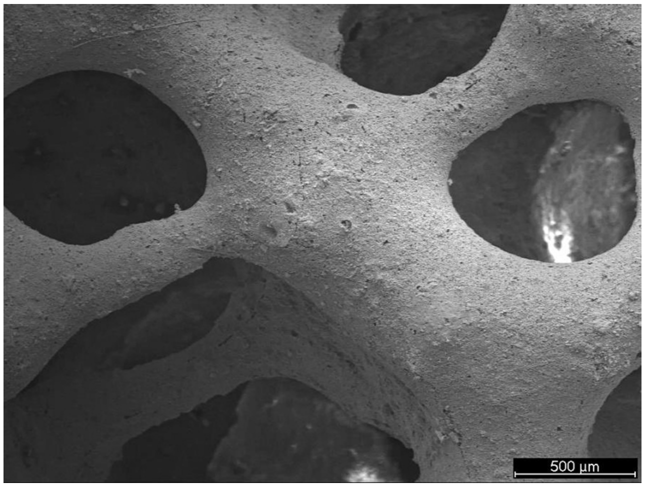

Figure 16 SEM image of an SiC-based foam filter. This photo was kindly transmitted from Drache Umwelttechnik GmbH, Diez, Germany.

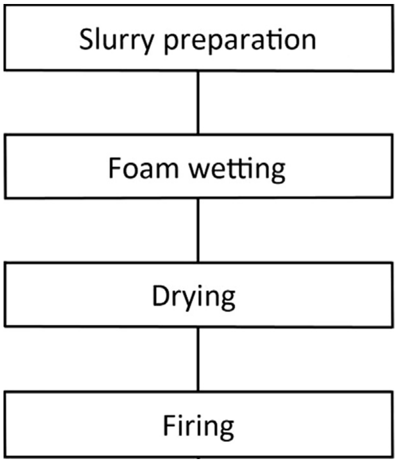

Figure 17 Flow sheet of the processing route for SiC-based foam filter.

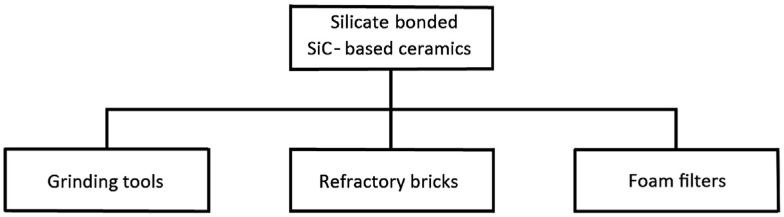

Figure 18 Silicate bonded SiC-based ceramics.

demand (Figure 18). The particular benefit of such materials lies in the fact that the process technologies for their manufacturing is comparable to the processing routes of the well-known traditional silicate ceramics, hence the processing can be regarded as less complex. Additionally maximum firing temperature is expected to be moderate. The idea of interconnecting SiC particle with a silicate bond is old: two of the mentioned three material groups are existing for more than 100 years. But yet most of them are up to date even today. The third material group, the foam filters, is fairly new and yet has been successfully marketed. This shows that it might be reasonable even at present to develop ceramics with a traditional silicate bond.

2.04.4.2 Sintered Silicon Carbide-Based Ceramics

Despite obvious benefits in terms of simplification of the technology, the materials scientist had regretted that silicate bonded SiC-based ceramics could not fully utilize the potentials of the SiC compound. The silicate bond bridges between the SiC grains proved to be relatively weak in comparison to the highly covalent bonded SiC. At elevated temperatures the silicate matrix softens, thus the high temperature strength is even further reduced. SiC has a high intrinsic thermal conductivity, but the poor heat conducting of the silicate bridges between the SiC grains reduces the heat flow between the grains to a great extent. The silicate matrix also has a negative effect on the chemical resistance of the SiC-based material.

Hence, materials researchers had to face the challenge to improve the properties of SiC-based materials through either reduction of the amount of silicate phases or replacement of the silicates by chemically stable and refractory phases. The decrease of the amount of additives and reduction of SiC particle size alone proved to be not enough for achieving an acceptable sintering activity.

2.04.4.2.1 Hot Pressed Silicon Carbide

Initial signs of success toward this objective were achieved through axial HP, which can be regarded as a pressure-assisted firing technique. Hot presses consist of resistance or inductive furnaces with thermal isolated and water-cooled combustion chambers, which contain integrated graphite pressing units. Hot presses run under vacuum or protective gas (mostly argon or nitrogen) and reach temperatures up to 2500 °C (for SiC

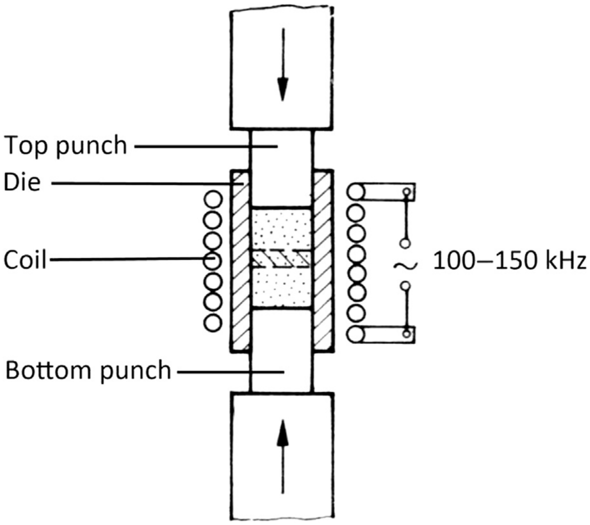

Figure 19 Scheme of an inductive hot pressing device.

usually 2050 °C is sufficient) and pressures up to 50 MPa provided that the die and the punches ordinarily consist of graphite. If the mold parts consist partly of carbon–fiber–carbon (CFC; C/C) and additionally only flat plates are manufactured, higher pressures are possible, temporarily up to 200 MPa. Figure 19 shows the scheme of an inductive HP device (the chamber and isolation are omitted).

In the first publication concerning hot pressed silicon carbide (HPSiC), a fine-grained SiC powder with slight additions of aluminum and iron, in both elementary and in oxide forms, was hot pressed up to a uniform density of 98% of the theoretical density (Aliegro, Coffin, & Tinklepough, 1956). Lange (1975) used alumina as a sintering aid, which besides adhering silica on the SiC particles creates a liquid aluminosilicate phase at elevated temperatures. This phase gives rise to a liquid-phase sintering (LPS) process which promotes densification up to 99% of the theoretical density through a solution reprecipitation mechanism. Load rate-depending tests were carried out on an HPSiC (Evans & Lange, 1975). The results indicated that at room temperature, where the grain boundary silicate phase is a rigid glass, the subcritical crack growth (see below) is moderate. However, at elevated temperatures it is highly significant since the glassy phase softens. Weaver and Olson (1974) hot pressed SiC powders containing >5% elementary aluminum powder and achieved true density. It can be assumed that also a liquid aluminosilicate phase was formed in this case (Kriegesmann, Lipp, Reinmuth, Schwetz, & Struensee, 1979).

Figure 20 demonstrates the model of subcritical crack growth due to grain boundary sliding. It shows part of a polycrystalline microstructure under tensile stress σ (Evans & Langdon, 1976). The primary crack may have been formed during the fabrication process, for instance through thermal stressing during the cooling stage after sintering. Let us suppose that the grain boundaries contain a soft phase. In this case, two adjacent grains under load in the neighborhood of the primary crack are sliding on each other along the grain boundaries. This effect is more evident as the closer the angle between the stress and the grain boundary is to 45°. Grain boundaries perpendicular to the stress cannot slide, they only may crack through stressing. Thus if a microstructure of a polycrystalline ceramic with "soft" grain boundaries is tensile stressed, a network of secondary cracks develops in front of a primary crack. In this way the bearing cross-section will gradually decrease and thus the strength of the material will be reduced. Since the grain boundaries have been proven as the weakest areas in the microstructures, the fracture surface is typically intergranular. Grain boundary sliding is the reason for the reduced strength at high temperatures for most ceramics.

Structural ceramics for both low and high temperatures use should not show any strength drop at high temperature. In order to reach this goal the idea was to modify the grain boundary in such a way that the fracture surface turns out to become transgranular.

Figure 21 shows two plots of bending strength as a function of temperature for HPSiC. In one case (Figure 21(a)), 1.5 wt.% elementary aluminum powder had been used as sintering aid (Kriegesmann, Lipp, Reinmuth, & Schwetz, 1983). The strength drops above 800 °C when the glassy phase begins to soften. It can be assumed that the strength loss at elevated temperatures was caused by subcritical crack growth. In the other case

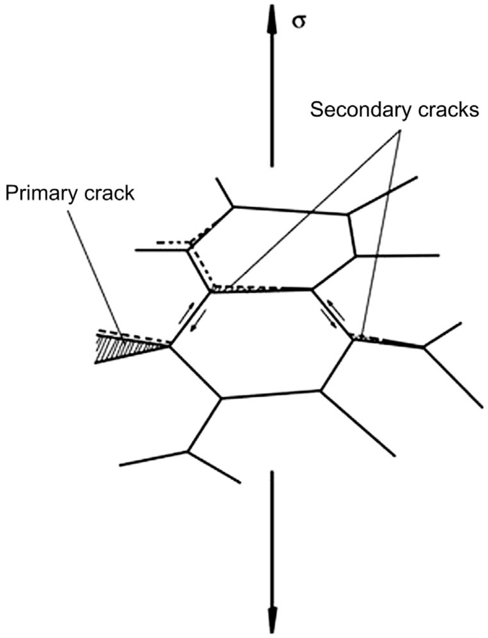

Figure 20 Scheme of the subcritical crack growth due to grain boundary sliding.

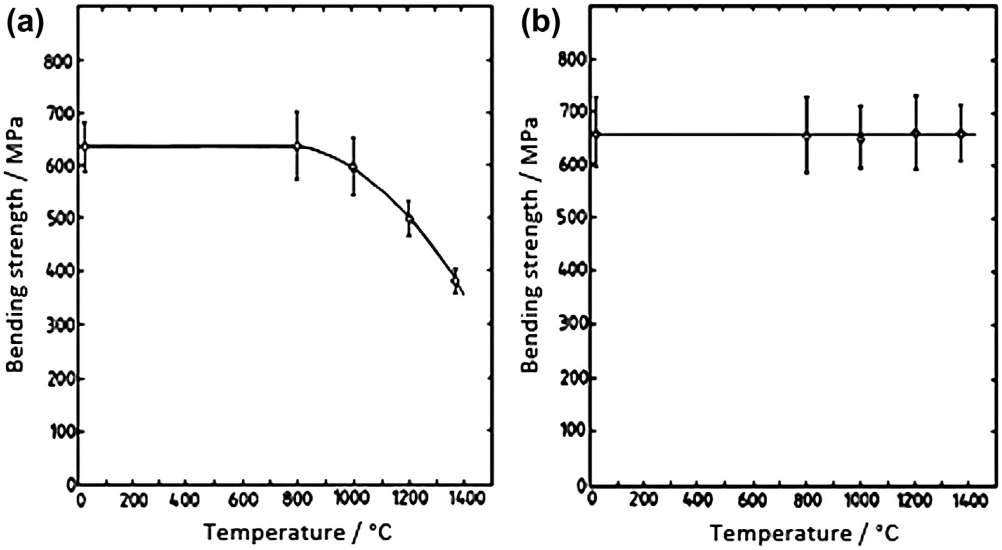

Figure 21 Bending strength versus temperature for HPSiC (micron-sized α-SiC starting powder): (a) doped with 1.5 wt.% Al and (b) doped with 0.3 wt-% Al. The copyright of this image is held by the author of this article.

(Figure 21(b)), the amount of the sintering aid was reduced drastically down to 0.3 wt.%, but it was still enough to reach true density. The room temperature strength is in the same range for both grades, but only the low-doped grade keeps such a level at least up to 1360 °C.

Figure 22 shows the SEM micrographs of the fracture surfaces for the two discussed HPSiC grades. As indicated above, (a) the high-doped and (b) the low-doped grades exhibit intergranular and transgranular fractures, respectively. According to Lange (1975) an LPS mechanism is responsible for the densification of the high-doped grade. It can be assumed for the low-doped grade that the solubility limit for aluminum in SiC is not exceeded so that aluminum is dissolved in the SiC grains and the grain boundaries are thus free from the secondary phase. It can be furthermore supposed that in this case a solid-state sintering mechanism is predominant. If α-type SiC starting powder is used for HP, no remarkable strength drop occurs up to at least

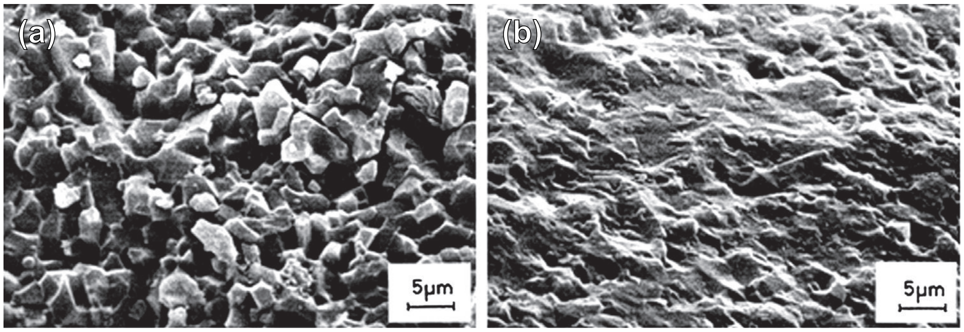

Figure 22 Fracture surfaces of HPSiC (micron-sized α-SiC starting powder): (a) doped with 1.5 wt.% Al and (b) doped with 0.3 wt.% Al. The copyright of these images is held by the author of this article.

1500 °C as far as the aluminum amount does not exceed 0.4 wt.% (Kriegesmann, Lipp, & Reinmuth, 1984). On the other hand, if the SiC starting powder contains the β-type, the amount of aluminum sintering aid might be increased up to 1 wt.% without strength drop at high temperatures (Kriegesmann, Lipp, & Reinmuth, 1982).

For an HPSiC-doped with boron or B_4C (Prochazka, 1974; Prochazka & Charles, 1973; Prochazka & Donalski, 1978) the strength is also kept high at elevated temperature even if the solubility limit of boron in SiC is exceeded (Kriegesmann, Lipp, Reinmuth, et al., 1979). The reason is that undissolved boron does not form a glassy phase at the grain boundaries but remains refractory.

True density of HPSiC can only be achieved through the addition of sintering aids. Available temperatures and pressures have proved to be too low for achieving it using just pure SiC powders, due to the extremely low sintering activity of this covalent material. Hence first successful attempts to generate fully dense and pure SiC ceramics required extremely high temperatures and pressures approaching diamond synthesis conditions (Balchan & Cowan, 1968; Hall, 1964; Nadeau, 1973).

2.04.4.2.2 Hot Isostatic Pressed Silicon Carbide

Commercial undoped micron-sized α- and β-SiC powders could be fully densified through HIP technique at a temperature of 2000 °C at a pressure of 200 MPa (Kriegesmann, Hunold, Lipp, Reinmuth, & Schwetz, 1986).

Both HP and HIP are pressure-assisted firing techniques. Unlike HP, the pressure in an HIP unit is transferred isostatically so that properties of the resulting materials are omnidirectional. Since the main pressure-transfer medium is not a strength-limited solid but a compressed inert gas (usually argon), the pressure is only limited through the walls of the unit itself and thus the allowable pressure might be much higher (up to 300 MPa). The water-cooled thick-walled and thermally isolated combustion chamber can be regarded as both a furnace and a high-pressure autoclave.

Two methods of powder HIP techniques are usually applied for the manufacture of hot isostatic pressed silicon carbide (HIPSiC). The first one (Figure 23(a)) is mostly used for scientific research when the dimensional accuracy of the sintered body is unimportant. In this case highly melted metal (e.g. tungsten, molybdenum, and tantalum) or glass (silica glass) casings are filled with powder. Silica glass proved to be the best-suited material for HIPing SiC. The powder-filled casing has to be vacuum-tight sealed, before the HIP cycle

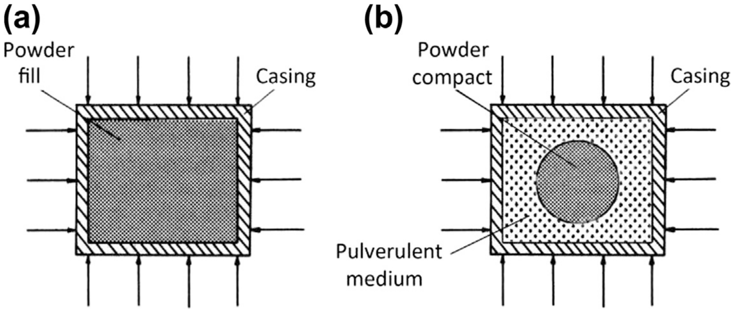

Figure 23 Principles of pressure transfer on powder HIP: (a) starting with powder and (b) starting with a shaped powder compact.

can be started. The second method (**Figure 23(b)**) is used for shaped powder compacts. In order to transfer the pressure to the shaped compact an additional pressure-transfer medium between the casing and the powder compact has to be inserted. This medium should be a heat-resistant and nonreactive pulverulent material, e.g. coarse hexagonal Boron nitride (BN) powder (Hunold, Reinmuth, & Lipp, 1983), since it should react with neither the SiC powder compact nor the sinter itself.

The above-mentioned renunciation of sintering aids is one way to reduce the defect concentration and the critical defect size in ceramics, respectively. Another possibility can be offered through reduction of the powder particle size of the powder with the goal of achieving ceramics with small grain sizes. However, because of the high-specific surface and energy of these fine powders, conventional sintering of them can lead to extreme grain growth. Through pressure-assisted sintering, the maximum sintering temperature can be reduced and thus rapid grain growth may be prevented. Ceramics with more than 95% of the theoretical density and mean grain size of 150 nm could be generated through HIP of boron- and carbon-doped (see below) β-SiC starting powders, with grain size <20 nm (Vassen, Stöver, & Uhlenbusch, 1991). The maximum HIP temperature at 1500 °C was comparatively low. The grain boundary reduction resulted in an increase of Vickers hardness, although together with a reduction of fracture toughness (Vassen & Stöver, 1997). On the other hand, if the grain size distribution becomes bimodal with coarse-grained inclusions in a nanosized matrix, the fracture toughness can be increased noticeably (Förster, Vassen, & Stöver, 1995). The technique was further improved by annealing the shaped bodies in vacuum before encapsulating in silica glass casings (Vassen, Buchkremer, & Stöver, 1999; Vassen & Stöver, 1999). In this way the residual oxygen content in the powder could be minimized, which enabled the researchers to control the grain size distribution in the HIPed bodies much better. Thus it was possible to achieve bodies with mean grain size smaller than 80 nm.

Nanosized (grain size < 100 nm) microstructures provide the possibility to improve the mechanical properties and the reliability of the SiC ceramics. However, it should be noticed that nanosized powders cannot be treated in the same simple way as conventional micron- or submicron-sized powders (Cannon, Danforth, Flint, Haggerty, & Marra, 1982). For instance, nanosized powders show deteriorated flow characteristics, lower oxidation resistance, as well as insufficient apparent and pressing density. Moreover, and above all other considerations, the higher costs for the nanosized powders must be taken into account (Schwetz & Lipp, 1978).

The HIP technique will be recalled later as an additional densification method to pressureless sintered SiC.

2.04.4.2.3 Silicon Carbide Ceramics Manufactured by the Field-Assisted Sintering Process

The field-assisted sintering technique (FAST) belongs to a novel class of sintering processes, which utilizes a pulsed direct current to enhance consolidation (Hennicke & Kessel, 2004). This consolidation technique principally is a modified HP process. We treat it here as a final pressure-assisted powder sintering technique, since it is regarded as highly topical by many experts. The principle was invented in the 1960s (Innoue 1966a, 1966b, 1967) and further developed by Sumitomo Coal Mining Co., Ltd, Tokyo, Japan (Tokita, 2001) calling this technique spark plasma sintering (SPS), though this term is debatable, since no evidence has been given that sparks or a plasma occur during this sintering process. We will use the term FAST because this acronym describes the process more precisely, though it must be admitted that the acronym SPS gains increasing acceptance.

In **Figure 24**, the two HP methods are compared with each other (Kessel & Hennicke, 2010). In classical HP devices (heated either inductively or via an ohmic resistance) (**Figure 24**(a)), a considerable temperature gradient between the inner (T_I) and the outer (T_A) section of the sample is present. In this case a long holding time t^* up to temperature adjustment will be necessary, in particular if the articles are supposed to be bulky. As a result the microstructural homogeneity is limited. Since normally pressure application should be started after temperature adjustment is reached, the HP cycle requires a comparatively long period.

In the case of FAST the heating current is conducted via the punches directly through the sintering body. In this way the temperature gradients are much smaller (but inverse: center hotter than outside) and thus higher heating rates can be permitted (**Figure 24**(b)). Since the time for the temperature adjustment is very small, the processing time is additionally reduced and thus the energy and cost efficiency further improved.

Through FAST it is possible to improve distinctly the sintering activity. One reason is the already mentioned uniform heating of the whole sample volume. However, a second and even more remarkable one is the fact that high current densities occur just locally at the grain–grain contact points, yielding there higher temperatures which enhance the sintering phenomena without grain growth. Some other effects have been observed with FAST (Kessel & Hennicke, 2010), which are not discussed here. In the case of SiC particles, it is important to mention that the resistivity of the electrically isolating oxide layers covering each particle with thicknesses on an

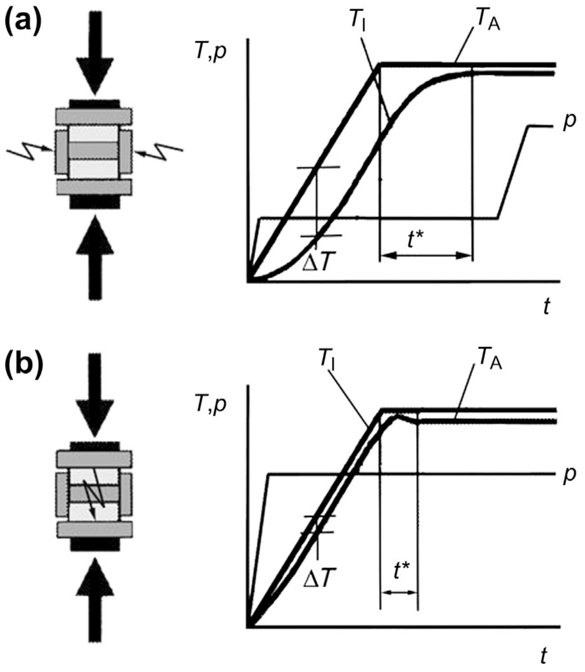

Figure 24 Axial hot pressing in comparison. (a) Hot pressing (HP). (b) Field-assisted sintering technology (FAST). Reproduced with kind permission of HvB-Verlag GbR, Ellerau, Germany.

atomic scale can be overcome by tunnel effects. These can be supported by the pulse character of the heating current. Each powdered material shows specific features during FAST sintering and thus requires specific process guidelines. Because of the high electrical conductivity of SiC, the corresponding powders should be well suited for FAST.

Following the above ideas, it is understood that FAST was also tested for SiC-based compositions. Cho, Munir, and Lee (2008) examined the microstructural changes in SiC ceramics doped with aluminum (Al), boron (B) and carbon (C) by FAST sintering at pressures of 40 MPa. They used β-SiC powder as starting material. At a sintering temperature of 1800 °C, 99.0% of the theoretical density was achieved in spite of a high heating rate and short holding times (10 min). It was assumed that an LPS mechanism is responsible for the sintering behavior, which was comparable with results found for similar compositions densified by using the conventional HP technique (Cao, MoberlyChan, De Jonghe, Gilbert, & Ritchie, 1996). Until 1700 °C the microstructure of this FAST SiC consists of globular grains, though a slight $\beta \rightarrow \alpha$ transformation had already been observed at 1700 °C. The growth of plate-like grains in a fine-grained matrix was observed in specimens at 1750 °C, so that a bimodal grain size distribution was present. At 1800 °C a platelet interlocking microstructure was generated. Further it was noticed that the grain growth rate decreases with an increase in the amount of total additive content in SiC. On the other hand, the volume fraction and the aspect ratio of the platelets in the sintered body rose with an increase of the additive amount.

The composition of Cho et al. (2008) is atypical in comparison with those usually being taken for liquid sintered SiC (LPS-SiC). FAST results for typical LPS-SiC compositions are presented below in connection with the LPS of SiC.

It would be interesting to consider whether it is possible to achieve a fully densified SiC ceramic by FAST without the usage of sintering additives, which had been succeeded with powder HIP already (Kriegesmann et al., 1986). Though it has to be admitted that FAST is superior to HIP in many respects, there is at least one item where HIP seems to be superior to FAST. For FAST the ultimate pressure transmitted to the specimen should be limited through the strength characteristics of the graphite molds, whereas ultimate pressure for HIP is only limited through the construction of the facility. Generally the limited applied pressure for HIP might rise to 300 MPa since the pressing power for FAST should, like HP, not exceed 50 MPa, unless some precautions had been taken (see above).

β-SiC powders activated through centrifugal ball milling were sintered by FAST using pressures between 50 and 150 MPa, maximum sintering temperatures between 1650 and 2200 °C and holding times between 3 and

10 min (Lara, Rapoyato, Muñoz, Ortiz, & Dominguez-Rodriguez, 2010). Full sinterization was obtained at 1900 °C and above. The sintering was accompanied with grain growth. The grains distribution ranged from 1.0 to 2.5 μm. It was noted that grain growth in these experiments strongly depends on holding time but less on sintering temperature.

Nanometric SiC powders were synthesized by using a mechanochemical process by reactive high-energy ball milling of Si and C mixtures (Yamamoto, Kitaura, Kodera, & Ishii, 2004). The powders were sintered without sintering additives in an FAST apparatus. At maximum sintering temperatures of 1700 °C with holding times of 10 min and axial pressures of 40 MPa, FAST resulted in specimens of relative densities of 98%. The crystallite size was 30–50 nm. Between 1600 and 1700 °C, the cubic structure underwent significant structural changes, which induced a rapid increase in densification.

Similar investigations were reported in another publication (Réau, Tenegal, & Galy, 2011). The powder synthesis, however, had been conducted in a different way using laser pyrolysis (Réau, Guizard, Canel, Galy, & Tenegal, 2012). The isostatically pressed specimens were heated in the FAST apparatus rapidly (100 K min^{-1} to 1750 °C, followed by 50 K min^{-1} to 1850 °C) at pressures of 130 MPa. The maximum sintering temperature (1850 °C) was shortly held (2 min). The corresponding sintered specimens reached relative densities up to 97% with average grain size of 46 nm.

2.04.4.2.4 Solid-State Sintered Silicon Carbide

The invention of the pressureless sintering for consolidating SiC powders into ceramics exhibiting closed porosity by Svante Prochazka can be regarded as one of the greatest steps forward for the processing of SiC-based ceramics (Prochazka 1973, 1977a, 1977b, 1981). Furthermore, pressureless sintered SiC by itself was considered to be one of the milestones within the field of the structural ceramics since it had opened areas of applications only occupied by metallic materials up to then.

Just like other covalently bonded pulverulent materials, submicron SiC powders cannot be sinter densified without any special aids. One reason is certainly the relatively low volume and grain boundary self-diffusion of Si and C atoms. Another one is the gas-phase relations (evaporation–condensation mechanism) which either compete with the sinter densification or even exclude it (Kriegesmann, 1988). For solid-state sintered SiC (SSiC) basically two sintering aids are needed (Prochazka, 1973). Usually about 1 wt.% boron and 1 wt.% carbon are added to the submicron-sized SiC powders exhibiting specific surface areas of at least 10 $\mathrm{m}^2\,\mathrm{g}^{-1}$. Boron might be present in elementary form or as a compound like boron carbide (B_4C), boron nitride (BN), boron phosphide (BP), aluminum tetraboride (AlB_4) and silicon borides (SiB_4 or SiB_6), respectively. Carbon can be introduced into the powder mixture as carbon black or as an organic component with high carbon content such as phenolic resin or novolak. Graphite has proved to be unfavorable because of insufficient homogenization ability.

In the literature there is a large number of partly controversial proposals concerning the sintering mechanism of SSiC (Telle, 1994), which we will not elaborate on here. Diffusional motions are difficult to comprehend in covalent solids, since point defects in these materials are not well investigated in literature. Even an LPS mechanism cannot be fully excluded for SSiC doped with boron. On the other hand, the solubility of boron is high in the lattices of SiC polytypes (Tajima & Kingery, 1982), pointing out the assumption of the solid-state sintering as probable. It is assumed that boron atoms occupy both Si- and B-lattice sites (Prochazka, 1989).

Carbon acts as deoxidization and desiliconization agent by removing both the inherent silica layer on the SiC particles and the elementary silicon (Prochazka & Scalan, 1975). Through the removal of the silica layer the competing shrinking-free evaporation–condensation mechanism is prevented (Kriegesmann 1988; Kriegesmann & Jodlauk, 2002). A higher amount of finely dispersed carbon in SSiC prevents grain growth and thus increases the strength (Seshadri, Srinivason, & Chia, 1989).

Boron and its compounds can be replaced by other efficient sintering aids. Among them, aluminum should be underlined (Böcker, Landfermann, & Hausner, 1979; Schwetz & Lipp 1980a, 1980b; Tanaka, Inomata, Hara, & Hasegawa, 1985), added in elementary form and as a compound like aluminum oxide (Al_2O_3) (Suzuki, 1986), aluminum nitride (AlN), aluminum carbide (Al_4C_3), aluminum diboride (AlB_2), aluminum phosphide (AlP) and aluminum silicon carbide (Al_4SiC_4). Additional sintering aids like gallium (Ga) (Papenburg, Goetz, & Kriegesmann, 1990) and Beryllium (Be) or its compounds (Smoak, 1979) cannot be recommended for industrial use because of cost efficiency reasons and physiological harmfulness.

The starting powder might be either cubic β-type (Prochazka, 1973) or predominantly hexagonal α-type SiC (Coppola & McMurtry, 1976; Coppola, Hailey, & McMurtry, 1979; Coppola, Hailey, & McMurtry, 1982). In general, submicron-sized powders (<1 μm) are used for commercial production.

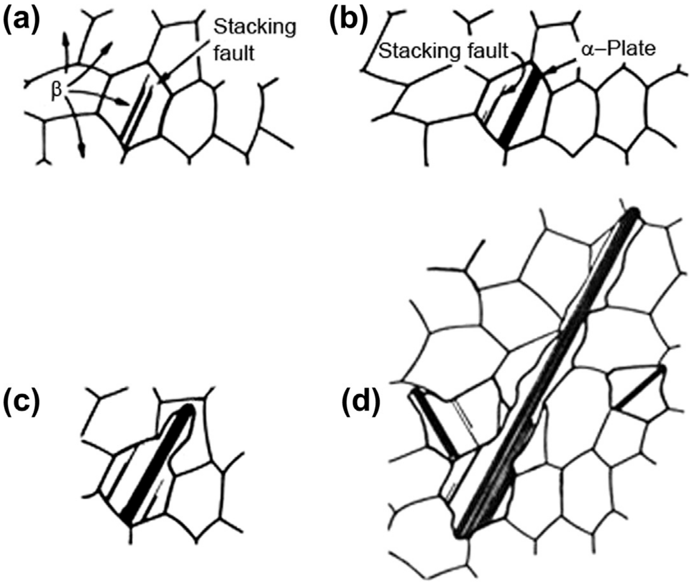

Figure 25 Schematic sequential microstructural development of fine-grained sintered β-SiC. (a) Stacking faults in a β-SiC crystal. (b) Formation of an α-plate (lamella) within a β-SiC crystal. (c) Extension of the α-plate beyond the initial β-SiC crystal. (d) Further elongation of the α-plate. Reproduced with kind permission of Springer Science + Business Media.

If the starting powder mixture contains β-SiC and a small amount of boron as a sintering aid (besides carbon), a globular fine-grained microstructure of β-crystals (3C polytype) is built up, after the sintering has been started. Some β-crystals get partly disordered containing stacking faults, which are nuclei for α-crystallites forming 4H, 6H or 15R polytype lamellae at temperatures above 1900 °C. The polytype lamellae first develop in the confines of the initial β-grains (Shinozaki & Kinsman, 1978). For the polytype evolution during the sintering process it should be noted that grain boundaries between the β-grains are normal, i.e. incoherent grain boundaries with a relatively high-specific interfacial energy. On the other hand the interfaces between the β-phase and the newly formed α-regions within a grain are coherent to each other with comparatively low specific interfacial energy. For an ordinary fine-grained ceramic with only normal grain boundaries a rise in sintering temperature usually induces the grains to grow. However, if there are both high-energetic incoherent and competing low-energetic coherent interfaces within a microstructure of a ceramic, the driving force of sintering will mainly effect the growth of the coherent interfaces for energetic reasons (Kriegesmann, 2005a). In Figure 25, the sequential microstructural change of fine-grained sintered β-SiC with rising temperature is shown schematically (Shinozaki & Kinsman, 1978). The α-lamellae extend beyond the initial β-grains, but since the α/β crystallographic relationships should kept fixed during lamella growth, the lamella edge (i.e. coherent interface) elongates accompanied by the local adjustment of adjacent β-phase to its original orientation.

The complex polytypic transformations for β-SiC starting powder with boron addition are shown in Figure 26 (Williams, Juterbock, Peters, & Whalen, 1984). The further nucleation of polytypes induced through the alteration of stacking sequences forms packets of plates of the same orientation. Thus the α-polytypes do not remain stable, parts of them experiencing lengthwise transformation to thin “feather” crystals of different polytypes.

The substitution of boron through aluminum as a sintering aid for β-SiC starting powders is in principle possible, but high densification has been found difficult to achieve, this being strongly dependent on the sintering conditions (Stutz, Prochazka, & Lorenz, 1985). During sintering huge plate-like crystals grow leaving large pores behind. β-SiC is completely transforming to 4H-polytype during the sintering process.

A combined doping of boron and aluminum is resulted in a better sintering activity than the simple boron doping (Stutz, Prochazka, & Lorenz, 1985). However, the improved sintering behavior is accompanied by an even stronger tendency to polytypic transformation. That means that a combined Al/B-addition seems to increase the mass transport during sintering. This can be attributed to a transient liquid phase in the system SiC–Al_4C_3–B_4C (Inomata, Tanaka, Inoue, & Kawabata, 1980). On the other hand, Stutz et al. (1985) could

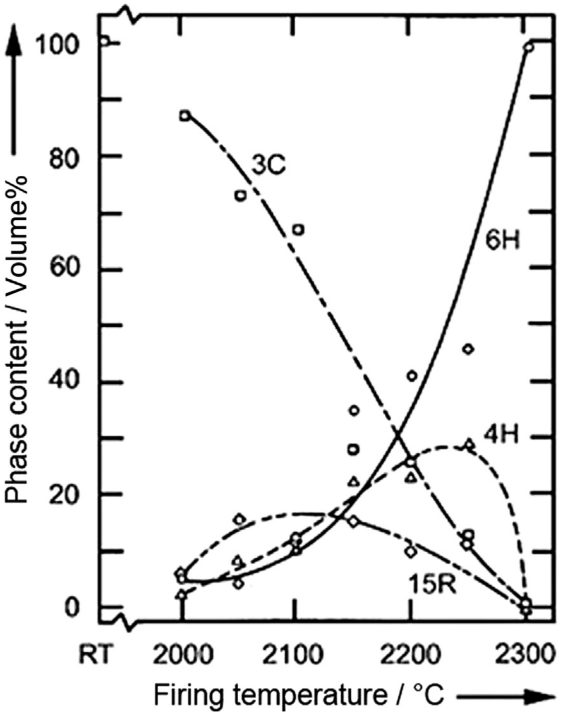

Figure 26 Change of polytype composition with temperature for a boron-doped β-SiC powder (doped with 0.6 wt.% B and 2.8 wt.% C). Reproduced with kind permission of John Wiley & Sons Ltd.

demonstrate that the polytype transformation rate and thus the tendency of exaggerated grain growth can be reduced considerably for such combined Al/B-doped β-SiC powder batches if an additional holding time just below polytype transformation temperature is introduced in the sintering process. The somehow lower sinter activity can be compensated through a slight increase in the maximum sintering temperature.

It should be noted that a distinctive polytypic behavior must not simply be regarded to be quality degrading, especially for some mechanical properties like wear. The polytypes differ from each other only in their stacking sequences but not in their densities, so that no residual stresses on coherent or incoherent interfaces can develop through the polytype transformation. On the other hand the polytype transformation is generally connected with exaggerated grain growth, which induces a strength loss through the grain size effect. Additionally the pores are trapped by the growing grains. These intragranular pores, which cannot be closed during sintering, reduce the load-bearing cross-section of the ceramic and thus cause further strength loss.

For SSiC ceramics obtained from β-SiC powders it can be concluded that it has been demonstrated that the polytype forming induced grain growth effects can be reduced through processing means (Stutz, Prochazka, & Lorenz, 1985). On the other hand slightest changes in the composition can negatively affect the sintering behavior. Thus the microstructures can hardly be controlled.

If α-SiC is used as the starting powder, polytype transformations can occur as well, but the transformation kinetics are much easier to assess. The grain morphology is determined by the B/C relation (Böcker & Hausner, 1978). Uniform microstructure with globular grains was confirmed for a maximum sintering temperature of 2060 °C, if the B/C relation was 0.125. For the same sintering temperature, a B/C relation of 0.33 resulted in a microstructure with faceted plates of nonuniform size. The increase of the relation to 0.8 is connected with a strong growing of the plates of the 6H polytype (>100 μm). Above 2100 °C exaggerated grain growth generally occurs, which can be stabilized with an adjusted amount of boron (Prochazka 1981). The original content relationship of the polytypes 6H and 4H gradually will reverse above 2200 °C according to Figure 27 (Williams, Juterbock, Peters, & Whalen, 1984). Since the maximum firing temperatures for SSiC are hardly above 2100 °C, these polytype changes should not be relevant in industrial practice. Figure 28 shows an etched microstructure of a commercial SSiC manufactured from boron- and carbon-doped α-SiC powder. The crystals are globular or moderately elongated. Some of them indicate a beginning polytypic transformation, recognized by the straight coherent interface boundaries.

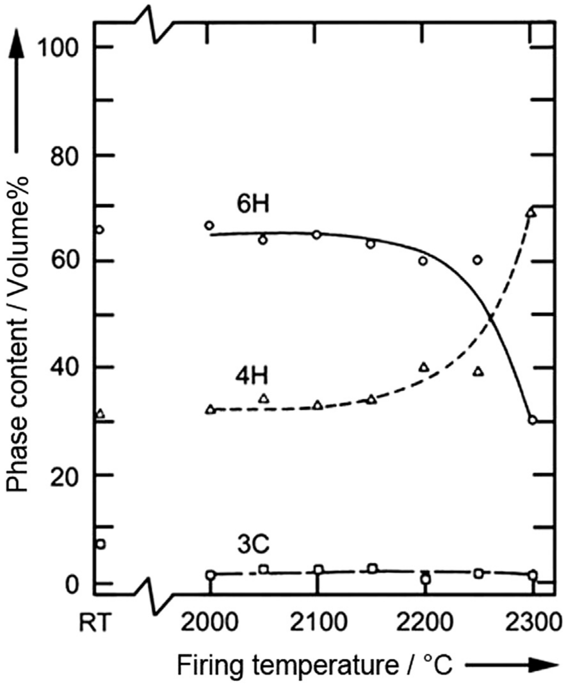

Figure 27 Change of polytype composition with temperature for a boron-doped α-SiC powder (doped with 0.6 wt.% B and 2.8 wt.% C). Reproduced with kind permission from John Wiley & Sons Ltd.

It can be concluded that solid-state sintering of submicron-sized SiC powders with appropriate additives results in dense, i.e. closed pores containing shaped ceramics with relative densities of 95–98% of theoretical density. The room temperature bending strength matches values up to 430 MPa, which is lower of course than the bending strength of optimized HPSiC or HIPSiC grades because of the lower relative density of SSiC (Table 5).

Higher densifications should be possible when even finer SiC powders are used. Datta, Bandyopadhyay and Chaudhuri (2002) achieved relative densities of nearly 99% by pressureless sintering of attrition milled and chemically treated nanosized α-SiC powders doped with B_4C (0.5 wt.%) and carbon (0.5 wt.%) at 2050 °C. The sintered bodies had an average grain size of 5.7 μm, thus they may not longer be described as nanoceramics.

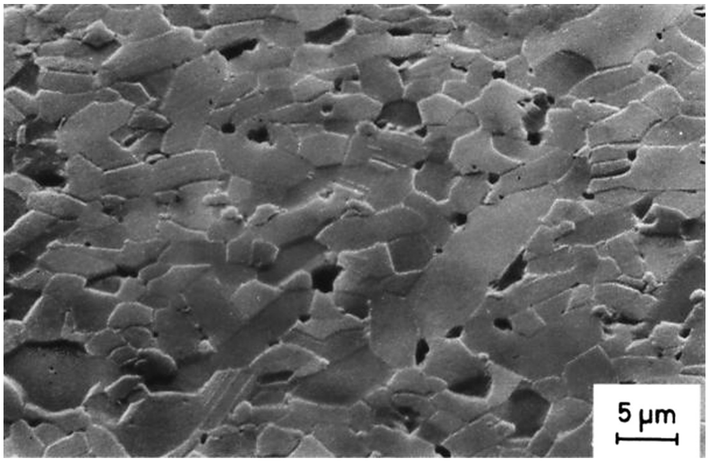

Figure 28 Microstructure of commercial SSiC (polished SEM microsection, etched with Murakami solution). This photo was kindly transmitted from ESK Ceramics GmbH & Co KG, Kempten, Germany.

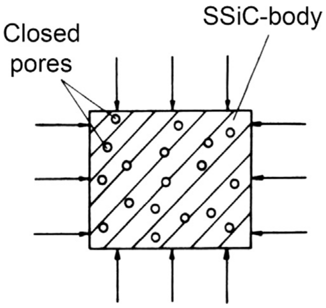

Figure 29 Principle of pressure transfer on SSiC body to generate HIPSSiC.

2.04.4.2.5 Hot Isostatic Pressed Solid-State Sintered Silicon Carbide

SSiC with closed pores can be further densified to more than 99% of the theoretical density through subsequent HIP. The main advantage of this hot isostatic pressed solid-state sintered silicon carbide (HIPSSiC) over the directly powder-HIPed HIPSiC (Figure 23) is the omission of vacuum-tight casings (Figure 29). In order to achieve an additional densification through HIP it is necessary that the presintered body (SSiC) has sufficient residual sintering activity (Hunold, 1984/1985), i.e. the presintered body should still have a sufficiently fine-grained microstructure.

Early HIP systems only permitted high gas pressures. Thus sintering and subsequent HIP could only be realized step-by-step in two different firing aggregates. Modern HIP systems can operate in a wide range of applied gas pressures, from vacuum to HIP conditions. Using these systems, it is possible to carry out sintering and HIP in a single firing aggregate and thus in a single cycle (Hunold, 1984/1985; Oberacker, Kühne, & Thümmler, 1987; Oberacker, Thümmler, & Fetahagic, 2001). The main temperature and pressure characteristics of the two system variants are shown in Figure 30, respectively.

It should be noted that generally the sintering temperature is higher than the HIP temperature. If both temperatures are in the same range, the holding time of the complete sintering process will be prolonged to presintering. As a consequence, grain growth and strength lessening are induced. The reduction of

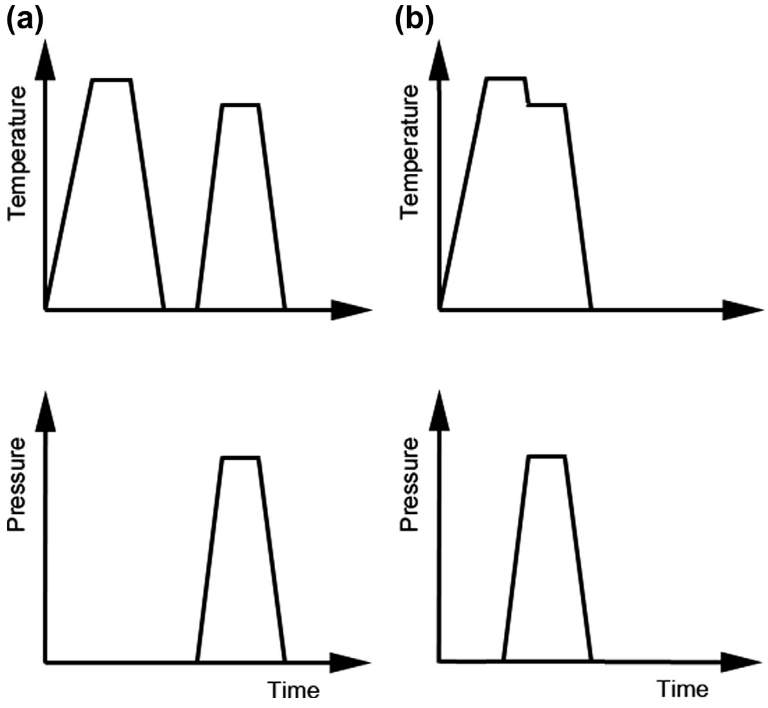

Figure 30 System variants of HIPS: (a) sintering and HIP and (b) sinter-HIP.

HIP temperature decreases the effect of holding time prolongation and thus keeps the microstructure widely stable.

The gas pressure sintering (GPS) is similar to post-HIP technique; hence, temperature and pressure characteristics are also represented by Figure 30(b). The real difference between the two techniques is the value of applied pressure during sintering. Whereas HIPing is conducted at gas pressures of at least 100 MPa, GPS only requires pressures up to 10 MPa. The pressure transferring medium in GPS units is generally nitrogen. Often different reasons for using the respective techniques are given: post-HIP is usually applied for closing the pores of a material, whereas GPS shall inhibit a potential decomposition tendency of a material by shifting the balance of the decomposition reaction to the solid. Through GPS the maximum sintering temperature can be raised with low risk of decomposition. The GPS technique was first applied for the sintering of silicon nitride (→ GPSSN) (Greskovich & Palm, 1980), since Si_3N_4 decomposes at elevated temperatures. GPS technique has sometimes been applied successfully for obtaining liquid-phase sintered SiC (LPS-SiC) ceramics, as it will be seen later.

It has been demonstrated that via additional HIP it is possible to obtain almost fully dense SSiC. Both SiC ceramic variants, SSiC and HIPSSiC, generally show a transgranular fracture mode (see above); and as a consequence, they exhibit stable bending strength up to about 1400 °C. However, the transgranular fracture mode also involves a severe disadvantage as it is fairly smooth, indicating a fast crack propagation character. It can be inferred from this that both SiC ceramics should be extremely brittle. In fact the fracture toughness of SSiC measured using the bridge method (sharp crack) reached values of only 2.2–2.5 MPa $m^{0.5}$ (Schwetz, Sigl, & Pfau, 1997). It can even be argued that SSiC (including HIPSSiC) is one of the most brittle ceramics at all.

2.04.4.2.6 Liquid-Phase Sintered Silicon Carbide

Following the above ideas, it was clear that advances in technical progress of SiC-based ceramics should be aimed to attaining tougher materials exhibiting intergranular fracture as well as to achieve fully dense ceramics through a single pressureless or at most low-pressure-assisted firing technique. The basic idea for recreating SiC ceramics was borrowed from the process engineering of silicon nitride (Si_3N_4) ceramics (Riley, 2004), where yttria (Y_2O_3) containing amorphous or semicrystalline silicates induce LPS. Two reasons can be given for the rather late evolution of LPS-SiC. The first one was the success of SSiC, which had created possibilities for new applications and markets. The second one had been processing problems concerning decomposition effects of the compositions, which had to be overcome or at least had to be reduced first. In spite of the difficult start (Omori & Takei, 1982) it had been recognized relatively early that the microstructures of LPS-SiC carbide can be influenced through a wide range of actions (Padture, 1994; Padture & Lawn, 1994), so that many approaches could be attempted. Today we can already say that LPS-SiC ceramics are the most widely studied SiC-based ceramics at all.

In order to render comprehensible the liquid sintering mechanisms of LPS-SiC and its material variants let us focus on some theoretical aspects of the solution-reprecipitation mechanism, which is decisive for the medium stage of LPS. Figure 31 outlines the basic principle of solution reprecipitation represented by a two-particle model. When two solid particles are surrounded by a liquid (melt), one of them (with higher surface energy) will be dissolved in the liquid starting from its surface. The dissolved material is then moved via an atomic mass transport (diffusion) to the surface of the other (seed) particle (with lower surface energy). Thus,

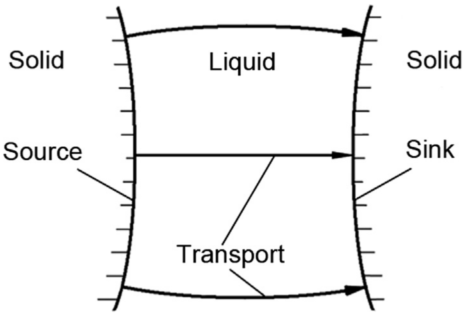

Figure 31 Basic principle of solution reprecipitation mechanism.

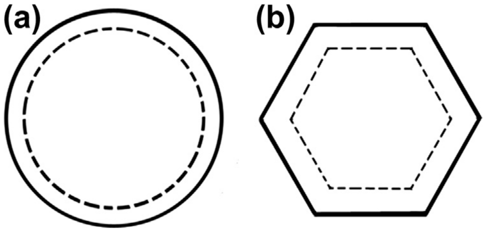

Figure 32 Xenomorhic (a) and idiomorphic (b) growth of crystals.

the surface of one particle is the source and the surface of the other particle is the sink for the mass transport. The solution reprecipitation process consists of three time dependent steps: solution, transport and reprecipitation. Let us just consider the relation between transport and reprecipitation. First, we presume that the solution is the fastest of the three steps. Under this assumption, if the rate controlled step is the mass transport, relatively few species get to the sink surface of the seed; hence, the species are immediately reprecipitated with the result that the crystal growth will be in a xenomorphic (globular and equiaxed) way. If on the other hand the reprecipitation is rate controlled, there are always enough species around the seed with the result that the crystal will grow idiomorphically (Figure 32).

Considering both the dissolving and the reprecipitated solid phases, there might be two different options for solution reprecipitation according to Table 4 (Kriegesmann, 2005b). If the dissolving phase and the reprecipitated one are identical, the solution reprecipitation can be regarded as homogeneous. Otherwise, if the dissolving and the reprecipitated phases are different, we can describe it as heterogeneous solution reprecipitation.

For the principle of the homogeneous solution reprecipitation, described again using two-particle models, two borderline cases are the Ostwald ripening (Ostwald, 1900) and the Kingery mechanism, respectively (Kingery, 1959). The precondition for both models is that the contact angle is low and the dihedral angle is zero so that the wetting of the liquid phase is complete (German, 1996).

The basic concept of Ostwald ripening (Figure 33a) is that the solubility of a particle in its surrounded melt varies inversely with its grain size. Small particles have a higher energy and thus a higher solubility than large ones because of their stronger curvature. The difference in solubilities implicates a concentration gradient in the

Table 4 Solid phases of the solution reprecipitation mechanism versions

Procedure	*Dissolving phase*	*Reprecipitated phase*
Homogeneous	α	α
Heterogeneous	α	β

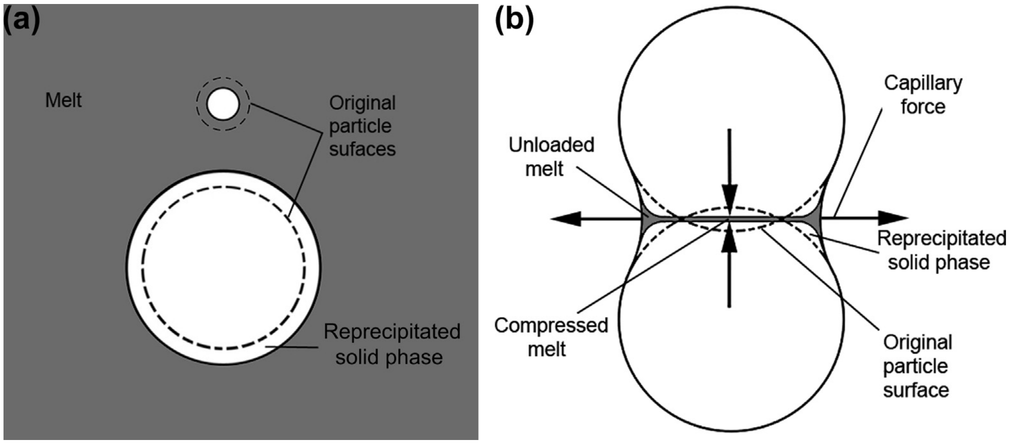

Figure 33 Mechanisms of homogeneous solution reprecipitation for liquid-phase sintering: (a) Ostwald ripening. (b) Kingery mechanism. The copyright of image (b) is held by the author of this article.

melt, and the concentration balance can be achieved through the material transport from the small particles to the large ones by viscosity dependent diffusion through the melt. Through this mass transfer the melt in the vicinity of the large particles will be supersaturated. The result is the advancing growth of larger particles at the expense of the smaller ones giving fewer particles with a larger average grain size. This "pure" Ostwald ripening model presupposes a high amount of melt, so that the particles are relatively far apart from each other, thus no grain shape accommodation will occur. The large amount of melt is the reason that this solution reprecipitation itself will not supply any contribution to densification, since fully density can already be achieved beforehand in the initial stage of sintering by rearrangement.

If the particles have the same size, there is no energy difference between them and thus no reason for any sintering effect providing that the amount of melt remains high. If the melt content, however, is reduced, the situation might be modified. The capillary forces give rise to the particles attraction (but because of the zero dihedral angle they will never contact each other directly). At locations where the particles come closer together a compression zone is formed in the melt, which causes a higher solubility there. Consequently local dissolution results in both grain shape accommodation (contact flattening) and excess of dissolved species in the compressed zone. The corresponding concentration gradient will be compensated through the diffusive mass transport from the compressed melt zone to the unloaded area in the melt, where the solubility limit might be exceeded. Due to this supersaturation the reprecipitation occurs on the particle surface adjacent to the unloaded areas. The principle of the Kingery mechanism according to a two-particle model is shown in **Figure 33**(b) (Kriegesmann, 2007). Through grain shape accommodation this Kingery approach supplies a particular contribution to densification as it implies that sintering occurs without any grain growth.

In general ceramic powders have a relatively wide range of grain size distributions (usual size range over one order of magnitude) and the amount of melt being generated during the sintering process should be low with respect of the properties of the corresponding designed ceramic. In this supposed case, the quantity of melt is not sufficient enough to fill all pore space if the particles remain spherical (exhibiting minimum energy) during sintering. However, the solution reprecipitation permits the growing solid particles to deviate from the spherical shape to fill space better. For a given grain volume, a sphere has a lower surface area than the adjusted grain shape, but the elimination of pores and the corresponding surface energy provides the net energy decrease. The corresponding more practical sintering model is termed "shape accommodated Ostwald ripening" (Kayser, Žyskovič, & Petzow, 1985). It combines the typical characteristics of both models like grain shape accommodation, grain growth and densification, and thus can be regarded as a combination of Ostwald ripening and Kingery model.

In the mechanisms described so far the reprecipitation of the solid phase occurs on undissolved particles of the starting material. However, if the particles of the starting phase transform before the sintering is concluded, the reprecipitation cannot occur on preexisting particles but rather crystal nuclei of transformed phase (thermodynamically stable) will develop which then will grow further.

The original powder particles will simultaneously be downsized and will finally disappear provided that the holding or annealing times are sufficiently long. Both described solution reprecipitation versions can be regarded as heterogeneous. Modeling approaches for them can be proposed according to Ostwald ripening, Kingery mechanism and shape accommodated Ostwald ripening, respectively. **Figure 34** shows a Kingery approach for the heterogeneous solution reprecipitation.

It should be noted that systems with high-temperature stable phases may show also homogeneous solution reprecipitation, when the liquid sintering starts before the transformation temperature is reached. In this case no phase transformation will occur of course if the transformation temperature is not crossed during the sintering experiment. But if the transformation temperature is exceeded in the later period of the sintering experiment, the heterogeneous solution reprecipitation will initiate. Let us suppose that the homogeneous solution reprecipitation causes xenomorphic crystal growth and the heterogeneous solution reprecipitation induces idiomorphic grain formation, respectively. This gives rise to a bimodal grain size distribution first. But since those low-temperature phase crystals, which had been grown through homogeneous reprecipitation, might be dissolved again through later occurring heterogeneous solution reprecipitation, the corresponding microstructure will have only idiomorphic crystals provided that the heterogeneous solution reprecipitation had been concluded in this sintering experiment.

The heterogeneous solution reprecipitation has been first discovered in ceramics from the sintering behavior of dense silicon nitride (Ziegler, Heinrich, & Wötting, 1987). During the sintering of silicon nitride the low-temperature modification α-Si_3N_4 is dissolved in the silicate melt and reprecipitated as β-Si_3N_4 nuclei, which grow as idiomorphic needle-shaped crystals with a high aspect ratio. Following the ideas commented on

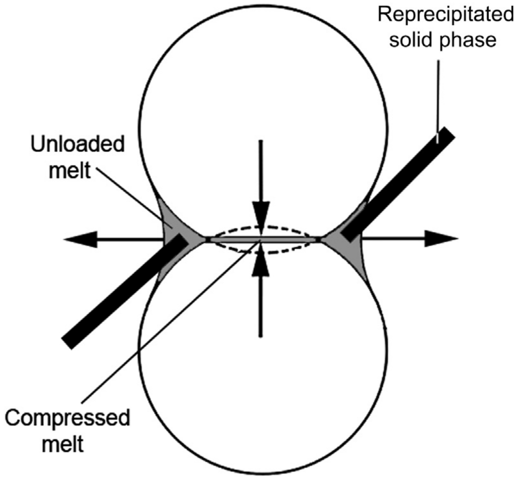

Figure 34 Kingery mechanism of heterogeneous solution reprecipitation for liquid-phase sintering. The copyright of this image is held by the author of this article.

Figure 32, crystal growth is rate controlled here. The modification β-Si_3N_4 is stable at sintering temperatures. These grown crystals can be regarded as in situ generated whiskers, which are largely responsible for the high toughness and the high strength of silicon nitride ceramics. If on the other hand the starting powder contains only β-Si_3N_4 particles besides the sintering additives, the solution reprecipitation will run in a homogeneous way, which only results in a microstructure exhibiting globular β-Si_3N_4 crystals (Lange, 1978) because of a rate-controlled diffusion in the melt. As a result, the corresponding mechanical properties would be worse. Thus it is typical for sintered silicon nitride that a beneficial product may only be achieved if the sintering is run via a heterogeneous solution reprecipitation mechanism.

Up to now, it has been assumed that the starting powder contains only particles of one phase (apart from the sintering additives). Now let us assume a third case when the starting powder contains particles of both modifications. The particles consisting of a high-temperature stable phase are indicated as seed crystals. Although both kinds of particles will make their contributions to the sintering of the corresponding bodies, the microstructure to be developed during the sintering process will be the result of the corresponding energy balance. The particles consisting of the low-temperature phase will preferentially dissolve in the melt at sintering temperatures provided their grains are fine enough. The reprecipitation will mainly occur on the preexisting seed crystals. Thus if the number of seed crystals in the starting powders is small, mainly few crystals will grow up to an enormous grain size, inhibited only through mutual growth of crystals. Since it will take some time, until all low-temperature stable phase particles are dissolved completely, the microstructural evolution is normally characterized through a bimodel grain size distribution with a matrix of small low temperature stable particles containing elongated large crystals of the high-temperature stable phase. Since the phases of the dissolving and the reprecipitated crystals differ from each other, this kind of solution reprecipitation must be regarded as a heterogeneous solution reprecipitation as well.

After this excursion on the general theory of LPS let us go back to the LPS-SiC again. Compared to SSiC, which must be sintered at least at about 2050 °C, the sintering temperature of LPS-SiC is lower (usually 1850–2000 °C) (Cutler & Jackson, 1989; Mulla & Krstic, 1991) which results in an almost fully dense microstructure with smaller grain sizes (average grain sizes <1 μm are possible) provided α-SiC powder is used as a raw material. The corresponding room temperature bending strength of such LPS-SiC is much higher than that of SSiC.

First successful approaches of LPS-SiC were presented by Omori and Takei (1982, 1985, 1986), who sintered β-SiC powders containing oxide additions or corresponding precursors. The choice of the sintering aids, however, had been purely empirical at the time of those investigations (Izhevskyi, Genova, Bressani, & Bressani 2000a, 2000b). A serious problem with using oxide mixtures as sintering additives for SiC is the fact that chemical interactions may occur during sintering, resulting in gaseous species formation which may cause tremendous weight losses in the bodies and thus a composition alteration during the firing. A thermodynamic analysis (Negita, 1986) demonstrated that only few oxides do not decompose SiC during the sintering process.

The situation is further aggravated through the silica layer adhering to each SiC powder particle. Generally alumina (Al_2O_3), yttria (Y_2O_3) and combinations of the two oxides like yttria alumina garnet (YAG, $Y_3Al_5O_{12}$) and some rare-earth oxides combined usually with alumina have proved to be effective oxide additives for LPS-SiC (Böcker & Hamminger, 1991; Cordery, Niesz, & Shanefield, 1990; Cutler & Jackson, 1989; Cutler, Virkar, & Hurford, 1989; Kim & Kim, 1995; Kostic, 1988; Martin & Adler, 2002; Mulla & Krstic, 1994; She & Ueno, 1999; van Dijen & Mayer, 1996; Wolf, Hübner, & Adler, 1993). The oxides react with the silica, which is always present on each SiC particle of the starting powder, to form a silicate melt and enhance densification. If the amount of silica on the surface of SiC starting powder particles is too low, some SiO_2 should be added in the form of highly dispersed silica (fused or fumed silica and aerosol).

The oxide-doped LPS-SiC ceramics should be sintered using either GPS (about 10 MPa argon pressure) or a powder bed (Figure 35). If these conditions are not satisfied, volatile and gaseous reaction products are formed through the reaction of SiC with the oxides. For instance the following redox reactions occur at temperatures lower than the sintering ones for the usually applied additives of the system Al_2O_3–Y_2O_3(SiO_2) if such gas preventive precautions are omitted (Grande, Sommerset, Hagen, Wiik, & Einarsrud, 1997; Mulla & Krstic, 1991).

$$SiO_2 + SiC \leftrightarrow 3SiO\uparrow + CO\uparrow \tag{7}$$

$$Al_2O_3 + SiC \leftrightarrow Al_2O\uparrow + SiO\uparrow + CO\uparrow \tag{8}$$

Early research activities of LPS-SiC were focused on starting compositions containing conventional Acheson α-SiC process powders (Section 2.04.3) (Chia & Lau, 1991; Cutler & Jackson, 1989; Padture & Lawn, 1994; She & Ueno, 1999; Sigl & Kleebe, 1993) because α-SiC is the most stable form of SiC at high temperatures and results in fine globular microstructures.

Sigl and Kleebe (1993) were the first authors to investigate detailed facts on solution reprecipitation for LPS-SiC. They used α-SiC as starting powder doped with YAG and sintered it at 1950 °C. Figure 36 shows a polished, plasma etched microsection of corresponding sintered specimen. A rim/core structure is visible, the corresponding interface being emphasized by the little arrows inserted into the image. The cores represent former coarse particles of the starting powder. The rim can be regarded as the reprecipitated SiC. The authors suggest Ostwald ripening by solution and reprecipitation. Strictly speaking, it should rather be regarded as a

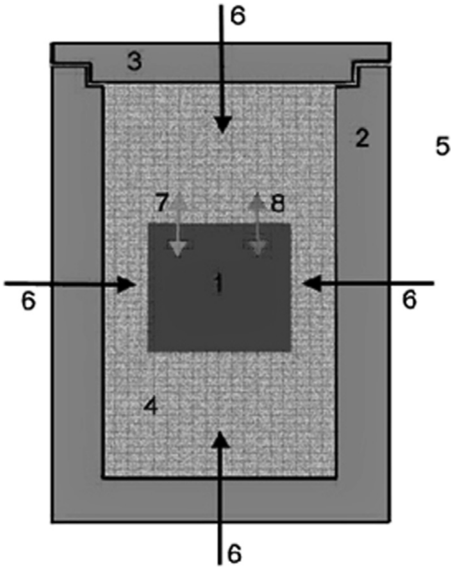

Figure 35 Sintering of LPS-SiC using powder bed. 1, specimen; 2, porous graphite crucible; 3, graphite cover; 4, powder bed consisting of SiC powder, coarse graphite or BN grains, sintering additives; 5, kiln chamber; 6, kiln gas atmosphere penetrating into the crucible; 7, decomposition and formation of SiC; 8, decomposition and formation of sintering additives. The copyright of this image is held by the author of this article.

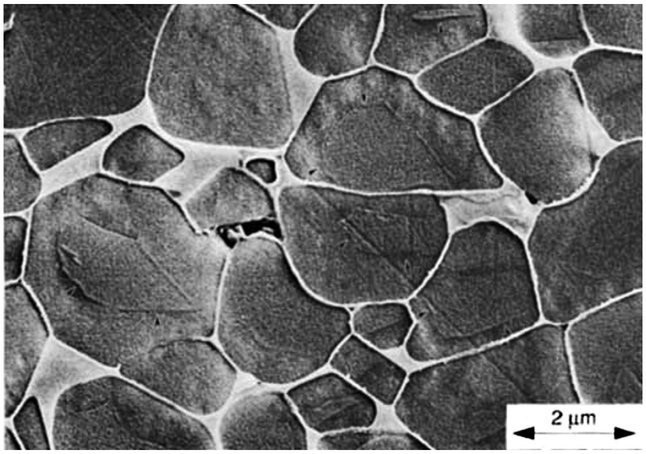

Figure 36 Microstructure of LPS-SiC doped with 10 vol.% YAG (polished SEM microsection, plasma etched). Reproduced with kind permission of John Wiley & Sons Ltd.

shape accommodated Ostwald ripening instead. There is a slight shift in the polytype composition in relation to the starting powder. However, it can be supposed that the corresponding faint polytype transformation is not affected by LPS. Thus, it can be deduced that the sintering behavior had been a homogeneous solution reprecipitation. Consequently, core and associated rim consists of the same polytypes (mainly 6H). Since during the sintering process a rim is built up through reprecipitation of atoms on the lattice of a starting grain (core), there should not be any grain boundary between core and rim. However, the authors supposed a coherent interface boundary between core and rim which cannot be considered conceivable because both structural constituents exhibit identical crystal structures. The different etching behavior of core and rim in the polished specimens can be explained only by the slight difference in the chemical composition, respectively, since the core is pure SiC and the rim contains traces of yttrium, aluminum and oxygen. The major crystalline secondary phase is YAG. Also, an amorphous intergranular film had been found.

The fracture toughness, however, could not be enhanced by employing "pure" α-SiC powders (at this stage of LPS-SiC research, see below). From previous studies on SSiC manufactured from β-SiC starting powders (Prochazka, 1973), it was known that β-SiC (3C polytype) transforms to α-polytypes near 1900 °C (**Figure 25**) generating flat platelets (**Figure 9**). Padture (1994) replaced the α-SiC starting powder mainly or completely through β-SiC powder, used Al_2O_3 and Y_2O_3 as sintering additives and sintered the corresponding shaped bodies at 1900 °C for 0.5 h and then annealed some selected specimens at 2000 °C for several hours. Whereas the only sintered specimens showed no significant polytype change after sintering, the additional annealing stage induced the microstructure during the sintering to develop a time-dependent $\beta \rightarrow \alpha$ transformation in accordance with the heterogeneous solution reprecipitation. The corresponding microstructures showed α-SiC platelets embedded in a YAG-matrix having a significant thermal expansion mismatch with SiC. The specimens had a distinctly improved toughness. These findings of Padture (1994) and the comparable results almost simultaneously published by a South Korean working group (Lee & Kim, 1994; Lee, Kim, & Kim, 1994) mark the beginning of a second generation of LPS-SiC ceramics.

The annealed LPS-SiC ceramics manufactured from β-SiC rich powders can be regarded as in situ platelet-reinforced materials, since the reinforcing particles are synthesized within the matrix during fabrication of the ceramics. This is in contrast to the common ex situ reinforced ceramics, where the reinforcing particles (whiskers, platelets or fibers) are synthesized separately and then inserted into a matrix during a secondary process. The ex situ reinforcement will be mentioned hereafter in this subsection but will be treated more comprehensively in the next subsection. The advantage of the in situ reinforcement is a simplification of the manufacturing technology.

Padture (1994) believed that α-SiC grains only grow form preexisting α-SiC seeds, though he got specimens with analog microstructure, when he had used "pure" β-SiC starting powder. He presumed that his β-SiC powder contained traces of α-SiC, which also were able to grow. Kim, Mitomo, Emoto and Lee (1998), however, found that the presence of β-SiC in the starting powder results in a formation of idiomorphic (anisotropic) α-SiC crystals during the annealing period of the sintering experiments even if α-SiC was absent. The average diameter of the idiomorphic crystals decreased with increasing α-SiC content. The maximum aspect ratio was achieved at 10% α-SiC and decreased with further increasing α-SiC in the starting material. Bending strength and fracture toughness of the sintered and additionally annealed specimens versus the α-SiC content in the starting powder showed opposite progressions: the highest bending strength value (477 MPa) was achieved for specimens manufactured from "pure" α-SiC powder and the optimum fracture toughness (6.8 MN $m^{0.5}$) was obtained when a "pure" β-SiC powder had been used.

The type of firing atmosphere has a strong influence on the evolution of LPS-SiC with oxide aids. The nitrogen atoms will be dissolved in the silicate melt during sintering: each introduced nitrogen atom connects three silicon atoms (instead of two in case of oxygen) (Schrimpf & Frischat, 1982), which generates a more tightly linked atomic network. Nitrogen increases the viscosity of the melt and thus reduces the atomic transport mechanisms. On the other hand, an argon atmosphere will not penetrate into the melt and thus will not alter it. According to the remarks given regarding Figure 32, this means that the nitrogen atmosphere should tend to shift the microstructure evolution to fine grained, xenomorphic crystals, whereas with argon atmosphere a tendency of microstructure evolution exhibiting idiomorphic grain structure is favored. Figure 37 shows two micrographs of LPS-SiC bodies manufactured from β-SiC powder with the additive system Al_2O_3–Y_2O_3 (Ortiz, Muñoz-Bernabé, Borrero-López, 2004). Both bodies had the same starting compositions, and the same processing procedures were used including firing temperature (1950 °C) and holding time (1 h) (Ortiz, Bhatia, Padture, & Pezzotti, 2002; Xu et al., 2001). The only difference had been the sintering atmosphere. The specimen of Figure 37(a) was sintered in nitrogen and the specimen of Figure 37(b) was sintered in argon. The comparison of the two micrographs demonstrate at the first glance, that the basis of the foregoing considerations of the author of this article seem to be sensible, since the nitrogen atmosphere favors a more globular microstructure whereas argon atmosphere promotes a microstructure with elongated grains. However, this interpretation of the atmospheric influence on the evolution of microstructure of LPS-SiC might probably be too simple, because this explanation model has not been found in literature yet.

Comparable results were obtained by Jun, Lee, Kim, Song, and Kim (2008) who investigated the role of sintering atmospheres on the microstructure evolution and the corresponding strength properties. They could confirm that nitrogen retards β → α phase transformation and formation of idiomorphic SiC crystals. Additionally they demonstrated that AlN addition to the sintering aids aims to the same effects on the microstructural evolution.

This leads us to another class of remarkable LPS-SiC ceramics, which are sintered by using an AlN–Al_2O_3 additive system. It should be noted that further material variants of LPS-SiC ceramics manufactured with oxide additive systems are to be discussed further below, since the full potential of this approach has not been demonstrated up to now in this article.

The suitability of the alternative additive system AlN–Y_2O_3 was first shown by Nader (1995) and by Chia, Boecker, and Storm (1994) independently of each other. AlN–Y_2O_3 additives for LPS-SiC proved to be superior to oxide additives systems in terms of mass loss and reproducibility of sintering behavior. In addition, it was demonstrated that the processing technique may run well without applying the laborious powder bed technique. Through the addition of a nitride component the corresponding silicate melt will be transferred to a silica

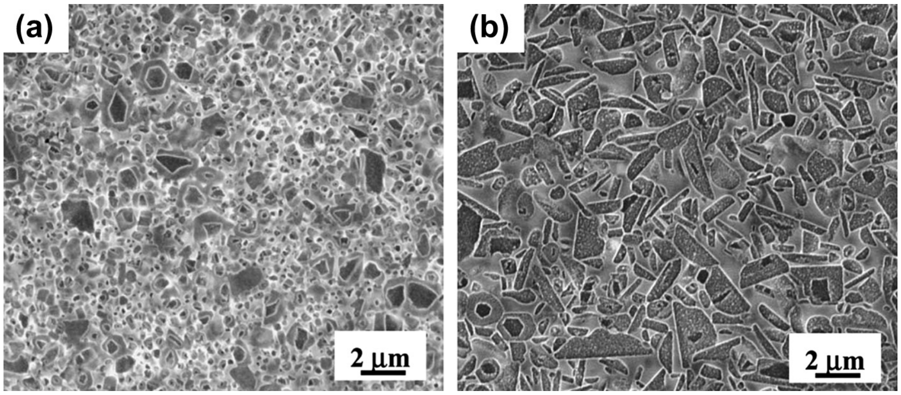

Figure 37 Microstructures of LPS-SiC processed in (a) N_2 atmosphere and (b) Ar atmosphere (polished SEM microsection, plasma etched). The copyright of these images is held by Elsevier B. V., Amsterdam, NL.

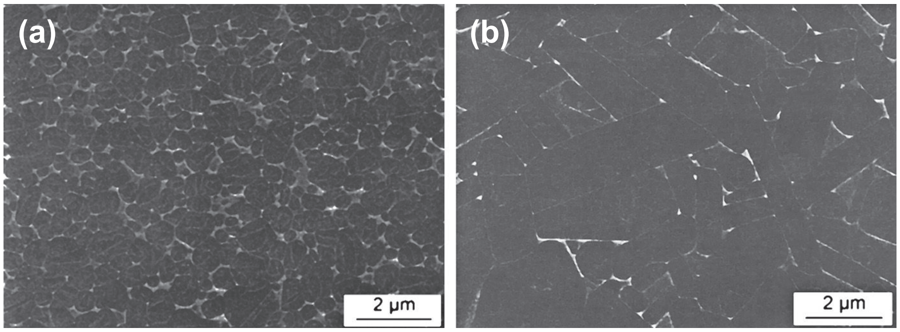

Figure 38 Microstructures of LPS-SiC doped with 10 vol.% AlN/Y_2O_3 (polished SEM microsection, plasma etched): (a) starting powder: α-SiC; sintered at 1950 °C, without annealing; (b) starting powder: 90% β-SiC, 10% α-SiC; sintered at 1970 °C, annealed 16 h. Reproduced with kind permission of HvB-Verlag GbR, Ellerau, Germany.

oxynitride melt. The melt is more stable at higher temperatures, but the kinetics of phase changes and grain growth phenomena are slowed down. Details about the corresponding solution reprecipitation of SiC in AlN–Y_2O_3–SiO_2 melts are reported elsewhere (Nader, 1995; Schwetz, Schäfer, Telle, 2003).

Rixecker, Wiedmann, Rosinus, and Aldinger (2001) argued that microstructural changes could be controlled better if an excess nitrogen pressure (0.2–10 MPa N_2) was used for sintering, because it suppresses the decomposition of AlN better. On the other hand, they admitted that a higher argon gas pressure (at least 10 MPa) should result in an HIP effect on the specimens. The latter statement supports the findings of Izhevskyi, Genova, Bressani, and Bressani (2001), who found a better densification using the sinter-HIP technique. Nevertheless, they favored argon as kiln atmosphere for their pressureless sintering experiments of LPS-SiC with the additive system AlN–Y_2O_3 (Izhevskyi et al., 2000a, 2000b, 2001). Thus the role of the firing atmosphere on LPS-SiC doped with AlN–Y_2O_3 is not clear (Izhevskyi et al., 2000a, 2000b).

Like for LPS-SiC with oxide additive systems, the kind of SiC starting powders (α-SiC or β-SiC) was considered a decisive factor for LPS-SiC manufactured via an AlN–Y_2O_3 system, whether the LPS of the SiC compositions can proceed either via xenomorphic or idiomorphic formation of crystals. Thus also this additive system permits the manufacture of LPS-SiC ceramics optionally via a homogeneous and a heterogeneous solution reprecipitation mechanism, respectively, each of them having its advantage and shortcomings for specific areas of application. The evolution of LPS-SiC manufactured using the AlN–Y_2O_3 system is more extensively demonstrated in the next paragraphs.

Microstructures of two completely densified LPS-SiC ceramics doped with AlN/Y_2O_3 (ratio 60:40) are presented in Figure 38 (Rixecker, Wiedmann, & Aldinger, 2001). The microstructure shown in Figure 38(a) has fine globular grain morphology (1.0 μm average grain size). The microsection shows the same core/rim structure already indicated in Figure 36. The starting raw material of the corresponding ceramic had been an α-SiC powder. It was sintered without additional annealing (holding time) at sintering temperature of 1950 °C. The grain morphology of microstructure shown in Figure 38(b) is totally different since it can be characterized by platelet-shaped grains. For the manufacture of the corresponding LPS-SiC a mixture of β- and α-SiC (90 β/10 α) was used as a starting raw material. At 1960 °C the specimen was annealed for 16 h. During this annealing period the characteristic platelet microstructure had developed via the β → α transformation, where preexisting α particles act as nuclei (seed crystals). The phase change was already completed after 8 h, where the average platelet size reached 2.2 μm with the (reverse) aspect ratio of 3.7. Longer annealing times reduce the aspect ratio and induce globular grain growth. It was noted by the authors that the specimens sintered with pure α-SiC powders never—even after longer annealing times—showed an anisotropic grain growth because of steric hindrance, since in this case each particle acts as nucleus for growing.

Figure 39 demonstrates the influence of the microstructural change as a result of phase transformation for the specimens characterized in Figure 34 (Rixecker, Wiedmann, & Aldinger, 2001). The specimen manufactured from α-SiC powder via homogeneous solution–reprecipitation shows no significant change of fracture toughness with annealing time at 1925 °C, because the annealing hardly affects the corresponding microstructure. On the other hand, a considerable increase of fracture toughness with annealing time is demonstrated for the specimen manufactured from the β-SiC-rich powder. The toughness increase can be explained by the platelet microstructure evolution due to heterogeneous solution reprecipitation during the annealing stage.

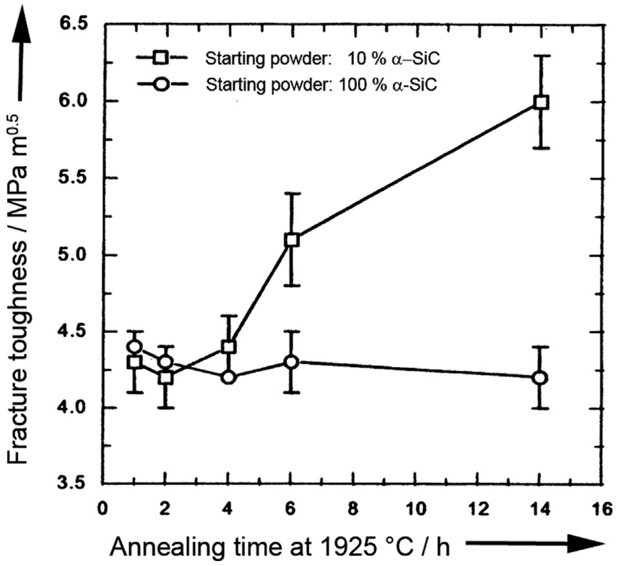

Figure 39 Fracture toughness versus annealing time at 1925 °C in nitrogen atmosphere for LPS-SiC ceramics of **Figure 34**. Reproduced with kind permission of HvB-Verlag GbR, Ellerau, Germany.

The energy dissipation-reinforcing mechanisms at room temperature are crack deflection, crack bridging, mechanical interlocking and platelet fracture. Pull-out effects are seldom observed at room temperatures but will be enhanced at higher temperatures when the intergranular glass phase may begin to soften (Wiedmann, 1998).

It was demonstrated by the investigations of Rixecker, Wiedmann, and Aldinger (2001) that a thermal treatment after sinter densification can improve the mechanical properties of an LPS-SiC manufactured from β-SiC-rich powders. The authors could show that also the LPS-SiC variant prepared from α-SiC powders could be upgraded through a short-time aging operation at 1200 °C, which improves both fracture toughness and bending strength explicitly. It was suggested that the oxinitride phase will be oxidized through this after treatment, which causes a volume increase in the interface, thus the generated internal compressive stress will reinforce the surface.

All previously presented in situ toughened LPS-SiC variants have been based on the β → α phase transformation in the annealing stage of sintering, where a microstructure with elongated grains evolves. We attributed it to a heterogeneous solution reprecipitation mechanism of LPS. However, it should be kept in mind that SiC also offers other phase transformations. This idea was followed by Schwetz, Schäfer, and Telle (2003), who sintered commercial submicron-sized α-SiC powders doped with sintering aids (7 vol.%) on the basis of AlN-YAG. They fired it in a gas pressure kiln first at slightly increased pressures (0.5 MPa Ar) to 1950 °C followed by an increased gas pressure (9.5 MPa Ar) at this temperature. During this sintering period the SiC polytype composition hardly altered the microstructure showing globular shaped crystals. Some specimens were subsequently annealed at 2050 °C (2.0 MPa Ar; $\geq$ 4 h). In this annealing stage the grains changed their shapes from globular to plate-like. The platelets started to develop after completion of 6 H → 4 H polytype transformation. The lower the 4 H content was in the starting powder, the larger developed the aspect ratio of the platelets. The evolution of elongated grain structure was intimately related to an increase in fracture toughness, thus this α-SiC polytype transformation had induced the in situ toughening of LPS-SiC. Since the α-form had been survived in this LPS-SiC ceramic during the annealing stage, this version should be included into below presented group, which is called "α-LPS-SiC".

Most of the publications about LPS-SiC ceramics presented up to now had been focused on scientific aspects. However, it should be noticed that the presented LPS-SiC materials had still been proven to be insufficient from an industrial and commercial point of view for two reasons. The first reason is that the goal of combining both high strength and toughness could only be achieved through individual actions. Thus an LPS-SiC ceramic could either have good strength or toughness but not both characteristics together. Secondly, an optimization of an LPS-SiC ceramic with regard to both strength and toughness requires additional time and energy consuming processing steps. Thus the aim of the enterprise ESK Ceramics was to develop an LPS-SiC ceramic, which had

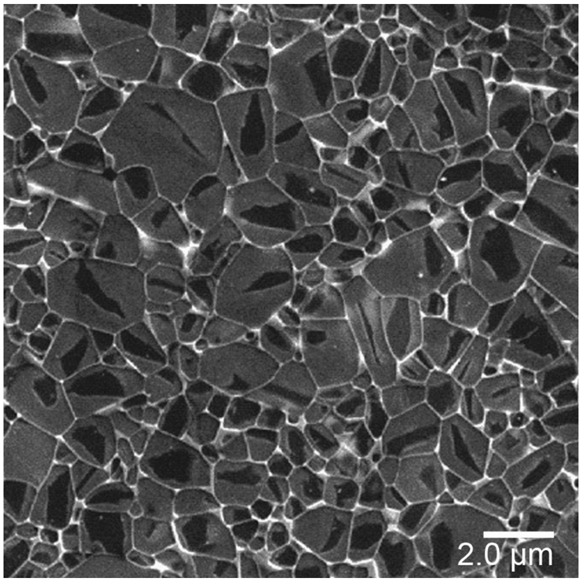

Figure 40 Microstructure of LPS-SiC with the tradename EKasic® T (polished SEM microsection, plasma etched). This photo was kindly transmitted from ESK Ceramics GmbH & Co KG, Kempten, Germany.

both improved strength and toughness together without costly aging or annealing actions (Schwetz, Sigl, Kempf, & Victor, 2003). The raw material for the commercial LPS-SiC (trade name EKasic® T, **Figure 40**) was usual submicron-sized Acheson powder (α-SiC) doped with YAG–AlN or Y_2O_3–AlN. An organic binder was added to the mixture. The debinding stage after shape forming (usually pressing) was conducted in two steps, first firing the specimen in inert gas (nitrogen) below 700 °C and secondly in air below 500 °C. The latter step should reduce the free-carbon content of the green body to ≤ 0.1 wt.% and simultaneously increase the adhering SiO_2 content to additional 1.0–1.5 wt.% through oxidation. The enhanced content of SiO_2 is necessary for the formation of the liquid phase during sintering. However, an excess of more than 1.5 wt.% SiO_2 during the debinding period should be avoided since it causes an increasing mass loss according to the reaction:

$$2SiO_2 + SiC \rightarrow 3SiO + CO \tag{9}$$

Even more important is the decarburization of SiC, since it permits the sinter densification up to high densities with a reduced amount of sintering additives (1–3 vol.%). The debound and decarbonized bodies are sintered (0.5 MPa Ar) in an autoclave-type kiln (sinter-HIP assembly or gas-pressure unit) at temperatures 1900–2000 °C until the pores get closed at about 95% relative density. Subsequently the pressure will be increased up to 2–100 MPa (Ar) in order to eliminate the residual porosity. The Y–Si–Al–O–N melt had been developed already far below the maximum sintering temperature. The fine-grained SiC particles dissolve in the melt at about 1850 °C and reprecipitate as Si–C–Al–O–N solid solution at preexisting coarser particles. Since the solution reprecipitation is homogeneous exhibiting a slight isotropic grain growth, the microstructure is fine grained. Moreover, the fracture toughness values are in the same range or even higher than those for in situ platelet reinforced LPS-SiC qualities. It should be noted that the usage of nitrogen containing atmosphere instead of argon has proven to be detrimental, because it causes an undesirable increase in viscosity of the melt and changes the melt composition. It is interesting to know that this decarburization changes the color of SiC particles and also the corresponding LPS-SiC ceramic from black to green color.

It had been demonstrated that assisting of high pressures is not always necessary for the sintering of submicron SiC powders with Al_2O_3–Y_2O_3 or AlN–Y_3O_3 additive systems. On the other hand it should be interesting to see, whether modern high pressure assisted firing techniques like FAST (SPS) (**Figure 24**) will influence the evolution of the microstructure and the mechanical properties during sintering. Hotta and Hojo (2009) sintered β-SiC submicron starting powders with 10 vol.% of the total AlN–Y_2O_3 additive system by using the FAST. At maximum sintering temperature of 1900 °C (holding time 5 min) and at pressures of 30 MPa at least 95% relative dense specimens were achieved. The AlN content was varied between 0 and 100 mol%. An increase of AlN resulted in a decrease of mean grain size. The highest bending strength of 1150 MPa was reached for specimen prepared by using 95 mol% AlN and 5 mol% Y_2O_3, where no grain growth at all during FAST sintering had been observed. All specimens densified by FAST exhibited microstructures with globular grains. At most slight phase transformations had been observed, which can be attributed to the low holding (annealing) time of only 5 min.

The reflections set out above show that LPS-SiC is not a single material. The term LPS-SiC covers a lot of different variants of SiC-based ceramics, which are linked only by the LPS. Though it is not possible in this survey to present a gapless visualization of LPS-SiC, there is still a lot left to report here about technological aspects, chances and limitations, which might be important for present and future applications of LPS-SiC ceramics. Compared to the SSiC, LPS-SiC offers major advantages in terms of processing (lower sintering temperature and complete densification) and materials engineering (higher toughness). However, there seems to be at least one domain where SSiC had been ahead, i.e. refractoriness. It will be shown that LPS-SiC scientists even have tried to surpass SSiC in terms of high temperature strength.

A better refractoriness of a ceramic material can be achieved through interfacial engineering either by reducing the amount of the intergranular matrix phase or by increasing the refractoriness of such phase. It should not be the goal of this development to change the interfacial conditions in such a manner that the fracture behavior turns out to be transgranular-like SSiC, because this would make the material more brittle. It follows from the above that the AlN–Al_2O_3 additive system offers a better refractoriness than the oxide systems.

Schneider, Biswas, Rixecker, and Aldinger (2003) studied the influence the molar ratio within a 10 vol.% additive system of AlN–Y_2O_3 on the creep resistance of LPS-SiC from β-SiC starting powders containing 10% α-SiC seeds. It was observed that the creep resistance will be improved as the molar ratio of AlN to Y_2O_3 is decreased. An increased Y_2O_3 portion increases the viscosity in the melt during sintering, which reduces the phase $\beta \rightarrow \alpha$ change rate and grain growth. An acceptable level of creep resistance was demonstrated for the molar ratio 2:3 of the additive system. A similar increase in creep resistance was achieved for a lower viscosity liquid phase of molar ratio 3:2 with a reduced additive amount. An oxide layer of $Y_2Si_2O_7$ was formed after long-time aging in air at elevating temperature without blistering or cracking. Further increase of creep resistance was obtained through a postsintering nitrogen anneal.

According to the old field strength theory of glasses (Dietzel, 1942), bond strength between the cation of an oxide additive and the oxygen ion rises with increasing valence state and decreasing cationic radius. Thus, if the amount of yttria in an AlN–Al_2O_3 additive system is replaced by an oxide of a heavier rare-earth element, the corresponding designed LPS-SiC should contain a more refractory intergranular phase, since the cationic radius of heavier rare-earth ion should be smaller than the ionic radius of Y^{3+}. Izhevskyi, Bressiani, and Bressiani (2005) used Yb_2O_3 in combination of AlN as an additive system for LPS-SiC from β-SiC starting powders containing 10% α-SiC seeds. The use of Ytterbia modified the liquid phase formed during sintering and reduced the phase change controlled formation of elongated grains, but fully dense specimens could be achieved. As reported in the paragraph above also the microstructures of these specimens could be improved through postsintering heat treatments in nitrogen. Though the $\beta \rightarrow \alpha$ transformation was retarded (annealing times at 1950 °C up to 32 h were used), especially with increase in Yb_2O_3 content in the additive system, in situ growth of elongated crystals could be achieved resulting in fracture toughness values of 4.5–5.0 MPa $m^{0.5}$. Increasing Yb_2O_3 content decreased the room temperature bending strength but improved the high-temperature strength. At 1400 °C about 60% of the room temperature strength could be retained.

Similar investigations were conducted by Kim et al. (2007). Three rare-earth oxides RE_2O_3 (10 wt.%) in combination with AlN were used as additive systems for a β-SiC starting powder containing 1 vol.% α-SiC seeds. The microstructures and the mechanical properties of the corresponding LPS-SiC ceramics after sintering and subsequent annealing were strongly influenced by the composition of the respective additive composition. The bending strength and fracture toughness values of the Lu_2O_3 containing LPS-SiC reached 700 MPa and 6 MPa $m^{0.5}$ at both room temperature and 1400 °C, respectively, what has to be considered as most notable. The high-temperature strength value exceeds by far the high-temperature strength value of SSiC. These results demonstrate the potentials of LPS-SiC ceramics. However, this does not mean that LPS-SiC will simply replace SSiC in high temperature applications; for it has to be considered that the manufacture of such a refractory LPS-SiC ceramics requires significant time, effort, energy consumption and material costs.

The idea of generating high viscous melts through additions of rare are oxides in sintering experiments was also pursued by Kumar et al. (2009) who tried to establish whether only a small amount of these additive systems can be sufficient to achieve dense LPS-SiC ceramics via HP technique. They used β-SiC powders (without α-SiC seeds), doped them with AlN combined with Y_2O_3, Lu_2O_3 or Sc_2O_3 as additive systems and hot pressed the corresponding mixtures (maximum sintering temperature: 2050 °C; pressure: 25 MPa; holding time: 6 h). In the case of Sc_2O_3 and Y_2O_3 the amount of only 3 wt.% was sufficient to manufacture densified (>97 relative density) LPS-SiC ceramics. The high viscosity formed during the LPS of SiC with the Lu_2O_3–AlN additive systems seemed to be responsible for the poorer density (~95% relative density). The corresponding microstructure had not developed elongated SiC crystals like the two other compositions. Only room temperature strength and fracture toughness values were measured.

The already presented investigations of Schwetz, Schäfer, et al. (2003) had demonstrated that it is possible to manufacture in situ toughened LPS-SiC without the need of any portion of β-SiC in the starting powder. The goal was achieved by replacing the usual $\beta \rightarrow \alpha$ transformation (or polytype change $3C \rightarrow 4H + 6H$) by the polytype change $6H \rightarrow 4H$. It was, however, recognized before that it seems possible to develop a self-reinforced microstructure from α-SiC starting powder without any polytype transformation. To demonstrate this we have to go back to LPS-SiC variants doped with the oxide additive systems. First in situ toughened LPS-SiC without a phase change was achieved with α-SiC starting powder containing relatively large α-SiC seeds (Kim, Mitomo, & Hirotsuru 1997; Lee, Kim, Cho, Lee, & Lim, 1998).

In the next step of evolution, Kim, Kim, Mitomo, Zhan, and Lee (1999) tried to find out whether the manufacture of in situ toughened LPS-SiC is possible without a phase change even if the fine α-SiC starting powders do not contain any large α-SiC seeds. They purified α-SiC powders chemically to remove both free carbon and SiO_2 and mixed them with 12 wt.% SiO_2 and YAG in various relations. The milled and dried powder mixtures were hot pressed at 1850 °C and after removal of pressure annealed at 1950 °C for 4 h under atmospheric pressure of argon to enhance grain growth. The hot pressed specimens showed microstructures consisting of relatively fine globular grains. The largest grains in the corresponding micrographs demonstrate the typical core/rim structure after plasma etching, indicating grain growth through solution reprecipitation. Obviously these larger grains give enough driving force to the system for the abnormal anisotropic growth of several grains, since the annealed specimens had bimodal grain size distributions consisting of 10 μm large SiC platelets embedded in a fine-grained matrix with an average grain size of 1 μm. The fracture toughness of the annealed specimens reached values of 6.1 MPa $m^{0.5}$. Both strength and toughness were optimized for the SiO_2/YAG relation of 0.5. Since there was no evidence of phase transformation it can be concluded that this in situ toughening was obtained through homogeneous solution reprecipitation.

In the next series of experiments (Kim, Kim, Rhee, & Kim, 2000) the influence of initial particle size on the evolution of microstructure of the LPS-SiC from initial α-SiC powders ("α-LPS-SiC") was investigated. The specimens were prepared in the same manner described in the previous paragraph, but with different average grain sizes (0.42; 0.50; 0.71 μm) of the starting α-SiC powders and a fixed SiO_2/YAG relation of 0.82. The specimens were hot pressed and annealed as described before. The finer the starting powder, the finer the microstructure developed during HP. Only the fine and medium grain-sized specimen could be induced to evolve in situ toughened bimodal microstructures with elongated grains, whereas the large grain-sized specimen maintained its unimodal grain size distribution after annealing. Again it could be assumed that a small number of larger grains should have been the prerequisites for the growth of platelets. The α-SiC grains which were considerably larger than the other matrix grains were supposed to act as nuclei for the growth of elongated anisotropic grains. It was supposed, however, that this anisotropic abnormal growth would occur only when the grain size is smaller than a certain critical limit. It was speculated that such threshold should be exceeded for specimens, which had been hot pressed with the coarser powders.

One could get the impression that the manufacture of in situ toughened α-LPS-SiC with oxide additive systems should only be possible via the HP technique. Jang, Kim, and Kang (2002) showed for instance that a successful manufacture of α-LPS-SiC can be achieved through a conventional pressureless powder bed sintering as well. The cited publication contains further interesting details concerning the influence of sintering atmosphere on the grain shape and grain size evolution.

A major technical advantage of the LPS approach for SiC compared to the solid-state sintering is the feasibility to manufacture an SiC ceramic with a homogeneous and fine-grained microstructure because of the lower temperature and the presence of the liquid phase (Padture 1994). Therefore it is a logical step that the material scientists concentrate on the manufacture of nanosized SiC-based ceramics, which are consolidated via LPS. The first success in this direction was achieved in the 1990s by a Japanese/South Korean research group (Mitomo, Hirotsuru, & Kim, 1997; Mitomo, Kim, & Hirotsuru, 1996). A fine β-SiC powder with an average particle size of 90 nm was densified by HP with an Al_2O_3–Y_2O_3–CaO additive system. An LPS-SiC nanoceramic with an average grain size of 110 nm was achieved. The ceramic could be superplastically deformed with a strain rates of $5.0 \times 10^{-4}\ s^{-1}$ at 1700 °C, which was the lowest temperature ever registered for superplasticity.

The same consortium (Lee, Kim, Mitomo, & Kim, 2003) achieved a fully dense nanostructured LPS-SiC ceramic through the quite different two-step sintering technique (S + S), which had been recently introduced by Chen and Wang (2000) in ceramic heat process technology for manufacturing nanometer-sized ceramics. The background of this new sintering technique is the fact that capillary driving force for sintering, which involves surfaces, and the grain growth, which involves grain boundaries, are comparable in magnitude, both being inversely proportional to grain size. The idea is the suppression of the grain growth in the final stage of sintering by exploiting the difference in the kinetics between grain boundary diffusion and grain boundary migration. A chemically cleaned ultrafine β-SiC powder was doped with additives having the same composition as mentioned in the previous paragraph. The mixture was milled in a vibrator mill to achieve a powder with a mean particle size of 20 nm. A specimen sintered in Ar under applied pressure of 20 MPa first taking a fast heating rate to 1750 °C (without holding) and then cooled down quickly to 1550 °C with 8 h holding time reached a relative density of 99% with a mean grain size of ∼40 nm. The new two-step sintering refers back to sinter HIP (**Figure 30**), where the first step is conducted at a higher temperature level than the second step. The intention had been the same in both cases: prevention of grain growth.

It was indicated above that the surface energy of nanosized powders is so high, that the challenge for sintering nanosized SiC powders lies in maintaining the grain size small during the sintering period. As already demonstrated for solid-state sintering of nanosized powders in this subsection, abnormal grain growth can be prevented relatively easy through pressure-assisted sintering techniques, since pressure assisting permits the reduction of the sintering temperature. The FAST (SPS) sintering technique described in connection with **Figure 24** seems to be a good choice for the manufacture of nanostructured SiC via an LPS approach.

A series of research activities concerning sintering of LPS-SiC with nanosized β-SiC powders by FAST have been published by Hotta and his colleagues from the Advanced Manufacturing Research Institute, National Institute of Advanced Industrial Science and Technology (AIST), Nagoya, Japan already (Hotta, Enomoto, & Hojo, 2006; Hotta & Hojo, 2006, 2010; Hotta, Kita, & Hojo, 2011). They used the additive system AlN–Y_2O_3 in various proportions mostly in a total amount of 10 vol.% and revealed that the AlN-rich additive were effective to retard grain growth during sintering. Only slight phase transformation occurred. Thus only xenomorphic (globular) crystals developed in the microstructure during FAST sintering. Fully dense (>99% relative density) SiC ceramics were obtained through FAST sintering for nanosized β-SiC powders (40 nm) with at least 5 vol.% total amount of the additive system AlN–Y_2O_3 with the molar ratio of 95:5 of the components. **Figure 41** shows the plasma etched SEM micrographs of the specimens sintered at 1900 °C for 10 min with 1, 5 and 10 vol.% AlN–Y_2O_3 additive amount, respectively (Hotta et al., 2011). It could be demonstrated that increasing amount of additive retards grain growth. The mean grain diameter of the sintered body with 10 vol.% additive was 80 nm (**Figure 41**(c)).

It has been shown that many approaches had been incorporated for the evolution of LPS-SiC ceramics. **Figure 42** shows a proposal for a classification scheme of the different groups using a dual principle, even if the designations could be a bit confusing to the reader of this article. Therefore an explanation of the different designations seems to be necessary. The term oxide or oxynitride in the second level is related to the additive system. The starting powder in the third level can consist of either α- or β-SiC, the latter may contain α-SiC seeds as well. The fourth level should demonstrate that LPS-SiC can be divided into eight groups. The designations α-LPS-SiC and β-LPS-SiC do not refer to the kind of SiC crystallites within the sintered ceramics, but to the (major) kind of starting powders used, respectively. In situ toughened LPS-SiC ceramics contain elongated (idiomorphic) crystals, which have been evolved as a result of high-temperature annealing. Untoughened LPS-SiC ceramics have globular (xenomorphic) crystals. It should be noted that the latter might even exhibit high fracture toughness. Refractory LPS-SiC are only imaginable for the oxynitride additive system. Nanosized LPS-SiC ceramics have developed for both oxide and oxynitride additive systems, up to now only untoughened versions have been developed. It should be noted that not all of the LPS-SiC ceramics can be fitted into the proposed scheme of **Figure 42**, especially those which are not designed for mechanical but for electrical functions (Martin & Adler, 2002). It should also be taken into account that the literature on LPS-SiC is most comprehensive. Thus not all aspects and materials of LPS-SiC could be considered in this article. For instance the porous LPS-SiC ceramics (Adler, Klose, & Piwonski, 1999; Adler, Teichgräber, Klose, & Stöver, 1998; Ihle, 2004; Piwonski, 2005) have not been considered.

2.04.4.2.7 Silicon Carbide Composites

SiC has been the dominant compound in all mentioned SiC-based ceramics of this chapter. There are, however, some sintered SiC-based ceramics, in which additionally a second compound is dispersed homogeneously for

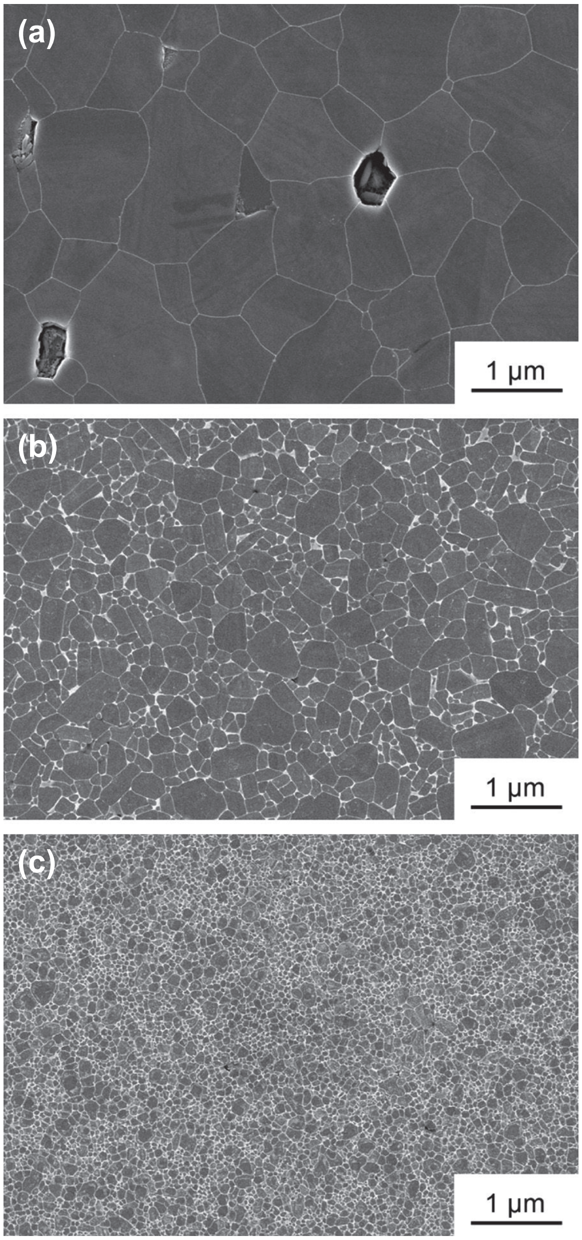

Figure 41 SEM micrographs of plasma-etched specimens FAST sintered at 1900 °C with 50 MPa pressure for 10 min with (a) 1, (b) 5 and (c) 10 vol.% AlN–Y_2O_3 additive (molar ratio: 95:5). Reproduced with kind permission of M. Hotta and the Ceramic Society of Japan.

different reasons. Only some of these sintered SiC-based composites should be mentioned shortly in this review article in order to preserve clarity in this overview over this multifaceted range of sintered SiC-based ceramics.

Ceramics for structural applications should exhibit high-strength values and good fracture toughness. To reach these goals three general preconditions must be aimed by technological means. The first precondition is that the material reaches high density. It would be best if the theoretical density can be achieved. If the obtained density is not sufficient enough, we can use pressure-assisted sintering techniques. A dense ceramic only exhibits good strength values if its microstructure has been controlled so that the grains are small sized. The grain growth can be inhibited through the inserting of heterogeneous phases (the reader may compare for instance the grain growth inhibiting effect of carbon for SSiC). High fracture toughness can be obtained for a dense ceramic if in situ or ex situ elongated particles with high aspect ratios (whiskers or platelets) are inserted and dispersed in the microstructure. If a dense material shall exhibit both high strength and toughness simultaneously, the elongated particles with high aspect ratios should also be small.

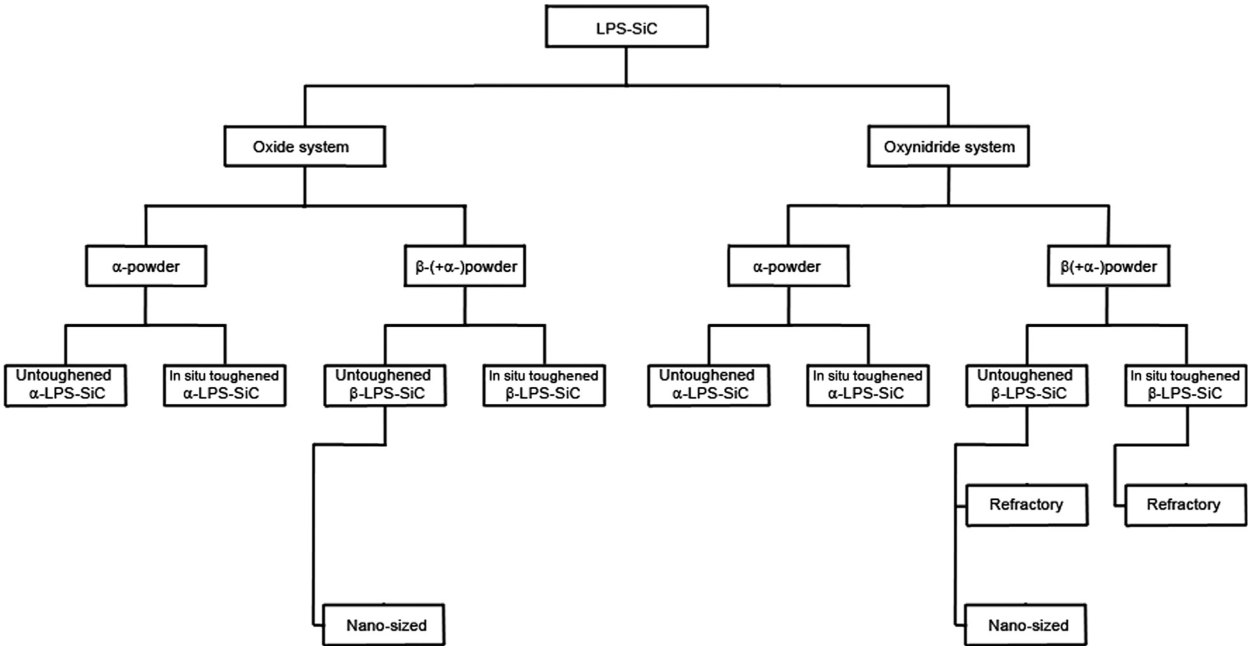

Figure 42 Classification of LPS-SiC ceramics.

Both high strength and toughness could be obtained for SiC–TiC composites (Doan, 1988; Endo, Ueki, & Kubo, 1990; Janney, 1987; Shaoming, Dongliang, Shouhong, & Jingkun, 1996; Wei & Becher, 1984). The addition of TiC particles reduces grain growth, thus the bending strength level could be increased to 700–800 MPa. The improvement of fracture toughness to 6.5–7.5 MPa $m^{0.5}$ is explained through the mismatch between the thermal coefficients of SiC and TiC, which causes radial tensile stresses in the grain boundaries and tangential compressive stresses in the matrix. The stresses cause crack deflection, crack branching and microcrack formation. Also LPS-SiC–TiC composites had been developed (Kim, Lee, & Lee, 2000; Sand & Adler, 1999).

SiC composites with diborides (TiB_2, ZrB_2) combine both the high thermal and electrical conductivity of the diborides with the enhanced oxidation resistance of SiC (Janney, 1987; Jimbou, Takahashi, Matsushia, & Kosugi, 1986; McMurtry, Boecker, Seshadri, Zanghi, & Garnier, 1987). The reinforcement is also explained through the mismatch of the thermal coefficients of the components. The toughening mechanisms are analyzed by Cai, Gu, and Faber (1990). SiC–TiB_2 composites could also be manufactured by LPS (Schwetz, Kempf, Saldsieder, & Telle, 2004). The toughening can be increased through both the in situ toughened SiC platelets and the ex situ inserted TiB_2 particles.

It has been demonstrated in this subsection that there are many different groups of densely sintered SiC-based ceramics available. The processing routes of the groups contain major differences. It would go beyond the scope of this review article to discuss the processing details of each group. Most of the mentioned materials were generated in a laboratory scale. Scientists, who are developing materials, do often not have to pay attention to commercial aspects. In our reflections now on processing of densely sintered SiC-based ceramics, both technical and commercial points of views shall be figured.

The flow sheet shown in Figure 43 shall represent the whole lot of densely sintered SiC-based ceramics as much as possible. However, not all processing steps shown here are necessarily applied for each material. On the other hand some further steps could be added for some materials or at least more precisely specified for the practice. The flow sheet shows a main line with a major sequence of processing steps and a branch with only one step. The firing steps are marked, since so far they were referred to in this subchapter with particular regard. The main line of the flow sheet represents the processing route for pressureless firing (firing 1) (S) sometimes supplemented through an additional pressureless or pressure-assisted firing step (S + S, GPS, HIPS). The first step (powder synthesis) is normally not executed by the ceramics company but by a raw material supplier. It should be noted that commercial submicron SiC powders are routinely chemically purified with hydrofluoric acid in order to remove the powder particles from adhering SiO_2. This cost increasing action is necessary for the

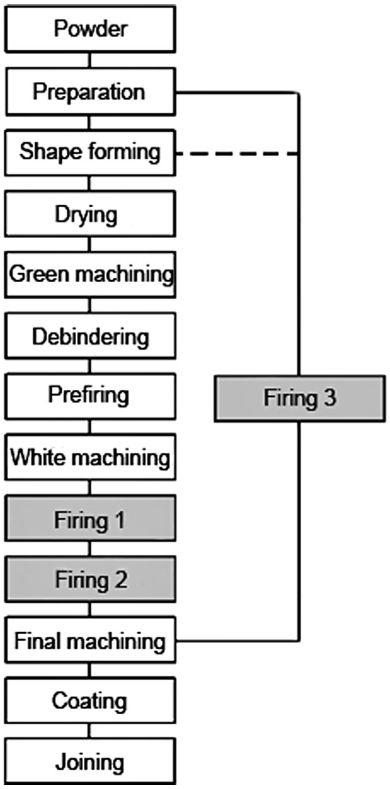

Figure 43 Flow sheet of the processing routes of densely sintered SiC-based ceramics.

production of SSiC but not for LPS-SiC since SiO_2 is a useful sintering additive for the latter. On the other hand it has been shown in this review (Kim et al., 1999) that the powders for LPS-SiC should be decarburized. Thus the raw material suppliers should be encouraged to reflect these insights.

Sometimes the next processing step, the powder preparation, can be reasonably conducted by the raw material supplier as well, if the supplied ceramic company is a small or medium-sized enterprise. In most cases the powder preparation, however, is done by the ceramic producer himself. The powder preparation includes milling and blending of compounds regularly consisting of SiC powder, sintering additives and organic aids (liquefiers and binders). Though most scientists cited in this article successfully used organic solvents and dispersants, it should be assessed whether the usage of water instead could be risked, since the powder preparation in aqueous systems is simpler and more cost-effective than the powder preparation in organic systems. The powder preparation includes conditioning of the powder mixtures for the subsequent shape forming, so there are slurries, plastic pastes and press-forming masses, respectively.

There are lots of shape-forming processes available in the ceramic technology. The purpose of this processing step is not only the generating of a desired shape but also a precise and smooth surface should be guaranteed. Furthermore, grain- and/or pore-oriented microstructures should be avoided and green densification should generally be high. Also economic considerations are important for choice of an appropriate shape-forming technique such as attainable shaping rates, costs of shaping tools and investment expenses for the whole shaping facility. It can be argued whether the various demands give reasons for the lot of different shape forming techniques, since none of the shape-forming techniques can fulfill all demands. Thus, always a compromise has to be made for the best choice of shape-forming technique. For the manufacture of densely sintered SiC-based ceramics principally all common shape-forming techniques can be applied like slip casting, tape casting, gel casting, electrophoretic shaping, extruding, hot molding, injection molding, wet pressing, axial dry pressing, cold isostatic pressing (CIP) and various rapid prototyping methods. Serious problems can arise, when slurries are poured into porous molds as for slip casting or pressure slip casting, where the fine powder particles penetrate into the molds via its open pores, which might then be clogged.

The residual humidity has to be removed in the next processing step. Since the complete removal of the humidity takes time, the drying is regularly conducted in drying chambers, especially when the moisture content in the green body is high ($\geq 3\%$). Microwave drying has not yet completely established. If the humidity is low, e.g. for dry pressed parts, the moisture removal can be integrated into the thermal process chain.

In spite of best adapted shape-forming techniques a net-shape forming is rarely possible for structural parts like densely sintered SiC-based ceramics. Thus the parts almost always require a special surface finish. The best surface finish can be achieved through final machining. There are several relatively new final machining methods available, e.g. laser cutting, electrical discharge machining (spark erosion technique), water cutting, sandblasting and ultrasonic machining. In most cases, however, the best surface finish is obtained by using grinding techniques. Computerized Numerical Control (CNC) machining operations are often used for this. Because of the high hardness of SiC products only diamond multicut tools can be used for grinding, thus this kind of grinding is extremely cost-intense. For reducing the costs it is suitable to shift the machining to an early stage of production, where the bodies are still relatively weak. The green machining can reduce the machining costs considerably, though the single cut tool consist of polycrystalline diamond because of the abrasive SiC powder particles in the green bodies. The demanded high-quality surface finish cannot be obtained only by green machining, which thus can reduce the machining costs but not avoid final machining completely. A compromise to a certain degree is the so-called white machining, conducted on 1200–1300 °C prefired bodies. For white machining of theses porous bodies, the same kind of multicut tools can be taken as for final machining.

The shaped bodies have to be debound in a separate debinding furnace, if the amount of binder used is high, for instance when extruding or injection molding had been taken as shape forming methods. The shaped SSiC parts have to be debound in a different way as LPS-SiC parts. SSiC green bodies should be debound in nitrogen or argon, because the sintering additive carbon should remain in the body to improve the densification during sintering and the detrimental oxidation of the SiC particles being then prevented. The LPS-SiC bodies must not contain carbon but additional silica on the surface of the powder particles may be advantageous for the sintering. Therefore LPS-SiC-shaped green bodies are favorably debound in air. In order to reduce carbon, a decarburization step of the green bodies is recommended in literature (Schwetz, Sigl, et al., 2003).

For the firing of SSiC in principle vacuum, argon or nitrogen can be used. A higher densification can be achieved through sintering in vacuum rather than in argon or nitrogen, since no gases counteracting the densification are entrapped during the vacuum sintering. However, through the vacuum treatment the surface is getting porous due to the reaction

$$\mathrm{SiC_s} \leftrightarrow \mathrm{Si_g} + \mathrm{C_s} \tag{10}$$

and the surface enriches elementary carbon. For this reason it is often beneficial to start the sintering process in vacuum, as long as the porosity is still open, and to conclude it in argon, when the pores are closing. The atmospheric conditions for sintering LPS-SiC ceramics had already been discussed above.

Ceramics are often coated for different reasons, for instance to generate structured functional surfaces or to install protective layers for a better oxidation resistance or better resistance against any other chemical attack. It must be admitted that coatings for densely sintered SiC ceramics are unusual.

SiC ceramics can be used at high temperatures in oxygen-rich atmospheres, since a thin self-healing layer of refractory silica will be formed through oxidation. Corrosion problems can arise, however, when alkali containing compounds are present. At temperatures above 800 °C alkali oxides react with the formed silica layer and cause the formation of a less refractory liquid with a low viscosity. Oxygen can diffuse in this case rapidly through the layer and to the SiC, which corrodes by oxidation to CO_2 and SiO_2. The CO_2 may be trapped in the low viscous silica melt, which causes bubbles. To avoid this, alumina-based coatings are recommended (Federer, 1990).

In order to reduce the friction of wear couples (see below) the polished SiC surface can be graphitized either through pure thermal decomposition (Thaler, Schwetz, & Kayser, 2004) or through chemical decomposition by chlorine (Ersoy, McNallan, Gogotsi, & Erdemir, 2000). These "carbide-derived-carbon" coatings have good adhesive strength but their use is limited because of abrasive wear due to the low hardness of graphite.

Extremely low friction coefficients can be achieved by amorphous "diamond-like-carbon" coatings on SSiC (Fundus & Knoch, 1997). The 1–3 µm thick, very hard coatings generated through plasma-activated chemical vapor deposition have insufficient adhesive strength and wear resistance at high pressures and high sliding speeds.

Modern facilities, engines, motors or automotives usually do not consist of a single material. They are represented by systems of different materials instead. Generally most structural materials in such systems are still metals, only few might be ceramics. In engineering systems, the materials must be compatible to each other.

It is often not easy to achieve a sensible design adjustment of two adjacent materials. Ceramics for instance have quite different properties than metals, this is the reason that the design with ceramic materials is so difficult and by far not all criteria for it have been explored yet. Adjacent components are joined together by form-locking, force-locking or firmly bonded methods. This final step of the flow sheet (Figure 43) is normally not the matter of the ceramics producers since materials are used to be joined together in mechanical engineering companies.

The processing of the direct pressure-assisted sintered SiC ceramics is represented by the branch shown in Figure 43, which indicates that the number of processing steps is reduced compared to the main line of the flow sheet. This simplification of process technique must be regarded, however, as disadvantageous, since it involves a loss of flexibility. For instance the usage of these techniques does not permit the application of cost-efficient green or white machining steps. The starting powder mixtures must not contain organic binders, because the decomposed gas species cannot escape through the molds during the high-temperature treatment. With the HP techniques HP and FAST (SPS) only single, simply shaped parts can be fabricated within one firing cycle. In terms of energy consumption it should be noticed that for each firing cycle the mold has to be heated up together with the article to be sintered. Finally parts of the mold have to be replaced after each HP cycle, because a strong conjunction between the mold and the sintered ceramic occurs. HIP specimens might be preshaped to some extent (Figure 23(b)), but since the pressure transfer is not completely uniform, often the specimens are deformed after the cycle (dotted line in Figure 43). Unlike HP many specimens corresponding to the kiln capacity can be sintered simultaneously within one cycle through HIP. On the other hand it should be noted, however, that the filling of the casings and the vacuum-tight sealing is laborious and casing materials are expensive and have to be replaced completely after each HIP cycle. It can be concluded that all direct pressure-assisted techniques justify only an industrial production of SiC-based ceramics, if the improved properties are really demanded.

It is not reasonable and often not possible to compare the main properties of all those in this subsection treated SiC-based ceramics with each other, since most of them are fabricated only in a laboratory scale and not all properties are available. Additionally it should be regarded that the materials evolution is an area of continuous development, thus it is hard to decide which quality should be listed. Hence Table 5 contains only some properties of six commercially proven or at least preproven sintered SiC ceramics, five densely sintered qualities. The final porous one (RSiC) will be presented at the end of this subsection. In addition, the list contains properties of some reaction bonded SiC-based ceramics treated in the following subsection. The listed SSiC is boron- and carbon-doped version of Figure 28, LPS-SiC is the untoughened α-LPS-SiC of Figure 40, the HIPSiC is an undoped version, the aluminum-doped HPSiC had been characterized in Figure 22(b).

The best bending strength values are achieved with the pressure-assisted versions (HIPSiC, HIPSSiC and HPSiC). It is interesting to see that the listed HIPSiC has an intergranular fracture mode (I) and consequently loses its strength at elevated temperatures, though no sintering additives had been used. The reason is that the SiO_2 content present as an impurity cannot decompose at elevated temperatures because of the high pressure,

Table 5 Properties of some sintered and reaction bonded SiC-based ceramics.

SiC ceramic			*SSiC*	*LPS-SiC*	*HIPSiC*	*HIPSSiC*	*HPSiC*	*RSiC*	*SiSiC*	*NSiC*	*CVD-SiC*	*CSiC*
Density	ρ	$g\ cm^{-3}$	3.10	3.24	3.21	3.21	3.21	2.75	3.07	2.80	3.21	1.95
Porosity	P	%	3	<1	<1	<1	<1	15.5	0	<10	0	15
Young's modulus	E	GPa	430	420	440	450	450	240	370	260	460	Not known
Bending strength (RT)	σ_B	MPa	400	550	640	640	640	110	320	170	450	18
Weibull modulus	m		10	15	10	10	10	10	10	10	15	10
Bending strength (1400 °C)	σ_B	MPa	400	Not known	430	640	640	110	–	Not known	520	Not known
Fracture mode	T/I		T	I	I	T	T	T	T	T	T	I
Fracture toughness	K_{IC}	$MPa\ m^{0.5}$	3.5	6	4	3.5	3.5	3.1	3.5	3.1	3.0	Not known
Thermal expansion coefficient	α	$10^{-6}\ K^{-1}$	3.8	4.1	3.8	3.8	3.8	3.8	4.4	5	3,8	Not known
Thermal conductivity	λ	$W\ m^{-1}\ K^{-1}$	130	80	120	130	130	70	110	105	300	25

thus it has to remain in the body during sintering. In the form of intergranular silica glass melt it enhances grain boundary sliding when loading at high temperatures. In HP units, the SiO_2 can escape through the gaps of the molds, therefore the residual SiO_2 content in hot pressed specimens is lower than in corresponding hot isostatic pressed ones. The scheduled LPS-SiC does not attain the strength level of the pressure-assisted SiC ceramics, but it has better Weibull modulus and a better fracture toughness instead. The room temperature strength of the LPS-SiC is better than the one of SSiC, because the lower grain size (LPS-SiC: 2 μm; SSiC: 5 μm) and higher density of the former as compared to the latter. The bending strength of LPS-SiC at high temperature has not been measured yet. However, due to the observed intergranular fracture mode (I) it can be assumed that the bending strength should drop at high temperatures. In contrast, the bending strength levels of the densely sintered SSiC, HIPSSiC and HPSiC exhibiting transgranular fracture mode (T) are kept up to high temperatures. The correlation between bending strength versus temperature curve and corresponding fracture mode had been explained in the remarks given regarding **Figures 21** and **22**.

The Young's modulus strongly depends on the phase composition and the porosity of a material. Consequently the relatively pure and dense pressure-assisted SiC materials scheduled in **Table 5** show high Young's modulus levels. It is also consistent with the theory that the more porous pure SSiC exhibits a lower Young's modulus. However, the intergranular phase containing dense LPS-SiC has a comparatively low Young's modulus. Obviously this phase itself has a lower Young's modulus because of the higher portion of ionic bond than the covalent compound SiC and thus, due to the mixing rule, it reduces the overall Young's modulus of the material.

The intergranular phase in LPS-SiC has a higher thermal expansion coefficient and lower thermal conductivity than pure SiC. This explains the higher overall thermal expansion coefficient and the lower thermal conductivity of LPS-SiC, which has a relatively high intergranular phase content (Kriegesmann 2005a). It should be noted that the thermal expansion coefficient is not influenced by the densification degree of a ceramic.

It has already been highlighted in this article that through Prochazka's invention of SSiC (Prochazka, 1973) the research activities on technical ceramics started to emerge in all industrialized countries. This new lightweight, strong, chemical-resistant and high-temperature stable material seemed to open up new fields of application which had been considered impossible for ceramics before. The potentials that had been esteemed first for SSiC referred to its good mechanical properties at high temperatures (Srinivasan, 1989). The application of common metals as structural components are generally restricted to temperatures below 1400 °C, whereas SSiC ceramics sustains at least 1400 °C under load in oxygen-containing atmospheres.

Therefore in many industrialized countries state support funds were granted at that time for ambitious research projects concerning the high-temperature applications of SiC ceramics and other new advanced ceramics such as silicon nitride. The most ambitious project had been gas turbine engine for automotives. **Figure 44** shows the design of the gas turbine engine, which contains many ceramic components. All technical problems could have been solved, thus the gas turbine engine worked well. Nevertheless the gas turbine engine was not adopted in industrial production. The reasons were the high costs involved in the manufacturing of ceramic materials. Since further ambitious ceramic projects concerning high-temperature applications in automotives like the ceramic turbochargers and ceramic valves have unfortunately failed to be taken up by production, the interest in ceramics for structural use at high temperatures has faded.

Today the main application field of densely sintered ceramics is tribology (friction and wear). One of the first successful products in this area had been the sliding and counter rings (wear couples) of mechanical seals for centrifugal pumps in the chemical industry. SiC ceramics has forced out the chemically less resistant tungsten carbide and the less thermal shock-resistant aluminum oxide from the market (Zeus, 1991). **Figure 45** contains some recent SiC seal rings.

For tribological applications the strength is not a decisive factor. ESK Ceramics successfully developed a coarse-grained version of SSiC with elongated grains with the tradename EKasic® C (**Figure 46**). It has proved to be extremely corrosion resistant, even against hot water attack, because of its low specific interface area. This SSiC sustains higher load capacities so that the surface pressure can be increased in tribological systems, which ensures a good smooth running. The microstructure of **Figure 46** recalls the microstructure of Prochazka's SSiC prepared from β-SiC starting powders (Prochazka, 1973), which did not have commercial success in spite of its trendsetting significance.

A good dry run capability for a mechanical seal is usually achieved through a sliding ring made of hard ceramic like SSiC and a counter ring of a smoother material like hard coal because of their corresponding low coefficient of friction. ESK ceramics developed coarse-grained SSiC with a microstructure similar to that of **Figure 46** but with evenly distributed graphite particles sized 50–120 μm. Since this material with the

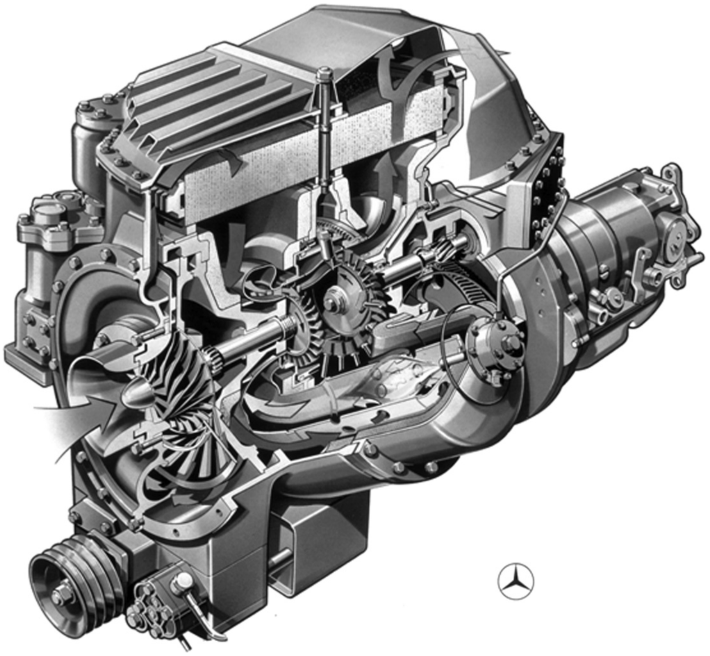

Figure 44 Design and principle of the gas turbine engine for automotives. This image was kindly transmitted from Daimler AG, Stuttgart, Germany.

tradename EKasic® G combines the properties of hard coal and coarse-grained SiC, sliding ring and counter ring could now be consisting of the same material for systems with a risk of dry running and the requirement of high chemical resistance.

LPS-SiC has good edge stability because of its combined high strength and fracture toughness. Such characteristic points it out for special structural applications like dewatering elements in paper machines. Because of its good mechanical properties and fine-grained microstructure, untoughened LPS-SiC can be used for miniaturized structural components. LPS-SiC is more cost-effective to manufacture than sintered silicon nitride (Schwetz, 2000).

In spite of their good properties, the pressure-assisted SiC ceramics HPSiC and HIPSiC are too costly to permit series production at present.

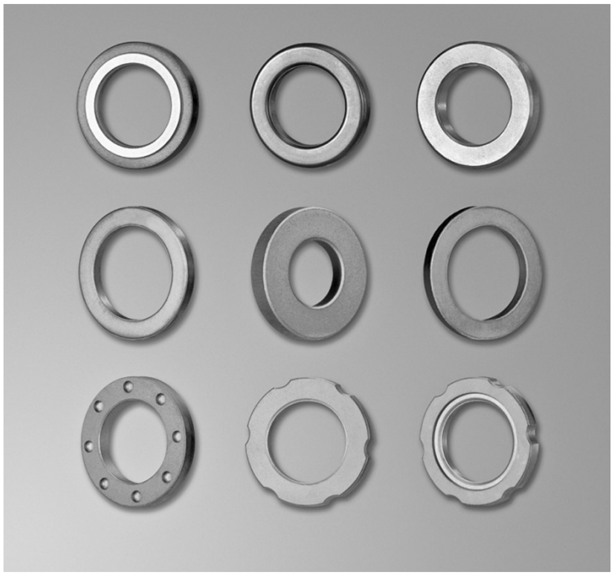

Figure 45 SSiC seal rings. This image was kindly transmitted from ESK Ceramics, Kempten, Germany.

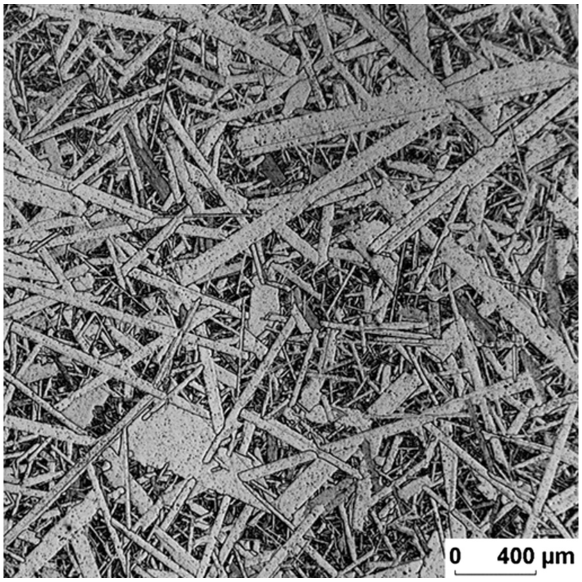

Figure 46 Microstructure of an SSiC with the trade name EKasic® C. This image was kindly transmitted from ESK Ceramics, Kempten, Germany.

2.04.4.2.8 Recrystallized Silicon Carbide

A SiC ceramic for structural application should have good mechanical properties in order to guarantee high strength and/or low friction. Pores within a ceramic strongly affect its mechanical properties. Therefore, one prominent goal of the mentioned processing techniques in this subsection was to achieve SiC-based ceramics exhibiting high or (even better) full densification. However, the final material treated in this subsection, the RSiC, which sinters with low or even without shrinkage, is a highly open-porous one. Because of its complete different microstructure compared to microstructures of the densely sintered SiC-based ceramics, it may be assumed that RSiC has quite different requirements and application areas. For this reason, the processing and applications of RSiC are described here separately from the other sintered SiC-based ceramics.

RSiC is the oldest of the SiC-based ceramics of this subsection. The first patent was granted at the beginning of the twentieth century (Fitzgerald, 1900). But many years passed before this material could be exploited economically, since only later efficient, controllable and manageable kilns had become available. Normally RSiC does not require any sintering additives. The typical particle structure of the green body is represented by bimodal grain size distribution (Weaver & Logan, 1978). Traditionally almost all bimodal grain size distributions for RSiC raw material batches used to consist of a coarse fraction with a narrow size range and mean diameter of 100 μm, and a fine one whose particles should preferably fill the gaps formed by coarse particles. This idea had been adapted from the particle structure in green bodies for refractories (Litzow, 1930) (Section 2.04.4.1). Anyhow the bimodal grain size distribution implements a high green density, which might be important, since no further contribution to densification can be expected because of nonexisting shrinkage effects during sintering.

The bimodal grain size distribution is not mandatory for the occurring sintering mechanism of RSiC (Kriegesmann, 1992) but promotes the formation of a homogeneous pore distribution (Kriegesmann, 2004a). It was assumed that an evaporation–condensation mechanism controls the sintering behavior (Kriegesmann, 1986, 1988), which causes the nonshrinking sintering (Kuczynski, 1949; Kingery & Berg, 1955). Hence, it should be noted that for SiC, besides the solid-state sintering (S) and the LPS, a third sintering mechanism exists: the evaporation–condensation mechanism (R). This can be regarded as a gas-phase sintering mechanism (Kriegesmann, 2005a).

In principle, an Ostwald ripening conception (Ostwald, 1900) can be proposed for this sintering mechanism (Kriegesmann, 2005a). Figure 47 demonstrates a two-particle model of Ostwald ripening for evaporation–condensation. Small- and coarse-sized particles are located adjacently in a gas space. At elevated temperature the partial pressure of the sublimating gas species will be higher over the small particle, due to its greater curvature, than over the large particle. The concentration gradient caused by the difference in vapor

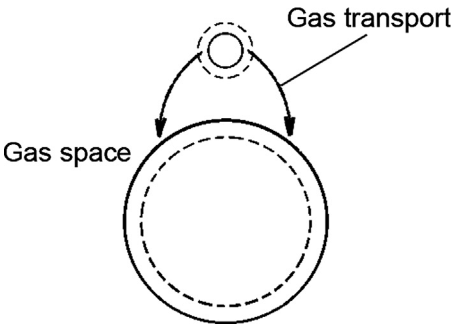

Figure 47 Ostwald ripening model for evaporation–condensation.

pressure gives rise to a concentration balance. The latter causes a supersaturation of the sublimating species over the large particle, which induces a deposition of the species at its surface. Over the course of the sintering process, the coarse particle is growing further. Simultaneously, the fine one is shrinking until it finally disappears.

The Ostwald ripening model implies that the deposition locations of the condensed species is arbitrary and thus random. Investigations of the sintering behavior of bimodal grain spectra with particular large coarse particles (within mm range) showed, however, that the surface of the coarse particles contains favorable and unfavorable locations for the sinks of the transport of the vapor species (Kriegesmann, Kraus, & Gros, 1998). The view of the coarse-grained RSiC in Figure 48 shows a (0001) lattice plane of a hexagonal α-SiC crystal with cone-shaped configurations of growing lattice planes. The heads of these cones are grown together with other sections of the crystal. The adjacent secondary sections have the same crystallographic orientations among each other, and obviously form a macrocrystal together with the former mother crystal of the coarse grained fraction. Only few (at most) primarily tabular shaped crystals show different orientations. Dislocations are assumed in the center of the cones. The cone-shaped or screw-shaped growth occurs in the direction of the dislocations by attachment of the condensed species at their crystal exit sites. Hence, new lattice planes in form of plates or spirals are generated, which spread two-dimensionally on the growth front of the plates by attachment of new condensed material. Cones are formed by creating new lattice planes, before the former has reached the edge of the crystal.

The formation of conical objects was not observed, when finer sized RSiC batches were sintered. However, it was noticed that the pitches of the terraces are larger as the sintering temperature gets higher. Furthermore it can

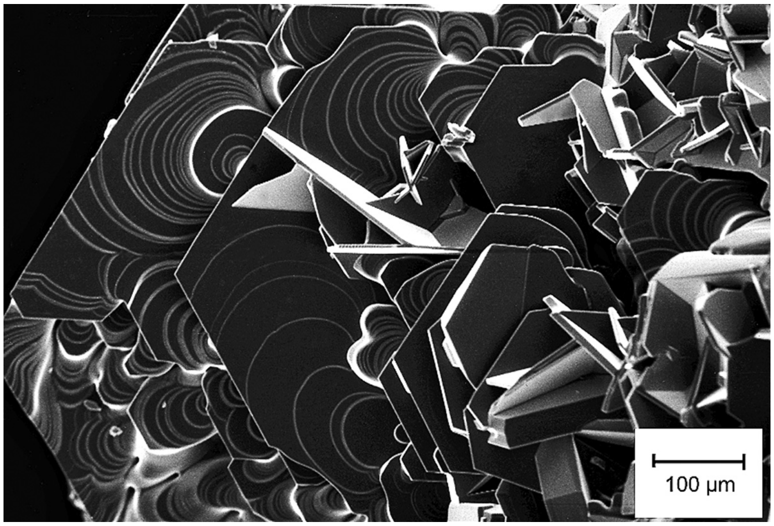

Figure 48 Coarse-grained RSiC surface. Sintering temperature, 2200 °C. The copyright of this image is held by the author of this article.

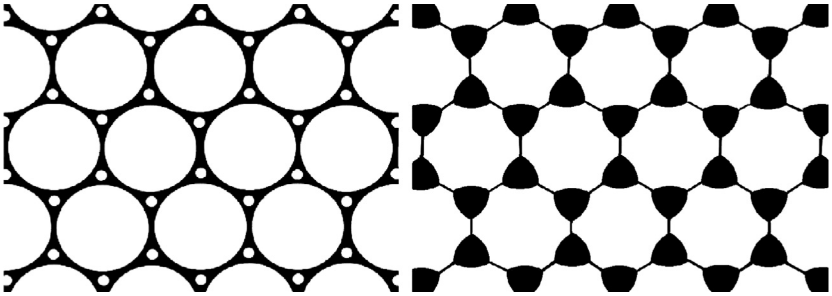

Figure 49 Schematic of bimodal grain size distribution in the green body (left) and the corresponding sintered body (right) (light areas: grains; dark areas: pores and grain boundaries). The copyright of this image is held by the author of this article.

be assumed that the concentration of lattice defects increases with decreasing grain size. This means that the deposition mechanism of evaporation–condensation approaches the Ostwald ripening conception as the particles of the starting powders are finer and the maximum sintering temperature is lower, since the depositions occurs in a more random order.

Figure 49 schematically shows both an ideally structured green body with bimodal grain size distribution and a corresponding body sintered via evaporation–condensation provided that the Ostwald ripening model is permissible (Kriegesmann, 2005a). In the sintered body (right) the fine particles are completely sublimated. They have left pores behind with a definite dihedral angle and the condensed species have been deposited on the coarse grains. Through the resulting grain growth, adjacent grains connect with each other and thus form grain boundaries. The fracture surface of a specimen with 70 wt.% coarse fraction (mean grain size 25 μm) and 30 wt.% fine fraction (6 μm and finer) is shown in Figure 50 (Kriegesmann, 1992). It resembles the schematic drawing of Figure 49 (right). The fracture mode is transgranular, the mean dihedral angle Φ being 120°.

It could be demonstrated that evaporation–condensation results in growth of preexisting grains. Thus it should be noted that the term "recrystallized silicon carbide" is indeed misleading, since no new formation of crystals occur.

The evaporation–condensation mechanism for RSiC cannot be a simple sublimation and recondensation, since gaseous SiC molecules do not exist. According to the present state of research (Kriegesmann, 2004b), evaporation–condensation is opened with a reduction or decomposition of the adherent silica through the reaction:

$$\mathrm{SiO}_{2\mathrm{s}} \leftrightarrow 2\mathrm{SiO}_{\mathrm{g}} + \mathrm{O}_{2\mathrm{g}} \tag{11}$$

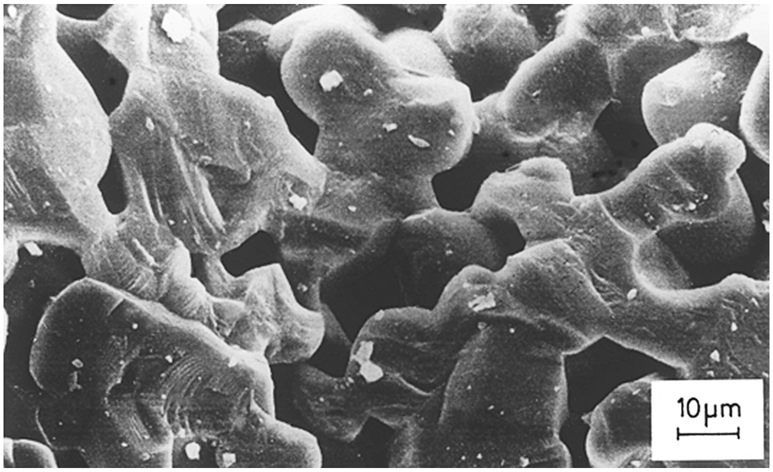

Figure 50 SEM fracture surface of RSiC (maximum sintering temperature, 2200 °C; relative density, 79.1%). The copyright of this image is held by the author of this article.

which should cause the uncovering of the surface of the SiC particles and simultaneously an enrichment of molecular oxygen in the vicinity of the particles. Oxygen is—according to the proposed model—necessary to decompose the fine-grained (submicron sized) SiC particles by active oxidation (in argon atmosphere):

$$\mathrm{SiC_s + O_{2g} \leftrightarrow SiO_g + CO_g} \tag{12}$$

The monoxides should then react in the inverse direction on the exit sites of dislocations at the surface of the coarse (micron-sized) SiC grains. This yields formation of secondary SiC and emission of molecular oxygen again, the latter becoming then available for further decomposition of the fine-grained SiC. The active oxidation could be maintained as long as small particles exist during the sintering process.

It should be noted that generation of SiC single crystals by the Lely process (Lely, 1955) should proceed following a similar mechanism. However, for the single-crystal formation a different evaporation–condensation mechanism was proposed with reactions among the gaseous species Si, Si_2C and SiC_2 (Sudarshan, 2010). Hence, there are some research needs left in terms of the gas reaction mechanism of RSiC.

The sintering temperatures necessary for the production of RSiC parts are the highest (2200–2500 °C), compared to the sintering temperatures needed for the commercial SiC-based ceramics of this subsection. Thus the kiln power is regularly too low for the study of overfiring effects. In order to investigate the sintering behavior of RSiC including overfiring effects, the grain size of the coarse fraction of the bimodal SiC grain mixture was extremely reduced with the idea of enhancing the sintering activity and thus reducing the sintering temperature (Kriegesmann & Jodlauk, 2002).

In Figure 51 the linear shrinkage of such a fine-grained RSiC is plotted against the firing temperature. It could be demonstrated that up to a specific temperature (1840 °C) termed T_R, actually no shrinkage at all had been observed. At T_R the specimen started to shrink noticeably, even if the amount of shrinkage was low. The microstructural changes during the firing were monitored by means of SEM analysis of fractured surfaces of the sintered specimens. The microstructures sintered below T_R showed both coarse and fine grains. By increasing the firing temperature, however, more and more fine particles vanished. At T_R only isolated fine particles could be discovered in the microstructure (Figure 52).

The sintering behavior of this initially nonshrinking ceramic could not—as usual in ceramic systems—be controlled through shrinkage or density measurements. Hence, the change in specific surface area measured by the Brunauer, Emmett, & Teller (1938) method overfiring temperature proved to be an effective method to characterize the sintering behavior of such a ceramic (Figure 53). The specific surface area decreases steadily with increasing firing temperature until T_R is reached, indicating the gradual loss of the fine-grained fraction. Beyond T_R the specific surface area decreases further on with rising temperature owing to the starting shrinkage. This effect has, however, only a slight influence on the thermal change of the specific surface area so that there is a clear kink in the curve at T_R.

At present only two application areas exist for RSiC. The first generation of SiC-based kiln furniture for firing silicate ceramics (porcelain and sanitary ware) above 1300 °C had been silicate (clay) bonded. In the 1970s these ones had been gradually replaced by RSiC lightweight kiln furniture (plates, beams and cases) having lower heat capacity, better strength, higher thermal conductivity and better thermal shock resistance. Figure 54

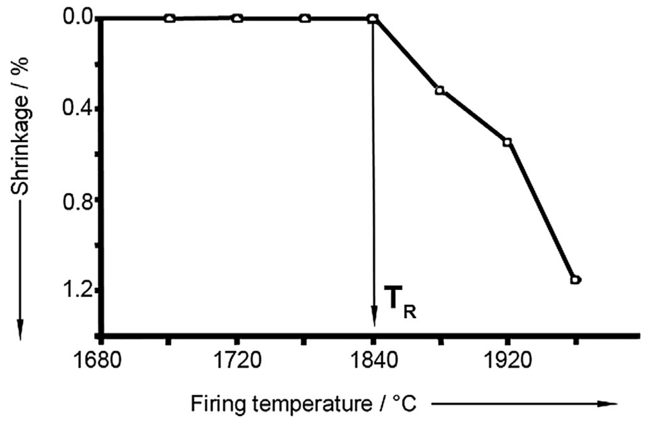

Figure 51 Linear shrinkage of slip cast RSiC as function of temperature (Starting powder mixture: 70 wt.% coarse powder (mean grain size 3 μm), 30 wt.% fine powder (submicron sized), holding time 1 h). The copyright of this image is held by the author of this article.

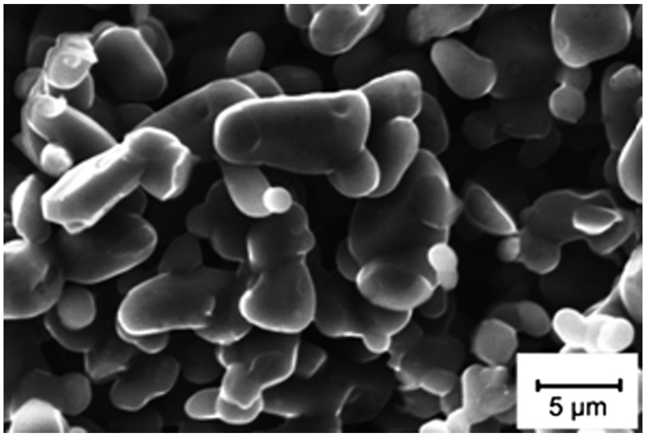

Figure 52 Microstructure of slip cast RSiC sintered at T_R (1840 °C). The copyright of this image is held by the author of this article.

shows RSiC kiln furniture carrying porcelain ware. The plates are usually covered by zirconia or zirconium silicate containing engobes in order to avoid contact reactions with the silicate ceramic article lying across.

Originally the only industrially used shape forming technique for RSiC was slip casting (Fredrisson, 1960), which allows the production of thin-walled, complexly shaped structural parts. Compared to other shape forming methods, the slip casting technique provides the possibility of shape forming without using organic binders in the RSiC batches. For this reason a debinding step could be omitted during the processing of RSiC. For batches with organic additives like binders for press forming, the debinding originally was mandatory. Otherwise the additives are reduced to carbon black during the sintering process in argon atmosphere, which inhibits the evaporation–condensation mechanism considerably (Kriegesmann, 1986, 1988). Within this context, it should be noted that the use of carbon as a sintering additive for SSiC is not only for removing the silica layer from the surface of SiC particles but also for preventing nonshrinking evaporation–condensation of SSiC, which competes with the shrinking solid state sintering.

The properties of the RSiC for kiln furniture are listed in Table 5. The Young's modulus is low because of its high porosity. Compared with the other commercial sintered SiC ceramics of Table 5, RSiC has the lowest room temperature bending strength due to both low relative density and large mean grain size. Important for the use

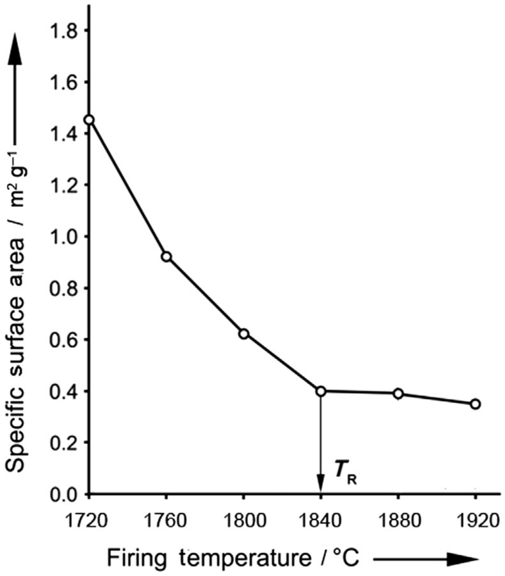

Figure 53 Specific surface area versus firing temperature of the slip cast RSiC. The copyright of this image is held by the author of this article.

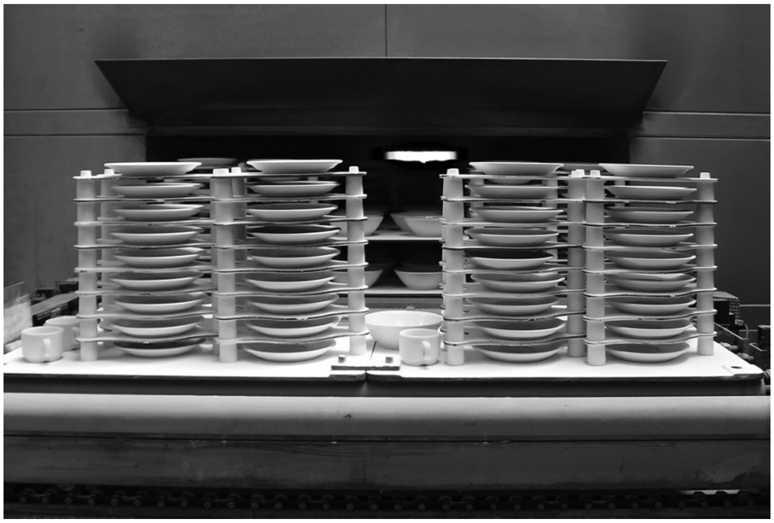

Figure 54 RSiC kiln furniture carrying porcelain ware. This image was kindly transmitted by Saint-Gobain Industrie Keramik Rödental GmbH, Rödental, Germany.

of kiln furniture is the fact that RSiC keeps its strength up to elevated temperature due to the transgranular fracture (Figure 50). The large grain size and the transgranular fracture mode probably are the main reasons for the low fracture toughness. Obviously the pores do not reduce the crack rate noticeably like it is the case in some other porous refractory materials. The thermal conductivity of RSiC is comparatively high in spite of its high porosity, reaching almost the level of the dense LPS-SiC. The main reason behind it is the fact that RSiC is a pure SiC ceramic and does not contain any intergranular second phases. The thermal coefficient is comparable to the other "pure" SiC ceramics, since—as already mentioned above—the thermal expansion coefficient does not depend on the degree of densification.

The second current application of RSiC is the Diesel particulate filter (DPF) monolith. In spring 2000 the automobile company Peugeot Société Anonyme (PSA) equipped its Peugeot 607 with a DPF. It was the first serially equipped DPF fully functional in the world. It contained a wall-flow RSiC filter monolith of the Ibiden Comp. Ltd (Yoshimi, 1991) (Figure 55). Since then, different filter materials have been used for DPF, although RSiC is still regarded as the best choice (Adler, 2005). The reason is not only the good strength compared to alternative materials, together with the high thermal conductivity and corrosion resistance, but also the technical abilities that makes RSiC an outstanding filter material. For instance through the modification of its bimodal grain size distribution it is possible to adjust almost any desired pore size, which additionally exhibits extremely narrow pore size distributions. This is demonstrated through Figure 56, which shows a pore size

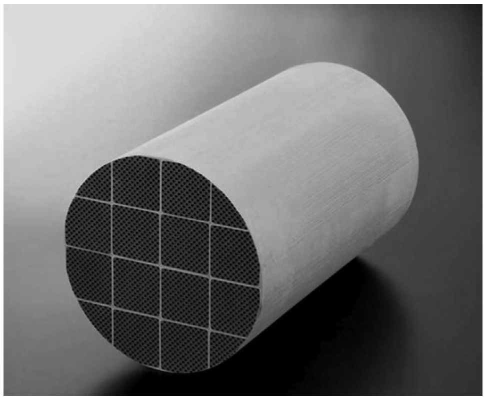

Figure 55 Wall-flow Diesel particulate filter monolith. This image was kindly permitted from Koji Shimato, Ibiden Comp. Ltd., Europe.

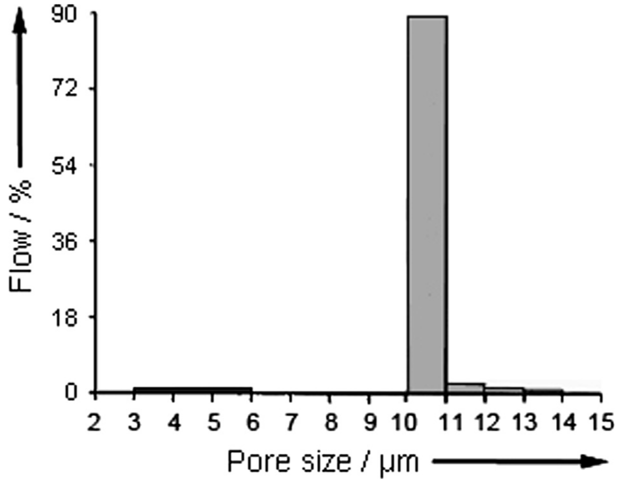

Figure 56 Pore size distribution of tape cast RSiC controlled by capillary flow porometry. The copyright of this image is held by the author of this article.

distribution of tape cast RSiC ceramic measured by a capillary flow porometer (Kriegesmann, Büchler, Rejic, & Ersen, 2009). The size of almost 90% of the pores is between 10 and 11 μm.

The principle of Diesel particulate filtration is shown in Figure 57. The presently most common used particulate filter is designed according to the honeycomb structure, which has been realized already for catalysts but at which the cells are closed at alternating ends. The main shape-forming technique applied for this wall-flow filter is extrusion molding. The filtration occurs in such a way that the exhaust gases penetrate the porous walls, which collect particles sizes between 50 and 1000 nm.

The microstructures of both RSiC variants for kiln furniture and for DPFs can only be compared phenomenologically. RSiC for kiln furniture should be as dense as possible for achieving better strength, thermal conductivity and above all oxidation resistance. DPF monoliths also need sufficient strength, but other properties are more important. There are two main requirements which both depend on the pore structure of a filter. However, the first is met best with small pores and the other with large ones. Hence, a compromise has to be found. Higher filtration efficiency is achieved through filter elements with smaller pores. On the one hand, a reduction of pore size causes a higher pressure drop of the exhaust gases, which should be as low as possible for a good engine output. For the requirement of sufficient strength the porosity of an RSiC monolith should not be higher than 60%. On the other hand, the porosity should not be lower than 50% since the lower the porosity the higher is the pressure drop. For the compromise between filtration efficiency and pressure drop a mean pore size of 10 μm seems to be adequate.

The author of this article and his team have alternatively proposed a wall-flaw filter via a tape casting technique (Kriegesmann, 2003; 2004a; Kriegesmann et al., 2009; Kriegesmann, Strate, Ersen, & Büchler, 2004; Rickmann, Büchler, & Kriegesmann, 2007). In order to realize such a filter conception, first a flexible tape cast foil containing a bimodal SiC grain size distribution had to be first developed. Figure 58 demonstrates the flexibility of the developed foil. Its consistency could have been adjusted as required simply by changing the amount of water and by controlling the rheological parameters. Because of the low-to-zero shrinking sintering,

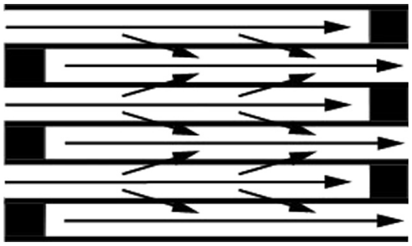

Figure 57 Principle of wall-flow Diesel particulate filter.

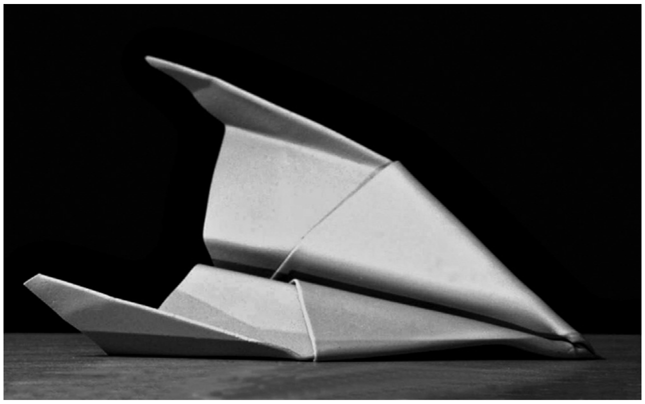

Figure 58 Pleatable green foil containing bimodal SiC grain size distribution. The copyright of this image is held by the author of this article.

the pleated structures survive the firing without cracking. **Figure 59** shows a fired prototype model of DPF made via tape casting.

The slurry for tape casting contains a high amount organic binder, which usually has to be removed through an additional oxidative debinding step. However, it is also possible to drop the debinding step if the slurry contains a certain amount of additional silica (e.g. in form of fine quartz sand) (Kriegesmann, 2010). **Figure 60** demonstrates the relevance of silica addition to the batch of a binder-containing slurry for the evolution of the corresponding microstructure of the sintered body. The batch of the RSiC corresponding to the microstructure of **Figure 60(a)** did not contain any additional quartz. The argon atmosphere pyrolyzed the binder only leaving fine carbon black particles behind. In the microstructure of **Figure 60(b)** only small relics of carbon could be detected. The corresponding raw material batch contained fine quartz sand which had oxidized the binder during the sintering process in spite of argon kiln atmosphere so that carbon could be reduced through this action.

Besides flexibility, tape casting offers a further benefit since two or more tape cast foils can be laminated together. This is especially noteworthy in view of a low-to-zero shrinking ceramic material. Even if two laminated foils have different RSiC compositions, there will be no deformation during sintering, since both foils show roughly zero shrinkage during firing. Hence, at the first glance it seems to be simple to realize a

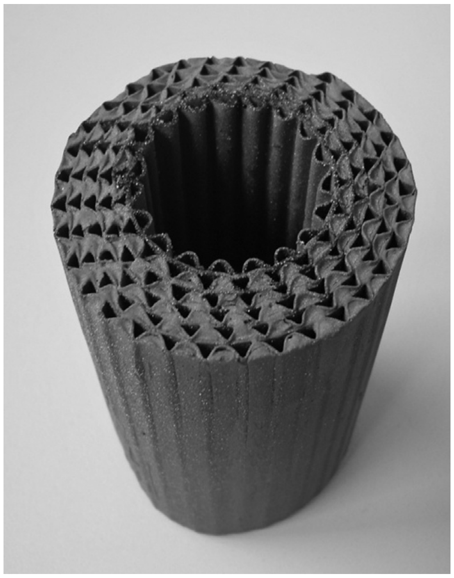

Figure 59 DPF model made via a tape casting process. The copyright of this image is held by the author of this article.

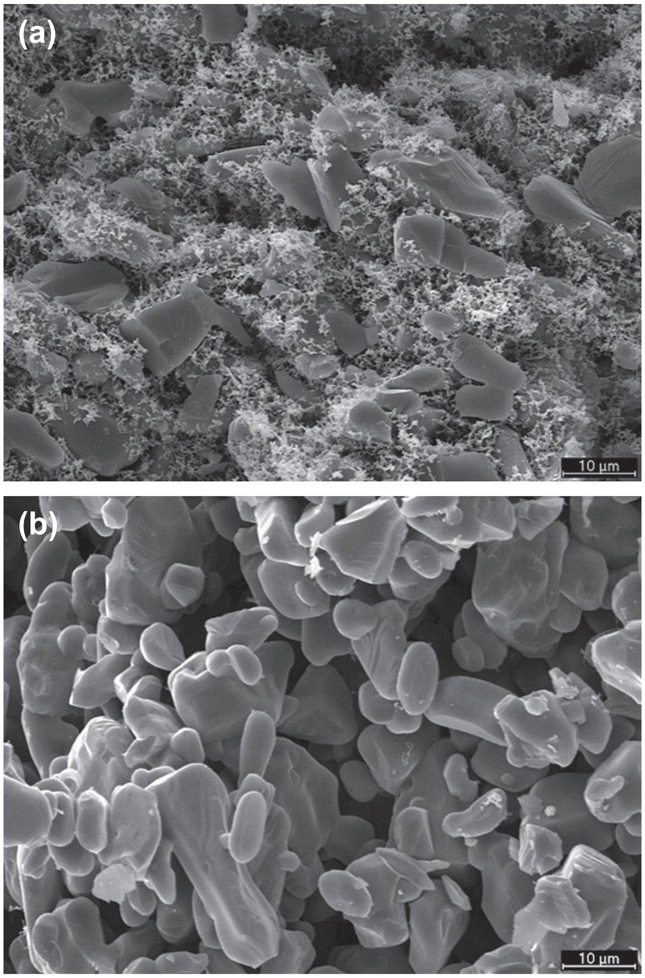

Figure 60 The influence of additional quartz in the binder-containing slurry on the microstructure of the corresponding sintered RSiC ceramic fired at 2050 °C: (a) without additional quartz and (b) with 15 wt.% quartz (referred to the amount of SiC in the slurry). The copyright of these images is held by the author of this article.

multilayered RSiC with graded structures. Although first trials of generating graded structured RSiC were promising at the beginning, they had two severe deficiencies. The first one refers to the microstructures of the layers. The raw material composition for each layer is different. Hence, a coarse pored RSiC needs a coarser grained fraction of the bimodal grain size distribution than a fine-pored RSiC. Consequently powder compositions with coarser grained fractions need higher sintering temperatures than those with finer grained fractions. Provided there is only a bilayered body to be sintered, in this case either one layer is sintered properly and the other is not or both layers have improper microstructures, if a compromise is made. The second deficiency refers to the adhesion between the layers. Because of the different sintering activity of each layer, a satisfying connection between the layers could only partly be achieved even if the laminated green foils had sticked together well. Many delaminations appeared in the bi- or multilayered specimens, some being even visible.

In order to remove the first deficiency, sintering tests with single-layered specimens were conducted including microstructural control over the whole temperature range. The standard recipes were—unusual for RSiC—altered through additional sintering aids, which should either promote or inhibit the sintering activity (Sahin & Kriegesmann, 2013). By this means it became possible to shift the optimum sintering temperature for each composition to lower and higher temperatures, respectively. Next step was to combine two compositions with the same optimum sintering temperature but one with an expected coarse- and the other with an expected fine-pored microstructure after sintering. Putting this into practice they were tape cast, laminated to a bilayer and sintered at maximum temperature. In this manner it became possible to generate bilayered RSiC specimens, where pore size of one layer could be quite different from the other one but each of the layers was optimum concerning its microstructure. This was possible through the addition of promoting or inhibiting sintering aids and variations of their contents. After realizing a lot of different pore size combinations in bilayered samples the same procedure was realized with a compound with more than two layers.

The second deficiency had the same cause, but its solution afforded a different approach (Sahin and Kriegesmann, 2013). The problem of avoiding delaminations during the sintering step was solved through inserting a few micrometer-thick intermediate layers into the interface between two adjacent layers. The recipe for this additional layer was composed in such a way that they contained besides fine (submicron-sized) powders both coarse powder fractions of the adjacent foil batches (both micron sized, but differing in grain size). Hence, the batch of the intermediate layer exhibited a three-modal grain size distribution which simultaneously fulfilled the sintering activity requirements of both adjacent layers.

Figure 61 shows the microstructure of a three-layered RSiC. The fit of the layers is so good that the borderline had to be marked in the figure to make it visible. The lower coarse-grained layer has coarse pores, the center medium-grained layer has medium-sized ones and the upper fine-grained layer has fine ones, respectively. The filtration efficiency of such a three-layered RSiC filtration system proved to be excellent at acceptable drop losses. It should be noted that via the LPS method another multilayer asymmetric SiC filter system (membrane) had been verified (Piwonski, 2005).

As already indicated above the exhaust catalyst is designed in a similar way as DPFs. Thus it would be interesting to know, if a porous ceramic like RSiC can fulfill both functions simultaneously, the function of a particulate filter and the function of a catalyst. Catalysts need the functionalization of their surface, i.e. they have to be coated with an active catalytic layer. There are many different coating methods available. For the reported investigations (Sahin, Pesch, Kolozsvári, & Kriegesmann, 2009) the technique of PVD had been applied. The corresponding experiments should only be considered as pretrials since many preliminary questions had to be answered first. Owing to cost restraints these basic tests were executed by using comparatively cheap titanium as coating element. Penetration depths of 75 μm could be achieved. The coating enhanced the strength of RSiC. The clogging of the pores could be prevented, thus the filtering efficiency could still be guaranteed after coating. On the other hand, it should be admitted that the pressure drop has been increased a bit. Up to the present only dense materials have been coated by PVD, thus such a "physical vapor infiltration" (PVI analog to the chemical vapor infiltration, CVI, see Section 2.04.4.3) should coat inner surfaces of the pores. These first experiments demonstrated that PVD technique can successfully be used for coating of porous materials.

It has been indicated in the previous paragraph that the inner pore surface area of RSiC could be used for sensoric applications. RSiC was coated with active layers of copper and copper oxide using several methods in order to develop an improved detection capacity of the sensor system for tracking the explosive triacetone triperoxide (TATP). First results showed that traces of the decomposition reaction of TATP could be identified, but additional work has still to be done (Warmer, 2010).

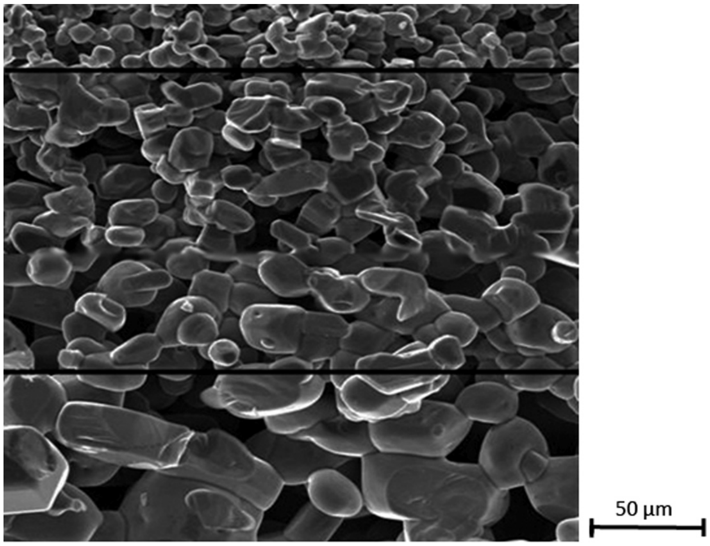

Figure 61 Three-layered RSiC. The copyright of this image is held by the author of this article.

It has been shown that RSiC is a very brittle ceramic (Table 5). The homogeneous pore structure, however, offers good space for inserting fibers into an RSiC matrix. Additionally through the absence of shrinkage there will not evolve shrinkage-induced stresses on the fibers during sintering. Two approaches have been realized.

The first approach (Kriegesmann, Meistring, Neumann, & Nixdorf, 1999; Neumann, 2002) is based on the original concept of "weak" interface (Evans & Marshall, 1989) between fiber and the strong matrix of ceramic matrix composites. Slip casting was used as a shape-forming technique. Within a plaster mold the singly inserted SiBCN and Hi-Nicalon™ fibers coated with BN or C (Section 2.04.3.2.) were covered with the slurry containing a bi- or monomodal SiC grain size distribution. After demolding and additional drying the specimen was sintered in argon atmosphere at temperatures up to 1800 °C. It should be noted that temperatures higher than 1800 °C could not be used when SiBCN fibers were used, since this would exceed the stability limit of the fibers. The sintered porous specimens were impregnated with phenolic resin, hardened and finally siliconized at 1560 °C in vacuum.

The second approach (Kriegesmann & Schumacher, 2004) was based on the concept of "strong" interface between fiber and the weak matrix (Tu, Lange, & Evans, 1996), since in this case the impregnating and siliconizing steps had been deliberately abandoned. The fiber-reinforced ceramic materials had been developed consisting of fine-grained RSiC matrix and an SiC-fiber fabric (Hi-Nicalon S). Tape casting was used as a shape-forming technique. The obtained flexible green tapes were laminated using different methods. After firing the corresponding composite specimens exhibited a typical sandwich structure with alternating layers of RSiC and more or less RSiC-containing fiber fabrics. Strengths testing showed that the fiber reinforcement improved the toughness of RSiC ceramics. Two different toughening effects were identified. The fiber fabric could sustain sintering temperatures up to 1900 °C.

It should be noted that most of the ceramic fibers are not stable much above 1250 °C. Therefore usually manufacture of fiber-reinforced ceramics is carried out using reaction bonding techniques at relatively low temperatures. These two approaches show, however, that there exist fibers which are stable up to high temperatures, making the manufacture of fiber-reinforced ceramics via an appropriate sintering technique possible. Since these ex situ toughened ceramics have an RSiC matrix, in line with the abbreviations used for the other SiC ceramic matrix composites, they can be identified as SiBCN/RSiC and SiC/RSiC, respectively.

In most cases there are a large number of criteria for classifying a group of related elements. This statement applies to the ceramics treated in this subsection as well. It is reasonable to classify ceramics according to their applied consolidation techniques and/or their consolidation mechanisms, since—as already mentioned before—consolidation can be regarded as the most important ceramic processing step, because it converts a shaped body into a ceramic product. In Figure 62 the main groups of the sintered SiC ceramics are classified according to this principle. The low-pressure-sintered SiC represent the pressureless sintered and the gas-pressure-sintered SiC ceramics, respectively. GPS has only been applied for some special LPS-SiC variants.

For the presentation of the SiC ceramics in this subsection we have not followed this clearly displayed pattern. Ceramics for mechanical engineering should normally be as dense as possible. Therefore the emphasis

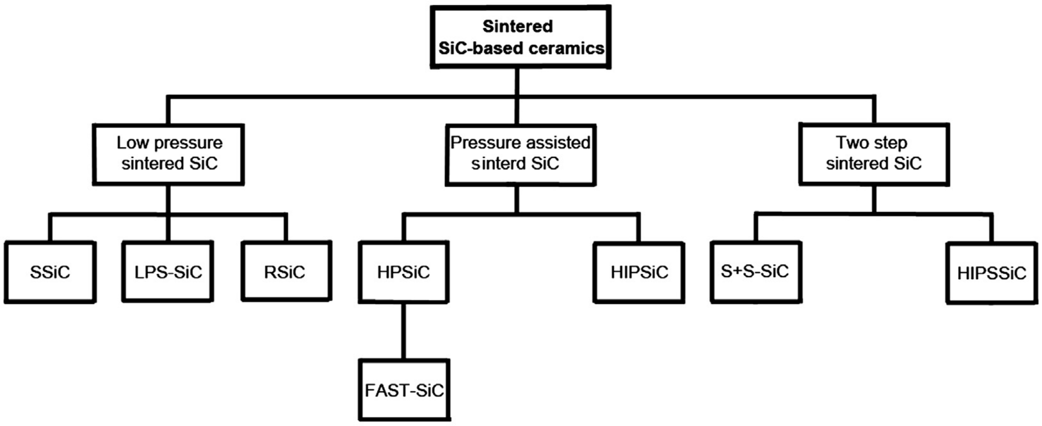

Figure 62 Classification of the sintered SiC-based ceramic corresponding to the applied consolidation techniques and sintering mechanisms, respectively.

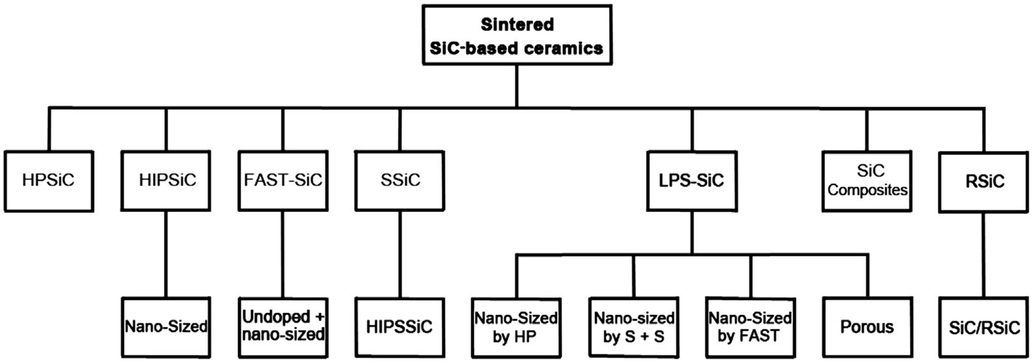

Figure 63 The sintered SiC-based ceramics classified according to the sequence in this subchapter.

has been paid to dense SiC-based ceramics first. The porous RSiC offers quite different applications; hence it was treated separately at the end of this subsection. A particular attention is devoted to the historical sequence of the ceramic materials and classes. The first dense SiC-based ceramic had been an HPSiC (Aliegro et al., 1956). That is comprehensible since it is easier to densify a difficult sinterable ceramic powder by a pressure-assisted technique than by pressureless sintering. Therefore the pressure-assisted sintering techniques were treated first in this subsection corresponding to their historical sequence. When SSiC was invented (Prochazka, 1973), the pressure sintering lost their significance noticeably, since it must have been regarded as extremely laborious. The main reason that pressure-assisted sintering techniques are still in use today is the fact that nanostructured ceramics can be verified by this techniques in a relatively problem-free way. It is surprising that even at the beginning of nanostructured SiC ceramics, a pressureless sintering method (S + S) became familiar (Lee et al., 2003). In Figure 63 the sintered SiC-based ceramics are listed corresponding to their sequence in this subsection.

2.04.4.3 Reaction Bonded Silicon Carbide-Based Ceramics

The consolidation techniques for SiC-based ceramics presented in previous subsections are based on the classical sintering process, which might have been modified through pressure-assisting techniques in order to achieve particular improved microstructures and related good properties. Sintering techniques are deeply rooted in ceramic tradition, since as people began manufacturing ceramics more than 10,000 years ago, they already had been using sintering techniques for these ancient materials. Sintering processes are governed by stochastic atomic site changes (diffusional motions) and surface or interface reactions. Typical chemical two-component reactions, however, are not characteristic for the sintering procedures.

In the second half of the twentieth century a consolidation phenomenon for ceramics became known, which controlled the ceramic bond as well, but was based upon two-component reactions anyway. Unfortunately, the designation for this phenomenon has not been uniformly fixed, which could be confusing sometimes for the newcomers of the ceramic technologies. The terms self-bonding, reaction sintering (RS), reaction bonding (RB) and reaction forming (RF) are most frequently used in literature. We will only use the term reaction bonding (RB) for this phenomenon and the term reaction bonded ceramics for the corresponding products. Though many reaction bonded ceramics have been created (Haggerty & Chiang, 1990), the most familiar one is still the reaction bonded silicon nitride (RBSN), which had been developed in the late 1950s (Par, Martin, & May, 1960; Popper & Ruddlesden, 1961). It has kept its high appreciation by materials scientists in spite of the loss of commercial relevance in recent years.

Reaction bonded ceramics include a broad materials category, thus they are not combined through collective properties and comparable processing procedures. But many of them consolidate with low-to-zero shrinkage. Hence, the corresponding manufacturing process has the potential of complex and large shapes with near net-shape capability. The nonshrinking consolidation has proved to be particularly advantageous for the manufacture of ceramic matrix composites (CMCs), since sinter densification cannot be achieved properly without pressure assistance for compositions with fiber contents of more than 10 vol.%. In addition, for pressure-assisted sintering of CMCs a significant amount of liquid phase is necessary in order to support relief sequence for shrinkage-induced stresses on the fibers. For many reaction bonding procedures the processing temperatures are much lower and sometimes the processing times are much shorter than for conventional sintering. This not only represents a significant commercial benefit but also enables the manufacture of some CMCs since many fibers are not stable at elevated temperatures.

2.04.4.3.1 Reaction Bonded Silicon Infiltrated Silicon Carbide

The reaction bonded silicon infiltrated silicon carbide (SiSiC) combines two consolidation procedures: infiltration of a primarily liquid phase into a porous structure and a reaction bonding. It belongs to a group of SiC-based ceramics which are consolidated by solid–liquid reactions. Generally a dried and debound (in nitrogen) green body ("preform") consists of commercial α-SiC powder and "carbon carriers" (graphite, carbon black and/or cracking substances of binder and lubricants), which is heated up above the melting point of silicon (1410 °C) in vacuum, where it is contacting a Si melt. For scientific investigations the usage of primary SiC is sometimes omitted (Hucke, 1983; Messner & Chiang, 1990; Wang, Tan, & Jiang, 2004). The Si melt soaks into the porous preform, driven by the capillary forces. The penetration is very fast due to both its good wetting characteristics for carbon and SiC and its low viscosity. The penetrating melt reacts with the contacting carbon particles to form SiC:

$$\mathrm{C_s + Si_l \leftrightarrow SiC_s} \tag{13}$$

Since the strongly exothermic reaction shows fast kinetics as well, the whole process is very rapid. It should be noted that it was assumed in early works (Forrest, Kennedy, & Shennan, 1972; Popper, 1960; Whalen, Noakes, & Terner, 1978) that secondary SiC generally should consist of the β-form. Later investigations, however, showed that the secondary SiC grown on the primary SiC consists of the same α-polytype. Only those secondary SiC grains with no contacts to the primary particles are composed of β-SiC (Ogbuji, Mitchell, Heuer, & Shinozaki, 1979; Page & Sawyer, 1980; Sawyer & Page, 1978). If, however, preforms were used, which did not contain primary SiC, only secondary β-SiC would be reprecipitated (Messner & Chiang, 1990).

The excess portion of Si melt, which is not needed for the reaction, fills the pores. Thus provided that the processing is optimized, a pore-free product can be manufactured. A typical SiSiC ceramic consists of SiC and 6–15 vol.% elementary silicon. **Figure 64** shows a typical microstructure of an SiSiC ceramic. The light areas represent elementary silicon and the dark ones primary and secondary SiC, respectively. Both components create an interpenetrating microstructure.

It should be mentioned that processing problems like thermal stress cracking often arise from too fast reaction rates. Therefore often a wick infiltration assembly is used, which is demonstrated in **Figure 65**. The graphite supports act as wicks for the infiltration, which control the rate of the infiltration and the amount of needed melt for the process.

During the liquid silicon infiltration (LSI) the exterior volume of the preform remains constant, but the new formation of SiC is associated with a volume increase. Hence, the secondary SiC grows into preexisting pores. Large pores support a complete infiltration but may result in a noncomplete chemical interaction and in formation of a structure with high residual elementary silicon and unreacted carbon. If the preform pores are small,

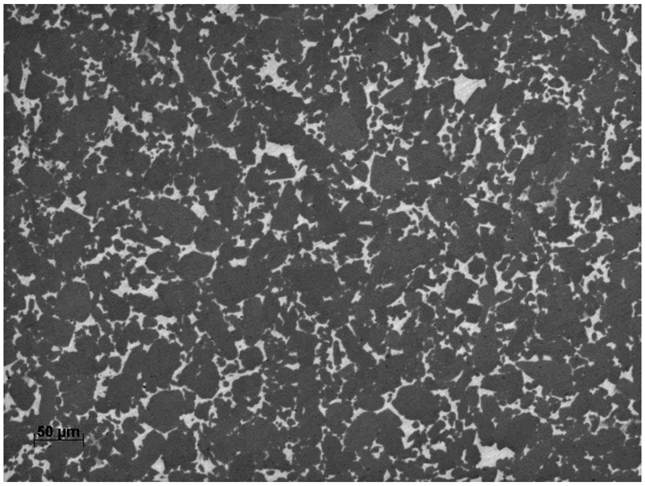

Figure 64 Light micrograph of SiSiC. This image was kindly transmitted by Schunk Ingenieurkeramik GmbH, Willich, Germany.

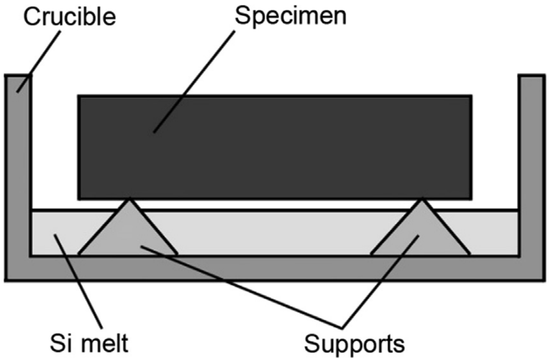

Figure 65 Wick infiltration assembly.

the chemical reaction will be complete but infiltration will be blocked due to chocking off the infiltration channels. In order to facilitate the infiltration of Si into the body, a certain amount of silica (quartz sand) can be added to the silicon in the crucible. When the silicon melts, some SiO is formed, which removes some carbon from the surface of the body by the following reaction

$$2C_s + SiO_g \leftrightarrow SiC_s + CO_g \tag{14}$$

and thus opens the surface-near pores (Forrest, Kennedy, & Shennan, 1970, 1972). Another way of removing the excess carbon from the surface area is a short-time heat up at 370–455 °C in an oxygen-containing nitrogen atmosphere before the infiltration process starts (Cohrt & Thümmler, 1985). In order to allow the reaction to take place completely and to prevent the pores from clogging through growing secondary SiC, the pore volume of the green body should be taken higher than needed for the volume growth induced by the reaction. Enough capacity can be achieved through the removal of the excess carbon from the interior of the body by annealing the bodies at 1540 °C in an oxygen-free nitrogen atmosphere with 0–10% hydrogen. As a result, nitrogen converts the SiO_2 into Si_3N_4, which will be decomposed through an additional annealing procedure in vacuum (Noakes, Sato, & Terner, 1978).

The final cooling down should be done slowly, because the slightly different thermal expansion coefficients of both solids Si and SiC in the microstructure could result in tensile stresses, which may cause cracking or at least form residual tensile stresses. Additionally it should be considered that silicon interacts abnormally with the adjacent SiC during solidification, since it solidifies with a volume change of 10% (Cohrt & Thümmler, 1985). This might result in induced tensile stresses especially when thick-walled parts are manufactured. After firing the excess silicon has to be removed through sandblasting with corundum, followed by the usual final machining.

The flow sheet of the processing route is comparable with the main line (with a single firing step) of the flow sheet of densely sintered SiC-based ceramics shown in Figure 43. Attempting to get better strength values, the usage of finer powders should be favored. However, fine powders are difficult to be densified, since as a result a large amount of free silicon is captured during siliconization. Further it should be considered that fine powders tend to agglomerate due to their high surface energy. Better green densities can be achieved with bimodal grain size distributions (Blecha, Schmid, Krauth, & Wruss, 1990).

It had already been mentioned above that raw material batches for SiSiC ceramics contains a large amount of "carbon carriers". Those shape-forming techniques are particularly favorable for the fabrication of SiSiC, which need a high amount of binder, like extruding, injection molding or tape casting. Here the binder simultaneously fulfills two requirements, facilitating the shape forming and delivering the required amount of carbon for the consolidation. For dry pressing the amount of binder is low (<3 wt.%), thus the composition should contain some carbon black in addition to the binder. More difficult should be slip casting, because usually such slurries do not contain binders and the carbon is difficult to distribute evenly in a dispersion agent, which normally is water. Slurries should contain bimodally distributed SiC particles as well, since coarser particles can be better stabilized in a slurry.

For SiSiC some interesting techniques had been developed to join parts together in order to manufacture large or complex shaped parts. SiSiC bodies can be soldered by depositing silicon or germanium on the joining surface first. The actual soldering process is conducted at temperatures above 1100 °C in vacuum and it takes only few minutes (Cohrt & Thümmler, 1985; Iseki, Yamashita, & Suzuki, 1981). For the preparation of diffusion bonding (Torti, Lucek, & Weaver, 1978) the joining surfaces have to be carefully plane grinded and pressed together. The diffusion bonding itself is conducted in vacuum or in protective gas at 1200 °C. The luting, the third method of joining, is conducted either by filling the junction between two reaction-bonded parts with the green mixture followed by a reaction siliconizing step or through joining and densification of the green bodies in a single step. Finally a joining method should be mentioned where a preceramic polymer (silicone resin) has been used at 800–1200 °C without applying any pressure (Colombo, Sglavo, Pippel, & Woltersdorf, 1998).

SiSiC is the most remarkable material from the processing point of view, since fully densification can be achieved without any shrinkage. This is only possible due to combination of infiltration and reaction bonding. Such a consolidation behavior is not possible with a sintering technique. Furthermore this is obtained at relatively low temperatures, thus the manufacture of SiSiC is quite cost efficient. So it is no wonder that presently SiSiC products are widespread throughout the world. Finally the siliconizing step can even eliminate shaping defects to a limited degree.

SiSiC was invented 50 years ago (Popper, 1960, 1966). The inventor Paul Popper belongs to the eminent pioneers of SiC-based ceramics at all like Edward Goodrich Acheson and Svante Prochazka. Additionally it should be mentioned that Popper was also trendsetting for silicon nitride ceramics. SiSiC was developed further at the United Kingdom Atomic Energy Authority (UKAEA) (Forrest et al., 1970, 1972) registered as trademark "REFEL".

Table 5 (Section 2.04.4.2) contains typical properties of SiSiC. They are often compared with the properties of SSiC because both materials started with their applications at almost the same time. In spite of higher densification the room temperature strength is a bit lower than that of SSiC. A laboratory SiSiC reached bending strength values up to 700 MPa, for which uniform microporous carbon preforms were used derived from organic precursors in order to obtain finer grained microstructures (Hucke, 1983). At high temperatures, the principal deficiency is a marked degradation in strength. The silicon component in SiSiC starts to become soft due to impurities before reaching the melting point. Additionally the silicon starts to exudate at about 1300 °C. Thus conventional SiSiC should not be applied at temperatures above 1300 °C.

Like all covalently bonded materials silicon is highly inert, even against hydrofluoric acid. However, it will be dissolved in diluted alkali lyes to form silicates. SiC is resistant against all kinds of acids and lyes. Therefore the application of elementary silicon containing SiSiC is restricted to $\mathrm{pH} = 10$, unlike SSiC. Apart from this restriction SiSiC has the same application field than SSiC for structural applications. **Figure 66** shows a counter ring of SiSiC for a mechanical seal. They do not differ visibly from SSiC rings. Since the nonshrinking consolidation of SiSiC allows the manufacture of large parts, the SiSiC processing is also used for the production of kiln furniture like beams, saggars, plates, frames, covers and supports, respectively. It should, however, be regarded that—as mentioned in the previous paragraph—ordinary SiSiC cannot be used at real high temperatures.

Figure 66 Counter ring of SiSiC for a mechanical seal. This image was kindly transmitted by Schunk Ingenieurkeramik GmbH, Willich, Germany.

Besides liquid siliconization in vacuum it is also possible to infiltrate via vapor phase in argon at temperature at about 2000 °C. Wang et al. (2004) demonstrated through comparative investigations that Si vapor infiltration can lead to deeper infiltration than Si liquid infiltration. They achieved the best result with vapor infiltration of porous carbon prefoms. The resulted SiSiC exhibiting 8 vol.% Si had a density of 3.12 g cm^{-3} and a bending strength of 630 MPa.

In this context, it is noteworthy to mention that an antecedent exists for SiSiC since RSiC has been impregnated with a liquid organic resin, carbonized chemically or via pyrolysis and finally heated in a silicon containing atmosphere at temperatures above 2200 °C (Taylor, 1965).

In order to improve the high-temperature properties many approaches had been performed to replace elementary silicon by refractory components. Lim, Yano, and Iseki (1989) were the first, who offered a solution to the problem. They first manufactured common SiSiC, and then they evacuated the silicon at 1600 °C and infiltrated the resulting pores by molten $MoSi_2$. This manufacturing process, however, involved high temperatures since $MoSi_2$ has a melting point of 2020 °C. The temperature could be reduced considerably (to 1625 °C), when alloyed silicon infiltrants were used (Chakrabarti and Das, 2000; Chiang and Messner, 1992; Messner and Chiang, 1988, 1990). During the reactive formation of SiC the solutes are reacted into the remaining melt enriching it until a precipitation of a refractory silicide occurs. For an Si–Mo melt system the reaction is

$$(x + 2y)\mathrm{Si} + y\mathrm{Mo} + x\mathrm{C} \leftrightarrow x\mathrm{SiC} + y\mathrm{MoSi_2} \qquad (15)$$

By infiltration of Si–Mo melts infiltration depth of >10 mm could be achieved with relative densities of >90%. The Si melt was completely replaced by the refractory and oxidation-resistant $MoSi_2$. Similar results had been obtained with alloyed Si–Nb (Singh & Behrendt, 1994) and Si–Ta (Simmer, Xiao, & Derby, 1998) melt systems to produce both disilicides Nb_2Si and Ta_2Si precipitated reaction bonded SiC ceramics, respectively. The elementary silicon, however, had not been completely removed.

The requirements in the aerospace technology originally only affected the evolution of the ceramic matrix composites (CMCs; fiber-reinforced ceramics) (Fitzer & Gadow, 1986; Gadow, 1986; Krenkel & Hald, 1989). In recent years the properties and manufacturing techniques have been consistently further developed so that they are broadly applicable across other branches of industry as well. The potential for marketable products is high. However, even today the CMCs are only involved in niche applications, because its manufacturing, in particular its tooling, induces high costs.

The CMCs differ from all other composites in their microporous and cracked matrix. On the one hand, a fully dense matrix cannot be realized due to process related reasons. On the other hand, due to the different thermal expansion behaviors of fiber and matrix, microcracks arise in the ceramic matrix during the cooling down period of the manufacturing process or at least in the application. Microcracks give rise to an open porosity, which may be up to 20% depending on the processing and on the fiber architecture (Krenkel, 2003). Compared to structural metals, CMCs must be regarded as relatively brittle. Compared to monolithic (untoughened) ceramics (0.1%), however, the breaking strain of CMCs might be one order of magnitude higher (1.0%). Hence, this higher breaking strain combined with the non-linear-elastic stress–strain behavior enables the CMCs to act as structural ceramic materials with quasi-ductile fracture behavior. Because of their low material densities, CMCs offer mass-specific strength values above 1000 °C which cannot be achieved by any other structural material (Krenkel, 2003).

Generally the properties of ceramic materials strongly depend on their microstructure and on its manufacturing process. This statement, however, applies to CMCs in particular, since the microstructures can be altered in many ways, which results in a wide diversity in terms of properties and application fields.

2.04.4.3.2 Carbon Fiber Silicon Carbide Matrix Composites via Liquid Silicon Infiltration (LSI-C/SiC)

The liquid silicon infiltration (LSI) is considered the most promising technique for a future large-scale production of CMCs. Through the variation of process parameters the properties of the corresponding carbon fiber silicon carbide matrix composite (C/SiC) can be optimized for special applications in a targeted fashion or can alternatively be adjusted for a wide range of applications. The main expectations, however, are grounded in sound economic analysis. Figure 67 schematically shows the manufacturing process of LSI-C/SiC exemplarily demonstrated for a two-dimensional (2D) woven fabric structure (Müller, 2001). The three production steps are only once passed through during the production line, which involves short processing and kiln occupancy periods. The material costs are relatively low, since commercially available C fibers and resins can be applied (Krenkel, 2003).

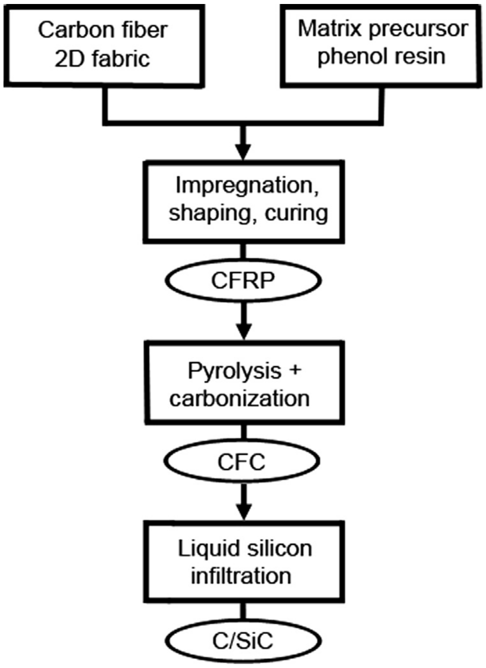

Figure 67 Flow sheet of the processing route of LSI-C/SiC With a 2 D woven fabric.

The first step of processing is the manufacture of carbon fiber-reinforced plastic (CFRP). Though the properties of the resulted C/SiC can be improved through the application of finer C fiber fabrics, often the coarser variants are preferred since both the price for fine fabrics and the work input for their processing in the fabrication line of the composite bodies are high. Usually fibers are chosen on the basis of high tensile stresses (HT fibers). These fibers are produced on the basis of polyacrylonitrile, which pass the production process at lower temperatures than those high-modulus fibers (HM) and thus reduce the fabrication costs of the C/SiC.

Suited matrix precursors are phenol resins because of their high carbon yield (55–65%) and low price. Phenol resins of the type novolac require the addition of a curing agent like hexamethylenetetramine.

The CFRP green bodies are achieved through liquid-phase impregnation of the fiber fabrics. The processability of the resin solution, i.e. the ability of fiber wetting, is improved when its viscosity is low. On the other hand, there is a risk that too little resin spots adhere to the fibers. The layed-up preimpregnated fiber fabrics (prepregs) are molded for instance through winding or stacking. The complete fusion of the resin requires temperatures above 100 °C. At 120 °C the crosslinking reaction starts with increasing viscosity. During the curing procedure the stacks are pressed together at pressures of 20 MPa. The curing temperature is about 200 °C. The whole curing process takes about 12 h (Müller, 2001).

The next processing step (pyrolysis + carbonization) results in the formation of the CFC or C/C preform, where the conversion of the cured phenol resin to glassy carbon occurs. Actually the decomposition of resin should give rise to large shrinkage. A free three-dimensional shrinkage, however, is not possible, since the carbon fibers reduce the shrinkage in axial direction due to their dimensional stability. This one-dimensional shrinkage reduction is partly compensated through a more significant shrinkage in the two other directions (Müller, 1998). The complex shrinkage behavior results in a characteristic crack pattern within the fiber bundles. If the fiber/matrix connection in the CFC preform is not too high, the cracks will be deflected along the fiber surfaces and thus should not damage the preform. They should rather cause a positive effect for the further processing, since it opens up access of the silicon melt to the inner regions of the preform for the subsequent infiltration process. Pyrolysis and carbonization is conducted between 850 and 1000 °C through rinsing with protective gas in order to facilitate the removal of pyrolysis products.

The final step, the LSI, is carried out in vacuum between 1450 and 1650 °C. Table 6 shows a typical characteristic parameters measured by Müller (2001) for each processing step. Noteworthy are the large noncontinuous density and porosity changes between the steps. It should additionally be mentioned that the radial dimensional changes are only small.

Table 6 The change of typical material parameters for 2-D C/SiC processing steps depending on temperature

Step	*Temperature (°C)*	*Density (g cm^{-3})*	*Fiber volume (%)*	*Porosity (%)*
CFRP	190	1.53	69	7
CFC	900	1.37	68	18
C/SiC	1550	2.10	ca 70	4

(Müller, 2001).

There is a great and an unsolved problem concerning the LSI. It cannot be expected that the liquid silicon will only react with the glassy carbon. There will also be an implementation of the carbon fiber as well. It is not conceivable that the fibers transform completely to secondary SiC, but they are definitely damaged by this reaction. Additionally it results in a strong adhesion between fibers and matrix so that pull-out effects, largely responsible for damage tolerance of CMC ceramics, will be prevented or at least impaired. As a consequence, a brittle fracture behavior usually typical for untoughened ceramics will occur accompanied by a low strength level. The portion of damaged fibers must not be too high in an LSI-C/SiC, since otherwise the advantage of CMC over full-ceramic SiC disappears (Müller, Mentz, Buchkremer, & Stöver, 2001). Therefore the CMC matrix generally consists not only of pure SiC and load-bearing carbon fibers but also of excess elementary silicon and of some unreacted carbon. Hence, some scientists designate these CMCs as C/C-SiC ceramics (Krenkel, 2003). Figure 68 shows a three-dimensional computer-tomography image of a 2D C/SiC microstructure. It demonstrates the anisotropic and heterogeneous mounting of the microstructure.

In principle there are some processing options to protect the carbon fibers from damage. The fiber can be coated by pyrolythic carbon (PyC) from gaseous precursors (Savage, 1993). Thick layer could as sacrificial layers protect the fibers against the attack of liquid silicon. Even better are coatings of SiC or BN, deposited from the gas phase (CVD). It should be beared in mind, however, that the main advantage of LSI, the low process cost level, disappears through the application of elaborated CVD techniques.

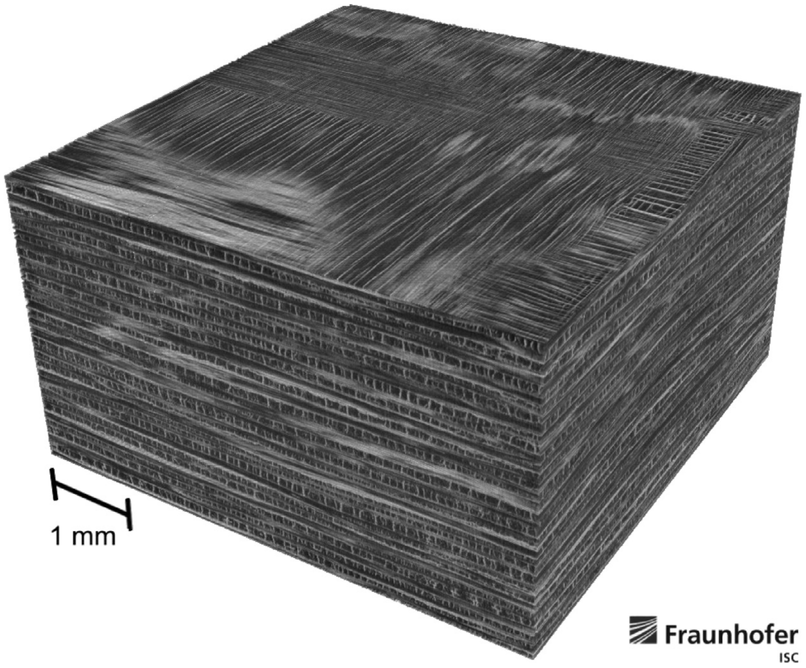

Figure 68 CT-image of a 2D LSI-C/SiC microstructure. This image was kindly released by Walter Krenkel from Fraunhofer Center Lightweight Materials and Design, Bayreuth, Germany, holding the copyright.

Figure 69 Carbon ceramic brake disc. This image was kindly transmitted by Brembo SGL Carbon Ceramic Brakes GmbH, Meitingen, Germany.

Finally it should be mentioned that LSI-C/SiC achieved an essential breakthrough for commercial civil applications by the insertion of ceramic high-performance brake disc for some automotives like Porsche and Mercedes (Krenkel, 2002; Wüllner, 2003; Zuber & Heidenreich, 2006). These usually designated carbon ceramic brake discs (Figure 69) are saving more weight and have longer durabilities than conventional cast iron discs. The carbon fibers are chopped for the corresponding processing route in order to facilitate the shape forming by using a simple axial pressing technique. Carbon ceramic brake disc could also be useful for high-speed trains.

Most damage-tolerant CMCs have relied on a “weak” interphase between fiber and matrix (strong matrix/weak interface concept). The role of the interface is to induce debonding and sliding effects, which permits dissipation through internal friction, leading to flaw-tolerant behavior (Evans & Marshall, 1989). The new concept is based on flaw tolerance through a strong interface but a weak matrix (Tu et al., 1996). At the end of previous subsection two approaches were described for CMCs with RSiC matrix, one was based on the weak interface concept and the other on the weak matrix concept. Another approach of the new concept is demonstrated in the next paragraph.

2.04.4.3.3 Carbon Fiber Silicon Carbide Matrix Composites via Internal Siliconization (IS-C/SiC)

Like the LSI-C/SiC concept the internal siliconizing approach (Müller, 2003) uses liquid silicon. The carbon matrix of CFC body was formed through the common pyrolysis of the precursor (usually phenol resin). Fine Si particles had been dispersed in the resin solution, which had been—as described above—impregnated into the fiber preform. During the subsequent pyrolysis the dispersion of Si filler particles could be maintained, since the pyrolysis is running only in the solid state. The final step, the reaction bonding was done according to the LSI route, though actually no infiltration had taken place. A damage of fibers could be avoided by this internal siliconizing concept. But unfortunately the fiber matrix bond was too low and the matrix porosity too high to achieve high bending strength and interlaminar shear strength values.

2.04.4.3.4 Silicon Carbide Fiber Silicon Carbide Matrix Composite via Liquid Silicon Infiltration (LSI-SiC/SiC)

The ceramic matrix composites have been developed for the use at elevated temperatures. But it should be regarded that the carbon fiber and the residual glassy carbon have a low oxidation resistant. To improve the oxidation resistance, the carbon fiber could be replaced by SiC fibers. But since silicon is wetting SiC as good as carbon, the risk of to strong bond between fiber and matrix is involved for SiC fibers as well.

The activity of the melt may be influenced by doping. Hagerty and Chiang (1990) argue that aluminum should retard the reaction rate. Singh, Dickerson, Olmstead, and Eldridge (1997) used a silicon alloyed with a slight amount of Mo as a melt infiltrant instead of pure silicon in order to achieve both a reduction of the activity of silicon in the melt and a reduction of the amount of elementary silicon in the matrix. They use

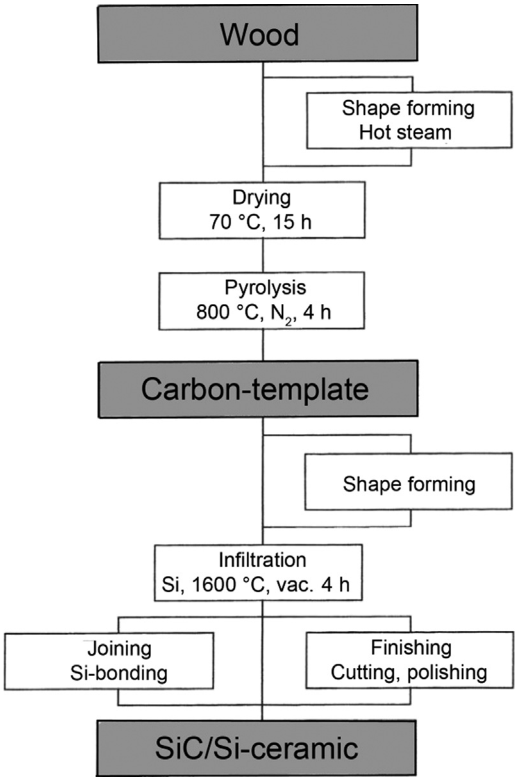

Figure 70 Flow sheet of cellular SiC ceramic (SiC/Si) from wood via LSI.

unidirectional SiC fiber (SCS-6) tapes for their ex situ toughening. Those fibers have an outer carbon-rich coating applied by the manufacturer. The authors demonstrated that the fibers did not need an additional interfacial coating on the SiC fibers. The minimal damage to the fiber coating had been attributed to the structure of the precursor carbon in the performance. Hence most of the "weak" coatings could survive and allow the debonding of fibers.

2.04.4.3.5 Biomorphic SiC/Si Ceramics

Biomimetics (also known as biomimicry, bionics, bioinspiration and biognosis) refers to the transformation of in-nature proven systems and functional principles toward the design of engineering systems. Biomorphic SiC-based ceramics with an anisotropic pore structure can be manufactured from natural wood. The pyrolysis of wood induces the thermal decomposition of the polyaromatic biopolymers. A carbon body (charcoal) is generated, which reflects the anatomy of the starting wooden body. The carbon body may act as a shape forming tool (template) for various reaction processes. For instance the liquid vacuum infiltration of an oak template with tetraethyl orthosilicate and subsequent annealing at 1400 °C formed an SiC skeleton. Since the yield of this conversion was low, the procedure had to be repeated several times (Ota et al., 1995). A better conversion can be achieved by LSI or Si vapor (de Arellano-López et al., 2004; Greil, 1999; Greil, 2001; Greil, Lifka, & Kaindl, 1998; Kaindl, 1999; Sieber, Kaindl, Schwarze, Werner, & Greil, 2000).

Figure 70 shows the flow sheet of cellular SiC ceramic (SiC/Si) from wood via LSI (Greil, 1999). The starting wood is dried after shape forming (e.g. via hot steam procedure). The formation of the carbon template is achieved through pyrolysis. The pyrolysis temperature may vary between 800 and 1800 °C depending on the kind of wood used. The selected temperature is particular significant for the molecular structure of resulting template, which may influence the wetting behavior of the Si melt. The infiltration is conducted after cutting-shaping process where required. The infiltration process may be used for joining two parts together. The processing is concluded by surface finishing or by acid leach of residual Si in order to generate a body with a definite porosity.

An alternative method to the conventional powder-ceramic processing route is the application of wood flour as starting powder (Schmidt & Aoki, 2006), which should be cost-effective compared to ceramic powders.

The base mixture may contain carbon fiber and powder as fillers and a phenol resin. Mixtures are axially pressed at 170 °C with pressures of 15 MPa to achieve a green density of 0.8–0.9 g cm^{-3}. The further processing steps are comparable to those procedures outlined in the previous process (pyrolysis and Si infiltration), respectively. The resulting biomorphic plates reach relatively high bending strength values (300 MPa) and high Young's moduli (385 GPa). The various grades mainly differ from each other in the amount of free carbon.

Paper can also be used as a preceramic precursor material for biomorphic SiC/Si ceramics (Greil, 2005; Kollenberg & Travitzky, 2010; Travitzky, Windsheimer, Fey, & Greil, 2008). After shaping (pleating, minting, winding and laminating) the paper is pyrolyzed between 300 and 900 °C to obtain the carbon templates, which are infiltrated via LSI or Si vapor. Similar complex structures can be achieved as through tape casting (compare Figures 58 and 59).

The next group of SiC-based ceramics refers to materials in which gas-phase reactions result in the formation of new solid phases.

2.04.4.3.6 Nitride Bonded Silicon Carbide

In the first treated material the SiC particles are silicon nitride bonded (Fickel & Völker, 1988), which is closely related to the well-known gas-phase reaction bonded silicon nitride (RBSN) (Moulson, 1979).

A shaped green body containing a mixture of relatively coarse SiC particles and elementary silicon is fired at 1400 °C in nitrogen atmosphere. The reaction between silicon and nitrogen results in formation of Si_3N_4 whiskers

$$3Si + 2N_2 \rightarrow Si_3N_4 \tag{16}$$

probably attributed to the VLS mechanism (Gribkov, Silaev, Shchetanov, Umantsev, & Isaikin, 1972). As catalyst for the VLS mechanism might act elementary Fe, which is usually present in silicon. It should be noted that the VLS mechanism for Si- and SiC whiskers had already been described in connection with Figure 8 in this article. The principle of the evolution of nitride bonded silicon carbide (NSiC) is demonstrated in Figure 71 according to a two-particle model. Figure 72 shows the microstructure of NSiC developed in our laboratory (Müller, 2000).

Table 5 (Section 2.04.4.2) contains the properties of commercial NSiC. In view of implementing application task for NSiC its properties should be compared with the properties of RSiC. The comparison illustrates that NSiC seems to be superior to RSiC in nearly every respect. This obvious predominant NSiC and the markedly lower firing temperature are the reasons that NSiC is more and more replacing RSiC as high-temperature-resistant kiln furniture (Figure 54). For the production of NSiC kiln furniture usually slip casting is used as shape-forming technique. For the improvement of the oxidation resistance the kiln furniture parts generally are briefly preoxidized at 1200 °C to form silica protective layers on their surfaces. For kilns for firing porcelain or sanitary ware the plates should be covered by zirconia or zirconium silicate containing engobes.

2.04.4.3.7 Chemical Vapor Deposited Silicon Carbide

CVD belongs to reaction bonding processes, where solids are formed through deposition from the vapor phase. Through CVD solid compounds are deposited via a chemical reaction in a vapor phase. A CVD device consists of three components: gas supply, reactor, and gas disposal.

$$A_g + B_g \rightarrow C_s + D_g. \tag{17}$$

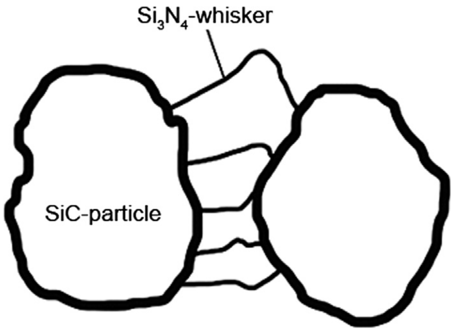

Figure 71 Bonding in NSiC.

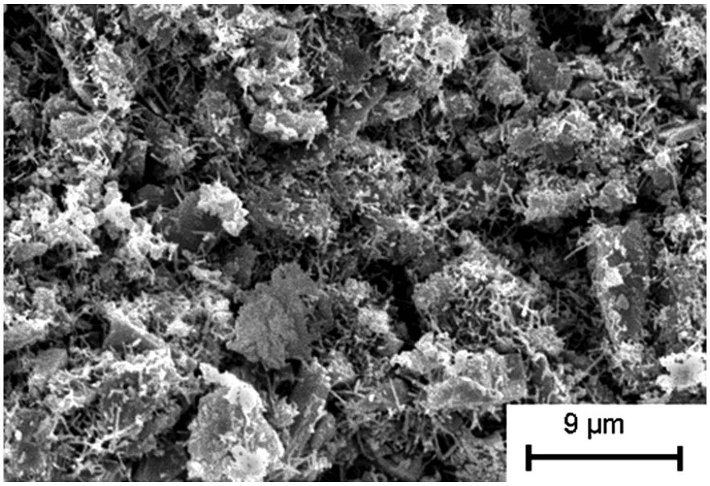

Figure 72 SEM micrographs of fracture surfaces of NSiC. The copyright of this image is held by the author of this article.

The basic principle of CVD is schematically shown in Figure 73. Usually two hot-reactant gases A_g and B_g and a carrier gas are piped into the reaction space (reactor), where the reactant gases react with each other, the solid reaction product C_s is deposited at particularly hot areas (typically at hot surfaces of substrates) and gaseous reaction product are disposed together with the exhaust gases. If there is not any hot substrate in the reactor but only a special hot gaseous region, powder particles are generated as solid deposition products. The SiC powder synthesis by several CVD methods had been treated in Section 2.04.3.1 and the preparation of SiC fibers via the CVD method in Section 2.04.3.2. Normally the CVD technique is used for generating coatings for functionalizing substrate surfaces. But the matter of interest here should not be the manufacture of coated layers but the manufacture of a monolithic material. Thus if the deposited material should be used in a self-contained way as a (thin walled) material, it has to be removed from the substrate.

For the manufacture of chemical vapor deposited silicon carbide (CVD-SiC) several reactant gas combinations are possible. Vaporized methyltrichlorsilane (MTS) as single reactant is a preferred precursor for depositing stoichiometric SiC, because the 1:1 atomic ratio of silicon and carbon (Carter, Davis, & Bentley, 1984; Choi, Park, & Kim, 1997; Galasso, 1991; Lohner, 1999):

$$CH_3SiCl_{3g} \rightarrow SiC_s + 3HCl_g \tag{18}$$

Hydrogen (H_2) is commonly used as carrier gas. The graphite substrate can be taken for the ohmic resistance heating in order to get a cold wall type reactor at about 1400 °C (Wang, Sasaki, & Hirai, 1991). Additionally graphite is a preferential substrate material for CVD-SiC since the soft graphite can easily be ground away.

Alternative substrates for the manufacture of CVD might be silicon wafers, because silicon might easily be etched by HF/HNO_3. This technique (for deposition temperatures up to 1300 °C) was used to generate both SiC and Si–SiC hybrid microengine structures via positive, negative and hybrid mold configurations by selectively dissolving the silicon for microelectromechanical systems (Lohner, 1999; Lohner, Chen, Ayon, & Spearing, 1998).

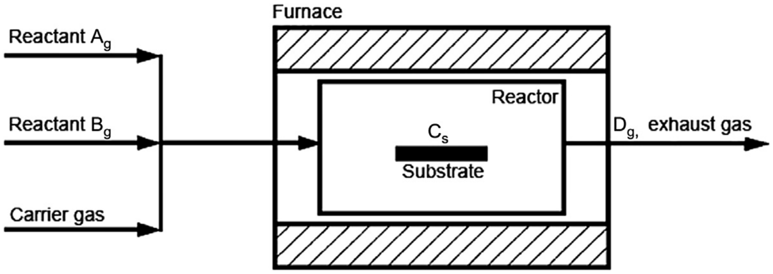

Figure 73 Scheme of a common CVD device for the reaction.

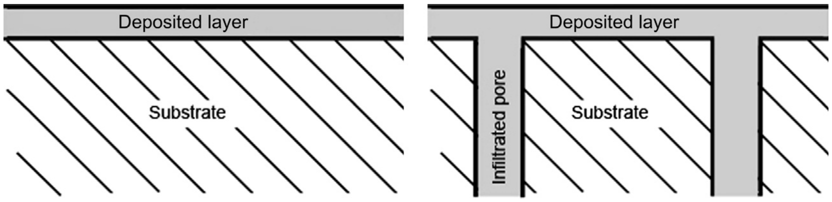

Figure 74 Difference between CVD (left) and CVI (right).

CVD-SiC can be manufactured up to theoretically density exhibiting high purity (>99.9995%). For this reason this polycrystalline β-SiC ceramic (mean grain size 5 μm) has some outstanding properties being compiled in Table 5 (Section 2.04.4.2) like extremely high thermal conductivity and Young's modulus. The bending strength (with transgranular fracture mode) even increases with increasing temperature. Laboratory mean bending strength values reach 724 MPa (Lohner, 1999).

Compact CVD-SiC parts are used for packages of electronic components, as elements for wafer treatments, kiln furnitures for the diode manufacturing and substrates for computer hard disks. CVD-SiC plates can be polished to flatnesses down to 0.3 nm (Hirai & Sasaki, 1991).

The chemical vapor infiltration (CVI) applies CVD reactions. The difference between CVD and CVI is shown in Figure 74. The substrate for CVD coating is a dense material, thus a layer is deposited on its surface only. For CVI the vapor species should not only be transported to the surface of the substrates, where a layer is deposited, but also via channel pores to the interior of the ceramic preform material in order to be deposited on its pore walls. It is intrinsically difficult to achieve a uniform deposition on the pore walls without clogging the pores.

2.04.4.3.8 Carbon and Silicon Carbide Fiber Silicon Carbide Matrix Composites via Chemical Vapor Infiltration (CVI-C/SiC; CVI-SiC/SiC)

The CVI-technique is commonly used for the manufacture of SiC-based CMCs. The porous preform typically is made from reinforcing C or SiC nD-fiber fabrics (with $n = 2, 3, 4$), the deposited SiC from an MTS precursor forms the matrix corresponding Eqn (18). With pyrolythic carbon (PyC) or boron nitride (pBN) precoated fiber fabrics should be used for achieving better toughening during the loading of the related CMCs due to fiber debonding from the matrix and enhanced pull-out effects.

There are different versions of CVI processes available (Naslain, Langlais, Vignoles, & Pailler, 2008; Xu & Yan, 2010, pp. 165–214). The isothermal-isobaric CVI (I-CVI) is the most commonly used type (Fitzer & Gadow, 1986; Gadow, 1986; Lamicq, Bernhart, Dauchier, & Mace, 1986; Rossignol, Langlais, & Naslain, 1984). The preform is kept at uniform temperature and the reactant gases are supplied to the preform at uniform pressure. The CVI process is very slow due to the low diffusion rate. In the temperature gradient CVI device (TG-CVI) the vapor precursor is transported through the preform from the colder surface to the hotter inside areas (Kulik, Kulik, Ramm, & Makarov, 2004). The corresponding temperature gradient enhances the diffusional motion of the gas. The precursor preferentially decomposes in the hot inner areas, since the reaction rate is higher at higher temperatures. TG-CVI permits a better and more uniform densification of the ceramic preform due to preventing an early pore clogging. The isothermal-forced flow CVI device (IF-CVI) utilizes a pressure gradient of the gas pressure penetrating into the uniformly heated preform (Roman, de Croon, & Metselaar, 1995; Roman, Kotte, & de Croon, 1995). The rate of the interior deposition is increased through the enhanced motion of the forced reactant gas species. The thermal gradient-forced flow (F-CVI) combines the effects of the latter two devices (Igawa et al., 2002; Wang, Tang, & Chen, 2008). The temperature gradient in the performance is achieved by heating the top region while cooling down the bottom region at the same time. The pressure gradient can be measured by the pressure differences between incoming and leaving gases. Compared to the conventional I-CVI, where the process period takes several weeks, the process period of F-CVI can be reduced to less than 24 h and the filler load degree can be enhanced to over 90%.

As a general rule, CVI represents the most effective process to manufacture CMCs with excellent properties and potentials. Hence the stoichiometry, the crystal orientation and the morphology of the deposit can be manipulated. High purity levels can be achieved for the deposit. Low infiltration temperatures result in low residual stresses and low fiber damage. An important feature is the absence of matrix shrinkage around the dimensionally reinforcing fibers. Technologically advantageous is the fact that complexly shaped preforms can be used. It should, however, not be overlooked that CVI has some inherent problems to the process, which are rather significant: the reactants are expensive, corrosive, toxic and explosive and the deposition rates are generally low.

2.04.4.3.9 Biomorphic SiC Ceramics by Chemical Vapor Infiltration (Biomorphic CVI-SiC)

Recently the CVI method has been used to convert preceramic precursors (especially papers) via MTS to biomorphic SiC ceramics (Streitwieser, Popovska, & Gerhard, 2006).

2.04.4.3.10 Carbon Bonded Silicon Carbide

The synthesis of ceramic materials via pyrolysis is often regarded as a new processing route. However, the group which should be mentioned here first is a traditional refractory product. The origin of the carbon bonded silicon carbide (CSiC)-based ceramics could not find out by the author of this article, but it can be assumed that the corresponding ceramics already emerged shortly after Acheson's invention. CSiC is an important product with a considerable market share even today. It can predominately be regarded as an in situ formed *c*arbon based ceramic with an SiC filler. **Figure 75** shows a CSiC crucible, which might be more than 1 m high.

The raw materials, graphite and relatively coarsely grained SiC powder, are mixed with pitch and other suitable synthetic resins (e.g. phenol resin) in counter flow intensive mixers, double arm kneaders or ploughshare mixers. The pitch resin compound should be warmed up to a temperature level above its softening temperature (200–400 °C) either during or before the mixing procedure. The shape forming techniques are isostatic pressing or pressing with pneumatic rams by hand. During the pressing operation the mixture should be kept in uniform hot condition in order to avoid manufacturing defects. The firing is carried out in shuttle kilns. The maximum firing temperature is about 1350 °C for carbonizing and pyrolyzing the binder. For the creation of an appropriate "reducing" atmosphere the green crucibles are usually placed into saggars tightly packed with reducing agents such as coke dust or graphite powder. During the firing process the crucible will shrink depending on the amount of binder in the starting mixture, since the weight loss of the binder is between 30% and 40%. For the protection against oxidation the crucibles might be glazed. It should be noted that the pitch derived carbon has a surprisingly high oxidation resistance for a carbonaceous material.

Table 5 shows some available properties of CSiC. The crucibles (**Figure 72**) used for melting nonferrous metals such as brass, copper, nickel, chromium as well as their alloys due to their good resistance to wetting to molten metals combined with a good thermal conductivity, low thermal expansion and good resistance against thermal shocks.

2.04.4.3.11 Polymer-Derived Silicon Carbide

An extension of the polymer pyrolysis route of pitch based raw material components to carbon-rich materials is the pyrolysis of polymers containing additional inorganic components (element organic polymers, inorganic polymers, hybrid polymers) like silicon to manufacture in situ generated nonoxide ceramics including those

Figure 75 Carbon bonded SiC crucible with spout. This image was kindly transmitted by Morgan Molten Metal Systems GmbH, Berkatal-Frankenhain, Germany.

here only considered SiC ceramics (Rice, 1983; Riedel, 1992; Riedel & Dressler, 1996; Riedel, Passing, Schönfelder, & Brook, 1992; Wynne & Rice, 1984). The corresponding polymer-derived SiC (PD-SiC) is one of the so-called polymer-derived ceramics (PDCs). It had been demonstrated in the previous subsection, that the manufacture of SiC rich ceramics generally requires temperatures of more than 1800 °C. Thus the main goal of monolithic PD-SiC evolution had been the manufacture of dense SiC ceramics at much lower temperatures.

In the first step of PD-SiC manufacture monomer element organic compounds (precursors) are converted to oligomer or polymer intermediates (Burkhard, 1949) through a reduction reaction:

$$(CH_3)_2SiCl_2 + Na/K \rightarrow \left[(CH)_3Si\right]_n \tag{19}$$

In the second step the polymer is converted to preceramic materials; this process is generally called "ceramization":

$$\left[(CH)_3Si\right]_n \xrightarrow{1200\ ^\circ C} SiC + CH_4 + H_2 \tag{20}$$

The latter conversion starts above 400 °C and is concluded at about 1200 °C. The separation of gaseous species is associated with high shrinkage and a strong increase of densification. At the end of decomposition the thermodynamically stable crystalline SiC (β-SiC) is not generated but rather metastable amorphous solids (preceramic material) form. The crystallization often occurs far above 1000 °C (Riedel, 1992). Relatively dense SiC ceramics without cracks could be achieved at firing temperatures of 1000 °C (in argon) by this powder-free method. The grain sizes of the pyrolytically based SiC ceramics are partly in the nanosized range exhibiting narrow size distributions.

The synthesis of ceramic materials via pyrolysis of polymer precursors has led to great interest among the researching ceramists. The researchers used a wide range of polymers to generate covalent bonded compounds such as silicon nitride (Si_3N_4), aluminum nitride (AlN), BN, B_4C and primarily SiC in fibrous, bulk or even ceramics form.

The polymer pyrolysis route has a difficult set of processing issues. Hence problems may arise through the huge shrinkage, which is understandable, if one remembers that the starting precursors have a density far below 1 g cm^{-3}, whereas SiC has a theoretical density of about 3.2 g cm^{-3}, and through the volume decrease due to both material change and gas loss, which is more than 50% during the thermal treatment. The shrinkage can cause cracking and the gas loss may leave poorly distributed pores behind. The loss of large mass fraction is also the reason for reduced yields from generally expensive reactants. It is sometimes difficult to retain the as-formed shape throughout the pyrolysis steps, since the polymers become low viscous. Shape stabilization can be achieved either by crosslinking the polymer before the pyrolysis is started (Atwell, Hauth, Jones, Langley, & Arons, 1987) or by producing oxide skins (Rice, 1983; Wynne & Rice, 1984). Furthermore it is unlikely that the polymers will leave constituent elements in precisely stoichiometric ratios, thus the pyrolysis products are inclined to be amorphous.

The polymer-derived fabrication route has, however, also some additional advantages besides the low-temperature requirement compared to the traditional powder route. For instance monomer and polymer starting materials can be prepared with a high degree of purity. Additionally the method had been successfully used to fabricate fibers (Yajima et al., 1978), which had been described in Section 2.04.3.2, and finally it is applied for the manufacture of C- or SiC–fiber-reinforced ceramics, which is characterized in the next paragraphs.

2.04.4.3.12 Carbon and Silicon Carbide Fiber Silicon Carbide Matrix Composites via Liquid Polymer Infiltration (LPI-C/SiC; LPI-SiC/SiC)

In this subsection two alternative methods had already been described for the production of C/SiC or SiC/SiC ceramic matrix composites exhibiting dense matrices. For the third method a liquid element organic precursor is impregnated into the porous perform consisting of reinforcing C or SiC nD-fiber fabrics (with $n=2, 3, 4$) followed by pyrolysis (Fitzer & Gadow, 1986; Gadow, 1986). The method is usually called liquid polymer infiltration (LPI) or polymer infiltration and pyrolysis.

Figure 76 shows the flow sheet of the fabrication of CMCs with 2D fiber fabrics using the LPI method (Schmitz, 1993). The start of the procedure resembles the start of the processing route of the LSI CMCs (Figure 66), since it begins with the fabrication of a prepreg (preimpregnated body) as well followed by shape forming (laminating), curing and pyrolyzing of the performances. As already reported above, the pyrolysis of

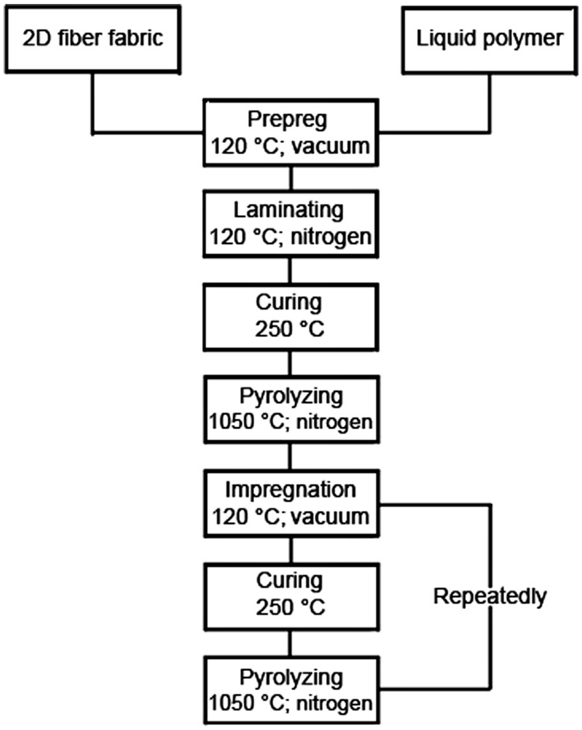

Figure 76 Flow sheet of the processing route of LPI-C/SiC and LPI-SiC/SiC with a 2D woven fabric.

"element organic" polymers is accompanied with large loss of mass fraction. Thus, the processing of CMCs via liquid polymer infiltration is an extremely labor-intensive process with a high consumption of expensive materials, since the pyrolyzing cycle has to be repeated several times to get a sufficiently dense CMC. The laboratory scale fabrication of single LPI-SiC specimen can take more than a couple of weeks (Schmitz, 1993).

In order to achieve a real tough LPI-SiC/SiC PyC or pBN precoated fiber fabrics should be used. To demonstrate the significance of this statement, two fracture surfaces of LPI-SiC/SiC specimens containing Hi-Nicalon™ fiber fabrics are shown in Figure 77 (Schmitz, 1993). Both specimens were impregnated with polyvinylsilane (PVS), the impregnation cycle was repeated seven times to achieve a CMC with residual 7% open porosity. The specimen of Figure 77(a) contained noncoated fibers. The corresponding fracture surface shows a smooth fracture surface indicating a brittle fracture behavior, thus no fiber pull-out effects are visible. The fiber fabric of the specimen of Figure 77(b) was coated with a 40 nm thick PyC layer. The corresponding fracture surface demonstrates toughening effects through debonding and pull-out. Specimen (a) reached a bending strength of only 65 MPa with a breaking strain of only 0.1%, the latter being typical for any brittle untoughened

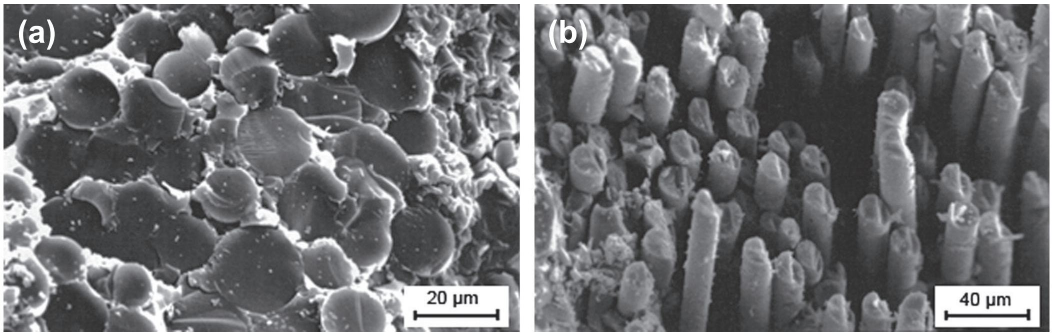

Figure 77 SEM micrographs of fracture surfaces of LPI-SiC/SiC. (a) Uncoated SiC fibers. (b) SiC fibers coated with PyC. The copyright of these images is held by the author of this article.

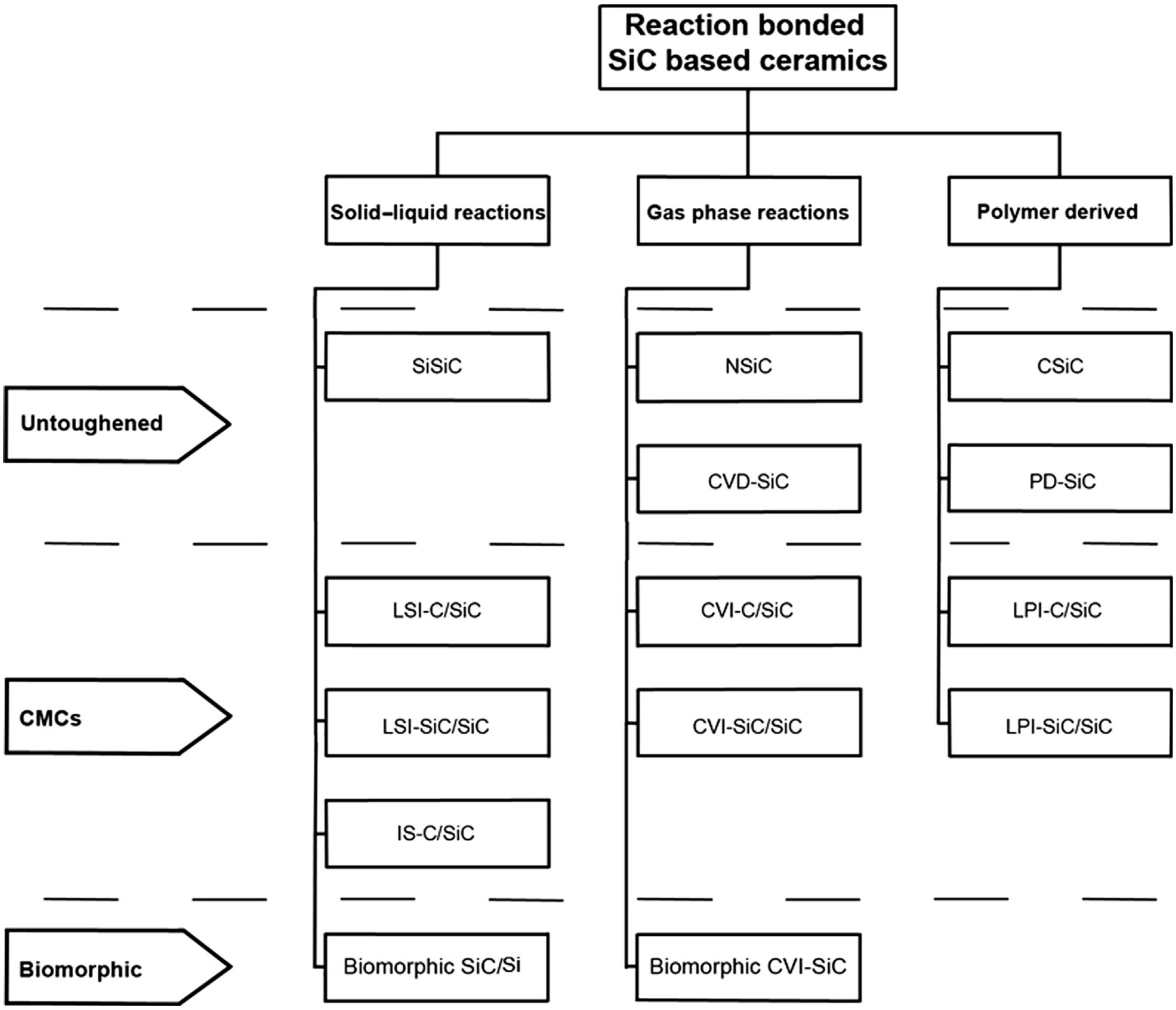

Figure 78 Reaction bonded SiC-based ceramics (RBSC).

ceramic. On the other hand specimen (b) discloses higher bending strength values of 330 MPa and even more important braking strain values reached 0.65%.

In this subsection some details of the processing aspects of reaction bonded SiC-based ceramics (RBSCs) have been reviewed. Three different manufacturing routes could have been distinguished for the SiC-based materials of this subchapter: solid–liquid reactions, gas-phase reactions and polymer-derived processing methods (Figure 78). The siliconization via vapor phase has not been attributed to the gas phase reactions, since the corresponding SiC-based ceramics are more similar to those ceramics consolidated by solid–liquid reactions. All RBSC ceramics except PD-SiC exhibit low-to zero shrinkage during final consolidation, IS-C/SiC is even swelling. The reaction bonding process for all listed RBSC ceramics except NSiC and CSiC is associated with in situ formation of SiC particles. All three groups of RBSC ceramics contain untoughened ceramics as well as ex situ toughened CMCs. Two groups include biomorphic ceramics.

2.04.5 Summary and Prospects

Due to its excellent intrinsic properties SiC can be regarded as one of the most commercially viable and important carbides. More than 100 years ago Edward Goodrich Acheson succeeded in synthesizing SiC raw materials for large-scale production. This was a good enough reason to start developing SiC-based ceramics.

First approaches used the processing knowledge of the classical silicate ceramics. By applying those processing principles SiC-based ceramics could be produced at fairly moderate temperatures. The properties of the corresponding silicate bonded SiC-based ceramics, however, could not meet all expectations. Thus their property levels proved to be too low to be used for structural applications. Therefore, it was tried to alter the kinds of sintering additives and to reduce their amount in order to evolve ceramics, whose properties should come close to the intrinsic characteristics of the compound SiC. Due to the low reactivity of the covalent bonded SiC compound this initiative proved to be difficult to be realized. In spite of reducing the grain size to submicron range first successful approaches could only be obtained through pressure-assisted sintering. A real breakthrough could be achieved after Svante Prochazka's invention of SSiC, since from then on it was possible to use marketable SiC-based ceramics for structural applications even at elevated temperatures and in conjunction with severe chemical attacks. The ceramics, however, proved to be extremely brittle. Through LPS-SiC, the brittleness could be reduced not only due to a change of fracture mode but particularly clearly through in situ toughening effects. The LPS could even be utilized for the manufacture of nanostructured and high-temperature stress-resistant SiC-based ceramics. LPS and gas-phase sintering methods were used to evolve porous ceramics even with graded pore structures for special filtering requirements. In general the maximum consolidation temperatures for all these nonsilicate ceramic-derived sintered ceramics have been extremely high. Through reaction bonding the consolidation temperature could considerably be reduced. Three different reaction bonding approaches resulted in untoughened and ex situ fiber-reinforced SiC-based ceramics. In most cases small volume changes occurred during final consolidation. Reaction bonding could also be successfully used for converting natural products into SiC-based ceramics.

Though the history of SiC-based ceramics is relatively short, they frame a huge class of ceramic materials. Some of them achieve high market shares like SiC grinding tools, SSiC, RSiC, SiSiC, CSiC and NSiC. Not all of these ceramics have been matter of intensive research activities. For others the sales volume is low or the ceramics are not scaled up from laboratory scale. Looking ahead to the future, challenges for the SiC-based ceramics should not only be faced by creating new processing techniques and new materials but also by scaling some powerful ceramics up from laboratory scale to industrial scale. The latter can generally be achieved through the transfer of research findings to industrial products, through restructuring and rationalization actions and thus through an improved cooperation between research institutes and industrial enterprises.

Acknowledgments

The author of this article is greatly indebted to all those people, who had provided him with image material and permitted him to reproduce it in this article.

References

Acheson, E. G. (1893). Production of artificial crystalline carbonaceous materials. US Patent No. 492,767.

Adler, J. (2005). Ceramic diesel particulate filters. *International Journal of Applied Ceramic Technology, 2*, 429–439.

Adler, J., Klose, T., & Piwonski, M. (1999). SiC-Keramik mit Porengrößen von Nanometer bis Mikromenter. Stand, Entwicklungs- und Anwendungsperspektiven. In A. Kranzmann & U. Gramberg (Eds.), *Werkstoffwoche '98. Band 3* (pp. 287–292). Weinheim, Germany: Wiley-VCH.

Adler, J., Teichgräber, M., Klose, T., & Stöver, H. (1998). Poröse Siliciumcarbidkeramik und Verfahren zu ihrer Herstellung. German Patent No. DE 19727115 A1.

Aliegro, R. A., Coffin, L. B., & Tinklepaugh, J. R. (1956). Pressure-sintered silicon carbide. *Journal of the American Ceramic Society, 39*, 386–389.

de Arellano-López, A. R., Martínez-Fernández, J., González, P., Domíngez, C., Fernández-Quero, V., & Singh, M. (2004). Biomorphic SiC: a new engineering material. *International Journal of Applied Ceramic Technology, 1*, 56–67.

Atwell, W. H., Hauth, W. E., Jones, R. E., Langley, N. R., & Arons, R. M. (1987). Advanced ceramics based on PoMer processing. DARPA Report AFWAL-TR-85-4099 Vol. I and II.

Balchan, A. S., & Cowan, G. R. (1968). Method of treating solids with high dynamic pressure. US Patent No. 3,667,911.

Baldus, H. P., Passing, G., Sporn, D., & Thierauf, A. (1995). Si-B-(N, C) a new material for high performance applications. In *High-temperature ceramic-matrix compsites II* (pp. 75–84). Westerville, OH: The American Ceramic Society.

Baumgartner, H. R., & Rossing, B. R. (1989). Pressureless sintering and properties of plasma synthesized SiC powder. In J. D. Cawley & C. E. Semler (Eds.), *Ceramic transactions: Vol. 2. Proceedings of the silicon carbide '87* (pp. 3–16). Westerville, OH: The American Ceramic Society.

Benecke, T., Korsten, A., Petersen, F., & Wiebke, G. (1976). Collector apparatus for gaseous reaction products. US Patent No. 3,976,829.

Blecha, M., Schmid, W., Krauth, A., & Wruss, W. (1990). Herstellung grobkörniger, auf hohen SiC-Gehalt optimierter SiC-C-Grünkörper für die Herstellung von SiSiC. *Sprechsaal, 123*, 263–268.

Boecker, W. D. G., Chwastiak, S., Frechette, F., & Lau, S. K. (1989). Single phase α-SiC reinforcements for composites. In J. D. Cawley & C. E. Semler (Eds.), *Ceramic transactions: Vol. 2. Proceedings of the silicon carbide '87* (pp. 407–420). Westerville, OH: The American Ceramic Society.

Böcker, W., & Hamminger, R. (1991). Advancements in sintering of covalent high performance ceramics. *Interceram, 40*, 520–525.

Böcker, W., & Hausner, H. (1978). The influence of boron and carbon additions on the microstructure of sintered silicon carbide. *Powder Metallurgy International, 10*, 87–89.

Böcker, W., Landfermann, H., & Hausner, H. (1979). Sintering of alpha silicon carbide with additions of aluminium. *Powder Metallurgy International, 11*, 83–85.

Brunauer, S., Emmett, P. H., & Teller, E. (1938). Adsorption of gases in multimolecular layers. *Journal of American Chemical Society, 60*, 309–319.

Burkhard, C. A. (1949). Polymethylsilane. *Journal of the American Chemical Society, 71*, 963–964.

Cai, H., Gu, W. H., & Faber, K. T. (1990). Microcrack toughening in SiC-TiB_2 composite. In *Proceedings of the American society for composites, 5th technical conference on composite materials* (pp. 892–901). Lancaster, PA: Technomic Publishing Company.

Cannon, W. R., Danforth, S. C., Flint, J. H., Haggerty, J. S., & Marra, R. A. (1982). Sinterable ceramic powders from laser-driven reactions: I, process description and modeling. *Journal of the American Ceramic Society, 65*, 324–330.

Cao, J. J., MoberlyChan, W. J., De Jonghe, L. C., Gilbert, C. J., & Ritchie, R. O. (1996). In situ toughened silicon carbide with Al-B-C additions. *Journal of the American Ceramic Society, 79*, 461–469.

Carter, C. H. J. R., Davis, R. F., & Bentley, J. (1984). Kinetics and mechanisms of high-temperature creep in silicon carbide: II, chemically vapor deposited. *Journal of the American Ceramic Society, 67*, 732–740.

Chakrabarti, O., & Das, P. K. (2000). Reactive infiltration of Si-Mo alloyed melt into carbonaceous preforms of silicon carbide. *Journal of the American Ceramic Society, 83*, 1548–1550.

Chen, L., Goto, T., & Hirai, T. (1996). Preparation and pressureless sintering of chemical vapour deposited SiC-B composite powder. *Journal of Materials Science, 31*, 679–683.

Chen, I.-W., & Wang, X. H. (2000). Sintering dense nanocrystalline ceramics without final-stage grain growth. *Nature (London), 404*, 168–171.

Chia, K. Y., Boecker, W. D. G., & Storm, R. S. (1994). Silicon carbide bodies having high toughness and method of making same. US Patent No. 5,298,470.

Chia, K. Y., & Lau, S. K. (1991). High toughness silicon carbide. *Ceramic Engineering and Science Proceedings, 12*, 1845–1861.

Chiang, Y.-M., & Messner, R. P. (1992). Method of preparing refractory silicon carbide composites and coatings. US Patent No. 5,079,195.

Cho, K.-S., Munir, Z. A., & Lee, H.-K. (2008). Microstructure of spark plasma sintered silicon carbide with Al-B-C. *Journal of Ceramic Processing Research, 9*, 500–505.

Choi, B. J., Park, D. W., & Kim, D. R. (1997). Chemical vapor deposition of silicon carbide by pyrolysis of methyltrichlorosilanes. *Journal of Material Science Letters, 16*, 33–36.

Cohrt, H., & Thümmler, F. (1985). Herstellung, Eigenschaften und Anwendung von reaktionsgebundenem, siliziertem Siliziumkarbid. *Zeitschrift für Werkstofftechnik, 16*, 277–285.

Colombo, P., Sglavo, V., Pippel, E., & Woltersdorf, J. (1998). Joining of reaction-bonded silicon carbide using a preceramic polymer. *Journal of Materials Science, 33*, 2405–2412.

Coppola, J. A., Hailey, N., & McMurtry, C. H. (1979). Sintered alpha silicon carbide ceramic body having equiaxed microstructure. US Patent No. 4,179,299.

Coppola, J. A., Hailey, N., & McMurtry, C. H. (1982). Sintered alpha silicon carbide ceramic body having equiaxed microstructure. US Patent No. 4,346,049.

Coppola, J. A., & McMurtry, C. H. (1976). Substitution of ceramics for ductile materials in design. In *Ceramics in the service of man. National symposium held June 7–9, 1976, Carnegie Institution, Part 3*. Washington, D.C.: National Academic Science.

Cordery, L., Niesz, D. E., & Shanefield, J. (1990). Sintering of silicon carbide with rare earth oxide additions. *Ceramic transactions, 7*, 618–636.

Cutler, R. A., & Jackson, T. B. (1989). Liquid phase sintered SiC. In V. J. Tennery (Ed.), *Proceedings of the 3rd international conference on ceramic materials and components for engines* (pp. 309–318). Westerville, OH: The American Ceramic Society.

Cutler, R. A., Virkar, A. V., & Hurford, A. C. (1989). Liquid sintering of silicon carbide. US Patent No. 4,829,027.

Datta, M. S., Bandyopadhyay, A. K., & Chaudhuri, B. (2002). Sintering of nano crystalline α silicon carbide by doping with boron carbide. *Bulletin of Materials Science, 25*, 181–189.

DeBolt, H. E., Krukonis, V. J., & Wawner, F. E. (1974). High strength, high modulus silicon carbide filaments via chemical vapor deposition. In R. B. Marshall, J. W. Faust & C. E. Ryan (Eds.), *Silicon carbide 1973* (pp. 168–175). Columbia, SC: University of South Carolina Press.

DiCarlo, J. A., & Yun, H. M. (2005). Non-oxide (silicon carbide) fibers. In N. P. Bansal (Ed.), *Handbook of ceramic composites* (pp. 33–52). New York, NY: Kluwer Academic Press.

Dietzel, A. (1942). Die Kationenfeldstärken und ihre Beziehung zu Entglasungsvorgängen, zur Verbindungsbildung und zu den Schmelzpunkten von Silikaten. *Zeitschrift für Elektrochemie, 48*, 9–23.

Doan, L. N. (1988). Gefügeverstärkung von SiC-Keramiken. PhD thesis, University of Stuttgart, Germany.

Eckert, K. L., Kara, M., & Kerber, A. (1994). Investigation of microstructure and strength of mullite bonded silicon carbide. *Ceramic Forum International/Berichte der Deutschen Keramischen Gesellschaft, 71*, 218–220.

Endo, H., Ueki, M., & Kubo, H. (1990). Hot pressing of SiC-TiC composites. *Journal of Materials Sciences, 25*, 2503–2506.

Ersoy, D. A., McNallan, M. J., Gogotsi, Y., & Erdemir, A. (2000). Tribological properties of carbon coatings produced by high temperature chlorination of SiC. *Tribology Transactions, 43*, 809–815.

Evans, A. G., & Langdon, T. G. (1976). Structural ceramics. In *Progress in materials sciences*, Vol. 21 (pp. 171–441). Oxford, New York: Pergamon Press.

Evans, A. G., & Lange, F. F. (1975). Crack propagation and fracture in silicon carbide. *Journal of Materials Science, 10*, 1659–1664.

Evans, A. G., & Marshall, D. B. (1989). The mechanical behavior of ceramic matrix composites. *Journal of the American Ceramic Society, 37*, 2567–2583.

Federer, J. I. (1990). Alumina base coatings for protection of SiC ceramics. *Journal of Materials Engineering, 12*, 141–149.

Feng, C. F. (Ed.). (2010). *SiC power materials, devices and applications*. Berlin, Heidelberg: Springer-Verlag.

Fickel, A., Völker, W. (1988). Modern refractory materials for blast furnace shafts. Interceram, Aachen Proceedings 1988, 38–40.

Fitzer, E., & Gadow, R. (1986). Fiber-reinforced silicon carbide. *American Ceramic Society Bulletin, 65*, 326–335.

Fitzgerald, F. A. J. (1900). Process of making carborundum materials. US Patent No. 650,234.

Forrest, C. W., Kennedy, P., & Shennan, J. V. (1970). The fabrication and properties of self-bonded silicon carbide bodies. UKEA Reactor Group Report. TRG report 2053 (s).

Forrest, C. W., Kennedy, P., & Shennan, J. V. (1972). The fabrication and properties of self-bonded silicon carbide bodies. In P. Popper (Ed.), *Special ceramics*, Vol. 5 (pp. 99–123). Stoke-on-Trent, U.K.: British Ceramic Research Association.

Förster, J., Vassen, R., & Stöver, D. (1995). Improvement of fracture-toughness in hot isostatically pressed mixtures of ultrafine and coarse-grained SiC ceramics. *Journal of Materials Science Letters, 14*, 214–216.

Frank, H. (1998). Schleifkörper aus keramisch gebundenem Schleifmittel. In J. Kriegesmann (Ed.), *Technische Keramische Werkstoffe* (pp. 1–94). Ellerau, Germany: HvB Verlag GbR. Loose-leaf-collection, Chapter 8.3.6.2., 43th Supplement.

Fredriksson, J. I. (1960). Process of making recrystallized silicon carbide. US Patent No. 2,964,823.

Fundus, M., & Knoch, H. (1997). Diamond like carbon coatings – tribological possibilities and limitations in applications on sintered silicon carbide bearing and seal faces. In *Proceedings of the 14th international pump users symposium* (pp. 93–98). Houston, USA: Texas A &M University System.

Gadow, R. (1986). Die Silizierung des Kohlenstoffs. PhD thesis, University of Karlsruhe, Germany.

Galasso, F. S. (1991). *Chemical vapor deposited materials*. Boca Raton, Fla: CRC Press.

German, R. M. (1996). *Sintering theory and practice*. New York, Chichester, Brisbane, Toronto, Singapore: John Wiley & Sons, 225–312.

Goldberger, W. M (1985). Method for continuous production of carbides. US Patent No. 4,543,240.

Goldberger, W. M., & Reed, A. K. (1984). Method of making ultra-microcrystallite silicon carbide product. US Patent No. 4,435,444.

Goldberger, W. M., & Reed, A. K. (1985). Ultra-microcrystalite silicon carbide product. US Patent No. 4,547,430.

Grande, T., Sommerset, H., Hagen, E., Wiik, K., & Einarsrud, M.-A. (1997). Effect of weight loss on liquid phase sintered silicon carbide. *Journal of the American Ceramic Society, 80*, 1047–1052.

Greil, P. (1999). Keramik aus Holz. In J. Kriegesmann (Ed.), *Technische Keramische Werkstoffe* (pp. 1–44). Ellerau, Germany: HvB Verlag GbR. Loose-leaf-collection, (Chapter 4).3.2.1., 50th supplement.

Greil, P. (2001). Biomorphous ceramics from lignocellulosics. *Journal of the European Ceramic Society, 21*, 105–118.

Greil, P. (2005). Verfahren zur Herstellung eines porösen Verbundkörpers aus Keramik. European Patent No. EP 1528049 A1.

Greil, P., Lifka, T., & Kaindl, A. (1998). Biomorphic cellular silicon carbide ceramics from wood; I. Processing and microstructure; II. Mechanical properties. *Journal of the European Ceramic Society, 18*, 1961–1973, 1975–1983.

Greskovich, G., & Palm, J. A. (1980). Development of high performance sintered Si3N4. Report No. AMMRC Tr. 80–46.

Gribkov, V. N., Silaev, V. A., Shchetanov, B. V., Umantsev, E. L., & Isaikin, A. S. (1972). Growth mechanism of silicon nitride whiskers. *Soviet Physics, Crystallography, 16*, 852–854.

Haggerty, J. S., & Chiang, Y.-M. (1990). Reaction-based processing methods for ceramics and composites. *Ceramic Engineering and Science Proceedings, 11*, 757–781.

Hall, H. T. (1964). Method of making high compressive strength silicon carbide and product thereof. US Patent No. 3,158,442.

Hayashi, J., Omori, M., & Yajima, S. (1978). Silicon carbide fibers having high strength and a method for producing said fibers. US Patent No. 4,100,233.

Hennicke, J., & Kessel, H. U. (2004). Field assisted sintering technology ("FAST") for the consolidation of innovated materials. *Ceramic Forum International/Berichte der Deutschen Keramischen Gesellschaft, 81*(11), E14–E16.

Hirai, T., & Sasaki, M. (1991). Silicon carbide prepared by chemical vapor deposition. In *Silicon carbide ceramics – 1 fundamental and solid reaction* (pp. 77–98). Barking, Essex: Elsevier Applied Sciences.

Hotta, M., Enomoto, N., & Hojo, J. (2006). Liquid-phase sintered silicon carbide with aluminum nitride and rare-earth oxide additives. *Key Engineering Materials, 317–318*, 111–114.

Hotta, M., & Hojo, J. (2006). Microstructural development of SiC ceramics by liquid-phase sintering with spark plasma sintering technique. *Materials Science Forum, 510–511*, 1022–1025.

Hotta, M., & Hojo, J. (2009). Effect of AlN additive on densification, microstructure and strength of liquid-phase sintered SiC ceramics by spark plasma sintering. *Journal of the Ceramic Society of Japan, 117*, 1009–1012.

Hotta, M., & Hojo, J. (2010). Inhibition of grain growth in liquid sintered SiC ceramics by AlN additive and spark plasma sintering. *Journal of the European Ceramic Society, 30*, 2117–2122.

Hotta, M., Kita, H., & Hojo, J. (2011). Nanostructured silicon carbide ceramics fabricated through liquid-phase sintering by spark plasma sintering. *Journal of the Ceramic Society of Japan, 119*, 129–132.

Hucke, E. E. (1983). Process development for silicon carbide based structural ceramics. AMMRS Report TR 83–85.

Hunold, K. (1984/1985). Hot isostatic pressing of SiC. *Powder Metallurgy International, 16*, 236–238, 17, 91–93.

Hunold, K., Reinmuth, K., & Lipp, A. (1983). Process for manufacture of substancially pore-free shaped polycrystalline articles by isostatic hot-pressing in glass casings. US Patent No. 4,381,931.

Igawa, N., Taguchi, T., Snead, L. L., Katoh, Y., Jitsukawa, S., Kohyama, A., et al. (2002). Optimizing the fabrication process for superior mechanical properties in the FCVI SiC matrix/stoichiometric SiC fiber composite system. *Journal of Nuclear Materials, 307–311*(Part 2), 1205–1209.

Ihle, J. (2004). Phasenausbildungen im System Al_2O_3-Y_2O_3-SiC und elektrische Eigenschaften von porösem flüssigphasengesinterten Siliciumcarbid. PhD thesis, Technical University Bergakademie Freiberg, Germany.

Inomata, Y., Tanaka, H., Inoue, Z., & Kawabata, H. (1980). Phase relations in SiC-Al_4C_3-B_4C at 1800 °C. *Kogyo Kyokaishi, 88*, 49–51.

Inoue, K. (1966a). Electric-discharge sintering. US Patent No. 3,241,956.

Inoue, K. (1966b). Apparatus for electrically sintering discrete bodies. US Patent No. 3,250,892.

Inoue, K. (1967). Method of an apparatus for controlling the porosity of electrically sintered bodies. US Patent No. 3,317,705.

Iseki, T., Yamashita, K., & Suzuki, H. (1981). Joining of self-bonded silicon carbide by germanium metal. *Journal of the American Ceramic Society, 64*, C13–C14.

Ishikawa, T. (1991). SiC continuous fiber, nicalon. In S. Somiya & Y. Inomata (Eds.), *SiC ceramics*, vol. 2 (pp. 81–98). Amsterdam: Elsevier.

Izhevskyi, V. A., Bressiani, A. H. A., & Bressiani, J. C. (2005). Effect of liquid phase sintering on microstructure and mechanical properties of Yb_2O_3-AlN containing SiC-based ceramics. *Journal of the American Ceramic Society, 88*, 1115–1121.

Izhevskyi, V. A., Genova, L. A., Bressani, J. C., & Bressani, A. H. A. (2000a). Review article: silicon carbide. Structure, properties and processing. *Cerâmica, 46*, 4–13.

Izhevskyi, V. A., Genova, L. A., Bressani, A. H. A., & Bressani, J. C. (2000b). Liquid-phase sintered SiC. Processing and transformation controlled microstructure tailoring. *Materials Research, 3*, 131–138.

Izhevskyi, V. A., Genova, L. A., Bressani, A. H. A., & Bressani, J. C. (2001). Liquid-phase sintered SiC based ceramics with AlN-Y_2O_3 and AlN-La_2O_3 additives. In J. G. Heinrich & F. Aldinger (Eds.), *Ceramic materials and components of engines* (pp. 593–598). Weinheim, Germany: Wiley VCH.

Jang, C.-W., Kim, J., & Kang, S.-J. L. (2002). Effect of sintering atmosphere on grain shape and grain growth in liquid-phase-sintered silicon carbide. *Journal of the American Ceramic Society, 85*, 1281–1284.

Janney, M. A. (1987). Mechanical properties and oxidation behavior of a hot-pressed SiC-15 vol % TiB_2 composite. *American Ceramic Society Bulletin, 66*, 322–324.

Jepps, N. W., & Page, T. F. (1983). Polytypic transformation in silicon carbide. *Progress in Crystal Growth and Characterization, 7*, 259–307.

Jimbou, R., Takahashi, K., Matsushia, Y., & Kosugi, T. (1986). SiC-ZrB_2 electroconductive ceramic composite. *Advanced Ceramic Materials, 1*, 341–345.

Jun, H.-W., Lee, H.-W., Kim, G.-H., Song, H.-S., & Kim, B.-H. (2008). Effect of sintering atmosphere on the microstructure evolution and the mechanical properties of silicon carbide ceramics. In J. P. Singh (Ed.), *Ceramic engineering and science proceedings: Vol. 18. Proceedings of the 21st annual conference on composites, advanced ceramics, materials, and structures – B.* Hoboken, NJ: John Wiley & Sons. http://dx.doi.org/10.1002/9780470294444.ch57. Issue 4.

Kaindl, A. (1999). Zellulare SiC-Keramik aus Holz. PhD thesis, University of Erlangen-Nürnberg, Germany.

Kayser, W. A., Žyskovič, M., & Petzow, G. (1985). Shape accommodation during grain growth in the presence of liquid phase. *Journal of Materials Science, 20*, 578–584.

Kessel, H. U., & Hennicke, J. (2010). FAST/SPS – Schnellsintertechnik und ihre Anwendung im Labor und Produktion. In J. Kriegesmann (Ed.), *Technische Keramische Werkstoffe* (pp. 105–118). Ellerau, Germany: HvB Verlag GbR. Loose-leaf-collection, (Chapter 3).6.7.1., 114th supplement.

Kim, Y.-W., Chun, Y.-S., Lee, S.-H., Park, J. Y., Nishimura, T., Mitomo, M., et al. (2007). Microstructure and mechanical properties of heat-resistant silicon carbide ceramics. *Key Engineering Materials, 336–338*, 1409–1413.

Kim, W. J., & Kim, Y.-W. (1995). Liquid phase sintering of silicon carbide. *Journal of the Korean Ceramic Society, 32*, 1655–1658.

Kim, J.-Y., Kim, Y.-W., Mitomo, M., Zhan, G.-D., & Lee, J.-G. (1999). Microstructure and mechanical properties of alpha-silicon carbide sintered with yttrium-aluminum garnet and silica. *Journal of the American Ceramic Society, 82*, 441–444.

Kim, Y.-W., Kim, J.-Y., Rhee, S. H., & Kim, D.-Y. (2000). Effect of initial particle size on microstructure of liquid-phase sintered silicon carbide. *Journal of the European Ceramic Society, 20*, 945–949.

Kim, Y.-W., Lee, S.-G., & Lee, Y.-I. (2000). Pressureless sintering of SiC-TiC composites with improved fracture toughness. *Journal of Materials Science, 35*, 5569–5574.

Kim, J. K., & Mai, Y.-W. (1998). *Engineered interfaces in fiber reinforced composites.* Oxford UK: Elsevier Science Ltd.

Kim, Y.-W., Mitomo, M., Emoto, H., & Lee, J.-G. (1998). Effect of initial α-phase content on microstructure and mechanical properties of sintered silicon carbide. *Journal of the American Ceramic Society, 81*, 3136–3140.

Kim, Y.-W., Mitomo, M., & Hirotsuru, H. (1997). Microstructural development of silicon carbide containing large seed grains. *Journal of the American Ceramic Society, 80*, 99–105.

Kingery, W. D. (1959). Densification during sintering in the presence of a liquid phase. *Journal of Applied Physics, 30*, 301–306.

Kingery, W. D., & Berg, M. (1955). Study of initial stages of sintering solids by viscous flow, evaporation-condensation and self-diffusion. *Journal of Applied Physics, 26*, 1205–1212.

Kistler-De Coppi, P. A., & Richarz, W. (1986). Phase transformations and grain growth in silicon carbide powders. *International Journal of High Technology Ceramics, 2*, 99–113.

Kleykamp, H., & Schumacher, G. (1993). The constitution of silicon-carbon system. *Berichte der Bunsengesellschaft für Physikalische Chemie, 97*, 799–804.

Knippenberg, W. F. (1963). Growth phenomena in silicon carbide. *Philips Research Reports, 18*, 161–274.

Kollenberg, W., & Travitzky, N. (2010). PT-Keramik®: Herstellung und Anwendungspotenziale papiertechnologisch hergestellter Keramik. In J. Kriegesmann (Ed.), *Technische Keramische Werkstoffe* (pp. 1–21). Ellerau, Germany: HvB Verlag GbR. Loose-leaf-collection, (Chapter 4).9.1.0., 116th Supplement.

Kostic, E. (1988). Sintering of silicon carbide in the presence of oxide additives. *Powder Metallurgy International, 20*, 28–29.

Krebs, R. (2008). Unshaped refractory materials (monolithics). In R. Routschka (Ed.), *Pocket manual: Refractory materials. Design, properties, testing* (3rd ed.). (pp. 233–303) Essen, Germany: Vulkan Verlag.

Krenkel, W. (2002). Design of ceramic brake pads and discs. *Ceramic Engineering Science Proceedings, 23*, 319–329.

Krenkel, W. (2003). Anwendungspotenziale faserverstärkter C/C-SiC-Keramiken. In W. Krenkel (Ed.), *Keramische Verbundwerkstoffe* (pp. 220–241). Weinheim, Germany: Wiley-VCH Verlag.

Krenkel, W., & Hald, H. (1989). Liquid infiltrated C/SiC – an alternative material for hot space structures. In *Proceedings of the ESA/EATEC conference on spacecraft structures and mechanical testing* (pp. 325–328). Paris, France: European Space Agency Publications Division.

Kriegesmann, J. (1986). Sintering phenomena in silicon carbide. *Powder Metallurgy International, 18*, 341–343.

Kriegesmann, J. (1988). Competing sintering mechanisms in silicon carbide. *Interceram, 37*, 301–303.

Kriegesmann, J. (1992). Processing phenomena for recrystallized silicon carbide. In K. Ishizaki, K. Niihara, M. Isotani & R. G. Ford (Eds.), *JFCC workshop series: Materials, processing and design*: *Grain boundary controlled properties of fine ceramics* (pp. 176–188). London, New York: Elesevier Applied Science.

Kriegesmann, J. (2003). Feinteiliges rekristallisiertes Siliciumcarbid – ein Werkstoff für Dieselpartikelfilter. In J. G. Heinrich & H. Gasthuber (Eds.), *Keramik im Fahrzeugbau* (pp. 131–138). Cologne, Germany: Deutsche Keramische Gesellschaft e.V.

Kriegesmann, J. (2004a). Finely layered recrystallized silicon carbide for diesel particulate filters. *Ceramic Forum International/Berichte der Deutschen Keramischen Gesellschaft, 81*(10), E25–E29.

Kriegesmann, J. (2004b). Microstructure control during consolidation of fine grained recrystallized silicon carbide. In H. Mandal & L. Öveçoĝlu (Eds.), *Euro ceramics VIII, proceedings of the 8th conference and exhibition of the European Ceramic Society in Istanbul, 2003* (pp. 2199–2202). Zürich, Switzerland: Trans Tech Publications Ltd.

Kriegesmann, J. (2005a). SSiC, LPSSiC und RSiC – Modellwerkstoffe zur Erläuterung von Sintervorgängen. In J. Kriegesmann (Ed.), *Technische Keramische Werkstoffe* (pp. 1–50). Ellerau, Germany: HvB Verlag GbR. Loose-leaf-collection, (Chapter 4).3.2.4., 84th supplement.

Kriegesmann, J. (2005b). Sintern von keramischen Werkstoffen. In J. Kriegesmann (Ed.), *Technische Keramische Werkstoffe* (pp. 105–118). Ellerau, Germany: HvB Verlag GbR. Loose-leaf-collection, (Chapter 4).3.2.4., 87th supplement.

Kriegesmann, J. (2007). Sintern von keramischen Werkstoffen. In J. Kriegesmann (Ed.), *Technische Keramische Werkstoffe* (pp. 119–154). Ellerau, Germany: HvB Verlag GbR. Loose-leaf-collection, (Chapter 4).3.2.4., 96th supplement.

Kriegesmann, J. (2010). Batch for producing a fireproof ceramic moulded body, method for production of the same and use thereof as a diesel particulate filter. European Patent No. EP 1776323 B1.

Kriegesmann, J., Büchler, R., Rejic, I., & Ersen, B. (2009). Foliengegossenes rekristallisiertes Siliciumcarbid für Dieselpartikelfilter. In J. Kriegesmann (Ed.), *Technische Keramische Werkstoffe* (pp. 1–48). Ellerau, Germany: HvB Verlag GbR. Loose-leaf-collection, (Chapter 8).3.1.9., 110th supplement.

Kriegesmann, J., Glagovsky, B. A., Moskowenko, I. B., & Schmid, H. A. (1993). Zerstörungsfreie Bestimmung der Härte an Schleif- und Honwerkzeugen. *Industrie Diamanten Rundschau, 27*, 58–61.

Kriegesmann, J., Hunold, K., Lipp, A., Reinmuth, K., & Schwetz, K. A. (1986). Shaped polycrystalline silicon carbide articles and isostatic hot-pressing process. US Patent No. 4,564,601.

Kriegesmann, J., & Jodlauk, J. (2002). Characterizing the consolidation of bimodally distributed fine-grained silicon carbide powders. *Ceramic Forum International/Berichte der Deutschen Keramischen Gesellschaft, 79*(12), E37–E44.

Kriegesmann, J., Kraus, M., & Gros, A. (1998). Gefügeausbildung von rekristallisiertem SiC. *Ceramic Forum International/Berichte der Deutschen Keramischen Gesellschaft, 75*(4), 83–88.

Kriegesmann, J., Lipp, A., & Reinmuth, K. (1982). Dense shaped articles of polycrystalline β-silicon carbide and process for the manufacture thereof by hot-pressing. US Patent No. 4,326,039.

Kriegesmann, J., Lipp, A., & Reinmuth, K. (1984). Dense shaped articles of polycrystalline α-silicon carbide and process for the manufacture thereof by hot-pressing. US Patent No. 4,467,043.

Kriegesmann, J., Lipp, A., Reinmuth, K., & Schwetz, K. A. (1983). Strength and fracture toughness of silicon carbide. In E. M. Lenoe, R. N. Katz & J. J. Burke (Eds.), *Ceramics for high performance applications. III. Reliability* (pp. 737–751). New York, London: Plenum Press.

Kriegesmann, J., Lipp, A., Reinmuth, K., Schwetz, K. A., & Struensee, D. von (1979). Entwicklung und Herstellung hochwarmfester Formkörper aus Siliciumkarbid, insbesondere für den Gasturbinenbau. *BMFT Forschungsbericht T*, 79–137.

Kriegesmann, J., Meistring, R., Neumann, N., & Nixdorf, R. (1999). Verfahren zur Herstellung eines Körpers mit einer porösen Matrix aus mindestens einem rekristallisiertem Werkstoff. European Patent No. EP 0899251 A1.

Kriegesmann, J., Rasch, H., & Büchler, R. (2002). Development of corundum and silicon carbide containing ceramics for grindings tools. Unpublished work.

Kriegesmann, J., & Schumacher, M. (2004). Silicon carbide fiber reinforced recrystallized silicon Carbide. In H. Mandal & L. Öveçoĝlu (Eds.), *Euro ceramics VIII, proceedings of the 8th conference and exhibition of the European Ceramic Society in Istanbul, 2003* (pp. 1063–1066). Zürich, Switzerland: Trans Tech Publications Ltd.

Kriegesmann, J., Strate, P., Ersen, B., & Büchler, R. (2004). Flachmembranstapel und Verfahren zur Herstellung einer solchen. German patent No. DE 103 29 229.

Kuczynski, G. C. (1949). Self-diffusion in sintering of metallic particles. *Transactions of the American Institute of Mining, Metallurgical, and Petroleum Engineers (AIME), 185*, 169–178.

Kulik, V. I., Kulik, A. V., Ramm, M. S., & Makarov, Y. N. (2004). Modelling of SiC-matrix composite formation by thermal gradient chemical vapour infiltration. *Materials Science Forum, 457–460*, 253–256.

Kumar, B. V., Roh, M.-H., Kim, Y.-W., Kim, W., Park, S.-W., & Seo, W.-S. (2009). Effect of additive composition on microstructure and mechanical properties of SiC ceramics sintered with small amount of RE_2O_3 (RE: SC, LU, Y) and AlN. *Journal of Materials Science, 44*, 5939–5943. http://dx.doi.org/10.1007/s10853-009-3818-8.

Lamicq, P. J., Bernhart, G. A., Dauchier, M. M., & Mace, J. G. (1986). SiC/SiC composite ceramics. *American Ceramic Society Bulletin, 66*, 336–338.

Lange, F. F. (1975). Hot-pressing behavior of silicon carbide powders with additions of aluminum oxide. *Journal of Materials Science, 10*, 314–320.

Lange, F. F. (1978). Dense silicon nitride ceramics: fabrication and interrelations with properties. In H. Palmour III, R. F. Davies & T. M. Hare (Eds.), *Materials science research: Vol. 11. Processing of crystalline ceramics* (pp. 597–614). New York: Plenum Press.

Lara, A., Rapoyato, R., Muñoz, A., Ortiz, A. L., & Dominguez-Rodriguez, A. (2010). Spark plasma sintering and microstructural characterization of additive-free polycrystalline ß-SiC. *Key Engineering Materials, 423*, 67–72.

Lee, J. G., & Cutler, I. B. (1975). Formation of silicon carbide from rice hulls. *American Ceramic Society Bulletin, 54*, 195–198.

Lee, S. K., & Kim, C. H. (1994). Effects of α-SiC versus β-SiC starting powders on microstructure and fracture toughness of SiC sintered with Al_2O_3-Y_2O_3 additives. *Journal of the American Ceramic Society, 77*, 1655–1658.

Lee, C. S., Kim, Y.-W., Cho, D. H., Lee, H. B., & Lim, H. J. (1998). Microstructure and mechanical properties of self-reinforced alpha-silicon carbide. *Ceramics International, 24*, 489–495.

Lee, S. K., Kim, Y. C., & Kim, C. H. (1994). Microstructural development and mechanical properties of pressureless-sintered SiC with plate-like grains using Al_2O_3-Y_2O_3 additives. *Journal of Materials Science, 29*, 5321–5326.

Lee, Y.-I., Kim, Y.-W., Mitomo, M., & Kim, D.-Y. (2003). Fabrication of dense nanostructured silicon carbide ceramics through two-step sintering. *Journal of the American Ceramic Society, 86*, 1803–1805.

Lely, J. A. (1955). Darstellung von Einkristallen von Silicium Carbid und Beherrschung von Art und Menge der eingebauten Verunreinigungen. *Berichte der Deutschen Keramischen Gesellschaft, 32*, 229–236.

Lely, J. A. (1958). Sublimation process for manufacturing silicon carbide Crystals. US Patent No. 2,854,364.

Lim, C. B., Yano, T., & Iseki, T. (1989). Microstructure and mechanical properties of RB-SiC/$MoSi_2$ composite. *Journal of Materials Science, 24*, 4144–4151.

Litzow, R. (1930). Über den Einfluß der Kornverteilung der Schamotte auf die Dichte feuerfester Materialien. *Glastechnische Berichte, 8*, 149–153.

Lohner, K. A. (1999). Microfabricated refractory ceramic structures for micro turbomachinery. Master thesis of Massachusetts Institute of Technology, Cambridge, Ma.

Lohner, K. A., Chen, K.-S., Ayon, A. A., & Spearing, S. M. (1998). Microfabricated silicon carbide microengine structures. *Materials Research Society Symposium Proceedings Series, 546*, 1–6.

Martin, H.-P., & Adler, J. (2002). Design elektrischer und thermischer Eigenschaften von flüssigphasengesintertem Siliciumcarbid. In J. Kriegesmann (Ed.), *Technische Keramische Werkstoffe* (pp. 1–35). Ellerau, Germany: HvB Verlag GbR. Loose-leaf-collection, (Chapter 4).3.2.3., 68th Supplement.

McMurtry, C. H., Boecker, W. D. G., Seshadri, S. G., Zanghi, J. S., & Garnier, J. E. (1987). Microstructure and material properties of SiC-TiB$_2$ particulate composites. *American Ceramic Society Bulletin, 66*, 325–329.

Meier, B., Hamminger, R., & Nold, E. (1990). Characterization of SiC-platelets. *Microchimica Acta, 11*, 195–205.

Messner, R. P., & Chiang, Y.-M. (1988). Processing of reaction-bonded silicon carbide without residual silicon phase. *Ceramic Engineering and Science Proceedings, 9*, 1052–1060.

Messner, R. P., & Chiang, Y.-M. (1990). Liquid-phase reaction bonding of silicon carbide using alloyed silicon-molybdenum melts. *Journal of the American Ceramic Society, 73*, 1193–1200.

Milewski, J. V., Gac, F. D., Petrovic, J. J., & Skaggs, S. R. (1985). Growth of beta-silicon carbide whiskers by the VLS process. *Journal of Materials Science, 20*, 1160–1166.

Mitomo, M., Hirotsuru, H., Kim, Y.-W. (1997). Superplastic silicon carbide sintered body. US Patent No. 5,591,685.

Mitomo, M., Kim, Y.-W., & Hirotsuru, H. (1996). Fabrication of silicon carbide nanoceramics. *Journal of Materials Research, 11*, 1601–1604.

Moissan, H. (1904). Nouvelles recherché aur la meteorite de Canon Diabolo. *Comptes Rendus, 139*, 773–786.

Moulson, A. J. (1979). Review: reaction-bonded silicon nitride: its formation and properties. *Journal of Materials Science, 14*, 1017–1051.

Mulla, M. A., & Krstic, V. D. (1991). Low-temperature presureless sintering of β-silicon carbide with aluminum oxide and yttrium oxide additions. *American Ceramic Society Bulletin, 70*, 439–443.

Mulla, M. A., & Krstic, V. D. (1994). Pressureless sintering of β-SiC with Al$_2$O$_3$ additions. *Journal of Materials Science, 29*, 934–938.

Müller, M. (1998). Über den Einfluss der Oberflächenstruktur und -chemie von Hochfest-Kohlenstofffasern auf die Eigenschaften von kohlenstofffaserverstärktem Kohlenstoff mit Phenolharz als Matrixausgangsstoff. PhD thesis, University of Karlsruhe, Germany.

Müller, C. (2000). Überbrandversuche bei nitridgebundenem SiC. Diploma-thesis, University of Applied Sciences Koblenz, Höhr-Grenzhausen, Germany.

Müller, M. (2001). Herstellung von C/SiC nach dem Flüssigsilicierverfahren. In J. Kriegesmann (Ed.), *Technische Keramische Werkstoffe* (pp. 1–27). Ellerau, Germany: HvB Verlag GbR. Loose-leaf-collection, (Chapter 4).4.1.5., 63th supplement.

Müller, M. (2003). Herstellung und Eigenschaften von C/SiC mit poröser Matrix. In J. Kriegesmann (Ed.), *Technische Keramische Werkstoffe* (pp. 1–26). Ellerau, Germany: HvB Verlag GbR. Loose-leaf-collection, (Chapter 4).4.1.6., 74th supplement.

Müller, M., Mentz, J., Buchkremer, H. P., & Stöver, D. (2001). Origin and effect of fiber attack for processing of C/SiC. In W. Krenkel (Ed.), *High temperature ceramic matrix composites* (pp. 66–72). Weinheim, Germany: Wiley-VCH Verlag.

Nadeau, J. S. (1973). Very high pressure hot pressing of silicon carbide. *American Ceramic Society Bulletin, 52*, 170–174.

Nader, M. (1995). Untersuchungen der Kornwachstumsphänomene an flüssigphasengesinterten SiC-Keramiken und ihre Möglichkeit zur Gefügeveränderung. PhD thesis, University of Stuttgart, Germany.

Naslain, R., Langlais, F., Vignoles, G., & Pailler, R. (2008). The CVI-process: state of the art and perspective. In R. Tandon, A. Wereszczak & E. Lara-Curzio (Eds.), *Ceramic engineering and Science Proceedings: Vol. 27. Mechanical properties and performance of engineering ceramics II* (pp. 373–386). Hoboken, NJ: John Wiley & Sons. Issue 2.

Negita, K. (1986). Effective sintering aids for silicon carbide ceramics: reactivities for silicon carbide with various additives. *Journal of the American Ceramic Society, 69*, C308–C310.

Neumann, N. (2002). Reaktionsgebildete SiC-Matrices für Faserverbundkeramiken. PhD thesis, University of Erlangen-Nürnberg.

Noakes, J. E., Sato, H., Terner, L. L. (1978). Method of forming a silicon carbide article. US Patent No. 4,067,955.

Oberacker, R., Kühne, A., & Thümmler, F. (1987). Einsatzmöglichkeiten für die Sinter-HIP-Technik für die Herstellung keramischer Hochleistungswerkstoffe. *Powder Metallurgy International, 19*, 43–50.

Oberacker, R., Thümmler, F., & Fetahagic, T. (2001). Aspects of sintering additives for processing and microstructure development of HIP-SSiC. *Zeitschrift für Metallkunde, 92*, 135–140.

Ogbuji, L. U., Mitchell, T. E., Heuer, A. H., & Shinozaki, J. (1979). Discussion of "microstructural characterization of "REFEL" (reaction-bonded) silicon carbides". *Journal of Materials Science, 14*, 2267–2271.

Omori, M., & Takei, H. (1982). Pressureless sintering of SiC. *Journal of the American Ceramic Society, 65*, C-92.

Omori, M., & Takei, H. (1985). Composite silicon carbide sintered shapes and its manufacture. US Patent No. 4,502,983.

Omori, M., & Takei, H. (1986). Method of preparing sintered shapes of silicon carbide. US Patent No. 4,564,490.

Ortiz, A. L., Bhatia, T., Padture, N. P., & Pezzotti, G. (2002). Microstructural evolution in liquid-phase-sintered SiC: III, effect of nitrogen-gas sintering atmosphere. *Journal of the American Ceramic Society, 88*, 1835–1840.

Ortiz, A. L., Muñoz-Bernabé, A., Borrero-López, O., Domõnguez-Rodrõguez, A., Guiberteau, F., & Padture, N. P. (2004). Effect of sintering atmosphere on the mechanical properties of liquid-phase-sintered SiC. *Journal of the European Ceramic Society, 24*, 3245–3249.

Ostwald, W. (1900). Über die vermeintliche Isometrie des roten und gelben Quecksilberoxyds und die Oberflächenspannung fester Körper. *Zeitschrift für Physikalische Chemie, 34*, 495–503.

Ota, T., Takahashi, M., Hibi, T., Ozawa, M., Suzuki, S., Hikichi, Y., et al. (1995). Biomimetic process for producing SiC "wood". *Journal of the American Ceramic Society, 78*, 3409–3411.

Padture, N. P. (1994). In situ-toughened silicon carbide. *Journal of the American Ceramic Society, 77*, 519–523.

Padture, N. P., & Lawn, B. R. (1994). Toughness properties of silicon carbide with an in situ induced heterogeneous grain structure. *Journal of the American Ceramic Society, 77*, 2518–2522.

Page, T. F., & Sawyer, G. R. (1980). Discussion of "microstructural characterization of "REFEL" (reaction bonded) silicon carbides": authors reply. *Journal of Materials Science, 15*, 1850–1856.

Papenburg, U., Goetz, U., & Kriegesmann, J. (1990). Verfahren zur Herstellung von hochverdichteter polykristalliner Formkörper aus α- und β-Siliciumcarbid durch drucklose Sinterung. German Patent No. DE 3902528.

Par, N. L., Martin, G. F., & May, E. R. W. (1960). Preparation, microstructure, and mechanical properties of silicon nitride. In P. Popper (Ed.), *Special ceramics* (pp. 102–135). London: Heywood Press.

Petersen, F., & Korsten, B. (1979). Electrical resistance furnace for production of silicon carbide. US Patent No. 4,158,744.

Piwonski, M. (2005). Keramische Membranen auf Basis von LPS-SiC: Schlickerentwicklung und Beschichtungsverfahren. PhD thesis, Technical University Bergakademie Freiberg, Germany.

Popper, P. (1960). The preparation of dense self-bonded silicon carbide. In P. Popper (Ed.), *Special ceramics* (pp. 209–219). London: Heywood Press.

Popper, P. (1966). Production of dense bodies of silicon carbide. US Patent No. 3,275,722.

Popper, P., & Ruddlesden, S. N. (1961). The preparation, properties, and structure of silicon nitride. *Transactions of the British Ceramic Society, 60*, 603–626.

Prener, J. S. (1963). Method of making silicon carbide. US Patent No. 3,085,863.

Prochazka, S. (1972). Investigation of ceramics for high-temperature turbine vanes. General Electric Report SRD-72–171, Final Report on Navy Contract N00019-72-C-0129.

Prochazka, S. (1973). *Sintering of silicon carbide*. Technical Report 73-CRD-325. Schenectady NY: General Electric Corporation.

Prochazka, S. (1974). Hot pressed silicon carbide. US Patent No. 3,853,566.

Prochazka, S. (1977a). Sintered dense silicon carbide. US Patent No. 4,004.934.

Prochazka, S. (1977b). Silicon carbide sintered body. US Patent No. 4.041.117.

Prochazka, S. (1981). *The sintering process for SiC, a review*. Technical Report 81-CRD-314. Schenectady NY: General Electric Corporation.

Prochazka, S. (1989). *Why is it difficult to sinter covalent substances?*. Technical Report 89-CRD-314. Schenectady NY: General Electric Corporation.

Prochazka, S., & Charles, R. J. (1973). Strength of boron-doped hot-pressed silicon carbide. *American Ceramic Society Bulletin, 52*, 885–891.

Prochazka, S., & Donalski, W. J. (1978). Hot pressed silicon carbide. US Patent No. 4.108.929

Prochazka, S., & Scalan, R. M. (1975). Effect of boron and carbon on sintering of SiC. *Journal of the American Ceramic Society, 58*, 72–74.

Raju, C. B., & Verma, S. (1997). SiC whiskers from rice hulls: formation, purification, and characterization. *British Ceramic Transactions, 96*, 112–115.

Ramsdell, L. S. (1947). Studies on silicon carbide. *American Mineralogist, 32*, 64–82.

Réau, A., Guizard, B., Canel, J., Galy, J., & Tenegal, F. (2012). Silicon carbide nanopowders: the parametric study of synthesis by laser pyrolysis. *Journal of the American Ceramic Society, 95*, 153–158.

Réau, A., Tenegal, F., & Galy, J. (2011). Process for preparing a silicon carbide part without the need for any sintering additives. US Patent No. 2011/0180977 A1.

Rice, R. W. (1983). Ceramic from polymer pyrolysis, opportunities and needs - a materials perspective. *American Ceramic Society Bulletin, 62*, 889–892.

Rickmann, K., Büchler, R., & Kriegesmann, J. (2007). Dieselpartikelfilter. German Patent No. DE 102005008832 B4.

Riedel, R. (1992). Alternative Verfahren zur Herstellung keramischer Werkstoffe. In Keramikverbund Karlsruhe – Stuttgart (Ed.), *Hochleistungskeramik: Von Pulvern zu Bauteilen; Forschungs- und Technologietrends* (pp. 23–29). Düsseldorf, Germany: VDI – Verlag.

Riedel, R., & Dressler, W. (1996). Chemical formation of ceramics. *Ceramics International, 22*, 233–239.

Riedel, R., Passing, G., Schönfelder, H., & Brook, R. J. (1992). A novel process for fabrication of dense silicon based ceramic components. *Nature, 355*, 714–717.

Riley, F. L. (2004). Silicon nitride and related materials. *Journal of the American Ceramic Society, 83*, 245–265.

Rixecker, G., Wiedmann, I., & Aldinger, F. (2001). Flüssigphasensintern von Siliciumcarbid mit oxinitridischen Zusätzen. In J. Kriegesmann (Ed.), *Technische Keramische Werkstoffe* (pp. 119–154). Ellerau, Germany: HvB Verlag GbR. Loose-leaf-collection, (Chapter 4).3.2.4., 96th supplement.

Rixecker, G., Wiedmann, I., Rosinus, A., & Aldinger, F. (2001). High-temperature effects in the fracture mechanical behaviour of silicon carbide liquid-phase sintered with AlN-Y_2O_3 additives. *Journal of the European Ceramic Society, 21*, 1013–1019.

Roman, Y. G., de Croon, M. H. J. M., & Metselaar, R. (1995). Analysis of the isothermal forced flow chemical vapour infiltration process. Part II: experimental study. *Journal of the European Ceramic Society, 15*, 887–898.

Roman, Y. G., Kotte, J. F. A. K., & de Croon, M. H. J. M. (1995). Analysis of the isothermal forced flow chemical vapour infiltration process. Part I: theoretical aspects. *Journal of the European Ceramic Society, 15*, 875–886.

Rossignol, J. Y., Langlais, F., & Naslain, R. (1984). A tentative modelization of titanium carbide CVI within the pore network of two-dimensional carbon-carbon performs. In *Proceedings of the 9th conference on chemical vapor deposition*. Pennington, NJ: Electrochemical Society, 596–614.

Sahin, C., & Kriegesmann, J. (2013). Ceramic filter and method for producing a ceramic filter. European patent No. 2425885 B1.

Sahin, C., Pesch, P., Kolozsvári, S., & Kriegesmann, J. (2009). Oberflächenfunktionalisierung von RSiC-Filtern mittels PVD-Technologie. In J. Kriegesmann (Ed.), *Technische Keramische Werkstoffe* (pp. 1–20). Ellerau, Germany: HvB Verlag GbR. Loose-leaf-collection, (Chapter 3).8.6.2., 111th supplement.

Sand, C., & Adler, J. (1999). Eigenschaften drucklos gesinterter TiC-Keramik und TiC/SiC-Composite. In J. Heinrich, W. Hermel, G. Ziegler & H. Riedel (Eds.), *Werkstoffwoche '98, Band 7: symposium 9: Keramik* (pp. 419–424). Weinheim: Wiley-VCH.

Savage, G. (1993). *Carbon-carbon composites*. London, U.K.: Chapmen & Hall.

Sawyer, G. R., & Page, T. F. (1978). Microstructural characterization of "REFEL" (reaction bonded) silicon carbides. *Journal of Materials Science, 13*, 885–904.

Schmidt, J., & Aoki, R. (2006). Prozessentwicklung und Qualitätssicherung von biomorphen SiC-Strukturkeramiken. In J. Kriegesmann (Ed.), *Technische Keramische Werkstoffe* (pp. 1–27). Ellerau, Germany: HvB Verlag GbR. Loose-leaf-collection, (Chapter 4).3.2.5., 91th supplement.

Schmitz, D. (1993). Verfahrensentwicklung zur Herstellung von keramischen Faserverbundwerkstoffen mittels metallorganischen Precursoren. Diploma-thesis, University of Applied Sciences Koblenz, Höhr-Grenzhausen, Germany.

Schneider, J., Biswas, K., Rixecker, G., & Aldinger, F. (2003). Microstructural changes in liquid-phase-sintered silicon carbide during creep in an oxidizing environment. *Journal of the American Ceramic Society, 86*, 501–507.

Schrimpf, C., & Frischat, G. H. (1982). Some properties of nitrogen-containing Na_2O-CaO-SiO_2 glasses. *Journal of Non-crystalline Solids, 52*, 479–485.

Schwetz, K. A. (2000). Silicon carbide based hard materials. In R. Riedel (Ed.), *Handbook of ceramic hard materials* (pp. 683–748). Weinheim: Wiley-VCH.

Schwetz, K. A., Kempf, T., Saldsieder, D. W., & Telle, R. (2004). Toughness and hardness of LPS-SiC and LPS-SiC based composites. *Ceramic Engineering and Science Proceedings, 25*, 579–588.

Schwetz, K. A., & Lipp, A. (1978). Herstellung und Eigenschaften ultrafeiner Beta-SiC Sinterpulver. *Radex-rundschau*, 479–498.

Schwetz, K. A., & Lipp, A. (1980a). Dense sintered shaped articles of polycrystalline alpha-silicon carbide and process for their manufacture. US Patent No. 4,230,497.

Schwetz, K. A., & Lipp, A. (1980b). The effect of boron and aluminium sintering additives on the properties of dense sintered alpha silicon carbide. *Science of Ceramics, 10*, 149–158.

Schwetz, K. A., Schäfer, E., & Telle, R. (2003). Influence of powder properties on in-situ platelet reinforcement of LPS-SiC. *ceramic forum international/Berichte der Deutschen Keramischen Gesellschaft, 80*(3), E40–E45.

Schwetz, K. A., Sigl, L. S., Kempf, T., & Victor, G. (2003). Liquid-phase-sintered SiC shaped bodies with improved fracture toughness and a high electric resistance. US Patent No. 6,531,423.

Schwetz, K. A., Sigl, L. S., & Pfau, L. (1997). Mechanical properties of injection molded B_4C-C Ceramics. *Journal of Solid State Chemistry, 133*, 68–76.

Seshadri, S. G., Srinivason, M., & Chia, K. Y. (1989). Micostructure and mechanical properties of pressureless sintered alpha SiC. In J. D. Cawley & C. E. Semler (Eds.), *Ceramic transactions: Vol. 2. Proceedings of the silicon carbide '87* (pp. 215–226). Westerville, Ohio: The American Ceramic Society.

Shaffer, P. T. B. (1994). *Silicon carbide whiskers. Handbook of Advanced Ceramic Materials*. Buffalo NY: Advanced Refractory Technologies, Inc.

Shaoming, D., Dongliang, J., Shouhong, T., & Jingkun, G. (1996). Mechanical properties of SiC/TiC composites by hot isostatic pressing. *Journal of Materials Science Letters, 15*, 394–396.

She, J. H., & Ueno, K. (1999). Effect of additive content on Liquid-Phase sintering on silicon carbide ceramics. *Materials Research Bulletin, 34*, 1629–1636.

Shinozaki, S., & Kinsman, K. R. (1978). Evolution in polycrystalline silicon carbide. In H. Palmour III, R. F. Davis & T. M. Hare (Eds.), *Materials science research: Vol. 11. Processing of crystalline ceramics* (pp. 641–652). New York, London: Plenum Press.

Shyne, J. J., & Milewski, J. V. (1971). Method of growing silicon carbide whiskers. US Patent 3,622,272.

Sieber, H., Kaindl, A., Schwarze, D., Werner, J. P., & Greil, P. (2000). Light-weight cellular ceramics from biological derived preforms. *Ceramic Forum International/Berichte der Deutschen Keramischen Gesellschaft, 77*(1–2), E21–E24.

Sigl, L. S., & Kleebe, H. J. (1993). Core/rim structure of liquid phase sintered silicon carbide. *Journal of the American Ceramic Society, 76*, 773–776.

Simmer, S. P., Xiao, P., & Derby, B. (1998). Processing and microstructural characterization of RBSiC-$TaSi_2$ composites. *Journal of Materials Science, 33*, 5557–5568.

Singh, M., & Behrendt, D. R. (1994). Reactive malt infiltration of silicon-niobium alloys in microporous carbon. *Journal of Materials Research, 9*, 1701–1708.

Singh, M., Dickerson, R. M., Olmstead, F. A., & Eldridge, J. I. (1997). SiC (SCS-6) fiber reinforced-reaction formed SiC matrix composites: microstructure and interfacial properties. *Journal of Materials Research, 12*, 706–713.

Smoak, R. H. (1979). Pressureless sintering beryllium containing powder composition. US Patent No. 4,172,109.

Srinivasan, M. (1989). The silicon carbide family of structural ceramics. In J. B. Wachtman (Ed.), *Structural ceramics – Treatise on materials Science and technology*, Vol. 29 (pp. 100–159). San Diego, CA: Academic Press.

Streitwieser, D. A., Popovska, N., & Gerhard, H. (2006). Optimization of the ceramization process for the production of three-dimensional biomorphic porous SiC ceramics by chemical vapor infiltration (CVI). *Journal of the European Ceramic Society, 26*, 2381–2387.

Stroke, F. G. (1981). Submicron beta silicon carbide powder and sintered articles of high density prepared therefrom. US Patent No. 4,295,890.

Stutz, D. H., Prochazka, S., & Lorenz, J. (1985). Sintering and microstructure formation of β-Silicon Carbide. *Journal of the American Ceramic Society, 68*, 479–482.

Sudarshan, T. (2010). Materials science and engineering of bulk silicon carbides. In C. F. Feng (Ed.), *SiC power materials, devices and applications* (pp. 1–61). Berlin, Heidelberg: Springer-Verlag.

Suyama, Y., Marra, R. A., Haggerty, J. S., & Bowen, H. K. (1985). Synthesis of ultrafine SiC powders by laser driven gas phase reactions. *American Ceramic Society Bulletin, 64*, 1356–1359.

Suyama, Y., & Yamaguchi, T. (1991). Powders for advanced ceramics. In P. Vincenzini (Ed.), *Fundamentals of ceramic engineering* (pp. 121–151). London, New York: Elsevier Applied Science.

Suzuki, K. (1986). Pressureless sintering of SiC with addition of aluminium oxide. Reports of the research laboratory, Asahi Glass Corporation Ltd, 36, 25–36.

Tairov, Y. M., & Tsvetkov, V. F. (1981). General principals of growing large-size single crystals of various silicon carbide polytypes. *Journal of Crystal Growth, 52*, 146–150.

Tairov, Y. M., & Vodakov, Y. A. (1977). Group IV materials (mainly SiC). In J. I. Pankove (Ed.), *Electroluminiscence: Vol. 17. Topics of applied physics* (pp. 31–61). Berlin, Heidelberg, New York: Springer-Verlag.

Tajima, Y., & Kingery, W. D. (1982). Solid solubility of aluminum and boron in silicon carbide. *Journal of the American Ceramic Society, 65*, C-27–C-29.

Tanaka, H., Inomata, Y., Hara, K., & Hasegawa. (1985). Normal sintering of Al-doped β-SiC. *Journal of Materials Science Letters, 4*, 315–317.

Taylor, K. M. (1965). Cold molded dense silicon carbide articles and method of making the same. US Patent No. 3,205,043.

Telle, R. (1994). Boride and carbide ceramics. In R. W Cahn, P. Haasen E. J.Kramer (Eds), Materials science and technology, Vol. 11: M. V Swain (Ed), Structure and properties of ceramics. Weinheim, New York, Cambridge, Tokyo: VCH Verlagsgesellschaft, pp. 173–266.

Thaler, H., Schwetz, K. A., & Kayser, A. (2004). Graphite-coated shaped body made of sintered silicon carbide. US Patent No. 6,777,076 B2.

Tokita, M. (2001). Mechanisms of spark plasma sintering. In K. Kosuge & H. Nagai (Eds.), *Proceedings of the 2000 powder metallurgy World Congress* (pp. 729–732). Kyoto, Japan: Japanese Society of Powder and Powder Metallurgy.

Torti, M. L., Lucek, J. W., & Weaver, G. Q. (1978). Densified silicon carbide – an interesting material for diesel applications. Society of Automotive Engineers (SAE) Technical Paper 780071.

Travitzky, N., Windsheimer, H., Fey, T., & Greil, P. (2008). Preceramic paper derived ceramics. *Journal of the American Ceramic Society, 91*, 3477–3492.

Tu, W.-C., Lange, F. F., & Evans, A. G. (1996). Concept for a damage-tolerant ceramic composite with "strong" interfaces. *Journal of the American Ceramic Society, 79*, 417–424.

van Dijen, F. K., & Mayer, E. (1996). Liquid phase sintering of silicon carbide. *Journal of the European Ceramic Society, 16*, 413–420.

van Dijen, F. K., & Metselaar, R. (1989). Chemical reaction engineering aspects of a rotary reactor for carbothermal synthesis of SiC. *Journal of the European Ceramic Society, 5*, 55–61.

Vassen, R., Buchkremer, H. P., & Stöver, D. (1999). Verfahren zum Herstellen feinkristalliner Siliciumkarbidkörper. German Patent No. DE 19642753.

Vassen, R., & Stöver, D. (1997). Properties of silicon based ceramics produced by hiping ultrafine powders. *Philosophical Magazine B, 76*, 585.

Vassen, R., & Stöver, D. (1999). Processing and properties of nanograin silicon carbide. *Journal of the American Ceramic Society, 82*, 2583–2593.

Vassen, R., Stöver, D., & Uhlenbusch, J. (1991). Sintering and grain growth of ultrafine amorphous SiC-Si powder mixtures. In G. Ziegler & H. Hausner (Eds.), *Euro-ceramics II: Vol. II. Proceedings of the 2nd European ceramic society conference, Augsburg 1991: Deutsche Keramische Gesellschaft* (pp. 791–797).

Wagner, R. S., & Ellis, W. C. (1964). Vapor–liquid–solid mechanism of single crystal growth. *Applied Physics Letters, 4*, 89.

Wang, Y., Sasaki, M., & Hirai, T. (1991). Thermal properties of chemical vapor-deposition SiC-C nanocomposites. *Journal of Materials Science, 26*, 5495–5501.

Wang, Y., Tan, S., & Jiang, D. (2004). The effect of porous carbon preform and the infiltration process on the properties of reaction-formed SiC. *Carbon, 42*, 1833–1839.

Wang, C., Tang, J., & Chen, Y. (2008). Oxidation resistance of 2D C/SiC composites fabricated by FCVI. *Key Engineering Materials, 368–372*, 1056–1058.

Warmer, J. (2010). Funtionalisierung von RSiC-Filtern für Anwendungen in der Gassensorik. Diploma-thesis, University of Applied Sciences Koblenz, Höhr-Grenzhausen, Germany.

Weaver, G. Q., & Olson, B. A. (1974). Sintered silicon carbide. US Patent No. 3,836,673.

Weaver, G. Q., & Logan, C. (1978). Process of forming silicon carbide bodies. US Patent No. 4,127,629.

Wecht, E. H. P. (1977). *Feuerfest-Siliciumcarbid*. Wien: Springer Verlag.

Wei, G. C. (1983). Beta SiC powders produced by carbothermal reduction of silica in a high-temperature rotary furnace. *Journal of the American Ceramic Society, 66*, c111–c113.

Wei, G. C., & Becher, P. F. (1984). Improvements in mechanical properties in SiC by addition of TiC. *Journal of the American Ceramic Society, 67*, 571–574.

Whalen, T. J., Noakes, J. E., & Terner, L. L. (1978). Progress on injection-molded reaction-bonded SiC. In J. J. Burke, E. N. Lenoe & R. N. Katz (Eds.), *Ceramics for high performance applications II* (pp. 179–192). Chestnut Hill, MA: Brook Hill Publishing Co.

Wiebke, G., Korndörfer, L., Korsten, A., Benecke, T., & Petersen, F. (1976). Furnace installation operated by direct electrical heating according to the resistance principle, in particular for the preparation of silicon carbide. US Patent No. 3,989,883.

Wiedmann, I. (1998). Herstellung und mechanische Eigenschaften von flüssigphasengesintertem Siliziumcarbid. Ph.D thesis, University of Stuttgart, Germany.

Williams, R. M., Juterbock, B. J., Peters, C. R., & Whalen, T. J. (1984). Forming and sintering behavior of B- and C- doped α- and β-SiC. *Journal of the American Ceramic Society, 67*, c111–c113.

Wolf, C., Hübner, H., & Adler, J. (1993). Mechanical behaviour of pressureless sintered SiC at high temperature. In P. Duran & J. F. Fernandez (Eds.), *Third EuroCeramics – engineering ceramics*, Vol. 3 (pp. 465–470). Castellon, Spain: Faenza Edritice Iberica.

Wüllner, A. (2003). Carbon-Keramik-Bremsen – Revolution im Hochleistungsbereich. *Ceramic Forum International/Berichte der Deutschen Keramischen Gesellschaft, 80*(8), D13–D38.

Wynne, K. J., & Rice, R. W. (1984). Ceramics via polymer pyrolysis. *Annual Review of Materials Science, 14*, 297–334.

Xu, H., Bhatia, T., Deshpande, S. A., Padture, N. P., Ortiz, A. L., & Cumbrera, F. L. (2001). Microstructural evolution in liquid-phase-sintered SiC: I, effect of starting SiC powder. *Journal of the American Ceramic Society*, 1578–1584.

Xu, Y., & Yan, X.-T. (2010). *Chemical vapour deposition. An integrated engineering design for advanced materials*. London, Dordrecht, Heidelberg, New York: Springer-Verlag.

Yajima, S., Hasegawa, Y., Hayashi, J., & Limura, M. (1978). Synthesis of continuous silicon carbide fibre with high tensile strength and high Young's modulus. Part 1 synthesis of polycarbosilane as precursor. *Journal of Materials Science, 13*, 2569–2576.

Yajima, S., Hayashi, J., & Omori, M. (1975). Continuous silicon carbide fiber of high tensile strength. *Chemical Letters*, 931–934.

Yajima, S., Hayashi, J., & Omori, M. (1977). Method of producing organosilicon high molecular weight compounds having silicon and carbon as main skeleton components and said organosilicon high molecular weight compounds. US Patent No. 4,052,430.

Yajima, S., Hayashi, J., Omori, M., & Okamura, K. (1976). Development of a silicon carbide fibre with high tensile strength. *Nature, 261*, 683–685.

Yajima, S., Okamura, K., Hayashi, J., & Omori, M. (1976). Synthesis of silicon carbide fiber with high tensile strength. *Journal of the American Ceramic Society, 59*, 324–327.

Yamamoto, T., Kitaura, H., Kodera, Y., & Ishii, T. (2004). Consolidation of nanostructured β-SiC by spark plasma sintering. *Journal of the American Ceramic Society, 87*, 1436–1441.

Yoshimi, O. (1991). Manufacture of porous SiC ceramics with high strength and low pressure loss. Japanese Patent No. JP 03215374 A2.

Zeus, D. (1991). How the use of advanced ceramics as tribomaterial has affectesd the evolution of mechanical seals. *Ceramic Forum International/Berichte der Deutschen Keramischen Gesellschaft, 68*(1/2), E36–E45.

Ziegler, G., Heinrich, J., & Wötting. (1987). Review. Relationship between processing, microstructure and properties of dense and reaction-bonded silicon nitride. *Journal of Materials Science, 22*, 3046–3086.

Zuber, C., & Heidenreich, B. (2006). Development of a net shape manufacturing method for ventilated brake discs in single piece design. *Materialwissenschaft und Werkstofftechnik, 37*, 301–308.

This page intentionally left blank

2.05 Spark Plasma Sintering of Nanoceramic Composites

Brahma Raju Golla, Engineering Ceramics Research Group, Korea Institute of Materials Science, Changwon, Gyeongnam, Korea
Bikramjit Basu, Materials Research Center, Indian Institute of Science, Bangalore, India

© 2014 Elsevier Ltd. All rights reserved.

2.05.1 Introduction

In the past few decades, ceramic nanomaterials have drawn considerable research interest in the materials community, in view of their attractive mechanical, physical and tribological properties (Basu & Balani, 2011; Basu & Kalin, 2011; Mukhopadhyay & Basu, 2007; Viswanathan, Laha, Balani, Agarwal, & Seal, 2006). Nanostructured materials are broadly defined as the materials having grain sizes or structural units with a size scale of <100 nm in any dimension. The length scale refers to particle diameter, grain size, layer thickness or even the width of a conducting line on an electronic chip. The nanostructured materials can be classified as zero-dimensional (nanoparticles), one-dimensional (nanotubes and nanowires), two-dimensional (thin films and multilayer systems) and three-dimensional (bulk materials with at least one nanocrystalline phase) materials (Basu & Balani, 2011; Mukhopadhyay & Basu, 2007; Viswanathan et al., 2006). The ceramic nanocomposites can also be classified into two categories based on the microstructure: (1) nanocomposites, fabricated by dispersion of nanosized particles within micron-sized matrix grains or at the grain boundaries of the matrix and (2) nano/nanocomposites, in which matrix grains are also in the nanosize scale (Basu & Balani, 2011; Mukhopadhyay & Basu, 2007; Nihara, 1991; Nihara & Suzuki, 1999).

It is well known that sintering is the major processing route for forming dense ceramics. The driving force for sintering is the reduction in surface free energy of the consolidated mass/powders. The reduction in surface energy can be accomplished by the diffusional mass transport processes that lead to either densification of the powder compact or grain growth. Classically, sintering can be divided into solid-state sintering and liquid-phase sintering. Solid-state sintering occurs when the powder compact is densified entirely in solid state at the sintering temperature, while liquid-phase sintering occurs when a liquid phase is present in the powder compact during sintering (Basu & Balani, 2011). In solid-state sintering, grain growth/coarsening may dominate the densification process and results in poor density, whereas the liquid-phase sintering enhances the densification in and some instances with abnormal grain growth. In order to obtain desired microstructure, the sintering parameters have to be tailored. For oxide ceramics, it is mostly the fine microstructure (finer grain sizes), that is desired to obtain a better combination of hardness, strength and toughness. However, elongated grains in some nonoxide ceramics, like Si_3N-based ceramics, enhance the toughness properties. Various processing parameters such as starting powders (size distribution and purity), sinter-aid/binder (type and amount), heating rate, sintering temperature, sintering time and sintering atmosphere significantly controls the densification process (**Figure 1**). A complete and detailed coverage of sintering mechanisms is not within the scope of this chapter and can be found elsewhere (Basu & Balani, 2011).

http://dx.doi.org/10.1016/B978-0-08-096527-7.00024-6

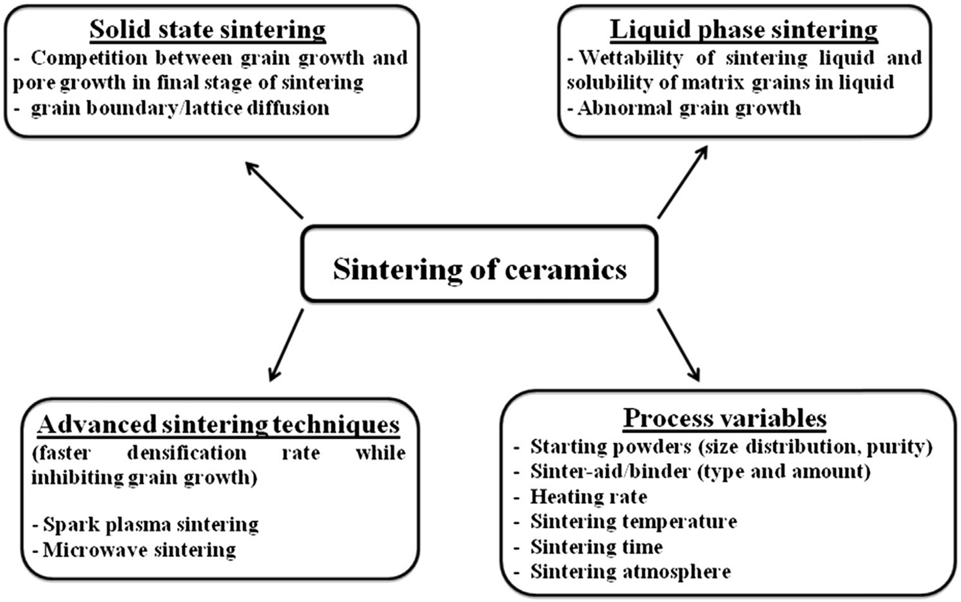

Figure 1 Summary of various factors controlling the sintering of ceramics as well as issues related with solid-state and liquid-phase sintering (Basu & Balani, 2011).

As far as the processing of nanoceramics is concerned, the control of grain growth during sintering remains the major challenge with conventional sintering techniques. In the above backdrop, various advanced sintering techniques such as spark plasma sintering (SPS), sinter forging, sinter-hot isostatic pressing were adopted to develop nanomaterials (Basu & Balani, 2011; Mukhopadhyay & Basu, 2007). Some of the major processing-related challenges in the development of nanoceramics and nanoceramic composites are illustrated in Figure 2. Adopting proper cost-effective synthesis route to obtain nonagglomerated *nanopowders*, forming green compact without cracks or density gradients and selecting appropriate densification technique in order to inhibit grain growth at the final stage of sintering are the key factors to be controlled in producing nanocrystalline materials.

Nanoceramics have distinct advantages in terms of superior hardness and strength, when compared to materials with micron or submicron microstructure. Mechanical properties can be significantly improved in ceramics by nanocomposite design. In particular, some nanoceramic composites can exhibit better

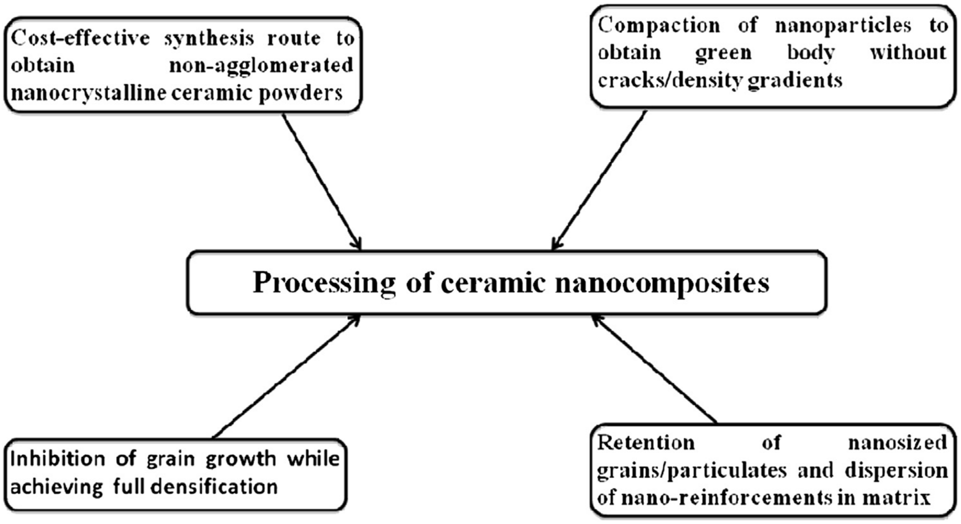

Figure 2 Schematic illustrates the major challenges in developing nanoceramic composites (Mukhopadhyay & Basu, 2007).

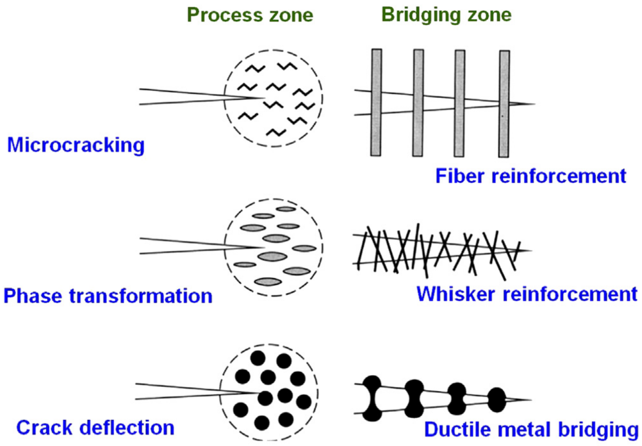

Figure 3 A schematic shows various toughening mechanisms in ceramic-based materials (Lawn, 1993).

high-temperature mechanical properties like hot hardness, high-temperature strength retention, creep and fatigue fracture resistance (Niihara, 1991; Niihara & Suzuki, 1999). One of the major concerns regarding mechanical properties of many technologically important ceramic systems is enhancement of fracture toughness. Lawn (1993) described that in ceramic-based materials, various toughening mechanisms such as microcracking, phase transformation, crack deflection, fiber/whisker reinforcement and ductile bridging, and so on have been possible by carefully controlling processing route and microstructure (**Figure 3**). However up to now, only a few of the toughening mechanisms have been explored in enhancing toughness of nanoceramic composites. In order to achieve high toughness in the nanostructured ceramic composites, perhaps more attempts to explore the suitability of fiber reinforcement and whisker reinforcement composites need to be pursued.

SPS has been one of the most widely used advanced sintering techniques in processing bulk nanoceramics/composites (Grasso, Sakka, & Maizza, 2009; Munir, Quach, & Ohyanagi, 2011; Munir, Tamburin, & Ohyanagi, 2006; Nishimura, Xu, Kimotoa, Hirosakia, & Tanaka, 2007; Orru, Licheri, Locci, Cincotti, & Cao, 2009; Raj, Cologna, & Francis, 2011). SPS is a versatile technique in developing a wide variety of materials such as nanomaterials, biomaterials, functional or functional graded materials, ultrahigh-temperature materials, transparent materials, porous materials, and so on (Basu, Katti, & Kumar, 2009; Chaim & Mardera, 2010; Chen, Khor, Chan, & Yu, 2004; Faiz et al., 2012; Gupta, Mukhopadhyay, Pavani, & Basu, 2012; Kalmodia et al., 2010; Nath, Biswas, & Basu, 2008; Nath, Tripathi, & Basu, 2009; Ran & Gao, 2012; Venkateswaran, Basu, Raju, & Kim, 2006; Zhang, Lin, Chang, Lu, & Ning, 2008). A summary of grain-size data on spark plasma sintered (SPSed) nanoceramics vis-a-vis starting powder particle size are summarized in **Table 1**. It is noteworthy that with the

Table 1 A comparison of starting powder particle size and final grain size of different oxide and nonoxide ceramics after spark plasma sintering (Mukhopadhyay & Basu, 2007)

Material	*Starting powder particle size (nm)*	*Final grain size after SPS (nm)*
ZrO_2 (3 mol% yttria)	27	70–80
ZrO_2 (3 mol% yttria)	60	100
ZnO	20	100
TiO_2	20	200
WC	7	25
γ-Al_2O_3–20 vol% SiC_w	32	118
WC–12 wt% Co (process: PPS)	40–80	50–110
ZrO_2–10 mol% Al_2O_3	<10	<100
3Y-TZP–40 vol% HAP	10	50
Si_3N_4–30 vol% TiN	5–20	50
Mullite–10 vol% SiC	100	240

PPS, pulse plasma sintering.

exception of TiO_2 and mullite composites, most of the materials can retain grain size below 100 nm after SPS processing.

There has been a growing research interest to develop strong and tough ceramics using either designed microstructure or adopting novel processing routes (Basu, Lee, & Kim, 2004; Basu, 2005; Basu, Venkateswaran, & Kim, 2006; Garmendia et al., 2011; Kumar, Prakash, Cheang, & Khor, 2005). Ceramics based on stabilized zirconia have received increasing attention since the discovery of transformation toughening. The toughened ZrO_2 materials have potentiality for biomedical and structural applications in view of their excellent biocompatibility, wear resistance, high corrosion resistance and mechanical properties. The various commercial applications of ZrO_2-based materials include femoral ball heads, dental restoratives, extrusion dies and cutting tool inserts, seals, thrust bearings, valve guides for turbocharger rotors, pump parts, knives and scissors used in paper industries, diesel engine parts, roller guide, bearings in seal-less pumps, magnetic drives and milling media, etc. (Basu, 2005; Basu, Lee, & Kim, 2004; Basu et al., 2006; Garmendia et al., 2011; Kumar et al., 2005).

Among nonoxide ceramics, transition metal carbides are refractory compounds and they are characterized with high hardness and strength. Among them, cemented carbides (both conventional as well as nanostructured) possess an excellent combination of mechanical and tribological properties and are one of the most extensively used ceramic-based materials for demanding engineering applications (Fang, Wang, Ryu, Hwang, & Sohn, 2009; Mukhopadhyay & Basu, 2011). WC-based cermets are conventionally used as cutting tools, wear parts, tools and dies, etc. in view of their attractive properties including high hardness, high elastic modulus, superior wear resistance, good thermal conductivity and low thermal expansion coefficient (Fang et al., 2009; Mukhopadhyay & Basu, 2011). Even though the metallic binder phase is responsible for the superior fracture toughness of these composites, it is the softer component, which limits the performance and hinders the use of such materials, particularly in applications requiring high hardness and good high-temperature properties. Hence, there has been a surge toward the development of dense novel WC-based materials by replacing the metallic binder phase partially or fully by ceramic sinter additives (Basu et al., 2004; Mukhopadhyay & Basu, 2011; Mukhopadhyay, Chakrabarty, & Basu, 2010; Sun, Kan, & Zhang, 2011; Venkateswaran, Sarkar, & Basu, 2005). One of the aims of this chapter is to discuss the development of high-performance WC-based ceramic nanocomposites to meet the demands of engineering applications. However, in the absence of metallic binder phase, extremely high sintering temperatures (1700–1900 °C) are necessary to obtain dense WC ceramics even with the use of SPS.

This chapter starts with an account of basic introduction pertaining to development of bulk nanoceramics/nanoceramic composites using SPS process. Section 2.05.2 describes the SPS processing and phenomena, driving forces for the process, and advantages and limitations of SPS. It also highlights the efficacy of novel multistage SPS to achieve uniform microstructure and superior properties in nanoceramics. The state-of-art knowledge in understanding thermal and electric field distribution of SPS is presented in Section 2.05.3. In particular, it is shown how various simulation models validate experimental results in connection with the thermal and electric field distribution of SPS. Section 2.05.4 highlights the development of oxide-based nanoceramics using SPS and in particular, ZrO_2 nanoceramic composites processing and properties is illustrated. As a case study, the tribological properties and wear mechanisms of YTZP nanoceramics is presented in view of its potentiality for various structural and tribological applications. The processing, microstructure, mechanical and tribological properties of WC–ZrO_2 nanocomposites are presented in detail in Section 2.05.5. Finally, Section 2.05.6 concludes with a brief overview of the present status of SPS usage in producing nanoceramics and unresolved issues related to both the mechanistic as well as operational aspects of SPS and emerging challenges in obtaining nanoceramic composites with superior properties.

2.05.2 Spark Plasma Sintering: Phenomenological Description

As mentioned earlier, the SPS has been most widely used in processing bulk nanoceramics/composites. SPS is a class of novel sintering techniques that employ mechanical pressure in combination with electric and thermal fields in order to produce dense materials of a powder compact (**Figure 4(a)**). SPS is also known under different names such as field-assisted sintering technique (FAST), plasma-activated sintering (PAS) or pulse electric current sintering, and plasma pressure compaction (PPC) (Basu & Balani, 2011; Cremer, 1944; Groza and Zavaliangos, 2000; Mukhopadhyay & Basu, 2007; Viswanathan et al., 2006). In the SPS processing, the starting materials can be in the form of either powders or green compacts. Phenomenologically, the process involves

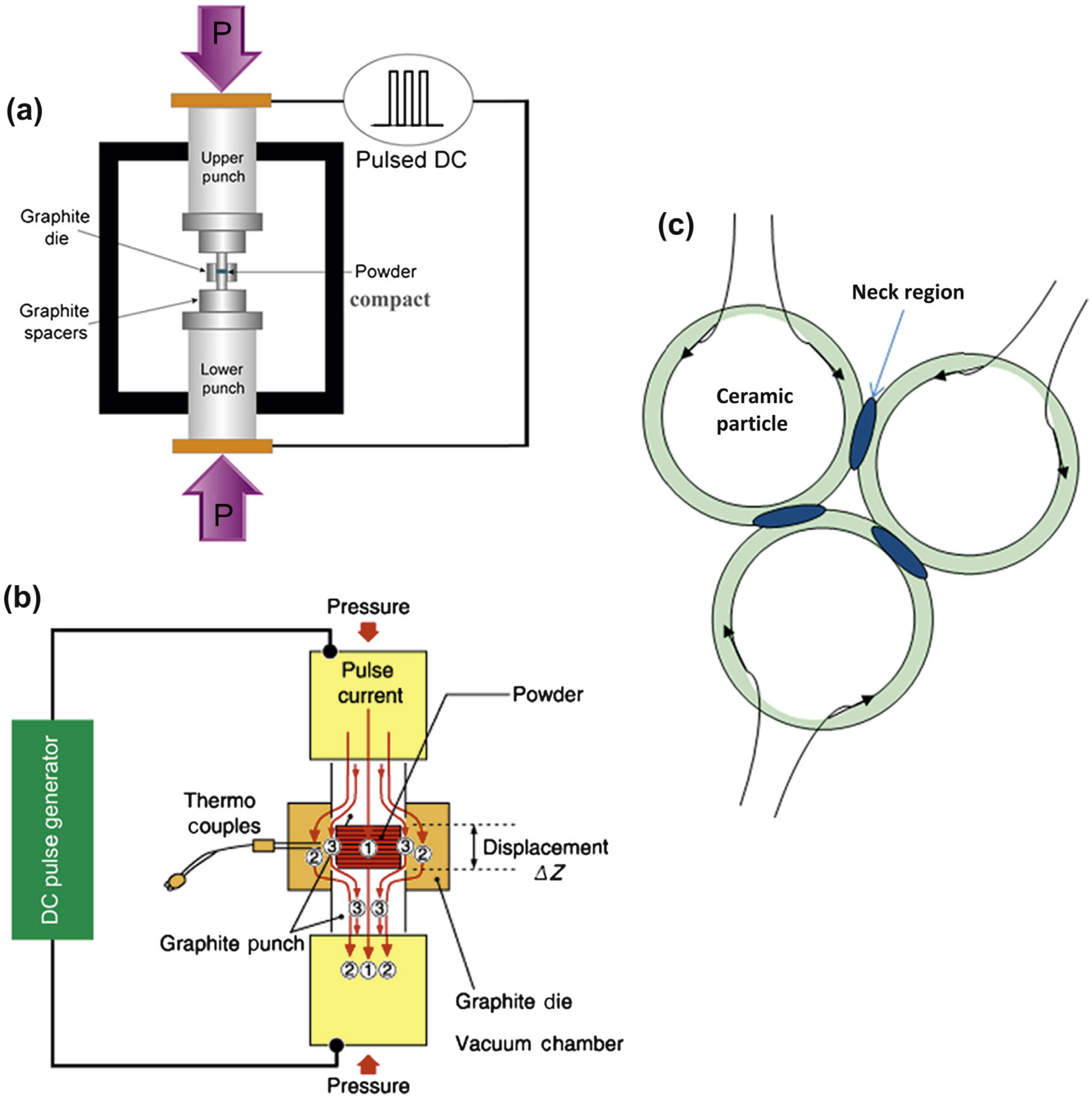

Figure 4 (a) Schematic of the spark plasma sintering process equipment (P is the applied external load) (Munir et al., 2011), (b) schematic of the physical process, involving the current flow during the spark plasma sintering process (Tiwari et al., 2009) and (c) current flow through powder particles in SPS.

heating a porous powder compact, by means of direct current (DC) pulse, which is applied through electrodes at the top and bottom punches of the graphite die.

SPS process is basically a modification of hot pressing and the fundamental difference is that high electric current passes directly through the pressing mould and powder compact, whereas a powder compact in a die-punch assembly is heated by external heating source in hot pressing (Mamedov, 2002; Shen, Zhao, Peng, & Nygren, 2002; Tokita, 2001). Typically, the die-punch assembly in hot pressing is heated by external heating with the heating coils being placed around the inner wall of the vacuum chamber. On the contrary, the sample and die in the SPS process are heated by Joule's heating with the current passing partly through die and rest through the powder compact, depending on temperature and thermophysical properties of the powder compact (Figure 4(b)). As far as the characteristics of the starting powders are concerned, conducting powders are heated by Joule effect and by heat transfer from the die-punch, while the nonconductive powders are heated only through the heat transfer from the die-punch. The SPS process utilizes pulsed high DC along with uniaxial pressure to enhance consolidation of powders. During the process, the combination of a low-voltage, high-intensity pulsed DC and uniaxial pressure are simultaneously applied, which in turn offers the possibilities of using rapid heating rates and very short holding times to obtain highly dense samples.

More importantly, the SPS process is driven by three mechanisms: (1) activation by pulsed current, (2) resistive heating and high heating rate and (3) pressure application. The primary purpose of the imposed electric currents is to provide the required amount of resistive heat. **Figure 4(c)** illustrates how current flows through powder particles in the SPS process. Joule heating that is generated by the power supply enhances the densification of materials. The surface of powder particles purify during SPS as a strong electrical field is produced in the small gaps of the particles to make the electrons, cations and anions striking the surface of the opposite particle. The electric current additionally enhances sintering of powders by activating various mass transport mechanisms such as surface oxide removal, electromigration and plasticity. The resistive heat in SPS consists of a localized and massive heat. The localized heat is concentrated at particle interfaces and facilitates particles bonding and the latter promotes plastic deformation and densification. Heating rates as high as 1000 °C min^{-1} are possible, although it is hard to apply a heating rate of more than 80 °C min^{-1} with most of the conventional sintering techniques.

According to Munir et al. (2006), the SPS process can be performed with or without pressure application to make either dense or porous compacts. In another work, Munir et al. (2011) mentioned that mechanical pressures of up to 1 GPa could be applied dynamically during SPS. The sinterability of powders increases under an applied pressure along with temperature. The application of pressure results in particle rearrangement and the breaking of agglomerates, particularly in the case of nanosized powders. The significance of the pressure on sintering depends on the relative magnitudes of particle size and surface energy. The relative contribution of the pressure becomes significant as the particle size increases. The effect of pressure on sintering can be assessed from the following equation:

$$\frac{d\rho}{(1-\rho)dt} = B\left(g\frac{\gamma}{x} + P\right) \tag{1}$$

where ρ is the fractional density, t is the time, B is a term that includes diffusion coefficient and temperature, g is a geometric constant, γ is the surface energy, x is the parameter that represents a size scale (related to particle size), and P is the applied external pressure. The first term on the right-hand side of Eqn (1) (within parentheses) represents the intrinsic driving force for sintering, while the second term represents the intrinsic contribution to the driving force by the applied pressure.

It has been believed that at initial stage, the pulsed DC current generates the spark discharge between the powder particles. The gases existing in the sample can be ionized and transformed into plasma. The generated spark discharges and plasma promote the elimination of absorbed gases and oxide layers on the surface of powder particles. Hence, the particle surfaces are cleaned and activated, which provide the favorable diffusion bonding between particles, thus accelerates the densification of the compact. The claim that the pulses generate spark discharges and this in combination with the existence of plasma between the powder particles explained the reason of the process being called SPS (Hansen, Rusin, Teng, & Johnson, 1992; Lee, Kang, Sato, Tezuka, & Kamio, 2003; Omori, 2000; Tokita, 2003; Wang, Chen, Hirai, & Kang, 1999). However, the experimental evidences for the spark discharge and plasma are still lacking. Moreover, the quantification of the effects of pulsed DC on densification of the conducting powders has not been well-explored yet. It is noteworthy to mention that a specific advantage of FAST, over traditional hot pressing or hot isostatic pressing, is controlled grain growth, which results in improved mechanical, physical or optical properties or corrosion and oxidation resistance properties (Khor, Cheng, Yu, & Boey, 2003; Shen, Johnson, Zhao, & Nygren, 2002; Su et al., 2004).

Li and Gao (2000) pointed out that despite having specific advantages like rapid rate of heating and lower processing time, one of the major disadvantages of SPS process is massive sparking, which occurs during the rapid heating and this expedites abnormal grain growth during sintering. Another disadvantage is that uniform densification depends on size of the sample (Angerer, Yu, Khor, Korb, & Zalite, 2005; Tamburini, Gennari, Garay, & Munir, 2005). Although not reported extensively in literature, SPS process can lead to nonuniformity in densification and concomitant variation in material properties across the sample width/thickness (Tiwari, Basu, & Biswas, 2009; Vanmeensel, Laptev, Hennicke, Vleugels, & Van Der Biest, 2005). These restrict wider industrial applications of the SPS process. Reddy, Kumar, and Basu (2010a) recently proposed that multistage SPS schedule can be adopted to consolidate nanoceramics with uniform and better mechanical properties than the widely researched single-stage SPS schedule. In this new processing approach, a porous powder compact is held for 5 min at temperature of $0.45T_m$ to promote initial surface activation, then heating quickly to a temperature of $0.5T_m$ and holding there for 5 min and finally sintering at $0.55T_m$ for another 5 min, where T_m is the

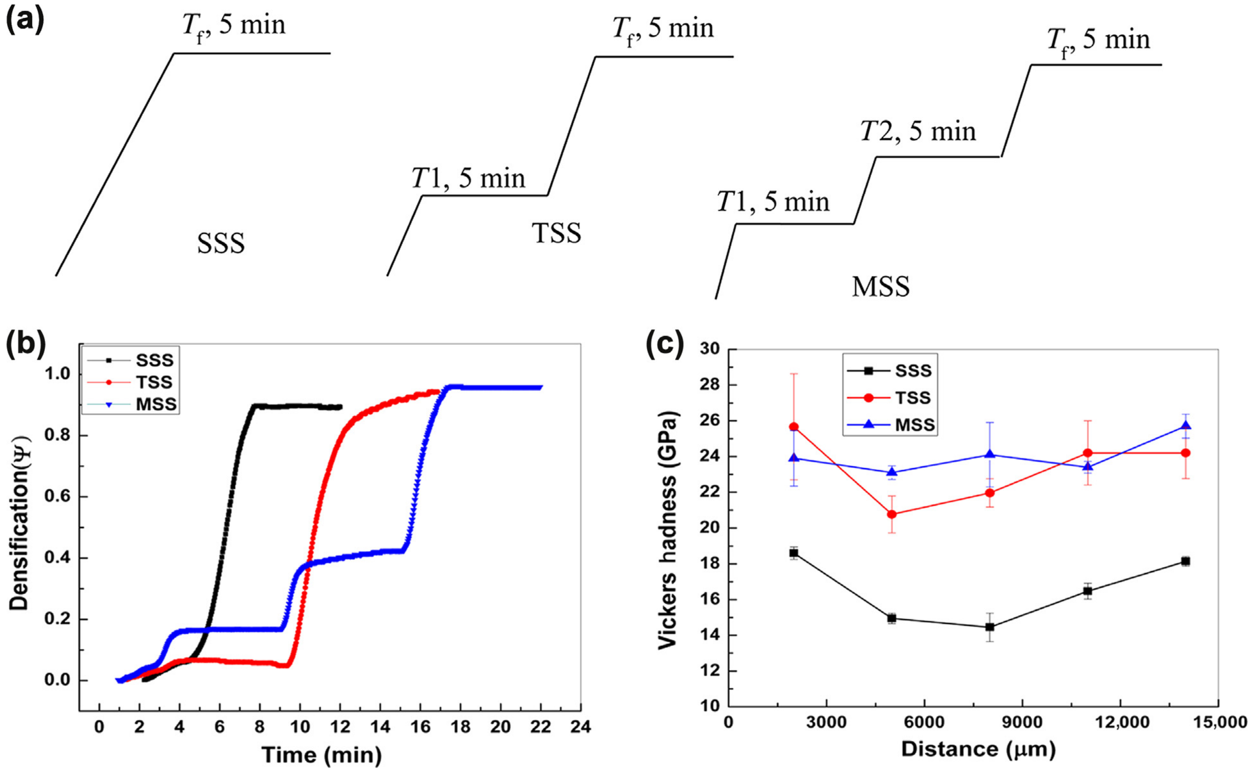

Figure 5 (a) Heating schedules of SSS, TSS and MSS, (b) a plot representing densification parameter ($\Psi = (\rho_t - \rho_i)/(\rho_{th} - \rho_i)$) as a function of heating time and (c) variation of Vickers microhardness with radial distance from center of sample for α-Al_2O_3 sintered via three different heating schedules of SSS, TSS and MSS [where $T1$ and $T2$ are intermediate temperatures, T_f is the final sintering temperature, ρ_t is instantaneous density, ρ_i is the initial density and ρ_{th} is the theoretical density of the compact; SSS, single-stage sintering; TSS, two-stage sintering; MSS, multistage sintering] (Reddy et al., 2010a).

melting point in degree Celsius. Such a heating scheme is based on the expectation that the multistage sintering (MSS) would be more effective than conventional single-stage sintering (SSS) or even two-stage sintering (TSS) using SPS. The latter involves the heating of powder compact to $0.45T_m$, holding it for 5 min and then sintering at $0.5T_m$ for 5 min. Also, any given porous powder compact is directly heated to $0.55T_m$ and then held for 5 min in SSS route. A schematic representation of heating schedules of SSS, TSS and MSS is presented in Figure 5(a) and Figure 5(b) illustrates how the densification parameter, $\psi = \frac{\rho_t - \rho_i}{\rho_{th} - \rho_i}$, where ρ_t is the instantaneous density at time, $t = t$, ρ_i is the initial density at the onset of SPS and ρ_{th} is the theoretical density, i.e. density of 100% dense compact) varies with heating time during three different sintering schemes (SSS, TSS, and MSS). Importantly, more shrinkage is observed during second holding stage at MSS process. However, the holding at final sintering temperature for 5 min does cause any noticeable shrinkage. In order to illustrate the effectiveness of this new approach of heating cycle in case of α-Al_2O_3, the evolution of densification parameter as a function of time and the variation of Vickers microhardness with radial distance from center of sample after three different SPS heating schedules (SSS, TSS and MSS) is shown in Figure 5(c). Al_2O_3 ceramic, densified using MSS scheme, exhibits significantly less variation as well as uniformly higher hardness values when compared to SSS/TSS ceramics (Figure 5(c)).

2.05.3 Spark Plasma Sintering: Thermal and Electric Field Distribution

The high heating rate in SPS causes a temperature gradient within the die. Typically, temperatures in SPS processing above 1000 °C are read by a pyrometer on the surface of the die. This temperature is not truly representative of the specimen temperature since there exists temperature difference between specimen center and surface of the die. For example, Tomino, Watanabe, and Kondo (1997) reported a temperature difference between specimen center and die surface of ~200 °C for copper and ~110 °C for alumina powders. Zavaliangos, Zhang, Krammer, and Groza (2004) also reported of microstructural inhomogeneities within SPS processed specimen, e.g. presence of coarser microstructure at the outer surface of WC specimens than in the center. Hence, temperature gradients in SPS must be evaluated carefully in order to make proper comparison with the other conventional sintering techniques and also to optimize processing in larger size specimen.

Yucheng and Zhengyi (2002) calculated 2-D temperature distribution inside the die and reported that the higher the thermal conductivity of the material, the lower is the temperature difference between the center and die surface. They concluded that temperature difference is directly related to heating rate, i.e. higher the heating rate, greater is the temperature difference which can be as high as 450 K when sintering temperature at sample center is 1873 K. In a different study, Zavaliangos et al. (2004) performed finite-element simulation to evaluate the similar problem of temperature distribution during field-activated sintering. Their study enables a proper comparison between SPS and conventional sintering technique and also indicates how to optimize processing parameters in larger size specimens. Additionally, considerable temperature gradient, both in radial and axial directions, was analyzed in their work. They attempted to rationalize the finite-element calculations from physical aspects of SPS, Joule's heat generation in the die setup and heat transfer within and out of die setup. Another important observation of their work was that almost a linear co-relation exists between die surface temperature and the sample temperature.

Tamburini et al. (2005) used the CFD-ACE+ code to examine the effect of sample conductivities on the current and temperature distributions. They showed that the sample conductivities significantly affect both thermal and electric field distributions. In another work, Vanmeensel, Laptev, Van der Biest, and Vleugels (2007) used FEM calculations to model the evolution of current density and temperature distribution in SPS system. In an effort to validate the model predictions, they performed experiments on electrically conducting titanium nitride and electrically insulating zirconia powder compact. They concluded that a largely inhomogeneous temperature distribution could be expected to exist in the case of titanium nitride, when compared to zirconia under identical SPS cycles. Such difference can be attributed to difference in current flow in zirconia (current flow through punch and die) and titanium nitride (current flow through sample). Because of such a likely temperature distribution effect, a guideline to closely capture the temperature profile is proposed. It has been suggested that if a pyrometer is placed at the bottom of bore hole inside the upper punch (about 5 mm away from specimen center), a better temperature control can be ensured with a temperature difference between the center and carefully placed pyrometer limited to 5 K or lower.

In another paper, Tiwari et al. (2009) reported finite-element simulations to determine the temperature distribution (both in radial and axial direction), heat and electric flux-field in the powder compact/die/punch assembly during the SPS process. The simulation studies were conducted using both ABAQUS and MATLAB and a range of power input, varying thermal conductivity of powder compact and the effect of time variation on both thermal and electric field evolution were considered. The major inference from MATLAB results is that if SPS processing needs to be carried out at a temperature region corresponding to graphite die surface temperature of 1000 °C or higher, the electrical power supply enabling power input to the SPS system needs to be more than 0.5×10^7 W/m^3 (**Figure 6(a)**). An increase in die surface temperature from 1000 to 1700 K can be realized with a seven times increase in power input, i.e. from 0.5 to 3.5×10^7 W/m^3. Also, the temperature decreases with an increase in radial distance, irrespective of thermal conductivity (**Figure 6(b)**). However, such a decrease strongly depends on the relative difference in thermal conductivity of various powder samples.

ABAQUS simulations were also used to evaluate temperature field over the SPS system (Tiwari et al., 2009). After 450 s, the surface temperature is in the range of 1301–1355 K (average ~1325 K), which is slightly lower (~14–15°) than obtained by MATLAB analysis (value ~1339 K) for a given set of input conditions (**Figure 6(c)**). As far as the simulated distribution of electric current density (ECD) is concerned, a clear difference in ECD between graphite punch and die surface can be seen (**Figure 6(d)**). Specifically, the electric current is maximum at the part of the punch outside the die, due to the smallest cross-section area (red region/band). For this simulated application, the magnitude of the current varies during sintering and the pattern of current flow is practically independent of time. The punches experience mostly high ECD and therefore, Joule's heating is in accordance with ECD. It can be realized that Joule's heating dominates in the punch part, as it should be. ABAQUS simulation results revealed the lowest ECD on the die surface, while intermediate level of ECD at the punch area.

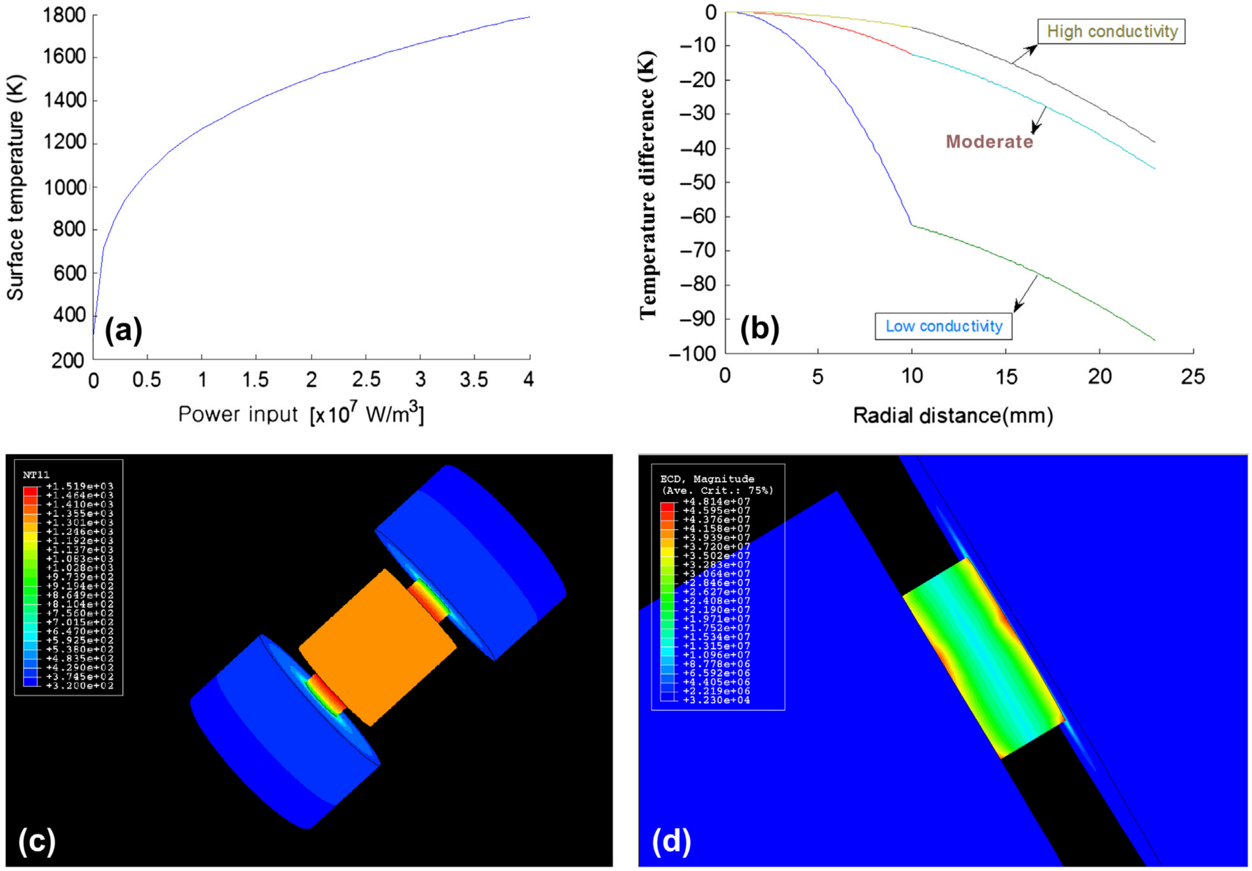

Figure 6 (a) The results of MATLAB estimation of graphite die surface temperature with variation in electrical power input, (b) the MATALAB simulation depicting the thermal heat flow evolution in the powder compact/die system for radial temperature profile in the middle cross-section of the sample, (c) ABAQUS FEM simulations visualizing the temperature distribution on the die and punch surface after 450 s operation of spark plasma sintering and (d) the ABAQUS FEM simulations visualizing the temperature distribution on the die and punch surface of spark plasma sintering after 450 s of soaking. For simulations in (b), (c) and (d) a constant Joule heat density of 1.25×10^7 W/m^3 is considered (Tiwari et al., 2009).

2.05.4 SPS of Oxide Nanoceramics

In view of the superior material properties, considerable research efforts have been carried out toward the processing and characterization of nanomaterials (Cha, Kim, Lee, Mo, & Hong, 2005; Nygren & Shen, 2003). While processing nanoceramics using SPS, it is important to select highly pure and well-deagglomerated precursor powders. Above a critical temperature, the grain growth rate of materials is largely determined by the characteristics of the starting powders, such as particle size, reactivity, degree of agglomeration, and so on. The densification behavior and resultant microstructure of some important oxide nanoceramics processed by SPS (under pressure 50 MPa, holding time 3 min and heating rate 100 °C/min) is shown in **Figure 7** (Nygren & Shen, 2003). As it can be seen in **Figure 7(a),(b)**, shrinkage starts at 900, 800 and 600 °C for Al_2O_3, ZrO_2 (doped with 3% yttria—3Y), and ZnO, respectively, and full density for the respective ceramic can be obtained at 1250, 1100 and 850 °C. The microstructures of SPSed samples reportedly exhibited an average grain size of 500 nm for alumina, and <100 nm for zirconia, whereas the precursor powders had an average particle size around 400 and 60 nm, respectively (**Figure 7(c),(d)**). It is widely known that the densification and grain growth are two competing processes during final stage of sintering. Marder, Chaim, and Estournes (2010) stated in developing high-performance nanoceramics that it is mostly desirable to achieve maximum densification with minimal grain coarsening. A close control of grain growth and densification is critical in optimizing the microstructure and properties of sintered materials (Zeng, Gao, Gui, & Guo, 1999). In a recent work, Reddy, Kumar, and Basu (2010b) reported that

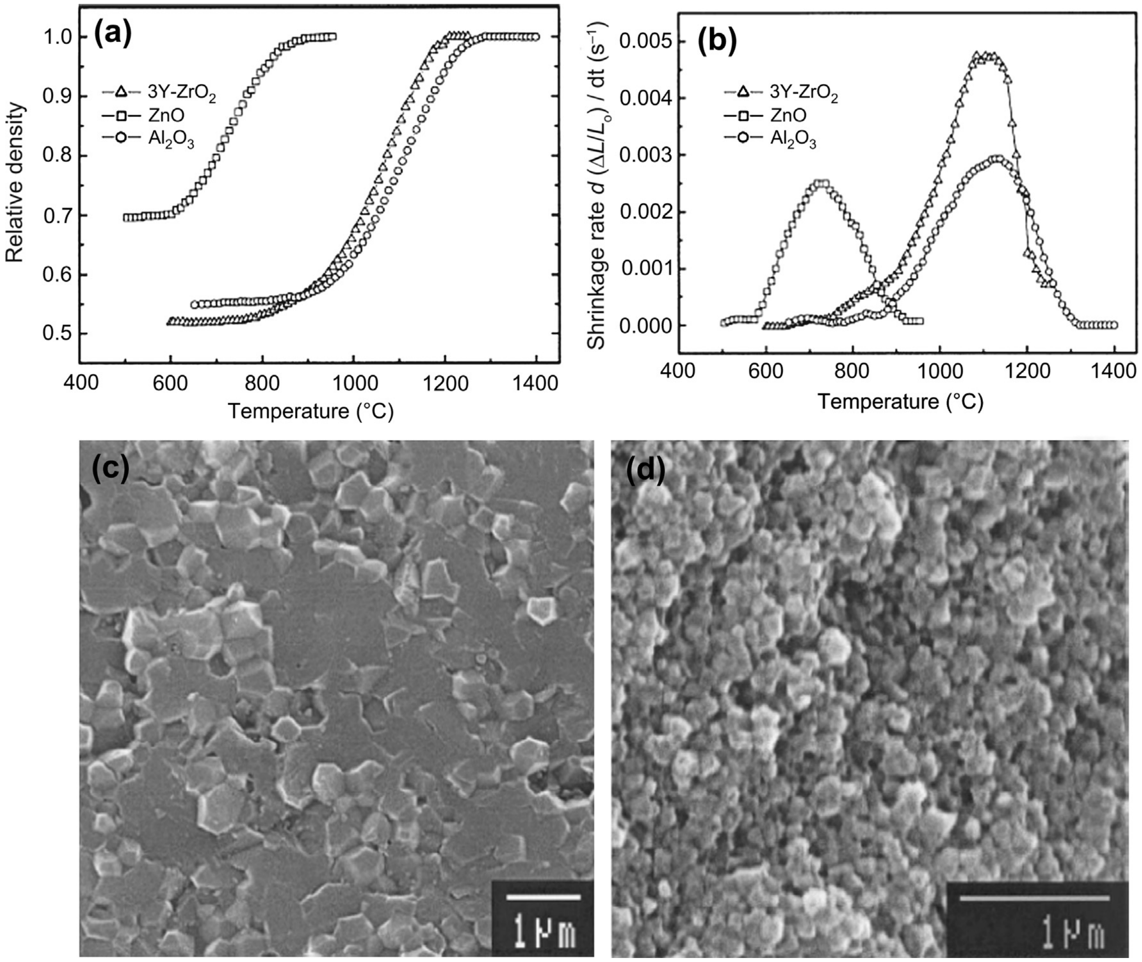

Figure 7 (a) Densification of ZnO, ZrO_2 (doped with 3% yttria), and α-Al_2O_3 ceramics as a function of temperature, and (b) shrinkage rate of the ZnO, ZrO_2 (doped with 3% yttria), and α-Al_2O_3 ceramics processed via SPS using a heating rate of 100 °C/min (c) SEM micrographs depicting the nano-sized microstructures of fully densified α-Al_2O_3 and (d) yttria-doped ZrO_2 (Nygren & Shen, 2003).

grain growth of nano-ZrO_2 and Al_2O_3 ceramics can be effectively inhibited using multistage SPS when compared to single-stage SPS (**Figure 8**). An important aspect of MSS proposed by Reddy et al. (2010b) is that such sintering scheme enables near-full densification (98% ρ_{th}) at lower grain size than that in conventional pressureless sintering in case of Al_2O_3 (**Figure 8(b)**). Also, an increase in relative density from 98 to 100% ρ_{th} takes place much more sharply compared to conventional sintering, while the variation of grain size with density remains qualitatively similar in case of SSS, MSS and conventional sintering (**Figure 8(b)**). Interestingly, not much difference in grain size variation is observed in case of 3 mol% yttria-stabilized ZrO_2, when they are sintered using TSS, MSS scheme at the same final sintering temperature (**Figure 8(a)**). More uniform grain size distribution is observed in case of ZrO_2 compared to Al_2O_3 with latter showing more bimodal grain size distribution (**Figure 8(c),(d)**).

The nanocomposite approach is reported to be promising in achieving higher fracture strength/fracture toughness of ceramics. Among various alumina nanocomposites, Al_2O_3–SiC nanocomposites, characterized by uniform dispersion of nano-SiC within submicron Al_2O_3 matrix, have been widely investigated (Gao et al., 1999; Merino & Todd, 2005; Ohji, Jeong, Choa, & Niihara, 1998; Sternitzke, 1997; Sun et al., 2005). The reinforcement of nano-SiC in Al_2O_3 matrix resulted in a significant increase in fracture strength along with a modest improvement in fracture toughness. Crack deflection and crack bridging by nano-SiC reinforcements are reported to lead to the improved fracture properties of the nanocomposites. The reinforcement of second phase can result in the enhancement of fracture toughness of materials due to the toughening mechanisms, like transformation toughening as for ZrO_2, ferroelastic domain switching as for

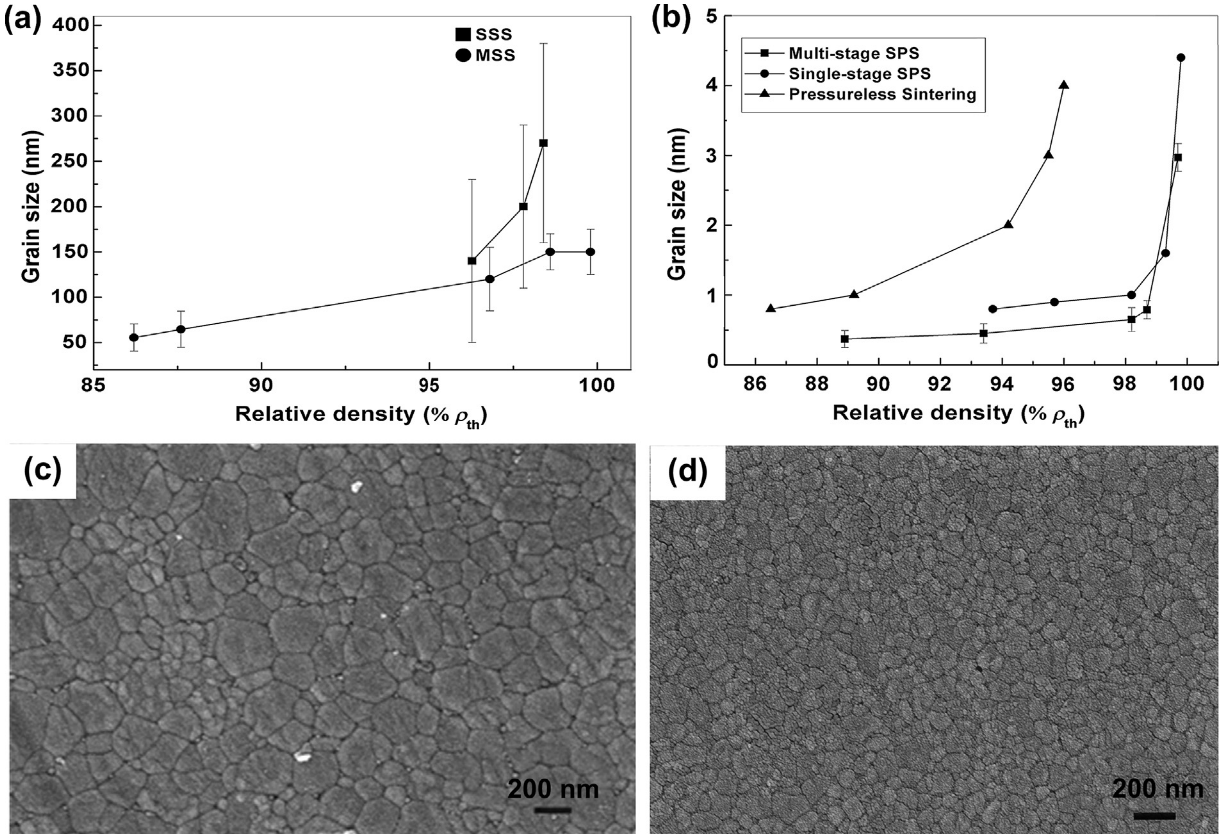

Figure 8 (a) Relative density versus grain size plot for 3 mol% yttria-stabilized ZrO_2 during single-stage sintering (SSS) and multistage sintering (MSS). (b) Relative density versus grain size map for α-Al_2O_3 for single-stage spark plasma sintering, single-stage spark plasma sintering and pressureless sintering. (c) SEM images of 3 mol% yttria-stabilized ZrO_2, multistage spark plasma sintered at 1250 °C. (d) Single-stage spark plasma sintered at 1250 °C (Reddy et al., 2010a; Zeng et al., 1999).

$BaTiO_3$ and ZrO_2 (Basu, 2005; Zhan, Kuntz, Wan, Garay, & Mukherjee, 2003a, 2003b). Zhan et al. (2003a) developed Al_2O_3–ZrO_2 nanocomposite via SPS route at 1100 °C. The densified nanocomposite had a finer microstructure with alumina matrix grain size of 96 nm and the zirconia reinforcements, having a size of 265 nm. A combination of mechanical properties, in particular, hardness of approximately 15.2 GPa and fracture toughness of around 8.9 MPa $m^{1/2}$, was reported with the Al_2O_3–20 vol% ZrO_2 nanocomposite. The toughness increment was attributed to ferroelastic domain switching of the ultra-fine t-ZrO_2. In case of Al_2O_3–SiC nanocomposites, SPS of Al_2O_3–5 vol% SiC powders at 1450 °C resulted in fully densified intragranular ceramic nanocomposite (Sun et al., 2005). The nanocomposites exhibited superior strength of around 980 MPa, which is much higher than 350 MPa (normally measured with monolithic Al_2O_3). Gao et al. (1999) fabricated Al_2O_3–SiC–ZrO_2 (3Y) nanocomposites via SPS under similar conditions and obtained maximum strength of ~1.2 GPa. In the following section, the development of ZrO_2-based nanocomposites is discussed.

2.05.4.1 SPS of ZrO_2-Based Nanoceramic Composites

Nanoceramics/nanocomposites based on ZrO_2 have been developed in order to improve mechanical properties of ZrO_2 by incorporation of other hard ceramics. Huang, Vanmeensel, Van der Biest, and Vleugels (2007) densified ZrO_2-based nanocomposites with 40 vol% WC addition by pulsed electric current sintering within 4 min at 1450 °C under a pressure of 60 MPa. An excellent combination of flexural strength of 2000 MPa, Vickers hardness of 16.2 GPa and fracture toughness of 6.9 MPa $m^{1/2}$ was obtained for a 2 mol% Y_2O_3-stabilized ZrO_2 nanocomposites. Such an improvement in mechanical properties of the ZrO_2 composites is due to the use of nano- or micrometer-sized WC starting powders. Yoshimura, Sando, Choa, Sekino, and Niihara (1999) sintered

ZrO_2–Al_2O_3 nanocomposites using the SPS route and nano-sized ZrO_2 grains of 50 nm characterize the microstructure.

Basu et al. (2006) developed fully dense yttria-stabilized tetragonal zirconia nanocomposites, reinforced with 30 vol% of ZrB_2 via SPS route (temperature of 1200 °C, holding time of 5 min and heating rate of 600K/min). The nanocomposite materials exhibited finer microstructure, with grain size of ZrO_2 in the range of 100–300 nm and ZrB_2 sizes of 2–3 μm. The hardness and fracture toughness of ZrO_2–ZrB_2 nanocomposites are shown in **Figure 9**. The hardness of the ZrO_2-based composites remained moderate, varying in the range of 12–14 GPa, while the fracture toughness reported in the range of 6–11 MPa $m^{1/2}$. The difference in toughness data was interpreted in terms of the difference in ZrO_2 matrix stabilization. A decrease in overall yttria content from 3 to 2 mol% considerably enhanced the fracture toughness. In addition to the transformation toughening mechanism, crack deflection by hard second phase led to the toughness improvement of the nanocomposites (**Figure 9(b),(c)**). An important observation was the occurrence of transformation toughening in ZrO_2–ZrB_2 nanocomposites.

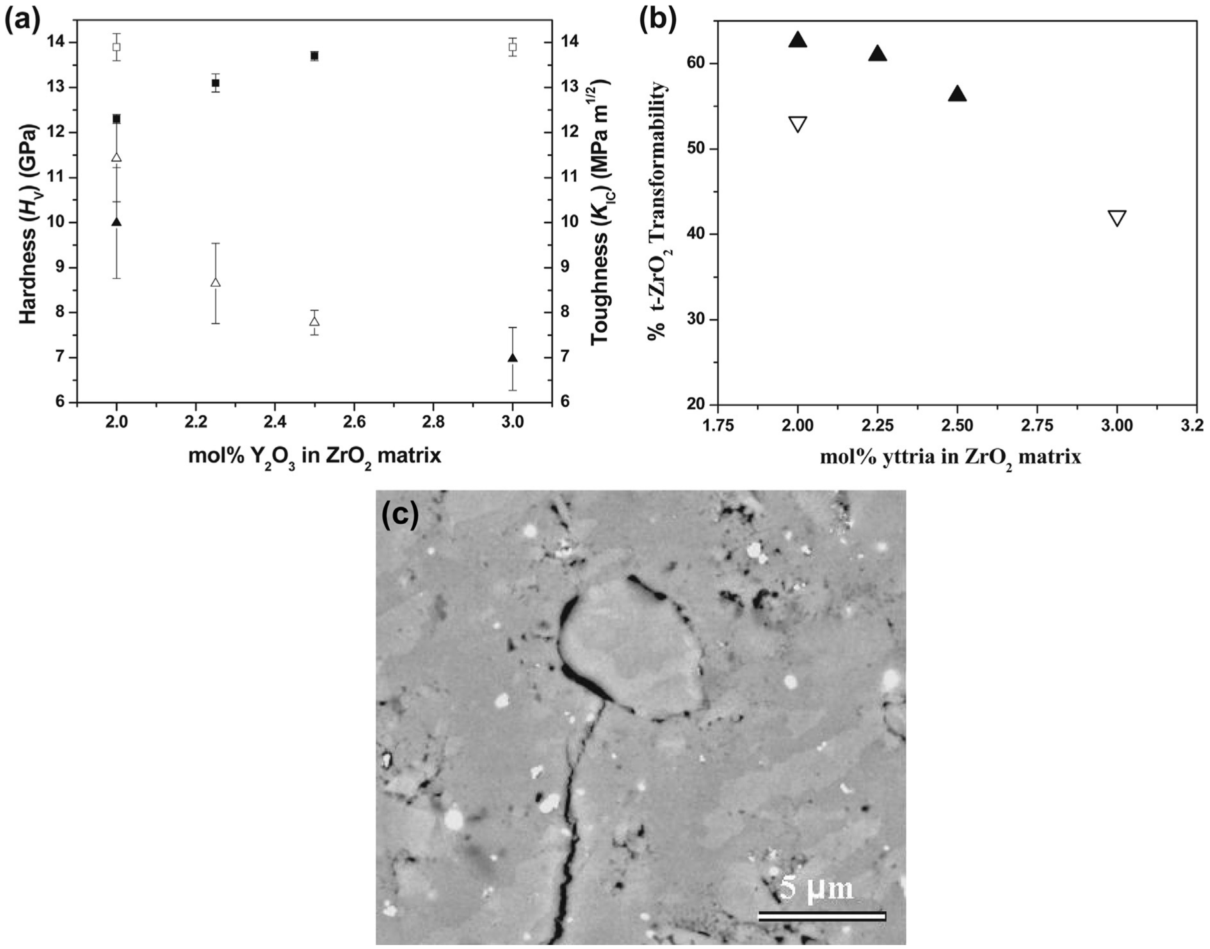

Figure 9 (a) Plot of hardness and toughness versus yttria stabilization ZrO_2 matrix for spark plasma sintered (1200 °C, 5 min) nanocomposites. Different symbols represent the mechanical property measured with various composites based on ZrO_2 matrix processed from either coprecipitated or mixed grade ZrO_2 powders: ■, H_{v10} of the mixed grades; □, H_{v10} of the coprecipitated grades; ▲, K_{Ic} of the co-precipitated grades (using Palmqvist formulae); Δ, K_{Ic} of the mixed grades (using Plamqvist formulae), (b) the percentage transformability of the ZrO_2 matrix against the mol% of yttria content in that matrix at sintering temperatures of 1200 °C. The t-ZrO_2 transformability is defined as [% m-ZrO_2 on the fractured surface-% m-ZrO_2 on the polished surface]. The transformability data of various composite grades processed from the use of ZrO_2 powders are indicated by different symbols: ▽, coprecipitated grades–mixed grades and (c) crack wake debonding of the coarser ZrB_2 particles at the interface in ZrO_2–2 mol% yttria (co-precipitated grades) nanocomposite, SPSed at 1200 °C for 5 min (Basu et al., 2006).

2.05.4.2 SPS of Y-TZP Nanoceramics Processing and Tribological Properties

Tetragonal zirconia polycrystals (TZP) have been extensively studied in view of its high fracture toughness. Its high fracture toughness (2–20 MPa m$^{1/2}$) stems from the crack tip shielding by volume increment due to stress-induced transformation of metastable tetragonal ‘t’-ZrO_2 to stable monoclinic ‘m’-ZrO_2 in the crack tip stress field, a phenomenon known as *transformation toughening* (Basu, 2005). In spite of having high fracture toughness and excellent strength (700–1200 MPa), conventional TZP monoliths possess lower hardness (10–11 GPa), in comparison to other structural ceramics, like Al_2O_3 or Si_3N_4, SiC (Basu & Balani, 2011).

Li and Gao (2000) achieved full density of yttria (Y)-stabilized tetragonal zirconia after SPS treatment (heating rate 600 °C/min) at 1400 °C for 3 min, and also at 1180 °C with holding time of 9 min. It should be mentioned that the specific advantage of the SPS process is not the general shift to a lower sintering temperature (1200 °C), but a shorter sintering time (5 min) due to faster densification mechanism. Nygren and Shen (2003) densified nanocrystalline powders (20 nm) of YTZP to near theoretical density, while maintaining the final grain size to below 100 nm after SPS at 1100 °C under 50 MPa pressure. ZrO_2 (nano powders of 27 nm) doped with 3 mol% yttria was fully densified by SPS at 1200 °C under 30 MPa pressure (Basu, Lee, et al., 2004). Transmission electron microscopy (TEM) characterization revealed the grain size of the sample was <90 nm and the nanoceramics exhibited higher hardness (~14.5 GPa) and moderate fracture toughness (5.2 MPa m$^{1/2}$) in comparison to that of conventionally sintered monolithic ZrO_2 (~11 GPa and 2.5 MPa m$^{1/2}$) (**Figure 10**). Importantly, the hardness of nanocrystalline zirconia is superior to those obtained by conventional composites of zirconia with 30 vol% hard ceramic reinforcements, like ZrB_2, TiB_2 and WC (Anne et al., 2005; Basu, Vleugels, & Van Der Biest, 2002; Basu, Vleugels, & Van Der Biest, 2004; Mukhopadhyay, Basu, Bakshi, & Mishra, 2007). In

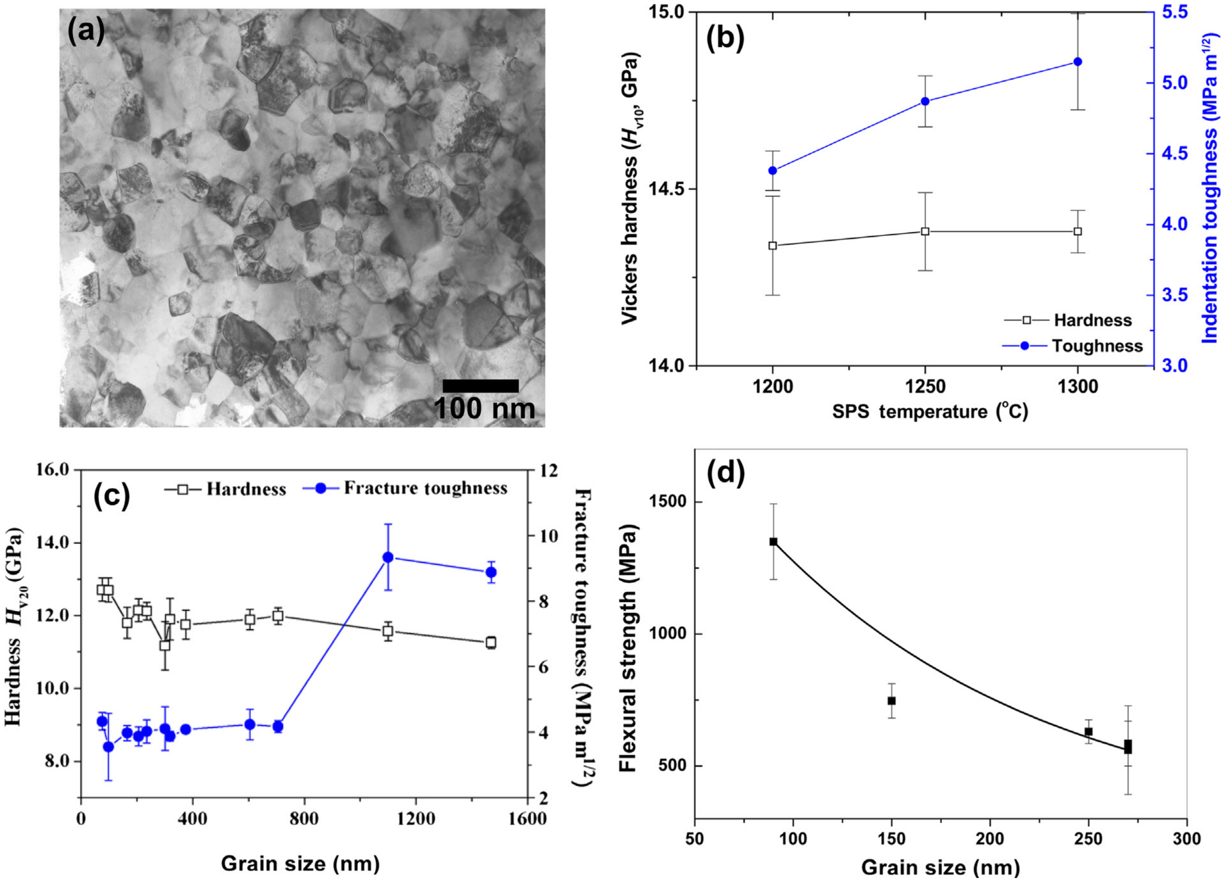

Figure 10 (a) Bright-field TEM image of the 3Y-TZP ceramic spark sintered at 1200 °C for 5 min (Basu, Lee, et al., 2004), (b) Vickers hardness and indentation toughness of the 3Y-TZP ceramics, spark plasma sintered in vacuum for 5 min at different temperatures (Basu, Lee, et al., 2004), (c) variation of Vickers hardness and indentation fracture toughness with grain size in Y-TZP (Kumar et al., 2010) and (d) the effect of grain size on flexural strength of ZrO_2 with 2 mol% yttria (Reddy et al., 2010c).

another work, Kumar, Kim, Hong, Bae, and Lim (2010) studied the effectiveness of various sintering techniques in processing nanocrystalline 3 mol% yttria-stabilized ZrO_2 ceramics. They reported that the average grain size of 75 nm is achievable for Y-TZP ceramics after SPS at 1150 °C for 10 min. The effect of YTZP grain size on Vickers hardness and indentation fracture toughness is shown in **Figure 10(c)**. It is noticeable that with decreasing grain size, the hardness slightly improved. In contrast, the fracture toughness significantly reduced from 9.0 MPa $m^{1/2}$ for 1100 nm grain size to 4.0 MPa $m^{1/2}$ for 700 nm grain size and the variation was negligible with further reduction of grain size of up to 75 nm. The grain size of YTZP has significant effect on the flexural strength (**Figure 10(d)**). The YTZP nanoceramic with grain size of around 90 nm exhibited flexural strength of ~1400 MPa, whereas the flexural strength is drastically lowered to 500 MPa with coarse grain structure of 275 nm. Overall, limited data (**Figure 10(d)**) reveal a significant increase in strength with a decrease in grain size from 275 nm to around 100 nm. However, it would be interesting to see how the strength of ZrO_2 would vary, when grain sizes are <100 nm and this will require some control experiments in future.

Ran et al. (2010) investigated the effect of SPS and subsequent annealing treatment on 3Y-TZP doped with 8 mol% CuO. Annealing after SPS resulted in grain growth and tetragonal to monoclinic zirconia phase transformation. It was reported that the grain size and monoclinic zirconia phase content are strongly dependent on the annealing temperature. Garmendia et al. (2011) developed nanostructured Y-TZP with the addition of a small volume fraction of partially coated multiwall carbon nanotubes by SPS. The resultant material exhibited an exceptional balance between aging and crack growth resistance due to the small grain size of the zirconia, which impedes the phase transformation that characterizes the aging. Crack bridging and carbon nanotubes pull-out were reported to be the main toughening mechanism. Li and Gao (2003) sintered nano-HAp–TZP (3Y) biocomposites using SPS. The rapid heating rate and short dwelling time of SPS process were attributed to the nano grain size of the biocomposites. It was proposed that SPS processing was effective in suppressing deleterious reaction between HAp and TZP; otherwise such reactions lead to the formation of unwanted TCP and cubic zirconia.

As a case study, tribological properties of YTZP ceramics are considered. In view of the potentiality of these ceramics for various structural applications ranging from biomedical to cutting tool and bearing applications, tribological property investigation is necessary. Although the wear behavior of zirconia ceramics has been widely studied for materials with micron and submicron grain sizes, very limited research on nanoceramics (<100 nm) (Kumar et al., 2010) has been reported. In case of TZP with coarse grains, the coefficient of friction (COF) was relatively high for self-mated zirconia ceramics, whereas dissimilar materials exhibited COF ranging from 0.3 to 0.5 (He et al., 1996; Klaffke, 1989; ZumGhar, 1989). The wear debris are reported to form as a result of internal stresses generated by mechanically or thermally induced phase transformation (Bundschuh & ZumGahr, 1991). As far as the wear mechanisms are concerned, plastic deformation, microcracking, and transgranular shear fracture of individual grains were dominant for fine grain size (~0.5 μm), while the increased tendency for intergranular fracture was observed for coarser grain size (~1.6 μm) (He et al., 1996).

Basu, Lee, et al. (2004) performed fretting wear tests (at ambient room temperature) for the YZP nanoceramics (90 nm), processed by SPS as well as conventional hot pressing. The fretting test of YTZP ceramics was carried out against steel ball (6 mm in diameter) and the test parameters include a normal load of 8 N, relative displacement of 150 μm, frequency of 8 Hz and testing duration of 100,000 cycles. This combination of fretting parameters establishes the "gross slip" fretting condition. The material removal of the YTZP ceramics was dominated by the abrasive wear and the SPS-processed material being harder than the conventional hot-pressed material, suffered less wear at the fretting contacts. In another work, Reddy, Mukhopadhyay, and Basu (2010) reported mechanical and tribological properties of dense yttria-stabilized t-ZrO_2 nanoceramics, which were developed via multistage and single-stage SPS. The fretting wear tests of ZrO_2 nanoceramics were studied against widely used Al_2O_3, ZrO_2 and bearing steel counter bodies at constant load (5 N) with an oscillating frequency of 5 Hz and 100 μm linear stroke for durations of 100,000 cycles. As far as the frictional behavior is concerned, the COF settled to a steady-state value of ~0.5 for both the ZrO_2 samples during fretting against steel. On the other hand, a slight difference in frictional behavior was observed for the ZrO_2 samples processed following two different processing schemes after fretting against the other two counter bodies. The COF recorded with the single-stage sintered (SSSed) ZrO_2 reached a value slightly higher than the steady-state COFs recorded with the multistage sintered (MSSed) samples (**Figure 11**). Furthermore, the COF of SSSed ZrO_2 samples against all the counter bodies over the entire test durations appeared to be relatively nonuniform, as compared to those recorded with the MSS ZrO_2 samples. The wear rate of the MSSed ZrO_2 samples (~10^{-7} mm^3/Nm) are nearly an order of magnitude lower than the corresponding wear rates measured with the SSSed ZrO_2 samples

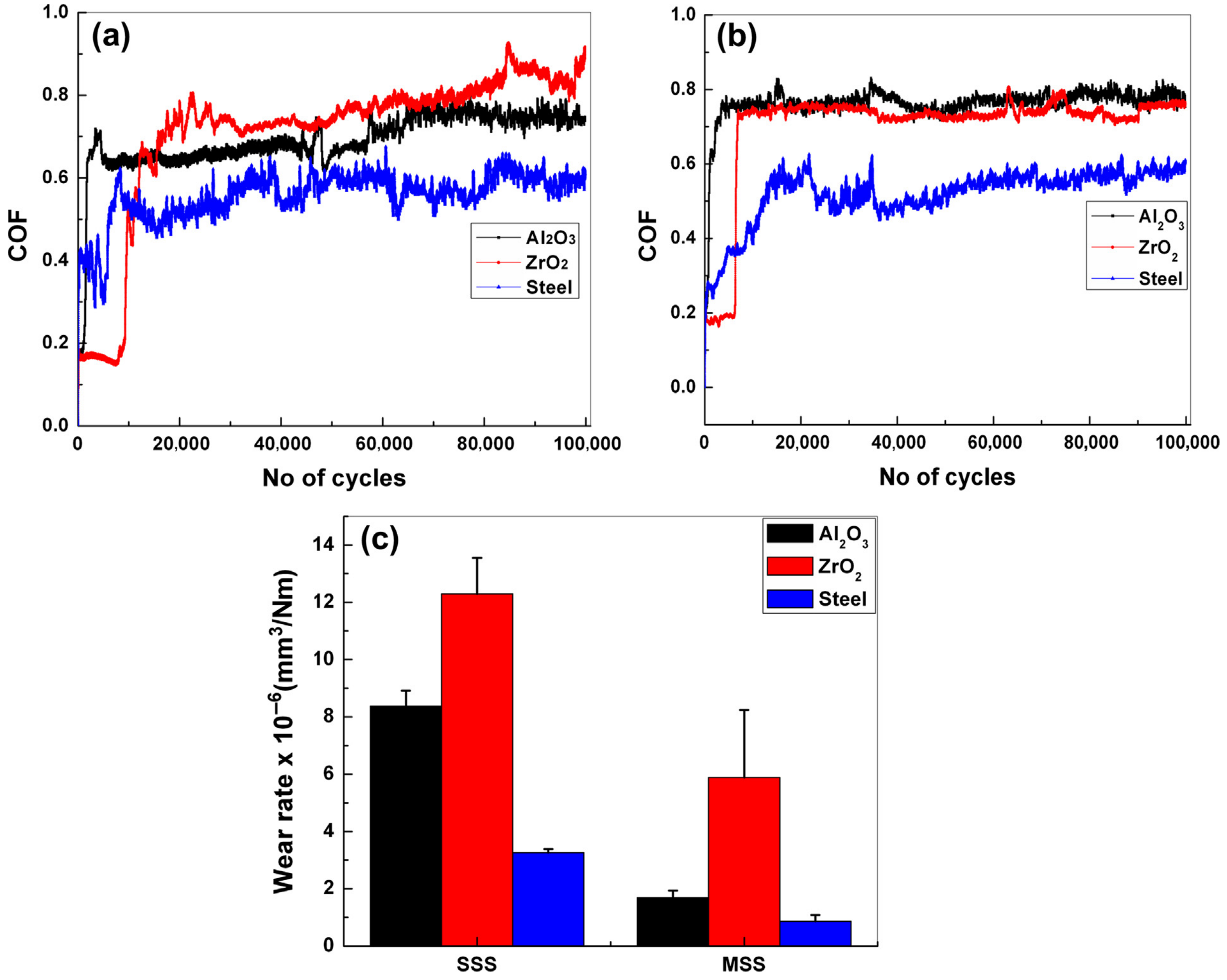

Figure 11 (a) Plot showing the variation of coefficient of friction (COF) with fretting duration (as number of cycles) for ZrO_2 with 2 mol% yttria, SPS processed via single-stage sintering (SSS) and (b) multistage sintering (MSS) and (c) wear rates measured for the SPS processed (via SSS and MSS) ZrO_2 samples. Fretting conditions: 5 N load, 5 Hz frequency, 100,000 cycles and 100 μm stroke length and the fretting experiments carried out against three different counter bodies (steel, ZrO_2 and Al_2O_3) (Reddy et al., 2010c).

($\sim 10^{-6}$ mm^3/Nm), irrespective of the counter body material that is used for the wear tests (**Figure 11(c)**). Whereas fretting against ZrO_2 self-mated system resulted in maximum wear loss, the tests against steel resulted in the minimum wear loss for both the ZrO_2 materials under investigation. SEM images of the worn surfaces revealed the abrasive scratches generated mainly due to the abrasive wear of both the types of ZrO_2 nanoceramics when fretted against the different counter bodies (**Figure 12**). A higher hardness of the MSS sample minimized the damage from abrasive wear and contributed to the improved wear resistance of the MSSed ZrO_2 nanoceramics, when compared to SSSed ZrO_2.

Kumar et al. (2010) reported the influence of grain size (ranging from 75 to 1470 nm) on wear behavior of fully densified Y-TZP ceramics. By employing SPS, microwave sintering and conventional pressureless sintering techniques, they could achieve zirconia with a wide range of grain sizes. A unidirectional ball-on-disc sliding wear tester was used to study wear behavior of Y-TZP against steel ball. In **Figure 13(a)**, the classical frictional response with initial increase in COF during initial running-in-period followed by a steady-state response, as obtained with ZrO_2 with various grain sizes, is shown. The COF varied over a narrow window of 0.35–0.44 (**Figure 13(b)**), while the wear rate reduced from 3.5 to 0.88×10^{-6} mm^3/Nm with decreasing grain size (**Figure 13(c)**). Mukhopadhyay and Basu (2007) in different work reported similar results for Y-TZP that the wear rate decreased with reduction of the grain size (**Figure 13(d)**). In case of nanocrystalline Y-TZP, the plastic deformation and microcracking contribute to the mild wear, whereas the delamination and spalling results in the increased wear for the coarser grain zirconia.

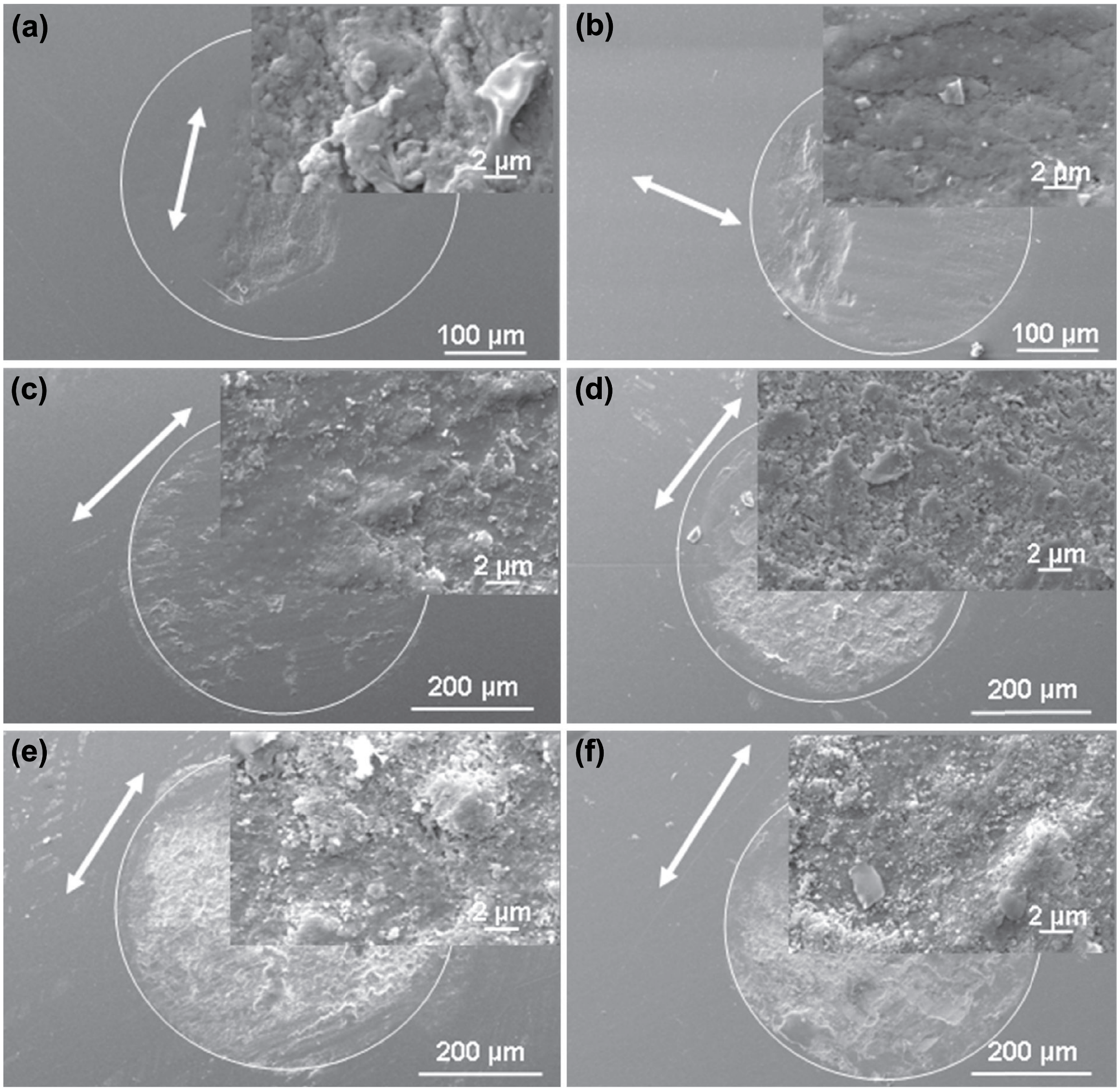

Figure 12 Low-magnification and corresponding higher magnification (as insets) SEM images obtained from the worn surfaces of SPS processed of Y-TZP ceramics, developed via (a), (c) and (e) single-stage sintering (SSS) and (b), (d) and (f) multistage sintering (MSS) schemes, fretted against (a), (b) Al_2O_3; (c), (d) steel and (e), (f) ZrO_2. Fretting conditions: 5 N load, 5 Hz frequency, 100,000 cycles and 100 μm stroke length (Reddy, Mukhopadhyay, et al., 2010).

2.05.5 Spark Plasma Sintering of WC-Based Nanoceramic Composites

Although WC-based cemented carbides have been extensively used for various technological applications since they were discovered about one century ago, the last two decades have witnessed tremendous surge for the development of fine-grained and ultrafine-grained cemented carbides (Berger, Porat, & Rosen, 1997). Cemented carbides or WC-based materials are one of the oldest and most successful commercial powder metallurgy products. Monolithic WC is not useful in technological applications despite its attractive properties because of processing difficulties and inherent brittleness. Conventional cemented carbides, having composition of WC–6 wt% Co exhibits high fracture toughness of 14 MPa $m^{1/2}$, which is significantly higher than the fracture toughness of monolithic WC (~4 MPa $m^{1/2}$). However, its hardness (~16 GPa) is low due to the presence of the softer metal binder phase (Venkateswaran, Sarkar, et al., 2006).

It has been reported that reduction in the WC grain size to a nanoscale range enhances the hardness and strength drastically. Sivaprahasam, Chandrasekar, and Sundaresan (2007) developed WC–12 wt% Co with

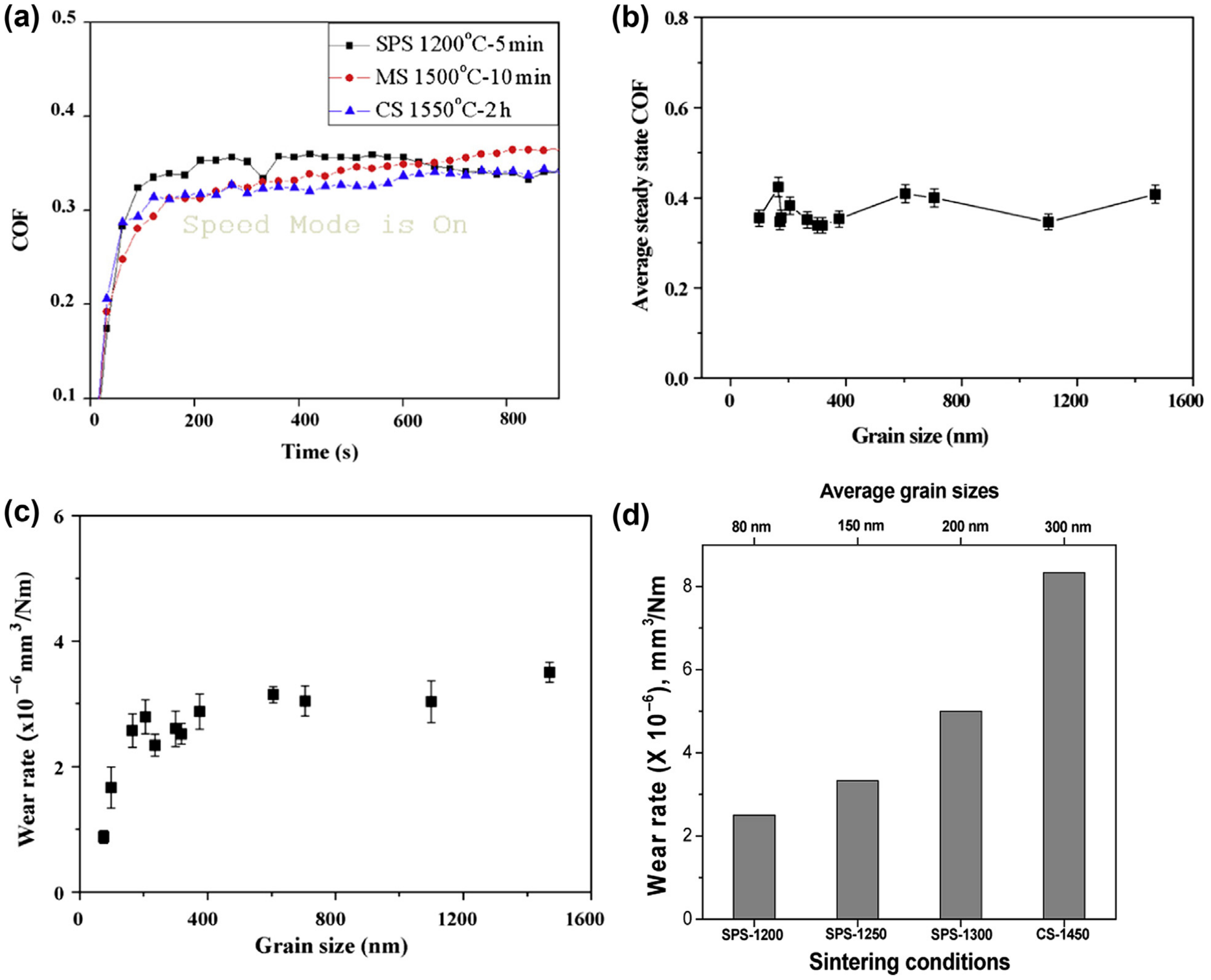

Figure 13 (a) The evolution of coefficient of friction (COF) with time (Kumar et al., 2010), (b) average COF with grain size (Kumar et al., 2010), (c) effect of grain size on the wear rate of Y-TZP ceramics (Kumar et al., 2010) and (d) variation of wear rates (unlubricated sliding) of the 3Y-TZP nanoceramics and conventionally sintered ceramic as a function of grain sizes (Mukhopadhyay & Basu, 2007). SPS, spark plasma sintered; CS, conventionally sintered (hot pressed).

higher hardness (~15.2 GPa) via SPS, as compared to conventional pressureless sintering (~13.8 GPa). The microstructural refinement was also reported by Cha, Hong, and Kim (2003) in SPS (1000 °C, 10 min, 50–100 MPa) processed WC–10 wt% Co nanomaterial, which possessed a hardness of ~18 GPa, while conventionally sintered (1100 °C) similar compositions had a maximum hardness of ~16 GPa. Higher hardness values of more than 20 GPa for bulk WC–Co nanomaterials have been reported by Jia, Fischer, and Gallois (1998). Interestingly, Richter and Ruthendorf (1999) reported that the hardness of nanocrystalline WC-based ceramics can reach a value close to, or even exceeding, that of WC single crystal. However, the fracture toughness of the nanocrystalline cemented carbides is inferior to that of cemented carbides with micron-sized grains. The fracture toughness of ultrafine and nanocrystalline WC–Co remained as low as 5–6 MPa m$^{1/2}$. The inferior fracture toughness has been attributed to an increase in constraint to plastic deformation, ahead of the propagating crack tip. From the above discussion, it can be stated that SPS is advantageous in obtaining fully dense WC-based composites with nanosized grains (<200 nm) by lowering the sintering temperatures (~1100–1200 °C) and sintering times (~5–10 min).

The presence of softer metallic phase in conventional as well as nanocrystalline WC-based materials limits the performance of these materials in applications involving high temperatures, high speeds or corrosive environments (Cha & Hong, 2003; Imasato, Tokumoto, Kitada, & Sakaguchi, 1995; Kim, Shon, Garay, & Munir, 2004; Kim, Shon, Yoon, Lee, & Munir, 2006; Mohan & Strutt, 1996; Suzuki, 1986, p. 262;

Suzuki, Hayashi, Yamamoto, & Nakajo, 1966). Hence, there has been a surge toward the development of dense, novel WC-based nanoceramics by replacing the metallic binder phase partially or fully with ceramic sinter additives (Basu, Venkateswaran, & Sarkar, 2005; Biswas, Mukhopadhyay, Basu, & Chattopadhyay, 2007; Eskandarany, 2000, 2005). However, the intriguing issue is the attainment of near-theoretical densification and prevention of the deterioration of fracture toughness in the absence of metallic phase.

Eskandarany (2000) successfully developed dense monolithic WC nanoceramics using PAS technique at 1700 °C. Kim et al. (2004, 2006) also achieved ~98% ρ_{th} densification during consolidation of submicron (~0.4 µm) binderless WC powders via SPS at 1600 °C for 2 min. The grain growth was insignificant during the sintering, even though some of the WC grains became faceted. It is now possible to develop dense monolithic WC possessing significantly higher hardness (24–28 GPa), when compared to cemented carbides. However, very poor fracture toughness of the binderless pure WC (~4–6 MPa $m^{1/2}$) render them unsuitable for use in demanding engineering applications as a replacements for cemented carbides.

In order to address the issue of brittleness associated with binderless monolithic WC, Eskandarany (2000) used PAS to develop WC–18 at% MgO nano/nanocomposite from nanosized matrix grains (WC ~25 nm) as well as the nanosized second phase particles (MgO ~50 nm). The fracture toughness was significantly improved up to ~14 MPa $m^{1/2}$ (as compared to 4 MPa $m^{1/2}$ for monolithic WC) with the addition of MgO sinter additive. However, such an improvement in fracture toughness was accompanied by a considerable deterioration in hardness (~15 GPa) with respect to monolithic WC (~23 GPa). Zhu, Wu, and Luo (2010) recently reported that an addition of 1.2–1.8 wt% stearic acid to the powder mixture leads to a change in the reaction mechanism from mechanically induced self-propagating reaction. This method improved yield and aided in refinement of the powder particle sizes with more uniform particle size distribution for the as-synthesized WC–MgO nanocomposites. In a different work, Eskandarany (2005) fabricated WC–32 at% Al_2O_3 nanocomposite. WC–Al_2O_3 nanocomposite also exhibited high fracture toughness of ~15 MPa $m^{1/2}$ with low hardness of ~16 GPa.

2.05.5.1 Microstructure Development in WC–ZrO_2-Based Nanoceramic Composite

A representative bright-field TEM image of the WC–ZrO_2 nanocomposite SPSed at 1300 °C for 5 min showed an overall fine microstructure with WC grains varying in the range of 0.3–0.5 µm along with ZrO_2 particles is shown in **Figure 14** (Biswas et al., 2007). The presence of ZrO_2 particulates of 60–90 nm in size is also observed at WC triple junctions and grain boundaries. One of the characteristic features is the faceted morphology of these nano-sized ZrO_2 particles. To observe the effect SPS holding time on microstructure a representative bright-field micrograph of WC–ZrO_2 nanocomposite SPSed at 1300 °C for 20 min is presented in **Figure 14(c)**. The average size of WC grains is around 0.4–0.5 µm. This observation indicates that the grain growth is restricted even on sintering for longer duration of 20 min. This is in contrast to Omori (2000), who reported abnormal grain growth (about 1 mm grain size) of binderless WC on holding for just over 1 min, although at higher spark sintering temperature of 1900 °C. An observation of SPSed WC–ZrO_2 nanocomposite samples also indicates that abnormal grain growth of WC is restricted considerably in contrast to that in binderless WC, reported by Cha et al. (2003). Therefore, ZrO_2 particles are effective in inhibiting grain growth even at longer holding times. A high-resolution TEM micrograph reveals atomically clean interface between the WC grains in the WC–ZrO_2 nanocomposite (**Figure 14(d)**).

TEM images (**Figure 14**) observations indicate the presence of a significant fraction of the nanocrystalline ZrO_2 particles along the WC grain boundaries. These intergranular zirconia particles can potentially restrict WC matrix grain boundary mobility during sintering. Such pinning effect due to ZrO_2 particles can explain considerable inhibition of grain growth of WC during spark sintering at 1300 °C. Since grain boundary provides faster diffusion path, the increase of grain boundary area due to nano-ZrO_2 can lead to faster mass transport. The volume fraction of ZrO_2 is ~14% and the nano-sized ZrO_2 particles are well dispersed in the WC matrix (**Figure 14**). The presence of zirconia can effectively result in a local increase in temperature around a number of WC/ZrO_2 interfaces. Such phenomenon can result in an enhancement of mass transport with concomitant augmentation of necking and hence resultant sintering kinetics. Additionally, the presence of α-W_2C at the boundary between WC and ZrO_2 is observed (**Figure 14(c)**).

The formation of W_2C results from a possible reaction between WC and ZrO_2 at the interface:

$$\mathrm{ZrO}_{2-x} + 2yWC = yW_2C + ZrO_{2-x-y} + yCO \tag{2}$$

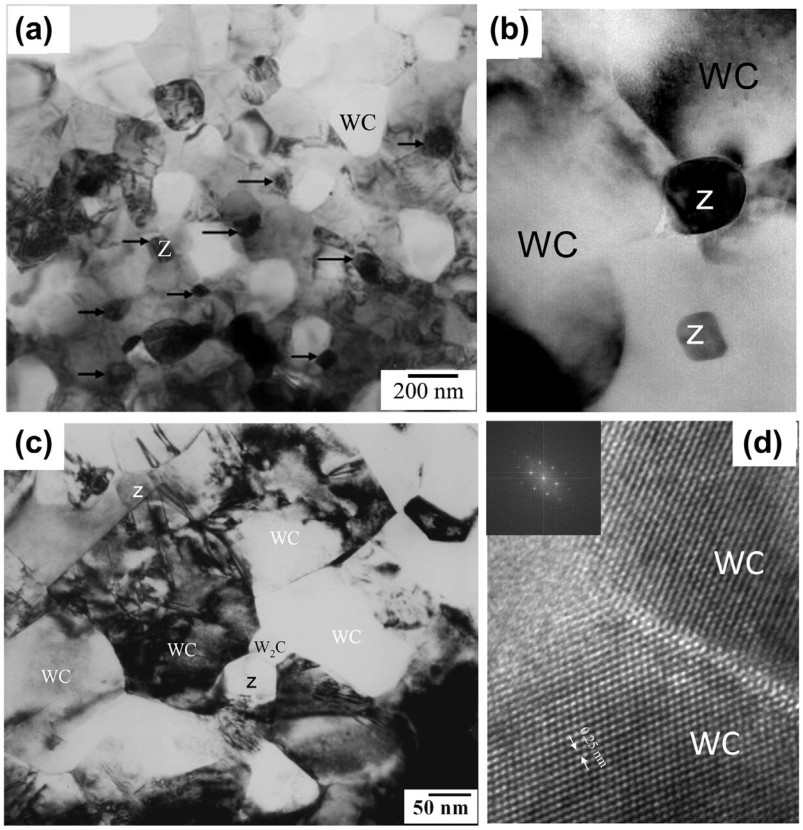

Figure 14 (a) Bright-field TEM image of WC–6 wt% ZrO_2 nanocomposite (spark plasma sintered for 5 min at 1300 °C) showing distribution of nanocrystalline ZrO_2 particles (indicated by arrows) in submicron WC matrix, (b) ZrO_2 particles are distributed in the WC matrix at the triple junction and at the grain boundary and interior of a WC grain (Z stands for ZrO_2), (c) bright-field TEM micrograph of WC–6 wt% ZrO_2 nanocomposite, spark plasma sintered sample for 20 min. The microstructural regions (second phase particles) corresponding to ZrO_2 are marked as Z and (d) high-resolution micrograph revealing atomically clean interface between the WC grains (Biswas et al., 2007).

where x is the oxygen vacancy concentration in the ZrO_2 as a result of the dopant concentration and y is the additional vacancy concentration created in the ZrO_2 due to reaction with WC. The above reaction creates additional oxygen vacancies and forms a layer of W_2C. The availability of additional oxygen vacancies may enhance the diffusivity to certain extent, resulting in faster mass transport and hence increased sintering kinetics.

Partial or full replacement of Co (metallic phase) with ZrO_2 can affect the microstructure and enhance the mechanical properties of WC-based ceramic nanocomposites (Mukhopadhyay et al., 2010). SPS experiments were carried out at 1300 °C for 0 min with the heating rate of ~175 K/min. The replacement of Co by ZrO_2 did not seem to have any significant influence on densification of WC–ZrO_2–Co system. Most of WC grains in the WC–6 wt% Co cermets were observed to be faceted, with the presence of Co phase along the grain boundaries (**Figure 15**). The development of triangular prism-shaped WC grains, as seen in **Figure 15(a)**, is commonly observed in WC-based cermets and is considered to be detrimental toward the mechanical properties (Mukhopadhyay & Basu, 2011). The average matrix grain size in the cermet was around 0.4 μm. In contrast, many WC grains appear to be equiaxed in the SPS processed WC–6 wt% ZrO_2 ceramic (**Figure 15(b)**). Hence, the addition of ZrO_2 suppresses the formation of the deleterious "truncated trigonal prism"-shaped WC grains. It can be more clearly observed from **Figure 15(b)** that the ZrO_2 particles present along the matrix grain boundaries are slightly coarser than those within the grains. More precisely, the intragranular ZrO_2 particles have sizes between 10 and 40 nm (average size: 28 nm), while the sizes of most of the intergranular particles lie between 60 and 80 nm (average size: 71 nm). **Figure 15(c)** presents the ultrafine microstructure of the WC–10 wt% ZrO_2 nanocomposites. Though the ZrO_2 size distribution is similar to that of WC–6 wt% ZrO_2 nanocomposite, clustering of ZrO_2 particles can be observed at many locations throughout the microstructure. Such agglomeration of the ZrO_2 nanoparticles was not observed in case of the WC–6 wt% nanocomposites

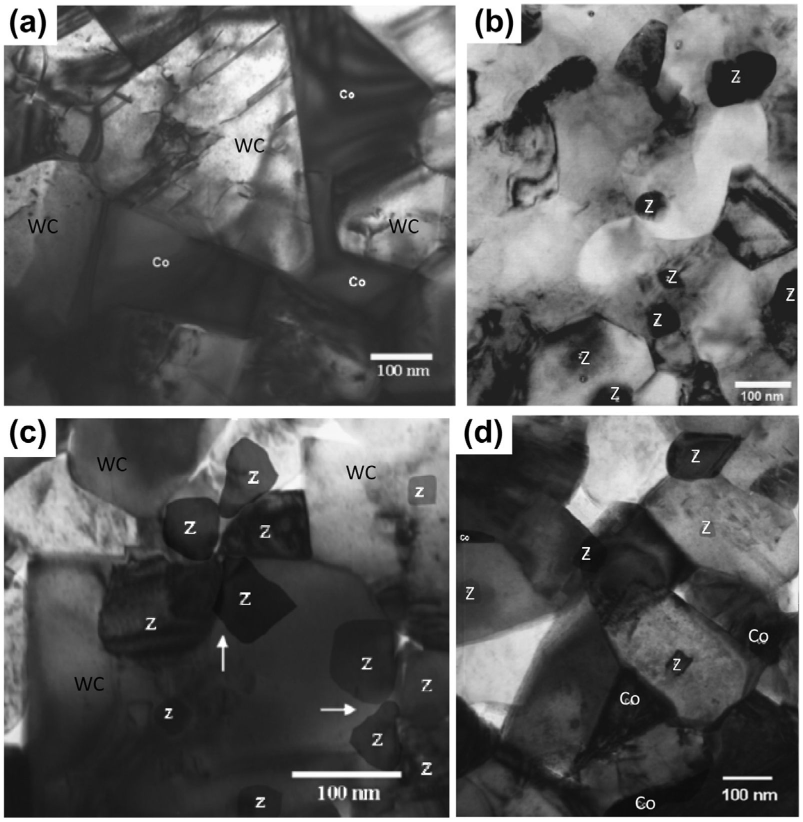

Figure 15 (a) Bright-field TEM image of SPS processed WC–6 wt% Co. The microstructural regions (secondary phase) corresponding to cobalt are marked as Co, (b) bright-field TEM image of SPS processed WC–6 wt% ZrO_2 nanocomposite. The microstructural regions (second phase particles) corresponding to ZrO_2 are marked as Z, (c) Lower magnification bright-field TEM image of SPS processed WC–10 wt% ZrO_2 nanocomposite. The microstructural regions (second phase particles) corresponding to ZrO_2 are marked as Z. Arrows indicate clustering of the ZrO_2 particles and (d) higher magnification bright-field TEM image of SPS processed WC–4 wt% ZrO_2–2 wt% Co nanocomposite. The microstructural regions corresponding to the ZrO_2 particles and cobalt are marked as Z and Co, respectively. All the WC samples were spark plasma sintered at 1300 °C for 0 min with the heating rate of ~175 K/min (Mukhopadhyay et al., 2010).

(**Figure 15(b),(c)**). Based on TEM observations, SPS-processed WC–ZrO_2–Co microstructure can be described as inter/intragranular nanocomposite. In addition to inter as well as intragranular nanosized ZrO_2 particles, the presence of Co phase along with a few faceted WC grains were also observed in the TEM images, corresponding to WC–4 wt% ZrO_2–2 wt% Co nanocomposites (**Figure 15(d)**). In a recently reported work by Malek, Lauwers, Perez, Baets, and Vleugels (2009), near-theoretical density for WC–(5/10 vol%) ZrO_2 composites via SPS was achieved after holding for 2–5 min at a much higher temperature of 1700 °C, which resulted in the formation of reaction product phases, like ZrC and W_2C. However, the presence of W_2C phase was not reported in the SPS processed (at 1300 °C for 0 min) WC–ZrO_2–Co nanocomposites (Mukhopadhyay et al., 2010). Another important observation is the presence of t-ZrO_2 in all the WC–ZrO_2–Co composites.

2.05.5.2 Mechanical Properties of WC–ZrO_2 and WC–ZrO_2–Co-Based Nanoceramic Composite

WC–ZrO_2 composites were developed with an objective of exploiting the transformation toughening of ZrO_2 in improving the fracture toughness of binderless WC (Basu, 2005; Hannink, Kelly, & Muddle, 2000; Wang, Heusch, Lay, & Allibert, 2002). In order to compare the properties of the ceramic composite with the commercially used WC–6 wt% Co cemented carbide, Co was replaced by the same weight fraction of ZrO_2 (WC–6 wt% ZrO_2). The mechanical properties of SPS-processed WC–ZrO_2 composites are compared with the pressureless sintered materials in **Table 2**. The hardness and toughness values are comparable, independent of the processing route. Additionally, the hardness values of WC–ZrO_2 materials (21–24 GPa) are far more superior to WC–Co materials (15.5 GPa) with same binder content (6 wt%). The measured toughness is not

Table 2 Mechanical properties of nanoceramics and nanocomposites processed via SPS and other sintering techniques

System (material)	*Processing conditions*	*Heating rate (K/min)*	*Matrix grain sizes (nm)*	*Hardness (GPa)*	*Fracture toughness (K_{IC}) (MPa $m^{1/2}$)*	*Flexural strength (GPa)*	*References*
Monolithic WC	SPS at 1900 °C	–	–	24	–	1000 (3-P)	Mukhopadhyay and Basu (2007)
Monolithic WC	PAS at 1963 K for 0.18 Ks	–	25	23	4	–	
WC–6 wt% Co	PS	–	1–2 μm	16	14	–	
WC–10 wt% Co	SPS at 1000 °C for 10 min	100	<300 nm	18	12	–	
WC–18 wt% MgO	PAS at 1963 K for 0.18 Ks	–	MgO: 50 nm	15	14	–	
WC–6 wt% ZrO_2 (3Y)	SPS, 1200 °C, 5 min	600	WC: 400, ZrO_2: 60	21.3	5.6	–	Basu, Lee, et al. (2004)
WC–6 wt% ZrO_2 (3Y)	SPS, 1250 °C, 5 min	600	WC: 400, ZrO_2: 60	21.6	6.3	–	
WC–6 wt% ZrO_2 (3Y)	SPS, 1300 °C, 5 min	600	WC: 400, ZrO_2: 60	23.6	5.9	–	
WC–6 wt% ZrO_2 (2Y)	SPS, 1300 °C, 5 min	600	WC: 400, ZrO_2: 60	23.9	5.8	–	
WC–6 wt% ZrO_2 (0Y)	SPS, 1300 °C, 5 min	600	WC: 400, ZrO_2: 60	21.5	5.7	–	
WC–6 wt% ZrO_2 (3Y)	PS, 1700 °C, 1 h	–	WC: 1500, ZrO_2: 1000	23.3	4.5	–	
WC–6 wt% Co	SPS, 1400 °C, 5 min	600	400	15.3	13.2	–	
WC–6 wt% Co	PS, 1500 °C, 1 h	600	1500	16.8	14.0	–	
WC–6 wt% Co	SPS, 1300 °C, 0 min	600	200	20.7	12.4	1.1 (4-P)	Mukhopadhyay et al. (2010)
WC–6 wt% ZrO_2	SPS, 1300 °C, 0 min	175	WC: 200, ZrO_2: 27	20.5	10.9	1.3 (4-P)	
WC–10 wt% ZrO_2	SPS, 1300 °C, 0 min	175	WC: 200, ZrO_2: 27	23.2	10.1	0.9 (4-P)	
WC–5 wt% ZrO_2–1 wt% Co	SPS, 1300 °C, 0 min	175	WC: 200, ZrO_2: 27	22.5	6.8	1.2 (4-P)	
WC–4 wt% ZrO_2–2 wt% Co	SPS, 1300 °C, 0 min	175	WC: 200, ZrO_2: 27	22.5	10.7	1.2 (4-P)	

SPS, spark plasma sintering; PAS, plasma-assisted sintering; PS, pressureless sintering; 3-P, three-point; 4-P, four-point flexural strength.

suitable for tribological application and this has motivated the development of second-generation WC-based nanocomposites. Mukopadhyay et al. (2010) made a systematic study to minimize the Co binder content by partial replacement with ZrO_2 (4 and 5 wt%; rest Co) or completely eliminate the Co phase by full replacement with an equal weight fraction (6 wt%) of ZrO_2. The hardness, indentation fracture toughness and flexural strength of WC–ZrO_2–Co nanocomposites are presented in **Table 2**. The WC–6 wt% Co cermet exhibits higher fracture toughness ($\sim$12.5 MPa $m^{1/2}$) among all the investigated materials. Similar fracture toughness ($\sim$11–12 MPa $m^{1/2}$) values for SPS processed WC–Co cermets were also reported earlier. Also, a modest decrease ($\sim$16%) in fracture toughness occurs on replacement of the entire Co binder with ZrO_2 nanoparticles (6 wt%). However, toughness improvement is not observed on either replacing a part of the ZrO_2 content by Co (up to 2 wt%) or increasing the ZrO_2 content to 10 wt%.

The SPS processed WC–6 wt% ZrO_2 inter/intragranular nanocomposite possess an excellent combination of properties, such as high hardness ($\sim$20 GPa), flexural strength ($\sim$1.3 GPa) and fracture toughness ($\sim$10 MPa $m^{1/2}$). In contrast to modest reduction in fracture toughness, the strength improvement of $\sim$18% has been measured for the WC–6 wt% ZrO_2 ceramic nanocomposite ($\sim$1.3 GPa), with respect to the similarly processed WC–6 wt% Co cermet ($\sim$1.1 GPa). Among other ZrO_2 containing nanocomposites, WC–5 wt% ZrO_2–1 wt% Co and WC–4 wt% ZrO_2–2 wt% Co also possess higher flexural strength ($\sim$1.2 GPa) with respect to WC–6 wt% Co cermet. Such improvement can be expected due to refinement in microstructural scale and the absence of "truncated trigonal prism"-shaped matrix grains in the presence of nanosized ZrO_2 particles. However, considerable reduction in the flexural strength ($\sim$0.9 GPa) is measured on incorporation of 10 wt% ZrO_2. The presence of agglomerates and possibly processing defects is believed to account for such inferior strength of the nanocomposite (**Figure 15(c)**). Most of the ZrO_2-containing nanocomposites exhibited superior hardness of $\sim$23 GPa, with the exception of WC–6 wt% ZrO_2. Although the nanoscaled microstructure is believed to be the reason for the superior hardness and strength, a systematic investigation of the effect of variation in ZrO_2 and WC grain size on the mechanical properties is expected to further elucidate the microstructure–mechanical property relationships for this class of materials.

In a different work, Malek et al. (2009) also found that the mechanical properties, in particular, fracture toughness and flexural strength, of SPS processed WC–ZrO_2 composites deteriorate in the presence of agglomerated ZrO_2 particles. Overall, they recorded an improvement in fracture toughness by $\sim$25% and flexural strength by $\sim$170% without any deterioration in hardness, over that of similarly processed monolithic WC, on incorporation of 10 wt% ZrO_2 (2 mol% Y_2O_3 stabilized) particles. However, the use of a higher SPS temperature of 1700 °C leads to the formation of reaction product phase, like W_2C (Malek et al., 2009). The difference in toughness can be explained by the use of a different technique (indentation/short crack method). In order to overcome the problem of agglomeration of the second-phase ceramic particles in binderless WC-based composites, Yang, Zhao, and Ai (2009) and Yang, Zhao, Ai, and Yuan (2009) studied in detail the effects of using chemical dispersant (polyethylene glycol), ball milling, ultrasonication and varying the temperature of dispersing media (distilled water) to ensure uniform distribution of various phases. Considerable improvements in the mechanical properties were reported for WC–ZrO_2–VC composites on optimizing the initial powder particle sizes and dispersion conditions (Yang, Zhao, Ai, et al., 2009). Hence, the replacement of metallic Co with ceramic (ZrO_2), while at the same time attaining similar densification and maintaining similar fracture toughness, is a very important research achievement which solves the long-standing problem pertaining to the softening and degradation of the metallic phase during demanding applications of WC-based cermets.

A comprehensive survey of the processing, grain size and mechanical properties of WC-based materials sintered using SPS and conventional sintering techniques is presented in **Table 2**. It can be realized that SPS is effective in minimizing grain growth when compared to conventional pressureless sintering. It appears that low holding time during SPS is beneficial in refining the grain size or obtaining fine microstructure. Irrespective of type of processing, all monolithic WC exhibited similar mechanical properties even those with WC–6 wt% CO cermet. It is interesting to note that the SPSed WC–MgO shows similar mechanical properties as that of WC–Co cermet (**Table 2**). Importantly, the presence of relatively softer MgO does not degrade the hardness property. Thus, the WC–MgO nanocomposite can potentially replace conventional WC-based cermets in many existing as well as futuristic applications. Although WC–6 wt% ZrO_2 nanoceramic exhibits better hardness properties when compared to WC cermet, its fracture toughness is considerably lower. However, addition of small amount of Co to WC–ZrO_2 appears to be promising as the WC–4 wt% ZrO_2–2 wt% CO is characterized with better mechanical properties (hardness: 22.5 GPa, fracture toughness: 10.7 MPa $m^{1/2}$ and flexural strength: 1.2 GPa).

In summary, nanocrystalline WC–Co cemented carbides exhibit improved hardness against their conventional counterparts, which is advantageous with regarding their cutting efficiency and wear-resistant applications. In case of WC-based nanoceramics, the replacement of metallic binder by ceramic additives has been possible with better combination of mechanical properties.

2.05.5.3 Tribological Properties of WC–ZrO_2-Based Nanoceramic Composite

There have been recent reports indicating the potential application of ceramic nanocomposites in machining and tribological applications (Kusunose, Sekino, Choa, & Niihara, 2002; Suryanarayana, 1995). For example, Si_3N_4/BN nanocomposites, when compared to the microcomposite, have higher fracture strength and better machinability, as indicated by superior surface finish of the machined component (Kusunose et al., 2002). Also, nanocrystalline WC–Co composites are reported to have four times higher wear resistance, and more than double the lifetime in cutting applications than conventional coarse-grained composites (Suryanarayana, 1995).

However, very limited research was reported on WC-based nanoceramic composites. Staia et al. (2006) investigated tribological characterization of binderless WC processed via PPC route. After the PPC (at 1600 and 1700 °C), all WC samples were characterized with micron-sized grains despite the use of submicron- and micron-sized starting powders. Tribological tests were carried out using the ball-on-disk configuration with Al_2O_3 balls (6 mm diameter) as a counterpart. Wear tests were performed at room temperature in air with a relative humidity of 54–64% at a linear velocity of 0.1 m/s, a load of 10 N, contact radius of 7 mm and a sliding distance of 1000 m. All the WC samples, irrespective of their starting powders or processing temperature, exhibited excellent tribological performance with COF varying between 0.26 and 0.31 and very low wear rate of approximately 10^{-8} mm^3/Nm. In another work, the wear behavior of pressureless sintered (temperature in the range of 1500–1700 °C, time variation (1–3 h) and vacuum atmosphere) micron sized WC–6 wt% ZrO_2 composites against steel ball were reported (Venkateswaran, Sarkar, & Basu, 2006). Fretting wear experiments were carried out with varying loads (2, 5, and 10 N) and varying cycles (10,000, 50,000 and 100,000), at constant frequency (8 Hz) and constant displacement stroke (50 μm) at ambient room temperature conditions. The tribological experiments revealed that the optimized WC–6 wt% ZrO_2 (2Y) composite exhibited moderate COF $\sim$0.15–0.5 with load variation and a maximum wear rate of around $\sim 70 \times 10^{-6}$ mm^3/Nm was recorded after fretting at 10 N load for 100,000 cycles. Mild abrasion at lower load (2 N) and tribochemical wear followed by spalling at higher load ($\geq$5 N) were reported to be the dominant wear mechanisms.

Venkateswaran et al. (2005) studied the wear behavior of SPSed (vacuum of 5–6 Pa at 1300 °C for 5 min under a pressure of 30 MPa) WC–6 wt% ZrO_2 nanocomposite. Fretting wear tests of the WC nanocomposite against bearing steel were performed by varying loads (2, 5 and 10 N) and fretting cycles (10,000–100,000). The frictional behavior is shown in **Figure 16**. The WC–ZrO_2 nanoceramic composites exhibited lower COF of 0.1 at lower load of 2 N. A clear transition in frictional behavior, leading to high COF of 0.5, is recorded during fretting (100,000 cycles) at higher load of 5 N. At the highest load of 10 N, the frictional transition takes place earlier than that at 5 N load. The wear rate after different test duration against normal load can be seen in **Figure 16(b)**. The wear rate of the nanocomposites was quite low and was in the order of $\sim 10^{-8}$ mm^3/Nm, when compared to dense WC–6 wt% ZrO_2 composite (pressureless sintered at 1600 °C), which exhibit wear rates in the order of $\sim 10^{-6}$ mm^3/Nm (Venkateswaran, Sarkar, et al., 2006). After fretting for 10,000 cycles, the wear rate of the WC–ZrO_2 nanocomposites is low and does not vary much with normal load. Wear rate, measured after 50,000 cycles, increases as load increases from 2 to 5 N; but no further increase is noted at the highest load of 10 N. The measured wear rate after 100,000 fretting cycles shows a monotonic increase with normal load, varied between 2 and 10 N. The wear depth data (which was measured using Stylus profilometer) against fretting variable is shown in **Figure 16(c)**. At the lowest load of 2 N, the wear scar depth is not measurable after 10,000 and 50,000 cycles. The wear depth was around 0.15 μm after fretting for 100,000 cycles at 2 N loads. An increase in the wear depth from $\sim$0.20 to 0.24 μm with increasing fretting cycles (10,000–100,000 cycles) at intermediate load of 5 N was observed. However, this increase is considerable at the highest load of 10 N. A maximum depth of $\sim$0.55 μm is evident after fretting for 100,000 cycles at 10 N load. This indicates that the severity of the wear of the investigated ceramic nanocomposites, i.e. the amount of material removal at the fretting contact, increases with increase in load and test duration. The formation of mild abrasive scratches along with finer (submicron-sized) wear debris particles is the characteristic of worn surface of the nanocomposite at lower load (2 N). Tribochemical wear is the predominant wear mechanism of the material removal at higher load (5 N and 10 N). Crack-induced spalling of nonprotective tribolayer and the formation of sheet-like agglomerated wear debris are implicative of severe wear of the ceramic at high load.

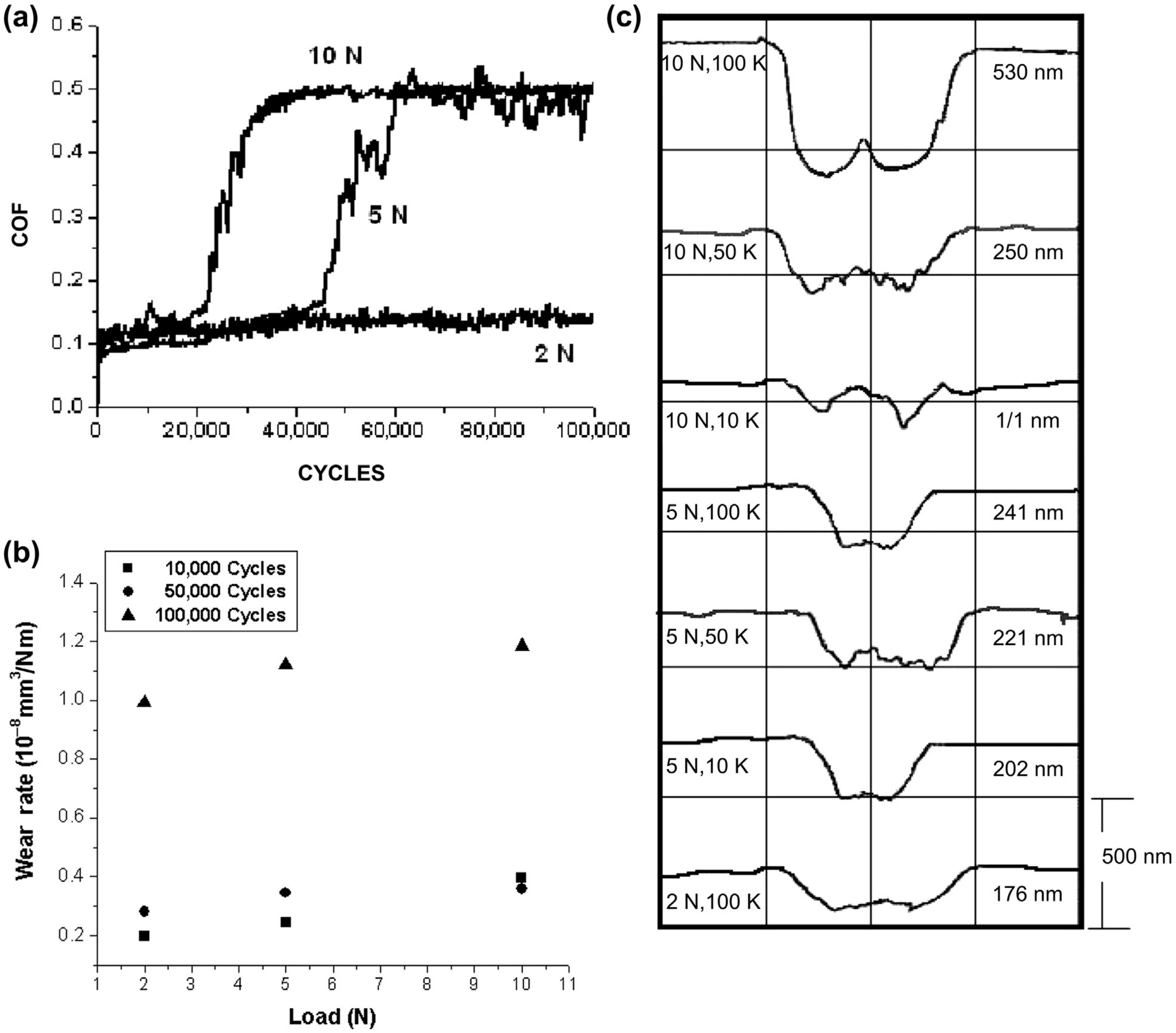

Figure 16 (a) The evolution of frictional behavior of WC–6 wt% ZrO_2/steel friction couple under the fretting conditions of 100,000 cycles with varying load at a constant frequency of 8 Hz and a constant displacement stroke of 50 μm, (b) wear rate of the WC–6 wt% ZrO_2 nanocomposite as a function of load and (c) surface profile characteristics of worn pit on WC–ZrO_2 composite, as traced by stylus profilometer for different fretting conditions [load (2–10 N), test duration (10–100 K) cycles]. Right-side marker indicates the vertical scale (Venkateswaran et al., 2005).

2.05.6 Conclusions and Outlook

SPS process has been a major success in developing bulk ceramic nanomaterials in various research laboratories by restricting grain growth during densification as SPS processing involves high heating rate, lower sintering temperatures and short holding times. Despite last two decades of research, to date, SPS processing of nanoceramics has been confined to laboratory scale development. The bottleneck for the use of SPS in industrial scale production of ceramic components has been due to two factors: (1) only regular geometric shape, like square, disc, rectangular or cylindrical shaped components can be made via SPS and (2) only one sample can be reliably sintered in one heating cycle. Although multiple die cavities within a large diameter graphite die can be used to make a number of small samples in a single heating cycle, often the difference in powder size uniformity or impurity can cause differences in shrinkage behavior, leading to difference in density among simultaneously sintered components. Also, the lab-scale SPS machine can make 10–20 mm diameter samples and the size of the samples also is determined by the final sintering temperature.

In particular, if the powder compact requires high sintering temperature of more than 1500 °C, then normal lab-scale SPS machine cannot be used to sinter larger diameter samples of more than 20 mm diameter. Some of the large capacity commercial machines can be used to densify samples of 50 mm diameter with 4–5 mm thickness even for difficult-to-sinter ceramics, like TiB_2, ZrB_2 and HfB_2, etc. This aspect needs to be considered while using SPS for commercial scale production, otherwise it is a great and fast processing tool to make nanomaterials.

A more fundamental concern is the sintering mechanisms responsible for superfast densification enabled by SPS technique. Perhaps, an important concern of SPS is the uncertainty in exactly confirming real sintering temperature as pyrometer temperature reading on the outer surface of the graphite die and actual sample temperature cannot be correlated reliably, when the sintering temperature is more than 1000 °C. Furthermore, since processing time involved in SPS is extremely short, temperature may not be uniform over the entire cross-section of the sample, which limits the size and shape of the products. This aspect has been the research focus of multiple research groups around the world, including that of Van Der Biest in Belgium, Munir in USA, Basu in India and others. This issue has been partly settled with FEM/MATLAB/ABAQUS/ANSYS-based simulation and some control experiments to probe into the reactivity during SPS process as well as with few experiments to validate the simulation predictions. Often, researchers do not measure properties across the diameter/thickness of the sample, and therefore do not report the inhomogeneity in basic mechanical properties (like hardness), that one would otherwise have measured. To this end, it has been recently demonstrated that problems arising from such nonuniform temperature distributions in SPS can be effectively minimized by using MSS scheme. However, more control experiments in future need to be carried out on high-conductivity metal as well as poorly conductive/insulating glass powders (transparent preferably) in the temperature range of intermediate stage of sintering so that the neck growth kinetics can be formulated. In such control experiments, liquid-phase sintering should be considered after establishing acceptable mechanisms for solid-state sintering, as the presence of liquid phase always provides additional diffusional path for faster mass transport. The activation energy for diffusion in electric field needs to be considered as well as the modified particle size-dependency on sintering time needs to be developed in case of SPS. With all such considerations and control experiments, it is expected that one can come up with modified neck growth equations, like those established for the classical solid-state sintering. Hence, it will require extensive research efforts. With better understanding of the underlying densification mechanisms of SPS, it would be possible to closely tune the SPS parameters to develop dense nanostructured materials in a large number of ceramic systems.

SPS has been extensively employed in developing ZrO_2-based nanoceramics. Almost fully dense yttria-stabilized tetragonal zirconia nanocomposites reinforced with 30 vol% of ZrB_2 can be achieved via SPS route at 1200 °C with a holding time of 5 min. It is noteworthy that the sintering temperature is (200–250 °C) less with lower processing time ($\sim$20–25 min), when compared to other conventional sintering techniques. SPSed 3 mol% yttria-doped ZrO_2 nanoceramics were characterized with better hardness, very high flexural strength and wear resistance in comparison to that of conventionally sintered monolithic ZrO_2. However, the fracture toughness of YTZP nanoceramics remained moderate. In the light of this, new experiments are to be designed in developing ZrO_2 nanoceramic composites by carefully selecting sintering additive and optimizing densification process in order to improve fracture toughness without compromising on its beneficial properties.

Binderless WC-based nanocomposites have been successfully developed to address some major problems with WC cermets such as the softening and preferential corrosion of the metallic binder phase. It has been demonstrated that partial/full replacement of Co (metallic phase) with nanosized t-ZrO_2 (ceramic phase) in WC–Co system, along with SPS, can lead to the development of high-performance WC-based ceramic nanocomposites. Our research has demonstrated that WC–2 wt% Co–4 wt% ZrO_2 nanocomposite can exhibit better combination of mechanical properties with fracture toughness of 10 MPa $m^{1/2}$ and strength of 1 GPa or more. A comparison in toughness property could not be made rigorously as many of the papers report the toughness values measured by conventional indentation toughness measurement techniques, which often overestimate the toughness properties and do not provide reliable measure of toughness. Nevertheless, the preliminary research has been encouraging for further development of novel WC-based materials to improve its performance in more demanding applications. More experiments in the near future are to be carried out to realize better performance potential of the WC–ZrO_2–Co nanocomposite over WC–Co hardmetals in tribological and machining applications.

Acknowledgments

The authors would like to thank Department of Science and Technology (DST), Government of India and Defence Research & Development Organisation (DRDO), Government of India for financial support which enabled our research involving SPS of ceramics and composites during the last decade.

References

Angerer, P., Yu, L. G., Khor, K. A., Korb, G., & Zalite, I. (2005). Spark-plasma-sintering (SPS) of nanostructured titanium carbonitride powders. *Journal of the European Ceramic Society, 25*, 1919–1927.

Anne, G., Put, S., Vanmeensel, K., Jiang, D., Vleugels, J., & Van Der Biest, O. (2005). Hard, tough and strong ZrO_2-WC composites from nanosized powders. *Journal of the European Ceramic Society, 25*, 55–63.

Basu, B. (2005). Toughening of Y-stabilized tetragonal zirconia ceramics. *International Materials Reviews, 50*(4), 239–256.

Basu, B., & Balani, K. (2011). *Advanced structural ceramics*. John Wiley & Sons, Inc., USA and American Ceramic Society, ISBN 9780470497111.

Basu, B., & Kalin, M. (2011). *Tribology of ceramics and composites: Materials science perspective*. John Wiley & Sons, Inc., USA and American Ceramic Society, ISBN 9780470522639.

Basu, B., Katti, D., & Kumar, A. (2009). *Advanced biomaterials: Fundamentals, processing and applications*. John Wiley & Sons, Inc., USA and American Ceramic Society. ISBN-10: 0470193409.

Basu, B., Lee, J. H., & Kim, D. Y. (2004). Development of nanocrystalline wear resistant Y-TZP ceramics. *Journal of the American Ceramic Society, 87*(9), 1771–1774.

Basu, B., Venkateswaran, T., & Kim, D. Y. (2006). Microstructure and properties of spark plasma sintered ZrO_2-ZrB_2 Nanoceramic composites. *Journal of the American Ceramic Society, 89*(8), 2405–2412.

Basu, B., Venkateswaran, T., & Sarkar, D. (2005). Pressureless sintering and tribological properties of WC-ZrO_2 composites. *Journal of the European Ceramic Society, 25*, 1603–1610.

Basu, B., Vleugels, J., & Van Der Biest, O. (2002). Development of ZrO_2-ZrB_2 Composites. *Journal of Alloys and Compounds, 334*(1–2), 200–204.

Basu, B., Vleugels, J., & Van Der Biest, O. (2004). Development of ZrO_2-TiB_2 composites: role of residual stress and starting powders. *Journal of Alloys and Compounds, 365*(1–2), 266–270.

Berger, S., Porat, R., & Rosen, R. (1997). A study of WC-based hard metals. *Progress in Materials Science, 42*, 311–320.

Biswas, K., Mukhopadhyay, A., Basu, B., & Chattopadhyay, K. (2007). Densification and microstructure development in spark plasma sintered WC-6 wt.% ZrO_2 nanocomposites. *Journal of Materials Research, 22*(6), 1491–1501.

Bundschuh, W., & ZumGahr, K.-H. (1991). Influence of porosity on friction and sliding wear of tetragonal zirconia polycrystal. *Wear, 151*, 175–191.

Cha, S. I., & Hong, S. H. (2003). Microstructures of binderless tungsten carbides sintered by spark plasma sintering process. *Materials Science and Engineering A, 356*, 381–389.

Cha, S. I., Hong, S. H., & Kim, B. K. (2003). Spark plasma sintering behavior of nanocrystalline WC–10Co cemented carbide powders. *Materials Science and Engineering A, 351*, 31–38.

Chaim, R., Mardera, R., & Estourne`s, C. (2010). Optically transparent ceramics by spark plasma sintering of oxide nanoparticles. *Scripta Materialia, 63*, 211–214.

Cha, S. I., Kim, K. T., Lee, K. H., Mo, C. B., & Hong, S. H. (2005). Strengthening and toughening of carbon nanotube reinforced alumina nanocomposite fabricated by molecular level mixing process. *Scripta Materialia, 53*, 793–797.

Chen, X. J., Khor, K. A., Chan, S. H., & Yu, L. G. (2004). Overcoming the effect of contaminant in solid oxide fuel cell (SOFC) electrolyte: spark plasma sintering (SPS) of 0.5 wt.% silica-doped yttria-stabilized zirconia (YSZ). *Materials Science and Engineering A, 374*, 64–71.

Cremer, G. D. (August 1944). Sintering together powders metals such as bronze, brass or aluminum. US Patent No. 2 355 954.

Eskandarany, M. S. E. (2000). Fabrication of nanocrystalline WC and nanocomposite WC–MgO refractory materials at room temperature. *Journal of Alloys and Compounds, 296*, 175–182.

Eskandarany, M. S. E. (2005). Fabrication and characterizations of new nanocomposite WC/Al_2O_3 materials by room temperature ball milling and subsequent consolidation. *Journal of Alloys and Compounds, 391*, 228–235.

Faiz, M. A., Kesarwani, P., Reddy, K. M., Kalmodia, S., Basu, B., & Balani, K. (2012). Functionally graded hydroxyapatite-alumina-zirconia biocomposite: synergy of toughness and biocompatibility. *Materials Science and Engineering C, 32*, 1164–1173.

Fang, Z. Z., Wang, X., Ryu, T., Hwang, K. S., & Sohn, H. Y. (2009). Synthesis, sintering, and mechanical properties of nanocrystalline cemented tungsten carbide – a review. *International Journal of Refractory Metals and Hard Materials, 27*, 288–299.

Gao, L., Wang, H. Z., Hong, J. S., Miyamoto, H., Miyamoto, K., Nishikawa, Y., et al. (1999). Mechanical properties and microstructure of nano-SiC-Al_2O_3 composites densified by spark plasma sintering. *Journal of the European Ceramic Society, 19*, 609–613.

Garmendia, N., Grandjean, S., Chevalier, J., Diaz, L. A., Torrecillas, R., & Obieta, I. (2011). Zirconia–multiwall carbon nanotubes dense nano-composites with an unusual balance between crack and ageing resistance. *Journal of the European Ceramic Society, 31*, 1009–1014.

Grasso, S., Sakka, Y., & Maizza, G. (2009). Electric current activated/assisted sintering (ECAS): a review of patents 1906–2008. *Science and Technology of Advanced Materials, 10*, 053001.

Groza, J. R., & Zavaliangos, A. (2000). Sintering Activation by External Electrical Field. *Materials Science and Engineering A, 287*(2), 171–177.

Gupta, N., Mukhopadhyay, A., Pavani, K., & Basu, B. (2012). Spark plasma sintering of novel ZrB_2-SiC-$TiSi_2$ composites with better mechanical properties. *Materials Science and Engineering A, 534*, 111–118.

Hannink, R. H. J., Kelly, P. M., & Muddle, B. C. (2000). Transformation toughening in zirconia-containing ceramics. *Journal of the American Ceramic Society, 83*, 461–487.

Hansen, J. D., Rusin, R. P., Teng, M. H., & Johnson, D. L. (1992). Combined-stage sintering model. *Journal of the American Ceramic Society, 75*(5), 1129–1135.

He, Y., Winnubst, L., Burggraaf, A. J., Verweij, H., van der Varst, P. G. Th., & de With, B. (1996). Grain-size dependence of sliding wear in tetragonal zirconia polycrystals. *Journal of the American Ceramic Society, 79*, 3090–3096.

Huang, S. G., Vanmeensel, K., Van der Biest, O., & Vleugels, J. (2007). Development of ZrO_2–WC composites by pulsed electric current sintering. *Journal of the European Ceramic Society, 27*, 3269–3275.

Imasato, S., Tokumoto, K., Kitada, T., & Sakaguchi, S. (1995). Properties of ultra-fine grain binderless cemented carbide RCCFN. *International Journal of Refractory Metals and Hard Materials, 13*, 305–312.

Jia, K., Fischer, T. E., & Gallois, B. (1998). Microstructure, hardness and toughness of nanostructured and conventional WC-Co composites. *Nanostructured Materials, 10*(5), 875–891.

Kalmodia, S., Goenka, S., Laha, T., Lahiri, D., Basu, B., & Balani, K. (2010). Microstructure, mechanical properties, and in vitro biocompatibility of spark plasma sintered hydroxyapatite–aluminum oxide–carbon nanotube composite. *Materials Science and Engineering C, 30*, 1162–1169.

Khor, K. A., Cheng, K. H., Yu, L. G., & Boey, F. (2003). Thermal conductivity and dielectric constant of spark plasma sintered aluminium nitride. *Materials Science and Engineering A, 347*, 300–305.

Kim, H. C., Shon, I. J., Garay, J. E., & Munir, Z. A. (2004). Consolidation and properties of binders sub-micron tungsten carbide by field-activated sintering. *International Journal of Refractory Metals and Hard Materials, 22*, 257–264.

Kim, H. C., Shon, I. J., Yoon, J. K., Lee, S. K., & Munir, Z. A. (2006). One step synthesis and densification of ultra-fine WC by high-frequency induction combustion. *International Journal of Refractory Metals and Hard Materials, 24*, 202–209.

Klaffke, D. (1989). Fretting wear of ceramics. *Tribology International, 22*, 89–101.

Kumar, B. V. M., Kim, W. S., Hong, S. H., Bae, H. T., & Lim, D. S. (2010). Effect of grain size on wear behavior in Y-TZP ceramics. *Materials Science and Engineering A, 527*, 474–479.

Kumar, R., Prakash, K. H., Cheang, P., & Khor, K. A. (2005). Microstructure and mechanical properties of spark plasma sintered zirconia-hydroxyapatite nanocomposite powders. *Acta Materialia, 53*, 2327–2335.

Kusunose, T., Sekino, T., Choa, Y.-H., & Niihara, K. (2002). Machinability of silicon nitride/boron nitride nanocomposites. *Journal of the American Ceramic Society, 85*(11), 2689–2695.

Lawn, B. R. (1993). *Fracture of brittle solids*. Cambridge: Cambridge University Press.

Lee, J.-M., Kang, S.-B., Sato, T., Tezuka, H., & Kamio, A. (2003). Fabrication of Al/Al_3Fe composites by plasma synthesis method. *Materials Science and Engineering A, 343*, 199–209.

Li, W., & Gao, L. (2000). Rapid sintering of nanocrystalline ZrO_2 (3Y) by spark plasma sintering. *Journal of the European Ceramic Society, 20*, 2441–2445.

Li, W., & Gao, L. (2003). Fabrication of HAp–ZrO_2 (3Y) nano-composite by SPS. *Biomaterials, 24*, 937–940.

Malek, O., Lauwers, B., Perez, Y., Baets, P. D., & Vleugels, J. (2009). Processing of ultrafine ZrO_2 toughened WC composites. *Journal of the European Ceramic Society, 29*, 3371–3378.

Mamedov, V. (2002). Spark plasma sintering as advanced PM sintering method. *Powder Metallurgy, 45*(4), 322–328.

Marder, R., Chaim, R., & Estournes, C. (2010). Grain growth stagnation in fully dense nanocrystalline Y_2O_3 by spark plasma sintering. *Materials Science and Engineering A, 527*, 1577–1585.

Merino, J. L. O., & Todd, R. I. (2005). Relationship between wear rate, surface pullout and microstructure during abrasive wear of alumina and alumina/SiC nanocomposites. *Acta Materialia, 53*(12), 3345–3357.

Mohan, K., & Strutt, P. R. (1996). Observation of Co nanoparticle dispersions in WC nanograins in WC–Co cermets consolidated from chemically synthesized powders. *Nanostructured Materials, 7*, 547–555.

Mukhopadhyay, A., & Basu, B. (2007). Consolidation-microstructure-property relationships in bulk nanoceramics and ceramic nanocomposites: a review. *International Materials Reviews, 52*(5), 257–288.

Mukhopadhyay, A., & Basu, B. (2011). Recent developments on WC-based bulk composites. *Journal of Materials Science, 46*, 571–589.

Mukhopadhyay, A., Basu, B., Bakshi, S. D., & Mishra, S. K. (2007). Pressureless sintering of ZrO_2-ZrB_2 composites: microstructure and properties. *International Journal of Refractory Metals and Hard Materials, 25*, 179–188.

Mukhopadhyay, A., Chakrabarty, D., & Basu, B. (2010). Spark plasma sintered WC-ZrO_2-co nanocomposites with high fracture toughness and strength. *Journal of the American Ceramic Society, 93*(6), 1754–1763.

Munir, Z. A., Quach, D. V., & Ohyanagi, M. (2011). Electric current activation of sintering: a review of the pulsed electric current sintering process. *Journal of the American Ceramic Society, 94*(1), 1–19.

Munir, Z. A., Tamburin, U. A., & Ohyanagi, M. (2006). The effect of electric field and pressure on the synthesis and consolidation of materials: a review of the spark plasma sintering method. *Journal of Materials Science, 41*, 763–777.

Nath, S., Biswas, K., & Basu, B. (2008). Phase stability and microstructure development in hydroxyapatite–mullite system. *Scripta Materialia, 58*, 1054–1057.

Nath, S., Tripathi, R., & Basu, B. (2009). Understanding phase stability, microstructure development and biocompatibility in calcium phosphate-titania composites, synthesized from hydroxyapatite and titanium powder mix. *Materials Science and Engineering C, 29*, 97–107.

Niihara, K. (1991). New design concept of structural ceramics-ceramic nano composites. *Journal of Ceramic Society of Japan. The Centennial Memorial Issue, 99*(10), 974–982.

Niihara, K., & Suzuki, Y. (1999). Strong monolithic and composite $MoSi_2$ materials by nanostructured design. *Materials Science and Engineering A, 261*, 6–15.

Nishimura, T., Xu, X., Kimotoa, K., Hirosakia, N., & Tanaka, H. (2007). Fabrication of silicon nitride nanoceramics—Powder preparation and sintering: a review. *Science and Technology of Advanced Materials, 8*, 635–643.

Nygren, M., & Shen, Z. (2003). On the preparation of bio-, nano- and structural ceramics and composites by spark plasma sintering. *Solid State Sciences, 5*, 125–131.

Ohji, T., Jeong, Y. K., Choa, Y. H., & Niihara, K. (1998). Strengthening and toughening mechanisms of ceramic nanocomposites. *Journal of the American Ceramic Society, 81*(6), 1453–1460.

Omori, M. (2000). Sintering, consolidation, reaction and crystal growth by the spark plasma system (SPS). *Materials Science and Engineering A, 287*, 183–188.

Orru, R., Licheri, R., Locci, A. M., Cincotti, A., & Cao, G. (2009). Consolidation/synthesis of materials by electric current activated/assisted sintering. *Materials Science and Engineering R, 63*, 127–287.

Raj, R., Cologna, M., & Francis, J. S. C. (2011). Influence of externally imposed and internally generated electrical fields on grain growth, diffusional creep, sintering and related phenomena in ceramics. *Journal of the American Ceramic Society, 94*(7), 1941–1965.

Ran, S., & Gao, L. (2012). Electrical properties and microstructural evolution of ZrO_2–Al_2O_3–TiN nanocomposites prepared by spark plasma sintering. *Ceramics International, 38*, 4923–4928.

Ran, S., Vleugels, J., Huang, S., Vanmeensel, K., Blank, D. H. A., & Winnubst, L. (2010). Manipulating microstructure and mechanical properties of CuO doped 3Y-TZP nano-ceramics using spark-plasma sintering. *Journal of the European Ceramic Society, 30*, 899–904.

Reddy, K. M., Kumar, N., & Basu, B. (2010a). Innovative multi-stage spark plasma sintering to obtain strong and tough ultrafine grained ceramics. *Scripta Materialia, 62*, 435–438.

Reddy, K. M., Kumar, N., & Basu, B. (2010b). Inhibition of Grain growth during the final stage of multi-stage spark plasma sintering of oxide ceramics. *Scripta Materialia, 63*, 585–588.

Reddy, K. M., Mukhopadhyay, A., & Basu, B. (2010c). Microstructure-mechanical-tribological property correlation of multistage spark plasma sintered tetragonal ZrO_2. *Journal of the European Ceramic Society, 30*, 3363–3375.

Richter, V., & Ruthendorf, M. V. (1999). On hardness and toughness of ultrafine and nanocrystalline hard materials. *International Journal of Refractory Metals and Hard Materials, 17*, 141–152.

Shen, Z., Johnson, M., Zhao, Z., & Nygren, M. (2002). Spark plasma sintering of alumina. *Journal of the American Ceramic Society, 85*(8), 1921–1927.

Shen, Z., Zhao, Z., Peng, H., & Nygren, M. (2002). Formation of tough interlocking microstructures in silicon nitride ceramics by dynamic ripening. *Nature, 417*, 266–269.

Sivaprahasam, D., Chandrasekar, S. B., & Sundaresan, R. (2007). Microstructure and mechanical properties of nanocrystalline WC–12Co consolidated by spark plasma sintering. *International Journal of Refractory Metals and Hard Materials, 25*(2), 144–152.

Staia, M. H., Torres, I. J., Castillo, C., Sudarshan, T. S., Lesage, J., & Chicot, D. (2006). Tribological study of WC produced by plasma pressure compaction. *International Journal of Refractory Metals and Hard Materials, 24*, 183–188.

Sternitzke, M. (1997). Review: structural ceramic nanocomposites. *Journal of the European Ceramic Society, 17*, 1061–1082.

Sun, S. K., Kan, Y. M., & Zhang, G. J. (2011). Fabrication of nanosized tungsten carbide ceramics by reactive spark plasma sintering. *Journal of the American Ceramic Society, 94*(10), 3230–3233.

Sun, X., Li, J. G., Guo, S., Xiu, Z., Duan, K., & Hu, X. Z. (2005). Intragranular particle residual stress strengthening of Al_2O_3–SiC nanocomposites. *Journal of the American Ceramic Society, 88*(6), 1536–1543.

Suryanarayana, C. (1995). Nanocrystalline materials. *International Materials Reviews, 40*(2), 41–64.

Su, X., Wang, P., Chen, W., Shen, Z., Nygren, M., Cheng, Y., et al. (2004). Effects of composition and thermal treatment on infrared transmission of Dy-α-sialon. *Journal of the European Ceramic Society, 24*, 2869–2877.

Suzuki, H. (1986). *Cemented carbide and sintered hard materials.* Tokyo, Japan: Maruzen.

Suzuki, H., Hayashi, K., Yamamoto, T., Nakajo, N. J. (1966). J. Jpn. Soc. of Powder Metal. 13:290, ASM International Handbook Committee, Metals Handbook, 9th ed. Vol. 13. Corrosion, pp. 855–857 (1987).

Tamburini, U. A., Gennari, S., Garay, J. E., & Munir, Z. A. (2005). Fundamental investigations on the spark plasma sintering/synthesis process II. Modeling of current and temperature distributions. *Materials Science and Engineering A, 394*, 139–148.

Tiwari, D., Basu, B., & Biswas, K. (2009). Simulation of thermal and electric field evolution during spark plasma sintering. *Ceramics International, 35*, 699–708.

Tokita, M. (2001). Mechanism of spark plasma sintering. In K. Kosuge, & H. Nagai (Eds.), *Proceedings of the 2000 powder metallurgy world congress (Kyoto, Japan, November 2000)* (pp. 729–732). Kyoto, Japan: Japanese Society of Powder and Powder Metallurgy.

Tokita, M. (2003). Large-size WC/Co functionally graded materials fabricated by spark plasma sintering (SPS) method. *Materials Science Forum, 39*, 423–425.

Tomino, H., Watanabe, H., & Kondo, Y. (1997). Electric current path and temperature distribution for spark Sintering. *Journal of the Japan Society of Powder and Powder Metallurgy, 44*(10), 974–979.

Vanmeensel, K., Laptev, A., Hennicke, J., Vleugels, J., & Van Der Biest, O. (2005). Modeling of the temperature distribution during field assisted sintering. *Acta Materialia, 53*, 4379–4388.

Vanmeensel, K., Laptev, A., Van der Biest, O., & Vleugels, J. (2007). Field assisted sintering of electro-conductive ZrO_2-based composites. *Journal of the European Ceramic Society, 27*(2–3), 979–985.

Venkateswaran, T., Basu, B., Raju, G. B., & Kim, D. Y. (2006). Densification and properties of transition metal borides-based cermets via spark plasma sintering. *Journal of the European Ceramic Society, 26*, 2431–2440.

Venkateswaran, T., Sarkar, D., & Basu, B. (2005). Tribological properties of WC-ZrO_2 nanocomposites. *Journal of the American Ceramic Society, 88*(3), 691–697.

Venkateswaran, T., Sarkar, D., & Basu, B. (2006). WC-ZrO_2 composites: processing and unlubricated tribological properties. *Wear, 260*(1–2), 1–9.

Viswanathan, V., Laha, T., Balani, K., Agarwal, A., & Seal, S. (2006). Challenges and advances in nanocomposite processing techniques. *Materials Science and Engineering R, 54*, 121–285.

Wang, S. W., Chen, L. D., Hirai, T., & Kang, Y. S. (1999). Microstructure inhomogeneity in Al_2O_3 sintered bodies formed during the plasma-activated sintering process. *Journal of Materials Science Letters, 14*(7), 1119–1121.

Wang, Y., Heusch, M., Lay, S., & Allibert, C. H. (2002). Microstructure evolution in the cemented carbides WC–Co I. Effect of the C/W ratio on the morphology and defects of the WC grains. *Physica Status Solidi, 193*, 271–283.

Yang, F., Zhao, J., & Ai, X. (2009). Effect of initial particulate and sintering temperature on mechanical properties and microstructure of WC-ZrO_2-VC ceramic composites. *Journal of Materials Processing Technology, 209*, 4531–4536.

Yang, F., Zhao, J., Ai, X., & Yuan, X. (2009). Effect of medium temperature on the dispersion of WC/ZrO_2/VC composite powders. *Journal of Materials Processing Technology, 209*, 2161–2166.

Yoshimura, M., Sando, M., Choa, Y. H., Sekino, T., & Niihara, K. (1999). Fabrication of dense ZrO_2 – based nano/nano type composites by new powder preparation method and controlled sintering process. *Key Engineering Materials, 161–163*, 423–426.

Yucheng, W., & Zhengyi, F. (2002). Study of temperature field in spark plasma sintering. *Materials Science and Engineering B, 90*(1–2), 34–37.

Zavaliangos, A., Zhang, J., Krammer, M., & Groza, J. R. (2004). Temperature evolution during field activated sintering. *Materials Science and Engineering A, 379*, 218–228.

Zeng, W., Gao, L., Gui, L., & Guo, J. (1999). Sintering kinetics of α-Al_2O_3 powder. *Ceramics International, 25*, 723–726.

Zhang, F., Lin, K., Chang, J., Lu, J., & Ning, C. (2008). Spark plasma sintering of macroporous calcium phosphate scaffolds from nanocrystalline powders. *Journal of the European Ceramic Society, 28*, 539–545.

Zhan, G. D., Kuntz, J., Wan, J., Garay, J., & Mukherjee, A. K. (2003a). Spark plasma sintered $BaTiO_3/Al_2O_3$ nanocomposites. *Materials Science and Engineering A, 356*, 443–446.

Zhan, G. D., Kuntz, J., Wan, J., Garay, J., & Mukherjee, A. K. (2003b). A novel processing route to develop a dense nanocrystalline alumina matrix ($<$100 nm) nanocomposite material. *Journal of the American Ceramic Society, 86*(1), 200–202.

Zhu, S. G., Wu, C. X., & Luo, Y. L. (2010). Effects of stearic acid on synthesis of nanocomposite WC-MgO powders by mechanical alloying. *Journal of Materials Science, 45*, 1817–1822.

ZumGahr, K. H. (1989). Sliding wear of ceramic-ceramic, ceramic-steel and steel-steel pairs in lubricated and unlubricated contact. *Wear, 133*, 1–22.

This page intentionally left blank

2.06 Advanced Manufacturing of Hard Ceramics

Rainer Gadow and Frank Kern, University of Stuttgart, Institute for Manufacturing Technology of Ceramic Components and Composites, Stuttgart, Germany

© 2014 Elsevier Ltd. All rights reserved.

2.06.1 Introduction

Manufacturing of engineering ceramics extends beyond the pure processing science which is specific for different materials. Manufacturing must equally respect economic and technical boundary conditions to select a processing cycle capable of producing ceramic components based on a set of requirements predefined by the application in terms of reproducibility, performance, and cost. The science of ceramic manufacturing in a competitive global environment must thus combine elements of basic material science, engineering and business economics.

In the 1970s and 1980s, which may be called the "golden age of engineering ceramics" new developments in ceramics manufacturing were dominantly performance driven, creating an ideal playground for material

http://dx.doi.org/10.1016/B978-0-08-096527-7.00025-8

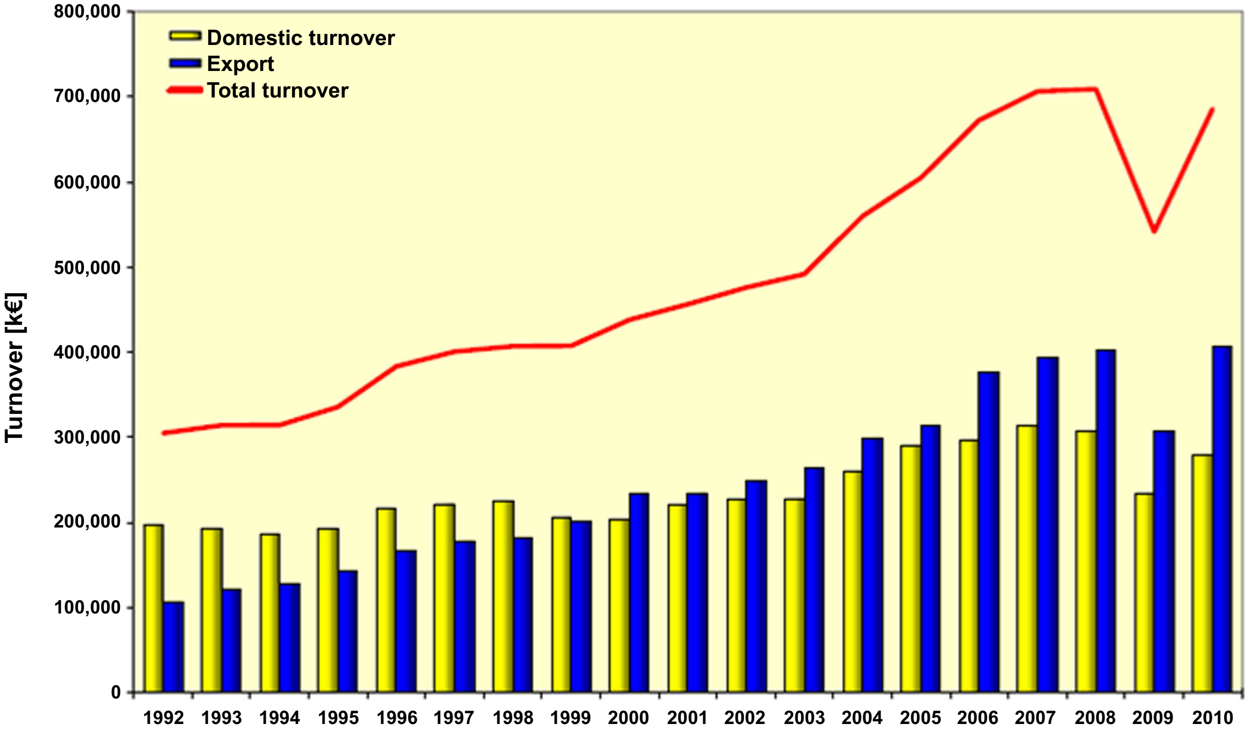

Figure 1 Domestic and total turnover over the past 20 years, Verband der keramischen Industrie E.V. (2011).

scientists to invent new materials with perpetually new and better properties. The cold war and the quest for even better materials for aerospace and military applications have contributed their share to this ceramic boom in the western countries.

Today the situation has changed dramatically. An overview of the trends of the turnover of ceramics manufacturers in Germany during the past 20 years is shown in Figure 1. Rising international competition to the established producers has led to a severe decline in pricing power. Thus a large fraction of new developments are cost driven aiming at making process cycles more efficient, if possible at the same level of component quality. The simpler engineering ceramic components have become commodities. Innovative developments are more or less restricted to some niche applications with high value addition such as biomedical, electronic and specialized mechanical engineering applications. While the structural ceramics have suffered from stagnation, functional materials, e.g. electronic devices, have become increasingly important.

However, structural ceramics especially hard ceramics are still of very high importance in engineering applications such as cutting tools, tribocomponents, engine components, biomedical implants and ceramic armor.

2.06.2 The Processing Chain of Ceramics Manufacturing

Typically, processing of all ceramics follows a scheme that is based on the properties of the material. Ceramics, with only a few exceptions, are produced from powders which are—with the help of additives and processing technology—conditioned in a very specific way to the needs of a forming process. The forming and shaping processes can be subdivided into three main groups: pressing processes, processing of plastic or plastified pastes and casting of liquid ceramic dispersions. The subsequent thermal treatment converts the as-formed green body to a ceramic material. To make ceramic components, the processing cycle must include technologies capable of supplying a specific geometry covering defined dimensional tolerances. This can be—in the ideal case—achieved by (near)-net-shape manufacturing processes. These processes are capable of producing green bodies of the desired size and shape reproducibly, respecting the shrinkage suffered during firing. Thus the sintered component requires little or no further machining processes. As pricing pressure has been ever

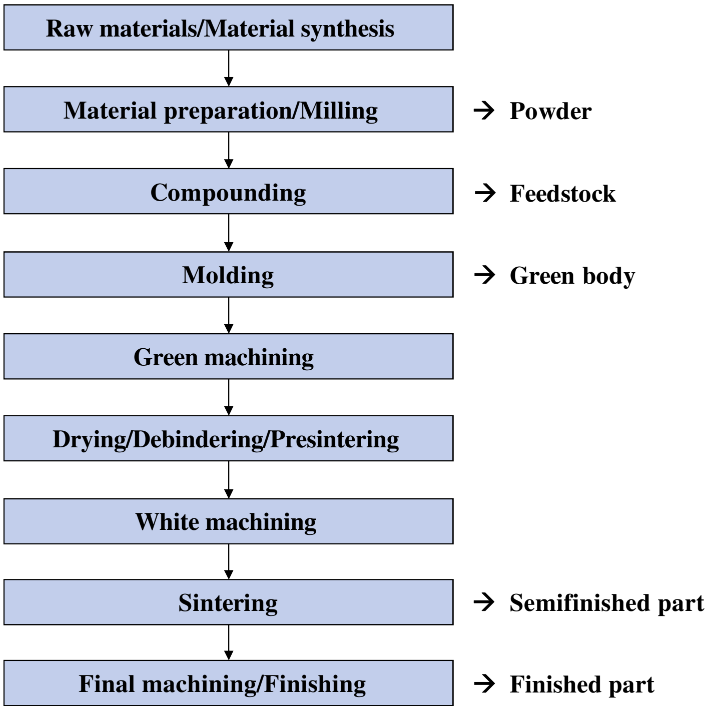

Figure 2 The processing chain of ceramics manufacturing.

increasing, the importance of near-net-shape processes in mass production of ceramic components has increased significantly.

Due to the properties of the product, hard ceramics are as a matter of fact difficult to machine in the final state. Machining should, if possible, be carried out before sintering in the green or white state where high removal rates are possible. However, this requires green bodies of sufficient strength to facilitate handling. In customized products which are produced in small lot sizes, final machining from a sintered blank is still of some importance. It has to be taken into account that the conventional machining processes like grinding, lapping and polishing do not allow for making all kinds of geometries. Inner contours or high aspect ratios are difficult to obtain in monolithic solutions, and very often assembling components from many subcomponents is necessary. New final machining methods like laser machining or electric discharge machining (EDM) may fill the gap. However, these machining methods may require modified or specially designed materials which are, e.g. electrically conductive.

Another new development which is promising for customized parts is the use of rapid prototyping processes like laser sintering, ink-jet printing and microextrusion, which are able to build up a complex shape ceramic in one cycle. Still, components derived from these technologies have not reached the structural integrity of conventionally produced parts, but for some special applications of ceramics which are not necessarily the classical ones, effective solutions exist.

In the scheme of a generalized production chain, we can observe a vertical structure defined by different groups of manufacturing processes (Figure 2) and a horizontal structure defined by the production stage. The following text will subdivide the manufacturing chapter into three blocks following the vertical dividing lines thus building three sections on pressing, plastic processing and casting processes. In most cases, structural parts require machining as a final stage; thus, it is treated individually in an additional section. Some case studies for manufacturing of ceramic components of different materials, sizes and numbers of pieces are finally discussed.

2.06.3 Before the Start—Definition of a Set of Requirements

The first step in manufacturing a ceramic is a process seldom described in the literature, as it has nothing to do with the processing itself. In most cases, the definition of the set of requirements of the customer is related to a completely new component design or the redesign of an existing component at lower price and having identical quality.

The customer has a certain application and defines the set of requirements making use of the expertise of the ceramics manufacturer. The set of requirements consists of three components: requirements of the material (strength, toughness, abrasion resistance, hardness, etc.), design features (size, shape, dimensional tolerances, surface quality, etc.) and economical boundary conditions (lot size, price targets, terms and conditions). Furthermore, original equipment manufacturers (OEMs) will define the terms of quality management and further regulatory restrictions (e.g. US Food and Drug Administration approval for medical devices). Based on this information, the manufacturer has to set up his production process to meet the customer demands and his economic targets.

The choice of a suitable manufacturing cycle becomes more or less straightforward as soon as the set of requirements, the existing process know-how and economic considerations are joined together. A detailed cost analysis has to cover the cost of required investments; the operating costs like material, energy and work force; as well as the cost of capital employed. On the other side, the number of components produced, the turnover per time and the cost targets defined are important. Other considerations which may influence the choice of the manufacturing process are capacity utilization, existing equipment already written off, customer preferences or regulatory restrictions.

The ceramics manufacturer can choose between three basic manufacturing technologies for forming and shaping of a component or manufacturing of a blank which is subsequently machined.

- Pressing of powders or granulates
- Casting of ceramic dispersions
- Thermoplastic forming

The following sections will describe these three groups.

2.06.4 Pressing

Pressing processes are by far the most important manufacturing processes for hard ceramics. This is due to the fast forming cycles and the comparatively short thermal treatment cycles where debindering can often be included in the regular firing cycle. While historically complicated shapes were produced by isostatically pressed blanks, progress in axial pressing processes using multilevel molds and presses allows for manufacturing sophisticated geometries rather than just disks, plates, and blocks. In recent years, pressing has regained the market share previously reserved for ceramic injection molding (CIM). Pressing technologies can be applied to manufacture alumina, silicon carbide, silicon nitride and various other hard ceramic composites.

2.06.4.1 Compounding

High-performance pressing processes, whether isostatic or axial, require pressing feedstocks which provide homogeneous and reproducible form filling, high green densities and green strength of the final components, as well as low abrasive wear of the molds.

While additives are sometimes omitted in materials science, stable manufacturing is impossible without the use of well-adapted additive recipes consisting of binders, plasticizers and surfactants. With the help of these additives, granulated powders of good flowability are produced today almost exclusively by spray granulation, leaving little space for other processes like build-up granulation or freeze-drying.

2.06.4.2 Spray Granulation

Spray granulation is carried out by atomizing liquid dispersions of ceramic powders in a flow of hot air or protective atmosphere. While granulated oxides are processed from aqueous slurries spray-dried in air, nonoxides (especially if very fine grained) are frequently atomized in nitrogen or argon atmosphere due to sensitivity to oxidation which would corrupt the feedstock quality. For the same reason, organic solvent may be applied to avoid chemical attack and tribo-oxidation during wet milling. Due to high cost, organic solvents and the gases needed to create the protective atmosphere are recycled in closed loop systems. These systems require explosion protection; this fact increases operating and investment cost.

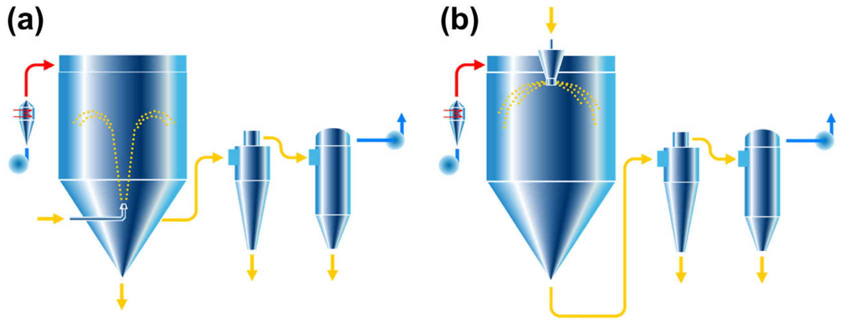

Figure 3 Setup of a spray dryer working: cocurrent (a) and countercurrent (b) (GEA Niro).

In the spray-drying process, the atomized dispersion and the hot gas/air may flow either cocurrent or counter current (Figure 3). Both systems have their specific advantages. Like in heat exchangers the countercurrent systems are energetically more efficient and allow for higher turnover. On the other hand, the cocurrent systems provide powders of more regular shapes and less granulate defects. Atomization of the liquid dispersion can be performed by the following different means:

- In two-component jets, the ceramic dispersion guided through a central tube is atomized by pressurized gas/air entering a concentric tube. The higher the gas pressure, the finer the spray and the resulting granulate. This technology is commonly used in pilot plants and smaller production units.
- In one-component jet, the dispersion is atomized by passing the pressurized dispersion through a nozzle. This atomization technique is used preferentially in large spray dryers with $>10\ \mathrm{kg\,h^{-1}}$ vaporization capacity.
- Other atomization techniques are limited to special cases. In spinners, the dispersion fed in the axis of a spinning wheel is atomized by centrifugal forces which breaks the jet into drops as soon as a certain critical velocity is reached.

The capacity of industrial-scale spray dryers may reach up to a few tons per hour of granulate.

The properties of the ceramic dispersion fed into the spray dryer have a strong influence on the yield and size distribution of the granulate. As the dispersion is exposed to strong shear forces in the nozzle and also in the suspension pump, a shear thinning or at least Newtonian behavior is favorable to provide good flowability and avoid clogging. Still high solid contents are favorable to increase productivity as the vaporization capacity of the spray dryer is limited. Manufacturing of the dispersions follows a procedure analogous to that of slip casting. Basics of spray drying technology are the subject of some comprehensive books (Cook & DuMont, 1991; Mujumdar, 2007, p. 710). New developments have dealt with producing powders with lower emissions of dust for better workplace hygiene (Shu, 2010). Pressing of nanomaterials with an increased internal friction due to large specific surface area also requires tailored spray granulation processes, capable of making powders which are compactable with standard equipment at acceptable pressing forces (Raghupathy, 2011).

2.06.4.3 Axial Pressing

Axial pressing starts with the filling of the mold. This—at first sight rather trivial process—strongly affects the product quality. The more homogeneously the mold filling process is carried out, the lower are the density gradients in the sintered part. Mold filling is commonly carried out volumetrically by a feed hopper which is drawn over the open mold. The powder ripples into the mold only by gravity forces. The air in the mold must escape countercurrent to the powder filled in. Specially in complex cavities with different depth levels, this effect may cause inhomogeneous filling. In case of mixed instead of spray granulated powder, segregation of the constituents may occur. Even in case of granulated feedstock, small and large granules may be enriched in different lateral levels leading to potential inhomogeneities.

In axial pressing, the powder is compacted in an axially symmetric die between two punches at high pressure. The compaction behavior of granulated ceramic powders strongly depends on the fraction and plasticity properties of the organic additives. Increasing binder fraction raises not only the required pressure for compaction but also the stability of the green body. The glass transition temperature of the binder should be lower than the working temperature to ensure good compaction. Humidity of powder and working atmosphere must be controlled to achieve reproducible results (Carneim & Messing, 2001; Shinohara, 1999). The exact compaction characteristics of a powder can be determined by instrumented compaction experiments (Klemm, Schöne, Svoboda, Fries, & Nebelung, 2010). Models of the mechanics of powder compaction are beneficial to help predict the densification behavior and limit experimental effort (Thompson, 1981). New approaches using Finite element modelling (FEM) have been demonstrated (Falgon, 2005). Depending on the requirements of the components and the complexity of the part, different designs and actuation forces can be selected. In case of very simple geometries and low strength and homogeneity requirements, toggle lever presses operating purely mechanically at high turnover are chosen. Granulate supply of presses for mass production is achieved volumetrically by automatized feed hoppers. This implies granulates of defined and reproducible bulk density to guarantee low fluctuations in component mass and size. It has been shown recently that axial pressing can compete with other shaping technologies in term of dimensional accuracy, reproducibility as well as green and sintered density (Kaiser, 2009).

Complex high-quality parts are produced in multilevel on hydraulic presses offering the opportunity to design pressing cycles with defined multistage loading and unloading cycles. The better the homogeneity of density in the pressed part, the lower the dimensional tolerances and distortion in the final components. The quality of the forming process thus has high effect on process economy as final machining costs can be reduced. Improved homogeneity can be achieved by evacuation of the mold (Kaiser, 2003). By ejection under an axial load, spallation of edges and delamination can be avoided.

The basic working principles of different uniaxial pressing setups are shown in **Figure 4**. In the classical setup A (fixed lower punch and mold floating upper punch), the densification is quite inhomogeneous, the neutral stress zone being closer to the bottom of the part. This can be slightly improved by setup B, where the mold is mechanically moved downward with the upper punch and mechanically returned with springs. Optimum conditions with a neutral zone at half height are reached in setup C with a fixed mold and lower and upper punch moving. This setup, however, requires having hydraulic pistons below the pressing level as well as placement of the press in a pit. Setup D can achieve equally good results in less space. Here the lower punch stays fixed but the upper punch and the mold are moved in optimum speed by independent hydraulic systems.

Multilevel pressing has gained importance over the past years. Technologies originally developed for powder metallurgy have been transformed to the field of ceramics manufacturing. Components mass produced on multilevel presses are, e.g. complex alumina faucet disks. On an axial press mounted on four columns, up to three upper and lower levels may be mounted. The main piston is attached to the base frame and two additional drives are then mounted on two opposite pillars each. By multilevel pressing, very complex shapes can be manufactured. The section of the different pistons has to be coordinated in such a way that the density of the powder in the individual sections is constant. Thus the different pistons must move with velocities inversely proportional to the component height in the section. Relative movement of the powder compact sections must be avoided.

In multilevel pressed components, the unloading cycle is a critical point. At high pressures, a high amount of elastic energy is stored in the compressed pistons; hence, sudden piston springback would cause lateral cracks in complex components. Thus, only with a controlled release of the axial load can such components be produced. While traditionally axial pressing was carried out against a fixed mechanical arrest, progress in hydraulic control units today allows for an extremely exact free positioning of the pistons. This enables exact positioning

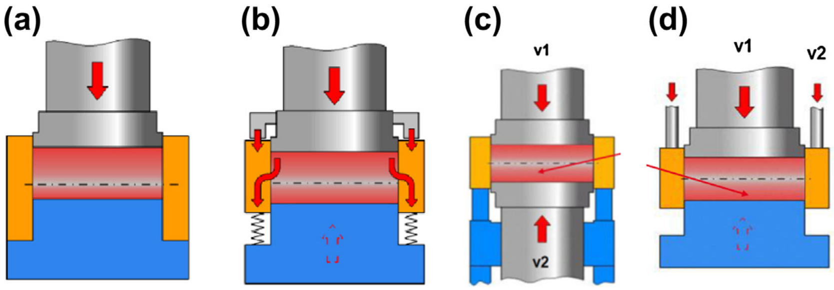

Figure 4 Uniaxial pressing principles (Laeis GmbH). (a) Fixed lower punch; (b) fixed lower punch, mold moved with upper punch and ejection springs; (c) fixed mold, upper and lower punch moving; and (d) fixed lower punch, mold moving independently. v1, v2 are punch velocities.

and controlled load release. Furthermore, the working principle of part ejection can be modified in such a way that it is no longer required to move the pressing die down with the lower punch in fixed position (draw-off principle). The new control units allow keeping the position of the die and eject the part by moving the lower piston (ejection principle). Specially in automated systems, part handling is facilitated as a handling unit can then take out the part easily as the upper level of the die is always in a fixed position. Traveling distance of the lower and upper punch is also reduced; therefore, in the same available space, higher components can be manufactured.

2.06.4.4 Cold Isostatic Pressing

In cold isostatic pressing (CIP), a powder compact contained in a flexible polymer bag is compacted by means of a liquid pressure transducer, in most cases water at high pressure. As the pressure acts evenly from all directions, the resulting powder compacts have high homogeneity and isotropic density (James, 1983; Reed, 1976). The CIP processes can be subdivided into wet bag and dry bag processes (Boyer, 1974).

In wet bag processes, the powder is filled into a flexible bag, which is then evacuated and closed with a plug. The bag (or many bags together) is placed into the water-filled recipient of the press and the compression takes place. In case of dry bag pressing, the powder is contained in a radially symmetric tool with flexible walls. Thus, the pressing cycle is not exactly isostatic but radial. The pressures employed in the CIP process may be extremely high (high-performance ceramics are often pressed at 200–300 MPa), the most performing machines being able to apply pressures up to 500 MPa. Compared to CIPed metal powders the degree of plastic deformation in compacted ceramic powders is negligible (Eksi, 2004). The process of densification can be calculated and visualized using FEM-based models (Gu, 2006; Lee, 2007). In case of less-sophisticated components from more coarse-grained material (easier to densify), pressures ranging between 50 and 100 MPa are sufficient. From a manufacturing point of view, the choice of the processing, dry or wet bag, is defined by the set of requirements. Wet bag pressing is a flexible manufacturing method where many parts of equal or different sizes may be produced in one cycle. However, the filling and unloading process is time consuming and personnel intensive. The parts produced may have odd shapes. Thus the wet bag process is suitable for large components with small lot sizes. On the other hand, in the dry bag process, mold filling and ejection of the produced parts can be completely automatized, making the process capable of mass-producing green bodies with narrow dimensional tolerances. The process is, e.g. used to manufacture isolators for spark plugs in millions of pieces. Ceramic hip joints of alumina, zirconia or ZTA are high-quality precision parts also produced by CIP. Due to the high requirements of density and structural homogeneity, compaction is carried out by CIP. In order to reduce the machining effort, the compaction process takes place in precision molds at extremely well-defined compaction parameters.

In most cases, CIPed compacts are subsequently green-machined. By pressing onto an incompressible insert, hollow parts like tubes can be produced with a defined inner geometry. In conventional dry bag pressing, the ends of the part which are not in contact with the flexible polymer membrane are not compacted equally. The compacts have a so-called *elephants foot*, which has to be removed prior to machining. Machining becomes possible as the green strength of CIPed compacts is high due to high green density and addition of binders to the granulate. The high degree of compaction in CIP has to be taken into account in designing the following debindering and sintering cycles, especially if very fine ceramic powders are used (Wang, 1992).

2.06.4.5 Machining of Pressed Components

2.06.4.5.1 Green Machining

Pressed components are commonly green-machined if required (Birkby, 1994). Only if the green strength is not sufficient, machining is carried out in the white state (presintered) or by final machining of the sintered part. Green machining requires a minimum strength of 10–20 MPa to be able to mount and fix the blanks for processing. Green machining may include drilling, turning, milling or grinding operations. It is always carried out dry without coolants or lubricants. The milling dust recovered from the exhaust system is returned to the compounding process to be recycled. As the blanks are sensitive, feed rates and advance are low. Milling is commonly performed with high-speed tools. Blanks from well-calibrated pressing processes with very reproducible sinter shrinkage can be green-machined in near-net-shape quality, so that the material allowance for final machining can be reduced to a minimum (Dhara, 2005). Blanks from the dry bag process with very reproducible shape may even be machined in automatized machining systems.

Further processes which may be included in the umbrella term of "green machining" are cleaning or chamfering of green bodies by means of compressed air or soft brushes. These processes are easily performed in the green state, while machining sharp edges resulting from the forming process becomes costly in the final sintered state.

2.06.4.5.2 White Machining

Blanks for white machining must be debindered and presintered prior to the machining process. The characteristics of white machining are slightly different from those of green machining; turning operations become more difficult, while milling is still possible with high-velocity diamond tools. If it is not carried out correctly, white machining may induce surface defects which cannot be healed during the sintering process (Song, 1997).

An example of white machining with economical relevance is the machining of zirconia blanks for dental crowns. Zirconia (3Y-TZP) blanks in the shape of blocks or disks are produced by axial or isostatic pressing and presintered to guarantee safe handling. Machining of dental crowns or bridges is then carried out based on patient-specific data sets by CAD-CAM systems respecting the sintering shrinkage (Hertlein, 2003).

2.06.4.6 Thermal Treatment

The thermal treatment of ceramic bodies includes the subprocesses debindering and sintering. During the debindering process, the organic additives are removed either by pyrolytic decomposition, evaporation or, most frequently, by combustion in air. In the subsequent sintering step, the final compaction to a dense ceramic material is achieved.

2.06.4.6.1 Debindering

Compared to, e.g. injection-molded parts with a much higher volumetric fraction of binder, the debindering of pressed components is relatively simple, as air may diffuse into the open porosity of the green bodies. Therefore—with the exception of materials consisting of nanoscale powders like Y-TZP—the debindering process can be included as an additional step at lower heating rate into the sintering cycle of oxide-based materials without much difficulty. In case of nonoxides, the debindering becomes more complicated as the materials are sensitive to oxidation at least at high temperature. In these cases, the debindering process must be performed at low temperatures to remove the organics without damaging the powder materials. If this is impossible, a nonoxidative process must be chosen. This does, however, require special binder systems which can be completely decomposed pyrolytically or waxlike systems which can be evaporated. In some cases like sintered silicon carbide (SSiC), it is even desired to obtain some carbon residue acting as a sintering aid together with boron carbide.

Debindering furnaces operating at larger scale require powerful exhaust systems with a post combustion unit to minimize emissions and avoid pollution. The thermomechanical behavior of ceramic bodies during debindering has been studied. It was found that removal of the organic binder phase leads to a fragile intermediate which is only held together by mechanical interlocking of particles (Gupta, 2010). Final debindering temperature is therefore often set above the level necessary to remove the binder in order to be able to safely handle the debindered bodies. A correct setup of debindering to achieve high quality and turnover can be performed using kinetic models based on results of thermal analysis (differential thermal analysis (DTA) / thermogravimetry (TG)) (Kern, 2011).

2.06.4.6.2 Sintering

Sintering processes may be subdivided into pressureless and pressure-assisted processes, by the different atmospheres (air, vacuum, protective, etc.) or by the sintering mechanisms (solid-state versus liquid-phase sintering). A comprehensive summary of sintering and the mechanisms involved is given by German and Kang (German, 1996; Kang, 2005).

From an economical view, pressureless sintering is always preferred as it is relatively simple technology and requires less investment. Operating costs are also lower. In manufacturing of hard ceramics, especially of nonoxides, pressure-assisted sintering technologies are applied as the pressureless processes either yield insufficient densification or lead to an undesired coarse microstructure. In some cases, the materials become thermodynamically unstable at high temperatures and atmospheric pressure. For example, silicon nitride decomposes to the elements at high temperature. In some sintering technologies, the forming and sintering step are carried out in one operation. These technologies are the axial hot pressing (HP) and hot isostatic pressing (HIP), which are now used for decades, and the pulsed electric current-assisted (PECS) or spark plasma sintering (SPS) technologies. While these technologies lead to materials of good quality at short processing times, they are not as favorable from a manufacturing point of view. The main reasons for this are that only one or a few parts can be produced at a time and that the components must be cost-intensively final machined from the pressed blanks. HIP and gas pressure sintering may be employed as an additional postdensification cycle. Net-shape formed parts which were pressurelessly presintered to a state of closed porosity are finally compacted to full density at high pressure. These sinter HIP or sinter gas pressure sintering (GPS) cycles are capable of producing components in net-shape quality and are becoming more and more important, especially in the manufacturing of cutting tools which were previously manufactured by hot axial pressing and subsequent machining.

The performance of sintering processes can be optimized by exploiting the kinetic data derived from the analysis of dilatometry measurements. Concepts using master sintering curve have been applied to different materials systems and for pressureless as well as for pressure-assisted sintering (Guillon, 2010; Pouchly, 2010). Black box models exploiting transient dilatometry data from measurements of different heating rates, neglecting the intrinsic processes on atomic level and describing the densification by systems of differential equations (thermokinetic modeling), can lead to extremely accurate predictions of the sintering behavior (Palmero, 2011).

2.06.4.6.2.1 Pressureless Sintering

At industrial-scale pressureless sintering is carried out either in large chamber furnaces or in tunnel furnaces. In chamber furnaces, a temperature program is run over the timescale. In tunnel furnaces, a fixed temperature profile is set up. The heating, cooling and dwell are determined by the lateral transport velocity of the part through the temperature profile furnace. Contrary to laboratory equipment, production furnaces, at least if sintering is carried out in air, are often directly heated by natural gas flames. In order to save energy, most modern kilns are equipped with heat exchanger units which allow for recuperation of a part of the thermal energy. The heat evolved from the kiln in the cooling stage can thus be used in the heating process. An overview of latest developments in industrial kiln and kiln furniture technology is given by Bertels and Sonntag (Bertels, 2000; Sonntag, 2008).

2.06.4.6.2.2 Pressure-Assisted Sintering

2.06.4.6.2.2.1 Hot Pressing

HP is carried out in heated graphite dies at axial pressures up to 20–80 MPa either in protective atmospheres or in vacuum. Depending on the reactivity of the material to be processed with carbon, the molds are clad with boron nitride suspension or ceramic and graphite are separated by a thin graphite foil. Hot presses exist from laboratory scale with a mold diameter of 30–50 mm up to industrial scale with 600–1000 mm diameter. The feedstock for HP is either an additive-free powder or a tailored spray granulate. Specially in the case of graphite molds with multiple inserts, axially precompacted parts are placed in the cavities of the die. In case of binder-containing feedstocks or preforms, the pressing cycle must include a dewaxing cycle to remove the binder by evaporation or decomposition prior to heating to final temperature.

Heating of the pressing die is either performed by radiation, through direct heating by DC current over the pistons, or by induction heating. In order to stand the high pressure, the die is surrounded by a ring of either graphite or a high-strength fiber-reinforced carbon–carbon composite.

In HP of alumina, the applied load has an influence on the mobility of grain boundaries. In the case of sintering of nano-Y-TZP, the applied load reduces activation energies (Li, 2000; Roy, 1993).

2.06.4.6.2.2.2 Pulsed Electric Current-Assisted Sintering (PECS/SPS)

PECS/SPS processes are a further development of HP technology. The basics of SPS and its opportunities for densification of various materials have been summarized by Garay (Garay, 2010). SPS is a powerful tool to produce extremely fine-grained materials not accessible by other processes. The feasibility of SPS processes has been demonstrated for Si_3N_4 and SiC as well as for alumina (Guillard, 2007; Meng, 2011; Nishimura, 2007).

In SPS, the die is heated by a pulsed electric DC or AC current introduced through the upper and lower punch of the hot press. This variation of heating allows much faster heating cycles. PECS/SPS sintering can be carried out at distinctly lower temperatures and shorter dwell.

The reasons for this have been controversially discussed for more than a decade. It is accepted that the pulsed electric current accelerates the diffusion processes, so that shorter processing cycles can be achieved. As in SPS equipment, the graphite die is placed in a double-walled water-cooled recipient with no further thermal insulation and very fast cooling cycles can be performed which further increases the performance. While typical HP cycles extend over 4–6 h, SPS cycles may be performed in one-third of this time. Processing conditions set up for HP cycles require not only adaptation but also complete redesign once transferred to SPS. Critical points are the interaction between the current and the powder compact and the current distribution over the volume of the compact. While in case of nonconductive materials (e.g. oxide ceramics) the current flows predominantly over the mold, in the case of conductive materials (nonoxides) the current flows, at least partially, through the sample. Therefore, different current and temperature distributions are achieved. These inhomogeneities of temperature may lead to strong fluctuations of properties over the component volume which may in some cases not be tolerated. Recent publications have come out with much lower heating rates than originally intended with the aim of obtaining ceramics of more homogeneous quality.

The main drawback of the HP or SPS process is the impossibility to directly produce parts with narrow dimensional tolerances. This drawback can be overcome by performing alternative machining processes like laser machining or EDM, which are independent of the hardness and toughness of the work piece. The application of these novel machining processes, however, requires tailored materials.

2.06.4.6.2.2.3 Gas Pressure Sintering/HIP

Gas pressure sintering and HIP are two processes with a similar fundamental idea. A compact is densified by the assistance of pressurized gas compressing a powder body either already presintered to a state of closed porosity or clad with a gas-impermeable shell of, e.g. glass or metal.

In classical HIP, the powder is filled into a steel sheath can which is subsequently evacuated and hermetically closed. The can is then placed into the recipient and heated up to a temperature where the metal shell becomes plastic. HIP parameters include applied pressure of up to 200 MPa and sintering temperatures of up to 2000 °C. While in CIP, the medium transferring the pressure is a liquid, in HIP, a pressurized gas, in most cases argon, is used. After pressure release and cooling, the can is removed (by grit blasting, cutting or dissolution in acid) and the pressed part has to be final machined. Lower machining allowances are obtained by using green-machined compacts instead of loose powder or granulate to load the mold. HIP leads to absolutely perfect microstructures. The high final machining cost has prevented widespread usage. Sinter-HIPing has thus become a feasible method to combine net-shape manufacturing with HIP. Here the powder compact of the final geometry respecting the sinter shrinkage is presintered to a density of ∼93–95% to close the open porosity. Then HIP can be performed without requiring a pressure-transducing shell, as such a role is played by the sintering skin itself. Materials produced by sinter-HIPing are, e.g. transparent alumina for armor (Krell, 2003) or high-density SSiC (Oberacker, 2001).

Gas pressure sintering is often applied for silicon nitride ceramics. In this case, the pressurized gas not only conveys pressing forces but also keeps the silicon nitride stable against decomposition above 1700 °C. According to the mass action law, high nitrogen pressure shifts the equilibrium toward the nitride side (Mittomo, 1990).

2.06.5 Manufacturing by Plastic Forming

Plastic forming includes extrusion, CIM in all its varieties as well as less-common processes like embossing. Liquid paste-based processes like screen printing or tape casting may be classified as either plastic forming or casting processes.

Unlike clay materials with inherent plasticity, hard ceramics require plasticizing additives to obtain feedstocks with sufficient flowability to apply plastic forming processes. These additives are either thermoplastic polymers which require elevated molding temperatures or, especially in extrusion, cellulose/water-based binders which can be processed at ambient temperature. The product spectrum producible by plastic forming processes ranges from very small complex components to large tubes or rods.

2.06.5.1 Ceramic Injection Molding

CIM, also called powder injection molding (PIM), is a process adapted from powder metallurgy in which a powder plastified by a binder is injected at high pressure into a closed die. By using a closed die, the part produced has a defined geometry and narrow dimensional tolerances, qualifying CIM as a net-shape production process. The basics of CIM/PIM are discussed in detail in the textbook by German (German, 1997).

By employing segmented tools, components of high complexity (including screw threads, undercuts, etc.) can be produced. Together with these advantages in geometric freedom some technical and economical restrictions exist. Molds must be very accurately machined, highly stiff and durable to stand the high injection pressures and abrasive forces of the ceramic paste. Cost of complex high-precision molds may range from 10,000 to >100,000 €. Thus the process becomes economical only in mass production processes, which enable to distribute the investment cost to a very large number of components. Depending on the added value of the parts, this point may be reached at 500–10,000 pieces. For a lower number of pieces, it is often more cost efficient to select a pressing and green milling process. The size of injection-molded parts may range from 1 to100 mm with weights from 100 mg to a few hundred grams. As the plastification of the paste requires a high fraction of organic binders, debindering becomes a critical issue especially at high wall thickness. Microstructural quality of CIM components seldom reaches the level of CIP components, due to process-intrinsic restrictions. The transient mold filling process may cause flow textures (Gadow, Fischer, & Lischka, 2005). Weld lines or abruptly changing cross-sections are critical points with reduced strength (Kern, 2010). Thus, the mold design is a crucial point to obtain CIM components of high quality. In plastics processing, mold filling simulations have become standard tools to solve this problem. Due to the complex thermorheological behavior of the two-component feedstocks, in CIM, simulation tools are still unavailable.

2.06.5.1.1 Compounding of CIM Feedstocks

CIM feedstocks require features which are in some aspects contradictory. The typical set of requirements includes (German, 1990):

- high solid loading
- good flowability/adjusted rheological properties
- high homogeneity
- good wetting of powder
- nonsticking to mold
- broad softening temperature interval
- low wear of mold
- economical cost

As the powder surfaces must be completely covered with binder and the sliding of the grains during the deformation of the paste must be possible at not too high shear forces, the total binder content in injection molding pastes is very high compared to that in pressing or casting feedstocks. Depending on the size, morphology and size distribution of the powder used, volumetric binder fractions range from 40% to 60%. As this leads to low inherent green density, a maximized solid load is very beneficial to reduce shrinkage and deformation during sintering. On the other hand, too high solid loading yields unfavorable rheological properties which would imply high injection pressures, high wear and injection-related shear cracks in the paste. This general problem can be attenuated by a proper selection of additives, although the production of a performing injection molding feedstock is always a compromise between solid load and viscosity.

Powder morphology has a strong influence on the performance of CIM feedstocks (Mannschatz, 2011). The word binder is used as a generic term for all the organic additives in the feedstock. It envelops among others the binder as such, plasticizers, surfactants as well as defoaming and release agents. The binders used are commonly waxes, paraffins or organic polymers. Special binder formulations may include soluble components such as polyethylene glycol (PEG) which can be solvent debindered prior to thermal debindering. A special group of binders based on polyoxymethylene (POM) are used to optimize green strength, allowing for manufacturing of thick-walled components. These POM-based systems are not thermally decomposed as the conventional ones but are monomerized to formaldehyde using acid catalysts (Stringari, 2011). A variety of feasible binder systems have been shown in the literature (Hanemann, 2011; Hausnerova, 2011; Zhang, 2005).

The compounding process itself must be very intensive to obtain a homogeneous feedstock in which all the grains are uniformly covered with the binder and powder agglomerations are absent. Homogeneous feedstocks are more complicated to obtain as the starting powder gets finer. Intragranular forces increase with the specific surface area. Thus, very fine grained powders in the submicrometer range require very high energy input. This cannot be achieved by standard mixers like sigma blade kneaders. Rather it requires machines like twin screw extruders or shear rollers which are capable of introducing high shear forces (Kern, 2010).

The rheological characteristics of the feedstocks must be shear thinning, so that at high shear forces (e.g. in the nozzle, in the gate or in thin channels in the mold), a lowered viscosity is obtained. Well-adjusted rheological characteristics are required to completely fill complex and narrow cavities. Measurement of rheological properties is commonly carried out in capillary rheometers. The measurement must cover the temperature range between the softening point of the paste and the plastification/injection temperature (Kern, 2009).

Besides the discussed thermoplastic feedstocks, it is possible to process thermosetting pastes. Here the binder is a resin which is polymerized by injection into a hot mold. The process has some relevance in manufacturing carbon components but is not applied for manufacturing of hard ceramics. The same is true for injection molding using moist clay materials which have sufficient self-plasticity to be molded without additives.

2.06.5.1.2 Injection Molding

Injection molding of ceramic feedstocks can basically be performed on standard machines for plastics processing. Electrically driven machines with high metering accuracy have become available recently. Computer-controlled hydraulic machines are still state of the art. The machines are gradually modified to meet the demands of the CIM process. Screws for CIM processing are usually hard chromium plated or coated with cemented carbides (e.g. WC/Co), to be able to stand the abrasive force of the ceramic pastes. The flank lead of the screws must be modified as the rheological properties of the high solid-loaded pastes are different. Plastifying the highly viscous ceramic feedstocks with standard screws for polymer processing leads to overheating of the paste in the plastification units during continuous operation. Screw geometries designed for metal injection molding are generally also well suited for CIM.

The newest developments in injection molding are production of microparts, high-precision molding, nonisothermal mold temperatures and special mold, gate and sprue geometries. Moreover, some progress toward mold filling simulation has been made (Moritz, 2010; Muller, 2010). An additional field may arise from joining different material systems during the forming stage by two-component-injection molding (Ruh, 2011).

In CIM, some specific features which are not common in injection molding of polymers must be respected. The rheological properties of the CIM feedstock strongly have to be considered in mold design. Flow paths in CIM must be shorter than in plastics processing to assure good mold filling. The paste should arrive at the cavity as hot as possible, therefore new gate systems were developed with either hot channel injection systems or nozzles diving deep into the mold to shorten the sprue runner. The mold may be evacuated prior to injection to avoid trapping of compressed air in corners. Dimensioning, positioning and shaping of the gate(s) is an essential point in CIM mold design. Due to the high viscosity of CIM pastes, jetting occurs if the paste is injected too fast through a too narrow gate. Moreover, high deformation speed can cause binder segregation and thus structural inhomogeneity or porosity in the sintered part. The ratio between component and gate diameters must be smaller than in plastics processing. In case of larger or very complex parts, if the mold has to be filled through more than one gate, weld lines inevitably occur. This is also the case for components with holes or some other unfavorable geometric conditions. Contrary to plastics manufacturing, weld lines do not heal out at a certain distance from their origin. The interdiffusion of the two subcurrents at the weld line is too weak to form a strong connection, especially at a larger distance to the gate. Thus, weld lines are weak links in CIM parts which may reduce the inherent material strength to about half values. Weld lines should thus be avoided. If this is not possible, they should be placed in regions of the components which do not bear maximum stress. As the mold filling is a transient fluid dynamic process, information on how mold filling takes place is valuable to improve mold design and process parameters. The easiest way to determine mold filling behavior is to carry out filling studies with increasing shot volume. It has to be considered that in case of noncubic powders, the flow texture also induces a crystallographic texture in the final component. Powders like alumina or SiC, no matter whether they are produced by milling or by precipitation, are nonspherical. Elongated shapes follow growth or cleavage planes. In the fluid flow, the particles orient in such a way as to reduce the flow resistance. The effect is comparable to the effect occurring in injection molding of birefringent polymers. This anisotropic orientation is amplified during sintering. Anisotropy applies not only to optical but also to mechanical properties. To determine the crystallographic anisotropy in the final sintered part, polarized light texture analysis carried out on thin sections of coarse-grained alumina samples produced with the specific mold geometry can be carried out.

The mold filling process is shown in Figure 5. First, the mold is closed and the nozzle is inserted into the sprue. Then the plastified paste is injected into the mold. This condition is held until the paste is solidified in the mold while a packing pressure is maintained until the sprue freezes off (the back flow of the paste is inhibited by a closed nonreturn valve). The screw is now pushed back and by rotation the feedstock is drawn in from the feed hopper. The feedstock is finally plastified in the multistage heated barrel until the melt cushion is rebuilt. After the mold is opened and the part is ejected, the cycle starts again.

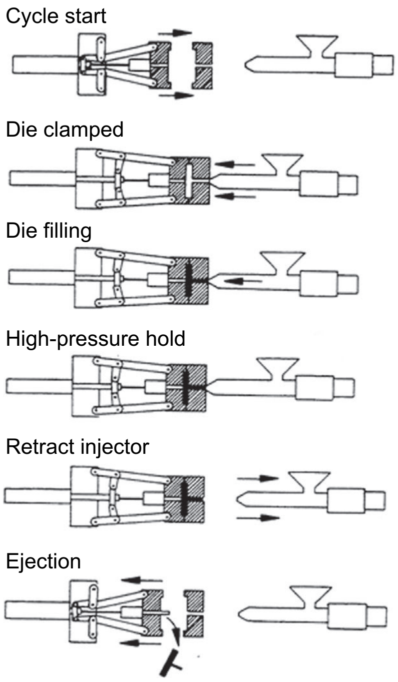

Figure 5 Injection molding cycle. German (1997).

The typical processing parameters in CIM are plastification temperatures of 100–200 °C, mold temperatures of 20–100 °C and molding pressures of 40–200 MPa. Injection speed depends on the machine and gate geometry and may vary between 5 and 100 cm^3; s^{-1}. As a general rule, molding pressures $<$100 MPa should be pursued. Moderate molding pressures and injection speeds are beneficial to the lifetime of the mold. CIM molds may need refurbishing after an average of 1000–20,000 shots depending on the abrasive properties of materials processed, paste properties and operating conditions.

Quality control is also an important issue in CIM. It may range from online control of machine parameters to testing the weight of molded parts (Walcher, 2010). A method applicable during process development and nondestructive testing is to detect internal flaws through computer tomography of manufactured specimens (Heldele, 2006).

2.06.5.2 Thermal Treatment

2.06.5.2.1 Debindering

As mentioned before, the binder fraction added to the feedstocks is extremely high. This binder content must be removed before sintering without causing damage by bloating or cracking. Moreover, contrary to pressed or cast components, the green bodies of CIM parts are nonporous. Thermal debindering is thus a very critical step in the CIM processing chain. It is commonly accepted that during the heat treatment the binder is incinerated or evaporated at the outer surface of the part. Then, as the debindering is carried out above the melting point of the thermoplastic binder, new binder is transported to the surface of the part by pore diffusion (German, 1997). This process takes place until all the pores are empty. It is evident that overheating of the component will lead to buildup of gas pressure in the part from either evaporated species or cracking products. This would inevitably lead to damaged parts. Purely thermal debindering processes needs thus to be carried out very slowly, in some cases extending over more than a week.

Powder and binder have different thermophysical properties. Thus residual stresses are built up during the solidification and cooling of the powder–binder mixture in the mold (Zotelief, 1996). Stress levels may reach the 10–130 MPa level which is in the range of the green strength. If these stresses are abruptly released during debindering, microscopic or even macroscopic cracking of the white bodies may occur.

New binder concepts have been developed to overcome this problem (see Section 2.06.5.1.1). A binder with a water-soluble fraction may be solvent debindered prior to thermal debindering. In an open porosity scenario, oxygen has access to the inner porosity so that bloating is efficiently suppressed. Using these two-component systems thus allows for higher heating rates and shorter and more economical debindering cycles. The second concept is based on a polymeric binder which is monomerized catalytically. POM binder can be monomerized to formaldehyde using vaporized acid catalysts. Besides polyoxymethylene (POM's) inherent very high green strength, this concept enables producing CIM green bodies of high wall thickness. During the debindering, the reaction front runs straight through the part without causing bloating problem (Krug, 2002). The disadvantages of the catalytic debindering process are: Enhanced safety precautions required due to the acid vapors involved, the requirement to purchase special furnace equipment including a combustion device for the furnace exhaust gases (formaldehyde and acid vapor).

In order to shorten process cycles, thermal debindering processes can be modeled and temperature time programs set up on the basis of thermogravimetry and differential thermoanalysis results (Kern, 2011).

2.06.5.2.2 Sintering

Sintering of CIM components is carried out in analogy to sintering of pressed or cast parts. However, there are some process specific peculiarities which must be respected. The green density of CIM parts is inevitably lower than that of high-quality pressed or cast parts. Moreover, unless perfectly carried out, a lower homogeneity must be considered. Sintering of ceramics produced by CIM thus requires slightly higher temperatures and may lead to slightly coarser microstructures. Flow-induced textures and density inhomogeneities may cause nonisotropic shrinkage and warping. In this case, the processing cycle—not only the sintering stage—has to be critically studied, and in the worst case, the design of the mold has to be revised.

2.06.5.3 Low-Pressure Injection Molding

Low-pressure ceramic injection molding or "hot-molding" (LP-CIM) is a variation of injection molding in which a very flowable feedstock based on wax or paraffin binder is employed which can be cast into a mold at much lower pressures (<20 MPa) (Lenk, 1995; Novak, 2004). Due to the lower pressures, the mold can be made from plastics or silicone, which drastically reduces the investment costs. The machines do, however, not allow the same extent of automatization as high-pressure CIM. Thus, the low-pressure process is well suited to produce prototypes or smaller series of components.

As the binder systems are mechanically less stable than in the case of conventional CIM, very often, debindering is carried out in a powder bed to prevent disintegration of the components. Microstructural quality is in most cases comparable or lower than in CIM. LP-CIM-processed materials are, e.g. alumina, zirconia and silicon carbide.

2.06.6 Manufacturing by Casting Processes

Casting processes cover all processing cycles which employ liquid dispersions, including slip casting and pressure slip casting, and also tape casting and screen printing. Dispersions are also the basis for granulated powders produced by spray drying. The liquid dispersions for these processes require tailored solid contents and rheological features to meet requirements of the forming processes.

2.06.6.1 Slip Casting and Pressure Slip Casting

Slip casting is commonly carried out with aqueous suspensions also called dispersions, slips or slurries. Criteria for good casting slips are low viscosity, high solid content, high homogeneity, absence of agglomerates and storage stability. Achieving these desired requirements is a matter of processing technology like mixing, milling and deairing and suitable additives such as surfactants, plasticizers and binders. The basics of colloid chemistry are well presented in the textbooks by Hunter and Russell (Hunter, 1989; Russel, 1989).

All ceramic powders, either oxides or nonoxides, contain an oxide shell with acidic or basic oxygen functionalities which interact with the solvent. In order to obtain a stable colloid, the individual particles have to be kept apart either by repulsive electrostatic forces, by adsorbed organic molecules or by combining both options (**Figure 6**) (Lu, 2006; Rajaiah, 1994). The principle of electrostatic stabilization is shown in **Figure 7**. Extremely small particles require high energy for perfect dispersion and proper surfactants to prevent recoagulation (Muller, 2004).

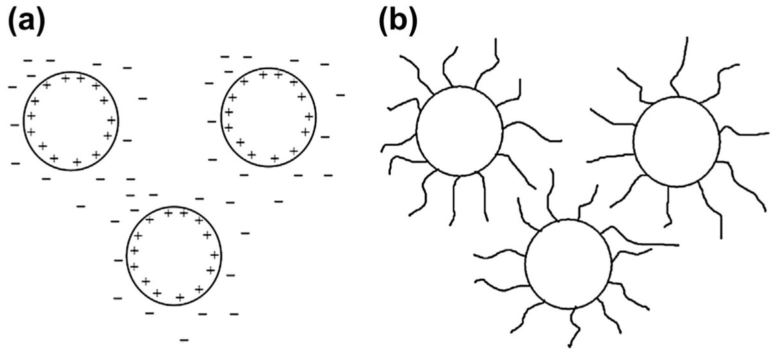

Figure 6 Schematic drawing of electrostatic stabilization (a) and steric stabilization (b).

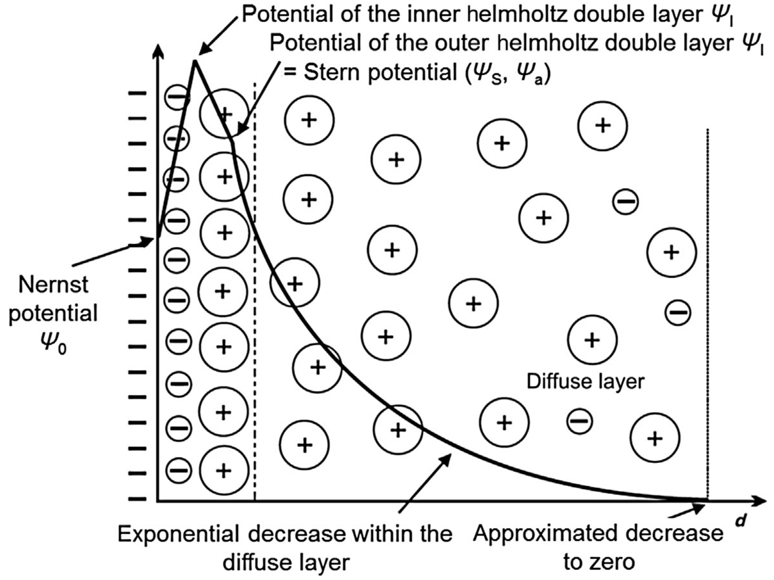

Figure 7 Characteristic of the potential within the layer model. Müller (1996).

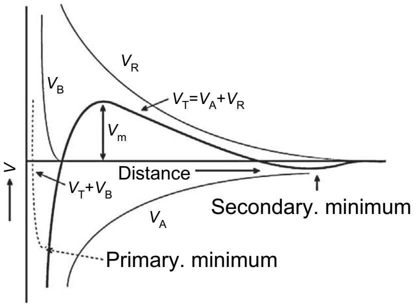

Figure 8 Characteristic of the interaction between the electrostatic repulsion (V_R), the van der Waals attraction (V_A) and Born's repulsion (V_B). Müller (1996).

Such a stabilized suspension can be destabilized by partial removal of the solvent. The particles then come closer to each other and once the interparticle forces change from repulsive to attractive, the particles begin to coagulate (Figure 8). This is basically the working principle of slip casting which is not a classical filtration process although the deposition speed of the process, like filtration, follows a parabolic kinetic (thickness $\sim \sqrt{t}$) (Figure 9).

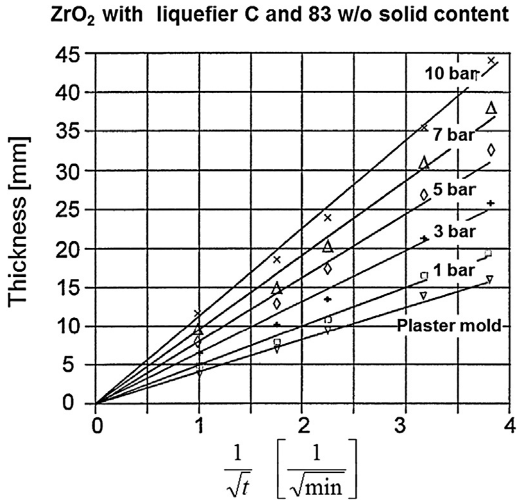

Figure 9 Body thickness dependent on time and pressure. Heinrich (2004).

After the slip is poured into the mold, water is drained by capillary forces into the open porosity of the mold. This process can be accelerated by pressure. As the dispersion in contact with the mold loses a part of the solvent, the stability of the dispersion breaks down and a layer—the ceramic green body—starts to form. As the attractive forces lead to a very close packing, cast green bodies are very dense and homogeneous because the process is carried out without external force. The individual particles even rotate during the green body formation in order to maximize attractive forces. Green density of cast green bodies is comparable to that of parts manufactured by axial pressing.

2.06.6.1.1 Slip Casting in Plaster Molds

Slip casting using plaster molds is a very versatile process to manufacture components of medium or large size. In slip casting lot sizes may vary from small numbers of customized parts of structural ceramics to mass production as in manufacturing of sanitary ware or tableware. Molds may be composed of several parts linked together by locking systems. The process thus requires little investment and is extremely flexible. Slip casting using plaster molds is a very versatile process for manufacturing of small- and medium-sized lots of components of medium to large size. Manufacturing of plaster molds is fast and rather inexpensive. By blending different types of plaster powder and choosing defined plaster/water ratios, the fraction of porosity and the pore size distribution of the plaster mold can be adjusted.

The principle of slip casting is not a simple filtration process but rather a controlled destabilization of a ceramic dispersion. The stable ceramic suspension is poured into a dry porous mold of plaster. The porous plaster soaks a part of the solvent contained in the suspension. Thus the solid content of the dispersion in contact with the interface increases and a ceramic body is deposited. As deposition proceeds, this interface migrates into the space formerly occupied by the slurry. Microscopically, the ceramic particles in the dispersion are kept apart by electrostatic forces or by polymers, which form an energy barrier against the coagulation of the particles. Once a part of the solvent is removed, the interparticle spacing is reduced, and as the distance is less than the distance of the energy barrier, attractive forces become dominant. This effect leads to a very dense and homogeneous packing of particles comparable to that in pressed parts. If proper measures are taken to produce agglomerate and gas-free dispersions, green bodies of high perfection can be obtained. Macroscopically, the casting process follows a parabolic time law similar to a pressure filtration; thus, very thick layers require long processing times, especially if very fine powders are used.

Casting is most frequently carried out as hollow casting. In this case, the process is stopped once a certain layer thickness is obtained, yielding a body with a defined outer geometry with some uncertainty in the wall thickness. Full bodies or bodies with an inner core may be cast by pouring dispersion until the complete mold is filled. However, there is always a contraction cavity in the middle of the part. After the completion of the casting process, the mold is turned around, the superfluous dispersion is drained and it can be recycled. The part is then left in the mold to predry to a semihard state. During this process, a shrinkage of ~0.25–1 vol.% occurs. In the semihard state, the body still contains some moisture. Due to the slight shrinkage, the ejection of the parts from the mold is facilitated. Depending on the geometries of the parts, the bodies may be simply drawn out of the mold containing a low inclination angle of 0°–2° (tubes, crucibles) or the molds are opened and the part is removed. Removal can be facilitated by flushing with compressed air from the back side through the porosity of the mold.

2.06.6.1.2 Pressure Slip Casting

Like in filtration, the pressurizing of the dispersion accelerates the formation of the green body (Salomoni, 2000). Pressure slip casting is often used in the production of sanitary ware (Waters, 2005). Recently, production of refractories was also reported (Klippel, 2011). Publications on the use of this processing method for advanced structural ceramics are relatively rare, although the feasibility of the process for nanoscale SiC and neodymium:yttrium-aluminum-garnet has been demonstrated (Kopylov, 2009; Matsunaga, 2010).

Molds must, however, be able to bear this additional load, so the first pressure slip casting processes were carried out in plaster molds reinforced with steel frames. This allowed for increasing the pressures to <10 bar. Higher pressures became possible by shifting from the traditional plaster molds to mold produced from sintered polymers like poly(methyl methacrylate).

Automatic pressure casting machines were developed in the 1970s, and since then have started to replace conventional slip casting in mass production of products like sanitary ware. From a manufacturing point of view, the pressure slip casting process using polymer molds has several decisive advantages. The polymer molds are mechanically durable. The porosity can be cleaned by backflushing with water so that no binder deposits are built up which clog the porosity with time. A manufacturing process can be run with a single mold which does not require drying. Changes in products are easily performed by changing the mold and reprogramming the machine and handling systems without the requirement to manufacture a multitude of plaster molds. However, the process requires higher investment in equipment compared to conventional slip casting.

Like in injection molding machines, the polymer molds which can be very complex and segmented are clamped in steel frames. Due to the structural integrity requirements of the polymer molds, high wall thickness of the polymers is required. In order to speed up the drainage of the water during the green body formation, draining channels are included into the mold. The process cycle can be divided into three stages: backflushing and closing of the mold, filling of the mold with ceramic dispersion and buildup of pressure for a defined time; and reducing the pressure, opening of the mold, and final ejection of the part.

Machine control units are programmable from memory. The removal of the parts and piling on the conveyor systems is done with robots or handling systems, especially for large-format components. In manufacturing of hard ceramics, the technology to date is scarcely used.

2.06.6.2 Gel Casting

As mentioned, colloidal techniques allow producing green bodies of high structural homogeneity. It is even more beneficial if the consolidation of the green bodies from a suspension is carried out without an external force that may induce anisotropy of the body (like in slip casting). In gel casting, a colloidal suspension is coagulated to obtain a rigid green body. Coagulation can be achieved by different mechanisms: polymerization of organic additives or shift in pH value resulting in destabilization of the ceramic suspension, among others. By gelation in a suitable mold of metal or plastics, green bodies can be produced in near-net-shape quality provided that the resulting gel has sufficient stability.

The preparation of the gel casting suspensions is basically carried out in analogy to dispersions for slip casting. High homogeneity is achieved by mixing with additives and milling.

Polymerization of organic additives may be induced catalytically or thermally. Cooled alumina dispersions stabilized at pH 3–4, containing a small percent of acrylic acid and N,N-methylenebisacrylamide, can be polymerized in nitrogen atmosphere by addition of peroxides and increase in temperature (Krell, 2003). Other binder systems based on polyvinyl alcohol (PVA) have also been proposed (Chabert, 2008).

Gel casting is one of the most effective methods to produce extremely defect-free green bodies (Krell, 1996). Direct coagulation casting works on a different basis. For instance, an alumina slurry with high solid content, electrostatically stabilized at acidic pH, is blended with a sufficient amount of urea which on addition of urease is enzymatically decomposed to carbon dioxide and ammonia. Ammonia shifts the pH toward the isoelectric point so that the suspension is coagulated (Baader, 1996).

While the wet green bodies have considerable strength, it is not trivial to dry these blocks in such a way to avoid warping and cracking. Gel-cast green bodies seldom exceed a green density of 50 vol.%, as the interparticle space contains large amounts of solvent/organics. As particles tend to reorient during the drying process, considerable stresses are built up which may lead to cracking of the bodies. Conventional drying must be carried out under extreme care in atmosphere with exact control of moisture and temperature. Green bodies must be placed on support plates allowing for sliding of the parts which shrink considerably during the drying process. Other concepts have made use of the osmotic principle. Wet green parts are transferred into a concentrated solution of, e.g. PEG. While the water is diffusing out, the PEG is diffusing into the green body resulting in stable parts which can then be conventionally dried, debindered and sintered (Trunec, 2011).

2.06.6.3 Tape Casting

Tape casting is very common for fabricating layered structures of functional ceramics. However, it is not often applied in manufacturing of structural hard ceramics. A good review on tape casting of ceramics was given by Hotza and Greil (Hotza, 1995).

The principle is now described briefly. First, a ceramic dispersion containing a high amount of binder and plasticizers is compounded. This suspension contained in a storage container is then continuously spread on a moving plastic conveyor belt with a doctor blade. The suspension is subsequently dried in a tunnel furnace and the resulting ceramic tape can be rolled up to be stored. From this stock, parts may be cut or punched. Stacks of these parts are then laminated under pressure, debindered and fired. All the functionalities required in the manufacturing process can be achieved only by a very proper recipe of the tape casting suspension. The solvent used is often nonaqueous to facilitate and speed up the drying process, and its rheological properties must be shear thinning so that the viscosity is low at high shear rates (to be able to spread the suspension on the substrate) and high at low shear rates (so that the suspension layer stays in shape). The organic content is much higher than in slip casting, as the flexibility of the tape and the integrity during the cutting or punching process must be tailored by using an appropriate mixture of binders and plasticizers.

2.06.7 Final Machining

Compared to machining of metals, hard machining of ceramics is much more complicated and requires special machinery with high stiffness to be able to accurately machine ceramic components. The type and quality of machining procedures strongly affects the mechanical properties of the machined ceramic part (Yondem, 2011).

Classical final machining is performed with high-speed diamond tools. Standard processes which can be carried out are grinding, honing, lapping and polishing. All these machining processes work with undetermined cutting edge and are capable to tool planar geometries and obtain surfaces with defined surface quality. Complicated geometries and sharp edges are difficult to obtain. The situation has improved since multiaxis ultrasonic grinding and milling with diamond tools is available which allows for producing complex shapes with a very high freedom of geometry (Zhao, 2008). Here, even inner contours can be produced which were previously inaccessible. Still very sharp radii and high aspect ratios cannot be produced.

New nonconventional machining processes like EDM (die sinking, wire cutting and milling) and laser machining have broadened the spectrum of ceramic component geometries accessible by hard machining. EDM machining requires electrically conductive materials (Luis, 2007). Traditionally, conductive materials like boron carbide, reaction bonded silicon infiltrated silicon carbide (SiSiC) and alumina/TiC with a narrow range of application were machined by EDM. Recently, new materials with oxide matrix (Y-TZP/WC or ZTA-TiC) and nonoxide basis (Si_3N_4/TiN, SiC/TiB_2) were developed which offer special features like higher hardness, toughness and bending strength. With these new materials it becomes possible to produce, e.g. abrasion-resistant tools or mold inserts with a high economic potential in mechanical engineering. **Figure 10** shows an image of recently developed ZTA-TiC composite material precision machined by wire-EDM (Landfried, 2011).

Laser machining has also become a state-of-the-art process for some special applications (Samant, 2009). In manufacturing of cubic boron nitride (CBN) cutting tools, the clamping trays are machined by lasers as conventional machining of the ultrahard substrate would be too costly. Laser cutting and laser drilling of ceramics have been successfully demonstrated. Nonoxides possess good laser machinability due to the following reasons: high thermal conductivity reduces thermoshock-induced cracking, nonoxides have a high absorption coefficient for the laser light and some nonoxides decompose instead of melting. This provides clean cutting planes or bore holes. As the processes are costly and as the total energy transferable to the work piece is limited, laser machining is only carried out where either only small quantities of materials have to be removed or other conventional processes are not applicable or uneconomical.

Figure 10 Wire-EDM machined ceramic components (Dimacer®) (Konstruktion, VDI).

2.06.8 Case Studies

Nowadays, hard ceramic materials are indispensable for applications deployed in extreme conditions of wear or high temperature. Hard ceramics can withstand such harsh environments due to their outstanding mechanical properties. However, the manufacturing of complex shape components is very challenging, because materials can be machined with diamond only. Thus, processing techniques of components must be selected carefully in order to produce hard ceramic parts with accepted cost–performance ratio.

2.06.8.1 Ceramic Injection Molding

CIM offers the ability of producing complex three-dimensional components for mass production. If mold design, feedstocks, processing parameters and the postprocessing of green parts are completely controlled, parts with extremely narrow tolerances can be produced without applying other finishing technologies. However, each processing step of the injection molding process is highly sophisticated.

As shown in detail in Section 2.06.5.1.2, the processing cycle of CIM is more complex than for most other forming and shaping technologies. The advantage of CIM is its capability of producing parts with complex shapes in one step in net-shape quality. **Figure 11** shows the size and complexity range covered by CIM.

The large parts are made from alumina and have a dimension of ~6 × 6 × 6 cm at a wall thickness of a few millimeters. The component has an extremely complex geometry (screw threads, undercuts, and high aspect

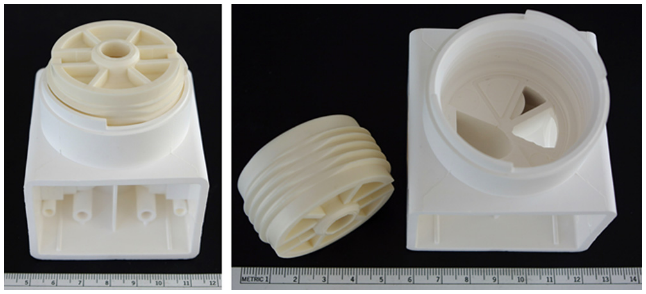

Figure 11 Alumina part for fluid technology (130 mm^3) (OxiMaTec GmbH).

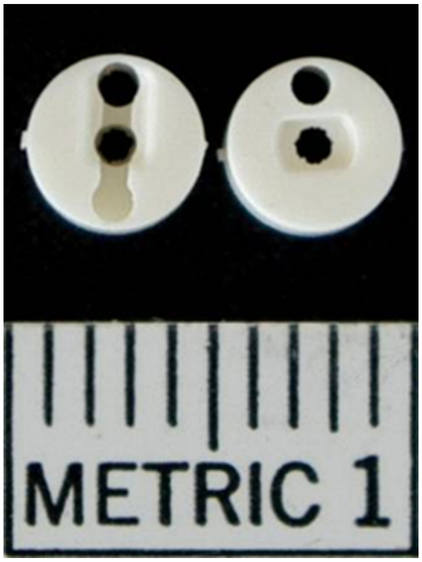

Figure 12 High-precision part of platelet-reinforced zirconia (OxiMaTec GmbH).

ratios). In case of this large part, which is not produced in extremely large lot sizes, the feasibility aspect plays the main role in selection of CIM. Producing such a complex shape in one piece from a cold isostatic pressed block would be extremely complicated if not impossible, the milling procedure being extremely time consuming. It would be required to change the clamping of the part several times and the delicate structure would be prone to chipping during the clamping or milling process. Furthermore, clamping in different positions always leads to higher dimensional tolerances. In this case, a lot size of a few hundred parts will be sufficient to justify an investment of some € 20,000 for a mold.

The precision parts displayed in Figure 12 are more typical for CIM components. They are small, complex-shaped parts of sophisticated structure with three levels in the front and two levels at the back side. The surface quality required is high. The material is platelet-reinforced zirconia (Y-TZP). A solution by pressing of blanks and milling would be possible but not economical at larger lot sizes. Here the cost of the mold will be moderate and justified at a lot size of approximately >1000 parts; a manifold tool insert would further boost performance of the CIM process.

2.06.8.2 Axial Pressing

Axial pressing of ceramics is one of the most frequently used manufacturing technologies for industrial applications. Production costs are relatively low when simple geometries without undercuts or semifinished products for further machining are desired.

2.06.8.2.1 Ballistic Armor

The armor ceramics shown in Figure 13 are among the simplest shapes possible in ceramics manufacturing. However, their fabrication is by no means trivial.

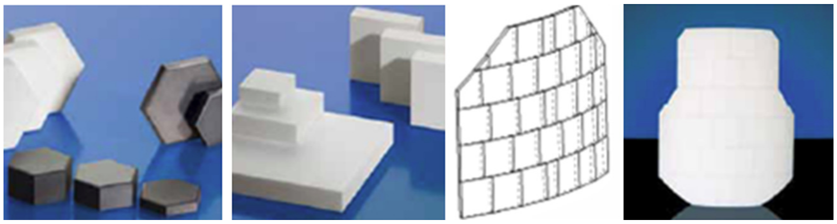

Figure 13 Armor tiles for protection of aircraft and automotive (CeramTec GmbH/Etec GmbH).

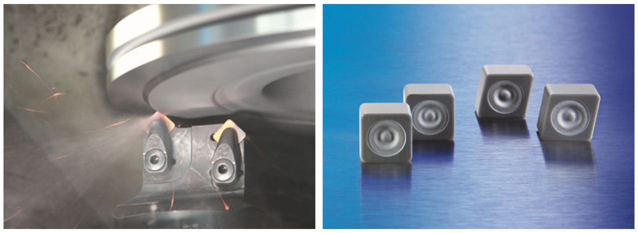

Figure 14 Cutting inserts (CeramTec GmbH).

Such plates of uniform thickness are typically made by axial pressing to shape. In case of the alumina and silicon carbide hexagons, the bevel may be formed during the shaping process or by subsequent grinding. Parts must be perfectly flat and within narrow dimensional tolerances to reduce machining effort. They also must be completely dense, as internal porosity would reduce hardness, stiffness and ballistic performance. Inhomogeneous green density from the surface to the center of the pressed part would cause warping or inhomogeneous density after sintering. Thus, the requirements to the quality of the pressed green bodies are high. To eliminate residual porosity, such materials are frequently post-HIPed after conventional sintering. Other manufacturing processes may also be applied but will not be economically competitive to mass production by axial pressing.

2.06.8.2.2 Cutting Tools

A second typical example for axial pressing is the manufacturing of cutting tools for machining of metals like gray cast iron for automotive brake disks (Figure 14). These tools are mass produced in millions of pieces in various geometries and from different hard materials. Cutting tools are usually cuboids or tetragonal prisms with a defined bevel. Today the spanning of these parts is facilitated by introducing a pit for the defined mounting of the tool in the holder. The pit is either formed during the pressing process or in some special cases (CBN tools) are made by laser machining. Pressing proceeds in automatic axial presses at up to 5–10 cycles per minute. After the pressing process, the tools are either pressurelessly sintered (e.g. alumina or ZTA) or gas pressure sintered (alumina/TiCN, Si_3N_4/TiN). Until recently HP in divided molds was also frequently used, obtaining excellent performance in application but with a certain tradeoff in manufacturing cost. As-fired components are machined by lapping to obtain coplanar top and down sides. Sides and bevels are machined by fine grinding in fully automatized machine units. Despite the fact that the geometry of the parts is very simple, a net-shape forming method is applied and machining is reduced to the minimum. The largest proportion of manufacturing cost is still spent on final machining.

2.06.8.3 CIP + Green Machining

Structural ceramic parts of highest strength and reliability are required for biomedical implants such as knee and hip prostheses (Figure 15). In the case of the knee, the shapes are complex, whereas for the hip joint, shapes are relatively simple. In order to obtain the highest possible level of structural perfection, blanks are produced by CIP. Pressing tools layout is such to come as close as possible to the final geometry. Some details like the mortise to place the ball on the titanium stem do require green machining. In the case of the knee, the whole contour has to be green machined from a blank. This requires not only extreme precision of the free form milling process but also excellent green stability and defined green density of the preformed blank. After pressureless presintering to closed porosity, the parts are post-HIPed not only to further boost strength but also to achieve 100% density, as

Figure 15 Ceramic hip and knee joint prosthesis components (CeramTec GmbH).

residual porosity increases the danger of low temperature degradation and inflammations of tissue in contact with the implant. High regulatory demand makes sophisticated quality control of the parts indispensable. Parts taken from the production line are extensively tested. Each component produced is labeled with a laser to ensure traceability.

2.06.9 Summary, Remarks, and Future Aspects

Hard ceramics today are used in a multitude of different applications with very specific requirements and performance. Such requirements may be high hardness, strength, wear resistance, high temperature and chemical resistance or even biocompatibility, and low temperature degradation resistance of medical devices.

Many publications have emphasized the material science aspects in the field. The manufacturing aspect is equally important to achieve the ability to economically produce performing hard ceramic components of high quality. The term quality here means to reach the demands of the set of requirements at a high level of precision, reliability and reproducibility.

As some ceramic components such as wear parts and cutting tools have become commodities, the economic aspect of manufacturing is becoming increasingly important. Near-net-shape forming strategies can contribute to reduce production cost. Low dimensional tolerances are the key to omit or reduce the final grinding or machining operations which are the dominant cost factor in hard ceramics production. The choice of an appropriate manufacturing route is governed by technical and economical considerations. A performing manufacturing process requires control over all stages of the processing chain. The typical hard ceramic materials have limited toughness. Processing- or machining-related defects must therefore be avoided in any case.

Today, pressing technologies have become the dominant forming and shaping technologies for hard ceramics with a low or moderate level of shape complexity. Pressing is fast and relatively simple; the low additive content of the pressed parts facilitates debindering and sintering. Parts of high complexity can be made by injection molding. The high degree of geometric freedom of the CIM process is, however, coupled with a more complex chemical and/or thermal treatment procedure.

CIP and milling processes are restricted to customized parts in small lot sizes.

Pressureless sintering of net-shape formed components is the economically most performing sintering process; in many cases, high-performance ceramics requiring full density and small grain size are postdensified by sinter-HIP or gas pressure sintering processes.

Pressure-assisted forming and sintering processes like HP, SPS sintering or HIP are only used in few high and/or niche applications and only if other processes are not applicable.

References

Baader, F. H. (1996). Direct coagulation casting – a new green shape technique.2. Application to alumina. *Industrial Ceramics, 16*(1), 46–80.

Bertels, F. (2000). Industrial kilns for advanced ceramics – modern applications. *Ceramic Forum International, 77*(10), E20.

Birkby, I. (1994). Factors affecting the machinability of fine ceramic powder compacts. *British Ceramic Transactions, 93*(5), 183.

Boyer, C. B. (1974). Equipment for cold isostatic pressing. *Mechanical Engineering, 96*(9), 60.

Carneim, R. D., & Messing, G. L. (2001). Response of granular powders to uniaxial loading and unloading. *Powder Technology, 115*, 131–138.

Chabert, F. (2008). Cross-linked polyvinyl alcohol as a binder for gelcasting and green machining. *Journal of the American Ceramic Society, 91*(10), 3138–3146.

Cook, E. M., & DuMont, H. D. (1991). *Process drying practice.* McGraw-Hill, Inc. ISBN 0070124620.

Dhara, S. (2005). Green machining to net shape alumina ceramics prepared using different processing routes. *International Journal of Applied Ceramic Technology, 2*(3), 262–270.

Eksi, A. K. (2004). Hardness and densification behaviour of cold isostatically pressed powders. *Metallurgica, 58*(10), 633–636.

Falgon, D. (2005). Identification procedure of a hardening law for powder compaction. *Powder Technology, 157*, 183–190.

Gadow, R., Fischer, R., & Lischka, M. (2005). Computer assisted colorimetric optical texture analysis for CIM components. *International Journal of Applied Ceramic Technology, 2*(4), 271–277.

Garay, J. E. (2010). Current-activated, pressure-assisted densification of materials. *Annual Review of Materials Research, 40*(1), 445–468.

German, R. E. (1997). *Injection molding of metals and ceramics.* Metal Powder Industry. ISBN-13: 978-1878954619.

German, R. M. (1990). *Powder injection molding.* Metal Powder Industries Fereration. ISBN: 0-918404-95-9.

German, R. M. (1996). *Sintering theory and practice.* John Wiley & Sons, Inc. ISBN 0-471-05786-X. 3.

Gu, Y. (2006). Visualizing isostatic pressing of ceramic powders using finite element analysis. *Journal of the European Ceramic Society, 26*, 2265–2272.

Guillard, F. (2007). Densitication of SiC by SPS-effects of time, temperature and pressure. *Journal of the European Ceramic Society, 27*(7), 2725–2728.

Guillon, O. (2010). Master sintering curve applied to the Field-Assisted Sintering Technique. *Journal of Materials Science, 45*(19), 5191–5195.

Gupta, S. (2010). Thermomechanical behavior of ceramic green bodies during presintering. *Journal of the American Ceramic Society, 93*(9), 2611–2616.

Hanemann, T. (2011). New methacrylate-based feedstock systems for micro powder injection moulding. *Microsystem Technologies, 17*(3), 451–457.

Hausnerova, B. (2011). Optimization of powder injection molding of feedstock based on aluminum oxide and multicomponent water-soluble polymer binder. *Polymer Engineering and Science, 51*(7), 1376–1382.

Heinrich, J. G. (2004). *Einführung in die Grundlagen der keramischen Formgebung*. Baden-Baden: Göller-Verlag.

Heldele, R. (2006). X-ray tomography of powder injection moulded micro parts using synchrotron radiation. *Nuclear Instruments and Methods in Physics Research B, 246*, 211–216.

Hertlein, G. (2003). Milling time vs. marginal fit of CAD/CAM-manufactured zirconia restorations. *Journal of Dental Research, 82*(Special issue: B), B194.

Hotza, D. (1995). Review: aqueous tape casting of ceramic powders. *Journal of Materials Science and Engineering A, 202*, 1–2.

Hunter, R. J. (1989). *Foundations of colloid science*. Oxford University Press.

James, P. J. (1983). *Cold isostatic pressing technology*. London, U.K: Applied Science.

Kaiser, A. (2003). Fast acting vacuum device – guaranteed quality for pressed refractories. *Interceram Refractories Manual*, 28–33.

Kaiser, A. (2009). Comparison of different shaping technologies for advanced ceramics production. *Ceramic Forum International/Berichte der DKG (Deutsche Keramische Gesellschaft, 86*(4), E41–E48.

Kang, S.-J. L. (2005). *Sintering* (1st ed.). Oxford: Elsevier, Butterworth Heinemann. ISBN 0-7506-6385-5.

Kern, F. (2009). Extrusion and injection molding of ceramic micro and nano composites. *International Journal of Material Forming, 2*(Suppl. 1), 609–612.

Kern, F. (2010). Thermoplastic ceramic injection molding of zirconia toughened alumina components. In T. Ohji, & M. Singh (Eds.), *Advanced processing and manufacturing technologies for structural and multifunctional materials IV: Ceramic engineering and science proceedings* (Vol. 31(8); pp. 223–238). The American Ceramic Society.

Kern, F. (2011). In C. Bonten, & M. R. Buchmeiser (Eds.), *Modellgestützte Auslegung von Entbinderungs- und Sinterprozessen im Keramischen Spritzguß* (Vol. 22). Stuttgart: Stuttgarter Kunststoff-Kolloquium. ISBN 978-3-00-034152-6, 2/V6 (in German).

Klemm, U., Schöne, B., Svoboda, H., Fries, M., & Nebelung, M. (2010). Instrumented compaction experiments under varied climatic conditions. *Journal of Ceramic Science and Technology, 1*(1), 59–66.

Klippel, U. (2011). Shaped coarse grained refractories by pressure slip casting. *Advanced Engineering Materials, 13*(1–2), 68–76.

Kopylov, Y. L. (2009). Development of Nd(3+):Y(3)Al(5)O(12) laser ceramics by high-pressure colloidal slip-casting (HPCSC) method. *Optical Materials, 31*(5), 707–710.

Krell, A. (1996). The influence of shaping method on the grain size dependence of strength in dense submicrometre alumina. *Journal of the European Ceramic Society, 16*(11), 1189–1200.

Krell, A. (2003). Transparent sintered corundum with high hardness and strength. *Journal of the American Ceramic Society, 86*(1), 12–18.

Krug, S. (2002). Reaction and transport kinetics for depolymerization within a porous body. *AIChE Journal, 48*(7), 1533–1541.

Landfried, R. (2011). Neue Mischkeramik erhöht Standzeiten von Werkzeugen. *Konstruktion, 9*, IW14–IW15 (in German).

Lee, S. C. (2007). A study on the Cap model for metal and ceramic powder under cold compaction. *Materials Science and Engineering A, 445*, 163–169.

Lenk, R. (1995). Hot moulding and interesting forming process. *Ceramic Forum International, 72*(10), 636–638.

Li, W. (2000). Analysis of the grain growth of nano Y-TZP materials. *Journal of Inorganic Materials, 15*(3), 536–540.

Lu, K. (2006). Colloidal dispersion and rheology study of nanoparticles. *Journal of Materials Science, 41*(17), 5613–5618.

Luis, C. J. (2007). Methodology for developing technological tables used in EDM processes of conductive ceramics. *Journal of Materials Processing Technology, 189*, 301–309.

Mannschatz, A. (2011). Influence of powder morphology on properties of ceramic injection moulding feedstocks. *Journal of the European Ceramic Society, 31*(14) (Special issue: SI), 2551–2558.

Matsunaga, N. (2010). Rheology and pressure filtration of aqueous SiC suspensions of nanometer-sized bimodal particles. *Ceramics International, 36*(5), 1581–1588.

Meng, F. (2011). Fabrication of ultrafine-grained alumina ceramics by two different fast sintering methods. *Ceramics International, 37*(6), 1973–1978.

Mittomo, M. (1990). Grain growth during gas pressure sintering of beta silicon nitride. *Journal of the American Ceramic Society, 73*(8), 2441–2445.

Moritz, T. (2010). Verification of the simulation results for mold filling processes in ceramic injection molding. *Ceramic Forum International, 87*(4), E28–E30.

Mujumdar, A. S. (2007). *Handbook of industrial drying*. CRC Press. ISBN 1574446681.

Muller, F. (2004). Dispersing nanoparticles in liquids. *International Journal of Mineral Processing, 74*, S31–S41.

Müller, R. H. (1996). *Zetapotential und Partikelladung in der Laborpraxis*. Stuttgart: Wissenschaftliche Verlagsgesellschaft mbH.

Muller, T. (2010). Ceramic micro parts produced by micro injection molding: latest developments. *Microsystem Technologies, 16*, 1419–1423.

Nishimura, T. (2007). Fabrication of silicon nitride nanoceramics – powder preparation and sintering: a review. *Science and Technology of Advanced Materials, 8*(7–8), 635–643.

Novak, S. (2004). Rheological properties of paraffin suspensions of surface-modified alumina powder for low-pressure injection moulding. *Rheologica Acta, 43*(5), 559–566.

Oberacker, R. (2001). Aspects of sintering additives for processing and microstructure development of HIP-SSiC. *Zeitschrift fuer Metallkunde, 92*(2), 135–140.

Palmero, P. (2011). Role of immiscible and miscible second phases on the sintering kinetics and microstructural development of nano-crystalline α-Al_2O_3-based materials. *Ceramics International*. http://dx.doi.org/10.1016/j.ceramint.2011.07.024.

Pouchly, V. (2010). Master sintering curve – a Practical approach to its construction. *Science of Sintering, 42*(1), 25–32.

Raghupathy, B. P. C. (2011). Spray granulation of nanometric zirconia particles. *Journal of the American Ceramic Society, 94*(1), 139–145.

Rajaiah, J. (1994). Rheology of sterically stabilized ceramic suspensions. *Industrial & Engineering Chemistry Research, 33*(10), 2336–2340.

Reed, J. S. (1976). Dry pressing. In F. F. Y. Wang (Ed.), *Treatise on materials science and technology* (Vol. 9; pp. 71–93). New York: Academic Press.

Roy, J. F. (1993). Alumina microstructural behaviour under pressureless sintering and hot-pressing. *Journal of the European Ceramic Society, 11*(4), 325–333.

Ruh, A. (2011). Development of two-component micropowder injection molding (2C-MicroPIM)—Process development. *International Journal of Applied Ceramic Technology, 8*(3), 610–616.

Russel, W. B. (1989). *Colloidal dispersions*. Cambridge: Cambridge University Press.

Salomoni, A. (2000). Pressure casting offers possibilities for technical ceramics. *American Ceramic Society Bulletin, 79*(11), 49–53.

Samant, A. N. (2009). Laser machining of structural ceramics-a review. *Journal of the European Ceramic Society, 29*(6), 969–993.

Shinohara, M. (1999). Effect of seasons on density strength of alumina. *American Ceramic Society Bulletin, 78*(2), 81–84.

Shu, Z. (2010). A novel approach of preparing press-powders for cleaner production of ceramic tiles. *Journal of Cleaner Production, 18*, 1045–1051.

Song, J. H. (1997). On the machinability of ceramic compacts. *Journal of the European Ceramic Society, 17*(14), 1665–1673.

Sonntag, A. (2008). Innovation in design and materials for complete kiln furniture solutions. *Ceramic Forum International, 85*(5), E54.

Stringari, G. B. (2011). Time-dependent properties of bimodal POM – application in powder injection molding. *Powder Technology, 208*(3), 590–595.

Thompson, R. A. (1981). Mechanics of powder pressing; model for powder densification. *American Ceramic Society Bulletin, 60*, 237–241.

Trunec, M. (2011). Osmotic drying of gelcast bodies in liquid desiccant. *Journal of the European Ceramic Society, 31*(14), 2519–2524. SI.

Walcher, H. (2010). Simple and efficient: quality assurance for powder injection moulding. *Ceramic Forum International, 87*(4), E33–E35.

Wang, J. (1992). Effect of pressing method on organic burnout. *Journal of the American Ceramic Society, 75*(9), 2627–2629.

Waters, B. (2005). Balancing firmness with packing in pressure casting sanitaryware. *Ceramic Forum International, 82*(3), E32–E36.

Yondem, I. (2011). The effect of different surface finishing procedures on surface roughness and fracture toughness in all-ceramic restorations. *International Journal of Applied Ceramic Technology, 8*(2), 437–445.

Zhang, J. Y. (2005). Research on SIPM-PEG as water-soluble binders applied in Ceramic Injection Molding. *Rare Metal Materials and Engineering, 34*(Suppl. 1), 593–596.

Zhao, B. (2008). Characteristics of surface deterioration layer of micro-nanocomposited ceramics under two dimensional ultrasonic vibration grinding. *Rare Metal Materials and Engineering, 37*(Suppl. 1), 832–835.

Zotelief, W. F. (1996). Residual thermal stresses in injection molded products. *Polymer Engineering & Science, 36*(14), 1886–1896.

2.07 Joining Methods for Hard Ceramics

Maria Isabel Osendi and Pilar Miranzo, Institute of Ceramics and Glass, CSIC. Kelsen, 5, Madrid, Spain

© 2014 Elsevier Ltd. All rights reserved.

2.07.1 Introduction

The development of suitable joining techniques to self-bond hard ceramics or for bonding to metals has been a major target before 2010, aiming at cutting edge applications of ceramics such as engine components and advanced gas turbines (Katano, Ando, Itoh, & Sasaki, 1993; van Roode, 2010; Waitz, Gauba, & Tzeng, 1998). Requirements for these joints include sufficient mechanical strength and the possibility to withstand moderate temperatures as many of these applications try to exploit the remarkable properties at high temperature of ceramics (Bocanegra-Bernal & Matovic, 2010; Naslain, 2005).

When bonding ceramics, the first difficulty is to get an intimate contact between the materials to be joined, that is to say, a continuous interface produced trough chemical/electronic interaction among the surfaces of both materials. Fundamental knowledge of the bonding interface is essential to reach full understanding of the underlying mechanisms and to get control over the properties of the joints as asserted by earlier works (Howe, 1993). Interface characterization includes usual techniques such as scanning electron microscopy (SEM) and electron microprobe (EPMA) analyses to identify the reaction degree and the potential diffusing species, whereas the use of transmission electron microscopy (TEM) is necessary when higher resolution is desirable (Ruhle, 1996). Modern techniques as focused ion beam in conjunction with TEM and X-ray spectral analysis have shown strong capabilities for analyzing joined interfaces (Loehman & Kotula, 2004).

When joining dissimilar materials and specially ceramics to metals, a main concern is the development of high residual stresses due to the difference in thermal expansion coefficients (CTE) of the considered materials. The usual way to decrease residual stresses is by interposing ductile metal layers that can reduce the strain through plastic deformation (Elssner & Petzow, 1990; Park, Mendez, & Eagar, 2005). The strain and stress levels at interfaces are commonly analyzed by numerical modeling methods like finite element analysis (FEA) (Kovalev, Miranzo, & Osendi, 1998), and through experimental methods like X-ray diffraction (XRD) (Lee & Kim, 1997), neutron diffraction (Martinelli, Drew, Fancello, Rogge, & Root, 1999) or high-resolution X-ray scanning diffractometry using synchrotron radiation (Vila et al., 2005).

http://dx.doi.org/10.1016/B978-0-08-096527-7.00026-X

A range of techniques have been devised for joining ceramic materials including alloy brazing (Akselsen, 1992a), metal diffusion bonding (Akselsen, 1992b) and via special ceramic or glass interlayers (Glass, Mahoney, Quillan, Pollinger, & Loehman, 1998; Perham, De Jonghe, Moberlychan, 1999). Some early work (Nicholas, 1990) and various review papers (Elssner & Petzow, 1990; Nicholas & Mortimer, 1985; Suganuma, 1990) dealing with different aspects of ceramic joining can be found in the specialized literature and, more recently, the excellent review on ceramic joining technologies for engineering ceramics aimed at high-temperature applications (Fernie, Drew, & Knowles, 2009).

In this chapter, a comprehensive updated review of joining methods used for hard oxide (Al_2O_3, ZrO_2) and nonoxide (Si_3N_4 and SiC) ceramics is presented. First, a definition and classification of the joining methods will be given. After that, direct joining methods will be briefly treated. The main body of this chapter will focus on the more generally used techniques like diffusion bonding, alloy brazing, and transient liquid-phase (TLP) methods. Furthermore, joining with interposing of glassy, glass ceramics or ceramic–metal interlayers will be introduced. The development of thermal stresses at the interfaces will be treated, also making reference to techniques for measuring and predicting residual stresses near the joining interface. The more common tests to evaluate the strength of the bonds will be briefly presented. Finally, current and foreseen applications will be discussed as well as the future trends for these joining methods.

2.07.2 Types and Classification of Ceramic Joining Methods

An earlier classification of joining methods considered three basic types (Nicholas & Mortimer, 1985)—mechanical joining, direct joining (two straight pieces), and indirect joining (a third interlayer material is interposed between the pieces to be bonded). Mechanical joining comprises methods such as using of bolts, screw threads (**Figure 1**), and shrink-fitting, which takes advantage of the higher CTE of metals that enclose the corresponding ceramic piece on cooling. These methods although interesting, in general, are not intended for high-temperature uses.

Another classification given by Fernie et al. (2009) considers two basic joining methods, the mechanical and the chemical that encompasses two techniques: those which entail formation of a liquid phase (alloy brazing, glass–ceramic interlayers, etc.) and those occurring in solid state (diffusion bonding, ultrasonic welding, etc.).

Figure 2 shows the schematic classification of joining methods excluding mechanical joining that tries to bring together both classifications. The direct joining essentially includes the diffusion bonding and welding method. In contrast, the indirect joining comprises diffusion bonding via solid—metallic or ceramic—nterlayer, bonding via an induced liquid like in the gas–metal eutectic bonding and transient liquid bonding, in both a small amount of liquid is formed that it is not detectable after bonding, and the properly liquid phase bonding processes. The interposing of intermediate metal foils and glass, glass–ceramics or oxide interlayers is common to all the indirect joining methods.

Figure 1 Silicon nitride component produced with a screw thread capable of attachment to a metal (http://www.twi.co.uk/content/ceramics_mech.html). Reproduced courtesy of TWI Ltd.

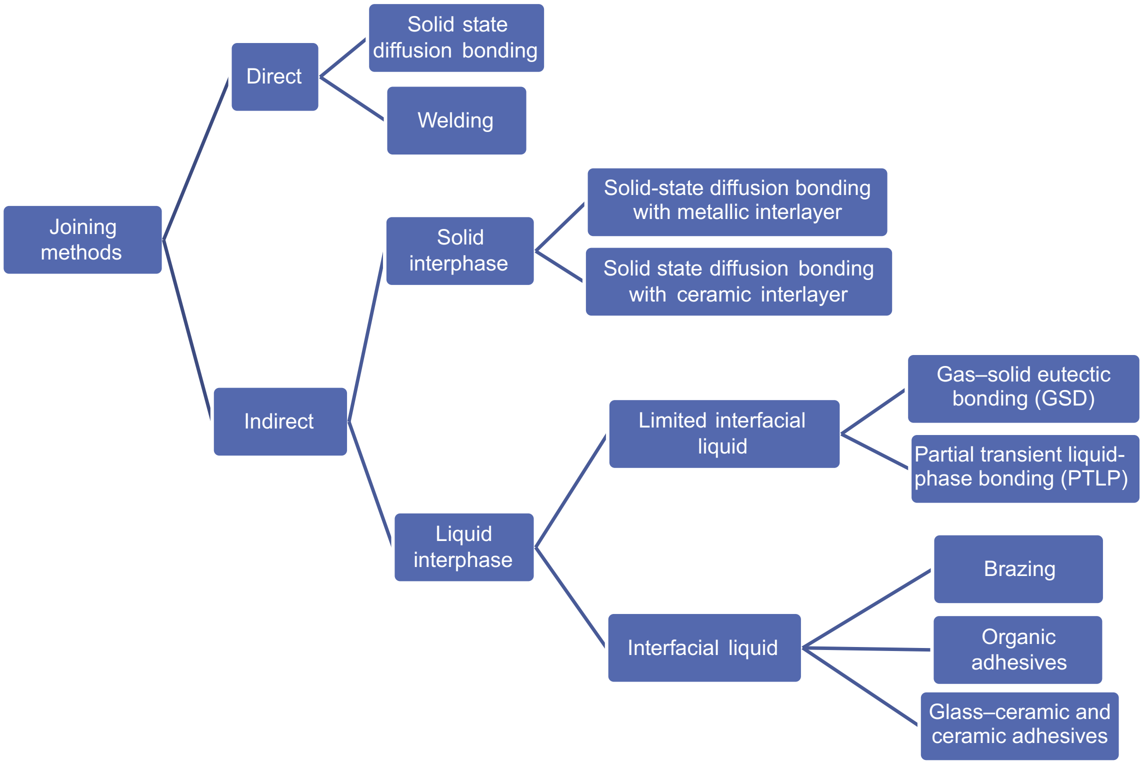

Figure 2 Classification and types of ceramic joining methods.

Generally, to achieve a successful joining, the adherents should not only be in close contact but the joined area should also be able to sustain certain level of stresses and thermal loads. Ceramic joining is a quite complex matter that depends on many parameters, but the basics of the phenomena rest on the interface formation. Usually, interface creation is more easily attained when a liquid is present, similar to a brazing alloy or a glass interlayer, whereas for application requiring higher loads and temperatures, joining is carried out under solid-state conditions as atoms have much lower mobility in that case (Klomp, 1972).

Chemical contact at the interface can take place by electronic interactions, short-range interdiffusion and chemical reaction (Howe, 1993). Therefore, the region affected by the joining interface can extend from few atomic layers to a few microns depending on the governing joining mechanism. Thermodynamic aspects of metal–ceramic interfaces have been studied for predicting interfacial reactions (Okamoto, 1990; van Loo & Kodentsov, 1998) and theoretical calculations have also been done to predict adhesion in some metal-oxide ceramic systems (Munoz, Gallego, Beltran, & Cerda, 2006; Zhang, Smith, & Evans, 2002). Many of these studies have been possible due to access to high-resolution microscopic techniques that provide information of the interface at the atomic level (Levay, Mobus, Vitek, Ruhle, & Tichy, 1999; Voue & De Coninck, 2000).

Other joining methods for ceramics have been the brazing alloy technique and the diffusion bonding, both have been extensively applied to hard engineering ceramics such as Al_2O_3, Si_3N_4, SiC, ZrO_2, etc., One important difference among these ceramics is the much lower CTE of silicon based ceramics compared to the others as can be seen in **Figure 3** (Chawla, 2003), which results in higher stresses when joined to common metals. Therefore, selection of metals with low CTE, if possible, designing graded joining compositions to reduce thermal stresses or interposing ductile metal interlayers have often been applied. Interlayers containing ceramics, glass, glass–ceramics or even ceramic precursors are mostly used for self-joining nonoxide ceramics and require relatively high temperatures, but much lower than the normal sintering temperatures of these ceramics. Therefore, there is a wide range of joining methods that can be used for joining ceramics, which have been developed during the last 30 years, and selection of one over other depends on the intended use and characteristics of the materials to be joined. Selected results and the main advantages of the most important methods are discussed in next sections.

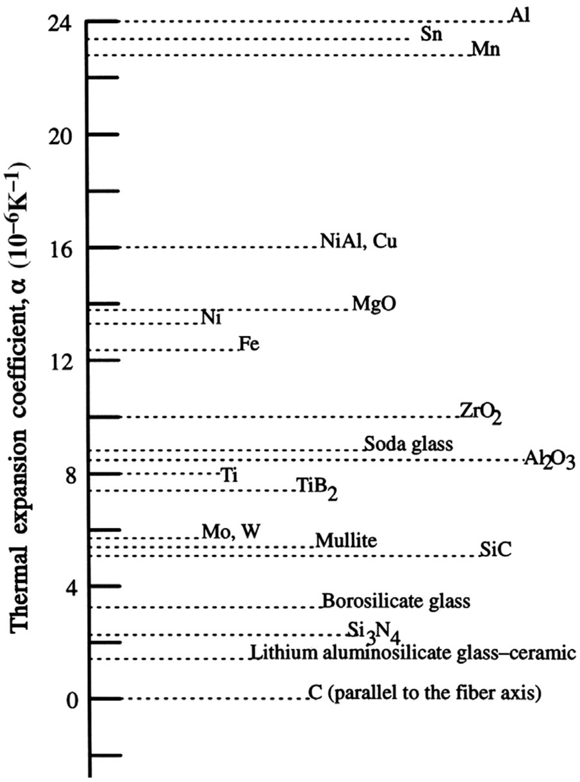

Figure 3 Coefficient of thermal expansion of representative ceramics and metals. Chawla, K. K. (2003). Ceramic matrix composites (2nd ed.). Kluwer Academic Publisher, Chap. 1, Figure 1.5, p. 7. Copyright 2003. Reproduced with kind permission from Springer Science + Business Media B.V.

2.07.3 Direct Bonding

Direct joining methods typically employ welding and diffusion bonding without using intermediate layers. In welding, the joining temperature must be raised close to the melting point of the pieces and effective results have been limited to few pairs of materials, such as Mo, Nb, Kovar–Al_2O_3 (Nicholas & Mortimer, 1985), mainly due to the stresses induced by CTE mismatch and thermal shock. Some ceramics like Si_3N_4 and SiC decompose instead of fusing and consequently cannot be fusion welded.

Friction welding, achieved by rotating and rubbing a metallic specimen against the surface of the ceramic piece, needs separate consideration. This method is essentially carried out at room temperature but the interface experiences a temperature rise owing to the surface friction. High rotating speeds, above 1000 rev min^{-1}, and selection of parameters to avoid ceramic cracking have resulted in the successful joining of Al_2O_3, ZrO_2, Si_3N_4 and SiC ceramics to Al alloys. In all cases tensile strengths above 60 MPa (Essa & Bahrani, 1991; Uday, Fauzi, Zuhailawati, & Ismail, 2010) have been reported. Typical local temperatures in these experiments are around 500 °C and pieces usually show some deformation around the bonded region (**Figure 4**).

Another technique that produces direct ceramic–metals joints is ultrasonic welding. In this method, an axial pressure is applied at room temperature and at the same time an ultrasonic signal, typically with frequencies around 20 KHz and power of 600–1200 W, is imposed to the joining area. Good joining results have been reported by this method in bonding ZrO_2, Al_2O_3, SiC, and Si_3N_4 ceramics to Al and Cu (Matsuoka, 1994). The process is mainly effective for softer metals and it has the advantage that joining can be achieved in a few seconds.

On the other hand, diffusion bonding is a temperature-activated solid-state process driven initially by plastic deformation at the contact asperities and by diffusion and creep in a second stage (Akselsen, 1992b). The application of load, temperatures in the range of 0.5–0.8 of the absolute melting temperature, and joining times in the range of hours are needed to achieve bonding. The formation of an interfacial reaction zone often takes place as this process involves atomic interdiffusion between both surfaces. Therefore, close contact between the

Figure 4 Ceramic plate friction welded to two Al bars: ceramics at TWI; friction welding of ceramics (http://www.twi.co.uk/content/ceramics_fsw.html). Reproduced courtesy of TWI Ltd.

surfaces to be joined entails flat contact and the absence of contaminants and foreign species. Accordingly, joining is predominantly done under high-vacuum conditions, although for nonoxide ceramics inert atmospheres are needed as well. Direct diffusion bonding of SiC (sintered with B and C additives) to itself has been done at temperatures above 1900 °C with an applied pressure of 27 MPa, obtaining bonds with bend strengths above 300 MPa that were in the order of the parent material strength (Deleeuw, 1992). Direct self-bonding of Si_3N_4 (sintered with Y_2O_3 additions) occurs at much lower temperatures than for SiC, explicitly at 1500 °C for a joining pressure of 50 MPa, producing joints with an average shear strength around 20 MPa (Polanco, De Pablos, Miranzo, & Osendi, 2004).

The direct diffusion bonding of Y-ZrO_2 to stainless steel at 1000 °C (Qin & Derby, 1993b), Si_3N_4 to Ni (Esposito, Bellosi, & Cetlotti, 1997; Vila et al., 2007) and to stainless steel (Stoop & Denouden, 1993) has been reported. Nevertheless, the majority of the work on diffusion bonding deals with the use of metal interlayers for self-joining of ceramics or for bonding to metal parts. Therefore, most of the data on diffusion bonding of ceramics will be referred in the next section.

2.07.4 Diffusion Bonding with Metallic Interlayers

In selecting the appropriate metallic interlayer, besides the stiffness of the layer, it is important to anticipate the possible reactions with the ceramic part in order to determine the optimum temperature conditions. Equilibrium reactions between oxides, nitrides or carbides and metals can be predicted from thermodynamic data (van Loo & Kodentsov, 1998). The possibility of reactions is generally desirable to promote rapid bonding, but extensive reaction can debilitate the joint strength. In some cases, good interfacial bonding without any detectable reaction between metal and ceramic parts has been reported. For example, a strong eutectic reaction was reported by diffusion bonding ZrO_2 to an NiCr alloy at temperatures above 1050 °C (Qin & Derby, 1993a), whereas Ni/ZrO_2 diffusion bonding (Vegter, Maeda, Naka, & Den Ouden, 2002) seemed to occur without the formation of a reaction layer (**Figure 5**) for alike temperatures. However, the formation of a reaction zone in this system was detected for joining temperatures of 1200 °C (Polanco, Miranzo, & Osendi, 2006) and bend strengths of 82 MPa were reported for ZrO_2/Ni/ZrO_2 bonds fabricated at 1100 °C under vacuum (Qin & Derby, 1992). In a similar way, Al_2O_3/Nb diffusion pairs bonded in the temperature range of 1500–1900 °C have been extensively studied showing dissolution of Al_2O_3 and diffusion of Al and O atoms into the Nb side that later

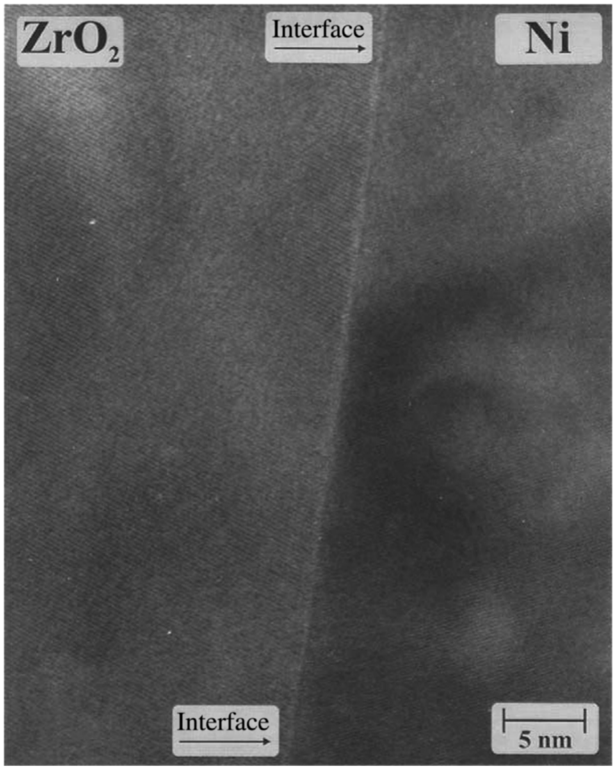

Figure 5 High-resolution TEM micrograph of an Ni/ZrO$_2$ interface diffusion bonded at 1050 °C for $t = 90$ min. Continuity across the interface in the atomic planes ZrO$_2$ and Ni is observed. Plane spacing of ZrO$_2$ is 0.253 nm and plane spacing of Ni is 0.203 nm (Vegter et al., 2002).

precipitate into Al_2O_3, but no new compounds were observed (Burger, Mader, & Ruhle, 1987). However, for Al_2O_3/Ni diffusion bonds at 1300 °C, several new phases, $NiAl_2O_4$ spinel (Trumble & Ruhle, 1991), nickel silicide (Lourdin, Juve, & Treheux, 1996) and $NiO \cdot 5Al_2O_3$ (Esposito, Bellosi, Guicciardi, & De Portu, 1998), have been reported, the differences being correlated to the purity of the Al_2O_3 and the bonding pressure. Maximum bend strengths of 149 MPa were obtained for self-joined Al_2O_3 with Ni interlayer at temperatures of 1350 °C (Esposito et al., 1998). Diffusion bonding of Al_2O_3 with a Ti layer was quite reactive producing intermetallic compounds for temperatures between 600 and 800 °C (Lu, Sass, Bai, Kohlstedt, & Gerberich, 1995).

Diffusion bonding with metallic interlayers has proven to be effective for self-joining Si_3N_4 ceramics as well as for joining them to metals. Among the more employed metal interlayers are iron and its alloys, such as Fe–Ni and different types of steels. At temperatures above 1050 °C (Silva, Oliveira, Castro, & Vieira, 1998), a strong interaction between Fe and Si_3N_4 occurs with diffusion of Si into the Fe phase (Heikinheimo, Isomaki, Kodentsov, & Vanloo, 1997; Oliveira, Silva, & Vieira, 2002). This can produce transformations from γ-Fe to α-Fe, and the evolution of N atoms from the Si_3N_4 that decomposes at the contact interface. When steel is used as a bonding interlayer (Polanco et al., 2004), the reactivity with Si_3N_4 increases as more elements are involved, specially Cr in the case of stainless steels, forming new species like Cr_2N, Fe_xSi_y and α-Fe while at the same time extensive diffusion of Si atoms into the steel layer takes place. Formation of the ternary $Cr_3Ni_5Si_2$ compound (**Figure 6**) was also detected at the contact interface with Si_3N_4 (Poza, Miranzo, & Osendi, 2008). Other minor elements in the stainless steel such as Mo and Ti also played an important role in the reactivity (Polanco et al., 2004) as well as the type of bonding atmosphere, argon or nitrogen (Shimoo, Shibata, & Okamura, 1998). Another often employed metal interlayer is Ni (Osendi, De Pablos, & Miranzo, 2001) that also produced diffusion of Si atoms into the Ni layer and the formation of Ni_xSi_y species (**Figure 7**) with the resulting bonds having a maximum shear strength of 80 MPa for a joining temperature of 1050 °C. Different types of Ni alloys such as Invar (Fe/Ni) and Kovar (Fe/Ni/Co) have produced high-strength joints when used as interlayer between Si_3N_4 and stainless steel (Stoop & Denouden, 1995). When Ti has been used as a bonding interlayer for joining Si_3N_4 at 1400 °C, relatively close to the melting temperature of Ti, a series of reaction species—Ti_5Si_3, TiSi, and

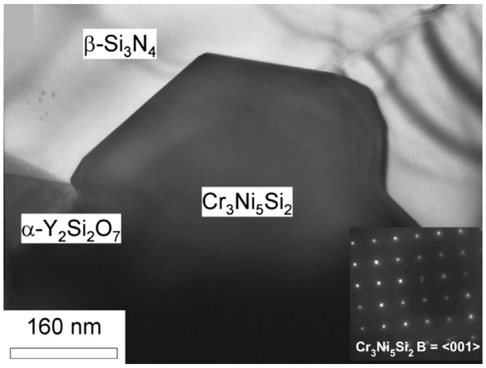

Figure 6 TEM image with nanobeam electron diffraction pattern identifying a crystal of $Cr_3Ni_5Si_2$, which is formed in the ceramic side of the joining interface. The image corresponds to an Si_3N_4 self-joined with a stainless steel interlayer at a bonding temperature of 1200 °C during 2 h (Poza et al., 2008).

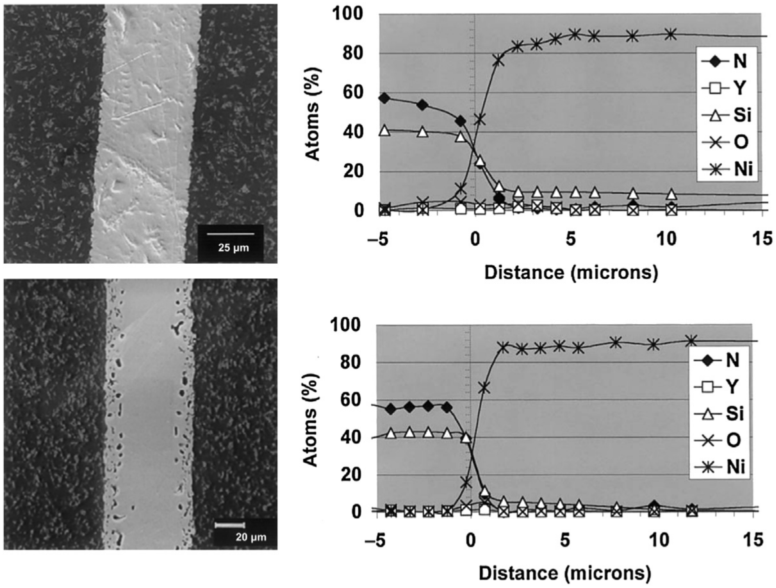

Figure 7 SEM micrographs of two Si_3N_4 bonds with Ni interlayer joined at 1050 (left) and 1150 °C (right). Corresponding electron probe microanalysis is shown at the bottom indicating the atomic interdiffusion in the bonding region. The origin of abscissas axis defines the Si_3N_4/Ni contact interface (Osendi et al., 2001).

TiN—formed at the interface (Lemus & Drew, 2003). Although solid-state bonding using a Mo interlayer has the advantage of its CTE being close to that of the Si_3N_4 (**Figure 3**), sound joints were only possible at 1400 °C in vacuum, and the presence of Mo_3Si and Mo_5Si_3 along with residual pores at the interface were reported (Martinelli & Drew, 1999). Using Nb as interlayer for self-joining Si_3N_4 in the 1200–1600 °C temperature range produced reaction interfaces formed by different silicides, Nb_5Si_3 and $NbSi_2$, depending on the temperature and time (Lemus-Ruiz, Leon-Patino, & Aguilar-Reyes, 2006).

Regarding SiC ceramics, much work has been done using Mo, Nb and Ti as bonding interlayers, all of them being refractory metals with relatively low CTE (**Figure 3**). With Mo interlayers, different types of Mo silicides as well as carbides were found at the interlayer depending on joining temperature, Mo_5Si_3 being the most harmful for the joint integrity. SiC bars joined with Mo foils at temperatures of 1500 °C for long times under vacuum showed high values of shear strengths, 182 MPa, that were practically maintained up to 1090 °C (Cockeram, 2005). In the case of Nb, bonding tests have been done in the 1000–1500 °C temperature range, with initial formation of Nb_5Si_3 which moved toward richer Si species ($NbSi_2$) when raising temperature (Naka, Saito, & Okamoto, 1987). In joining SiC to Ni, silicides of the type Ni_2Si, Ni_5Si_2, and Ni_3Si plus C developed for joining temperatures ~1000 °C and Ni_2Si and C for 1150 °C (Schiepers, Vanloo, & Dewith, 1988). Prereacting the SiC piece with a Cr coating produced a surface reaction interlayer of Cr_5Si_3C, which acted as a diffusion barrier when joining to an Ni foil, with reportedly better joining results (Bhanumurthy & SchmidFetzer, 1996). Diffusion bonding using Ni-based superalloys (Hastelloy X and Incoloy 909) in the 800–1000 °C temperature range showed successive reaction zones of carbides, silicides and free carbon. SiC ceramics were found more reactive with Ni superalloys than Si_3N_4 under similar conditions (Larker, Nissen, Pejryd, & Loberg, 1992). In the case of Ti interlayer, the stable ternary compound Ti_3SiC_2 that exhibits plastic behavior leading to a high joint strength was reported for bonding temperatures $\sim$1450 °C. These studies also indicated the likely formation of TiC and titanium silicides for bonding temperatures <1200 °C (Gottselig, Gyarmatti, Naoumidis, & Nickel, 1990).

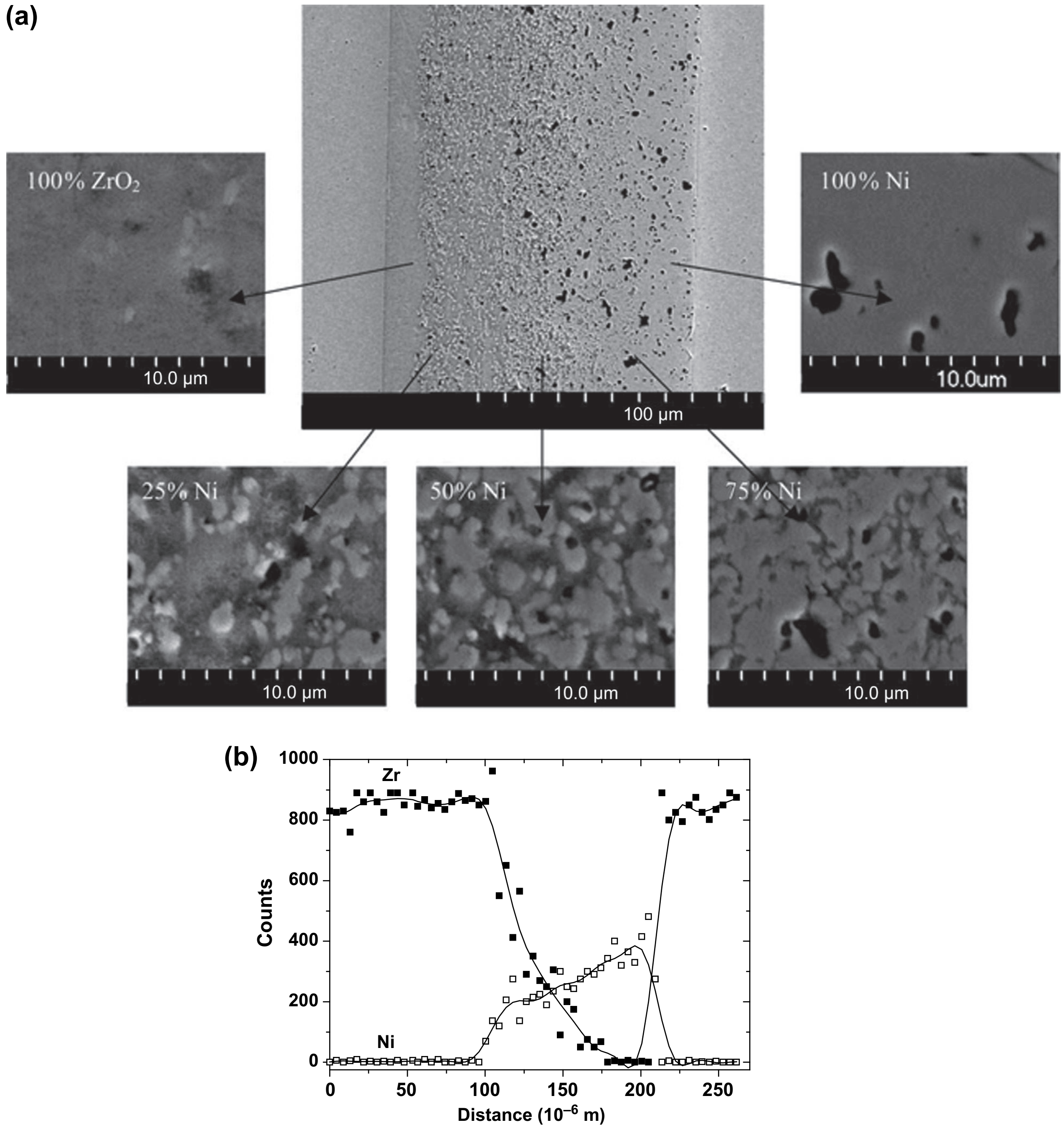

Figure 8 (a) SEM micrograph of a ZrO_2/Ni graded bonding interlayer between two ZrO_2 parts. The interlayer was produced by sequentially spraying inks prepared with graded mixtures of submicron ZrO_2 and Ni powders and sintering/bonding occurred at 1100 °C. Gradual composition remained after joining as shown by the microanalysis (b) (Polanco et al., 2006).

As presented above, Si_3N_4 and SiC ceramics react quite easily with most of the metals of interest, forming metal silicides of various kinds plus metal carbides in the case of SiC, consequently bonding is usually rapidly achieved but controlling the products as well as the reaction extension is required to achieve high bond strengths. Additional species produced by the decomposition of SiC and Si_3N_4 at the contact interfaces are C and N_2, the latter can be trapped as occluded pores often observed at the reaction zone (**Figure 7**), which can reduce the strength of the bond. Most of the reaction products can be predicted considering free-energy changes for possible reactions between Si_3N_4 or SiC and common metals (Okamoto, 1990; van Loo & Kodentsov, 1998).

Within this category, other types of diffusion bonding techniques such as the use of joining interlayers formed by graded metal–ceramic mixtures (Glaeser, 1997; Polanco et al., 2006, Polanco, Miranzo, & Osendi, 2007) can be considered. One example of this type of graded joining interlayer can be seen in **Figure 8** for a ZrO_2/Ni (Polanco et al., 2006), where diffusion bonding and solid-state sintering phenomena simultaneously occurred at the interfacial region.

2.07.5 Indirect Liquid-Phase Joining

Within the joining processes involving filler materials that melt at the joining temperature are the gas–metal eutectic or direct copper bonding (DCB) and TLP bonding (**Figure 2**). In these liquid-phase bonding processes, a small amount of liquid is formed but it is not detectable at the microscopic level after bonding. Brazing is by far the most widely used process when mechanically reliable and vacuum-tight joints operating at high temperature are required. It allows low-cost large-scale joining of intricate geometries as it is not restricted to flat surfaces.

DCB procedure involves the reaction of a gas with the surface of a metal to form a eutectic surface composition (Fernie et al., 2009; Greenhut, 2011). The interface melts by heating the assembly at a temperature between the melting point of the eutectic and the pure metal. This process, of particular relevance in the electronics industry, is used to join Al_2O_3 and AlN to copper. The assembly is heated to the joining temperature in a partial pressure of oxygen greater than the equilibrium partial pressure of oxygen over Cu_2O and bond takes place through the reaction of Cu_2O with Al_2O_3 to form a few nanometers layer of $CuAlO_2$. Since AlN ceramic substrates have a passivating surface oxide of Al_2O_3, the same technique has been used to bond AlN to copper but in this case joining is carried out in vacuum or nitrogen after an oxidation step.

TLP process involves placing an alloy interlayer between the parent surfaces with a composition close to that of the parent material, while also containing a melting point depressant such as Si, B or P in its chemical composition. This interlayer completely melts during the early stages of joining wetting the faying surfaces. As time progresses, the melting point depressant diffuses out of the alloy into the parent material, causing isothermal solidification of the interlayer, a schematic of the process is depicted in **Figure 9**. The final step is homogenizing the bond at a suitable heat-treating temperature. This process characteristically lies between diffusion bonding and brazing and for this reason, it is commonly called *diffusion brazing*. The main advantage of TLP bonding is that the resulting phases have a melting point above the bonding temperature. The kinetics of the process and the effect of the different bonding parameters are described in a recent review on this topic (Cook & Sorensen, 2011). The TLP process has been widely used in the aerospace industry for joining metals but it is less common for ceramics. A derivative of this process, the partial transient liquid phase (PTLP) joining, has been used for ceramics and deserves a special section (Section 2.07.5.1).

2.07.5.1 Partial Transient Liquid-Phase Bonding

While traditional TLP relies on chemically homogeneous filler interlayer, ceramic self-bonding by the PTLP method is based on an inhomogeneous three-part interlayer. Such an interlayer consists in cladding a low-melting point alloy to both sides of a more refractory metal core like the example in **Figure 10(a)** for SiC joined with an Ni–Si/Mo/Ni–Si three layer system (Liu, Valenza, Muolo, & Passerone, 2010). The two outer alloys melt during heating, wetting the ceramics and diffusing into the solid refractory metal core. As joining progresses, the liquid disappears through diffusion and isothermal solidification at the joining temperature, as reflected in **Figure 10(b)** for Al_2O_3 self-joined using an Ni/Nb/Ni interlayer (Hong, Bartlow, Reynolds, Mckeown, & Glaeser, 2008), which essentially differentiates PTLP from brazing. The main advantage of TLP and PTLP bonding is that the resulting bonds can operate at temperatures equal or above the bonding temperature. Another advantage is that the resulting bonding interphase often has microstructure and, therefore, mechanical properties similar to the properties of the base materials.

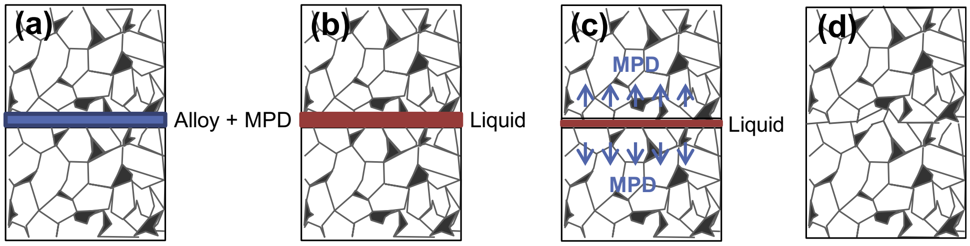

Figure 9 Schematic showing the main steps involved in the formation of a joint by the TLP process: (a) initial assembly, (b) melting of joining interlayer, (c) melting point depressant (MPD) diffuses out of the alloy into the parent materials, and (d) final joint.

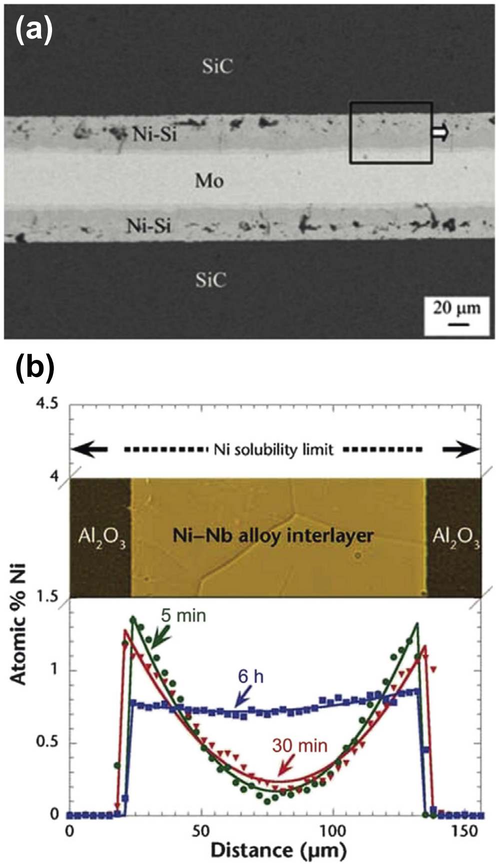

Figure 10 (a) SEM micrograph showing the interface of SiC self-bonded by the PTLP method at 1350 °C for 10 min, where the interlayer consisted in cladding a low melting point Ni-56 at.% Si alloy to both sides of a refractory Mo core (Liu et al., 2010). (b) Composition profile, analyzed using energy-dispersive spectroscopy and EPMA, of Al_2O_3 self-joined using an Ni/Nb/Ni interlayer by PTLP at 1400 °C, for times ranging from 5 min to 6 h, indicating that essentially complete homogenization takes place in 6 h (Hong et al., 2008).

Multilayered fillers of Cu/Ni/Cu have been used to self-join Si_3N_4, SiC and Al_2O_3 at temperatures of 950–1000 °C by PTLP, reporting reproducibly high joint-bend strengths (230–770 MPa) (Locatelli, Dalgleish, Nakashima, Tomsia, & Glaeser, 1997). Different types of interlayers based on Cu, like Cu/Pt/Cu (Shalz, Dalgleish, Tomsia, & Glaeser, 1993), Cr/Cu/Ni/Cu/Cr (Shalz, Dalgleish, Tomsia, & Glaeser, 1994) and Cu/Nb/Cu (Marks, Chapman, Danielson, & Glaeser, 2000), have been used to join Al_2O_3. Indium has also been used as a cladding material with an interlayer of both pure Ag and Ag-based active metal for PTLP bonding Al_2O_3 (Sugar et al., 2006). In the case of Ni/Nb/Ni, Al_2O_3 joints with fracture strengths of 500–520 MPa, yielding Nb-rich interlayers with very high remelting temperatures, have been reported (Hong et al., 2008).

Different TLP interlayers have been used to join alumina with metals, such as Ni and Ni–Cr cores with Cu cladding for alumina/stainless-steel bonds (Zhang, Chandel, & Seow, 2002), Ni/Ti/Ni multilayer for joining

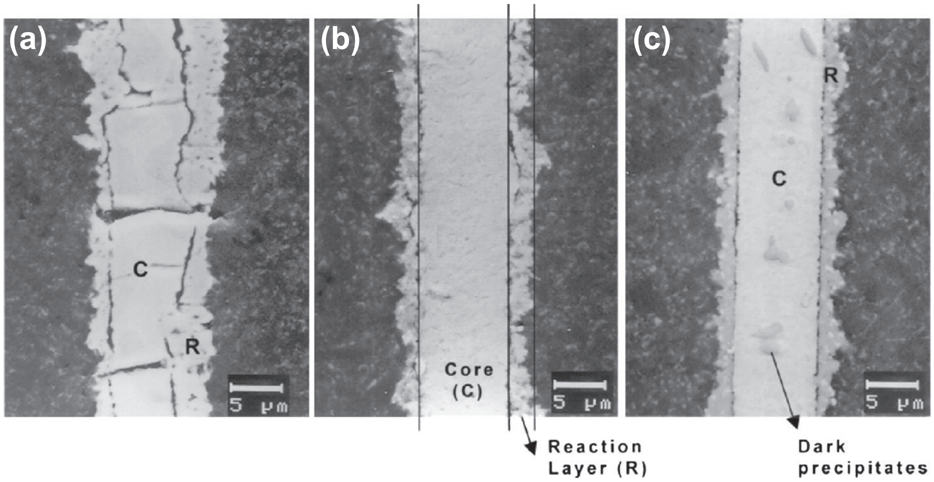

Figure 11 SEM micrographs of the joining cross-sections of Si_3N_4 ceramics PTLP joined using an Ni–Cr braze foil with B infused at its surface, at 1150 °C for 30 min applying the following joining pressures: (a) 7.5, (b) 30, and (c) 40 MPa. The joining region showed a diffusion zone, Ni[Cr, Si] solid solution with some CrN precipitates, at the middle of the interlayer and a reaction layer at the Si_3N_4/brazing alloy interface, which mainly consisted of CrN and BN (Liang, 2003a).

alumina to Kovar alloy (Zhang, Qiao, & Jin, 2002), and pure Cu foils for joining alumina with an aluminum metal matrix composite (Zhai, North, & Serratorodrigues, 1997).

Si_3N_4 has been self-joined using Ni–Cr alloys coated with either B (Liang, Osendi, & Miranzo, 2003a,b) or Au (Ceccone et al., 1996) at relatively low temperatures with this PTLP method. In both cases, strong bonds have been reported which were associated with the particular microstructure of the interface (**Figure 11**) consisting on a reaction layer formed by CrN and a diffusion layer of $Ni_{[Cr,Si]}$ solid solution with some CrN precipitates (Liang et al., 2003a; Liang et al. 2003b). Following a similar strategy, multiple layers of the type CuTi/Pd/CuTi, Ti/Cu/Ti and Ti/Ni/Ti have been successfully employed for joining Si_3N_4 specimens (Chen, Cao, Zhao, & Zou, 2004; Peteves, Paulasto, Ceccone, & Stamos, 1998), which benefits from the use of the active Ti metal and formation of a low-melting liquid which gradually disappears as the Ti dissolves in the core, forming higher melting point intermetallic phases. The resulting joint strength, 160 MPa, was retained when raising the temperature up to 600 °C (Chen et al., 2004). PTLP has also been successfully used for joining Si_3N_4 composites to metals, as is the case of Inconel 718 (Kim, Park, & Eagar, 2003), steel (Blugan, Janczak-Rusch, & Kuebler, 2004) or an iron aluminide intermetallic alloy (Brochu, Pugh, & Drew, 2004).

Less work has been done in the case of PTLP of SiC ceramics. Recently (Liu et al., 2010), SiC/SiC joints were fabricated by using an Ni–Si/Mo/Ni–Si structure (**Figure 10(a)**) whereas SiC was joined to Kovar using an Ni–Si coating as interlayer on the SiC side and the Mo directly attached to the Kovar. Finally, ZrO_2 materials have also been joined using PTLP via Al/Ni alloy/Al interlayer (Akashi, Nukui, & Kiyono, 2009).

2.07.5.2 Liquid-Phase Joining

Liquid-phase joining processes can be classified according to the type of joining medium (**Figure 2**), i.e. organic adhesives; metallic brazes or glass–ceramics and ceramic adhesives. The temperature capability is strongly dependent on the type of interlayer ranging from 200 °C in the case of organic adhesives up to 1200 °C for glass–ceramic interlayers. In nearly all cases, the joining medium is placed between the surfaces to be joined and either melted or cured. After cooling to room temperature, the joining interlayer is detectable as a third body between the joined materials. Among liquid phase joining advantages over the solid-state bonding are the ability to fill completely the gap between the contacting surfaces, which makes it not surface roughness dependent, and also the possibility of large-scale joining of intricate geometries as the method is not restricted to flat surfaces. In addition, it is a faster process compared to diffusion bonding and its main drawbacks are the lower oxidation resistance and temperature capability.

When the service temperature does not exceed 200 °C, conventional polymer-based adhesives can be used to join ceramics. In addition to their general low cost, speed and ease of application, adhesives minimize stresses because of their low-elastic moduli. However, due to the low-temperature useful range, there are few applications outside the electronics and dental ceramics for such joints. For increased service temperature, soldering (below ~450 °C) and brazing (above 450 °C) find widespread use in areas such as electronics, dental practice, jewellery applications, or cutting tools (Fernie et al., 2009; Lang, Yamaguchi, Ohashi, & Sato, 2011; Nicholas, 1998; Raic, Rudolf, Todorovic, Stamenkovic, & Anzel, 2010). In both soldering and brazing, the metal–alloy interlayer melts and reacts with the surfaces at the joining temperature to form the bond. Bend strengths of up to 500 MPa are achievable, depending on materials selection and design.

These processes rely on wetting of the ceramic surface by the filler metal or alloy, which is determined by the magnitude of the surface tensions and the reactivity of the involved species. The amount of wetting of a solid surface by a liquid is commonly evaluated from the contact angle, θ, using Young's equation (Kumar & Prabhu, 2007; Nicholas, 1998). Alternatively, the spreading coefficient defined as a balance between the involved interfacial energies and the work of adhesion—work per unit area needed to separate the liquid from the solid—is a useful concept. Whereas, under nonreactive conditions, wetting only depends on the physical properties of the involved materials and is represented by a stationary contact angle, a clear definition for wetting in solid/liquid reactive systems is still not available.

In the case of soldering, most studies have been devoted to develop low-melting point alloys modified either by the addition of active elements into the alloy or by the deposition of a thin film of an active metal and a thin film of solder on the ceramic surface. Recent research in this field includes lead-free solders based on either eutectics or low-melting point alloys like In–Sn, Cu–Sn, Cu–In or Au–Ge (Kumar & Prabhu, 2007; Lang et al., 2011). Commercial solders based on Sn–Ag and Zn–Al–Ag marketed by S-bond Technologies LLC (http://www.s-bond.com) with liquidus temperatures of 232 and 420 °C, respectively, are currently available.

Metallic brazes for joining ceramics are usually referred to in terms of the main element (e.g. Ag-based and Cu-based), which provides different temperature capability. In **Table 1**, the liquidus temperatures of different commercial braze alloys from Wesgo (www.wesgometals.com) are shown. The most widely used braze family is that of the Ag-based alloys, with the eutectic composition 72 Ag–28 Cu (in wt.%) that melts at 780 °C as the standard alloy. Two approaches have been considered to improve the poor wetting of ceramics by metals: the design of filler metals with improved wettability (Active Metal Brazes or AMB) or the modification of the ceramic surface to make it wettable by "metallization". One of the most common processes for the latter is the Mo–Mn (called molymanganese) process that was originally developed for joining zirconium and magnesium silicate bodies and oxide ceramics containing a secondary glassy phase. It consists on depositing layers of an Mn-based glassy phase and a refractory metal (Mo) onto the ceramics, with a final thin layer of Ni. During heating the Mo–Mn layers react with the glassy phase and favor wetting by the Ag–Cu braze (Mishra et al., 2005; Nono, Barroso, & Castro, 2006). Alternative metalizing methods that involve depositing an active element on a ceramic surface before brazing have been developed for ceramics such as Si_3N_4 and AlN (Fernie et al., 2009).

The reactive wetting or active metal brazing is achieved by adding extra elements, typically from Groups IV and V, to the filler alloy to induce wetting by decomposing a thin layer of the ceramic surface and forming a new phase, which diminishes the contact angle. Typically, Ti is the active metal added, but other metals such as

Table 1 Liquidus temperature of significant commercial Wesgo brazing alloys (technical information courtesy of MTC Wesgo Metals, http://www.wesgometals.com)

Trade names	*Nominal composition (wt.%)*	*Liquidus temperature (°C)*
Cusil®	72 Ag + 28 Cu	780
Incusil-10®	63 Ag + 27 Cu + 10 In	730
Incusil-15®	61.5 Ag + 23.5 Cu + 15 In	705
Silver-ABA®	Ag + 5 Cu + 1.25 Ti + 1 Al	912
Ticusil®	68.8 Ag + 26.7 Cu + 4.5 Ti	900
Cusil-ABA®	63 Ag + 1.75 Ti + 35.25 Cu	815
Incusil-ABA®	59 Ag + 27.25 Cu + 12.5 In + 1.25 Ti	715
35 Gold–65 copper®	35 Au + 65 Cu	1010
50 Gold–50 copper®	50 Au + 50 Cu	970
80 Gold–20 copper®	80 Au + 20 Cu	910
Gold-ABA™	96.4 Au + 3 Ni + 0.6 Ti	1030
Gold-ABA V™	97.5 Au + 0.75 Ni + 1.75 V	1090
Nioro®	82 Au + 18 Ni	955
Nioro-ABA®	82 Au + 16 Ni + 0.75 Mo + 1.25 V	960
Paloro-3V®	89.2 Au + 7.8 Pd + 3.0 V	1220
Copper-ABA®	Cu + 2 Al + 3 Si + 2.25 Ti	1024

Hf, Zr and V have also been tried, as they are known for having some degree of chemical interaction with most ceramics (Loehman, Hosking, Gauntt, Kotula, & Lu, 2005; Loehman & Kotula, 2004) and consequently decreasing the contact angle of different brazing alloy/ceramic systems (Eustathopoulos, 2005; Fernie et al., 2009; Nascimento, 2003). Reactive wetting has been modeled by Eustathopoulos (1998, 2005); he considered spreading kinetics mainly driven by the chemical reactions taking place at the solid/liquid/vapor triple-line interface and the transport of reactive species from the drop bulk to the triple line. Other models (Saiz, Tomsia, & Cannon, 1998) assume that adsorption of the reactive element at the initial interface is the important factor and subsequent wetting and spreading are controlled by the migration of a triple-line ridge. Numerical simulations of the kinetics of the triple-line motion were discussed in a recent review article (Kumar & Prabhu, 2007). Atomistic simulations by molecular dynamics methods of reactive and nonreactive wetting have been done in the years before 2010 (De Coninck & Blake, 2008; de Ruijter, Blake, & De Coninck, 1999; Swiler & Loehman, 2000).

2.07.5.2.1 Active Metal Brazing with Ag–Cu–Ti

The most commonly used AMB alloys for joining ceramics to either ceramics or metals are Cu and Ag–Cu alloys with additions of Ti. The melting point of Ag–Cu–Ti alloys ranges from 815 to 912 °C, as seen in **Table 1** for several commercial alloys, being the limit temperature of use around 600 °C because of both creep and oxidation effects (Fernie et al., 2009). The role of Ti in wetting and spreading has been discussed from a theoretical and thermodynamic perspective (Eustathopoulos, 1998) but most experimental studies concentrate on microstructural development. AMB of engineering ceramics, except for zirconia, follows the same general trend about microstructural changes at the interface: Ti within the molten braze migrates at the brazing temperature to the ceramic surface to form a discontinuous reaction layer of relatively simple compounds (Ti_xO, TiN and TiC); subsequent layer growth enlargement occurs by lateral growth until it becomes continuous; at this stage, a second chemical reaction begins and the free metal liberated by the first chemical reaction forms an intermetallic layer which is then wetted by the AMB (**Figure 12(a)**). Indium has also been used as a melting point depressant—e.g. Incusil ABA melts at 715 °C—and to offset the effects of CTE when joining to metals.

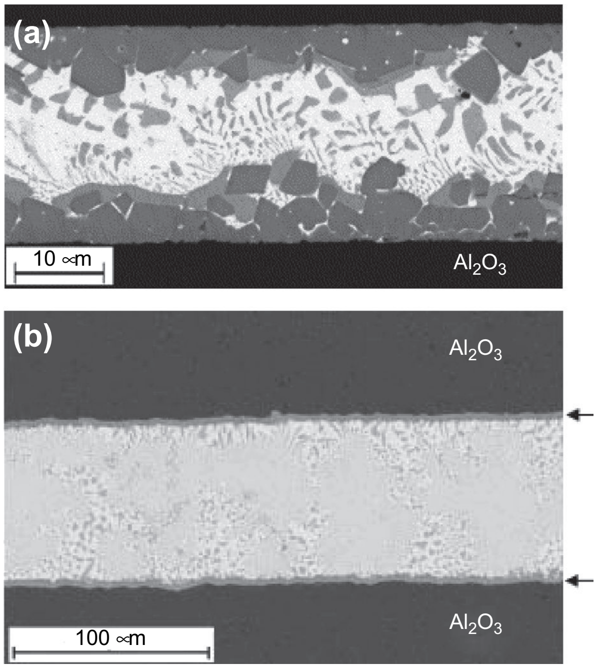

Figure 12 SEM images of joining interfaces for alumina/CuAg–Ti braze/alumina joints obtained: (a) with a CuAg–8 at.% Ti at 900 °C for 30 min, where a continuous 3–5-μm-thick reaction layer is formed consisting of the Ti_3Cu_3O and Ti_4Cu_2O compounds (Voytovych et al., 2006) and (b) by screen printing a Ti paste onto the alumina surface prior to brazing with the CuAg alloy at 850 °C for 15 min (the Ti content was 2.2 wt.%). A bilayer reaction zone formed by a Ti-rich oxide layer near alumina (arrows in the micrograph) and a layer of $Ti_3(Cu,Al)_3O$ on the braze side of the interface was observed (Kozlova et al., 2010).

Active metal brazing of alumina ceramics has been extensively investigated (Janickovic, Sebo, Duhaj, & Svec, 2001; Mandal & Ray, 2004; Paulasto & Kivilahti, 1998; Voytovych, Robaut, & Eustathopoulos, 2006), showing that the interfacial chemistry is directly correlated to wetting. Cu–Ag alloys do not wet alumina but contact angle decreases with Ti addition; 3 and 8 at.% Ti decreased below 10° the steady contact angle, which was related to the formation of M_6X—mixed oxides of the type Ti_3Cu_3O and Ti_4Cu_2O at the interface. From the mechanical point of view, it was observed that a higher amount of Ag in the filler improved the bond strength of alumina joints (Mandal & Ray, 2004) due to the increased Ti activity.

Ag–Cu–Ti alloys have also been used to join alumina to metals, particularly steels, Ti- and Ni-alloys and copper, although the sequence of interfacial chemical reactions is by far less clear. For example, in joining alumina to Ni parts (Arroyave & Eagar, 2003; Valette, Devismes, Voytovych, & Eustathopoulos, 2005), nickel dissolved in the braze alloy and dramatically decreased the chemical activity of Ti. This effect was not so intense for Fe substrates; in fact, for Al_2O_3 brazed to stainless steel, the presence of Ti_xO, Cu_3Ti_3O and FeTi phases at the Al_2O_3 interface, and FeTi and $Fe_{35}Cr_{13}Ni_3Ti_7$ intermetallics at the stainless-steel interface were confirmed (Kar, Mandal, Venkateswarlu, & Ray, 2007). The formation of a bilayer reaction zone, consisting of a Ti-rich oxide layer near the alumina and a layer of $Ti_3(Cu,Al)_3O$ on the braze side of the interface, was also reported for AMB of alumina to copper, performed by screen printing a Ti paste onto the alumina surface prior to brazing with the Cu–Ag alloy (Kozlova et al., 2010) (**Figure 12(b)**).

The presence of a Ti_xO-rich layer at the ceramic side of the interface has been reported for ZrO_2 and Al_2O_3/ZrO_2 composites as well. During brazing, Ti reacts with the ZrO_2 leading to an oxygen depletion at the surface region which induces its darkening (Hanson, Ironside, & Fernie, 2000). This nonstoichiometric layer did not show any effect on the mechanical performance of the ZrO_2–ZrO_2 joints, with reported strengths around 300 MPa measured by four-point bending. In addition to Ti_xO, other reaction layers such as M_6O mixed oxides have also been described (Muolo, Ferrera, Morbelli, & Passerone, 2004). The thickness of the Ti_xO layer at the ZrO_2 side was proved to be a critical feature for achieving a successful joint, as wetting and adhesion occurred only for specific thickness. For example, for ZrO_2/Ni-based superalloy joints brazed with the Ag–Cu–1.75 wt.% Ti alloy, the optimal layer thickness was <1 μm (Sciti, Bellosi, & Esposito, 2001); whereas, for ZrO_2 brazed to stainless steel and to itself, using Ag57Cu38Ti5 filler, the maximum shear strength was obtained for a 4.4-μm-thick layer (Hao, Wang, Jin, & Wang, 1995). The evolution of the interfacial microstructure with brazing conditions has also been studied on ZrO_2/Ti joints with Ag–Cu–1.75 wt.% Ti filler (Smorygo, Kim, Kim, & Eom, 2007). A comparative study on the self-brazing of ZrO_2 using two AMB alloys, Ag27Cu3Ti and Sn10Ag4Ti, shows higher flexural strengths for the first although the Ti_xO interfacial reaction layers for both brazing systems were of the same nature and formation kinetics (Chuang, Yeh, & Chai, 2000). More complex interfacial reactions were reported when TiH_2 powder was employed for improving wetting of Ag–Cu filler in joining ZrO_2 to stainless steel (Liu, Qiao, Wang, Yang, & Lu, 2008).

Scarce works have been done on AMB of Si_3N_4 using Ag–Cu–Ti alloys, but the formation of double layered reaction products consisting of Ti_5Si_3 and Ti_xN layers has been reported as well (Nomura, Iwamoto, & Tanaka, 1999). Similar reaction scheme has been observed for AlN and SiC ceramics, with formation of Ti_xN and TiC, respectively, at the ceramic/braze interface (Loehman & Tomsia, 1992; Palit & Meier, 2006; Prakash, Mohandas, & Raju, 2005).

Attempts have been made to improve the strength of AMB alloys through the addition of ceramic particles or fibers as reinforcements, which also leads to a reduction in the CTE of the braze alloy, and then in the CTE mismatch. For example, SiC self-joined with Ag–Cu–Ti filler achieved a 50% increase in the joint strength (up to 500 MPa) by incorporating SiC particles either as a coating on the braze foil or by including SiC powders into the brazing alloy (Knowles, Ormston, Conquest, Ecclestone, & Fernie, 2003). The ceramic/braze interface was mainly TiC containing some intermetallics of the type Ti_5Si_3 and Cu_5Si. Following the same rationale, the shear strength of carbon fiber-reinforced SiC matrix composites brazed to Ti alloys has been improved by adding different reinforcements to the Ag–Cu–Ti powdered braze, as tungsten particles, short carbon fibers and SiC particles (Lin, Huang, Zhang, & Liu, 2006; Lin, Huang, & Zhang, 2007; Xiong, Huang, Lin, Zhang, & Zhao, 2011). Finally, Si_3N_4 particles have been introduced into Ag–Cu–Ti filler alloy, in this case to braze Si_3N_4 to TiAl intermetallics (Song, Cao, Wang, & Feng, 2011), and SiC particles into a commercial active Ag–Cu–In–Ti alloy was used to join Si_3N_4–TiN composite to steel (Blugan, Kuebler, Bissig, & Janczak-Rusch, 2007) reporting joint strengths up to 500 MPa.

To minimize residual stresses at the metal–ceramic interface, layered braze structures have been proposed with alternating layers of the reinforced and unreinforced filler alloy (Galli, Botsis, & Janczak-Rusch, 2006). However, special care must be taken when selecting reinforcing particles as they can alter the chemical activity in

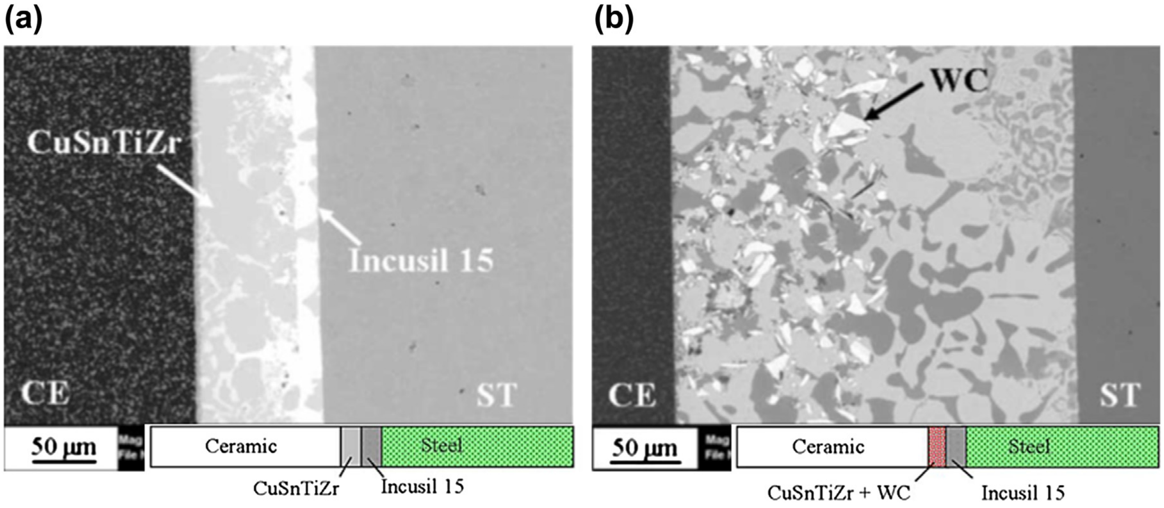

Figure 13 Cross-sectional SEM micrographs of Si_3N_4/TiN ceramics (CE)-steel (ST) joints brazed with double layer brazes. The ceramic was previously metalized with CuSnTiZr (a) or CuSnTiZr containing 35 vol% of WC particles (b) at 930 °C and then brazed to the steel using Incusil-15 at 740 °C for 10 min. Schematic representation of the joint partners and brazing filler alloy systems are included (Blugan et al., 2004).

the multilayered braze. In this way, distinct results have been reported for Si_3N_4/TiN composite-steel joints. Strength increases of 20% were reported for a three-layer structure consisting of a middle layer of Incusil-ABA reinforced with SiC particles between two foils of unreinforced Incusil-ABA when compared to the unreinforced single-layer braze (Galli et al., 2006). Conversely, when brazing with the two-layered system of CuSnTiZr and Incusil-15 (**Figure 13**), the addition of WC particles to the CuSnTiZr layer altered the chemical reactivity and decreased the strength (Blugan et al., 2004).

2.07.5.2.2 Ag-Based Reactive Air Brazing

Most of the AMB alloys must be brazed in inert gas or vacuum, but the recent development of reactive air brazing (RAB) technology overcomes this difficulty, thus minimizing the associated operating costs. Furthermore, these joints demonstrate high-temperature oxidation resistance. The technique has been used for joining electrochemically active ceramics such as zirconia ceramics and lanthanum strontium cobalt ferrite to oxidation-resistant materials like FeCrAlY. RAB can be applied for sealing solid-oxide fuel cells (SOFCs), where the need of vacuum heating can preclude the use of conventional AMB.

In RAB, the ceramic surface is reactively modified with a compound that has been dissolved in a noble metal solvent, e.g. silver, gold, or platinum, such that the remaining molten filler material wets the newly formed surface. Schuler, Stuck, Beck, Keser, and Tack (2000) were the first to recognize that the Ag–CuO system could be exploited to bond ceramics in air, reporting the successful joining of alumina using a 99Ag–1CuO (in mol%) braze. The Ag–CuO system presents two invariant points (the eutectic at 942 °C and $x_{Ag} = 0.99$ and a monotectic at 967 °C and $x_{Ag} = 0.36$) and two-phase liquid miscibility gap extending between these two points. Most basic Ag–CuO wetting research has been carried out on Al_2O_3 or ZrO_2 (Kim, Hardy, & Weil, 2005a,b; Schuler et al., 2000; Weil, Coyle, Darsell, Xia, 2005; Weil, Kim, & Hardy, 2005). Further refinements to the basic technology include the addition of low levels of TiO_2 to the basic Ag–CuO braze formulation to improve wetting (Kim et al., 2005b; Weil, Kim, Hardy, & Darsell, 2006a) or Pd, in an attempt to increase the upper limit temperature of the braze (Darsell, Hardy, Kim, & Weil, 2006; Weil, Kim, Hardy, & Darsell, 2006b). Other efforts comprise incorporating aluminum into the Ag braze to avoid the high-temperature embrittlement of silver occurring due to the reaction of hydrogen and oxygen dissolved in it when simultaneously exposed to dual reducing/oxidizing atmospheres in SOFC applications. As aluminum has higher oxygen affinity than hydrogen, it preferentially reacts with oxygen dissolved in the silver. Unlike the sealing techniques, based primarily on high-temperature glasses, the RAB joints exhibit excellent thermal cycling performance and long-term stability in both high-temperature oxidizing and reducing atmospheres (Weil, Coyle, et al., 2005; Weil, Kim, et al., 2005).

2.07.5.2.3 Other Braze Alloys

There is a whole range of commercially available Au-based alloys (35–80 wt.% of Au) mostly alloyed with Cu that show liquidus temperatures of 910–1010 °C (**Table 1**). They are usually nonactive metal compositions and therefore suitable for brazing to metalized ceramic substrates. There are also commercial AMB based on Au (Gold–ABA–V, Gold–ABA and Nioro–ABA from Wesgo Metals) with 80 wt.% Au, the rest Ni, and with either V or Ti as the active metal. The Au-based alloys have been used for brazing ceramics to a lesser extent than Ag- and Ag–Cu- based alloys. Au–15.5Ni–1.75V–0.75Mo alloy (Nioro-ABA) has been used for brazing Si_3N_4 (Peteves, S. D., Paulasto, M., Ceccone, G., & Stamos, V. (1998)) and Al_2O_3 (Rijnders & Peteves, 1999) achieving high-joint strengths. The formation of VN was reported in the case of Si_3N_4 whereas no reaction layer between the ceramic and braze alloy was found for Al_2O_3. Recent studies on Si_3N_4 ceramics brazing using Au–Ni–V (Zhang & Sun, 2010) and Au–Ni–Pd–V fillers (Sun, Zhang, Geng, Ikeuchi, & Shibayanagi, 2011) analyze the evolution of the bonding interlayer with brazing temperature and V content. The mechanical metallization of Si_3N_4 with Ti has been employed as an alternative route to deposit active metallic films prior to brazing with stainless steel using 82Au–18Ni (wt%) eutectic alloys (Do Nascimento & Martinelli, 2005). Good bonds have also been obtained for ZrO_2/ZrO_2 and ZrO_2/stainless steel AMB with Au-based fillers (gold–ABA and gold–ABA–V) (Singh, Shpargel, & Asthana, 2007).

The most widely used Cu-based alloy for ceramics is the copper-ABA (Wesgo metals, **Table 1**) with 92 wt.% Cu and the rest Ti, Al and Si, which has a liquidus temperature of 1025 °C, but different experimental Cu-based alloys with higher and lower melting points have also been developed. Durov, Kostjuk, Shevchenko, and Naidich (2000) reported high-strength ZrO_2/metal joints using a range of Cu–Ga and Cu–Sn alloys with Ti and V as active elements. Lin, Chen, and Shiue (2001) have discussed the wettability of Cu–Sn–Ti alloys on alumina for Ti content varying from 6 to 12 wt.%, proposing that 9 wt.% Ti was optimum. Si_3N_4 ceramics was joined to itself using different Cu-based filler alloys, such as (CuZn)(85)Ti-15 (Zhang, Liu, Naka, Meng, & Zhou, 2004) and Cu68Ti20Ni12 (Zou, Wu, & Zhao, 2005) and, recently, a Cu–Pd–Ti filler alloy (Liu, Zhang, Zhou, Meng & Naka, 2008; Zhang, Guo, Naka, & Zhou, 2008). The important role of Ti on the interfacial reaction is demonstrated in all of them, reporting formation of TiN and/or Ti_2N on the ceramic side and Cu solid solution at the center of the joint, in which some precipitates were observed.

Ni-based alloys (Ni–Cr–Si, Ni–V or Ni–Ti) have also been used for brazing ceramics, mainly Si_3N_4 and SiC (Hadian & Drew, 1996; Mao, Li, & Yan, 2008). Good wettability to Si_3N_4 substrates has been reported for Ni–V braze alloys if the V content is in excess of 34.5 wt.% (Xiong, Chen, et al., 2007), and to SiC for Ni–Cr alloys within the Cr content range of 10–60 wt.% (Mao, Mombello, & Baroni, 2011).

Co-based and Pd-based braze alloys have conventionally been thought for ultra-high-temperature applications such as those found in gas turbines or heat exchangers. SiC ceramics have been brazed to itself and to Ni-based superalloys with a series of experimental alloys based on CoFeNi(Si,B)–Cr–Ti (Xiong, Mao, et al., 2007; Xiong, Mao, Xie, et al., 2007). SiC/SiC joints showed a good strength at room temperature which was retained up to 1000 °C but strong chemical interfacial reactions and a large CTE mismatch limited the bond strength of SiC/Ni-based superalloys. Vanadium has been added to both Co- and PdNi-based alloys and used to join SiC (Xiong, Chen, et al., 2007). Other Pd alloys based on PdCu–Nb have been used to join Si_3N_4 to metals, producing bond strengths of up to 150 MPa (Chaumat, Drevet, & Vernier, 1997).

A new family of brazes purposely designed to join SiC/SiC composites is the BraSiC™ group (Fernie et al., 2009), including an Si–Co alloy with Co ranging from 1 to 18 wt.% and compositions based on binary Si alloys with Ce, Ir, Re, and Ru. The BraSiC™ family are nonreactive brazes which nevertheless have low contact angles on SiC.

2.07.5.2.4 Other Specific Liquid-Phase Joining Techniques

Glass-to-metal sealing is also included in liquid-phase joining techniques. Although now a mature technology, in recent years, there has been increasing interest in glass- and glass–ceramic-to-metal seals for SOFCs and coatings on titanium for biomedical applications. Excellent and comprehensive reviews on this topic can be found in the literature (Donald, 2009; Donald, Mallinson, Metcalfe, Gerrard, & Fernie, 2011; Fergus, 2005).

Another type of liquid-phase bonding method is based in the self-propagating high-temperature synthesis (SHS) technology. The classical example of SHS joining has its roots in the thermite process in which the powders are converted to liquid iron and alumina after ignition. Successful joining of SiC to itself and to Ni-based superalloys using SHS has been achieved with TiC–Ni functionally graded materials as filler and a tungsten sheet as an intermediate layer. The strength of brazed specimens increased with increasing thickness of the tungsten layer, as it effectively improved the distribution of process-induced thermal stresses in the joints, achieving strengths about 60% of that of the parent SiC (Li, Zhou, Duan, Qiu, & Zhang, 2003). A nickel aluminide reactive interlayer was used to join Si_3N_4 and FeCr alloy, attaining an average shear strength of 94.3 MPa (Jadoon, 2004). A similar approach was used to coat metallic pipes with an Al_2O_3–TiO_2–TiC multiphase ceramic layer joined with an intermediate intermetallic layer of AlFe–AlCrFe–NiFe, situated between the base metal and the ceramic layer (Meng et al., 2007).

Recently, novel reactive Al–Au nanomultilayered foils have been developed for rapid joining of similar and dissimilar materials, by using the multilayered nanofoils and two layers of braze (Raic et al., 2009). The thickness of the reactive foils was in the range 10–100 nm and contained many nanoscale layers alternated between materials with high mixing heats, such as Al and Au. The heat generated in the reactive nanofoil allows fast melting of the two layers of braze decreasing significantly the brazing time.

2.07.6 Joining through Ceramic and Glass Interlayers

Both types of joining will be treated together although it can fall into different categories such as PTLP or solid-state diffusion, depending on the occurrence of a liquid phase. Joining by interposing ceramic, glass interlayers or mixture of both has been essentially applied for self-joining ceramics looking for joints that are able to sustain high temperatures. The method has mostly been used for nonoxide ceramics and considers joining adhesives with compositions close to those typically used for the sintering of Si_3N_4 or SiC ceramics (Esposito, Bellosi, & Landi, 1999; Mecartney, Sinclair, & Loehman, 1985). These additives can be applied as a ceramic ink or slurry of the mixed powders that melt when heated, then wetting the ceramic parts and generally producing good bonds.

For joining Si_3N_4 materials, interlayer with compositions mix of different oxides like MgO–Al_2O_3–SiO_2 (Mecartney et al., 1985) or Y_2O_3–Al_2O_3–SiO_2 (Glass et al., 1998), and in some cases with Si_3N_4 additions (Xie, Mitomo, Huang, & Fu, 2000), have been used to achieve bonding interfaces of similar composition to the grain-boundary glassy phase of Si_3N_4 ceramics. Alternatively, the use of Al_2O_3 has been restricted to avoid formation of low viscosity liquids and just mixtures of rare-earth oxides and SiO_2 were applied as interlayers (Sainz, Miranzo, & Osendi, 2002). Relatively high strengths (around 600 MPa) that are maintained up to temperatures of 1000 °C have been reported for this joining method (Glass et al., 1998).

For SiC materials, glass forming interlayers with compositions of different mixtures, namely SiO_2–Al_2O_3–Y_2O_3, SiO_2–Al_2O_3–MgO and CaO–Al_2O_3, have been employed (Ferraris, Salvo, Casalegno, Ciampichetti, Smeacetto, & Zucchetti, 2008) looking for CTE close to the parent material and also resistance to radiation to meet nuclear applications needs. These powders mixtures have been previously reacted to form a glass that is applied as powdered glass slurry to the SiC parts. After joining, the glassy interlayer often disappears as glass infiltrates and becomes part of the ceramic microstructure. In the case of the CaO–Al_2O_3 mixtures, a glass–ceramic bonding interlayer was obtained (Ferraris, Salvo, Isola, Montorsi, & Kohyama, 1998). One variation of the method is the NITE (nanoinfiltration transient–eutectic-phase sintering) process that uses nanoparticles of SiO_2, Al_2O_3, and Y_2O_3, sometimes with SiC additions, to reduce shrinkage (Nozawa et al., 2009). Shear strengths in the range of 200–250 MPa were reported for the last type of joining.

Another method described for SiC using a ceramic interlayer consisted on tape casting a paste of SiC plus C with organics and later infiltration with molten Si that reacted with the C phase to form SiC (Rabin, 1990). Based on a similar reaction, Si_3N_4 was joined using a polyethylene film that after heating left C residues that reacted with the parent Si_3N_4 producing an SiC interlayer plus nitrogen. Flexural strengths of 200 MPa that kept constant up to 1200 °C (Nakamura Kubo, Kanzaki, & Tabata, 1987) were observed. A reaction forming process (Singh, 1997, 1999) has been used for joining SiC-based ceramics and fiber-reinforced ceramic matrix composites. In this process, a carbonaceous mixture is firstly applied on the joint area, holding the items to be joined in a fixture, and curing at 110–120 °C. Then, silicon or a silicon alloy in tape, paste, or slurry form is applied around the joint region and the whole assembly is heated to 1250–1425 °C for silicon or silicon-refractory metal alloy melting, infiltrating and reacting with carbon to form SiC. Joint thickness can be readily controlled through adjustments of the properties of the carbonaceous paste and the applied fixturing force. A variant on this methodology is the use of electrophoretic deposition of slurry containing SiC powders and a carbonaceous material (Lessing, Erickson, & Kunerth, 2000).

Within this group is joining using preceramic polymers that when polymerized at 1000 °C transform into amorphous ceramics, which crystallizes if treated at higher temperatures. Polymers such as polycarbosilanes or

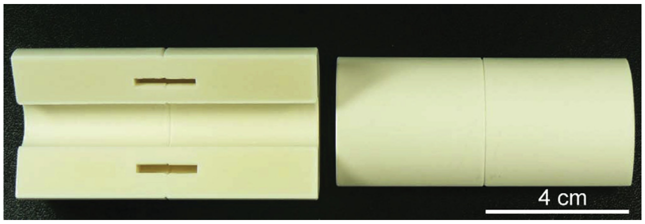

Figure 14 Photograph of an Al_2O_3 nozzle shaped with an internal circular channel joined at the middle part and its side view. Pieces were joined in green state with a paste of Al_2O_3 powders and polymeric additives that confer plasticity; green surfaces of the Al_2O_3 tube were coated with an organic to avoid fluid migration from the paste. The joined green parts were then sintered at 1650 °C (Han, 2011).

silicone resins (Pippel, Woltersdorf, Colombo, & Donato, 1997) have been used as interlayer in the joining of SiC, although the second was more effective. In fact, a bonding interlayer of an amorphous silicon oxycarbide ceramics formed at 1200 °C with strengths of 220 and 39 MPa in flexure and shear tests, respectively (Colombo Sglavo, Pippel, & Woltersdorf, 1998).

Different from the above methods is the green state joining that is commonly used in the clay-based ceramic industry to produce complex parts. Unfortunately, this method cannot be used for advanced ceramics as they do not have the required plasticity. However, some recent studies (Zheng & Akinc, 2001) have shown that by using a liquid polymer precursor, and adding SiC powders to the bonding paste, a joining interface indistinguishable from the matrix was achieved without the need of an applied pressure. Average bend strength of 323 MPa, comparable to that of the parent material was measured. A similar green joining process has been developed for Al_2O_3 ceramics (**Figure 14**), which uses an alumina slurry containing additives to confer plasticity to the interlayer and a previous coating of the surface of the green bodies to eliminate the excessive drying of the paste due to capillary pressure, thus large pieces and complex shapes can be joined with this method (Han, 2011).

2.07.7 Development of Residual Thermal Stresses

Since most metals have larger CTE (**Figure 3**) and lower elastic modulus than ceramics, large residual stresses often develop around the interfacial region, which are not totally relieved when cooling from the joining temperature. Residual stresses play a main role in the mechanical integrity of joints, since they may induce plastic deformations in the metal side and cracking in the ceramic side. The problem of determining the thermal stresses of joined interfaces and how they affect the strength values is very complex and there are not analytical models that can explain the effect of all the involved parameters, namely plastic deformation, system geometry and cooling pattern. Normally this problem is approached by numerical simulation using FEA, which also provide useful designing criteria and likely reduce the experimental workload.

For common but type symmetrical joints (ceramic–metal–ceramic) and away from the joint-free surface, the stresses parallel to the interface are commonly tensile in the metal side of the joint and compressive in the ceramics (Kirchner, Conway, & Segall, 1987), decreasing to zero toward the free edge. On the other hand, stresses normal to the interface are near zero throughout the joined elements except for a local near-surface region of the interface, where tensile stresses in the ceramics and compressive stresses in the metal develop (**Figure 15**). In fact, maximum tension in ceramics occurs near the free edge of the interface, where the stresses are singular (Kovalev et al., 1998). The concern about the validity of the peak thermal stresses calculated close to the interface singularity has been addressed by some authors, proposing different methods to deal with it, either by using finer meshing and comparing to analytical results (Kovalev et al., 1998) or by using the strain energy in the ceramics as a metric for failure (Park, Mendez, & Eagar, 2002). This tensile stress developed in the ceramic part may be the most important in affecting failure characteristics of the joint, often provoking the fracture of the ceramics at the edges and corners of interfaces (Park et al., 2002).

The influence of the metal interlayer thickness on thermal stresses developing has been predicted by FEA analysis. For Si_3N_4 ceramics joined using Ni interlayer (**Figure 16**), calculations indicated that below a given thickness ratio of the ceramic to the metal foil stresses did not change when decreasing interlayer thickness (Kovalev et al., 1998). Conversely, for nonsymmetric joints of the type Al_2O_3/Ni superalloy with Ni interlayer, computed stresses decreased with interlayer thickness (Hattali, Valette, Ropital, Mesrati, & Treheux, 2009). For these types of antisymmetric joints, FEA calculations including creep deformation of the metal part resulted in

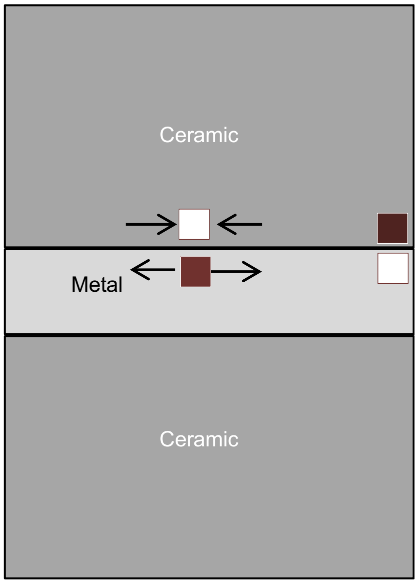

Figure 15 Drawing representing two ceramics bonded with a metallic interlayer and showing location of thermal elastic stress built-up around the interfacial region: compressive in the ceramic central section and in the metal corner, but tensile in the central metal side and in the ceramic corner (Kovalev et al., 1998).

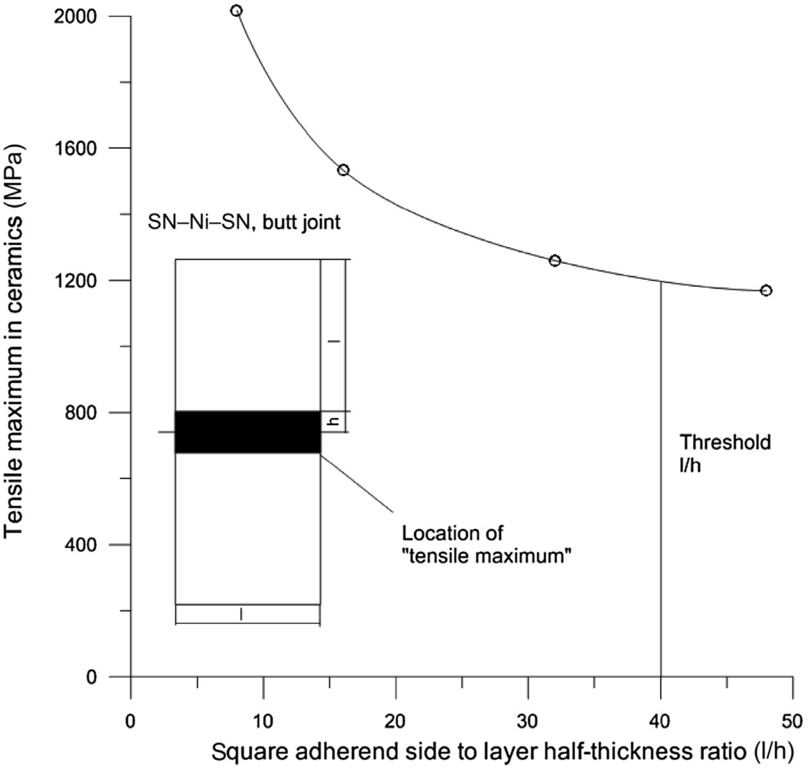

Figure 16 The influence of interlayer-to-ceramics thickness ratio on the tensile maximum of the ceramic side for an Si_3N_4–Ni–Si_3N_4 joint is represented. In the range of thin interlayers, this tensile maximum experiences insignificant influence of the layer thickness (Kovalev et al., 1998).

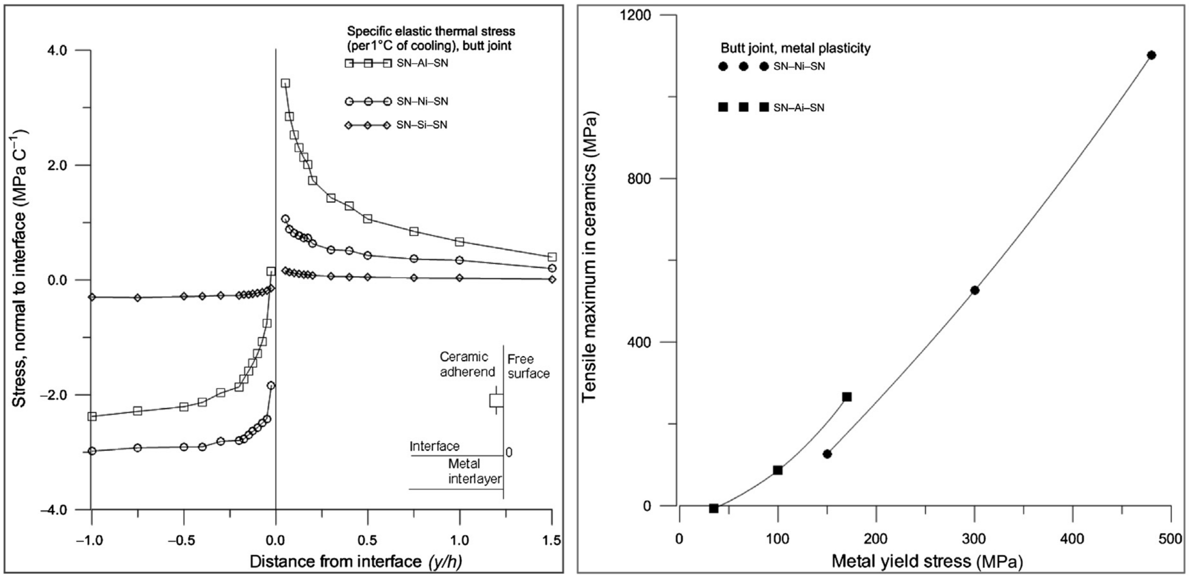

Figure 17 Comparison of surface elastic stress distribution near the interface-free edge per degree of cooling for an Si_3N_4 joint with different interlayer—Ni, Al and Si—showing their direct correlation with CTE mismatch (left). Relationship of the tensile maximum in the ceramics for different assumed values of metal yield stress computed for Ni and Al interlayers with no strain hardening (right) (Kovalev et al., 1998).

an increase of the residual stresses in the joining region, conversely to results for the symmetric Al_2O_3 joints with Ni interlayer that showed no difference by allowing creep deformation.

The effects of CTE and yield stress of the metal interlayer on the residual stresses have also been attempted using FEA methods, generally showing that selecting metal interlayers of low-yield stress and with CTE closer to the ceramic counterparts was beneficial for reducing thermal stresses (**Figure 17**). FEA has also been helpful in predicting stresses of complex joints with multilayered structures of alternating ductile and rigid interlayers, which accordingly reduced strain energy in the ceramic part by redistributing the stress and plastic strain if layers were properly arranged (Park et al., 2005).

Another important parameter influencing residual stresses is the geometry of the joint. In particular, it has been shown that elastic stresses in the ceramic side increased for lap joints compared to butt type joints of similar dimensions. Similarly, surface tensile stresses, measured near the interface using strain gages in asymmetric Si_3N_4/metal joints, were relatively smaller for cylindrical specimens compared to specimens having square corners and, besides, maximum stresses increased with the size of the joined area (Suganuma, 1990).

The effect of using graded interlayers for joining ceramic to metal parts in reducing stresses compared to a sharp interface has been investigated in Al_2O_3/Ni joints by computing stresses and plastic strains near the radial-free surface (Williamson, Rabin, & Drake, 1993). Analyses showed that the most significant reduction occurred for the shear component of the stress and equally for the shear plastic strain.

To validate computed results about residual stress distributions in ceramic–metal joints, commonly strength tests are carried out and results compared to maximum tensile stresses predictions. However, techniques like neutron diffraction (Martinelli et al., 1999; Vila et al., 2007) and high-energy XRD (Vila et al., 2005) can provide accurate deformation maps of the interface region, which seem more valuable for validating the results of analytical tools. Actually, high-energy XRD data can probe very small scattering volumes (typically $0.05 \times 1 \times 1$, in millimeters); consequently, the strain field can be determined with quite small position uncertainty, although due to X-ray absorption, specimen size should be about 1cm^3, whereas scattering volume for neutrons is about 1mm^3 and probed samples can have sizes in the order of tens of cubic centimeters (Vila et al., 2005). Strain analysis using low-energy X-ray sources has also been reported but data are restricted to a small zone typically $<10\ \mu\text{m}$ near the free surface (Hattali, Valette, Ropital, Mesrati, & Treheux, 2010).

The measurements of strains by diffraction techniques relay on the evidence that crystalline lattice spacing varies under stress (either tensile or compressive). This change can be detected as a shift in the angle at which the diffraction peaks appear, and by using diffraction Bragg's equation, the relative variation of the actual lattice spacing with respect to the strain-free spacing is translated into strain (Vila et al., 2007). These methods provide

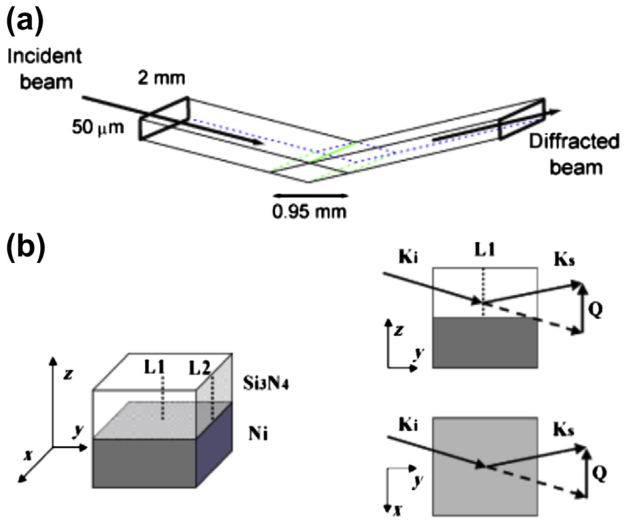

Figure 18 (a) Scheme of the scattering geometry and approximate scattering volume for Si_3N_4 (301)-diffraction peak for 60 keV incident X-rays and slit dimensions of 2 mm by 50 microns. (b) Perspective of selected—L1 and L2—scanning lines on the ceramic side approaching the joining interface with the metal, the metal side is too absorbent to allow measurement. The 2D schemes show the relative arrangement of the incident X-ray beam (Ki), the diffracted beam (Ks) and the transferred momentum (Q) (Vila et al., 2005).

the strain in the direction of the transferred moment (**Figure 18**) and specimens should be correspondingly aligned to obtain the different spatial components.

2.07.8 Testing the Joining Strength

At present, there are no universal methods for determining bond strength in joined ceramic–ceramic or ceramic–metal parts. The most commonly used testing configurations are bending and shear tests, and in lesser extension tensile tests. For the measurement of tensile joining strength, the main difficulties derive from the correct sample preparation and appropriate loading configuration to avoid bending effects.

Different types of shear tests have been employed (**Figure 19**), being interfacial shear strength simply obtained by dividing the fracture load by the joined surface area. A standard for testing shear strength of ceramic joints has recently been proposed (ASTM C1469-10). The main drawback of some of these methods is to assure that pure shear loading occurs but the key advantage of these methods is that specimens can be relatively small (**Figure 20**) and in some cases, joined specimens can be tested at once without further machining. The three- and four-point bending tests are also well accepted, as they are typically used for strength testing of bulk ceramics, and also have a corresponding standard method (ASTM C1161). Joint strengths are estimated from usual elastic expressions derived from bending theory of beams. Two main specimen types can be probed by these methods, the symmetric ceramic–ceramic and the ceramic–metal bars, in both cases the joint interface is at the middle of the test bar. In the case of the asymmetric test bars, caution should be taken when applying typical bend strength equations, as the stress distribution may not be symmetric (Galli et al., 2006). Commonly, specimens of the required geometry are machined and conditioned from larger joined parts.

Results for strength depend on the testing geometry employed; shear data often representing the lowest figure. Comparison among strength results for Si_3N_4/Inconel bonds using an Ag–37Cu–5.5Ti (in at.%) brazing alloy carried out under shear, tensile, three- and four-point bending configurations showed average strength values of 178, 233, 321, and 344 MPa, respectively (Lee, 1997). The negative sign of the difference between three- and four-point bending configurations was also observed for Si_3N_4/Si_3N_4 and Si_3N_4/304 stainless steel joints brazed with the same brazing alloy (Lee, 1997), in contradiction to what occurs for monolithic ceramics. Furthermore, data dispersion analyzed following Weibull statistics indicated that for three-point bending and tensile tests strength showed minor scattering than the shear and four-point bending tests. For high-temperature strength determination, bending and also shear are the preferred testing methods.

Inspection of tested bars shows that fracture often takes place along the joined interface or in the ceramic side near the interface, depending on the residual stresses developed and on the possible interfacial reactions

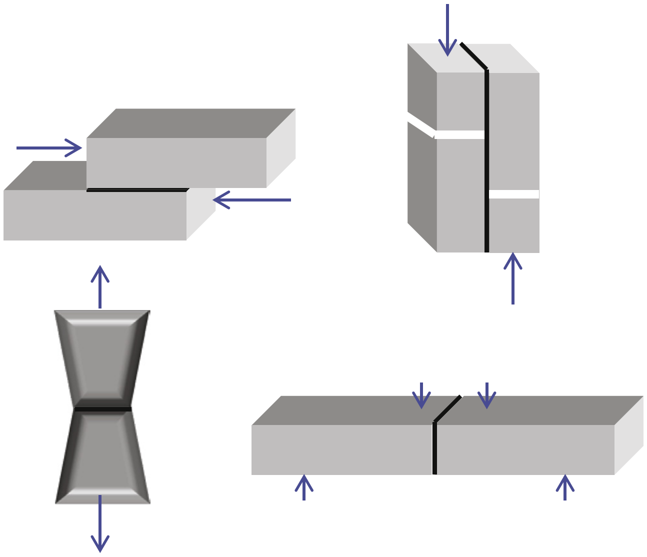

Figure 19 Illustration showing common configurations for bonding strength testing; two shear geometries are seen at the top, and four-point bending and tensile configurations at the bottom.

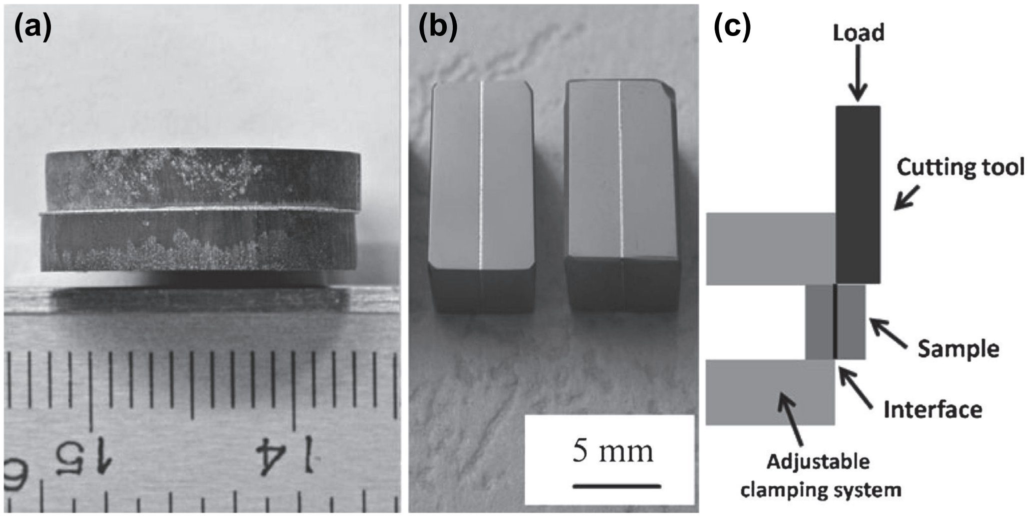

Figure 20 (a) Photograph of two SiC pieces joined at 1300 °C with multiple interlayers, Mo foil with layers of an Ni–Si alloy at both sides. (b) Specimen sectioned from the joined part for shear test. The scheme of the testing configuration is also shown in (c) (Liu et al., 2010).

(Figure 21). Therefore, a clear relationship between the strength level and the crack path cannot be drawn as opposite trends have been reported in the bibliography (Blugan et al., 2004; Kim, Chang, & Park, 2001; Park et al., 2002).

2.07.9 Examples and Applications

There is a general consensus that joining technologies can drive a wider range of applications for ceramics in the industry. A knowledgeable list of applications of ceramic joining technologies has recently been published (Fernie et al., 2009) making reference to the particular joining method involved. Among ceramic engineering applications that require joining technologies, we can highlight the use of Al_2O_3 substrates for electronic packaging where brazing methods are customary and also ZrO_2 ceramics for SOFC systems, which precise seals

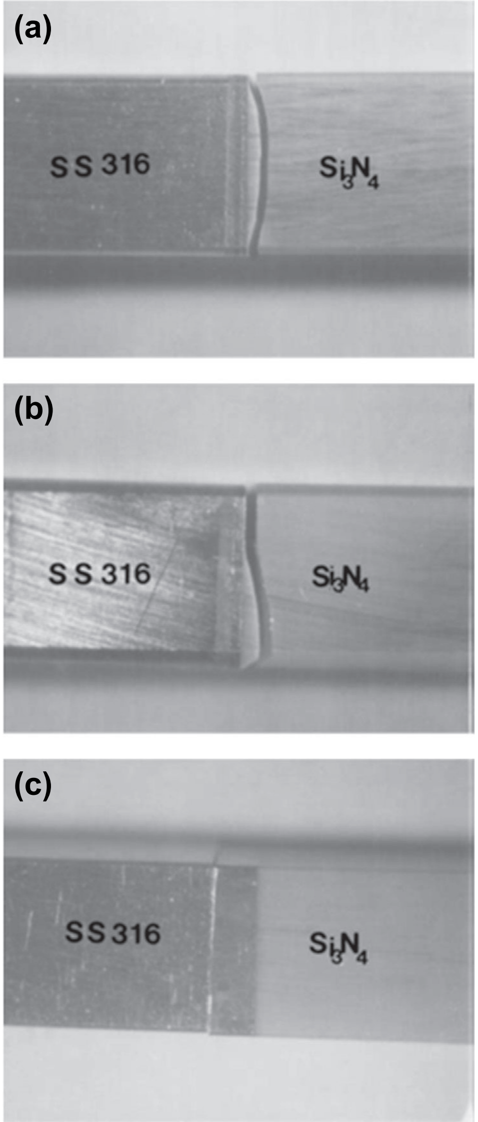

Figure 21 Different types of crack paths observed for Si_3N_4 joined to stainless steel, which corresponded to (a) low-, (b) intermediate- and (c) high-strength values (Kim et al., 2001).

and bonds for joining to metallic interconnectors (Smeacetto, Salvo, Ferraris, Casalegno, & Asinari, 2008). In the packaging of high-power SiC electronics devices which operate at higher temperatures than usual electronic systems (>350 °C), die attaching is an important step. For this purpose, SiC devices have been bonded by the TLP method to Si_3N_4 and Cu heat sink (Mustain, Brown, & Ang, 2010). The use of ceramics for sensors and all types of electronic displays in cars is steadily increasing as well (Okada, 2008).

In the steel-making and aluminum-casting industries, to enhance wear resistance of tubes and blowers used for transferring powders, Al_2O_3 is commonly bonded to inner steel tubes, although S_3N_4 is increasingly used for parts working under more severe environments (Gugel & Woetting, 1999; Okada, 2008). Solid solution of Si_3N_4 phase (SiAlON) stalks and sleeves for the transfer of molten aluminum in the low-pressure casting process have been employed with increased productivity; the stalks are attached to metallic ends, whereas SiAlON sleeves are inserted into metallic tubes for Al die casting (Okada, 2008).

Ceramic components for automotive parts were developed during the 1980s, like the ceramic turbocharger rotor, combustion chamber or glow plugs, all requiring joining technologies; although most of these developments were successful, they have not come into mass car production. Nevertheless, needs for wear-resistant and low-friction parts are still held (Okada, 2008). That is, for example, the case of ceramic tappets that are joined to the steel shaft by brazing methods (Matsuo, Ito, & Taniguchi, 1999).

Applications as cutting tools and drilling parts are important for Al_2O_3 and Si_3N_4 ceramics, which also require joining technologies for housing moving structures.

High-performance Si_3N_4 materials and SiC composites have been investigated to increase effectiveness and performance of gas turbines for aviation and power generation systems (van Roode, 2010). R&D programs on ceramics turbines focusing on higher efficiency and lower emissions have been implemented in many countries (Okada, 2008). Joining methods are applied for the turbine rotors and turbine nozzle, using shrink-fitting and tapper-fit joints, respectively (Foley, 1999). Applications of ceramics in nuclear fusion reactors are important for SiC/SiC composites (Lewinsohn, Jones, Colombo, & Riccardi, 2002). The NITE process has been applied for these composites as shown in **Figure 22** for a tube joint, where joined area shows the same composition as the parts. With this technology, the channel structure of a heat exchanger unit was fabricated (Nozawa et al., 2009). Another example can be seen in **Figure 23** for a gas-cooled reactor where SiC parts are brazed by the BraSiC™ process (www.liten.cea.fr).

Ceramics also find applications as biomedical implants in both dental restoration and femoral prosthesis, where joining is a basic issue. The materials of relevance are in this case Al_2O_3 and ZrO_2 (Hamadouche, Boutin, Daussange, Bolander, & Sedel, 2002; Manicone, Iommetti, & Raffaelli, 2007) although Si_3N_4 materials have received recent attention as bearing for hip implants (**Figure 24**) (Bal et al., 2009). The direct bonding of the

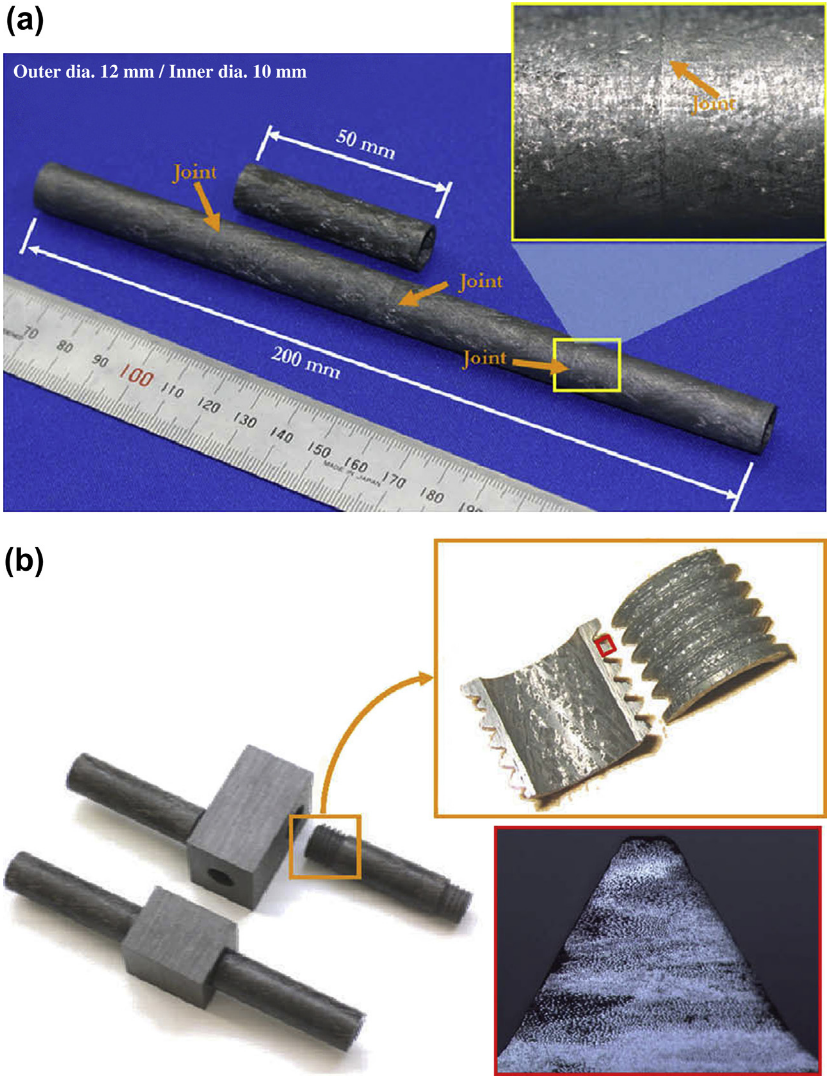

Figure 22 Image with different joints types in SiC/SiC composites for nuclear applications: (a) a 200-mm-long tube obtained by joining smaller parts using the NITE process and (b) a screw-threaded joint of this material (Nozawa et al., 2009).

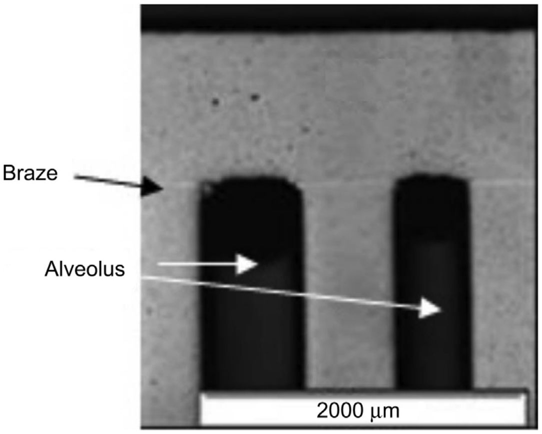

Figure 23 Details of the modular structure of an experimental gas-cooled SiC reactor joined with a brazing alloy (BraSiC). Reproduced courtesy of CEA Liten. (www.liten.cea.fr)

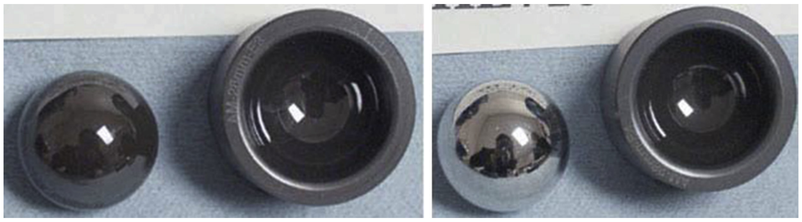

Figure 24 Images of Si_3N_4–Si_3N_4 (left) and Si_3N_4–CoCr (right) bearing couples investigated for total hip arthroplasty due to their favorable wear behavior (Bal et al., 2009).

ceramic ball to the metal stem using a modular approach with tapper design is preferred for hip implants (Heimke, 1994; Rahaman, Yao, Bal, Garino, & Ries, 2007). Conversely, glass formulations have been used for joining ZrO_2 and Al_2O_3 ceramics to veneer porcelain for all ceramic dental restorations as alternative to resin bonding (Ashkanani, Raigrodski, Flinn, Heindl, & Mancl, 2008; Saied, Lloyd, Haller, & Lawn, 2011).

2.07.10 Concluding Remarks

In this chapter, a full account of the existing joining technologies applied to hard ceramic materials has been reviewed. The many aspects of this wide topic have been covered, such as the chemical reactivity and wetting of the mating surfaces, the characterization and modeling of the bonding interface, the development of residual stresses, and the mechanical integrity of the joints. It can be said that the essentials of joining are well established, even though the mechanisms of interface formation remain as a matter of fundamental and experimental research. More technological aspects of joining methods like the prediction of residual stresses and of course, the methods for reducing them, as they play a major role on the mechanical integrity of joints, are a subject of continuous advance. Finally, the development of new/better joining procedures focused on producing joints that can sustain higher temperatures, harsh conditions, mechanical loads, may present biocompatibility, have sealant characteristics, etc., are the driving forces for the research in this field.

The current trends in joining deal with the use of multiple layers between the parent materials with different functionalities like strain reduction, increased reactivity or reinforcing purposes. These layers are often metallic but can also include glass or ceramic structures, like in the cases of the ceramic particles or fibers incorporated in brazing alloys as reinforcements or the multilayer architecture approach of TLP bonding that provides a liquid at reduced temperatures to favor bonding that, afterward, rapidly disappears. As reducing costs is another important issue to be considered, recent development of RAB technology allows overcoming the use of inert gas or vacuum during AMB brazing.

Innovative joining techniques for nonoxide ceramics based on ceramic or ceramic/metal interlayers for high-temperature applications have raised much interest. That is the case of novel reactive multilayered foils based on the SHS approach for rapid joining of similar and dissimilar materials, the NITE process that reduces shrinkage and the reaction-forming processes focused on producing high-refractory SiC ceramic joints. Within this group stands the use of preceramic polymers as joining interlayer, which also presents notable perspectives.

The green state joining that allows producing large pieces and complex shapes is noteworthy. By inducing the required plasticity, the method can be extended to advanced ceramics using either liquid polymer precursors or additives to confer plasticity to the slurries.

For a true optimization of the joining structure, modeling must advance in parallel to experiments providing guidelines that allow minimizing the workload. At the end, the selection of a particular joining method is constrained by the intended applications, which cover exciting areas of interest like electronic packaging, high-power electronics, SOFC systems, biomedical implants and high-temperature ceramic components for automotive parts, fusion reactors or aviation and static gas turbines.

Acknowledgments

The authors thank the financial support of the Spanish Ministry of Science (Materials Program) through different projects over the years. We also recognize the colleagues with whom we have collaborated in the course of these years on this topic.

References

Akashi, T., Nukui, T., & Kiyono, H. (2009). Liquid-phase oxidation joining of oxide ion conducting ceramics via Al/heat resistant alloy/Al multilayer interlayers. *Journal of the Ceramic Society of Japan, 117*, 983–986.

Akselsen, O. M. (1992a). Advances in brazing of ceramics. *Journal of Materials Science, 27*, 1989–2000.

Akselsen, O. M. (1992b). Diffusion bonding of ceramics. *Journal of Materials Science, 27*, 569–579.

Arroyave, R., & Eagar, T. W. (2003). Metal substrate effects on the thermochemistry of active brazing interfaces. *Acta Materialia, 51*, 4871–4880.

Ashkanani, H. M., Raigrodski, A. J., Flinn, B. D., Heindl, H., & Mancl, L. A. (2008). Flexural and shear strengths of ZrO_2 and a high-noble alloy bonded to their corresponding porcelains. *Journal of Prosthetic Dentistry, 100*, 274–284.

Bal, B. S., Khandkar, A., Lakshminarayanan, R., Clarke, I., Hoffman, A. A., & Rahaman, M. N. (2009). Fabrication and testing of silicon nitride bearings in total hip arthroplasty winner of the 2007 "HAP" PAUL award. *Journal of Arthroplasty, 24*, 110–116.

Bhanumurthy, K., & Schmidfetzer, R. (1996). Solid-state reaction bonding of silicon carbide (HIP-SiC) below 1000 °C. *Materials Science and Engineering A-Structural Materials Properties Microstructure and Processing, 220*, 35–40.

Blugan, G., Janczak-Rusch, J., & Kuebler, J. (2004). Properties and fractography of Si_3N_4/TiN ceramic joined to steel with active single layer and double layer braze filler alloys. *Acta Materialia, 52*, 4579–4588.

Blugan, G., Kuebler, J., Bissig, V., & Janczak-Rusch, J. (2007). Brazing of silicon nitride ceramic composite to steel using SiC-particle-reinforced active brazing alloy. *Ceramics International, 33*, 1033–1039.

Bocanegra-Bernal, M. H., & Matovic, B. (2010). Mechanical properties of silicon nitride-based ceramics and its use in structural applications at high temperatures. *Materials Science and Engineering A-Structural Materials Properties Microstructure and Processing, 527*, 1314–1338.

Brochu, M., Pugh, M. D., & Drew, R. A. L. (2004). PTLPB of Si_3N_4 to FA-129 using nickel as a core interlayer. *International Journal of Refractory Metals & Hard Materials, 22*, 95–103.

Burger, K., Mader, W., & Ruhle, M. (1987). Structure, chemistry and diffusion bonding of metal ceramic interfaces. *Ultramicroscopy, 22*, 1–13.

Ceccone, G., Nicholas, M. G., Peteves, S. D., Tomsia, A. P., Dalgleish, B. J., & Glaeser, A. M. (1996). An evaluation of the partial, transient liquid phase bonding of Si_3N_4 using Au coated Ni-22Cr foils. *Acta Materialia, 44*, 657–667.

Chaumat, G., Drevet, B., & Vernier, L. (1997). Reactive brazing study of a silicon nitride to metal joining. *Journal of the European Ceramic Society, 17*, 1925–1927.

Chawla, K. K. (2003). *Ceramic matrix composites* (2nd ed.). Dordrecht, The Netherlands: Kluwer Academic Publishers.

Chen, Z., Cao, M. S., Zhao, Q. Z., & Zou, J. S. (2004). Interfacial microstructure and strength of partial transient liquid-phase bonding of silicon nitride with Ti/Ni multi-interlayer. *Materials Science and Engineering A-Structural Materials Properties Microstructure and Processing, 380*, 394–401.

Chuang, T. H., Yeh, M. S., & Chai, Y. H. (2000). Brazing of zirconia with AgCuTi and SnAgTi active filler metals. *Metallurgical and Materials Transactions A-Physical Metallurgy and Materials Science, 31*, 1591–1597.

Cockeram, B. V. (2005). Flexural strength and shear strength of silicon carbide to silicon carbide joints fabricated by a molybdenum diffusion bonding technique. *Journal of the American Ceramic Society, 88*, 1892–1899.

Colombo, P., Sglavo, V., Pippel, E., & Woltersdorf, J. (1998). Joining of reaction-bonded silicon carbide using a preceramic polymer. *Journal of Materials Science, 33*, 2405–2412.

Cook, G. O., III, & Sorensen, C. D. (2011). Overview of transient liquid phase and partial transient liquid phase bonding. *Journal of Materials Science, 46*, 5305–5323.

Darsell, J. T., Hardy, J., Kim, J. Y., & Weil, K. S. (2006). Investigation of Pd-Modified Ag-CuO Air Braze Filler Metals. In *Brazing and Soldering: Proceedings of The Third International Brazing and Soldering Conference (April 24-26, 2006)* (p. 167). San Antonio, TX: ASM International.

De Coninck, J., & Blake, T. D. (2008). Wetting and molecular dynamics simulations of simple liquids. *Annual Review of Materials Research, 38*, 1–22.

De Ruijter, M. J., Blake, T. D., & De Coninck, J. (1999). Dynamic wetting studied by molecular modeling simulations of droplet spreading. *Langmuir, 15*, 7836–7847.

Deleeuw, D. (1992). Effects of joining pressure and deformation on the strength and microstructure of diffusion-bonded silicon-carbide. *Journal of the American Ceramic Society, 75*, 725–727.

Do Nascimento, R. M., & Martinelli, A. E. (2005). Microstructure of brazed joints between mechanically metallized Si_3N_4 and stainless steel. *Journal of Materials Science, 40*, 4549–4556.

Donald, I. W. (2009). *Glass-to-metal seals*. Sheffield: Society of Glass Technology.

Donald, I. W., Mallinson, P. M., Metcalfe, B. L., Gerrard, L. A., & Fernie, J. A. (2011). Recent developments in the preparation, characterization and applications of glass- and glass-ceramic-to-metal seals and coatings. *Journal of Materials Science, 46*, 1975–2000.

Durov, A. V., Kostjuk, B. D., Shevchenko, A. V., & Naidich, Y. V. (2000). Joining of zirconia to metal with Cu-Ga-Ti and Cu-Sn-Pb-Ti fillers. *Materials Science and Engineering A-Structural Materials Properties Microstructure and Processing, 290*, 186–189.

Elssner, G., & Petzow, G. (1990). Metal ceramic joining. *Isij International, 30*, 1011–1032.

Esposito, L., Bellosi, A., & Cetlotti, G. (1997). Silicon nitride-nickel joints through diffusion bonding. *Acta Materialia, 45*, 5087–5097.

Esposito, L., Bellosi, A., Guicciardi, S., & De Portu, G. (1998). Solid state bonding of Al_2O_3 with Cu, Ni and Fe: characteristics and properties. *Journal of Materials Science, 33*, 1827–1836.

Esposito, L., Bellosi, A., & Landi, S. (1999). Interfacial forces in Si_3N_4- and SiC-based systems and their influence on the joining process. *Journal of the American Ceramic Society, 82*, 3597–3604.

Essa, A. A., & Bahrani, A. S. (1991). The friction joining of ceramics to metals. *Journal of Materials Processing Technology, 26*, 133–140.

Eustathopoulos, N. (1998). Dynamics of wetting in reactive metal ceramic systems. *Acta Materialia, 46*, 2319–2327.

Eustathopoulos, N. (2005). Progress in understanding and modeling reactive wetting of metals on ceramics. *Current Opinion in Solid State & Materials Science, 9*, 152–160.

Fergus, J. W. (2005). Sealants for solid oxide fuel cells. *Journal of Power Sources, 147*, 46–57.

Fernie, J. A., Drew, R. A. L., & Knowles, K. M. (2009). Joining of engineering ceramics. *International Materials Reviews, 54*, 283–331.

Ferraris, M., Salvo, M., Casalegno, V., Ciampichetti, A., Smeacetto, F., & Zucchetti, M. (2008). Joining of machined SiC/SiC composites for thermonuclear fusion reactors. *Journal of Nuclear Materials, 375*, 410–415.

Ferraris, M., Salvo, M., Isola, C., Montorsi, M. A., & Kohyama, A. (1998). Glass-ceramic joining and coating of SiC/SiC for fusion applications. *Journal of Nuclear Materials, 258*, 1546–1550.

Foley, A. (1999). Ceramic joining applications in gas turbines. *Industrial Ceramics, 19*, 193–195.

Galli, M., Botsis, J., & Janczak-Rusch, J. (2006). Relief of the residual stresses in ceramic-metal joints by a layered braze structure. *Advanced Engineering Materials, 8*, 197–201.

Glaeser, A. M. (1997). The use of transient FGM interlayers for joining advanced ceramics. *Composites Part B-Engineering, 28*, 71–84.

Glass, S. J., Mahoney, F. M., Quillan, B., Pollinger, J. P., & Loehman, R. E. (1998). Refractory oxynitride joints in silicon nitride. *Acta Materialia, 46*, 2393–2399.

Gottselig, B., Gyarmatti, E., Naoumidis, A., & Nickel, H. (1990). Joining of ceramics demonstrated by the example of SiC/Ti. *Journal of the European Ceramic Society, 6*, 153–160.

Greenhut, V. A. (2011). Principles and methods of metal-ceramic bonding for PM applications. *International Journal of Powder Metallurgy, 47*, 57–76.

Gugel, E., & Woetting, G. (1999). Materials selection for ceramic components in automobiles. *Industrial Ceramics, 19*, 196–199.

Hadian, A. M., & Drew, R. A. L. (1996). Strength and microstructure of silicon nitride ceramics brazed with nickel-chromium-silicon alloys. *Journal of the American Ceramic Society, 79*, 659–665.

Hamadouche, M., Boutin, P., Daussange, J., Bolander, M. E., & Sedel, L. (2002). Alumina-on-alumina total hip arthroplasty – a minimum 18.5-year follow-up study. *Journal of Bone and Joint Surgery-American, 84A*, 69–77.

Han, J.-H. (2011). Joining alumina ceramics in green state using a paste of ceramic slurry. *Journal of Materials Processing Technology, 211*, 1191–1196.

Hanson, W. B., Ironside, K. I., & Fernie, J. A. (2000). Active metal brazing of zirconia. *Acta Materialia, 48*, 4673–4676.

Hao, H. Q., Wang, Y. L., Jin, Z. H., & Wang, X. T. (1995). Joining of zirconia ceramic to stainless-steel and to itself using Ag57-Cu38-Ti5 filler metal. *Journal of the American Ceramic Society, 78*, 2157–2160.

Hattali, M. L., Valette, S., Ropital, F., Mesrati, N., & Treheux, D. (2009). Effect of thermal residual stresses on the strength for both alumina/Ni/alumina and alumina/Ni/nickel alloy bimaterials. *Journal of Materials Science, 44*, 3198–3210.

Hattali, M. L., Valette, S., Ropital, F., Mesrati, N., & Treheux, D. (2010). Calculation and experimental determinations of the residual stress distribution in alumina/Ni/alumina and alumina/Ni/nickel alloy systems. *Journal of Materials Science, 45*, 4133–4140.

Heikinheimo, E., Isomaki, I., Kodentsov, A. A., & Vanloo, F. J. J. (1997). Chemical interaction between Fe and silicon nitride ceramic. *Journal of the European Ceramic Society, 17*, 25–31.

Heimke, G. (1994). The safety of ceramic balls on metal stems in hip-arthroplasty. *Advanced Materials, 6*, 165–170.

Hong, S. M., Bartlow, C. C., Reynolds, T. B., Mckeown, J. T., & Glaeser, A. M. (2008). Ultrarapid transient-liquid-phase bonding of Al_2O_3 ceramics. *Advanced Materials, 20*, 4799–4803.

Howe, J. M. (1993). Bonding, structure, and properties of metal-ceramic interfaces 1. Chemical bonding, chemical-reaction, and interfacial structure. *International Materials Reviews, 38*, 233–256.

Jadoon, A. K. (2004). Employing reactive synthesis for metal to ceramic joining for high temperature applications. *Journal of Materials Science, 39*, 593–604.

Janickovic, D., Sebo, P., Duhaj, P., & Svec, P. (2001). The rapidly quenched Ag-Cu-Ti ribbons for active joining of ceramics. *Materials Science and Engineering A-Structural Materials Properties Microstructure and Processing, 304*, 569–573.

Kar, A., Mandal, S., Venkateswarlu, K., & Ray, A. K. (2007). Characterization of interface of Al_2O_3-304 stainless steel braze joint. *Materials Characterization, 58*, 555–562.

Katano, Y., Ando, M., Itoh, T., & Sasaki, M. (1993). Application of ceramics to turbocharger rotors for passenger cars. *Journal of Engineering for Gas Turbines and Power-transactions of the Asme, 115*, 9–16.

Kim, T. W., Chang, H. S., & Park, S. W. (2001). Re-distribution of thermal residual stress in a brazed Si_3N_4/stainless steel joint using laminated interlayers. *Journal of Materials Science Letters, 20*, 973–976.

Kim, J. Y., Hardy, J. S., & Weil, K. S. (2005a). Effects of CuO content on the wetting behavior and mechanical properties of a Ag-CuO braze for ceramic joining. *Journal of the American Ceramic Society, 88*, 2521–2527.

Kim, J. Y., Hardy, J. S., & Weil, K. S. (2005b). Novel metal-ceramic joining for planar SOFCs. *Journal of the Electrochemical Society, 152*, J52–J58.

Kim, J. J., Park, J. W., & Eagar, T. W. (2003). Interfacial microstructure of partial transient liquid phase bonded Si_3N_4-to-Inconel 718 joints. *Materials Science and Engineering A-Structural Materials Properties Microstructure and Processing, 344*, 240–244.

Kirchner, H. P., Conway, J. C., & Segall, A. E. (1987). Effect of joint thickness and residual-stresses on the properties of ceramic adhesive joints 1. Finite-element analysis of stresses in joints. *Journal of the American Ceramic Society, 70*, 104–109.

Klomp, J. T. (1972). Bonding of metals to ceramics and glasses. *American Ceramic Society Bulletin, 51*, 683.

Knowles, K. M., Ormston, D. R., Conquest, D. B., Ecclestone, L. J., & Fernie, J. A. (2003). Particulate loading of high temperature brazes for joining engineering ceramics. *Advances in Joining of Ceramics, 138*, 103–118.

Kovalev, S. P., Miranzo, P., & Osendi, M. I. (1998). Finite element simulation of thermal residual stresses in joining ceramics with thin metal interlayers. *Journal of the American Ceramic Society, 81*, 2342–2348.

Kozlova, O., Braccini, M., Voytovych, R., Eustathopoulos, N., Martinetti, P., & Devismes, M. F. (2010). Brazing copper to alumina using reactive CuAgTi alloys. *Acta Materialia, 58*, 1252–1260.

Kumar, G., & Prabhu, K. N. (2007). Review of non-reactive and reactive wetting of liquids on surfaces. *Advances in Colloid and Interface Science, 133*, 61–89.

Lang, F. Q., Yamaguchi, H., Ohashi, H., & Sato, H. (2011). Improvement in joint reliability of SiC power devices by a diffusion barrier between Au-Ge solder and Cu/Ni(P)-metalized ceramic substrates. *Journal of Electronic Materials, 40*, 1563–1571.

Larker, R., Nissen, A., Pejryd, L., & Loberg, B. (1992). Diffusion bonding reactions between a SiC/SiC composite and a superalloys during joining by hot isostatic pressing. *Acta Metallurgica et Materialia, 40*, 3129–3139.

Lee, W. C. (1997). Strength of Si_3N_4/Ni-Cr-Fe alloy joints with test methods: shear, tension, three-point and, four-point bending. *Journal of Materials Science, 32*, 6657–6660.

Lee, S. B., & Kim, J. H. (1997). Finite-element analysis and X-ray measurement of the residual stresses of ceramic/metal joints. *Journal of Materials Processing Technology, 67*, 167–172.

Lemus-Ruiz, J., Leon-Patino, C. A., & Aguilar-Reyes, E. A. (2006). Interface behaviour during the self-joining of Si_3N_4 using a Nb-foil interlayer. *Scripta Materialia, 54*, 1339–1343.

Lemus, J., & Drew, R. A. L. (2003). Joining of silicon nitride with a titanium foil interlayer. *Materials Science and Engineering A-Structural Materials Properties Microstructure and Processing, 352*, 169–178.

Lessing, P. A., Erickson, A. W., & Kunerth, D. C. (2000). Electrophoretic deposition EPD applied to reaction joining of silicon carbide and silicon nitride ceramics. *Journal of Materials Science, 35*, 2913–2925.

Levay, A., Mobus, G., Vitek, V., Ruhle, M., & Tichy, G. (1999). Structure of misfit dislocations in niobium-sapphire interfaces and strength of interfacial bonding: an atomistic study. *Acta Materialia, 47*, 4143–4152.

Lewinsohn, C. A., Jones, R. H., Colombo, P., & Riccardi, B. (2002). Silicon carbide-based materials for joining silicon carbide composites for fusion energy applications. *Journal of Nuclear Materials, 307*, 1232–1236.

Liang, Y. N., Osendi, M. I., & Miranzo, P. (2003a). Effect of bonding pressure on silicon nitride joining using a nickel-chromium-boron metal filler. *Journal of the American Ceramic Society, 86*, 1226.

Liang, Y. N., Osendi, M. I., & Miranzo, P. (2003b). Joining mechanism in Si_3N_4 bonded with a Ni-Cr-B interlayer. *Journal of the European Ceramic Society, 23*, 547–553.

Li, S. J., Zhou, Y., Duan, H. P., Qiu, J. H., & Zhang, Y. (2003). Joining of SiC ceramic to Ni-based superalloy with functionally gradient material fillers and a tungsten intermediate layer. *Journal of Materials Science, 38*, 4065–4070.

Lin, C. C., Chen, R. B., & Shiue, R. K. (2001). A wettability study of Cu/Sn/Ti active braze alloys on alumina. *Journal of Materials Science, 36*, 2145–2150.

Lin, G. B., Huang, J. H., & Zhang, H. (2007). Joints of carbon fiber-reinforced SiC composites to Ti-alloy brazed by Ag-Cu-Ti short carbon fibers. *Journal of Materials Processing Technology, 189*, 256–261.

Lin, G. B., Huang, J. H., Zhang, H., & Liu, H. Y. (2006). Microstructure and mechanical performance of brazed joints of C-f/SiC composite and Ti alloy using Ag-Cu-Ti-W. *Science and Technology of Welding and Joining, 11*, 379–383.

Liu, G. W., Qiao, G. J., Wang, H. J., Yang, J. F., & Lu, T. J. (2008). Pressureless brazing of zirconia to stainless steel with Ag-Cu filler metal and TiH_2 powder. *Journal of the European Ceramic Society, 28*, 2701–2708.

Liu, G. W., Valenza, F., Muolo, M. L., & Passerone, A. (2010). SiC/SiC and SiC/Kovar joining by Ni-Si and Mo interlayers. *Journal of Materials Science, 45*, 4299–4307.

Liu, C. F., Zhang, J., Zhou, Y., Meng, Q. C., & Naka, M. (2008). Effect of Ti content on microstructure and strength of Si_3N_4/Si_3N_4 joints brazed with Cu-Pd-Ti filler metals. *Materials Science and Engineering A-Structural Materials Properties Microstructure and Processing, 491*, 483–487.

Locatelli, M. R., Dalgleish, B. J., Nakashima, K., Tomsia, A. P., & Glaeser, A. M. (1997). New approaches to joining ceramics for high-temperature applications. *Ceramics International, 23*, 313–322.

Loehman, R. E., Hosking, F. M., Gauntt, B., Kotula, P. G., & Lu, P. (2005). Reactions of Hf-Ag and Zr-Ag alloys with Al_2O_3 at elevated temperatures. *Journal of Materials Science, 40*, 2319–2324.

Loehman, R. E., & Kotula, P. G. (2004). Spectral imaging analysis of interfacial reactions and microstructures in brazing of alumina by a Hf-Ag-Cu alloy. *Journal of the American Ceramic Society, 87*, 55–59.

Loehman, R. E., & Tomsia, A. P. (1992). Reactions of Ti and Zr with AlN and Al_2O_3. *Acta Metallurgica et Materialia, 40*, S75–S83.

Lourdin, P., Juve, D., & Treheux, D. (1996). Nickel-alumina bonds: mechanical properties related to interfacial chemistry. *Journal of the European Ceramic Society, 16*, 745–752.

Lu, Y. C., Sass, S. L., Bai, Q., Kohlstedt, D. L., & Gerberich, W. W. (1995). The influence of interfacial reactions on the fracture toughness of Ti–Al_2O_3 interfaces. *Acta Metallurgica Et Materialia, 43*, 31–41.

Mandal, S., & Ray, A. K. (2004). Correlation between the mechanical properties and the microstructural behaviour of Al_2O_3-(Ag-Cu-Ti) brazed joints. *Materials Science and Engineering A-Structural Materials Properties Microstructure and Processing, 383*, 235–244.

Manicone, P. F., Iommetti, P. R., & Raffaelli, L. (2007). An overview of zirconia ceramics: basic properties and clinical applications. *Journal of Dentistry, 35*, 819–826.

Mao, Y. W., Li, S. J., & Yan, L. S. (2008). Joining of SiC ceramic to graphite using Ni-Cr-SiC powders as filler. *Materials Science and Engineering A-Structural Materials Properties Microstructure and Processing, 491*, 304–308.

Mao, Y. W., Mombello, D., & Baroni, C. (2011). Wettability of Ni-Cr filler on SiC ceramic and interfacial reactions for the SiC/Ni-51Cr system. *Scripta Materialia, 64*, 1087–1090.

Marks, R. A., Chapman, D. R., Danielson, D. T., & Glaeser, A. M. (2000). Joining of alumina via copper/niobium/copper interlayers. *Acta Materialia, 48*, 4425–4438.

Martinelli, A. E., & Drew, R. A. L. (1999). Microstructure and mechanical strength of diffusion-bonded silicon nitride-molybdenum joints. *Journal of the European Ceramic Society, 19*, 2173–2181.

Martinelli, A. E., Drew, R. A. L., Fancello, E. A., Rogge, R., & Root, J. H. (1999). Neutron diffraction and finite-element analysis of thermal residual stresses on diffusion-bonded silicon carbide-molybdenum joints. *Journal of the American Ceramic Society, 82*, 1787–1792.

Matsuo, Y., Ito, M., & Taniguchi, M. (1999). Ceramic-metal joining for automobiles. *Industrial Ceramics, 19*, 203–207.

Matsuoka, S. I. (1994). Ultrasonic welding of ceramic/metal. *Journal of Materials Processing Technology, 47*, 185–196.

Mecartney, M. L., Sinclair, R., & Loehman, R. E. (1985). Silicon-nitride joining. *Journal of the American Ceramic Society, 68*, 472–478.

Meng, Q. S., Chen, S. P., Zhao, J. F., Zhang, H., Zhang, H. X., & Munir, Z. A. (2007). Microstructure and mechanical properties of multilayer-lined composite pipes prepared by SHS centrifugal-thermite process. *Materials Science and Engineering A-Structural Materials Properties Microstructure and Processing, 456*, 332–336.

Mishra, P., Sengupta, P., Athavale, S. N., Pappachan, A. L., Grover, A. K., Suri, A. K., et al. (2005). Brazing of hot isostatically pressed-Al_2O_3 to stainless steel (AISI 304L) by Mo-Mn route using 72Ag-28Cu braze. *Metallurgical and Materials Transactions A-Physical Metallurgy and Materials Science, 36A*, 1487–1494.

Munoz, M. C., Gallego, S., Beltran, J. I., & Cerda, J. (2006). Adhesion at metal-ZrO_2 interfaces. *Surface Science Reports, 61*, 303–344.

Muolo, M. L., Ferrera, E., Morbelli, L., & Passerone, A. (2004). Wetting, spreading and joining in the alumina-zirconia-Inconel 738 system. *Scripta Materialia, 50*, 325–330.

Mustain, H. A., Brown, W. D., & Ang, S. S. (2010). Transient liquid phase die attach for high-temperature silicon carbide power devices. *IEEE Transactions on Components and Packaging Technologies, 33*, 563–570.

Nakamura, M., Kubo, K., Kanzaki, S., & Tabata, H. (1987). Joining of silicon-nitride ceramics by hot-pressing. *Journal of Materials Science, 22*, 1259–1264.

Naka, M., Saito, T., & Okamoto, I. (1987). Niobium silicides at interface between niobium and SiC. *Journal of Materials Science Letters, 6*, 875–876.

Nascimento, R. M. (2003). Review Article: recent advances in metal-ceramic brazing. *Cerâmica, 49*, 178–198.

Naslain, R. R. (2005). SiC-matrix composites: nonbrittle ceramics for thermo-structural application. *International Journal of Applied Ceramic Technology, 2*, 75–84.

Nicholas, M. G. (Ed.). (1990). *Joining of ceramics*. London, UK: Chapman and Hall.

Nicholas, M. G. (1998). *Joining processes: Introduction to brazing and diffusion bonding*. Dordrecht, The Netherlands: Kluwer Academic Publishers.

Nicholas, M. G., & Mortimer, D. A. (1985). Ceramic metal joining for structural applications. *Materials Science and Technology, 1*, 657–665.

Nomura, M., Iwamoto, C., & Tanaka, S. I. (1999). Nanostructure of wetting triple line in a Ag-Cu-Ti/Si_3N_4 reactive system. *Acta Materialia, 47*, 407–413.

Nono, M. C. A., Barroso, J. J., & Castro, P. J. (2006). Mechanical behavior and microstructural analysis of alumina-titanium brazed interfaces. *Materials Science and Engineering A-Structural Materials Properties Microstructure and Processing, 435*, 602–605.

Nozawa, T., Hinoki, T., Hasegawa, A., Kohyama, A., Katoh, Y., Snead, L. L., et al. (2009). Recent advances and issues in development of silicon carbide composites for fusion applications. *Journal of Nuclear Materials, 386*, 622–627.

Okada, A. (2008). Automotive and industrial applications of structural ceramics in Japan. *Journal of the European Ceramic Society, 28*, 1097–1104.

Okamoto, T. (1990). Interfacial structure of metal-ceramic joints. *Isij International, 30*, 1033–1040.

Oliveira, F. J., Silva, R. F., & Vieira, J. M. (2002). The reaction rate at Si_3N_4/steel interfaces as a function of sintering aids. *Journal of the European Ceramic Society, 22*, 2561–2570.

Osendi, M. I., De Pablos, A., & Miranzo, P. (2001). Microstructure and mechanical strength of Si_3N_4/Ni solid state bonded interfaces. *Materials Science and Engineering A-Structural Materials Properties Microstructure and Processing, 308*, 53–59.

Palit, D., & Meier, A. M. (2006). Reaction kinetics and mechanical properties in the reactive brazing of copper to aluminum nitride. *Journal of Materials Science, 41*, 7197–7209.

Park, J. W., Mendez, P. F., & Eagar, T. W. (2002). Strain energy distribution in ceramic-to-metal joints. *Acta Materialia, 50*, 883–899.

Park, J. W., Mendez, P. F., & Eagar, T. W. (2005). Strain energy release in ceramic-to-metal joints by ductile metal interlayers. *Scripta Materialia, 53*, 857–861.

Paulasto, M., & Kivilahti, J. K. (1995). Formation of interfacial microstructure in brazing of Si_3N_4 with Ti-activated Ag-Cu filler alloys. *Scripta Metallurgica et Materialia, 32*, 1209–1214.

Paulasto, M., & Kivilahti, J. (1998). Metallurgical reactions controlling the brazing of Al_2O_3 with Ag-Cu-Ti filler alloys. *Journal of Materials Research, 13*, 343–352.

Perham, T. J., De Jonghe, L. C., & Moberlychan, W. J. (1999). Joining of silicon carbide with a cordierite glass-ceramic. *Journal of the American Ceramic Society, 82*, 297–305.

Peteves, S. D., Paulasto, M., Ceccone, G., & Stamos, V. (1998). The reactive route to ceramic joining: fabrication, interfacial chemistry and joint properties. *Acta Materialia, 46*, 2407–2414.

Pippel, E., Woltersdorf, J., Colombo, P., & Donato, A. (1997). Structure and composition of interlayers in joints between SiC bodies. *Journal of the European Ceramic Society, 17*, 1259–1265.

Polanco, R., De Pablos, A., Miranzo, P., & Osendi, M. I. (2004). Metal-ceramic interfaces: joining silicon nitride-stainless steel. *Applied Surface Science, 238*, 506–512.

Polanco, R., Miranzo, P., & Osendi, M. I. (2006). Fabrication and microstructure of a ZrO_2-Ni functionally graded bonding interlayer using the airbrush spraying method. *Acta Materialia, 54*, 2215–2222.

Polanco, R., Miranzo, P., & Osendi, M. I. (2007). ZrO_2-Ni functionally graded joining interlayers: microstructure and properties. *Advanced Engineering Materials, 9*, 1005–1008.

Poza, P., Miranzo, P., & Osendi, M. I. (2008). Transmission electron microscopy study on silicon nitride/stainless steel bonded interfaces. *Thin Solid Films, 517*, 779–781.

Prakash, P., Mohandas, T., & Raju, P. D. (2005). Microstructural characterization of SiC ceramic and SiC-metal active metal brazed joints. *Scripta Materialia, 52*, 1169–1173.

Qin, C. D., & Derby, B. (1992). Diffusion bonding of nickel and zirconia – mechanical-properties and interfacial microstructures. *Journal of Materials Research, 7*, 1480–1488.

Qin, C. D., & Derby, B. (1993a). Diffusion bonding of a nickel (chromium) alloy to zirconia – mechanical-properties and interface microstructures. *Journal of Materials Science, 28*, 4366–4374.

Qin, C. D., & Derby, B. (1993b). Diffusion bonds between a stainless-steel and zirconia. *Journal of the American Ceramic Society, 76*, 232–234.

Rabin, B. H. (1990). Modified tape casting method for ceramic joining – application to joining of silicon-carbide. *Journal of the American Ceramic Society, 73*, 2757–2759.

Rahaman, M. N., Yao, A., Bal, B. S., Garino, J. P., & Ries, M. D. (2007). Ceramics for prosthetic hip and knee joint replacement. *Journal of the American Ceramic Society, 90*, 1965–1988.

Raic, K. T., Rudolf, R., Kosec, B., Anzel, I., Lazic, V., & Todorovic, A. (2009). Nanofoils for soldering and brazing in dental joining practice and jewellery manufacturing. *Materiali in Tehnologije, 43*, 3–9.

Raic, K. T., Rudolf, R., Todorovic, A., Stamenkovic, D., & Anzel, I. (2010). Liquid metal/ceramic interfaces in dental practice and jewellery manufacturing. *Materiali in Tehnologije, 44*, 59–66.

Rijnders, M. R., & Peteves, S. D. (1999). Joining of alumina using a V-active filler metal. *Scripta Materialia, 41*, 1137–1146.

Ruhle, M. (1996). Structure and composition of metal ceramic interfaces. *Journal of the European Ceramic Society, 16*, 353–365.

Saied, M. A., Lloyd, I. K., Haller, W. K., & Lawn, B. R. (2011). Joining dental ceramic layers with glass. *Dental Materials, 27*, 1011–1016.

Sainz, M. A., Miranzo, P., & Osendi, M. I. (2002). Silicon nitride joining using silica and yttria ceramic interlayers. *Journal of the American Ceramic Society, 85*, 941–946.

Saiz, E., Tomsia, A. P., & Cannon, R. M. (1998). Ridging effects on wetting and spreading of liquids on solids. *Acta Materialia, 46*, 2349–2361.

Schiepers, R. C. J., Vanloo, F. J. J., & Dewith, G. (1988). Reactions between alpha-silicon carbide ceramic and nickel or iron. *Journal of the American Ceramic Society, 71*, C284–C287.

Schuler, C. C., Stuck, A., Beck, N., Keser, H., & Tack, U. (2000). Direct silver bonding – an alternative for substrates in power semiconductor packaging. *Journal of Materials Science-Materials in Electronics, 11*, 389–396.

Sciti, D., Bellosi, A., & Esposito, L. (2001). Bonding of zirconia to super alloy with the active brazing technique. *Journal of the European Ceramic Society, 21*, 45–52.

Shalz, M. L., Dalgleish, B. J., Tomsia, A. P., & Glaeser, A. M. (1993). Ceramic joining I partial transient liquid-phase bonding of alumina via Cu/Pt interlayers. *Journal of Materials Science, 28*, 1673–1684.

Shalz, M. L., Dalgleish, B. J., Tomsia, A. P., & Glaeser, A. M. (1994). Ceramic joining II partial transient liquid-phase bonding of alumina via Cu/Ni-Cu multilayer interlayers. *Journal of Materials Science, 29*, 3200–3208.

Shimoo, T., Shibata, D., & Okamura, K. (1998). Interaction of Si_3N_4 with 18%Cr-8%Ni austenitic stainless steel. *Journal of the Ceramic Society of Japan, 106*, 545–550.

Silva, R. F., Oliveira, F. J., Castro, F. P., & Vieira, J. M. (1998). Modeling of chemical wear in ferrous alloys silicon nitride contacts during high speed cutting. *Acta Materialia, 46*, 2501–2507.

Singh, M. (1997). A reaction forming method for joining of silicon carbide-based ceramics. *Scripta Materialia, 37*, 1151–1154.

Singh, M. (1999). Design, fabrication and characterization of high temperature joints in ceramic composites. In K. Niihara, K. Nakano, T. Sekino, & E. Yasuda (Eds.), *Key engineering materials: Vols. 164–165. Proceedings of the 3rd international conference on high temperature ceramic matrix composites (HT-CMC 3), September 1998* (pp. 415–420). Osaka, Japan: Switzerland:Trans Tech Publications.

Singh, M., Shpargel, T. P., & Asthana, R. (2007). Brazing of stainless steel to yttria-stabilized zirconia using gold-based brazes for solid oxide fuel cell applications. *International Journal of Applied Ceramic Technology, 4*, 119–133.

Smeacetto, F., Salvo, M., Ferraris, M., Casalegno, V., & Asinari, P. (2008). Glass and composite seals for the joining of YSZ to metallic interconnect in solid oxide fuel cells. *Journal of the European Ceramic Society, 28*, 611–616.

Smorygo, O., Kim, J. S., Kim, M. D., & Eom, T. G. (2007). Evolution of the interlayer microstructure and the fracture modes of the zirconia/Cu-Ag-Ti filler/Ti active brazing joints. *Materials Letters, 61*, 613–616.

Song, X. G., Cao, J., Wang, Y. F., & Feng, J. C. (2011). Effect of Si_3N_4-particles addition in Ag-Cu-Ti filler alloy on Si_3N_4/TiAl brazed joint. *Materials Science and Engineering A-Structural Materials Properties Microstructure and Processing, 528*, 5135–5140.

Stoop, B. T. J., & Denouden, G. (1993). Diffusion bonding of silicon-nitride to austenitic stainless-steel without interlayers. *Metallurgical Transactions A-Physical Metallurgy and Materials Science, 24*, 1835–1843.

Stoop, B. T. J., & Denouden, G. (1995). Diffusion bonding of silicon-nitride to austenitic stainless-steel with metallic interlayers. *Metallurgical and Materials Transactions A-Physical Metallurgy and Materials Science, 26*, 203–208.

Suganuma, K. (1990). Recent advances in joining technology of ceramics to metals. *Isij International, 30*, 1046–1058.

Sugar, J. D., Mckeown, J. T., Akashi, T., Hong, S. M., Nakashima, K., & Glaeser, A. M. (2006). Transient-liquid-phase and liquid-film-assisted joining of ceramics. *Journal of the European Ceramic Society, 26*, 363–372.

Sun, Y., Zhang, J., Geng, Y. P., Ikeuchi, K., & Shibayanagi, T. (2011). Microstructure and mechanical properties of an Si_3N_4/Si_3N_4 joint brazed with Au-Ni-Pd-V filler alloy. *Scripta Materialia, 64*, 414–417.

Swiler, T. P., & Loehman, R. E. (2000). Molecular dynamics simulations of reactive wetting in metal-ceramic systems. *Acta Materialia, 48*, 4419–4424.

Trumble, K. P., & Ruhle, M. (1991). The thermodynamics of spinel interphase formation at diffusion-bonded Ni/Al_2O_3 interfaces. *Acta Metallurgica Et Materialia, 39*, 1915–1924.

Uday, M. B., Fauzi, M. N. A., Zuhailawati, H., & Ismail, A. B. (2010). Advances in friction welding process: a review. *Science and Technology of Welding and Joining, 15*, 534–558.

Valette, C., Devismes, M. F., Voytovych, R., & Eustathopoulos, N. (2005). Interfacial reactions in alumina/CuAgTi braze/CuNi system. *Scripta Materialia, 52*, 1–6.

Van Loo, F. J. J., & Kodentsov, A. A. (1998). Interfacial chemistry: reactions in inorganic systems. *Pure and Applied Chemistry, 70*, 501–508.

Van Roode, M. (2010). Ceramic gas turbine development: need for a 10 year Plan. *Journal of Engineering for Gas Turbines and Power-transactions of the ASME, 132*, 011301–011308.

Vegter, R. H., Maeda, M., Naka, M., & Den Ouden, G. (2002). The microstructure of ZrO_2-Ni-Si_3N_4 diffusion bonds. *Journal of Materials Science, 37*, 1179–1182.

Vila, M., Prieto, C., Miranzo, P., Osendi, M. I., Del Rio, J. M., & Perez-Castellanos, J. L. (2005). Measurements and finite-element simulations of residual stresses developed in Si_3N_4/Ni diffusion bonds. *Journal of the American Ceramic Society, 88*, 2515–2520.

Vila, M., Prieto, C., Zahr, J., Perez-Castellanos, J. L., Bruno, G., Jimenez-Ruiz, M., et al. (2007). Residual stresses in ceramic-to-metal joints: diffraction measurements and finite element method analysis. *Philosophical Magazine, 87*, 5551–5563.

Voue, M., & De Coninck, J. (2000). Spreading and wetting at the microscopic scale: recent developments and perspectives. *Acta Materialia, 48*, 4405–4417.

Voytovych, R., Robaut, F., & Eustathopoulos, N. (2006). The relation between wetting and-interfacial chemistry in the CuAgTi/alumina system. *Acta Materialia, 54*, 2205–2214.

Waitz, I. A., Gauba, G., & Tzeng, Y. S. (1998). Combustors for micro-gas turbine engines. *Journal of Fluids Engineering-transactions of the ASME, 120*, 109–117.

Weil, K. S., Coyle, C. A., Darsell, J. T., Xia, G. G., & Hardy, J. S. (2005). Effects of thermal cycling and thermal aging on the hermeticity and strength of silver-copper oxide air-brazed seals. *Journal of Power Sources, 152*, 97–104.

Weil, K. S., Kim, J. Y., & Hardy, J. S. (2005). Reactive air brazing: a novel method of sealing SOFCs and other solid-state electrochemical devices. *Electrochemical and Solid State Letters, 8*, A133–A136.

Weil, K. S., Kim, J. Y., Hardy, J. S., & Darsell, J. T. (2006a). The effect of TiO_2 on the wetting behavior of silver-copper oxide braze filler metals. *Scripta Materialia, 54*, 1071–1075.

Weil, K. S., Kim, J. Y., Hardy, J. S., & Darsell, J. T. (2006b). Investigation of Pd-modified Ag-CuO air braze filler metals. In J. J. Stephens, & K. S. Weil (Eds.), *Proceedings of the 3rd internation conference on brazing and soldering* (pp. 167–175). Materials Park, OH, USA: ASM International.

Williamson, R. L., Rabin, B. H., & Drake, J. T. (1993). Finite-element analysis of thermal residual-stresses at graded ceramic-metal interfaces. 1. Model description and geometrical effects. *Journal of Applied Physics, 74*, 1310–1320.

Xie, R. J., Mitomo, M., Huang, L. P., & Fu, X. R. (2000). Joining of silicon nitride ceramics for high-temperature applications. *Journal of Materials Research, 15*, 136–141.

Xiong, H. P., Chen, B., Kang, Y. S., Mao, W., Kawasaki, A., Okamura, H., et al. (2007). Wettability of Co-V, and PdNi-Cr-V system alloys on SiC ceramic and interfacial reactions. *Scripta Materialia, 56*, 173–176.

Xiong, J. H., Huang, J. H., Lin, G. B., Zhang, H., & Zhao, X. K. (2011). Joining of C(f)/SiC composite to TC4 using Ag-Cu-Ti-SiC composite filler material. *Powder Metallurgy, 54*, 269–272.

Xiong, H. P., Mao, W., Xie, Y. H., Chen, B., Guo, W. L., Li, X. H., et al. (2007). Control of interfacial reactions and strength of the SiC/SiC joints brazed with newly-developed Co-based brazing alloy. *Journal of Materials Research, 22*, 2727–2736.

Xiong, H. P., Mao, W., Xie, Y. H., Guo, W. L., Li, X. H., & Cheng, Y. Y. (2007). Brazing of SiC to a wrought nickel-based superalloy using CoFeNi(Si, B)CrTi filler metal. *Materials Letters, 61*, 4662–4665.

Zhai, Y., North, T. H., & Serratorodrigues, J. (1997). Transient liquid-phase bonding of alumina and metal matrix composite base materials. *Journal of Materials Science, 32*, 1393–1397.

Zhang, J. X., Chandel, R. S., & Seow, H. P. (2002). Effects of chromium on the interface and bond strength of metal-ceramic joints. *Materials Chemistry and Physics, 75*, 256–259.

Zhang, J., Guo, Y. L., Naka, M., & Zhou, Y. (2008). Microstructure and reaction phases in Si_3N_4/Si_3N_4 joint brazed with Cu-Pd-Ti filler alloy. *Ceramics International, 34*, 1159–1164.

Zhang, J., Liu, C. F., Naka, M., Meng, Q. C., & Zhou, Y. (2004). A TEM analysis of the Si_3N_4/Si_3N_4 joint with a Cu-Zn-Ti filler metal. *Journal of Materials Science, 39*, 4587–4591.

Zhang, C. G., Qiao, G. J., & Jin, Z. H. (2002). Active brazing of pure alumina to Kovar alloy based on the partial transient liquid phase (PTLP) technique with Ni-Ti interlayer. *Journal of the European Ceramic Society, 22*, 2181–2186.

Zhang, W., Smith, J. R., & Evans, A. G. (2002). The connection between ab initio calculations and interface adhesion measurements on metal/oxide systems: Ni/Al_2O_3 and Cu/Al_2O_3. *Acta Materialia, 50*, 3803–3816.

Zhang, J., & Sun, Y. (2010). Microstructural and mechanical characterization of the Si_3N_4/Si_3N_4 joint brazed using Au-Ni-V filler alloys. *Journal of the European Ceramic Society, 30*, 751–757.

Zheng, J., & Akinc, M. (2001). Green state joining of SiC without applied pressure. *Journal of the American Ceramic Society, 84*, 2479–2483.

Zou, J. S., Wu, B., & Zhao, Q. Z. (2005). Investigation on the interface structure and joining strength of Si_3N_4/Cu68Ti20Ni12. *Rare Metal Materials and Engineering, 34*, 102–106.

Standard References

ASTM C1469-10. (2010). *Standard test method for shear strength of joints of advanced ceramics at ambient temperature*. West Conshohocken, PA. http://dx.doi.org/10.1520/C1469-10 www.astm.org.

ASTM C1161-02c. (2008). *e1 Standard test method for flexural strength of advanced ceramics at ambient temperature*. West Conshohocken, PA. http://dx.doi.org/10.1520/C1161-02CR08E01 www.astm.org.

Website Citations

TWI Limited. http://www.twi.co.uk/content/ceramics_mech.html Accessed 05.08.11.
S-Bond Technologies. http://www.s-bond.com Accessed 17.10.11.
CEA Liten. http://www-liten.cea.fr Accessed 24.10.11.
MTC Wesgo Metals. http://www.wesgometals.com Accessed 24.10.11.

This page intentionally left blank

SECTION III

MICROSTRUCTURE AND PROPERTIES

This page intentionally left blank

2.08 Microstructural Characterization of Hard Ceramics

Gregory S. Rohrer, Department of Materials Science and Engineering, Carnegie Mellon University, Pittsburgh, PA, USA

© 2014 Elsevier Ltd. All rights reserved.

2.08.1 Introduction

The study of microstructures is motivated by the fact that nearly all engineered materials are used in a polycrystalline form. The realization that many of the macroscopic properties of polycrystalline solids are strongly influenced by the internal structure has motivated countless microstructure studies, most with the goal of establishing correlations between the microstructure and the properties.

This chapter will focus on the most recent developments in microstructural characterization and their applications to ceramics. However, at the outset, it is appropriate to note past reviews of this topic. For example, the relationship between carbide (Hollox, 1968; Tucker & McLachlan, 1993) and carbide composite microstructures (French, 1969; Gurland, 1988; Sherman & Brandon, 1999) and mechanical properties has been thoroughly reviewed. The application of electron microscopy to ceramic microstructure (Bando, 1995; Kleebe, Braue, Schmidt, Pezzotti, & Ziegler, 1996; Thomas, 1996) and grain boundaries (Ikuhara, 2001; Varela et al., 2005) has also been the subject of several comprehensive reviews.

While there are a few early examples of novel three-dimensional studies (Hull, 1988; Williams & Smith, 1952), the vast majority of microstructural information has been determined from the analysis of two-dimensional images. The microstructure is, of course, a three-dimensional object. Stereology, which is the interpretation of three-dimensional spatial information from two-dimensional sections, has been the link that allows volumetric information about the microstructures to be drawn from the planar images. However, all stereological results depend on an assumption of homogeneity and, in some cases, geometric models or assumptions about the true shapes of objects in three dimensions. In cases where these assumptions are valid, the stereological results are also valid (Russ, 1986). However, for many of the most interesting materials, the validity of the assumptions cannot be guaranteed.

Between 2001 and 2010, there has been a rapid expansion in capabilities for three-dimensional microstructure studies; this has provided an entirely new perspective on some "well-known" microstructures and pointed to the weakness of the assumptions used in stereology. As an example, one can point to a landmark study of the three-dimensional structure of cementite precipitates in a ferrous alloy which showed that structures historically classified as intragranular precipitates were actually branches connected to dendritic grain boundary precipitates and Widmanstätten structures (Kral & Spanos, 1999). Considering the expected value of these emerging capabilities for the materials science community, this chapter will emphasize the three-dimensional characterization of microstructures.

http://dx.doi.org/10.1016/B978-0-08-096527-7.00027-1

This recent revolution in our ability to characterize microstructures in three dimensions has occurred across a wide range of length scales from the atomic to the millimeter range (Robertson et al., 2011). At the atomic scale, there have been significant advances in field ion microscopy. Although this technique has been available for decades, the limited volume of material and the types of materials that could be imaged made it impractical for many studies. However, the recent development of laser-assisted, three-dimensional atom probe (3DAP) microscopy has made it possible to make three-dimensional, near-atomic resolution images of reasonable volumes of a wide range of materials (Kelly & Miller, 2007; Miller & Forbes, 2009; Seidman, 2007). At the same time, advances in electron tomography in the transmission electron microscope (TEM) have made it possible to make three-dimensional images at slightly lower resolution (Barnard, Sharp, Tong, & Midgley, 2006; Batenburg et al., 2009; Mobus & Inkson, 2001; Weyland et al., 2006). The dual beam, focused ion beam scanning electron microscope (DB-FIB SEM) makes three-dimensional imaging and crystallography mapping possible at the submicron level (Dillon & Rohrer, 2009b; Groeber, Haley, Uchic, Dimiduk, & Ghosh, 2006; Li, Dillon, & Rohrer, 2009; Rohrer et al., 2010; Uchic, Groeber, Dimiduk, & Simmons, 2006). At larger length scales, X-ray tomography (Chen et al., 2010; Chino & Dunand, 2008) and high-energy X-ray diffraction microscopy (HEDM) (Hefferan et al., 2009; Johnson, King, Honnicke, Marrow, & Ludwig, 2008; Larson, Yang, Ice, Budai, & Tischler, 2002; Poulsen et al., 2001) allow phase mapping and crystallographic mapping, respectively. Finally, at the largest length scale, "RoboMet" robotic polishing and metallography allows the three-dimensional imaging of samples with sizes up to the centimeter-size range (Spowart, Mullens, & Puchala, 2003).

In microstructure characterization, there is always a compromise between resolution and the number of features (for example, grains) that can be observed and the limits depend on the instruments used. This is especially true in three-dimensional studies. The compromises between resolution and the numbers of features are summarized by the schematic in Figure 1 (Rohrer, 2011b). Using current techniques and those anticipated in the near future, the approximate bounds on domains are shown by the solid lines; all these domains are expected to expand to the right with time. These techniques make it possible to create input for computational models that can be used to predict materials properties. One key aspect of Figure 1 is that, depending on the problem at hand, it may not be possible to characterize all the relevant length scales without using a combination of techniques.

Simulation and modeling are playing an increasingly important role in establishing structure–property relationships and there is an emerging vision of being able to rapidly develop and optimize new materials through an increased interplay between simulation and experiment (2011, Pollock et al., 2008). Realizing this vision, however, requires accurate, three-dimensional, microstructural data. These trends provide a renewed motivation for improved characterization and analysis techniques.

The remainder of this chapter is organized in the following way. First, the most important microstructural features that one can derive from characterization experiments are described and illustrated by some examples

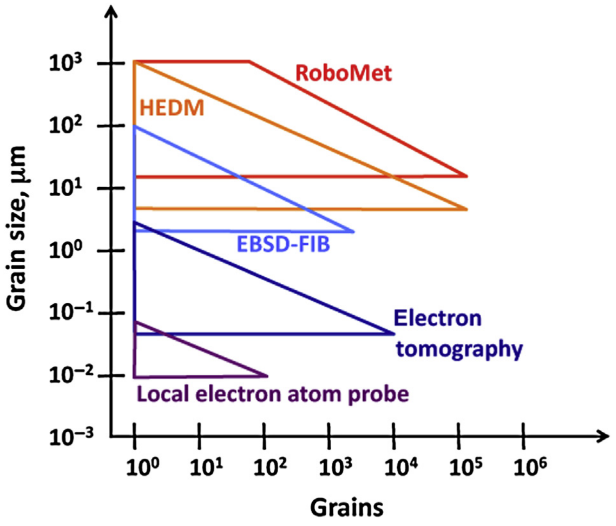

Figure 1 Approximate limitations on the numbers of grains that can be mapped in three dimensions using selected techniques. The bounds of the domains of these techniques are expected to expand to the right with time. Source: Rohrer, 2011b.

of data. Next, the most important recent advances in the three-dimensional microstructural characterization are described. Although examples from a wide range of materials types will be used, all the methods are applicable to ceramics and other hard materials. Finally, a summary and prognosis for future trends are provided.

2.08.2 Microstructural Parameters

2.08.2.1 Grain Sizes and Grain Size Distributions

As mentioned in the introduction, most materials are used in a granular form and are either polycrystalline (in the case of single-phase materials) or composites consisting of two or more phases. In all cases, the sizes of the component crystals are an important characteristic of the microstructure that is connected to physical properties including strength, hardness, and optical transparency, to name a few. From planar sections, the crystal size is usually measured using the linear intercept method. Using this method, the number of intercepts per length of test lines that are superimposed on the microstructure is used as a measure of the grain size. For example, for the image in Figure 2(a) of a WC/Co composite, a skeleton (Figure 2(b)) can be created that consists of all the carbide–carbide and carbide–binder interfaces, where Co is the binder. It is then relatively simple to count the number of times a line of fixed length intercepts each boundary (Kim, Massa, & Rohrer, 2008). The stereologically determined carbide grain size, L^*, is a function of the volume fraction of the carbide (f_c) and the average number of intercepts per unit length of test lines with carbide/carbide boundaries (N_{cc}) and binder/carbide interfaces (N_{bc}):

$$L^* = \frac{2f_c}{2N_{cc} + N_{bc}} \tag{1}$$

In the case that three-dimensional data are available, there is no need for a stereological interpretation and it is possible to determine grain sizes directly in terms of either their volume or spherical equivalent radii (Groeber, Haley, Uchic, Dimiduk, & Ghosh, 2006; Rowenhorst, Lewis, & Spanos, 2010). The distribution of crystal sizes is most frequently reported to be lognormal (Rohrer, 2005):

$$f_L(\rho) = \frac{1}{(2\pi)^{1/2}}\frac{1}{\beta\rho}\exp\left[-(\ln\rho - \alpha)^2/2\beta^2\right] \tag{2}$$

where $\rho = r/\langle r\rangle$, $\langle r\rangle$ is the average grain size, and α and β are the fitting parameters. On a coarse scale, the lognormal distribution provides a good account of distribution. For example, the data shown in Figure 3 for WC crystal sizes in WC–Co composites demonstrate that in many different samples, the width of the distribution is the same and only the mean varies (Kim et al., 2008). However, there can be significant deviations in the tails of the distribution that are not obvious in the plots such as Figure 3(a). For example, Figure 4 shows that the lognormal distribution is accurate for features that are within one standard deviation of the mean, but that there are more large grains than predicted by the lognormal distribution (Tucker, Chan, Rohrer, Groeber, & Rollett, 2012).

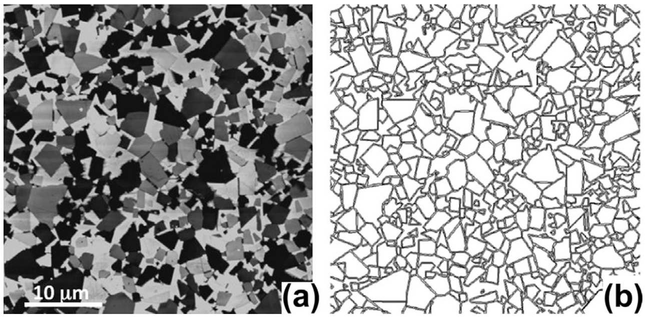

Figure 2 (a) Contact AFM image of a WC/Co sample with a carbide volume fraction of 0.82. The lightest contrast corresponds to Co and the carbide crystals are a variety of darker shades. (b) A skeletonized map determined from the AFM image by tracing the boundary positions. The average grain diameter is 1.53 μm and the contiguity of the carbide phase is 0.50. Source: Kim et al., 2008.

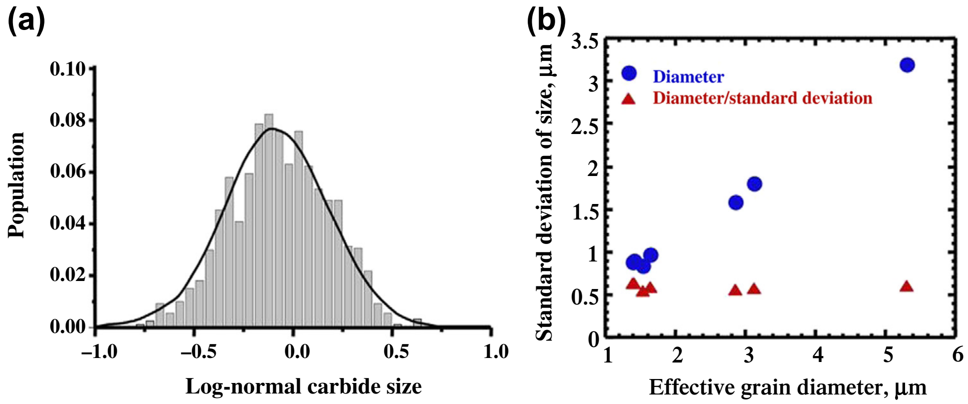

Figure 3 (a) The carbide grain size distribution of a WC/Co sample with a carbide volume fraction of 0.83. (b) The relationship between the mean grain diameter and standard deviation of the distribution of grain sizes for a range of specimens with different volume fractions and different grain sizes. Source: Kim et al., 2008.

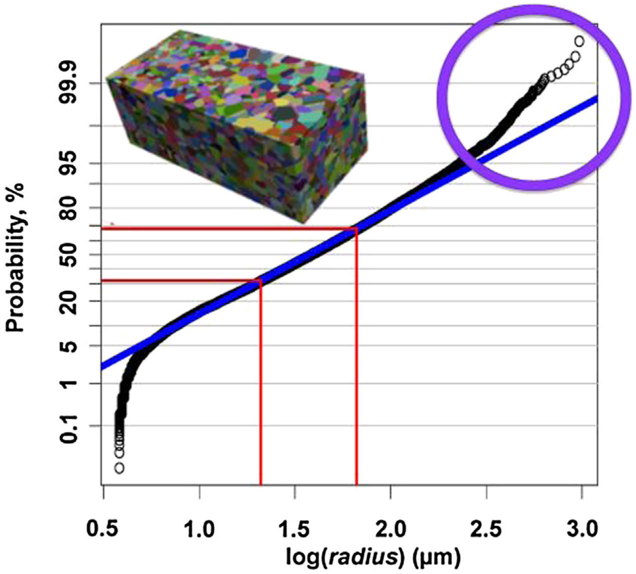

Figure 4 Distribution of ~5800 grain sizes measured in three dimensions compared to a lognormal distribution (blue line). Red lines are drawn at one standard deviation about the mean. The largest grains deviate from this distribution (purple circle). Source: Tucker et al., 2012.

While knowledge of the features close to the mean is sufficient for determining average materials properties, such as elastic response or thermal conductivity, it is the rare feature that frequently triggers dramatic changes in the microstructure, often with life-limiting consequences for applications. For example, recent simulations have shown that the long-term capacity of a rechargeable Li-ion battery depends on the extremes of the grain size distribution in the anode and cathode and that Li dendrite formation, which leads to unpredictable battery behavior, occurs on the smallest grains (Smith, Garcia, Horn, 2009). Similarly, when the size distribution of grains that initiate fatigue cracks in a Ti alloy are compared to the overall size distribution, it is found that the initiating grains are larger than the mean (Jha, Larsen, & Rosenberger, 2009).

2.08.2.2 Crystal Shape

Grain shapes are most frequently interpreted in terms of some model geometric shapes, such as a circle (sphere), an ellipse (ellipsoid), or a polygon (polyhedron) in two dimensions (three dimensions). For example, the transverse section of the chemical vapor deposition (CVD)-grown TiC_xN_{1-x} coating shown in Figure 5 has

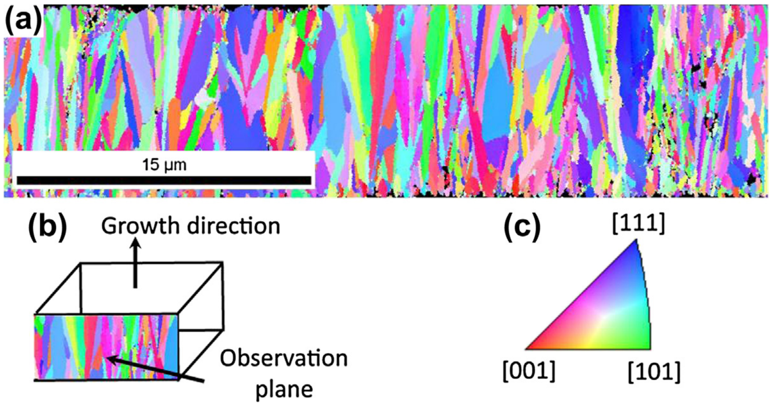

Figure 5 (a) Electron backscatter diffraction orientation map for a TiC_xN_{1-x} coating grown by chemical vapor deposition. (b) This is a transverse section of the coating, as indicated in this schematic. (c) Each color corresponds to a crystal orientation, defined by this key. Source: Chien et al., 2009.

grains elongated along the growth direction (Chien et al., 2009). Freely available software (Health) can be used to fit the grain shapes in the image to ideal ellipses. From this, it is possible to determine the average area and the average dimensions of the major and minor axes. For the materials shown in Figure 5, the ratio of the major to minor axis length is 7.2.

It is also possible to approximate crystals as polyhedra. However, in this case, it is also necessary to have a measure of crystal orientation, so electron backscatter diffraction (EBSD) data are necessary. A stereological technique has been developed to calculate the relative areas of different types of interfaces based on two-dimensional images (Saylor, El-Dasher, Adams, & Rohrer, 2004; Saylor & Rohrer, 2002). The required observations for the stereological analysis are line segments, in the sample reference frame, representing the crystal boundaries (Figure 6(a)), and the associated crystal orientations. From these data, the interface plane distribution (IPD), which is the relative areas of crystal planes as a function of orientation, can be calculated using freely available software. The IPD, $\lambda(n)$, can be measured for the grain boundaries in a single-phase material or the phase boundaries and grain boundaries in a composite (Kim et al., 2008; Kim & Rohrer, 2004; Sano, Kim, & Rohrer, 2005). The IPD has two parameters that specify the interface normal orientation and can be plotted as a continuous distribution, as in Figure 6(b).

For the case of regular faceted system, such as WC crystals in a Co matrix, the crystal shape can be modeled as a trigonal prism with $\{0001\}$ (Syha et al., 2012) basal facets and $(10\bar{1}0)$ prismatic facets (Figure 6(c); Kim et al., 2008; Kim & Rohrer, 2004). In this case, the shape can be parameterized by an aspect ratio computed as the ratio of the length along the edge of the (0001) basal facet (b) to its height (h) along a $(10\bar{1}0)$ facet. The results in Figure 6(c) show how the WC aspect ratio varies with the volume fraction of WC and Co. In a stereological determination of crystal shape, it is necessary to have a sufficient number of observations. To illustrate this, Figure 7 shows the aspect ratio of WC crystals calculated using different numbers of observations. Based on these results, it is clear that after approximately 500 observed line segments, the result is not affected by additional data. This provides a guideline for the minimum number of line segments that are required for an accurate IPD.

If the data are three-dimensional, then no stereological interpretation is required and grain shapes can be determined directly. In this case, it is possible to specify the ranges of shapes and how they vary. This is not straightforward for complex shapes, but parameters have been developed to quantify shape characteristics and their distributions. For example, MacSleyne, Uchic, Simmons, and De Graef (2009) have used moment invariants to quantify the three-dimensional shapes of precipitates in microstructures. Moment invariants are combinations of the moments of inertia of an object that are invariant with respect to certain transformations. For example, Figure 8 shows how the shapes of dendritically shaped precipitates can be classified using moment invariants. The vertical axis is an affine parameter that is invariant with respect to translations, rotations, anisotropic scaling, and shear. The horizontal axis is a shape parameter that measures of the volume-to-surface ratio (see MacSleyne, 2009 for the detailed definitions, which are beyond the scope of this chapter). This representation clearly separates highly branched structures (lower left) from more compact structures (upper right). While the application of these distributions is still being studied, they offer a promising path for the quantification of crystal shapes in microstructures.

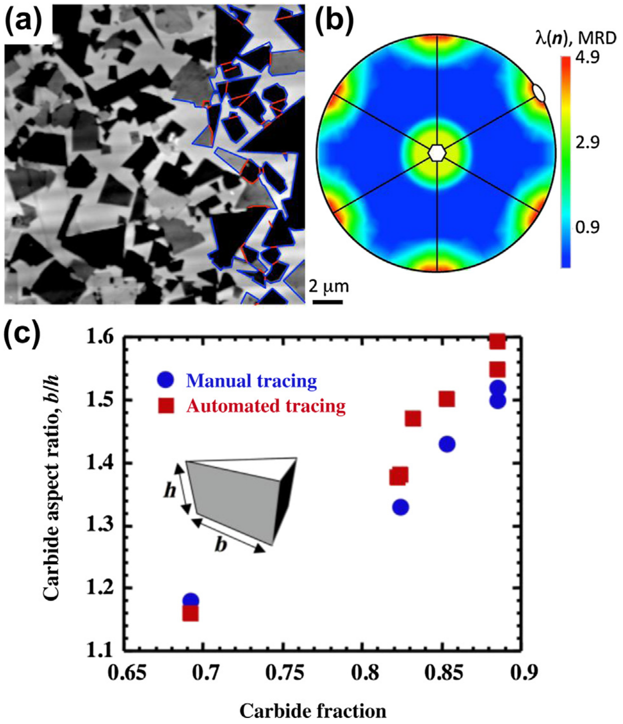

Figure 6 (a) An atomic force microscope image of a WC/Co composite after etching. The dark polygonal features are WC grains. (b) Interface plane distribution for the WC/Co interfaces in a WC/Co composite, showing that particles are dominantly bound by basal and prismatic surfaces. (c) Average base-to-height aspect ratios (*b*/*h*) for the carbide grains in the seven samples, plotted as a function of carbide volume fraction. Source: Kim et al., 2008.

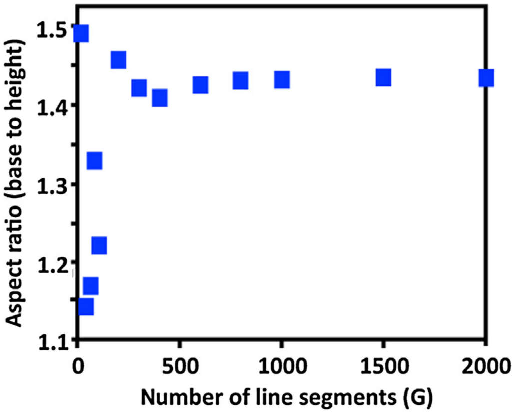

Figure 7 The base-to-height aspect ratio of WC crystals in a WC/Co sample with a carbide volume fraction of 0.85, determined using different numbers of observations. The result converges after 500 line segments. Source: Kim et al., 2008.

2.08.2.3 Contiguity

In composite materials, the contiguity of each phase can affect the mechanical properties, especially in the case where there is significant contrast in the properties. For the case of WC/Co composite, contiguity of the carbide phase (C) is computed according to the following expression:

$$C = \frac{2\sum_i l_{\text{cc}}^i}{\sum_{i,j}\left(2l_{\text{cc}}^i + l_{\text{bc}}^j\right)} \tag{3}$$

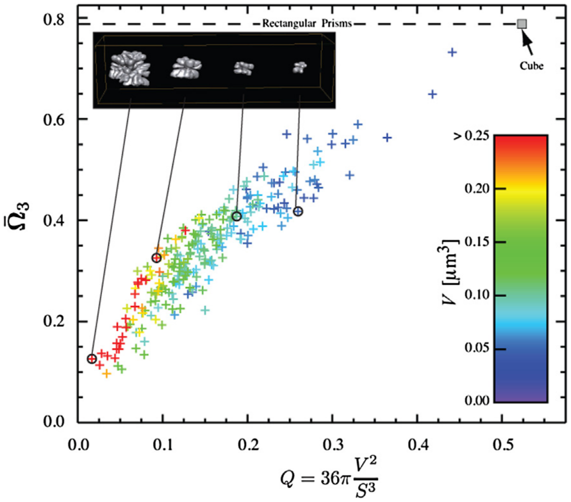

Figure 8 Plot of a moment invariant, $\overline{\Omega}_3$, as a function of a shape parameter, *Q*, for the 260 γ' precipitates from a René 88-DT superalloy. The color scheme corresponds to the particle volume. The precipitates shown in the inset correspond to the black circles. The horizontal dashed line indicates the location of the class of rectangular prisms, with the cube located at the position indicated on the far right. Source: From MacSleyne et al. (2009). Copyright Elsevier, reproduced with permission.

where l_{cc} is the length of a carbide–carbide grain boundary and l_{bc} is the length of a binder–carbide interface. These lengths can be extracted from micrographs such as those illustrated in Figures 2(a) and 6(a). Figure 9 illustrates data for the contiguity of WC crystals in WC/Co composites as a function of the WC volume fraction (Kim et al., 2008). While these data indicate that the contiguity is approximately linear with the carbide volume fraction over the range of compositions examined, more comprehensive studies, over a wider range of composition, have found that the contiguity increase is nonlinear (German, 1985). The data in Figure 9 also contain evidence that the carbide volume fraction/contiguity relationship is also scale invariant in the range of specimens studied: samples A and B have very different grain sizes (5.31 and 1.65 μm, respectively), but nearly the same carbide volume fractions and contiguity (Luyckx & Love, 2006).

Contiguity in three dimensions can be determined exactly. This is particularly important for devices such as solid-oxide fuel cells where the contiguity of the void space (to transport reactant gases) and of the three phase boundaries (where gases, ionic species, and electronic charge carriers can participate in reactions) influences the overall transport through the device and, therefore, the electrochemical characteristics. Wilson et al. (2006) studied the anode of a solid-oxide fuel cell comprised of Ni, yttria-stabilized zirconia (YSZ), and pore space and found that of all the three phase boundaries, 63% of the length formed an interconnected network.

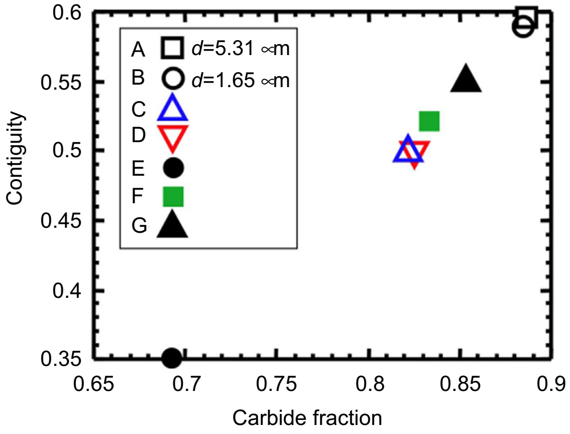

Figure 9 The WC contiguity as a function of the carbide volume fraction for seven different WC/Co specimens. The Co volume fraction (grain size) of each sample is: A = 0.88 (5.31 μm), B = 0.88 (1.65 μm), C = 0.82 (1.41 μm), D = 0.82 (1.53 μm), E = 0.69 (1.40 μm), F = 0.83 (3.12 μm), and G = 0.85 (2.59 μm). Source: Kim et al., 2008.

2.08.2.4 Crystallographic Distributions of Orientations and Interfaces

The term "texture" is usually used to refer to a nonrandom distribution of crystal orientations. However, it can also refer to a nonrandom distribution of misorientations or interface planes. Orientation textures are typically quantified using pole figures (distributions of the normal to a specific set of crystal planes in the sample reference frame) and inverse pole figures (distributions specific sample directions in the reference frame of the crystals) that are calculated from either X-ray or EBSD data. As an example, consider the EBSD orientation map of α-alumina in Figure 10 and the accompanying inverse pole figure and pole figure (Chien et al., 2009). This map is a transverse section of a coating grown by CVD, so the growth direction is vertically oriented in the plane of the figure. The dominance of blue and green colors in Figure 10(a) indicates that the prismatic orientations (those perpendicular to the [0001] axis) are perpendicular to the plane of the image and the [0001] axis is aligned along the growth direction. This is also reflected in the inverse pole figure (IPF) in Figure 10(b) and the pole figure in Figure 10(c). The IPF shows the distribution of crystal orientations along the growth direction of the coating. It is consistent with the conclusions from the color in the orientation map, but quantifies the preference for the alignment of the [0001] axis along the growth direction. The units, multiples of a random distribution (MRD), compare the actual distribution with the distribution expected for the case when the orientations are completely random. If the value is less than one, this indicates that the orientation occurs less frequently than one would expect in a random distribution. If it is greater than one, it occurs more frequently by that multiple. This is a common unit of measure in texture studies. The pole figure in Figure 10(c) also shows that the [0001] axes are preferentially aligned with the growth direction.

Interfaces and grain boundaries can also exhibit texture. In the most general sense, the relative areas of different types of grain boundaries are described by the grain boundary character distribution (GBCD) (Rohrer et al., 2004). The grain boundary type is specified by five parameters. As parameters for this distribution, we select a misorientation type by specifying an axis–angle combination (three parameters), and a grain boundary plane orientation by specifying a unit vector normal to the boundary (two parameters). It is possible to characterize the GBCD using fewer than five parameters and a variety of representations are illustrated in Figure 11 and are discussed in the following paragraph (Kim et al., 2008; Rohrer, 2011b).

Figure 11 shows the three different representations of the GBCD calculated using the same data. This example is for hexagonal WC. Figure 11(a) shows a single parameter distribution of disorientations, in which each boundary is classified by its minimum misorientation angle, without consideration of the misorientation axis. Compared to the random distribution, there is an enhancement of grain boundaries with 30° and 90° disorientations. When one considers the axis and angle of the misorientation, there are three independent

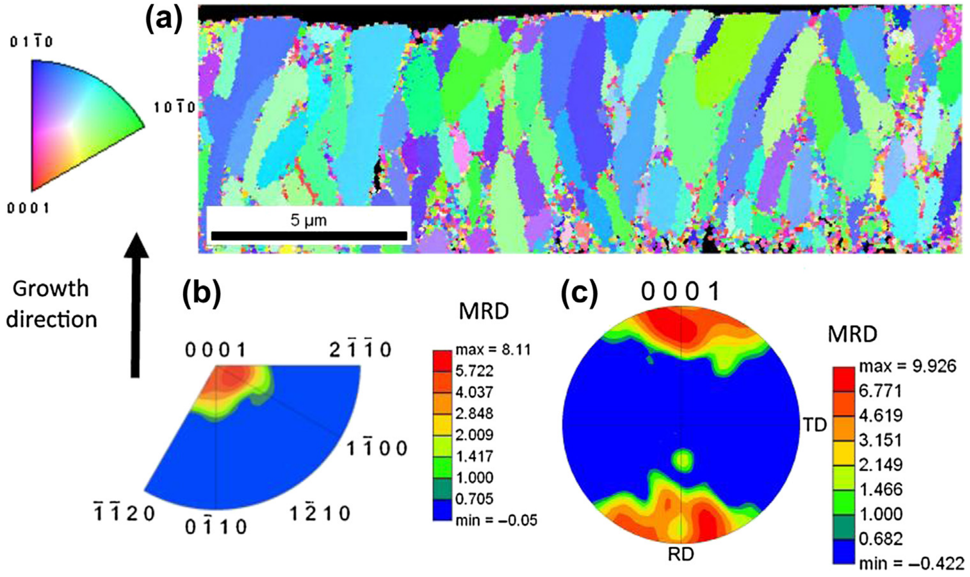

Figure 10 (a) Electron backscatter diffraction orientation map of a transverse section of an α-Al_2O_3 coating grown by chemical vapor deposition (color legend for the orientation is shown on the left). (b) Inverse pole figure for the growth direction of the sample. (c) Pole figure for the [0001] directions in the crystal. Source: Chien et al., 2009.

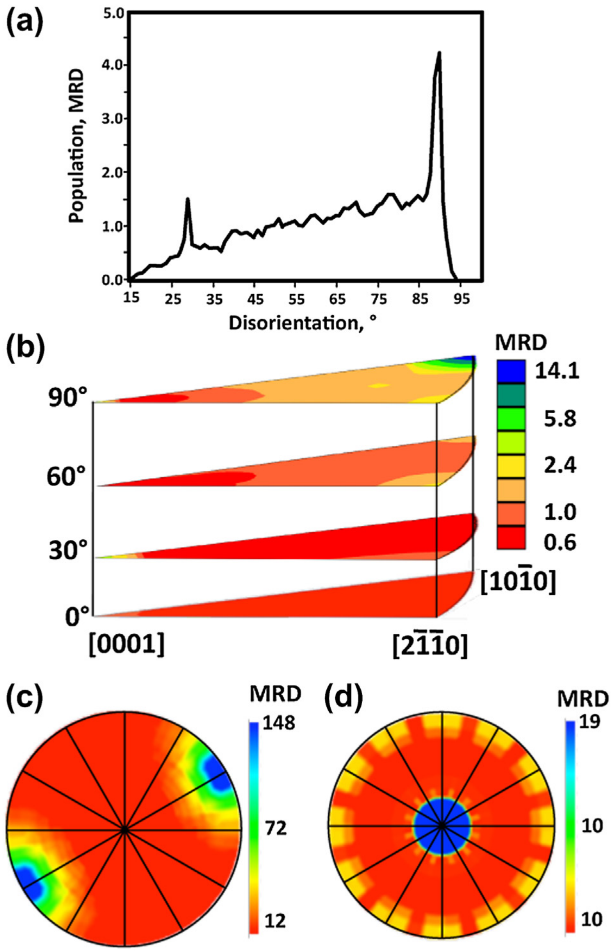

Figure 11 Three different representations of the distribution of relative areas of different types of grain boundaries. (a) Each boundary is classified by its minimum misorientation angle, without consideration of the misorientation axis. (b) Each position in this three-dimensional axis–angle space corresponds to a different misorientation. For any particular axis–angle combination, there is a distribution of grain boundary planes and the distributions for the two peaks in (b) are shown in (c) and (d). Source: Rohrer, 2011b.

parameters for each boundary, two for the axis direction and one for the rotation angle. Therefore, in Figure 11(b) each position in a three-dimensional space corresponds to a different grain boundary misorientation. In each layer of the axis–angle space, all possible axes are represented; the rotation angle varies along the vertical direction. Note that the peak for 30° in Figure 11(a) is concentrated at [0001], indicating that these are mostly 30° rotations about [0001], and the peak at 90° in Figure 11(a) is concentrated at [10-10], indicating that this is the dominant misorientation axis. For any particular axis–angle combination, there is a distribution of grain boundary planes, as shown for the examples in Figure 11(c) and (d). Note that when the misorientation axis, the misorientation angle, and the grain boundary plane are specified, there are five independent parameters. The grain boundary plane distributions in Figure 11(c) and (d) are the relative areas of different grain boundary planes for the misorientation of 90° about [10-10] and 30° about [0001], respectively. The plots are stereographic projections. The maxima show that the 90° [10-10] misorientation boundaries are concentrated on [10-10] planes, indicating that they are pure twist boundaries and the 30° [0001] boundaries are concentrated on [0001], indicating that they are also pure twist boundaries. The local maxima at the prismatic orientations correspond to asymmetric tilt boundaries. One final representation is to consider the distribution of grain boundary planes alone, with no reference to the misorientation. This is the two-parameter IPD. This type of distribution for WC/Co interfaces was already illustrated in Figure 6(b).

Describing the GBCD with a reduced number of parameters is often useful because the complete five-parameter space of grain boundary types is large; if the space is discretized in 10° intervals, then there are roughly 6×10^3 different grain boundaries for a material with cubic symmetry (Rohrer et al., 2004). The number of distinct boundaries increases rapidly for finer discretizations and crystals with reduced symmetry. So, until recently, the number of distinct grain boundary types was large compared to the number of observations it was possible to make. However, this is no longer the case. The development of high-speed EBSD mapping of orientations has made it possible to characterize and classify 10^4–10^5 boundaries (Adams, Wright, & Kunze, 1993; Schwartz, Kumar, Adams, & Field, 2009).

2.08.2.5 Interface Topology

While there have been many efforts during the past several years to characterize the GBCD, fewer studies have attempted to characterize the connectivity of grain boundaries in the microstructure. The statistics of triple junctions, twin related clusters, and percolation characteristics have all been explored as metrics for connectivity (Frary & Schuh, 2003, 2004, 2005; Kumar, King, & Schwartz, 2000; Minich, Schuh, & Kumar, 2002; Reed, Kumar, Minich, & Rudd, 2008; Schuh, Kumar, & King, 2003; Xia, Zhou, Chen, & Wang, 2006; Xia, Zhou, & Chen, 2008), and Schuh, Kumar, King (2003) found that boundary population is not a reliable indicator of network topology. While there is also a long history of applying the mathematical tools of topology to microstructures, there are still relatively few examples (Gameiro, Mischaikow, & Wanner, 2005; Steele, 1972; Mecke, 1996; Mecke & Sofonea, 1997; Mendoza, Savin, Thornton, & Voorhees, 2004, Mendoza, Thornton, Savin, & Voorhees, 2006; Wanner, Fuller, & Saylor, 2010).

In two dimensions, there are two topological metrics that measure the number of independent pieces of the network (referred to as B_0) and the number of closed loops (referred to as B_1) (Wanner et al., 2010). In the context of plane sections of grain boundary networks, B_0 measures the groups of grain boundaries not connected to the rest of the network and B_1 measures the continuous, closed paths of grain boundaries or the number of grains. It has recently been proposed that the ratio of B_0 to B_1, or the inverse connectivity, is a suitable metric for network connectivity (Rohrer & Miller, 2010). The ratio varies with the subset of boundaries considered and its variation as a function of the disorientation angle threshold is a characteristic of the type of microstructure, providing information beyond that available from relative area measurements.

As an example, Figure 12 compares two Ni microstructures (reference and grain boundary engineered) after separating the $\Sigma3^n$ and non-$\Sigma3^n$ boundaries (Rohrer & Miller, 2010). The $\Sigma3^n$ boundaries are $\Sigma3$, $\Sigma9$, and $\Sigma27$, in coincident site lattice notation. The network of $\Sigma3^n$ boundaries in the reference sample is clearly disconnected

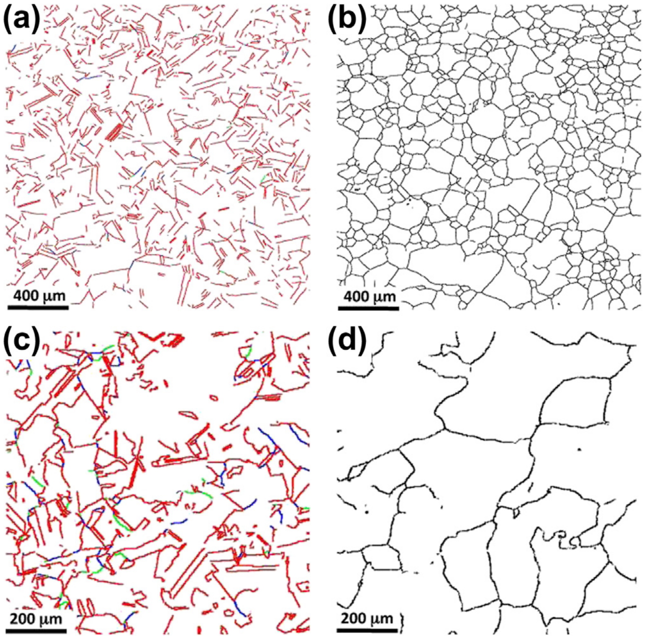

Figure 12 Grain boundary maps for the Ni samples. (a) All of the $\Sigma3^n$ boundaries in the low $\Sigma3$ Ni, $\beta_{01} = 3.1$; (b) all of the non-$\Sigma3^n$ boundaries in the low $\Sigma3$ Ni, $\beta_{01} = 0.12$; (c) all of the $\Sigma3^n$ boundaries in high $\Sigma3$ Ni, $\beta_{01} = 0.53$; (d) all of the non-$\Sigma3^n$ boundaries in high $\Sigma3$ Ni, $\beta_{01} = 8.6$. In (a) and (c), the $\Sigma3$ boundaries are colored red, the $\Sigma9$ boundaries in blue and the $\Sigma27$ boundaries in green. Source: Rohrer & Miller, 2010.

and this is reflected in an inverse connectivity that is greater than one. On the other hand, the network of non-$\Sigma 3^n$ boundaries (Figure 12(b)) is relatively connected and this is reflected in an inverse connectivity that is less than one and smaller than the value for the $\Sigma 3^n$ network. The situation is reversed for the grain boundary engineered sample. In this case, the inverse connectivity is less than one for the $\Sigma 3^n$ boundaries. The inverse connectivity of the network of non-$\Sigma 3^n$ boundaries is 16 times larger, indicating that it is relatively disconnected compared to the network of $\Sigma 3^n$ boundaries. This suggests that the main impact of grain boundary engineering in this case is to increase the connectivity of twin related boundaries while simultaneously decreasing the connectivity of random boundaries.

2.08.2.6 Curvature Distributions

The distribution of interface curvatures is not commonly evaluated, but is important for understanding microstructure evolution and verifying theories for capillarity-driven processes such as coarsening in multi-phased mixtures and grain growth in single-phase polycrystals. Most theories have been compared to experiments where only an average curvature was determined (Rohrer, 2005). Using the three-dimensional data, it is now possible to measure the spatial distribution of curvatures which are important for local morphological evolution (Alkemper & Voorhees, 2001). For example, a recent study of the curvatures of grain faces in three dimensions demonstrated that mean-field approaches to grain growth are flawed because the curvature and growth rate of a grain is strongly affected by the topology of its nearest neighbors (Rowenhorst et al., 2010).

2.08.3 Recent Advances in Microstructural Characterization Techniques

2.08.3.1 Three-Dimensional Atom Probe

3DAP is an increasingly powerful technique for the analysis of composition and structure on the near-atomic scale (Kelly and Miller, 2007; Miller and Forbes, 2009; Seidman, 2007). This technique is commonly referred to as "atomic probe tomography". However, this is somewhat misleading; while the method is used to visualize three-dimensional volumes, the underlining principle is closer to serial sectioning than tomography. 3DAP instruments combine a field-ion microscope with a mass spectrometer; as atoms are ionized and ejected from the sample, their trajectories are used to determine their original positions in the sample and their atomic masses are determined by mass spectroscopy. In the past, there were a number of aspects of atom probe technology that limited its applicability. First, the preparation of needle-shaped specimens by etching was laborious and labor intensive and made it difficult to locate specific features of interest. Second, the analysis was very slow. Finally, it was essentially impossible to examine ceramics and other insulators by this technique. However, progress in several different areas have eliminated or at least minimized these problems.

The DB-FIB SEM has made it feasible to create samples of specific areas for analysis in the 3DAP. For example, single grain boundaries can be selected for analysis and the FIB can be used to mill a needle-shaped specimen that contains the interface or region of interest. The introduction of the local electrode and a position sensitive area detector greatly increased both the efficiency and the rate of ion collection. Finally, using a pulsed laser to assist with ionization made it possible to analyze insulators. As the wavelengths of the lasers are reduced and the pulse rates are increased (approaching a megahertz), the rate of data collection has also greatly increased. With these latest advances, it is possible to image $\sim 10^8$ atoms in a period of hours; approximately 50% of all of the ionized atoms are analyzed, the composition sensitivity in the parts per million range, and spatial resolution is on the order of a nanometer.

As an example of these recent advancements to the study of ceramics and hard materials, laser-assisted 3DAP has recently been used to study the composition of a grain boundary in carbon-doped alumina (Marquis, Yahya, Larson, Miller, & Todd, 2010). An FIB was used to cut a needle shaped sample containing a grain boundary. As shown in Figure 13, there is an $\sim$10 nm wide region near the grain boundary that is enriched in carbon. This work is a significant advance because it shows that oxides and other insulting ceramics can now be characterized by 3DAP. Therefore, future applications to ceramics and hard materials are promising.

2.08.3.2 Electron Tomography

Three-dimensional TEM imaging by electron tomography has recently become more common in materials research (Barnard et al., 2006; Batenburg et al., 2009; Mobus & Inkson, 2001; Weyland et al., 2006). As with

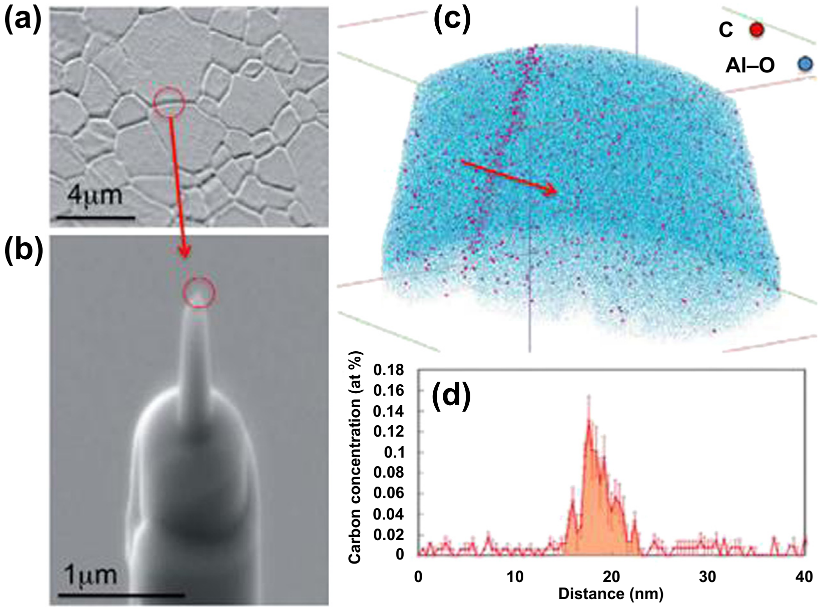

Figure 13 3DAP analysis of a grain boundary in carbon-doped alumina. (a) SEM image of the etched surface revealing grain boundaries. (b) FIB prepared 3DAP specimen containing a grain boundary near the apex of the specimen. (c) Atom-probe reconstruction showing carbon segregation at the grain boundary. (d) Concentration profile across grain boundary along the red arrow shown in (b). Source: From Marquis et al., 2010). Copyright Elsevier, reproduced with permission.

other tomographies, it involves recording a series of images from different perspectives over a large angular range. In principle, images should be recorded at all possible orientations and in small increments (on the order of 1°); in practice, the geometry of the sample holder and the microscope usually limits the range of rotation. While this is nonideal and can lead to some artifacts, it does not prevent application of the method. After the images are recorded, the three-dimensional volume is reconstructed and visualized using computer algorithms developed for this purpose. For example, the image in Figure 14 shows silica particles within a polymer/ceramics composite (Ikeda, Katoh, Shimanuki, & Kohjiya, 2004). While this technique has not been widely applied to ceramics and hard materials, it will clearly be useful for understanding the structure of composites.

The most common contrast mechanism for electron tomography is high-angle annular dark-field imaging in the scanning TEM (Robertson et al., 2011). Because this contrast mechanism is sensitive to variations in the atomic number, it creates clear phase contrast. However, electron tomography can also be carried out with bright-field or dark-field images, although competing contrast mechanisms can interfere with the three-dimensional reconstruction. It is also possible to create three-dimensional composition maps by coupling the images to electron energy loss or energy-dispersive spectroscopy. In addition to structural information in multiphased materials, electron tomography has also been used to study dislocation dynamics and magnetic domain structure (Robertson et al., 2011). The resolution of this technique is on the order of 1 nm.

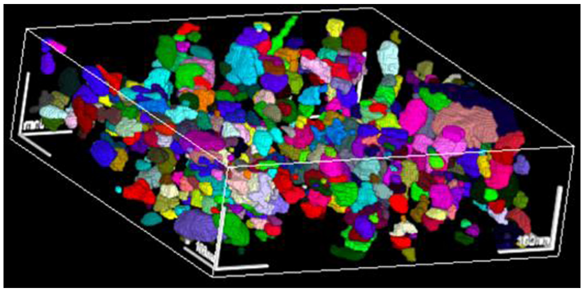

Figure 14 Volume rendered view of the reconstructed mass density distribution of silica inclusions in a rubber matrix. The frame is shown in reconstructed perspective geometry (length and width: 630 nm; thickness: 181 nm). The bar for each direction shows the distance of 100 nm. Source: From Ikeda et al. (2004). Copyright John Wiley and Sons, reproduced with permission.

2.08.3.3 X-ray Tomography

The basic principles of tomography can also be applied to a set of transmission X-ray radiographs to reconstruct a three-dimensional volume (Chen et al., 2010; Chino and Dunand, 2008). Contrast in the radiographs arises from differences in absorption coefficients, so it is generally applied to multiphased materials and composites. Compared to electron tomography, the imaging conditions are much more straightforward and there is no limit on the angular range. While the resolution is lower than electron tomography, it is also possible to image much larger volumes. The samples must be partially X-ray transparent so it is the absorption coefficient of the sample, along with the density, which controls the maximum sample size. There are commercial desktop instruments that are capable of creating three-dimensional images with resolutions in the 10 s of microns range and volumes on the order of 10^2 mm^3. Using the greater penetrating power of the higher energy X-rays available at a synchrotron, larger samples can be imaged at resolutions below 10 μm. Furthermore, recent advances in the ability to focus X-rays have made it possible to increase the resolution of synchrotron tomography to approximately 20 nm (Robertson et al., 2011).

An example of X-ray tomography is shown in Figure 15. The sample is an SiC fiber–SiC matrix composite formed by the chemical vapor infiltration of a woven fiber preform (Morales-Rodriguez, Reynaud, Fantozzi, Adrien, & Maire, 2009). This process leaves porosity in the material and this creates density contrast that can be imaged. This example was constructed from 1200 separate projections imaged with an 85 kV beam and a pixel size of 4.2 μm. The data can be analyzed to determine the volume fraction of pores, the connectivity of the pore space, and the tortuosity of the pores. Another example in which a ceramic/metal composite has been characterized is a study of damage accumulation around SiC particles in SiC/aluminum composites (Silva et al., 2010; Williams et al., 2010). Mo–TiC composites have also been imaged by this technique at the European Synchrotron Radiation Facility ID19 beam line and have a pixel size of 280 nm (Cedat et al., 2009). Data sets of this type are valuable as input to simulations of materials properties. As the resolution increases, X-ray tomography is likely to become a widespread technique for the study of composites containing hard materials.

2.08.3.4 DB-FIB/EBSD

Automated EBSD, which makes it possible to accumulate a map of crystal orientations on a surface, has had a transformative effect on the study of grain boundaries in polycrystals (Figure 16; Adams et al., 1993). It is currently possible to measure several hundred orientations per second, enabling the determination of the shapes and orientations of thousands of grains in a reasonable amount of time. In orientation maps such as that shown in Figure 16(c), four of the five grain boundary parameters can be specified: the lattice misorientation and the in-plane component of the grain boundary plane orientation. The most direct way to make an absolute determination of the final component of the boundary plane orientation is to remove a small amount of material (small compared to the grain size) and repeat the measurement; a process referred to as *serial sectioning*. Manual serial sectioning coupled with EBSD to determine grain boundary plane crystallography is technically demanding and time consuming. As a result, there are relatively few examples in the literature (Randle & Davies,

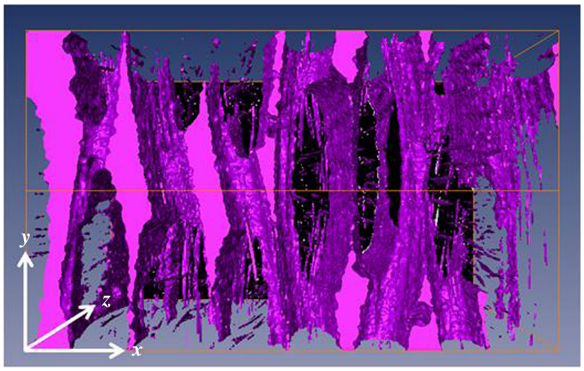

Figure 15 Three-dimensional volume rendering of the axial view of pores in two-dimensional SiC$_f$–SiC composites. The dimensions of the reconstructed three-dimensional volume are $x \sim 2.5$ mm, $y \sim 1.5$ mm and $z \sim 3.8$ mm (total volume ~ 14.3 mm^3). Source: From Morales-Rodriguez et al. (2009). Copyright Elsevier, reproduced with permission.

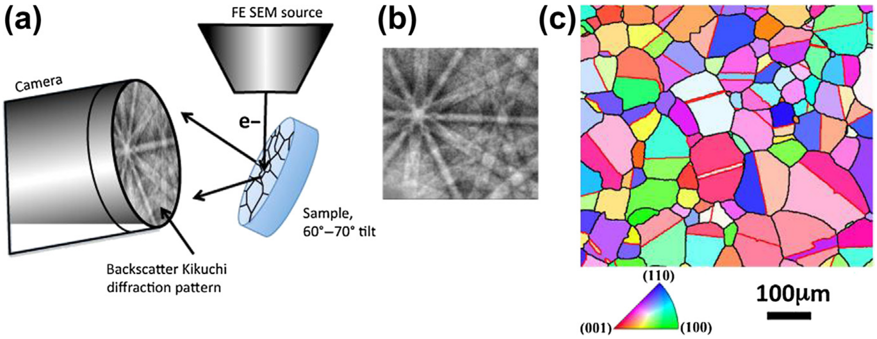

Figure 16 (a) Electron backscatter diffraction (EBSD) maps are recorded in SEM with the sample tilted at a large angle with respect to the beam. (b) A digital camera captures a diffraction pattern that is characteristic of the volume of material that interacted with the beam. (c) After recording local orientations on a grid of points, an orientation map can be plotted. The orientations of the TiO_2 sample are specified by colors defined in the legend. Source: Rohrer, 2011b.

2002; Rowenhorst, Gupta, Feng, & Spanos, 2006, Rowenhorst, Lewis, & Spanos, 2010; Rowenhorst & Voorhees, 2005; Saylor, El Dasher, Sano, & Rohrer, 2004; Saylor, Morawiec, & Rohrer, 2002, 2003b).

Dual beam microscopes that contain both an electron beam for EBSD mapping and an FIB for material removal have significantly reduced the experimental barriers imposed by serial sectioning (Dillon & Rohrer, 2009b; Groeber et al., 2006; Khorashadizadeh et al., 2011; Konrad, Zaefferer, & Raabe, 2006; Li, Dillon, & Rohrer, 2009; Rohrer et al., 2010; Uchic, Groeber, Dimiduk, & Simmons, 2006). The sequence of orientation mapping and removing thin layers can be fully automated so that data can be acquired without user intervention. This has enabled the collection of large three-dimensional images of materials from which statistical information can be derived. Examples of three-dimensional images of ceramics are illustrated in Figure 17. The three-dimensional images can also be used as the input to simulations of materials response (Lewis, Jordan, & Geltmacher, 2008; Rollett et al., 2010; Zaafarani, Raabe, Singh, Roters, & Zaefferer, 2006). It should also be noted that the FIB could be used for serial sectioning and imaging experiments without collecting orientation data. This type of three-dimensional imaging is somewhat simpler and considerably more widespread (MacSleyne et al., 2009; Singh, Chawla, & Shen, 2010).

These methods are easily applied to ceramics. For example, EBSD maps of Y_2O_3 were obtained on parallel layers separated by 200 nm (Figure 17(a); Dillon & Rohrer, 2009b). The choices of the in-plane and between-plane spacing of orientation points are important for the success of the measurement. It has been found that the spacing between planes should be no larger than 1/10th of the mean grain size and the spacing of orientation

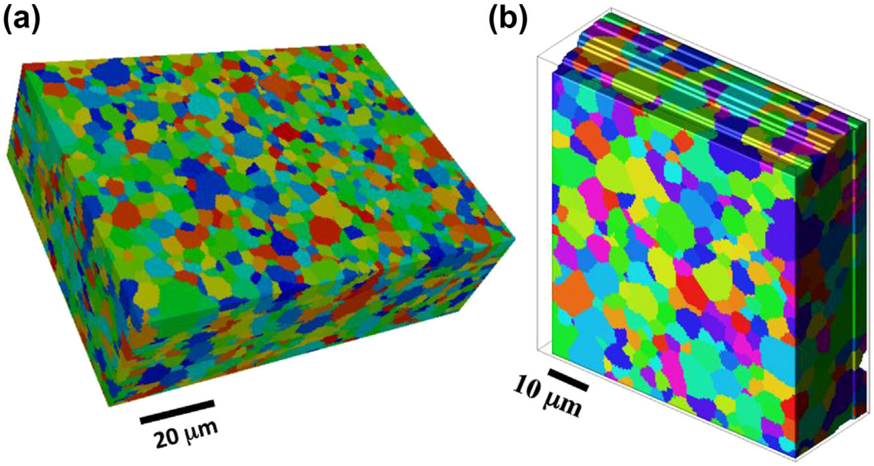

Figure 17 (a) A three-dimensional orientation map of yttria (Y_2O_3) based on 43 parallel EBSD maps (Dillon & Rohrer, 2009a). (b) A three-dimensional orientation map of 8% yttria (Y_2O_3)-stabilized zirconia (ZrO_2). Source: Helmick et al., 2011.

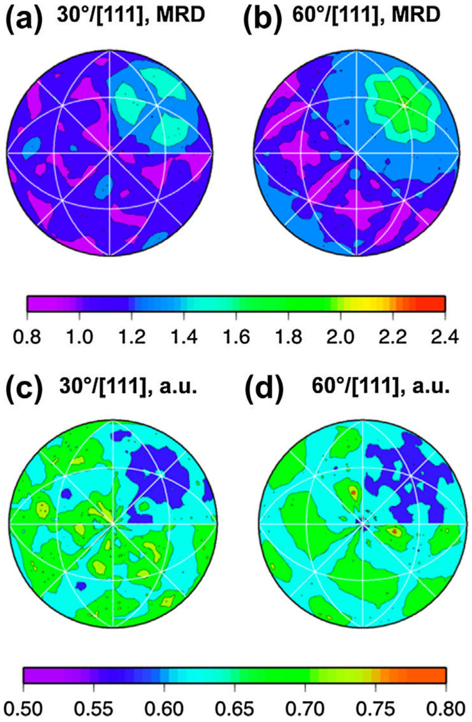

Figure 18 (a–b) The grain–boundary plane distribution at the fixed misorientations of 30°/[111] and 60°/[111], plotted in stereographic projection along [001]. The corresponding energy distributions are shown in (c) and (d). Source: Dillon & Rohrer, 2009a.

points in the plane should be at least one half of the spacing between planes. The processing of the data is also very important for the accurate calculation of the GBCD. In each EBSD map, average orientations were determined for each grain larger than 10 pixels and the grain boundaries were then approximated by a set of line segments. It was also found that subpixel alignment of the parallel layers was essential to achieve accurate results (Dillon & Rohrer, 2009b; Li et al., 2009; Rohrer et al., 2010). If it is assumed that in an equiaxed microstructure the triple lines should be randomly oriented, then their average orientation should be parallel to the milling direction. However, when the orientations of the triple lines are examined in the sample reference frame, they are typically biased. To correct for the effect, a rigid offset is applied to the positions in each layer so that the mean of the triple line direction is normal to the sample surface. In most cases, these adjustments are less than the pixel spacing.

The distribution of grain boundary planes in the yttria polycrystal for misorientations of 30° and 60° about [111] are shown in Figure 18(a) and (b) (Dillon & Rohrer, 2009b). In each distribution, there is a peak at the twist position, where the grain boundary is bounded on both sides by a (111) plane. The grain boundary energy distributions for the same misorientations are shown in Figure 18(c) and (d). The energy shows an approximate inverse relationship to the distribution; the minimum energy occurs at the (111) twist position where the grain boundary plane distribution reaches a maximum. Based on these results, there is an inverse relationship between the grain boundary population and the grain boundary energy. In fact, this inverse correlation persists throughout the domain of grain boundary population types of all of the materials that have been examined (Dillon & Rohrer, 2009b; Li et al., 2009; Rohrer, 2011a; Rohrer et al., 2010; Saylor, Saylor, Morawiec, & Rohrer, 2003a). This inverse correlation is thought to arise from the preferential elimination of higher energy boundaries during grain growth (Dillon & Rohrer, 2009a; Rohrer, 2011a).

Three-dimensional microstructural data is particularly important when the connectivity of a microstructure is important, as is the case for a solid-oxide fuel cell. For example, in the active cathode region, there is a three-phase mixture of lanthanum–strontium manganate (LSM), YSZ, and pore space. Oxidation is thought to only occur at the three-phase line where gaseous oxygen, oxide ion conducting YSZ, and electron conducting LSM meet. A representative section of data from this region is illustrated in Figure 19 (Dillon et al., 2011; Helmick et al., 2011). This study showed that the triple phase lines preferred [111] orientations and that this did not change in service (Dillon et al., 2011).

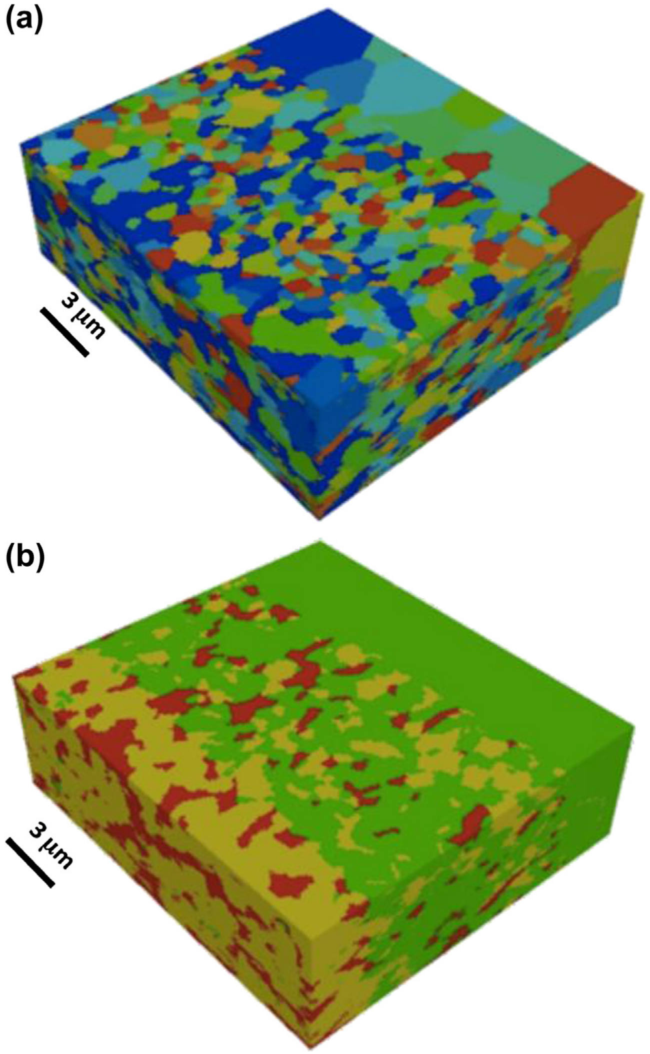

Figure 19 Oblique projections of the reconstructed three-dimensional volume of the active cathode of a solid oxide fuel cell. In the orientation map in (a), different colors are used to indicate different grains. In the phase map (b), green indicates YSZ, gold indicates LSM, and red indicates pores. Source: Helmick et al., 2011.

2.08.3.5 X-ray Diffraction Microscopy

X-ray tomography makes it possible to map the internal structure of a material nondestructively, but in its normal mode provides no crystallographic information. Three-dimensional orientation maps obtained by combining serial sections of planar EBSD orientation maps to reconstruct a three-dimensional volume (Section 2.08.3.4) provide the crystallographic information, but are destructive and do not permit time-dependent studies of polycrystalline structure. There are, however, a number of emerging high-energy X-ray techniques that allow orientation maps to be determined from transmitted X-ray beams (Hefferan et al., 2009; Johnson et al., 2008; Larson et al., 2002; Poulsen et al., 2001). This makes it possible to create a three-dimensional orientation map, subject the sample to external stimulus (mechanical, chemical, thermal, or electrical) and map the structure again.

The most promising X-ray orientation mapping methods are based on transmitted X-rays and, because of this, high-energy (50–100 kV) synchrotron radiation is necessary to achieve penetrations depths of millimeters to centimeters. High-energy diffraction microscopy uses multiple detectors to determine a diffracted beam's origin and, therefore, the physical location of each diffracting grain within a sample; it then combines information about the shapes of diffraction spots and the relative positions of diffraction spots to determine grain shape and orientation, respectively (Poulsen et al., 2001). Diffraction contrast tomography (DCT) is closely

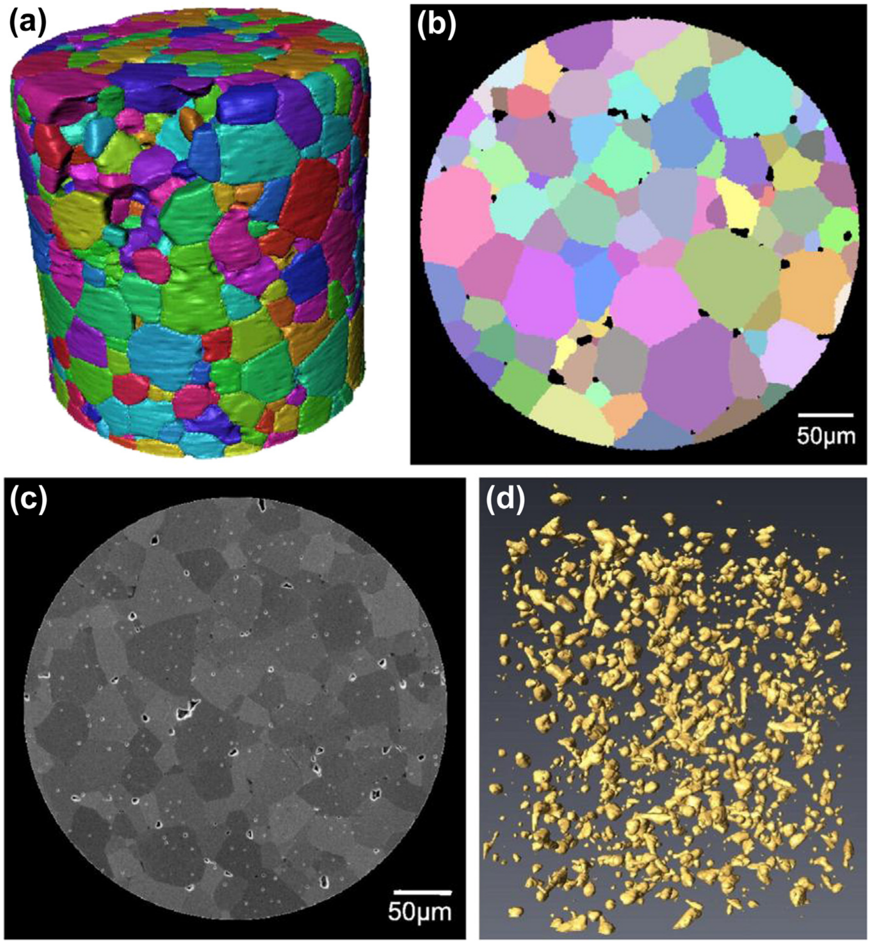

Figure 20 Three-dimensional view of an $SrTiO_3$ polycrystal (a) (colored randomly) and cross-section (colored according to crystallographic orientation) (b) of the reconstructed structure compared to an SEM micrograph (c) of the same material. Collective ensemble of intergranular pores (d). Source: Syha et al., 2012. Copyright Elsevier, reproduced with permission.

related to HEDM, but is a tomographic technique (Johnson et al., 2008). In X-ray tomography, the contrast is determined by density differences. However, if a monochromatic beam is used and the individual crystals are sufficiently large, then a portion of the transmitted beam is diffracted away, and this creates contrast in the radiograph that can be associated with the projected grain shape and location; the diffraction angles can be used to determine the grain orientation. This technique has been used to study the paths followed by cracks that advance by stress corrosion cracking (King, Johnson, Engelberg, Ludwig, & Marrow, 2008).

These techniques currently have resolutions in the range of 1–5 μm and have yet to be widely applied. One published application of DCT to a ceramic is a study of $SrTiO_3$ and an example of the results is shown in Figure 20 (Syha et al., 2012). This sample contains more than 800 grains and about half are internal and do not interact with the surface. The data can be used to determine both the grain and pore size distributions. In addition, the grain shapes and topologies can be determined. For example, the average number of faces per grain for the sample shown in Figure 20 is 12.8. Furthermore, because the data include crystallographic information, all textural data and the five-parameter GBCD can also be calculated.

2.08.4 Summary and Conclusions

Section 2.08.2 of this chapter summarized quantitative parameters that could be derived from microstructural characterization efforts. The recent implementation of three-dimensional microstructure characterization has led to both increasingly sophisticated and increasingly accurate descriptions of grain size distributions, grain shape descriptions, interface character distributions, and microstructural connectivity. This has mainly been enabled by the development of the advanced three-dimensional characterization techniques that were described in Section 2.08.3. While not all these have been applied widely to ceramics or other hard materials, they are applicable and will certainly have impact in the future.

There are three current trends in microstructural characterization that are likely to continue for some time. First, the numbers of features characterized will increase, structures will be characterized in three dimensions, and, in some cases, three-dimensional structures will be characterized as a function of time. Larger data sets will allow a representative volume of the material to be quantified, and three-dimensional and time-dependent data will allow mechanisms to be explored. The second trend is that structure data will be used as input for simulations of materials properties. Such studies will be necessary to validate simulations that can be used to study hypothetical structures. Finally, structural characterization will increasingly use multiple techniques to span length scales. It is anticipated that these trends will lead to increasingly powerful structure–property relationships for a wide range of ceramic and composite hard materials.

Acknowledgment

The work was supported by the MRSEC program of the National Science Foundation under Award Number DMR-0520425.

References

Adams, B. L., Wright, S. I., & Kunze, K. (1993). Orientation imaging - the emergence of a new microscopy. *Metallurgical Transactions A: Physical Metallurgy and Materials Science, 24*, 819–831.

Alkemper, J., & Voorhees, P. W. (2001). Three-dimensional characterization of dendritic microstructures. *Acta Materialia, 49*, 897–902.

Bando, Y. (1995). Microstructure analysis of advanced ceramics by high-resolution analytical transmission electron-microscopy. *Journal of Electron Microscopy, 44*, 115–123.

Barnard, J. S., Sharp, J., Tong, J. R., & Midgley, P. A. (2006). High-resolution three-dimensional imaging of dislocations. *Science, 313*, 319.

Batenburg, K. J., Bals, S., Sijbers, J., Kubel, C., Midgley, P. A., Hernandez, J. C., et al. (2009). 3D imaging of nanomaterials by discrete tomography. *Ultramicroscopy, 109*, 730–740.

Cedat, D., Libert, M., Le Flem, M., Fandeur, O., Rey, C., Clavel, M., et al. (2009). Experimental characterization and mechanical behaviour modelling of molybdenum-titanium carbide composite for high temperature applications. *International Journal of Refractory Metals & Hard Materials, 27*, 267–273.

Chen, Y. C. K., Chu, Y. S., Yi, J., Mcnulty, I., Shen, Q., Voorhees, P. W., et al. (2010). Morphological and topological analysis of coarsened nanoporous gold by X-ray nanotomography. *Applied Physics Letters, 96*.

Chien, H., Gao, M. C., Miller, H. M., Rohrer, G. S., Ban, Z. G., Prichard, P., et al. (2009). Microtexture and hardness of CVD deposited alpha-Al_2O_3 and TiC_xN_{1-x} coatings. *International Journal of Refractory Metals & Hard Materials, 27*, 458–464.

Chino, Y., & Dunand, D. C. (2008). Directionally freeze-cast titanium foam with aligned, elongated pores. *Acta Materialia, 56*, 105–113.

Dillon, S. J., Helmick, L., Miller, H. M., Wilson, L., Gemman, R., Petrova, R. V., et al. (2011). The orientation distributions of lines, surfaces, and interfaces around three-phase boundaries in solid oxide fuel cell cathodes. *Journal of the American Ceramic Society, 94*, 4045–4051.

Dillon, S., & Rohrer, G. (2009a). Mechanism for the development of anisotropic grain boundary character distributions during normal grain growth. *Acta Materialia, 57*, 1–7.

Dillon, S. J., & Rohrer, G. S. (2009b). Characterization of the grain-boundary character and energy distributions of yttria using automated serial sectioning and EBSD in the FIB. *Journal of the American Ceramic Society, 92*, 1580–1585.

Frary, M., & Schuh, C. A. (2003). Nonrandom percolation behavior of grain boundary networks in high-T_c superconductors. *Applied Physics Letters, 83*, 3755–3757.

Frary, M., & Schuh, C. A. (2004). Percolation and statistical properties of low- and high-angle interface networks in polycrystalline ensembles. *Physical Review B, 69*, 12.

Frary, M., & Schuh, C. A. (2005). Connectivity and percolation behaviour of grain boundary networks in three dimensions. *Philosophical Magazine, 85*, 1123–1143.

French, D. N. (1969). Microstructure and microproperties of WC–Co alloys. *International Journal of Powder Metallurgy, 5*, 47–60.

Gameiro, M., Mischaikow, K., & Wanner, T. (2005). Evolution of pattern complexity in the Cahn–Hilliard theory of phase separation. *Acta Materialia, 53*, 693–704.

German, R. M. (1985). The contiguity of liquid-phase sintered microstructures. *Metallurgical Transactions A: Physical Metallurgy and Materials Science, 16*, 1247–1252.

Groeber, M. A., Haley, B. K., Uchic, M. D., Dimiduk, D. M., & Ghosh, S. (2006). 3D reconstruction and characterization of polycrystalline microstructures using a FIB-SEM system. *Materials Characterization, 57*, 259–273.

Gurland, J. (1988). New scientific approaches to development of tool materials. *International Materials Reviews, 33*, 151–166.

Hefferan, C. M., Li, S. F., Lind, J., Lienert, U., Rollett, A. D., Wynblatt, P., et al. (2009). Statistics of high purity nickel microstructure from high energy X-ray diffraction microscopy. *CMC-Computers Materials & Continua, 14*, 209–219.

Helmick, L., Dillon, S. J., Gerdes, K., Gemmen, R., Rohrer, G. S., Seetharaman, S., et al. (2011). Crystallographic characteristics of grain boundaries in dense yttria-stabilized zirconia. *International Journal of Applied Ceramic Technology, 8*, 1218–1228.

Hollox, G. E. (1968). Microstructure and mechanical behavior of carbides. *Materials Science and Engineering, 3*, 121–137.

Hull, F. C. (1988). Plane section and spatial characteristics of equiaxed beta-brass grains. *Materials Science and Technology, 4*, 778–785.

Ikeda, Y., Katoh, A., Shimanuki, J., & Kohjiya, S. (2004). Nano-structural observation of in situ silica in natural rubber matrix by three dimensional transmission electron microscopy. *Macromolecular Rapid Communications, 25*, 1186–1190.

Ikuhara, Y. (2001). Grain boundary and interface structures in ceramics. *Journal of the Ceramic Society of Japan, 109*, S110–S120.

Jha, S. K., Larsen, J. M., & Rosenberger, A. H. (2009). Towards a physics-based description of fatigue variability behavior in probabilistic life-prediction. *Engineering Fracture Mechanics, 76*, 681–694.

Johnson, G., King, A., Honnicke, M. G., Marrow, J., & Ludwig, W. (2008). X-ray diffraction contrast tomography: a novel technique for three-dimensional grain mapping of polycrystals. II. The combined case. *Journal of Applied Crystallography, 41*, 310–318.

Kelly, T. F., & Miller, M. K. (2007). Invited review article: atom probe tomography. *Review of Scientific Instruments, 78*(031101), 1–20.

Khorashadizadeh, A., Raabe, D., Zaefferer, S., Rohrer, G. S., Rollett, A. D., & Winning, M. (2011). Five-parameter grain boundary analysis by 3D EBSD of an ultra fine grained CuZr alloy processed by equal channel angular pressing. *Advanced Engineering Materials, 13*, 237–244.

Kim, C. S., Massa, T. R., & Rohrer, G. S. (2008). Interface character distributions in WC–Co composites. *Journal of the American Ceramic Society, 91*, 996–1001.

Kim, C. S., & Rohrer, G. S. (2004). Geometric and crystallographic characterization of WC surfaces and grain boundaries in WC–Co composites. *Interface Science, 12*, 19–27.

King, A., Johnson, G., Engelberg, D., Ludwig, W., & Marrow, J. (2008). Observations of intergranular stress corrosion cracking in a grain-mapped polycrystal. *Science, 321*, 382–385.

Kleebe, H. J., Braue, W., Schmidt, H., Pezzotti, G., & Ziegler, G. (1996). Transmission electron microscopy of microstructures in ceramic materials. *Journal of the European Ceramic Society, 16*, 339–351.

Konrad, J., Zaefferer, S., & Raabe, D. (2006). Investigation of orientation gradients around a hard laves particle in a warm-rolled Fe_3Al-based alloy using a 3D EBSD-FIB technique. *Acta Materialia, 54*, 1369–1380.

Kral, M. V., & Spanos, G. (1999). Three-dimensional analysis of proeutectoid cementite precipitates. *Acta Materialia, 47*, 711–724.

Kumar, M., King, W. E., & Schwartz, A. J. (2000). Modifications to the microstructural topology in F.C.C. materials through thermomechanical processing. *Acta Materialia, 48*, 2081–2091.

Larson, B. C., Yang, W., Ice, G. E., Budai, J. D., & Tischler, J. Z. (2002). Three-dimensional X-ray structural microscopy with submicrometre resolution. *Nature, 415*, 887–890.

Lewis, A. C., Jordan, K. A., & Geltmacher, A. B. (2008). Determination of critical microstructural features in an austenitic stainless steel using image-based finite element modeling. *Metallurgical and Materials Transactions A: Physical Metallurgy and Materials Science, 39A*, 1109–1117.

Li, J., Dillon, S. J., & Rohrer, G. S. (2009). Relative grain boundary area and energy distributions in nickel. *Acta Materialia, 57*, 4304–4311.

Luyckx, S., & Love, A. (2006). The dependence of the contiguity of WC on Co content and its independence from WC grain size in WC–Co alloys. *International Journal of Refractory Metals & Hard Materials, 24*, 75–79.

Macsleyne, J., Uchic, M. D., Simmons, J. P., & De Graef, M. (2009). Three-dimensional analysis of secondary gamma-prime precipitates in rene-88 DT and UMF-20 superalloys. *Acta Materialia, 57*, 6251–6267.

Marquis, E. A., Yahya, N. A., Larson, D. J., Miller, M. K., & Todd, R. I. (2010). Probing the improbable: imaging C atoms in alumina. *Materials Today, 13*, 34–36.

Mecke, K. R. (1996). Morphological characterization of patterns in reaction-diffusion systems. *Physical Review E, 53*, 4794–4800.

Mecke, K. R., & Sofonea, V. (1997). Morphology of spinodal decomposition. *Physical Review E, 56*, R3761–R3764.

Mendoza, R., Savin, I., Thornton, K., & Voorhees, P. W. (2004). Topological complexity and the dynamics of coarsening. *Nature Materials, 3*, 385–388.

Mendoza, R., Thornton, K., Savin, I., & Voorhees, P. W. (2006). The evolution of interfacial topology during coarsening. *Acta Materialia, 54*, 743–750.

Miller, M. K., & Forbes, R. G. (2009). Atom probe tomography. *Materials Characterization, 60*, 461–469.

Minich, R. W., Schuh, C. A., & Kumar, M. (2002). Role of topological constraints on the statistical properties of grain boundary networks. *Physical Review B, 66*, 4.

Mobus, G., & Inkson, B. J. (2001). Three-dimensional reconstruction of buried nanoparticles by element-sensitive tomography based on inelastically scattered electrons. *Applied Physics Letters, 79*, 1369–1371.

Morales-Rodriguez, A., Reynaud, P., Fantozzi, G., Adrien, J., & Maire, E. (2009). Porosity analysis of long-fiber-reinforced ceramic matrix composites using x-ray tomography. *Scripta Materialia, 60*, 388–390.

National Insitutiutes of Health, Imagej. http://rsb.info.nih.gov/ij/.

Pollock, T. M., Allison, J. E., Backman, D. G., Boyce, M. C., Gersh, M., Holm, E. A., et al. (2008). *Integrated computational materials engineering: A transformational discipline for improved competitiveness and national security*. Washington, DC: National Academy of Sciences.

Poulsen, H. F., Nielsen, S. F., Lauridsen, E. M., Schmidt, S., Suter, R. M., Lienert, U., et al. (2001). Three-dimensional maps of grain boundaries and the stress state of individual grains in polycrystals and powders. *Journal of Applied Crystallography, 34*, 751–756.

Randle, V., & Davies, H. (2002). A comparison between three-dimensional and two-dimensional grain boundary plane analysis. *Ultramicroscopy, 90*, 153–162.

Reed, B. W., Kumar, M., Minich, R. W., & Rudd, R. E. (2008). Fracture roughness scaling and its correlation with grain boundary network structure. *Acta Materialia, 56*, 3278–3289.

Robertson, I. M., Schuh, C. A., Vetrano, J. S., Browning, N. D., Field, D. P., Jensen, D. J., et al. (2011). Towards an integrated materials characterization toolbox. *Journal of Materials Research, 26*, 1341–1383.

Rohrer, G. S. (2005). Influence of interface anisotropy on grain growth and coarsening. *Annual Review of Materials Research, 35*, 99–126.

Rohrer, G. S. (2011a). Grain boundary energy anisotropy: a review. *Journal of Materials Science, 46*, 5881–5895.

Rohrer, G. S. (2011b). Measuring and interpreting the structure of grain-boundary networks. *Journal of the American Ceramic Society, 94*, 633–646.

Rohrer, G. S., Li, J., Lee, S., Rollett, A. D., Groeber, M., & Uchic, M. D. (2010). Deriving grain boundary character distributions and relative grain boundary energies from three-dimensional EBSD data. *Materials Science and Technology, 26*, 661–669.

Rohrer, G. S., & Miller, H. M. (2010). Topological characteristics of plane sections of polycrystals. *Acta Materialia, 58*, 3805–3814.

Rohrer, G. S., Saylor, D. M., El Dasher, B., Adams, B. L., Rollett, A. D., & Wynblatt, P. (2004). The distribution of internal interfaces in polycrystals. *Zeitschrift Fur Metallkunde, 95*, 197–214.

Rollett, A. D., Lebensohn, R. A., Groeber, M., Choi, Y., Li, J., & Rohrer, G. S. (2010). Stress hot spots in viscoplastic deformation of polycrystals. *Modelling and Simulation in Materials Science and Engineering, 18*.

Rowenhorst, D. J., Gupta, A., Feng, C. R., & Spanos, G. (2006). 3D crystallographic and morphological analysis of coarse martensite: combining EBSD and serial sectioning. *Scripta Materialia, 55*, 11–16.

Rowenhorst, D. J., Lewis, A. C., & Spanos, G. (2010). Three-dimensional analysis of grain topology and interface curvature in a beta-titanium alloy. *Acta Materialia, 58*, 5511–5519.

Rowenhorst, D. J., & Voorhees, P. W. (2005). Measurements of the grain boundary energy and anisotropy in tin. *Metallurgical and Materials Transactions A: Physical Metallurgy and Materials Science, 36A*, 2127–2135.

Russ, J. C. (1986). *Practical stereology*. Springer.

Sano, T., Kim, C. S., & Rohrer, G. S. (2005). Shape evolution of $SrTiO_3$ crystals during coarsening in titania-rich liquid. *Journal of the American Ceramic Society, 88*, 993–996.

Saylor, D. M., El-Dasher, B. S., Adams, B. L., & Rohrer, G. S. (2004). Measuring the five-parameter grain-boundary distribution from observations of planar sections. *Metallurgical and Materials Transactions A: Physical Metallurgy and Materials Science, 35A*, 1981–1989.

Saylor, D. M., El Dasher, B., Sano, T., & Rohrer, G. S. (2004). Distribution of grain boundaries in $SrTiO_3$ as a function of five macroscopic parameters. *Journal of the American Ceramic Society, 87*, 670–676.

Saylor, D. M., Morawiec, A., & Rohrer, G. S. (2002). Distribution and energies of grain boundaries in magnesia as a function of five degrees of freedom. *Journal of the American Ceramic Society, 85*, 3081–3083.

Saylor, D., Morawiec, A., & Rohrer, G. (2003a). The relative free energies of grain boundaries in magnesia as a function of five macroscopic parameters. *Acta Materialia, 51*, 3675–3686.

Saylor, D. M., Morawiec, A., & Rohrer, G. S. (2003b). Distribution of grain boundaries in magnesia as a function of five macroscopic parameters. *Acta Materialia, 51*, 3663–3674.

Saylor, D. M., & Rohrer, G. S. (2002). Determining crystal habits from observations of planar sections. *Journal of the American Ceramic Society, 85*, 2799–2804.

Schuh, C. A., Kumar, M., & King, W. E. (2003). Analysis of grain boundary networks and their evolution during grain boundary engineering. *Acta Materialia, 51*, 687–700.

Schwartz, A. J., Kumar, M., Adams, B. L., & Field, D. P. (2009). *Electron backscatter diffraction in materials science*. New York: Springer.

Seidman, D. N. (2007). Three-dimensional atom-probe tomography: advances and applications. *Annual Review of Materials Research, 37*, 127–158.

Sherman, D., & Brandon, D. (1999). Mechanical properties of hard materials and their relation to microstructure. *Advanced Engineering Materials, 1*, 161–181.

Silva, F. D., Williams, J. J., Muller, B. R., Hentschel, M. P., Portella, P. D., & Chawla, N. (2010). Three-dimensional microstructure visualization of porosity and Fe-rich inclusions in SiC particle-reinforced Al alloy matrix composites by X-ray synchrotron tomography. *Metallurgical and Materials Transactions A: Physical Metallurgy and Materials Science, 41A*, 2121–2128.

Singh, D. R. P., Chawla, N., & Shen, Y. L. (2010). Focused ion beam (FIB) tomography of nanoindentation damage in nanoscale metal/ceramic multilayers. *Materials Characterization, 61*, 481–488.

Smith, M., Garcia, R. E., & Horn, Q. C. (2009). The effect of microstructure on the galvanostatic discharge of graphite anode electrodes in $LiCoO_2$-based rocking-chair rechargeable batteries. *Journal of the Electrochemical Society, 156*, A896–A904.

Spowart, J. E., Mullens, H. M., & Puchala, B. T. (2003). Collecting and analyzing microstructures in three dimensions: a fully automated approach. *JOM-Journal of the Minerals Metals & Materials Society, 55*, 35–37.

Steele, J. H. (1972). Application of topological concepts in stereology. In G. E. Pellissier, & S. M. Purdy (Eds.), *Stereology and quantitative metallography*. Philadelphia, PA: American Society for Testing and Materials.

Syha, M., Rheinheimer, W., Baurer, M., Lauridsen, E. M., Ludwig, W., Weygand, D., et al. (2012). Three-dimensional grain structure of sintered bulk strontium titanate from x-ray diffraction contrast tomography. *Scripta Materialia, 66*, 1–4.

Thomas, G. (1996). Electron microscopy and microanalysis of ceramics. *Journal of the European Ceramic Society, 16*, 323–338.

Tucker, J. C., Chan, L. H., Rohrer, G. S., Groeber, M. A., & Rollett, A. D. (2012). Tail departure of log-normal grain size distributions in synthetic three-dimensional microstructures. *Metallurgical and Materials Transactions A*. http://dx.doi.org/10.1007/s11661-011-0851-4. Available on line.

Tucker, M. O., & Mclachlan, N. (1993). Fracture and microstructure of graphites. *Journal of Physics D: Applied Physics, 26*, 893–907.

Uchic, M. D., Groeber, M. A., Dimiduk, D. M., & Simmons, J. P. (2006). 3D microstructural characterization of nickel superalloys via serial-sectioning using a dual beam FIB-SEM. *Scripta Materialia, 55*, 23–28.

Varela, M., Lupini, A. R., Van Benthem, K., Borisevich, A. Y., Chisholm, M. F., Shibata, N., et al. (2005). Materials characterization in the aberration-corrected scanning transmission electron microscope. *Annual Review of Materials Research, 35*, 539–569.

Wanner, T., Fuller, E. R., & Saylor, D. M. (2010). Homology metrics for microstructure response fields in polycrystals. *Acta Materialia, 58*, 102–110.

Weyland, M., Yates, T. J. V., Dunin-Borkowski, R. E., Laffont, L., & Midgley, P. A. (2006). Nanoscale analysis of three-dimensional structures by electron tomography. *Scripta Materialia, 55*, 29–33.

White House Office of Science, Technology, and Policy. (2011). *Materials genome initiative for global competitiveness*. http://www.whitehouse.gov/sites/default/files/microsites/ostp/materials_genome_initiative-final.pdf.

Williams, J. J., Flom, Z., Amell, A. A., Chawla, N., Xiao, X., & De Carlo, F. (2010). Damage evolution in SiC particle reinforced al alloy matrix composites by X-ray synchrotron tomography. *Acta Materialia, 58*, 6194–6205.

Williams, W. M., & Smith, C. S. (1952). A study of grain shape in an aluminum alloy and other applications of stereoscopic microradiography. *Journal of Metals, 4*, 755–765.

Wilson, J. R., Kobsiriphat, W., Mendoza, R., Chen, H. Y., Hiller, J. M., Miller, D. J., et al. (2006). Three-dimensional reconstruction of a solid-oxide fuel-cell anode. *Nature Materials, 5*, 541–544.

Xia, S. A., Zhou, B. X., & Chen, W. J. (2008). Effect of single-step strain and annealing on grain boundary character distribution and intergranular corrosion in alloy 690. *Journal of Materials Science, 43*, 2990–3000.

Xia, S., Zhou, B. X., Chen, W. J., & Wang, W. G. (2006). Effects of strain and annealing processes on the distribution of sigma 3 boundaries in a Ni-based superalloy. *Scripta Materialia, 54*, 2019–2022.

Zaafarani, N., Raabe, D., Singh, R. N., Roters, F., & Zaefferer, S. (2006). Three-dimensional investigation of the texture and microstructure below a nanoindent in a Cu single crystal using 3D EBSD and crystal plasticity finite element simulations. *Acta Materialia, 54*, 1863–1876.

2.09 Mechanical Characterization of Ceramics: Designing with Brittle Materials

Raul Bermejo and Robert Danzer, Institut für Struktur- und Funktionskeramik, Montanuniversität Leoben, Leoben, Austria

© 2014 Elsevier Ltd. All rights reserved.

Nomenclature

$\boldsymbol{a}$ Crack length
$\boldsymbol{a_c}$ Critical crack length
$\boldsymbol{a_c(\sigma_a)}$ Critical crack size in service
$\boldsymbol{a_c(\sigma_{pt})}$ Critical crack size in a proof test
$\boldsymbol{C}$ Material parameter
$\mathbf{d}\boldsymbol{a}$ Crack length increment
$\mathbf{d}\boldsymbol{t}$ Time increment
$\mathbf{d}\boldsymbol{N}$ Cycle increment
$\boldsymbol{E}$ Young's modulus
$\boldsymbol{F}$ Probability of failure
$\boldsymbol{F_S(\sigma)}$ Cumulative probability of fracture
$\boldsymbol{g(a)}$ Crack-size frequency density function
$\boldsymbol{G}$ Strain energy release rate
$\boldsymbol{K_I}$ Normal (mode I) stress intensity factor
$\boldsymbol{K_{II}}$ In-plane (sliding) shear stress intensity factor
$\boldsymbol{K_{III}}$ Out-of-plane (tearing) shear stress intensity factor
$\boldsymbol{K_{Ic}}$ Fracture toughness
$\boldsymbol{m}$ Weibull modulus
$\boldsymbol{n}$ SCCG exponent
$\boldsymbol{n_c(\sigma)}$ Mean number of critical cracks per unit volume
$\boldsymbol{n_c}(\sigma, \vec{r})$ Local critical crack density over the volume
$\boldsymbol{N}$ Number of load cycles
$\boldsymbol{N_f}$ Number of cycles to failure
$\boldsymbol{N_{c,S}(\sigma)}$ Mean number of critical cracks per specimen
$\tilde{n}$ SCCG exponent for cyclic fatigue
$\boldsymbol{p}$ Material constant
$\boldsymbol{R}$ Reliability
$\vec{r}$ Position vector
$\boldsymbol{t}$ Time to failure
$\boldsymbol{v}$ Crack growth velocity
$\boldsymbol{v_0}$ Material parameter
$\boldsymbol{V_{eff}}$ Effective volume
$\boldsymbol{V_0}$ Reference volume
$\boldsymbol{V_1}$ Reference volume of material 1
$\boldsymbol{V_2}$ Reference volume of material 2
$\boldsymbol{Y}$ Geometric factor
$\boldsymbol{\Delta C}$ Material parameter
$\boldsymbol{\Gamma_c}$ Energy absorbed (or consumed) per unit area of crack advance
$\boldsymbol{\upsilon}$ Poisson's ratio
$\boldsymbol{\sigma_a}$ Uniaxial applied stress
$\boldsymbol{\sigma_e}$ Equivalent stress
$\boldsymbol{\sigma_f}$ Fracture strength
$\boldsymbol{\sigma_{pt}}$ Applied stress during a proof test
$\boldsymbol{\sigma_r}$ Arbitrary reference stress
$\boldsymbol{\sigma_0}$ Characteristic strength
$\boldsymbol{\sigma_1(R)}$ Equivalent reference stresses for the material volume 1
$\boldsymbol{\sigma_2(R)}$ Equivalent reference stresses for the material volume 2
$\sigma(\vec{r})$ Tensile stress
$\dot{\sigma}$ Stress rate
B3B Ball-on-three balls
MU Measurement uncertainty
PIA Principle of independent action
SCCG Subcritical crack growth
SPT Strength–probability–time diagram

2.09.1 Introduction

The interest in the mechanical behavior of ceramic materials has always been motivated by the in-service demands made on structural components and machine parts which often require the application of brittle materials, particularly ceramics and glasses. The reason is certain outstanding properties such as high-temperature stability, oxidation and corrosion resistance, dimensional stability, hardness and wear resistance, as well as other special characteristics such as thermal, electrical or optical properties. Due to their inherent brittleness, ceramics have been used for many decades as structural elements, but almost always under compressive loading conditions. Currently, most of the new engineering designs need to withstand tensile stresses, which imply potential limitations for ceramics due to their low fracture toughness and sensitivity of their strength to the presence of defects. However, the use of special approaches in the design together with improved mechanical properties of modern engineering ceramics can enable their safe and optimal use as structural materials. Many examples of the successful and beneficial application of engineering ceramics for mechanically loaded components, especially at high temperatures and in aggressive environments, have already been established: from bearings, dies and cutting tools to valves for internal combustion engines, gas turbine components, solid oxide fuel cells, and bioimplants, among others.

The need for different design criterion for brittle materials based on probabilistic calculation of strength, as compared to that generally applied to conventional materials, comes from the different modes of failure criteria. This chapter discusses the reasons and presents the methodology for the probabilistic assessment of the reliability of structural components made of brittle materials. The peculiarities associated with designing for brittle materials are clearly pointed out, and design recommendations to improve their mechanical behavior are specified.

2.09.2 Fracture and Strength of Brittle Materials

The inherent brittleness of these materials is associated with the relatively immobile dislocations and consequently almost absence of plasticity during the fracture process (Davidge, 1979; Kingery, Bowen, & Uhlmann, 1976; Wachtman, 1996). Brittle fracture is controlled by the extension of small flaws which are dispersed in a material or on the surface of components and which behave like cracks. They can be generated in the production process, and also during handling and in service. Since the extremely high values of yield strength in brittle materials are difficult to reach, almost no dissipation of energy due to plastic flow is possible and the energy required for crack propagation is essentially consumed in the formation of new fracture surfaces. The propagation of such cracks leads, in most of the cases, to unexpected and catastrophic failure of the component. Hence, these materials have intrinsically low resistance to crack propagation.

The fracture of brittle materials can be described by the linear elastic fracture mechanics based on the well-known Griffith–Irwin energy balance criterion. Assuming linear elastic material behavior, a crack will propagate under a uniform applied tensile loading normal to the crack plane if a certain combination of the applied stress, σ, and the crack length, a, reaches a critical value. This can be expressed as (Griffith, 1920):

$$\sigma(\pi a)^{1/2} = \frac{1}{Y}(E'\Gamma_c)^{1/2} \tag{1}$$

where E' is the modulus of elasticity, E, for the plane stress and $E/(1-\nu^2)$ for the plane strain conditions, ν is the Poisson's ratio, and Γ_c is the energy absorbed (or consumed) per unit area of crack advance. Y is a dimensionless constant that depends on the crack configuration and geometry, and may also depend on the loading situation. For cracks, which are small compared to the component size (this is the general case in ceramics), Y is of the order of unity. Data for the geometric factor can be found in literature (Murakami, 1986; Newman & Raju, 1981; Tada, Paris, & Irwin, 1985).

The resistance of a material to crack propagation is determined by the material property called *fracture toughness*, which is defined as (Irwin, 1956):

$$K_{Ic} = (E'\Gamma_c)^{1/2} \tag{2}$$

The fracture toughness in brittle materials is measured normal to the direction of applied stress (mode I). It can be experimentally determined using the standardized single-edge V-notch beam method (ISO 23146, 2008). A crack-like notch is introduced in the specimen, which is loaded in four-point bending (4PB). The radius of the notch should be similar or smaller than the microstructural unit (e.g. grain size) in order to avoid overestimation of the fracture toughness (Damani, Gstrein, & Danzer, 1996). Typical values for the fracture toughness of hard ceramics are in the range from 3 to 20 MPa m$^{1/2}$. Some examples are silicon carbides (2.5–4 MPa m$^{1/2}$), alumina (3.5–4 MPa m$^{1/2}$), zirconia YTZP (4.5–5 MPa m$^{1/2}$), silicon nitrides

(4–8 MPa $m^{1/2}$), diamond-based materials (8–12 MPa $m^{1/2}$), and cemented carbides (7–20 MPa $m^{1/2}$) (Ashby, 1992; Munz & Fett, 1999).

The crack propagation is possible if the stress intensity factor at the crack tip, K_I, defined as $K_I = Y\sigma a^{1/2}$, equals or exceeds the intrinsic material toughness:

$$K_I \geq K_{Ic} \tag{3}$$

The stress intensity factor characterizes the stress field near the tip of a crack in a linearly elastic solid under mode I (normal to the crack plane) applied loading. When the criterion for crack propagation (according to Eqn (3)) is fulfilled, the propagation of the crack may occur either in a stable or an unstable manner. The latter will occur if the following inequality is also satisfied (Irwin, 1956):

$$\frac{\partial K_I}{\partial a} \geq \frac{\partial K_{Ic}}{\partial a} \tag{4}$$

where the first term describes the change of the applied stress intensity factor with the crack increment and the second term is the variation of the material toughness as the crack length increases. In monolithic brittle materials, K_{Ic} is generally constant and thus the second term in Eqn (4) is zero. Thus the inequality is automatically fulfilled when crack propagation occurs. In that case unstable crack propagation is expected, which implies catastrophic failure of the component. However, there exist materials where K_{Ic} is not constant, i.e. the crack growth resistance increases with the crack length increment. In such cases, it is said that the material shows "R-curve" behavior (Bradt, Hasselman, & Munz, 1996; Fett & Munz, 1993; Nishida, Hanaki, Nojima, & Pezzotti, 1995; Ramachandran & Shetty, 1991; Swain & Hannink, 1984; Shetty & Wang, 1989). The propagation of a crack upon an applied load does not imply unstable propagation, since Eqn (3) may not be fulfilled. This situation can be found in ceramic materials with toughened mechanisms (Duan, Mai, & Cotterell, 1995; Sbaizero, Roitti, & Pezzotti, 2003), doped ceramics (Anderson & Braun, 1990; Casellas, Feder, Llanes, & Anglada, 2001), multiphase materials (e.g. combining brittle and ductile phases Llanes, Torres, & Anglada, 2002; Torres, Bermejo, Llanes, & Anglada, 2008; Torres, Casellas, Anglada, & Llanes, 2001) or multilayer architectures such as layered ceramics (Bermejo, Deluca, 2013), containing layers with different mechanical properties (e.g. fracture toughness) (Bermejo et al., 2006; Lube, Pascual, Chalvet, & De Portu, 2007; Lugovy et al., 2005; Moon et al., 2002; Pascual, Lube, & Danzer, 2008; Sglavo & Bertoldi, 2006). In this sense, the geometry (layer thickness, distribution and build-up of the layers), material (brittle and ductile) and/or the presence of residual stresses (due to thermal mismatch between layers, among others) can influence the stable/unstable propagation of the crack through the material (see for instance Bermejo et al., 2006; Bermejo et al., 2007; Lugovy et al., 2005; Orlovskaya, Kübler, Subbotin, & Lugovy, 2002; Pascual, Chalvet, Lube, & De Portu, 2005; Sestakova, Bermejo, Chlup, & Danzer, 2011; Sglavo & Bertoldi, 2006). The R-curve behavior can be directly measured using compact tension specimens, where the crack length increment is monitored with an optical microscope. R-curve measurements have been reported for various classes of ceramic-based materials where the toughness can be enhanced through external mechanisms such as crack bridging (Becher, Hsueh, Angelini, & Tiegs, 1988; Evans & McMeeking, 1986; Steinbrech & Schenkel, 1988), domain switching (Bermejo, Grünbichler, Kreith, & Auer, 2010; Fett, Glazounov, Hoffmann, Munz, & Thun, 2001; Kolleck, Schneider, & Meschke, 2000; Meschke, Kolleck, & Schneider, 1997), transformation toughening (Alcalá & Anglada, 1998; Anderson & Braun, 1990; Casellas, Alcalá, Llanes, & Anglada, 2001), and so on.

The strength of brittle materials, σ_f, can be determined with standardized 4PB tests (EN 843-1, 1995). According to the Griffith analysis derived above, the strength scales with the fracture toughness, K_{Ic}, and is inversely proportional to the square root of the critical crack size a_c:

$$\sigma_f = \frac{K_{Ic}}{Y(\pi a_c)^{1/2}} \tag{5}$$

Strength test results on ceramic specimens show, in general, large scatter. This follows from the fact that in each individual specimen the size and location of the critical defect (or crack) can be different. Typical volume flaws, which may act as fracture origins, are second-phase regions, large pores, inclusions, large grains or agglomerations of small pores (Danzer, 2002; Morrell, 1999). Typical fracture origins at the surface are grinding scratches and contact damage. Even grooves at grain boundaries may act as fracture origins (Danzer, 2006). The stress measured at fracture (according to Eqn (5)) can thus differ from specimen to specimen depending on the loading level and on the size of the critical defect.

Another important mechanism affecting the strength of brittle materials is associated with the growth of defects under the application of mechanical stress well below the nominal strength of the material. The most relevant mechanism for this behavior is called subcritical crack growth (SCCG), also known as "delayed fracture" (see for instance Danzer, 1994b; Michalske & Freiman, 1983; Wiederhorn, 1974). This can occur in components operating for a long time under stationary loads. The environmental conditions (i.e. humidity and temperature) can also enhance this phenomenon (Bermejo, et al., 2013; Cho, Yoon, Kim, & Kim, 2000, Cho, Yoon, Lee, & Chu, 2003; Lube, Danzer, Kübler, et al., 2002; Richter, Kleer, Heider, & Röttenbacher, 1985).

As a result of the nondeterministic character of strength in brittle materials and components, a probabilistic analysis is necessary which describes the strength as a distribution function.

2.09.3 Probability of Brittle Failure

In brittle materials, strength depends on the size of the largest (or critical) defect in a specimen, and this can differ from component to component (Danzer, 1994a; Davidge, 1979; Kingery et al., 1976; Munz and Fett, 1999; Wachtman, 1996). Therefore, a single number cannot describe the strength uniquely; a strength distribution function is necessary and a large number of specimens are required for its characterization. Design with brittle materials such as ceramics has to be approached statistically (Rubeša, Smoljan, & Danzer, 2003). In other words, a component has a certain probability of failure or survival. Experimental observations have shown that the probability of failure increases with the magnitude of the load and the size of the specimens (Danzer, 1994a; Davidge, 1979; Wachtman, 1996; Munz & Fett, 1999). The strength–size effect is the most prominent and relevant consequence of the statistical behavior of strength of brittle materials. These observations cannot be explained in a deterministic way using the simple model of a single crack in an elastic body. Their interpretation requires the understanding of the behavior of many cracks distributed throughout a material, as it is derived below.

A cumulative probability of fracture $F_S(\sigma)$, which represents the probability that fracture occurs at a stress equal to or lower than a given σ, can be defined as (Danzer, 1992):

$$F_S(\sigma) = 1 - \exp\left(-N_{c,S}(\sigma)\right) \tag{6}$$

where $N_{c,S}(\sigma)$ is the mean number of critical cracks per specimen (i.e. the value of expectation). The symbol S designates the size and shape of a specimen. This function requires several assumptions: (1) cracks do not interact (this means that their separation is large enough for their stress fields not to overlap), (2) the stress state is uniaxial and homogenous, and (3) cracks are perpendicularly oriented to the stress axis.

The number $N_{c,S}(\sigma)$ depends on the applied load: at low loads, the number of critical cracks is small: $N_{c,S}(\sigma) << 1$. This is typical for the application of advanced ceramic components since they are designed to have a high reliability. In this case the probability of fracture becomes equal to the number of critical cracks per specimen: $F_S(\sigma) \approx N_{c,S}(\sigma) << 1$. At high loads this number may become high: $N_{c,S}(\sigma) >> 1$. Then, if flaws are statistically distributed, some of the specimens contain even more critical cracks than the mean value $N_{c,S}$. Nevertheless, the (small) probability still exists that, in some individual specimens, no critical crack occurs. Therefore, there is always a nonvanishing probability of survival for an individual specimen and the probability of fracture only asymptotically approaches one for very high values of $N_{c,S}(\sigma)$, as can be inferred from Eqn (6) (Danzer, Lube, Supancic, & Damani, 2008).

To establish analytically the dependence of the probability of failure on the applied load, more information on the crack population involved is needed (Jayatilaka & Trustrum, 1977; Hunt & McCartney, 1979; McCartney, 1979; Danzer, Reisner, & Schubert, 1992). If a homogeneous crack-size frequency density function $g(a)$ exists, the mean number of critical cracks per unit volume is:

$$n_c(\sigma) = \int_{a_c(\sigma)}^{\infty} g(a)\,\mathrm{d}a \tag{7}$$

and the mean number of critical cracks (Griffith cracks) per specimen is $N_{c,S}(\sigma) = V \cdot n_c(\sigma)$, with V being the volume of the specimen. (For an inhomogeneous crack size distribution the number of critical flaws per specimen results from integration of the local critical crack density $n_c(\sigma, \vec{r})$ over the volume, with $\vec{r}$ being the position vector.) The strength–size effect is a consequence of this relationship. The stress dependency of the critical crack density results from the stress dependence of the Griffith crack size, which is the lower integration limit in Eqn (7). In most materials the size frequency density decreases with increasing crack size, i.e. $g \propto a^{-p}$, with p being a material constant. A typical density flaw distribution is shown in **Figure 1**.

For such cases Eqn (7) can easily be integrated (Danzer, Lube, & Supancic, 2001; Danzer, Supancic, Pascual, & Lube, 2007; Jayatilaka & Trustrum, 1977). Inserting the result into Eqn (6) gives the well-known relationship for Weibull statistics (Weibull, 1939, 1951):

$$F(\sigma, V) = 1 - \exp\left[-\frac{V}{V_0}\left(\frac{\sigma}{\sigma_0}\right)^m\right] \tag{8}$$

The Weibull modulus m describes the scatter of the strength data. The characteristic strength σ_0 is the stress at which, for specimens of volume $V = V_0$, the failure probability is $F(\sigma_0, V_0) = 1 - \exp(-1) \approx 63\%$. Independent material parameters in Eqn (8) are m and $V_0\sigma_0^m$; the choice of the reference volume V_0 influences the value of the characteristic strength σ_0.

The material parameters in the Weibull distribution are related to the fracture toughness of the material and parameters from the size frequency density of the cracks. Details can be found in Danzer (2006). For example, as shown in the noteworthy paper of Jayatilaka & Trustrum (1977), the Weibull modulus only depends on the slope of the crack size frequency distribution: $m = 2(p-1)$. This derivation shows that the Weibull distribution is a special case out of a class of more general crack-size frequency distributions (Danzer, 1992; Danzer, Lube, & Supancic, 2001). In particular, the type of flaw distribution may have influence on the strength distribution function. This notwithstanding, almost all sets of strength data determined on ceramics reported so far can be fitted nicely by a Weibull distribution function. Typically, advanced ceramics have a Weibull modulus between 10 and 30, or even higher. For classical ceramics the modulus is between 5 and 10. As commented above, the Weibull modulus is associated with the scatter of strength data. In addition, measurement uncertainties (MU) associated with the testing procedure can influence the strength distribution, especially in advanced ceramics with relative low inherent scatter, i.e. with high Weibull modulus (Bermejo, Supancic, & Danzer, 2011). It is therefore recommended an analysis of possible MU for the corresponding testing procedure to determine the strength of brittle materials.

A special case of the Weibull distribution is found when cracks have a random orientation within a homogeneous uniaxial tensile stress field. If cracks are parallel to the uniaxial stress direction, the crack borders are not opened by the stresses and they do not disturb the stress field. Clearly, this type of loading is harmless. For any crack orientation between these extremes, some in-plane (sliding) or out-of-plane (tearing) shear loading (mode II and mode III) of the cracks occur. Then, the strain energy release rate is $G = K_I^2/E' + K_{II}^2/E' + K_{III}^2/E'$, where K_I, K_{II} and K_{III} are the stress intensity factors for each mode of loading (Lawn, 1993). Therefore, to describe the action of many cracks in a uniaxial stress field, not only the crack-size distribution but also the distribution of crack orientations should be known. Such analysis shows that the characteristic strength σ_0 is influenced by the fact that, in the general case, the number of critical cracks depends not only on the length but also on the orientation of the crack (Jayatilaka & Trustrum, 1977).

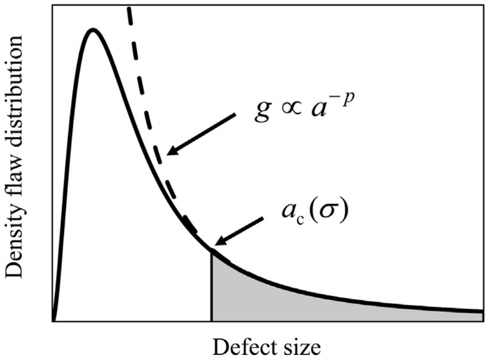

Figure 1 Density flaw distribution as a function of the defect size.

For inhomogeneous but uniaxial stress fields a generalization of Eqn (8) can be made (Weibull, 1939, 1951):

$$F(\sigma_{\mathrm{r}}, V_{\mathrm{eff}}) = 1 - \exp\left[-\frac{V_{\mathrm{eff}}}{V_0}\left(\frac{\sigma_{\mathrm{r}}}{\sigma_0}\right)^m\right] \tag{9}$$

where V_{eff}, the effective volume of a component, is given by the integration of the stress field over the volume:

$$V_{\mathrm{eff}} = \int\limits_{\sigma>0} \left(\frac{\sigma(\vec{r})}{\sigma_{\mathrm{r}}}\right)^m \mathrm{d}V \tag{10}$$

where σ_{r} is an arbitrary reference stress. The integration is done only over volume elements where the stress $\sigma(\vec{r})$ is tensile. Any damaging action of compressive stresses is, therefore, neglected. Usually, the effective volume is defined to be the volume of a tensile test specimen which would yield the same reliability as the component if loaded with the reference stress. The effective volume is related to the reference stress via the following equation:

$$\sigma_{\mathrm{r}}^m V_{\mathrm{eff}} = \sigma_0^m V_0 \tag{11}$$

In general, the maximum in the stress field is used as the reference stress (for example, in bending tests the outer fiber stress is commonly used). Since, for advanced ceramics, the Weibull modulus is a relatively high number (e.g. $m = 10\text{–}30$), only the most highly loaded volume elements (stress more than 80% of the maximum) contribute significantly to the effective volume and so the effective volume approximates to the "volume under high load". It should be noted that if a stress lower than the maximum tensile stress is selected as the reference stress, then the effective volume may become large—possibly larger even than the real size of the component. Hence, this should be taken with care.

For simple cases, e.g. the stress field in a bending specimen, the calculation of the integral in Eqn (10) can be made analytically, but in general, and especially in the case of components, a numerical solution is necessary. For each loading case the calculations have to be done only once because the integral scales with the magnitude of the load. As mentioned before, for modern ceramic materials the Weibull modulus can be high. Then, the numerical determination of the effective volume may become difficult, especially if high-stress gradients exist. Commercial tools which can postprocess data generated in an FE stress analysis are available. Examples are STAU (Brückner-Foit, Heger, & Munz, 1993) or CARES (Nemeth, Manderscheid, & Gyekenyesi, 1989). Effective volumes for standardized flexure bars and cylindrical rods in flexure have been published (Quinn, 2003a, 2003b).

In case of a multiaxial stress state, an equivalent stress should be defined. Many different proposals for the definition of the equivalent stress in ceramics can be found in the literature (Brückner-Foit, Fett, Munz, & Schirmer, 1997; Freudenthal, 1968; Lamon, 1990; Munz & Fett, 1999; Thiemeier, Brückner-Foit, & Kölker, 1991; Wachtman, 1996). The principle of independent action (PIA) is very much used and accounts for the action of all principle stresses (σ_{I}, σ_{II} and σ_{III}) independently (Freudenthal, 1968):

$$\begin{aligned} &\sigma_{\mathrm{e}} = \left(\sigma_{\mathrm{I}}^m + \sigma_{\mathrm{II}}^m + \sigma_{\mathrm{III}}^m\right)^{1/m} && \text{for} \quad \sigma_{\mathrm{I}} > 0 \\ &\text{and} \\ &\sigma_{\mathrm{e}} = 0 && \text{for} \quad \sigma_{\mathrm{I}} \le 0 \end{aligned} \tag{12}$$

The action of compressive stresses is neglected in both cases. Of course, the equivalent stress should also be used for the proper definition of the effective volume. This possibility is also accounted for in commercial FE programs (Brückner-Foit et al., 1993; Nemeth et al., 1989).

Furthermore, applied (uniaxial) constant loads over a certain period of time may cause "delayed failure" on a brittle component, thus the probability of failure may differ from that estimated using Eqn (8). The growth of defects (cracks) upon the action of loads over time (SCCG) can be described as crack velocity vs stress intensity (v–K) curves (Fett & Munz, 1985). For the technical relevant velocity region, i.e. between 10^{-13} and 10^{-6} m s^{-1}, a Paris type law can be used:

$$v = v_0 \left(\frac{K}{K_{\mathrm{Ic}}}\right)^n \tag{13}$$

where v_0 and the SCCG exponent n are the temperature- and environment-dependent material parameters. The corresponding Weibull distribution as a function of time taken into account the effects of SCCG can be then derived (Danzer et al., 2008):

$$F(\sigma_a, V_{\text{eff}}, t) = 1 - \exp\left[-\frac{V_{\text{eff}}}{V_0} \left(\frac{\sigma_a}{\sigma_0}\right)^m \cdot \left(\frac{\sigma_a^2}{C} t + 1\right)^{m/(n-2)} \right] \tag{14}$$

where σ_a is the uniaxial applied stress, t is the time to failure, and $C = 2K_{\text{Ic}}^2/(\pi Y^2 v_0 (n-2))$ is the material- and geometry-dependent parameter. If only little SCCG occurs (i.e. $\sigma_a^2 t/C << 1$), then Eqn (14) becomes equal to Eqn (8).

Analog to strength degradation due to SCCG, the application of variable loads over time (cyclic fatigue) has also been recognized as a possible damage mechanism in hard ceramics (Gilbert, Cao, Moberlychan, Dejonghe, & Ritchie, 1996; Gilbert, Dauskardt, & Ritchie, 1995; Gilbert & Ritchie, 1987; Ritchie, 1999; Reece, Guiu, & Sammur, 1989). Although not much data exit for engineering ceramics, there exists a Paris law for cyclic fatigue crack growth. The crack growth per load cycle can be expressed as:

$$\frac{da}{dN} = \left(\frac{\Delta a}{\Delta N}\right)_0 \left(\frac{\Delta K}{K_{Ic}}\right)^{\tilde{n}} \tag{15}$$

The material parameters, the factor $(\Delta a/\Delta N)_0$ and the SCCG exponent $\tilde{n}$, are dependent on mean stress and temperature. N is the number of load cycles and N_f is the number of cycles to failure. Cyclic crack growth influences lifetime in a manner similar to SCCG. Under conditions where cyclic fatigue is the dominating damage mechanism, the cyclic lifetime can be determined in an analogous way to the procedures discussed above. For example, the equation analogous to Eqn (14) is (Danzer, 1994a):

$$F(\sigma, V, N_f) = 1 - \exp\left[-\frac{V}{V_0} \left(\frac{\Delta\sigma}{\sigma_0}\right)^m \left(\frac{\Delta\sigma^2}{\Delta C} N_f + 1\right)^{m/(\tilde{n}-2)} \right] \tag{16}$$

where ΔC is the material parameter which is defined in a similar fashion as the parameter C. It should be noted that in the few cases reported, the SCCG exponent for cyclic fatigue is much larger than unity: $\tilde{n} >> 1$ (Dauskardt, James, Porter, & Ritchie, 1992; Gilbert et al., 1995; Liu & Chen, 1994). Thus, like SCCG, cyclic fatigue life is strongly dependent on the applied stress range and the size of the initial flaws. The action of cyclic fatigue and of SCCG can be assumed to be independent and the crack advance due to both mechanisms can be simply added. But since both growth rates strongly depend on the applied load and since the SCCG and cyclic fatigue exponents are, in general, different, it is quite likely that the growth rates are very different. Then the simplified model description can be used that only one of both mechanisms is dominating.

2.09.4 Designing with Brittle Materials

The Weibull distribution is widely used not only to describe strength data but also for designing with brittle materials in terms of reliability. For instance, the distribution function can be used to determine the relationship between reliability (defined as $R = 1 - F$) and the necessary equivalent design stress $\sigma_{e,r,R}(V_{\text{eff}})$. In this section, implications of Weibull distributions on the reliability of components are addressed and some guidelines for design with brittle materials are given. An example is shown in **Figure 2**, which shows the cumulative probability of failure versus 4PB strength data for a commercial silicon nitride ceramic (Lube, Danzer, Kübler, et al., 2002; Lube, Danzer, Steen, & , 2002; Lube & Dusza, 2007). The sample consisted of 42 individual experiments. The logarithmic scales have been chosen in such a way that the Weibull distribution is represented by a straight line. The distribution fits nicely to the measured data. The reference stress used is the maximum surface bending stress, $\sigma_{\max}$, and the normalizing volume used is $V_{\text{eff}} = V_0 = 7.7\ \text{mm}^3$. The Weibull modulus results in $m = 15.5$ [12.5 – 18.5] and the characteristic strength of the sample resulting from the sampling procedure $\sigma_0 = 844$ MPa [829 – 859]. The indicated scatter relates to the 90% confidence intervals. As derived in the previous section, the

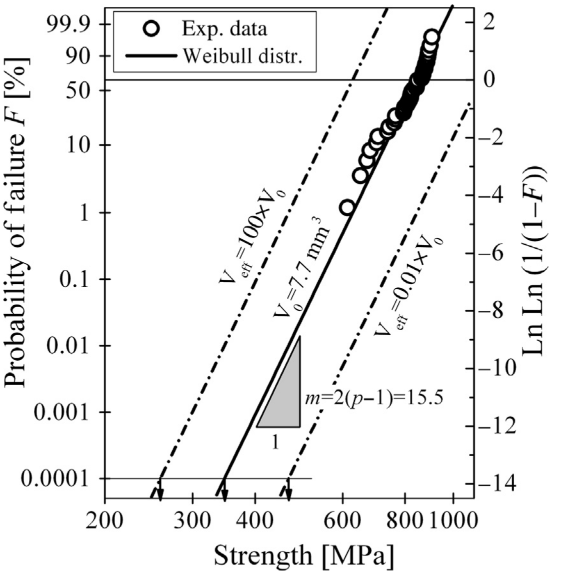

Figure 2 Four-point bending strength test results for a silicon nitride ceramic. Plotted is the probability of failure versus the strength. The straight lines represent the Weibull distributions. The measured Weibull distribution has a modulus of $m = 15.5$ and the characteristic strength is 844 MPa. Also shown are Weibull distributions for specimens with a 100 times larger (left) and a 100 times smaller (right) effective volume. Indicated are the 10^{-4}% failure probabilities and the design stresses for each set of specimens respectively.

equivalent stress necessary for a certain reliability R can be calculated for a component with an effective volume V_{eff} as:

$$\sigma_{\mathrm{e,r,R}}(V_{\mathrm{eff}}) = \sqrt[m]{\frac{V_0 \cdot \sigma_0^m}{V_{\mathrm{eff}}} \cdot \ln \frac{1}{R}} \tag{17}$$

To give an example, for $V_{\mathrm{eff}} = V_0$, let us determine the maximum allowable stress for a reliability of $R = 99.9999\%$ (i.e. one component out of 10^6 would fail) in the bending tests shown in Figure 2. Following Eqn (17) the stress is $\sigma_{\mathrm{e,r,R}}(V_{\mathrm{eff}}) = \sigma_0 \cdot (\ln 1/R)^{1/m}$. Inserting the numerical values for R, σ_0 and m gives $\sigma_{\mathrm{e,r,0.999999}}(V_0) = 0.41 \cdot \sigma_0 = 348$ MPa. In other words, it is expected that one specimen out of a million would fail at a stress ≤ 348 MPa. This stress is also indicated in Figure 2. Remember, the characteristic strength of the data set is 844 MPa. It should be noted that, for the selected example, the design stress determined by probabilistic means corresponds—in a deterministic design approach—to a "safety factor" of about 844 MPa/ 348 MPa = 2.4. The advantage in the probabilistic approach is that a realistic reliability can be determined and that total safety, which does not exist in reality, is not implied.

Now let us discuss the influence of the volume under load. For two sets of specimens of different volume (indicated by the indices 1 and 2) the (equivalent) stresses to achieve the same reliability R must follow the condition:

$$\sigma_1(R)^m V_1 = \sigma_2(R)^m V_2 \quad \text{or} \quad \sigma_2(R) = \sigma_1(R) \cdot \left(\frac{V_1}{V_2}\right)^{1/m} \tag{18}$$

where $\sigma_1(R)$ and $\sigma_2(R)$ are the corresponding equivalent reference stresses to get the desired reliability R and V_1 and V_2 are the corresponding effective volumes of the specimens, respectively. If, in the above example, the effective volume is increased 100 times, the design stress decreases by a factor of $100^{1/15.5} = 0.72$ and becomes 0.72×348 MPa = 234 MPa (for a 100 times smaller volume it becomes 451 MPa). These estimates assume a single flaw-type population initiating failure in all specimen sizes. The Weibull distributions functions for the large and the small specimens are also shown in Figure 2. It can be recognized that the Weibull line is shifted to lower strength values in the first case and to higher strength values in the latter case. The dependence of strength on the specimen size is the most significant effect caused by its probabilistic nature. As discussed above, it may

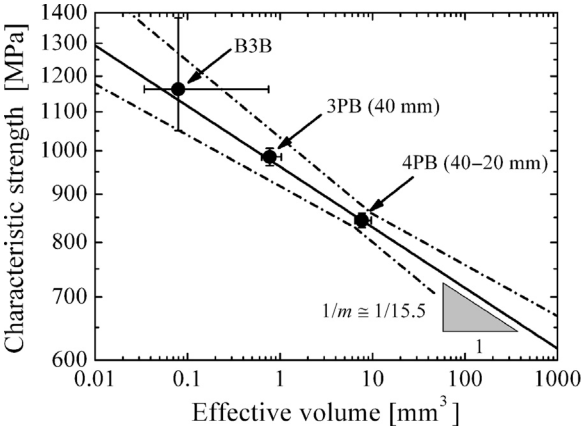

Figure 3 Strength test results of a silicon nitride ceramic. Shown are data from uniaxial and biaxial strength tests. To determine the equivalent stress the PIA criterion was used. Plotted in log–log scale is the characteristic strength of sets of specimens versus their effective volume. The solid line indicates the trend predicted by the Weibull theory. Scatter bars and the dashed lines refer to the 90% confidence intervals due to the sampling procedure. The relatively large scatter of the sample with the smallest effective volume results from the small number of tested specimens.

have a dramatic influence on the design stress. To demonstrate that influence, **Figure 3** shows experimental results from the reference material (Lube, Danzer, Kübler, et al., 2002; Lube, Danzer, Steen, &, 2002; Lube & Dusza, 2007). Results of three-point bending and 4PB tests (uniaxial stress fields) and of ball-on-three balls tests (biaxial stress field) are reported (for details of the testing procedures, see Börger, Supancic, & Danzer, 2002, 2004; Danzer, Harrer, et al., 2007; Lube, Danzer, Kübler, et al., 2002a;Lube & Dusza, 2007). The PIA criterion was used to calculate the equivalent stress. The effective volume of the specimens is in a range between about 10^{-3} and 10^2 mm^3. In this range the data follow the trend determined by the Weibull theory. The broken lines describe the limits of the 90% confidence interval for a data prediction based on the 4PB data presented in **Figure 2**. The characteristic strength of the individual samples varies from about 800 MPa (for the largest specimens) up to almost 1200 MPa (for the smallest specimens).

For the case of brittle materials susceptible to SCCG the lifetime prediction requires obtaining crack propagation data to describe the behavior of the component. Both direct and indirect methods may be employed. With direct methods crack velocity is measured on fracture mechanics-type specimens (e.g. double cantilever specimen and double torsion specimen with a crack) as a function of the applied stress intensity factor. With indirect methods the growth of internal defects causes a degradation of strength, which is used to derive the underlying crack propagation parameters. With this method only the average crack behavior can be measured. However, they allow direct testing of component-like specimens, so that extrapolation of data to real components is more accurate. Typical SCCG measurements are conducted with constant stress rate tests, as shown in **Figure 4**. The characteristic strength (σ_0) is plotted versus the stress rate ($\dot{\sigma}$) in a log–log diagram for an alumina ceramic tested in air at ambient temperature. The scatter bars (90% confidence interval) reflect the uncertainties due to the sampling procedure. For "low" stress rates (i.e. up to $\sim 10^2$ MPa s^{-1}) the data can be fitted according to $\sigma_\text{f} \propto \dot{\sigma}^{1/(n+1)}$, which yields an SCCG exponent $n \approx 33$. For stress rates higher than $\sim 10^2$ MPa s^{-1} the testing time is too short for significant SCCG and the strength is equal to the "inert strength", defined as the strength of the material without the effect of moisture. Two loading regions can be recognized: at low stress rates, a strong influence of SCCG on the strength exists; at (very) high stress rates, SCCG has no significant influence on the strength.

In this section it has been shown how we can estimate the reliability of a component when the distribution function of strength has been measured. Such function may depend on the size of the specimen, on how the load has been applied over time (e.g. static, cyclic) and on the environmental conditions where the component has been loaded. Certain predictions can be made employing the so-called strength–probability–time diagrams, which can be used twofold: (1) to calculate the probability of failure of a component under a constant applied stress after certain period of time, or (2) to estimate the maximum period that a component will work under a constant applied stress (with ca 100% probability of failure). However, in terms of design with brittle materials, in order to guarantee a component's minimum service life a "proof testing" technique is commonly used

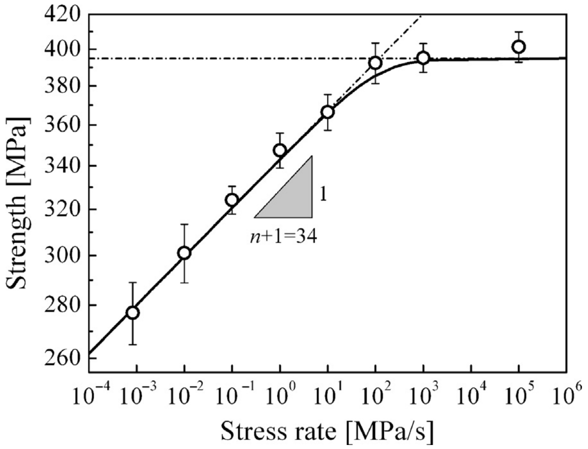

Figure 4 Characteristic strength versus stress rate for constant stress rate tests performed on alumina ceramic in air at ambient temperature (for details, see Lube, & Baierl, 2011). The SCCG exponent determined using this data is $n = 33$. The scatter bars reflect the 90% confidence interval.

(Davidge, 1979; Morrell, 1989; Munz & Fett, 1999; Soma, Ishida, Matsui, & Oda, 1987). In a proof test the component is loaded with a stress σ_{pt}, which is higher than the design service stress σ_{a}. According to Eqn (5), the critical flaw size in a proof test is $a_{\mathrm{c}}(\sigma_{\mathrm{pt}}) = (1/\pi)\cdot(K_{\mathrm{c}}/Y\sigma_{\mathrm{pt}})^2$. In a proof test all components containing equal or larger sized flaws are destroyed. In other words, the frequency distribution of flaws represented in **Figure 1** is truncated at $a = a_{\mathrm{c}}(\sigma_{\mathrm{pt}})$. The critical crack size in service is $a_{\mathrm{c}}(\sigma_{\mathrm{a}}) = (1/\pi)\cdot(K_{\mathrm{c}}/Y\sigma_{\mathrm{a}})^2$ with $a_{\mathrm{c}}(\sigma_{\mathrm{a}}) < a_{\mathrm{c}}(\sigma_{\mathrm{pt}})$. If the crack growth law is known, the time that the crack needs to grow from $a_{\mathrm{c}}(\sigma_{\mathrm{pt}})$ to the critical size $a_{\mathrm{c}}(\sigma_{\mathrm{a}})$ can be determined. In practice, however, neither the loading stress nor the crack growth law is precisely known. Consequently, proof testing is often done at much too high stresses, which results in an unnecessarily large proportion of rejections. An often occurring problem in proof testing is that the in-service stress fields of components cannot easily be simulated in a test. For example, the stress fields caused by temperature changes or by contact loading can hardly be reproduced in simple mechanical tests. In such cases, large parts of a component are often subjected to a too large proof stress, which increases the number of failures in the test. On the other hand, some parts of a component are subjected to too small proof stress. The proof test then only reduces the failure probability, but some in-service failures are still possible.

An alternative to proof test are the non-destructive evaluation (NDE) methods. Radioscopic testing and x-ray computed tomography (CT) are two approaches which are very commonly used due to their capability to visualise inner structures of the objects under investigation and the applicability to numerous materials. Computed tomography is a well-established method in the foundry-industry for identifying casting defects (Geier et al., 2009). It is is ideal for visualising internal structures such as pores, cavities or inclusions of higher or lower density than the base material. The test specimen is positioned between an x-ray source and a detector such that the area that is to be investigated is imaged completely on the detector. Depending on the size and type of detector, a few hundred to thousand radioscopic images are taken while the object is rotated step-wise through 360°. After this step of data acquisition, a three-dimensional volume is reconstructed from the x-ray images, which provides the full 3D-information of the object. The reconstruction of the 3D-volume is based on the findings of G. N. Hounsfield (Hounsfield, 1976) who was awarded the Nobel-Prize in Medicine in 1979. The most widely-spread algorithm for the majority of the CT-reconstructions used nowadays is the "FDK-Algorithm" (Feldkamp, Davis, & Kress, 1984). The resolution of the data depends on the size of the object and the position of the object between x-ray source and detector. Up to now the method is not common for the detection of cracks in ceramics since the crucial factor in such investigations is the size of the structures compared to the spatial resolution of the CT-data. The detection of cracks requires a crack width greater than the resolution of the CT-data. In other words: even a rather long crack will not be detected when it is not opened wide enough, which is the situation in most of (brittle) ceramic materials. The maximum resolution that can be obtained with microfocus x-ray-devices is about 4 μm. Cracks with widths in this range or less cannot be detected with these devices. Further development will be necessary to utilize this method as an alternative to proof testing in brittle materials.

2.09.5 Summary

The stochastic nature of brittle fracture originates from the random occurrence of microstructural defects in the material. They act as stress concentrators which allow the initiation of cracks, one of which may suddenly extend and result in fracture.

To design with brittle materials, a probabilistic approach is required based on the application of principles of probabilistic fracture mechanics. The strength of brittle materials is associated with the density flaw distribution in the component and can be described in most cases in the framework of Weibull statistics. The strength distribution function can be used to determine the relationship between reliability and the necessary equivalent design stress to cause failure. The key parameters which influence the strength are the size of the component (i.e. at a given stress level the probability of failure increases with the size of the component), and variations of tensile stresses (i.e. a precise knowledge of stress distribution over the volume of the component and the applied stress range is required).

In summary, according to the probability of failure, on which design calculations should be based, some considerations must be taken into account when designing with brittle materials:

(1) The calculation of strength is based on a probabilistic evaluation. Each level of applied stress is associated with a certain probability of failure.
(2) Since the Weibull modulus m, which typically takes high values, appears as an exponent in the Weibull distribution, the probability of failure is very sensitive to small variations in the highest tensile stresses that arise. Therefore the distribution of stresses should be kept as uniform as possible, and design-conditioned stress concentrations must be avoided in any case.
(3) Since stresses at every point in the component enter into the calculation of strength, a precise knowledge of stress distribution over the volume is required. This can generally be achieved only by means of computer aided numerical methods of analysis, such as the finite element method.
(4) The integration over the volume of the component brings about the size effect: at a given stress level the probability of failure of a component (i.e. the probability of encountering a critical defect) increases with the size of the component.
(5) The lifetime of brittle components can be reduced by the effect of static and cyclic loads applied over time. Delayed fracture can occur in components under applied constant loads over a certain period of time, as a consequence of the subcritical growth of defects. This is dependent on the applied stress range and the size of initial flaws. Thus a reduction of the size of initial flaws can significantly extend the lifetime of brittle components.

References

Alcalá, J., & Anglada, M. (1998). Indentation precracking of Y-TZP: implications to R-curves and strength. *Materials Science and Engineering, A245*, 267–276.

Anderson, R. M., & Braun, L. M. (1990). Technique for the R-curve determination of Y-TZP using indentation-produced flaws. *Journal of the American Ceramic Society, 73*, 3059–3062.

Ashby, M. F. (1992). *Materials selection in mechanical design*. Oxford: Pergamon Press.

Becher, P. F., Hsueh, C.-H., Angelini, P., & Tiegs, T. N. (1988). Toughening behavior in Whisker-reinforced ceramic matrix composites. *Journal of the American Ceramic Society, 71*, 1050–1061.

Bermejo, R., & Deluca, M. (2013). Layered Ceramics. In S. Somiya (Ed.), *Handbook of Advanced Ceramics:Materials, Applications, Processing, and Properties* (2nd ed.). Academic Press: Elsevier Inc.

Bermejo, R., Grünbichler, H., Kreith, J., & Auer, C. (2010). Fracture resistance of a doped PZT ceramic for multilayer piezoelectric actuators: Effect of mechanical load and temperature. *Journal of the European Ceramic Society, 30*, 705–712.

Bermejo, R., Supancic, P., & Danzer, R. (2011). Influence of measurement uncertainties on the determination of the Weibull distribution. *Journal of the European Ceramic Society, 32*, 251–255.

Bermejo, R., Supancic, P., Krautgasser, C., Morrell, R., & Danzer, R. (2013). Subcritical Crack Growth in Low Temperature Co-fired Ceramics under Biaxial Loading. *Engineering Fracture Mechanics, 100*, 108–121.

Bermejo, R., Torres, Y., Sanchez-herencia, A. J., Baudin, C., Anglada, M., & Llanes, L. (2006). Residual stresses, strength and toughness of laminates with different layer thickness ratios. *Acta Materialia, 54*, 4745–4757.

Bermejo, R., Torres, Y., Baudin, C., Sánchez-Herencia, A. J., Pascual, J., Anglada, M., et al. (2007). Threshold strength evaluation on an Al_2O_3–ZrO_2 multilayered system. *Journal of the European Ceramic Society, 27*, 1443–1448.

Börger, A., Supancic, P., & Danzer, R. (2002). The ball on three balls test for strength testing of brittle discs - stress distribution in the disc. *Journal of the European Ceramic Society, 22*, 1425–1436.

Börger, A., Supancic, P., & Danzer, R. (2004). The ball on three balls test for strength testing of brittle discs - part II: analysis of possible errors in the strength determination. *Journal of the European Ceramic Society, 24*, 2917–2928.

Bradt, R. C., Hasselman, D. P. H., & Munz, D. (1996). *Fracture mechanics of ceramics*. New York, London: Plenum Press.

Brückner-Foit, A., Fett, T., Munz, D., & Schirmer, K. (1997). Discrimination of multiaxiallity criteria with the Brazilian disc test. *Journal of the European Ceramic Society, 17*, 689–696.

Brückner-Foit, A., Heger, A., & Munz, D. (1993). Evaluation of failure probability of multiaxially loaded components using the STAU postprocessor. *Ceramic Engineering & Science Proceedings, 14*, 331.

Casellas, D., Alcalá, J., Llanes, L., & Anglada, M. (2001). Fracture variability and R-curve behavior in yttria-stabilized zirconia ceramics. *Journal of Materials Science, 36*, 3011–3025.

Casellas, D., Feder, A., Llanes, L., & Anglada, M. (2001). Fracture toughness and mechanical strength of Y-TZP/PSZ ceramics. *Scripta Materialia, 45*, 213–220.

Cho, S.-J., Yoon, K.-J., Kim, J.-J., & Kim, K.-H. (2000). Influence of humidity on the flexural strength of alumina. *Journal of the European Ceramic Society, 20*, 761–764.

Cho, S.-J., Yoon, K.-J., Lee, Y.-C., & Chu, M.-C. (2003). Effects of environmental temperature and humidity on the flexural strength of alumina and measurement of environment-insensitive inherent strength. *Materials Letters, 57*, 2751–2754.

Damani, R., Gstrein, R., & Danzer, R. (1996). Critical notch-root radius effect in SENB-S fracture toughness testing. *Journal of the European Ceramic Society, 16*, 695–702.

Danzer, R. (1992). A general strength distribution function for brittle materials. *Journal of the European Ceramic Society, 10*, 461–472.

Danzer, R. (1994a). Ceramics: mechanical performance and lifetime prediction. In D. Bloor, R. J. Brook, M. C. Flemings, S. Mahajan, & R. W. Cahn (Eds.), *The Encyclopedia of advanced materials*. Pergamon.

Danzer, R. (1994b). Subcritical crack growth in ceramics. In D. Bloor, R. J. Brook, M. C. Flemings, S. Mahajan, & R. W. Cahn (Eds.), *The Encyclopedia of advanced materials*. Pergamon Press.

Danzer, R. (2002). Mechanical failure of advanced ceramics: the value of fractography. *Key Engineering Materials, 223*, 1–18.

Danzer, R. (2006). Some notes on the correlation between fracture and defect Statistics: is the Weibull statistics valid for very small specimens? *Journal of the European Ceramic Society, 26*, 3043–3049.

Danzer, R., Harrer, W., Supancic, P., Lube, T., Wang, Z., & Börger, A. (2007). The ball on three balls test - strength and failure analysis of different materials. *Journal of the European Ceramic Society, 27*, 1481–1485.

Danzer, R., Lube, T., & Supancic, P. (2001). Monte-carlo simulations of strength distributions of brittle materials - type of distribution, specimen- and sample size. *Zeitschrift für Metallkunde, 92*, 773–783.

Danzer, R., Lube, T., Supancic, P., & Damani, R. (2008). Fracture of advanced ceramics. *Advanced Engineering Materials, 10*, 275–298.

Danzer, R., Reisner, G., & Schubert, H. (1992). Der einfluß von gradienten in der defektdichte und festigkeit auf die bruchstatistik von spröden werkstoffen. *Zeitschrift für Metallkunde, 83*, 508–517.

Danzer, R., Supancic, P., Pascual, J., & Lube, T. (2007). Fracture statistics of ceramics – Weibull statistics and deviations from Weibull statistics. *Engineering Fracture Mechanics, 74*, 2919–2932.

Dauskardt, R. H., James, M. R., Porter, J. R., & Ritchie, R. O. (1992). Cyclic fatigue-crack growth in a SiC-Whisker-reinforced alumina ceramic composite: long- and small-crack behavior. *Journal of the American Ceramic Society, 75*, 759–771.

Davidge, R. W. (1979). *Mechanical behaviour of ceramics*. Cambridge: Cambridge University Press.

Duan, K., Mai, Y.-M., & Cotterell, B. (1995). R-Curve effect on strength and reliability of toughened ceramic materials. *Journal of Materials Science, 30*, 1405–1408.

EN 843-1. (1995). Advanced technical ceramics, monolithic ceramics, mechanical properties at room temperature, part 1. *Determination of Flexural Strength*.

Evans, A. G., & Mcmeeking, R. M. (1986). On toughening of ceramics by strong reinforcements. *Acta Metallurgica, 34*, 2435–2441.

Feldkamp, L. A., Davis, L. C., & Kress, J. W. (1984). Practical Cone-Beam Algorithm. *Journal of the Optical Society of America A, 1*, 612–619.

Fett, T., Glazounov, A., Hoffmann, M. J., Munz, D., & Thun, G. (2001). On the interpretation of different R-curves for soft PZT. *Engineering Fracture Mechanics, 68*, 1207–1218.

Fett, T., & Munz, D. (1985). Determination of *v–K* curves by a modified evaluation of lifetime measurements in static bending tests. *Journal of the American Ceramic Society, 68*, C213–C215.

Fett, T., & Munz, D. (1993). Evaluation of R-curve effects in ceramics. *Journal of Materials Science, 28*, 742–752.

Freudenthal, A. M. (1968). Statistical approach to fracture. In H. Liebowitz (Ed.), *Fracture*. New York, London: Academic Press.

Geier, G., Rosc, J., Hadwiger, M., Fritz, L., Habe, D., Pabel, T., & Schumacher, P. (2009). Assessing Casting Quality Using Computed Tomography with Advanced Visualization Techniques, Shape casting. *Third International Symposium*. TMS 2009.

Gilbert, C. J., Cao, J. J., Moberlychan, W. J., Dejonghe, L. C., & Ritchie, R. O. (1996). Cyclic fatigue and resistance -curve behaviour of an *in situ* toughened silicon carbide with Al, B, C additions. *Acta Materialia, 44*, 3199–3214.

Gilbert, C. J., Dauskardt, R. H., & Ritchie, R. O. (1995). Behavior of cyclic fatigue cracks in monolithic silicon nitride. *Journal of the American Ceramic Society, 78*, 2291–2300.

Gilbert, C. J., Dauskardt, R. H., & Ritchie, R. O. (1997). Microstructural mechanisms of cyclic fatigue-crack propagation in grain-bridging ceramics. *Ceramics International, 23*, 413–418.

Gilbert, C. J., & Ritchie, R. O. (1987). Fatigue crack propagation in transformation toughened zirconia ceramic. *Journal of the American Ceramic Society, 70*, C248–C252.

Griffith, A. A. (1920). The phenomenon of rupture and flow in solids. *Philosophical Transactions of the Royal Society of London, A221*, 163–198.

Hounsfield, G. N. (1976). Picture Quality of Computed Tomography. *American Journal of Roentgenology, 127*, 3–9.

Hunt, R. A., & Mccartney, L. N. (1979). A new approach to fracture. *International Journal of Fracture, 15*, 365–375.

Irwin, G. R. (1956). Onset of fast crack propagation in high strength steel and aluminium alloys. *Sagamore Research Conference Proceedings, 2*, 289–305.

ISO 23146 2008. *Fine ceramics (advanced ceramics, advanced technical ceramics) – Test methods for fracture toughness of monolithic ceramics – Single-edge V-notch beam (SEVNB) method.*

Jayatilaka, A. D. S., & Trustrum, K. (1977). Statistical approach to brittle fracture. *Journal of Materials Science, 12*, 1426–1430.

Kingery, D. W., Bowen, H. K., & Uhlmann, D. R. (1976). *Introduction to ceramics*. New York: John Wiley & Sons.

Kolleck, A., Schneider, G. A., & Meschke, F. (2000). R-curve behaviour of BaTiO3 and PZT ceramics under the influence of an electric field applied parallel to the crack front. *Acta Materialia, 48*, 4099–4113.

Lamon, J. (1990). Ceramics reliability: statistical analysis of multiaxial failure using the Weibull approach and the multiaxial elemental strength. *Journal of the American Ceramic Society, 73*, 2204–2212.

Lawn, B. R. (1993). *Fracture of brittle solids* (2nd ed.). Cambridge: Cambridge University Press.

Liu, S.-Y., & Chen, I. W. (1994). Plasticity-induced fatigue damage in ceria-stabilized tetragonal zirconia polycrystals. *Journal of the American Ceramic Society, 77*, 2025–2035.

Llanes, L., Torres, Y., & Anglada, M. (2002). On the fatigue crack growth behavior of WC–Co cemented carbides: kinetics description, microstructural effects and fatigue sensitivity. *Acta Materialia, 50*, 2381–2393.

Lube, T., Danzer, R., Kübler, J., Dusza, J., Erauw, J.-P., Klemm, H., et al. (2002). Strength and fracture toughness of the ESIS silicon nitride reference material. In A. Neimitz, I. V. Rokach, D. Kocanda, & K. Golos (Eds.), *Fracture beyond 2000*. Sheffield: EMAS Publications.

Lube, T., Danzer, R., & Steen, M. (2002). A testing program for a silicon nitride reference material. In M. Matsui, S. Jahanmir, H. Mostgaci, M. Naito, K. Uematsu, et al. (Eds.), *Improved ceramics through new measurements, processing and standards*. Westerville: The American Ceramic Society.

Lube, T., & Dusza, J. (2007). A silicon nitride reference material - a testing program of ESIS TC6. *Journal of the European Ceramic Society, 27*, 1203–1209.

Lube, T., Pascual, J., Chalvet, F., & De Portu, G. (2007). Effective fracture toughness in Al_2O_3–Al_2O_3/ZrO_2 laminates. *Journal of the European Ceramic Society, 27*, 1449–1453.

Lube, T., & Baierl, R. G. A. (2011). Sub-Critical Crack Growth in Alumina – a Comparison of Different Measurement and Evaluation Methods. *Berg- und Hüttenmännische Monatshefte, 156*, 450–456.

Lugovy, M., Slyunyayev, V., Orlovskaya, N., Blugan, G., Kübler, J., & Lewis, M. H. (2005). Apparent fracture toughness of Si_3N_4-based laminates with residual compressive or tensile stress in surface layers. *Acta Materialia, 53*, 289–296.

Mccartney, L. N. (1979). Extensions of a statistical approach to fracture. *International Journal of Fracture, 15*, 477–487.

Meschke, F., Kolleck, A., & Schneider, G. A. (1997). R-curve behaviour of BaTiO3 due to stress-induced ferroelastic domain switching. *Journal of the European Ceramic Society, 17*, 1143–1149.

Michalske, T. A., & Freiman, S. W. (1983). A molecular mechanism for stress corrosion in vitreous silica. *Journal of the American Ceramic Society, 66*, 284–288.

Moon, R. J., Hoffmann, M., Hilden, J., Bowman, K., Trumble, K., & Rödel, J. (2002). R-curve behavior in alumina-zirconia composites with repeating graded layers. *Engineering Fracture Mechanics, 69*, 1647–1665.

Morrell, R. (1989). *Handbook of properties of technical & engineering ceramics, part 1: An introduction for the engineer and designer*. London: Her Majesty's Stationary Office.

Morrell, R. (1999). *Fractography of brittle materials*. Teddington: National Physical Laboratory.

Munz, D., & Fett, T. (1999). *Ceramics*. Berlin, Heidelberg: Springer.

Murakami, Y. (1986). *The stress intensity factor handbook*. New York: Pergamon Press.

Nemeth, N. N., Manderscheid, J. M., & Gyekenyesi, J. P. (1989). Designing ceramic components with the CARES computer program. *American Ceramic Society Bulletin, 68*, 2064–2072.

Newman, J. C., & Raju, I. S. (1981). An empirical stress-intensity factor equation for the surface crack. *Engineering Fracture Mechanics, 15*, 185–192.

Nishida, T., Hanaki, Y., Nojima, T., & Pezzotti, G. (1995). Measurement of rising R-curve behaviour in toughened silicon nitride by stable crack propagation in bending. *Journal of the American Ceramic Society, 78*, 3113–3116.

Orlovskaya, N., Kübler, J., Subbotin, V., & Lugovy, M. (2002). High toughness ceramic laminates by design of residual stress. *Materials Research Society Symposium Proceedings, 702*.

Pascual, J., Chalvet, F., Lube, T., & De Portu, G. (2005). R-curves in Al_2O_3–Al_2O_3/ZrO_2 laminates. *Key Engineering Materials, 290*, 214–221.

Pascual, J., Lube, T., & Danzer, R. (2008). Fracture statistics of ceramic laminates strengthened by compressive residual stresses. *Journal of the European Ceramic Society, 28*, 1551–1556.

Quinn, G. D. (2003a). Weibull effective volumes and surfaces for cylindrical rods loaded in flexure. *Journal of the American Ceramic Society, 86*, 475–479.

Quinn, G. D. (2003b). Weibull strength scaling for standardized rectangular flexure specimens. *Journal of the American Ceramic Society, 86*, 508–510.

Ramachandran, N., & Shetty, D. K. (1991). Rising-crack-growth resistance (R-curve) behaviour of toughened alumina and silicon nitride. *Journal of the American Ceramic Society, 74*, 2634–2641.

Reece, M. J., Guiu, F., & Sammur, M. F. R. (1989). Cyclic fatigue crack propagation in alumina under direct tension-compression loading. *Journal of the American Ceramic Society, 72*, 348–352.

Richter, H., Kleer, G., Heider, W., & Röttenbacher, R. (1985). Comparative study of the strength properties of slip-cast and of extruded silicon-infiltrated SiC. *Materials Science and Engineering, 71*, 203–208.

Ritchie, R. O. (1999). Mechanisms of fatigue-crack propagation in ductile and brittle solids. *International Journal of Fracture, 100*, 55–83.

Rubeša, D., Smoljan, B., & Danzer, R. (2003). Main features of designing with brittle materials. *Journal of Materials Engineering and Performance, 12*, 1–9.

Sbaizero, O., Roitti, S., & Pezzotti, G. (2003). R-curve behavior of alumina toughened with molybdenum and zirconia particles. *Material Science and Engineering A, 359*, 297–302.

Sestakova, L., Bermejo, R., Chlup, Z., & Danzer, R. (2011). Strategies for fracture toughness, strength and reliability optimisation of ceramic-ceramic laminates. *International Journal of Materials Research, 102*, 613–626.

Sglavo, V. M., & Bertoldi, M. (2006). Design and production of ceramic laminates with high mechanical resistance and reliability. *Acta Materialia, 54*, 4929–4937.

Shetty, D. K., & Wang, J.-S. (1989). Crack stability and strength distribution of ceramic that exhibits rising crack-growth-resistance (R-curve behavior). *Journal of the American Ceramic Society, 72*, 1158–1162.

Soma, T., Ishida, Y., Matsui, M., & Oda, I. (1987). Ceramic component design for assuring long-term durability. *Advanced Ceramic Materials, 2*, 809–812.

Steinbrech, R. W., & Schenkel, O. (1988). Crack-resistance curves of surface cracks in alumina. *Journal of the American Ceramic Society, 71*, C271–C273.

Swain, M. V., & Hannink, R. H. J. (1984). R-curve behaviour in zirconia ceramics. In N. Claussen, M. Rühle, & A. H. Heuer (Eds.), *Advances in ceramics, science and technology of zirconia II*. Columbus: American Ceramic Society.

Tada, H., Paris, P., & Irwin, G. R. (1985). *The stress analysis handbook*. St. Louis: Del Research Corporation.

Thiemeier, T., Brückner-Foit, A., & Kölker, H. (1991). Influence of fracture criterion on the failure prediction of ceramics loaded in biaxial flexure. *Journal of the American Ceramic Society, 74*, 48–52.

Torres, Y., Bermejo, R., Llanes, L., & Anglada, M. (2008). Influence of notch radius and R-curve behaviour on the fracture toughness evaluation of WC–Co cemented carbides. *Engineering Fracture Mechanics, 75*, 4422–4430.

Torres, Y., Casellas, D., Anglada, M., & Llanes, L. (2001). Fracture toughness evaluation of hardmetals: influence of testing procedure. *International Journal of Refractory Metals and Hard Materials, 19*, 27–34.

Wachtman, J. B. (1996). *Mechanical properties of ceramics*. New York, Chichester: Wiley-Interscience.

Weibull, W. (1939). *A statistical theory of the strength of materials*. Stockholm: Generalstabens Litografiska Anstalts Förlag.

Weibull, W. (1951). A statistical distribution function of wide applicability. *Journal of Applied Mechanics, 18*, 293–298.

Wiederhorn, S. M. (1974). Subcritical crack growth in ceramics. In R. C. Bradt, D. P. H. Hasselman, & F. F. Lange (Eds.), *Fracture mechanics of ceramics*. New York: Plenum.

2.10 Toughness, Fatigue and Thermal Shock of Ceramics: Microstructural Effects

Gilbert Fantozzi, INSA de Lyon, MATEIS (UMR CNRS 5510), Villeurbanne, France
Malika Saâdaoui, LERSIM Ecole Mohammadia d'Ingénieurs, Université Mohamed V Agdal, Rabat, Morocco

© 2014 Elsevier Ltd. All rights reserved.

2.10.1 Introduction

Ceramic materials are prone to damage or fracture under mechanical or thermal stresses, caused by crack extension from preexisting flaws, introduced during processing or surface machining. In the years before 2013, stronger and tougher materials were developed by controlling their composition and microstructural parameters such as grain size and shape. The toughness of advanced ceramics has been improved by tailoring their microstructures to provide toughening mechanisms. Flaw-tolerant materials were developed with microstructures that exhibit rising fracture toughness with crack extension, known as resistance curve or R-curve behavior, which is generally associated with the ability to activate toughening mechanisms. For monolithic ceramics, the toughening mechanisms are classified in two types depending on whether they involve (1) a process zone around the crack tip, like microcracking or phase transformation or (2) a crack-bridging zone behind the crack tip. For both mechanisms, the crack growth resistance, dominated by crack wake effects that shield the crack tip from the applied load, influences the fracture behavior.

In this chapter, the emphasis is placed on the influence of the microstructural toughening and the induced crack growth resistance on the fracture behavior, particularly during static or cyclic fatigue and thermal shock. Attention is focused on representative materials like polycrystalline alumina (Al_2O_3), silicon carbide (SiC), silicon nitride (Si_3N_4), known to exhibit R-curve behavior as a result of a grain-bridging mechanism, and zirconia (ZrO_2)-based ceramics exhibiting phase transformation toughening. The basic principles presented should be extended to other engineering ceramics.

2.10.2 Fracture Behavior

2.10.2.1 Toughness and R-curve

Based on linear elastic fracture mechanics, the fracture toughness of a brittle material, representing its resistance to crack growth, can be evaluated by the work of fracture at the opening mode, G_{Ic}, that often

http://dx.doi.org/10.1016/B978-0-08-096527-7.00029-5

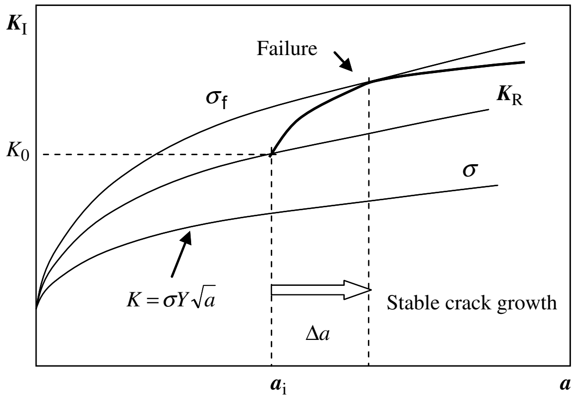

Figure 1 Schematic representation of an R-curve with its significance to crack stability.

approaches the surface free energy, $2\gamma_s$, necessary to create two new crack surfaces, or equivalently by the critical stress intensity factor, K_{Ic}, related to the fracture strength, σ_f, and the critical flaw size, a_c, as follows (Griffith, 1920):

$$K_{Ic} = \sigma_f Y \sqrt{a_c} \tag{1}$$

where Y is the nondimensional geometrical factor.

Typical values for the fracture toughness of ceramic materials are in the range from 1 to 10 MPa $m^{1/2}$. One successful approach to enhance crack growth resistance of these materials consists of controlling their microstructures so as to activate various reinforcement mechanisms (Becher, 1991; Evans, 1990; Green, Hannink, & Swain, 1989; Munz & Fett, 1999). In most cases, the toughness, instead of being a constant material property, increases with crack growth. The fracture behavior is thus described by a crack growth resistance curve (R-curve) representing the variation of the fracture resistance denoted by R, or the associated stress intensity factor, K_R (for plane strain, $R = K_R^2/E$, where E is the Young's modulus), with crack extension Δa (**Figure 1**). For a crack with an initial size a_i, K_R generally increases with a decreasing slope, from an initial value K_0, corresponding to the intrinsic fracture toughness, to a plateau value. For an applied tensile stress σ, the stress intensity factor $K_I = \sigma Y \sqrt{a}$ increases with the crack size a. When the stress is increased, there is no crack growth below the onset value K_0. Crack extension initiates when $K_I = K_0$ and the propagation is generally stable as $dK_I/da < dK_R/da$, so the stress needs to be increased for further crack growth. The crack becomes unstable when the strength, σ_f, is reached, which corresponds to the tangency condition between K and K_R curves ($K_I = K_R$ and $dK_I/da = dK_R/da$). A consequence of this condition is that the strength of a ceramic is related to the slope of the R-curve and not necessarily to the length of crack extension. Moreover, the initial part of the R-curve is the most important for designing high-strength, damage-tolerant ceramics (Kruzic, Satet, Hoffmann, Cannon, & Ritchie, 2008). However, some caution is necessary when using an R-curve as a fracture parameter, as its shape depends not only on the material but also on the specimen and crack geometry and test conditions (Miyazaki, Hyuga, Yoshizawa, Hirao, & Ohji, 2009; Munz, 2007).

2.10.2.2 Microstructural Toughening

The most important toughening mechanisms in polycrystalline ceramics are grain bridging and transformation toughening, discussed below. These mechanisms act as crack-shielding mechanisms due to the closure tractions in the wake of a propagating crack (Evans, 1990; Heuer, 1987; Knehans, Steinbrech, & Schaarwachter, 1983). The associated R-curve as a function of crack extension is commonly expressed as follows:

$$K_R(\Delta a) = K_0 + K_{sh}(\Delta a) \tag{2}$$

where K_0 is the intrinsic fracture toughness and K_{sh} is the microstructural toughening increment, which is higher for phase transformation (up to 15 MPa $m^{1/2}$) compared to grain bridging (2–5 MPa $m^{1/2}$).

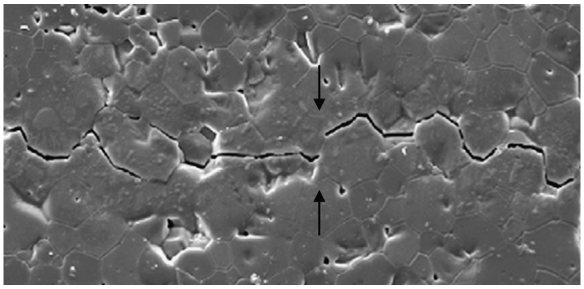

Figure 2 SEM micrograph of grain bridging in alumina.

2.10.2.2.1 Grain Bridging

Crack-tip shielding due to grain bridging (**Figure 2**) occurs in monolithic ceramics, such as alumina (Marshall, Evans, & Drory, 1983; Steinbrech, Reichl, & Schaarwachter, 1990; Swanson, Fairbanks, Lawn, Mai, & Hockey, 1987; Vekinis, Ashby, & Beaumont, 1990), SiC (Padture & Lawn, 1994; Gilbert, Cao, Moberlychan, Dejonghe, & Ritchie, 1996) and silicon nitride (Li & Yamanis, 1989; Li, Lee, & Lui, 1992) and arises from elastic and interfacial frictional stresses that act to reduce the crack opening as in fiber- or whiskers-reinforced ceramics (Becher, 1991; Becher, Hsueh, Alexander, & Sun, 1996; Evans, 1990; Zou et al., 2004). In this latter case, whisker frictional bridging occurs behind the crack tip when the whisker–matrix interface debonds and further, the whiskers are pulled out. The shielding effect depends on the whisker strength, volume fraction of whiskers, the size of whiskers, the Young's modulus and the interface properties.

Accumulation of shielding during crack propagation results in a reduction of the effective stress intensity factor at the crack tip and thus enhances the material toughness. As crack propagation is accompanied by crack opening, a saturation limit is reached for a critical value of the crack opening displacement, δ_c, beyond which grain bridging disappears (**Figure 3**). Crack bridging is often modeled by a compressive stress, σ_b, acting across the crack faces (**Figure 3(b)**). The relation between the bridging stress and the crack opening displacement, δ, is a material property for which different expressions can be used, depending on the bridging mechanism (Munz, 2007). For frictional effects, dominant in monolithic ceramics such as alumina and silicon nitride, the bridging stress function can be represented as (Mai & Lawn, 1987):

$$\sigma_b = \sigma_m \left(1 - \frac{\delta}{\delta_c}\right)^n \tag{3}$$

where σ_m is the maximum bridging stress, δ_c is the crack opening displacement at which the grain bridging disappears and the exponent n describes the stress decrease.

The magnitude of grain bridging is controlled by the expansion anisotropy, the interfacial roughness and microstructural parameters such as the grain size and morphology (aspect ratio), which can be controlled by additives or heat treatments (Chantikul, Bennison, & Lawn, 1990; El Attaoui, Saâdaoui, Chevalier, & Fantozzi,

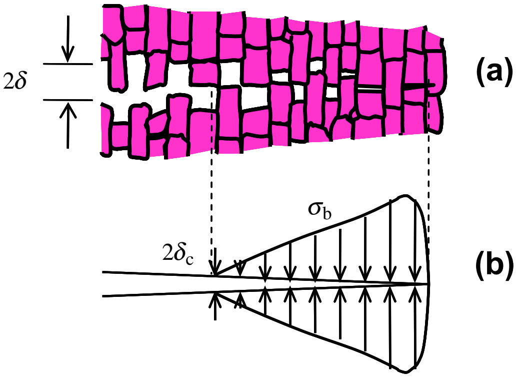

Figure 3 Schematic representation of (a) crack bridging zone and (b) associated closure stresses.

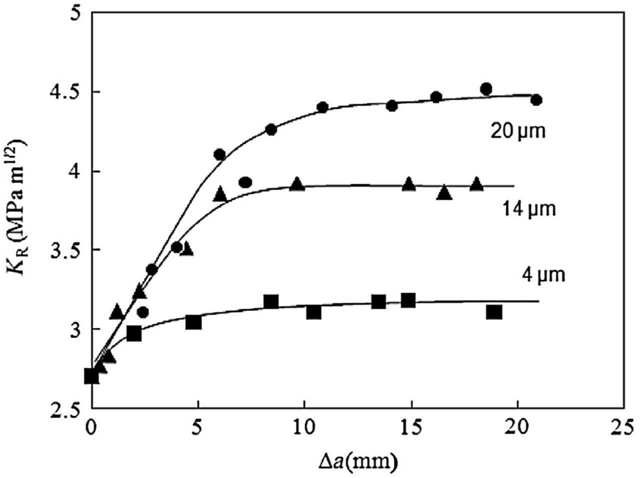

Figure 4 K_R curves obtained by the double torsion technique for alumina with different grain sizes (El Attaoui et al., 2005).

2005; Kleebe, Pezzotti, & Ziegler, 1999; Kovar, Bennison, & Ready, 2000; Satet, Hoffmann, & Cannon, 2006; Zheng, Knowles, Vieira, Lopes, & Oliveira, 2001). Coarsening and elongating the microstructure enhances the contribution of frictional bridging and pullout, resulting in a more pronounced R-curve behavior. Examples of such effects are shown in **Figures 4** and **5**, respectively, for coarse-grain alumina and the so-called self-reinforced silicon nitride, example of which is illustrated in **Figure 6**, characterized by a bimodal grain distribution, with in situ coarsened fibrous or elongated grains (Becher et al., 1998; Li & Yamanis, 1989; Miyazaki, Hyuga, Yoshizawa, Hirao, & Ohji, 2009; Tatarko et al., 2010). **Figure 5** corresponds to macrocrack R-curves obtained by Becher et al. (1998) for Si_3N_4 materials with different microstructures. For a nearly equiaxed submicrometer grain size material (1), the R-curve rises slowly, to a low plateau value of 3.5 MPa m$^{1/2}$. The toughness increased as both the grain size distribution and the proportion of large fibrous grains were increased (2 and 3). A steep rising R-curve with a steady-state value >10 MPa m$^{1/2}$ (4) was obtained for a bimodal material with large elongated grains (typically more than 1 µm diameter) dispersed in a fine grain-size matrix.

For many monolithic bridging ceramics, there is a discrepancy between the crack growth resistance curves obtained from long and small surface cracks, particularly for small crack extensions (Cook, Liniger, Steinbrech, & Deuerler, 1994; Gilbert, Cao, Dejonghe, & Ritchie, 1997; Li & Yamanis, 1989). An example of such discrepancy is shown in **Figure 7** where the R-curves for small indentation surface cracks (<400 µm) and for a long crack in compact tension specimen are represented for an in situ toughened SiC, so-called ABC-SiC (Gilbert et al., 1996).

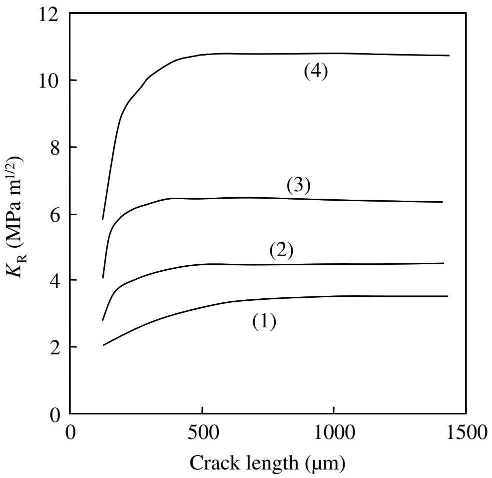

Figure 5 K_R curves for Si_3N_4 with (1) equiaxed submicrometer grain size, (2 and 3) coarsened and elongated microstructures and (4) bimodal microstructure with large elongated grains in a fine-grain size matrix. From Becher et al. (1998).

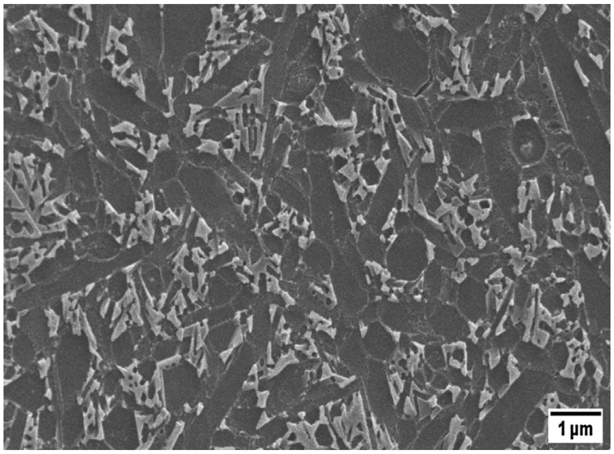

Figure 6 SEM micrograph of a self-reinforced Si_3N_4 ceramic (Tatarko et al., 2010).

This material, processed with addition of aluminum, boron, and carbon, consists of 25 vol.% cubic β-SiC and 75 vol.% hexagonal α-SiC and presents a dual-phase, plate-like morphology of the α grains, distributed as a three-dimensional interlocking network with an amorphous film along grain boundaries. This microstructure leads to a marked rising R-curve behavior, related to an intergranular fracture and the presence of the plate-shaped grains, which promote grain bridging and subsequent grain pullout. The long crack growth resistance (**Figure 7**) increases within 600 µm of crack extension, from an initial value of $K_0 = 5.5$ MPa $m^{1/2}$ to a steady-state plateau value of 9.1 MPa $m^{1/2}$. The results for small cracks are similar for crack extensions higher than about 120 µm. For lower crack extensions, a discrepancy appears, the long-crack growth resistance being higher with a lower initial slope. This discrepancy can be attributed to a difference in bridging contribution: the physical limited wake of the small cracks restricts the development of shielding, compared to that which can be reached with long cracks.

2.10.2.2.2 Transformation Toughening

Transformation toughening has been employed to increase the fracture toughness of a variety of zirconia-toughened ceramics (ZTC) classified into three different categories depending on their microstructures (Hannink, Kelly, & Muddle, 2000):

1. Dispersion-toughened ceramics with tetragonal zirconia particles in a ceramic matrix, such as zirconia-toughened alumina.

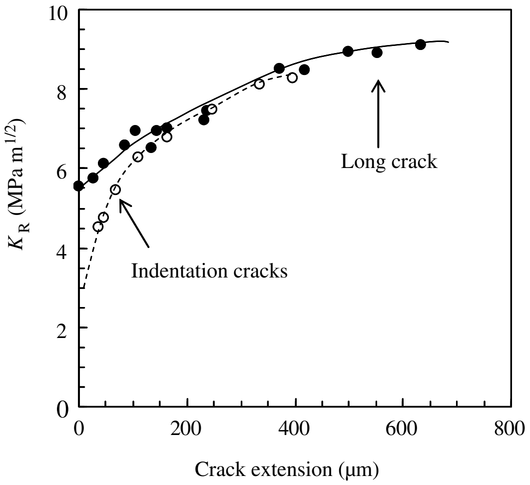

Figure 7 Comparison of the R-curves measured in ABC-SiC material for small and long cracks. From Gilbert, Cao, et al. (1997).

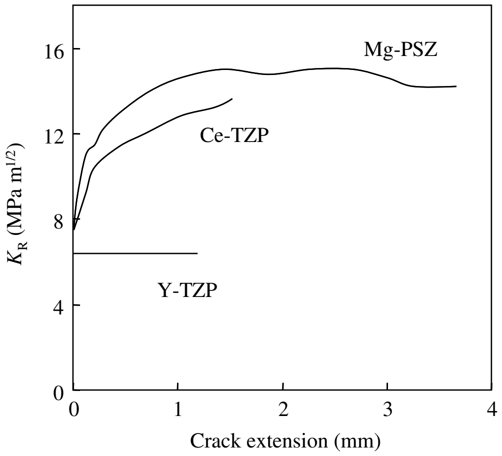

Figure 8 K_R curves for various zirconia-toughened ceramics. From Hannink et al. (2000).

2. Partially stabilized zirconia (PSZ) consisting of a cubic ZrO_2 matrix with a dispersion of tetragonal precipitates, obtained by doping with certain stabilizers like magnesia (Mg-PSZ).
3. Single-phase, tetragonal zirconia polycrystals (TZP) where the tetragonal phase is retained at room temperature; the most common Y-TZP and Ce-TZP ceramics are obtained using, respectively, yttria and ceria as stabilizer.

Transformation toughening is due to a stress-induced martensitic transformation of tetragonal (t) zirconia grains or particles to the monoclinic (m) phase in front of a crack. During crack propagation, the volume increase ($\sim$5%), accompanying the transformation, creates compressive stresses that shield the crack tip from the applied stress (Evans, 1990; Green et al., 1989; Hannink et al., 2000; Marshall et al. 1983). For further crack propagation, the applied stress intensity factor has to be increased to overcome the shielding contribution (K_{sh} in Eqn (2)). Thus, the crack growth resistance increases until a steady-state transformation zone is developed, corresponding to the R-curve plateau value. The magnitude of the transformation toughening is controlled by the stability of the tetragonal phase which is influenced by microstructural parameters such as particle or grain size, morphology and location of the t-phase (Becher & Swain, 1992; Casellas, Nagl, Llanes, & Anglada, 2005; Green et al., 1989). Phase transformation in ZTC is generally accompanied by other mechanisms as microcracking or grain bridging, which contribute to the material toughening (El Attaoui et al., 2007; Hannink et al., 2000). Crack growth resistance curves are shown in **Figure 8**, for some typical zirconia ceramics with different oxides as stabilizers. Particularly high R-curve effects are observed in Ce-TZP and Mg-PSZ materials.

2.10.3 Subcritical Crack Growth

2.10.3.1 Mechanisms and Basic Relations

In presence of a reactive environment, slow crack growth which can cause delayed failure occurs for most ceramics at a stress intensity factor lower than the toughness K_{IC}, due to stress-enhanced chemical interaction between environmental species (especially water) and the crack tip bonds. This crack propagation also called subcritical crack growth (SCG), or static fatigue, is governed by the stress intensity factor, K_I and generally characterized by a power law between the crack growth rate ($V = da/dt$), and K_I:

$$V = AK_I^n \tag{4}$$

where A and n are the parameters depending on the material, the temperature and the environment. Accurate determination of these parameters leads to lifetime prediction for ceramic components.

Typical V–K_I curves are shown for different environments in **Figure 9** for a 3Y-TZP zirconia doped with 3 mol % of Y_2O_3 material. The results show the presence of a threshold under vacuum, water and air, below which no propagation occurs. The V–K_I curve in air shows three different stages, which characterize stress-assisted

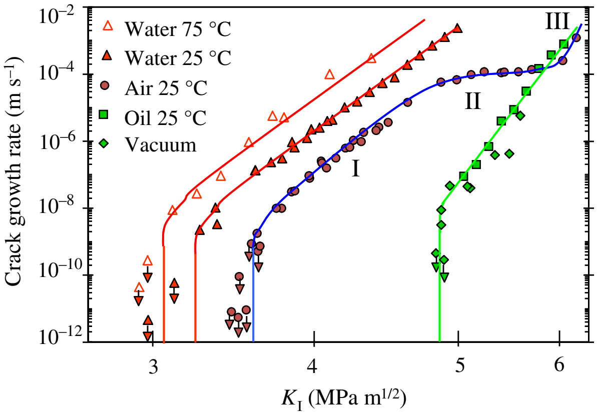

Figure 9 V–K_I curves of a Y-TZP polycrystalline tetragonal zirconia (Chevalier & Fantozzi, 2005).

corrosion by water. For stage I (low crack velocities), the rate-limiting mechanism is the thermally activated reaction kinetics between the ceramic and corrosive molecules at the crack tip (fracture of ceramic bonds by water), whereas, in stage II transport of molecules from the crack mouth toward the crack tip control the higher crack rates. Stage III occurs at even higher crack rates, which exceed the molecule transport rate and the fracture of ceramic bonds takes place without reaction with the environmental species (fracture under vacuum conditions). In water, only the stage I is observed while under vacuum or silicon oil where no water molecules are present, only stage III occurs for a stress intensity factor near K_{IC} (Chevalier & Fantozzi, 2005; Chevalier, Olagnon, & Fantozzi, 1999).

The sensitivity of ceramic materials to stress-assisted corrosion—hence to SCG—lies in their ability to react with water. A schematic representation of this sensitivity is shown for different materials in **Figure 10**, where the crack velocity in air is represented as function of the stress intensity factor rationalized by the threshold value in vacuum (V–$K_I/K_{I0vacuum}$). In this representation, very fine microstructures are considered to avoid R-curve effects which will be discussed below. It appears that the sensitivity to SCG is strongly linked to the ionic fraction of the bond (**Table 1**): the higher the ionic fraction, the higher the intrinsic susceptibility to SCG.

For polycrystalline ceramics, the microstructure plays a major role on the V–K_I curves obtained experimentally, particularly for reinforced materials, examples of which are discussed in the following sections. Due to the crack shielding associated with the reinforcement, the effective crack tip stress intensity factor, K_{tip}, corresponding to the driving force for crack growth may be expressed as follows:

$$K_{tip} = K_I - K_{sh} \tag{5}$$

where K_I is the applied stress intensity factor and K_{sh} is the shielding contribution due to the microstructure.

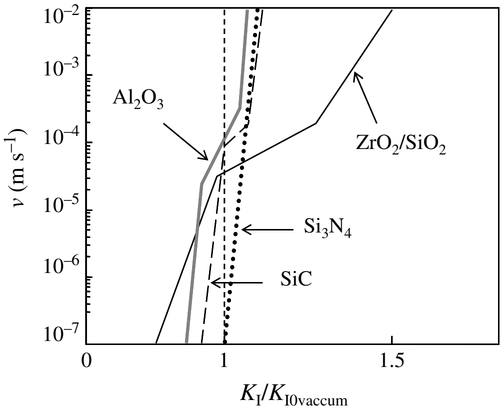

Figure 10 Susceptibility to SCG of different ceramics (Chevalier & Fantozzi, 2005).

Table 1 Ionic fraction and susceptibility to SCG for different ceramics (Chevalier & Fantozzi, 2005)

	ZrO_2	Si_3N_4	SiC
Ionic fraction	0.6	0.3	0.16
$K_{I0air}/K_{I0vacuum}$	~0.6	~0,9	~1

2.10.3.2 Influence of Grain Bridging

The grain size influences the SCG of nontransforming ceramics by modifying the grain bridging reinforcement, generally occurring in these materials. Increasing the grain size increases the shielding effect of bridging during crack propagation and thus, enhances the static fatigue limit and the apparent stress intensity factor, K_I (Eqn (5)), during SCG (Ebrahimi, Chevalier, & Fantozzi, 2000; El Attaoui et al., 2005). Munz and Fett (1999) showed that a crack velocity decrease could be observed at the beginning of the propagation of small cracks in alumina. **Figure 11(a)** shows V–K_I curves obtained by the relaxation method under constant displacement in air, by Ebrahimi et al. (2000), for three polycrystalline alumina materials with equiaxed grain morphology and grain sizes, d, between 2 and 13 μm. The crack propagation rate, controlled by stress corrosion is very sensitive to the stress intensity factor, K_I, below 2×10^{-5} m s^{-1} for the three alumina ceramics (region I) and K_I dependence becomes moderated in region II. In the stage I, the applied stress intensity factor needed to propagate the crack at a given velocity increases with the grain size.

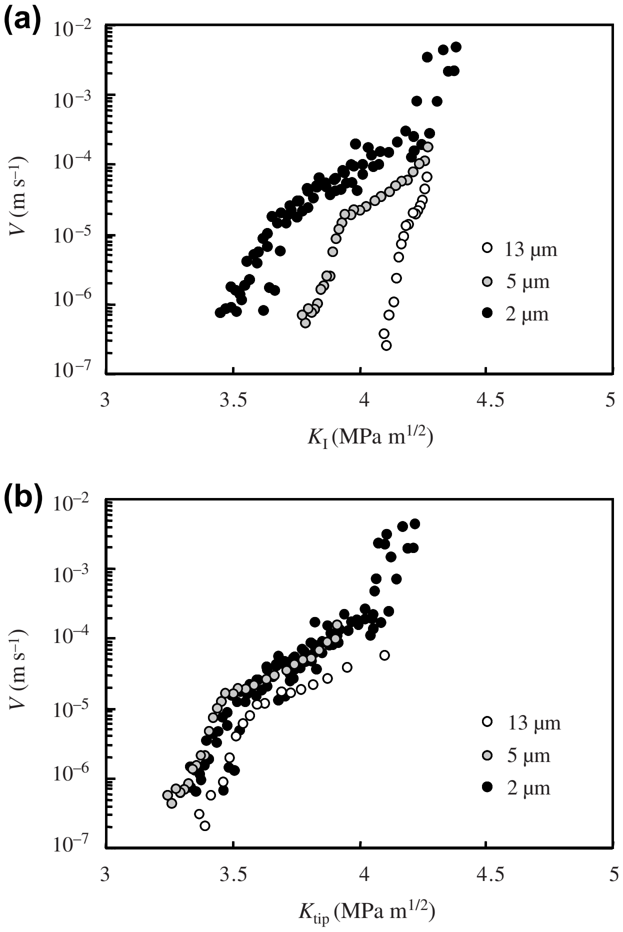

Figure 11 (a) V–K_I curves of three alumina with different grain sizes obtained by load relaxation in double torsion. The initial velocities are the highest and decreases when crack length increases, leading to an increase of the reinforcement. (b) Intrinsic V–K_{tip} curves obtained by subtracting the shielding contribution of crack bridging, obtained from the K_R curves of the materials (Ebrahimi et al., 2000).

We can also notice that the higher the grain size, the higher the slope of the crack growth law. Moreover, K_{I0}, defined as the minimum stress intensity factor that leads to measurable crack propagation during relaxation, is much higher ($\sim$25%) in coarse-grained alumina ($d = 13$ μm) than in fine-grained alumina ($d = 2$ μm). This is obviously related to grain bridging reinforcement that acts to shield the crack from the applied stress in coarse-grain materials, as discussed before. This also explains the convergence of the V–K_I curves at high crack growth rate corresponding to the beginning of the relaxation test from small crack lengths, for which bridging interactions are not yet fully developed. Considering the stress intensity factor at the crack tip by the subtraction of the reinforcement (Eqn (5)) leads to an intrinsic crack propagation curve, independent of the grain size (**Figure 11(b)**). Indeed, as the materials are processed from the same powder, the SCG mechanism is basically the same, the difference between the V–K_I curves and the apparent increase of the threshold arise from the extrinsic wake shielding due to crack bridging, the intensity of which increases with the grain size.

The influence of the grain size is highly dependent on the fracture mode as it can be seen in **Figure 12**, where V–K_I curves are plotted for high-purity alumina with mean grain sizes, between 6 and 53 μm (Ebrahimi et al., 2000). In this case, the grain size distribution is broader, with the appearance of elongated grains for highest grain sizes (50% of abnormal grains for the mean grain size 53 μm). For grain sizes ranging from 6 to 35 μm, the intergranular mode of fracture is prevalent and the conclusions are the same as before: the larger the grain size, the larger is the crack resistance. However, for the largest grain size (53 μm), a marked shift of the V–K_I curve toward low stress intensity factor is observed due to the appearance of transgranular fracture, which reduces the grain bridging effect.

Jacobs and Chen (1994) have studied the SCG behavior of hot-pressed silicon nitride materials constituted of β-Si_3N_4 crystalline phase, a small amount of α-Si_3N_4 and an intergranular oxynitride glass, with different microstructures: a material with a fine microstructure leading to a low toughness, and others with coarse and bimodal microstructures known to exhibit significant crack growth resistance due to grain bridging. **Figure 13** shows the SCG behavior of these materials for different environments, with the stress intensity factor normalized

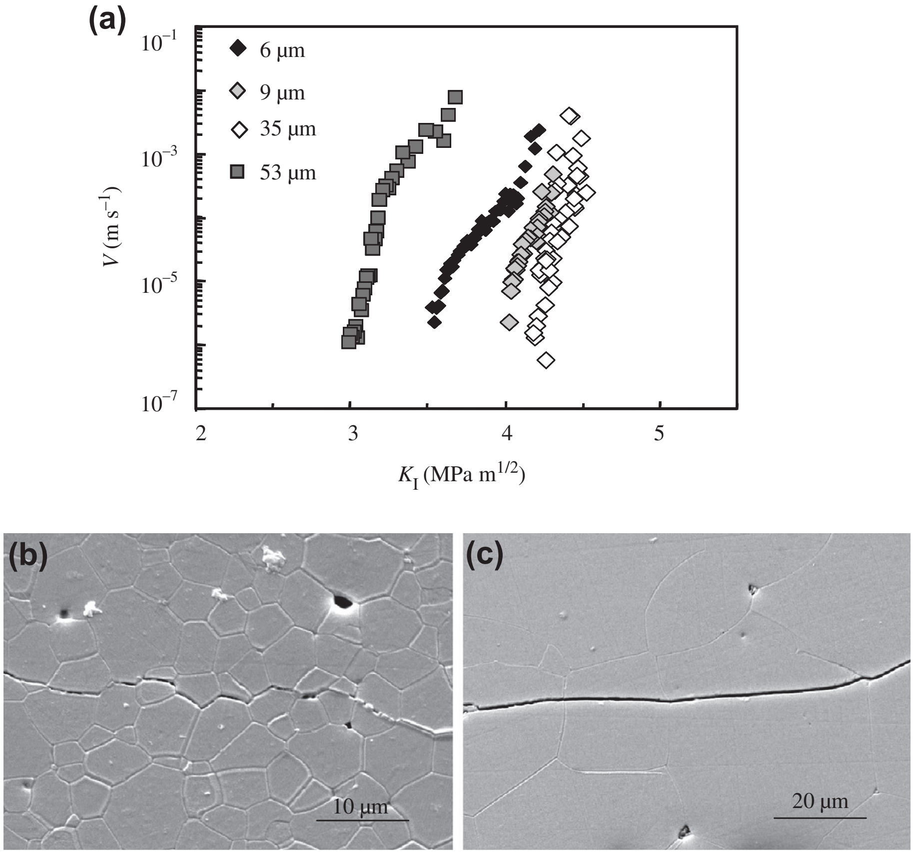

Figure 12 (a) V–K_I curves of high-purity alumina with grain sizes between 6 and 53 μm and (b, c) micrographs showing the transition from intergranular to transgranular fracture mode for the coarse grain material (Ebrahimi et al., 2000).

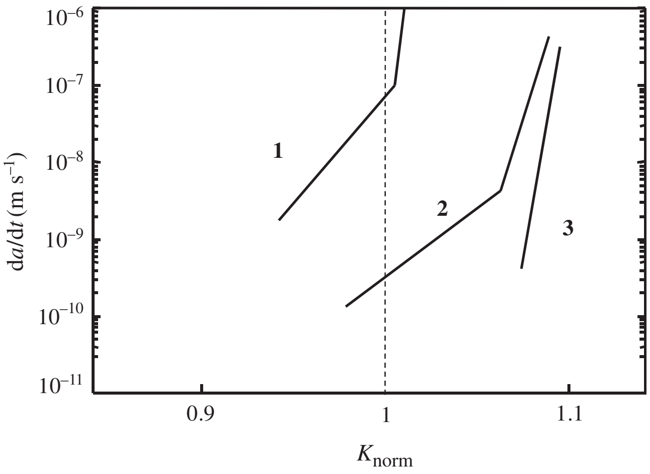

Figure 13 Subcritical crack growth under static loading for silicon nitride materials. Fine-grain material in (1) NaOH solution and (2) toughened material in moist air or water and (3) in NH_3. From Jacobs and Chen (1994).

by a parameter, N, equivalent to the material indentation toughness in water ($K_{norm} = K_I/N$). For a toughened material, the crack growth rates are similar in moist air and water (curve 2) and they are lower in NH_3 (curve 3). These results show a relative insensitivity of the silicon nitrides to SCG in a range of moist and dry environments (this behavior is similar to that of the Y–Si–Al–O–N oxynitride glass with a composition close to that found in silicon nitride intergranular glassy phases (Bhatnagar, Hoffman, & Dauskardt, 2000)). The effect of the microstructure is similar to that discussed above for alumina: the toughened Si_3N_4 material exhibits lower crack growth rates at a given K_{norm}, compared to the fine-grain material (curve 1) and, its SCG curve shows a lower slope at low K_{norm}, corresponding to a region where the crack shielding contribution K_{sh} (Eqn (5)) is increasing.

2.10.3.3 Effect of Phase Transformation Toughening

In the case of zirconia ceramics, the transformation zone size which governs the transformation mechanism is related to the applied stresses: the higher the stresses, the larger the transformation zone. The shielding stress intensity factor is proportional to the applied one (Chevalier et al., 1999; McMeeking & Evans, 1982):

$$K_{sh} = C_{sh} \cdot K_I \tag{6}$$

where C_{sh} is the parameter which increases with the material transformability.

And as a consequence of Eqn (5), the stress intensity factor at the crack tip, K_{Itip}, can be expressed as follows:

$$K_{Itip} = (1 - C_{sh})K_I \tag{7}$$

If we assume that the intrinsic mechanism of SCG in a given ceramic is given by

$$V = A_0 \cdot K_{Itip}^n \tag{8}$$

then, the experimentally determined V–K_I law in the presence of transformable zirconia particles is

$$V = A_0 \cdot (1 - C_{sh})^n \cdot K_I^n = A \cdot K_I^n \tag{9}$$

This means that the effect of transformation toughening on slow crack growth is to shift the V–K_I law toward high stress intensity factors, preserving the n exponent of the slow crack growth power law. C_{sh} can be modified by changing the stability of the tetragonal phase for example by changing the grain size. Figure 14 shows the V–K_I curves of yttria-stabilized zirconia ceramics with too different grain sizes (0.3 and 1 μm), compared to that of zirconia single crystal. Increasing the grain size leads to a shift toward higher stress intensity factors, expressing an increase of crack resistance due to higher transformability. At the same time, the curves run parallel, as a signature of the "intrinsic" zirconia n exponent.

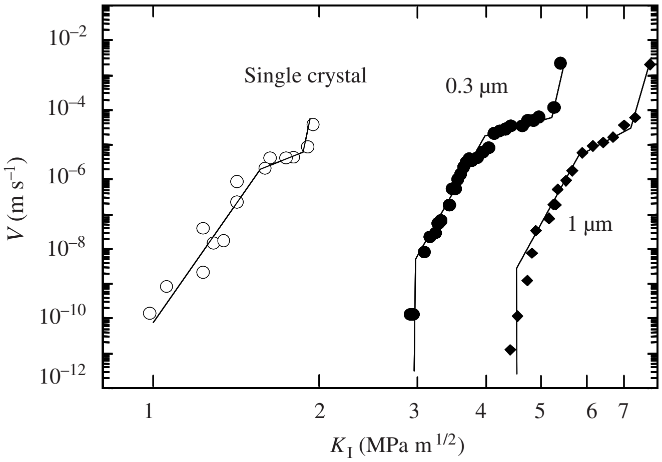

Figure 14 Effect of grain size on V–K_I diagrams for yttria-stabilized zirconia and comparison with a single crystal (Chevalier & Fantozzi, 2005).

Transformation toughening requires zirconia particles with a size distribution ranging between the critical size for spontaneous transformation on cooling to room temperature after sintering, D_c, and the critical size for stress-induced transformation, D'_c (Claussen & Rühle, 1981). D_c is in the range of 0.5–0.8 µm for unstabilized zirconia in an alumina ceramic matrix and D'_c is in the order of 0.1 µm.

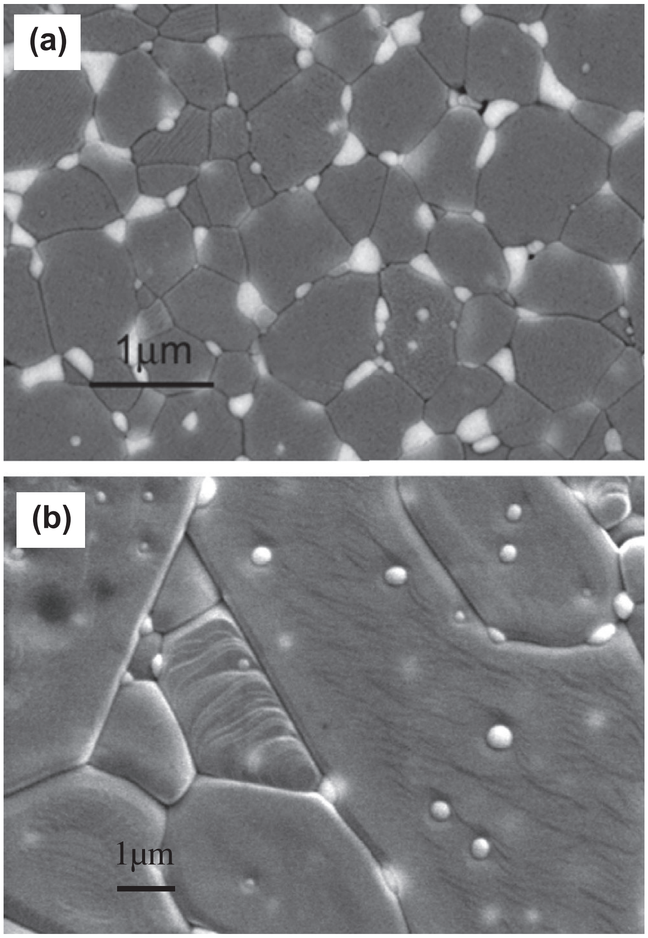

Figure 15 SEM micrograph showing the microstructure of the (a) A-10Z and (b) A-2.5Z nanocomposites (De Aza et al., 2003).

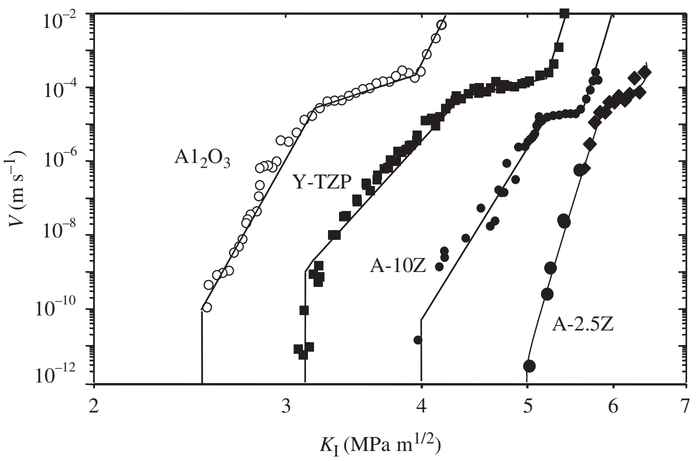

Figure 16 V–K_I curves for alumina, 3Y-TZP zirconia, and nanocomposites A10Z and A2.5Z. From De Aza et al. (2003).

Using a colloidal processing, De Aza, Chevalier, Fantozzi, Schehl, and Torrecillas (2003) obtained alumina–zirconia nanocomposites with a narrow distribution of nanosized ZrO_2 particles, homogeneously distributed in micrometer Al_2O_3 matrix. Ten volume percent of transformable zirconia particles, with a size ranging between 100 and 600 nm, corresponds to the maximum amount of transformation toughening. The microstructure of this nanocomposite, named, A-10Z, is shown in **Figure 15**, where a micrograph of the nanocomposite obtained with 1.7 vol.% (2.5 wt%) zirconia nanoparticles, named A-2.5Z is also represented. The V–K_I curves of the nanocomposites are compared in **Figure 16** to those of a fine-grain alumina, and a 3Y-TZP zirconia. Due to its optimized particles size and distribution, the A-10Z composite exhibits high transformation toughening rate and thus high fracture resistance properties, which shifts the V–K_I curve toward higher K_I values, compared to that of alumina and zirconia or a composite with the same composition obtained by conventional powder mixing techniques (Chevalier et al., 2005; De Aza et al., 2003). The A-2.5Z nanocomposite exhibits a peculiar behavior: both the toughness and the threshold are significantly increased, although the quite small size of zirconia particles, <100 nm, is below the critical size for phase transformation (i.e. $< D'_c$). In this case, there is no transformation toughening, even at the crack tip. Moreover, this behavior cannot be attributed to crack bridging, since the R-curve of this composite is flat and the mode of failure is predominantly transgranular. In this nanocomposite, a compressive residual stress field appears in the alumina matrix, which retards the crack front opening when an external stress is applied. The relative effect of the residual stress intensity factor is higher for lower applied stress intensity factors, which explains the higher slope for the A-2.5Z V–K_I curve.

2.10.4 Cyclic Fatigue

2.10.4.1 Fatigue Crack Propagation

Engineering ceramics are prone to cyclic fatigue, particularly those undergoing crack growth resistance. Cyclic loading enhances crack propagation compared to static loading at equivalent stress level. Crack growth rates ($V = \mathrm{d}a/\mathrm{d}t$) can be several orders of magnitude greater than those corresponding to static conditions and they show a marked sensitivity to the maximum applied stress intensity factor, $K_{\max}$, traduced by a high value of the exponent m, compared to that of the stress intensity range ΔK (p) in the modified Paris law (Dauskardt, James, Porter, & Ritchie, 1992; Liu & Chen, 1991):

$$\frac{\mathrm{d}a}{\mathrm{d}t} = A \cdot (\Delta K)^p \cdot K_{\max}^m \tag{10}$$

Examples of m and p exponents are given in **Table 2** for different ceramic materials. Moreover, the threshold values, below which no crack growth is detected, are much smaller for cyclic loading, compared to static loading. It is now well recognized (El Attaoui et al., 2005; Jacobs & Chen, 1995) that the intrinsic response to static or

Table 2 Examples of the exponents *m* and *p* for different ceramic materials

Material	*m*	*p*	*References*
Al_2O_3	21.8	9.8	Gilbert, Dauskard, et al. (1997)
SiC	36	1.9	Gilbert et al. (1996)
Al_2O_3–SiC whisker	18	4.8	Dauskardt et al. (1992)
Si_3N_4	29	1.3	Gilbert et al. (1995)
Y-TZP	15	–	Chevalier et al. (1999)

cyclic loading is the same, but there is a degradation of the reinforcement under alternate loading. Thus, the cyclic fatigue behavior is influenced by the microstructural parameters controlling the reinforcement. Additionally, crack size effects are generally observed in toughened ceramics (Han, Kim, Gilbert, & Ritchie, 2001; Kruzic, Cannon, & Ritchie, 2004; Steffen, Dauskardt, & Ritchie, 1991). Short cracks (in the range of natural flaw size) are less resistant to cyclic fatigue than long cracks, which is traduced by a lower fatigue threshold and accelerated crack growth at the same level of applied load. This difference is attributed to the incomplete shielding development in the short cracks.

2.10.4.2 Influence of Microstructural Toughening

For nontransforming ceramics, the toughening derives essentially from crack bridging and the fatigue mechanism is extrinsic: during cyclic loading, a degradation of the bridging zone occurs leading to a reduction of its shielding capacity (El Attaoui et al., 2005; Gilbert, Dauskardt, & Ritchie, 1995; Gilbert & Ritchie, 1998; Gilbert et al., 1996; Hu & Mai, 1992). Accumulation of frictional-wear damage at the grain/matrix interface and reduction of frictional sliding resistance of partially debonded grains decreases bridging stresses (Eqn (3)), and thus enhances crack-growth rates under cyclic loading (Ritchie, Gilbert, & McNaney, 2000). An example of such degradation can be seen in **Figure 17** for the coarse-grain alumina (20 μm) exhibiting R-curve behavior shown in **Figure 4**. The sample was first monotonically loaded leading to an increase of the crack growth resistance, K_R, until a fully bridged crack was formed (plateau of the R-curve) and was subsequently submitted to cyclic mode, taking care not to propagate the crack. The sample was subsequently reloaded monotonically in order to repropagate the crack. The degradation for a constant crack length can therefore be quantified by the drop of K_R. During cyclic fatigue, the crack length is not constant but generally increases and the net crack driving force can be considered as the resultant of two phenomena: increase of K_{sh} associated with crack extension and decrease of K_{sh} by cyclic damage accumulation. In this respect, the crack growth rate under cyclic loading can be described as a balance between those two effects (El Attaoui et al., 2005; Jacobs & Chen, 1995) and a steady state with a constant crack velocity can be reached. Steady-state crack growth rates measured as a function of K_{Imax} during cyclic loading of A4 and A20 alumina (with respective grain size of 4 and 20 μm) are plotted in **Figure 18**, in which static loading results are also included for comparison. For the fine-grain material, cyclic loading slightly accelerates

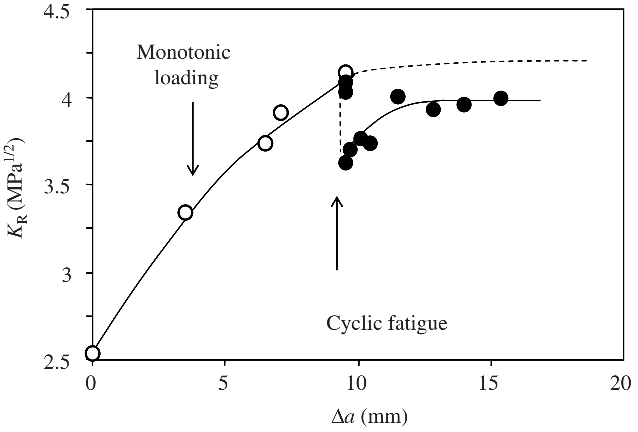

Figure 17 Degradation of the reinforcement by cyclic loading in 20 μm grain-size alumina (El Attaoui et al., 2005).

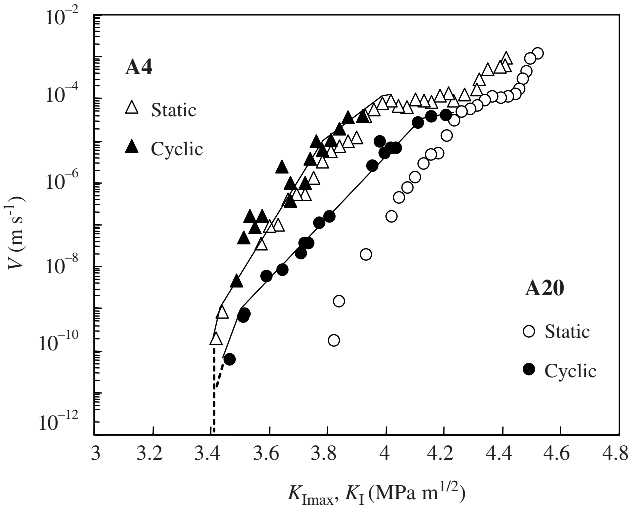

Figure 18 Crack velocity versus the maximum applied stress intensity factor, K_{Imax}, during cyclic loading, for A4 and A20 alumina compared to static V–K_{I} curves. From El Attaoui et al. (2005).

crack propagation suggesting that cyclic fatigue effect is very limited in this material. For the coarse-grain alumina, crack propagation rate is comparable to that of static loading in the high crack growth rate region and becomes higher up to several orders of magnitude in the low crack growth rate region. As the crack growth rate decreases, the difference between the static and the cyclic stress intensity factors increases due to shielding degradation during cyclic fatigue. Important is that the threshold of cyclic crack propagation for the coarse grain material tends toward that of the fine-grain one. This means that the benefit of crack bridging is entirely lost at low cyclic load.

Identical cyclic fatigue effect due to crack shielding degradation was observed for the ABC-SiC SiC described in Section 2.11.2.2.1, whereas no fatigue effect was observed for an equiaxed grain size SiC with a low constant toughness (Gilbert et al., 1996). For the ABC-SiC material, cyclic fatigue crack-growth rates are significantly faster than those under static loading at the same stress intensity level (**Figure 19**). Determination of the bridging tractions from in situ measurements of the crack-opening profiles under an applied load in a scanning electron microscope provided a quantitative evidence of progressive bridging degradation during cyclic loading for this material. In particular, a near-threshold crack is significantly more open than a crack grown near instability (i.e. at high crack growth rates) and its profile approaches that of a traction-free crack (Gilbert & Ritchie, 1998).

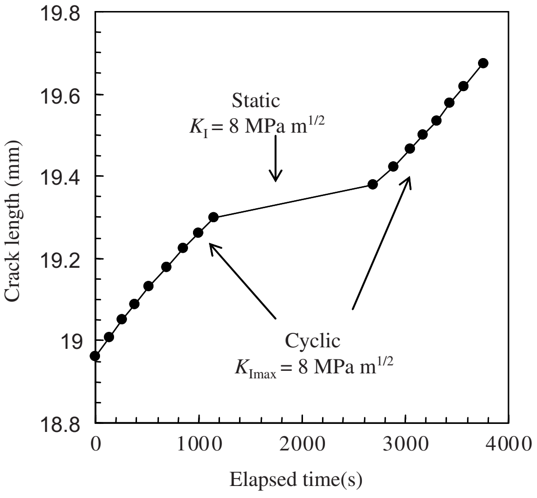

Figure 19 Comparison of crack growth rates in ABC-SiC under static and cyclic loading. From Gilbert et al. (1996).

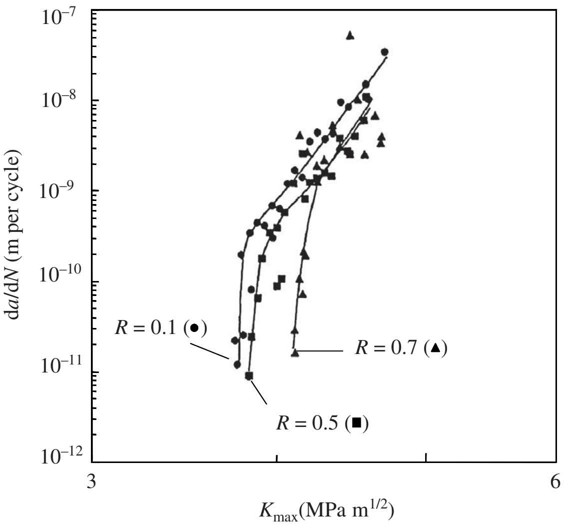

Figure 20 Effect of load ratio, R, on cyclic crack growth rates as a function of K_{max} in silicon nitride. From Gilbert et al. (1995).

Cyclic fatigue effects were also observed in silicon nitride (Bermudo, Osendi, Lib, & Reece, 1997; Gilbert et al., 1995; Jacobs & Chen, 1994). **Figure 20** shows the influence of the load ratio $R = K_{min}/K_{max}$, on crack growth rates plotted as a function of K_{max}, for a silicon nitride material exhibiting a significant rising R-curve behavior, due to the presence of columnar β-Si_3N_4 grains (Gilbert et al., 1995). Below 10^{-9} m per cycle, crack growth rates are decreased with increasing R at a given K_{max}, in accordance with the grain-bridging mechanism: increasing the load ratio leads to a reduction in the sliding distance along the grain bridge/matrix interface, and thus to less degradation in crack-tip shielding per loading cycle. Similar results were obtained for SiC at low crack-growth rates (Gilbert et al., 1996) and for alumina, over the entire range of crack growth rates (Gilbert, Dauskard, Ritchie, 1997).

For zirconia transforming ceramics, in addition to the damage by bridging degradation occurring in polycrystalline ceramics, fatigue effects can be induced by a reduction of the transformation zone shielding under cyclic loading (Dauskardt, Marshall, & Ritchie, 1990; Guiu, Reece, & Vaughan, 1991; Hoffman, Dauskardt, Mai, & Ritchie, 1993; Tsai, Belnap, & Shetty, 1995). For example, cyclic loading experiments were conducted by El Attaoui et al. (2007) on Ce-TZP materials with identical grain sizes and different amounts of transformation toughening, ranging from no phase transformation to highly autocatalytic transformation. Fatigue effects were evidenced in all the materials, even in nontransformation one and the degradation increased with the transformation rate. In this case, the phase transformation induced two other toughening mechanisms operative at different proportions depending on the amount of transformation and the degradation of which contribute to fatigue effects: crack bridging by monoclinic transformed grains resulting from crack arrest due to the shielding effect of the transformation zone, and crack branching operating within a large zone in the presence of autocatalytic transformation.

2.10.5 Thermal Shock Behavior

2.10.5.1 Strength Degradation

According to their low thermal conductivity, ceramic materials are sensitive to thermal shock, which occurs when a material is subjected to a sudden temperature change, especially during cooling. Transient thermal stresses are generated and can become large enough to induce damage such as microcracking, or complete fracture of the material. From Hasselman's classical approach (Hasselman, 1969), brittle materials are classified into two categories: low-strength materials resistant to thermal shock damage (**Figure 21(a)**) and high-strength materials resistant to crack initiation (**Figure 21(b)**). The thermal shock strength degradation is conveniently evaluated from quenching experiments in water and the measure of the retained strength, σ_R. For monolithic ceramics, σ_R generally remains constant until the applied temperature difference, ΔT, reaches a

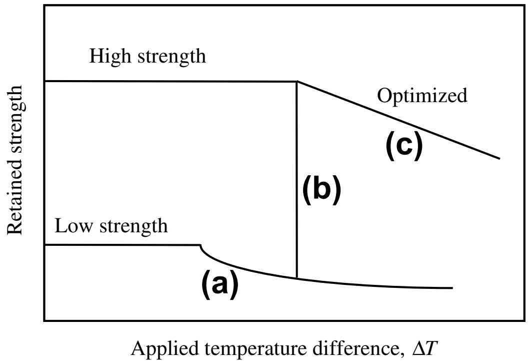

Figure 21 Illustration of the strength degradation from thermal shock for (a) low-strength and (b) high-strength materials and (c) optimized microstructures.

critical value, ΔT_c, and then decrease discontinuously or gradually above this value. ΔT_c often used as a thermal shock parameter indicating the resistance to crack initiation is given by the following equation:

$$\Delta T_c = \sigma_f \frac{1-\nu}{E\alpha} \tag{11}$$

where σ_f is the strength, ν is the Poisson's ratio, E is the Young's modulus, and α is the coefficient of thermal expansion.

The thermal shock resistance of ceramics is influenced by the specimen shape and size and the heat transfer conditions, in addition to the material properties such as Young's modulus, thermal expansion coefficient, tensile strength and fracture toughness (Becher & Warwick, 1993; Pettersson, Johnsson, & Shen, 2002). For example, the incorporation of second-phase particles into a ceramic matrix can increase the thermal shock resistance due to modified material properties (Nieto, Martinez, Mazerolles, & Baudin, 2004) or to microstructural toughening as for alumina–zirconia ceramics (Weimi, Lei, Xudong, Tong, & Guanming, 2007) and Si_3N_4–TiC nanocomposites (Tian, Jiang, & Liu, 2011). Moreover, increasing the crack growth resistance of ceramics increases their thermal shock resistance as will be discussed below, and allows obtaining an optimal state between resistance to crack initiation and resistance to crack propagation (**Figure 21(c)**).

2.10.5.2 Fracture Mechanical Approach: Microstructural Effects

A fracture mechanics approach in terms of stress intensity factor or energy release rate (Bahr, Fett, Hahn, Munz, & Pflugbeil, 1993; Evans & Charles, 1977; Pompe, 1993; Swain, 1990) was developed, allowing to take into account the impact of toughness behavior on thermal shock resistance. The crack extension during thermal shock can be described by a diagram representing the applied thermal shock stress intensity factor, K_{TS}, as a function of crack length at several times. A schematic representation of such diagram is shown in **Figure 22**, for an applied temperature difference larger than the critical value. As the thermal shock is a transient phenomena, K_{TS} increases with time for a given crack length, displays a peak value and then decreases. At a fixed time, K_{TS} passes through a maximum and all the curves have a common envelope (dashed line) which allows anticipating crack propagation modes and arrest, depending on the material behavior and thermal shock conditions.

A crack with an initial length a_i will extend following stable or unstable sequences depending on the toughness behavior. For a material with a constant toughness, K_{Ic} (**Figure 22**, curve (1)), crack propagation occurs when K_{TS} reaches K_{Ic}. The propagation first unstable ($dK_{ST}/da > 0$), becomes stable when ($dK_{ST}/da < 0$), and the crack arrest occurs with a final crack length, a_1, determined by the envelope curve. Materials exhibiting R-curve behavior are generally characterized by three consecutive stages of crack propagation (**Figure 22**, curve (2)). The onset of crack propagation occurs when K_{TS} reaches the initial value of the R-curve. If the R-curve is steep enough, the crack extension is first stable (as $dK_{ST}/da < dK_{ST}/da$), then unstable (when $dK_{ST}/da > dK_{ST}/da$), and becomes stable again. The final crack length is reduced ($a_2 < a_1$), which leads to higher retained strength in the R-curve material, compared to that obtained with the constant toughness material. The different sequences of crack growth have been observed as a function of thermal

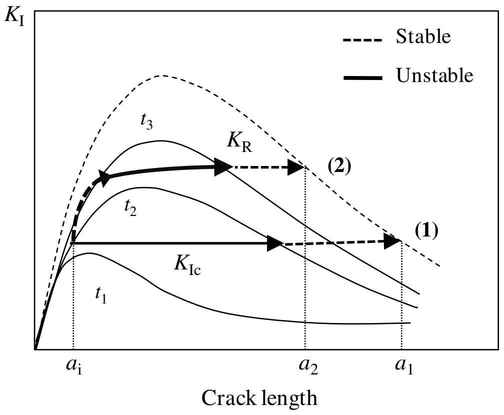

Figure 22 Illustration of crack growth under thermal shock loading for a material with (1) constant toughness and (2) rising R-curve behavior.

stress intensity by Schneider, Magerl, Hahn, and Petzow (1993) during model thermal loading experiments of ceramic discs by lamp irradiation. For quantitative analysis, suitable R-curves under thermal shock conditions have to be considered as they are generally different from those determined under mechanical loading (Bahr et al., 1993; Saâdaoui & Fantozzi, 1998). However, although the R-curve is not unique, a correlation between the R-curve shape, which depends on microstructural effects for the same conditions, and the strength degradation after thermal shock has been established. For example, it has been demonstrated that for alumina with different grain sizes, the retained strength after thermal shock increases linearly with the slope of the R-curve (Steinbrech, 1992). For Si_3N_4 ceramics, it has been shown that the thermal shock resistance can be enhanced using SiC whisker reinforcement (Jia, Zhou, & Lei, 1996) or by coarsening and elongating the microstructure (Hoffman, Schneider, & Petzow, 1993; Lee, Moretti, Readey, & Lawn, 2002). Controlled grain coarsening inducing a high crack growth resistance allows to maintain a high initial strength, which decreases gradually after thermal shock, compared to the typical catastrophic strength loss observed in a fine grain material (**Figure 23**).

Lutz, Swain, and Claussen (1991) have shown that the thermal shock behavior of high strength alumina–zirconia composites can be significantly modified by incorporating pressure zones in a duplex structure that induce crack growth resistance. The thermal shock damage resistance of such materials was enhanced with pronounced R-curve behavior represented by a power function ($K_R \propto a^{\tau}$): $\tau = 0$ corresponds to constant toughness and $\tau > 0$ indicates pronounced R-curve behavior, the intensity of which increases with τ (**Figure 24**).

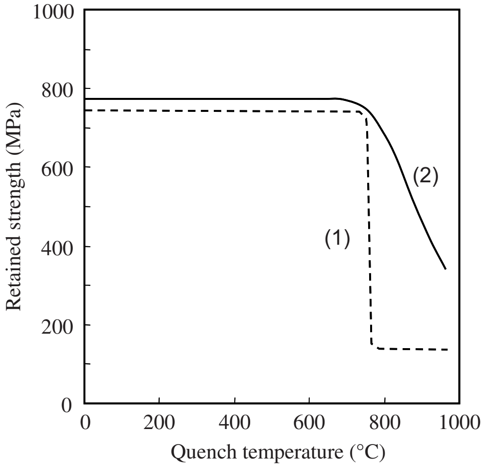

Figure 23 Thermal shock behavior of Si_3N_4 ceramics: (1) fine grain size and (2) optimally coarsened microstructure. Reproduced from Hoffman et al. (1993).

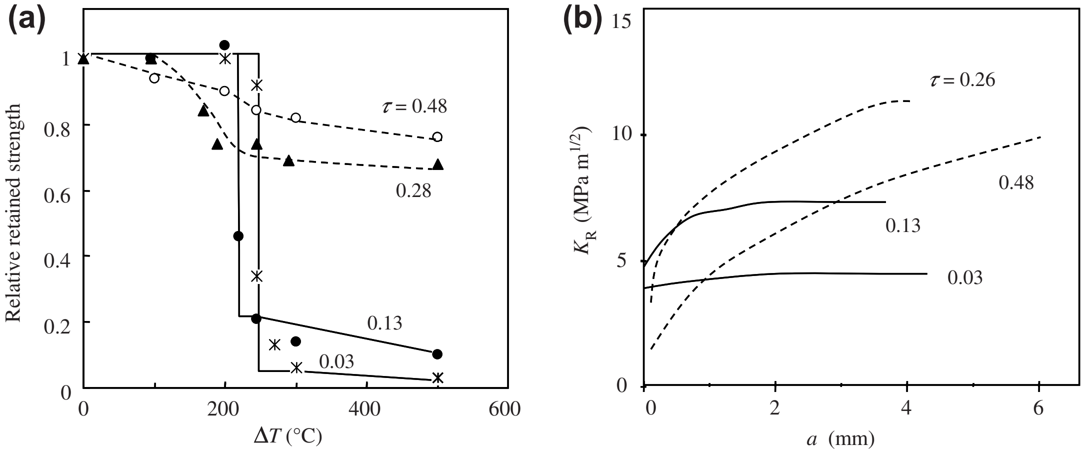

Figure 24 (a) Relative retained strength and (b) corresponding R curves for duplex alumina-zirconia composites. From Lutz et al. (1991).

2.10.6 Concluding Remarks and Future Trends

In this chapter, the fracture behavior of ceramic materials has been analyzed in relation with their microstructure and some examples are given for representative materials. For highly brittle ceramics, especially single crystals, the fracture toughness is equivalent to the surface energy, which is very low for ceramic materials. The development of specific microstructures has led to "flaw-tolerant" materials with improved fracture toughness. The presence of dissipating mechanisms, like crack bridging or phase transformation, leads to the reinforcement of the material, generally accompanied by an increase of the fracture toughness with crack extension (R-curve effect). This toughening is a consequence of crack-shielding mechanisms, which decrease the net crack-tip driving force, due to closure tractions in the wake of a propagating crack. In the preceding sections, we have considered only the toughening due to a single mechanism. In the presence of multiple mechanisms, interaction between them must be considered. This interaction can produce synergism between mechanisms, leading to higher reinforcement, as it is the case of the association of whisker crack bridging and transformation toughening (Amazigo & Budiansky, 1988; Becher & Tiegs, 1987; Evans 1990).

It has been shown that the microstructural toughening decreases the susceptibility to SCG under static loading, and increases the thermal shock resistance. However, toughened materials are more susceptible to degradation under cyclic loading. Thus, tailoring the microstructure of a material must be achieved according to the more important or critical properties intervening in its application.

This short review is not exhaustive as several important points have not been treated in detail. This includes the influence of the toughness behavior on the strength (Kruzic et al., 2008; Munz 2007), which is important for the reliability of ceramic materials. Moreover, the examples given in this chapter concern essentially long-crack behavior. However, in ceramic materials, crack-size effects can be significant (Dauskardt et al. 1992; Gilbert, Cao, et al., 1997; Han et al., 2001; Kruzic et al., 2004; Munz, 2007; Steffen et al. 1991). For example, in grain bridging materials, the critical flaw sizes are often much smaller than the length of the steady-state bridging zones and small cracks propagate at higher growth rates than long cracks at equivalent static or cyclic loading. Consequently, component design cannot be based only on the long crack behavior of a material. Furthermore, the fracture behavior is very often analyzed at room temperature and for the future, a more extensive study of the fracture behavior as a function of temperature should be necessary, the ceramics being widely used at high temperatures.

This work is focused on some monolithic ceramics and associated toughening mechanisms. In recent years, new design concepts were used leading to improved mechanical behavior. Among them, multilayered ceramic composites and ceramic nanocomposites offer new perspectives on the development of engineering ceramic materials. The concept of ceramic nanocomposites proposed by Niihara (1991) consists of dispersing second-phase nanosize particles within matrix grains or along the grain boundaries. A number of combinations of reinforcement and matrix have been reported in the literature, but most studies were essentially concentrated on Al_2O_3 or Si_3N_4 matrices reinforced with SiC nanoparticles (Sternitzke, 1997). Significant enhancements in mechanical properties such as fracture strength, fracture toughness and thermal shock resistance can be obtained with these materials. The strengthening and toughening mechanisms for nanocomposites were discussed based on the effect of residual stresses generated by the mismatch of thermal expansion coefficients between the matrix and the dispersed particles, and the development of dislocations in these materials (Awaji, Choi, & Yagi, 2002).

Ceramic composites with a layered structure (Bermejo, Pascual, Lube, & Danzer, 2008; Bermejo et al., 2006; Lugovy et al., 2005; Sglavo & Bertoldi, 2006) exhibit increased apparent fracture toughness and a non-catastrophic failure behavior due to energy-dissipating mechanisms such as crack deflection or bifurcation which reduce the crack-driving force and lead to an increasing R-curve behavior. One of the most important multilayer designs consists of an alternate tensile–compressive residual stresses with the compressive layers located at the surface or internally, leading respectively to mechanical resistance or damage tolerance, traduced by an enhanced crack growth resistance. In the latter case, the material reliability can be significantly increased, the strength becoming independent on the flaw size, and a threshold strength below which no fracture occurs can be evidenced as for alumina–zirconia multilayered ceramic (Bermejo et al., 2007). For this material, it has also been shown (Bermejo, Torres, Anglada, & Llanes, 2008) that the fatigue resistance is enhanced compared to that of monolithic ceramics, with a crack growth threshold of about 70% of the apparent fracture toughness and the toughening mechanisms (compressive residual stresses, crack bifurcation, and delamination at interfaces) are always effective, independently of the loading conditions.

References

Amazigo, J. C., & Budiansky, B. (1988). Interaction of particulate and transformation toughening. *Journal of the Mechanics and Physics of Solids, 36*, 581–595.

Awaji, H., Choi, S. M., & Yagi, E. (2002). Mechanisms of toughening and strengthening in ceramic-based nanocomposites. *Mechanics of Materials, 34*, 411–422.

Bahr, H. A., Fett, T., Hahn, I., Munz, D., & Pflugbeil, I. (1993). Fracture mechanics treatment of thermal shock and the effect of bridging stresses. In G. A. Schneider, & G. Petzow (Eds.), *Thermal shock and thermal fatigue behaviour of advanced ceramics* (pp. 105–117). Dordrecht: Kluwer Academic Publishers.

Becher, P. F. (1991). Microstructural design of toughened ceramics. *Journal of the American Ceramic Society, 74*, 255–269.

Becher, P. F., Hsueh, C.-H., Alexander, K. B., & Sun, E. Y. (1996). Influence of reinforcement content and diameter on the R-curve response in SiC-whisker-reinforced alumina. *Journal of the American Ceramic Society, 79*, 298–304.

Becher, P. F., Sun, E. Y., Plucknett, K. P., Alexander, K. B., Hsueh, C. H., Lin, H. T., et al. (1998). Microstructural design of silicon nitride with improved fracture toughness: I, effects of grain shape and size. *Journal of the American Ceramic Society, 81*, 2821–2630.

Becher, P. F., & Swain, M. V. (1992). Grain-size-dependent transformation behaviour in polycrystalline tetragonal zirconia. *Journal of the American Ceramic Society, 75*, 493–502.

Becher, P. F., & Tiegs, T. N. (1987). Toughening behaviour involving multiple mechanisms: whisker reinforcement and zirconia toughening. *Journal of the American Ceramic Society, 70*, 651–654.

Becher, P. F., & Warwick, W. H. (1993). Factors influencing the thermal shock behaviour of ceramics. In G. A. Schneider, & G. Petzow (Eds.), *Thermal shock and thermal fatigue behaviour of advanced ceramics* (pp. 37–48). Dordrecht: Kluwer Academic Publishers.

Bermejo, R., Pascual, J., Lube, T., & Danzer, R. (2008). Optimal strength and toughness of Al_2O_3–ZrO_2 laminates designed with external or internal compressive layers. *Journal of the European Ceramic Society, 28*, 1575–1583.

Bermejo, R., Torres, Y., Anglada, M., & Llanes, L. (2008). Fatigue behavior of Alumina–Zirconia multilayered ceramics. *Journal of the American Ceramic Society, 91*, 1618–1625.

Bermejo, R., Torres, Y., Baudin, C., Sanchez-Herencia, A. J., Pascual, J., Anglada, M., et al. (2007). Threshold strength evaluation on an Al_2O_3–ZrO_2 multilayered system. *Journal of the European Ceramic Society, 27*, 1443–1448.

Bermejo, R., Torres, Y., Sanchez-Herencia, A. J., Baudin, C., Anglada, M., & Llanes, L. (2006). Residual stresses, strength and toughness of laminates with different layer thickness ratios. *Acta Materialia, 54*, 4745–4757.

Bermudo, J., Osendi, M. I., Lib, M., & Reece, M. J. (1997). Cyclic fatigue behaviour of silicon nitride materials. *Journal of the European Ceramic Society, 17*, 1135–1860.

Bhatnagar, A., Hoffman, M. J., & Dauskardt, R. H. (2000). Fracture and subcritical crack-growth behaviour of Y-Si-Al-O-N glasses and Si_3N_4 ceramics. *Journal of the American Ceramic Society, 83*, 585–596.

Casellas, D., Nagl, M. M., Llanes, L., & Anglada, M. (2005). Microstructural coarsening of zirconia-toughened alumina composites. *Journal of the American Ceramic Society, 88*, 1958–1963.

Chantikul, P., Bennison, S. J., & Lawn, B. R. (1990). Role of grain size in the strength and R-curve properties of alumina. *Journal of the American Ceramic Society, 73*, 2419–2427.

Chevalier, J., Deville, S., Fantozzi, G., Bartolomé, J. F., Pecharroman, C., Moya, J. S., et al. (2005). Nanostructured ceramic oxides with a slow crack growth resistance close to covalent materials. *Nanoletters, 7*, 1297–1301.

Chevalier, J., & Fantozzi, G. (2005). Slow crack propagation in ceramics at the nano- and micro-scale: effect of microstructure. In R. C. Bradt, D. Munz, M. Sakai, & K. W. White (Eds.), *Fracture mechanics of ceramics* (Vol. 14; pp. 173–190). New York: Springer.

Chevalier, J., Olagnon, C., & Fantozzi, G. (1999). Crack propagation and fatigue in zirconia-based composites. *Composites: Part A, 30*, 525–530.

Claussen, N., & Rühle, M. (1981). Design of transformation-toughening ceramics. In A. H. Heuer, & L. W. Hobbs (Eds.), *Science and technology of zirconia I: Vol. 3. Advances in ceramics* (pp. 137–163). Colombus, OH: American Ceramic Society.

Cook, R. F., Liniger, E. R., Steinbrech, R. W., & Deuerler, F. (1994). Sigmoidal indentation-strength characteristics of polycrystalline alumina. *Journal of the American Ceramic Society, 77*, 303–314.

Dauskardt, R. H., James, M. R., Porter, J. R., & Ritchie, R. O. (1992). Cyclic fatigue-crack growth in a SiC-whisker-reinforced alumina ceramic composite: long- and small-crack behavior. *Journal of the American Ceramic Society, 75*, 759–771.

Dauskardt, R. H., Marshall, D. B., & Ritchie, R. O. (1990). Cyclic fatigue-crack propagation in magnesia-partially-stabilized zirconia ceramics. *Journal of the American Ceramic Society, 73*, 893–903.

De Aza, A. H., Chevalier, J., Fantozzi, G., Schehl, M., & Torrecillas, R. (2003). Slow crack growth behavior of zirconia-toughened alumina ceramics processed by different methods. *Journal of the American Ceramic Society, 86*, 115–120.

Ebrahimi, M. E., Chevalier, J., & Fantozzi, G. (2000). Slow crack-growth behaviour of alumina ceramics. *Journal of Materials Research, 15*, 142–147.

El Attaoui, H., Saâdaoui, M., Chevalier, J., & Fantozzi, G. (2005). Quantitative analysis of crack shielding degradation during cyclic fatigue of alumina. *Journal of the American Ceramic Society, 88*, 172–178.

El Attaoui, H., Saâdaoui, M., Chevalier, J., & Fantozzi, G. (2007). Static and cyclic crack propagation in Ce-TZP ceramics with different amounts of transformation toughening. *Journal of the European Ceramic Society, 27*, 483–486.

Evans, A. G. (1990). Perspective on the development of high-toughness ceramics. *Journal of the American Ceramic Society, 73*, 187–206.

Evans, A. G., & Charles, E. A. (1977). Structural integrity in severe thermal environments. *Journal of the American Ceramic Society, 60*, 22–28.

Gilbert, C. J., Cao, J. J., Dejonghe, L. C., & Ritchie, R. O. (1997). Crack-growth resistance-curve behavior in silicon carbide: small versus long cracks. *Journal of the American Ceramic Society, 80*, 2253–2261.

Gilbert, C. J., Cao, J. J., Moberlychan, W. J., Dejonghe, L. C., & Ritchie, R. O. (1996). Cyclic fatigue and resistance-curve behavior of an in situ toughened silicon carbide with Al-B-C additions. *Acta Metallurgica et Materialia, 44*, 3199–3214.

Gilbert, C. J., Dauskard, R. H., & Ritchie, R. O. (1997). Microstructural mechanisms of cyclic Fatigue-crack propagation in-grain-bridging ceramics. *Ceramics International, 23*, 413–418.

Gilbert, C. J., Dauskardt, R. H., & Ritchie, R. O. (1995). Behavior of cyclic fatigue cracks in monolithic silicon nitride. *Journal of the American Ceramic Society, 78*, 2291–2300.

Gilbert, C. J., & Ritchie, R. O. (1998). On the quantification of bridging tractions during subcritical crack growth under monotonic and cyclic fatigue loading in a grain-bridging silicon carbide ceramic. *Acta Metallurgica et Materialia, 46*, 609–616.

Green, D. J., Hannink, R. H. J., & Swain, M. V. (1989). *Transformation toughening of ceramics*. Boca Raton, FL: CRC Press.

Griffith, A. A. (1920). Fracture of brittle solids. *Philosophical Transactions of the Royal Society, 221A*, 162–198.

Guiu, F., Reece, M. J., & Vaughan, D. A. J. (1991). Cyclic fatigue of ceramics. *Journal of Materials Science, 26*, 3275–3286.

Han, Y. S., Kim, D. K., Gilbert, C. J., & Ritchie, R. O. (2001). Cyclic fatigue–crack propagation behavior in silicon carbide: long- and small-crack behavior. *Journal of the American Ceramic Society, 80*, 551–554.

Hannink, R. H. J., Kelly, P. M., & Muddle, B. C. (2000). Transformation toughening in zirconia-containing ceramics. *Journal of the American Ceramic Society, 83*, 461–487.

Hasselman, D. P. H. (1969). United theory of thermal shock fracture initiation and crack propagation in brittle ceramics. *Journal of the American Ceramic Society, 52*, 600–604.

Heuer, A. H. (1987). Transformation toughening in ZrO_2-containing ceramics. *Journal of the American Ceramic Society, 70*, 689–698.

Hoffman, M. J., Dauskardt, R. H., Mai, Y.-W., & Ritchie, R. O. (1993). A review of the mechanics and mechanisms of cyclic fatigue-crack propagation in transformation-toughened zirconia ceramics. In S. P. S. Badwal, M. J. Bannister, & R. H. J. Hannink (Eds.), *Science and technology of zirconia* (pp. 321–338). Lancaster: Technomic Publishing.

Hoffmann, M. J., Schneider, G. A., & Petzow, G. (1993). The potential of Si_3N_4 for thermal shock applications. In G. A. Schneider, & G. Petzow (Eds.), *Thermal shock and thermal fatigue behaviour of advanced ceramics* (pp. 49–58). Dordrecht: Kluwer Academic Publishers.

Hu, X., & Mai, Y. W. (1992). Crack-bridging analysis for alumina ceramics under monotonic and cyclic loading. *Journal of the American Ceramic Society, 75*, 848–853.

Jacobs, D. S., & Chen, I. W. (1994). Mechanical and environmental factors in the cyclic and static fatigue of silicon nitride. *Journal of the American Ceramic Society, 77*, 1153–1161.

Jacobs, D. S., & Chen, I. W. (1995). Cyclic fatigue in ceramics: a balance between crack shielding accumulation and degradation. *Journal of the American Ceramic Society, 78*, 513–520.

Jia, D. C., Zhou, Y., & Lei, T. C. (1996). Thermal shock resistance of SiC whisker reinforced Si_3N_4 ceramic composites. *Ceramics International, 22*, 107–112.

Kleebe, H. J., Pezzotti, G., & Ziegler, G. (1999). Microstructure and fracture toughness of Si_3N_4 ceramics: combined roles of grain morphology and secondary phase chemistry. *Journal of the American Ceramic Society, 82*, 1857–1867.

Knehans, R., Steinbrech, R., & Schaarwachter, W. (1983). Increase of crack resistance during slow crack growth in Al_2O_3 bend specimens. *Journal of Materials Science, 18*, 265–270.

Kovar, D., Bennison, S. J., & Ready, M. J. (2000). Crack stability and strength variability in alumina ceramics with rising toughness-curve behaviour. *Acta Materialia, 48*, 565–578.

Kruzic, J. J., Cannon, R. M., & Ritchie, R. O. (2004). Crack-size effects on cyclic and monotonic crack growth in polycrystalline alumina: quantification of the role of grain bridging. *Journal of the American Ceramic Society, 87*, 93–103.

Kruzic, J. J., Satet, R. L., Hoffmann, M. J., Cannon, R. M., & Ritchie, R. O. (2008). The utility of R-curves for understanding fracture toughness-strength relations in bridging ceramics. *Journal of the American Ceramic Society, 91*, 1986–1994.

Lee, S. K., Moretti, J. D., Readey, M. J., & Lawn, B. R. (2002). Thermal shock resistance of silicon nitrides using an indentation–quench test. *Journal of the American Ceramic Society, 85*, 279–281.

Li, C. W., Lee, D. J., & Lui, S. C. (1992). R-curve behaviour and strength for in-situ reinforced silicon nitrides with different microstructures. *Journal of the American Ceramic Society, 75*, 1777–1785.

Liu, S. Y., & Chen, I. W. (1991). Fatigue of yttria-stabilized zirconia; I: fatigue damage, fracture origins and lifetime prediction. *Journal of the American Ceramic Society, 74*, 1197–1205.

Li, C. W., & Yamanis, J. (1989). Super-tough silicon nitride with R-curve behaviour. *Ceramic Engineering and Science Proceedings, 10*, 632–645.

Lugovy, M., Slyunyayev, V., Orlovskaya, N., Blugan, G., Kuebler, J., & Lewis, M. (2005). Apparent fracture toughness of Si_3N_4-based laminates with residual compressive or tensile stresses in surface layers. *Acta Materialia, 53*, 289–296.

Lutz, E. H., Swain, M. V., & Claussen, N. (1991). Thermal shock behaviour of duplex ceramics. *Journal of the American Ceramic Society, 74*, 19–24.

Mai, Y. W., & Lawn, B. R. (1987). Crack interface grain bridging as a fracture resistance mechanism in ceramics: II A model. *Journal of the American Ceramic Society, 70*, 289–294.

Marshall, D. B., Evans, A. G., & Drory, M. (1983). Transformation toughening in ceramics. In R. C. Bradt, A. G. Evans, D. P. H. Hasselman, & F. E. Lange (Eds.), *Fracture mechanics of ceramic* (Vol. 6; pp. 289–307). New York: Plenum Press.

McMeeking, R. M., & Evans, A. G. (1982). Mechanisms of transformation toughening in brittle materials. *Journal of the American Ceramic Society, 65*, 242–246.

Miyazaki, H., Hyuga, H., Yoshizawa, Y., Hirao, K., & Ohji, T. (2009). Relationship between fracture toughness determined by surface crack in flexure and fracture resistance measured by indentation fracture for silicon nitride ceramics with various microstructures. *Ceramics International, 35*, 493–501.

Munz, D. (2007). What can we learn from R-curve measurements? *Journal of the American Ceramic Society, 90*, 1–15.

Munz, D., & Fett, T. (1999). *Ceramics: Mechanical properties, failure behaviour, materials selection*. Berlin, Heidelberg: Springer.

Nieto, M. I., Martinez, R., Mazerolles, L., & Baudin, C. (2004). Improvement in the thermal shock resistance of alumina through the addition of submicron-sized aluminium nitride particles. *Journal of the European Ceramic Society, 24*, 2293–2301.

Niihara, K. (1991). New design concept of structural ceramics-ceramic nanocomposites. *Journal of the Ceramic Society of Japan, 99*, 974–982.

Padture, N. P., & Lawn, B. R. (1994). Toughness properties of a silicon carbide with an in situ induced heterogeneous grain structure. *Journal of the American Ceramic Society, 77*, 2518–2522.

Pettersson, P., Johnsson, P., & Shen, Z. (2002). Parameters for measuring the thermal shock of ceramic materials with an indentation-quench method. *Journal of the European Ceramic Society, 22*, 1883–1889.

Pompe, W. E. (1993). Thermal shock behavior of ceramic materials – modeling and measurement. In G. A. Schneider, & G. Petzow (Eds.), *Thermal shock and thermal fatigue behaviour of advanced ceramics* (pp. 3–14). Dordrecht: Kluwer Academic Publishers.

Ritchie, R. O., Gilbert, C. J., & McNaney, J. M. (2000). Mechanics and mechanisms of fatigue damage and crack growth in advanced materials. *International Journal of Solids and Structures, 37*, 311–329.

Saâdaoui, M., & Fantozzi, G. (1998). Crack growth resistance under thermal shock loading of alumina. *Materials Science and Engineering, A247*, 142–151.

Satet, R. L., Hoffmann, M. J., & Cannon, R. M. (2006). Experimental evidence of the impact of rare-earth elements on particle growth and mechanical behaviour of silicon nitride. *Materials Science and Engineering, A422*, 66–76.

Schneider, G. A., Magerl, F., Hahn, I., & Petzow, G. (1993). In situ observations of unstable and stable crack propagation and R-curve behaviour in thermally loaded disks. In G. A. Schneider, & G. Petzow (Eds.), *Thermal shock and thermal fatigue behaviour of advanced ceramics* (pp. 229–244). Kluwer Academic Publishers.

Sglavo, V. M., & Bertoldi, M. (2006). Design and production of ceramic laminates with high mechanical resistance and reliability. *Acta Materialia, 54*, 4929–4937.

Steffen, A. A., Dauskardt, R. H., & Ritchie, R. O. (1991). Cyclic fatigue life and crack-growth behavior of microstructurally small cracks in magnesia-partially-stabilized zirconia ceramics. *Journal of the American Ceramic Society, 74*, 1259–1268.

Steinbrech, R. W. (1992). R curve behaviour of ceramics. In R. C. Bradt, et al. (Eds.), *Fracture mechanics of ceramics* (Vol. 9; pp. 187–208). New York: Plenum Press.

Steinbrech, R. W., Reichl, A., & Schaarwachter, W. (1990). R-Curve behaviour of long cracks in alumina. *Journal of the American Ceramic Society, 73*, 2009–2015.

Sternitzke, M. (1997). Review: structural ceramic nanocomposites. *Journal of the European Ceramic Society, 17*, 1061–1082.

Swain, M. V. (1990). R-curve behaviour and thermal shock resistance of ceramics. *Journal of the American Ceramic Society, 73*, 621–628.

Swanson, P. L., Fairbanks, C. J., Lawn, B. R., Mai, Y.-W., & Hockey, B. J. (1987). Crack-interface grain bridging as a fracture resistance mechanism in ceramics: I, experimental study on alumina. *Journal of the American Ceramic Society, 70*, 279–289.

Tatarko, P., Kasiarova, M., Dusza, J., Morgiel, J., Sajgalik, P., & Hvizdos, P. (2010). Wear resistance of hot-pressed Si_3N_4/SiC micro/nanocomposites sintered with rare-earth oxide additives. *Wear, 269*, 867–874.

Tian, C., Jiang, H., & Liu, N. (2011). Thermal shock behaviour of Si_3N_4–TiN nano-composites. *International Journal of Refractory Metals and Hard Materials, 29*, 14–20.

Tsai, J. F., Belnap, J. D., & Shetty, D. K. (1995). Cyclic fatigue of Ce-TZP/Al_2O_3 composites: role of the degradation of transformation zone shielding. *Journal of the American Ceramic Society, 78*, 599–608.

Vekinis, G., Ashby, M. F., & Beaumont, P. W. R. (1990). R-Curve behavior of alumina ceramics. *Acta Metallurgica et Materialia, 38*, 1151–1162.

Weimi, M., Lei, W., Xudong, S., Tong, C., & Guanming, Q. (2007). Thermal shock resistance of $A1_20_3/Zr0_2$ (Y_2 O_3) composites. *Journal of Rare Earths, 25*, 53–57.

Zheng, Y. S., Knowles, K. M., Vieira, J. M., Lopes, A. B., & Oliveira, F. J. (2001). Microstructure, toughness and flexural strength of self-reinforced silicon nitride ceramics doped with yttrium oxide and ytterbium oxide. *Journal of Microscopy, 201*, 238–249.

Zou, L. H., Huang, Y., Park, D. S., Cho, B. U., Kim, H. D., & Han, B. D. (2004). R-curve behavior of Si_3N_4 whisker-reinforced Si_3N_4 matrix composites. *Ceramics International, 31*, 197–204.

This page intentionally left blank

2.11 High-Temperature Mechanical Behavior of Hard Ceramics

Joaquin Ramírez-Rico and Julián Martínez-Fernández, Dpto. Física de la Materia Condensada—ICMS, Universidad de Sevilla—CSIC, Sevilla, Spain

© 2014 Elsevier Ltd. All rights reserved.

Nomenclature

ϵ strain
$\dot{\epsilon}$ steady-state strain rate or creep rate (s^{-1})
σ externally applied uniaxial stress (MPa)
σ_0 threshold stress for creep (MPa)
G shear modulus (GPa)
b Burgers vector (Å)
d average grain size (μm)
k Boltzmann constant (1.38×10^{-23} J K^{-1})
R gas constant (8.31 J mol^{-1} K^{-1})
D self-diffusion constant (m^2 s^{-1})
Q activation energy for self-diffusion (J mol^{-1})
n stress exponent for creep
p grain size exponent for creep
Ω atomic volume (Å^3)
δ grain boundary thickness (Å)
η viscosity (MPa s)
f volume fraction
K_1 rate of solution and precipitation (m s^{-1} J^{-1})
h intergranular glassy layer thickness (Å)

2.11.1 Introduction

Ceramics are regarded as interesting materials for high-temperature applications due to their good thermomechanical properties, which arise from their high melting points and low densities. Wherever their properties at high temperatures differ from those measured at room-temperature plastic deformation, i.e. the permanent, irreversible deformation of the material under applied stress, is usually responsible for these differences. In a broad sense, plasticity is due to the formation and movement of defects in the ceramics, whether they are point defects, dislocations, twins, grain boundaries or secondary phases. For this reason, plastic deformation can only be understood by considering the microstructure as a defining characteristic of the material and therefore is intricately related to processing.

Most technical ceramics of interest for thermomechanical applications that can be manufactured reproducibly and in large quantities are polycrystalline and they are the main focus of this chapter. Plastic deformation of single crystals, although fascinating and important to many applications, is not treated here, but the reader can find many entry level texts in the literature, such as Poirier (1985).

This chapter is divided into three main sections. Section 2.11.2 describes creep in ceramics and summarizes the mechanisms most often invoked to explain plastic deformation in polycrystalline materials. As examples of these mechanisms, the creep behavior of some ceramics interesting from a technological point of view is reviewed in Section 2.11.3. Finally, in Section 2.11.4, the concept of creep rupture and the mechanisms of high-temperature static fracture of ceramics are briefly introduced.

2.11.2 Creep Mechanisms in Polycrystalline Materials

Creep can most simply be defined as the sustained plastic deformation of a material under the application of a constant stress, usually at high temperatures over half the melting point. In a typical experiment, a dead-weight loading apparatus is used to impart a constant stress in a sample of prismatic or cylindrical shape, either in tension or compression, and the elongation and thus the strain ϵ is recorded as a function of time. If a plot of strain versus time is made, such as that of **Figure 1**, three different stages can be distinguished. The first one is termed *primary creep* and is a transient stage, while the second one represents *steady-state creep* and is characterized by a constant rate of deformation. A third stage characterized by an acceleration in strain until failure (*tertiary creep*) is often observed for materials tested in tension, and is due to formation of a neck in the tensile specimen.

The steady-state creep rate $\dot{\epsilon}$ depends on temperature, applied stress and on one or more characteristic parameters describing the microstructure, usually the grain size in polycrystalline ceramics. It is often found empirically that the relationship between creep rate and experimental conditions and microstructure can be described by the Mukherjee–Bird–Dorn equation (Mukherjee, Bird, & Dorn, 1969):

$$\dot{\epsilon} = \frac{AD_0Gb}{kT}\left(\frac{b}{d}\right)^p\left(\frac{\sigma}{G}\right)^n e^{-\frac{Q}{RT}} \tag{1}$$

where D_0 is the frequency factor, G is the shear modulus, d is the grain size, b is the modulus of the Burgers' vector, σ is the applied stress, T is the temperature and Q is the activation energy for creep. In many cases, the activation energy for creep coincides with that of diffusion, $Q = Q_\mathrm{d}$ and then D is the diffusion coefficient:

$$D = D_0e^{-\frac{Q_\mathrm{d}}{RT}} \tag{2}$$

The term n is termed the *stress exponent* and d is the *grain size exponent*. In most oxides, it is found that the strain rate normally depends also on the testing environment and shows a potential relationship with the oxygen partial pressure P_{O_2}. For very fine-grained ceramics, a threshold stress σ_0 for deformation is often observed, leading to a relationship of the type $\dot{\epsilon} \propto (\sigma - \sigma_0)^n$.

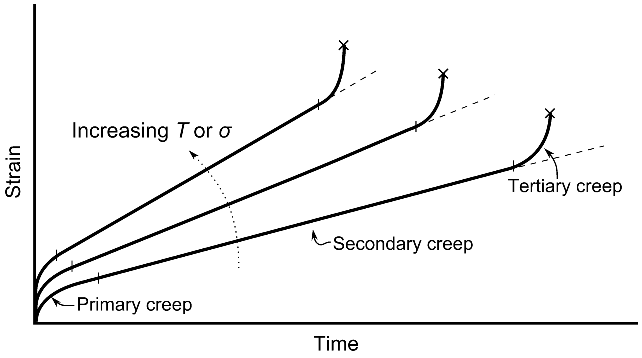

Figure 1 Typical strain vs time plot for a constant stress experiment. Three zones can be distinguished, corresponding to primary, secondary (steady-state) and tertiary creep. In the steady state, the creep rate is constant and increases with increasing stress or temperature.

Table 1 Parameters predicted by some models for creep in ceramics

Mechanism	n	p	Q	*Ref.*
Diffusional creep				
Nabarro–Herring	1	2	Q_l	(Herring, 1950; Nabarro, 1948)
Coble	1	3	Q_{gb}	(Coble, 1963)
Grain boundary sliding				
By diffusion	1[a]	2,3	Q_l, Q_{gb}	(Ashby & Verrall, 1973)
Interface reaction control	2	1	Q_l	(Burton, 1972)
	2	2	Q_{gb}	(Schneibel & Hazzledine, 1983)
By dislocations	2	2	Q_{gb}	(Gifkins, 1976)
Solution-precipitation				
Controlled by diffusion	1	3		(Raj & Chyung, 1981)
Controlled by interface reaction	1	1		
Viscous flow	1	[b]	Q_{visc}	(Dryden & Wilkinson, 1997)
Dislocation mechanisms				
Glide and climb controlled by climb	4.5	0	Q_l	(Weertman, 1957b)
Glide and climb controlled by glide	3	0	Q_{ci}	(Weertman, 1957a)
Climb from Bardeen–Herring sources controlled by lattice diffusion	3	0	Q_l	(Nabarro, 1967)
Climb from Bardeen–Herring sources controlled by pipe diffusion	5	0	Q_p	(Nabarro, 1967)

[a] *With a threshold stress inversely proportional to grain size.*

[b] *Strain rate is proportional to the cube of the volume fraction of the secondary phase.*

A typical experimental study of creep in ceramics involves testing a large number of specimens, either in tension or compression, at different loads, temperatures and grain sizes. For each of the tests, the steady-state creep rate is determined and the data fitted to Eqn (1) to obtain values of n, p and Q. Then, an attempt is made to identify the possible rate-controlling mechanism by comparing these values with theoretical predictions of different models for creep. Unfortunately, a set of n, p and Q values does not always allow for unambiguous identification of the underlying mechanism, and microstructural observation of crept samples is necessary. Additionally, it is important to check that the microstructure of the material stayed constant during the course of the experiment, i.e. that no grain growth has taken place in the ceramic, as otherwise the measured strain rate might not be a true steady-state rate. If that is the case, and assuming that microstructural evolution does not change the rate-controlling mechanism, it is still possible to determine at least n and Q by performing instantaneous changes in applied stress or temperature, respectively, and comparing the rate before and after the step.

Cannon and Langdon (1988, 1983), as well as Chokshi and Langdon (1991), have classified the physical mechanisms responsible for creep into lattice mechanisms, which take place inside the individual grains of the ceramic and independently of the grain boundaries ($p = 0$), and boundary mechanisms, which rely on the presence of grain boundaries and must therefore depend on the total amount of boundaries through the grain size of the ceramic ($p \geq 1$). Lattice mechanisms occur in both single crystal and polycrystalline ceramics while, by definition, boundary mechanisms occur only in polycrystalline materials. A summary of creep models along with their predicted values for n, p, and Q is included in **Table 1**.

2.11.2.1 Diffusional Creep

In diffusional creep, plastic deformation is entirely due to matter transport between the different boundary surfaces of each grain through diffusion of vacancies, either through the grain or along the grain boundaries. As noted by Nabarro (1948), when a nonhydrostatic stress field is applied to a crystal, the local concentration of point defects (i.e. vacancies) is modified from the equilibrium value so a higher concentration exists in the tensile faces of the crystal, and a lower concentration appears in the compressive faces (**Figure 2**). This concentration gradient in turn produces a flux of vacancies through the crystal that is equivalent to a flux of matter in the opposite direction, which produces a macroscopic permanent deformation of the crystal. With this hypothesis, Herring (1950) later arrived to the following expression for the steady-state creep rate:

$$\dot{\epsilon} = \frac{B\Omega\sigma}{kT\,d^2} D_l \qquad (3)$$

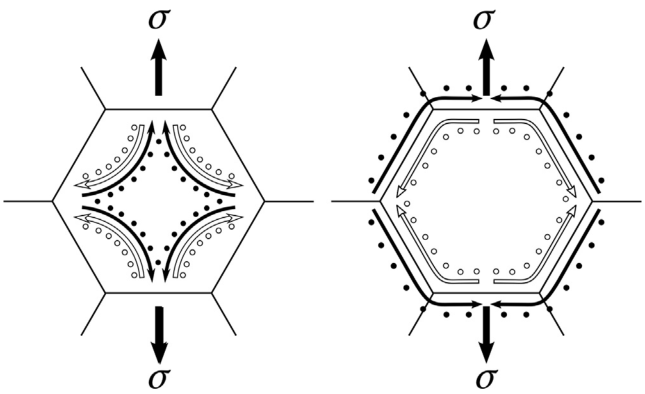

Figure 2 Schematic of vacancy (○) and atomic (●) flow in diffusional creep. (a) Nabarro-Herring creep. (b) Coble creep.

This predicts a linear dependence of strain rate with stress and an inverse square dependence with the grain size. In the above expression, Ω is the atomic volume and D_l is the coefficient of self-diffusion. Nabarro–Herring creep is sometimes observed at very high temperatures ($T \approx 0.9\ T_m$) and very low stresses ($\sigma \leq 10^{-6}$ G).

In addition to bulk diffusion, defects and thus matter can be transported through diffusion along the grain boundaries, which is usually faster (**Figure 2**). This extension is due to Coble (1963) and yields

$$\dot{\epsilon} = B\frac{\pi\Omega\sigma}{kT\,d^3}\delta D_{gb} \tag{4}$$

Here δ is the grain boundary thickness and D_{gb} is the self-diffusion coefficient through the grain boundaries. In Coble creep, dependence with the cubed inverse of the grain size is then predicted, which makes this mechanism favored for polycrystalline ceramics with small grain sizes. Additionally, since the activation energy for self-diffusion through the grain boundary is normally smaller than that for bulk self-diffusion, Coble creep is more commonly observed at lower temperatures.

In the general case where matter is transported independently through both paths, the steady-state creep rate can be written as

$$\dot{\epsilon} = B\frac{\Omega\sigma}{kT\,d^2}\left(D_l + \frac{\pi\delta}{d}D_{gb}\right) \tag{5}$$

Self-diffusion in ceramics involves the transport of both the anions and the cations in the appropriate stoichiometric ratio. There are two possible diffusion paths (through the grain and along the grain boundaries) and (usually) two ionic species, so a total of four possible rate-controlling mechanisms exist (Gordon, 1973). Then, creep is controlled by the slower diffusing species along the faster path.

Until now, we have considered the creep of isolated grains, which become elongated due to diffusive transport of matter from the compressive faces to the tensile ones. It must be noted that if this were the only mechanism responsible for deformation, extensive formation of cavities and small cracks would have to take place. In order to maintain compatibility of the deformation, a grain boundary sliding (GBS) mechanism must take place. When GBS occurs so that the grains elongate along the tensile axis and maintain their adjacent neighbors, it is termed Lifshitz sliding (Lifshitz, 1963) and is depicted schematically in **Figure 3**. While Lifshitz sliding accounts for part of the total strain, diffusion is usually the rate-controlling process.

In the above discussion, we have implicitly accepted that grain boundaries act as perfect sinks and sources of point defects, but if this is not the case then creep can be controlled by reaction of formation and annihilation of vacancies at the grain boundaries. Several theories exist for interface reaction control (Arzt, Ashby, & Verrall, 1983; Ashby, 1969; Burton, 1972; Greenwood, 1970; Schneibel & Hazzledine, 1983), most of them predicting values of $n = 2$ and $p = 1$.

2.11.2.2 Grain Boundary Sliding and Superplasticity

Diffusional creep predicts a change in the shape of the grains, which become elongated in the tensile direction from the (usually) equiaxed initial configuration. However, many ceramic materials maintain an equiaxed grain

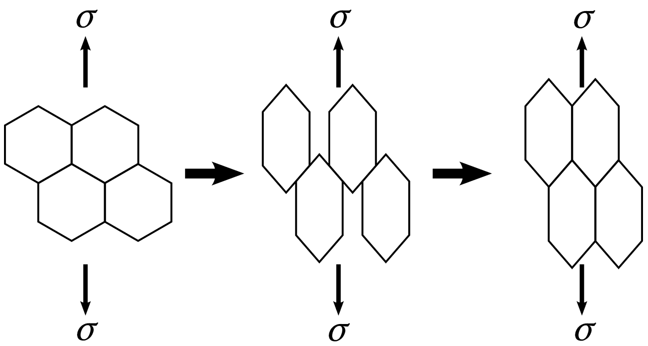

Figure 3 Schematic representation of Lifshitz grain boundary sliding which accompanies diffusional creep. The grains in the initial configuration (a) become elongated due to diffusive flow (b) and grains slide to maintain cohesion of the polycrystal (c). The grains maintain their adjacent neighbors. This sliding process accounts for part of the total creep strain.

shape even after undergoing large deformations, which implies that a different mechanism must be taking place. Rachinger sliding (Rachinger, 1952) considers that the adjacent neighbors of each grain can change during deformation, in contrast with Lifshitz sliding. This permits the ceramic to undergo large deformations without a change in grain morphology and is the basis for the superplastic behavior observed in many ceramics. Sliding of grains past each other would, however, generate stresses at multigrain junctions and irregularities in the grain boundaries that would increase until opposing the applied stress, stopping deformation, or would create cracks at grain boundaries. Therefore, an accommodation mechanism that relaxes such stresses must be present.

Two main groups of GBS theories exist depending on whether the rearrangement is considered in terms of individual grains or groups of grains (cooperative grain boundary sliding). A review of these mechanisms and their geometrical implications for the topology of the grains can be found in Zelin and Mukherjee (1996). Ashby and Verrall (1973) proposed a model for sliding accommodated by diffusion in which grain switching occurs in groups of four grains by an intermediate neck position, and gives rise to a threshold stress that is inversely dependent on the grain size. They predict a stress exponent of $n = 1$ and a grain size exponent $p = 2$ if diffusion occurs through the bulk and $p = 3$ if diffusion occurs through the grain boundaries, and an activation energy accordingly to the diffusion path. Other mechanisms involve accommodation by dislocations in a volume in the periphery of each grain but not inside them (Gifkins, 1976), or accommodation by an interface-reaction-controlled process (Burton, 1972; Schneibel & Hazzledine, 1983). The phenomenon of superplasticity and its relationship with GBS has been studied in great detail and it is outside of the scope of this chapter, but many reviews exist and a good starting point can be found in Maehara and Langdon (1990), Langdon (1991), and Chokshi, Mukherjee, and Langdon (1993).

2.11.2.3 Viscous Flow Creep

Many ceramics contain secondary, usually vitreous phases that are the result of the addition of sintering aids to promote densification. Usually distributed as an intergranular film and in pockets at multigrain junctions, this vitreous phase can have a dramatic effect on the high-temperature mechanical properties of the material, and especially on creep. Since viscosity falls at high temperatures, redistribution of this glassy phase alone can account for at least a fraction of the plastic strain in many ceramics. This mechanism, however, must be transient in nature as the action of an external stress makes the grains approach each other and the secondary phase is therefore squeezed out; the grains finally become interlocked and deformation must proceed through another mechanism, such as one of those described earlier.

Dryden et al. (Dryden, 2000; Dryden & Wilkinson, 1997; Dryden, Kucerovsky, Wilkinson, & Watt, 1989) obtained an expression for viscous flow creep by idealizing the microstructure as a set of cubic grains embedded in an incompressible Newtonian fluid. The creep rate is related to stress by

$$\dot{\epsilon} = \frac{f^3}{27\eta} S\left(\frac{\epsilon}{f}\right)\sigma \tag{6}$$

In the above expression, f is the volume fraction of the glassy phase and η is its viscosity which contains the dependence with temperature. The function $S\left(\frac{\epsilon}{f}\right)$ is termed the "strain factor" and goes to zero as the strain increases. This is to be expected since creep by viscous flow is a transient process, and thus the strain rate must decrease with time. This function does, however, decrease faster when load is compressive than when it is tensile, and this mechanism can explain, at least partially, the asymmetry between creep in compression and tension observed in many ceramics.

2.11.2.4 Solution-Precipitation Creep

In many ceramics containing a secondary vitreous phase, an additional mechanism can be responsible for creep provided that the crystalline phase of the grains is at least partially soluble in the glass. This mechanism, first due to Raj and Chyung (1981), implies that the crystal is dissolved into the glass at the grain boundaries subjected to compression. Diffusion of the crystal's species occurs along the liquid phase toward the grain boundaries in tension, where they precipitate back into a crystalline material. This sequential mechanism, which is essentially the process by which liquid-phase densification occurs, consists of two processes with different kinetics: solution and precipitation at grain boundaries, and material transport along the glassy phase. The slowest of these processes will be the rate-controlling one.

If creep is controlled by interface reaction (solution and precipitation), then the strain rate is given by

$$\dot{\epsilon} = \frac{\Omega}{2kT}\frac{K_1}{d}\sigma \tag{7}$$

where K_1 is the rate at which the atoms are exchanged between the glass and the crystal at the interface and contains the temperature dependence. If the creep is controlled by diffusion through the glass,

$$\dot{\epsilon} = 3.7\frac{\Omega c}{\eta}\frac{\alpha}{d^3}\sigma \tag{8}$$

where c is the average molar concentration of the solute in the liquid phase, η is the viscosity and $\alpha = h\Omega^{-\frac{1}{3}}$, where h is the glass thickness at the grain boundaries. A schematic of this model is presented in Figure 4.

2.11.2.5 Power-Law Creep

Lattice mechanisms are independent of the presence of grain boundaries and therefore for them $p = 0$. They are all based on the intragranular motion of dislocations, which is generally less important for ceramic than it is for metals. This is mainly due to two reasons: on the one hand, ionic solids exhibit much higher Peierls stresses for

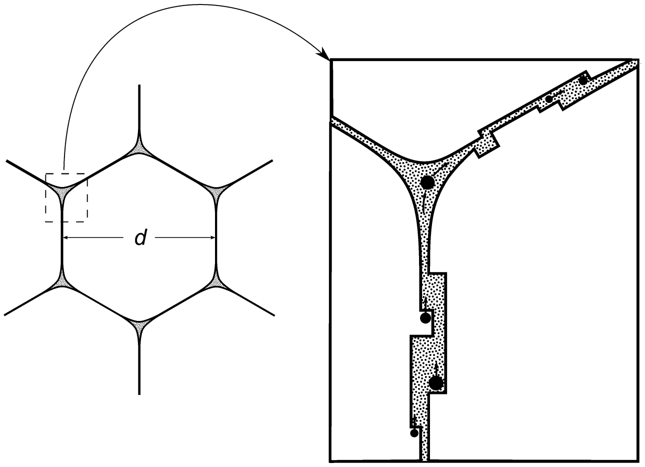

Figure 4 Schematic representation of the microstructure in the solution-precipitation creep model of Raj and Chyung. Adapted from Raj and Chyung (1981).

glide due to electrostatic forces, which determine the slip systems for easy glide. In the case of covalent solids, the directional nature of the atomic bonding makes dislocation glide even more difficult. The Burgers vector in ceramic materials is usually much larger than in metals, which in turn requires higher shear stresses for glide. On the other hand, crystal structure in ceramics is usually much more complex, which makes it less likely for several slip systems to be simultaneously operative. Since the number of slip systems is limited, only certain components of strain can be produced and in polycrystalline materials it is not possible for individual, randomly oriented grains to undergo arbitrary deformation and conform to the macroscopic deformation of the specimen. A minimum of five independent slip systems is required for a crystal to be able to undergo arbitrary changes in shape.

Nevertheless, creep deformation by dislocation motion is often observed at very high stresses and in ceramics with a very large grain size, in which diffusion paths are large and diffusional creep is therefore limited. When lattice mechanisms are observed in ceramics, measured stress exponent tends to cluster around values of 3 and 5, in analogy with metals where the exponents are interpreted in terms of control by glide or climb of dislocations, respectively. Due to the observation of stress exponents higher than unity, creep by motion of dislocations is termed *power-law creep*.

2.11.2.6 Combined Creep Mechanisms

Until now creep has been attributed to only one of the many possible mechanisms, but in reality many ceramics can undergo a transition from one rate-controlling mechanism to another depending on applied stress or temperature (Figure 5). More than one mechanism can be active simultaneously, depending on the microstructural characteristics of the material. For instance, for very fine-grained ceramics, a mechanism involving accommodation by diffusion would be expected since the paths for matter transport are short. However, since strain rate in this case depends inversely on some power of the grain size, in large-grained ceramics, the creep rate produced by diffusional accommodation is very small, and lattice mechanisms involving dislocations might become relevant. Interface reaction control might be rate limiting at very low stresses, while at sufficiently high applied stress, diffusional control might be recovered. Another example, in this case of an "apparent" transition, occurs in ceramics that exhibit a threshold stress for deformation so $\dot{\epsilon} \propto (\sigma - \sigma_0)^n$; the apparent stress exponent is $\partial\,\mathrm{In}\,\dot{\epsilon}/\partial\,\mathrm{In}\,\sigma = n\sigma/(\sigma - \sigma_0)$ and very high "apparent" values of n can be observed at stresses higher but close to the threshold stress. Transitions in the activation energy for creep can also be observed: the ratio of creep rates produced by Nabarro–Herring to Coble creep is proportional to the grain size, $\dot{\epsilon}_{\mathrm{NH}}/\dot{\epsilon}_{\mathrm{Coble}} \propto d$, so for the same applied stress and temperature, a fine-grained ceramic might accommodate deformation by Coble creep but Nabarro–Herring creep might be more important for larger grain sizes. A change in the observed activation energy will then be observed as grain size is increased, from $Q = Q_{\mathrm{gb}}$ to $Q = Q_{\mathrm{lattice}}$.

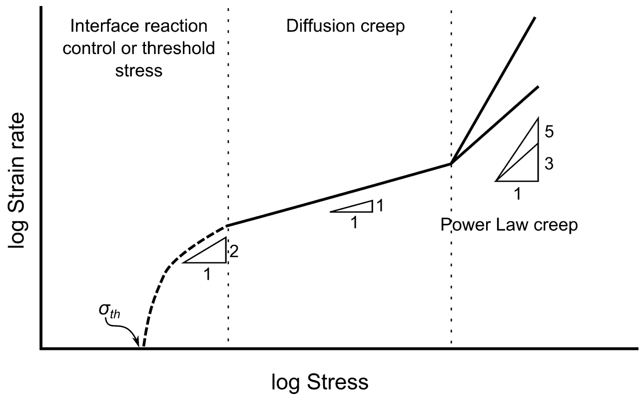

Figure 5 Schematic illustration showing possible creep mechanism transitions with applied stress. Adapted from Chokshi and Langdon (1991).

2.11.2.7 Creep in Particulate Composites

In cases where the volume fractions of the different phases composing the polycrystalline ceramic are similar, the microstructure can be referred to as *duplex* (French, Zhao, Harmer, Chan, & Miller, 1994) and in these cases, a simple approach exists that allows prediction of the creep properties of the composite if the properties of the individual phases are known. For simplicity, we will consider a two-phase ceramic composite with volume fractions f_1 and f_2 that is subjected to a uniaxial stress σ undergoing steady-state creep at a rate $\dot{\epsilon}$. Then, a simple rule of mixtures can be applied to relate either the strain rates of each of the phases to the macroscopic rate, or the load partitioning in each of the phases to the total external applied stress.

In the first case the composite is said to be deforming under *isostress* conditions, in parallelism to the Reuss model of continuum elastic micromechanics. Both phases of the material are under the same average stress σ and are deforming at such a rate that their sum weighted by each phase's volume fraction equals the total macroscopic strain rate:

$$\begin{aligned} \sigma &= \sigma_1 = \sigma_2 \\ \dot{\epsilon} &= f_1\dot{\epsilon}_1 + f_2\dot{\epsilon}_2 \end{aligned} \tag{9}$$

Let us assume that each phase is deforming according to its own equation of state, which will be written as $\dot{\epsilon}_i = B_i\sigma_i^{n_i}$, with $B_i = A_i \exp(-Q_i/RT)$. The composite strain rate is then

$$\dot{\epsilon} = f_1B_1\sigma^{n_1} + f_2B_2\sigma^{n_2} \tag{10}$$

where the isostress condition was used. The composite creep equation can be written as follows:

$$\dot{\epsilon} = A\sigma^n \exp(Q/RT) \tag{11}$$

Now n and Q contain the dependence of the macroscopic strain rate on applied stress and temperature, and might not be constants but change depending on the experimental conditions. By using

$$n = \frac{\partial \ln \epsilon}{\partial \ln \sigma} \qquad Q = \frac{\partial \ln \epsilon}{\partial (1/T)} \tag{12}$$

the apparent stress exponent and activation energy in the composite can be obtained as a function of the stress exponents and activation energies of each of the phases as well as their relative volume fractions:

$$n = n_1f_1\frac{\dot{\epsilon}_1}{\dot{\epsilon}} + n_2f_2\frac{\dot{\epsilon}_2}{\dot{\epsilon}} \qquad Q = Q_1f_1\frac{\dot{\epsilon}_1}{\dot{\epsilon}} + Q_2f_2\frac{\dot{\epsilon}_2}{\dot{\epsilon}} \tag{13}$$

A consequence of this relationship is that, for a given composite with fixed volume fractions, the apparent values of n and Q will depend on applied stress and will be closer to that of the phase deforming at a faster rate of the two.

The second case corresponds to *isostrain* conditions, in which both phases deform at the same rate, equal to the macroscopic strain rate, and the externally applied stress is partitioned between them according to their relative volume fractions, i.e.

$$\begin{aligned} \sigma &= f_1\sigma_1 + f_2\sigma_2 \\ \dot{\epsilon} &= \dot{\epsilon}_1 = \dot{\epsilon}_2 \end{aligned} \tag{14}$$

This is conceptually analogous to the Voigt approximation in elastic micromechanics. Now the applied stress can be written as a function of the strain rate as

$$\sigma = f_1\left(\frac{\dot{\epsilon}}{B_1}\right)^{1/n_1} + f_2\left(\frac{\dot{\epsilon}}{B_2}\right)^{1/n_2} \tag{15}$$

Now, the apparent stress exponent and activation energy of the composite are

$$\frac{1}{n} = f_1\frac{1}{n_1}\frac{\sigma_1}{\sigma} + f_2\frac{1}{n_2}\frac{\sigma_2}{\sigma} \qquad Q = Q_1f_1\frac{n}{n_1}\frac{\sigma_1}{\sigma} + Q_2f_2\frac{n}{n_2}\frac{\sigma_2}{\sigma} \tag{16}$$

Again, the values of n and Q for the composite will change with experimental conditions, but in this case, they will be closer to that of the phase that would deform by itself at a lower rate of the two.

2.11.3 High-Temperature Creep Behavior of Technical Ceramics

In this section, the properties of some of the most widely studied technical ceramics for high-temperature applications are summarized in the context of the physical mechanisms described above. As with any other material or physical property, mechanical properties of ceramic materials are highly dependent on processing as well as testing conditions, so caution must be exercised if the data presented here are to be used. In each case, the reader must refer to the original publication to determine whether the conditions at which the data were obtained apply to the problem at hand.

The list of materials for which data are compiled below is by no means exhaustive: data that exemplifies specific behaviors have in some instances been included instead of more general cases, and wherever possible, data from commercial materials have been included.

2.11.3.1 Alumina Ceramics

Alumina is perhaps the most widely studied technical ceramic, and an extensive body of data exists in the literature. It is generally found that creep deformation in polycrystalline alumina occurs by diffusional flow, with a stress exponent $n \sim 1$ and grain size exponents $p \sim 2$–3, which are indicative of Nabarro–Herring or Coble creep, for example, Folweiler (1961) and Cannon, Rhodes, and Heuer (1980). The former is typical of large-grained alumina ($d > 10\ \mu\text{m}$) while the latter is observed for finer grained materials. Ultra-fine-grained alumina ($d < 1\ \mu\text{m}$) exhibits stress exponents closer to $n \sim 2$, indicative of a GBS mechanism or interface-reaction-controlled creep, for example, Xue and Chen (1990). The rate-controlling process is Al^{3+} lattice diffusion for Nabarro–Herring creep ($Q_l\ [Al^{3+}] = 476\ \text{kJ mol}^{-1}$ (Paladino & Kingery, 1962) or $510\ \text{kJ mol}^{-1}$ (Legall, Lesage, & Bernardini, 1994)) as it is much faster than oxygen diffusion ($Q_l\ [O^{2-}] = 620$–$635\ \text{kJ mol}^{-1}$ (Oishi & Kingery, 1960; Prot & Monty, 1996)). In the case of creep accommodated by grain boundary diffusion, oxygen diffusion is usually rate controlling ($Q_{gb}\ [O^{2-}] = 460\ \text{kJ mol}^{-1}$ (Oishi & Kingery, 1960)). **Figure 6** shows the creep rates for hot-pressed alumina as a function of applied stress for temperatures ranging from 1000 to 1800 °C.

Several studies have shown that creep in alumina is very sensitive to even small concentrations of dopants or impurities. In particular, the addition of lanthanides such as Y or La has the effect of reducing the creep rate by one to two orders of magnitude when compared to undoped alumina (Cho, Harmer, Chan, Rickman, & Thompson, 1997; French et al., 1994; Lartigue-Korinek, Carry, & Priester, 2002; Li et al., 1999; Yoshida, Ikuhara, & Sakuma, 1999). It is generally believed that the effect of doping with isovalent ions is to inhibit grain boundary diffusion, increasing the apparent activation energy from 400–500 to 700–800 kJ mol^{-1}. Grain size-normalized tensile creep rates are shown in **Figure 7** as a function of reciprocal temperature for hot-pressed

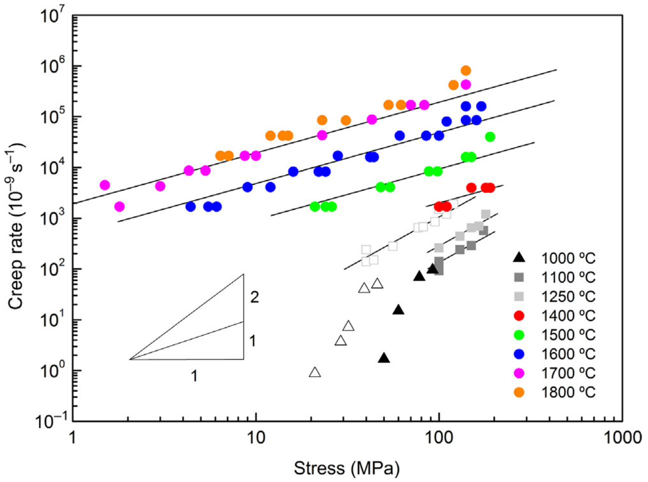

Figure 6 Creep rates of alumina in bending (solid symbols) and tension (hollow symbols) as a function of applied stress for different temperatures. Circles represent data from Folweiler (1961), squares from Ferber, Jenkins, Nolan, and Yeckley (1994) and triangles from Robertson, Wilkinson, and Caceres (1991).

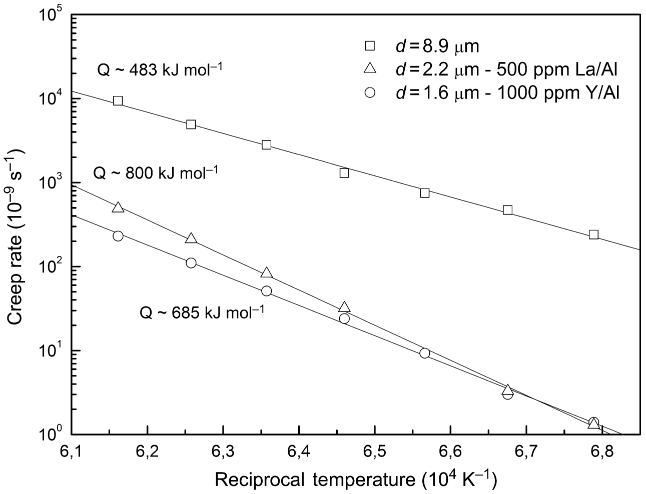

Figure 7 Grain size normalized tensile creep rates as a function of reciprocal temperature for hot-pressed alumina doped with Y and La, and comparison with undoped alumina. A decrease in creep rate as well as an increase in apparent activation energy is observed. Data are from Cho et al. (1997).

alumina doped with Y and La, as well as undoped alumina (Cho et al., 1997). A decrease in creep rate as well as an increase in apparent activation energy is observed, from 483 kJ mol^{-1} in pure alumina to 685 kJ mol^{-1} in alumina doped with 1000 ppm Y and to 800 kJ mol^{-1} in 500 ppm La-doped alumina. Similar results have been obtained by Yoshida, Ikuhara, and Sakuma (1998), who studied creep rates in alumina with 1 μm grain size doped with 0.045 mol.% of La_2O_3, Y_2O_3 and Lu_2O_3. They found that activation energy increases from 410 kJ mol^{-1} in undoped alumina to 810 kJ mol^{-1} when doped with La_2O_3, 830 kJ mol^{-1} when doped with Y_2O_3, and 780 kJ mol^{-1} if doped with Lu_2O_3.

Although fine-grained alumina exhibits a stress exponent typical of superplastic ceramics and fulfills the microstructural requirements for superplasticity, pure alumina shows very high boundary energy. This provides a high driving force for concurrent grain growth during creep leading to strain hardening and an increase in flow stress, but also makes the grain boundaries have relatively low cohesive strength, leading to cavitation and cracking during creep (Xue & Chen, 1990). It has been found that the addition of a second phase can inhibit grain growth during deformation, leading to superplastic behavior in alumina composites. For instance, Xue, Wu, and Chen (1991) found that the addition of 10% ZrO_2 in volume led to negligible grain growth during creep, and the material showed constant flow stress up to very high strains at strain rates of 10^{-4} s^{-1}. Several alumina composites have been studied for its superplastic properties, for example in Kim, Hiraga, Morita, and Sakka (2001), where it was found that the addition of 10 vol.% zirconia and 10 vol.% spinel leads to tensile strains of 850% at 5×10^{-4} s^{-1} and 1500 °C.

Small diameter, composite grade commercial alumina fibers have been developed since the 1970s and now find many uses in oxide–oxide ceramic matrix as well as metal–matrix composites. The most widely used are those from the Nextel family manufactured by 3M. Many fiber compositions exist with various amounts of SiO_2, although only two are considered suitable for composite production: Nextel 610, which is 99% pure alumina fiber, and Nextel 720, which is an alumina/mullite fiber. For ease of reading, their properties are summarized and compared in Section 2.11.3.3.

2.11.3.2 Zirconia Ceramics

ZrO_2 ceramics have been widely studied due to its good mechanical properties at high temperatures when it is stabilized in one of its high-temperature phases, either tetragonal or cubic. The most common oxides to stabilize zirconia are MgO, CaO, CeO_2 and Y_2O_3, the effect of the last being the most studied. The most interesting zirconia ceramics for technical applications are partially stabilized zirconia, which consists of a mixture of cubic and tetragonal phases and, especially, fully stabilized tetragonal zirconia polycrystal (TZP), which are nearly 100% tetragonal. TZP is interesting for thermomechanical applications because the tetragonal-monoclinic transformation in the presence of a stress field leads to a toughening mechanism due to the volume increase associated with the transformation, which is of a martensitic nature (Garvie, Hannink, & Pascoe, 1975;

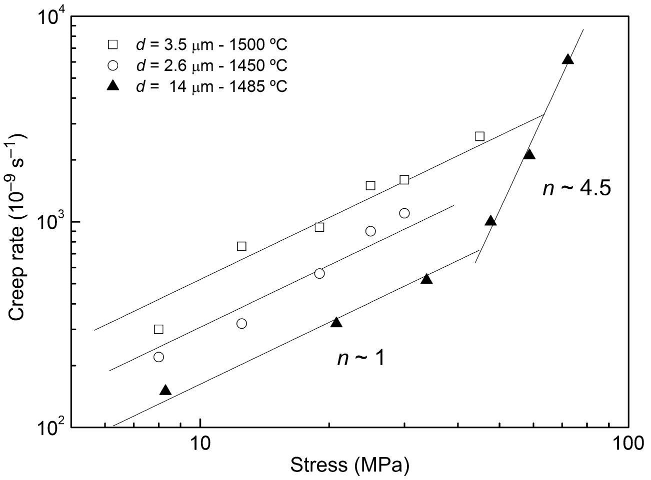

Figure 8 Creep in coarse-grained yttria-stabilized zirconia. Filled triangles are from Evans (1970) and hollow symbols from Dimos and Kohlstedt (1987).

Lange, 1982a, 1982b, 1982c, 1982d, 1982e). Ultrafine grains are required in TZP to avoid spontaneous tetragonal to monoclinic transformation, for which nucleation statistics are grain size-dependent (Chen, Chiao, & Tsuzaki, 1985), and this has led to the development of very fine-grained TZP materials that show superplastic behavior, as was first demonstrated by Wakai, Sakaguchi, and Matsuno (1986).

The first studies of creep in partially stabilized zirconia were due to Evans (1970), who studied 6 mol.% yttria- and Scandia-stabilized zirconia polycrystals of a nominal grain size of ~14 μm. A transition in stress exponent was found with stress, from $n \sim 1$ to ~ 3, which was attributed to a transition from diffusional to dislocation-controlled creep. A later study by Dimos and Kohlstedt (1987) on finer grained ($d \sim$ 2.6–9.5 μm), fully stabilized (25 mol.% Y_2O_3) cubic zirconia confirmed that creep occurs by diffusional flow; these authors obtained an activation energy of 550 kJ mol^{-1} and a stress exponent $n \sim 1$. Creep rates as a function of stress from both works are shown in **Figure 8**.

The fine-grained characteristics of TZP doped with small amounts of Y_2O_3 (Y-TZP) can be attributed to the segregation of dopant cations to the grain boundary, which lowers the grain boundary mobility and the grain boundary energy. This in turn both limits static grain growth, allowing fine-grained, fully dense Y-TZP ceramics to be obtained, as well as inhibits cavity nucleation during plastic deformation, fulfilling the two requirements for superplasticity. It is therefore no surprise that 3 mol% Y_2O_3-doped zirconia (Y-TZP) has become the universal choice to demonstrate superplastic deformation in ceramics (Chen & Xue, 1990). The first report of superplasticity in 3Y-TZP is due to Wakai et al. (1986), who were able to obtain tensile strains up to 160% at 1450 °C. They observed a stress exponent in the range of $n = 1.5$ at 1150 °C to $n = 1.9$ at 1450 °C and an activation energy of 573–590 kJ mol^{-1}. Later studies of Nieh, Mcnally, and Wadsworth (1988) on a nominally identical material showed a stress exponent of $n = 3$; this apparent discrepancy was attributed to the different purity of the starting powders used in those works. It is now accepted that creep behavior of Y-TZP depends on the impurity content of the material. For low-purity materials a stress exponent of $n \sim 2$ is observed over the entire stress range and a glassy intergranular film is present in the ceramic, while for high-purity Y-TZP, a change in stress exponent is observed, from $n = 2$ at high stresses to higher values of n at lower stresses. Moreover, the stress at which this transition occurs seems to depend on grain size. An example of this is shown in **Figure 9**, which contains data from Owen and Chokshi (1998).

Most of the data on creep of fine-grained 3Y-TZP has been successfully rationalized by Jimenez-Melendo and Dominguez-Rodriguez (2000), Jimenez-Melendo, Dominguez-Rodriguez, and Bravo-Leon (1998) and Dominguez-Rodriguez, Bravo-Leon, Ye, and Jimenez-Melendo (1998), who attribute the transitions in stress exponent as well as the disparities in measured activation energies to the presence of a threshold stress for creep similar to that observed for metals. They rationalized the data available in the literature by the empirical relationship

$$\dot{\epsilon} = 3 \cdot 10^{10} \frac{(\sigma - \sigma_0)^2}{Td^2} \exp\left(-\frac{460\ \text{kJ mol}^{-1}}{RT}\right) \tag{17}$$

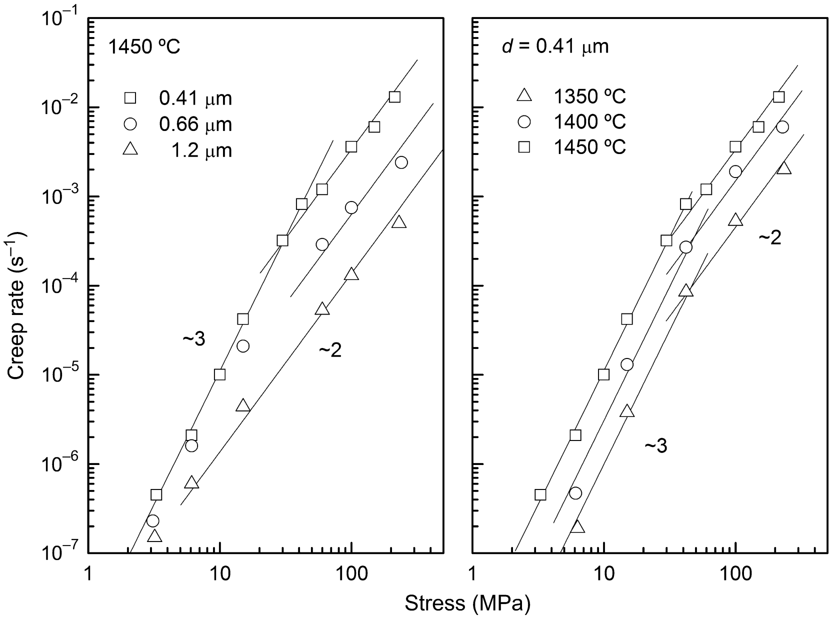

Figure 9 Creep rate of high-purity 3Y-TZP as a function of applied stress for different grain sizes and temperatures (Owen & Chokshi, 1998). A change in apparent stress exponent with stress can be seen. The "transition" stress depends on grain size but not on temperature.

where $\dot{\epsilon}$ is given in s^{-1}, σ in MPa, T in K and d in μm. The threshold stress σ_0 is given by

$$\sigma_0 = 5 \cdot 10^{-4} \frac{1}{d} \exp\left(\frac{120 \text{ kJ mol}^{-1}}{RT}\right) \tag{18}$$

It appears that this threshold stress is related to the segregation of dopants at the grain boundaries, which explains its dependence with the inverse of the grain size. While the existence of this threshold stress appears to rationalize the superplastic behavior of 3Y-TZP well, there is still ongoing debate regarding its physical origin.

2.11.3.3 Mullite Ceramics

Mullite ($3Al_2O_2 \cdot 2SiO_2$) is an interesting material for thermomechanical applications due to its low thermal expansion coefficient, low creep rate and high melting point. Creep of mullite has been studied in some detail for example by (de Arellano-Lopez et al., 2002; Dokko, Pask, & Mazdiyasni, 1977; Hynes & Doremus, 1991; Lessing, Gordon, & Mazdiyasni, 1975; Ohira, Ismail, Yamamoto, Akiba, & Somiya, 1996; Okamoto, Fukudome, Hayashi, & Nishikawa, 1990; Rhanim, Olagnon, Fantozzi, & Torrecillas, 1997), among others. Generally, the stress exponent is $n \sim 1$ for high-purity mullite, which indicates a diffusional mechanism for deformation, either Nabarro–Herring or Coble creep, although some authors have measured higher stress exponents and invoke a GBS mechanism. In bimodal microstructures formed by both equiaxed and elongated grains, cavitation and slow crack growth, probably due to unaccommodated GBS, have been observed at high stresses, leading to very high stress exponents in that range (Rhanim et al., 1997). Creep data obtained in bending by Okamoto et al. (1990) and Ohira et al. (1996) is plotted in **Figure 10**, showing a stress exponent slightly higher than one. With that data, a grain size exponent of $p \sim 2.5$ is obtained, which the authors attributed to simultaneous diffusion along the grain boundaries and the lattice of the grains. The range of activation energies vary considerably, changing from ~400 kJ mol^{-1} at temperatures up to 1600 °C to 700–800 kJ mol^{-1} at higher temperatures. These values agree reasonably well with the activation energy for interdiffusion in mullite (703 kJ mol^{-1} reported by Hynes and Doremus (1991)) and with oxygen diffusion, from a value of 397 kJ mol^{-1} reported by Ikuma et al. (1999) to 433 kJ mol^{-1} as obtained by Fielitz et al. (2001). **Figure 11** shows the data from Okamoto et al. (1990) and Rhanim et al. (1997).

When Y_2O_3 is added as a sintering aid, mullite is found to exhibit superplastic-like behavior, showing stress exponents close to two and a transition to one at higher stresses (>5 MPa) (de Arellano-Lopez et al., 2002).

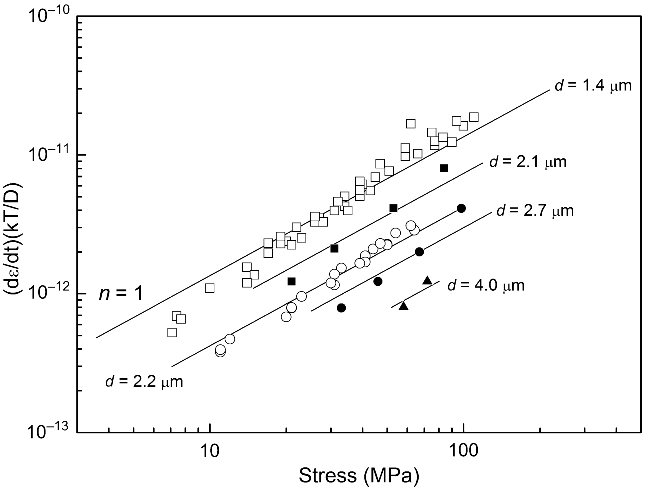

Figure 10 Temperature-compensated creep rate of high-purity mullite with different grain sizes as a function of applied stress. Hollow symbols are from Okamoto et al. (1990) while filled symbols are from Ohira et al. (1996).

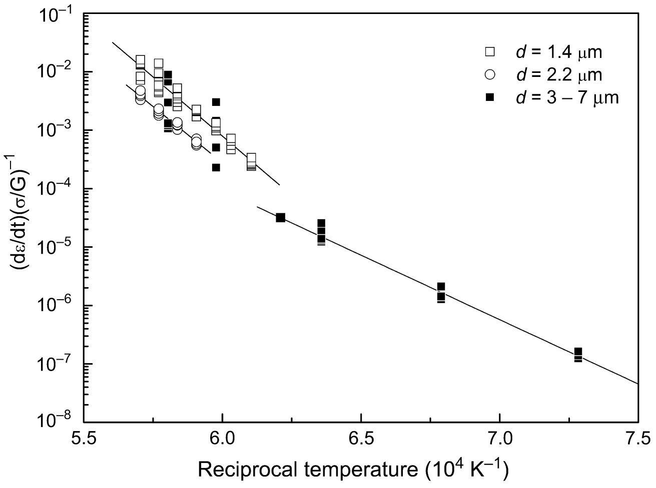

Figure 11 Stress-compensated creep rate of high-purity mullite with different grain sizes as a function of reciprocal temperature. Hollow symbols are from Okamoto et al. (1990) while filled symbols are from Rhanim et al. (1997). Activation energy changes from ~420 kJ mol^{-1} at low temperatures to ~737 kJ mol^{-1} at high temperatures.

The added Y_2O_3 forms a glassy phase in the grain boundaries and multigrain junctions that can be partially crystallized by heat treatment to form $Y_2Si_2O_7$. Although this has little effect on the creep rates, which are three orders of magnitude higher than that of high-purity mullite, when the grain boundary phase was crystallized extensive cavitation was observed and lower total strains could be attained before failure. Apparent activation energies were very high, in the range of 1000–2000 kJ mol^{-1}, and were not attributed to a rate-controlling process.

2.11.3.3.1 Small Diameter Oxide Fibers

The Nextel 610 and 720 fibers, developed and manufactured by 3M, are the most commonly used ceramic fibers in oxide–oxide ceramic matrix composites. Although the high-temperature capabilities of these materials are poorer than those of SiC-based composites, they are sometimes preferred due to their lower processing costs and higher stability in oxidizing atmospheres. Both types of fiber are obtained from a sol–gel route using aluminum carboxylates, and they differ in their composition: the 610 is an ~99% pure alumina fiber while the 720 contains 85 wt.% alumina and 15 wt.% silica, and is actually an alumina/mullite composite fiber.

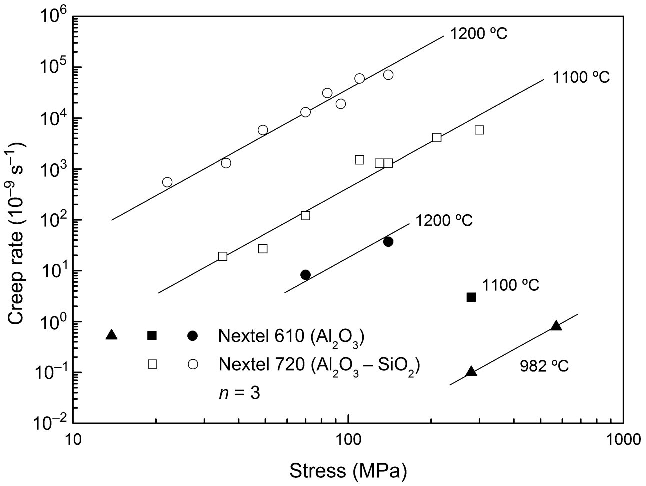

Figure 12 Creep rates of Nextel 610 and 720 fibers (Tompkins, 1995).

The Nextel 610 fiber contains 1.12 wt.% of impurities, 0.67 wt.% of Fe_2O_3 as a nucleating agent and 0.35 wt.% of silica as a grain growth inhibitor. These impurities are thought to reduce the creep resistance of Nextel 610 fiber, which shows a stress exponent of approximately 3 and an apparent activation energy around 660 kJ mol^{-1} between 1000 and 1200 °C. Failure occurs via the coalescence of cavities over the whole gauge length.

The Nextel 720 fiber is an alumina/mullite composite with a microstructure consisting of mosaic grains composed of fine mullite grains embedding elongated alumina grains. This microstructure is thought to give Nextel 720 a much better creep resistance, with creep rates two orders of magnitude lower than Nextel 610 (**Figure 12**).

2.11.3.4 Silicon Carbide Ceramics

Many commercial grades of silicon carbide ceramics have been developed and studied from 1990 to 2010 that fall into two main categories: sintered and reaction-bonded silicon carbide (RBSC). Because silicon carbide is a covalent material, bulk diffusion is too slow to achieve full density without sintering aids, and carbon and boron are used for this purpose. The role of carbon is to remove SiO_2 from the surface of the grains and convert it to silicon carbide, while the role of boron is not fully clear, although it is thought to affect grain boundary energy. After sintering at temperatures >2000 °C, a dense α-SiC with an equiaxed microstructure is obtained, such as Hexoloy-SA produced by Carborundum (now Saint Gobain). At lower temperatures, dense SiC/Si materials can be obtained by partially sintering a powder compact of α-SiC with carbon and then infiltrating it with molten silicon, which reacts partially with the carbon to form β-SiC. The volume fraction of SiC ranges from about 67% to about 92%, and this material is termed RBSC. Commercial grades of RBSC are SCRB210 (Coors, Golden, CO, 18% volume fraction Si) and KX01 (Carborundum, Niagara Falls, NY, 33% volume fraction Si) (Wiederhorn, Hockey, & French, 1999). In both cases contact areas between the SiC grains are small and creep is controlled by deformation of the residual silicon (Hockey & Wiederhorn, 1992).

The creep rates of several grades of silicon carbide as a function of temperature are plotted in **Figure 13**. Data obtained in compression for sintered SiC (Lane, Carter, & Davis, 1988) show a change in activation energy that was attributed to a transition in deformation mechanism with temperature, from GBS accommodated by grain boundary diffusion and low dislocation activity, to GBS accommodated by bulk diffusion and high dislocation activity. They observed stress exponents in the range of ~1.5 which are consistent with a GBS mechanism. For comparison, tensile creep data of three RBSC commercial materials are included (Tressler & McNallan, 1989).

In RBSC, as in other ceramics with a secondary bonding phase (such as Si_3N_4, see next section), differences between tensile and compressive creep are often observed. We summarize the results of Wiederhorn, Roberts, and Chuang (1988) for KX01, a siliconized SiC ceramic produced by Sohio Corp. containing 33 vol.% silicon. Their results, which are plotted in **Figure 14**, can be described by a power law with two different stress exponents, $n \sim 3.5$ at low stresses and $n > 10$ at high stresses. At the low-stress region, creep is attributed to a lattice

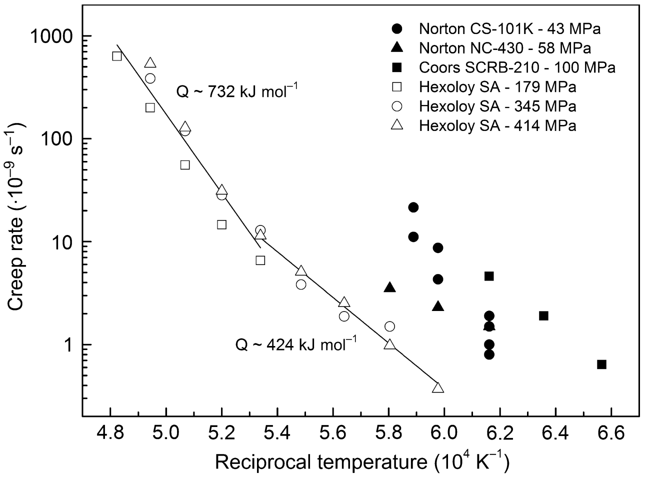

Figure 13 Creep of SiC as a function of temperature. Filled symbols correspond to a sintered α-SiC (Hexoloy) tested in compression and represent data from Lane et al. (1988). Hollow symbols correspond to RBSC commercial materials tested in tension (Tressler & McNallan, 1989).

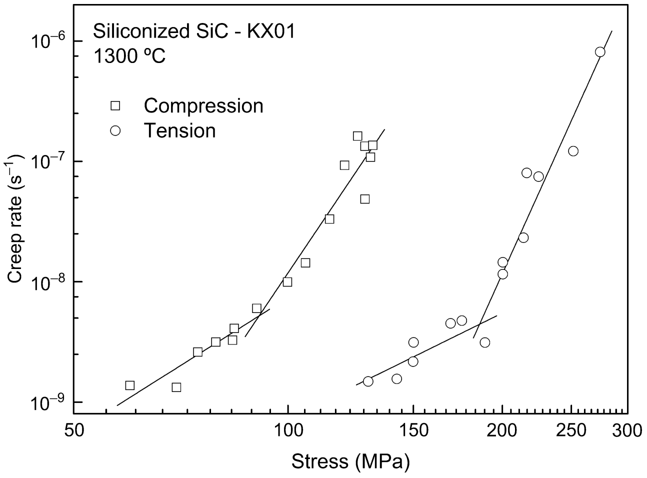

Figure 14 Comparison of tensile and compressive creep in KX01 reaction-bonded SiC (Wiederhorn et al., 1988).

mechanism involving dislocations, although these were only observed at the contact regions between the SiC grains, while no physical explanation was given for the very high values of *n* at high stresses. Up to three orders of magnitude difference in creep rates were observed between results obtained in tension and compression, which were attributed to extensive cavitation observed in the tensile specimens, while the compressive specimens had no cavities; this led authors to conclude that the high-stress exponents could not be attributed to a creep mechanism involving cavitation. They indicate that friction between SiC grains could modify the stress state of the silicon phase affecting creep properties, and concluded that deformation is produced by motion of SiC clusters with limited deformation of the grains in the contact areas.

Reaction-formed SiC (RFSC) (Chiang, Messner, Terwilliger, & Behrendt, 1991) is another type of siliconized silicon carbide material that is obtained by melt infiltration of porous carbon preforms with silicon: reaction of carbon and silicon produces β-SiC forming a continuous network with some residual silicon distributed along channels where the pores in the carbon preform were initially. Martinez-Fernandez et al. (2003) studied creep in RFSC and observed that no steady state was reached even for stresses higher than 600 MPa at 1350 °C. Instead, strain rate decreased as strain increased. Differences in the rate of deceleration in RFSC materials with different silicon content allowed the authors to attribute this saturation effect to viscous flow of the silicon phase, which was confirmed by microstructural observations of silicon depletion in the crept specimens.

2.11.3.4.1 Small Diameter Silicon Carbide Fibers

SiC/SiC ceramic matrix composites have been studied in detail for a range of high-temperature structural applications, and it has been shown that they exhibit a matrix damage mechanism that determines their primary creep behavior but that secondary creep (if at all present) and maximum strain at fracture are controlled by the creep properties of the fibers. For a detailed analysis, the reader is referred to Section 2.07.6 of Chapter 2.07 in this volume.

Many SiC fibers have been developed for use as building blocks in ceramic–matrix composite materials, with the goal of obtaining high creep and oxidation resistance. Small diameter ($\sim 10\ \mu m$) fibers are prepared by melt spinning, cross-linking and pyrolysis of an organosilicon polymer, most commonly polycarbosilane, polytitanocarbosilane, or polyaluminocarbosilane; several reviews of the processing and properties of precursor-derived SiC fibers exist, for example, Bunsell and Berger (2000) and Ishikawa (2005). In the first generation of fibers, the polymer was cross-linked by heating in air, which introduced oxygen that remained during the subsequent pyrolysis process, which involves heating in an inert atmosphere at around 1200 °C. Examples of this generation of fibers are Nicalon, produced by Nippon Carbon, and Tyranno-LoxM (containing Ti) and Tyranno-ZMI (containing Zr) by Ube Industries. These fibers have an oxygen content of $\sim$8–12 wt.% and a large amount of residual carbon surrounding the small SiC grains ($\sim$10 nm); their microstructural stability is limited, which results in a loss of mechanical properties at high temperatures. Figure 15 shows the room-temperature tensile strength of several SiC fibers after exposing them to high temperatures for 1 h in an Ar atmosphere; both Nicalon and Tyranno-LoxM exhibit a marked loss of tensile strength after annealing at temperatures of 1300 °C or higher. The second generation of SiC fibers was produced by cross-linking the polymer precursor by electron irradiation to avoid the introduction of oxygen at this stage. Examples are Hi-Nicalon fibers, which show better strength retention and higher Young's modulus. Although they show lower oxygen content, significant free carbon still exists in these fibers, which limits their creep resistance and oxidative stability. A significant effort was made for the third generation of SiC fibers, which are near stoichiometric and use higher pyrolysis temperatures, which results in larger grain sizes, higher crystallinity and the development of a sintered microstructure. Examples of these fibers are Hi-Nicalon S, Tyranno-SA and Sylramic, manufactured by Dow Corning. Hi-Nicalon S is obtained from polycarbosilane, like previous generations, which is cross-linked by electron irradiation and pyrolyzed at temperatures in excess of 1500 °C in carefully controlled atmospheres. In Tyranno-SA, a polyaluminocarbosilane precursor is cured by oxidation, and pyrolyzed in two stages, first at 1300 °C to produce an oxygen-rich fiber, and then at up to 1800 °C to allow the outgassing of CO and sintering. The aluminum present in the precursor doubles as

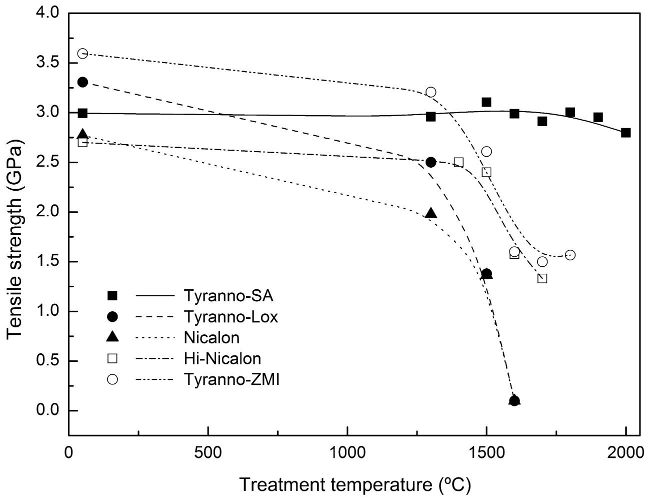

Figure 15 Room-temperature tensile strength of different SiC fibers after exposing them to high temperatures for 1 h in Ar atmosphere. Adapted from Ishikawa (2005).

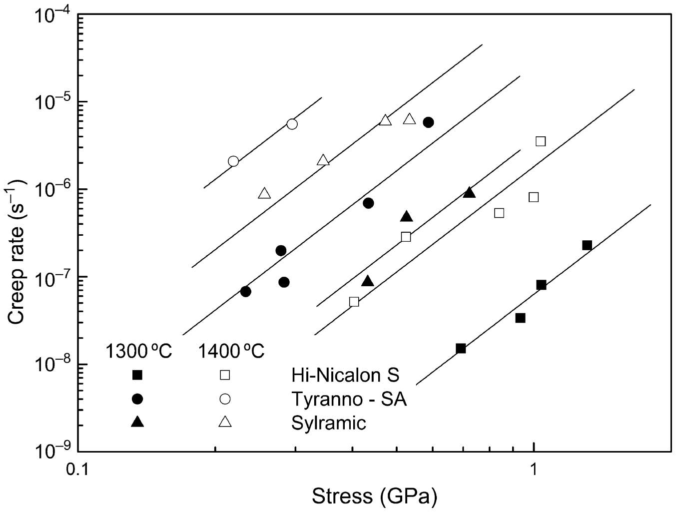

Figure 16 Creep rates as a function of stress at 1300 and 1400 °C for three near-stoichiometric SiC fibers. Adapted from Ishikawa (2005).

both a sintering aid and to enhance corrosion resistance of the fiber against alkaline contaminants. The resulting fiber shows large SiC grains (~200 nm) with some free carbon still present in the fiber core. In Sylramic, a polytitanocarbosilane precursor is oxygen-cured and doped by chemical vapor infiltration with boron as a sintering aid, and later pyrolyzed at 1600 °C to obtain a near-stoichiometric fiber with large SiC grains (~100–200 nm) and smaller grains of TiB_2 and B_4C. Near-stoichiometric fibers show excellent creep resistance as seen in **Figure 16**. Hi-Nicalon S shows the higher creep resistance, a result of the electron curing process that gives the lowest oxygen content, at the penalty of higher processing costs, while the sintering aids in Tyranno-SA and Sylramic increase the creep rate of these fibers by enhancing diffusion rates at the grain boundaries.

2.11.3.5 Silicon Nitride Ceramics

Creep in silicon nitride has been extensively studied, and a critical review exists for data published until 2004 (Melendez-Martinez & Dominguez-Rodriguez, 2004). Due to its covalent nature, it is nearly impossible to obtain fully dense silicon nitride ceramics without sintering aids, and most of these materials are densified with the addition of secondary phases (most commonly Y_2O_3, MgO and Al_2O_3) in which silicon nitride is totally or partially soluble and which form a glass with the SiO_2 on the powder surface at sintering temperatures. Densification thus occurs via a solution-precipitation process via the liquid phase, and the result is a biphasic material of silicon nitride grains more or less surrounded by a secondary phase that is normally glassy but can be partially devitrified. As in the case of siliconized silicon carbide, both the microstructure and the creep behavior of silicon nitride is affected by the nature and amount of this secondary phase, which manifests itself, among other things, in a marked tendency to cavitation and in differences in creep behavior when tested in tension or compression.

Although viscous flow creep due to redistribution of the secondary phase is transient in nature, it can account for some of the measured strain and, as was shown in Section 2.11.2.3, the strain at which this transient effect saturates in tension is approximately twice of that in compression. In any case, an additional mechanism able to produce steady-state creep must be active, and the solution-precipitation model of Raj (Section 2.11.2.4) is commonly invoked. This is characterized by a stress exponent of $n=1$ which is commonly observed in compression (**Figure 17**) although higher values have been sometimes observed. Activation energies range between 412 kJ mol^{-1} (Backhaus-Ricoult, Eveno, Castaing, & Kleebe, 1995) and 770 kJ mol^{-1} (Bernardgranger, Crampon, Duclos, & Cales, 1997), which can be attributed to a variety of activation energies of solution or diffusion; in silicon nitride, several deformation mechanisms are simultaneously active and it is difficult to identify the rate-controlling process (Melendez-Martinez & Dominguez-Rodriguez, 2004).

In tension, the picture is very different as it is accepted that formation of cavities amounts for most of the observed strain. If Eqn (1) is used to fit the experimental data, very high values of n, which increase with

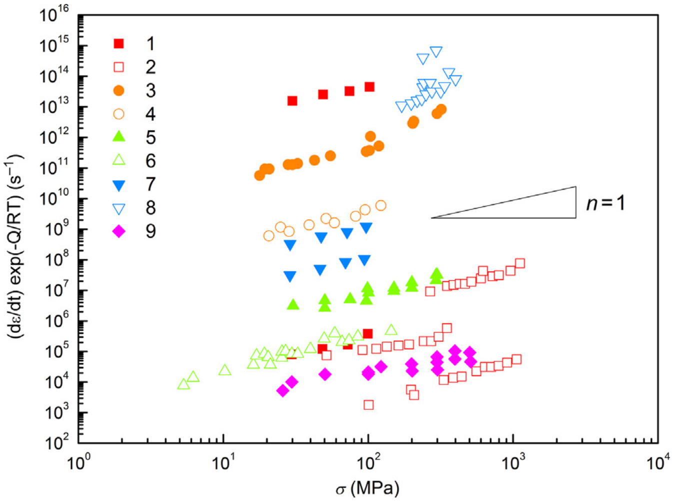

Figure 17 Compressive creep of silicon nitride ceramics, adapted from Melendez-Martinez and Dominguez-Rodriguez (2004). Data presented are from 1, Yoon, Akatsu, and Yasuda (1996); 2, Backhaus-Ricoult et al. (1995); 3, Boling-Risser, Goretta, Routbort, and Faber (2000); 4, Xie, Mitomo, and Zhan (2000); 5, Yoon et al. (2000); 6, Zhan, Mitomo, Ikuhara, and Sakuma (2000); 7, Yoon, Akatsu, and Yasuda (1997); 8, Birch and Wilshire (1978); 9, Wereszczak et al. (1999).

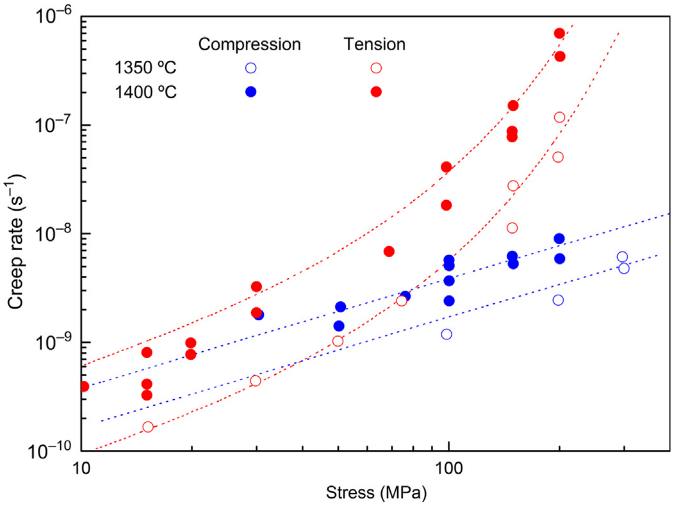

Figure 18 Differences between compressive creep in tension and compression for silicon nitride (Yoon et al., 2000).

applied stress, are observed. At low stresses, however, a stress exponent of one is often recovered and tensile creep resistance approaches that measured in compression. Data from Yoon, Wiederhorn, and Luecke (2000) for SN88 silicon nitride manufactured by NGK insulators is plotted in **Figure 18** and illustrates this effect. According to Luecke and Wiederhorn (1999), strain rate is related with the stress by an exponential relationship:

$$\dot{\epsilon} \propto \sigma \exp(\alpha\sigma) \tag{19}$$

where α is related to the stress required to cavitate the intergranular silicate phase and depends on temperature. These authors found that such a cavitation creep mechanism, acting in parallel to solution-precipitation as in compression, could rationalize the differences between tension and compression and why these approach each other at low stresses (**Figure 19**).

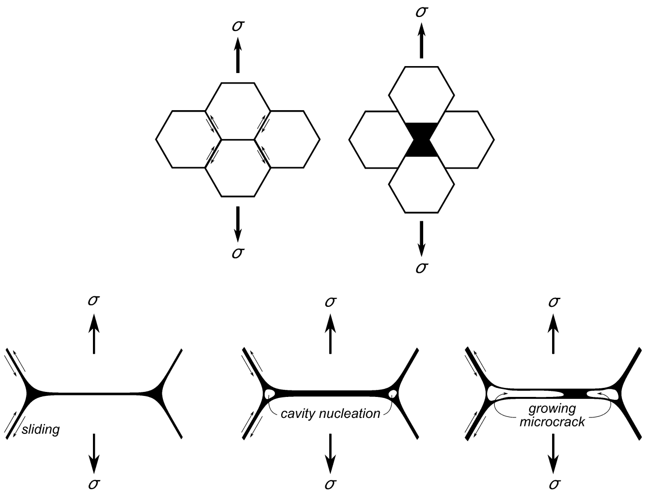

Figure 19 Examples of creep damage that can lead to fracture at high temperatures. Top: Cavitation produced by unaccommodated grain boundary sliding in "pure" ceramics. Bottom: cavitation at glassy intragranular pockets in ceramics containing vitreous phases. Adapted from Tsai and Raj (1982).

2.11.4 Creep Rupture of Ceramics

As it was shown, creep might produce nucleation of microstructural defects such as voids or cavities at multigrain junctions that can have a profound impact on high-temperature fracture. These defects can grow and coalesce until a crack is formed that is large enough to propagate catastrophically, or can form microcracks that then grow subcritically by means of cavitation ahead of the crack tip. In any case, fracture of ceramics at high temperatures is normally controlled by flaws different from those responsible for fracture at low temperatures. Chan and Page (1993) have reviewed creep damage by distinguishing among two classes of polycrystalline ceramics: single phase materials with "clean" boundaries free of glassy phase, and ceramics with a secondary bonding phase, either glassy or crystalline, that is the result of the addition of sintering additives (i.e. liquid-bonded or reaction-bonded ceramics). In the case of pure ceramics with clean boundaries, cavitation can be the result of unaccommodated GBS, while in vitreous bonded ceramics or materials containing small amounts of vitreous phase cavities appear at multigrain junctions that are subjected to negative pressures when the grains slide past each other (Tsai & Raj, 1982). As it would be expected from such mechanisms, creep fracture in "pure" ceramics clean of glassy phases is normally dominated by nucleation of cavities, while in ceramics with a secondary phase growth and coalescence of such defects dominate.

Creep leads to time-dependent slow crack growth phenomena similar to the environmentally assisted subcritical growth often observed in ceramics and specially glasses and room temperature, and this means that at high temperatures, ceramics can fracture at stresses much lower than the tensile strength if load is applied for long enough time. Usually creep-crack growth in ceramics at stress intensity factors much lower than K_{IC} is governed by a power law that relates crack growth velocity with applied stress intensity by

$$v = AK_I^N \tag{20}$$

Prediction of lifetime under creep-fracture conditions is usually done by the Monkman-Grant projection technique (Monkman & Grant, 1956), which assumes that fracture occurs after a certain amount of strain which is a material parameter that depends on temperature:

$$t_f = C\dot{\epsilon}^{-M} \tag{21}$$

The parameter M is often found to be unity. Experimental determinations of creep fracture are often performed at constant stress in static fatigue experiments; in those cases a relationship similar to the one above exists for time to fracture and applied stress:

$$t_f = D\dot{\epsilon}^{-S} \tag{22}$$

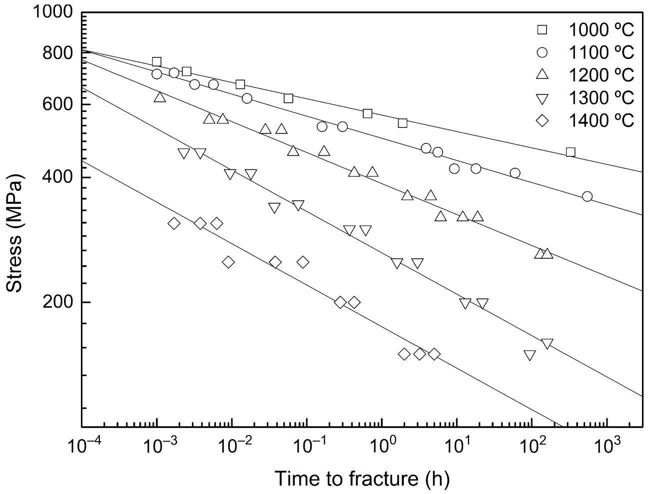

Figure 20 Creep rupture of hot-pressed silicon nitride (Norton NC132) in four-point bending showing the log–log relation between applied stress and lifetime, for different temperatures. Adapted from Quinn (1990).

Now *D* and *S* are temperature dependent and *S* must be related to both *M* and the creep parameters of the material. An example of this behavior is presented in **Figure 20**, where applied stress in four-point bending static fatigue is plotted as a function of lifetime, for different temperatures in a commercial grade hot-pressed silicon nitride (Norton NC312). Changes in fracture mechanisms and/or creep parameters will lead to different values of the parameters in the Monkman-Grant approach and this leads to the concept of fracture mechanism maps that identifies regions of different fracture mechanisms in a stress vs temperature plots (Quinn & Braue, 1990).

2.11.5 Concluding Remarks

As it has been shown, creep in ceramics is a complex process that involves the creation and interaction of at least one, but often more, types of defect (vacancies, dislocations, precipitates, grain boundaries…) and is thus highly dependent on the microstructure of the material. Although most of the theories for creep presented here are widely accepted, in some cases they are introduced *ad-hoc* based on empirical observation and lack an underlying theoretical framework. This is especially notorious in the case of superplasticity, where no comprehensive theory exists even for seemingly simple ceramic systems such as TZP. It is clear that more work is needed in this direction.

Efforts to obtain ceramics with higher creep resistance have focused on two approaches. The first one is based on reducing or eliminating the use of sintering aids that promote the formation of vitreous films at the grain boundaries: Techniques such as microwave-assisted of spark-plasma sintering allow for fast, very high-temperature densification of powders requiring fewer additives. Another possibility is to use directional solidification techniques to eliminate the grain boundaries altogether: in this case the ceramic is grown from the melt resulting in ceramic composites with clean interphases and no grain boundaries (Llorca & Orera, 2006).

The second approach consists of novel compositions with higher melting point and therefore higher intrinsic creep resistance: it is the case of the so-called ultra high temperature ceramics (UHTC), normally composites of rare earth borides (ZrB_2 and HfB_2) and SiC to enhance their oxidation resistance and sinterability (Chamberlain, Fahrenholtz, Hilmas, & Ellerby, 2004; Levine et al., 2002). The possibility of obtaining UHTCs of controlled microstructure has been opened again by the development of novel sintering techniques such as those described above. Currently, however, there is a lack of data on creep properties of these materials due to the high temperatures at which they need to be tested.

References

de Arellano-Lopez, A. R., Melendez-Martinez, J. J., Cruse, T. A., Koritala, R. E., Routbort, J. L., & Goretta, K. C. (2002). Compressive creep of mullite containing Y_2O_3. *Acta Materialia, 50*, 4325–4338.

Arzt, E., Ashby, M. F., & Verrall, R. A. (1983). Interface controlled diffusional creep. *Acta Metallurgica, 31*, 1977–1989.

Ashby, M. F. (1969). On interface-reaction control of Nabarro-Herring creep and sintering. *Scripta Metallurgica, 3*, 837–842.

Ashby, M. F., & Verrall, R. A. (1973). Diffusion-accommodated flow and superplasticity. *Acta Metallurgica, 21*, 149–163.

Backhaus-Ricoult, M., Eveno, P., Castaing, J., & Kleebe, H. J. (1995). High temperature creep behavior of high purity hot-pressed silicon nitride. In R. C. Bradt, C. A. Brookes, & J. L. Routbort (Eds.), *Plastic deformation of ceramics*. New York: Plenum Press.

Bernardgranger, G., Crampon, J., Duclos, R., & Cales, B. (1997). High temperature creep behaviour of beta'-Si3N4/alpha-YSiAlON ceramics. *Journal of the European Ceramic Society, 17*, 1647–1654.

Birch, J. M., & Wilshire, B. (1978). Compression creep-behavior of silicon-nitride ceramics. *Journal of Materials Science, 13*, 2627–2636.

Boling-Risser, M. A., Goretta, K. C., Routbort, J. L., & Faber, K. T. (2000). Effect of microstructure on high-temperature compressive creep of self-reinforced hot-pressed silicon nitride. *Journal of the American Ceramic Society, 83*, 3065–3069.

Bunsell, A. R., & Berger, M. H. (2000). Fine diameter ceramic fibres. *Journal of the European Ceramic Society, 20*, 2249–2260.

Burton, B. (1972). Interface reaction controlled diffusional creep – consideration of grain-boundary dislocation climb sources. *Materials Science and Engineering, 10*, 9–14.

Cannon, W. R., & Langdon, T. G. (1983). Creep of ceramics I. Mechanical characteristics. *Journal of Materials Science, 18*, 1–50.

Cannon, W. R., & Langdon, T. G. (1988). Creep of ceramics II. An examination of flow mechanisms. *Journal of Materials Science, 23*, 1–20.

Cannon, R. M., Rhodes, W. H., & Heuer, A. H. (1980). Plastic-deformation of fine-grained alumina (Al_2O_3). 1. Interface-controlled diffusional creep. *Journal of the American Ceramic Society, 63*, 46–53.

Chamberlain, A. L., Fahrenholtz, W. G., Hilmas, G. E., & Ellerby, D. T. (2004). High-strength zirconium diboride-based ceramics. *Journal of the American Ceramic Society, 87*, 1170–1172.

Chan, K. S., & Page, R. A. (1993). Creep damage development in structural ceramics. *Journal of the American Ceramic Society, 76*, 803–826.

Chen, I. W., Chiao, Y. H., & Tsuzaki, K. (1985). Statistics of martensitic nucleation. *Acta Metallurgica, 33*, 1847–1859.

Chen, I. W., & Xue, L. A. (1990). Development of superplastic structural ceramics. *Journal of the American Ceramic Society, 73*, 2585–2609.

Chiang, Y. M., Messner, R. P., Terwilliger, C. D., & Behrendt, D. R. (1991). Reaction-formed silicon-carbide. *Materials Science and Engineering. A. Structural Materials Properties Microstructure and Processing, 144*, 63–74.

Cho, J. H., Harmer, M. P., Chan, H. M., Rickman, J. M., & Thompson, A. M. (1997). Effect of yttrium and lanthanum on the tensile creep behavior of aluminum oxide. *Journal of the American Ceramic Society, 80*, 1013–1017.

Chokshi, A. H., & Langdon, T. G. (1991). Characteristics of creep deformation in ceramics. *Materials Science and Technology, 7*, 577–584.

Chokshi, A. H., Mukherjee, A. K., & Langdon, T. G. (1993). Superplasticity in advanced materials. *Materials Science & Engineering R-Reports, 10*, 237–274.

Coble, R. L. (1963). A model for boundary diffusion controlled creep in polycrystalline materials. *Journal of Applied Physics, 34*, 1679–1682.

Dimos, D., & Kohlstedt, D. L. (1987). Diffusional creep and kinetic demixing in yttria-stabilized zirconia. *Journal of the American Ceramic Society, 70*, 531–536.

Dokko, P. C., Pask, J. A., & Mazdiyasni, K. S. (1977). High-temperature mechanical-properties of mullite under compression. *Journal of the American Ceramic Society, 60*, 150–155.

Dominguez-Rodriguez, A., Bravo-Leon, A., Ye, J. D., & Jimenez-Melendo, M. (1998). Grain size and temperature dependence of the threshold stress for superplastic deformation in yttria-stabilized zirconia polycrystals. *Materials Science and Engineering. A. Structural Materials Properties Microstructure and Processing, 247*, 97–101.

Dryden, J. R. (2000). On the creep in ceramics due to a viscous grain boundary phase. *Journal of the Mechanics and Physics of Solids, 48*, 2115–2135.

Dryden, J. R., Kucerovsky, D., Wilkinson, D. S., & Watt, D. F. (1989). Creep deformation due to a viscous grain-boundary phase. *Acta Metallurgica, 37*, 2007–2015.

Dryden, J. R., & Wilkinson, D. S. (1997). Three-dimensional analysis of the creep due to a viscous grain boundary phase. *Acta Materialia, 45*, 1259–1273.

Evans, P. E. (1970). Creep in yttria-stabilized and scandia-stabilized zirconia. *Journal of the American Ceramic Society, 53*, 365–369.

Ferber, M. K., Jenkins, M. G., Nolan, T. A., & Yeckley, R. L. (1994). Comparison of the creep and creep-rupture performance of 2 hiped silicon-nitride ceramics. *Journal of the American Ceramic Society, 77*, 657–665.

Fielitz, P., Borchardt, G., Schneider, H., Schmucker, M., Wiedenbeck, M., & Rhede, D. (2001). Self-diffusion of oxygen in mullite. *Journal of the European Ceramic Society, 21*, 2577–2582.

Folweiler, R. (1961). Creep behavior of pore-free polycrystalline aluminum oxide. *Journal of Applied Physics, 32*, 773–778.

French, J. D., Zhao, J. H., Harmer, M. P., Chan, H. M., & Miller, G. A. (1994). Creep of duplex microstructures. *Journal of the American Ceramic Society, 77*, 2857–2865.

Garvie, R. C., Hannink, R. H., & Pascoe, R. T. (1975). Ceramic steel. *Nature, 258*, 703–704.

Gifkins, R. C. (1976). Grain-boundary sliding and its accommodation during creep and superplasticity. *Metallurgical Transactions. A. Physical Metallurgy and Materials Science, 7*, 1225–1232.

Gordon, R. S. (1973). Mass-transport in diffusional creep of ionic solids. *Journal of the American Ceramic Society, 56*, 147–152.

Greenwood, G. W. (1970). The possible effects on diffusion creep of some limitation of grain boundaries as vacancy sources or sinks. *Scripta Metallurgica, 4*, 171–173.

Herring, C. (1950). Diffusional viscosity of a polycrystalline solid. *Journal of Applied Physics, 21*, 437–445.

Hockey, B. J., & Wiederhorn, S. M. (1992). Effect of microstructure on the creep of siliconized silicon-carbide. *Journal of the American Ceramic Society, 75*, 1822–1830.

Hynes, A. P., & Doremus, R. H. (1991). High-temperature compressive creep of polycrystalline mullite. *Journal of the American Ceramic Society, 74*, 2469–2475.

Ikuma, Y., Shimada, E., Sakano, S., Oishi, M., Yokoyama, M., & Nakagawa, Z. E. (1999). Oxygen self-diffusion in cylindrical single-crystal mullite. *Journal of the Electrochemical Society, 146*, 4672–4675.

Ishikawa, T. (2005). Advances in inorganic fibers. *Advances in Polymer Science, 178*, 109–144.

Jimenez-Melendo, M., & Dominguez-Rodriguez, A. (2000). High temperature mechanical characteristics of superplastic yttria-stabilized zirconia. An examination of the flow process. *Acta Materialia, 48*, 3201–3210.

Jimenez-Melendo, M., Dominguez-Rodriguez, A., & Bravo-Leon, A. (1998). Superplastic flow of fine-grained yttria-stabilized zirconia polycrystals: constitutive equation and deformation mechanisms. *Journal of the American Ceramic Society, 81*, 2761–2776.

Kim, B. N., Hiraga, K., Morita, K., & Sakka, Y. (2001). Superplasticity in alumina enhanced by co-dispersion of 10% zirconia and 10% spinel particles. *Acta Materialia, 49*, 887–895.

Lane, J. E., Carter, C. H., & Davis, R. F. (1988). Kinetics and mechanisms of high-temperature creep in silicon-carbide. 3. Sintered alpha-silicon carbide. *Journal of the American Ceramic Society, 71*, 281–295.

Langdon, T. G. (1991). The physics of superplastic deformation. *Materials Science and Engineering: A-Structural Materials Properties Microstructure and Processing, 137*, 1–11.

Lange, F. F. (1982a). Transformation toughening. 1. Size effects associated with the thermodynamics of constrained transformations. *Journal of Materials Science, 17*, 225–234.

Lange, F. F. (1982b). Transformation toughening. 2. Contribution to fracture-toughness. *Journal of Materials Science, 17*, 235–239.

Lange, F. F. (1982c). Transformation toughening. 3. Experimental-observations in the ZrO_2–Y_2O_3 system. *Journal of Materials Science, 17*, 240–246.

Lange, F. F. (1982d). Transformation toughening. 4. Fabrication, fracture-toughness and strength of Al_2O_3–ZrO_2 composites. *Journal of Materials Science, 17*, 247–254.

Lange, F. F. (1982e). Transformation toughening. 5. Effect of temperature and alloy on fracture-toughness. *Journal of Materials Science, 17*, 255–262.

Lartigue-Korinek, S., Carry, C., & Priester, L. (2002). Multiscale aspects of the influence of yttrium on microstructure, sintering and creep of alumina. *Journal of the European Ceramic Society, 22*, 1525–1541.

Legall, M., Lesage, B., & Bernardini, J. (1994). Self-diffusion in alpha-Al_2O_3. 1. Aluminum diffusion in single-crystals. *Philosophical Magazine. A. Physics of Condensed Matter Structure Defects and Mechanical Properties, 70*, 761–773.

Lessing, P. A., Gordon, R. S., & Mazdiyasni, K. S. (1975). Creep of polycrystalline mullite. *Journal of the American Ceramic Society, 58*, 149.

Levine, S. R., Opila, E. J., Halbig, M. C., Kiser, J. D., Singh, M., & Salem, J. A. (2002). Evaluation of ultra-high temperature ceramics for aeropropulsion use. *Journal of the European Ceramic Society, 22*, 2757–2767.

Lifshitz, I. M. (1963). On the theory of diffusion-viscous flow of polycrystalline bodies. *Soviet Physics Jetp-Ussr, 17*, 909–920.

Li, Y. Z., Wang, C. M., Chan, H. M., Rickman, J. M., Harmer, M. P., Chabala, J. M., et al. (1999). Codoping of alumina to enhance creep resistance. *Journal of the American Ceramic Society, 82*, 1497–1504.

Llorca, J., & Orera, V. M. (2006). Directionally solidified eutectic ceramic oxides. *Progress in Materials Science, 51*, 711–809.

Luecke, W. E., & Wiederhorn, S. M. (1999). A new model for tensile creep of silicon nitride. *Journal of the American Ceramic Society, 82*, 2769–2778.

Maehara, Y., & Langdon, T. G. (1990). Superplasticity in ceramics. *Journal of Materials Science, 25*, 2275–2286.

Martinez-Fernandez, J., Munoz, A., Lopez, A. R. D., Feria, F. M. V., Dominguez-Rodriguez, A., & Singh, M. (2003). Microstructure-mechanical properties correlation in siliconized silicon carbide ceramics. *Acta Materialia, 51*, 3259–3275.

Melendez-Martinez, J. J., & Dominguez-Rodriguez, A. (2004). Creep of silicon nitride. *Progress in Materials Science, 49*, 19–107.

Monkman, F. C., & Grant, N. J. (1956). An empirical relationship between rupture life and minimum creep rate in creep-rupture tests. *Proceedings of the ASTM, 56*, 593.

Mukherjee, A. K., Bird, J. E., & Dorn, J. E. (1969). Experimental correlations for high-temperature creep. *ASM Transactions Quarterly, 62*, 155–179.

Nabarro, F. R. N. (1948). *Deformation of crystals by the motion of single ions*. Report of a Conference on Strength of Solids. Bristol: The Physical Society.

Nabarro, F. R. N. (1967). Steady-state diffusional creep. *Philosophical Magazine, 16*, 231–237.

Nieh, T. G., Mcnally, C. M., & Wadsworth, J. (1988). Superplastic properties of a fine-grained yttria-stabilized tetragonal polycrystal of zirconia. *Scripta Metallurgica, 22*, 1297–1300.

Ohira, H., Ismail, M. G. M. U., Yamamoto, Y., Akiba, T., & Somiya, S. (1996). Mechanical properties of high purity mullite at elevated temperatures. *Journal of the European Ceramic Society, 16*, 225–229.

Oishi, Y., & Kingery, W. D. (1960). Self-diffusion of oxygen in single crystal and polycrystalline aluminum oxide. *Journal of Chemical Physics, 33*, 480–486.

Okamoto, Y., Fukudome, H., Hayashi, K., & Nishikawa, T. (1990). Creep deformation of polycrystalline mullite. *Journal of the European Ceramic Society, 6*, 161–168.

Owen, D. M., & Chokshi, A. H. (1998). The high temperature mechanical characteristics of superplastic 3 mol% yttria stabilized zirconia. *Acta Materialia, 46*, 667–679.

Paladino, A. E., & Kingery, W. D. (1962). Aluminum ion diffusion in aluminum oxide. *Journal of Chemical Physics, 37*, 957–962.

Poirier, J. P. (1985). *Creep of crystals: High-temperature deformation processes in metals, ceramics and minerals.* Cambridge: Cambridge University Press.

Prot, D., & Monty, C. (1996). Self-diffusion in alpha-Al_2O_3. 2. Oxygen diffusion in 'undoped' single crystals. *Philosophical Magazine. A. Physics of Condensed Matter Structure Defects and Mechanical Properties, 73*, 899–917.

Quinn, G. D. (1990). Fracture mechanism maps for advanced structural ceramics. 1. Methodology and hot-pressed silicon-nitride results. *Journal of Materials Science, 25*, 4361–4376.

Quinn, G. D., & Braue, W. R. (1990). Fracture mechanism maps for advanced structural ceramics. 2. Sintered silicon-nitride. *Journal of Materials Science, 25*, 4377–4392.

Rachinger, W. A. (1952). Relative grain translations in the plastic flow of aluminium. *Journal of the Institute of Metals, 81*, 33–41.

Raj, R., & Chyung, C. K. (1981). Solution-precipitation creep in glass-ceramics. *Acta Metallurgica, 29*, 159–166.

Rhanim, H., Olagnon, C., Fantozzi, G., & Torrecillas, R. (1997). Experimental characterisation of high temperature creep resistance of mullite. *Ceramics International, 23*, 497–507.

Robertson, A. G., Wilkinson, D. S., & Caceres, C. H. (1991). Creep and creep fracture in hot-pressed alumina. *Journal of the American Ceramic Society, 74*, 915–921.

Schneibel, J. H., & Hazzledine, P. M. (1983). The role of coble creep and interface control in superplastic Sn-Pb alloys. *Journal of Materials Science, 18*, 562–570.

Tompkins, T. L. (1995). Ceramic oxide fibers: building blocks for new applications. *Ceramic Industry, 144*, 45–50.

Tressler, R. E., & Mcnallan, M. (1989). Performance verification of new, low-cost ceramics. In J. R. Hellmann, & B. K. Kennedy (Eds.), *Projects within the center for advanced materials*. Pennsylvania State University.

Tsai, R. L., & Raj, R. (1982). Creep fracture in ceramics containing small amounts of a liquid-phase. *Acta Metallurgica, 30*, 1043–1058.

Wakai, F., Sakaguchi, S., & Matsuno, Y. (1986). Superplasticity of yttria-stabilized tetragonal ZrO_2 polycrystals. *Advanced Ceramic Materials, 1*, 259–263.

Weertman, J. (1957a). Steady-state creep of crystals. *Journal of Applied Physics, 28*, 1185–1189.

Weertman, J. (1957b). Steady-state creep through dislocation climb. *Journal of Applied Physics, 28*, 362–364.

Wereszczak, A. A., Ferber, M. K., Kirkland, T. P., Barnes, A. S., Frome, E. L., & Menon, M. N. (1999). Asymmetric tensile and compressive creep deformation of hot-isostatically-pressed Y_2O_3-doped-Si_3N_4. *Journal of the European Ceramic Society, 19*, 227–237.

Wiederhorn, S. M., Hockey, B. J., & French, J. D. (1999). Mechanisms of deformation of silicon nitride and silicon carbide at high temperatures. *Journal of the European Ceramic Society, 19*, 2273–2284.

Wiederhorn, S. M., Roberts, D. E., & Chuang, T. J. (1988). Damage-enhanced creep in a siliconized silicon-carbide – phenomenology. *Journal of the American Ceramic Society, 71*, 602–608.

Xie, R. J., Mitomo, M., & Zhan, G. D. (2000). Superplasticity in a fine-grained beta-silicon nitride ceramic containing a transient liquid. *Acta Materialia, 48*, 2049–2058.

Xue, L. A., & Chen, I. W. (1990). Deformation and grain-growth of low-temperature-sintered high-purity alumina. *Journal of the American Ceramic Society, 73*, 3518–3521.

Xue, L. A., Wu, X., & Chen, I. W. (1991). Superplastic alumina ceramics with grain-growth inhibitors. *Journal of the American Ceramic Society, 74*, 842–845.

Yoon, S. Y., Akatsu, T., & Yasuda, E. (1996). The microstructure and creep deformation of hot-pressed Si_3N_4 with different amounts of sintering additives. *Journal of Materials Research, 11*, 120–126.

Yoon, S. Y., Akatsu, T., & Yasuda, E. (1997). Anisotropy of creep deformation rate in hot-pressed Si_3N_4 with preferred orientation of the elongated grains. *Journal of Materials Science, 32*, 3813–3819.

Yoon, K. J., Wiederhorn, S. M., & Luecke, W. E. (2000). Comparison of tensile and compressive creep behavior in silicon nitride. *Journal of the American Ceramic Society, 83*, 2017–2022.

Yoshida, H., Ikuhara, Y., & Sakuma, T. (1998). High-temperature creep resistance in rare-earth-doped, fine-grained Al_2O_3. *Journal of Materials Research, 13*, 2597–2601.

Yoshida, H., Ikuhara, Y., & Sakuma, T. (1999). High-temperature creep resistance in lanthanoid ion-doped polycrystalline Al_2O_3. *Philosophical Magazine Letters, 79*, 249–256.

Zelin, M. G., & Mukherjee, A. K. (1996). Geometrical aspects of superplastic flow. *Materials Science and Engineering. A. Structural Materials Properties Microstructure and Processing, 208*, 210–225.

Zhan, G. D., Mitomo, M., Ikuhara, Y., & Sakuma, T. (2000). Effects of microstructure on superplastic behavior and deformation mechanisms in beta-silicon nitride ceramics. *Journal of the American Ceramic Society, 83*, 3179–3184.

This page intentionally left blank

2.12 Mechanical Behavior of SiC Fiber-Reinforced Ceramic Matrix Composites

Gilbert Fantozzi and Pascal Reynaud, INSA de Lyon, MATEIS (UMR CNRS 5510), Villeurbanne, France

© 2014 Elsevier Ltd. All rights reserved.

2.12.1 Introduction

Space and aeronautic applications need light and nonbrittle materials even at high temperature. For example in airplane engines, materials have to maintain their long-term mechanical properties under high temperature and oxidizing atmospheres even when subjected to complex mechanical loads. Ceramic–matrix composites (CMCs) are interesting candidates for such applications, because they have low density, are tolerant to damage and have better mechanical properties at high temperature than metallic alloys (Aveston, Cooper, & Kelly, 1971; Bouillon et al., 2000; Evans, Zok, & McMeeking, 1995; Evans, 1997; Fantozzi, Reynaud, & Rouby, 2001; Halverson & Curtin, 2002; Lamicq & Jamet, 1995; Lamon, 2005; Vandenbulke, Fantozzi, Goujard, & Bourgeon, 2005).

CMCs are composite materials made with long woven ceramic fibers embedded in a ceramic matrix deposited by chemical vapor infiltration (**Figure 1**). In these composites, fracture strain on fibers is higher than the fracture strain in the matrix. Then, when a load is applied on a composite, the matrix cracks first and the fibers bridging this crack sustain the load. Due to the difference of stresses between bridging fibers and matrix at the level of the matrix crack, interface between fiber and matrix is subjected to a shear stress leading to debonding of fibers and matrix. In the debonded zone, around the matrix crack, bridging fibers slide with friction in the surrounding matrix. This interfacial friction is characterized by the interfacial frictional shear stress τ corresponding to the shear stress at fiber/matrix interface necessary for fibers to slide in the matrix (Aveston et al., 1971).

Due to these fiber/matrix interactions, CMCs are composites tolerant to damage and mechanically behave like nonbrittle materials under monotonic loading. Under cyclic fatigue, the load applied oscillates between a valley load and a peak load. During each loading/unloading cycle, the mechanical behavior of composite described in a stress versus strain diagram is characterized by a stress/strain loop where the area is the energy dissipated during each cycle which is linked to the interfacial shear stress τ (Fantozzi et al., 2001; Rouby, Penas, & Reynaud, 2001; Solti, Robertson, & Mall, 2000; Vandenbulke et al., 2005).

When CMCs are subjected to cyclic fatigue, interfacial shear stress may decrease due to interfacial wear and this evolution leads to a variation of internal friction. At high temperature in air, during static fatigue a recession of fiber/matrix interphases may occur leading also to a change of the composite deformation during time. To obtain longer lifetimes, a protection against oxidation is required, and enhanced SiC matrices and self-healing matrices do that. Nevertheless at higher temperatures creep of fibers may occur leading to high deformations of the composites and to lower lifetimes.

2.12.2 Micromechanical Analysis

Several fiber-reinforcement architectures have been developed on CMCs. The simplest one is unidirectional (1D) reinforcement, where long fibers are aligned along one direction. However, CMCs are often cross-weaved

http://dx.doi.org/10.1016/B978-0-08-096527-7.00031-3

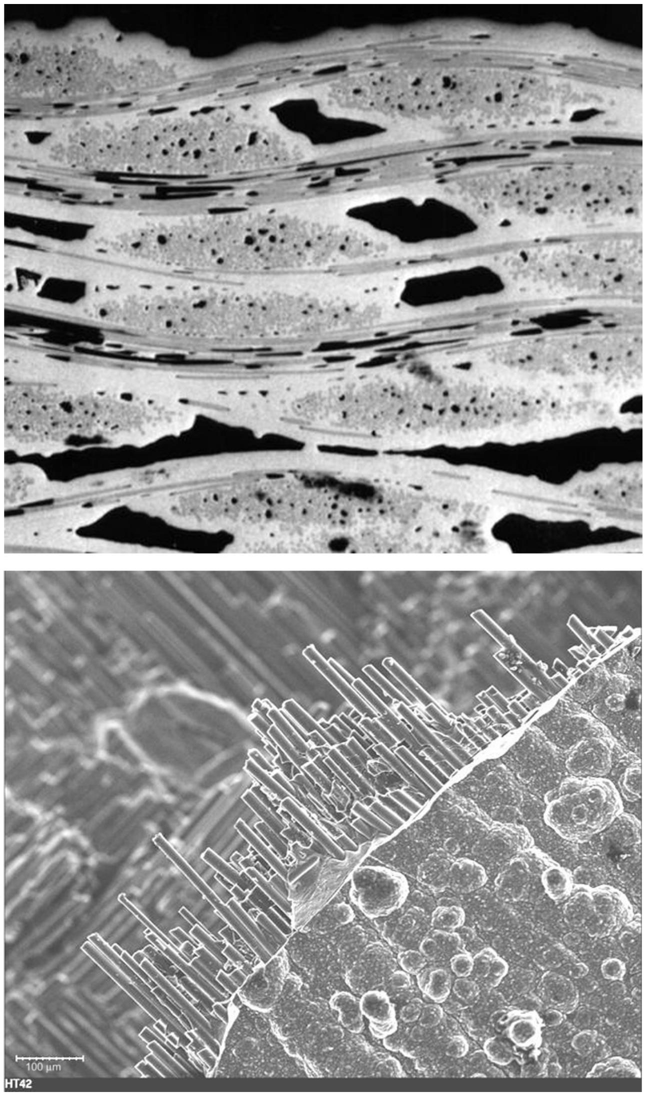

Figure 1 Typical microstructure and fracture surface of cross-weaved CMC (example of a 2D SiC/SiC).

or cross-plied, where the fiber reinforcement is done following two perpendicular directions. When subjected to a uniaxial loading aligned with one direction of fibers, the damage of CMCs is similar to the damage of a 1D composite, with a fiber fraction corresponding to the fraction of fibers aligned with the loading direction. That is the reason why the micromechanical analysis of damage is usually developed on 1D composite as described below.

For a 1D composite, when a load is applied parallel to the axis of fibers, the mechanical behavior is characterized first by an elastic behavior, and the load applied on the composite is shared between fibers and matrix according to their volume fraction. The stress sustained by fibers and matrix is given by:

$$\sigma_c = \sigma_m v_m + \sigma_f v_f \tag{1}$$

where σ_c is the stress applied on the composite, σ_m and σ_f are the stresses sustained, respectively, by matrix and fibers, and v_m and v_f are the volume fraction of matrix and of fibers, respectively.

When the stress σ_c applied on the composite is high enough to reach the fracture stress of matrix σ_{mR}, the matrix cracks and the cracks develop along a section of the composite perpendicular to the axes of fibers. At the level of this matrix crack, fibers are not broken but bridge the crack, and are overloaded due to the matrix unloading. Because of this difference of stresses at the level of crack, fiber/matrix interface is subjected to a shear stress leading to a debonding of fibers and surrounding matrix. According to the differences of

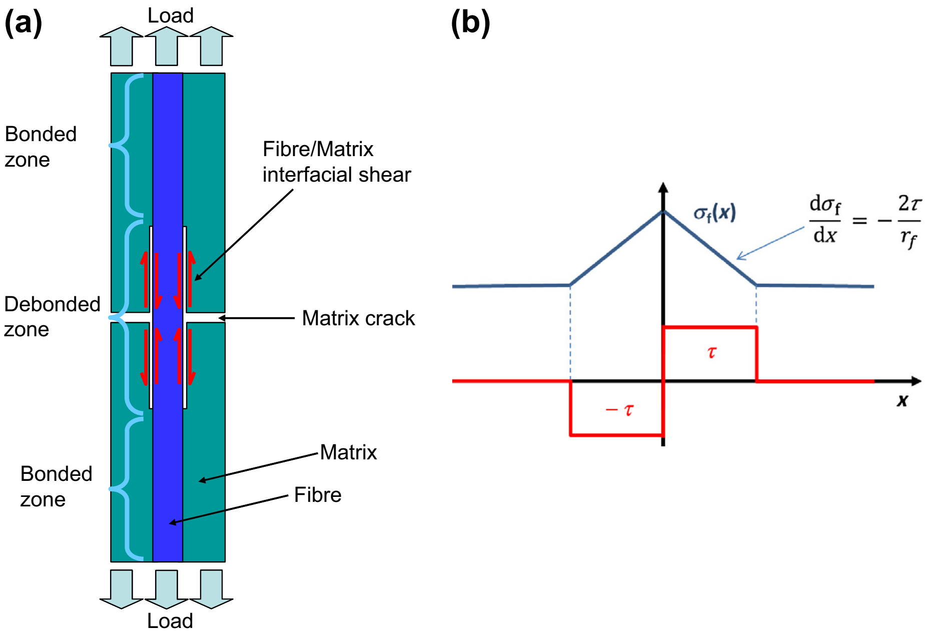

Figure 2 Elementary damage mechanism on 1D CMC: (a) unbroken fiber bridging a matrix crack and fiber/matrix sliding with friction and (b) stress profile along the bridging fiber close to the matrix crack.

elongations between bridging fibers and cracked matrix, fibers slide in the debonded zone with friction. Hence, along the fibers close to the matrix crack stresses and strains are maximal at the crack level, and then decrease down to a minimum value at the limit of the debonded zone. This decrease is given by (Aveston et al., 1971):

$$\frac{d\sigma_f}{dx} = -\frac{2\tau}{r} \quad \text{and} \quad \frac{d\varepsilon_f}{dx} = -\frac{2\tau}{rE_f} \tag{2}$$

with x, the distance from the matrix crack; τ, the interfacial frictional shear stress; r, the radius of fibers; and E_f, the Young's modulus of fibers. The end of the debonded zone corresponds to the distance from the crack where the strain of fibers equals the strain of matrix, which is also the strain of the composite. Typical bridging fibers and cracked matrix strain profiles around a matrix crack are shown in Figure 2.

Out of the debonded zone, the stress in matrix is maximal and a new matrix crack can be created, leading to a new debonded zone. Hence the damage mechanism induced by the load applied on the composite is first a multicracking of matrix associate to localized debonding of fibers (Figure 3(a)).

When the number of matrix cracks is high enough to debond fibers all along their length, no more matrix cracks can be created and multicracking of matrix is saturated. The distance between each matrix crack is randomly distributed between two limit values d_{min} and d_{max} and is given by (Aveston et al., 1971):

$$d_{min} = \frac{v_m}{v_f}\frac{r}{2\tau}\sigma_{mR} \tag{3a}$$

and

$$d_{max} = 2d_{min} \tag{3b}$$

Due to the high density of matrix cracks this saturation can be described by a mean distance d. After saturation of matrix multicracking, fibers are totally debonded and the typical strain profile is given in Figure 3(b).

When a matrix crack occurs, fibers are less broken under the stress applied. After saturation of matrix multicracking, the stress applied on the composite is sustained only by unbroken fibers, and as far as this stress increases the fraction of broken fibers increases. When all fibers are broken the strength of the composite is reached (Evans, 1997; Halverson & Curtin, 2002).

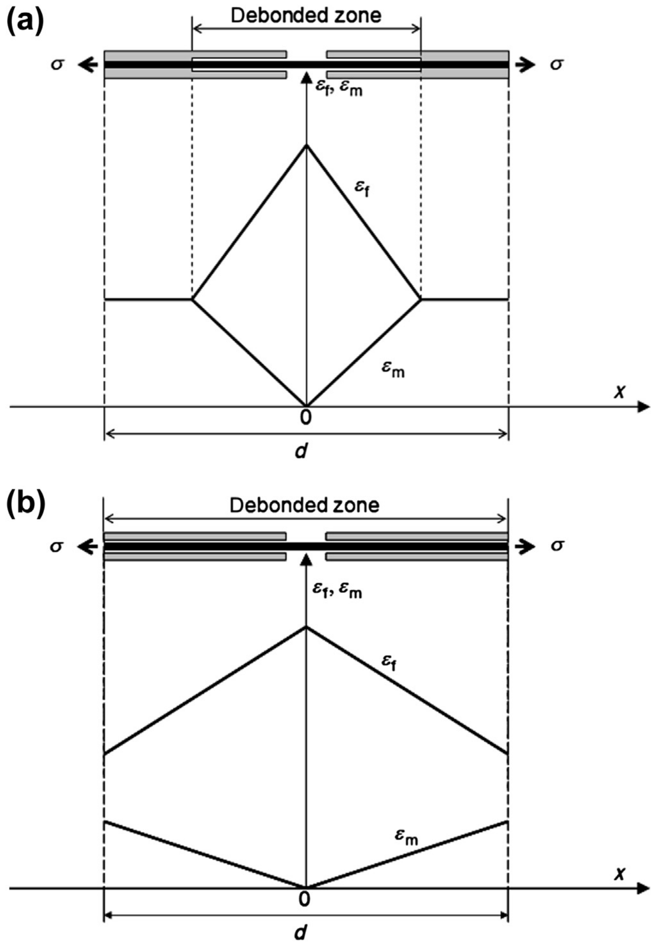

Figure 3 Strain profile of unbroken fiber bridging a matrix crack and of surrounding matrix for (a) partially debonded fibers and (b) totally debonded fibers.

For cyclic fatigue test (Evans et al., 1995; Fantozzi et al., 2001; Zawada, Butkus, & Hartman, 1991), the stress applied on the composite oscillates between a valley stress and a peak stress, with a peak stress S lower than the strength of the composite. During first loading, multiple cracking of matrix occurs, and the mean distance between matrix cracks d is controlled by statistical distribution of matrix defects, which are critical under this peak stress. For subsequent cycles only to-and-fro sliding of fibers occurs close to each matrix crack. This repeated sliding of fibers is done with friction, characterized by the interfacial shear stress τ, in a zone lower or equal to the debonded zone created during the first cycle. Hence the strain profile of fibers is more complex.

According to the level of the peak stress S and the mean distance between matrix cracks d, debonding of bridging fibers during first loading is localized close to each matrix cracks (Figure 3(a)) if the interfacial shear stress τ is higher than a limit value $2\tau^*$. This limit value is calculated from strain profiles in the fibers and is given by:

$$\tau^* = \frac{\alpha r E_f S}{2 d E_c} \tag{4}$$

where $\alpha = E_m v_m / E_f v_f$ and E_c is the elastic modulus of the composite ($E_c = E_m v_m + E_f v_f$). If τ is lower than $2\tau^*$, the debonding of the fibers is total (Figure 3(b)).

During repeated loading/unloading cycles, bridging fibers slide close to each matrix crack, and the sliding zone extends as far as the load is increasing during loading step, or decreasing during unloading step. This phenomenon leads to a complex strain profile (Figure 4), where three cases have to be considered: (1) if $\tau > 2\tau^*$: sliding of bridging fibers is localized close to each matrix crack during the first loading and during subsequent cycles; (2) if $2\tau^* > \tau > \tau^*$: sliding is total during the first loading and localized close to each matrix

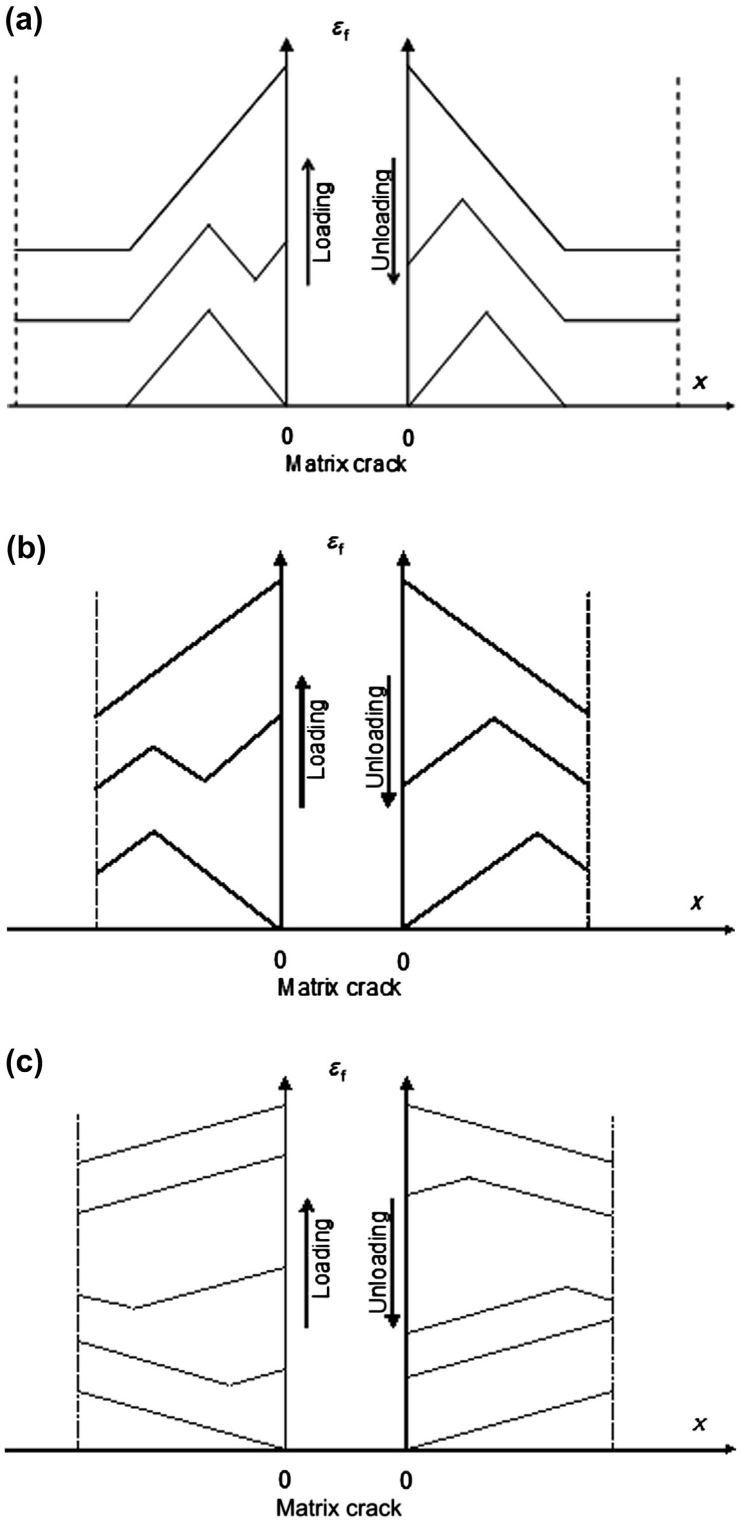

Figure 4 Theoretical evolution of strain profile of bridging fibers under loading/unloading cycle according to the interfacial shear stress level (a: $\tau > 2\tau^*$; b: $\tau^* < \tau < 2\tau^*$; c: $0 < \tau < \tau^*$).

cracks during subsequent cycles; (3) if $0 < \tau < \tau^*$: fibers slide in matrix all along their length both during first loading and during cycles.

From these strain profiles it is possible to theoretically calculate the strain ε of the composite in relation to the stress applied σ_c by integration of the local fibers strains along the strain profiles (Fantozzi & Reynaud, 2009).

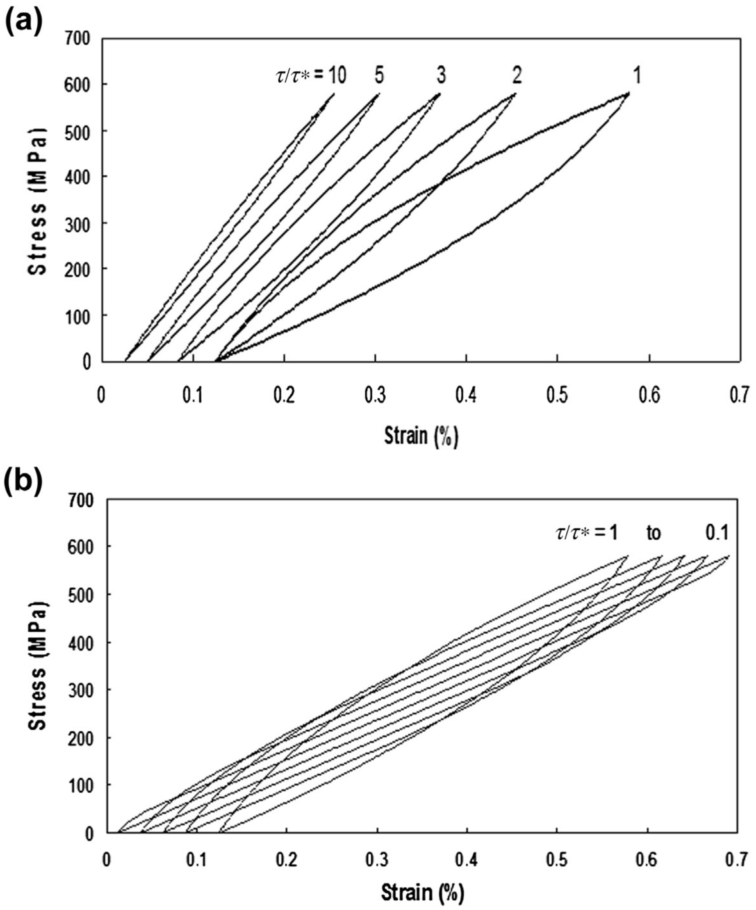

Figure 5 Theoretical stress/strain loops during cyclic fatigue with decreasing interfacial shear stress (a: $\tau > \tau^*$; b: $\tau > \tau^*$).

It is then possible to plot in stress/strain diagram the mechanical hysteresis loops described by a 1D CMC under cyclic fatigue. These theoretical loops are given in Figure 5 for $\tau > \tau^*$ and $\tau < \tau^*$ cases. Under these diagrams it can be seen that loops are opened and that some energy can be dissipated during a cycle. This dissipation of energy is a direct consequence of the friction between fibers and matrix during to-and-fro slides, and may be calculated theoretically.

To characterize the dissipation of energy during a loading/unloading cycle, several parameters may be calculated as: the area of the stress/strain loop ΔW, the internal friction $\Delta W/W_e$ (where W_e is the maximum elastic energy stored during the cycle), and also the width of the loop at midstress $\Delta\varepsilon$. The theoretical expressions of ΔW and $\Delta W/W_e$ are:

$$\text{if} \quad \tau/\tau^* > 1: \ \Delta W = \frac{\alpha}{6}\frac{\tau^*}{\tau}\frac{S^2}{E_c} \quad \text{and} \quad \frac{\Delta W}{W_e} = \frac{\alpha}{3\left(\frac{\alpha}{2}+\frac{\tau}{\tau^*}\right)} \tag{5a}$$

$$\text{if} \quad \tau/\tau^* < 1: \ \Delta W = \frac{\alpha}{6}\frac{\tau^*}{\tau}\frac{S^2}{E_c}\left(3-2\frac{\tau}{\tau^*}\right) \quad \text{and} \quad \frac{\Delta W}{W_e} = \alpha\frac{\tau}{\tau^*}\frac{1-\frac{2}{3}\frac{\tau}{\tau^*}}{1+\alpha\left(1-\frac{1}{2}\frac{\tau}{\tau^*}\right)} \tag{5b}$$

It can be seen that internal friction $\Delta W/W_e$ is only dependent of the parameter α (representative of the elastic properties of the constituents) and of the ratio τ/τ^*. During cyclic fatigue, the repeated to-and-fro slides of fibers

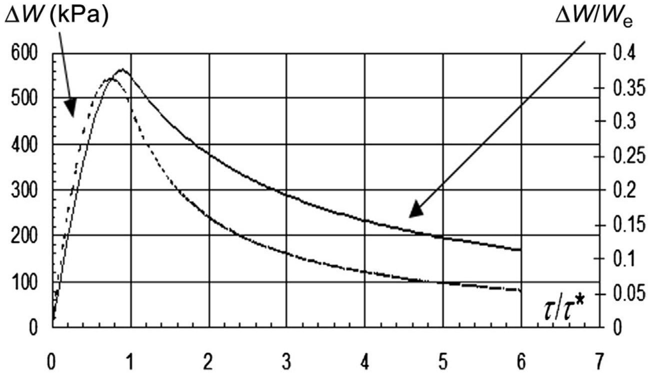

Figure 6 Theoretical relationships between dissipated energy (ΔW) or internal friction ($\Delta W/W_e$) and normalized interfacial shear stress τ/τ^*.

close to each matrix crack can introduce an interfacial wear between fibers and surrounding matrix (Evans, 1997; Fantozzi et al., 2001). This phenomenon may be described by a decrease of the interfacial shear stress τ as far as the number of cycles increases. Then the effect of interfacial wear on dissipation may be described by the relation between area of the loops ΔW, internal friction $\Delta W/W_e$ or loop width at midstress $\Delta\varepsilon$ and interfacial shear stress τ or the normalized interfacial shear stress τ/τ^*. The plotting of these three parameters versus the normalized interfacial shear stress gives curves starting and ending by zero for zero and infinite normalized interfacial shear stress and crossing to a maximum for a normalized interfacial shear stress close to 1 (**Figure 6**).

For a given composite, initial dissipation energy corresponds to the area of loops, or internal friction, for an initial value of interfacial shear stress τ_0/τ^*. Its evolution during cyclic fatigue is given by the subsequent values associate to interfacial shear stress values τ_N/τ^* decreasing from τ_0/τ^*. Hence, if the initial normalized interfacial shear stress τ_0/τ^* is on the right hand or on the left hand regard to the maximum, the evolution during cyclic fatigue due to interfacial wear can increase, decrease or go through a maximum. These theoretical evolutions have been observed experimentally and are described later (Section 2.12.5.1).

This analysis may be used also to describe the evolution of deformation during time of CMCs under static fatigue at high temperatures. In that case the decrease of interfacial shear stress is due to oxidation and recession of interphases, leading to an increase of the deformation during time, as observed experimentally and described below (Section 2.12.5.2).

For more complex CMCs like cross-weaved or cross-plies composites loaded in a direction parallel to one direction of fibers, the mechanical behavior of transverse plies is usually elastic and less dissipative. Hence the mechanical hysteresis during cyclic fatigue of 2D composites is mainly due to longitudinal fibers, whose behavior is similar to a 1D composite.

2.12.3 Monotonic Tensile Behavior

For damage study of CMCs, the knowledge of the mechanical behavior under monotonic tensile loading is fundamental because the main damage mechanisms are developed under this type of loading, that gives the initial damage of these composites for long tests like fatigue or creep tests.

When a CMC is loaded under monotonic tension in a direction aligned with one direction of fibers, the mechanical behavior of CMC is characterized by the following three domains:

- Below the first matrix crack stress σ_{le}: the composite is not damaged and the mechanical behavior of the composite is linear elastic behavior with an elastic modulus corresponding to the load bearing by the fibers and the matrix ($E_c = E_f v_f + E_m v_m$).
- Above the first matrix crack stress σ_{le} and below matrix crack saturation at σ_{sat}: fiber/matrix sliding occurs. The mechanical behavior of the composite is nonlinear due to matrix multicracking and fiber/matrix interactions, which are characterized by the interfacial shear stress τ.
- Above the matrix crack saturation stress σ_{sat}: the mechanical behavior of the composite is again linear elastic, but with a lower tangential elastic modulus corresponding to a load bearing by the fibers only.

Experimental results are given in **Figure 7**. The initial elastic domain is often observed, and the nonlinear domain can be more or less extended. The nonlinear domain corresponds to a stage where matrix multicracking

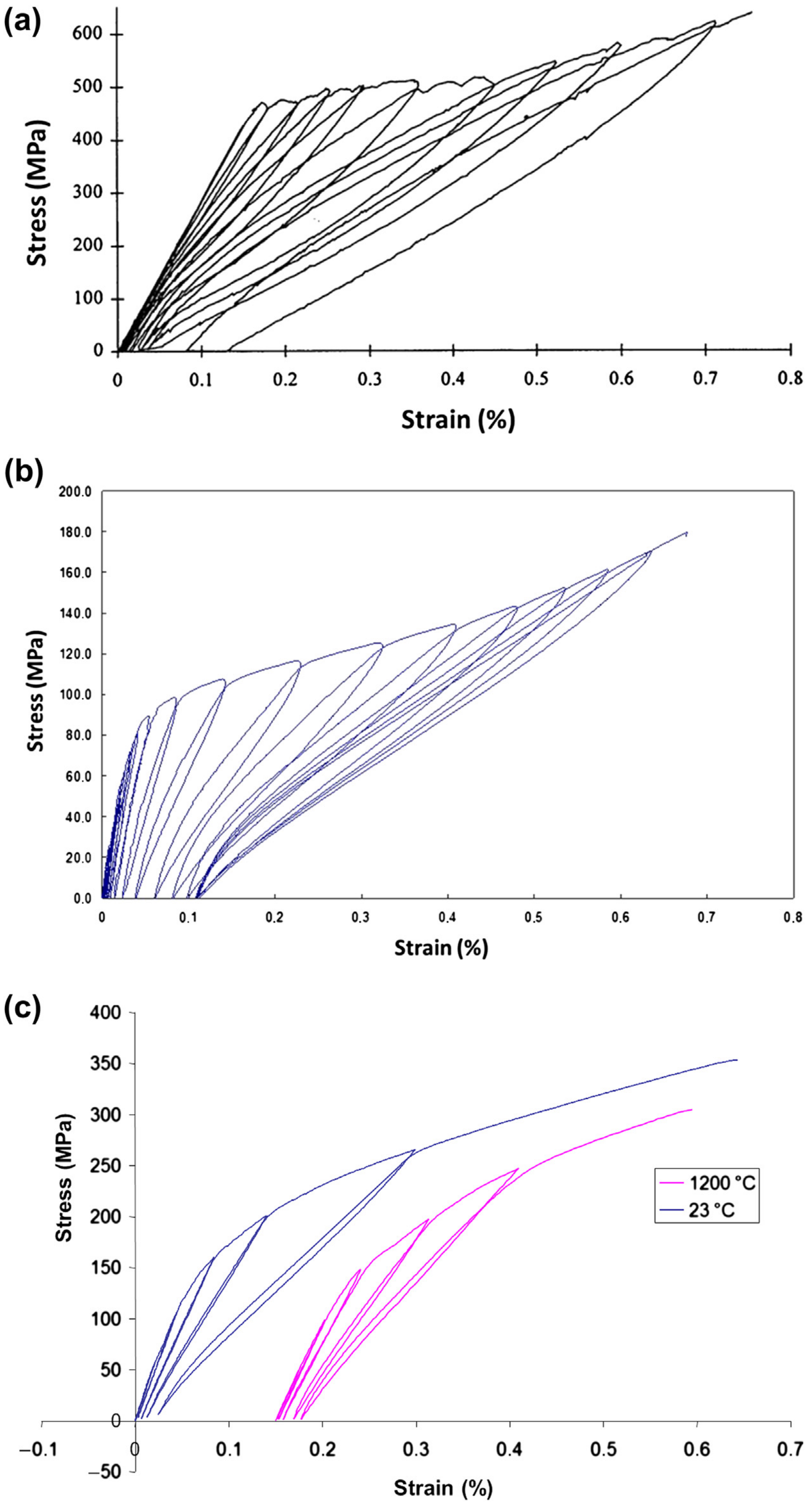

Figure 7 Experimental mechanical behavior of CMC under monotonic tension (a) SiC/Si_3N_4 at room temperature, (b) SiC/[Si–B–C] at room temperature, (c) Hi-Nicalon/[Si–B–C] at room temperature and at high temperature.

occurs and where the mean distance between two neighboring cracks decreases as the stress applied increases. The end of this stage corresponds to the damage status where fibers are totally debonded and where overloading profiles of fibers overlap. According to the Weibull statistic of defects in the matrix, the stress of first matrix crack σ_{le} and the stress of matrix multicracking saturation σ_{sat} can be close or not. When these two stresses are similar, the mechanical behavior of the composite is characterized by a stress/strain curve with a "plateau". This is the case, for example, of the 1D SiC/Si_3N_4 at room temperature (Figure 7(a)). If the stress of matrix multicracking saturation is different with the stress of first matrix crack, the mechanical behavior is nonlinear until the saturation stress σ_{sat}, and then becomes linear due to the load bearing by the fibers only. In that case, the tangential elastic modulus is $E_f \cdot v_f$. An example of such behavior is given in Figure 7(b) for an SiC/[Si–B–C] composite. If the strength of the composite is lower than the saturation stress σ_{sat}, the mechanical behavior is nonlinear above the elastic domain and until the fracture stress of the composite. This is the case, for example, of the Hi-Nicalon/[Si–B–C] composite as shown in Figure 7(c).

These three experimental cases can be described by the micromechanical approach described in the previous section, including the effect of the stress applied on the mean distance between two neighbor matrix cracks. This effect can be for example described by the following equation when $\sigma_{le} \le \sigma_c \le \sigma_{sat}$:

$$\frac{1}{d} = \frac{1}{d_{sat}} \frac{(\sigma_c - \sigma_{le})}{(\sigma_{sat} - \sigma_{le})} \tag{6}$$

and the overlapping condition of fibre strain profiles leads to:

$$\sigma_{sat} = \frac{\tau d_{sat} E_c}{\alpha r_f E_f} \tag{7}$$

The last equation describes the fact that for a given d_{sat}, the stress σ_{sat} increases with the interfacial shear stress. These three cases are described theoretically by the Figure 8 for a 1D composite.

Whatever is the status of damage in the composite, the maximum loading of the fibers is close to each matrix crack and the fracture of the composite occurs when all the bridging fibers break. The strength σ_R of the composite is therefore given by:

$$\sigma_R = V_f \sigma_{fR} \tag{8}$$

where σ_{fR} is the mean strength of the fibers. This equation shows that if ageing of the composite leads to a damage of the fibers, a decrease in their strength occurs, leading to a decrease in the composite strength as shown by Xu, Braun, Ostertag, and Krause (1995) on SiC/Si_3N_4 composites at high temperatures. But a change in the fiber–matrix interphases may lead also to a decrease in composite strength, as described in the next section.

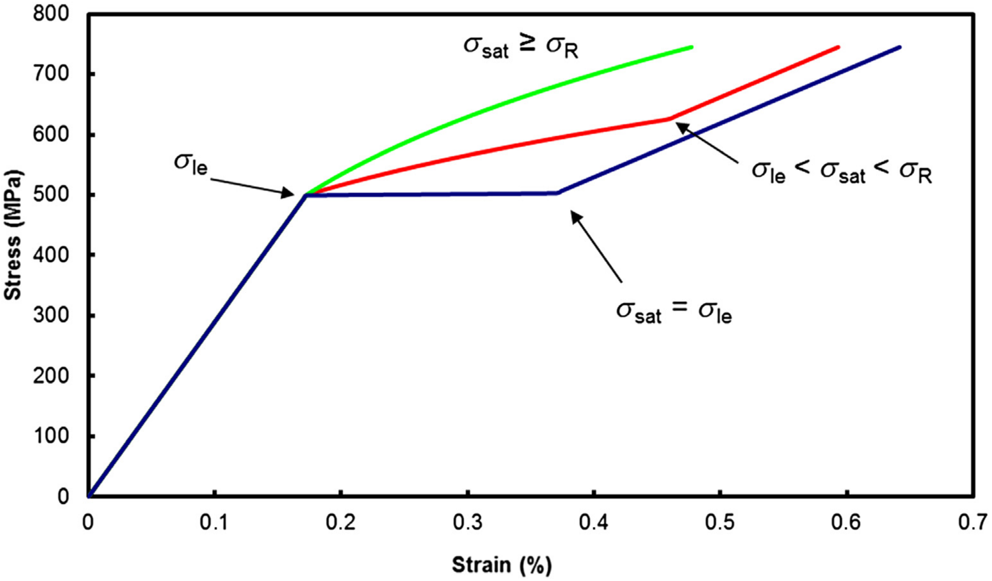

Figure 8 Theoretical behavior under monotonic tension of 1D CMC according to the stress saturation σ_{sat}.

2.12.4 Effects of Oxidation on Mechanical Behavior

The ceramic matrix composites reinforced with long fibers exhibit good mechanical properties such as high elastic modulus or high strength at high temperatures. The SiC-based ceramics show a good oxidation resistance due to the formation of a protective layer of silica. The mechanical behavior of CMCs is linked to the fiber/matrix bonding and a thin layer of interphase is interposed between the matrix and the fiber, this thin layer exhibiting a low shear strength interface. Very often, this compliant thin layer is constituted by carbon and this carbon interphase is sensitive to oxidation (Filipuzzi and Naslain, 1994).

An example of evolution of the room bending fracture strength as a function of oxidation time under air at 800 °C is shown in **Figure 9** (Frety, Molins, & Boussuge, 1992). Two SiC–SiC composites were studied and they were processed by a chemical vapor infiltration process into cross-weaved 0°/90° Nicalon fiber preforms. A thin layer of pyrolithic carbon was deposited on the fiber preform. They contained 40 vol% SiC fibers and had a porosity of 10%. The two investigated composites differ in the pyrocarbon interphase thickness: 35–70 nm for the composite 1 and 140–200 nm for the composite 2.

At 800 °C, the two composites exhibit a similar behavior: the fracture strength decreases significantly as a function of oxidation time. The overall mechanical behavior changes from tough to brittle.

At 1400 °C, the variation of the fracture strength is given by **Figure 10**. The fracture strength of the composite 1 is almost constant whereas the strength of the composite 2 decreases quickly. The modifications of the mechanical properties are linked to the oxidation of the materials and especially to the oxidation of the carbon interphase.

The different phenomena, which take place have been described by Filipuzzi et al. (1994) and are schematically described in **Figure 11**. The oxidation begins by the oxidation of the carbon interphase with production of gaseous species CO or CO_2. An annular pore is formed and the reactant species must diffuse along the pore. The fibers and the matrix react with oxygen and there is formation of silica and carbon oxides. The growth of the silica layers on the pore walls leads to a decrease in the pore width. When the pore is sealed by silica the reactant must diffuse through silica and so the oxygen flux is strongly reduced inside the pore. At low temperatures, diffusion in the gas phase along the pore and oxidation in the bulk material occur whereas at high temperatures, oxidation of carbide from the pore walls and of near surface occurs.

So, at 800 °C, the carbon interphase is replaced by silica, leading to a dramatic increase of the interfacial debonding/sliding shear stress with a decrease of the fiber pull-out length owing to a strong bonding and then to a brittle behavior (with a flat fracture facies). If the ageing is done under vacuum, no oxidation of fiber–matrix interface occurs and the mechanical behavior of the composites remains unchanged as shown in **Figure 9**.

At 1400 °C for the composite 1, the pores are quickly sealed by silica and so the composite is protected against oxidation and keeps its mechanical properties. On the other hand, for the composite 2, which presents a thicker interphase, the pores sealing by silica do not occur because carbon is consumed before

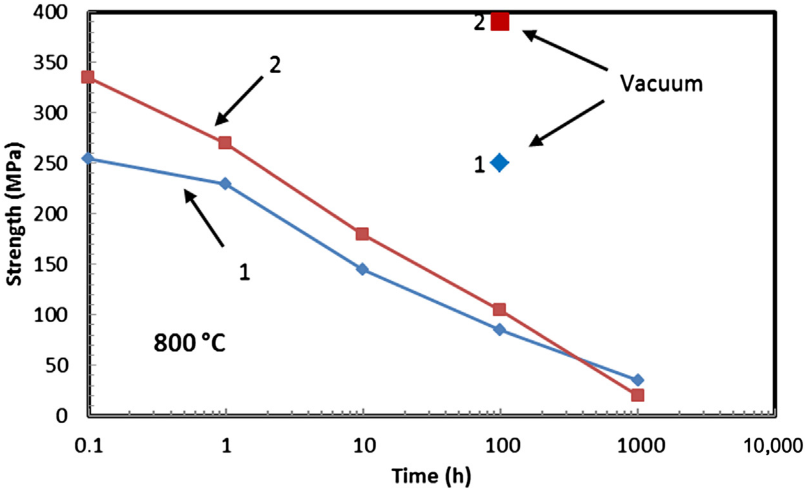

Figure 9 Effect of ageing under air of SiC/SiC composites strength (composite 1: interface thickness 70 nm; composite 2: interface thickness 200 nm) at 800 °C and comparison with aging under vacuum. From Frety et al. (1992).

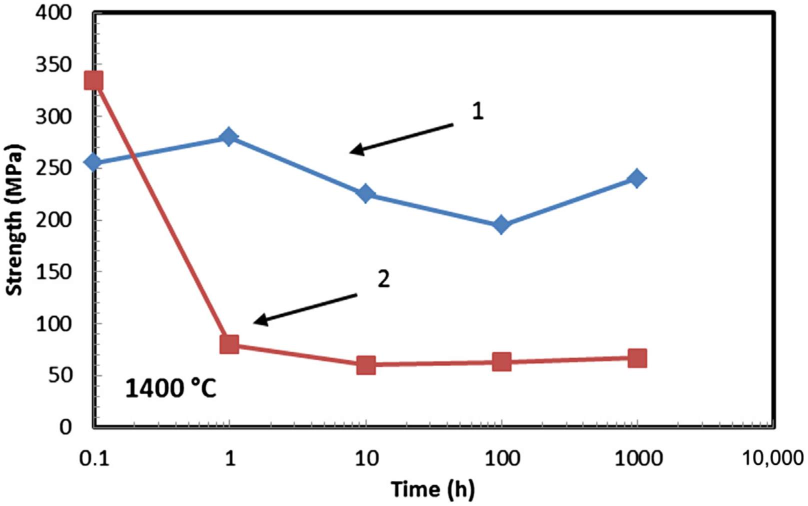

Figure 10 Effect of ageing under air of SiC/SiC composites strength (composite 1: interface thickness 70 nm; composite 2: interface thickness 200 nm) at 1400 °C and comparison with aging under vacuum. From Frety et al. (1992).

silica seals the pores. Therefore, the mechanical properties of the composite 2 decrease dramatically and quickly at 1400 °C.

These results exhibit the significant effect of the thickness of the pyrocarbon on the evolution of the mechanical behavior during oxidation. A low thickness of the pyrocarbon interphase (about 50 nm) gives a better oxidation resistance.

In order to improve the low oxidation resistance of the carbon interphase, some new composites have been developed as suggested by Fox and Nguyen (1995) with the incorporation in the matrix of glass-forming, boron-based particulates which react with oxygen and form a sealant glass which inhibits the oxidation of the carbon layer. The mechanical behavior of these enhanced long fiber-reinforced CMCs has been studied by Zhu et al. (1998) who have shown that the addition of the glass-forming particulates in the matrix improves the oxidation resistance of the composite as seen in **Figure 12**. The tensile stress-strain curve of the enhanced SiC–SiC composite in air at 1300 °C shows that the fracture strength is about the same than that of the standard SiC–SiC composite without incorporation of boron-based particulates under argon at the same temperature. The deformation at the fracture strength is higher for the enhanced composite, which exhibits a ductility increase contrarily to the standard composite that becomes brittle under air.

Another way to increase the oxidation resistance of the CMCs is to use a multi-layered matrix constituted of three different constituents (silicon carbide, boron carbide, and a SiBC phase) as described by Viricelle, Goursat, and Bahloul-Hourlier (2001) (see **Figure 13**). An effective protection against oxidation takes place in the temperature range 650–900 °C due to the formation of the boron oxide, which protects the carbon interphase. At higher

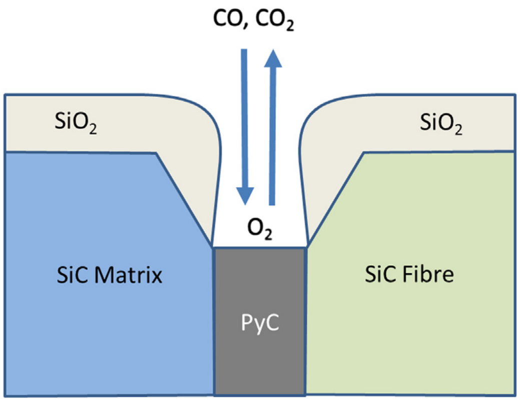

Figure 11 Theoretical oxidation mechanism at high temperatures of fiber/matrix interfaces. From Filippuzzi and Naslain (1994).

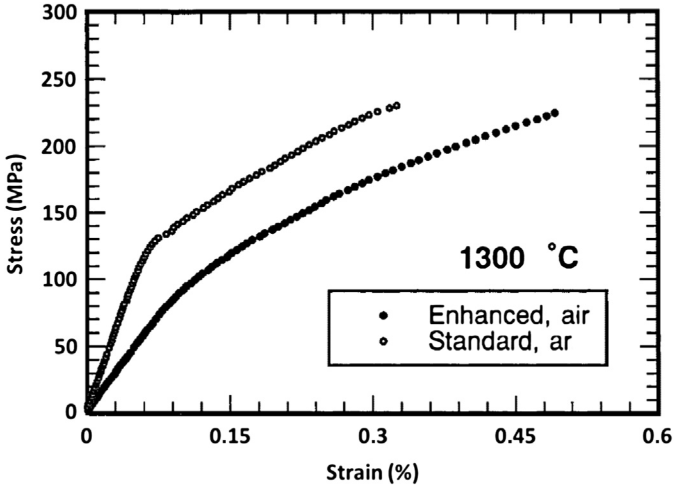

Figure 12 Monotonic tensile behavior at 1300 °C of standard SiC/SiC composite in argon and enhanced SiC/SiC composite under air. From Zhu et al. (1998).

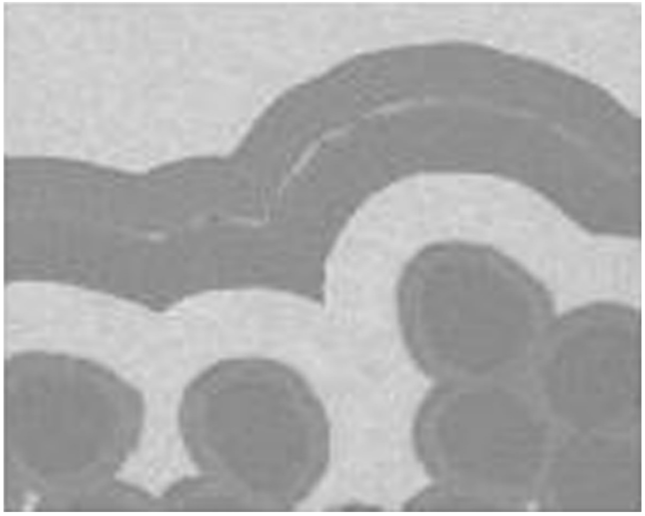

Figure 13 SEM image of a multilayer SiC/[Si–B–C] composite. From Vandenbulke et al. (2005).

temperatures, boron oxide is volatile and is no more protective but the two other constituents of the matrix, SiC and SiBC, form borosilicate and silica which conduct to a self-healing behavior. However, below about 600 °C, the oxidation of the boron carbide is too low in order to protect the carbon interphase against the oxidation.

2.12.5 Cyclic and Static Fatigue

CMCs are interesting materials because they are light and nonbrittle even at high temperatures. Therefore, their mechanical properties under long tests below their strength have to be known for long-term applications. That is the reason why their mechanical behavior under cyclic and static fatigues have been investigated to determine the evolutions of the mechanical behavior during these tests, to identify the micromechanical mechanisms leading to these evolutions, and evaluate the lifetimes associated. These two types of behaviors (cyclic fatigue and static fatigue) are described below.

2.12.5.1 Cyclic Fatigue

When a CMC is subjected to a cyclic loading between a valley stress and a peak stress, during the first loading its mechanical behavior and damage are similar to the monotonic tensile test (matrix multicracking

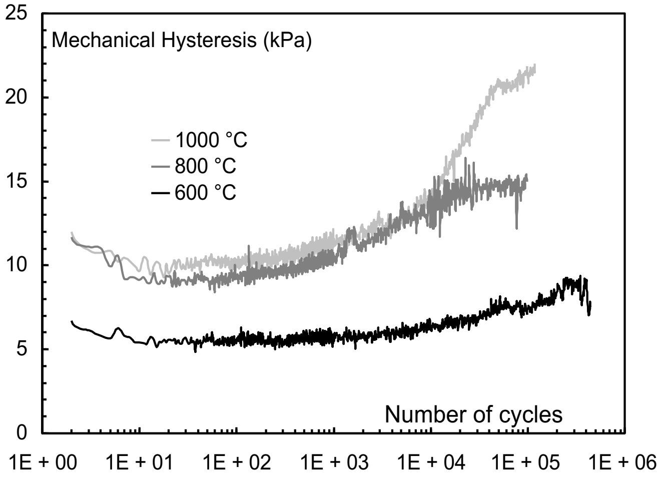

Figure 14 Evolution of internal friction under cyclic fatigue under inert atmosphere at high temperature of SiC/SiC composite.

and fiber/matrix sliding with initial value of interfacial shear stress) but stopped when the peak load is reached. But under subsequent cycles, damage of the composites expands. This should lead usually to an increase of the energy dissipated during a loading/unloading cycle. This phenomenon has been observed on Nicalon SiC/SiC composites at room temperature and at high temperature under inert atmosphere (**Figure 14**). On this composite dissipated energy per cycle increases during fatigue, and is higher when the temperature increases (Fantozzi et al., 2001). But for some composites (Nicalon SiC/MAS-L, C/SiC, and Nextel/Al_2O_3) internal friction can decrease during fatigue (Fantozzi et al., 2001; Ruggles-Wrenn, Mall, Eber, & Harlan, 2006; Staehler, Mall, & Zawada, 2003; Zawada et al., 1991). This is also the case of self-healing Hi-Nicalon SiC/[Si–B–C] composites under low stresses (up to 200 MPa) (**Figure 15**). The decrease of internal friction during fatigue is observed at both 600 and 1200 °C (Reynaud, Rouby, & Fantozzi, 2005).

This evolution is not classical because usually internal friction increases during fatigue as far as the material is damaged. But, as mentioned in the previous section, in CMCs a general phenomenon occurring during cyclic fatigue is wear of the fiber/matrix interface due to to-and-fro sliding of fibers in the matrix near a matrix crack (Evans, 1997; Fantozzi et al., 2001). This effect leads to a progressive decrease of the interfacial frictional shear stress τ as the number of cycles applied increases.

As described in Section 2.12.2, when the interfacial frictional shear stress τ is higher than the limit value $\tau*$ (Eqn (4)), sliding of fibers is located near the matrix cracks, and when τ is lower than τ^* sliding is total. For a

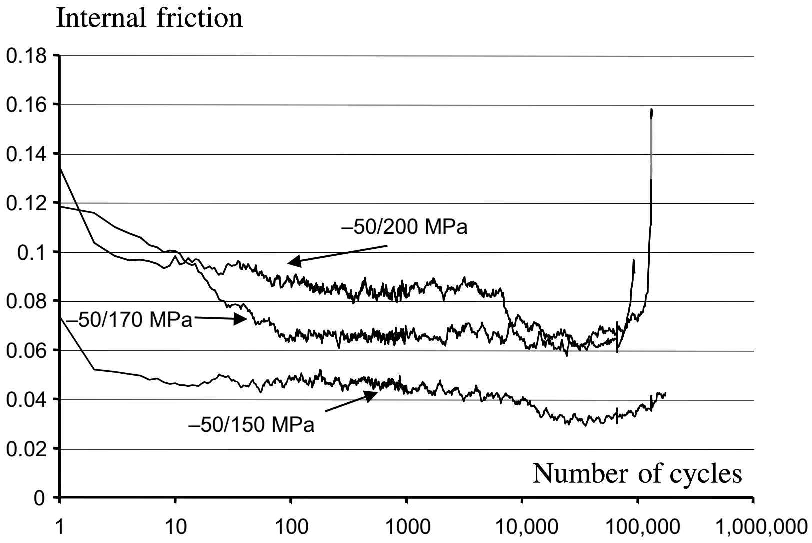

Figure 15 Evolution of internal friction under cyclic fatigue under air at high temperature of SiC/[Si–B–C] composite.

given composite and a given peak stress S, the initial interfacial shear stress τ_0 can be higher or lower than τ^*. If τ_0 is higher than τ^*, the representative point on "internal friction versus interfacial shear stress" diagram ("$\Delta W/W_e$ versus τ/τ^*" diagram) is on the right-hand side ($\tau_0/\tau^* > 1$). During cyclic fatigue if interfacial shear stress decreases due to interfacial wear, internal friction increases (case of SiC/SiC composites) (**Figures 14** and **16**). On the other hand, if τ_0 is lower than τ^*, the representative point is on the left side of "$\Delta W/W_e$ versus τ/τ^*" diagram and during fatigue the decrease of τ leads to a decrease in internal friction (case of Hi-Nicalon SiC/[Si–B–C]) (**Figures 15** and **16**).

For the Hi-Nicalon SiC_f/[Si–B–C] composite, at 600 °C there is no fiber creep, but a total sliding of fibers is possible if the initial interfacial shear stress τ_0, due to radial thermal stresses in tension at the fiber/matrix interfaces, is lower than the limit value τ^* (Reynaud et al., 2005). At 1200 °C thermal stresses are lower than at 600 °C, but a creep of fibers appears (Farizy, Chermant, Sangleboeuf, & Vicens, 2003). This can lead also to the complete debonding of fibers due to the reduction of their diameter. Therefore the sliding can occur along the whole fiber length (total sliding) and internal friction can decrease due to interfacial wear, as observed experimentally (**Figure 15**).

As shown in **Figure 6**, internal friction is maximal for a normalized interfacial shear stress τ/τ^* close to 1. Therefore, during cyclic fatigue a peak of internal friction is possible if the initial interfacial shear stress τ_0/τ^* is close to 1 and if the interfacial wear is sufficient to decrease τ/τ^* below this maximum. This effect has been observed experimentally on 2D SiC/SiC composites (**Figure 17**) after a heat treatment under vacuum leading to a removal of PyC interface by oxidation from free-oxygen atoms in the Nicalon fibers. In that case the initial interfacial shear stress τ_0 has decreased enough to be close to the maximum of internal friction and go through this maximum due to interfacial wear (Fantozzi et al., 2001; **Figure 16**).

Internal friction is an interesting parameter to analyze the evolutions of the composites during cyclic fatigue, mainly at the fiber/matrix interface level. Shear-lag modeling of equivalent 1D composite gives theoretical relation between internal friction and the normalized interfacial shear stress τ/τ^*. Hence from experimental data it is possible to assess the value of the interfacial shear stress τ (Evans, 1997). But to determine this value, the crack density of matrix cracks d has to be known to determine the value of τ^*. For example, on Hi-Nicalon/[Si–B–C] composite, the mean distance between matrix cracks is about 20 μm and internal friction is about 0.1 at 1200 °C under a peak stress of 200 MPa. These experimental data lead to a theoretical value of τ^* of 150 MPa and an apparent interfacial shear stress τ of 20 MPa.

From hysteresis stress/strain loops shapes it is also possible to assess the value of interfacial shear stress τ from the tangential elastic modulus, and an experimental decrease of τ during cyclic fatigue has been shown on SiC/[MAS] composites by this way (Evans, 1997).

During cyclic fatigue tests, even if the applied peak stress is lower than the strength of CMCs, a delayed fracture of the composite may occur, and the number of cycles necessary to obtain the fracture of the

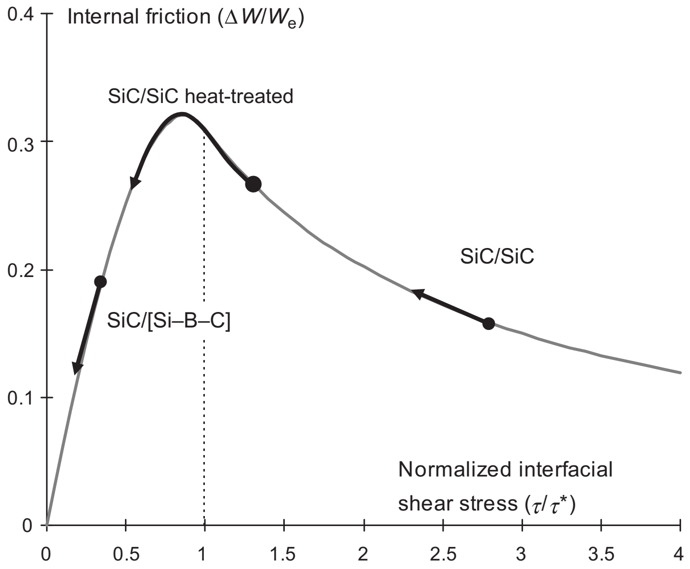

Figure 16 Theoretical evolution of internal friction during cyclic fatigue for different level of initial interfacial shear stress.

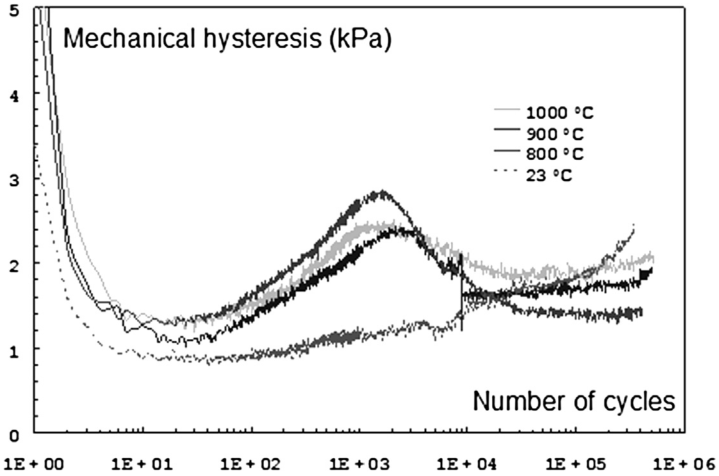

Figure 17 Effect of ageing under vacuum at different temperatures on the mechanical hysteresis at room temperature during cyclic fatigue on SiC/SiC composite.

composites corresponds to the lifetime. To study the lifetimes under cyclic fatigue for a given composite, several tests have to be performed at various levels of peak stresses until fracture of the composite or stopped after a limit number of cycles (10^6 or 10^7 cycles for example). From these tests, lifetime diagrams are plotted where each test corresponds to a point whose coordinates are the number of cycle at fracture and the peak stress. An example of such diagram is given in Figure 18. This type of diagram is very useful to summarize the performances of a given composite (monotonic strength, fatigue limit, and lifetimes under limited endurance), and also to show the effect of environment or temperatures on the fatigue properties for a given composite. This type of diagram is also interesting to compare the properties of several composites as shown in Figure 18. In this diagram, the lifetimes at high temperature under air of a CMC with a self-healing matrix are given and compared to the lifetimes at room temperature of a standard SiC/SiC of first generation. This comparison points out the better properties of the composite with self-healing matrix at high temperatures under air due to the better resistance against oxidation of this composite. Another way to illustrate these better properties is to plot lifetimes for a given peak stress as a function of temperature (Figure 19). In this figure, the comparison is done at 120 MPa between a standard Nicalon/SiC composite, a Hi-Nicalon/SiC composite and a Hi-Nicalon/[Si–B–C] composite with self-healing matrix. The better properties of the Hi-Nicalon fiber at high temperature than the Nicalon fiber is visible, as well as the better resistance against oxidation of CMCs by self-healing matrices.

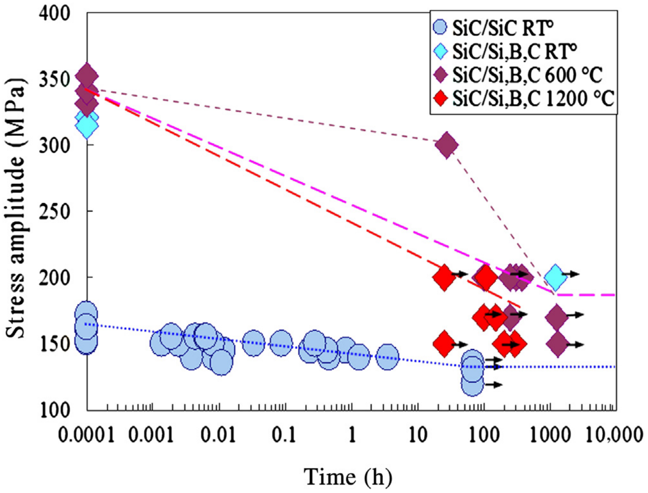

Figure 18 Lifetime diagram of SiC/SiC composite at room temperature and of SiC/[Si–B–C] at high temperature under air.

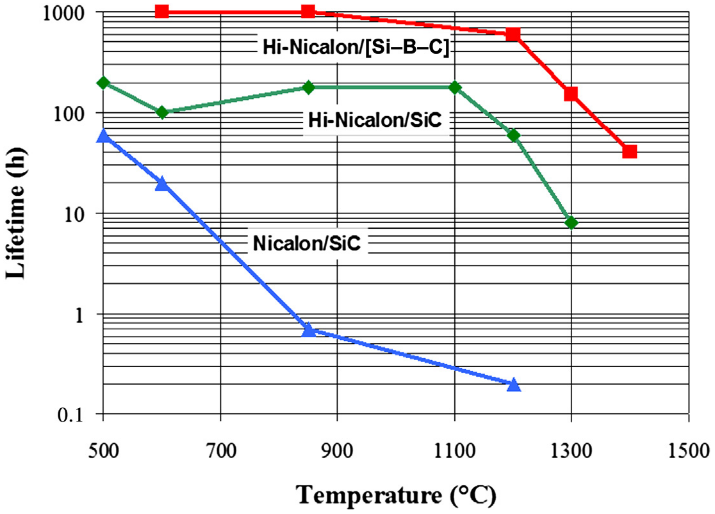

Figure 19 Effect of temperature on the lifetime under cyclic fatigue (120 MPa) under air of different composites. From Bouillon et al. (2000).

2.12.5.2 Static Fatigue

For static fatigue tests, applying a steady load on a composite points out the effects of time on the mechanical behavior, and mainly the effects of oxidation at high temperature under air.

This kind of test has been applied on SiC/[Si–B–C] composites at intermediate temperatures. This mechanical test may be conducted as follows: a steady load is applied on the composite, and periodically (between 6 and 12 h according to the duration of the test) an unloading/reloading sequence is performed to obtain stress/strain loops and to follow evolutions of the composites.

Figure 20 shows this evolution for an SiC/[Si–B–C] composite at 450 °C. Areas of stress/strain loops after a static fatigue of 1500 h under a steady stress of 150 MPa have changed during time and the strain has increased fast at the beginning of the tests, then more and more slowly. Like for cyclic fatigue, this phenomenon is attributed to a decrease of interfacial shear stress. But for static fatigue the decrease of τ is due to time-dependent phenomena like fiber/matrix PyC interface recession by oxidation. As for cyclic fatigue, the calculation of internal friction from stress/strain loops recorded during static fatigue allow to assess the decrease of τ/τ^* during time. Nevertheless, in that case also, the value of the mean distance between matrix cracks (or matrix cracks density) is required to reach the value of interfacial shear stress τ.

The evolution of the deformation during time measured experimentally by an extensometer may be calculated theoretically by the 1D micromechanical analysis developed in Section 2.12.2, by introducing a

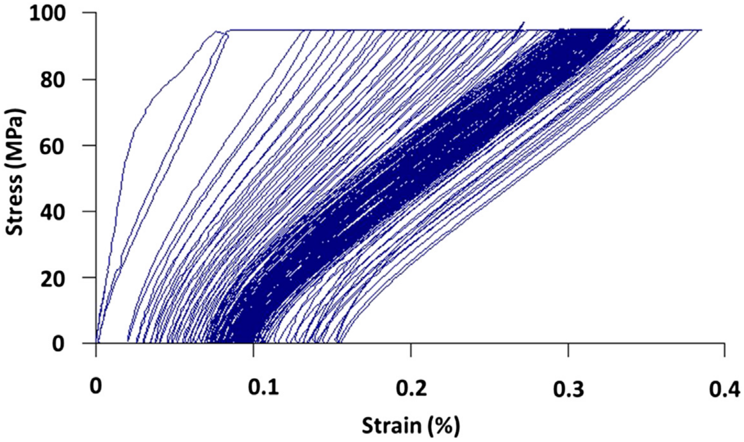

Figure 20 Experimental stress/strain loops evolution during static fatigue of a SiC/[Si–B–C] composite at 450 °C under air.

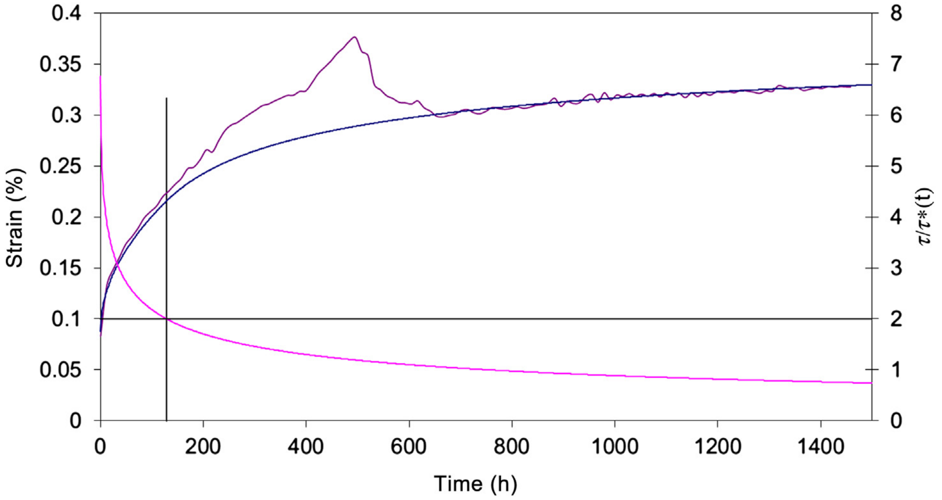

Figure 21 Experimental evolution of strain during static fatigue of SiC/[Si–B–C] composite at 450 °C under air and theoretical description based on shear-lag model.

mathematical law of τ decrease during time. An example of theoretical fit is given in Figure 21 for a SiC/[Si–B–C] composite tested at 150 MPa under air at 450 °C. On this diagram the experimental increase of the deformation during time is well described by the theoretical model. This model allows an extrapolation of this evolution for longer durations, and shows also that the overlapping of strain overloading in fibers occurs at the beginning of the test during the first hundreds of hours. Then the fibers are totally debonded but the friction between fibers and the surrounding matrix continue to decrease progressively.

During these tests fibers are also subjected to slow crack growth due to oxidation of free carbon around the SiC grains in the fibers (Gauthier & Lamon, 2009). Their embrittlement is developed, leading hence to a delayed final fracture of the composite. This phenomenon is pointed out by lifetime diagrams for a Hi-Nicalon/[Si–B–C] composite tested under air at 500 °C, as shown in Figure 22. At this temperature, this diagram shows that the lifetime decreases when the fatigue stress is higher and the relationship between lifetime and fatigue stress is theoretically described by the law:

$$t_R \cdot \sigma^n = A_0 \exp\left(\frac{E_A}{RT}\right) \tag{9}$$

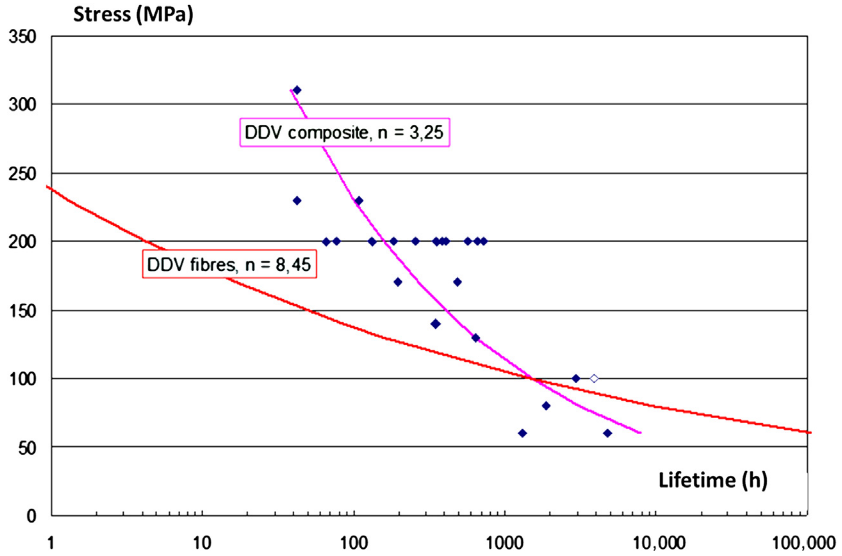

Figure 22 Lifetime diagram under static fatigue at 500 °C under air of an SiC/[Si–B–C] composite and comparison with lifetime of fibers.

where t_R is the lifetime, σ is the fatigue stress, n is a parameter characteristic of slow crack growth phenomenon, A_0 is a constant, E_A is the activation energy, R is the gas constant, and T is the absolute temperature of the test.

A comparison between static fatigue of the composite and the fibers shows that at intermediate and high stresses the lifetime of the composite is longer than the lifetime of the fibers (Moevus, 2007). This is characterized by two different values of n; n is equal to 3.25 for the composite and to 8.45 for the fibers. For this range of applied stress, slow crack growth of the fibers is controlled by diffusion of oxygen. In the composite the diffusion of oxygen toward the fiber surfaces is slowed down due to consumption of oxygen by reaction with self-healing matrices and interphases. Under lower stresses, the lifetime of the composite and fiber bundles are similar. For this low level of stresses, reaction kinetics with fiber surfaces are slower than diffusion kinetics of oxygen into the matrix crack. Hence the slow crack growth kinetics in the dry bundles and fibers of the composites are similar.

From the lifetimes obtained under static fatigue at various temperatures between 450 °C and 750 °C, the activation energy has been determined at 130 kJ mol^{-1} for the composite and 180 kJ mol^{-1} for the fibers. For this range of temperature, several mechanisms of oxidation may be involved (oxidation of self-healing matrix, oxidation of interphases between fibers and matrices) that could influence slow crack growth kinetics in fibers according to the temperature and control of the lifetime of the composites. Nevertheless, the activation energy determined experimentally for the composite give a good description of temperature effects on lifetimes below 600 °C where self-healing is low. For higher temperatures where self-healing is important, lifetime of composites are longer than those determined by the previous equation with an energy of activation equal to 130 kJ mol^{-1}.

Static fatigue corresponds to tests under steady loading performed under intermediate temperatures, where oxidation mechanisms are mainly involved in the evolution of composites during tests. At higher temperatures (more than 1000 °C for example), creep of fibers and eventually matrices may occur, leading to a different mechanical behavior and lifetimes. These phenomena are described in the next section.

2.12.6 Creep

To perform creep tests, the loading is similar to static fatigue loading (steady stress with an unloading/reloading sequence each 6 or 12 h) but the temperature is higher to enable creep of constituents and may be conducted under inert atmosphere or air. When conducted under air, oxidation phenomena act in addition to creep phenomena (Casas & Martinez-Esnaola, 2003).

During creep tests, the deformation of CMCs increases, exhibiting a transient primary stage and a second stage. Tertiary stage is seldom observed, only for very high stresses and temperatures (see **Figure 23**).

For a 2D SiC/[Si–B–C] tested under argon no oxidation occurs, but the total strain after 50 h of tensile creep at 120 MPa may reach or exceed 1% for temperatures higher than 1200 °C (Chermant et al., 2002). The creep resistance for stresses lower than 170 MPa and a temperature lower than 1200 °C is good for SiC/[Si–B–C] composites with a strain rate lower than $2 \times 10^{-8}\ \mathrm{s}^{-1}$. For stresses higher than 170 MPa and temperatures higher than 1200 °C the strain rate increases up to $10^{-7}\ \mathrm{s}^{-1}$ or more (see **Figure 24**).

The classical phenomenological approach by the general Norton formalism, linking the strain rate during the steady state to the activation energy and the stress exponent, is not relevant for CMCs, and a damage-creep approach is more adequate (Fantozzi, Chevalier, Olagnon, & Chermant, 2000). To describe and classify the different damage modes during creep, a useful parameter is the creep mismatch ratio (CMR) defined as:

$$\mathrm{CMR} = \frac{\dot{\varepsilon}_\mathrm{f}}{\dot{\varepsilon}_\mathrm{m}} \tag{10}$$

which describes the stress redistribution between the constituents of the composites ($\dot{\varepsilon}_\mathrm{f}$ and $\dot{\varepsilon}_\mathrm{m}$ being the creep strain rates of respectively the fibers and the matrix). For glass–ceramic composites CMR is usually below 1 because the creep resistance of matrices is lower than the fibers, and CMR is above 1 for ceramic matrix composites like Si_3N_4 or SiC matrices which are more creep resistant than fibers.

In the ceramic matrix CMCs, the creep mechanism takes place in two stages. Under the first loading and at the beginning the composite is mainly subjected to matrix multicracking in transverse yarns and in longitudinal

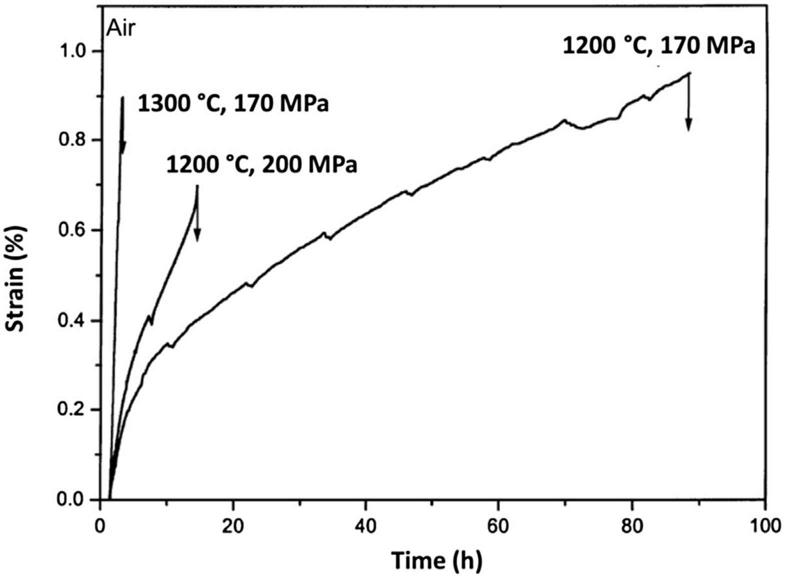

Figure 23 Creep strain versus time for an SiC/[Si–B–C] composite under air at 1200 °C (170 and 200 MPa) and at 1300 °C and 170 MPa. From Farizy et al. (2003).

yarns until saturation. Then the opening of these cracks increases progressively during time and if stress and temperature are high enough, creep of bridging fibers may appear controlling the strain rate during the steady state and the maximum strain at final fracture of the composite.

For SiC/[Si–B–C] composites under air an additional effect of oxidation is introduced leading to creation of glasses in the self-healing matrices leading to a good creep resistance up to 1200 °C and 170 MPa (Farizy et al., 2003). Nevertheless at higher temperatures, crystallization of several matrix layers and modification of Hi-Nicalon fibers may appear leading to SiC grain growth both under air and inert atmospheres. Under air, partial oxidation of fiber–matrix interfaces and matrix interlayers and glass forming in matrix cracks are observed in addition. But their effects on creep resistance of the composite require a better determination, mainly by comparison with creep tests under inert atmosphere.

Creep and cyclic fatigue are two different loading modes leading to delayed fracture after a long duration. It is important to compare these two types of damage mode to determine if a steady loading or a periodic loading is

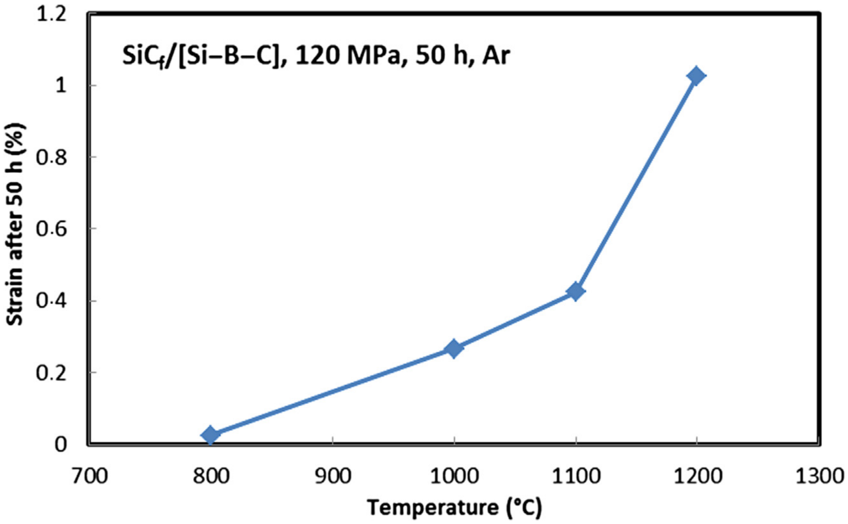

Figure 24 Effect of temperature on creep strain after 50 h under 120 MPa of an SiC/[Si–B–C] composite under inter atmosphere. From Chermant et al. (2002).

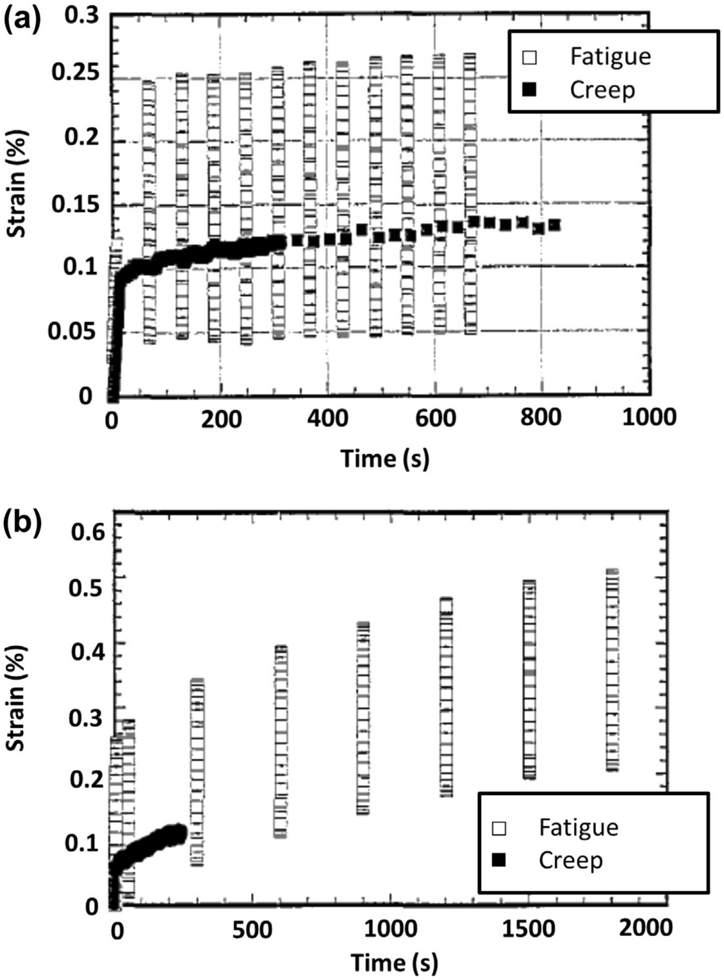

Figure 25 Comparison between cyclic fatigue and creep under argon on SiC/SiC at (a) 1000 °C and 180 MPa and (b) 1300 °C and 120 MPa. From Zhu et al. (1997).

more damaging for these CMCs at high temperatures. Such comparison has been done by Zhu et al. (Zhu et al., 1997, Zhu, Mizuno, Kagawa, & Mutoh, 1999) on a standard SiC–SiC at 1000 and 1300 °C under inert atmosphere (**Figure 25**). This study shows that at 1000 °C fatigue, creep resistance are similar, but at 1300 °C creep resistance is lower than fatigue resistance. At 1000 °C fracture of the composite under cyclic fatigue is due to interfacial wear by cyclic loading and creep of fibers. The effect of interfacial degradation by cyclic loading is visible on the maximum strain of the composite which is higher under cyclic fatigue than under creep test. This may be due to a lower interfacial shear stress under cyclic fatigue. At 1300 °C creep of fibers is predominant, leading to lower lifetimes of the composites.

2.12.7 Conclusions

CMCs demonstrate nonbrittle mechanical behavior due to the high strength of their fibers, and because of optimized fiber/matrix interactions after matrix multicracking. Interactions between fibers and matrix act mainly at the interface level and when fibers and matrix are debonded in a zone close to a matrix crack, bridging fibers slide with friction in the surrounding matrix. This friction is characterized by the interfacial frictional shear stress (τ) and is the main phenomenon leading to energy dissipation during cyclic fatigue of CMCs.

Under monotonic tension, their mechanical behavior is nonlinear due to the multicracking of matrix and fiber bridging, and under cyclic or static fatigue at high temperature, interfacial effects change with the number of cycles or during time leading to a change of the energy dissipation and the maximum strain. Under cyclic fatigue wear of fibers and the surrounding matrix may explain the decrease of interfacial shear stress, and under static fatigue a recession by oxidation may also lead to a decrease of interfacial shear stress. The introduction of these mechanisms in a shear-lag model can help describe mechanical behavioral changes with the number of cycles or with duration. At higher temperatures, creep of fibers may occur and be predominant, leading to high strain rates and a limited lifetime.

For composites with SiC fibers and SiC matrices, lifetime under fatigue and creep may be affected by oxidation, mainly at the fiber/matrix interfaces and by slow crack growth in the fibers. Hence protection of interphases and fibers allows longer lifetimes at high temperatures in air, as for example observed on self-healing SiC matrices.

Nowadays, the major problem concerning fiber-reinforced CMCs is linked to the evaluation and assessment of long lifetimes under various conditions of loading, test temperatures, and atmospheres. These conditions involve different damage mechanisms: wear and oxidation of interphases leading to changes of interfacial characteristics, evolution of matrix cracks networks and their self-healing, creep of fibers at high temperatures. It would be significant to determine the relationships between these damage mechanisms and the lifetimes of the composites, more particularly at high, intermediate and low temperatures where oxidation resistance is different. The monitoring of damage during use or testing is necessary to follow the degradation of the mechanical properties and to evaluate the remaining lifetime. For example acoustic emission has been used in that sense (Moevus, 2007; Moevus, Rouby, Godin, et al., 2008). In addition micromechanical analysis and modeling is a way to forecast lifetime with a better accuracy, mainly when lifetimes are difficult to reach experimentally. Nevertheless a good theoretical description of critical damage is required and is ongoing. An outcome such as improving the resistance against oxidation in air by using self-healing matrices is a good example.

References

Aveston, J., Cooper, G. A., & Kelly, A. (1971). Single and multiple fracture. In *Proc. of conference on the properties of fibre composites of the national physical laboratory* (pp. 15–26). Guildford, UK: IPC Science and Technology Press.

Bouillon, E., Abbe, F., Goujard, S., Pestourie, E., Habarou, G., & Dambrine, B. (2000). Mechanical and thermal properties of a self-healing matrix composite and determination of the lifetime duration. *Ceramic Engineering and Science Proceedings, 21*, 459–467.

Casas, L., & Martinez-Esnaola, J. M. (2003). Modelling the effect of oxidation on the creep behavior of fibre-reinforced ceramic matrix composites. *Acta Materialia, 51*, 3745–3757.

Chermant, J. L., Boitier, G., Darzens, S., Farizy, G., Vicens, J., & Sangleboeuf, J. C. (2002). The creep mechanism of ceramic matrix composites at low temperature and stress, by a material science approach. *Journal of the European Ceramic Society, 22*, 2443–2460.

Evans, A. G. (1997). Design and life prediction issues for high-temperature engineering ceramics and their composites. *Acta Materialia, 45*, 23–40.

Evans, A. G., Zok, F. W., & McMeeking, R. M. (1995). Fatigue of ceramic matrix composites. *Acta Metallurgica et Materialia, 43*, 859–875.

Fantozzi, G., Chevalier, J., Olagnon, C., & Chermant, J. L. (2000). Creep of ceramic matrix composites. In A. Kelly, & C. Zweben (Eds.), *Comprehensive composite materials* (pp. 115–162). Elsevier.

Fantozzi, G., & Reynaud, P. (2009). Mechanical hysteresis in ceramic matrix composites. *Materials Science and Engineering A, 521--522*, 18–23.

Fantozzi, G., Reynaud, P., & Rouby, D. (2001). Thermomechanical behaviour of long fibres ceramic-ceramic composites. *Sil Industrial, 66*, 109–119.

Farizy, G., Chermant, J. L., Sangleboeuf, J. C., & Vicens, J. (2003). SiC_f–SiBC composites: microstructural investigations of the as received material and creep tested composites under an oxidative environment. *Journal of Microscopy, 210*, 176–186.

Filipuzzi, L., & Naslain, R. (1994). Oxidation mechanisms and kinetics of 1D-SiC/C/SiC composite materials: II, modeling. *Journal of the American Ceramic Society, 77*, 467–480.

Filipuzzi, L., Camus, G., & Naslain, R. (1994). Oxidation mechanisms and kinetics of 1D-SiC/C/SiC composite materials: I, an experimental approach. *Journal of the American Ceramic Society, 77*, 459–466.

Fox, D. S., & Nguyen, Q. N. (1995). Oxidation kinetics of enhanced SiC/SiC. *Ceramic Engineering and Science Proceedings, 16*, 877–884.

Frety, N., Molins, R., & Boussuge, M. (1992). Oxidizing ageing effects on SiC-SiC composites. *Journal of Materials Science, 27*, 5084–5090.

Gauthier, W., & Lamon, J. (2009). Delayed failure of Hi-Nicalon and Hi-Nicalon S multifilament tows and single filaments at intermediate temperatures (500°–800 °C). *Journal of the American Ceramic Society, 92*, 702–709.

Halverson, H. G., & Curtin, W. A. (2002). Stress rupture in ceramic-matrix composites: theory and experiment. *Journal of the American Ceramic Society, 85*, 1350–1365.

Lamicq, P. J., & Jamet, J. F. (1995). Thermostructural CMCs: an overview of the French experience. In A. G. Evans, & R. Naslain (Eds.), *Proceedings of the second international conference on high-temperature ceramic-matrix composites* (Vol. 57; pp. 1–12). Westerville, USA: Ceramic Transactions.

Lamon, J. (Ed.). (2005). *Recent advances in ceramic-matrix composites.* Cachan, France: Lavoisier.

Moevus, M. (2007). Mécanisme d’endommagement, émission acoustique et durée de vie en fatigue statique du composite SiCf/[Si-B-C] aux températures intermédiaires. PhD thesis, France: INSA de Lyon.

Moevus, M., Rouby, D., Godin, N., R’Mili, M., Reynaud, P., Fantozzi, G., et al. (2008). Analysis of damage mechanisms and associated acoustic emission in two SiC/SiBC composites exhibiting different tensile behaviours. Part I: damage pattern and acoustic emission activity. *Composites Science and Technology, 68*, 1250–1257.

Moevus, M., Godin, N., R'Mili, M., Rouby, D., Reynaud, P., Fantozzi, G., et al. (2008b). Analysis of damage mechanisms and associated acoustic emission in two SiC/SiBC composites exhibiting different tensile behaviours. Part II: unsupervised acoustic emission data clustering. *Composites Science and Technology, 68*, 1258–1265.

Reynaud, P., Rouby, D., & Fantozzi, G. (2005). Cyclic fatigue behaviour at high temperature of a self-healing ceramic matrix composite. *Annales de Chimie Science des Matériaux, 30*, 649–658.

Rouby, D., Penas, O., & Reynaud, P. (2001). Anelastic behaviour of ceramic matrix composites during cyclic fatigue. In W. Krenkel, R. Naslain, & H. Schneider (Eds.), *Proc. of high temperature ceramic matrix composites 4* (pp. 429–439). Weinheim, Germany: Wiley-Vch.

Ruggles-Wrenn, M. B., Mall, S., Eber, C. A., & Harlan, L. B. (2006). Effects of steam environment on high temperature mechanical behavior of Nextel^{TM}720/alumina (N720/A) continuous fibre ceramic composite. *Composites: Part A, 37*, 2029–2040.

Solti, J. P., Robertson, D. D., & Mall, S. (2000). Estimation of interfacial properties from hysteretic energy loss in unidirectional ceramic matrix composites. *Advanced Composite Materials, 9*, 161–173.

Staehler, J., Mall, S., & Zawada, L. (2003). Frequency dependence of high-cycle fatigue behaviour of CVI C/SiC at room temperature. *Composites Science and Technology, 63*, 2121–2131.

Vandenbulke, L., Fantozzi, G., Goujard, S., & Bourgeon, M. (2005). Outstanding ceramic matrix composites for high temperature applications. *Advanced Engineering Materials, 7*, 137–142.

Viricelle, J. P., Goursat, P., & Bahloul-Hourlier, D. (2001). Oxidation behaviour of a multi-layered ceramic-matrix composite $(SiC)_f/C/(SiBC)_m$. *Composites Science and Technology, 61*, 607–614.

Xu, H. K., Braun, L. M., Ostertag, C. P., & Krause, R. F. (1995). Failure modes of SiC/Si_3N_4-matrix composites at elevated temperatures. *Journal of the American Ceramic Society, 78*, 388–394.

Zawada, L. P., Butkus, L. M., & Hartman, G. A. (1991). Tensile and fatigue behaviour of silicon carbide fiber-reinforced aluminosilicate glass. *Journal of the American Ceramic Society, 74*, 2851–2858.

Zhu, S., Mizuno, M., Kagawa, Y., & Mutoh, Y. (1999). Monotonic tension, fatigue and creep behavior of SiC-fiber-reinforced SiC-matrix composites: a review. *Composites Science and Technology, 59*, 833–851.

Zhu, S., Mizuno, M., Kagawa, Y., Cao, J., Nagano, Y., & Kaya, H. (1997). Creep and fatigue behavior of SiC fiber reinforced SiC composite at high temperatures. *Materials Science and Engineering, A225*, 69–77.

Zhu, S., Mizuno, M., Nagano, Y., Cao, J., Kagawa, Y., & Kaya, H. (1998). Creep and fatigue behavior in an enhanced SiC/SiC composite at high temperature. *Journal of the American Ceramic Society, 81*, 2269–2277.

2.13 Resistance to Contact Deformation and Damage of Hard Ceramics

Emilio Jiménez-Piqué, Luis Llanes, and Marc Anglada, Departament de Ciència dels Materials i Enginyeria Metal·lúrgica,
Universitat Politècnica de Catalunya · Barcelona Tech, Barcelona, Spain

© 2014 Elsevier Ltd. All rights reserved.

Glossary

Hertzian Contact Blunt contact produced between two spheres or between a sphere and a plane.

Blunt contact Elastic contact produced between two bodies, although a fracture can occur.

Ring crack Shallow crack appearing close to the indentation area in brittle materials.

Cone crack Unstable progression of the ring crack inside the material, at a given angle with the surface.

Quasiplasticity Inelastic deformation caused by a large amount of microcracks underneath the contact area, driven by the shear stress produced under contact.

Nomenclature

a	radius of contact
c	cone crack length
E	Young's modulus of the indented material
E_i	Young's modulus of the indenter
E_{eff}	effective Young's modulus
H	hardness
K_{Ic}	mode I fracture toughness
K_I	mode I stress intensity factor
P	applied load
P_c	critical load to produce fracture (ring crack/cone crack)
P_Y	critical load to produce quasiplastic damage
p_0	contact pressure
R	radius of the indenter
α	cone crack angle
ν	Poisson's ratio of the indented material
ν_i	Poisson's ratio of the indenter
σ_{tm}	tensile stress produced along the contact perimeter
τ_m	shear stress

2.13.1 Introduction

Due to their inherent hardness and stiffness, as well as their corrosion and high temperature resistance, advanced ceramics are being increasingly used in many industrial applications, from manufacturing to transportation and energy generation. However, brittleness is the limiting factor for expanding their use to other relevant applications. Being brittle implies that the strength of the component is not an intrinsic parameter, but it is dependent on the initial flaw size that translates to poor mechanical reliability. Most of the research done on

http://dx.doi.org/10.1016/B978-0-08-096527-7.00032-5

the failure of ceramics has been devoted to understanding the strength in terms of intrinsic flaws, that is, defects induced during processing. However, if damage is induced during service, similar information on how structural integrity is affected as a function of microstructure is rather scarce.

Advanced ceramics are used in many extreme applications with high thermomechanical loads. Among these, contact loadings play a significant role, as in wear components, hard body impacts, rollers, ball bearings, gears, axes, as well as biomedical and dental implants. Although these contact loadings can produce catastrophic failure directly (especially if overloading, impact, or cyclic loading is produced), in most of the cases contact loads produce small fissures or microcracks that are not critical for fracture by themselves but produce a degradation of the strength of the material. It is then important to understand the mechanics of contact loading, and the different types of damage produced in hard ceramics, in order to understand the generation and the evolution of extrinsic damage introduced in the material. This understanding is fundamental for the increased reliability and better performance of hard ceramic components.

In this framework of ideas, Hertzian (spherical) contact loading characterization provides an excellent tool for understanding the damage produced during in-service conditions. In addition, because the volume of the material tested is relatively small compared to other mechanical testing protocols, it allows for the characterization of small samples or components, as well as coatings, composites and graded materials.

Hertzian contact mechanics have been used extensively by the ceramic community, specially by Lawn and coworkers (for a review see Lawn, 1998), evidencing that it is a very effective method to (1) introduce extrinsic damage to test the damage tolerance of ceramics; (2) simulate blunt contact in-service loadings; (3) obtain indentation stress–strain curves; (4) produce stable cracks and estimate fracture toughness; and (5) study contact fatigue and stress corrosion cracking by cycling the load or maintaining the load for a given time, even in the presence of fluids or temperature.

Such an experimental and analytical approach has proven to be successful in the assessment of contact damage in polycrystalline ceramics (e.g. Giberteau, Padture, Lawn 1994; Lawn, & Wilshaw, 1975; Lawn, 1998), single crystals (Hammond & Armstrong 1988), brittle layer structures (Lawn et al., 2002), coatings (Pajares, Wei, Lawn, & Berndt, 1996; Pavon et al., 2006), and more recently in cemented carbides (Góez et al., 2012; Tarres, Ramírez, Gaillard, Jimenez-Pique, & Llanes, 2009; Zhang & Fang, 2008; Zhang, Fang, & Belnap, 2007).

In this chapter, the basics of Hertzian contact damage on hard ceramics will be reviewed, with special emphasis on Al_2O_3, SiC, and Si_3N_4. The intent is to focus on the practical issues of Hertzian indentation as well as on the relevant methodologies to extract data. For more in-depth reviews, the reader is referred to the existing reviews in the literature (Fischer-Cripps, 2000; Johnson, 1987; Lawn, 1998).

2.13.2 Experimental Setup for Hertzian Indentation

The experimental setup for Hertzian contact testing is, in most cases, quite simple. It consists of indenting at a given force a flat surface of the material to be studied with a sphere of a known material. Normally, the indenter material is harder than the target material in order to avoid deformation of the indenter. The preferred choices for indenter material are WC-based composites (particularly WC–Co and WC–Ni), diamond, and sapphire, although there is no limitation to use any material (even softer ones). Curved surfaces can also be tested as long as the radius of the material is taken into account (Eqn (3)). **Figure 1** presents a typical indentation test on a hard ceramic sample tested with a WC–Ni 10-mm sphere.

Indentation can be performed on any machine capable of applying a controlled load, from a simple hardness tester to a universal testing machine or an impact test machine. The only concern to be taken into account is that the sample and the indenter should be properly fixed, as otherwise there will be lateral movements that will invalidate the test. If the sample is lightly abraded on the surface, then there will be a lower scatter in the fracture loads (Franco, Roberts, & Warren, 1997).

From this basic setting, several improvements can be made. For example, an acoustic emission detector can be placed near the contact area in order to detect any unstable crack propagation. Likewise, this testing can be done in water or other fluids in order to simulate realistic environments (Kelly, 1999; Pavon et al., 2006).

In some cases, it is important to observe the subsurface damage produced by indentation. In this regard, the deformation or fracture during indentation was easily observed in transparent ceramics (Cook & Pharr, 1990). However, if the sample is opaque, several techniques may be implemented.

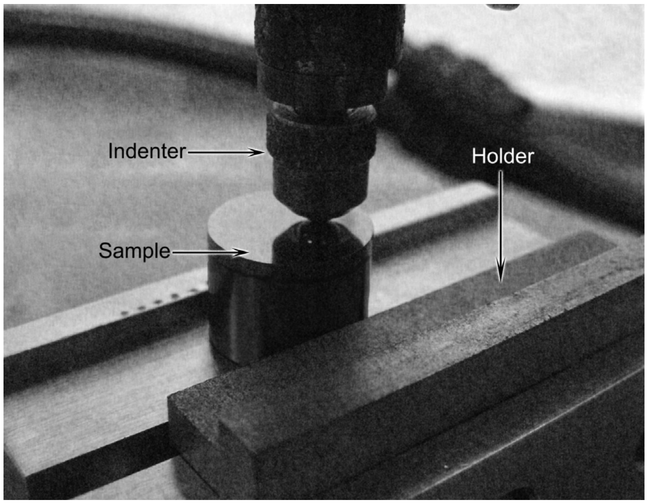

Figure 1 Typical setup of an indentation test on a hard ceramic. A WC–Co indenter with a diameter of 5 mm is pressed against a clamped specimen in a universal testing machine.

One common approach is the clamped interface technique (e.g. Cai, Stevens Kalceff, & Lawn, 1994; Giberteau, Padture, & Lawn 1994; Miranda, Pajares, Guiberteau, Deng, & Lawn, 2003). This technique consists of (1) selecting the region of interest and cutting the sample into two in that region, (2) polishing the surfaces that have been produced from cutting the sample, (3) gluing or clamping back the surfaces, (4) polishing the top surface if necessary in order to level the surface, (5) performing indentation tests at the interface, and (6) ungluing or unclamping both halves in order to observe the damage produced.

This is a relatively easy technique to observe the damage and cracks produced during indentation, which yields valuable qualitative observations. However, the production of this kind of samples can be cumbersome in hard ceramics due to the low velocity in polishing, possible grain pullout, and rounding of the edge. In addition, the damage observed may not be the same as that produced in a massive sample, because the stress state in the clamped interface is not the same as in the bulk material (Helbawi, Zhang, & Zarudi, 2001). Finally, special care has to be taken in order to ensure that no movement of the interface occurs while indenting, which can happen specially during cyclic testing.

Another approach is to indent the sample and afterward remove a given depth of material in order to see the damage, either from the top of the sample or from the side. As in the previous case, for hard ceramics, special care has to be taken to avoid grain pullout or introducing other damage. In the case of polishing from the side, it is important to ensure that the edges are not rounded and that the polishing is done perpendicularly to the surface, with a maximum of a 5° deflection. At the indentation, some material removal may happen if the sample is not constrained because of all the preexisting fissures.

These issues are avoided if the removal of the material is done from the top of the sample. If the thickness of removed material is known, the damage produced at any depth can be easily observed. If the procedure is repeated sequentially, information at different depths can be obtained. This sequence of images can be combined to yield a tomographic three-dimensional reconstruction of the cracks and damage. This method can be somewhat time consuming even in softer ceramics, but it produces reliable data on the damage created in dental porcelain (Rueda, Seuba, Anglada, & Jimenez-Pique, 2013). Sequential polishing is done normally by the mechanical removal of material, although broad ion beam techniques may also be employed. The use of Focused Ion Beam is not recommended, as typical indentations are in the order of 100 μm and focused ion beam topographies are in the order of tenths of microns. A graphical representation of the different methods for visualizing damage is presented in **Figure 2**.

Recently, some advanced observation techniques have been applied to visualize the cone crack without the need of material removal. For example, Liu et al. have successfully visualized cone cracks in Si_3N_4 by crosspolarized confocal microscopy (Liu, Sun, & Pei, 2011). On the other hand, thermal wave analysis was applied by Wei and Lawn (Wei & Lawn, 1996) to visualize both cone cracking and quasiplastic deformation.

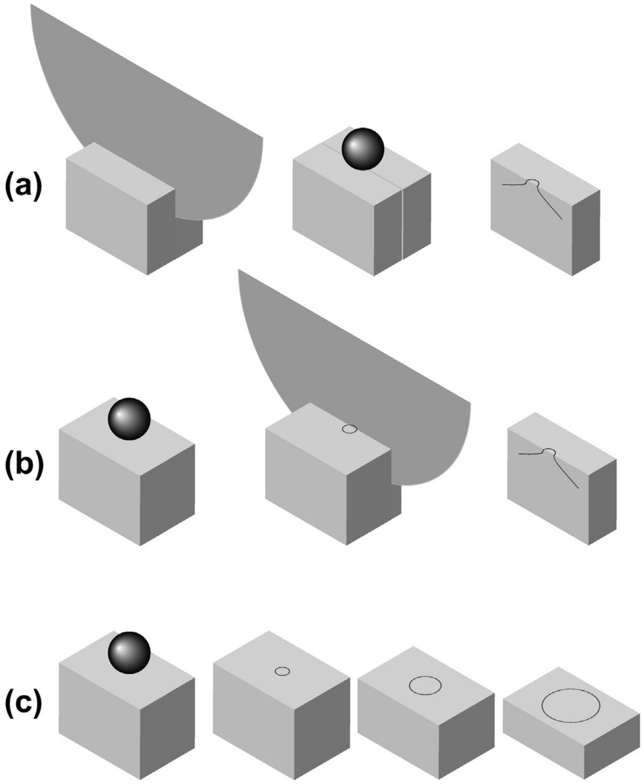

Figure 2 Methods to visualize the damage produced during indentation: (a) Clamped interface: the sample is cut and polished and clamped back, indentation is performed, and the sample is unclamped later for visualization. (b) Inspection of the damage produced by cross-sectioning the sample after the test. (c) Sequential removal of surface material to visualize the subsurface damage.

2.13.3 Mechanics of Elastic Spherical Contact

The elastic contact between two bodies was first described by Hertz in 1882, and the equations describing this response are usually known as Hertzian equations (Hertz, 1896). Hertz showed that, when a sphere of radius R is pressed against a flat solid, the relationship between the contact radius (a) and the load (P) for small penetration depths equals to

$$a^3 = \frac{3}{4}\frac{PR}{E_{\mathrm{eff}}} \tag{1}$$

where E_{eff} is the effective modulus between the sample and the indenter, which is defined as

$$\frac{1}{E_{\mathrm{eff}}} = \frac{1-\nu^2}{E} + \frac{1-\nu_{\mathrm{i}}^2}{E_{\mathrm{i}}} \tag{2}$$

with the subscript i indicating the indenter material (e.g. for diamond, $E_{\mathrm{i}} = 1140$ GPa and $\nu_{\mathrm{i}} = 0.07$; for alumina $E_{\mathrm{i}} = 380$ GPa and $\nu_{\mathrm{i}} = 0.28$, and for WC–Co, depending on the grade, $E_{\mathrm{i}} = 450$–700 GPa and $\nu_{\mathrm{i}} = 0.21$–0.24).

If the tested material has a radius of curvature (R_{m}), then instead of using the radius of the indentation sphere in the equations, the effective radius of curvature (R') has to be used:

$$\frac{1}{R'} = \frac{1}{R_{\mathrm{m}}} + \frac{1}{R} \tag{3}$$

The mean pressure between the indenter and the material (p_0) is

$$p_0 = \frac{P}{\pi a^2} = \frac{4E_{\mathrm{eff}}}{3\pi}\left(\frac{a}{R}\right) \tag{4}$$

In the case of spherical indentation, by plotting p_0 against a/R it is possible to display the stress–strain contact relationship. These types of curves are very useful to study the elastic range and the onset of inelastic deformation. However, they have to be treated with care when analyzing the plastic region, as it cannot be directly compared with a uniaxial test.

If the indenter is instrumented, that is, the displacement of the indenter (h) is recorded together with the load, the relationship between load and displacement is

$$P = \left(\frac{4}{3}E_{\mathrm{eff}}\sqrt{R}\right)h^{3/2} \tag{5}$$

The maximum tensile stress (σ_{tm}) is produced along the contact perimeter of the contact, and is equal to

$$\sigma_{\mathrm{tm}} = \frac{1}{2}(1-2\nu)p_0 \tag{6}$$

The maximum shear stress (τ_{m}) is produced beneath the indentation axis at a depth close to $0.5a$, and is equal to

$$\tau_{\mathrm{m}} = 0.46p_0 \tag{7}$$

In most materials, and according to the Tresca criterion, when the value of τ_{m} reaches a certain limit ($\tau_{\mathrm{m}} = \sigma_{\mathrm{y}}/2$ where σ_{y} is the yield strength of the material), the material will start to plastically flow and create a permanent deformation, making a transition from an elastic response to an elastoplastic response. This criterion has been also invoked to explain the nucleation of the dislocations during pop-in events (Gaillard, Tromas, & Woirgard, 2003; Lorenz et al. 2003). In this case, p_0 will equal the hardness of the material. However, hard ceramics have high yield stress, and other inelastic deformation mechanisms may be activated before dislocation movement or twin formation are active.

2.13.4 Damage in Hard Ceramics

Equations (6) and (7) summarize a competition between two stress components that will produce two different types of damage. One stress is tensile at the surface (Eqn (6)), and the other is shear beneath the surface (Eqn (7)).

On the one hand, tensile stresses around the contact area will trigger the growth of surface flaws around the indentation to produce a shallow ring crack (Warren, Hills, & Dai, 1995). This crack is usually a few microns in depth and has a radius of around 1.12 times the contact radius. If the load is increased, the crack will then propagate into the material at an angle with the surface, generating a crack with truncate cone geometry. This type of crack is known as cone crack, and has been thoroughly studied in the literature (Frank & Lawn, 1967). Because the load comes from an indentation, as the crack progresses into the material the stress field diminishes. This will cause the stress intensity factor to decrease despite the increase in the crack length, down to a value lower than the fracture toughness of the material, and consequently the crack stops. Further increases in the load will produce a stable growth in the cone crack length. The critical load to produce cone cracks scales linearly with the radius of the indenter for a range of radius up to several millimeters, and not with the contact area. This dependency is known as Auberbach's law (Auberbach, 1891) and it is a consequence of the highly decreasing stress fields generated by indentation, as explained by Frank and Lawn (Frank & Lawn, 1967).

On the other hand, another type of damage is produced by shear stresses underneath the surface at a depth of around $0.5a$. This damage consists of the microcracking of the material by a K_{II} type of load (as the material is under hydrostatic compression), and it is generally known as quasiplastic damage. The microcracking of the material will produce an inelastic deformation of the material, and a visible imprint in the surface (Lawn, Padture, Cai, & Guiberteau, 1994). Because shear stress controls the deformation, this type of damage is known as quasiplasticity, although no relevant dislocation movement may be involved.

2.13.4.1 Cone Cracking versus Quasiplastic Damage

Knowing which type of damage will be produced at the lowest load is relevant to understand the degradation of mechanical properties and the subsequent failure of hard ceramics. These two types of damage are essentially

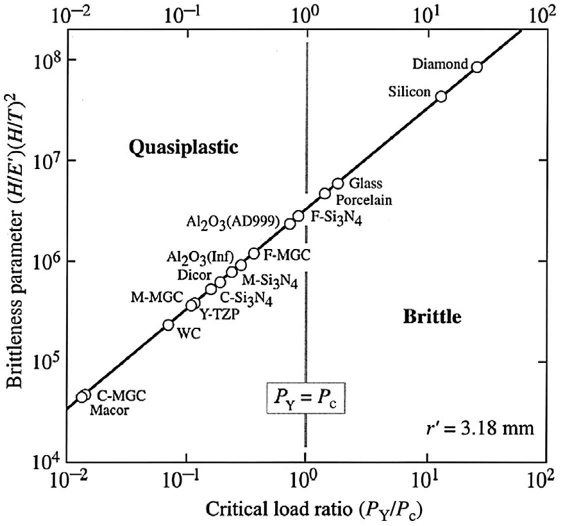

Figure 3 Predictive index as developed by Lawn and coworkers to estimate whether the first damage to occur will be cone crack or quasiplastic damage. Observe that all data are for a WC–Co indenter of a 3.18-mm radius. The change in the indenter material or size may result in a switch in the damage type. Observe that most hard ceramics are close to the region where both types of damage will appear at different loads. Reproduced from Rhee et al. (2001) with permission.

controlled by the geometry of the indenter and the mechanical properties of the material. Lawn and coworkers have developed a relationship to predict which type of damage will occur first (Rhee, Kim, Deng, & Lawn, 2001) in terms of the ratio between the critical load for quasiplastic damage (P_Y) and the one for cone cracking (P_c):

$$\frac{P_Y}{P_c} = D(\nu)\frac{H^3}{E_{\text{eff}}K_{\text{Ic}}^2}R \tag{8}$$

where $D(\nu)$ is a constant that depends on the Poisson ratio (ν) of the material and should be experimentally calibrated. H is the hardness of the material and K_{Ic} is the fracture toughness. If $P_Y/P_c > 1$, then the sample develops cone cracking. Otherwise, the material deforms inelastically by quasiplastic deformation. Figure 3 (extracted from Rhee et al., 2001) presents graphically such a predictive index for a variety of materials for a fixed indenter size.

By inspecting Eqn (8), it is straightforward to see that brittle materials with a low fracture toughness, such as glass or porcelain, as well as very hard materials such as diamond, will develop cone cracks under spherical indentation (except with very small indentation radii typical of nanoindentation testing).

Hard and tough ceramics, such as SiC, Al_2O_3, or Si_3N_4, yield values in the vicinity of 1, and will swap between the two damages depending on the radius and the material of the indenter used and, particularly, between the precise values of the mechanical properties, such as hardness or fracture toughness.

These mechanical properties are dependent on microstructural features and processing routes and a change in these can yield very different indentation responses. In this respect, Figure 4, taken from the work of Guiberteau, Padture, and Lawn (Guiberteau et al., 1994), presents the behavior of the Hertzian indentation in alumina with different grain sizes. It can be seen that for small grain sizes (and hence, a relatively low K_{Ic} and high H) the material presents a well-developed cone crack, whereas for large grain sizes (i.e. a relatively high K_{Ic} and relatively low H), the material presents quasiplastic damage.

However, it is also usual that both damages coexist in a narrow range of loads, as presented in Figure 5, especially for materials such as alumina, silicon carbide, or silicon nitride. In this case, a critical evaluation regarding the effective critical load has to be made as both damage types will be simultaneously present in the material.

2.13.4.2 Can the Fracture Toughness be Calculated from Cone Cracking?

If a cone crack is generated from the indentation, it should be, in theory, easy to estimate the fracture toughness of the material. Considering that the applied load is known, it could be approached following a procedure

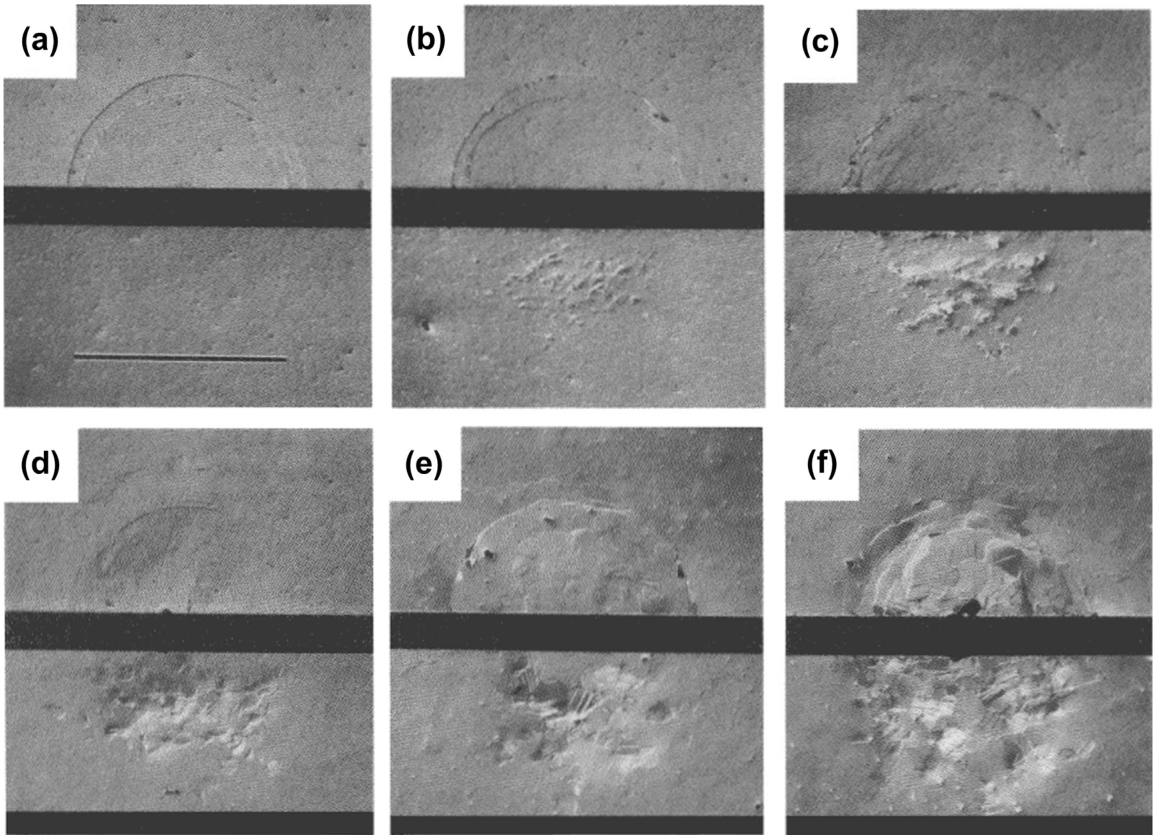

Figure 4 Hertzian damage on alumina with increasing grain sizes from fine (a) to coarse (f) indented under the same conditions. It is seen how a change in the microstructure produces a transition between damage modes. Scale bar corresponds to 550 μm. Figure reproduced from Guiberteau, Padture and Lawn (1994) with permission.

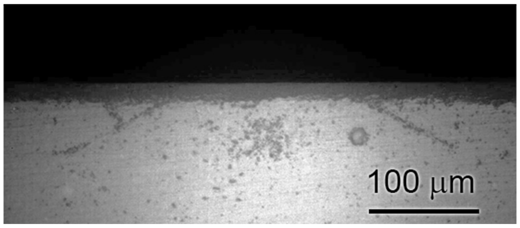

Figure 5 Cross-section of an indented alumina (grain size is 3 μm) with a WC–Co sphere at 350 N. Both cone crack and quasiplastic damage can be seen, as the critical loads to generate both damages are very close.

similar to the one used in Vickers indentation. However, this is not the case, as there are no analytical universal formulas for calculating fracture toughness.

Using spherical indentation to estimate K_{Ic} is an attractive method because only a small volume of the material is required, and a fracture is produced in the elastic regime (if no quasiplasticity is produced). The relationship between the critical load to produce a crack (P_{c}) and K_{Ic} can be expressed as (Fischer-Cripps, 1997)

$$P_{\mathrm{c}} = \left(\frac{a^3\pi^3}{4(1-\nu)\phi(c/a)}\right)^{1/2} K_{\mathrm{Ic}} \tag{9}$$

where c is the crack length and $\phi(c/a)$ is an integral without an analytical solution, whose solution depends on the mechanical properties of both the material and the indenter. Because there is no analytical solution and the results are very sensitive to the variations of ν and to the material used as an indenter, Hertzian contact is not extensively used to measure K_{Ic}.

There are, however, several methodologies based on Hertzian contact and developed to measure the fracture toughness of brittle materials, especially the one proposed by Warren and coworkers (Roberts, Lawrence, Bisrat, Warren, & Hills, 1999; Warren, 1995) where the relationship between P_{c} and K_{Ic} equals to

$$K_{\mathrm{Ic}} = \left(\frac{E_{\mathrm{eff}} P_{\mathrm{c}}}{C(\nu) R}\right)^{1/2} \tag{10}$$

where $C(\nu)$ is a numerical parameter that depends on ν (calibrated for some materials by Warren, 1995). However, in order to apply this equation, both the indenter and the material should have the same elastic modulus (Warren & Hills, 1994) and the contact should be frictionless (Paliwalw, Tandon, Buchheit, & Rodelas, 2011).

2.13.4.3 Contact Damage and Strength

Depending on the type of damage induced in the ceramic component, the strength degradation will proceed in different ways: in the case of a cone crack, the growth will be unstable until a certain length c. The length of the cone cracks is related to the applied load by

$$P = K_{\mathrm{Ic}} \frac{(c + a/\cos\alpha)^{3/2}}{\chi} \tag{11}$$

where α is the cone base angle and χ a geometric parameter. If the cone crack is larger than the natural defects of the material, then there will be a sudden drop in the strength, as the failure of the component will start from the cone crack (Ceseracciu, Jimenez-Pique, Fett, & Anglada, 2008; Lawn, Wiederhorn, & Johnson, 1975), and not from a natural defect. If the sample is loaded with larger loads, the cone crack will grow stably and there will be degradation in strength with increasing indentation load, but without any further drops.

Materials with a quasibrittle behavior will generate an array of microcracks that will grow underneath the indenter. This means that the microcracks will grow steadily and that the degradation in strength will be smooth.

Therefore, ceramics with a quasibrittle behavior will be more damage tolerant than brittle ceramics, in the sense that the strength will deteriorate progressively without a sudden drop (Lawn, Lee, Peterson, & Wuttiphan, 1998; Lee & Lawn, 1998). In contrast, brittle ceramics are usually harder and perform better in wear tests (Cho, Hockey, Lawn, & Bennison, 1989). Therefore, when choosing a ceramic for a contact application it is very important to foresee all the mechanical solicitations that the component will suffer, and to not make the material selection just based on a single parameter (e.g. hardness). Similar trends are found for composite materials such as cemented carbides, although here the analysis of the experimental data is more complex because the transition from brittle to quasiplastic damage modes is more gradual (Goez et al., 2012).

2.13.4.4 Angle of the Cone Crack

As said before, the generation of a cone crack will result in a sudden decrease in the mechanical strength of the material, which will result in lowering the reliability of the component. Therefore, it is important to impede the generation of the cone crack by materials with enhanced fracture toughness or with damage tolerance, either by a quasibrittle approach or by other strategies such as laminate composites (Bermejo et al., 2006; Bermejo et al., 2007; Clegg, Kendall, Alford, Button, & Birchall, 1990; Rao, Sanchez-Herencia, Beltz, McMeeking, & Lange, 1999; Sanchez-Herencia, Pascual, He, & Lange, 1999).

The first estimations of such angles were based on the analysis of the principal stresses of the uncracked body, assuming that the crack will follow the direction orthogonally to the greatest tensile stress. However, as the crack propagates, the stress field is modified and the trajectories should necessarily be different. This was overlooked in the past, as in the works of Frank and Lawn (1967), which set the foundation of the topic. The cone crack trajectory observed by these authors in a soda-lime glass matched quite well with the predicted path of 21°, but later it was found that an unrealistic Poisson ratio of 0.3 was assumed in the calculation, whereas the real value is around 0.18 (Lawn, Wilshaw, & Hartley, 1974).

Table 1 Prediction of the cone crack geometry for alumina only taking account of the Poisson's ratio, and observed values. The discrepancy disappears if the R-curve is taken into account

Material	*Relative crack length (c/a)*	*Cone crack angle*
Calculated (no R-curve)	2.8	18.5°
Experimental (with R-curve)	1.8 ± 0.3	27 ± 2°

Kocer and Collins (Kocer & Collins, 1998; Kocer, 2002) and Fett et al. (Fett, Rizzi, & Diegele, 2004) noted that the Poisson ratio will influence the cone crack geometry. Both authors obtained more accurate results with methods based on the finite-element (FE) analysis of the stress field on cracked materials, applied, respectively, to an incremental crack propagation model and to the determination of the weight functions. Results from these authors are in agreement with the experimental angles in glasses reported in the literature; however, disagreement with experimental observations was found for polycrystalline materials, such as alumina or silicon nitride.

There are two other material parameters that strongly affect the geometry of the cone crack, assuming that the crack is larger than the microstructure and that can be altered by material engineering: R-curve and residual stress (Ceseracciu, Anglada, & Jimenez-Pique, 2008).

The R-curve is relevant in many polycrystalline ceramics, especially if they fracture along grain boundaries. In this case, the crack path is tortuous and friction between adjacent grains on the opposite lips of the crack acts as an applied stress. This opposes both opening and sliding forces and progressively increases the resistance to crack propagation, up to a value coinciding with a crack length equal to the zone of effective shielding. This friction will result in an increase in the effective fracture toughness as the crack length increases. Of course, several other mechanisms can contribute to the R-curve behavior such as crack bridging, phase transformation, or microcrack nucleation.

In principle, R-curve materials are always desired for increasing the resistance to crack growth and reducing the length of the cracks. However, in the case of cone cracking, the situation is not so straightforward. While R-curves will indeed decrease the crack length, the mode II present in the shielding will effectively make the angle more acute. **Table 1** presents the comparison between the experimental cone crack geometry of an alumina with a grain size of approximately 3 μm with the predicted values if no R-curve existed (Ceseracciu et al., 2008).

Therefore, a toughening mechanism such as crack bridging effectively decreases the crack length, but at the price of increasing the cone crack angle as well (Widjaja, Ritter, & Jakus, 1996).

A more effective way of decreasing the length and angle of the cone crack is by the use of residual stresses. The introduction of compressive stresses at the surface will effectively decrease both the length and angle of the crack, increasing the resistance to strength degradation by contact loadings. These residual stresses can be introduced by a variety of methods that do not alter much the microstructure of the material, such as by thermal treatments, functional gradient microstructure (Jitcharoen, Padture, Giannakopoulos, & Suresh, 1998), or laminates (Jimenez-Pique et al., 2006).

In **Figure 6** a plot of the crack trajectories simulated by finite element method (FEM) is presented (Ceseracciu et al., 2008). It is seen how the introduction of compressive residual stresses decreases the angle of the cone crack, whereas the introduction of tensile stresses increases the angle of the crack with the resulting decrease of strength.

From this work, the variation of angle as a function of the residual stress (σ_{res}) can be taken as approximately linear, and approximated to

$$\Delta\alpha \propto \frac{\sigma_{\text{res}}}{p_0} \cdot \frac{c}{a} \tag{12}$$

2.13.4.5 Elastic Modulus of the Indenter

Most investigations reported in the literature use a hard sphere, usually of WC–Co to perform Hertzian testing. This choice is very convenient because the sphere will remain elastic for the whole test for most materials and will not fracture or deform, as well as being easy to obtain at an affordable price. However, several authors do

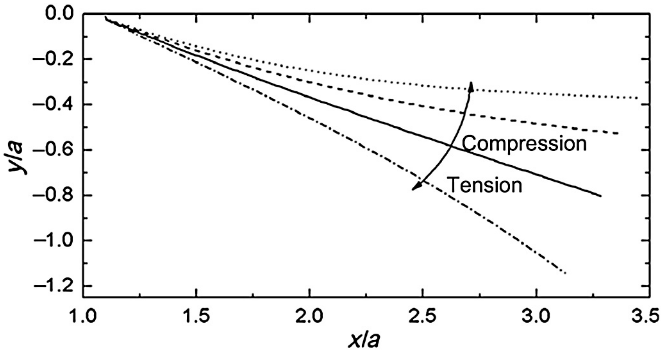

Figure 6 Crack path trajectories calculated by the FEM under different residual stress levels. Tensile residual stresses produce an increment in both the angle and the length of the cone crack, both being features detrimental to residual stress. Reproduced from Ceseracciu, Anglada, Jimenez-Pique (2008) with permission.

not take into account the importance of the elastic mismatch between the indenter and the material, as pointed out by Warren and Hills (1994).

There are two main issues to consider when indenting with dissimilar materials: (1) The stress fields, and hence the critical load for fracture will be altered; and (2) there will be a relative displacement between the material and the indenter and friction will play a relevant role (Paliwalw et al., 2011).

These two effects cause the load for producing cone cracks to increase as the relative elastic modulus of the indenter increases. In addition, if cyclic loads are being applied, the relative displacement between the indenter and material will result in wear around the contact area. For an excellent paper on the subject, see Wereszczak, Daloz, and Strong (2011).

2.13.4.6 Cyclic Loading and Prolonged Loading

Hertzian contact is an attractive technique to study fatigue and stress corrosion cracking properties of materials due to the small volumes used and the resemblance with real loading conditions. However, the analysis of contact data is not straightforward due to the complex stress field and the different types of damages produced. First of all, if the material is brittle or quasiplastic, it will behave differently under cyclic loading. In addition, for brittle materials, several types of cracks can be used to study fatigue: ring crack, cone crack, or inner secondary cracks that appear during cyclic loading.

First of all, the appearance of a superficial ring crack can be monitored as a function of the number of cycles or the time under contact. This is an easy to implement technique, which can be used to relate the number of cycles to effective failure with the applied load as a function of the Paris exponent, by either considering that the ring crack coalesces from different microcracks (Pavon, Jimenez-Pique, Anglada, Saiz, & Tomsia, 2006) or that it grows around the perimeter with a small increase in the depth (Jimenez-Pique, Ceseracciu, Chalvet, Anglada, & de Portu, 2005). However, a ring crack is shallow and may have a minor impact on the strength degradation of the material.

Cone crack propagation under cyclic (Guiberteau, Padture, Cai, & Lawn, 1993) and static loads (Kocer, 2003) can be also studied to estimate fatigue parameters. However, the cone crack increase in length has to be observed in order to yield precise data, and this can be cumbersome if the materials to be studied are not transparent. Kocer (Kocer, 2003) has developed an attractive methodology based on gently disturbing the crack path in order to pair the crack growth with the load and time. Despite these difficulties in observing the crack propagation, the strength degradation can be easily obtained by just fracturing the sample, yielding valuable information of how the material behaves under service.

There are also types of damage exclusive of contact fatigue tests. For brittle materials, under cyclic loadings an inner cone crack that is well inside the contact region can appear. This inner crack is provoked by the hydraulic pumping as explained by Chai and Lawn (Chai & Lawn, 2005) and has a more acute angle than the outer cone crack. Consequently, it can be more deleterious to strength.

Materials with quasiplastic behavior will not be sensitive to stress corrosion, as microcracks are not at the surface in contact with humidity. However, when cyclic loads are present, the microcracks will grow due to the sliding friction forces, which degrade the internal cohesion of the crack. These microcracks will grow and

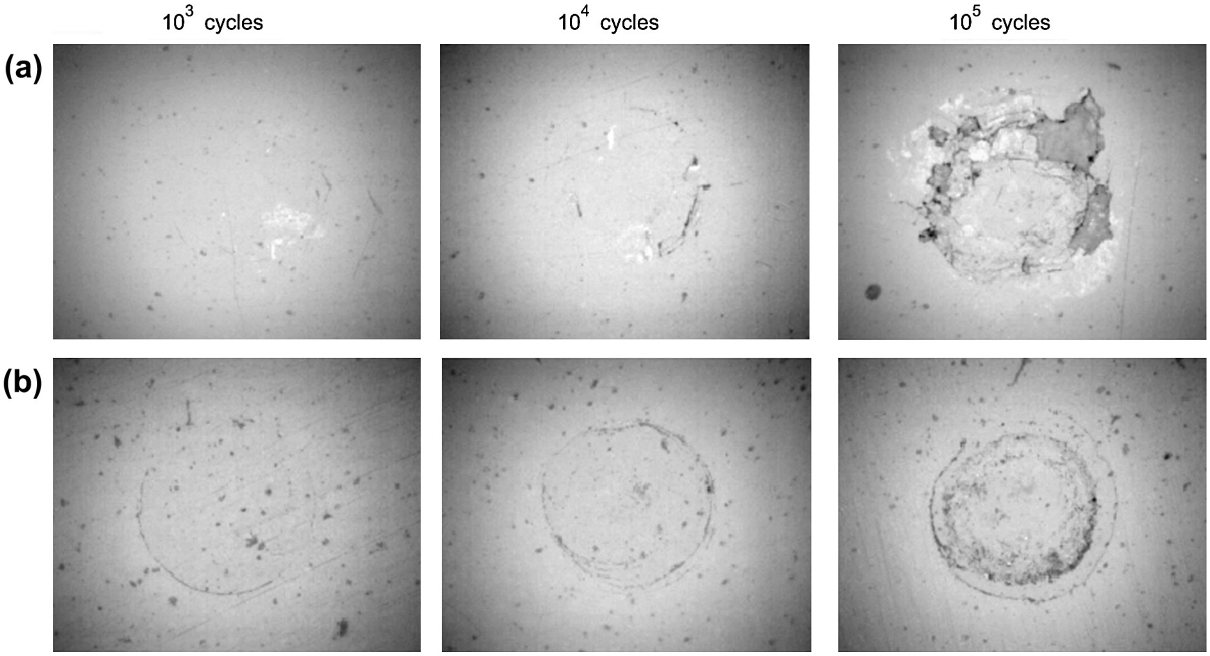

Figure 7 Cyclic indentation tests on a ceramic that develops quasibrittle damage (a) and cone crack (b) and as a first damage. Ceramic b presents a higher resistance to the appearance of damage, but the loss of cohesion becomes evident after 10^5 cycles due to the coalescence of the microcracks. Reproduced from Ceseracciu, Chalvet, de Portu, Anglada, and Jimenez-Pique (2005) with permission.

eventually coalesce. As damage increases, this will lead to a progressive degradation of the strength of the material (Lee et al., 2000). If loading is repeated for a large amount of cycles, the microcracking may be large enough to affect the integrity of the material even causing the loss of material as seen in **Figure 7**.

Therefore, designing ceramics against contact fatigue is not a simple question and a compromise has to be made between damage-tolerant ceramics that are able to restrict the growth of cone crack, and hard ceramics that are able to resist the degradation of the surface of the material due to the coalescence of microcracks.

2.13.5 Some Examples in the Literature

In **Tables 2–4**, examples of the results obtained in different investigations on Hertzian indentation of hard ceramics are presented. **Table 2** summarizes the works related to Al_2O_3, **Table 3** on SiC, and **Table 4** on Si_3N_4. All these studies were on indentation at room temperature, for bulk materials. Data presented do not include work related to impact (Akimune, Akiba, & Ogasawara, 1995; Holmquist & Wereszczak, 2010), composites (Lee et al., 2011), layered materials (Lee, Wuttiphan, Hu, Lee, & Lawn, 1998), rolling contact fatigue (Kida, Saito, & Kitamura, 2005; Wang & Hadfield, 2001), or high temperature (Sánchez-González, Miranda, Guiberteau, & Pajares, 2009).

As can be seen in these tables, several types of damage can be obtained by varying either microstructure or experimental parameters such as the indenter diameter. It is noteworthy that most of the experimental works have been performed with WC–Co spheres.

In this context, it is important to emphasize that although broad predictions of the contact response of a given material can be given, the intrinsic variability of the response implies that experimental studies are necessary to correctly evaluate the precise response of a given indenter material system. This is especially true if the indenter material is different from the standard WC–Co choice.

2.13.6 Conclusions

Hertzian contact testing is a very versatile experimental technique to explore the mechanical properties of hard ceramics. It allows for testing under a wide range of environments and loading conditions with a relatively small

Table 2 Some examples in the literature on Hertzian indentation on Al_2O_3 ceramics. The columns describe Sintering with the approximate grain size and comments on microstructure; Indenter material; Radius of indenter; range of loads applied; type of damage observed (Cone = cone cracking, qp = quasiplastic damage, ring = ring cracking); Comments

	Sintering, approximate grain size, (comments on microstructure)	*Indenter material*	*Radius of indenter* R *(mm)*	*Load applied* P *(N)*	*Damage type observed*	*Comments*
Laugier (1984)	Pressureless (PL), 2 μm (+4% zirconia)	WC–Co	0.5–6	400–3800	Cone	Auberbach law
Guiberteau et al. (1993)	PL, 23 μm	WC–Co	1.98–12.7	Up to 3500	qp	Cyclic loading
Guiberteau et al. (1994)	PL, 3–48 μm	WC–Co	1.98–12.7		Cone/qp	
Bouras and Bouzabata (1996)	PL, 2–10 μm	WC–Co	1–11	150–900	Cone	Influence of Zr ion implantation
Wei and Lawn (1996)	PL, 3–48 μm	WC–Co	3.18	2000	Cone/qp	Thermal wave analysis
Widjaja et al. (1996)	4–17 μm	WC–Co	2		Cone crack	
Franco et al. (1997)	Hot pressed (HP) & PL; 1.2, 3.8, and 14.1 μm	Al_2O_3	2.5	350–600	Cone crack	Influence of the surface state
Latella, O'Connor, Padture, and Lawn (1997)	PL, 1–4 μm (highly porous)	WC–Co	0.79–2.70	1000	Cone/qp/ collapse	Studies porosity form 2%–18%, cyclic loads
Anya (1998)	PL	Al_2O_3	2.5		Cone	Compares with Al_2O_3/SiC composite
DiGiovanni, Chan, Harmer, and Nied (1999)	Liquid phase (LP), 5 μm (6% vol porosity)	WC–Co	3.175	1180	qp	Observation of the microcracking
An (1999)	PL, 1–25 μm (textured)	WC–Co	6.36	1000	Cone/qp	Influence of the texture of grains on contact fatigue
An (2000)	PL, 1–25 μm (textured)	WC–Co	1.98–12.7 mm	2000	qp	Cross-sections of qp damage
Guo and Chan (2000)	PL (textured)	WC–Co	3.18	2500	qp	Influence of the texture on cracking
DiGiovanni, Chan, Harmer, and Nied (2001)	LP, 1–4 μm (0–8% vol porosity)	WC–Co	1.59–4.76	45–4000	qp	Different porosity levels on response
Ceseracciu et al. (2005)	PL, 2 μm with residual stress	WC–Co	2.5	200–600	Ring/qp	Evolution of damage with cycles and residual stress
Jimenez-Pique et al. (2005)	PL, 2–5 μm with residual stress	WC–Co	2.5	200–600	Ring	Influence of residual stress on appearance of damage by cyclic loads
Bouras, Zerizer, Gheldane, Bouazza, and Bouzabata (2008)	HP, 2–14 μm	WC–Co	1–14	200–2500	Cone	R-curve measurement

Table 3 Some examples in the literature on the Hertzian indentation on SiC ceramics. Columns describe Sintering with the approximate grain size and comments on the microstructure; Indenter material; Radius of the indenter; range of loads applied; type of damage observed (Cone = cone cracking, qp = quasiplastic damage, ring = ring cracking); Comments

	Sintering route, approximate grain size, (comments on microstructure)	*Indenter material*	*Radius of indenter* R *(mm)*	*Load applied* P *(N)*	*Damage type observed*	*Comments*
Lawn et al. (1994)	4–25 μm	WC–Co	3.18	1000	Cone/qp	Describes both damage mechanisms as a function of microstructure
Padture and Lawn (1994)	LP, 4 and 25 μm	WC–Co	1.58–1.27	1–300	Cone/qp	Effect of microstructure on damage type
Padture and Lawn (1995a)	PL, 25 μm (20% yttrium aluminum garnet)	WC–Co	3.18	1000	Cone/qp	Cyclic loading, compares with other materials
Padture and Lawn (1995b)	LP, 4 and 25 μm	WC–Co	3.18	1000	Cone/qp	Cyclic loading, effects of microstructure
Ortiz et al. (2004)	10 μm (elongated)	WC–Co	1.98–12.7	15–3500	qp	Different microstructures produced by different sintering atmospheres
Wereszczak, Johanns, and Jadaan (2009)	HP, 1.8–3 μm	Diamond	1–2.5	60–200	Ring	Acoustic Emission detection, different microstructures
Hegedűsová, Kovalčíková, Ceniga, and Dusza (2010)	HP, 1 μm	Steel	2–3.5	4900	Cone/qp	Compares SiC and Si_3N_4 on contact and contact strength
Wereszczak et al. (2011)	HP, 3–5.5 μm	Various	1.2–2	100–700	Ring	Evidences the importance of elastic mismatch in the critical load for cracking

Table 4 Some examples in the literature on Hertzian indentation on Si_3N_4 ceramics. Columns describe Sintering with the approximate grain size and comments on microstructure; Indenter material; Radius of the indenter; range of loads applied; type of damage observed (Cone = cone cracking, qp = quasiplastic damage, ring = ring cracking); Comments

	Sintering route, approximate grain size, (comments on microstructure)	*Indenter material*	*Radius of indenter* R *(mm)*	*Load applied* P *(N)*	*Damage type observed*	*Comments*
Xu, Wei, Padture, Lawn, and Yeckley (1995)	Hot isostatic pressing (HIP), 0.5–2 μm	WC–Co	1.98	2–300	Cone/qp	Thermal wave imaging
Miller and Bowman (1996)	HP, 0.4 μm (textured)	WC–Co	3.2	500	Cone	Deformation of cracks due to anisotropy
Lee, Wuttiphan, and Lawn (1997), Lee and Lawn (1998)	HP, 0.4–9 μm	WC–Co	1.59–3.18	4500	Cone/qp	Extensive study on damage types and strength depending on microstructure
Lee, Lee, Lawn, and Kim (1998)	HP (different α/βphases)	WC–Co	1.98	4000	Cone/qp	Effect of α/βratio phases
Kim, Jung, Peterson, and Lawn (1999)	4 μm	WC–Co	1.98, 3.18	1000, 2200	Cone/qp	Fatigue and strength degradation on fine grain Si_3N_4
Lee et al. (2000)	0.4–9 μm	WC–Co	1.98	4000	Cone/qp	Cyclic loading. dependency of damage with grain size
Bashkansky, Lewis, Pujari, Reintjes, and Yu (2001)		Si_3N_4	28.6		Cone	Coherence tomography observation of cracks on contact between two spheres
Yoshida, Chaudhri, and Hoshi (2002)		Diamond	1, 2		Cone	Compares with impact
Shea, Yanga, Beppub, and Ohjia (2003)	PL (37% porous)	WC–Co	1.67	100–2000	qp	Highly porous
Belmonte, Miranzo, and Osendi (2007)	HP 1–7 μm (textured)	WC–Co	2.	500–3000	Cone/qp	Influence of the texture
Lin, Lakshminarayanan, and Shetty (2007)	HIP&PL 2–9 μm	WC–Co	2	1750–2500	Cone/qp	Compares two materials with two different processing routes
Guahk, Han, and Lee (2008)	PL 0.5–3.5 μm	WC–Co	1.98–3.56	900	qp	Fatigue and strength degradation on fine grain Si_3N_4
Hegedűsová et al. (2010)	5 μm	Steel	2, 2.5, 3.5	4900	Cone/qp	Compares SiC and Si_3N_4 on contact and contact strength
Liu et al. (2011)	0.5–20 μm	WC–Co	3.96	2400–3600	Cone	Confocal imaging of cone cracks

amount of sample material. Several types of damage can be induced in the material by using different indenter types, and indenter material. Despite this, it is not the best method for evaluating K_{Ic} due to the lack of an analytical solution and to the experimental difficulty in assessing the crack length.

The damage induced by Hertzian indentation is representative of in-service contact loading conditions. By evaluating the strength degradation of the materials, it is possible to extrapolate the results to the performance of materials and components during use.

However, in order to do so, it is important to choose the appropriate geometry and indenter material if in-service conditions are to be simulated. Differences in geometry and material will result in different critical loads and different types of damage.

Therefore, although the basic mechanics of contact on hard ceramics are understood, there is still a lack of data on more realistic indentation counterparts and under more realistic conditions.

Acknowledgments

For fruitful discussions on the topic, the authors would like to thank Dr L. Ceseracciu, Dr A. Rueda, and Dr F. García-Marro as well as Prof. J. Pavon and Prof. Y. Gaillard. The work was funded in part through projects MAT2008-03398 and MAT2011-23913 of the Ministry of Science and Innovation of Spain.

References

Akimune, Y., Akiba, T., & Ogasawara, T. (1995). Damage behaviour of silicon nitride for automotive gas turbine use when impacted by several types of spherical particles. *Journal of Materials Science, 15*, 1000–1004.

An, L. (1999). Indentation fatigue in random and textured alumina composites. *Journal of the American Ceramic Society, 82*, 178–182.

An, L. (2000). Contact-damage behavior of textured and random alumina ceramics under Hertzian indentation. *Journal of the American Ceramic Society, 83*, 410–412.

Anya, C. C. (1998). Hertzian flaw analysis and models for the prediction of flexural fracture strength of Al_2O_3 and Al_2O_3/SiCp nanocomposites. *Journal of Materials Science, 33*, 977–984.

Auberbach, F. (1891). Measurement of hardness. *Annual Physical Chemistry, 43*, 61–100.

Bashkansky, M., Lewis, D., III, Pujari, V., Reintjes, J., & Yu, H. Y. (2001). Subsurface detection and characterization of Hertzian cracks in Si_3N_4 balls using optical coherence tomography. *NDT&E International, 34*, 547–555.

Belmonte, M., Miranzo, P., & Osendi, M. I. (2007). Mechanical properties and contact damage behavior in aligned silicon nitride materials. *Journal of the American Ceramic Society, 90*, 1157–1163.

Bermejo, R., Torres, Y., Baudin, C., Sanchez-Herencia, A. J., Pascual, J., Anglada, M., et al. (2007). Threshold strength evaluation on an Al_2O_3–ZrO_2 multilayered system. *Journal of the European Ceramic Society, 27*, 1443–1448.

Bermejo, R., Torres, Y., Sanchez-Herencia, A. J., Baudin, C., Anglada, M., & Llanes, L. (2006). Residual stresses, strength and toughness of laminates with different layer thickness ratios. *Acta Materialia, 54*, 4745–4757.

Bouras, S., & Bouzabata, B. (1996). Study of Hertzian indentation on a transparent vitroceramic and on an alumina. *Materials Chemistry and Physics, 43*, 127–134.

Bouras, S., Zerizer, I., Gheldane, F., Bouazza, M. T., & Bouzabata, B. (2008). Study of the resistance to crack propagation in alumina by acoustic emission. *Ceramics International, 34*, 1857–1865.

Cai, H., Stevens Kalceff, M. A., & Lawn, B. R. (1994). Deformation and fracture of mica-containing glass-ceramics in Hertzian contacts. *Journal of Material Research, 9*, 762–770.

Ceseracciu, L., Anglada, M., & Jimenez-Pique, E. (2008). Hertzian cone crack propagation on polycrystalline materials: role of R-curve and residual stresses. *Acta Materialia, 56*, 265–273.

Ceseracciu, L., Chalvet, F., de Portu, G., Anglada, M., & Jimenez-Pique, E. (2005). Surface contact degradation of multilayer ceramics under cyclic subcritical loads and high number of cycles. *International Journal of Refractory Metals & Hard Materials, 23*, 375–381.

Ceseracciu, L., Jimenez-Pique, E., Fett, T., & Anglada, M. (2008). Contact strength of ceramic laminates. *Composites Science and Technology, 68*, 209–214.

Chai, H., & Lawn, B. R. (2005). Hydraulically pumped cone fractures in brittle solids. *Acta Materialia, 53*, 4237–4244.

Cho, S.-J., Hockey, B. J., Lawn, B. R., & Bennison, S. J. (1989). Grain-size and R-curve effects in the abrasive wear of alumina. *Journal of the American Ceramic Society, 72*, 1249–1252.

Clegg, W. J., Kendall, K., Alford, N. M., Button, T. W., & Birchall, J. D. (1990). A simple way to make tough ceramics. *Nature, 347*, 455–461.

Cook, R. F., & Pharr, G. M. (1990). Direct observation and analysis of indentation cracking in glasses and ceramics. *Journal of the American Ceramic Society, 73*, 787–817.

DiGiovanni, A. A., Chan, H. M., Harmer, M. P., & Nied, H. F. (1999). Synergistic effects of porosity and glass on quasi-ductility under Hertzian contact in liquid-phase-sintered alumina. *Journal of the American Ceramic Society, 82*, 749–752.

DiGiovanni, A. A., Chan, H. M., Harmer, M. P., & Nied, H. F. (2001). Micromechanics of deformation in porous liquid-phase-sintered alumina under Hertzian contact. *Journal of the American Ceramic Society, 84*, 1844–1850.

Fett, T., Rizzi, G., & Diegele, E. (2004). Weight functions for cone cracks. *Engineering Fracture Mechanics, 71*, 2551–2560.

Fischer-Cripps, A. C. (1997). Predicting Hertzian fracture. *Journal of Material Science, 32*, 1277–1285.

Fischer-Cripps, A. C. (2000). A review of analysis methods for sub-micron indentation testing. *Vacuum, 58*, 569–585.

Franco, A., Roberts, S. G., & Warren, P. D. (1997). Fracture toughness, surface flaw sizes and flaw densities in Al_2O_3. *Acta Materialia, 45*, 1009–1015.

Frank, F. C., & Lawn, B. R. (1967). On the theory of Hertzian fracture. *Proceedings of the Royal Society of London, A299*, 291–306.

Gaillard, Y., Tromas, C., & Woirgard, J. (2003). Pop-in phenomenon in MgO and LiF: observation of dislocation structures. *Philosophical Magazine Letters, 9*, 553–561.

Góez, A., Coureaux, D., Ingebrand, A., Reig, B., Tarrés, E., Mestra, A., et al. (2012). Contact damage and residual strength in hardmetals. *International Journal of Refractory Metals and Hard Materials, 30*, 121–127.

Guahk, K. H., Han, I. S., & Lee, K. S. (2008). Strength degradations from Hertzian contact damages in nitrided pressureless sintered silicon nitride ceramics. *International Journal of Modern Physics B, 22*, 1819–1826.

Guiberteau, F., Padture, N. P., & Lawn, B. R. (1994). Effect of grain size on Hertzian contact in alumina. *Journal of the American Ceramic Society, 77*, 1825–1831.

Guiberteau, F., Padture, N. P., Cai, H., & Lawn, B. R. (1993). Indentation fatigue: a simple cyclic Hertzian test for measuring damage accumulation in polycrystalline ceramics. *Philosophical Magazine A, 68*, 1003–1016.

Guo, Y., & Chan, H. M. (2000). Influence of texture on Hertzian indentation behavior of alumina. *Journal of Materials Science Letters, 19*, 327–330.

Hammond, B. L., & Armstrong, R. W. (1988). Recovered elastic and plastic strains at residual micro-indentations in a MgO crystal. *Philosophical Magazine Letters, 57*, 41–47.

Hegedűsová, L., Kovalčíková, A., Ceniga, L., & Dusza, J. (2010). Contact strength and crack formation in monolithic ceramic materials. *Materials Science and Engineering: A, 527*, 1179–1184.

Helbawi, H., Zhang, L., & Zarudi, I. (2001). Difference in subsurface damage in indented specimens with and without bonding layer. *International Journal of Mechanical Sciences, 43*, 1107–1121.

Hertz, H. (1896). *Hertz's miscellaneous papers*. London, UK: MacMillan.

Holmquist, T. J., & Wereszczak, A. A. (2010). Using Hertzian indentation to understand the strength and ballistic resistance of silicon carbide. *International Journal of Applied Ceramic Technology, 7*, 625–634.

Jimenez-Pique, E., Ceseracciu, L., Chalvet, F., Anglada, M., & de Portu, G. (2005). Hertzian contact fatigue on alumina/alumina–zirconia laminated composites. *Journal of the European Ceramic Society, 25*, 3393–3401.

Jimenez-Pique, E., Ceseracciu, L., Gaillard, Y., Barch, M., de Portu, G., & Anglada, M. (2006). Instrumented indentation on alumina–alumina/zirconia multilayered composites with residual stresses. *Philosophical Magazine, 86*, 5371–5382.

Jitcharoen, J., Padture, N. P., Giannakopoulos, A. E., & Suresh, S. (1998). Hertzian-crack suppression in ceramics with elastic-modulus-graded surfaces. *Journal of the American Ceramic Society, 81*, 2301–2308.

Johnson, K. L. (1987). *Contact mechanics*. Cambridge, UK: Cambridge University Press.

Kelly, J. R. (1999). Clinically relevant approach to failure testing of all-ceramic restorations. *The Journal of Prosthetic Dentistry, 81*, 652–661.

Kida, K., Saito, M., & Kitamura, K. (2005). Flaking failure originating from a single surface crack in silicon nitride under rolling contact fatigue. *Fatigue & Fracture of Engineering Materials & Structures, 28*, 1087–1097.

Kim, D. K., Jung, Y.-G., Peterson, I. M., & Lawn, B. R. (1999). Cyclic fatigue of intrinsically brittle ceramics in contact with spheres. *Acta Materialia, 47*, 4711–4725.

Kocer, C. (2002). An automated incremental finite element study on Hertzian cone crack growth. *Finite Elements in Analysis and Design, 39*, 639–660.

Kocer, C. (2003). Using the Hertzian fracture system to measure crack growth data: a review. *International Journal of Fracture, 121*, 111–132.

Kocer, C., & Collins, R. (1998). Angle of Hertzian cone cracks. *Journal of the American Ceramic Society, 81*, 1736–1742.

Latella, B. A., O'Connor, B. H., Padture, N. P., & Lawn, B. R. (1997). Hertzian contact damage in porous alumina ceramics. *Journal of the American Ceramic Society, 80*, 1027–1031.

Laugier, M. T. (1984). Hertzian indentation of sintered alumina. *Journal of Materials Science, 19*, 254–258.

Lawn, B. R. (1998). Indentation of ceramics with spheres: a century after Hertz. *Journal of the American Ceramic Society, 81*, 1977–1994.

Lawn, B. R., Deng, Y., Miranda, P., Pajares, A., Chai, H., & Kim, D. K. (2002). Overview: damage in brittle layer structures from concentrated loads. *Journal of Material Science, 17*, 3019–3036.

Lawn, B. R., Lee, K. S., Peterson, I. M., & Wuttiphan, S. (1998). Model of strength degradation from Hertzian contact damage in tough ceramics. *Journal of the American Ceramic Society, 81*, 1509–1520.

Lawn, B. R., Padture, N. P., Cai, H., & Guiberteau, F. (1994). Making ceramics ductile. *Science, 263*, 1114–1116.

Lawn, B. R., Wiederhorn, S. M., & Johnson, H. (1975). Strength degradation of brittle surfaces: blunt indenters. *Journal of the American Ceramic Society, 58*, 428–432.

Lawn, B. R., & Wilshaw, T. R. (1975). The indentation fracture: principles and applications. *Journal of Material Science, 10*, 1049–1081.

Lawn, B. R., Wilshaw, T. R., & Hartley, N. E. W. (1974). A computer simulation study of Hertzian cone crack growth. *International Journal of Fracture, 10*, 1–16.

Lee, K. S., Jang, K. S., Park, J. H., Kim, T. W., Han, I. S., & Woo, S. K. (2011). Designing the fiber volume ratio in SiC fiber-reinforced SiC ceramic composites under Hertzian stress. *Materials & Design, 32*, 4394–4401.

Lee, K. S., Jung, Y.-G., Peterson, I. M., Kim, D. K., Lawn, B. R., & Lee, S. K. (2000). Model for cyclic fatigue of quasiplastic ceramics in contact with spheres. *Journal of the American Ceramic Society, 83*, 2255–2262.

Lee, S. K., & Lawn, B. R. (1998). Role of microstructure in Hertzian contact damage in silicon nitride: II Strength degradation. *Journal of the American Ceramic Society, 81*, 997–1003.

Lee, S. K., Lee, K. S., Lawn, B. R., & Kim, D. K. (1998). Effect of starting powder on damage resistance of silicon nitrides. *Journal of the American Ceramic Society, 81*, 2061–2070.

Lee, S. K., Wuttiphan, S., & Lawn, B. R. (1997). Role of microstructure in Hertzian contact damage in silicon nitride: I. Mechanical characterization. *Journal of the American Ceramic Society, 80*, 2367–2381.

Lee, K. S., Wuttiphan, S., Hu, X. Z., Lee, S. K., & Lawn, B. R. (1998). Contact-induced transverse fractures in brittle layers on soft substrates: a study on silicon nitride bilayers. *Journal of the American Ceramic Society, 81*, 571–580.

Lin, G. Y., Lakshminarayanan, R., & Shetty, D. K. (2007). Contact damage initiation in silicon nitride in Hertzian indentation: role of microstructure. *Journal of Materials Science, 42*, 3508–3519.

Liu, Z., Sun, J., & Pei, Z. (2011). Cross-polarization confocal imaging of subsurface flaws in silicon nitride. *International Journal of Applied Ceramic Technology, 8*, 411–422.

Lorenz, D., Zeckzer, A., Hilpert, U., Grau, P., Johansen, H., & Leipner, H. S. (2003). Pop-in effect as homogeneous nucleation of dislocations during nanoindentation. *Physical Review B, 67*, 172101.

Miller, P. D., & Bowman, K. J. (1996). Hertzian fracture of textured Si_3N_4. *Acta Materialia, 44*, 3025–3034.

Miranda, P., Pajares, A., Guiberteau, F., Deng, Y., & Lawn, B. R. (2003). Designing damage-resistant brittle-coating structures: I. bilayers. *Acta Materialia, 51*, 4347–4356.

Ortiz, A. L., Muñoz-Bernabé, A., Borrero-López, O., Domínguez-Rodríguez, A., Guiberteau, F., & Padture, N. P. (2004). Effect of sintering atmosphere on the mechanical properties of liquid-phase-sintered SiC. *Journal of the European Ceramic Society, 24*, 3245–3249.

Padture, N. P., & Lawn, B. R. (1994). Toughness properties of a silicon carbide with an in-Situ-induced heterogeneous grain structure. *Journal of the American Ceramic Society, 77*, 2518–2522.

Padture, N. P., & Lawn, B. R. (1995a). Fatigue in ceramics with interconnecting weak interfaces: a study using cyclic Hertzian contacts. *Acta Metallurgica et Materialia, 43*, 1609–1617.

Padture, N. P., & Lawn, B. R. (1995b). Contact fatigue of a silicon carbide with a heterogeneous grain structure. *Journal of the American Ceramic Society, 78*, 1431–1438.

Pajares, A., Wei, L. H., Lawn, B. R., & Berndt, C. C. (1996). Contact damage in plasma-sprayed alumina-based coatings. *Journal of the American Ceramic Society, 79*, 1907–1914.

Paliwalw, B., Tandon, R., Buchheit, T. E., & Rodelas, J. M. (2011). An assessment of the effectiveness of the Hertzian indentation technique for determining the fracture toughness of brittle materials. *Journal of the American Ceramic Society, 94*, 2153–2161.

Pavon, J., Jimenez-Pique, E., Anglada, M., Lopez-Esteban, S., Saiz, E., & Tomsia, A. (2006). Stress–corrosion cracking by indentation techniques of a glass coating on Ti_6Al_4V for biomedical applications. *Journal of the European Ceramic Society, 26*, 1159–1169.

Pavon, J., Jimenez-Pique, E., Anglada, M., Saiz, E., & Tomsia, A. (2006). Monotonic and cyclic Hertzian fracture of a glass coating on titanium-based implants. *Acta Materialia, 54*, 3593–3603.

Rao, M. P., Sanchez-Herencia, A. J., Beltz, G. E., McMeeking, R. M., & Lange, F. F. (1999). Laminar ceramics that exhibit a threshold strength. *Science, 286*, 102–105.

Rhee, Y.-W., Kim, H.-W., Deng, Y., & Lawn, B. R. (2001). Brittle fracture versus quasiplasticity in ceramics: a simple predictive index. *Journal of the American Ceramic Society, 84*, 561–565.

Roberts, S. G., Lawrence, C. W., Bisrat, Y., Warren, P. D., & Hills, D. A. (1999). Determination of surface residual stresses in brittle materials by Hertzian indentation: theory and experiment. *Journal of the American Ceramic Society, 82*, 1809–1816.

Rueda, A. O., Seuba, J., Anglada, M., & Jiménez-Piqué, E. (2013). Tomography of indentation cracks in feldspathic dental porcelain on zirconia. *Dental Materials, 29*, 348–356.

Sánchez-González, E., Miranda, P., Guiberteau, P., & Pajares, A. (2009). Effect of temperature on the pre-creep mechanical properties of silicon nitride. *Journal of the European Ceramic Society, 29*, 2635–2641.

Sanchez-Herencia, A. J., Pascual, C., He, J., & Lange, F. F. (1999). ZrO_2/ZrO_2 layered composites for crack bifurcation. *Journal of the American Ceramic Society, 82*, 1512–1518.

Shea, J., Yanga, J.-F., Beppub, Y., & Ohjia, T. (2003). Hertzian contact damage in a highly porous silicon nitride ceramic. *Journal of the European Ceramic Society, 23*, 1193–1197.

Tarres, E., Ramírez, G., Gaillard, Y., Jimenez-Pique, E., & Llanes, L. (2009). Contact fatigue behavior of PVD-coated hardmetals. *International Journal of Refractory Metals and Hard Materials, 27*, 323–331.

Wang, Y., & Hadfield, M. (2001). Ring crack propagation in silicon nitride under rolling contact. *Wear, 250*, 282–292.

Warren, P. D. (1995). Determining the fracture toughness of brittle materials by Hertzian indentation. *Journal of the European Ceramic Society, 15*, 201–207.

Warren, P. D., & Hills, D. A. (1994). The influence of elastic mismatch between indenter and substrate on Hertzian fracture. *Journal of Materials Science, 29*, 2860–2866.

Warren, P. D., Hills, D. A., & Dai, D. N. (1995). Mechanics of Hertzian cracking. *Tribology International, 28*, 357–362.

Wei, L., & Lawn, B. R. (1996). Thermal wave analysis of contact damage in ceramics: case study on alumina. *Journal of Material Research, 11*, 939–947.

Wereszczak, A. A., Daloz, W. L., & Strong, K. T., Jr (2011). Effect of indenter elastic modulus on Hertzian ring crack initiation in silicon carbide. *International Journal of Applied Ceramic Technology, 8*, 885–894.

Wereszczak, A. A., Johanns, K. E., & Jadaan, O. M. (2009). Hertzian ring crack initiation in hot-pressed silicon carbides. *Journal of the American Ceramic Society, 92*, 1788–1795.

Widjaja, S., Ritter, J. E., & Jakus, K. (1996). Influence of R-curve behaviour on strength degradation due to Hertzian indentation. *Journal of Materials Science, 31*, 2379–2384.

Xu, H. H. K., Wei, L., Padture, N. P., Lawn, B. R., & Yeckley, R. L. (1995). Effect of microstructural coarsening on Hertzian contact damage in silicon nitride. *Journal of Materials Science, 30*, 869–878.

Yoshida, H., Chaudhri, M. M., & Hoshi, Y. (2002). Quasistatic indentation and spherical particle impact studies of turbine-grade silicon nitrides. *Philosophical Magazine A, 82*, 2031–2040.

Zhang, H., & Fang, Z. Z. (2008). Characterization of quasi-plastic deformation of WC-Co composite using Hertzian indentation technique. *International Journal of Refractory Metals and Hard Materials, 26*, 106–114.

Zhang, H., Fang, Z. Z., & Belnap, J. (2007). Quasi-plastic deformation of WC-Co composites loaded with a spherical indenter. *Metallurgical and Materials Transactions A, 38A*, 552–561.

This page intentionally left blank

2.14 Wear of Hard Ceramics

Goffredo de Portu and Stefano Guicciardi, National Research Council of Italy (CNR), Chemical Science & Materials Technology Department, Institute of Science and Technology for Ceramics (ISTEC), Faenza, Italy

© 2014 Elsevier Ltd. All rights reserved.

2.14.1 Introduction

The science of tribology has received special attention between in the last 50 years. However, the most critical progress has been made between in the last 20 years with the introduction of new techniques and instruments that have allowed an in-depth understanding of wear mechanisms.

In many cases the only available option to improve the performances of metallic tribo-components is to replace them with ceramics. Ceramics exhibit excellent properties at both room and high temperatures (i.e. high hardness and strength, chemical inertness and low density), and therefore they are ideal candidates for tribological applications (for example, for high-speed, high-load-bearing applications, as suggested by Richerson (1992)). Since the tribological behavior of ceramics has been extensively investigated, a better understanding of their complex wear phenomenon is now available. However, the potential of ceramics in many applications is limited by their relatively low toughness. Under wear conditions with high Hertzian contact stresses and cyclic loads, such as in roller bearings, the risk of catastrophic failure, surface fatigue and crack formation is more important than abrasive wear. Under such conditions, a tougher and stronger material can be expected to perform better. For these reasons in the last decades, important efforts and progress have been made to produce tougher, and, in general, defect-tolerant ceramics.

Since tribology is defined as "the science and technology of interacting surfaces in relative motion" (Hutchings, 1992), it involves the study of friction and wear. It turns out that the friction coefficient and wear resistance are not intrinsic properties of the investigated material but the result of chemical, physical and mechanical interactions of a system that includes two or more bodies.

Williams (1994) indicated "perhaps as much as one third of our global energy consumption is consumed wastefully in friction". Even today the situation has not changed much. This waste of energy has, of course, direct consequences in terms of pollution and costs involved in manufacturing. Components with improved tribological properties are essential for an efficient utilization of industrial processes. This could lead to a reduction of pollution, improving our quality of life, and costs related to the replacement of prematurely worn components.

In this chapter several combinations of ceramic/ceramic or ceramic/metal systems are discussed with the aim of developing an understanding of the tribological behavior of ceramics both as bulk materials and composites.

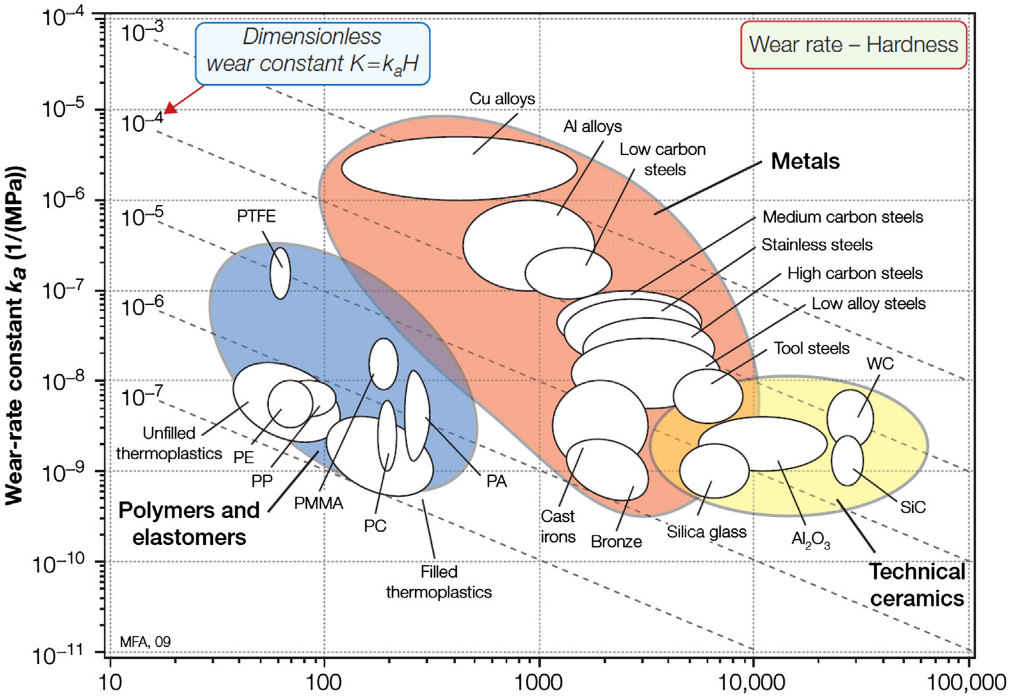

Figure 1 Wear rate as a function of hardness for several classes of materials. From Materials: Engineering, Science , Processing and Design, edited by Ashby, Shercliff and Cebon, Elsevier (2007).

Technical ceramics exhibit the highest hardness and the lowest wear rate, as evident from the rate–hardness relationship of many materials (Figure 1).

2.14.2 Definitions and Experimental Methods

As mentioned before tribology deals with the interaction of surfaces in relative motion. To quantify this interaction the following two main parameters are used to identify the tribological behavior of this system.

1. The *coefficient of friction* or friction coefficient (μ) which defines the resistance encountered by a body moving over another.
2. The *specific wear rate* (usually specific wear or wear rate) that is the volume (or sometimes the mass) loss per unit force per unit distance of a body in motion against another one.

The coefficient of friction (μ) is the ratio of the tangential force F_t necessary to move a body over a counterface to the applied normal load W; consequently, it is a dimensionless constant and can be expressed as

$$\mu = \frac{F_t}{W} \tag{1}$$

The complexity of the phenomena related to the wear of a material is simplified by the Archard equation (Archard, 1953) that introduces the wear coefficient K.

According to Archard theory the volume of the material removed per unit distance (Q) is proportional to K and the normal load (W) but inversely proportional to its hardness (H). This relationship is expressed by the equation:

$$Q = \frac{KW}{H} \tag{2}$$

K is a dimensionless constant and always less than unity.

However from an engineering point of view, the amount of material removed from a surface is usually expressed by the *specific wear rate* (or wear coefficient) κ that is usually quoted as volume loss (ΔV) divided by

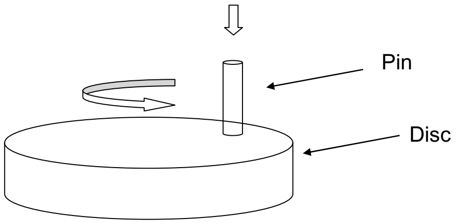

Figure 2 Schematic of pin-on-disc configuration.

applied load (P) and sliding distance (L), i.e.

$$\kappa = \frac{\Delta V}{P \cdot L} \tag{3}$$

(commonly expressed in $\mathrm{mm}^3\ \mathrm{N}^{-1}\ \mathrm{m}^{-1}$).

A deeper theoretical discussion of this point is outside of the aim of this work, so we refer an interested reader to appropriate publications (Archard, 1953; Hutchings, 1992; Williams, 1994).

To determine the tribological behavior of ceramics, several testing methods have been developed (Hutchings, 1992) with the aim of defining robust testing procedures that enable the production of reliable data. Czichos, Becker, and Lexov (1987) reported the results of an international program such as the VAMAS exercise on the pin-on-disc wear test, carried out to verify if this method responds to the prerequisites above mentioned. The results suggested that such a method or ball-on-disc (standard, ISO 20808:2004) can be considered the most suitable one for obtaining comparable wear data and, consequently, they are the most widely used for sliding wear test of ceramics. For this reason this chapter focuses mainly on this method. However it is noteworthy, as it will be discussed in Section 2.14.3.2, that a large scatter in results is intrinsic to tribological tests of ceramics. Thus the term "reliable" has a relative meaning in tribology. A schematic of pin-on-disc wear test is shown in **Figure 2** and full details concerning this method can be found in the publication of Bayer (2004). Usually pins are cylinders with spherical caps (in this way they simulate the ball-on-disc configuration). This configuration has the disadvantage that when wear occurs the contact area increases, and therefore for a constant applied load, the normal pressure decreases. This implies that the theoretical failure analysis based on Hertzian stress distribution may not be appropriate (Ravikiran, 2000; Ravikiran & Jahanmir, 2001; Ravikiran, Nagarajan, Biswas, & Pramila Bai, 1995). However a flat surface of the pin with sharp edges can lead to ploughing phenomena or chipping of the pin. Consequently the measurement of wear and friction can be severely affected. This event is considered worse than the previous one.

The information that researchers wish to obtain from tribo-tests are the wear behavior and related mechanisms of the coupling studied as well as the trend of the friction coefficient as a function of the experimental parameters.

While the wear can be explained with wear mechanisms friction, sometimes, it is more difficult to explain.

Factors influencing the wear and friction of ceramics in sliding contacts are summarized in **Figure 3**. It can be seen that a large number of factors must be taken into account in evaluating the tribological behavior. In general many of them are present at the same time and it is difficult to identify the influence of each one. Some models developed in the attempt of rationalizing the influence of each factor in the wear mechanisms are discussed in the next paragraph. Observations of microstructural features of the worn surface can allow identifying the different phenomena.

Figure 4 shows an example of delamination and subsurface cracking (Conoci, Melandri, & De Portu, 1999) while in **Figure 5**, an example of tribochemical reaction on Si_3N_4 surface is reported (Jones, Dobedoe, & Lewis, 2001). In this figure the presence of rolls of hydroxylated silicon oxide is visible. The presence of a third body between the two sliding surfaces is a key factor in determining their wear behavior. **Figure 6** shows the material transfer from steel and 3Y–tetragonal zirconia polycrystals (TZP) balls on the surface of an alumina–chromium–zirconia composite (Scheppokat, Hannink, Janssen, De Portu, & Claussen, 2005) while **Figure 7** shows the WC transfer from the pin on the surface of an alumina–zirconia–zirconia laminate (Tarlazzi, Roncari, Pinasco, Guicciardi, Melandri, & De Portu, 2000).

Sliding wear of ceramics

Microfracture
trans- and intergranular

Surface cracking
- stress concentration
- second phases
- flaws
- high Young's modulus

Subsurface cracking
- residual stresses
- inclusions
- flaws
- second phases

- low fracture toughness

Delamination fracture
subsurface cracking due to fatigue

- third body layer
- plastic deformed layer
- tribochemical reaction layer
- residual stresses
- inclusions, second phases
- flaws

Tribochemical reaction

- surface layer
  (non-oxide ceramics, e.g. Si_3N_4, SiC)
- stress corrosion cracking
  (oxide ceramics, e.g. Al_2O_3, ZrO_2
- surface effects, e.g. Rehbinder, Joffee etc.

Thermophysical reaction

- surface softening/plastic deformation
  (e.g. high temperature or sliding speed)
- structural changes
  (e.g. crystal structure, second phases
- thermal shock cracking

Third body layer

- transferred material (adhesion, surface roughness)
- loose wear debris
- compacted wear debris

Surface grooving (abrasion)

- microcutting/microploughing
- microfatigue
- microcracking
- spalling

Figure 3 Factors contributing to friction and wear of ceramics in sliding contact. From Bundschuh, W. and Zum Gahr, W.-H.(1991). Influence of porosity on friction and sliding wear of tetragonal zirconia polycrystal. *Wear* **152**, 175–191.

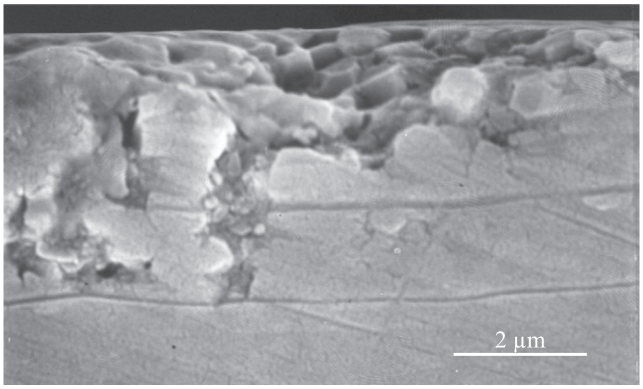

Figure 4 Cracks parallel to the surface, underneath the worn groove of transformed 3Y-TZP. From Conoci, S., Melandri, C., De Portu, G. (1999). Wear of 3Y-TZP containing compressive residual stresses at the surface. *Journal of Materials Science* **34**, 1009–1015.

2.14.2.1 Wear Mechanisms

Wear depends on several factors such as thermomechanical material properties, contact and sliding conditions, lubrication, test temperature and so on. Attempts to capture the whole tribological behavior have been pursued by the so-called wear maps (Hokkirigawa, 1991; Hsu & Shen, 1996; Lim & Ashby, 1987; Ting & Winer, 1989). General considerations and limitation of the wear map concept can be found in Adachi, Kato, and Chen (1997). Especially in the severe regime (wear rate $> 10^{-6}$ $mm^3\ N^{-1}\ m^{-1}$), one of the main material removal mechanisms in ceramics is abrasive wear that is triggered by microfracture (Bhushan, 2001; Jahanmir, 1994; Ludema, 1996; Zum Gahr, 1987). According to this, several models have been proposed in order to predict the specific wear rate (V) as a function of material properties and experimental details, some of which are reported in **Table 1**.

The influence of fracture toughness on ceramic wear models has been however critically reviewed by Ajayi and Ludema (1988). Moreover, in ceramics with a rising R-curve behavior, the fracture toughness is a function of crack length and its relationship with the wear resistance must be carefully considered (Miyazaki, Hyuga, Yoshizawa, Hirao, & Ohji, 2009).

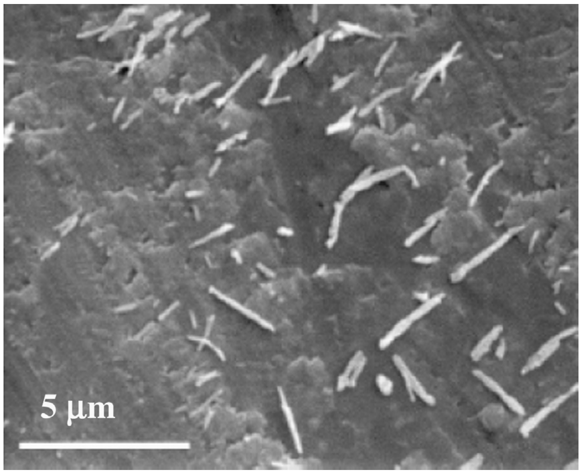

Figure 5 Rolls of hydroxylated silicon oxide due to tribochemical reaction on Si_3N_4 surface. From Jones, A. H., Dobedoe, R. S., Lewis, M. H. (2001). Mechanical properties and tribology of Si_3N_4-TiB_2 ceramic composites produced by hot pressing and hot isostatic pressing. *Journal of the European Ceramic Society* **21**, 969–980.

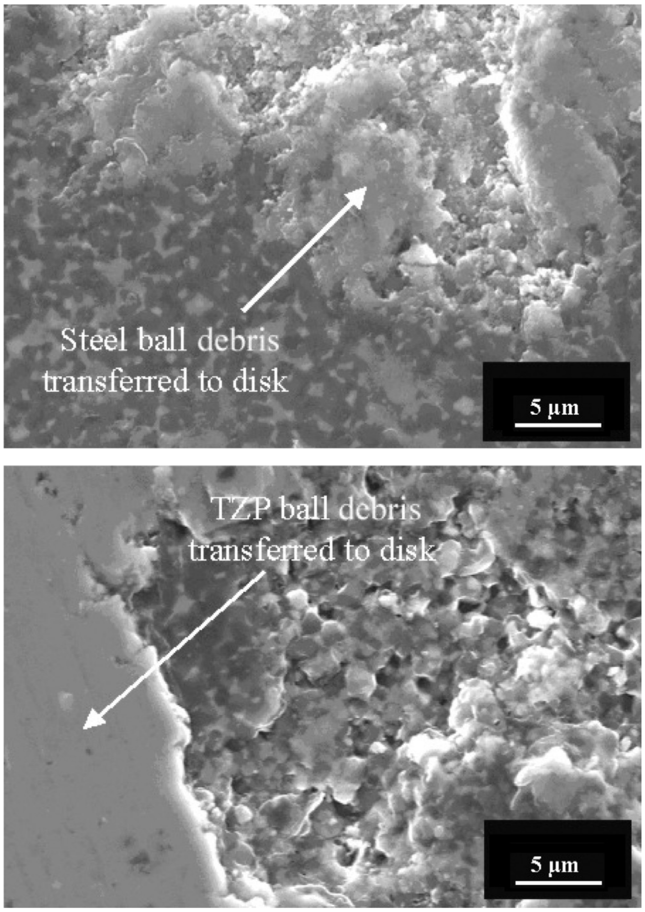

Figure 6 SEM micrographs of the wear track in a Al_2O_3-Cr-ZrO_3 composite disc, showing material transfer from counter face materials: (a) steel ball and (b) 3Y-TZP ball. From Scheppokat, S., Hannink, R., Janssen, R., De Portu, G., Claussen, N. (2005). Sliding wear of Cr-Al_2O_3-ZrO_2 and Mo-Al_2O_3-ZrO_2 composites. *Journal of the European Ceramic Society* **25**, 837–845.

As an example, Figure 8 shows the comparison of one of the models (Evans and Marshall) with some selected experimental data available in literature.

The poor fit with the experimental data is evident. The inaccuracy in representing a trend obtained by experimental data is evidenced also by the other models. This testifies the difficulties of defining a model, based on mechanical properties of the materials involved in the process, able to represent and foresee the tribological behavior of ceramics.

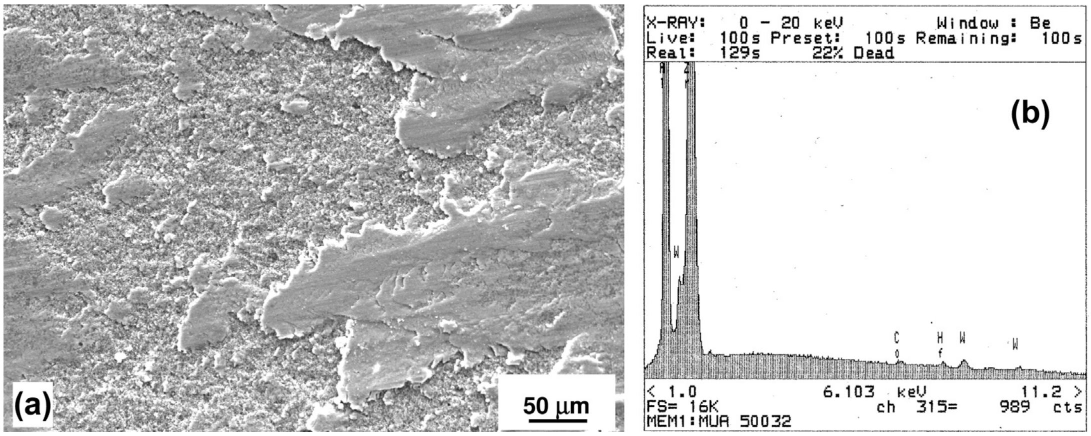

Figure 7 (a) SEM micrograph of the surface of an alumina-zirconia/zirconia laminate worn against a WC pin. Material plastically deformed and smeared on the surface is visible. (b) The presence of tungsten (W) and cobalt (Co) testifies the material transfer from pin to the disc. From Tarlazzi, A., Roncari, E., Pinasco, P., Guicciardi, S., Melandri, C., De Portu, G. (2000). Tribological behaviour of Al_2O_3/ZrO_2-ZrO_2 laminated composites. *Wear* **244**, 29–40.

Table 1 Some models used to described the wear rate of ceramics

Model	*Reference*
$V = C\dfrac{F_n^{9/8}}{K_{Ic}^{1/2}\mathrm{Hv}^{5/8}}\left(\dfrac{E}{\mathrm{Hv}}\right)^{4/5}D$	Evans and Marshall (1980)
$V = C\mathrm{Sc}^{5.46}$ with $\mathrm{Sc} = \dfrac{P_0^2\sqrt{R_{\max}}}{K_{Ic}}$	Kato (1990)
$V = C\dfrac{\sigma_{\max}}{\sigma_D}\dfrac{DF_n}{\mathrm{Hv}}$	Wang et al. (1990)
$V = Ct + \dfrac{d}{d^*}\left[\dfrac{\sigma_{\max} + \sigma_D + \sigma_R}{\sigma_R} - \left(\dfrac{d^*}{d}\right)^{1/2}\right]$	Liu and Fine (1993)

F_n, normal load; K_{Ic}, fracture toughness; Hv, hardness; E, elastic modulus; D, sliding distance; P_0, maximum Hertzian contact pressure; $R_{\max}$, maximum surface roughness; d, mean grain size; d^*, critical grain size; t, time; C, M, constants; σ_D, critical external damage stress; $\sigma_{\max}$, maximum tensile stress; σ_R, residual thermal stress.

2.14.3 Oxides

Oxides are widely used as structural ceramics. This is due to their good mechanical properties and sufficiently simple processing and sintering methods. In addition they can operate even at relatively high temperature, with the obvious advantage of no oxidation.

Among oxides the most used ceramics are alumina and zirconia. The first one has the advantage of high hardness, Young's modulus and compressive strength, valuable chemical inertness and potential operation up to 1000 °C.

The latter one can exhibit toughening mechanisms related to the tetragonal to monoclinic (t → m) phase transformation that leads to a higher value of toughness. However zirconia cannot operate at temperatures as high as alumina and has drastic property degradation in humid atmospheres especially in the temperature range 150–200 °C.

Nevertheless both of them are finding increasing use in engineering applications as wear-resistant materials. The fields of application range from components for engines, pumps, seals, nozzles, to extrusion dies; from crucibles for foundries to bioceramics, both orthopedics and orthodontics usage.

In this section we will focus attention on these two classes of oxides.

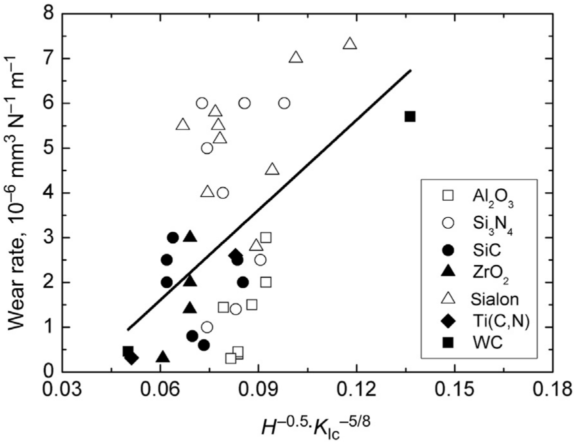

Figure 8 Comparison of the model proposed by Evans and Marshall with some selected experimental data available in literature.

2.14.3.1 Alumina

Alumina is probably the most widely used engineering ceramic. Its development started in the middle of the twentieth century and since that time enormous progress has been made. Due to its chemical, physical and mechanical properties it has been extensively studied as a wear-resistant material.

Many authors have investigated the wear behavior of alumina under different testing conditions (Andersson & Blomberg, 1993; Blomberg, Hogmark, & Lu, 1993; He, Wang, Wallace, & Hsu, 1993; Jeng & Yan, 1993; Liu & Fine, 1993; Sasaki, 1989; Senda, Drennan, & McPherson, 1995; Takadoum, 1993).

Wide ranges of specific wear rates have been reported. The magnitudes comprised from 10^{-9} to 10^{-3} mm^3 N^{-1} m^{-1}. This relative large variation can be attributed to the different wear mechanisms active during the tests, testing conditions and test method itself.

The wear mechanisms depend on many factors such as materials properties, grain size, porosity, hardness, toughness and test conditions, such as sliding speed, applied load, media (for example amount of humidity in the testing atmosphere), temperature, etc.

In order to predict the wear of ceramics, it is essential to understand the wear mechanisms that determine their behavior under specific stress conditions. In the next section the relationships among some of the above mentioned parameters and the tribological behavior of alumina will be analyzed.

2.14.3.1.1 Effect of Grain Size

Many investigations have studied the relationship between wear rate, the coefficient of friction, and grain size (Krell & Klaffke, 1996; Liu & Fine, 1993; Mukhopadhyay & May, 1993; Senda, Yasuda, Kaji, & Bradt, 1999; Singha Roy, Basu, Chanda, & Mitra, 2007; Singha Roy, Guchhait, Chanda, Basu, & Mitra, 2007; Xu, Jahanmir, & Wang, 1995; Zum Gahr, Bundschuh, & Zimmerlin, 1993). It has been generally observed that the wear rate of polycrystalline alumina increases with increasing grain size while the coefficient of friction (μ) is slightly affected by the grain size.

The primary wear mechanism associated with alumina is brittle microfracture along the grain boundaries, larger grain size being associated with larger flaw size. Cho, Hockey, Lawn, and Bennison (1989) demonstrated that the presence of large grain size reduces the critical stress for microfracture. Thermal expansion anisotropy of the crystals and dislocation-induced stresses, larger at the grain boundaries for larger grain-sized material, contribute to the grain boundaries fracture with consequent pull out of the grains (Senda et al., 1999; Toschi et al., 2003; Singha Roy & Guchhait, 2007; Singha Roy & Basu, 2007). It is evident that the pull out of a single large grain causes the removal of a volume of material much greater than that by pulling out of a smaller grain. Usually brittle intergranular fracture and grain dislodgement are observed but in some cases transgranular fracture of larger grains is also present (Figure 9). Also the presence of very fine debris is always detected as the grains comminute. The debris can act as a third body leading to abrasive wear. Larger grains produce more abrasive debris. Alumina with small grain size generates finer debris that easily reacts with the atmosphere producing aluminum hydroxide (see discussion below). In some experimental conditions (i.e. high load and high temperature), the debris is plastically deformed, compacted and smeared on the surface of the worn track

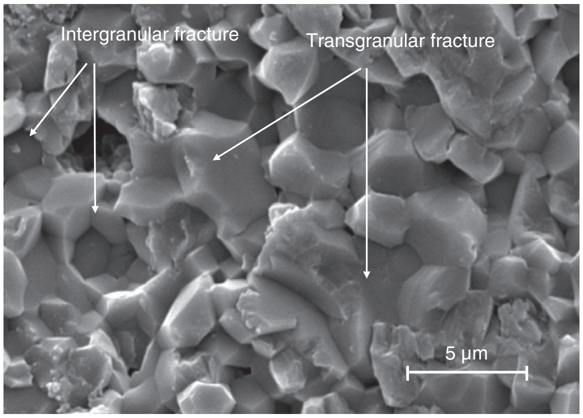

Figure 9 Intergranular and transgranular fracture of monolithic alumina, applied load 150 N; sliding speed 0.15 m/s.

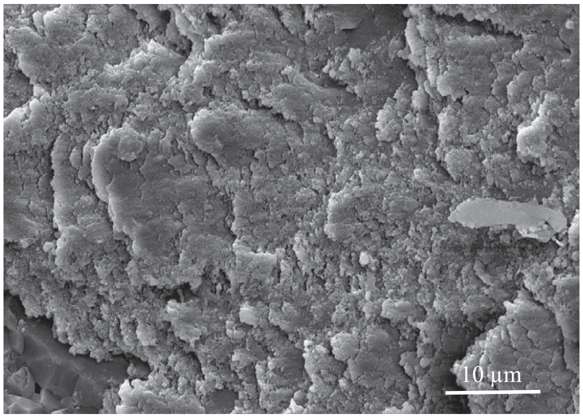

Figure 10 Plastically deformed debris spread over the surface of monolithic alumina tested at 150 N (applied load) and 0.15 m/s (sliding speed).

(Figure 10) forming a compacted layer that protects the surface from subsequent wear. This layer is weakly bonded on the surface of a large-grained alumina if compared with a finer one and is more prone to microcracking, induced by the thermal–mechanical fatigue generated during sliding. It turns out that in higher grained alumina, large parts of the layer are more easily detached from the surface. This exposes the original sliding surface to a new attack that causes inter- and transgranular fracture leading to a high specific wear rate (Senda et al., 1999; Singha Roy & Basu, 2007; Singha Roy & Guchhait, 2007; Toschi et al., 2003).

However in spite of the evidence reported by the authors mentioned, regarding the wear resistance improvement with decreasing grain size, Xiong, Manroy, Ward, Terheci, and Lathabay (1997) reported a completely different behavior. They observed that the wear resistance improved with increasing grain size. The authors attributed this behavior mainly to the test configuration, pointing out the difference in wear mechanism from round-pin configuration (increasing contact area) and flat-pin configuration (constant contact area). With the latter configuration a larger amount of debris is trapped between the rubbing surfaces generating abrasive wear by the third body. In addition they found that fine-grained alumina produced more debris than the coarser one.

However also Singha Roy and Guchhait (2007) and Singha Roy and Basu (2007) used flat pins and obtained completely different results from those reported by Xiong et al. (1997).

These contradictory results confirm the importance of test configuration and experimental parameters used to assess the tribological behavior of ceramics and the need for developing comparable experimental procedures to obtain reliable and comparable results for a deep understanding of the phenomenon.

Nevertheless there is broad agreement that alumina wear resistance is improved with decreasing grain size.

The macroscopic fracture associated to the grain size is also a direct consequence of the applied load. According to Xiong and Manory (1999), in a ball-on-disc configuration, the related Hertzian stress can exceed 1 GPa.

Jahanmir and Dong (1992) reported that the wear of alumina, and consequent transition from mild to severe wear, strongly depends on the contact stress.

2.14.3.1.2 Effect of the Atmosphere

Alumina can react with moisture in the atmosphere to form aluminum hydroxide (Gee, 1992; Perez-Unzueta, Beynon, & Gee, 1991). This hydroxide (boehmite—$AlO(OH)$) was found to form at a temperature of about 200 °C while at temperatures of about 100 °C the formation of aluminum trihydroxide (bayerite—$Al(OH)_3$) is favored. It was proposed that stresses and temperatures in the contact junction cause a phase transformation from an alpha alumina to a transition alumina. The transition alumina subsequently reacts with water to form a lubricous hydroxide layer and reduces friction and wear.

The effects of this tribochemical reaction are quite controversial. They can be beneficial if the resultant reaction product is stable, forming a protective layer that separates the two surfaces, reducing wear and friction. Or it can be deleterious if the reaction products are not coherent and can be easily removed. The consequent formation of debris can lead to abrasive wear by a third body that causes high wear rate and friction (Kapelski, Platon, & Boch, 1988).

Water has been found to exert significant effects on the tribological behavior of alumina. A film-like substance was found on the surfaces of water-lubricated alumina wear surfaces, suggesting the possibility of tribochemical reaction between water and alumina in the contact junction.

Buckley (1974) observed that the friction increased with increasing temperature up to 500 °C, and then it decreased. He attributed this initial rise in friction to the removal of absorbed water from the surface.

Contradictory results (Gates, Hsu, & Klaus, 1989; Gee, 1992) have been reported about the mechanisms involved in the formation of tribofilms.

Nevertheless many authors reported that water can act as a lubricant medium reducing wear and friction of alumina under sliding conditions (Andersson, 1992; Guicciardi, Melandri, & De Portu, 1999; Löffelbein, Woydt, & Habig, 1993; Singha Roy & Basu, 2007).

Reduction of wear rate has been verified also in alumina for biomedical applications when tested in physiological media simulation (Ikeuchi, Kusaka, & Yoshida, 2000). Kalin, Novac, and Vizintin (2003) reported that the pH of the water plays an important role. High specific wear is observed in very acid and very alkaline conditions as well as around the isoelectric point of an aqueous environment because the tribolayers do not form, while in the intermediate pH region the tribolayers always form. On the contrary in the latter case, the coefficient of friction was found to be very high while in the extreme regions of pH (very acid or very alkaline) the coefficient of friction was low. These results are in contrast with the results obtained by Löffelbein et al. (1993) that stated that the nature of the aqueous solution is of minor importance. Again these contradictory results can be attributed to the different methods and experimental conditions used by the different authors. Also in this case the difficulties in defining a unique tribological behavior of a ceramic material reiterate the need for further investigations.

2.14.3.2 Zirconia

When Garvie, Hannink, and Pascoe (1975) proposed to use the tetragonal (t) to monoclinic (m) phase transformation to improve both the toughness and the strength of zirconia alloys, great excitement was aroused in the scientific community. This concept was a great breakthrough in ceramic science and produced a revolutionary change in engineering ceramics. The increase of volume related to the t → m phase transformation in the wake or in front (it depends on the stabilizer) of a propagating crack generates a compressive stress that hinders the crack propagation, enhancing the toughness of zirconia-based ceramics. Even if zirconia exhibits lower hardness than alumina, the availability of a ceramic with improved mechanical properties generated great interest also among tribologists.

In zirconia-based ceramics, the physical–mechanical properties depend on the proportion and distribution of the different phases. This depends on the type and amount of the different stabilizers (i.e. Y_2O_3, MgO, CeO_2, and CaO) as well as on appropriate sintering temperature and heat treatment that must be controlled to suit the purpose for which the zirconia-based ceramics are to be used.

Zirconia has excellent chemical stability; it is resistant to most common acids and alkalis and to many molten salts. Obviously it is immune from oxidation but some problems can arise from its low thermal conductivity (about $2\ W\ m^{-1}\ K^{-1}$) that is an order of magnitude lower than that of alumina. Depending on the stabilizer zirconia exhibits a thermal instability at relatively low temperature. This suggests that zirconia–zirconia sliding couples may be unsatisfactory unless heat generation at the interface is negligible (i.e. small load and low sliding speeds).

Hannink, Murray, and Scott (1984) using a reciprocating hemispherical slider on flat measured the friction and wear properties of magnesia–partially stabilized zirconia (Mg–PSZ or more general PSZ) at very low sliding speed (10^{-3}–10^{-2} m s^{-1}) in unlubricated conditions. In most of the experiments they used the same material (i.e. PSZ) for both the slider and the flat.

They found that PSZ exhibited a friction coefficient μ of about 0.3. In the presence of water μ increased markedly to 0.5 while in lubricant (0.5% stearic acid in *n*-tridecane) it reduced to 0.1.

Temperature also had an effect: up to 500 °C the friction increased but after this temperature it decreased.

The wear rate was found to be in the range of 10^{-7}–10^{-8} mm^3 m^{-1} N^{-1} even if a large scatter of the data resulted from the experiments. This scatter was attributed to the fact that the amount of material removed was comparable to the grain size of PSZ that ranged typically from 50 to 70 μm. However it must be pointed out that a large scatter in results can be intrinsic to tribological tests of ceramics as shown by Almond and Gee (1987), Almond and Gee (1988), Czichos (1992), pp. 480–488, and Guicciardi, Melandri, Lucchini, and De Portu (2002).

The presence of water increased remarkably the wear rate of PSZ by one or two orders of magnitude. This behavior was correlated with the increased friction under these conditions. Unexpectedly the authors found that in spite of the reduction in friction observed in lubricating conditions, the stearic acid lubricant also increased the wear rate by about one order of magnitude. An explanation for this behavior was not provided.

The effect of temperature on wear of PSZ (but in general on all types of zirconia, and among them, in particular yttria–PSZ, 3Y–TZP) is quite puzzling. At room temperature and between 300 and 500 °C, the PSZ shows good wear resistance. However at temperatures around 200 °C an anomalous increase of wear was observed. It was correctly hypothesized that this high wear rate was due to an exaggerated tetragonal to monoclinic phase transformation. This phenomenon was later explained in depth by several researchers (Watanabe, Satoshi, & Fukuura, 1984; Winnubst & Burggraaf, 1988).

The important point emerging from this early study is that in selecting a zirconia-based ceramic for tribological application, great attention must be paid to evaluating the service conditions (i.e. temperature, environment, lubricants, etc.).

Indeed this consideration can be extended to ceramics in general.

The occurrence of phase transformation in zirconia that gives superior mechanical properties to zirconia alloys introduces additional complications in the evaluation of the tribological behavior of this class of ceramics.

A great difference in microstructure, type and amount of different phases in zirconia stabilized with different oxides also leads to a great range of results in terms of wear and friction behavior.

For example Mg–PSZ, as described above, mainly consists of large cubic grains (typically 50 μm–70 μm) with lenticular tetragonal precipitates and a certain amount of fine monoclinic phase within the large cubic grains and monoclinic grains at the grain boundaries. Consequently Mg–PSZ contains four different phases: cubic matrix, transformable tetragonal, matrix monoclinic and grain boundaries monoclinic (Green, Hannink, & Swain, 1989; Hannink, 1983). The distribution of the phases and the size of the tetragonal precipitates can be varied with appropriate thermal treatments. Obviously different microstructures lead to different physical and mechanical properties. Mg–PSZ has good thermal shock resistance, good strength (up to 600–700 MPa) and excellent toughness (up to 11 MPa $m^{1/2}$). Yttria–PSZ, generally called TZP and usually identified as 3Y–TZP (3 stands for the mol% of the stabilizer), has completely different microstructure. It consists of a homogeneous fine-grained structure with the grain size typically around 0.3 μm. This structure confers on 3Y–TZP very high strength up to 1 GPa, higher hardness than Mg–PSZ (about 13 and 9 GPa, respectively) but lower toughness (4–8 MPa $m^{1/2}$) (Green et al., 1989).

Stachowiak and Stachowiak (1989) tested both Mg–PSZ and 3Y–TZP against two zirconia ceramics and three metallic materials, namely Mg–PSZ, 3Y–TZP and EN26 steel, cast iron (gray), brass (leaded). They performed a pin-on-plate test at a sliding speed of 0.08 m s^{-1} with the applied normal load ranging from 2 to 15 N. It was confirmed that the friction coefficient depends on the environment (humidity) and sliding surface conditions (severity of the surface damage). Ceramic–ceramic sliding pairs were more sensitive to the environment than ceramic–metal pairs. In general μ was in the range of 0.4–0.7 for most of the tested sliding pair combinations but ceramic–ceramic pairs had a higher friction coefficient. No significant differences in terms of friction coefficient were observed between the two different zirconia ceramics. In spite of their significant differences in grain size and phase compositions, both Mg–PSZ and 3Y–TZP exhibited similar wear behavior. The wear rate was higher for the self-mated ceramic pairs while the damage on zirconia ceramics was limited when the counterface was a metallic material. In this latter case metal transfer to the ceramic was observed as reported later for other ceramic–metal pairs (Scheppokat et al., 2005).

Due to the interesting physical–mechanical properties mentioned above, Y–TZP (especially containing 3 mol% of yttria) attracted the attention of many researchers interested in the understanding of its tribological behavior.

Several studies have been performed on this material coupled with several different materials, both ceramics and metals. Consequently many results have been provided, some of them contradictory, with some aspects related to specific microstructural features not completely clarified (i.e. the role of phase transformation). From these data, it is difficult to establish well-defined relationships between composition, test configuration, and wear properties. However a number of conclusions can be made on the results available:

1. The zirconia–zirconia pairs are the worst both in terms of friction and wear. As a matter of fact this behavior is generally observed with all the ceramics. A ceramic against itself is the worst possible coupling.
2. With zirconia-based ceramics the contact and flash temperature is an important issue, as it will be shown later. Since zirconia has lower thermal conductivity $\sim 2\ \mathrm{W\ m^{-1}\ K^{-1}}$, in zirconia–zirconia pairs quite high temperatures can be reached. Hvizdoš, Maestra, and Anglada (2010), since they were not able to find monoclinic phase in the worn surface, suggested the presence of reversible phase transformation from monoclinic to tetragonal. Ravikiran and Pramila Bai (1995) and Annamalai, Anantharamu, Gokularathnam, and Krishnamurty (1991) also hypothesized a similar behavior due to the high temperature at contact. Alternatively it can be supposed that the temperature was so high that no driving force was available for $t \rightarrow m$ transformation. When the counterface material is a metal or a ceramic with high thermal conductivity (i.e. the thermal conductivity of steel ranges from about 16 to 45 $\mathrm{W\ m^{-1}\ K^{-1}}$ and that of alumina or SiC is about 30 and 150 $\mathrm{W\ m^{-1}\ K^{-1}}$, respectively), the expected temperature at the contact is lower because the heat generated during sliding can be more easily dissipated.

On the contrary to the findings by the above-mentioned authors other researchers observed the presence of monoclinic phase at the surface of a worn zirconia (Birkby, Harrison, & Stevens, 1989) even if in a very thin surface layer ($<1\ \mu\mathrm{m}$) (Bundschuh & Zum Gahr, 1991).

The question of $t \rightarrow m$ phase transformation is the main issue. This phenomenon characterizes the zirconia behavior and makes this material so interesting in terms of mechanical properties. However from the tribological point of view, it can play a contradictory role.

At small load and low sliding speed (i.e. 9.8 N and $10^{-3}\ \mathrm{m\ s^{-1}}$, respectively) when the transformation is moderate or small, at the beginning of the wear process, it can be beneficial because the transformation induces compressive stress at the surface preventing the formation or hindering the crack propagation that would result from the tensile stresses in the wake of the rubbing contact. This reduces the wear rate and retards the transition from mild wear to severe wear as observed by Fischer, Anderson, and Jahanmir (1989).

On the contrary when the transformation is fast and massive, for example in very severe testing conditions, the result is a rapid increase in friction coefficient and wear rate. This phenomenon occurs because the $t \rightarrow m$ phase transformation induces microcracking around the monoclinic grains. In this situation the monoclinic grains are poorly bonded with the rest of the body and are easily removed from the surface. This leads to two main consequences: (1) a large volume of material is removed and (2) a large amount of debris is available and can act as a third body promoting abrasive wear. In addition under high load, this debris is plastically deformed and smeared on the surface. During the progress of sliding contact the layer formed by the smeared debris cracks and large flakes are removed from the surface leaving fresh fractured surfaces prone to transformation and the cycle continued. This process has, of course, a direct influence on friction and wear.

The behavior described before generates some doubts about the effectiveness of zirconia as wear-resistant material.

2.14.4 Nonoxide Ceramics

Nonoxide ceramics have mechanical properties usually better than oxide ceramics, in particular at high temperature. The benefits of higher performance are counterbalanced by higher production costs. Nonoxide ceramics are currently used for wear-resistant applications: bearings (Si_3N_4), seals (SiC), machining tools (Si_3N_4, sialon, TiC), furnace rollers (Si_3N_4), and dies (sialon). Values of mechanical and physical properties for

Table 2 Some properties of selected nonoxide ceramics

Property	*SiC*	*Si_3N_4*	*Sialon*	*TiC*
Density (g cm^{-3})	3.1	3.2	3.2	4.9
Thermal conductivity (W m^{-1} K^{-1})	61	31	21	35
Coefficient of thermal expansion (10^{-6} °C^{-1})	4.4	2.9	3	8
Heat capacity (J kg^{-1} K^{-1})	2800	810	620	600
Vickers hardness	2200	1800	1780	3000
Young's modulus (GPa)	380	290	290	430
Poisson ratio	0.19	0.24	0.28	0.19
Flexural strength (MPa)	700	800	945	250
Fracture toughness (MPa m$^{0.5}$)	4.0	6.1	7.7	2.5

these nonoxide ceramics are listed in **Table 2** (ASM Handbook Vol. 18, 1992; Bhushan, 2001; Nomura, Yoshimi, Konno, & Hanada, 2000).

These values are just reference values as for each material, they are strongly dependent on raw powders, composition, sintering route, microstructure, finishing and test methodology.

2.14.4.1 Effect of Texture and Intergranular Phase Content

The microstructure of nonoxide ceramics can greatly vary depending on the starting raw powders, the use of different sintering aids, when needed, and the sintering cycle. The resulting microstructural parameters, such as grain size, grain shape, grain orientation, porosity and grain boundary structure, can all affect the tribological behavior of ceramics (Ajayi & Ludema, 1992; Borrero-Lopez, Ortiz, Guiberteau, & Padture, 2005; Dogan & Hawk, 2001; Wang, She, & Ma, 1995).

Moreover, due to processing, the wear resistance can also be dependent on the direction of testing if the final microstructure is anisotropic. As an example, **Table 3** shows how the testing direction and content of β-phase in the initial powder mixture can affect the wear rate of different Si_3N_4 samples made by slip casting (Nakamura, Hirao, Yamauchi, & Kanzaki, 2003). The wear tests were conducted in a block-on-ring arrangement where the ring was a commercially supplied Si_3N_4. The β-phase is one of the two polymorphs of Si_3N_4 and is characterized by a high aspect ratio, the other one being the α-phase that is almost globular. The slip casting technique orients the long β-grains parallel to the slip casting direction onto the slip plane. C-perp and C-para refer to the sliding direction of the ring on the slip plane of the block perpendicular and parallel to the aligned β-grain, respectively. S refers to the sliding direction in the block plane perpendicular to the long axis of β-grains. The β-phase is less hard than the α-phase but due to its higher aspect ratio promotes higher fracture toughness. The different trends of wear resistance with the initial β-phase content and testing direction can be explained with the different fracture toughness values measured along the various directions with respect to the slip casting direction and preferential β-grain orientation. These results seem to support the importance of fracture properties for the wear resistance of ceramics. A beneficial effect of the β-phase content on the wear resistance of self-mated Si_3N_4 was observed also up to 700 °C in a pin-on-disc configuration by Gomes, Oliveira, Silva, Osendi, and Miranzo (2000). The authors found that for each coupling, the friction coefficient was almost independent of the sliding speed with values in the range 0.5–0.8. A marked effect of α/β phase ratio can be found also on the wear performances of Y-sialon (Jones, Hirao, Hyuga, Yamauchi, & Kanzaki, 2003). With two different experimental

Table 3 Specific wear rate as a function of β-phase content and testing direction for slip cast Si_3N_4

	Specific wear rate, w *($\times 10^{-5}$ mm^3 N^{-1} m^{-1})*		
β content (wt.%)	*C-perp*	*C-para*	*S*
5.7	0.22	1.32	0.89
17.2	0.31	1.03	0.22
36.2	0.38	15.30	0.22
57.3	1.05	10.70	0.16

arrangements, ball-on-disc and block-on-ring, those authors showed that under mild testing conditions the α-sialon performed better due to their higher hardness, but under severe testing conditions, when the main wear mechanism was triggered by microcracking, the sialon with low α-phase content had better wear characteristics due to their higher toughness. Using a fretting configuration, Kumar, Acikbas, Kara, Mandal, and Basu (2009) found that the wear rate of another series of sialon ceramics had an inverse linear correlation with the β-sialon content and the substitution parameter z. The substitution parameter is the variable in the chemical formula of sialon ($Si_{6-z}Al_zO_zN_{8-z}$). In those experiments the friction coefficient was in the range 0.59–0.64 and no clear correlation with the microstructural parameters was found. Borrero-Lopez, Ortiz, Guiberteau, and Padture (2007) have shown that increasing the aspect ratio of the grains has a beneficial effect on the tribological properties of SiC ceramics due to the higher fracture toughness.

Dense Si_3N_4 ceramics are usually obtained by adding sintering aids to promote densification by the formation of liquid phase. On cooling, this liquid phase forms an intergranular glassy phase which bonds the Si_3N_4 grains together. Usually, the specific wear rate decreases with decreasing the intergranular glassy phase content. Such a behavior was for example observed in two Si_3N_4 ceramics, with different interfacial bonding, sliding against a commercially available Si_3N_4 ball (Hyuga, Sakaguchi, Hirao, Yamauchi, & Kanzaki, 2001). The increase of wear rate with the increase of the intergranular phase content was observed also in SiC by Borrero-Lopez et al. (2005). In particular, these authors found that the increase of the intergranular phase decreases the hardness of the material and increases the internal tensile residual stress. The effect of the amount of glassy phase on the friction coefficient and wear resistance of Si_3N_4 ceramics sliding against gray cast iron under lubricated conditions was shown to be dependent on the lubricant. When water was used as lubricant the wear rate increased with the increase of glassy phase content. In contrast when sodium silicate solution was used no effect was observed (Fang, Gao, & Zhang, 1999). In water the friction coefficient as a function of time was different for each coupling while it was almost independent on the coupling in the sodium silicate solution. The initial values, which were in the range 0.6–0.8, dropped to about 0.02 in the sodium silicate solution, but remained as high as 0.6 in most of the cases in water. Using different experimental methods—fretting, ball-on-disc and drilling—Campbell, Laoui, Celis, and VanderBiest (1996) assessed the tribological properties of several sialon ceramics worn against steel and cast iron bodies. They found that the higher the intergranular phase content was the lower the hardness and wear resistance were, but the friction coefficient was around 0.4 in all cases. In a recent paper, Kurama, Schulz, and Herrmann (2011) showed that in (Y_2O_3, Nd_2O_3)-doped sialon ceramics obtained from two different sintering routes, i.e. gas-pressure sintering and plasma spark sintering, and coupled to steel balls, the coarsening of the grain size was more beneficial than the reduction of the intergranular phase. On the other hand, using the same sintering route, the increase of intergranular phase reduced the wear resistance. When the applied load was reduced to 10 N, the wear behavior was almost reversed. The friction coefficient, which was in the range 0.8–1.4, was found to be strongly influenced by hardness. According to Zhang, Cheng, and Lathabai (2001), in Ca-doped α-sialon ceramics there is an optimum glassy phase content to optimize the erosive wear performance.

Besides quantity, also the composition of the intergranular phase could play an important role in the wear resistance of nonoxide ceramics. Skopp, Woydt, and Habig (1990) did not find any influence of the phase composition on the wear rate or the friction coefficient for three self-mated Si_3N_4 ceramics. However, experimental results very often indicate the opposite. With a block-on-ring method, Kitaoka, Tsuji, Katoh, Yamaguchi, and Sato (1994) tested three Si_3N_4 ceramics with different sintering aids at 120 °C in water. The sintering aids were MgO and Al_2O_3 for SN-1 and Y_2O_3 and Al_2O_3 for SN-2 and SN-3. The grain boundary phase in SN-1 and SN-2 was amorphous while in SN-3 it was partially crystalline. At low sliding speeds, the wear was influenced by the presence of NH_3, produced by the chemical reaction. In this condition the composition containing MgO exhibited a specific wear rate higher than the one with Y_2O_3. At sliding speeds above 0.4 $m\ s^{-1}$, however, when wear was controlled by oxidation and microfracture, the specific wear rates were larger for the Si_3N_4 containing crystalline secondary phase. The friction coefficient of SN-2 was almost constant at about 0.3, while for the other Si_3N_4 varied with the sliding speed. Using a commercial Si_3N_4 ball in ball-on-disc configuration tests, Hyuga, Jones, Hirao, and Yamauchi (2004) have shown that rare-earth additives such as Yb_2O_3 and Lu_2O_3 make Si_3N_4 twice more wear resistant than when Y_2O_3 is used. The same trend was observed in the ball counter bodies. The authors attributed this behavior to the weaker grain–grain boundary bonding strength in Y_2O_3-doped Si_3N_4 and to the higher oxidation resistance of the rare-earth-doped Si_3N_4. It should be noted that the hardness of the three Si_3N_4 materials was almost the same and that the fracture toughness of the Lu_2O_3-doped Si_3N_4 was lower than that of the Y_2O_3-doped Si_3N_4. Also in sialon ceramics, the composition of the intergranular phase affects the tribological properties. When Lu_2SiO_5 is used as sintering aid, the silicate grain boundary phase promotes a higher wear rate, but when Lu_2O_3 is used, the wear rate can be comparable to the equiaxed Lu-α sialon (Jones, Hyuga, Hirao, & Yamauchi, 2004). Microstructural parameters such as interphase bond strength and residual stresses seem to play a greater role than either bulk hardness or fracture toughness on the erosion wear of TiC-based cermets (Hussainova, 2003).

2.14.4.2 Grain Size

Grain refinement usually implies better mechanical properties. For this reason, nanosized materials have been considered very promising substitutes for more conventional structural materials for tribological applications (Andrievski, 2009; Gleiter, 1989; Hahn & Padmanabhan, 1995; Han, Lavernia, & Mohamed, 2005; Mukhopadhyay & Basu, 2007; Vassen & Stover, 2001; Weertman et al., 1999). As reported in Section 2.14.3.1.1 for the oxide ceramics there is a general agreement on the fact that a reduction of the grain size leads to an increase of wear resistance. In particular, according to the well-known Hall–Petch relation, the finer the grain the harder is the material. As hardness is a crucial parameter in the wear resistance of a material (Section 2.14.2.1), nonoxide nanosized grain ceramics have the potential to perform better than the corresponding materials with microsized microstructure. The first improvement of the wear resistance of Si_3N_4 with the refinement of the grain size was reported by Herrmann et al. (1998). These authors observed also a reduction of the friction coefficient in ultrafine Si_3N_4 ceramics. Kim, Kumar, Hong, and Kim (2010) characterized several Si_3N_4 ceramics with mean grain size in the range 90–241 nm. They observed that the hardness increased but the fracture toughness decreased with decreasing grain size. The wear rate of the finest material was about one order of magnitude lower than that of the coarsest one. In the finest ceramic, wear was mainly due to delamination of the layer formed by the tribochemical reaction while in the coarsest material, fracture and pull out of large elongated grains was the main wear mechanism. The friction coefficient was not influenced by the microstructure.

The benefit of grain refinement of the Si_3N_4 matrix on the wear behavior of a Si_3N_4–TiN composite was reported also by Yoshimura, Komura, and Yamakawa (2001). They observed that the wear rate of the nanocomposite was almost half that of the conventional composite, both in air and vacuum.

Guicciardi, Sciti, Melandri, and Pezzotti (2007) studied the dry sliding behavior of nano- and microstructured SiC pins against SiC and Si_3N_4 discs. They also observed that the friction coefficient and the pin wear rate were not influenced by the pin grain size. On the other hand, the disc wear rate was about one order of magnitude higher when worn against microstructured SiC pins than against nanostructured SiC pins. The rationale of these findings was that the nanostructured SiC pins released debris much finer and softer than the corresponding debris coming from the microstructured SiC pins. The smaller size makes the debris less abrasive while the lower hardness promotes the formation of soft debris layer which can be smeared on the surface and reduce the contact pressure.

Improved wear resistance has been observed also in nanocrystalline diamond films (Erdemir et al., 1999; Uhlmann, Rosiwal, Bayerlein, & Rohner, 2010), and TiC-based cermet coatings (Qi et al., 2006).

However, for Ti_3SiC_2 ceramics an inverse trend of wear resistance and grain size was reported (El-Raghy, Blau, & Barsoum, 2000). These authors stated that the coarse-grained materials were more wear resistant than the fine-grained materials due to the larger number of energy-dissipating mechanisms, such as delamination, crack bridging, grain deformation microcracking and grain fracture.

2.14.4.3 Environment and Temperature

The ambient atmosphere can greatly influence the wear performances of nonoxide ceramics. Moreover, there can be a combined effect of the environment and the testing conditions. The wear of Si_3N_4 depends in a very complex way on sliding speed and humidity, dry conditions being the worst in most of the cases (Gee & Butterfield, 1993). Using bearing steel as disc material, Lee and Kim (1994) found that the wear rates of two Si_3N_4 materials were strongly dependent on sliding speed and humidity. High humidity and a low sliding speed led to the highest wear rate. As the sliding speed was increased, the wear rate decreased and the effect of the humidity on the wear rate was reduced. The same trend was observed in the friction coefficient which was in the range 0.4–0.7. However, in this case the effect of humidity on the friction coefficient was maintained also at high sliding speed. Even the oxygen content in the atmosphere can influence the wear rate. Si_3N_4 ceramics sliding against cast iron and steel, in a pin-on-disc tests configuration, showed a decrease in wear rate when the oxygen concentration of the atmosphere was reduced (Tennenhouse & Runkle, 1986) As nonoxide ceramics like Si_3N_4 and SiC are used as water pump seals, the effect of water on their tribological behavior is an important issue. Water usually reduces both friction coefficient and wear rate by forming a lubricant interlayer, after the initial smoothing of the surface, by tribochemical reactions (Andersson, 1992; Chen, Kato, & Adachi, 2001; Fischer, 1990). The reduction of wear rate can be of about 1–2 orders of magnitude (Fischer & Tomizawa, 1985; Sasaki, 1989). However, there can be a combined effect of sliding speed and applied load on the wear in water. In a series of ball-on-disc tests on three different self-mated ceramics in water, Rani, Yoshizawa, Hyuga, Hirao, and Yamauchi (2004) found that the wear rate of Si_3N_4 and SiC ceramics generally increased with increasing applied load and decreasing sliding speed. The different extent of tribochemical reactions and the resulting smoothing of the mating surfaces were indicated as the reason for such a behavior. The friction coefficients of Si_3N_4 were lower than that of the SiC, however they both were below 0.1 with a slight dependence on the sliding speed for Si_3N_4 and no dependence on the applied load for both ceramics. The reader interested in a deep discussion of this topic can refer to Matsuda, Kato, and Hashimoto (2011) for the influence of water from different sources on the tribological properties of SiC; Umeda, Enomoto, Mitsui, and Mannami (1993) for the influence of water on the tribological behavior of some boride ceramics; Hibi and Enomoto (1989), Nakamura and Hirayama (1990), Winn, Dowson, and Bell (1995a, 1995b), and Zhao, Liu, and Fischer (1998) for the effect of lubricants other than water on the tribological properties of nonoxide ceramics.

The possibility of using nonoxide ceramics for high-temperature applications requires, besides other things, the knowledge of their high-temperature tribological behavior. Generally, the increase of temperature promotes the decrease of both hardness and fracture toughness which, in turn, broadly determine the wear performances of ceramics (**Figure 8**). However, Lin and Chen (1995) have shown that the change in stress intensity factor affects the wear rate of Si_3N_4 more than fracture toughness at least in the range of 25–550 °C. Moreover, usually an increase in temperature in an oxygen-rich atmosphere promotes also oxidation and the formation of tribochemical products that are loosely bonded to the sliding surfaces and can be easily removed by sliding process. Many authors explored the field of the wear and friction–temperature relationship. In particular Si_3N_4 and SiC were extensively studied and a large number of data are available. From these data it can be confidently stated that, in general, the wear rate of nonoxide ceramics increases with the increase of the temperature (Gee, Matharu, Almond, & Eyre, 1990; Gomes, Miranda, Vieira, & Silva, 2001; Kim, Chae, & Kim, 2000; Park, Danyluk, & McNallan, 1992; Skopp et al., 1990) even if some different behavior can be observed in particular testing conditions. Melandri, Gee, De Portu, and Guicciardi (1995) found that the wear rate of a Si_3N_4 increased up to 900 °C and then dropped to nearly the same value of room temperature at 1200 °C. This behavior was caused by the melting of the intergranular glassy phase, which protected the specimens from further wear.

Other parameters like environment (i.e. humidity, air, and vacuum), sliding speed or applied load influence the effect of the temperature on the wear and friction of nonoxide ceramics. Park et al. (1992) showed that at constant temperature the presence of humidity induces tribochemical reactions with the formation of roll debris that decreased the wear rate.

When tested at high temperature in air, obviously, nonoxide ceramics oxidize. In these conditions oxidation products, which remain on the samples, can mask the actual entity of material removed by wear. However test carried out in vacuum confirmed that the wear rate increased with increasing testing temperature (Gee et al., 1990). Similar results were obtained by Hisakado and Tani (1999) testing Si_3N_4, SiC and TiC in vacuum up to 600 °C. They observed an increase of the wear rate up to 400 °C but at 600 °C only the wear rate of the TiC ceramic continued to increase, while that of Si_3N_4 and SiC dropped to the value at room temperature. This behavior was attributed to the presence of a protecting film formed by the debris generated during the sliding process.

The sliding speed also plays a role in the wear at high temperature. It has been observed (Gomes et al., 2001) with Si_3N_4/iron alloy that keeping the temperature constant the wear rate decreases with increasing slinging speed. Woydt and Habig (1989) also found that the lower the sliding speed, the greater is the effect of the testing temperature. In SiSiC ceramics they observed that at a low sliding speed, the wear rate increased with the temperature while at high sliding speed (3 m s^{-1}), it was almost constant independently from the temperature. Also in this case, tribooxidation was the predominant wear mechanism at sliding speeds higher than 1 m s^{-1}. Moreover at 800 °C, the wear rate was nearly independent of the applied load. However, Kim et al. (2000) found that the wear rate increases as a function of applied load up to 1000 °C.

An increase in wear rate with increasing temperature was also observed in SiC (Xiao & Senda, 1997) although in some cases it remains constant up to 500 °C (Yang, Senda, Kotani, & Hirose, 2004). Nevertheless in all the cases, the authors reported a decrease of the wear rate at temperature $\geq$1000 °C (800 °C in vacuum). This phenomenon was caused by the formation of a dense tribofilm of very fine debris.

In general the friction coefficient of Si_3N_4 also increases with increasing temperature (Gee et al., 1990; Hisakado & Tani, 1999; Melandri et al., 1995; Skopp et al., 1990). However the friction coefficient was also found to decrease with the temperature or remaining constant (0.6–0.7) in vacuum (Park et al., 1992). Invariance of the friction coefficient with the temperature was also observed in Si_3N_4/iron alloy (Gomes et al., 2001)

Also in SiC a reduction of μ as a function of temperature was observed (Gee et al., 1990) but it could be independent of, or very much affected by, the testing temperature depending on the applied load.

The influence of temperature on the tribological behavior of many other nonoxide ceramics has been studied. However, for reasons of limited space, the results of these studies will not be discussed in this section. The reader is referred to the appropriate publications listed below: Si_3N_4 composites (Gomes, Osendi, Miranzo, Oliveira, & Silva, 1999; Melandri et al., 1995; Woydt, Skopp, & Habig, 1991), Si_3N_4 films (Miyoshi, Pouch, Alterovitz, Pantic, & Johnson, 1989), SiC composites (Woydt et al., 1991), sialon composites (Park, Han, Lim, & Yeo, 1997), TiC bulks (Tkachenko, Yurchenko, Sibel, & Murzin, 1998; Zhao, Liu, Zhu, Ouyang, & Xue, 1998), TiCN bulks (Meng, Lu, Wang, & Yang, 2006), TiCN coatings (Polcar, Novak, & Siroky, 2006), cubic boron nitride (c-BN) coatings (Yu, Inagawa, & Jin, 1994), TiN–TiB_2 composites (Yang, Ouyang, Liu, & Liang, 2010), and several nitride-based coatings (Lopez & Staia, 2005; Polcar et al., 2006; Sue & Chang, 1995; Wilson & Alpas, 1996; Wilson & Alpas, 1997).

2.14.5 Composites

With the aim of improving mechanical and tribological properties, ceramic composites have been developed. They are generally formed from a matrix reinforced with one or more secondary phases to enhance a specific property. When thermomechanical properties are the target, usually an increase of wear resistance can be expected according to the various models reported in Section 2.14.2.1. However, as shown by several investigations, microstructural features seem to be more important than bulk properties in the determination of the wear resistance of a ceramic composite (Hu, Li, & Llewellyn, 2005; Hussainova, 2005; Hussainova, Kolesnikova, Hussainov, & Romanov, 2009). When a secondary phase is introduced in a ceramic matrix, residual stresses develop due to the different thermal expansion coefficients. Moreover, the quality of interface bonding is of paramount importance for a good structural performance.

Many combinations of ceramic–metal or ceramic–ceramic composites with different couplings have been studied. Due to the specific nature of this chapter only few examples of results obtained from these studies will be analyzed, and cemented carbides are not discussed. We refer the interested reader to refer the chapter on wear of cemented carbides.

2.14.5.1 Ceramic–Metal Composites

Assuming that the main wear mechanisms in ceramics are brittle microfracture along the grain boundaries, it is essential to limit this phenomenon. Toughness plays a key role in hindering the crack propagation and reducing the severity of the wear mechanisms. With the aim of increasing the toughness of ceramics, addition of high-melting point metallic particles have been considered by many researchers as toughening reinforcing phases (Breval, Deng, Chiou, & Pantano, 1992; Budiansky, Amazigo, & Evans, 1988; Chou & Tuan, 1995; De Portu, Guicciardi, Melandri, & Monteverde, 2007; De Portu, Guicciardi, Melandri, & Sbaizero, 1999; Scheppokat et al., 2005; Sekino, Nalajima, Ueda, & Niihara, 1997). Ideally they can combine the good properties of both classes of materials, i.e. the hardness and wear resistance of ceramics with the toughness and damage tolerance of metals.

De Portu et al. (2007) investigated the behavior of Al_2O_3–Mo and Al_2O_3–Nb particulate composites containing different amounts of secondary phase and particles dimension. The composites were tested on a disc-on-pin apparatus, using WC as counterface material, with loads ranging from 10 to 150 N at a sliding speed of $0.5\ m\ s^{-1}$. It was found that the friction coefficient decreased with increasing applied loads for all the composites. The rate of decrease was greater up to 50 N and lower for higher applied load. No significant difference was found between the different materials. The reduction in friction was attributed to the characteristic of the debris film observed. At higher contact loads, higher temperatures were generated and the metal particles embedded in the debris easily oxidized increasing the lubrication properties of the films.

The friction coefficient of these composites was similar to that measured by De Portu et al. (1999) with pure alumina sliding against WC in similar testing conditions. In terms of wear the two composites behaved quite

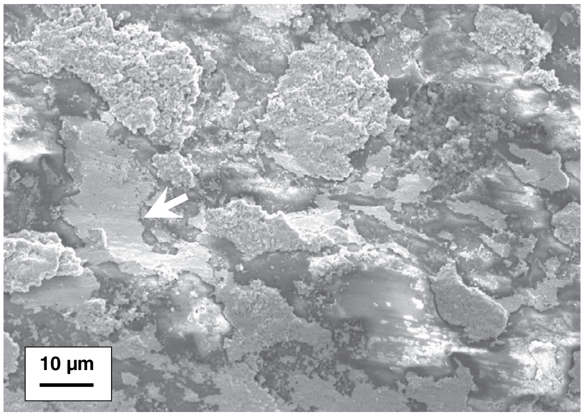

Figure 11 Nb inclusion in Al_2O_3-Nb composite, deformed and ploughed (arrowed) after test at 150 N. From De Portu. G., Guicciardi, S., Melandri, C., Monteverde F. (2007). Wear Behaviour of Al_2O_3-Mo and Al_2O_3-Nb Composites. *Wear* **262**, 1346–1352.

differently. The wear resistance of Al_2O_3–Mo composites was very low. Due to the weak adhesion of the molybdenum particles to the alumina matrix, the wear resistance of this composite was very poor even under relatively low loads, especially when coarse (2.5 μm) Mo particles were used. The Nb-containing composites were more wear resistant. Due to their ductility and limited thermal expansion mismatch with respect to Al_2O_3, the Nb particles were more strongly bonded to the matrix and were more difficult to remove from the surface during the sliding. As these particles are much softer than the matrix, they can be prone to ploughing (**Figure 11**) and the alumina matrix mainly supports the contact pressure. This can explain why the wear behavior of this composite is very similar to that observed for pure alumina (De Portu et al., 1999). Chang, Binner, and Higginson (2010) also verified that if a soft secondary phase is present in a ceramic matrix composite, after the initial part of the sliding process almost all the load is carried by the matrix. They prepared Al(Mg)/Al_2O_3 interpenetrating composites starting from alumina foams infiltrated by Al–8 wt.% Mg alloy and studied the wear behavior in reciprocating sliding conditions against a WC ball. The composites exhibited better wear resistance than that of the Al(Mg) alloy. When the density and the cell size of the alumina foams were changed different wear mechanisms were observed. Foams with lower density facilitated the ploughing of the soft Al (as already observed for Al_2O_3–Nb composites mentioned above) which exhibited deep grooves or were cut by the counter ball as flakes and plates. The composites with the higher foam density showed fewer, shallower grooves and a protruding alumina network as already observed by Kork (2006) in alumina-reinforced aluminum alloy composites. In this situation, the alumina structure bears the load and the wear process is governed by alumina wear resistance and consequently the tribological behavior is better than that of the aluminum alloys.

Composites containing more than one secondary phase have also been studied. Scheppokat et al. (2005) evaluated the tribological performance of Cr–Al_2O_3–ZrO_2 and Mo–Al_2O_3–ZrO_2 composites sliding against stainless steel and 3Y–TZP ball under different loads and at a sliding speed of 0.75 $m\ s^{-1}$. A well-defined relationship between composition, test configuration, and wear properties was not established. However the authors verified that

1. the specific wear rate of most metal–alumina composites varies by only one order of magnitude and the wear mechanism is related to surface fatigue and brittle macrofracture rather than microbreakout or machining;
2. the composites containing the greater amounts of both chromium and zirconia showed specific wear rates more than an order of magnitude lower than the 3Y–TZP reference material, although they had slightly lower hardness than 3Y-TZP. This was the case against both stainless steel and 3Y–TZP balls;
3. no clear correlation could be found between disc metal content, hardness and specific wear rate under the chosen test conditions. It was suggested that this may have partly been due to the transfer of slider ball materials to the sample disc (**Figure 6**).

From the results analyzed and from additional data from the referred literature, it can be concluded that addition of metal to ceramics in many cases does not lead to an improvement of tribological performance. In some circumstances, depending on experimental conditions, microstructure of the composites and coupling, a reduction of friction coefficient can be observed due to the formation of lubricious tribofilms. However metal–ceramic composites do not seem to provide a general solution for large industrial applications.

2.14.5.2 Ceramic–Ceramic Composites

In order to overcome the problems mentioned above, attention has been concentrated on ceramic–ceramic composites. These composites can exhibit mechanical properties superior to those of the ceramic matrix itself and, at the same time, potentially better tribological performance.

Many compositions with different matrix and secondary phases have been explored.

Gomes et al. (1999) studied the tribological behavior of Si_3N_4 ceramics reinforced with SiC platelets or SiC nanoparticles in self-mated conditions. They found no net differences in wear rate between matrix and composites, at least at room temperature. However, the platelet-reinforced composite worn more due to large dimension of the SiC reinforcement which promoted an easy debonding. The friction coefficients, which were in the range 0.35–0.75 for all the testing conditions, were shown to be almost independent of the sliding speed and slightly affected by the testing temperature with the highest values measured at 350 °C. The friction coefficient of the Si_3N_4 matrix was intermediate between the SiC platelet-reinforced composite, which had the lowest friction coefficient, and the SiC nanoparticle-reinforced composite. The interfacial failure between reinforcement and matrix was also the reason for the higher wear rate of BN-reinforced Si_3N_4 ceramics with respect to the matrix alone (Carrapichano, Gomes, & Silva, 2002). The wear rate was observed to increase with the content of BN reinforcement in a nonlinear way. The introduction of BN platelets was successful in order to reduce the friction coefficient which passed from 0.8 for the Si_3N_4 matrix to about 0.65–0.70 for the BN-reinforced composites, in this case almost independently of the BN content. Dogan and Hawk (2000) have shown that the addition of SiC whiskers to a Si_3N_4 matrix increased Young's modulus, hardness and fracture toughness but decreased the wear resistance due to tensile stresses at the whisker/matrix interface. A similar behavior was observed also in Si_3N_4 whisker-reinforced sialon composites (Park et al., 1997). The effect of Si_3N_4 whisker orientation on the tribological properties of several Si_3N_4 composites was studied by Liang et al. (Liang, Lee, & Park, 1999). The addition of carbon fibers to a Si_3N_4 matrix decreased the original mechanical properties but increased the wear resistance due to the lubricant effect of the carbon reinforcement. The friction coefficient in fact was reduced from 0.7 of the starting Si_3N_4 matrix down to 0.3 for the C-reinforced composites. Being strongly anisotropic, moreover, the fibers had a different effect depending on the testing orientation with respect to their long axis (Hyuga, Jones, Hirao, & Yamauchi, 2005).

Woydt et al. (1991) and Skopp and Woydt (1995), with the aim of finding a material suitable for increasing the efficiency of engines, studied SiC and Si_3N_4 ceramics and several composites using those materials as matrix. Titanium carbide (TiC) and titanium diboride (TiB_2) were added to SiC, while BN, titanium carbide (TiC) and titanium nitride (TiN) were added to Si_3N_4. Also a binary carbonitride (Ti, Mo)(C,N) cemented with 13 wt.% Ni was considered.

For a successful application in engines as unlubricated tribosystems, the ceramic components should exhibit a friction coefficient lower than 0.2 and a wear coefficient lower than $10^{-6}\,mm^3\,N^{-1}\,m^{-1}$ (i.e. mild wear regime). Both these parameters must be independent from sliding velocity and ambient temperature (Platzer, 1990).

The results obtained with the composites tested against them in a pin-on-disc configuration were very promising.

It was found that addition of TiC, TiB_2, TiN and BN generally improved the mechanical properties of the ceramic matrix and, at the same time, considerably improved the tribological properties with respect to the matrices.

In particular Si_3N_4–TiN and SiC–TiC approached the bench mark expected for the above-mentioned applications. Both showed wear coefficients below $10^{-6}\,mm^2\,N^{-1}\,m^{-1}$, at room and high temperatures, and friction coefficient about 0.3. Wear and friction coefficients were almost independent from sliding velocity especially at room temperature. On the same type of composite, Melandri et al. (1995) found that the TiN-reinforced Si_3N_4 composite worn slightly more than the matrix alone. The wear resistance was even lower when TiN was replaced by TiC. The friction coefficient of the composites was about 0.6 and that of the matrix about 0.45. On the other hand, an improvement of the wear resistance of a TiN-reinforced Si_3N_4 was observed by Liu and Huang (2004) in a series of pin-on-disk tests where the ceramic composite was mated to steel balls. Also the friction coefficient was lower for the composite, about 0.49, than for the matrix, about 0.70. When TiB_2 particles were used as reinforcement in a Si_3N_4 matrix, Jones et al. observed an improvement in hardness, fracture toughness and wear resistance (Jones et al., 2001). A lower wear rate was also found when an Si_3N_4 matrix was reinforced with few percent of Mo_5Si_3 or W_2C particles due to the formation of lubricant layers. A reduction of the friction coefficient was observed for the composites with respect to the matrices (Iizuka & Kita, 2005; Iizuka, Kita, Hirai, & Osumi, 2004). The modification of thermal conductivity and oxidation resistance was the explanation given by Hooper et al. for the improvement of wear performances of TiC–c-BN tools with respect to the c-BN alone (Hooper, Shakib, & Brookes, 1988).

Addition of BN to Si_3N_4 was effective only at temperatures below 100–200 °C, in humid atmosphere. In those conditions, in spite of the reduction of mechanical properties (compared with pure Si_3N_4), the friction coefficients were as low as 0.1–0.2 and the wear rate stays in the mild regime.

The binary (Ti, Mo)(C,N)-based carbonitride, due to the formation of self-lubrication oxides, showed a remarkable decrease in wear coefficient at both room and high temperatures with values lower than those observed in many nonmetallic and polymeric materials.

Ceramics that exhibit the formation of self-lubricious oxides as the result of tribochemical reaction are very promising for decreasing friction and/or wear and particular attention must be paid to their development and characterization.

Due to the large literature body on their tribological behavior, we refer the interested reader to some recent papers regarding the applications of nonoxide ceramic composites in brake applications (Fan et al., 2011; Fan, Zhang, Cheng, Tian, & Yang, 2010; Matejka et al., 2010; Shu et al., 2010; Wu, Zeng, Yu, & Fan, 2010).

Janxing, Zeliang, Jun, Jianfeng, and Tongkun (2006) focused their attention on alumina-based composites. In this case TiC, Ti(C,N), (W,Ti)C and SiC-whiskers were added to an alumina matrix and tested against a cemented carbide. It was found that all the composites showed better mechanical properties than pure alumina and a decrease in friction coefficient with increasing sliding speed and, particularly, of the applied load.

Under the same testing conditions Al_2O_3/(W,Ti)C exhibited the lowest friction coefficient (0.3–0.5) while the Al_2O_3/SiC_w is the highest (0.5–0.7). On the other hand this latter composite showed the highest wear resistance. Such behavior can be attributed to the whisker pull out during the wear. The protruding whiskers, observed in the worn track, created a rough surface that was responsible for the high μ but, at the same time, the pull out was a toughening mechanism that led to a low wear rate.

Among alumina-based composites, Al_2O_3–SiC has received intensive attention. One of the most interesting outcomes from these studies is that the transition from mild to severe wear, usually observed in alumina after a certain period of sliding, is suppressed in Al_2O_3–SiC composites (Bajwa, Rainforth, & Lee, 2005; Melmonte, Nieto, Osendi, & Miranzo, 2006). Another important result from studies on alumina/silicon carbide composites is that the improvement of the tribological properties is greater than that of the mechanical properties. It turns out that the theory proposed by Evans (1979) and Evans and Marshall (1980), which relates the improvement of tribological behavior directly to the mechanical properties, is questionable.

The fracture mode is important in determining the transition from mild wear to severe wear but it is difficult to ascribe the change in fracture mode directly to mechanical properties or, at least, just to them (Guicciardi, Sciti, Melandri, & Bellosi, 2005; Merino & Todd, 2005; Chen, Rainforth, & Lee, 2000).

In order to verify the influence of mechanical properties and the fracture mode on tribological behavior of alumina-based composites, Zhang, Luo, Wang, Robert, and Todd (2008) and Luo, Zhang, and Robert (2008) studied the abrasive wear of Al_2O_3–SiC and alumina/mullite composites. They confirmed that the wear resistance of the composites was greater (two to four times) than that of the monolithic alumina. It was evident that the different materials had different fracture modes. The improvement in wear resistance was attributed to a combination of improved mechanical properties and transition from intergranular fracture, in alumina, to transgranular fracture in the composites.

Wear-resistant ceramics, such as alumina, are widely used as biomedical components in orthopedics (for example, hip joints). So the possibility of improving the tribological properties of such a ceramic through the addition of a secondary phase was considered attractive.

Begin-Colling, Mocellin, Von Stebut, Bordji, and Mainard (1998) studied the wear behavior of Al_2O_3 and Al_2O_3–TiN particulate composite in a simulated biological environment. However, in spite of the different mechanisms of material removal observed in the two materials, no clear evidence of improved tribological properties by the composite was found.

There is no space in this chapter to analyze in detail other valuable publications available on ceramic–ceramic composites. Among them the readers interested in this topic are referred to the publications of Lee (1999), Chen and Breslin (2002), Rainforth (2004), Gomes et al. (1999), Melandri et al. (1995), and Woydt et al. (1991) for Si_3N_4 composites, Woydt et al. (1991) for SiC composites and Park et al. (1997) for sialon composites.

Ceramic–metal composites showed improved mechanical properties but not necessarily better tribological properties. In some cases the friction was reduced due to the formation of lubricious film from tribochemical reaction, mainly of the metallic secondary phase. However because of the ductility of those particles they are often deformed and easily worn from the surface leaving the ceramic matrix to bear all the load. Consequently the wear behavior exhibited by these composites is that of the matrix.

Ceramic–ceramic composites generally show better mechanical and tribological properties than bulk single phase ceramics. The improvement in wear resistance is attributed to a combination of improved mechanical properties and transition (change in fracture mode) from intergranular, in alumina, to transgranular in the composites. In addition, alumina–SiC composites have been shown to delay or suppress the time-dependent transition from mild wear to severe wear.

Due to their performances and potential applications these materials deserve particular attention for further studies.

2.14.6 Laminated Structures

As already pointed out by Perez-Unzueta et al. (1991) and Hutchings (1992) the performance of wear-resistant materials is mainly related to the properties of thin surface layers. Consequently improvement in surface toughness appears to be a promising way to improve the tribological behavior of ceramics. In fact, since removal of material in engineering ceramics under sliding conditions is generally caused by the propagation of surface cracks resulting from tensile stresses in the wake of rubbing contact, an increase in surface toughness should lead to an improvement in wear resistance. Fischer et al. (1989) observed that when toughness increases, wear resistance increases by approximately three orders of magnitude, measured in air at room temperature at small loads and very low sliding speed. However as shown before, zirconia phase transformation can increase substantially surface toughness but not necessarily the wear resistance (Conoci, Melandri, & De Portu, 1997, 1999). Many authors (Cai, Green, & Messing, 1998; Clegg, Kendall, Alford, Button, & Birchall, 1990; Kuo & Kriven, 1997; Lakshminarayanan, Shetty, & Cutler, 1996; Russo, Harmer, Chan, & Miller, 1992; She, Scheppokat, Janssen, & Claussen, 1998) have shown that an effective method for improving the surface toughness of a material is to produce laminated structures designed to induce compressive residual stresses at the surface by combining the different thermophysical characteristics (i.e. thermal expansion and shrinkage on sintering) of the different materials used.

Sergo, Lipkin, De Portu, and Clarke (1997), Rao, Sánchez-Herencia, Beltz, McMeeking, and Lange (1999), Kiefer, Moon, and Lange (2005), De Portu, Micele, and Pezzotti (2006), and De Portu and Micele (2007) developed laminated structures with the aim of improving their surface properties such as hardness and toughness by inducing compressive residual stresses at the surface.

Toschi et al. (2003) investigated the tribological behavior of such symmetric hybrid composites containing alumina outer layers under compression (**Figure 12**). They carried out sliding wear tests on a disc-on-pin apparatus in unlubricated conditions. Pins of pure dense alumina as the reference material were used as counterface material. The hybrid-laminated composites with a compressive stress of about 140 MPa showed the lowest values of friction coefficient (μ) under all the experimental conditions, except for the test carried out at

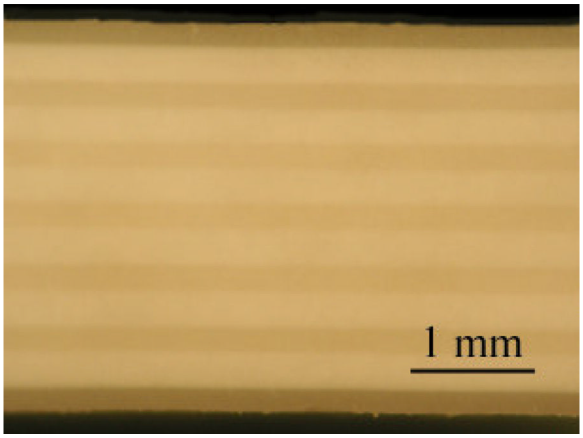

Figure 12 Sections of alumina/alumina-zirconia laminated structures. Darker layers alumina, brighter layers alumina-zirconia composites. From, De Portu, G., Micele, L. and Pezzotti, G. (2006). Laminated Ceramic Structures from Oxide Systems. *Composites: Part B, Engineering* **37**, 556–567.

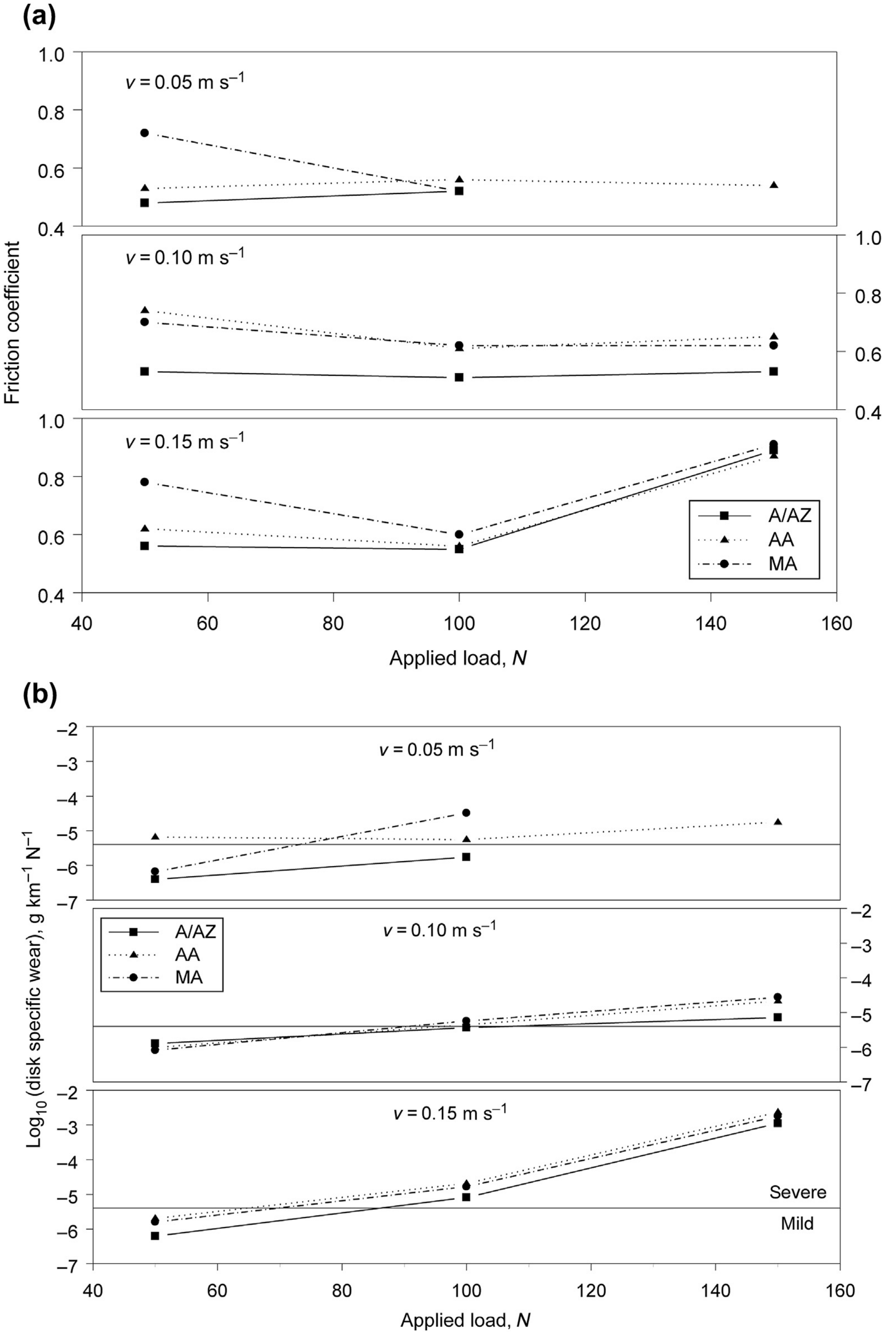

Figure 13 Friction coefficients and specific wear of alumina/alumina-zirconia (A/AZ) and pure alumina (AA) laminates and monolithic alumina (MA) as a function of different experimental conditions. The straight line is the boundary between mild and severe wear regime. From Toschi, F., Melandri, C., Pinasco, P., Roncari, E., Guicciardi, S. and de Portu G. (2003). *"Influence of Residual Stress on the Wear Behaviour of Alumina/Alumina-Zirconia Laminated Composites"*, Journal of the American Ceramic Society **86** [9] 1547–1553.

the most severe testing condition (150 N and 0.15 m s^{-1}), for which the value was closer to that of the bulk alumina. Additional relevant information acquired from that publication is that the friction coefficient of the hybrid composites was almost constant regardless of the applied loads, except for the most severe conditions. The authors explained this behavior in terms of reduced adhesion. In fact when a severe wear regime is present, the friction coefficient tends to increase with the severity of the test. This means that the increased amount of debris formed during sliding, then plastically deformed between the disc and pin, offers a large contact surface for the two materials, thus leading to an increase in adhesive friction. As the wear of hybrid laminates results in a lower amount of debris than other materials, the direct consequence is a lower friction. Regarding the wear behavior it was found that the wear of hybrid-laminated composites was always less than the values measured on the stress-free materials (**Figure 13**). In such laminated composites, four main wear mechanisms were identified: microcracking, macrocracking, abrasion from the third body while considerable plastic deformation, that can be synergetic with the others, seemed to be predominant under the severest testing conditions. A cracked layer formed by compacted debris was observed on the worn surface.

The debris, its comminution and subsequent compaction, was caused by cracking of the grains at the early stage of the process as previously observed by Guicciardi et al. (1999). This result suggests that microcracking is the main wear mechanism active under the described experimental conditions. For a material with a given flaw size, the critical condition for the onset of cracking at the surface occurs when the stress intensity factor K_I, due to the maximum principal tensile stress ($\sigma_{1\max}$), is greater than or equal to the local fracture toughness K_{Ic}. The presence of compressive residual stresses increases the apparent surface fracture toughness and, as it opposes the tensile stress generated in the wake of the sliding contact, it prevents the formation and propagation of cracks.

Undoubtedly laminated structures exhibit substantial improvements in wear resistance, as discussed before, but if they are not properly designed the increased resistance to static contact damage (i.e. increased apparent surface toughness) may not be effective in sliding condition. Tarlazzi et al. (2000) have shown that when zirconia is present in the surface, under severe operating conditions, an exaggerated phase transformation from tetragonal to monoclinic symmetry occurs while high contact temperatures can be reached by the material pairs. Because the mechanical properties of alumina show a strong degradation with temperature (Alpert, Chan, Bennison, & Lawn, 1988; Fett, Missbach, & Munz, 1994; Shimada et al., 1984), this can result in lower wear resistance when the wear mechanism is controlled by instantaneous or fatigue-induced brittle fractures. Moreover, the temperature increase in the AZ/Z laminated composite may have relaxed the residual stress to some extent and, also, favored material transfer from the pin to the disc (**Figure 7**) creating the conditions for abrasive wear by a third body. In these conditions the increased surface toughness is ineffective in enhancing the wear resistance of the laminated composite.

Regarding nonoxide layered composites, no improvements in wear resistance or friction coefficient was observed in Si_3N_4–TiN multilayer laminates in spite of a threefold increase in fracture toughness exhibited by the layered composite with respect to the single layer. This was explained considering that in wear the contact is on micrometer or submicrometer level while the fracture toughness was measured on a much larger scale (Hadad et al., 2006).

2.14.7 Conclusions

The interaction of solid surfaces in relative motion is a very complex phenomenon. The tribological behavior depends on several factors such as physical, chemical, microstructural and thermomechanical properties of the coupled materials. In addition experimental conditions such as the type of contact, contact pressure, sliding speed and distance, lubrication, test temperature and surrounding environment (i.e. humidity level) play an important role in defining the response of materials exposed to a wear process. In hard ceramics, this is further complicated by their inherent brittle behavior according to which any small defect in the microstructure can trigger microfracture under the stress generated by contact. This could be one of the reasons for the great scatter of the results that are generally observed under nominally identical test conditions.

However, notwithstanding the difficulties just mentioned and in spite of their brittleness, due to the remarkable chemical, physical and mechanical properties, hard ceramics occupy a major market share in wear-resistant applications. Moreover, due to their refractoriness and the growing demand for high-temperature materials they seem to be the unique candidate for extremely demanding and technical appliances.

In addition the development of new tough and flaw-resistant ceramics is ongoing. Some of them exhibit improved toughness due to phase transformation (namely zirconia-based ceramics), some by incorporating secondary phases (metallic or ceramics), some by nanosizing the microstructure, and some by introducing residual surface stress as in multilayer composites.

However, zirconia ceramics must be handled carefully. In some conditions (small load and low temperature) they can perform quite well. However under high loads and temperature or in presence of humid atmospheres (even at temperature as low as 200 °C) they exhibit high friction and poor wear resistance. In addition the occurrence of phase transformation generates additional complication that leads to contradictory results.

Ceramic–metal composites generally do not show performances of particular interest. Although the presence of plastically deformed particles adds to better they have a negative effect on the wear resistance.

Ceramic–ceramic composites are more promising. Improvement of mechanical properties as well as of tribological behavior can be achieved especially when reducing the grain size of both matrix and secondary phase. Some interesting results have been obtained with nanocomposites even if a clear indication of remarkable improvement of performances has not been demonstrated so far. These materials cannot be considered a real breakthrough as they have been demonstrated in other fields.

Improved wear resistance can be also obtained by introducing residual surface compressive stresses, as it can be done by producing laminated composites, to contrast the tensile stresses which are generated between two sliding surfaces in contact.

In order to improve and enhance the utilization for structural ceramics in industrial applications, standard testing procedures should be defined and followed.

References

Adachi, K., Kato, K., & Chen, N. (1997). Wear map of ceramics. *Wear, 203*, 291–301.

Ajayi, O. O., & Ludema, K. C. (1988). Surface damage of structural ceramics – implications for wear modeling. *Wear, 124*, 237–257.

Ajayi, O. O., & Ludema, K. C. (1992). The effect of microstructure on wear modes of ceramic materials. *Wear, 154*, 371–385.

Almond, A. G., & Gee, M. G. (1987). Results from a UK inter-laboratory project on dry sliding wear. *Wear, 120*, 101–116.

Almond, A. G., & Gee, M. G. (1988). Effects of wear variables on wear testing of ceramics. *Materials Science and Technology, 4*, 877–884.

Alpert, C. P., Chan, H. M., Bennison, S. J., & Lawn, B. R. (1988). Temperature dependence of alumina-based ceramics. *Journal of the American Ceramic Society, 71*, C-371–C-373.

Andersson, P. (1992). Water-lubricated pin-on-disc tests with ceramics. *Wear, 154*, 37–47.

Andersson, P., & Blomberg, A. (1993). Alumina in unlubricated sliding point, line and plane contacts. *Wear, 170*, 191–198.

Andrievski, R. A. (2009). Size-dependent effects in properties of nanostructured materials. *Reviews on Advanced Materials Science, 21*, 107–133.

Annamalai, V. E., Anantharamu, B. L. A., Gokularathnam, C. V., & Krishnamurty, R. (1991). Transformation behaviour of yttria tetragonal zirconia polycrystals in a metal-cutting environment. *Journal of Materials Science Letters, 10*, 1374–1376.

Archard, J. F. (1953). Contact and rubbing of flat surfaces. *Journal of Applied Physics, 24*, 981–988.

ASM International. Handbook Committee. (1992). *Friction, lubrication, and wear technology*. Materials Park, Ohio: American Society for Metals.

Bajwa, S., Rainforth, W. M., & Lee, W. E. (2005). Sliding wear behavior of SiC-Al_2O_3 nanocomposites. *Wear, 259*, 553–561.

Bayer, R. G. (2004). *Mechanical wear fundamentals and testing* (2nd ed.). New York: Marcel Dekker, Inc.

Begin-Colling, S., Mocellin, A., Von Stebut, J., Bordji, K., & Mainard, D. (1998). Al_2O_3 and Al_2O_3-TiN wear resistance in a simulated biological environment. *Journal of Materials Science, 3*, 2837–2843.

Bhushan, B. (Ed.). (2001). *Modern tribology handbook*. Boca Raton, FL: CRC Press.

Birkby, I., Harrison, P., & Stevens, R. (1989). The effect of surface transformation on the wear behavior of zirconia TZP ceramics. *Journal of the European Ceramic Society, 5*, 37–45.

Blomberg, A., Hogmark, S., & Lu, J. (1993). An electron microscopy study of worn surfaces. *Tribology International, 26*, 369–381.

Borrero-Lopez, O., Ortiz, A. L., Guiberteau, F., & Padture, N. P. (2005). Effect of microstructure on sliding-wear properties of liquid-phase-sintered alpha-SiC. *Journal of the American Ceramic Society, 88*, 2159–2163.

Borrero-Lopez, O., Ortiz, A. L., Guiberteau, F., & Padture, N. P. (2007). Microstructural design of sliding-wear-resistant liquid-phase-sintered SiC: an overview. *Journal of the European Ceramic Society, 27*, 3351–3357.

Breval, E.-., Deng, Z., Chiou, S., & Pantano, C. G. (1992). Sol gel prepared Ni-alumina composite materials, part I – microstructure and mechanical properties. *Journal of Materials Science, 27*, 1464–1468.

Buckley, D. H. (1974). Friction and wear behavior of glasses and ceramics. In *Surfaces and interfaces of glass and ceramic*. New York: Plenum.

Budiansky, B., Amazigo, J. C., & Evans, A. G. (1988). Small scale crack bridging and the fracture toughness of particulate-reinforced ceramics. *Journal of the Mechanics and Physics of Solids, 36*, 167–187.

Bundschuh, W., & Zum Gahr, W.-H. (1991). Influence of porosity on friction and sliding wear of tetragonal zirconia polycrystal. *Wear, 152*, 175–191.

Cai, P. Z., Green, D. J., & Messing, G. L. (1998). Mechanical characterization of Al_2O_3/ZrO_2 hybrid laminates. *Journal of the European Ceramic Society, 5*, 2025–2034.

Campbell, P., Laoui, T., Celis, J. P., & VanderBiest, O. (1996). The influence of intergranular phases on the tribological performance of sialons. *Materials Science and Engineering A-Structural Materials Properties Microstructure and Processing, 207*, 72–86.

Chang, H., Binner, J., & Higginson, R. (2010). Dry sliding wear behaviour of Al(Mg)/Al_2O_3 interpenetrating composites produced by a pressureless infiltration technique. *Wear, 268*, 166–171.

Carrapichano, J. M., Gomes, J. R., & Silva, R. F. (2002). Tribological behaviour of Si_3N_4-BN ceramic materials for dry sliding applications. *Wear, 253*, 1070–1076.

Chen, M., Kato, K., & Adachi, K. (2001). Friction and wear of self-mated SiC and Si_3N_4 sliding in water. *Wear, 250*, 246–255.

Chen, H. J., Rainforth, W. M., & Lee, W. E. (2000). The wear behavior of Al_2O_3-SiC ceramic nanocomposites. *Scripta Materialia, 42*, 555–560.

Chen, M. Y., & Breslin, M. G. (2002). Friction behavior of co-continuous alumina/aluminum composites with and without SiC reinforcement. *Wear, 249*, 868–876.

Cho, S.-J., Hockey, B. J., Lawn, B. R., & Bennison, S. J. (1989). Grain size and R-curve effects in the abrasive wear of alumina. *Journal of the American Ceramic Society, 72*, 1249–1252.

Chou, W. B., & Tuan, H. W. (1995). Toughening and strengthening of alumina with silver inclusions. *Journal of the European Ceramic Society, 15*, 291–295.

Clegg, W. J., Kendall, K., Alford, N. M., Button, T. W., & Birchall, J. D. (1990). A simple way to make tough ceramics. *Nature, 347*, 455–457.

Conoci, S., Melandri, C., & De Portu, G. (1997). Effect of surface residual stresses on surface crack behaviour and wear of Y-TZP. In J. Baxter, L. Cot, R. Fordham, V. Gabis, J. Hellot, M. Lefebvre, et al. (Eds.), *Key engineering materials: Vols. 132–136, Part 3. Proceedings of euro ceramics V* (pp. 1501–1504). Switzerland: Trans Tech Publications.

Conoci, S., Melandri, C., & De Portu, G. (1999). Wear of 3Y-TZP containing compressive residual stresses at the surface. *Journal of Materials Science, 34*, 1009–1015.

Czichos, H. (1992). *Design of friction and wear experiments* (pp. 480–488). ASM handbook18: Friction, lubrication and wear technology. USA: The Materials Information Society.

Czichos, H., Becker, S., & Lexov, J. (1987). Multilaboratory tribotesting: results from the Versailles advanced materials and standards programme on wear test methods. *Wear, 114*, 109–130.

De Portu, G., Guicciardi, S., Melandri, C., & Sbaizero, O. (1999). Wear behaviour of Al_2O_3-Mo composites. In P. Vincenzini (Ed.), *Ceramics: Getting into the 2000's – part C, advances in science and technology* (pp. 771–778). Faenza: Techna.

De Portu, G., Guicciardi, S., Melandri, C., & Monteverde, F. (2007). Wear behaviour of Al_2O_3-Mo and Al_2O_3-Nb composites. *Wear, 262*, 1346–1352.

De Portu, G., Micele, L., & Pezzotti, G. (2006). Laminated ceramic structures from oxide systems. *Composites: Part B, Engineering, 37*, 556–567.

De Portu, G., & Micele, L. (2007). Lamination process to obtain structures with tailored residual stress distribution. In M. Anglada, E. Jiménez-Piqué, & P. Hvizdoš (Eds.), *Key engineering materials: Vol. 333. Proceeding of the SICMAC summer school on layered, functional gradient ceramics, and thermal barrier coatings* (pp. 27–37). Switzerland: Trans Tech Publications.

Dogan, C. P., & Hawk, J. A. (2000). Influence of whisker toughening and microstructure on the wear behavior of Si_3N_4- and Al_2O_3-matrix composites reinforced with SiC. *Journal of Materials Science, 35*, 5793–5807.

Dogan, C. P., & Hawk, J. A. (2001). Microstructure and abrasive wear in silicon nitride ceramics. *Wear, 250*, 256–263.

El-Raghy, T., Blau, P., & Barsoum, M. W. (2000). Effect of grain size on friction and wear behavior of Ti_3SiC_2. *Wear, 238*, 125–130.

Erdemir, A., Fenske, G. R., Krauss, A. R., Gruen, D. M., McCauley, T., & Csencsits, R. T. (1999). Tribological properties of nanocrystalline diamond films. *Surface and Coatings Technology, 120*, 565–572.

Evans, A. G. (1979). In J. B. Hockey, & R. W. Rice (Eds.), *NBS spec. publ. 562, the science of ceramic machining and surface finishing, II* (pp. 1–14). National Bureau of Standards, U.S. Department of Commerce.

Evans, A. G., & Marshall, D. B. (1980). Wear mechanisms in ceramics. In D. A. Rigney (Ed.), *Fundamentals of friction and wear of materials* (pp. 439–452). Metals Park, OH: American Society for Metals.

Fan, S. W., Zhang, L. T., Cheng, L. F., Tian, G. L., & Yang, S. J. (2010). Effect of braking pressure and braking speed on the tribological properties of C/SiC aircraft brake materials. *Composites Science and Technology, 70*, 959–965.

Fan, S. W., Zhang, L. T., Cheng, L. F., Zhang, J. X., Yang, S. J., & Liu, H. Y. (2011). Wear mechanisms of the C/SiC brake materials. *Tribology International, 44*, 25–28.

Fang, L., Gao, Y. M., & Zhang, Z. (1999). Tribology of Si_3N_4 with different glassy phase content sliding against grey cast iron lubricated with water. *Wear, 225*, 896–904.

Fett, T., Missbach, M., & Munz, D. (1994). Failure behaviour of Al_2O_3 with glassy phase at high temperatures. *Journal of the European Ceramic Society, 13*, 197–209.

Fischer, T. E. (1990). Friction and wear of ceramics. *Scripta Metallurgica et Materialia, 24*, 833–838.

Fischer, T. E., Anderson, M. P., & Jahanmir, S. (1989). Influence of fracture toughness on the wear resistance of yttria-doped zirconium oxide. *Journal of the American Ceramic Society, 72*, 252–257.

Fischer, T. E., & Tomizawa, H. (1985). Interaction of tribochemistry and microfracture in the friction and wear of silicon-nitride. *Wear, 105*, 29–45.

Garvie, R. C., Hannink, R. H., & Pascoe, R. T. (1975). Ceramic steel? *Nature, 258*, 703–704.

Gates, R. S., Hsu, M., & Klaus, E. E. (1989). Tribochemical mechanism of alumina with water. *Tribology Transaction, 32*, 357–363.

Gee, M. G. (1992). The formation of aluminium hydroxide in the sliding wear of alumina. *Wear, 153*, 201–227.

Gee, M. G., & Butterfield, D. (1993). The combined effect of speed and humidity on the wear and friction of silicon-nitride. *Wear, 162*, 234–245.

Gee, M. G., Matharu, C. S., Almond, E. A., & Eyre, T. S. (1990). The measurement of sliding friction and wear of ceramics at high-temperature. *Wear, 138*, 169–187.

Gleiter, H. (1989). Nanocrystalline materials. *Progress in Materials Science, 33*, 223–315.

Gomes, J. R., Miranda, A. S., Vieira, J. M., & Silva, R. F. (2001). Sliding speed-temperature wear transition maps for Si3N4/iron alloy couples. *Wear, 250*, 293–298.

Gomes, J. R., Oliveira, F. J., Silva, R. F., Osendi, M. I., & Miranzo, P. (2000). Effect of alpha-/beta Si_3N_4-phase ratio and microstructure on the tribological behaviour up to 700 degrees C. *Wear, 239*, 59–68.

Gomes, J. R., Osendi, M. I., Miranzo, P., Oliveira, F. J., & Silva, R. F. (1999). Tribological characteristics of self-mated couples of Si_3N_4-SiC composites in the range 22-700 degrees C. *Wear, 233*, 222–228.

Green, D. J., Hannink, R. H. J., & Swain, M. V. (1989). *Transformation toughening of ceramics.* Boca Raton, FL: CRC Press.

Guicciardi, S., Melandri, C., & De Portu, G. (1999). Wear behaviour of electroconductive Al_2O_3 based composites. In P. Walls, C. Sorrell, & A. Ruys (Eds.), *Proceedings of the second international meeting of Pacific Rim Ceramic Societies* (pp. 513–519). Menai, NSW, Australia: Australasian Ceramic Society.

Guicciardi, S., Melandri, C., Lucchini, F., & De Portu, G. (2002). On data dispersion in pin-on-disk wear tests. *Wear, 252*, 1001–1006.

Guicciardi, S., Sciti, D., Melandri, C., & Bellosi, A. (2005). Dry sliding wear behavior of Al_2O_3-SiC submicro- and nano-composites. *Journal of the American Ceramic Society, 88*, 179–183.

Guicciardi, S., Sciti, D., Melandri, C., & Pezzotti, G. (2007). Dry sliding wear behavior of nano-sized SiC pins against SiC and Si_3N_4 discs. *Wear, 262*, 529–535.

Hadad, M., Blugan, G., Kubler, J., Rosset, E., Rohr, L., & Michler, J. (2006). Tribological behaviour of Si_3N_4 and Si_3N_4-%TiN based composites and multi-layer laminates. *Wear, 260*, 634–641.

Hahn, H., & Padmanabhan, K. A. (1995). Mechanical response of nanostructured materials. *Nanostructured Materials, 6*, 191–200.

Han, B. Q., Lavernia, E. J., & Mohamed, F. A. (2005). Mechanical properties of nanostructured materials. *Reviews on Advanced Materials Science, 9*, 1–16.

Hannink, R. H. J. (1983). Microstructural development of sub eutectoid aged MgO-ZrO_2 alloys. *Journal of Materials Science, 18*, 457–470.

Hannink, R. H., Murray, M. J., & Scott, H. G. (1984). Friction and wear of partially stabilized zirconia: basic science and practical applications. *Wear, 100*, 355–366.

He, C., Wang, Y. S., Wallace, J. S., & Hsu, S. M. (1993). Effect of microstructure on the wear transition of zirconia-toughened alumina. *Wear, 162–164*, 314–321.

Herrmann, M., Schulz, I., Schubert, C.., Hermel, W., Dresden, I., Zalite, I., et al. (1998). Ultrafine Si_3N_4 material with low coefficients of friction and wear rates. *Ceramic Forum International, 75*, 38–45.

Hibi, Y., & Enomoto, Y. (1989). Tribochemical wear of silicon-nitride in water, normal-alcohols and their mixtures. *Wear, 133*, 133–145.

Hisakado, T., & Tani, H. (1999). Effects of elevated temperatures and topographies of worn surfaces on friction and wear of ceramics in vacuum. *Wear, 224*, 165–172.

Hokkirigawa, K. (1991). Wear mode map of ceramics. *Wear, 151*, 219–228.

Hooper, R. M., Shakib, J. I., & Brookes, C. A. (1988). Microstructure and wear of tic cubic bn tools. *Materials Science and Engineering A-Structural Materials Properties Microstructure and Processing, 106*, 429–433.

Hsu, S. M., & Shen, M. C. (1996). Ceramic wear maps. *Wear, 200*, 154–175.

Hu, J., Li, D. Y., & Llewellyn, R. (2005). Computational investigation of microstructural effects on abrasive wear of composite materials. *Wear, 259*, 6–17.

Hussainova, I. (2003). Effect of microstructure on the erosive wear of titanium carbide-based cermets. *Wear, 255*, 121–128.

Hussainova, I. (2005). Microstructure and erosive wear in ceramic-based composites. *Wear, 258*, 357–365.

Hussainova, I., Kolesnikova, A., Hussainov, M., & Romanov, A. (2009). Effect of thermo-elastic residual stresses on erosive performance of cermets with core-rim structured ceramic grains. *Wear, 267*, 177–185.

Hutchings, I. M. (1992). *Tribology: Friction and wear of engineering materials*. London: Edward Arnold.

Hvizdoš, P., Maestra, Á., & Anglada, M. (2010). Effect of heat treatment on wear damage mechanisms in 3Y-TZP ceramics. *Wear, 269*, 26–30.

Hyuga, H., Jones, M. I., Hirao, K., & Yamauchi, Y. (2004). Influence of rare-earth additives on wear properties of hot-pressed silicon nitride ceramics under dry sliding conditions. *Journal of the American Ceramic Society, 87*, 1683–1686.

Hyuga, H., Jones, M. I., Hirao, K., & Yamauchi, Y. (2005). Friction and wear properties of Si_3N_4/carbon fiber composites with aligned microstructure. *Journal of the American Ceramic Society, 88*, 1239–1243.

Hyuga, H., Sakaguchi, S., Hirao, K., Yamauchi, Y., & Kanzaki, S. (2001). Influence of microstructure and grain boundary phase on tribological properties of Si_3N_4 ceramics. *Ceramic Engineering Science Proceedings, 22*, 197–202.

Iizuka, T., & Kita, H. (2005). Tribological behavior of Mo_5Si_3 particle reinforced Si_3N_4 matrix composites. *Wear, 258*, 877–889.

Iizuka, T., Kita, H., Hirai, T., & Osumi, K. (2004). Tribological behavior of W_2C nano-particle reinforced Si_3N_4 matrix composite. *Wear, 257*, 953–961.

Ikeuchi, K., Kusaka, J., & Yoshida, H. (2000). Tribology for all-ceramic joint prostheses. *Journal of Ceramic Processing Research, 1*, 53–56.

ISO 20808:2004, Fine ceramics (advanced ceramics, advanced technical ceramics) – Determination of friction and wear characteristics of monolithic ceramics by ball-on-disc method.

Jahanmir, S. (Ed.). (1994). *Friction and wear of ceramics*. New York, USA: Marcel Dekker.

Jahanmir, S., & Dong, X. (1992). Mechanism of mild to severe wear transition in alpha alumina. *ASME, Transactions, Journal of Tribology, 114*(3), 403–411.

Janxing, D., Zeliang, D., Jun, Z., Jianfeng, L., & Tongkun, C. (2006). Unlubricated friction and wear behavior of various alumina-based ceramic composites against cemented carbide. *Ceramics International, 32*, 499–507.

Jeng, M.-C., & Yan, L.-Y. (1993). Environmental effects on wear behavior of alumina. *Wear, 161*, 111–119.

Jones, A. H., Dobedoe, R. S., & Lewis, M. H. (2001). Mechanical properties and tribology of Si_3N_4-TiB_2 ceramic composites produced by hot pressing and hot isostatic pressing. *Journal of the European Ceramic Society, 21*, 969–980.

Jones, M. I., Hirao, K., Hyuga, H., Yamauchi, Y., & Kanzaki, S. (2003). Wear properties of Y-alpha/beta composite sialon ceramics. *Journal of the European Ceramic Society, 23*, 1743–1750.

Jones, M. I., Hyuga, H., Hirao, K., & Yamauchi, Y. (2004). Wear properties under dry sliding of Lu-alpha sialons with in situ reinforced microstructures. *Journal of the European Ceramic Society, 24*, 3581–3589.

Kato, K. (1990). Tribology of ceramics. *Wear, 136*, 117–133.

Kalin, M., Novac, S., & Vizintin, J. (2003). Wear and friction behavior of alumina ceramics in aqueous solution with different pH. *Wear, 254*, 1141–1146.

Kapelski, G., Platon, F., & Boch, P. (1988). Wear and friction properties of some engineering ceramics. In Derek Taylor (Ed.), *Proceedings of 14th international conference of science of ceramics* (pp. 781–786). Stoke-on-Trent: The Institute of Ceramics.

Kiefer, T., Moon, H., & Lange, F. F. (2005). Compressive surface layer to avoid edge cracking in laminar ceramic composite. *Journal of the American Ceramic Society, 88*, 2855–2858.

Kim, J. H., Kumar, B. V. M., Hong, S. H., & Kim, H. D. (2010). Fabrication of silicon nitride nanoceramics and their tribological properties. *Journal of the American Ceramic Society, 93*, 1461–1466.

Kim, S. S., Chae, Y. H., & Kim, D. J. (2000). Tribological characteristics of silicon nitride at elevated temperatures. *Tribology Letters, 9*, 227–232.

Kitaoka, S., Tsuji, T., Katoh, T., Yamaguchi, Y., & Sato, K. (1994). Effect of sintering aids on tribological characteristics of Si_3N_4 ceramics at 120-degrees-C in water. *Wear, 179*, 63–67.

Kork, M. (2006). Abrasive wear of alumina particle reinforced aluminium alloy composites fabricated by vortex method. *Composites A, 37*, 457–464.

Krell, A., & Klaffke, D. (1996). Effect of grain size and humidity on fretting wear in fine-grained alumina, Al2O3/TiC, and zirconia. *Journal of the American Ceramic Society, 79*, 1139–1145.

Kumar, R., Acikbas, N. C., Kara, F., Mandal, H., & Basu, B. (2009). Microstructure-mechanical properties-wear resistance relationship of sialon ceramics. *Metallurgical and Materials Transactions A-Physical Metallurgy and Materials Science, 40A*, 2319–2332.

Kuo, D-H., & Kriven, W. M. (1997). A strong and damage-tolerant oxide laminate. *Journal of the American Ceramic Society, 80*, 2421–2424.

Kurama, S., Schulz, I., & Herrmann, M. (2011). Wear properties of alpha- and alpha/beta-SiAlON ceramics obtained by gas pressure sintering and spark plasma sintering. *Journal of the European Ceramic Society, 31*, 921–930.

Lakshminarayanan, R., Shetty, D. K., & Cutler, R. A. (1996). Toughening of layered ceramic composites with residual surface compression. *Journal of the American Ceramic Society, 79*, 79–87.

Lee, K. H., & Kim, K. W. (1994). Effects of humidity and sliding speed on the wear properties of si3n4 ceramics. *Materials Science and Engineering A-Structural Materials Properties Microstructure and Processing, 186*, 185–191.

Lee, S. W. (1999). Tribological characterization in ceramic based composites. In K. Niihara, T. Sekino, E. Yasuda, & T. Sasa (Eds.), *Key engineering materials: Vols. 161–163. The science of engineering ceramics II* (pp. 593–598).

Liang, Y. N., Lee, S. W., & Park, D. S. (1999). Effects of whisker distribution and sintering temperature on friction and wear of Si_3N_4-whisker-reinforced Si_3N_4-composites. *Wear, 225*, 1327–1337.

Lim, S. C., & Ashby, M. F. (1987). Wear-mechanism maps. *Acta Metallurgica, 35*, 1–24.

Lin, J. F., & Chen, Y. N. (1995). The relationship between the change in stress intensity factor and wear rate at elevated-temperatures for ceramics. *Wear, 185*, 131–139.

Liu, C. C., & Huang, J. L. (2004). Tribological characteristics of Si_3N_4-based composites in unlubricated sliding against steel ball. *Materials Science and Engineering A-Structural Materials Properties Microstructure and Processing, 384*, 299–307.

Liu, H. Y., & Fine, M. E. (1993). Modeling of grain-size-dependent microfracture-controlled sliding wear in polycrystalline alumina. *Journal of the American Ceramic Society, 76*, 2393–2396.

Löffelbein, B., Woydt, M., & Habig, K-H. (1993). Sliding friction and wear of ceramics in neutral, acid and basic aqueous solutions. *Wear, 162–164*, 220–228.

Lopez, G., & Staia, M. H. (2005). High-temperature tribological characterization of zirconium nitride coatings. *Surface and Coatings Technology, 200*, 2092–2099.

Ludema, K. C. (1996). *Friction, wear, lubrication: A textbook in tribology*. Boca Raton, FL: CRC Press.

Luo, H. H., Zhang, F. C., & Robert, S. G. (2008). Wear resistance of reaction sintered alumina/mullite composites. *Materials Science and Engineering A, 478*, 270–275.

Matejka, V., Lu, Y. F., Jiao, L., Huang, L., Martynkova, G. S., & Tomasek, V. (2010). Effects of silicon carbide particle sizes on friction-wear properties of friction composites designed for car brake lining applications. *Tribology International, 43*, 144–151.

Matsuda, M., Kato, K., & Hashimoto, A. (2011). Friction and wear properties of silicon carbide in water from different sources. *Tribology Letters, 43*, 33–41.

Melandri, C., Gee, M. G., de Portu, G., & Guicciardi, S. (1995). High temperature friction and wear testing of silicon nitride ceramics. *Tribology International, 28*, 403–413.

Melmonte, M., Nieto, M. I., Osendi, M. I., & Miranzo, P. (2006). Influence of the SiC grain size on the wear behavior of Al_2O_3/SiC composites. *Journal of the European Ceramic Society, 26*, 1273–1278.

Merino, J. L. O., & Todd, R. I. (2005). Relationship between wear rate, surface pull-out and microstructure during abrasive wear of alumina and alumina/SiC nanocomposites. *Acta Materialia, 53*, 3345–3357.

Meng, J. H., Lu, J. J., Wang, J. B., & Yang, S. R. (2006). Tribological behavior of TiCN-based cermets at elevated temperatures. *Materials Science and Engineering A-Structural Materials Properties Microstructure and Processing, 418*, 68–76.

Miyazaki, H., Hyuga, H., Yoshizawa, Y., Hirao, K., & Ohji, T. (2009). Correlation of wear behavior and indentation fracture resistance in silicon nitride ceramics hot-pressed with alumina and yttria. *Journal of the European Ceramic Society, 29*, 1535–1542.

Miyoshi, K., Pouch, J. J., Alterovitz, S. A., Pantic, D. M., & Johnson, G. A. (1989). Adhesion, friction, and wear of plasma-deposited thin silicon-nitride films at temperatures to 700°C. *Wear, 133*, 107–123.

Mukhopadhyay, A. K., & May, Y.-W. (1993). Grain size effect and abrasive wear mechanisms in alumina ceramics. *Wear, 162–164*, 258–268.

Mukhopadhyay, A., & Basu, B. (2007). Consolidation microstructure property relationships in bulk nanoceramics and ceramic nanocomposites: a review. *International Materials Reviews, 52*, 257–288.

Nakamura, M., Hirao, K., Yamauchi, Y., & Kanzaki, S. (2003). Wear behaviour of alpha-Sb_3N_4 ceramics reinforced by rod-like beta-Sb_3N_4 grains. *Wear, 254*, 94–102.

Nakamura, Y., & Hirayama, S. (1990). Effect of liquid lubricants on the wear of gray cast-iron against sialon ceramic. *Wear, 137*, 91–97.

Nomura, N., Yoshimi, K., Konno, T., & Hanada, S. (2000). Fracture toughness improvement of TiC by Nb and Mo precipitates. *Journal of Materials Science Letters, 19*, 1879–1881.

Park, D. S., Danyluk, S., & McNallan, M. J. (1992). Influence of tribochemical reaction-products on friction and wear of silicon-nitride at elevated-temperatures in reactive environments. *Journal of the American Ceramic Society, 75*, 3033–3039.

Park, D. S., Han, B. D., Lim, D. S., & Yeo, L. W. (1997). A study on wear and erosion of sialon-Si_3N_4 whisker ceramic composites. *Wear, 203*, 284–290.

Perez-Unzueta, A. G., Beynon, J. H., & Gee, M. G. (1991). The effect of surrounding atmosphere on the sliding wear of alumina. *Wear, 146*, 179–196.

Platzer, W. (1990). *The role of future emission regulation on the tribology of truck diesel engines*. Bad Nauheim 19/20.

Polcar, T., Novak, R., & Siroky, P. (2006). The tribological characteristics of TiCN coating at elevated temperatures. *Wear, 260*, 40–49.

Qi, X. M., Aust, E., Eigen, N., Gartner, F., Klassen, T., & Bormann, R. (2006). TiC-based cermet coatings: advanced wear performance by nanocrystalline microstructure. *Advanced Engineering Materials, 8*, 427–433.

Rainforth, W. M. (2004). The wear behavior of oxide ceramics-a review. *Journal of Materials Science, 39*, 6705–6721.

Rani, D. A., Yoshizawa, Y., Hyuga, H., Hirao, K., & Yamauchi, Y. (2004). Tribological behavior of ceramic materials (Si_3N_4, SiC and Al_2O_3) in aqueous medium. *Journal of the European Ceramic Society, 24*, 3279–3284.

Rao, M. P., Sánchez-Herencia, A. J., Beltz, G. E., McMeeking, R. M., & Lange, F. F. (1999). Laminar ceramics that exhibit a threshold strength. *Science, 286*, 102–105.

Ravikiran, A., Nagarajan, V. S., Biswas, S. K., & Pramila Bai, B. N. (1995). Effect on speed and pressure on dry sliding interactions on alumina against steel. *Journal of the American Ceramic Society, 78*, 356–364.

Ravikiran, A., & Pramila Bai, B. N. (1995). Sliding wear of YTZP ceramics against steel: observations of ceramic transfer and wear transition. *Journal of Materials Science, 30*, 1999–2007.

Ravikiran, A. (2000). Influence of apparent pressure on wear behavior of self mated alumina. *Journal of the American Ceramic Society, 83*, 1302–1304.

Ravikiran, A., & Jahanmir, S. (2001). Effect of contact pressure and load on wear of alumina. *Wear, 251*, 980–984.

Richerson, D. W. (1992). *Modern ceramic engineering*. New York: Marcel Dekke, ISBN 0-8247-8634-3.

Russo, C. J., Harmer, M. P., Chan, H. M., & Miller, G. A. (1992). Design of a laminated ceramic composite for improved strength and toughness. *Journal of the American Ceramic Society, 75*, 3396–3400.

Sasaki, S. (1989). The effects of the surrounding atmosphere on the friction and wear of alumina, zirconia, silicon-carbide and silicon-nitride. *Wear, 134*, 185–200.

Scheppokat, S., Hannink, R., Janssen, R., De Portu, G., & Claussen, N. (2005). Sliding wear of Cr-Al_2O_3-ZrO_2 and Mo-Al_2O_3-ZrO_2 composites. *Journal of the European Ceramic Society, 25*, 837–845.

Sekino, T., Nalajima, T., Ueda, S., & Niihara, K. (1997). Reduction and sintering of a nickel-dispersed-alumina composite and its properties. *Journal of the American Ceramic Society, 80*, 1139–1148.

Senda, T., Drennan, J., & McPherson, R. (1995). Sliding wear of oxide ceramics at elevated temperatures. *Journal of the American Ceramic Society, 78*, 3018–3024.

Senda, T., Yasuda, E., Kaji, M., & Bradt, R. C. (1999). Effect of grain size on the sliding wear and friction of alumina at elevated temperature. *Journal of the American Ceramic Society, 82*, 1505–1511.

Sergo, V., Lipkin, D. M., De Portu, G., & Clarke, D. R. (1997). Edge stresses in alumina/zirconia laminates. *Journal of the American Ceramic Society, 80*, 1633–1638.

She, J., Scheppokat, S., Janssen, R., & Claussen, N. (1998). Reaction bonded three-layer alumina-based composites with improved damage resistance. *Journal of the American Ceramic Society, 81*, 1374–1376.

Shimada, M., Matsushita, K., Kuratani, S., Okamoto, T., Koizumi, M., Tsukuma, K., et al. (1984). Temperature dependence of Young's modulus and internal friction in alumina, silicon nitride and partially stabilized zirconia ceramics. *Journal of the American Ceramic Society, 67*, C-23–C-24.

Shu, Y., Jie, C., Qizhong, H., Xiang, X. O., Tong, C., & Yunping, L. (2010). Effect of braking speeds on the tribological properties of carbon/carbon composites. *Materials Transactions, 51*, 1038–1043.

Singha Roy, R., Guchhait, H., Chanda, A., Basu, D., & Mitra, M. K. (2007). Improved sliding wear resistance of alumina with sub-micron grain size: a comparison with coarser grained material. *Journal of the European Ceramic Society, 27*, 4737–4743.

Singha Roy, R., Basu, D., Chanda, A., & Mitra, M. K. (2007). Distinct wear characteristic of submicrometer-grained alumina in air and distilled water: a brief analysis of experimental observation. *Journal of the American Ceramic Society, 90*, 2987–2991.

Skopp, A., & Woydt, D. (1995). Ceramic and ceramic composite materials with improved friction and wear properties. *Tribology Transaction, 38*, 233–242.

Skopp, A., Woydt, M., & Habig, K. H. (1990). Unlubricated sliding friction and wear of various Si_3N_4 pairs between 22°C and 1000°C. *Tribology International, 23*, 189–199.

Stachowiak, G. W., & Stachowiak, G. B. (1989). Unlubricated friction and wear behavior of toughened zirconia ceramics. *Wear, 132*, 151–171.

Sue, J. A., & Chang, T. P. (1995). Friction and wear behavior of titanium nitride, zirconium nitride and chromium nitride coatings at elevated temperatures. *Surface and Coatings Technology, 76*, 61–69.

Takadoum, J. (1993). Tribological behavior of alumina sliding on several kinds of materials. *Wear, 170*, 285–290.

Tarlazzi, A., Roncari, E., Pinasco, P., Guicciardi, S., Melandri, C., & De Portu, G. (2000). Tribological behaviour of Al_2O_3/ZrO_2-ZrO_2 laminated composites. *Wear, 244*, 29–40.

Tennenhouse, G. J., & Runkle, F. D. (1986). The effects of oxygen on the wear of Si_3N_4 against cast-iron and steel. *Wear, 110*, 75–81.

Ting, B. Y., & Winer, W. O. (1989). Friction-induced thermal influences in elastic contact between spherical asperities. *Journal of Tribology-Transactions of the ASME, 111*, 315–322.

Tkachenko, Y. G., Yurchenko, D. Z., Sibel, A. S., & Murzin, L. M. (1998). High-temperature friction and wear of titanium carbide hard alloys with an addition of a solid lubricant. *Powder Metallurgy and Metal Ceramics, 37*, 421–424.

Toschi, F., Melandri, C., Pinasco, P., Roncari, E., Guicciardi, S., & De Portu, G. (2003). Influence of residual stress on the wear behaviour of alumina/alumina-zirconia laminated composites. *Journal of the American Ceramic Society, 86*, 1547–1553.

Uhlmann, E., Rosiwal, S., Bayerlein, K., & Rohner, M. (2010). Influence of grain size on the wear behavior of CVD diamond coatings in micro-EDM. *International Journal of Advanced Manufacturing Technology, 47*, 919–922.

Umeda, K., Enomoto, Y., Mitsui, A., & Mannami, K. (1993). Friction and wear of boride ceramics in air and water. *Wear, 169*(1), 63–68.

Vassen, R., & Stover, D. (2001). Processing and properties of nanophase non-oxide ceramics. *Materials Science and Engineering A-Structural Materials Properties Microstructure and Processing, 301*, 59–68.

Wang, D. F., She, J. H., & Ma, Z. Y. (1995). Effect of microstructure on erosive wear behavior of SiC ceramics. *Wear, 180*, 35–41.

Wang, Y. S., Hsu, S. M., & Munro, R. G. (1990). A wear model for alumina sliding wear. In *Proc. Japan int. tribology conf.* (Vol. 2; pp. 1225). Tokyo, Japan: Japan Society of Tribologists.

Watanabe, M., Satoshi, I., & Fukuura, I. (1984). Aging behavior of Y-TZP. In N. Claussen, M. Rühle, & H. Heuer (Eds.), *Proceeding of the second international conference on the science and technology of zirconia (zirconia '83)* (pp. 391–398). Columbus, Ohio: The American Ceramic Society, Inc.

Weertman, J. R., Farkas, D., Hemker, K., Kung, H., Mayo, M., Mitra, R., et al. (1999). Structure and mechanical behavior of bulk nanocrystalline materials. *Mrs Bulletin, 24*, 44–50.

Williams, J. A. (1994). *Engineering tribology*. Oxford: Oxford Science Publications, Oxford University Press.

Wilson, S., & Alpas, A. T. (1996). Dry sliding wear of a PVD TiN coating against Si_3N_4 at elevated temperatures. *Surface and Coatings Technology, 86*, 75–81.

Wilson, S., & Alpas, A. T. (1997). Effect of temperature and sliding velocity on TiN coating wear. *Surface and Coatings Technology, 94–95*, 53–59.

Winn, A. J., Dowson, D., & Bell, J. C. (1995a). The lubricated wear of ceramics 1. The wear and friction of silicon nitride, alumina and steel in the presence of a mineral oil based lubricant. *Tribology International, 28*, 383–393.

Winn, A. J., Dowson, D., & Bell, J. C. (1995b). The lubricated wear of ceramics 2. The wear and friction of silicon nitride and steel in the presence of mineral oil or an ester based lubricant. *Tribology International, 28*, 395–402.

Winnubst, A. J. A., & Burggraaf, A. J. (1988). The aging behavior of ultrafine-grained Y-TZP in hot water. In S. Sōmiya, N. Yamamoto, & H. Yanagida (Eds.), *Proceeding of the third international conference on the science and technology of zirconia* (pp. 39–47). Columbus, Ohio: The American Ceramic Society, Inc.

Woydt, M., & Habig, K. H. (1989). High-temperature tribology of ceramics. *Tribology International, 22*, 75–88.

Woydt, M., Skopp, A., & Habig, K. H. (1991). Dry friction and wear of self-mated sliding couples of SiC-TiC and Si_3N_4-TiN. *Wear, 148*, 377–394.

Wu, Y. Q., Zeng, M., Yu, L., & Fan, L. R. (2010). Synergistic effect of nano- and micrometer-size ceramic fibers on the tribological and thermal properties of automotive brake lining. *Journal of Reinforced Plastics and Composites, 29*, 2732–2743.

Xiao, H. N., & Senda, T. (1997). Friction and wear of silicon carbide at elevated temperatures. *Journal of the Ceramic Society of Japan, 105*, 750–755.

Xiong, F., Manroy, R. R., Ward, L., Terheci, M., & Lathabay, S. (1997). Effect of grain size and test configuration on the wear behavior of alumina. *Journal of the American Ceramic Society, 80*, 1310–1312.

Xiong, F., & Manory, R. R. (1999). The effect of test parameters on alumina wear under low contact stress. *Wear, 236*, 240–245.

Xu, H. H. K., Jahanmir, S., & Wang, Y. (1995). Effect of grain size on scratch interaction and material removal in alumina. *Journal of the American Ceramic Society, 78*, 881–891.

Yang, Q., Senda, T., Kotani, N., & Hirose, A. (2004). Sliding wear behavior and tribofilm formation of ceramics at high temperatures. *Surface and Coatings Technology, 184*, 270–277.

Yang, Z. L., Ouyang, J. H., Liu, Z. G., & Liang, X. S. (2010). Wear mechanisms of TiN-TiB(2) ceramic in sliding against alumina from room temperature to 700°C. *Ceramics International, 36*, 2129–2135.

Yoshimura, M., Komura, O., & Yamakawa, A. (2001). Microstructure and tribological properties of nano-sized Si_3N_4. *Scripta Materialia, 44*, 1517–1521.

Yu, Z. M., Inagawa, K., & Jin, Z. J. (1994). Tribological properties of c-bn coatings in vacuum at high-temperature. *Surface and Coatings Technology, 70*, 147–150.

Zhang, F. C., Luo, H. H., Wang, T. S., Robert, S. G., & Todd, R. I. (2008). Influence factors on wear resistance of two alumina matrix composites. *Wear, 265*, 27–33.

Zhang, Y., Cheng, Y. B., & Lathabai, S. (2001). Influence of microstructure on the erosive wear behaviour of Ca alpha-sialon materials. *Journal of the European Ceramic Society, 21*, 2435–2445.

Zhao, X. Z., Liu, J. J., & Fischer, T. E. (1998). Effects of lubricant rheology and additive chemistry in the wear of Si_3N_4 sliding on steel. *Wear, 223*, 37–43.

Zhao, X. Z., Liu, J. J., Zhu, B. L., Ouyang, J. L., & Xue, O. J. (1998). Tribological properties of TiC-based ceramic high speed steel pairs at high temperatures. *Ceramics International, 24*, 13–18.

Zum Gahr, K.-H. (1987). *Microstructure and wear of materials*. Oxford, UK: Elsevier.

Zum Gahr, K.-H., Bundschuh, W., & Zimmerlin, B. (1993). Effect of grain size on friction and sliding wear of oxide ceramics. *Wear, 162–164*, 269–279.

2.15 Corrosion of Ceramic Materials

Mathias Herrmann and Hagen Klemm, Fraunhofer-Institut für Keramische Technologien und Systeme IKTS, (www.ikts.fraunhofer.de) Dresden, Germany

© 2014 Elsevier Ltd. All rights reserved.

2.15.1 Introduction

The term *corrosion* is defined as localized or large-scale reaction of a material with the surrounding media, resulting in degradation or even in destruction of the material or component. Corrosion behavior is therefore a property not of the material, but of the system including the material, the media and conditions such as temperature, pressure, medium type and volume or flow rate, and tribological as well as mechanical loads. Therefore, a simple statement concerning corrosion resistance of a material cannot be given because the material may be stable under one set of conditions, but unstable under another set of conditions (Jacobson, 1986; Klemm, 2010; Nickel & Gogotsi, 2000; Nickel, Quirmbach, & Pötschke, 2010; Petzow & Herrmann, 2002; Schmalzried & Schwetz, 2010).

Fundamentally two distinctly different types of corrosion can occur, namely, active or passive.

If the corrosion products are removed from the surface, i.e. if species with high vapor pressures or components soluble in the corrosion media are formed, the corrosion reaction is characterized by removal of the corrosion products and hence reduction in size and mass of the ceramic material. This type of corrosion is called *active corrosion*. Active corrosion is usually characterized by a linear time dependence of the mass loss or the decrease in dimensions (**Figure 1(a)**).

$$\Delta x = Kt \tag{1}$$

where x is the mass or dimensions and K, the rate constant.

If the reaction product of the corrosion reaction is a solid or a high-viscosity liquid (e.g. a silicate) that is insoluble in the corrosion media, the corrosion is often controlled by the properties of the formed surface layer. If the surface layer is dense and the rate of diffusion of the reactants or reaction products through this layer is low, the formed layer acts as a corrosion barrier and the corrosion is controlled by this barrier. This case is called *passive corrosion* (**Figure 1(b)**).

For times longer than the time necessary for the formation of the passive layer, the change in mass or dimensions is proportional to the square root of time:

$$\Delta x = k\sqrt{t} + C_1, \tag{2}$$

where Δx is the thickness of the layer and the constant k is the rate constant, C_1 includes the processes up to formation of a stable layer. The layer thickness and mass change can be recalculated using the equation of the chemical reaction and the component densities. The equation has the physical meaning that the diffusion through the barrier is rate-controlling and as a result, the thickness of the barrier increases with $\sqrt{t}$. More complicated equations have been derived for short reaction times (formation of the stable oxide layer) (Nickel et al., 2010; Nickel & Gogotsi, 2000). The above equation is valid for steady-state systems, i.e. in which the material surfaces and surface layer properties can be considered to be constant. If any of these parameters is

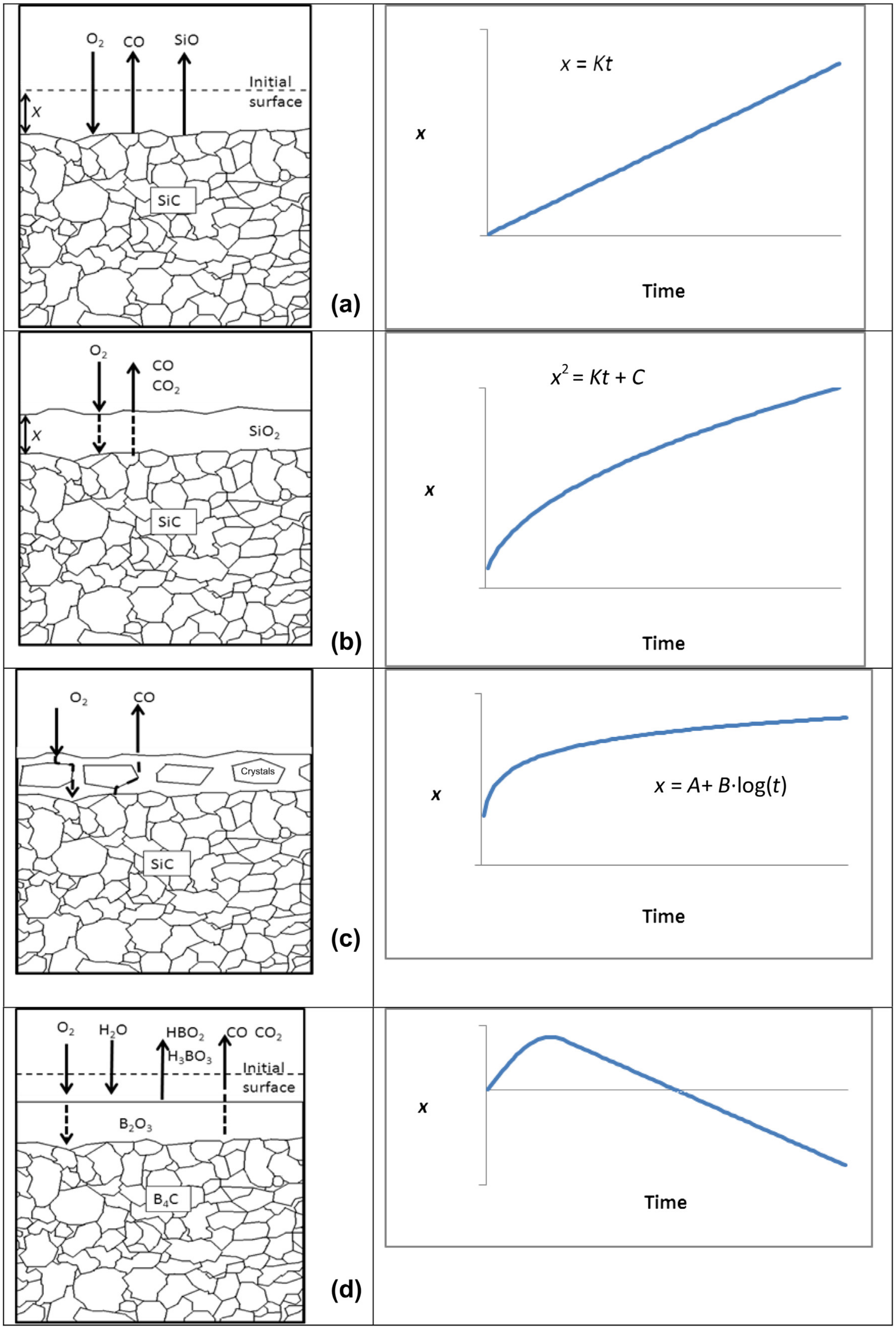

Figure 1 Schematics of different types of corrosion: (a) active (b) and (c) passive with amorphous and crystallized oxide layer respectively, in silicon carbide ceramics (d) paralinear (active) behavior in boron carbide ceramics.

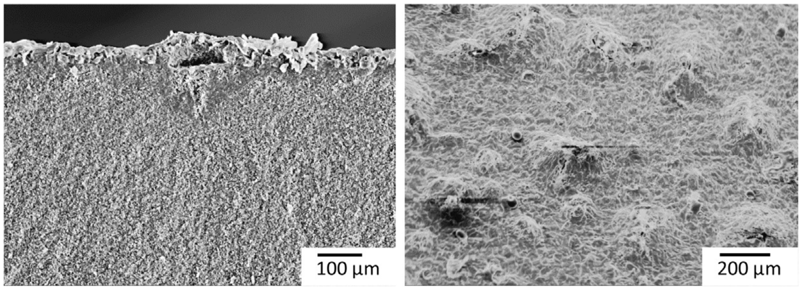

Figure 2 Pits formed in Si_3N_4 ceramics during oxidation (Klemm, Taut, & Wötting, 2003).

changed, more complicated equations must be used to describe the process (Nickel et al., 2010; Nickel & Gogotsi, 2000). It was shown that if the layer crystallizes and the diffusion through the crystals is slow, the equation changes to $\Delta x = A + B \log(t)$, where A and B are constants (**Figure 1(c)**).

The active and passive corrosion mechanisms are shown schematically in **Figure 1** for the oxidation of SiC.

A detailed derivation of the equations depending on the mechanism and the sample geometry is given in the literature (Hou & Chou, 2009; Nickel & Gogotsi, 2000; Nickel et al., 2010; Persson & Nygren, 1994; Herrmann, 2013).

Besides large-scale homogeneous corrosion, more intense corrosion can take place locally (pitting). Pitting can be caused by inhomogeneities in the ceramic (pores, cracks or segregated secondary phases with lower corrosion resistivity) or by locally damaged corrosion layers (through gas bubble formation or impurities from the corroding atmospheres). Pitting is mainly responsible for the decrease in strength of ceramics due to corrosion (**Figure 2**).

A material's corrosion behavior is often distinguished by the surrounding media:

- Corrosion in gases
- Corrosion in liquid media.

This classification is based on the differences in media, transport mechanisms and experimental methods of investigation. Gas corrosion often occurs at higher temperatures and plays a significant role in high-temperature applications, especially for nonoxide materials. Water- or organic-based systems play an important role in industrial processes in which ceramics and hard materials are used, e.g. as seals, bearings or valves. These processes take place near ambient temperature. Nevertheless, if the interaction with metal or glass melts is taken into account, high temperatures are also involved. However, corrosion in these systems is very specific and therefore beyond the scope of this chapter. This chapter is focused on corrosion in air, combustion gases and water vapor-containing gases as well as in acidic and basic solutions and under hydrothermal conditions.

2.15.2 Corrosion in Gases

This chapter concentrates on corrosion in air, combustion gases and water vapor-containing gases due to the practical importance of these processes. Corrosion in halogenides and SO_2/SO_3 is not treated (see Jacobson & Fox, 1988; Jacobson, 1993; Marra, Kreidler, Jacobson, & Fox, 1988; Nickel & Gogotsi, 2000; Nickel et al., 2010; Presser, Heon, & Gogotsi, 2011; Readey, 1998; Van der Biest, Barnes, Corish, & Norton, 1987). Presser and co-workers (Presser et al., 2011) provide an overview of the reaction of different carbides with Cl_2. The halogenides—e.g. Cl_2 and HCl—extract the metal from the carbon, leaving a porous carbon material. The goal of the investigations of the interaction was to gain an understanding of the process of formation of porous carbon (carbon derived from carbides, or CDC materials), not of the corrosion behavior.

For unknown systems, an initial estimate of the corrosion behavior can be made by means of the gas reactions and the associated thermodynamic data. A corrosion reaction generally becomes possible when the Gibbs free energy ($\Delta G_{reaction}$) of the corresponding reaction is negative. If condensed phases are formed, passive corrosion can occur depending on the properties of the formed phases. Active corrosion is likely if the thermodynamic calculations predict the formation of gaseous phases only. In this case, the reaction can also take place if $\Delta G_{reaction}$ is positive. This only means that the partial pressure of the gaseous product has a

Table 1 Overview of corrosion data for nonoxide ceramics (EN12923, 2006)

Material	*Mechanism/Remarks*	*Literature*
Overview of corrosion of ceramics		Jacobson, 1993; Nickel & Gogotsi, 2000; Nickel et al., 2010; Opila, 2003
Testing procedures		Advanced, 2006; dos Santos e Lucato, Sudre, & Marshall, 2011; Fritsch, 2008; Jacobson, 1993; Nickel & Gogotsi, 2000; Nickel et al., 2010; Opila, 2003
Si_3N_4	Passive oxidation, influence of material properties	Backhaus-Ricoult, Guerin, & Urbanovich, 2002; Klemm et al., 2003; Klemm, 2002, 2010; Klemm, Herrmann, & Schubert, 1998; Nickel & Gogotsi, 2000; Nickel et al., 2010; Petzow & Herrmann, 2002
	Gas turbine conditions	Fritsch, 2008; Fritsch, Klemm, Herrmann, Michaelis, & Schenk, 2010; Klemm, 2002; Klemm, 2010; Opila, 2003; Parthasarathy, Rapp, Opeka, & Kerans, 2009
SiC	Passive/transition from passive to active	Balat, 1996; Balat, Berjoan, Pichelin, & Rochmann, 1998; Charpentier, Balat-Pichelin, & Audubert, 2010; Charpentier, Balat-Pichelin, Glénat, et al., 2010; Charpentier, Maître, Balat-Pichelin, et al., 2009; Costello & Tressler, 1986; Courtright, 1991; Dawi, Balat-Pichelin, Charpentier, et al., 2012; dos Santos e Lucato et al., 2011; Heuer & Lou, 1990; Kim & Moorhead, 1990a, 1990b; More, Tortorelli, Walker, et al., 2003; Narushima, Goto, Yokoyama, et al., 1994a, 1994b; Narushima, Goto, Yokoyama, Iguchi, & Hirai, 1993; Nickel & Gogotsi, 2000; Nickel et al., 2010; Opila & Serra, 2011; Osada, Nakao, Takahashi, & Ando, 2009; Presser & Nickel, 2008; Presser, Loges, Hemberger, et al., 2009; Presser, Loges, Wirth, et al., 2009; Ramberg & Worrell, 2001; Schmalzried & Schwetz, 2010; Schneider, Guette, Naslain, et al., 1998; Vaughn & Maahs, 1990; Wang, Zhang, Zeng, Vignoles, & Guette, 2008
	Gas turbine conditions	Fritsch et al., 2010; Fritsch, 2008; Hisamatsu, Etori, & Yamamoto, 2003; Jacobson & Farmer, 1999; Jacobson, 1993; Nickel & Gogotsi, 2000; Opila & Myers, 2004; Opila & Serra, 2011; Opila, 2003; Opila, Smialek, Robinson, Fox, & Jacobson, 1999; Roode, 2010
EBC for Si_3N_4 and SiC and oxide ceramics	Environmental barrier coatings	Fritsch & Klemm, 2006; Fritsch & Klemm, 2008; Fritsch, 2008; Klemm, 2002; Klemm, 2010; Roode, 2010
BN/B_4C/borides	Passive/active, influence of moisture	Eichler & Lesniak, 2008; Fahrenholtz, Hilmas, Talmy, & Zaykoski, 2007; Hu, Zhang, Han, Guang, & Du, 2010; Jacobson & Farmer, 1999; Nickel & Gogotsi, 2000; Nickel et al., 2010; Parthasarathy et al., 2009; Schmalzried & Schwetz, 2010; Sciti et al., 2005
AlN		Dutta, Mitra, & Rabenberg, 1992

partial pressure of <1 atm. For example, under gas turbine conditions a partial pressure of the reaction products of 10^{-7} MPa results in a degradation rate of Si_3N_4 ceramics of approximately 400 μm per 1000 h (Fritsch, 2008). A 100 times higher pressure would result in approximately 100 times higher recession rate. For gas reactions (active corrosion), the lower the partial pressure of the reaction products, the lower the corrosion rate.

The basic principles of the interaction of nonoxide ceramics with air or combustion gases will be outlined in the following chapter using the examples of SiC and Si_3N_4 ceramics due to the abundance of studies performed on them and their predominance in high-temperature applications. **Table 1** gives a summary of important literature in which the behavior of the materials is explained in detail. Presser and Nickel (2008) gives a comprehensive overview concerning the oxidation of SiC materials and single crystals.

2.15.2.1 Oxidation

All nonoxide ceramics are thermodynamically unstable in air, exhibiting passive oxidation behavior up to high temperatures. Therefore, their stability is connected with the stability of the oxide layer and diffusion of the oxygen through the formed oxide films. At ambient temperatures, nanometer-thick or even thinner oxide films are sufficient for stabilizing the nonoxide material (passive oxidation). At higher temperatures, the film thickness increases due to faster diffusion and oxidation reactions. The diffusion coefficients of the oxides and the resulting typical parabolic oxidation rates for selected ceramics are given in **Figure 3**. The data reveal that SiO_2 is superior to other oxides as an oxidation barrier. SiO_2 has an additional advantage in that it forms amorphous layers up to high temperatures, thus preventing the formation of grain boundaries (with accordingly higher diffusion coefficients) in the oxide scale and the destruction of the oxide scale due to the volume change during crystallization. The highly viscous character of the silica in the layer also allows the healing of cracks and, at least above the glass transition temperature, the relaxation of stresses between the oxide layer and the matrix. These simple principles are responsible for the high oxidation resistance of silica-forming systems (SiC, Si_3N_4 and $MoSi_2$) (**Figure 3**).

The data also indicate that the oxidation resistance of transition metal carbides, nitrides and borides alike (ZrB_2, TiC, ZrC, ZrN, and WC) is poor due to the high oxygen diffusion coefficients of the oxides. Composites with SiC are often used to improve the oxidation behavior of these materials. SiO_2 forms as an oxidation product of SiC, followed by a protective layer which includes the oxides or silicates of the other components. This method is used for example to improve the stability of the so-called ultrahigh-temperature materials (Fahrenholtz et al., 2007; Hu et al., 2010; Parthasarathy et al., 2009; Sciti, Brach, & Bellosi, 2005).

The properties of the protective oxide scales also depend on factors other than the main component of the material. Secondary phases such as those found in liquid phase-sintered materials can react with the oxide scale, usually reducing the viscosity and increasing the diffusion coefficients in the oxide scale. This was investigated in detail for Si_3N_4 materials. The oxidation stability of Si_3N_4 ceramics with different sintering additives at temperatures above 1200 °C was found to increase in the following order:

MgO, MgO/Al_2O_3, $MgO/R_2O_3 < R_2O_3/Al_2O_3 << R_2O_3$ ($R =$ rare-earth metal) (Petzow & Herrmann, 2002).

Oxidation at high temperatures does not take place only at the surface of the component if the diffusion along the grain boundaries is faster than the oxidation reaction. This is the case in liquid phase-sintered materials that have amorphous grain boundaries that allow relatively fast process of oxygen transport into the bulk (Klemm et al., 1998; Klemm et al., 2003; Petzow & Herrmann, 2002).

The differences between the chemical potentials of the components in the surface oxide layer and the grain boundary in the bulk also result in the diffusion of the additives or impurities toward the surface and in diffusion of unreacted oxygen and oxides formed by oxidation into the material. These processes lead to damage in the bulk of the material due to segregation of the grain boundaries and pore formation and ultimately to degradation of the material (Klemm et al., 2003). This can be alleviated by crystallization of the grain boundaries as well as at least partial crystallization of the formed oxides. The high oxidation resistance and remarkable increase in long-term stability of Si_3N_4/SiC and $Si_3N_4/MoSi_2$ composite materials result from in situ crystallization of Si_2N_2O in the near-surface area (Klemm et al., 1998; Klemm, 2010). These processes are shown in **Figure 4**.

Solid phase-sintered materials such as SiC and Si_3N_4 with minimal additive contents (Si_3N_4 HIPed without additives), have a higher oxidation resistance than the analogous liquid phase-sintered materials due to the low extent of diffusion of oxygen into the bulk of these ceramics, oxidation taking place only on the outer surface (**Figure 4(a)**).

Small amounts of alkaline oxide or fluorine impurities strongly reduce the viscosity of the amorphous grain boundary phase and hence the oxidation and creep resistance in Si_3N_4 materials. Therefore for high-temperature materials, pure raw materials must be used. Impurities in the gas phase can also change the diffusion coefficients in the oxide scale. Alkaline, sulphate and vanadium impurities in combustion gases have a significant negative effect on the oxidation stability of Si_3N_4 and SiC (Jacobson, 1993; Klemm, 2010; Nickel et al., 2010; Nickel & Gogotsi, 2000; Petzow & Herrmann, 2002).

Si_3N_4 ceramics with nitrogen-rich grain boundary phases exhibit accelerated oxidation, so-called *catastrophic oxidation*, in the range of 900–1100 °C due to the absence of a dense oxide layer. Stresses caused by the volume increase during oxidation result in formation of microcracks and ultimately in rapid destruction of the material (Sciti et al., 2005; Petzow & Herrmann, 2002). "Pest oxidation" of $MoSi_2$ is another example of incomplete formation of a protective oxidation scale at intermediate temperatures (electric heaters at temperatures <1000 °C).

Oxidation of nitrides and carbides also results in gaseous reaction products (N_2 and CO/CO_2 respectively). If the diffusion of these gases is much lower than the diffusion of oxygen through the layer, bubbles can be formed in the oxide layer, resulting in locally increased oxidation rates and pitting (**Figure 2**). These pores/bubbles in the oxide layer were found in Si_3N_4 materials at oxidation temperatures above 1200–1300 °C due to the low

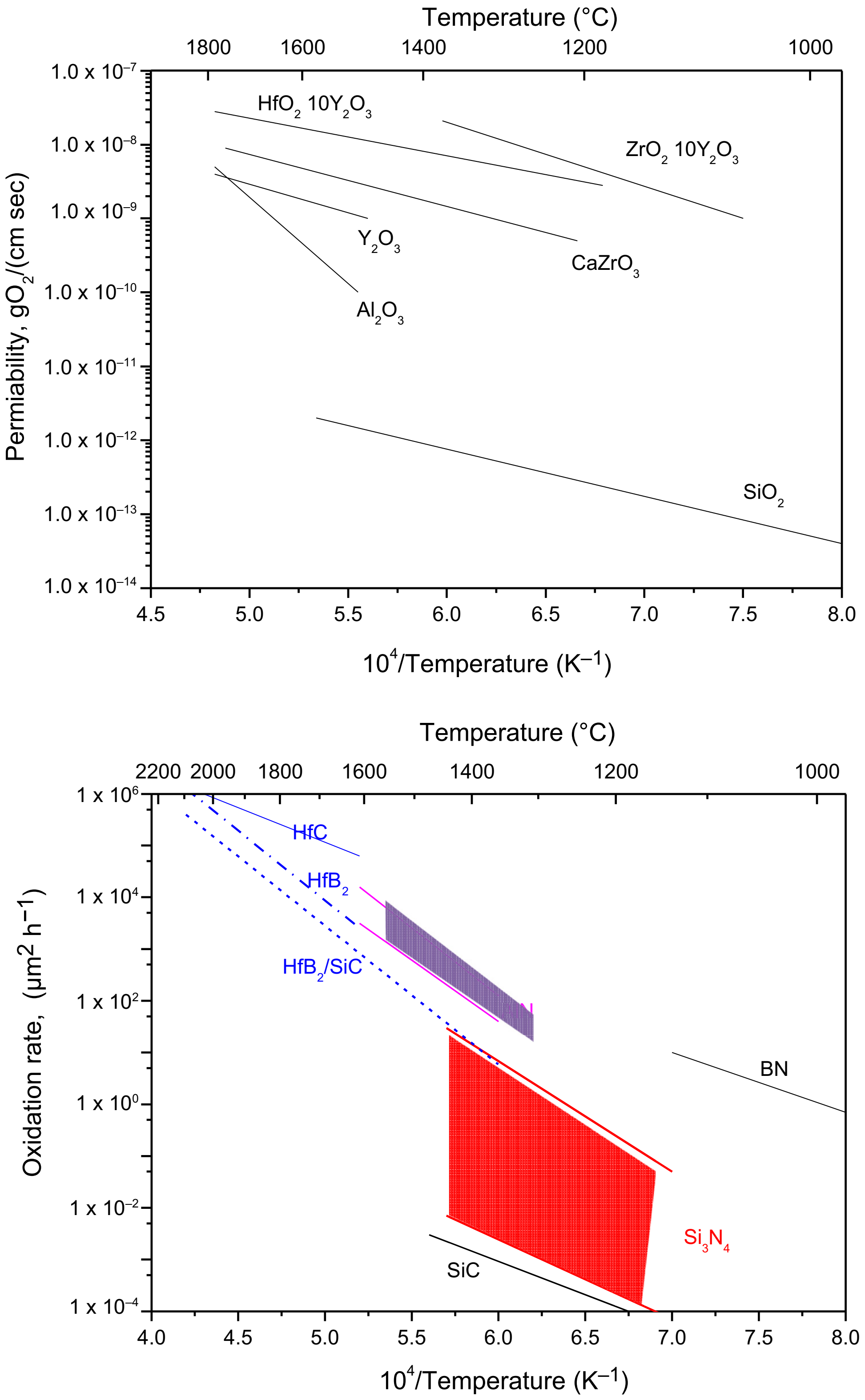

Figure 3 Oxygen permeability in oxides (Courtright, 1991) and typical parabolic oxidation constants (Courtright, 1991; Jacobson & Farmer, 1999; Petzow & Herrmann, 2002).

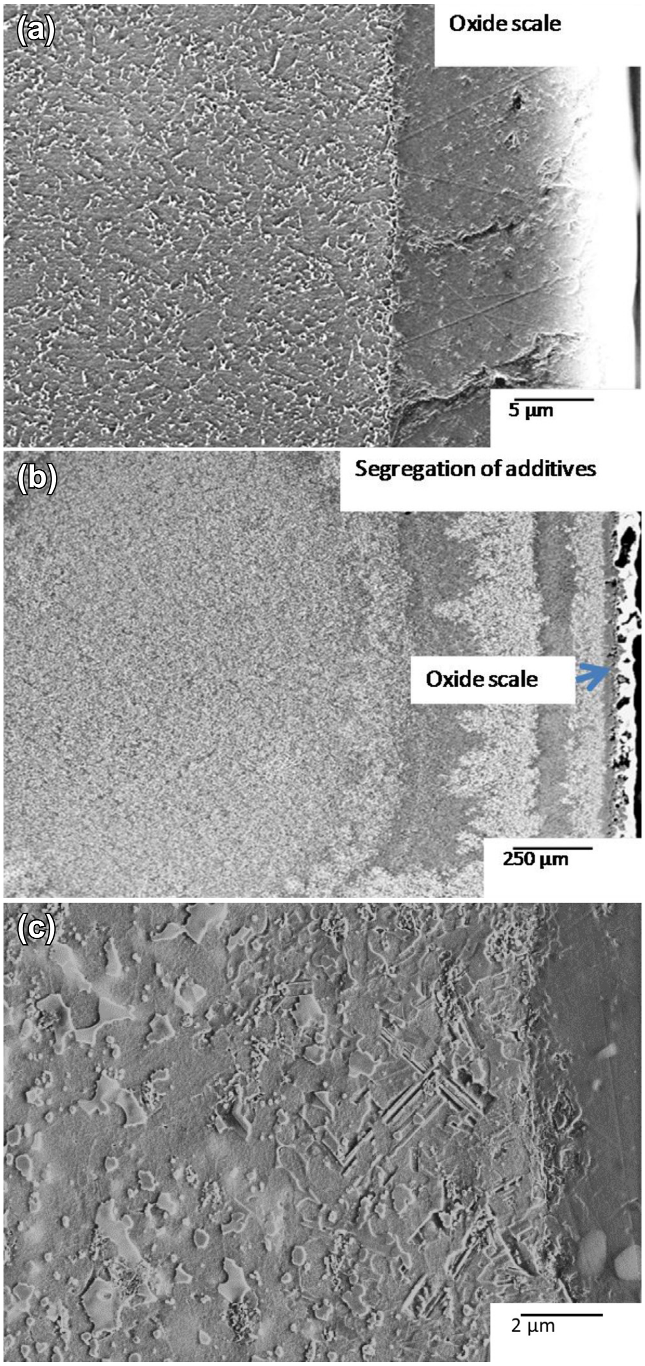

Figure 4 SEM micrographs of cross-oxidized sections of at 1500 °C. (a) Si_3N_4 without sintering additives oxidized for 2500 h (b) Si_3N_4 material with Y_2O_3/Al_2O_3 additives oxidized for 1000 h. (c) Si_3N_4 material with Y_2O_3 and $MoSi_2$ additives oxidized for 2500 h.

solubility and low diffusion rate of the nitrogen formed as a reaction product of oxidation (Backhaus-Ricoult et al., 2002; Jacobson, 1986; Klemm, 2010; Klemm et al., 1998;). Bubbles can also be formed by impurities with higher oxidation rates (e.g. carbon in SiC) (Nickel et al., 2010; Nickel & Gogotsi, 2000; Presser & Nickel, 2008; Schmalzried & Schwetz, 2010).

Oxidation is strongly influenced by the porosity in the material. All open pores provide sites for oxidation and hence porous materials oxidize faster than dense materials. Depending on the pore structure and the oxidation rate, small pores can be closed by the oxidation product due to the volume increase usually observed during oxidation, thus reducing or preventing internal oxidation (oxidation in the bulk). For example, the rate of oxidation of porous reaction-bonded Si_3N_4 and of recrystallized SiC materials decreases with increasing temperature in the range between 900 and 1200 °C due to faster pore closure. This process is described in detail in the literature (Jennings, 1983).

Depending on the oxygen partial pressure and the temperature, the oxide layers can become unstable, resulting in a change from passive to active oxidation.

The theory of *active oxidation* was first developed by Wagner for Si and then modified by different authors for SiC and Si_3N_4 (**Table 1**). The idea behind the theory was that during active oxidation, the flux of the oxygen or water to the surface must be as high as the fluxes of the reaction products away from the surface (**Figure 1(b)**) and the partial pressure of the reaction products must be lower than the equilibrium concentration necessary for the formation of the oxide layer. Based on these ideas, combining thermodynamic equilibrium and transport equations in the gas phase, the oxygen partial pressure at which the change from active to passive oxidation takes place can be calculated as a function of temperature. The transition boundary between active and passive oxidation for Si_3N_4 and SiC in air is shown in **Figure 5**. In the literature, different equilibria determining the critical partial pressure are proposed for SiC, e.g. Heuer and Lou (1990) proposed the condition where SiO_2 smoke is formed near the surface:

$$SiO + O_2 \Rightarrow SiO_{2(smoke)} \tag{3}$$

(For silicon-based ceramics, the main silicon-containing species in the gas phase in the region of active oxidation in dry atmospheres is silicon monoxide (SiO) (Heuer & Lou, 1990)).

Based on the consideration of zero weight change during oxidation, Wang et al. (2008) proposed another condition, according to the following reaction:

$$SiC + 4/3\ O_2 \Leftrightarrow 2/3\ SiO_{2(cond.)} + 1/3\ SiO_{(g)} + CO_{(g)} \tag{4}$$

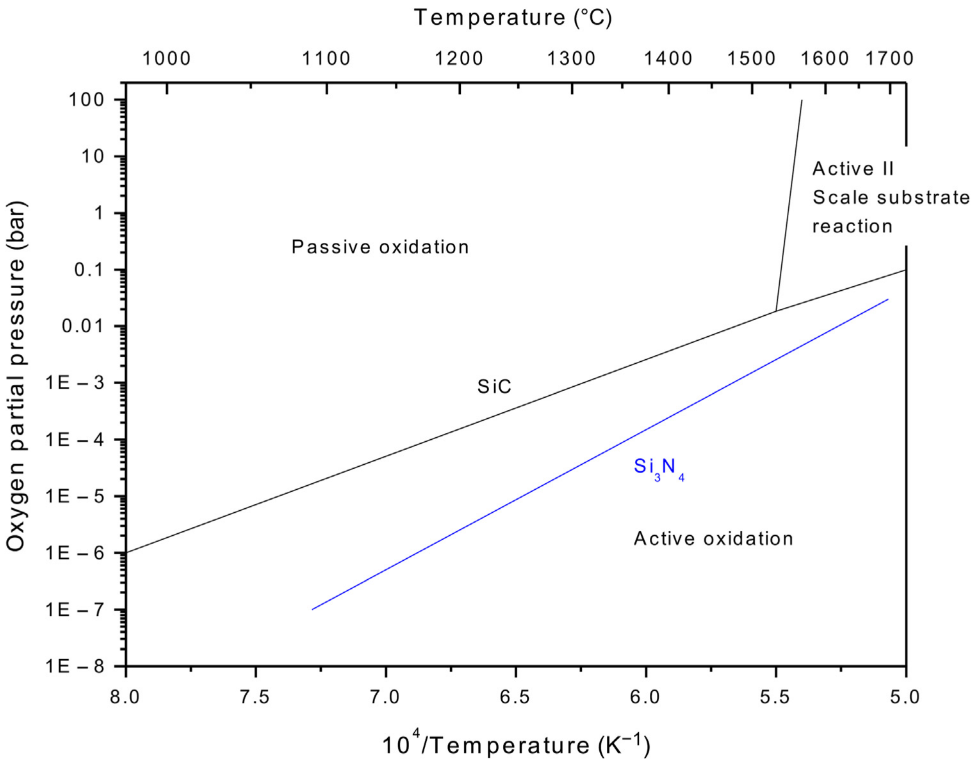

Figure 5 Dependence of the transition from active to passive oxidation on temperature and oxygen partial pressure in air for Si_3N_4- and SiC ceramics.

Nevertheless, all these equations result in similar values for the boundaries (e.g. oxygen partial pressure as a function of temperature). Additional uncertainty is introduced by the fact that the precise values of the diffusion coefficients of the gaseous species and the thickness of the diffusion layer are not known exactly. On the other hand, the experimental data concerning the transition point for the change from active to passive oxidation exhibit a certain amount of scatter, making it difficult for the most precise boundary conditions to be identified (Presser & Nickel, 2008).

The change in the activity of SiO_2 in the oxide scale by formation of silica melts due to diffusion of additives into the surface layer (rare earth, Al_2O_3 in Si_3N_4 or LPSSiC materials or impurities in the gas phase) also influences the theoretical boundary (Charpentier et al., 2009; Klemm, 2010).

For Si_3N_4-based materials, the boundary depends on both the oxygen partial pressure and the nitrogen pressure in the system (increasing the nitrogen pressure suppresses the active oxidation process). For SiC-based materials, the CO/CO_2 pressure in the atmosphere has an effect on the boundary. A higher CO pressure stabilizes the oxide, thus suppressing the change to active oxidation. Kim and Moorhead (1990a) showed that the strength of SSiC decreases linearly with mass loss during active oxidation.

The stability regime of the oxide layer also depends on the gas velocity, with a high gas velocity expanding the active oxidation temperature/pressure region. In addition, water vapor influences the decomposition process.

Besides the described region of active oxidation, a second region exists for SiC. The transition from passive to active oxidation takes place at high temperature nearly irrespective of the oxygen pressure if the interaction of the SiO_2 surface layer with the SiC results in a partial pressure which is higher than or equal to the overall pressure. Therefore, the reaction

$$SiC + 3/2\ O_2 \Rightarrow SiO_2 + CO \tag{5}$$

results in the formation of large bubbles in the oxide layer on the surfaces of the SiC components and a transition from passive to active oxidation (active II) (Jacobson, 1993; Narushima et al., 1994b) (**Figure 5**). The same mechanism is also known for Si_3N_4 ceramics

Above the oxide scale decomposition temperature, simple decomposition and evaporation reactions of SiC into Si and carbon and of Si_3N_4 materials into Si and N can also take place.

The same active oxidation mechanism described here is also active in humid atmospheres, especially in combustion atmospheres with high water vapor pressures.

2.15.2.2 Reactions in Humid Atmospheres

In humid atmospheres, corrosion is usually accelerated even in the region of passive oxidation due to the higher reactivity of water vapor and higher diffusion coefficients. Water vapor can also react to form hydroxides which can evaporate at high temperatures. For the common boride ceramic materials, H_3BO_3 or HBO_2 has the highest partial pressure (**Figure 6**).

Therefore boride, BN and B_4C materials are moisture-sensitive much below 1000 °C. For boride systems, the oxidation law can be changed from parabolic for passive oxidation in dry air to paralinear, indicative of active oxidation (**Figure 1(d)**). The mechanism behind this is that the oxidation process determined by the diffusion through the oxide layer has the same rate as the evaporation process and hence the thickness of the oxide layer remains constant with time, but the material dimensions decrease. Hydroxides of Si, Al, Mg and of some of the transition metals have low partial pressures even at high temperatures. In static (nonflowing) atmospheres, the evaporation of hydroxides is of little significance, but the situation is completely different in atmospheres with high gas stream velocities and high water vapor pressures such as those found in gas turbine environments (Fritsch, 2008; Hisamatsu et al., 2003; Jacobson, 1993; Klemm et al., 1998; Klemm, 2010; Opila et al., 1999; Opila, 2003). In these conditions, even alumina, SiC and Si_3N_4 materials can undergo severe degradation (Fritsch & Klemm, 2008; Fritsch et al., 2010; Fritsch, 2008; Hisamatsu et al., 2003; Jacobson & Farmer, 1999; Jacobson, 1993; Klemm et al., 1998; Klemm, 2010; Opila & Myers, 2004; Opila et al., 1999; Opila, 2003). **Table 2** gives the dependencies of the corrosion mechanism on the flow rate of the hot gas. Measured regression rates of different nonoxide and oxide materials are compiled in **Figure 7**.

Therefore, for application of these materials in gas turbine environments, environmental barrier coatings (EBCs) must be used. These coatings have the function of suppressing or preventing the evaporation of the hydroxides. Up to now the best results have been observed with compounds of the transition metals (ZrO_2, HfO_2, Y_2O_3 and Yb_2O_3). Besides possessing this chemical function, these materials must have similar thermal

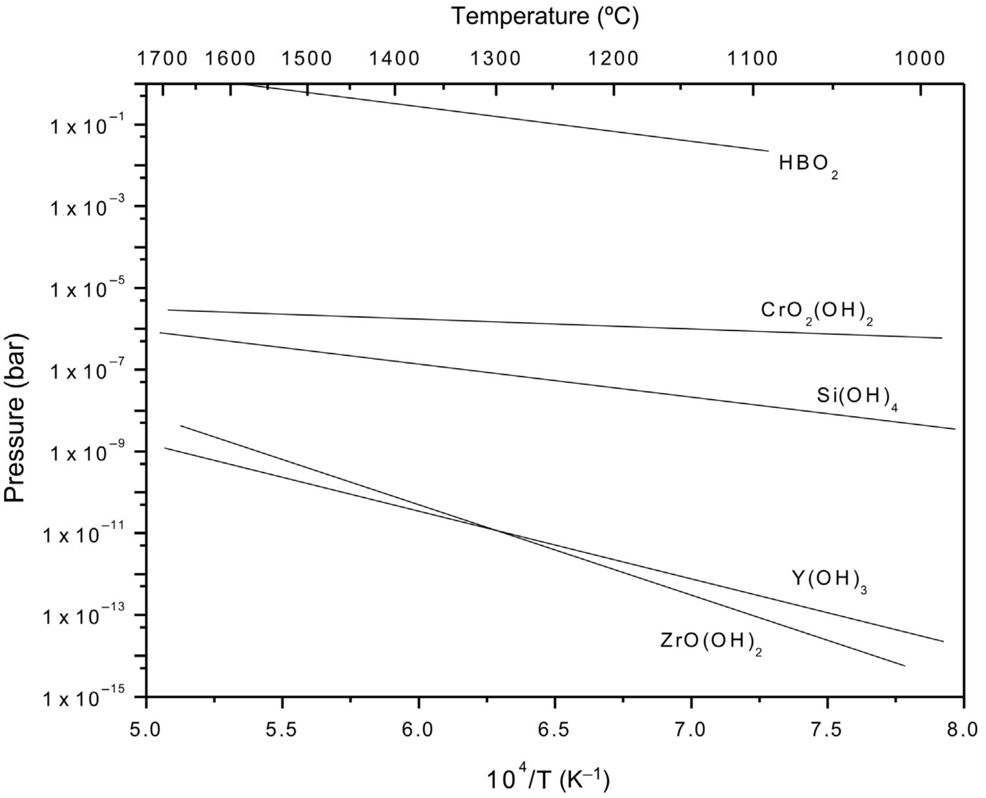

Figure 6 Partial pressure of different hydroxides at 1 bar pressure (0.1 bar oxide pressure and 0.1 bar water pressure) as a function of the temperature (Fritsch, 2008 and data calculated using SGTE database).

expansion coefficients to that of the substrate and must be stable in relation to the oxide scale and the substrate material. In the ideal case, the coating forms directly from the bulk to enable self-healing. Layered systems are also being considered to achieve the complex functionalities required for these coatings. A detailed overview of the current status of EBCs for Si_3N_4 and other nonoxides is given by Klemm (Fritsch & Klemm, 2006, 2008; Fritsch, 2008; Hong-fei & Klemm, 2011; Roode, 2010).

The functionality of an EBC in nonoxide (Si_3N_4) and oxide (Al_2O_3) materials is demonstrated in Figure 8. The micrograph show polished cross-sections of the surface region after hot gas testing. Corrosion was not evident in the surface region protected by the EBC, but material loss was found in the unprotected region.

Table 2 Principle categories of corrosion attack of structural ceramics in water vapor-rich hot gas environments (tests performed at 1200–1500 °C, 7.5–100% water vapor, 1–18 bar total pressure and 100–5000 h exposure times; a detailed compilation of literature results is given in Fritsch et al. (2010))

Type	*Test equipment*	*Flow rate (m s^{-1})*	*Corrosion value* K_w *(mg cm^{-2} h^{-1})*
Passive corrosion/oxidation	Furnace	10^{-4}–10^{-2}	Si_3N_4, SiC ~ weight gain, Al_2O_3 stable
Paralinear corrosion	Thermogravimetry	10^{-2}–10^{-1}	Si_3N_4, SiC, Al_2O_3 ~ 10^{-3}–10^{-2}
Active corrosion	Burner rig/test turbine	20–300	Si_3N_4, SiC, Al_2O_3 ~ 10^{-2}–10^{-1}

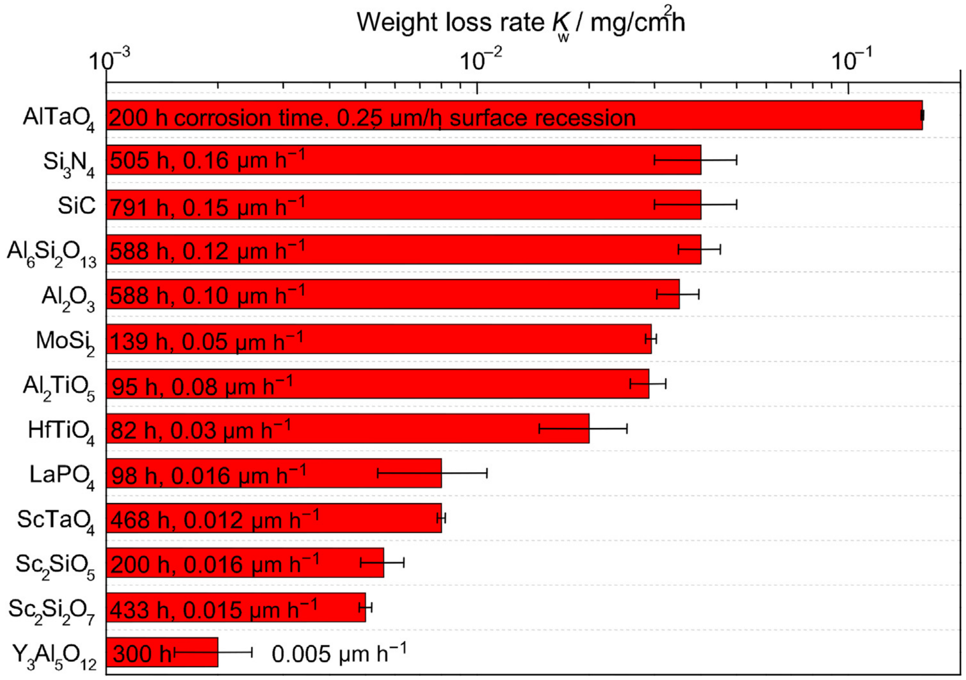

Figure 7 Ranking of ceramic materials in terms of hot-gas-corrosion recession with linear weight loss rate measured in a gas burner test at 1450 °C at flow rate of 100 m s^{-1}, $P_{H_2O} = 0.28$ atm and overall pressure of 1 atm (Fritsch et al., 2010).

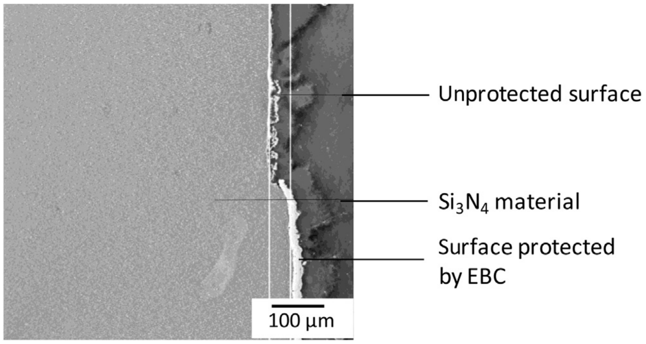

Figure 8 Functionality of EBC on Si_3N_4 ceramics after hot gas testing at 1450 °C for 100 h.

2.15.3 Corrosion in Aqueous Solutions

2.15.3.1 Basic Processes

Ceramic materials exhibit a unique combination of properties such as hardness, wear and corrosion resistance, enabling them to be used in pumps and seals (mainly SiC and alumina), ball bearings (mainly Si_3N_4 ceramics), chemical apparatus, valves and a wide variety of other applications. Despite the high corrosion resistance in comparison with that of many metals, the suitable material for the given application must be chosen carefully with respect to mechanical load, tribological conditions and corrosion.

Therefore, a detailed understanding of the corrosion behavior is necessary. In contrast to metals, which undergo redox reactions (oxidation of metal) during corrosion, ceramics undergo acid–base reactions in corrosive conditions:

$$M_xO_y + 2y\,H^+ \Rightarrow x\,Me^{(2y/x)+}(aq.) + y\,H_2O \tag{6}$$

or hydration of metal oxide

$$M_xO_y + n\,H_2O \Rightarrow M_xO_y \cdot n\,H_2O \tag{7}$$

or hydrolysis of covalent bonds (shown below for AlN)

$$AlN + 3\,H_2O \Rightarrow Al(OH)_3 + NH_3 \tag{8}$$

The few electrically conductive ceramic materials, e.g. SiC, TiN, TiC, $MoSi_2$, hardmetals MAX phases and conductive composites, can undergo electrochemically driven redox reactions like metals. This can change the corrosion behavior strongly and will be explained at the end of this chapter. For a better understanding of the corrosion stability, it is convenient to distinguish solid phase- and liquid phase-sintered materials. The solid phase-sintered materials are usually single-phase materials and do not contain continuous grain boundary phases; examples include high-purity Al_2O_3, ZrO_2 and SiC. The stability of the material is hence determined by the stability of the main ceramic component. Liquid phase-sintered materials (e.g. sintered Si_3N_4-ceramics, liquid phase-sintered SiC (LPSSiC), porcelain, mullite and Al_2O_3 with glassy phase) or materials produced by infiltration (e.g. Si-infiltrated SiC) contain continuous grain boundary phase skeletons that can be leached out of the ceramics even under conditions in which the main components are stable. Therefore the stability of the grain boundary phase is often the parameter determining the stability of the ceramic. Alumina ceramics can be either solid- or liquid phase sintered depending on the silica content of the starting composition. The weight gain of alumina as a function of the silica content in HCl at 150 °C is given in **Figure 9** (Genthe & Hausner, 1989). The glassy grain boundary phase was less stable than alumina in the acid and strongly reduced the stability of the alumina ceramics. A similar strong change in the stability in acids as a function of the grain boundary composition was observed for Si_3N_4 materials (**Figure 10**). A change in weight loss of more than two orders of magnitude was found for certain compositions. The two examples illustrate the strong dependence of the corrosion resistance on composition and microstructure.

In order to assess the corrosion behavior of ceramics in advance, it is necessary to evaluate their thermodynamic and kinetic stabilities in aqueous media. To achieve a high corrosion resistance, it is advantageous to have the lowest possible solubility of the ceramic or its most unstable component. Generally corrosion reaction only becomes possible when the Gibbs free energy ($\Delta G_{reaction}$) of the corresponding dissolution reaction is negative. These parameters can be assessed at least by pH-dependent activities of the metal ions in equilibrium with the solids, e.g. of the oxides (Conradt, 2008; Franks & Gan, 2007; Iler, 1982; Schilm, 2004). Information

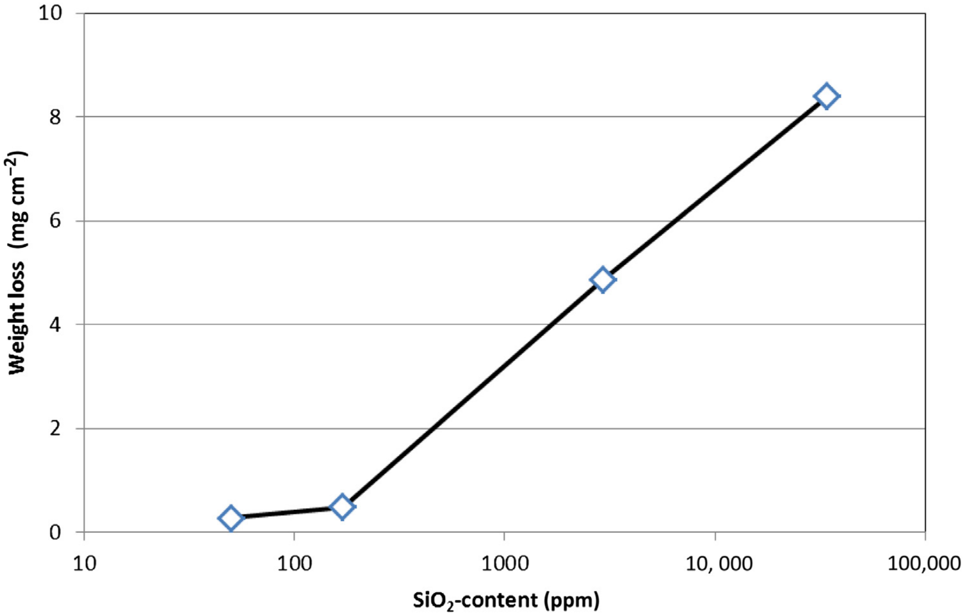

Figure 9 Dependence of the weight loss of Al_2O_3 ceramics in 1 M HCl as a function of the silica content of the alumina ceramics (MgO content approximately 500 ppm (Genthe & Hausner, 1989)).

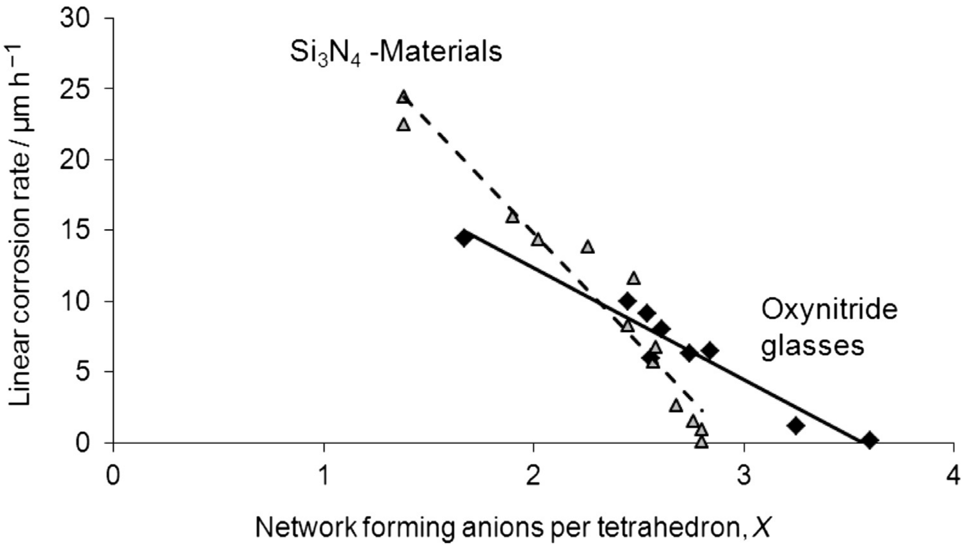

Figure 10 Dependence of the linear corrosion rate of Si_3N_4 materials and oxynitride glasses (with similar composition as the grain boundary phase of silicon nitride ceramics) as a function of the structure of the glass network (after Herrmann, 2013).

about glass stability in aqueous media obtained from extensive studies in the field of glass corrosion can also be applied to ceramic materials with glassy grain boundary phases (Clark, Dilmore, Ethridge, & Hench, 1976; Conradt, 2008; Freiman, Wiederhorn, & Mecholsky, 2009; Iler, 1982; Risbud, 1981; Schilm, 2004; Schilm, Herrmann, & Michael, 2004b; Scholze, 1991). For example, the low solubility of glasses with high SiO_2 contents at low pH values (Conradt, 2008; Iler, 1982) corresponds to a high stability of Si_3N_4 ceramics with SiO_2-rich grain boundary phases in concentrated mineral acids (except HF) up to 100 °C (Herrmann, 2005; Schilm, 2004; Schilm, Herrmann, & Michael, 2007; Herrmann, 2013).

However, if solubility limits are reached during the corrosion process, precipitation of solid phases, i.e. formation of compounds with low solubility, occurs. These phases deposit inside the ceramic material or on its surface, resulting in the formation of protective layers. These layers reduce the rate or completely prevent further corrosion reactions.

Whereas thermodynamics provides basic information about the possibility ($\Delta G_{\text{reaction}} < 0$) or impossibility ($\Delta G_{\text{reaction}} >> 0$) of corrosive attack, kinetic examinations yield information about the reaction rates. Thus, for example, the thermodynamic instability of Al_2O_3 ceramics in acids is countered by high activation energy for the dissolution reaction, which is responsible for the high-corrosion stability. In general, corrosive attack involves several reactions or material transport processes depending on the ambient parameters (temperature, concentration ratios in corrosive media, composition and grain boundary phase content). The individual processes overlap each other, often resulting in complex corrosion behavior determined by the slowest and thus rate-limiting process. **Figure 11** schematically illustrates three common types of corrosion in ceramics interfacial (reaction) controlled, limited by the diffusion of the species or passivating due to the formation of a nonsoluble reaction product. The corrosion behavior of Si_3N_4 ceramics in 1 N H_2SO_4 is a good example (**Figure 11(b)**) for the illustration of the different kinetics. In this case, a media temperature change of just 30 K is sufficient to realize the different behaviors. A detailed discussion of the corrosion equation is given in the literature (Herrmann & Schilm, 2009; Herrmann, Schilm, Hermel, & Michaelis, 2006; Schilm, 2004; Schilm, Gruner, Herrmann, & Michael, 2006; Seipel & Nickel, 2003; Herrmann, 2013).

The locally increased attack and resultant damage in the ceramics is called *pitting* and is the main factor determining the strength of the materials after corrosion (residual strength). A pronounced reduction in strength is typically observed in the initial stage of corrosion. This is caused by the fact that in the initial period, the corrosion is accelerated at existing inhomogeneities. Also the relation between strength (σ) and defect size (a)

$$\sigma \sim \frac{1}{\sqrt{a}} \tag{9}$$

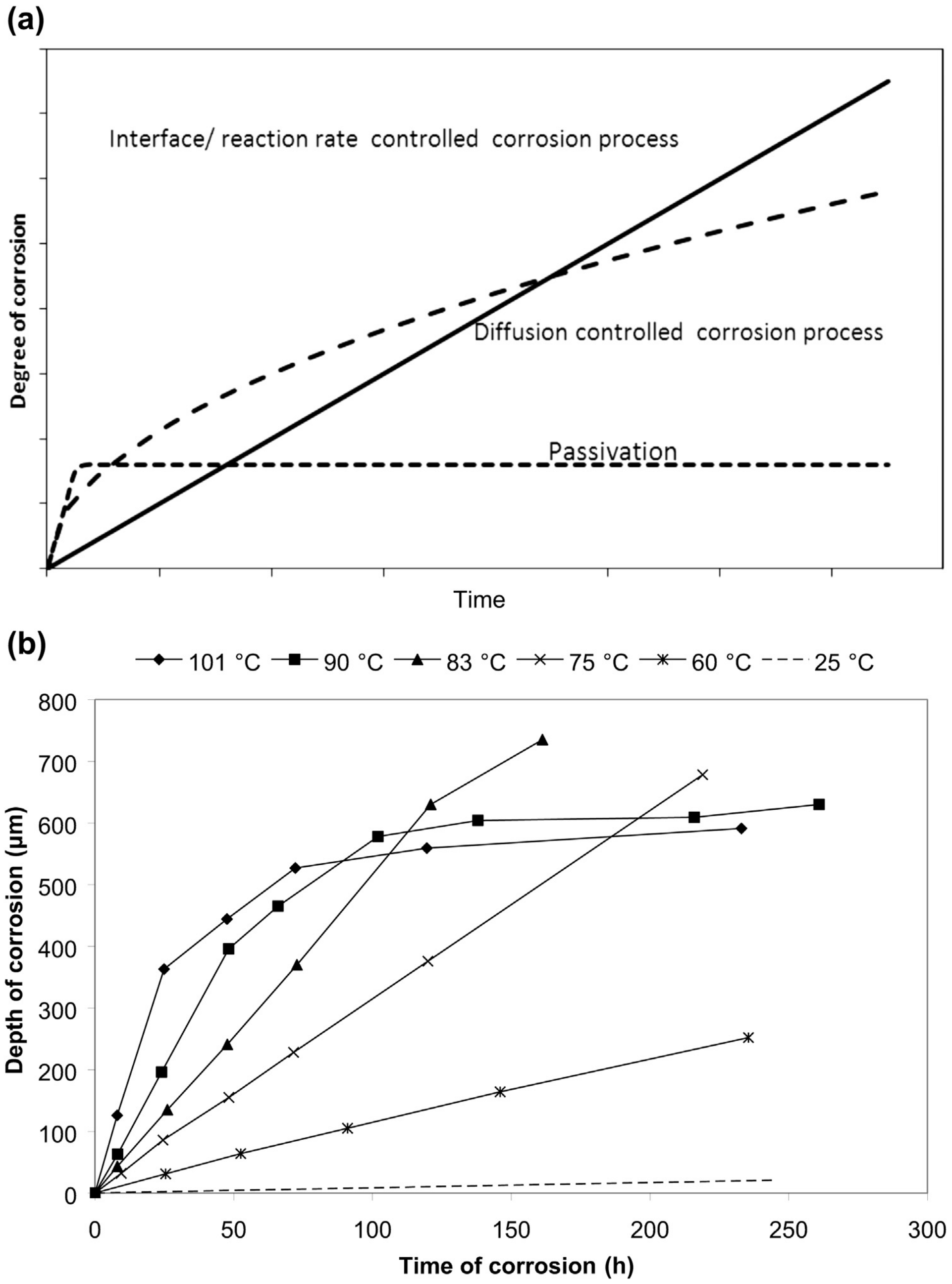

Figure 11 (a) Schematic view of the different corrosion kinetics, (b) Time dependence of the thickness of the corrosion layer of a Si_3N_4 ceramic as a function of temperature in 0.5 mol H_2SO_4 (Si_3N_4 material with 6 wt% Y_2O_3 and 4 wt% Al_2O_3) (Herrmann, 2013).

directly results in a stronger dependence of strength on defect size for small defect sizes, strongly growing in the initial period. The mechanisms of pitting have been poorly studied thus far and it is very specific for the different materials. They presumably involve growth of existing inhomogeneities (pores, chemical impurities, cracks and local stress).

Apart from chemically caused corrosive degradation, stress occurring in the ceramics may significantly influence the stability. The low stability of yttria-stabilized tetragonal zirconia (Y-TZP) ceramics in hot acids and under hydrothermal conditions is mainly caused by the chemically induced transformation of zirconia from the metastable tetragonal phase (t-ZrO_2) to the monoclinic phase (m-ZrO_2) (see below).

Subcritical crack growth is accelerated if the external tensile stress below the fracture stress is accompanied by a corrosion process. Local chemical corrosion at the crack tip may increase the crack growth rate by several orders of magnitudes, resulting in a significant reduction in lifetime (Barinov, Ivanov, Orlov, & Shevchenko, 1998; Chevalier, Olagnon, & Fantozzi, 1999; Freiman et al., 2009; Lawson, 1995; Lughi & Sergo, 2010; Salmang & Scholze, 2007; Schneider et al., 2008). Corrosive attack in suspensions combined with abrasive wear may result in a significant increase in the corrosion rate (Fang, Sidky, & Hocking, 1997; Presser, Berthold, Wirth, & Nickel, 2008; Kitaoka, Toshidhide, Toshio, Yamaguchi, & Kashiwagi, 1992, 1994a, 1994b; Presser, Nickel, Krummhauer, & Kailer, 2009). **Table 3** gives an overview of the corrosion behavior of different ceramics under various conditions and **Figure 12** gives the strengths of various ceramic materials in different media. Because the corrosion depends strongly on microstructure and impurities, these data can only serve as a guideline for the corrosion behavior of the materials.

The corrosion behavior of different thermally sprayed coatings in bases and acids was investigated by Berger et al. (Stahr, Berger, Herrmann, & Deska, 2008; Toma et al., 2010; Herrmann & Toma, 2014). Despite having similar compositions to those of the ceramics, the coatings were much less stable than the ceramics. This reveals the strong influence of the microstructure on the corrosion behavior. A detailed derivation of the equations depending on the mechanism and the sample geometry is given in the literature (Hou & Chou, 2009; Nickel & Gogotsi, 2000; Nickel et al., 2010; Herrmann, 2013).

Additional results concerning the corrosion of the main structural ceramics are given below in more detail.

2.15.3.2 Corrosion of Different Ceramics in Aqueous Solutions

Pure *alumina ceramics* have a high-corrosion resistance in bases and acids and under hydrothermal conditions. Even in supercritical water, they exhibit a high-corrosion resistance (Franks & Gan, 2007; Galuskova et al., 2011a; Genthe & Hausner, 1989; Genthe & Hausner, 1992; Hirata et al., 2003; Hoppert, 2010; Kitaoka et al., 1992; Mikeska et al., 2000; Mikeska, 1999; Oda & Yoshio, 1997; Sato et al., 1991). Silica and alkaline additives in alumina often used to reduce the sintering temperature are leached out in acids and under hydrothermal conditions (**Figures 9** and **13**). MgO results in the formation of spinel phases which are chemically stable and do not degrade. Therefore these materials are more stable than the alumina ceramics with silica impurities (**Figure 13**b) (Hoppert, 2010; Genthe & Hausner, 1989; Genthe & Hausner, 1992).

Zirconium oxide (ZrO_2) has different crystallographic modifications. The cubic modification (fluorite structure) stable at high temperatures transforms to the tetragonal modification at 2370 °C. The tetragonal modification transforms to the monoclinic modification at 1170 °C. The tetragonal-to-monoclinic phase transformation is associated with a volume expansion of nearly 5%, resulting in cracking of the material. Therefore, pure ZrO_2 is of no practical use; the tetragonal and cubic modifications can be stabilized through the addition of rare-earth or earth alkali oxides. The following types of zirconia exist (organized according to the degree of stabilization) (Chevalier et al., 2009; Iio, Okada, Asano, & Yoshimura, 1992; Lughi & Sergo, 2010):

- Fully stabilized (cubic) zirconia has moderate strength and toughness and is mostly used as an oxide conductor, e.g. in sensors or solid oxide fuel cells. Very few results concerning the corrosion stability of this material are available. In general, it is highly stable in solutions and in humid air. Fully stabilized ZrO_2 is also used as thermal barrier coatings in gas turbine applications, making use of its high stability in water vapor (Chevalier et al., 2009; Fritsch et al., 2010; Yoshimura et al., 1986). Yoshimura (Yoshimura et al., 1986) investigated the stability of yttrium stabilized zirconia in different media and at different temperatures.
- Partially stabilized zirconia (PSZ) exhibits a cubic matrix with fine tetragonal precipitates (typically ~200 nm) formed during cooling. Typically these materials are prepared with MgO as the stabilizer. If a load is applied, the tetragonal phase can transform to the monoclinic phase, resulting in transformation toughening. These materials are used as wear parts and in chemical equipment and have a higher stability than and similar corrosion mechanisms to those of Y-TZP materials (Chen & Lu, 2003; Chevalier et al., 2009; Herrmann et al., 2003; Schacht et al., 1998; Tan et al., 1996).
- Tetragonal zirconia polycrystalline (TZP) ceramics consist of metastable tetragonal grains which when loaded can transform to the tetragonal phase, resulting in transformation toughening. The typical material is 2–3 mol yttria-stabilized ZrO_2 which can reach strengths of >1 GPa and a fracture toughness of $\geq$ 6 MPa m$^{1/2}$. CeO_2-stabilized materials can reach even higher fracture toughness, but lower strength, levels. Besides the described zirconia ceramics, several composites are used, with the most prominent being zirconia-toughened alumina containing 10–20 vol% ZrO_2 (ZTA) and alumina-toughened zirconia (ATZ). Y-TZP is widely used in cutting applications and dental implants and hence the hydrothermal stability of this material has been

Table 3 Stabilities of different technical ceramics in aqueous solutions

Material	*Medium*	*Stability*	*Notes*	*Literature*
Al_2O_3 (>99.9%)	H_2SO_4; HCl; $<100\ ^\circ C$, NaOH, H_2O	High	Stability depends on the impurity content	Barinov et al., 1998; Franks & Gan, 2007; Galuskova, Hnatko, Galusek, & Sajgalik, 2011a; Genthe & Hausner, 1989; Genthe & Hausner, 1992; Hirata, Ota, & Morimoto, 2003; Hoppert, 2010; Kitaoka et al., 1992; Mikeska, 1999; Mikeska, Bennison, & Grise, 2000; Nielsen, 1992; Oda & Yoshio, 1997; Sato, Sato, Okuwaki, & Tanaka, 1991
Al_2O_3 (<97%)	H_2SO_4; HCl, NaOH, H_2O	Low	Corrosion resistance is determined by the composition of the grain boundary phase	
			SiO_2 in the material reduces the stability	
ZrO_2 Y-TZP	$H_2SO_4 > RT$ $H_2O > 100\ ^\circ C$	Low	Degradation of the ceramic material occurs due to stress which is caused by a corrosion-related transformation to monoclinic ZrO_2	Bartolome, Montero, Diaz, et al., 2004; Chen & Lu, 2003; Chevalier et al., 1999; Chevalier, Gremillard, Virkar, & Clarke, 2009; Gremillard, Chevalier, Epicier, & Fantozzi, 2002; Guo & Schober, 2004; Hannink, Kelly, & Muddle, 2000; Herrmann, Seipel, Schilm, et al., 2005; Johannes & Schneider, 2012; Kern, 2011; Kimel & Adair, 2002; Lawson, 1995; Li & Watanabe, 1998; Lughi & Sergo, 2010; Marro, Chintapalli, Hvizdos, et al., 2009; Munnoz-Saldan, Balmori-Ramirez, Jaramillo-Vigueras, Iga, & Schneider, 2003; Ramalingam, Reimanis, Fuller, & Haftel, 2010; Schacht, Boukis, Dinjus, et al., 1998; Schneider, Begand, Kriegel, et al., 2008; Tan, Gill, & Lawson, 1996; Yashima, Nagatome, Noma, et al., 1995; Yasuda, Goto, & Takeda, 2001; Yoshimura, Hiuga, & Somiya, 1986
Mg-PSZ	$H_2SO_4 > RT$ $H_2O < 200\ ^\circ C$	Higher than Y-TZP	Material is strong and much less prone to degradation than Y-TZP	
ZTA (10–15 wt% ZrO_2)	H_2SO_4; NaOH $<$ 100 °C	High	Material exhibits almost no degradation if it is free of SiO_2	
	$H_2O > 200\ ^\circ C$	Medium	Degradation of the ceramic material occurs due to stress which is caused by a corrosion-related transformation to monoclinic ZrO_2	
SiC	Acid; bases; HF	High		Adler & Petasch, 2012; Andrews, Herrmann, Sephton, Machio, & Michaelis, 2007; Barringer, Faiztompkins, Feinroth, et al., 2007; Cook, Little, & King, 1994; Divakar, Seshadri, & Srinivasan, 1989; Gogotsi, 1994; Herrmann et al., 2003; Hirayama, Kawakubo, & Goto, 1989; Kailer, Amann, Krummhauer, Herrmann, & Sydow, 2011; Kitaoka et al., 1994; Kumar, Balasubramaniam, & Basu, 2007; Loenhout & Traets, 2009; Mallik, Reddy, Acikbas, et al., 2011; Meschke & Kailer, 2004; Murthy, Kobayashi, Tsurekawa, et al., 2004; Presser et al., 2008; Presser, Nickel, et al., 2009; Rendtel, 2010; Schmalzried & Schwetz, 2010; Schwetz & Hassler, 2002a, 2002b; Sydow, Herrmann, Schneider, Kleebe, & Michaelis, 2011; Sydow, Schneider, Herrmann, Kleebe, & Michaelis, 2010; Sydow, Sempf, Herrmann, et al., 2011; Tan, Allen, & Barringer, 2009
SiSiC	Acid, bases, hydrothermal	High Low	Dissolution of free silicon occurs	
LPSSiC	Acid; bases; hydrothermal	Medium or high	Corrosion resistance is strongly dependent upon the composition of the grain boundary phase	
Si_3N_4	Concentrated HCl, HNO_3, H_2SO_4	High stability	SiO_2 surface layer formation results in passivation	Fang et al., 1997; Galuskova, Hnatkoe, Galusek, & Sajgalik, 2011b; Herrmann, 2005; Herrmann, 2012; Herrmann et al., 2006; Herrmann & Schilm, 2009; Herrmann, Schilm, Michael, Meinhardt, & Flegler, 2003; Kitaoka et al., 1994; Kleebe, Cinibulk, Cannon, & Rühle, 1993; Monteverde, Mingazzini, Giorgi, & Bellosi, 2001; Nagae, Koyama, Yasutake, & Yoshio, 2006; Nagae, Yoshio, & Oda, 2006; Oda, Yoshio, Miyamoto, & Koizumi, 1993; Okada & Yoshimura, 1996; Sato et al., 1988b; Sato, Sato, Tamura, & Okuwaki, 1992; Sato, Tokunaga, Endo, et al., 1988a, 1988b; Schilm et al., 2006; Schilm et al., 2007; Schilm, 2004; Schilm, Herrmann, & Michael, 2003; Schilm, Herrmann, & Michael, 2004a, 2004b; Seipel & Nickel, 2003; Sharkawy & El-Aslabi, 1998; Shimada & Sato, 1989; Somiya, 2001
	HF	Very low	Dissolution of grains and grain boundary phase occurs	
	Diluted acids, bases $H_2O < 250\ ^\circ C$	High or low	Stability depends on the amount and composition of the grain boundary phase; the stability varies depending on composition and medium	
	$H_2O > 250\ ^\circ C$	Medium/low	Increased dissolution of Si_3N_4 grains occurs	
AlN				Krnel & Kosmac, 2000; Krnel & Kosmac, 2002; Li, Nakamura, Shirai, et al., 2006; Svedberg, Arndt, & Cima, 2000; Tamai, Hamauzu, Ryumon, et al., 2000

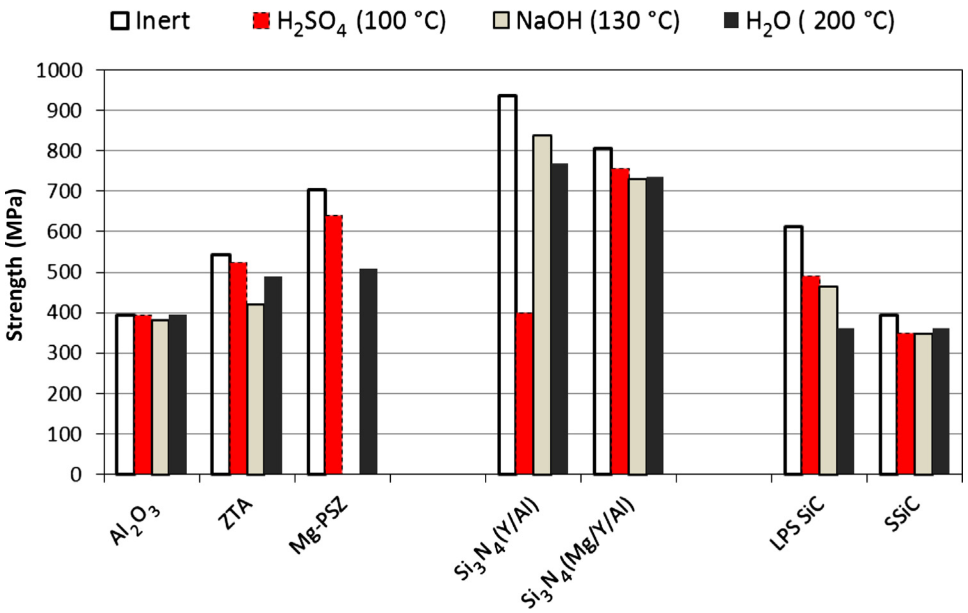

Figure 12 Strengths of different ceramic materials after corrosion in 1 N NaOH, H_2SO_4 and water at elevated temperatures (temperature is given in the graph) after 200h (Herrmann, Schilm, & Michael, 2003).

thoroughly investigated (Bartolome et al., 2004; Chevalier et al., 2009; Kimel & Adair, 2002; Lawson, 1995; Lughi & Sergo, 2010).

Transformation toughening of the zirconia ceramics is based on stress-induced phase transformation of the metastable tetragonal phase to the stable monoclinic phase accompanied by a volume increase at the crack tip. This volume increase results in compressive stress at the crack tip. The phase transformation can be initiated by mechanical loading as well as by corrosion. The same mechanism that causes toughening results in accelerated aging/corrosion of ZrO_2 ceramics: water or even water vapor can destabilize t-ZrO_2. If the monoclinic phase content is high, the arising stresses result in the formation of microcracks and grain lifting (spalling) (Bartolome et al., 2004; Chevalier et al., 2009; Lawson, 1995; Li & Watanabe, 1998; Lughi & Sergo, 2010; Marro et al., 2009; Tan et al., 1996). This process starts on the surface, increasing the surface roughness and influencing the wear behavior. The formed microcracks create pathways for water penetration into the ceramic, resulting in further transformation, microcracking and ultimately formation of macrocracks. Thus the phase transformation leads to accelerated aging of the material. The interrelation between aging behavior, stresses and wear and the effect on the integrity of zirconia devices are illustrated in **Figure 14**. The same mechanism that results in toughening, i.e. improvement of the mechanical behavior, also results in accelerated aging/corrosion of ZrO_2.

Details of the destabilization mechanism in ZrO_2 are still under discussion. The main process is the water adsorption and diffusion of OH^- into the ZrO_2 lattice, resulting in filling of the vacancies in the oxygen sublattice by OH^- (Chevalier et al., 2009; Guo & Schober, 2004; Yoshimura et al., 1986) or O^{2-} (Chevalier et al., 2009). Incorporation of water strongly depends on the partial pressure of the water vapor (Yoshimura et al., 1986).

The microstructure and the corrosion conditions mainly control the kinetics. Most investigations were carried out under hydrothermal conditions (sterilization of medical products at 135 °C in water for 5 h). Additionally, Y-TZP ceramics have the lowest stability in the temperature range between 200 and 300 °C (Bartolome et al., 2004; Chevalier et al., 2009; Guo & Schober, 2004; Lawson, 1995; Lughi & Sergo, 2010; Yashima et al., 1995). The stability under hydrothermal conditions can be increased by different factors:

- Reduction of the grain size results in an increase in the stability of t-ZrO_2. Above the critical grain size of approximately 0.3–0.5 μm, the corrosion is strongly accelerated. This makes precise temperature control during sintering necessary. Nanocrystalline materials show an strongly improved corrosion stability (Johannes & Schneider, 2012)
- Increasing of the stabilizer content results in reduced transformation toughening and therefore reduced fracture toughness and strength of the material. Therefore an optimum has to be found. It was proposed that by inhomogeneous yttria distribution (higher yttria content in the outer shells of the grains), the stability could be increased without a reduction in toughness.

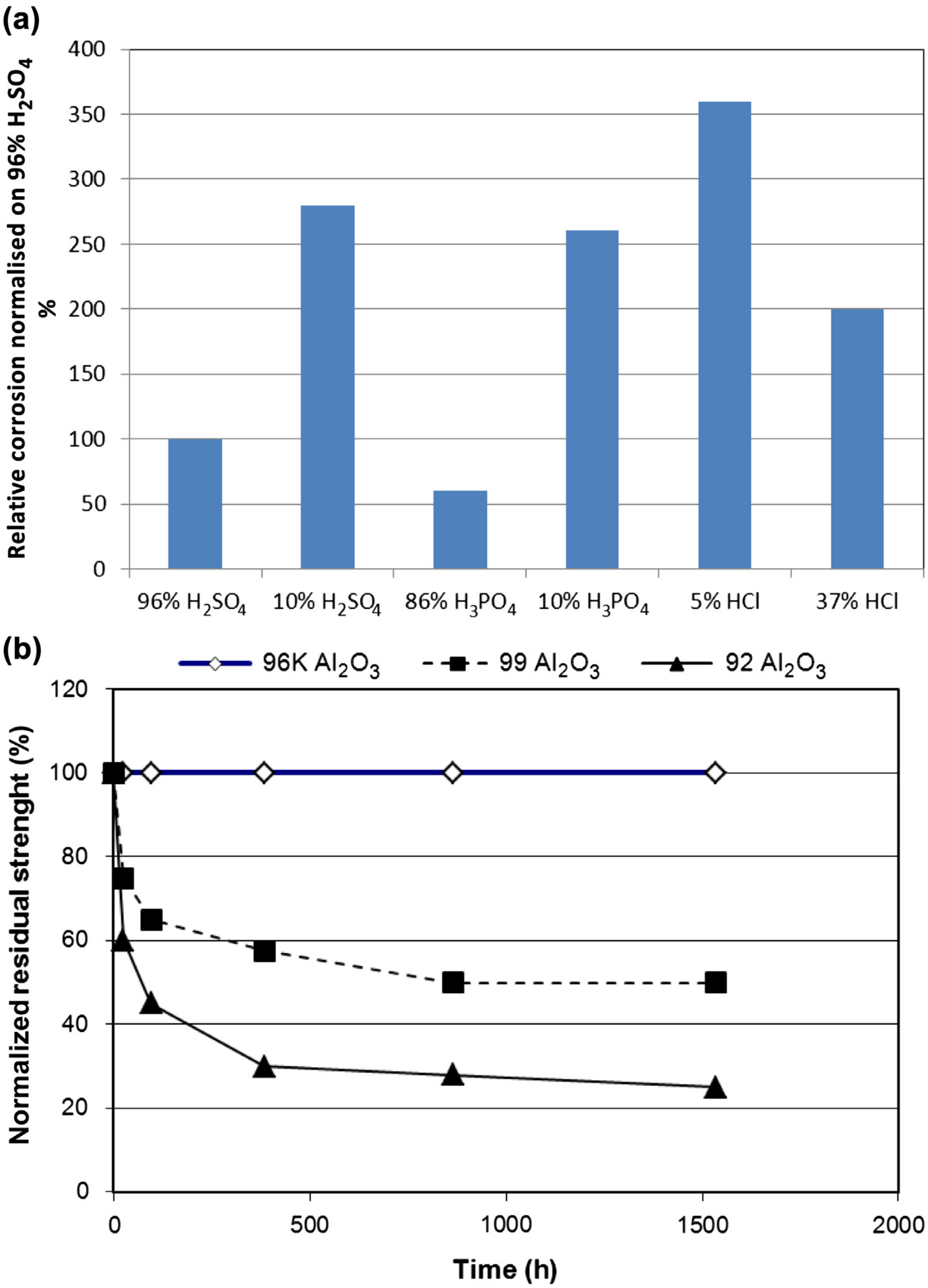

Figure 13 Corrosion rate and change in residual strength during corrosion (Hoppert, 2010). (a) Relative corrosion volume of a 92% Al_2O_3 ceramic after 121 days at 20 °C in different acids results normalized with respect to the corrosion of the ceramics in 96% H_2SO_4). (b) Residual strength of different Al_2O_3 ceramics in 5% H_2SO_4 at 100 °C (96 K Al_2O_3: 96% Al_2O_3 with crystalline secondary phase; 99 Al_2O_3; 92 Al_2O_3: Al_2O_3 ceramic with 99% and 92% purity and glassy grain boundary phase).

- Additional doping with other oxides (Chevalier et al., 2009; Lawson, 1995; Lughi & Sergo, 2010; Schacht et al., 1998), mainly CeO_2 (Chevalier et al., 2009; Lawson, 1995; Lughi & Sergo, 2010; Schacht et al., 1998), increases the stability. The higher stability can be explained by the different solubilities of CeO_2 and Y_2O_3 as well as by the different concentrations of oxygen vacancies (no vacancies in CeO_2 in CeO_2-stabilized ZrO_2) which play an important role in the corrosion mechanism.
- Increasing the Al_2O_3 content in Y-TZP reduces the extent of phase transformation during corrosion and therefore increases the stability. Al_2O_3/ZrO_2 have also been observed to show improved corrosion resistance

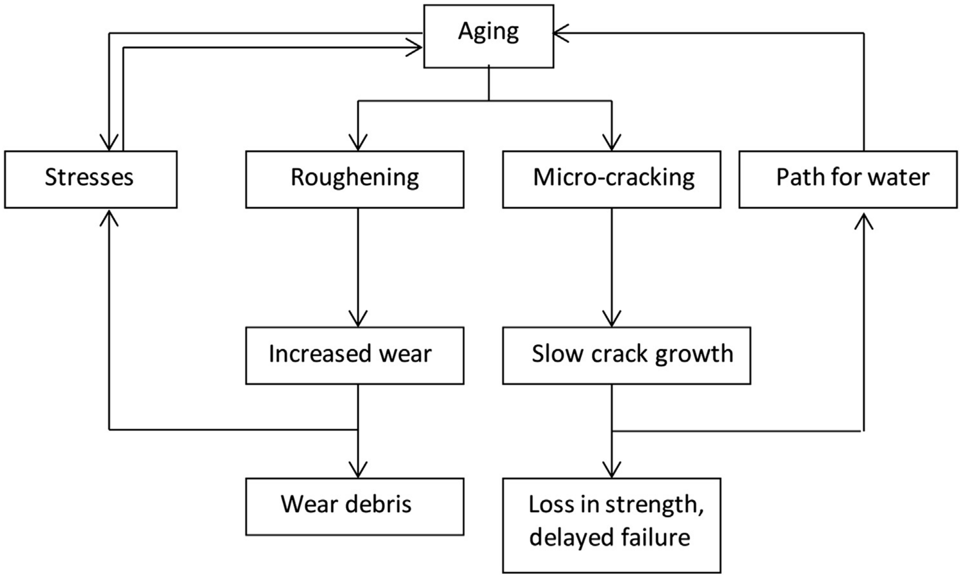

Figure 14 Potential effect of corrosion on the integrity of zirconia components (after Chevalier et al., 2009).

in comparison with that of pure TZP (Johannes & Schneider, 2012). MgO, spinel and transition metal oxide additives exhibit similar effects (Lawson, 1995).

- Use of pore-free microstructures and materials also results in improved stability.

The Mg-PSZ ceramics are more stable than the Y-TZP ceramics are under hydrothermal conditions. Direct comparison of Ce-TZP, Mg/Y-PSZ, and Mg-PSZ in different acids (HCl, H_2SO_4 and H_3PO_4) at 390 °C was carried out by Schacht (Schacht et al., 1998). The results yielded an increase in stability in the order Mg-PSZ < Mg/Y-PSZ, << Ce-TZP. The lowest stability was observed in H_2SO_4 solutions. A similar result was observed for YSZ ceramics (Yoshimura et al., 1986). Selective dissolution of yttria was observed in these materials. ZrP_2O_7 formed during corrosion in H_3PO_4 at 600–700 °C and 100 MPa.

Subcritical crack growth and phase transformation in Y-TZP ceramics were investigated in detail to predict the lifetime of ZrO_2 implants (Bartolome et al., 2004; Chevalier et al., 1999; Yashima et al., 1995). Schneider carried out detailed studies of the phase transformation of alumina-toughened ZrO_2 (Schneider et al., 2008) and found a much lower extent of aging in humid atmospheres for these materials than for 3Y-TZP ceramics. A transformation of approximately 50% of the ZrO_2 fraction was calculated to take place in only about 50 years (extrapolated from higher temperatures) at 37 °C and was observed to take place after <100 h at 134 °C (Schneider et al., 2008).

Thus transformation-toughened ZrO_2 materials can only be used in solutions or humid air at higher temperatures if a detailed selection process has been carried out to determine the right material, microstructure and processing.

Silicon nitride materials are usually liquid phase-sintered materials containing amorphous grain boundary phases. In Si_3N_4 ceramics, the grain boundary phase is distributed among the triple junctions and the thin films between the grains. The triple junctions form a three-dimensional network and have cross-sectional diameters of <1–2 μm (**Figure 15**). The thin grain boundary films between adjacent grains have thicknesses typically in the range of 1–2 nm, strongly depending on the grain boundary composition (Petzow & Herrmann, 2002; Kleebe et al., 1993). In materials with 5–10 vol% additives more than 90% of the grain boundary phase is concentrated in the triple junctions. These microstructural features must be taken into account in the interpretation of the corrosion resistance.

Typical sintering additives are rare-earth oxides and Al_2O_3/AlN or MgO or MgO/Al_2O_3 (Petzow & Herrmann, 2002). Because of their different additive contents and processing/sintering, the ceramics have different grain boundary phase amounts and compositions. Studies of the corrosion resistance of Si_3N_4 materials revealed a strong relationship between the stability of the grain boundary and the corrosion resistance of the ceramic material (Galuskova et al., 2011b; Herrmann & Schilm, 2009; Herrmann et al., 2003; Herrmann et al., 2006; Herrmann, 2005; Herrmann, 2012; Kitaoka et al., 1994; Kleebe et al., 1993; Nagae, Koyama, et al., 2006; Sato

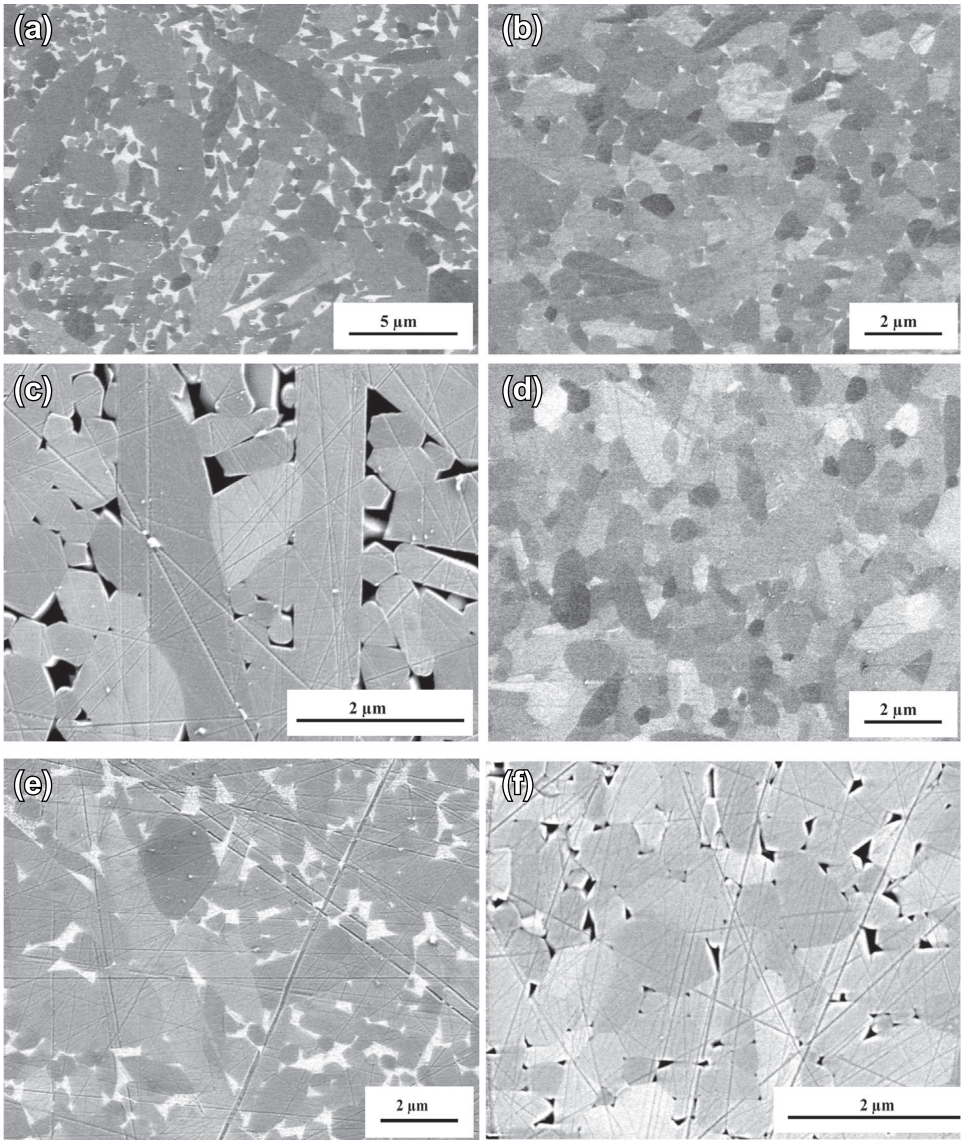

Figure 15 FESEM micrographs of polished sections (a, c and e) with Y_2O_3/Al_2O_3 additives and (b, d and f) with $Y_2O_3/MgO/Al_2O_3$ additives before and after corrosion (Herrmann, 2005). (a and b) initial state, (c and d) corroded in 1 N H_2SO_4 at 90 °C, and (e and f) corroded in 1 N NaOH at 90 °C.

et al., 1988a, 1988b; Sato et al., 1992; Schilm et al., 2003; Schilm et al., 2004a; Schilm et al., 2006; Schilm et al., 2007; Schilm, 2004; Seipel & Nickel, 2003; Shimada & Sato, 1989; Somiya, 2001).

Materials sintered conventionally with Y_2O_3/Al_2O_3 have much lower strengths after corrosion in acids at elevated temperatures due to grain boundary phase dissolution in the acids. This dissolution of the grain boundary phase can occur to depths of several micrometers without the three-dimensional network of the Si_3N_4 grains being destroyed (Figures 11(b) and 16(a)). Even materials with completely dissolved grain boundaries exhibit strengths of 400–500 MPa.

Comprehensive investigations of the relationship between grain boundary phase composition and corrosion behavior were carried out by Herrmann and Schilm et al. (Herrmann, 2005; Herrmann, 2012; Herrmann et al., 2003; Herrmann et al., 2006; Herrmann & Schilm, 2009; Schilm, 2004; Schilm et al., 2003; Schilm et al., 2004a; Schilm et al., 2006; Schilm et al., 2007; Seipel & Nickel, 2003) who found that the corrosion behavior of silicon nitride ceramics with amorphous grain boundary phases exposed to H_2SO_4, HCl, other mineral acids except HF (Monteverde et al., 2001; Schilm et al., 2004a; Sharkawy & El-Aslabi, 1998; Shimada & Sato, 1989) and bases at temperatures to at least 100–130 °C depends on the stability of the grain boundary phase: under these

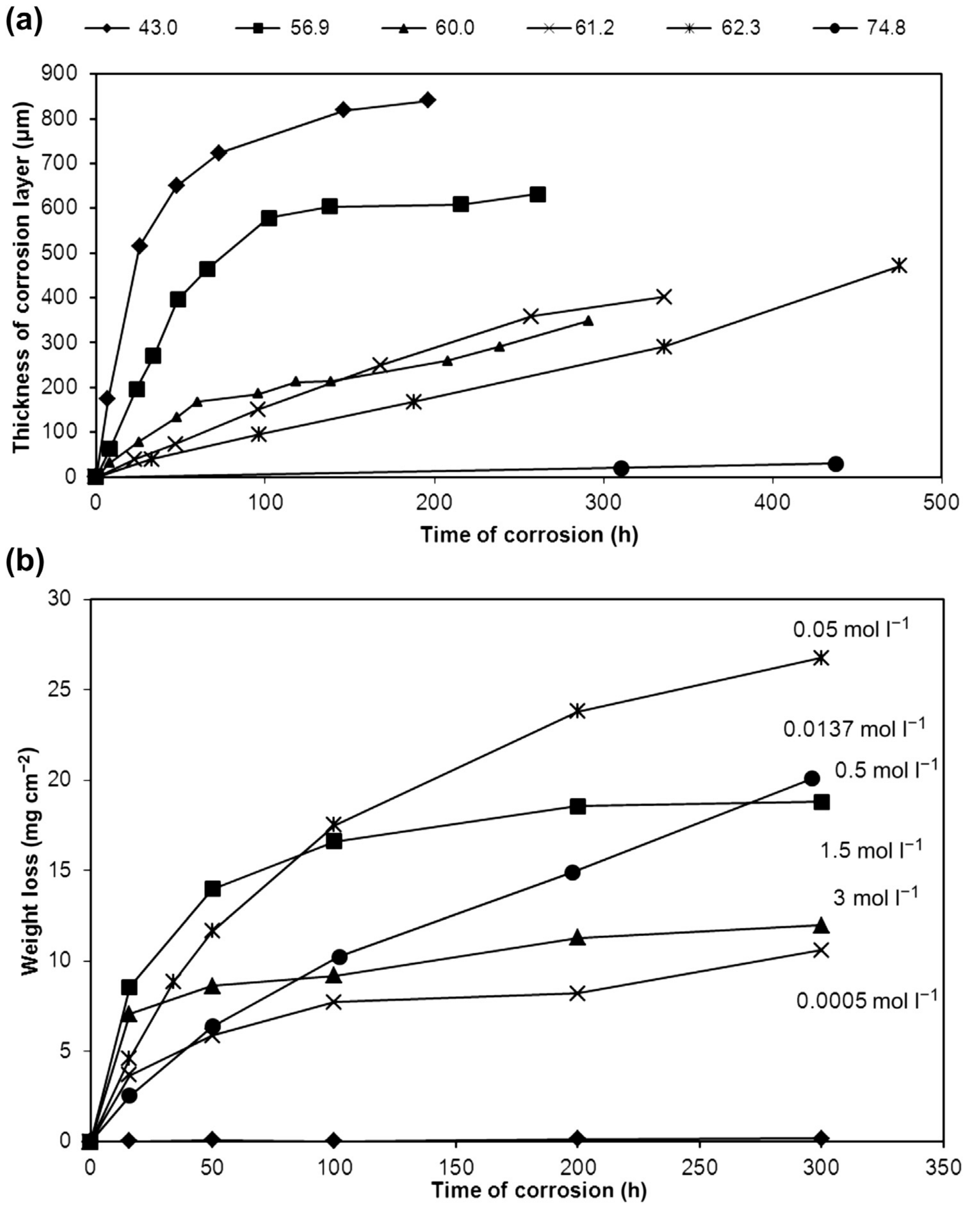

Figure 16 Time dependence of the thickness of the corrosion layer and weight loss during corrosion of silicon nitride materials (Schilm et al., 2007): (a) for Si_3N_4 materials with grain boundary phases with different SiO_2 and constant Y_2O_3/Al_2O_3 contents at 90 °C in 0.5 mol H_2SO_4 following Schilm et al. (Schilm, 2007; Herrmann, 2013) (mol% SiO_2 given in the diagram); (b) dependence of weight loss on corrosion time for the Si_3N_4 material with 6 wt% Y_2O_3 and 4 wt% Al_2O_3 in H_2SO_4 at different concentrations at 90 °C (concentrations given the diagram).

conditions, the silicon nitride grains themselves show a high stability. The stability of the grain boundary phase can be described using basic relations known from glass science (Herrmann, 2013; Herrmann, 2005; Schilm, 2004; Schilm et al., 2004b). Typically the glass network modifiers (in Si_3N_4 ceramics Y^{3+}, rare earth, Mg^{2+}, and, as intermediates, Al^{3+}) dissolve in the acids and a hydrated network remains. In the second step, the Si–O–Si bonds in the network break and the SiOx units dissolve in the acids. This process is shown schematically in Figure 17. The destruction of the network is normally the process with the lowest rate. Therefore more strongly linked networks are more stable. A strong correlation between the observed linear reaction rates and the structures of the grain boundaries has been found (Figure 10). Based on these data and the proposed corrosion mechanism, it can be concluded that the main factor influencing the stability of grain boundary phases in acids is the amount of bridging anions and network-forming cations, i.e. the SiO_2 content of the grain boundary

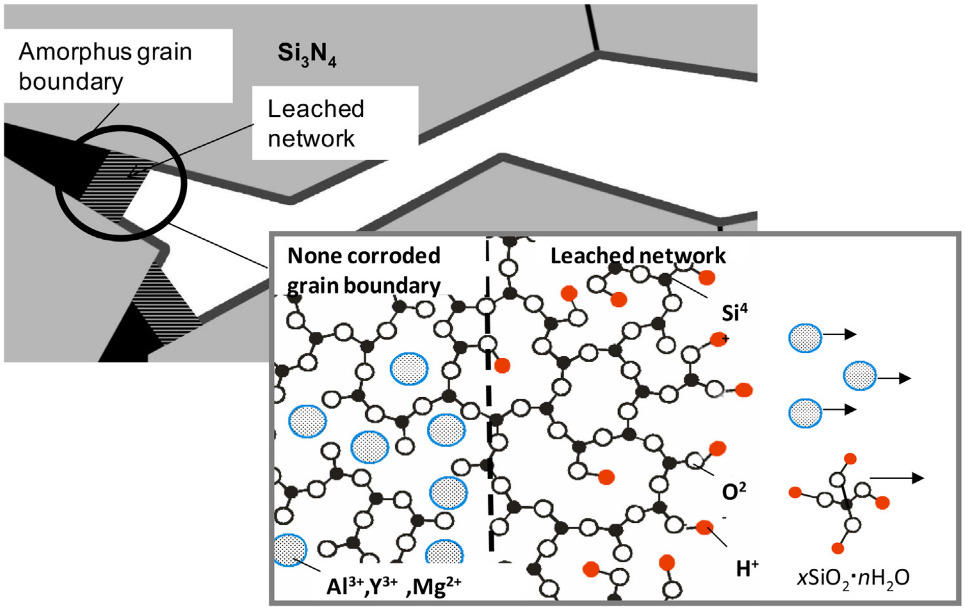

Figure 17 Schematic diagram illustrating the corrosion process in acids.

phase. This finding is confirmed by the fact that HIPed Si_3N_4 materials without sintering additives show very high corrosion resistance in acids (Herrmann, 2005; Oda et al., 1993). The nature of the network-modifying ions (e.g. Y^{3+}, rare earth, Mg^{2+} and/or Ca^{2+}) has a much lower influence. The kinetics of corrosion is rather complex and is often described by different laws. A detailed analysis of the different types of behavior is given in the literature (Herrmann, 2013; Herrmann et al., 2006; Herrmann & Schilm, 2009; Schilm, 2004; Schilm et al., 2003; Schilm et al., 2006; Seipel & Nickel, 2003). For short corrosion times, a reaction-controlled mechanism is usually observed, whereas for longer times, the process can be greatly slowed down by passivation mechanisms (**Figures 11** and **16**). The change in mechanism depends on the grain boundary composition, the temperature and the concentration of the acid (**Figures 11** and **16**).

The reason for this passivation is the formation of SiO_2-rich deposits in the pores. The detailed mechanisms and conditions of formation of these layers are discussed in the literature (Herrmann, 2013; Herrmann, 2005; Herrmann et al., 2003; Herrmann et al., 2006; Herrmann & Schilm, 2009; Schilm, 2004; Schilm et al., 2003; Schilm et al., 2004a, 2004b; Schilm et al., 2006; Schilm et al., 2007; Seipel & Nickel, 2003). Such hydrated networks are also known to form in glasses, although formation of these hydrated networks is much more pronounced in the pores of Si_3N_4 ceramics than in glasses. This is due to kinetic factors as well as hydrolysis of the surfaces of the Si_3N_4 grains (a few nm in 100 h). The strong remaining skeleton of Si_3N_4 grains stabilizes this layer. The formation of a SiO_2-rich passivating layer in Si_3N_4 also leads to a much higher corrosion resistance in acids of high concentration than in acids of medium concentration (**Figure 16(b)**).

The anions in HCl, HNO_3 and H_2SO_4 do not appear to have any special effects. Fluorine anions strongly influence the corrosion of Si_3N_4 ceramics due to their ability to dissolve SiO_2 (Sharkawy & El-Aslabi, 1998; Schilm et al., 2004a; Shimada & Sato, 1989). Even at low concentrations, the fluorine ions prevent the formation of passivating layers and dissolve the thin films between the Si_3N_4 grains, resulting in a nonadhering corrosion layer from which the Si_3N_4 grains can be removed very easily. This also results in a significant reduction in strength (Schilm et al., 2004a). The corrosion rate is found to be lower in H_3PO_4 solutions than in HCl and other mineral acids due to the formation of low-solubility rare-earth phosphates (Herrmann, 2013; Petzow & Herrmann, 2002).

The influence of the microstructure on corrosion can be summarized as follows: ceramics with high corrosion resistance in acids are those with low amounts of grain boundary phase and large numbers of bridging anions, i.e. grain boundary phases with high SiO_2 contents. This is shown schematically in **Figure 18**.

Crystallization of the grain boundary can also yield an improvement in corrosion behavior. Very little information about the influence of grain boundary crystallization on corrosion resistance can be found in the literature (Herrmann, 2013; Oda et al., 1993). This could be a way to increase the corrosion stability of Si_3N_4

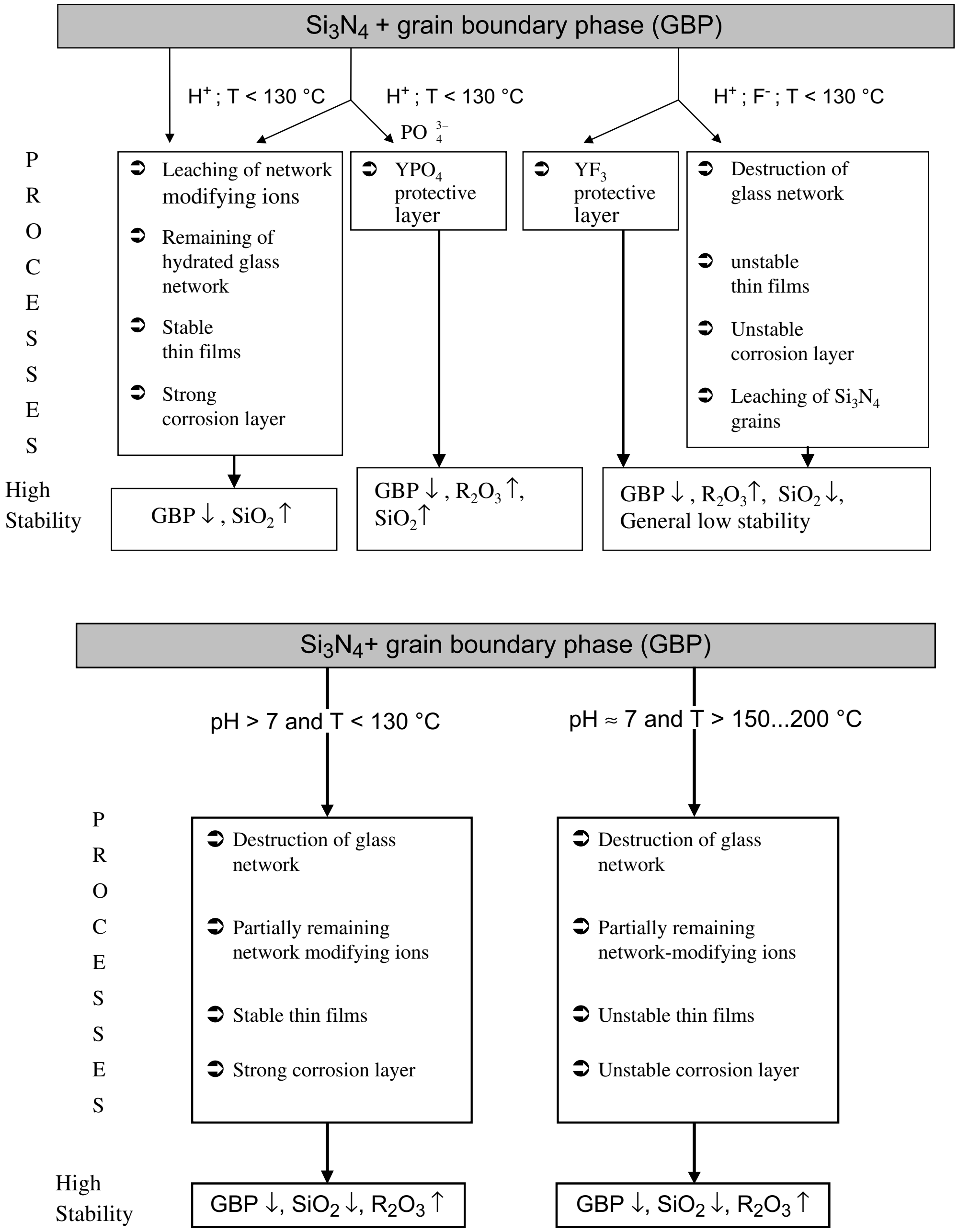

Figure 18 Corrosion resistance as a function of the grain boundary phase for Si_3N_4 ceramics in acids, bases and hydrothermal conditions (GPB = grain boundary phase; 'thin films' mean thin grain boundary films between adjacent Si_3N_4 grains).

ceramics. The lowered grain boundary phase content in α- and β-SiAlON materials also improves the corrosion resistance. Figure 19 shows that the corrosion stability of the α-SiAlON is strongly reduced in comparison with Si_3N_4 materials. The higher stability is caused by the lower amount of the grain boundary phase and the changed composition.

The mechanisms underlying corrosion resistance in bases and under hydrothermal conditions are the same. For standard Si_3N_4 materials, the weight loss and the corrosion depth are much lower in bases at least up to concentrations of 1 mol l^{-1} and temperatures up to 130 °C than in acids. This can also be explained by the stability of the grain boundary phase and the relations known from glass science. At medium concentrations of bases, Y_2O_3 and Al_2O_3 form hydroxides passivating the grain boundaries. Under very strong alkaline conditions, Al_2O_3, MgO and SiO_2 constituents of the grain boundary can easily be dissolved and therefore under

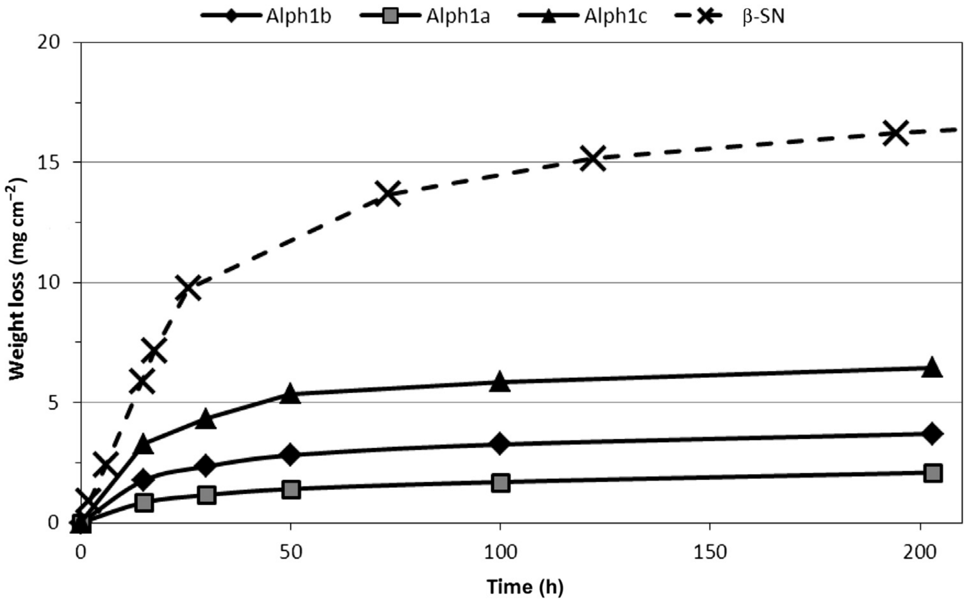

Figure 19 Weight loss of α-sialon materials with different grain boundary phase contents in 1 N H_2SO_4 at 90 °C in comparison to a standard β-Si_3N_4 material (volume content of additives of the sialon material increases from Alph1a to Alph1c (maximum app. 4 vol% for Alph1c; β-SN silicon nitride with 11 wt% Y_2O_3/Al_2O_3 additives)).

these conditions, the corrosion stability is reduced. In summary, the materials that are the most stable in acids due to a high SiO_2 content in the grain boundary phase are less stable in basic solutions.

Under hydrothermal conditions at temperatures of >200–250 °C, the grains and the thin films between the grains are seen to dissolve, resulting in a corrosion layer α-sialon (Galuskova et al., 2011b; Herrmann, 2005; Herrmann et al., 2003; Nagae, Yoshio, et al., 2006; Oda et al., 1993; Schilm et al., 2007). Under these conditions, the SiO_2-rich grain boundaries are less stable than the Y_2O_3/Al_2O_3 grain boundary phases. The ceramics that are most stable in bases and under hydrothermal conditions are less stable in acids. At temperatures >250 °C, the dissolution of the Si_3N_4 grains become a pronounced corrosion mechanism (Herrmann, 2005; Herrmann et al., 2003; Schilm et al., 2007). Recently (Galuskova et al., 2011b), it was shown that the hydrothermal corrosion stability of β-sialon materials is not superior to that of β-Si_3N_4 materials at 290 °C. In both cases, pronounced corrosion of the grains takes place. This explains the determined less stability of Si_3N_4 materials in comparison to LPSSiC and SSiC materials (Figure 20).

The presented corrosion data show the main correlations between composition, structure and corrosion behavior, allowing materials to be preselected for the given conditions. Nevertheless, the materials still have to be evaluated further to determine their suitability for the given applications.

Up to now, no silicon nitride ceramics with the same universal corrosion stability as that of SSiC could be developed. However, ceramics with low amounts of $Y_2O_3/MgO/Al_2O_3$ represent a good compromise with high stability in acids, bases and hydrothermal conditions (Herrmann, 2005; Herrmann et al., 2003).

The group of silicon carbide ceramics is made up of different materials with different properties. The main dense materials are solid phase-sintered SiC (SSiC), Si-infiltrated SiC (SiSiC) and LPSSiC. Porous materials such as recrystallized SiC (RSiC), nitride-bonded silicon carbide and clay-bonded silicon carbide also exist.

The different kinds of silicon carbide ceramics exhibit different corrosion behavior (Figures 12, 20, 21) (Schmalzried & Schwetz, 2010; Schwetz & Hassler, 2002a, 2002b). Whereas the dense SSiC exhibits very high-corrosion stability in different media and at different temperatures, SiSiC and LPSSiC show lower stabilities due to their compositions and microstructures. The SSiC is mostly a single-phase material used in seals and bearings and exhibits pure grain boundary phases. Occasionally existing secondary phases such as graphite or boron carbide are normally only present as local inclusions with grain sizes of <5–10 μm and therefore corrosion of these phases does not have a weakening effect on the SSiC. The high grain boundary purity and the high corrosion stability in acids, bases and hydrothermal conditions inherent to SiC are the reasons for the superior corrosion resistance of these materials in comparison with Si_3N_4 materials and other structural ceramics. SSiC is the only dense Si-containing ceramic with good stability in HF-containing liquids. SiC can be passivized not only by the formation of a SiO_2 layer (which can easily be dissolved in HF-containing solutions), but also by the dissolution of SiO_2 and subsequent formation of carbon-containing passivating layers. This explains the high stability in HF-containing solutions and under hydrothermal conditions (Figure 21).

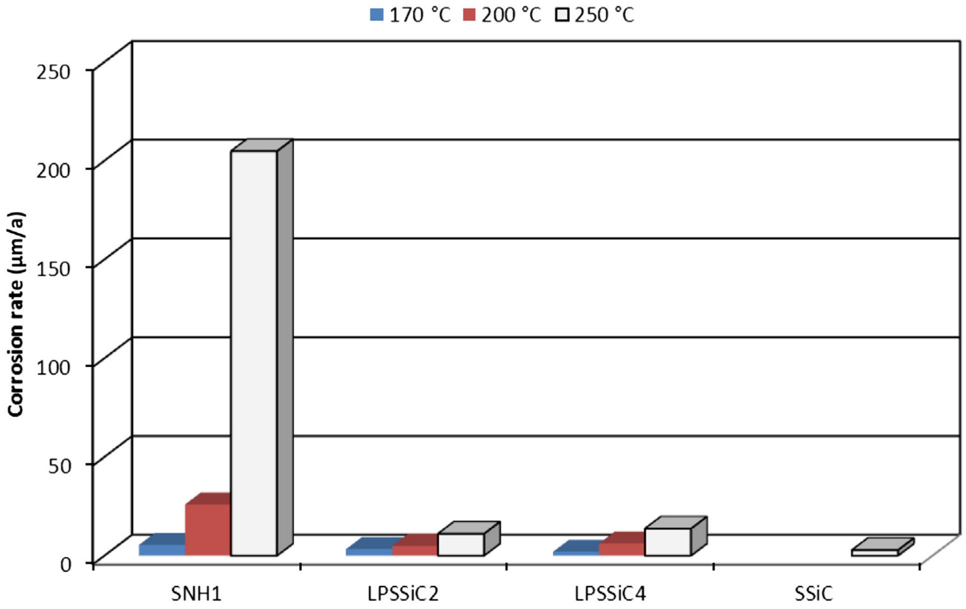

Figure 20 Hydrothermal stability of SSiC, LPSSiC (2 and 4% additives) and Si_3N_4 (SNH1) at different temperatures (calculated from the weight loss) (Herrmann et al., 2003).

In silicon-infiltrated SiC, clay-bonded SiC and LPSSiC ceramics, a continuous secondary phase of lower stability determines the overall corrosion resistance of the material.

The SiSiC ceramics contain residual silicon which dissolves in basic solutions at elevated temperatures. The silicon can even decompose water to generate hydrogen.

$$Si + (n + 2)\ H_2O \Rightarrow SiO_2 \times n\ H_2O + 2H_2 \tag{11}$$

The silica formed dissolves in highly basic solutions and therefore no passivation takes place in bases. In contrast, in neutral and acidic solutions, passivation takes place due to the low solubility of SiO_2 in the solutions. Because the solubility increases greatly with increasing temperature (Iler, 1982), the corrosion stability decreases strongly with increasing temperature even in neutral solutions.

The stability of LPSSiC is determined by the oxide grain boundary phases formed. They are nearly fully crystallized in the sintered materials (usually $Y_3Al_5O_{12}$; Al_2O_3, $YAlO_3$; and/or $Y_4Al_2O_9$) and are quite stable in

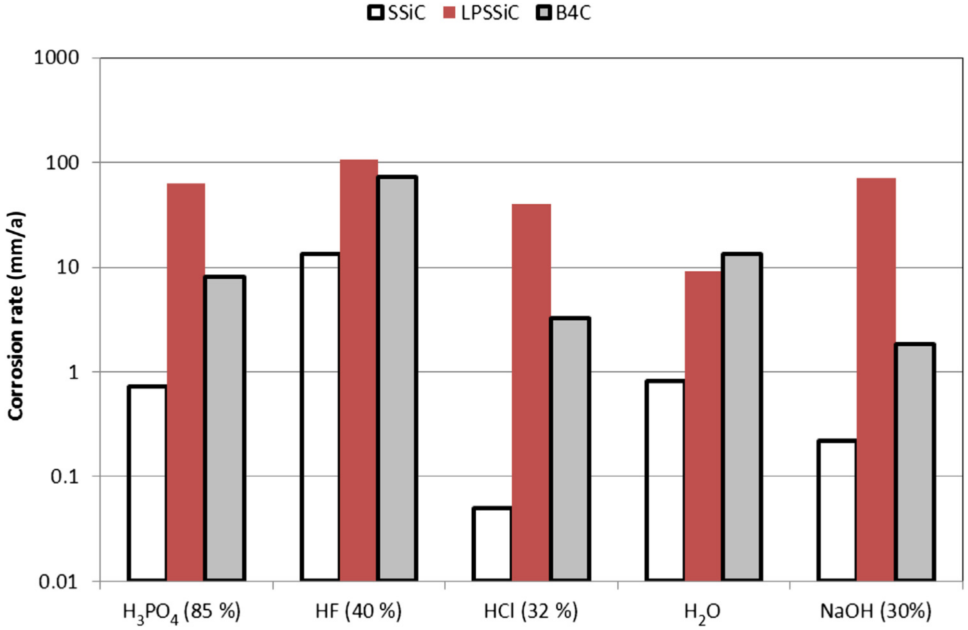

Figure 21 Corrosion resistance of EKasic® C(SSiC) and EKasic® Tplus (LPSSiC) in different acids and bases at 220 °C (calculated from the thickness of affected surface layer) (Rendtel, 2010).

acids and bases of medium concentration. However, they can dissolve in concentrated acids and bases at elevated temperatures (Herrmann et al., 2003; Kitaoka et al., 1994; Rendtel, 2010; Schwetz & Hassler, 2002b). Under hydrothermal conditions, the grain boundary phases are much more stable than the grain boundaries in Si_3N_4 materials, but nevertheless a strong reduction in strength is observed (**Figures 20** and **21**). A detailed analysis has shown that the strength-determining defects are pits formed from residual porosity in the material (Herrmann et al., 2003). Therefore retention of the properties under corrosive conditions is connected with minimization of defects (segregation of additives and pores).

Kitaoka et al. (1994), Presser et al. (2008), Presser, Nickel, et al. (2009) investigated the acceleration of wear under hydrothermal conditions in detail for SSiC. Kitaoka showed that $SiO_2 \times n\, H_2O$ forms between room temperature and 300 °C in water and nearly completely dissolves in the liquid during corrosion at 120–300 °C. At 120 and 300 °C, the formation of gases was detected. The main gaseous reaction products observed were H_2, CO_2 (25% of the amount of H_2 (mol per mol)), CH_4 (<10% of H_2) and, additionally at 300 °C, C_2H_6 (<1% of the amount of H_2). In the presence of dissolved oxygen in the water, CO_2 and CO were dominant reaction products.

Like SSiC, recrystallized SiC is composed of a three-dimensional SiC network with very pure grain boundaries. It usually contains 15–20% porosity. This porosity increases the reactivity, but the chemical stability is similar to that of SSiC materials. Due to this high stability, such materials lend themselves well to use as refractory materials and diesel particle filters (Adler & Petasch, 2012).

The clay-bonded SiC materials can be produced cost-effectively due to the low sintering temperature (800–1200 °C), but the corrosion stability is limited by the relatively low stability of the silicate bonds in the SiC grains in comparison with that of RSiC or NSiC.

As already mentioned in the introduction, SiC ceramics are semiconductors. The specific resistivity at room temperature can be in the range of more than 1 MΩm to <1 Ωm depending on the doping of the grains and the grain boundary phase (Ihle, Martin, Herrmann, et al., 2006; Kleebe & Siegel, 2003; Sauti, Can, McLachlan, & Herrmann, 2007; Schmalzried & Schwetz, 2010; Siegelin, Kleebe, & Sigl, 2003). The reaction of SiC with acids, bases and water is a redox reaction and therefore a chemical potential in contact with water can be formed as in the case of metals (**Figures 22** and **23**; standard potentials are given in the literature (Sydow, Sempf, et al., 2011)). Therefore, electrochemical corrosion can cause material degradation of SiC materials like in cermets or hardmetals (Kumar et al., 2007). The corrosion rates of SiC ceramics are generally low in comparison with those of metals. Nevertheless, damage patterns for SiC seals have been reported under conditions (pure water at room and elevated temperatures) in which pure chemical corrosion as described above would not be expected (Loenhout & Traets, 2009; Meschke & Kailer, 2004). This is strongly suggestive of electrochemical corrosion as the primary cause. The detailed mechanism underlying this behavior has not yet been elucidated, but a possible reason could be, besides electrochemical corrosion, streaming potential. The initial formation of local pits could be enhanced by cavitation.

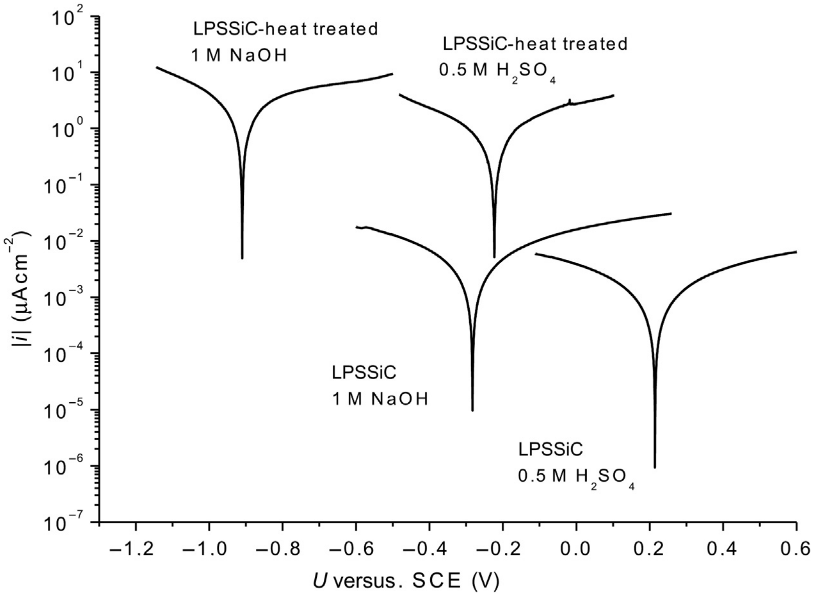

Figure 22 Linear voltammetric scans in 1 M NaOH and 0.5 M H_2SO_4 of a liquid phase-sintered material and an additionally heat-treated LPSSiC (scan rate: 0.5 mV s^{-1}; Sydow, Herrmann, et al., 2011).

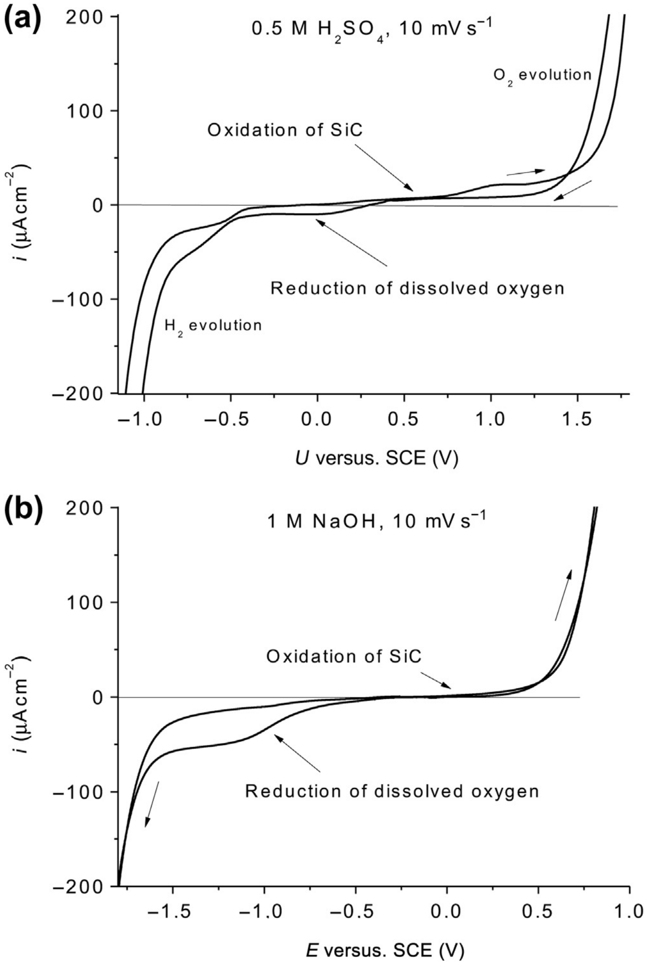

Figure 23 Cyclic voltammetry measurements of SSiC in (a) 0.5 M H_2SO_4 and (b) 1 M NaOH electrolytes (Sydow et al., 2010).

Studies have been carried out to investigate the electrochemical corrosion behavior of SSiC, SiSiC and LPSSiC (Andrews et al., 2007; Cook et al., 1994; Divakar et al., 1989; Sydow et al., 2010; Sydow, Herrmann, et al., 2011; Sydow, Sempf, et al., 2011). SiC ceramics were found to exhibit corrosion potentials (open circuit potentials) of greater than −150 mV (in comparison with NHE, normal hydrogen electrode) in 1 N acids and higher than −200 mV in 1 N NaOH. For LPSSiC, somewhat lower values were observed (−450 mV in 0.5 mol H_2SO_4 (1 N H_2SO_4) and −660 mV in NaOH (Andrews et al., 2007; Sydow, Herrmann, et al., 2011; Sydow, Sempf, et al., 2011)). During immersion in the solution, these potentials shifted to positive values (up to +500 mV in acid and up to 0 mV in 1 M NaOH) due to the formation of surface layers. Through treatment in HF solutions, the potential could be returned to the original value (Andrews et al., 2007). At least in basic and neutral solutions, the formation of a $SiO_2 \times n\, H_2O$ surface layer was directly shown by scanning electron microscopy/energy-dispersive X-ray spectroscopy investigations. This $SiO_2 \times n\, H_2O$ layer was found to passivate the SiC surface partially and resulted in reduction of the corrosion current (Andrews et al., 2007; Cook et al., 1994; Sydow et al., 2010). The most pronounced corrosion of SiC ceramics was found to occur if the applied voltage was in the region of water decomposition to oxygen. Under these conditions, the formation of CO gas was also observed (Sydow, Herrmann, et al., 2011).

Evidence of corrosion is provided by the micrographs in **Figure 24**. Immersion of SiC in acid without application of a voltage yielded no visible reactions, whereas application of 2 V in H_2SO_4 resulted in the formation of a 100-nm-thick SiO_2 layer. In 1 N NaOH, severe etching of the grains took place.

Electrochemical corrosion is greatly reduced through reduction of the conductivity of the SiC ceramics (Sydow et al., 2010; Sydow, Sempf, et al., 2011). Core-rim structures are observed in SiC materials due to the dependence of the conductivity of the grains on the doping level (Al, B).

Recently it was observed that the wear and friction coefficients of SiC materials can be improved by the application of a potential less than the corrosion potential (Kailer et al., 2011).

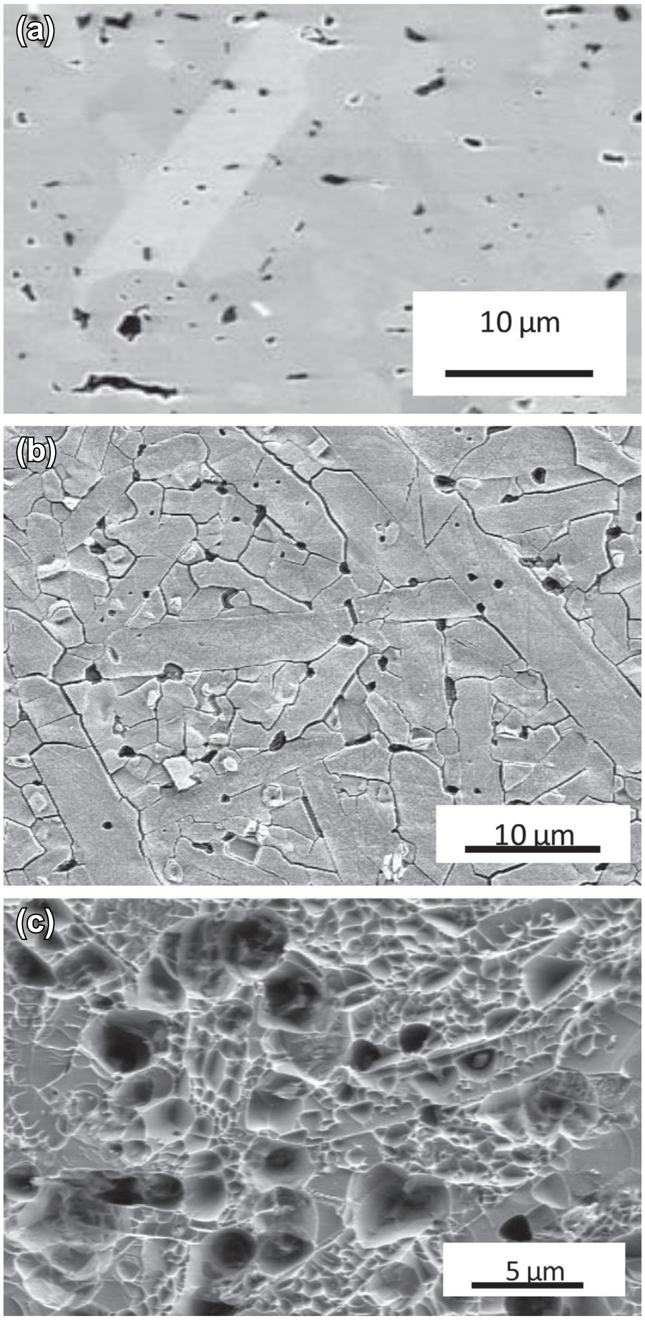

Figure 24 SEM micrographs of SSiC in H_2SO_4 (a) with no applied voltage and (b) with a voltage of 2 V applied for 1 h and (c) in NaOH with an applied voltage of 2 V (Sydow et al., 2010).

2.15.4 Final Remarks

This chapter revealed that ceramic materials exhibit high-corrosion stability at both room and elevated temperatures. Nevertheless the corrosion behavior of the different ceramic materials strongly depends on the corrosion conditions, the microstructure and composition of the ceramic materials. Therefore, a careful selection of the materials for applications under the different conditions is necessary.

In the past 20 years, a deep understanding of the behavior of the ceramic materials in air and combustion gasses at high temperatures has been achieved, and special long-term mechanical and corrosion resistant materials have been developed. The development of EBCs to control the interaction with the high-speed moisture-containing gas stream is an actual research topic to meet the complex thermomechanical and corrosive loading under gas turbine conditions.

The interaction of the ceramics with special gasses like chlorine, hydrogen chlorine or in a plasma has not been investigated in the same depth as the interaction with oxygen or water vapor. This would be necessary with the increasing range of applications under harsh conditions in chemical or microelectronic production processes.

Also the corrosion behavior of ceramic materials in aqueous solutions is well understood. This knowledge can be used for the selection of materials for different applications. The corrosion behavior of the materials strongly depends on the existence and composition of small amounts of impurities, grain boundary phases (e.g. Si_3N_4-; Al_2O_3-ceramics) or grain size or dopants of the main component (especially ZrO_2 ceramic (TZP)). Therefore a careful selection of the materials for a given application has to be carried out.

The detailed mechanisms of pit formations are not clear. Nevertheless it can be summarized that inhomogeneities (inclusions, pores, and local stresses) result in pitting formation and therefore have to be avoided. The influence of the different corrosion conditions on subcritical crack growth is investigated in detail only for zirconia and alumina for water-based systems in connection with medical applications. However, these processes have to be taken into account for the application of ceramics under load in corrosive environments because it can strongly reduce the lifetime.

The influence of superimposing wear and corrosion is still not investigated in detail due to the wide range of possible parameters and has to be specified for a given application. In common, the wear reduces the corrosion resistance.

Future research in the field of corrosion of ceramics will be focused in different directions: to ensure the reliability of future applications of components, the evaluation of the behavior under the special conditions of the applications and the prediction of lifetime is necessary. On the other hand, new developed materials have to be tested as well.

New analytical methods and modeling of the processes on atomic level will in future allow a more detailed insight in the corrosion process and may be result in new ideas for further improvement of the corrosion stability of ceramics materials.

References

Adler, J., & Petasch, U. (2012). Diesel particulate filters. In S. Somya (Ed.), *Handbook of advanced ceramics*. London: Elsevier.

Andrews, A., Herrmann, M., Sephton, M., Machio, C., & Michaelis, A. (2007). Electrochemical corrosion of solid and liquid phase sintered silicon carbide in acidic and alkaline environments. *Journal of the European Ceramic Society, 27*, 2127–2135.

Backhaus-Ricoult, M., Guerin, V., & Urbanovich, V. S. (2002). High-temperature oxidation behavior of high-purity α-, β-, and mixed silicon nitride ceramics. *Journal of the American Ceramic Society, 85*, 385–392.

Balat, M. J. H. (1996). Determination of the active-to-passive transition in the oxidation of silicon carbide in standard and microwave-excited air. *Journal of the European Ceramic Society, 16*, 55–62.

Balat, M., Berjoan, R., Pichelin, G., & Rochmann, D. (1998). High-temperature oxidation of sintered silicon carbide under pure CO at low pressure: active–Passive transition. *Applied Surface Science, 133*, 115–123.

Barinov, S. M., Ivanov, M. V., Orlov, S. V., & Shevchenko, V. J. (1998). Influence of environment on delayed failure of alumina ceramics. *Journal of the European Ceramic Society, 18*, 2057–2063.

Barringer, E., Faiztompkins, Z., & Feinroth, H. (2007). Corrosion of CVD silicon carbide in 500°C Supercritical water. *Journal of the American Ceramic Society, 90*, 315–318.

Bartolome, J. F., Montero, I., Diaz, M., et al. (2004). Accelerated aging in 3-mol%-yttria-stabilized tetragonal zirconia ceramics sintered in reducing conditions. *Journal of the American Ceramic Society, 87*, 2282–2285.

Charpentier, L., Balat-Pichelin, M., & Audubert, F. (2010). High temperature oxidation of SiC under helium with low-pressure oxygen – part 1: sintered α-SiC. *Journal of the European Ceramic Society, 30*, 2653–2660.

Charpentier, L., Balat-Pichelin, M., Glénat, H., Beche, E., Caborde, E., & Audubert, F. (2010). High temperature oxidation of SiC under helium with low-pressure oxygen. Part 2: CVD β-SiC. *Journal of the European Ceramic Society, 30*, 2661--2670.

Charpentier, L., Maître, A., Balat-Pichelin, M., Faucoud, S., & Adubert, F. (2009). Influence of alumina on the passive oxidation at low oxygen pressure of hot-pressed α-SiC. *Scripta Materialia, 60*, 481–484.

Chen, S. Y., & Lu, H.-Y. (2003). Low-temperature ageing map for 3mol% Y_2O_3–ZrO_2. *Journal of Materials Science, 24*, 453–456. *Journal of Materials Science*, 18, 2415–2426 (1989)).

Chevalier, J., Gremillard, L., Virkar, A. V., & Clarke, D. R. (2009). The tetragonal–monoclinic transformation in zirconia: lessons learned and future trends. *Journal of the American Ceramic Society, 92*, 1901–1920.

Chevalier, J., Olagnon, C., & Fantozzi, G. (1999). Crack propagation and fatigue in zirconia-based composites, composites. Part A. *Applied Science and Manufacturing, 30*, 525–530.

Clark, D. E., Dilmore, M. F., Ethridge, E. C., & Hench, L. L. (1976). Aqueous corrosion of soda-silica and soda-lime-silica glass. *Journal of the American Ceramic Society, 59*, 62–65.

Conradt, R. (2008). Chemical durability of oxide glasses in aqueous solutions: a review. *Journal of the American Ceramic Society, 91*, 728–735.

Cook, S. G., Little, J. A., & King, J. E. (1994). Corrosion of silicon carbide ceramics using conventional and electrochemical methods. *British Corrosion Journal, 29*, 183.

Costello, J. A., & Tressler, R. E. (1986). Oxidation kinetics of silicon carbide crystals and ceramics: I, in dry oxygen. *Journal of the American Ceramic Society, 69*, 674–681.

Courtright, L. E. (1991). Engineering property limitations of structural ceramics and ceramic composites above 1600°C. *Ceramic Engineering and Science Proceedings, 12*, 1725–1744.

Dawi, K., Balat-Pichelin, M., Charpentier, L., & Adubert, F. (2012). High temperature oxidation of SiC under helium with low-pressure oxygen. Part 3: β-SiC–SiC/PyC/SiC. *Journal of the European Ceramic Society, 32*, 485–494.

Divakar, R., Seshadri, S. G., & Srinivasan, M. (1989). Electrochemical techniques for corrosion rate determination in ceramics. *Journal of the American Ceramic Society, 72*, 780–784.

dos Santos e Lucato, S. L., Sudre, O. H., & Marshall, D. B. (2011). A method for assessing reactions of water vapor with materials in high-speed, high-temperature flow. *Journal of the American Ceramic Society, 94*, 186–195.

Dutta, I., Mitra, S., & Rabenberg, L. (1992). Oxidation of sintered aluminum nitride at near-ambient temperatures. *Journal of the American Ceramic Society, 75*, 3149–3153.

Eichler, J., & Lesniak, C. (2008). Boron nitride (BN) and BN composites for high temperature applications. *Journal of the European Ceramic Society, 28*, 1105–1109.

EN 12923-1. (2006). *Advanced technical ceramics – Monolithic ceramics – Part 1: General practice for undertaking corrosion tests*.

Fahrenholtz, W. G., Hilmas, G. E., Talmy, I. G., & Zaykoski, J. A. (2007). Refractory diborides of zirconium and hafnium. *Journal of the American Ceramic Society, 90*, 1347–1364.

Fang, Q., Sidky, P. S., & Hocking, M. G. (1997). The effect of corrosion and erosion on ceramic materials. *Corrosion Science, 39*, 511–527.

Franks, G. V., & Gan, Y. (2007). Charging behavior at the alumina–water interface and implications for ceramic processing. *Journal of the American Ceramic Society, 90*, 3373–3388.

Freiman, S. W., Wiederhorn, S. M., & Mecholsky, J. J. (2009). Environmentally enhanced fracture of glass: a historical perspective. *Journal of the American Ceramic Society, 92*, 1371–1382.

Fritsch, M. (2008). *Heißgaskorrosion keramischer Werkstoffe in H_2O-haltigen Rauchgasatmosphären* (Dissertationsschrift). TU Dresden: Fraunhofer IRB Verlag, ISBN: 978-3-8167-7588-1.

Fritsch, M., & Klemm, H. (2006). The water vapor hot gas corrosion behavior of Al_2O_3-Y_2O_3 materials, Y_2SiO_5 and $Y_3Al_5O_{12}$-coated alumina in a combustion environment. *Ceramic Engineering and Science Proceedings, 27*, 149–159.

Fritsch, M., & Klemm, H. (2008). The water vapor hot gas corrosion behavior of oxide based ceramic materials in a combustion atmosphere. *Journal of the European Ceramic Society, 28*, 2353–2358.

Fritsch, M., Klemm, H., Herrmann, M., Michaelis, A., & Schenk, B. (2010). The water vapour hot gas corrosion of ceramic materials. *Ceramic Forum International (Berichte der Deutschen Keramischen Gesellschaft), 87*, 11–12.

Galuskova, D., Hnatko, M., Galusek, D., & Sajgalik, P. (2011a). Corrosion of structural ceramics under sub-critical conditions in aqueous sodium chloride solution and in deionized water, part II: dissolution of Al_2O_3-based ceramics. *Journal of the American Ceramic Society, 94*, 3044–3052.

Galuskova, D., Hnatko, M., Galusek, D., & Sajgalik, P. (2011b). Corrosion of structural ceramics under subcritical conditions in aqueous sodium chloride solution and in deionized water, part I: dissolution of Si_3N_4-based ceramics. *Journal of the American Ceramic Society, 94*, 3035–3043.

Genthe, W., & Hausner, H. (1989). Corrosion of alumina in acids. In G. de With, R. A. Terpstra, & R. Metselaar (Eds.), *Euro-ceramics 1* (Vol. 3; pp. 463–467). London: Elsevier.

Genthe, W., & Hausner, H. (1992). Influence of chemical composition on the corrosion of alumina in acids and caustic solutions. *Journal of the European Ceramic Society, 9*, 417–425.

Gogotsi, Y. G. (1994). Hydrothermale Korrosion von SiC – Betrachtung der schädlichen und nützlichen Aspekte in Keramik in Wissenschaft und Praxis. In R. Telle (Ed.), *Korrosion und Verschleiß von keramischen Werkstoffen* (pp. 114–122). FoB DKG.

Gremillard, L., Chevalier, J., Epicier, T., & Fantozzi, G. (2002). Biomedical grade zirconia ceramic by addition of silica. *Journal of the American Ceramic Society, 85*, 401–407.

Guo, X., & Schober, T. (2004). Water incorporation in tetragonal zirconia. *Journal of the American Ceramic Society, 87*, 746–748.

Hannink, R. H. J., Kelly, P. M., & Muddle, B. C. (2000). Transformation toughening in zirconia-containing ceramics. *Journal of the American Ceramic Society, 83*, 461–487.

Herrmann, M. (2005). *Gefügeausbildung in Siliciumnitridkeramiken und der Einfluss des Gefüges auf ausgewählte Werkstoffeigenschaften*. Habilitation BTU.

Herrmann, M. (2012). Ceramic bearings and seals. In S. Somya (Ed.), *Handbook of advanced ceramics*. London: Elsevier.

Herrmann, M. (2013). Corrosion of Silicon Nitride Materials in Aqueous Solutions. *Journal of American Ceramic Society, 96*, 3009–3022.

Herrmann, M., & Schilm, J. (2009). Shape dependence of corrosion kinetics of Si_3N_4 ceramics in acids. *Ceramics International, 35*, 797–802.

Herrmann, M., Schilm, J., & Michael, G. (2003). Corrosion behaviour of different technical ceramics in acids, basic solutions and under hydrothermal condition. *Ceramic Forum International, 80*(4), E27–E34.

Herrmann, M., Schilm, J., Michael, G., Meinhardt, J., & Flegler, R. (2003). Corrosion of silicon nitride materials in acidic and basic solutions and under hydrothermal conditions. *Journal of the European Ceramic Society, 23*, 585–594.

Herrmann, M., Schilm, J., Hermel, W., & Michaelis, A. (2006). Corrosion behaviour of silicon nitride ceramics in aqueous solutions. *Journal of the Ceramic Society of Japan, 114*, 1069–1075.

Herrmann, M., Seipel, B., Schilm, J., Nickel, K. G., Michael, G., & Krell, A. (2005). Hydrothermal corrosion of zirconia-toughened alumina (ZTA) at 200°C. *Journal of the European Ceramic Society, 25*, 987–1013.

Herrmann, M. F.-L., Toma, F. L., Berger, L. M., Kaiser, G., & Stahr, C. C. (2014). Comparative study of the corrosion resistance of thermally sprayed ceramic coatings and their bulk ceramic counterparts. *Journal of the European Ceramic Society, 34*, 493–504.

Heuer, A., & Lou, V. L. K. (1990). Volatility diagrams for silica, silicon nitride, and silicon carbide and their application to high-temperature decomposition and oxidation. *Journal of the American Ceramic Society, 73*, 2785–3128.

Hirata, T., Ota, S., & Morimoto, T. (2003). Influence of impurities in Al_2O_3 ceramics on hot corrosion resistance against molten salt. *Journal of the European Ceramic Society, 23*, 91–97.

Hirayama, D., Kawakubo, T., & Goto, A. (1989). Corrosion behavior of silicon carbide in 290°C water. *Journal of the American Ceramic Society, 72*, 2049–2053.

Hisamatsu, T., Etori, Y., & Yamamoto, T. (2003). Degradation of silicon carbide in combustion flow at high temperature and speed. In *ASME turbo expo 2003, Munich.* ASME-paper no. 2003-GT-38886.

Hong-fei, C., & Klemm, H. (2011). Environmental barrier coatings for silicon nitride. *Key Engineering Materials, 484*, 139–144.

Hoppert, H. (2010). Korrosionsverhalten von Aluminiumoxiden in flüssigen Phasen. Fachausschusssitzung “Werkstoffanwendung” Mannheim.

Hou, X. M., & Chou, K.-C. (2009). Quantitative interpretation of the parabolic and nonparabolic oxidation behavior of nitride ceramic. *Journal of the European Ceramic Society, 29*, 517–523.

Hu, P., Zhang, X.-H., Han, J.-C., Guang, L. C., & Du, S.-Y. (2010). Effect of various additives on the oxidation behavior of ZrB_2-based ultra-high-temperature ceramics at 1800°C. *Journal of the American Ceramic Society, 93*, 345–349.

Ihle, J., Martin, H. P., Herrmann, M., Obenaus, P., Adler, J., & Hermel, W. (2006). The influence of porosity on the electrical properties of liquid phase sintered silicon carbide. *International Journal of Materials Research (Zeitschrift für Metallkunde), 97*, 649–656.

Iio, S., .Okada, A., .Asano, T., & .Yoshimura, M. (1992). Corrosion behaviour of silicon nitride ceramics in aqueous solutions. *Journal of the Ceramic Society of Japan (International Edition), 100*, 954–956.

Iler, R. K. (1982). *Chemistry of silica* (Russian translation). Mockva: Mir, 286 ff, 320.

Jacobson, N. S. (1986). Kinetics and mechanism of corrosion of SiC by molten salts. *Journal of the American Ceramic Society, 69*, 74–82.

Jacobson, N. S. (1993). Corrosion of silicon-based ceramics in combustion environments. *Journal of the American Ceramic Society, 76*, 3–28.

Jacobson, N., & Farmer, S. (1999). High-temperature oxidation of boron nitride: I, monolithic boron nitride. *Journal of the American Ceramic Society, 82*, 393–398.

Jacobson, N., & Fox, D. S. (1988). Molten-salt corrosion of silicon nitride: II, sodium sulfate. *Journal of the American Ceramic Society, 71*, 139–148.

Jennings, M. (1983). Reaction between silicon and nitrogen. *Journal of the Materials Science, 18*, 951–967.

Johannes, M., & Schneider, J. (2012). Processing of nanostructured zirconia composite ceramic with high aging resistance. *Journal of Ceramic Science and Technology, 3*, 151–158.

Kailer, A., Amann, T., Krummhauer, O., Herrmann, M., & Sydow, U. (2011). Influence of electric potentials on the tribological behaviour of silicon carbide. *Wear, 27*, 1922–1927.

Kern, F. (2011). 2.75Yb-TZP ceramics with high strength and aging resistance. *Journal of Ceramic Science and Technology, 2*, 147–154.

Kim, H. E., & Moorhead, A. J. (1990a). Effects of active oxidation on the flexural strength of α-silicon carbide. *Journal of the American Ceramic Society, 73*, 1868–1872.

Kim, H. E., & Moorhead, A. J. (1990b). High-temperature gaseous corrosion of Si_3N_4 in H_2-H_2O and Ar-O_2 environments. *Journal of the American Ceramic Society, 73*, 3007–3014.

Kimel, R. A., & Adair, J. H. (2002). Aqueous degradation and chemical passivation of yttria-tetragonally-stabilized zirconia at 25°C. *Journal of the American Ceramic Society, 85*, 403–408.

Kitaoka, S., Toshidhide, T., Toshio, K., Yamaguchi, Y., & Kashiwagi, K. (1992). Tribological characteristics of α-alumina ceramics in high temperature water. *Journal of the American Ceramic Society, 75*, 3075–3080.

Kitaoka, S., Toshidhide, T., Toshio, K., Yamaguchi, Y., & Kashiwagi, K. (1994a). Tribological characteristics of Si_3N_4 ceramics in high temperature and high pressure water. *Journal of the American Ceramic Society, 77*, 580–588.

Kitaoka, S., Toshidhide, T., Toshio, K., Yamaguchi, Y., & Kashiwagi, K. (1994b). Tribological characteristics of SiC ceramics in high temperature and high pressure water. *Journal of the American Ceramic Society, 77*, 1851–1856.

Kleebe, H.-J., Cinibulk, M. K., Cannon, R. M., & Rühle, M. (1993). Statistical analysis of the intergranular film thickness in silicon nitride ceramics. *Journal of the American Ceramic Society, 76*, 1969–1977.

Kleebe, H.-J., & Siegel, F. (2003). Schottky barrier formation in liquid-phase sintered silicon carbide. *Zeitschrift für Metallkunde, 94*, 211–217.

Klemm, H. (2002). Corrosion of silicon nitride materials in gas turbine environment. *Journal of the European Ceramic Society, 22*, 2735–2740.

Klemm, H. (2010). Silicon nitride for high-temperature applications. *Journal of the American Ceramic Society, 93*, 1501–1522.

Klemm, H., Herrmann, M., & Schubert, C. (1998). High temperature oxidation and corrosion of silicon-based nonoxide ceramics. In *ASME turbo expo ’98, Stockholm, Sweden 1998.* ASME paper 98-GT-480.

Klemm, H., Taut, C., & Wötting, G. (2003). Long-term stability of nonoxide ceramics in an oxidative environment at 1500°C. *Journal of the European Ceramic Society, 23*, 619–627.

Krnel, K., & Kosmac, T. (2000). Reactivity of aluminum nitride powder in dilute inorganic acids. *Journal of the American Ceramic Society, 83*, 1375–1378.

Krnel, K., & Kosmac, T. (2002). Reactivity of aluminum nitride powder in aqueous silicon nitride and silicon carbide slurries. *Journal of the American Ceramic Society, 85*, 484–486.

Kumar, B. V. M., Balasubramaniam, R., & Basu, B. (2007). Electrochemical behavior of TiCN–Ni-based cermets. *Journal of the American Ceramic Society, 90*, 205–210.

Lawson, S. (1995). Environmental degradation of zirconia ceramics. *Journal of the European Ceramic Society, 15*, 485–502.

Li, J., Nakamura, M., Shirai, T., Shirai, T., Matsumaru, K., Ishizaki, C., & Ishizaki, K. (2006). Mechanism and kinetics of aluminum nitride powder degradation in moist air. *Journal of the American Ceramic Society, 89*, 937–943.

Li, J.-F., & Watanabe, R. (1998). Phase transformation in Y_2O_3-partially-stabilized ZrO_2 polycrystals of various grain sizes during low-temperature aging in water. *Journal of the American Ceramic Society, 81*, 2687–2691.

Loenhout, v. G., & Traets, J. (2009). Laser-machining silicon carbide seal faces helps them withstand electrokinetic-driven corrosion. *Sealing Technology*, 7–11.

Lughi, V., & Sergo, V. (2010). Low temperature degradation – aging – of zirconia: a critical review of the relevant aspects in dentistry. *Dental Materials, 26*, 807–820.

Mallik, A. K., Reddy, M. K., Acikbas, N. C., Kara, F., & Mandal, H. (2011). Influence of SiC addition on tribological properties of SiAlON. *Ceramics International, 37*, 2495–2504.

Marra, J. E., Kreidler, E. R., Jacobson, N. S., & Fox, D. S. (1988). Reaction of silicon-based ceramics in mixed oxidation chlorination environments. *Journal of the American Ceramic Society, 71*, 1067–1073.

Marro, F. G., Chintapalli, R., Hvizdos, P., Soldera, F., Mücklich, F., & Anglada, M. (2009). Study of near surface changes in yttria-doped tetragonal zirconia after low temperature degradation. *International Journal of Materials Research, 100*, 92.

Meschke, F., & Kailer, A. (2004). Electrically driven cold water corrosion of SiC. *Ceramic Forum International, 81*, E19–E22.

Mikeska, K. R. (1999). Corrosion of alumina in aqueous hydrofluoric acid. *Journal of the American Ceramic Society, 82*, 3561–3566.

Mikeska, K. R., Bennison, S., & Grise, S. (2000). Corrosion of ceramics in aqueous hydrofluoric acid. *Journal of the American Ceramic Society, 83*, 1160–1164.

Monteverde, F., Mingazzini, C., Giorgi, M., & Bellosi, A. (2001). Corrosion of silicon nitride in sulphuric acid aqueous solution. *Corrosion Science, 43*, 1851–1863.

More, K. L., Tortorelli, P. F., Walker, L. R., Miriyala, N., Price, J. R., & van Roode, M. (2003). High-temperature stability of SiC-based composites in high-water-vapor-pressure environments. *Journal of the American Ceramic Society, 86*, 1272–1281.

Munnoz-Saldan, J., Balmori-Ramirez, H., Jaramillo-Vigueras, D., Iga, T., & Schneider, G. A. (2003). Mechanical properties and low-temperature aging of tetragonal zirconia polycrystals processed by hot isostatic pressing. *Journal of Materials Research, 18*, 2415–2426.

Murthy, V. S. R., Kobayashi, H., Tsurekawa, S., Tamari, N., Watanabe, T., & Kato, K. (2004). Influence of humidity and doping elements on the friction and wear of SiC in unlubricated sliding. *Tribology International, 37*, 353–364.

Nagae, M., Koyama, Y., Yasutake, S., & Yoshio, T. (2006). Corrosion behavior of sialon ceramics in supercritical water. *Journal of the American Ceramic Society, 89*, 3550–3553.

Nagae, M., Yoshio, T., & Oda, K. (2006). Corrosion behavior of structural ceramics in supercritical water. *Advanced Science and Technology, 45*, 173–177.

Narushima, T., Goto, T., Yokoyama, Y., Iguchi, Y., & Hirai, T. (1994a). High-temperature active oxidation and active-to-passive transition of chemically vapor-deposited silicon nitride in N_2-O_2 and Ar-O_2 atmospheres. *Journal of the American Ceramic Society, 77*, 2369–2375.

Narushima, T., Goto, T., Yokoyama, Y., Iguchi, Y., & Hirai, T. (1994b). Active-to-passive transition and bubble formation for high-temperature oxidation of chemically vapor-deposited silicon carbide in CO-CO, atmosphere. *Journal of the American Ceramic Society, 77*, 1078–1082.

Narushima, T., Goto, T., Yokoyama, Y., Iguchi, Y., & Hirai, T. (1993). High-temperature active oxidation of chemically vapor-deposited silicon carbide in CO-CO_2 atmosphere. *Journal of the American Ceramic Society, 76*, 2521–2524.

Nickel, K. G., & Gogotsi, Y. G. (2000). Corrosion of hard materials. In *Handbook of ceramic hard materials* (pp. 140–182). Wiley-VCH.

Nickel, K. G., Quirmbach, P., & Pötschke, J. (2010). High temperature corrosion of ceramics and refractory materials. In *Shreir's corrosion* (Vol. 1; pp. 668–690).

Nielsen, K. A. (1992). Corrosion of different ceramic materials in H_2SO_4, H_3PO_4, H_2O and NAOH at 90 °C. *Euro Ceramics II, 2*, 1309–1313.

Oda, K., & Yoshio, T. (1997). Hydrothermal corrosion of alumina ceramics. *Journal of the American Ceramic Society, 80*, 3233–3236.

Oda, K., Yoshio, T., Miyamoto, Y., & Koizumi, M. (1993). Hydrothermal corrosion of pure, hot isostatically pressed silicon nitride. *Journal of the American Ceramic Society, 76*, 1365–1368.

Okada, A., & Yoshimura, M. (1996). Mechanical degradation of silicon nitride ceramics in corrosive solutions of boiling sulphuric acid. *Key Engineering Materials, 113*, 227–236.

Opila, E. J. (2003). Oxidation and volatilization of silica formers in water vapor. *Journal of the American Ceramic Society, 86*, 1238–1248.

Opila, E. J., & Myers, D. L. (2004). Alumina volatility in water vapour at elevated temperatures. *Journal of the American Ceramic Society, 87*, 1701–1705.

Opila, E., & Serra, J. L. (2011). Oxidation of carbon fiber-reinforced silicon carbide matrix composites at reduced oxygen partial pressures. *Journal of the American Ceramic Society, 94*, 2185–2192.

Opila, E. J., Smialek, J. L., Robinson, R. C., Fox, D., & Jacobson, N. S. (1999). SiC recession caused by SiO_2 scale volatility under combustion conditions: II, thermodynamics and gaseous-diffusion model. *Journal of the American Ceramic Society, 82*, 1826–1834.

Osada, T., Nakao, W., Takahashi, K., & Ando, K. (2009). Kinetics of self-crack-healing of alumina/silicon carbide composite including oxygen partial pressure effect. *Journal of the American Ceramic Society, 92*, 864–869.

Parthasarathy, T. A., Rapp, R. A., Opeka, M., & Kerans, R. J. (2009). Effects of phase change and oxygen permeability in oxide scales on oxidation kinetics of ZrB_2 and HfB_2. *Journal of the American Ceramic Society, 92*, 1079–1086.

Persson, J., & Nygren, M. (1994). The oxidation kinetics of β-sialon ceramics. *Journal of the European Ceramic Society, 13*, 467–484.

Petzow, G., & Herrmann, M. (2002). Silicon nitride ceramics. In M. Jansen (Ed.), *Structure and bonding* (Vol. 102; pp. 43–163). Berlin Heidelberg: Springer-Verlag.

Presser, V., Berthold, C., Wirth, R., & Nickel, K. G. (2008). Structural characterisation of tribologically influenced silicon carbide ceramic surfaces. *Current Opinion in Solid State and Materials Science, 12*, 73–80.

Presser, V., Heon, M., & Gogotsi, Y. (2011). Carbide-derived carbons – from porous networks to nanotubes and graphene. *Advanced Functional Materials, 21*, 810–833.

Presser, V., Loges, A., Hemberger, Y., & Nickel, K. H. (2009). Microstructural evolution of silica on single-crystal silicon carbide. Part I: denitrification and oxidation rates. *Journal of the American Ceramic Society, 92*, 724–731.

Presser, V., Loges, A., Wirth, R., & Nickel, K. H. (2009). Microstructural evolution of silica on single crystal silicon carbide. Part II: influence of impurities and defects. *Journal of the American Ceramic Society, 92*, 1796–1805.

Presser, V., & Nickel, G. (2008). Silica on silicon carbide. *Critical Reviews in Solid State and Materials Sciences, 33*, 1–99.

Presser, V., Nickel, K. G., Krummhauer, O., & Kailer, A. (2009). A model for wet silicon carbide tribo-corrosion. *Wear, 267*, 168–176.

Ramalingam, S., Reimanis, I. E., Fuller, E. R., & Haftel, D. (2010). Slow crack growth behavior of zirconia-toughened alumina and alumina using the dynamic fatigue indentation technique. *Journal of the American Ceramic Society*, 1–8.

Ramberg, C. E., & Worrell, W. L. (2001). Oxygen transport in silica at high temperatures: implications of oxidation kinetics. *Journal of the American Ceramic Society, 84*, 2607–2616.

Readey, D. W. (1998). Corrosion of ceramics in halogen-containing atmospheres. *Journal of the American Ceramic Society, 18*, 2383–2387.

Rendtel, A. (2010). Korrosionsbeständigkeit von Nichtoxidkeramiken in wässrigen Medien. In *Fachausschusssitzung "Werkstoffanwendung" Mannheim*.

Risbud, S. H. (1981). Analysis of bulk amorphous oxynitride structures using the network theory of glasses. *Physics and Chemistry of Glasses, 22*, 168–170.

Roode, M. (2010). Ceramic gas turbine development need for a 10 year plan. *Journal of Engineering for Gas Turbines and Power, 132*, 1–8.

Salmang, H., & Scholze, H. (2007). *Keramik* (7. Voll. Neubearbeitete Auflage). Springer.

Sato, T., Sato, S., Okuwaki, A., & Tanaka, S.-i (1991). Corrosion behavior of alumina ceramics in caustic alkaline solutions at high temperatures. *Journal of the American Ceramic Society, 74*, 3081–3084.

Sato, T., Sato, S., Tamura, K., & Okuwaki, A. (1992). Corrosion behaviour of silicon nitride ceramics in caustic alkaline solutions at high temperatures. *British Ceramic Transactions and Journal, 91*, 117–120.

Sato, T., Tokunaga, Y., Endo, T., Shimada, M., Komeya, K., Komatsu, M., et al. (1988a). Corrosion of silicon nitride ceramics in aqueous hydrogen chloride solutions. *Journal of the American Ceramic Society, 71*, 1074–1079.

Sato, T., Tokunaga, Y., Endo, T., et al. (1988b). Ceramics in aqueous chloride solutions. *Journal of the American Ceramic Society, 71*, 1074–1079.

Sauti, G., Can, A., McLachlan, D. S., & Herrmann, M. (2007). The AC conductivity of liquid-phase-sintered silicon carbide. *Journal of the American Ceramic Society, 90*, 2446–2453.

Schacht, M., Boukis, N., Dinjus, E., Ebert, K., Janssen, R., Meschke, F., et al. (1998). Corrosion of zirconia ceramics in acidic solutions at high pressures and temperatures. *Journal of the European Ceramic Society, 18*, 2373–2376.

Schilm, J. (2004). *Korrosionsverhalten von Siliciumnitridkeramiken in Säuren, Promotion IKTS/TU BAF*.

Schilm, J., Gruner, W., Herrmann, M., & Michael, G. (2006). Corrosion of Si_3N_4-ceramics in aqueous solutions, part I: characterisation of starting materials and corrosion in 1N H_2SO_4. *Journal of the European Ceramic Society, 26*, 3909–3917.

Schilm, J., Herrmann, M., & Michael, G. (2003). Kinetic study of the corrosion of silicon nitride materials in acids. *Journal of the European Ceramic Society, 23*, 577–584.

Schilm, J., Herrmann, M., & Michael, G. (2004a). Leaching behaviour of silicon nitride materials in sulphuric acid containing KF. *Journal of the European Ceramic Society, 24*, 213–221.

Schilm, J., Herrmann, M., & Michael, G. (2004b). Corrosion of YSiAlON-glasses in acidic and caustic media. *Silicates Industriels, 69*, 317–324. Special issue.

Schilm, J., Herrmann, M., & Michael, G. (2007). Corrosion of Si_3N_4-ceramics in aqueous solutions: part 2. Corrosion mechanisms in acids as a function of concentration, temperature and composition. *Journal of the European Ceramic Society, 27*, 3573–3588.

Schmalzried, K. H., & Schwetz. (2010). Silicon carbide and boron carbide based hard materials. In R. Riedel, & C. Chen (Eds.), *Ceramic science and technology* (pp. 131–225). Wiley VCH.

Schneider, B., Guette, A., Naslain, R., Cataldi, M., & Costecalde, A. (1998). A theoretical and experimental approach to the active-to-passive transition in the oxidation of silicon carbide experiments at high temperatures and low total pressures. *Journal of Materials Science, 33*, 535–547.

Schneider, J., Begand, S., Kriegel, R., Kaps, C., Glien, W., & Oberbach, T. (2008). Low-temperature aging behavior of alumina-toughened zirconia. *Journal of the American Ceramic Society, 91*, 3613–3618.

Scholze, H. (1991). *Glass – nature, structure and properties*. New York, Berlin: Springer verlag.

Schwetz, K. A., & Hassler, J. (2002a). Zur Beständigkeit von Hochleistungskeramiken gegen Flüssigkorrosion. *Ceramic Forum International (Berichte der Deutschen Keramischen Gesellschaft), 79*(10), D15–D18.

Schwetz, K. A., & Hassler, J. (2002b). Zur Beständigkeit von Hochleistungskeramiken gegen Flüssigkorrosion. *Ceramic Forum International (Berichte der Deutschen Keramischen Gesellschaft), 79*(11), D14–D19.

Sciti, D., Brach, M., & Bellosi, A. (2005). Long-term oxidation behavior and mechanical strength degradation of a pressureless sintered ZrB_2–$MoSi_2$ ceramic. *Scripta Materialia, 53*, 1297–1302.

Seipel, B., & Nickel, K. G. (2003). Corrosion of silicon nitride in aqueous acidic solutions: penetration monitoring. *Journal of the European Ceramic Society, 23*, 594–602.

Sharkawy, S. W., & El-Aslabi, A. M. (1998). Corrosion of silicon nitride ceramics in aqueous HCl and HF solutions at 27-80°C. *Corrosion Science, 40*, 1119–1129.

Shimada, M., & Sato, T. (1989). Corrosion of silicon nitride ceramics in HF and HCl solutions. *Ceramic Transactions Symposium, 10*, 355–364.

Siegelin, F., Kleebe, H.-J., & Sigl, S. (2003). Interface characteristics affecting electrical properties of Y-doped SiC. *Journal of Materials Research, 18*, 2608–2617.

Somiya, S. (2001). Hydrothermal corrosion of nitride and carbide of silicon. *Materials Chemistry and Physics, 67*, 157–163.

Stahr, C. C., Berger, L.-M., Herrmann, M., & Deska, D. (2008). Corrosion of alumina-based coatings. In *International thermal spray conference & exhibition ITSC 2008, conference proceedings* (pp. 374–377). DVS-Verlag GmbH.

Svedberg, L. M., Arndt, K. C., & Cima, M. J. (2000). Corrosion of aluminum nitride (AlN) in aqueous cleaning solutions. *Journal of the American Ceramic Society, 83*, 41–46.

Sydow, U., Schneider, M., Herrmann, M., Kleebe, H.-J., & Michaelis, A. (2010). Electrochemical corrosion of silicon carbide ceramics part 1: electrochemical investigation of sintered silicon carbide (SSiC). *Materials and Corrosion, 61*, 657–664.

Sydow, U., Herrmann, M., Schneider, M., Kleebe, H.-J., & Michaelis, A. (2011). Electrochemical corrosion of SSiC and LPS-SiC ceramic materials. In *EUROCORR, Stockholm*.

Sydow, U., Sempf, K., Herrmann, M., Schneider, M., & Michaelis, A. (2011). Electrochemical corrosion of liquid-phase sintered silicon carbide. *Materials and Corrosion, 62*, 9999.

Tamai, H., Hamauzu, T., Ryumon, A., Aoki, K., Oda, K., & Yoshio, T. (2000). Hydrothermal corrosion and strength degradation of aluminum nitride ceramics. *Journal of the American Ceramic Society, 83*, 3216–3218.

Tan, H. C., Gill, C., & Lawson, S. (1996). The effect of sintering additives on the hydrothermal and corrosive degradation of Y TZP. *Key Engineering Materials*, 199–206.

Tan, L., Allen, T. R., & Barringer, E. (2009). Effect of microstructure on the corrosion of CVD-SiC exposed to supercritical water. *Journal of Nuclear Materials, 394*, 95–101.

Toma, F. L., Stahr, C. C., Berger, L. M., Saaro, S., Herrmann, M., Deska, D., et al. (2010). Michael; corrosion resistance of APS- and HVOF-sprayed coatings in the Al_2O_3-TiO_2 system. *Journal of Thermal Spray Technology, 19*, 137–147.

Van der Biest, O. O., Barnes, J., Corish, J., & Norton, J. F. (1987). Corrosion of a silica-bearing ceramic in sulfur-oxygen atmospheres. *Journal of the American Ceramic Society, 70*, 456–459.

Vaughn, W. L., & Maahs, H. G. (1990). Active-to-passive transition in the oxidation of silicon carbide and silicon nitride in air. *Journal of the American Ceramic Society, 72*, 1540–1543.

Wang, J., Zhang, L., Zeng, Q., Vignoles, G. L., & Guette, A. (2008). Theoretical investigation for the active-to-passive transition in the oxidation of silicon carbide. *Journal of the American Ceramic Society, 91*, 1665–1673.

Yashima, M., Nagatome, T., Noma, T., Ishizawa, N., Suzuki, Y., & Yoshimura, M. (1995). Effect of dopant species on tetragonal (f)-to-monoclinic phase transformation of arc-melted ZrO_2-$RO_{1,5}$ (R = Sm, Y, Er, and Sc) in water at 200°C and 100 MPa pressure. *Journal of the American Ceramic Society, 78*, 2229–2232.

Yasuda, K., Goto, Y., & Takeda, H. (2001). Influence of tetragonality on tetragonal-to-monoclinic phase transformation during hydrothermal aging in plasma-sprayed yttria-stabilized zirconia coatings. *Journal of the American Ceramic Society, 84*, 1037–1042.

Yoshimura, M., Hiuga, T., & Somiya, S. (1986). Dissolution and reaction of yttria-stabilized zirconia single crystals in hydrothermal solutions. *Journal of the American Ceramic Society, 69*, 583–584.

SECTION IV

COATINGS AND APPLICATIONS

This page intentionally left blank

2.16 PVD and CVD Hard Coatings

Christian Mitterer, Department of Physical Metallurgy and Materials Testing, Montanuniversität Leoben, Leoben, Austria

© 2014 Elsevier Ltd. All rights reserved.

Glossary

a-C	Amorphous carbon
a-C:H	Amorphous hydrogenated carbon
CVD	Chemical vapor deposition
d.c.	Direct current
DLC	Diamond-like carbon
DSC	Differential scanning calorimetry
fcc	Face-centered cubic
HiPIMS	High-power impulse magnetron sputtering
HPPMS	High-power pulse magnetron sputtering
PACVD	Plasma-assisted chemical vapor deposition
PLD	Pulsed laser deposition
PVD	Physical vapor deposition
r.f.	Radiofrequency
SZD	Structure zone diagram
ta-C	Tetrahedral carbon
ta-C:H	Tetrahedral hydrogenated carbon

2.16.1 Introduction

Hard coatings with a thickness of a few microns are widely applied to improve the performance of tools, for example, for cutting, forming and casting applications, and components, for example, in automotive and aerospace applications (Mayrhofer, Mitterer, Hultman, & Clemens, 2006). Originally starting with thermally activated chemical vapor deposition (CVD), different methods have been developed including plasma-assisted physical vapor deposition (PVD), plasma-assisted chemical vapor deposition (PACVD), and laser-assisted methods such as pulsed laser deposition. The coatings synthesized with these methods offer high hardness, oxidation and wear resistance, thermal stability, diffusion barrier properties, and in some cases also low friction and even smart, self-adaptive properties. The present chapter reviews deposition techniques to grow these hard coatings and selected relations between synthesis conditions, the resulting coating structure and properties for some of the most important representatives of hard coating materials.

2.16.2 Coating Deposition Techniques

Most of the industrially applied hard coatings are deposited either by CVD or PVD methods; thus, only these techniques and the main thin film growth mechanisms will be shortly described in this section.

http://dx.doi.org/10.1016/B978-0-08-096527-7.00035-0

2.16.2.1 Chemical Vapor Deposition

The term CVD summarizes all techniques utilizing gaseous precursor materials, which are introduced into a reaction chamber, to synthesize a coating (Pierson, 1999). The necessary surface reaction usually is most often thermally activated, for example, by high temperatures or by laser assistance; however, kinetic activation by plasma in PACVD is used as well. The feed of less stable precursor compounds (e.g., metal-organic CVD) induces chemical reactions that are activated at lower temperatures, but the widely used halide precursor gases (e.g., $TiCl_4$, BCl_3, $AlCl_3$) are more stable and the deposition temperature often is in the range of 950–1150 °C (thermally activated CVD). Further, deposition processes are distinguished, whether the reactor wall, the substrate, and the gas mixture are heated (hot-wall CVD, the reactor wall is also coated) or if only the substrate is heated (cold-wall CVD) (Fredriksson & Carlsson, 1993a). Apart from the deposition temperature, the deposition pressure (ranging between atmospheric pressure and a few 10 mbar) plays a major role, as internal gas stream velocities (i.e., residence times) and boundary-layer thickness (i.e., reactant diffusion to the substrate surface) are depending on pressure. Hence, pressure influences the homogeneity of the deposition process within the reactor, and also the supersaturation of the precursor gases is an important deposition parameter. **Figure 1** illustrates the basic steps involved in a CVD process (Spear, 1982). Concerning the surface reaction rate limits, mass transport controlled and surface kinetics controlled regimes are distinguished. The former describes the case where the diffusion from the laminar gas stream to the surface (via the gaseous boundary layer) occurs slower than the reaction of adsorbed species, and vice versa is valid for the latter. Higher temperatures and lower pressures suppress the mass transport controlled regime, due to increased diffusion and decreased boundary-layer thickness, respectively. Usually, the surface kinetics controlled regime offers a more uniform deposition within the reactor, whereas fewer deposition processes might be operated in the mass transport controlled regime—aiming for maximized deposition rates. Eventually, deposition rates drop at still higher temperatures due to homogeneous deposition, that is, formation of solids within the gas stream and not at the substrate surface (Choy, 2003; Pierson, 1999).

Thermal hot-wall CVD utilizing halide precursors was the first method for the deposition of TiN, TiC, TiC_xN_{1-x}, and Al_2O_3 coatings in the 1970s (Kornmann, Schachner, Funk, & Lux, 1975; Schintlmeister & Pacher, 1975). A common precursor gas composition contains species such as $TiCl_4$, N_2, CH_4, and H_2 for TiC_xN_{1-x}, or $AlCl_3$, CO_2, and H_2 for Al_2O_3, respectively. The conventional TiC_xN_{1-x} process, needing deposition temperatures of approximately 1000 °C, has been almost completely substituted by the medium-temperature TiC_xN_{1-x} process, utilizing acetonitrile (CH_3CN) as an organic C/N source and deposition temperatures of 750–800 °C (Prengel, Pfouts, & Santhanam, 1998). This is on the one hand related to the hindered coarsening of the coating. On the other hand, the formation of the undesired η-phase, that is, a brittle double carbide phase of type Co_6W_6C at the interface between the carbide and the cobalt phase, facilitating adhesion failure of the coating, is hindered at lower deposition temperatures.

Typical advantages of CVD are the high throwing power, the possibility of large batch sizes (e.g., several thousands of cutting tool inserts) and high achievable coating thicknesses (up to 25 μm). The expression "throwing power" describes the ability of a coating technology to deposit at substrate regions that are not directly in the line of sight of the deposit's origin. That is, a high throwing power allows a more uniform film

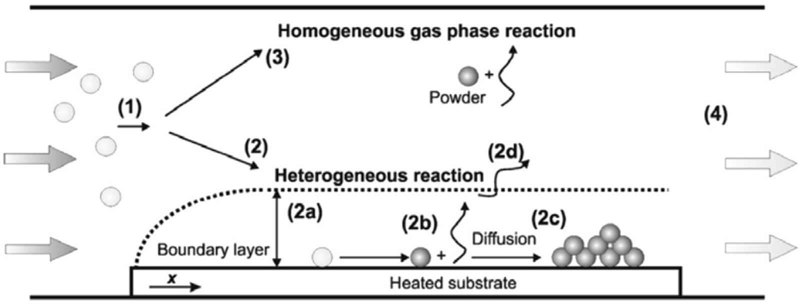

Figure 1 Schematic illustration of the basic process steps involved in CVD: gas feed (1), heterogeneous reaction (2), homogeneous reaction (3), and gas exhaust (4). The heterogeneous reaction comprises transport of the reactants through the boundary layer and adsorption (2a), chemical reactions at the substrate surface (2b), nucleation and growth (2c), and desorption of by-products (2d). Redrawn after Spear (1982) and Choy (2003).

deposition at substrates with a complex three-dimensional shape. Disadvantages are the usually tensile coating stresses (limiting the coating performance in interrupted cutting) and the sometimes high coating roughness; both demanding posttreatment processes such as sand blasting (Klaus, Genzel, & Holzschuh, 2008).

2.16.2.2 Physical Vapor Deposition

In contrast to CVD, PVD methods utilize solid precursors (i.e., the so-called targets) and—in addition to thermal activation—also kinetic activation of film growth. Thus, coatings synthesized with these methods are usually far away from thermodynamic equilibrium and characterized by high defect densities and compressive stresses, small grain sizes, and/or metastable phases. In the last four decades, a huge variety of different deposition techniques has been developed, with the goal to increase process efficiency and to stimulate film growth. In the following sections, the two general techniques evaporation and sputtering will be shortly described. For the synthesis of hard coatings, most often reactive processes are used, where a reactive gas, for example, N_2, C_2H_2, or O_2, is additionally introduced into the vacuum chamber, creating the respective nitride, carbide or oxide coating. All these techniques are carried out in vacuum and are line-of-sight processes, which means that only those areas of the substrate that are directly exposed to the target are coated. Thus, multifold targets and sophisticated substrate rotation are required to obtain a homogeneous coating distribution on three-dimensional parts. To promote the activation of film growth, usually negative substrate bias voltages are applied, accelerating positive ions to the coating surface and promoting film growth by atomic scale heating (Petrov, Barna, Hultman, & Greene, 2003).

2.16.2.2.1 Evaporation

In evaporation, the solid target is transferred to the vapor state by applying heat, for example, by resistance or inductive heating, by electron or laser beam heating, or by the formation of an arc. While the first techniques are widely applied for growing coatings for optical applications or as permeation, diffusion or thermal barrier films, the deposition of hard coatings is dominated by cathodic arc evaporation. There, the vapor phase is created in a vacuum chamber by an arc discharge between two electrodes, where the target forms the cathode. The arc discharge occurs at low voltages ranging from 20 to 100 V and high currents between 30 A and several kiloamperes. Under these conditions, a few micrometer-sized nonstationary spot of high current density (in the order of 10^{12} Am^{-2}) is formed on the cathode surface. These so-called cathode spots move randomly over the cathode surface (Figure 2) and create a high flux of ionized target material and electrons, leading to the formation of a self-sustained plasma with ionization rates of up to 100% (Anders, 2008). Spot ignition most

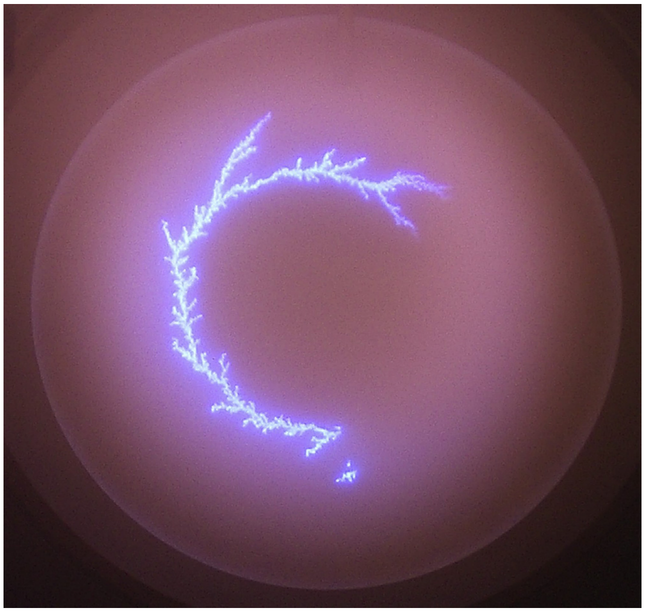

Figure 2 Cathode spot on an AlCr target moving along the race track as forced by the magnetic field configuration used.

likely occurs at surface asperities of the target, where the electrical field is concentrated. The extreme heating due to the localized field results in the explosion-like evaporation of target material and its ionization. Ignition and explosion usually take place within 1–10 ns, with a lifetime of the cathode spot in the order of a 100 ns. The ions present in the formed plasma can reach charge states of three or four or even above and may reach a kinetic energy of about 20 eV for light and 200 eV for heavy elements. The high ion energy, charge state, and ionization of the vapor generated by cathodic arc discharges are the basis for its excellent control of coating growth at relatively low substrate temperatures (typically between 200 and 600 °C). A major disadvantage is, however, the emission of macrodroplets from the cathode spot, which are incorporated as defects into the growing film. While magnetic filtering may be applied to separate the flux of ions from the droplets (Sanders & Anders, 2000), the majority of hard coatings is deposited without filtering, making polishing necessary for applications where low surface roughness is needed, for example, in automotive applications (Tomanik, 2008).

2.16.2.2.2 Sputtering

Sputtering is a process that involves the physical evaporation of atoms from the target surface by momentum transfer from bombarding highly energetic ions. These ions, typically originating from a heavy inert gas, impinge on the target surface, ejecting material primarily in atomic form (Mattox, 2010). To provide this ion bombardment, the vacuum chamber is backfilled with an inert gas such as Ar, to a pressure in the 10^{-3}–10^{-2} mbar range, and an electric discharge is ignited between the target forming the cathode and the substrates forming the anode. The energy of the positive Ar ions bombarding the target is in the range from 100 to 1000 eV, creating a collision cascade in the target material and ejecting atoms with energies varying from 10 to 40 eV. To overcome the limitation of low deposition rates, permanent magnetic fields are applied in magnetron sputtering (**Figure 3**), allowing the concentration and densification of the plasma in the space immediately above the target. As a result of trapping the electrons near the target surface, the ion bombardment and, hence, the sputtering rates, are significantly enhanced. In addition, unacceptable substrate heating due to electron bombardment can be avoided. Depending on the magnetic field lines looping between the central and the outer magnets, magnetrons can be balanced or unbalanced. In a conventional balanced magnetron, all field lines loop between these two magnets. If the magnetic field lines are partially open toward the substrates, as in **Figure 3**, the plasma is allowed to expand away from the target area. This configuration is known as unbalanced magnetron (Window, 1996) and enables intense low energy ion irradiation of the growing film, thus promoting film growth (Section 2.16.2.3).

Sputtering can be done in d.c., pulsed d.c. and radiofrequency (r.f.) modes (Arnell & Kelly, 1999). D.c. offers the possibility of cheap power supplies and easy process control; however, its major disadvantage is related to reactive sputtering, in particular to the so-called poisoning of the target surface. This means that the sputter yield is typically much lower for the compound film formed on the target surface (e.g., a nitride when sputtering in Ar + N_2 atmosphere) compared to that on the metal, resulting in dramatically reduced deposition rates (Heller, 1973). This situation is even worse when less-conducting or even nonconducting films, for

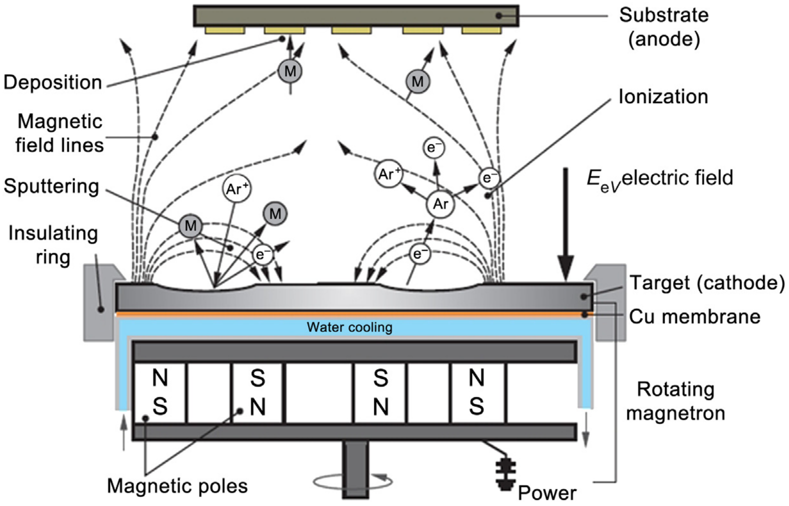

Figure 3 Schematic of a direct current unbalanced magnetron sputtering system.

example, oxides, are formed, which leads to charging and arcing phenomena (Arnell & Kelly, 1999). While target poisoning can be overcome by efficient control of sputter power and partial pressure of the reactive gas, charging and arcing can only be mastered by discharges operating in the kilohertz (i.e., pulsed d.c. sputtering) or megahertz frequency range (i.e., r.f. sputtering).

The advantage of sputtering is the avoidance of droplet formation, which results in smooth films. However, its major disadvantage is the low ionization rate, where typically only a fraction of approximately 1% of the species sputtered from the target is ionized (Mattox, 2010). Application of pulses in the megawatt and microsecond range (i.e., high-power impulse magnetron sputtering or high-power pulse magnetron sputtering) is an emerging sputter technique enabling significantly higher ionization rates, with values up to 30% and higher charge states of the target ions (Kouznetsov, Macák, Schneider, Helmersson, & Petrov, 1999).

2.16.2.3 Thin Film Growth

During exposure of the substrate surface to the vapor phase, impinging species are either reflected immediately, reevaporate after some residence time, or condense on the surface. Energetic species condense on the surface at extremely high cooling rates of up to 10^{13} K s^{-1} (Barbee, Holmes, Keith, Pyzyna, & Ilonca, 1977) by losing their energy, finding preferential nucleation sites, like lattice defects, atomic steps, point defects, or grain boundaries and bonding to other atoms. At high impingement rates, metastable and stable clusters are formed and can continue to grow by binding of diffusing adatoms or by direct capture of atoms from the vapor phase. Subsequent film formation may occur according to three basic growth modes: island or Volmer–Weber growth, which occurs when the smallest stable clusters nucleate on the substrate and grow in three dimensions to form islands; layer by layer or Frank–Van der Merve growth takes place when the binding energy between film atoms is equal to or less than that between the film atoms and the substrate; and Stransky–Krastanov growth, a combination of the two, where first one or more monolayers are formed and then, when it becomes energetically favorable, three-dimensional islands are formed (Ohring, 2002). Growth of hard coatings usually follows the island growth mode, where coalescence occurs when neighboring islands get in contact (Barna & Adamik, 1998).

Film growth depends on both nucleation and growth kinetics, determining the coating structure. To link the observed structure to growth parameters, structure zone diagrams (SZDs) have been developed. The first SZD was introduced by Movchan and Demchishin for thick films grown by thermal evaporation and sputtering (Movchan & Demchishin, 1969), where they relate the observed structures to the homologous temperature (i.e., the substrate temperature divided by the melting temperature of the coating material). According to thermal activation, they distinguished between three different zones, where zone 1 is determined by small or even zero surface mobility of condensing atoms, resulting in porous columnar structures. Zone 2 is governed by surface diffusion processes, where shadowing effects are overcome and dense films are formed. Zone 3 is assumed to be determined by bulk diffusion, showing a recrystallized structure. This SZD was expanded later by taking into account deposition parameters typical for PVD processes, that is, total pressure or ion energy. There, also a so-called transition zone T was introduced, which is formed between zones 1 and 2, characterized by a dense fibrous structure (Thornton, 1977). Very recently, Anders proposed a new SZD (Anders, 2010), still considering the originally proposed three structure zones and the transition zone (**Figure 4**). There, film growth is classified according to the thermal activation T^*, considering the homologous temperature and a thermal shift caused by the potential energy of particles arriving at the film surface, and the kinetic activation E^*, describing displacement and heating effects caused by the kinetic energy of bombarding particles (i.e., atomic scale heating (Petrov et al., 2003)). A third axis considers the net film thickness t^*, which provides to maintain the qualitative illustration of film structure while indicating thickness reduction by densification and sputtering. The diagram also includes a "negative thickness" due to the effect of ion etching at excessive ion energies and intensities.

2.16.3 Nitrides and Carbonitrides

Coatings based on transition metal nitrides like the golden–yellow face-centered cubic (fcc) TiN, deposited by CVD in the 1970s (Schintlmeister & Pacher, 1975) and later in the 1980s by PVD (Mayrhofer et al., 2006), have been the first to be commercially applied for the reduction of tool wear. There, the application

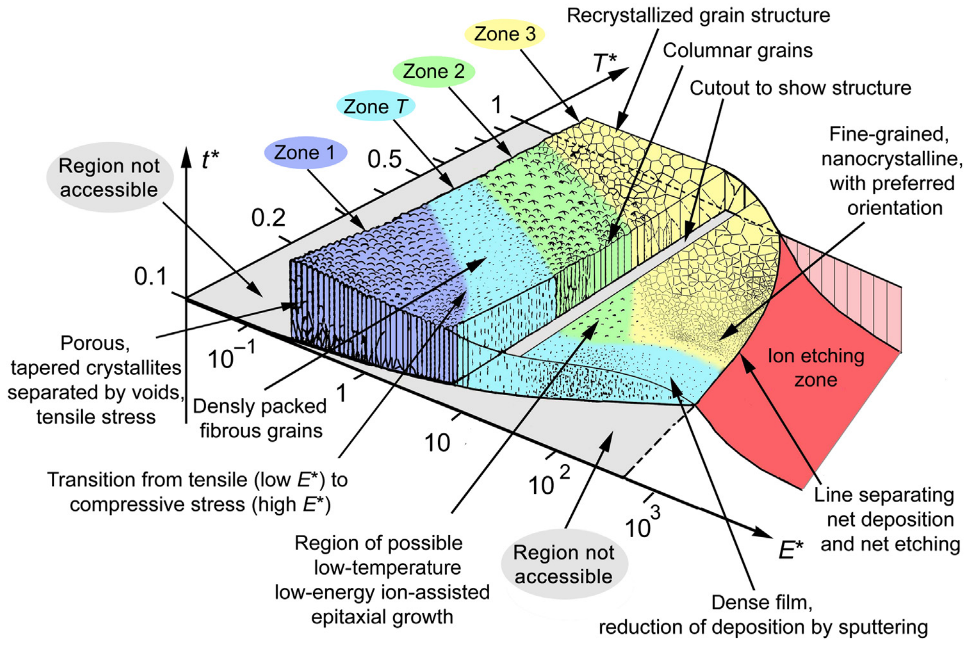

Figure 4 Structure zone model after Anders for thin film growth (Anders, 2010).

temperatures may be extremely different ranging from low temperatures for cold forming dies to above 1000 °C for cemented carbide dry-cutting tools. These extremely different loading conditions, the necessity of increased performance and the demand to master difficult-to-machine materials, have driven the specific development of wear-resistant coatings within the last three decades to meet the individual requirements of the given application. To enhance the abrasion and erosion resistance of TiN (which is still often the standard coating used for a huge variety of applications), carbon is added at the expense of nitrogen, which results in the formation of a stable solid solution TiC_xN_{1-x} (Bergmann, Kaufmann, Schmid, & Vogel, 1990). In particular, TiC_xN_{1-x} is also of interest because of its excellent friction properties, where the friction coefficient of TiN in the order of 0.6–0.8 (Fateh, Fontalvo, Gassner, & Mitterer, 2007; Franklin & Beuger, 1992) against alumina is reduced to approximately 0.2 due to the formation of the TiC_xN_{1-x} solid solution (Rebelo de Figueiredo et al., 2008). This has recently been related to the in situ formation of self-lubricious reaction layers after a short running-in period in dry sliding contacts (**Figure 5**), where the carbon released from the coating forms in humid environments an easy shearable, a few nanometer thick reaction layer characterized by weak C–H bonds (Rebelo de Figueiredo et al., 2010). TiC_xN_{1-x} is thus an early example for a smart, self-adaptive coating with multifunctional properties, combining wear resistance and low friction. For applications where the tool is applied under tribological and corrosive loads, the fcc CrN, which shows an increased corrosion resistance (Navinšek, Panjan, & Milošev, 1997) and quite low friction coefficients of about 0.4 (Cheng, Browne, & Heckerman, 2011), is the standard choice.

While transition metal nitrides like TiN and CrN have dominated in the 1980s and 1990s, metastable solid solutions such as $Al_xTi_{1-x}N$ and $Al_xCr_{1-x}N$ have continuously replaced the simple nitrides in the last decade for severe cutting applications. $Al_xTi_{1-x}N$ had been introduced in 1986 (Münz, 1986), where Al replaces the Ti atoms in TiN forming a metastable fcc $Al_xTi_{1-x}N$ solid solution. The outstanding properties of $Al_xTi_{1-x}N$ coatings have been related to its superior oxidation resistance, where the onset of oxidation could be shifted from approximately 550 °C for TiN or approximately 500 for TiC_xN_{1-x} to approximately 700 °C for $Al_xTi_{1-x}N$ (Münz, 1986). This is attributed to the formation of a dual-layer protective oxide scale, with a dense α-Al_2O_3-rich top layer and a rutile-type TiO_2-rich layer underneath (McIntyre, Greene, Håkansson, Sundgren, & Münz, 1990). Coating failure is then related to breakaway oxidation, where the spallation of the porous rutile layer occurs. Similar considerations have lead to the introduction of $Al_xCr_{1-x}N$ (Reiter, Derflinger, Hanselmann, Bachmann, & Sartory, 2005), where stable and protective α-Al_2O_3-rich and Cr_2O_3-rich layers are formed in oxidative environments (Reiter, Mitterer, & Sartory, 2007). Due to the formation of these dense layers, the oxidation onset could be raised to temperatures >1000 °C. For achieving these improvements in

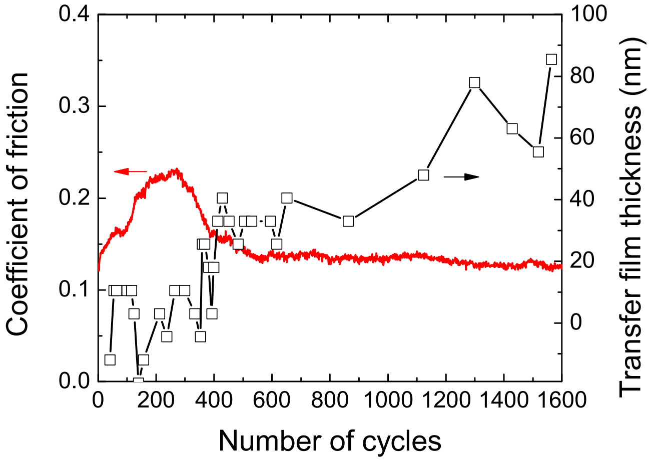

Figure 5 Coefficient of friction and transfer film thickness formed on a TiC_xN_{1-x} coating plotted versus the number of cycles for a reciprocating sliding test against an Al_2O_3 counterbody performed in an atmosphere with 35–45% relative humidity (Rebelo de Figueiredo et al., 2010).

oxidation resistance, it is of vital importance to choose Al contents as close as possible to the solubility limit of the respective transition metal nitride in fcc AlN (Makino, 2005), for example, $x = 0.67$ for $Al_xTi_{1-x}N$ and $x = 0.7$ for $Al_xCr_{1-x}N$. Traditionally, this necessitates the application of PVD methods with high ionization rates and high kinetic energies of film-forming species like unbalanced magnetron sputtering and cathodic arc evaporation (PalDey & Deevi, 2003).

More recently, it has been reported that the metastable solid solutions $Al_xTi_{1-x}N$ and $Al_xCr_{1-x}N$ undergo spinodal decomposition and age hardening at elevated temperatures. For example, the $Al_xTi_{1-x}N$ phase decomposes in the temperature range between 700 and 900 °C in fcc TiN and fcc AlN domains (Mayrhofer et al., 2003), giving rise to a hardness increase due to coherency strains (**Figure 6**). For higher annealing temperatures, overaging with a coarsening of these domains and transformation of the fcc AlN into the stable hexagonal wurtzite-type AlN phase, as evidenced by differential scanning calorimetry (DSC, **Figure 6**), results in a loss of hardness. Direct evidence for the decomposition has recently been provided by three-dimensional atom probe tomography, making the resulting compositional modulations in the fully decomposed structure visible (**Figure 7**) (Rachbauer, Stergar, Massl, Moser, & Mayrhofer, 2009). $Al_xCr_{1-x}N$ shows a slightly different decomposition route, where first wurtzite AlN is formed, whereas the CrN-enriched matrix decomposes in a two-step reaction into Cr_2N and finally Cr under the release of N_2 (Willmann et al., 2006). Also the formation of the incoherent AlN domains is connected to a slight hardness

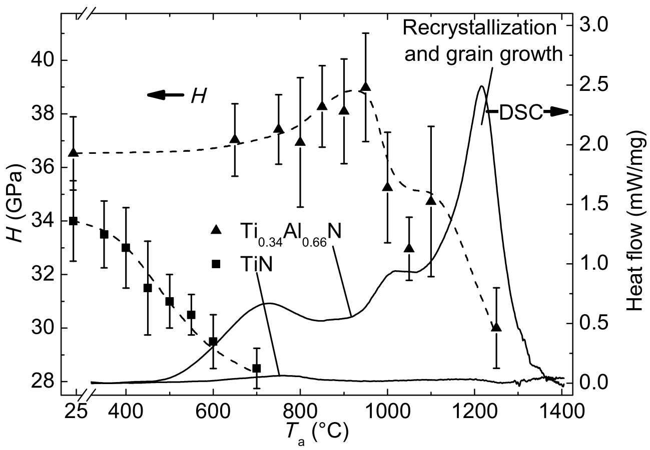

Figure 6 Hardness H as a function of annealing temperature T_a (isothermal annealing was conducted in nitrogen for 120 min) and dynamical DSC measurements (heating rate: 50 K min^{-1}) of $Al_{0.66}Ti_{0.34}N$ and TiN films. Redrawn after Mayrhofer et al. (2003).

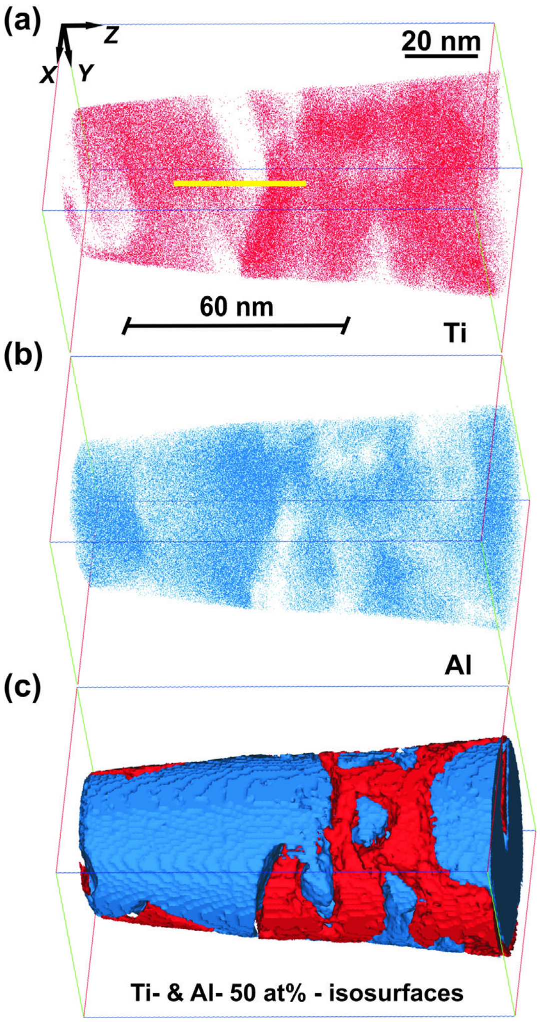

Figure 7 Three-dimensional atom probe tomography images of an $Al_{0.54}Ti_{0.46}N$ coating after annealing to 1350 °C revealing a coarsened network of TiN and AlN. (a) 3D maps of Ti (red) and (b) Al (blue) within a representative probe volume of length of 120 nm, (c) combined isoconcentration surfaces of Ti (red) and Al (blue) (Rachbauer et al., 2009).

increase between 600 and 700 °C (Willmann, Mayrhofer, Hultman, & Mitterer, 2008). It should be noted here that the formation of the already mentioned protective dual-layer α-Al_2O_3-rich and Cr_2O_3-rich oxide scale shifts the onset of CrN decomposition to approximately 200 °C higher temperatures, due to the hindered release of nitrogen (Mayrhofer, Willmann, Hultman, & Mitterer, 2008).

In the last decade, research on these metastable coatings has been stimulated by theoretical approaches, where, for example, solubility limits and elastic properties of the formed phases have been predicted by ab initio calculations of electron band structures using the density functional theory (Mayrhofer, Music, & Schneider, 2007). While it has been believed that the synthesis of the described metastable solid solutions is an exclusive domain of plasma-assisted PVD methods, $Al_xTi_{1-x}CN$ with extremely high Al contents has recently also been synthesized by thermal CVD using $TiCl_4$, $AlCl_3$, NH_3, H_2, N_2, Ar, and ethylene as carbon source at temperatures between 800 and 900 °C (Endler et al., 2010). There, the carbon is claimed to be incorporated as an amorphous grain boundary phase, whereas an fcc $Al_xTi_{1-x}N$ solid solution with x values between 0.76 and 0.87 has been found. The scientific background behind achieving these high AlN contents above the solubility limit is not clear up to now; nevertheless, excellent performance of these coatings in milling applications has been found. Several other transition metal nitrides forming similar metastable solid solutions, for example, $Al_xHf_{1-x}N$ (Franz, Lechthaler, Polzer, & Mitterer, 2010a; Howe et al., 2007), $Al_xZr_{1-x}N$ (Franz, Lechthaler, Polzer, & Mitterer, 2012; Sheng, Zhang, & Veprek, 2008) and $Al_xNb_{1-x}N$ (Franz, Lechthaler, Polzer, & Mitterer, 2010b; Holec, Franz, Mayrhofer, & Mitterer, 2010), have also been investigated in the past years; however, it still needs to be elucidated if an industrial relevance similar to $Al_xTi_{1-x}N$ and $Al_xCr_{1-x}N$ might be achieved in the future.

During the last decade, several attempts have been made to improve application-related properties of these metastable transition metal nitrides further by doping and alloying. These attempts can be divided into (1) enhancement of hardness, wear, and oxidation resistance and (2) reduction of friction. Transition metal elements such as Zr, Hf, and Ta have been shown to be incorporated into the $Al_xTi_{1-x}N$ solid solution, replacing Ti atoms (Donohue, Cawley, Brooks, & Münz, 1995; Rachbauer, Blutmager, Holec, & Mayrhofer, 2012; Rachbauer, Holec, & Mayrhofer, in press). Thus, solid solution hardening was observed, and, more important, a limited kinetics for the formation of wurtzite AlN, thus enhancing the thermal stability of the coating. In the case of Ta, this is related to an increase of the cohesive energy with increasing Ta content due to a Ta-induced strengthening of the covalent and metallic bonds in comparison with the Ta-free $Ti_{1-x}Al_xN$ system (Rachbauer, Holec, et al., in press). Ta has also been reported to improve the oxidation resistance of $Al_xTi_{1-x}N$ up to 900 °C (Pfeiler, Scheu, et al., 2009). Although there are only preliminary results available, these approaches combining ab initio calculations with experimental work allow for a tailored design of phases, enabling a knowledge-driven materials development.

Low contents of alloying elements such as Si and B have been described to be incorporated into the $Al_xTi_{1-x}N$ and $Al_xCr_{1-x}N$ phase, respectively, and to improve oxidation resistance by affecting the formation of protective oxide scales (Pfeiler, Zechner, et al., 2009). Similarly, Y additions have been used to increase the oxidation resistance of these coatings (Donohue, Smith, Münz, Petrov, & Greene, 1997). Higher Si contents have been reported to promote the formation of a nanocomposite structure consisting of fcc TiN or $Al_{1-x}Ti_xN$ nanocrystals, respectively, surrounded by a few monolayers thick amorphous SiN_x tissue phase (Veprek, Männling, Jilek, & Holubar, 2004; Veprek & Reiprich, 1995; Veprek & Veprek-Heijman, 2008). Based on the assumption that dislocation-driven plasticity in nanocrystals can essentially be neglected (Schiøtz, Vegge, Di Tolla, & Jacobsen, 1999) and that plastic deformation of the tissue phase by grain boundary sliding is limited because of its low thickness, hardness values well beyond the rule of mixture of the phases involved can be obtained. This nanocomposite approach has even been claimed to be suitable to synthesize coatings with hardness exceeding that of diamond (Veprek et al., 2000), although the accurate measurement of hardness of these superhard materials and the validity of these data is seriously discussed (Fischer-Cripps, 2006; Fischer-Cripps, Bull, & Schwarzer, 2012).

Typically, $Al_xTi_{1-x}N$ and $Al_xCr_{1-x}N$ show excellent wear resistance at elevated temperatures; however, friction coefficients are high, with values between 0.7 and 1 against alumina at a temperature of 700 °C (Kuschej, Mayrhofer, & Kathrein, 2005). Since common solid lubricants such as diamond-like carbon (DLC) or MoS_2 fail at temperatures above 200 °C due to oxidation, attempts have been made to benefit from formation of the so-called Magnéli phase oxides (Magnéli, 1953), which are expected to act as lubricants in high-temperature sliding contacts. Magnéli phases are oxygen-deficient oxides of selected transition metals, in particular Mo, V, W, and Ti, being described as crystallographic shear structures that can be derived from the parent perovskite ReO_3. Homologous series of Magnéli phases have been constructed for vanadium oxides, such as the V_nO_{2n-1} series between the borderline phases V_2O_3 ($n = 2$) and VO_2 ($n = \infty$) (Andersson, 1954) and the V_nO_{2n+1} series between the borderline phases VO_2 ($n = \infty$) and V_2O_5 ($n = 2$) (Tilley & Hyde, 1970), or for tungsten oxides, such as the W_nO_{3n-2} series (Wadsley, 1955) and the W_nO_{3n-1} series (Magnéli, 1953). Among these oxides, the formation of V_2O_5 by the oxidation of V on top of either $Al_xTi_{1-x}N$/VN superlattices (Mayrhofer, Hovsepian, Mitterer, & Münz, 2004) or as V alloyed to $Al_xTi_{1-x}N$ (Kutschej, Mayrhofer, Kathrein, Polcik, & Mitterer, 2004) and $Al_xCr_{1-x}N$ (Franz et al., 2006) has been studied. While the superlattices seem to lose their mechanical integrity due to the oxidation of the VN layers, oxidation of V can be controlled by outdiffusion through the $Al_xTi_{1-x}N$ or $Al_xCr_{1-x}N$ matrix (Franz et al., 2008). Since the melting temperature of the formed V_2O_5 phase is about 650 °C, a liquid lubricating V_2O_5 film is formed on the coating surface, yielding friction coefficients between 0.2 and 0.4 at 700 °C (Franz et al., 2006; Kutschej et al., 2004). **Figure 8** shows a comparison of friction coefficients measured in a ball-on-disc test against Al_2O_3 balls at 700 °C versus the sliding distance for a V-free and a V-alloyed $Al_xCr_{1-x}N$ coating. While the friction coefficient of the standard $Al_xCr_{1-x}N$ is approximately 0.6 with high scattering of the data, it can be reduced to values of approximately 0.2 by adding 28 mol% VN (Franz et al., 2006). Although no unambiguous evidence was found up to now for the beneficial effect of this in situ formation of Magnéli phases in cutting processes, V or W containing $Al_xTi_{1-x}N$ coatings have been suggested or even successfully evaluated in severe cutting applications (Kathrein, Michotte, Penoy, Polcik, & Mitterer, 2005; Reeswinkel, Music, & Schneider, 2011).

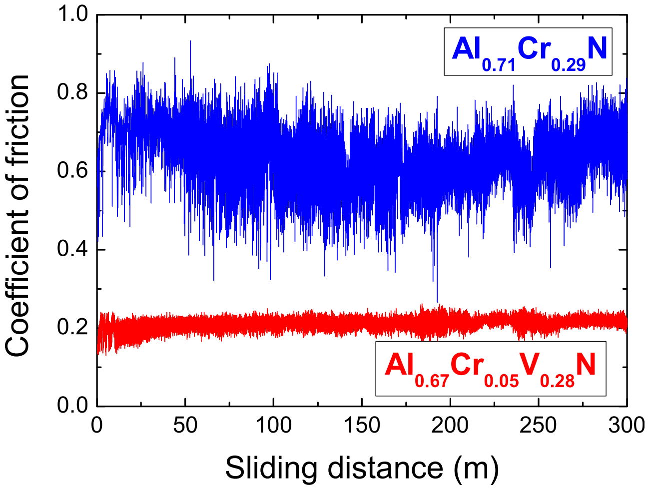

Figure 8 Coefficient of friction of V-free and V-alloyed $Al_xCr_{1-x}N$ coatings tested against Al_2O_3 at 700 °C counterparts versus sliding distance. Redrawn after Franz et al. (2006).

2.16.4 Carbides

Among the transition metal carbides, TiC was the CVD coating dominating the coating market in the early 1970s (Ruppi, 2001; Schintlmeister & Pacher, 1975). This interest arose due to the higher hardness of TiC compared to that of TiN, which is a consequence of its more covalent bonding characteristics (Sundgren & Hentzell, 1986). Despite its success at that time, the essential drawback of CVD TiC coatings is that a large amount of the carbon needed is also supplied from the cemented carbide substrate. This results in decarburization and formation of the brittle η-phase in surface-near zones of the substrate. TiC is furthermore characterized by a lower crater wear resistance compared to TiN when machining steels, which is related to its lower efficiency as a diffusion barrier (Schintlmeister & Pacher, 1975). Despite its higher hardness and the consequently higher abrasion resistance, TiC coatings have thus been widely substituted by TiC_xN_{1-x} (Ruppi, 2001).

Carbides have also been investigated using PVD methods. However, compared to transition metal nitrides, the growth for carbides is more complicated due to the hydrocarbon precursors used, which could on the one hand result in hydrogen incorporation in the coating. On the other hand, in particular for carbon to metal ratios exceeding 1, a dual-phase structure of the respective transition metal carbide plus a carbon modification is formed (Zehnder, Schwaller, Munnik, Mikhailov, & Patscheider, 2004). The properties of these coatings are essentially dominated by the bonding within the carbon phase and its morphological arrangement, for example, in a nanocomposite structure; consequently, more information on these coating materials can be found in Sections 2.16.7 and 2.16.8.

2.16.5 Borides

Unlike the transition metal nitrides and carbides with their dominating metallic binding character, the structure of borides is governed by covalent B–B bonds (Etourneau & Hagenmüller, 1985), resulting in a higher bond strength and consequently hardness, elastic modulus, and melting temperature. While hexaboride coatings such as LaB_6, SmB_6, and CeB_6 have been studied in the 1990s for decorative applications (Mitterer, 1997; Mitterer, Waldhauser, Beck, & Reiners, 1996) and because of their low work function for electron emission (Waldhauser, Mitterer, Laimer, & Störi, 1998), commercial success has up to now only been achieved for TiB_2 coatings, grown by CVD and magnetron sputtering, respectively, for machining of aluminum alloys (Mitterer, Rauter, & Rödhammer, 1990; Pierson & Mullendore, 1982). In CVD processes, usually $TiCl_4$ and BCl_3 are used as titanium and boron sources (Pierson & Mullendore, 1982). In contrast, PVD processes for boride coatings are usually based on the respective boride target. Since boride targets are usually prone to thermal shock and thus thermal cracking during arc evaporation, boride coatings are almost exclusively grown by sputter deposition.

TiB_2 as a coating material is of interest due to its high hardness and chemical inertness, in particular against aluminum (Berger & Hogmark, 2002; Samsonov & Kovenskaya, 1977), which has a pronounced adhesion tendency to nitride coatings in cutting applications, forming build-up edges. Due to its highly covalent nature with a two-dimensional B network formed in a hexagonal lattice, TiB_2 coatings often have an extremely high hardness, reaching values of >40 GPa (Mayrhofer, Mitterer, Wen, Greene, & Petrov, 2005; Mitterer et al., 1990). These values are well above those of bulk TiB_2 (approximately 34 GPa (Kieffer & Benesovsky, 1963)) and have been on the one hand related to the often-observed high compressive stresses within these coatings (Berger, Karlsson, Larsson, & Hogmark, 2001). Since these high stresses limit the coating thickness, efforts on the out-annealing of defects in sputtered coatings by bombardment of the film surface with electrons due to the application of bipolar pulsed bias voltages have been undertaken (Berger et al., 2001). Using this approach, coating thicknesses of up to 60 μm have been reached (Berger, 2002). On the other hand, a nanocolumnar structure formed by self-organization in sputtered overstoichiometric TiB_{2+x} coatings has been suggested to explain the extremely high hardness values (**Figure 9**; Mayrhofer et al., 2005). Such nonstoichiometric $TiB_{2\pm x}$ coatings are often found in sputtering from TiB_2 targets, due to the different scattering probabilities of Ti and B atoms during the transport from the target to the substrate (Neidhardt et al., 2008). There, columns with a (0001) preferred orientation of the hexagonal TiB_2 phase and diameters of approximately 20 nm are encapsulated in the excess B (Mayrhofer et al., 2005). The columns themselves are composed of bundles of coherent approximately 5-nm diameter TiB_2 subcolumns that are separated by a disordered 1–2 monolayers thin B-rich tissue phase. The observed nanostructure is extremely stable, and does not undergo thermal changes upon annealing up to 700 °C.

Besides TiB_2, other diborides have been investigated as well. Examples are ZrB_2, which is characterized by lower hardness but an excellent corrosion resistance (Ürgen, Çakır, Eryılmaz, & Mitterer, 1995) and HfB_2, which is as well characterized by high hardness values (Herr, Berg, Friedrich, Broszeit, & Kloos, 1994; Jayaraman et al., 2006). In many attempts, nitrogen has been added to diboride coatings, with the goal to increase toughness by forming a nanocomposite structure consisting of the respective diboride and nitride phases (Herr et al., 1994; Jayaraman et al., 2006; Mitterer et al., 1990; Ürgen et al., 1995). Recently, coatings within the ternary Ti–B–N system have also been deposited by reactive cathodic arc evaporation from Ti–B targets with B/Ti atomic ratios of 1/5 and 3/5 (Neidhardt, Czigány, et al., 2006; Neidhardt, Czigány, Sartory, Tessadri, & Mitterer, 2010; Neidhardt, O'Sullivan, et al., 2006). A nanocomposite structure within the TiN–TiB_x–BN system has been obtained. Very similar results have also been reported for the Cr–B–N system (Polychronopoulou et al., 2009; Polychronopoulou et al., 2008).

2.16.6 Oxides

Among the oxides, Al_2O_3 is dominating as a wear-protective coating for cutting tools, due to its unique combination of chemical inertness, thermal stability, and hot hardness. Beside the stable hexagonal α-Al_2O_3 (also

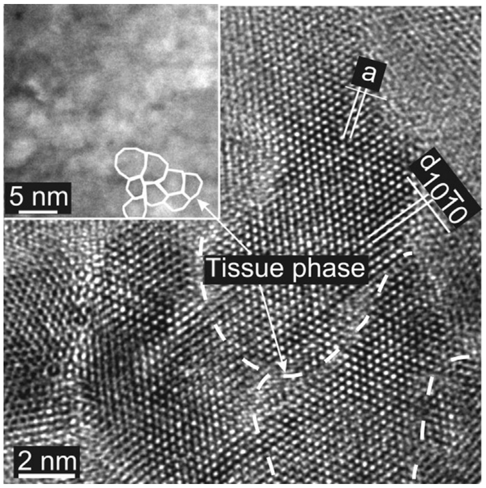

Figure 9 Bright-field plan-view (0001) high-resolution transmission electron microscopy image of a $TiB_{2.4}$ layer. The inset is a lower resolution Z-contrast image (Mayrhofer et al., 2005).

denoted as corundum, sapphire, or α-alumina), several metastable polymorphs (γ, δ, κ, η, θ, χ) exist. The phase formed is determined by the deposition process itself and its parameters, with α- and κ-Al_2O_3 usually being synthesized by CVD and γ-Al_2O_3 by PVD processes. Among the process conditions, essentially the substrate temperature and the application of seed templates determine the formation of these polymorphs. In CVD, $AlCl_3$ and CO_2 are used as precursors (Tingey, 1966). Typically, below a deposition temperature of approximately 800 °C, amorphous Al_2O_3 is formed (Fredriksson & Carlsson, 1993b); however, the formation of moderate temperature (700–950 °C) crystalline coatings using the NO–H_2–HCOOH system has been reported (Connelly, Pattanaik, & Sarin, 2005). Furthermore, the deposition conditions during Al_2O_3 nucleation (Ruppi, 2005) and surface treatment procedures of the substrate (Danzinger, Haubner, & Lux, 1991) are crucial for the phase formation. Most often, a TiC_xN_{1-x} base layer is used in CVD, to provide the necessary adhesion of the Al_2O_3 top layer and to match its properties with those of the cemented carbide substrates. Whether an oxidation step of this TiC_xN_{1-x} base layer is done or not determines if the Al_2O_3 top layer grows in the stable α-Al_2O_3 or a metastable modification (most often κ-Al_2O_3) (Ruppi, 2005). κ-Al_2O_3 is characterized by a significantly lower thermal conductivity compared to that of α-Al_2O_3 (Cahill, Lee, & Selinder, 1998), which results in an improved thermal shielding and a consequently reduced thermal load of the cutting tool. Transformation of κ-Al_2O_3 into the stable α-Al_2O_3 modification occurs at a temperature of approximately 1000 °C (Hochauer et al., 2010), and results in coating cracking and delamination due to the associated volume change. Nevertheless, despite its metastable nature, κ-Al_2O_3 coatings are characterized by usually smaller grain sizes and lack of voids compared to α-Al_2O_3 (Vuorinen & Skogsmo, 1990), giving rise to benefits in some cutting operations.

The PVD of Al_2O_3 coatings is still a challenge, mainly due to their electrically insulating nature, requiring pulsed d.c. or r.f. plasmas. At low deposition temperatures, coatings are reported to be X-ray amorphous (Chou, Adamson, Mardinly, & Nieh, 1991). Temperatures between 350 and 550 °C are needed to grow crystalline γ-Al_2O_3 (Cremer et al., 1999; Schütze & Quinto, 2003), while for the desired α-Al_2O_3 modification, temperatures of 700 °C are needed (Zywitzki & Hoetzsch, 1997). The γ-Al_2O_3 phase formed in sputtered coatings is characterized by a remarkable thermal stability, where no phase transformation within well-crystalline coatings has been observed for an annealing temperature of 1000 °C (Edlmayr et al., 2011; Edlmayr, Moser, Walter, & Mitterer, 2010).

Since the exploitation of α-Al_2O_3 as a wear-protective coating on high-speed steel cutting tools would require deposition temperatures below 600 °C to avoid the softening of the substrate, several approaches have been undertaken to promote nucleation and growth of the α-Al_2O_3 phase by applying suitable deposition conditions, templates, or stabilizers. For the growth of α-Al_2O_3 at 720 °C, a critical Al^+ ion energy of 40 eV has been reported to be necessary (Music, Nahif, Sarakinos, Friederichsen, & Schneider, 2011). The most efficient template or stabilizer for α-Al_2O_3 growth known up to now is Cr_2O_3 (escolaite), which is isostructural with corundum. Cr_2O_3 has successfully been used as template, fostering the epitaxial growth of α-Al_2O_3 at substrate temperatures of 400–450 °C (Eklund, Sridharan, Sillassen, & Bøttiger, 2008; Jin et al., 2002). Recently, solid solutions within the system Al_2O_3–Cr_2O_3 have been synthesized by cathodic arc evaporation (Pohler, Franz, Ramm, Polcik, & Mitterer, 2011; Ramm et al., 2007) and by magnetron sputtering (Pederson, Bøttiger, Sridharan, Sillassen, & Eklund, 2010), showing that the corundum structure is already formed in the temperature range between 300 and 550 °C. However, also for the Al_2O_3–Cr_2O_3 solid solution special care has to be taken to optimize the ion bombardment conditions to obtain well-crystalline coatings. **Figure 10** shows an example of X-ray diffraction patterns of coatings grown by reactive cathodic arc evaporation from an $Al_{0.7}Cr_{0.3}$ target with different duty cycles, that is, the ratio of the negative pulse duration over the total pulse length of the bipolar pulsed d.c. bias voltage. The peaks of the top layer are found in between the positions of the α-Al_2O_3 and the Cr_2O_3 positions, indicating the formation of a solid solution according to Vegard's law (Ramm et al., 2007). The rising duty cycle, that is, the increasing duration of the period with ion bombardment at the expense of that with electron bombardment, results in an increasing crystallinity of the solid solution, as evidenced by the increasing peak intensity in **Figure 10**. Although cathodic arc evaporation of the Al_2O_3–Cr_2O_3 solid solution has been demonstrated on an industrial scale (Ramm et al., 2007), the application potential of these coatings is still under investigation.

2.16.7 Diamond-like Carbon

The general term DLC describes hydrogenated as well as nonhydrogenated carbon materials. Being a metastable form of amorphous carbon containing a significant fraction of sp^3 bonds, DLC films can have a high hardness,

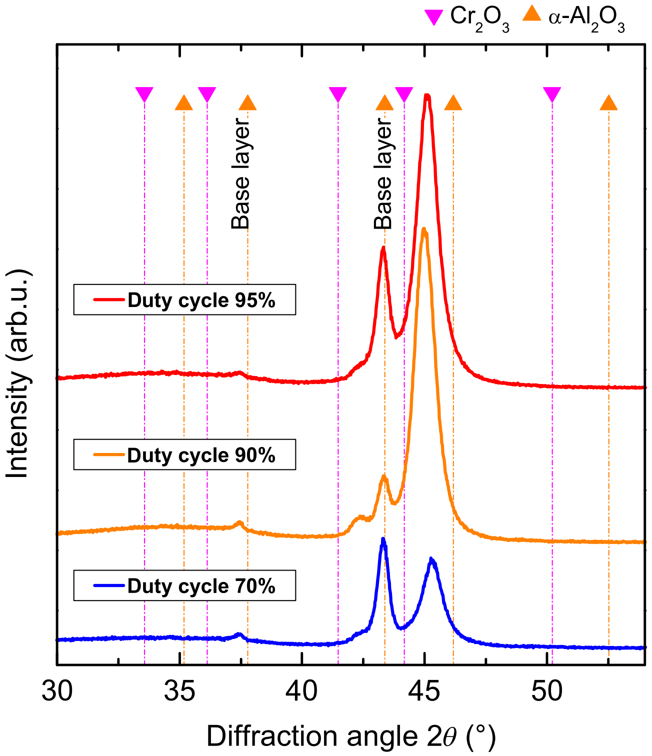

Figure 10 XRD patterns of coatings grown by reactive cathodic arc evaporation from $Al_{0.7}Cr_{0.3}$ targets using different duty cycles on a $Al_{1-x}Ti_xN$ base layer.

chemical inertness, optical transparency, that is, diamond-like properties, and act at the same time as solid lubricants, which is a typical property of graphite (Robertson, 2002). As a consequence, DLC films have found widespread applications as protective and self-lubricious coatings in areas such as automotive parts, magnetic storage discs, and biomedical coatings. Since DLC coatings have a metastable nature, they have to be synthesized by plasma-assisted PVD or PACVD processes (Grill, 1999), typically at temperatures not exceeding 200 °C.

Carbon forms a large variety of crystalline and disordered structures as it is able to exist in three hybridizations, that is, sp^1, sp^2, and sp^3. In the sp^3 configuration, as in diamond, the four valence electrons of carbon are assigned to a tetrahedrally directed sp^3 orbital, which makes a strong directional σ bond to an adjacent atom. In the threefold coordinated sp^2 configuration, as in graphite, three of the four valence electrons enter trigonally directed sp^2 orbitals, which form σ bonds in a plane. The fourth electron of the sp^2 atom is in the $p\pi$ orbital, which lies normal to the σ bonding plane. This π orbital forms a weaker π bond with a π orbital with one or more neighboring atoms. Thus, graphite has strong intralayer σ bonding and weak van der Waals bonding between its layers, resulting in its outstanding lubricious properties. In the sp^1 configuration, two of the four valence electrons enter σ orbitals, each forming a σ bond directed along the $\pm x$-axis, and the other two electrons enter $p\pi$ orbitals in the y and z directions (Robertson, 1986).

DLC thin films owe some extreme properties similar to diamond deriving from the strong σ bonds, but these are achieved in isotropic disordered films with no grain boundaries, being much cheaper and easier to be produced than diamond itself. The structure of such DLC coatings is amorphous with very short range ordered sp^3 and sp^2 bonds (Grill, 1999). DLC can be classified according to a ternary phase diagram first suggested by Jacob and Moller (Ferrari, 2004; Jacob & Moller, 1993) (**Figure 11**). There, a-C:H designates DLC materials containing up to 50 at% hydrogen and typically sp^3 fractions of $<50\%$, while tetrahedral carbon films (ta-C) and tetrahedral hydrogenated carbon films can contain $\geq 85\%$ sp^3 bonds. The hydrogen is required to obtain and stabilize the diamond-like properties mentioned above and is introduced by reacting with the dangling bonds via the formation of C–H bonds, thus introducing many sp^3 sites in the films. Generally, the observed rather high intrinsic compressive stresses for films with high sp^3 fractions affect their adhesion to the substrate and often cause delamination and buckling, when thicknesses of >2 μm are achieved (Grill, 1999). However, hydrogen incorporation was found to decrease its rigidity and thus brittleness. In a similar approach, metals

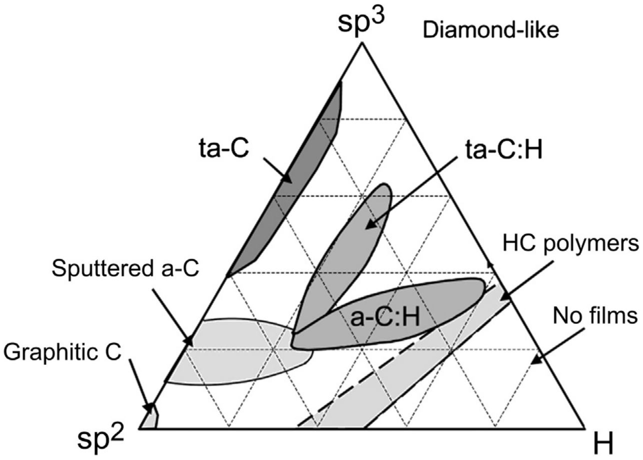

Figure 11 Ternary phase diagram of amorphous carbons. The three corners correspond to diamond (sp^3 configuration), graphite (sp^2 configuration), and hydrogen, respectively (Ferrari, 2004).

such as W, Cr, and Si have been added to a-C:H (Gassner, Patscheider, Mayrhofer, & Mitterer, 2006) and a-C coatings (Field, Jarratt, & Teer, 2004), allowing to reduce stresses and hardness (e.g., from 40–80 GPa for a-C to values of 10–30 GPa (Grill, 1999)) to adapt the coating surface to the given tribological counterpart.

The most important feature of DLC coatings is their excellent tribological behavior, with friction coefficients in the range of 0.007–1. The large spread of data is a result of the different bonding structures and compositions of DLC films and also of the environmental conditions. The extremely low friction coefficients are related to the retransformation of the as-deposited metastable structure to a few nanometers thin, weakly bonded graphitic planes in the sliding contact enabling velocity accommodation (Berthier, Godet, & Brendle, 1989), that is, again a smart, self-adaptive behavior is observed. Its formation can be significantly enhanced by the availability of hydrogen from humid atmospheres or the coating itself (Erdemir, 2001). However, a significant drawback of both hydrogenated and nonhydrogenated DLC coatings is their low thermal stability, since the metastable structure will transform toward the stable graphite at elevated temperatures. The consequently deteriorating wear resistance determines the application limit of these materials. While first changes within the DLC structure, for example, the release of hydrogen, has been reported to start at temperatures as low as 100 °C (Gassner, Mayrhofer, Patscheider, & Mitterer, 2007), no structural changes have been reported for hydrogen-free ta-C up to 600 °C (Grierson et al., 2010). Due to their unique combination of self-lubricious and wear protection properties, DLC coatings are assumed to be one of the key materials in reducing fuel and oil consumption as well as fine dust and CO_2/NO_x emissions in the automotive industry, in particular due to the friction reduction of engine and drive-train components (Holmberg, Andersson, & Erdemir, 2012).

2.16.8 Multilayers, Nanolaminates, and Nanocomposites

Coating architectures with base and top layers have been applied since a long time with the primary goal to adjust elastic properties and thermal expansion of the top layer to those of the substrate material. In the late 1980s, the hard coatings community learned to benefit from exploring size effects, that is, the strengthening of a coating due to microstructural and dimensional constraints (Arzt, 1998). The first representatives of such coating architectures have been based on superlattice approaches, that is, a layer-by-layer arrangement with sharp interfaces and periodicities in the order of a few nanometers. Such lamellar materials, either designed by an alternating growth of individual layers in an artificial superlattice (e.g., TiN/VN (Helmersson et al., 1987)) or inherently nanolaminated phases (e.g., the so-called $M_{n+1}AX_n$ ($n = 1$–3) phases (Barsoum, 2000), where M is a transition metal, A represents a group A element such as Al or Si, and X is C and/or N, or the already mentioned Magnéli phases (Magnéli, 1953)) are promising materials as they combine high hardness and toughness. Superlattices represent challenges for coating synthesis, for example, by maintaining the layered structure on three-dimensional substrates; however, due to the possibility of synthesis of superhard (i.e., with hardness >40 GPa) and thus highly wear-resistant materials they have been successfully transferred to production (Hovsepian & Münz, 2003). In the 1990s, nanocomposite structures have been developed, primarily also with the goal to reach superhardness. Besides the already mentioned system based on TiN nanocrystals surrounded by an amorphous SiN_x tissue phase (Veprek & Reiprich, 1995), several other systems based on hard phases [e.g., TiN–TiB_2 and TiC–TiB_2 (Mitterer et al., 1999)] or combinations of hard and soft phases [e.g., ZrN–Cu (Musil, 2000)] have been suggested. Later on, the know-how on deposition techniques and the progress in self-organization phenomena lead to the development of smart, multifunctional coating materials with complex multiphase structures. Well-known representatives for these nanocomposite materials are coatings with high wear resistance, supertoughness, and low-friction behavior, where the latter adapts itself to different ambient atmospheres. For example, nanosized WC grains provide the necessary wear resistance, DLC offers low friction in humid and WS_2 in dry atmospheres (Baker, Chromik, Wahl, Hu, & Voevodin, 2007; Voevodin & Zabinski, 2000). Recently, double oxide phases combining a transition metal and a noble metal, having crystals with a layered atomic structure with weak interplanar bonds like silver molybdate [e.g., $Ag_2Mo_2O_7$; (Stone et al., 2010)], have been suggested to provide low friction up to 600 °C. Also other layered compounds have been explored, for example, Mo_2BC, which is characterized by an unusually high stiffness and moderate ductility (Emmerlich et al., 2009). The development of these complex phases requires the combined efforts of theoretical approaches, for example, based on the prediction of phase stabilities and elastic properties, and experimental work. However, in combination with vapor phase deposition methods allowing one to synthesize materials far away from thermodynamical equilibrium, it enables to enter a new age in advanced materials design.

2.16.9 Summary and Outlook

This chapter has presented an overview on vapor phase deposition methods and the present state of the art in wear-resistant hard coatings. In the past decades, there has been a growing interest in these thin film materials, due to their widespread application as wear and oxidation protective coatings for tools and low-friction films for engine and drive-train components. CVD and PVD techniques have reached a status of maturity, which allows one to effectively control film growth and thus to synthesize tailormade coating materials, often with multifunctional or even smart self-adaptive properties. Many of the coatings grown by plasma-assisted deposition methods are largely nonstoichiometric, they contain impurities, growth-induced defects, metastable phases and may have grain sizes in the nanometer range; they are thus far away from thermodynamic equilibrium conditions and often show unique property combinations. A huge variety of hard coatings based on transition metal nitrides and carbonitrides, carbides, borides, oxides, and carbon have been successfully synthesized, with TiN, CrN, TiC_xN_{1-x}, TiC, $Al_{1-x}Ti_xN$, $Al_{1-x}Cr_xN$, TiB_2, Al_2O_3, and DLC being successful representatives on the coating market. In addition, coating architectures based on bilayers and multilayers, superlattices and nanocomposites have been developed, with the goal to adjust the elastic and thermal properties of the top layer to the substrate materials or to achieve unique property combinations like high hardness and toughness or even self-lubrication. The further development of hard coatings materials and architectures is fostered by combined theoretical and experimental approaches based on the available theoretical prediction of phase stabilities and their corresponding properties and experimental work. The combination of these approaches with the possibility to grow those materials atom by atom in well-controlled vapor deposition processes will open up a new area in materials science.

Acknowledgments

Financial support of this work by the Austrian Nanoinitiative within the Research Project Cluster NanoCoat is highly appreciated. The author gratefully acknowledges the following people for comments on this review, general discussions, figures and/or technical assistance: Christoph Czettl, Robert Franz, Gert Gassner, Markus Kahn, Regina Kranz, Paul Mayrhofer, Marlene Mühlbacher, Markus Pohler, Richard Rachbauer, Marisa Rebelo de Figueiredo, and Angelika Tremmel.

References

Anders, A. (2008). *Cathodic arcs: From fractal spots to energetic condensation.* New York: Springer.
Anders, A. (2010). A structure zone diagram including plasma-based deposition and ion etching. *Thin Solid Films, 518*, 4087–4090.

Andersson, G. (1954). Studies on vanadium oxides. *Acta Chemica Scandinavica, 8*, 1599–1606.

Arnell, R. D., & Kelly, P. J. (1999). Recent advances in magnetron sputtering. *Surface and Coatings Technology, 112*, 170–176.

Arzt, E. (1998). Size effects in materials due to microstructural and dimensional constraints: a comparative review. *Acta Materialia, 46*, 5611–5626.

Baker, C. C., Chromik, R. R., Wahl, K. J., Hu, J. J., & Voevodin, A. A. (2007). Preparation of chameleon coatings for space and ambient environments. *Thin Solid Films, 515*, 6737–6743.

Barbee, T. W., Jr., Holmes, W. H., Keith, D. L., Pyzyna, M. K., & Ilonca, G. (1977). Synthesis of amorphous niobium–nickel alloys by vapor quenching. *Thin Solid Films, 45*, 591–599.

Barna, P. B., & Adamik, M. (1998). Fundamental structure forming phenomena of polycrystalline films and the structure zone models. *Thin Solid Films, 317*, 27–33.

Barsoum, M. W. (2000). The $M_{n+1}AX_n$ phases: a new class of solids; thermodynamically stable nanolaminates. *Progress in Solid State Chemistry, 28*, 201–281.

Berger, M. (2002). Thick physical vapour deposited TiB_2 coatings. *Surface Engineering, 18*, 219–223.

Berger, M., & Hogmark, S. (2002). Evaluation of TiB_2 coatings in sliding contact against aluminium. *Surface and Coatings Technology, 149*, 14–20.

Berger, M., Karlsson, L., Larsson, M., & Hogmark, S. (2001). Low stress TiB_2 coatings with improved tribological properties. *Thin Solid Films, 401*, 179–186.

Bergmann, E., Kaufmann, H., Schmid, R., & Vogel, J. (1990). Ion-plated titanium carbonitride films. *Surface and Coatings Technology, 42*, 237–251.

Berthier, Y., Godet, M., & Brendle, M. (1989). Velocity accommodation in friction. *Tribology Transactions, 32*, 490–496.

Cahill, D. G., Lee, S. M., & Selinder, T. I. (1998). Thermal conductivity of κ-Al_2O_3 and α-Al_2O_3 wear resistant coatings. *Journal of Applied Physics, 83*, 5783–5786.

Cheng, Y. H., Browne, T., & Heckerman, B. (2011). Mechanical and tribological properties of CrN coatings deposited by large area filtered cathodic arc. *Wear, 271*, 775–782.

Chou, T. C., Adamson, D., Mardinly, J., & Nieh, T. G. (1991). Microstructural evolution and properties of nanocrystalline alumina made by reactive sputtering deposition. *Thin Solid Films, 205*, 131–139.

Choy, K. L. (2003). Chemical vapour deposition of coatings. *Progress in Materials Science, 48*, 57–170.

Connelly, R., Pattanaik, A. K., & Sarin, V. K. (2005). Development of moderate temperature CVD Al_2O_3 coatings. *International Journal of Refractory Metals and Hard Materials, 23*, 317–321.

Cremer, R., Witthaut, M., Neuschütz, D., Erkens, G., Leyendecker, T., & Feldhege, M. (1999). Comparative characterization of alumina coatings deposited by RF, DC and pulsed reactive magnetron sputtering. *Surface and Coatings Technology, 120*, 213–218.

Danzinger, M., Haubner, R., & Lux, B. (1991). Influence of etching the TiC underlayer with $CH_4/AlCl_3/H_2$ on the CVD formation of κ-Al_2O_3. *Journal de Physique II, 1/C2*, 579–586.

Donohue, L. A., Cawley, J., Brooks, J. S., & Münz, W. D. (1995). Deposition and characterization of TiAlZrN films produced by a combined steered arc and unbalanced magnetron sputtering technique. *Surface and Coatings Technology, 74–75*, 123–134.

Donohue, L. A., Smith, I. J., Münz, W. D., Petrov, I., & Greene, J. E. (1997). Microstructure and oxidation-resistance of $Ti_{1-x-y-z}Al_xCr_yY_zN$ layers grown by combined steered-arc/unbalanced-magnetron-sputter deposition. *Surface and Coatings Technology, 94–95*, 226–231.

Edlmayr, V., Harzer, T. P., Hoffmann, R., Kiener, D., Scheu, C., & Mitterer, C. (2011). Effects of thermal annealing on the microstructure of sputtered Al_2O_3 coatings. *Journal of Vacuum Science and Technology A, 29*, 041506.

Edlmayr, V., Moser, M., Walter, C., & Mitterer, C. (2010). Thermal stability of sputtered Al_2O_3 coatings. *Surface and Coatings Technology, 204*, 1576–1581.

Eklund, P., Sridharan, M., Sillassen, M., & Bøttiger, J. (2008). α-Cr_2O_3 template-texture effect on α-Al_2O_3 thin-film growth. *Thin Solid Films, 516*, 7447–7450.

Emmerlich, J., Music, D., Braun, M., Fayek, P., Munnik, F., & Schneider, J. M. (2009). A proposal for an unusually stiff and moderately ductile hard coating material: Mo_2BC. *Journal of Physics D: Applied Physics, 42*, 185406.

Endler, I., Höhn, M., Herrmann, M., Holzschuh, H., Pitonak, R., Ruppi, S., et al. (2010). Aluminum-rich TiAlCN coatings by low pressure CVD. *Surface and Coatings Technology, 205*, 1307–1312.

Erdemir, A. (2001). The role of hydrogen in tribological properties of diamond-like carbon films. *Surface and Coatings Technology, 146–147*, 292–297.

Etourneau, J., & Hagenmüller, P. (1985). Structure and physical features of the rare-earth borides. *Philosophical Magazine, 52*, 589–610.

Fateh, N., Fontalvo, G. A., Gassner, G., & Mitterer, C. (2007). Influence of high-temperature oxide formation on the tribological behaviour of TiN and VN coatings. *Wear, 262*, 1152–1158.

Ferrari, A. C. (2004). Diamond-like carbon for magnetic storage disks. *Surface and Coatings Technology, 180–181*, 190–206.

Field, S. K., Jarratt, M., & Teer, D. G. (2004). Tribological properties of graphite-like and diamond-like carbon coatings. *Tribology International, 37*, 949–956.

Fischer-Cripps, A. C. (2006). Critical review of analysis and interpretation of nanoindentation test data. *Surface and Coatings Technology, 200*, 4153–4165.

Fischer-Cripps, A. C., Bull, S. J., & Schwarzer, N. (2012). Critical review of claims for ultra-hardness in nanocomposite coatings. *Philosophical Magazine, 92*, 1601–1630.

Franklin, S. E., & Beuger, J. (1992). A comparison of the tribological behaviour of several wear-resistant coatings. *Surface and Coatings Technology, 54/55*, 459–465.

Franz, R., Lechthaler, M., Polzer, C., & Mitterer, C. (2010a). Investigation on structure and properties of arc-evaporated HfAlN hard coatings. *Journal of Vacuum Science and Technology A, 28*, 528–535.

Franz, R., Lechthaler, M., Polzer, C., & Mitterer, C. (2010b). Structure, mechanical properties and oxidation behaviour of arc-evaporated NbAlN coatings. *Surface and Coatings Technology, 204*, 2447–2453.

Franz, R., Lechthaler, M., Polzer, C., & Mitterer, C. (2012). Oxidation behavior and tribological properties of arc-evaporated ZrAlN hard coatings. *Surface and Coatings Technology, 206*, 2337–2345.

Franz, R., Neidhardt, J., Mitterer, C., Schaffer, B., Hutter, H., Kaindl, R., et al. (2008). Oxidation and diffusion processes during annealing of AlCrVN hard coatings. *Journal of Vacuum Science and Technology A, 26*, 302–308.

Franz, R., Neidhardt, J., Sartory, B., Kaindl, R., Tessadri, R., Polcik, P., et al. (2006). High-temperature low-friction properties of vanadium-alloyed AlCrN coatings. *Tribology Letters, 23*, 101–107.

Fredriksson, E., & Carlsson, J. O. (1993a). Chemical vapor deposition of aluminum oxides from various gas mixtures. *Journal of Chemical Vapor Deposition, 1*, 333–417.

Fredriksson, E., & Carlsson, J. O. (1993b). Factors influencing the κ-$Al_2O_3 \rightarrow \alpha$-$Al_2O_3$ phase transformation during CVD growth. *Surface and Coatings Technology, 56*, 165–177.

Gassner, G., Mayrhofer, P. H., Patscheider, J., & Mitterer, C. (2007). Thermal stability of nanocomposite CrC/a-C: H thin films. *Thin Solid Films, 515*, 5411–5417.

Gassner, G., Patscheider, J., Mayrhofer, P. H., & Mitterer, C. (2006). Structure of sputtered nanocomposite CrC_x/a-C: H thin films. *Journal of Vacuum Science and Technology B, 24*, 1837–1843.

Grierson, D. S., Sumant, A. V., Konicek, A. R., Friedmann, T. A., Sullivan, J. P., & Carpick, R. W. (2010). Thermal stability and rehybridization of carbon bonding in tetrahedral amorphous carbon. *Journal of Applied Physics, 107*, 033523.

Grill, A. (1999). Diamond-like carbon: state of the art. *Diamond and Related Materials, 8*, 428–434.

Heller, J. (1973). Reactive sputtering of metals in oxidizing atmospheres. *Thin Solid Films, 17*, 163–176.

Helmersson, U., Todorova, S., Barnett, S. A., Sundgren, J.-E., Markert, L. C., & Greene, J. E. (1987). Growth of single-crystal TiN/VN strained-layer superlattices with extremely high mechanical hardness. *Journal of Applied Physics, 62*, 481–484.

Herr, W., Berg, G., Friedrich, C., Broszeit, E., & Kloos, K. H. (1994). Investigation of fundamental properties and tribological behavior of HfB_2 and Hf(B, N) coatings. *Materialwissenschaft und Werkstofftechnik, 25*, 175–179.

Hochauer, D., Mitterer, C., Penoy, M., Michette, C., Martinz, H. P., & Kathrein, M. (2010). Thermal stability of doped CVD κ-Al_2O_3 coatings. *Surface and Coatings Technology, 204*, 3713–3722.

Holec, D., Franz, R., Mayrhofer, P. H., & Mitterer, C. (2010). Structure and stability of phases within the NbN–AlN system. *Journal of Physics D: Applied Physics, 43*, 145403.

Holmberg, K., Andersson, P., & Erdemir, A. (2012). Global energy consumption due to friction in passenger cars. *Tribology International, 47*, 221–234.

Hovsepian, P. Eh, & Münz, W. D. (2003). Recent progress in large-scale production of nanoscale multilayer/superlattice hard coatings. *Vacuum, 96*, 27–36.

Howe, B., Bareno, J., Sardela, M., Wen, J. G., Greene, J. E., Hultman, L., et al. (2007). Growth and physical properties of epitaxial metastable $Hf_{1-x}Al_xN$ alloys deposited on MgO(001) by ultrahigh vacuum reactive magnetron sputtering. *Surface and Coatings Technology, 202*, 809–814.

Jacob, W., & Moller, W. (1993). On the structure of thin hydrocarbon films. *Applied Physics Letters, 63*, 1771.

Jayaraman, S., Gerbi, J. E., Yang, Y., Kim, D. Y., Chatterjee, A., Bellon, P., et al. (2006). HfB_2 and Hf–B–N hard coatings by chemical vapor deposition. *Surface and Coatings Technology, 200*, 6629–6663.

Jin, P., Xu, G., Tazawa, M., Yoshimura, K., Music, D., Alami, J., et al. (2002). Low temperature deposition of α-Al_2O_3 thin films by sputtering using a Cr_2O_3 template. *Journal of Vacuum Science and Technology A, 20*, 2134–2136.

Kathrein, M., Michotte, C., Penoy, M., Polcik, P., & Mitterer, C. (2005). Multifunctional multi-component PVD coatings for cutting tools. *Surface and Coatings Technology, 200*, 1867–1871.

Kieffer, R., & Benesovsky, F. (1963). *Hartstoffe*. Wien: Springer.

Klaus, M., Genzel, Ch, & Holzschuh, H. (2008). Residual stress depth profiling in complex hard coating systems by X-ray diffraction. *Thin Solid Films, 517*, 1172–1176.

Kornmann, M., Schachner, H., Funk, R., & Lux, B. (1975). Nucleation of alumina layers on TiC and cemented carbides by chemical vapor-deposition. *Journal of Crystal Growth, 28*, 259–262.

Kouznetsov, V., Macák, K., Schneider, J. M., Helmersson, U., & Petrov, I. (1999). A novel pulsed magnetron sputter technique utilizing very high target power densities. *Surface and Coatings Technology, 122*, 290–293.

Kutschej, K., Mayrhofer, P. H., & Kathrein, M. (2005). Structure, mechanical and tribological properties for sputtered $Ti_{1-x}Al_xN$ coatings with $0.5 \leq x \leq 0.75$. *Surface and Coatings Technology, 200*, 2358–2365.

Kutschej, K., Mayrhofer, P. H., Kathrein, M., Polcik, P., & Mitterer, C. (2004). A new low-friction concept for $Ti_{1-x}Al_xN$ based coatings in high-temperature applications. *Surface and Coatings Technology, 188–189*, 358–363.

Magnéli, A. (1953). Structures of the ReO_3-type with recurrent dislocations of atoms—homologous series of molybdenum and tungsten oxides. *Acta Crystallographia, 6*, 495–500.

Makino, Y. (2005). Prediction of phase change in pseudobinary transition metal aluminum nitrides by band parameters method. *Surface and Coatings Technology, 193*, 185–191.

Mattox, D. M. (2010). *Handbook of physical vapor deposition (PVD) processing* (2nd ed.). Oxford: Elsevier.

Mayrhofer, P. H., Hörling, A., Karlsson, L., Sjölén, J., Larsson, T., Mitterer, C., et al. (2003). Self-organized nanostructures in the Ti–Al–N system. *Applied Physics Letters, 83*, 2049–2051.

Mayrhofer, P. H., Hovsepian, P. Eh., Mitterer, C., & Münz, W. D. (2004). Calorimetric evidence for frictional self-adaptation of TiAlN/VN superlattice coatings. *Surface and Coatings Technology, 177–178*, 341–347.

Mayrhofer, P., Mitterer, C., Hultman, L., & Clemens, H. (2006). Microstructural design of hard coatings. *Progress in Materials Science, 51*, 1032–1114.

Mayrhofer, P. H., Mitterer, C., Wen, J. G., Greene, J. E., & Petrov, I. (2005). Self-organized nanocolumnar structure in superhard TiB_2 thin films. *Applied Physics Letters, 86*, 131909.

Mayrhofer, P. H., Music, D., & Schneider, J. M. (2007). Ab initio calculated binodal and spinodal of cubic $Ti_{1-x}Al_xN$. *Applied Physics Letters, 90*, 029902.

Mayrhofer, P. H., Willmann, H., Hultman, L., & Mitterer, C. (2008). Influence of different atmospheres on the thermal decomposition of Al–Cr–N coatings. *Journal of Physics D: Applied Physics, 41*, 155316.

McIntyre, D., Greene, J. E., Håkansson, G., Sundgren, J. E., & Münz, W. D. (1990). Oxidation of metastable single-phase polycrystalline $Ti_{0.5}Al_{0.5}N$ films—kinetics and mechanisms. *Journal of Applied Physics, 67*, 1542–1553.

Mitterer, C. (1997). Borides in thin film technology. *Journal of Solid State Chemistry, 133*, 279–291.

Mitterer, C., Mayrhofer, P. H., Beschliesser, M., Losbichler, P., Warbichler, P., Hofer, F., et al. (1999). Microstructure and properties of nanocomposite Ti–B–N and Ti–B–C coatings. *Surface and Coatings Technology, 120–121*, 405–411.

Mitterer, C., Rauter, M., & Rödhammer, P. (1990). Sputter deposition of ultrahard coatings within the system Ti–B–C–N. *Surface and Coatings Technology, 41*, 351–364.

Mitterer, C., Waldhauser, W., Beck, U., & Reiners, G. (1996). Structure and properties of decorative rare-earth hexaboride coatings. *Surface and Coatings Technology, 86/87*, 715–721.

Movchan, B. A., & Demchishin, A. (1969). Investigation of the structure and properties of thick vacuum-deposited films of nickel, titanium, tungsten, alumina, and zirconium dioxide. *Physics of Metals and Metallography, 28*, 653–660.

Münz, W. D. (1986). Titanium aluminum nitride films: a new alternative to TiN coatings. *Journal of Vacuum Science and Technology A, 4*, 2717–2725.

Music, D., Nahif, F., Sarakinos, K., Friederichsen, N., & Schneider, J. M. (2011). Ab initio molecular dynamics of Al irradiation-induced processes during Al_2O_3 growth. *Applied Physics Letters, 98*, 111908.

Musil, J. (2000). Hard and superhard nanocomposite coatings. *Surface and Coatings Technology, 125*, 322–330.

Navinšek, B., Panjan, P., & Milošev, I. (1997). Industrial applications of CrN (PVD) coatings, deposited at high and low temperatures. *Surface and Coatings Technology, 97*, 182–191.

Neidhardt, J., Czigány, Zs., Sartory, B., Kaindl, R., Tessadri, R., Polcik, P., et al. (2006). Nanocomposite Ti–B–N coatings synthesized by reactive arc evaporation. *Acta Materialia, 54*, 4193–4200.

Neidhardt, J., Czigány, Zs., Sartory, B., Tessadri, R., & Mitterer, C. (2010). Wear-resistant Ti–B–N nanocomposite coatings synthesized by reactive cathodic arc evaporation. *International Journal of Refractory Metals and Hard Materials, 28*, 23–31.

Neidhardt, J., Mráz, S., Schneider, J. M., Strub, E., Bohne, W., Liedke, B., et al. (2008). Experiment and simulation of the compositional evolution of Ti–B thin films by sputtering of a compound target. *Journal of Applied Physics, 104*, 063304.

Neidhardt, J., O'Sullivan, M., Reiter, A. E., Rechberger, W., Grogger, W., & Mitterer, C. (2006). Structure–property-performance relations of high-rate reactive arc-evaporated Ti–B–N nanocomposite coatings. *Surface and Coatings Technology, 201*, 2553–2559.

Ohring, M. (2002). *The materials science of thin films—deposition and structure* (2nd ed.). San Diego: Academic Press.

PalDey, S., & Deevi, S. C. (2003). Single layer and multilayer wear resistant coatings of (Ti, Al)N: a review. *Materials Science and Engineering A, 342*, 58–79.

Pedersen, K., Bøttiger, J., Sridharan, M., Sillassen, M., & Eklund, P. (2010). Texture and microstructure of Cr_2O_3 and $(Cr, Al)_2O_3$ thin films deposited by reactive inductively coupled plasma magnetron sputtering. *Thin Solid Films, 518*, 4294–4298.

Petrov, I., Barna, P. B., Hultman, L., & Greene, J. E. (2003). Microstructural evolution during film growth. *Journal of Vacuum Science and Technology A, 21*, 117–128.

Pfeiler, M., Scheu, C., Hutter, H., Schnöller, J., Michotte, C., Mitterer, C., et al. (2009). On the effect of Ta on improved oxidation resistance of Ti–Al–Ta–N coatings. *Journal of Vacuum Science and Technology A, 27*, 554–560.

Pfeiler, M., Zechner, J., Penoy, M., Michotte, C., Mitterer, C., & Kathrein, M. (2009). Improved oxidation resistance of TiAlN coatings by doping with Si or B. *Surface and Coatings Technology, 203*, 3104–3110.

Pierson, H. O. (1999). *Handbook of chemical vapor deposition (CVD).* Park Ridge: Noyes Publications.

Pierson, H. O., & Mullendore, A. W. (1982). Thick boride coatings by chemical vapor deposition. *Thin Solid Films, 95*, 99–104.

Pohler, M., Franz, R., Ramm, J., Polcik, P., & Mitterer, C. (2011). Cathodic arc deposition of $(Al, Cr)_2O_3$: macroparticles and cathode surface modifications. *Surface and Coatings Technology, 206*, 1454–1460.

Polychronopoulou, K., Baker, M. A., Rebholz, C., Neidhardt, J., O'Sullivan, M., Reiter, A. E., et al. (2009). The nanostructure, wear and corrosion performance of arc evaporated CrB_xN_y nanocomposite coatings. *Surface and Coatings Technology, 204*, 246–255.

Polychronopoulou, K., Neidhardt, J., Rebholz, C., Baker, M. A., O'Sullivan, M., Reiter, A. E., et al. (2008). Synthesis and characterization of Cr–B–N coatings deposited by reactive arc-evaporation. *Journal of Materials Research, 23*, 3048–3055.

Prengel, G. G., Pfouts, W. R., & Santhanam, A. T. (1998). State of the art in hard coatings for carbide cutting tools. *Surface and Coatings Technology, 102*, 183–190.

Rachbauer, R., Blutmager, A., Holec, D., & Mayrhofer, P. H. (2012). Effect of Hf on structure and age hardening of Ti–Al–N thin films. *Surface and Coatings Technology, 206*, 2667–2672.

Rachbauer, R., Holec, D., & Mayrhofer, P. H. (2012). Increased thermal stability of Ti–Al–N thin films by Ta alloying. *Surface and Coatings Technology, 211*, 98–103.

Rachbauer, R., Stergar, E., Massl, S., Moser, M., & Mayrhofer, P. H. (2009). Three-dimensional atom probe investigations of Ti–Al–N thin films. *Scripta Materialia, 61*, 725–728.

Ramm, J., Ante, M., Bachmann, T., Widrig, B., Brändle, H., & Döbeli, M. (2007). Pulse enhanced electron emission (P3e™) arc evaporation and the synthesis of wear resistant Al–Cr–O coatings in corundum structure. *Surface and Coatings Technology, 202*, 876–883.

Rebelo de Figueiredo, M., Muratore, C., Franz, R., Chromik, R. R., Wahl, K. J., Voevodin, A. A., et al. (2010). In situ studies of $TiC_{1-x}N_x$ hard coating tribology. *Tribology Letters, 40*, 365–373.

Rebelo de Figueiredo, M., Neidhardt, J., Kaindl, R., Reiter, A., Tessadri, R., & Mitterer, C. (2008). Formation mechanisms of low-friction tribo-layers on arc-evaporated $TiC_{1-x}N_x$ hard coatings. *Wear, 265*, 525–532.

Reeswinkel, T., Music, D., & Schneider, J. M. (2011). Structure and mechanical properties of TiAlN–WN_x thin films. *Surface and Coatings Technology, 205*, 4821–4827.

Reiter, A. E., Derflinger, V. H., Hanselmann, B., Bachmann, T., & Sartory, B. (2005). Investigation of the properties of $Al_{1-x}Cr_xN$ coatings prepared by cathodic arc evaporation. *Surface and Coatings Technology, 200*, 2114–2122.

Reiter, A. E., Mitterer, C., & Sartory, B. (2007). Oxidation of arc evaporated $Al_{1-x}Cr_xN$ coatings. *Journal of Vacuum Science and Technology A, 25*, 711–720.

Robertson, J. (1986). Amorphous carbon. *Advances in Physics, 35*, 317–374.

Robertson, J. (2002). Diamond-like amorphous carbon. *Materials Science and Engineering Reports, 37*, 129–281.

Ruppi, S. (2001). Advances in chemically vapour deposited wear resistant coatings. *Journal de Physique IV, 11*, 847–859.

Ruppi, S. (2005). Deposition, microstructure and properties of texture-controlled CVD α-Al_2O_3 coatings. *International Journal of Refractory Metals and Hard Materials, 23*, 306–316.

Samsonov, G. V., & Kovenskaya, B. A. (1977). The electronic structure of boron compounds and the nature of chemical bond in borides. In V. I. Matkovich (Ed.), *Boron and refractory borides* (pp. 5–19). Berlin: Springer.

Sanders, D. A., & Anders, A. (2000). Review of cathodic arc deposition technology at the start of the new millennium. *Surface and Coatings Technology, 133–134*, 78–90.

Schintlmeister, W., & Pacher, O. (1975). Preparation and properties of hard-material layers for metal machining and jewelry. *Journal of Vacuum Science and Technology, 12*, 743–748.

Schiøtz, J., Vegge, T., Di Tolla, F. D., & Jacobsen, K. W. (1999). Atomic-scale simulations of the mechanical deformation of nanocrystalline metals. *Physical Review B, 60*, 11971–11983.

Schütze, A., & Quinto, D. T. (2003). Pulsed plasma-assisted PVD sputter-deposited alumina thin films. *Surface and Coatings Technology, 162*, 174–182.

Sheng, S. H., Zhang, R. F., & Veprek, S. (2008). Phase stabilities and thermal decomposition in the $Zr_{1-x}Al_xN$ system studied by ab initio calculation and thermodynamic modeling. *Acta Materialia, 56*, 968–976.

Spear, K. E. (1982). Principles and applications of chemical vapor deposition (CVD). *Pure and Applied Chemistry, 54*, 1297–1311.

Stone, D., Liu, J., Singh, D. P., Muratore, C., Voevodin, A. A., Mirhra, S., et al. (2010). Layered atomic structures of double oxides for low shear strength at high temperatures. *Scripta Materialia, 62*, 735–738.

Sundgren, J.-E., & Hentzell, H. T. G. (1986). Critical review: the present state of art in hard coatings. *Journal of Vacuum Science and Technology A, 4*, 2259–2279.

Thornton, J. A. (1977). High rate thick film growth. *Annual Review of Materials Science, 7*, 239–260.

Tilley, R. J. D., & Hyde, B. G. (1970). An electron microscopic investigation of decomposition of V_2O_5. *Journal of Physics and Chemistry of Solids, 31*, 1613–1619.

Tingey, G. L. (1966). Kinetics of water-gas equilibrium reaction. Part I: reaction of carbon dioxide with hydrogen. *Journal of Physical Chemistry, 70*, 1406–1412.

Tomanik, E. (2008). Friction and wear bench tests of different engine liner surface finishes. *Tribology International, 41*, 1032–1038.

Ürgen, M., Çakır, A. F., Eryılmaz, O. L., & Mitterer, C. (1995). Corrosion properties of zirconium boride and zirconium boron nitride coated steels. *Surface and Coatings Technology, 71*, 60–66.

Veprek, S., Männling, H. D., Jilek, M., & Holubar, P. (2004). Avoiding the high-temperature decomposition and softening of $(Al_{1-x}Ti_x)N$ coatings by the formation of stable superhard nc-$(Al_{1-x}Ti_x)N$/a-Si_3N_4 nanocomposite. *Materials Science and Engineering A, 366*, 202–205.

Veprek, S., Niederhofer, A., Moto, K., Bolom, T., Männling, H.-D., Nesladek, P., et al. (2000). Composition, nanostructure and origin of the ultrahardness in nc-TiN/a-Si_3N_4/a- and nc-$TiSi_2$ nanocomposites with $H_V = 80$ to ≥ 105 GPa. *Surface and Coatings Technology, 133–134*, 152–159.

Veprek, S., & Reiprich, S. (1995). A concept for the design of novel superhard coatings. *Thin Solid Films, 268*, 64–71.

Veprek, S., & Veprek-Heijman, M. J. G. (2008). Industrial applications of superhard nanocomposite coatings. *Surface and Coatings Technology, 202*, 5063–5073.

Voevodin, A. A., & Zabinski, J. S. (2000). Supertough wear-resistant coatings with 'chameleon' surface adaptation. *Thin Solid Films, 370*, 223–231.

Vuorinen, S., & Skogsmo, J. (1990). Characterization of α-Al_2O_3, κ-Al_2O_3, and α-κ multioxide coatings on cemented carbides. *Thin Solid Films, 193–194*, 536–546.

Wadsley, A. D. (1955). The crystal chemistry of non-stoichiometric compounds. *Reviews of Pure and Applied Chemistry, 5*, 165–193.

Waldhauser, W., Mitterer, C., Laimer, J., & Störi, H. (1998). Sputtered thermionic hexaboride coatings. *Surface and Coatings Technology, 98*, 1315–1323.

Willmann, H., Mayrhofer, P. H., Hultman, L., & Mitterer, C. (2008). Hardness evolution of Al–Cr–N coatings under thermal load. *Journal of Materials Research, 23*, 2880–2885.

Willmann, H., Mayrhofer, P. H., Persson, P. O.Å., Reiter, A. E., Hultman, L., & Mitterer, C. (2006). Thermal stability of Al–Cr–N hard coatings. *Scripta Materialia, 54*, 1847–1851.

Window, B. (1996). Issues in magnetron sputtering of hard coatings. *Surface and Coatings Technology, 81*, 92–98.

Zehnder, T., Schwaller, P., Munnik, F., Mikhailov, S., & Patscheider, J. (2004). Nanostructural and mechanical properties of nanocomposite nc-TiC/a-C: H films deposited by reactive unbalanced magnetron sputtering. *Journal of Applied Physics, 95*, 4327–4334.

Zywitzki, O., & Hoetzsch, G. (1997). Correlation between structure and properties of reactively deposited Al_2O_3 coatings by pulsed magnetron sputtering. *Surface and Coatings Technology, 94–95*, 303–308.

2.17 Thermal and Environmental Barrier Coatings for Si-Based Ceramics

Soumendra N. Basu and Vinod K. Sarin, Division of Materials Science and Engineering, Department of Mechanical Engineering, Boston University, Boston, MA, USA

© 2014 Elsevier Ltd. All rights reserved.

2.17.1 Introduction

Gas turbines are currently a $42B industry worldwide with 65% accounting for aircraft engines and 35% for power generation (Clarke, Oechsner, & Padture, 2012). Over the next two decades, a significant increase in electricity demand and a projected doubling of airline traffic is expected to result in substantial growth. Concurrently, the need for higher efficiencies and a reduction in high-altitude NO_x emissions requires that these turbines operate at increasingly higher temperatures.

Figure 1 shows the evolution of gas turbine operation temperatures over time (Zhu, Miller, & Fox, 2008). Superalloy development, with air-cooling capabilities led to a modest increase in temperature capabilities, but plateaued around ~1100 °C (2000 F). Introduction of ceramic matrix composites (CMCs) increased the operational temperature range to ~1300 °C (2400 F). This increase was matched and exceeded demand for high ~1375 °C (2500 F) by the use of thermal barrier coatings (TBCs) on superalloys. Current peak demand on combustion temperatures in aerospace applications is approaching 1650 °C (3000 F). This requires the development of CMCs in conjunction with TBCs. However, since TBCs are not diffusion barriers, they cannot protect the CMCs from high-temperature degradation, and hence need environmental barrier coatings (EBCs) for protection. This chapter discusses the developments in TBCs and EBCs used in hot sections of gas turbines.

TBCs are used to protect the metallic components in the hot sections of gas turbines. Due to their low thermal conductivity, TBCs can maintain a significant temperature drop across their thickness, as seen in **Figure 2** (Padutre, Gell, & Jordan, 2002). This allows the metallic components, typically made of high-temperature superalloys, to be exposed to lower temperatures, thereby increasing the service lifetimes. It has been predicted that a 30–60 °C reduction of the superalloy temperature will double the lifetime of that turbine section (Belmonte, 2006). This is due to a combination of factors, including a reduction of creep, oxidation, corrosion, and thermal fatigue of the substrate (Brindley & Miller, 1989). In fact, the benefits of using a TBC are considered to be equivalent to three decades of superalloy development (Levi, 2004). A characteristic configuration of a TBC coating system with a bond-coat between the superalloy substrate and the low thermal conductivity topcoat is shown in **Figure 2**. The bond-coat, typically made of an aluminide or an Al-rich alloy, helps bond the

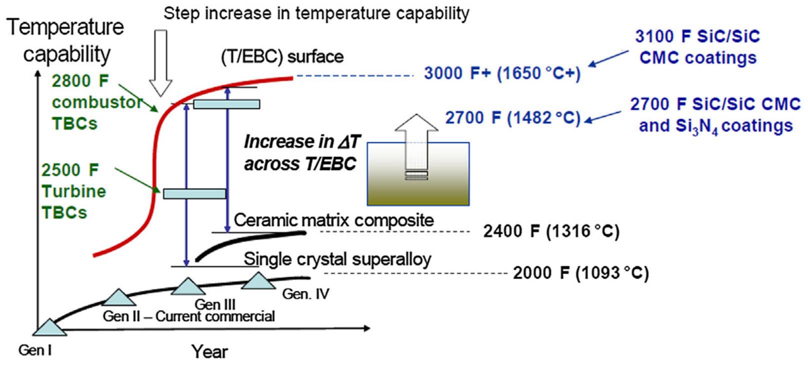

Figure 1 Role of coatings in increasing temperature capabilities of gas turbines (Zhu et al., 2008).

TBC to the substrate by forming a thermally grown oxide that adheres to the ceramic topcoat, and also acts as a diffusion barrier that protects the substrate from the harsh environment.

2.17.2 Environmental Barrier Coatings

The need to go to extreme temperatures (**Figure 1**) necessitates the use of CMCs. These CMCs are typically made of Si-based ceramics, i.e. SiC and Si_3N_4. They form dense SiO_2 (silica) scales when exposed to clean, dry oxygen environments, which act as excellent diffusion barriers, and protect the ceramic substrates from further oxidation. However, sinter additives like yttrium, magnesium, and aluminum can migrate from the grain boundary phase of the substrate to the silica. This causes pore formation and crystallization leading to microcracking of the protective oxide layer, compromising its effectiveness as a diffusion barrier.

Si-based ceramics are also susceptible to hot corrosion in the presence of elements such as Na, Va, and S, leading to the formation of corrosive oxides such as Na_2O, V_2O_5, SO_2, and SO_3. These oxides react with the protective silica scales formed on the Si-based ceramics forming nonprotective low-melting-temperature silicates, leading to severe pit formation, material loss, and increased porosity (Jacobson, 1993). **Figure 3(a)** shows the extensive porosity in an SiC substrate due to hot corrosion (Auger & Sarin, 1997). Additionally, in the presence of high-pressure water vapor, the protective silica scale volatilizes to gaseous Si–O–H species, exposing the ceramic surface (Moore, Tortorelli, Ferber, & Keiser, 2000). This leads to an accelerated oxidation of the ceramic surface to SiO_2, which in turn volatilizes. This repeated cycling of oxidation and volatilization leads to a rapid recession of the surface of the Si-based ceramic. **Figure 3(b)** shows that the extent of surface recession by this mechanism can be extensive over the period of operation of the gas turbines (Robinson & Smialek, 1999).

For the above reasons, CMCs used in gas turbines at high temperatures require protective EBCs. Lee (2000b) summarized the requirements of an effective EBC. The coatings need to resist reacting with the aggressive environments to avoid degrading themselves, and they need to act as excellent diffusion barriers to effectively

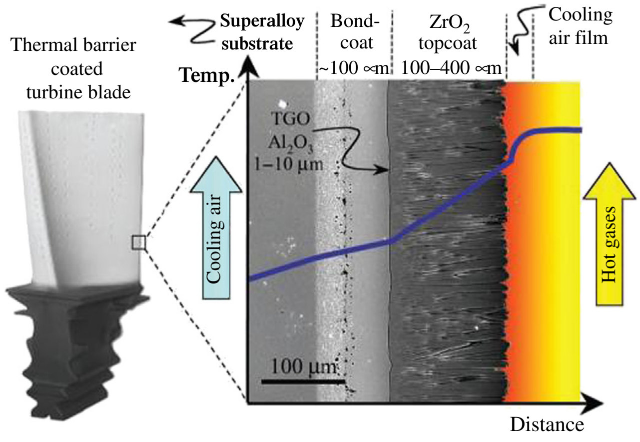

Figure 2 Role of TBC in temperature drop to the substrate (Padutre et al., 2002).

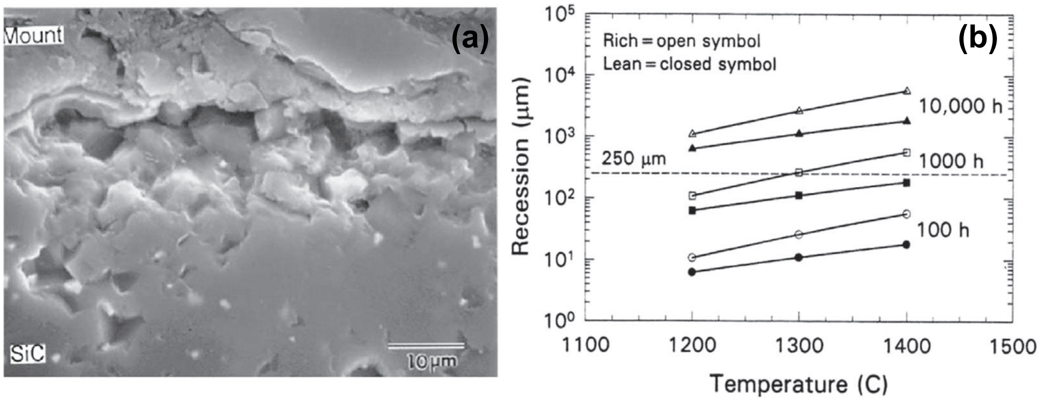

Figure 3 Degradation mechanisms of uncoated SiC under harsh environments at elevated temperatures. (a) SEM micrograph of porosity due to hot corrosion in SiC (Auger & Sarin, 1997). (b) Recession rates of SiC under different operating conditions (Robinson & Smialek, 1999).

separate the substrate from the environment. In addition, the coatings must have a coefficient of thermal expansion (CTE) compatible with the substrate in order to avoid excessive residual stresses on thermal cycling, must maintain phase stability under prolonged high temperature, particularly avoiding the formation of new phases that are accompanied by large volumetric changes, and must be chemically compatible with the substrates to avoid detrimental chemical reactions at the coating/substrate interface during high-temperature exposures.

2.17.2.1 Mullite-Based Chemically Vapor Deposited Coatings

Mullite ($3Al_2O_3{\cdot}2SiO_2$) has received considerable attention as a candidate material for EBCs for protection of Si-based ceramics and composites used in hot sections of gas turbines (Butt, Mecholsky, Roode, & Price, 1990; Price, van Roode, & Stala, 1992). Mullite has a good CTE match, especially with SiC (**Table 1**). Additionally, mullite has excellent corrosion resistance, creep resistance, high-temperature strength and toughness, and can exist over a wide composition range. The last attribute can be exploited for deposition of functionally graded coatings. It is expected that functionally grading the mullite to alumina-rich compositions at the gas/coating interface will decrease the silica activity of the EBC in contact with the aggressive atmosphere and the coating will thus exhibit superior hot corrosion and recession resistance.

Chemical vapor deposition (CVD) is not a line-of-sight deposition process, and lends itself readily for control of coating uniformity and thickness, even on complex parts with edges, corners, and curvatures. Furthermore, the CVD process leads to coatings that have substantially lower residual stresses due to the lack of rapid quenching inherent to the plasma spray process, thereby avoiding porosity and microcracks.

2.17.2.1.1 Coating Deposition

Mullite coatings have been deposited on Si-based ceramic substrates using the $AlCl_3$–$SiCl_3$–CO_2–H_2 system in a hot-wall CVD reactor shown in **Figure 4**. $AlCl_3$ vapor is produced by passing Cl_2 gas over heated Al chips, while

Table 1 Coefficient of thermal expansion and thermal conductivity of substrate and coating materials of interest (de Faoite, Browne, Chang-Díaz, & Stanton, 2012; Jacobson et al., 2005; Lee, Eldridge, et al., 2005)

Material	*CTE (10^{-6} per °C)*	*Thermal Conductivity (W m^{-1} K^{-1})*
SiC	4.3–5.6	40–170
Si_3N_4	3.1–3.3	20–150
YSZ	7.0–10.1	2.2–2.9
Al_2O_3	7.2–9.1	6–19
Mullite	5–6	2.2–2.8
BSAS (monoclinic celsian)	4–5	2.5–3
Y_2SiO_5	5–6	1.6–1.9
Sc_2SiO_5	5–6	2.3–3.5
Yb_2SiO_5	7–8	1.3–1.4
Er_2SiO_5	7–8	1.3–1.4

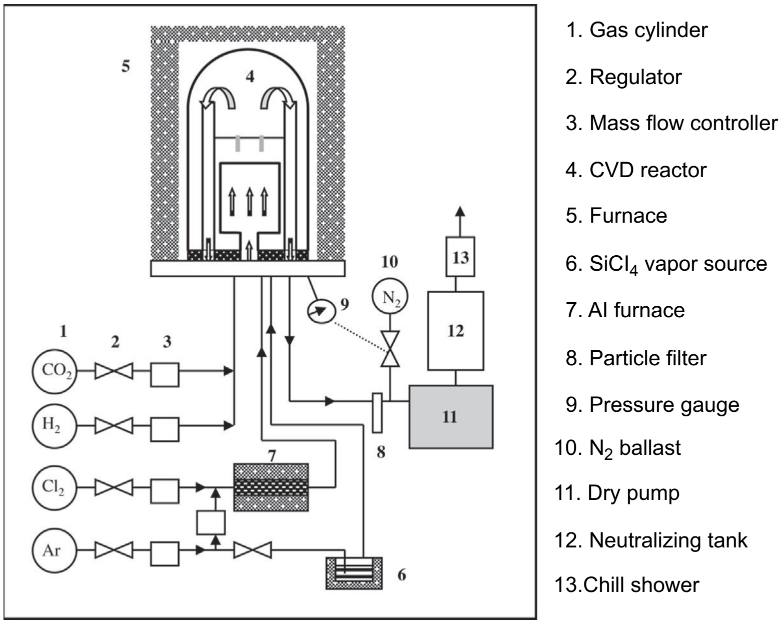

Figure 4 Schematic of the CVD reactor for growth of mullite-based EBCs.

$SiCl_4$ vapor is produced by heating liquid $SiCl_4$ and using Ar carrier gas. The metal chlorides ($AlCl_3$ and $SiCl_4$) are premixed before being introduced into the hot zone of the CVD reactor for mullite deposition using the overall reaction (Basu & Sarin, 2005b; Sarin & Mulpuri, 1998):

$$6AlCl_3(g) + 2SiCl_3(g) + 13CO_2(g) + 13H_2(g) \rightarrow 3Al_2O_3 \cdot 2SiO_2(s) + 13CO(g) + 26HCl(g) \tag{1}$$

Mulpuri and Sarin (1996) carried out detailed thermodynamic analysis of the $AlCl_3$–$SiCl_4$–CO_2–H_2 system and constructed CVD ternary phase diagrams for various partial pressures of H_2. Their analysis showed that CVD mullite deposition should be carried out in the CO_2-rich regime to avoid the incorporation of C and carbides in the coating. They also reported that deposition below 800 °C favors the formation of sillimanite ($Al_2O_3 \cdot SiO_2$) over mullite, and that deposition above 1200 °C did not improve the deposition efficiency, defined as the fraction of Al and Si in the input chlorides ending up as mullite.

Auger and Sarin (2001) studied the kinetics of CVD mullite growth and reported that under the typical deposition conditions of CVD mullite, the kinetic rate-limiting step was the intermediate water gas shift reaction (Tingly, 1966):

$$CO_{2(g)} + H_{2(g)} \rightarrow H_2O_{(g)} + CO_{(g)}. \tag{2}$$

Basu, Kulkarni, Wang, and Sarin (2008) reported the effect of deposition parameters on the growth rate and overall morphology of the coatings. The trends in their findings are summarized qualitatively in Figure 5. A significant increase in the growth rate of the coatings with deposition temperature was observed, consistent with an Arrhenius temperature dependence of growth rate. The increase in the growth rate with temperature also leads to an increase in the coating grain size with temperature. However, a decrease in the coating deposition rate was observed when the deposition temperature was too high due to gas-phase powder formation that depletes the input constituents for coating deposition. Figure 5(e) and (f) shows a desired coated sample with no powder formation, and a coated sample with significant gas phase powder formation, respectively.

A similar increase in the deposition rate of the coatings with increasing total reactor pressure was found up to a critical pressure. At low deposition pressures, the growth is controlled by transport of gaseous species through the boundary layer. Increasing the overall pressure increases the flux through the boundary layer resulting in an increase in the deposition rate. Also, the CVD system increases the total reactor pressure at a constant volumetric flow rate by decreasing the speed of gas removal. Since the residence time of the gaseous species in the reaction zone of the hot-wall CVD reactor is inversely proportional to rate of removal, an increase in the total pressure corresponds to an increase in the residence time of the gases. This increase in the residence time would also lead

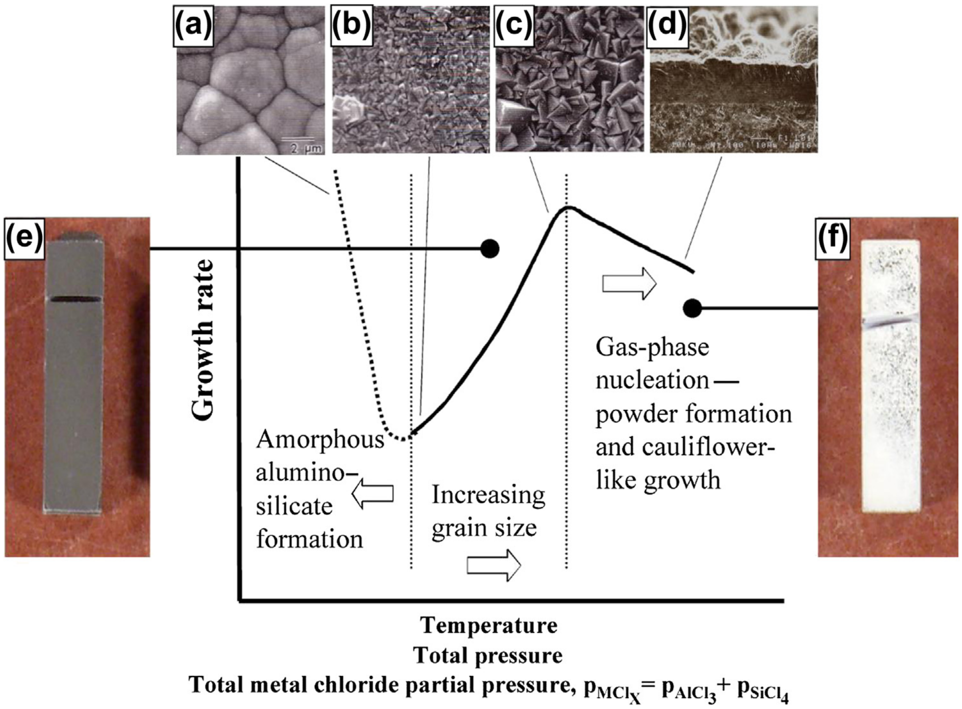

Figure 5 Schematic of the variation of growth rate of CVD-mullite coatings with increasing deposition temperature, total reactor pressure, and total metal chloride partial pressure. (a) Very fast growing amorphous aluminosilicates form at very low metal chloride partial pressures. Increasing the total metal chloride partial pressure leads to (b) crystalline mullite, whose (c) grain size increases with temperature, pressure and total metal chloride partial pressure. (d) However, further increase in these parameters lead to a decrease in deposition rate due to gas phase nucleation and cauliflower-like outgrowths in the coatings. (e) Sample with no gas phase powder formation. (f) Sample with excessive gas phase powder formation (Basu et al., 2008).

to enhanced growth rates. The increase in growth rates is also reflected in a clear increase in the coating grain size with increasing total reactor pressure. However, after a critical pressure is reached, there is a decrease in the coating deposition rate with increasing pressure due to gas phase powder formation accompanied by cauliflower-like growth features on the coating surface (**Figure 5(d)**). These observations are consistent with kinetic modeling of this system reported by Nitodas et al. (Nitodas & Sotirchos, 2000).

2.17.2.1.2 Coating Structure

Mullite coatings have been deposited on Si-based ceramics using CVD. **Figure 6** shows the SEM micrographs of fracture cross-sections of coatings deposited on flat SiC (Basu, Hou, & Sarin, 1999) and highly curved SiC fibers (Varadarajan, Pattanaik, & Sarin, 2001), the latter demonstrating the ability of the CVD process to deposit uniform coatings on parts with complex shapes with large curvatures. The coatings are dense and free of cracks and pores. **Figure 7** shows the coatings to be phase-pure, i.e. all nonsubstrate peaks in the X-ray diffraction (XRD) scan can be indexed to mullite (Doppalapudi & Basu, 1997).

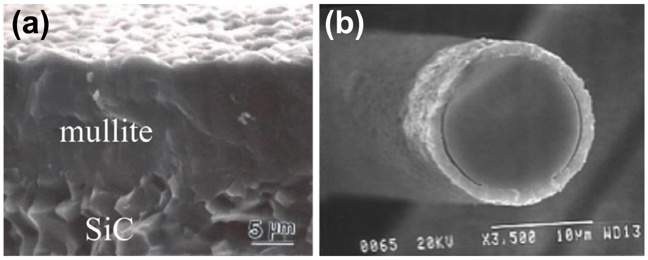

Figure 6 CVD-mullite coatings on (a) planar and (b) curved SiC surfaces.

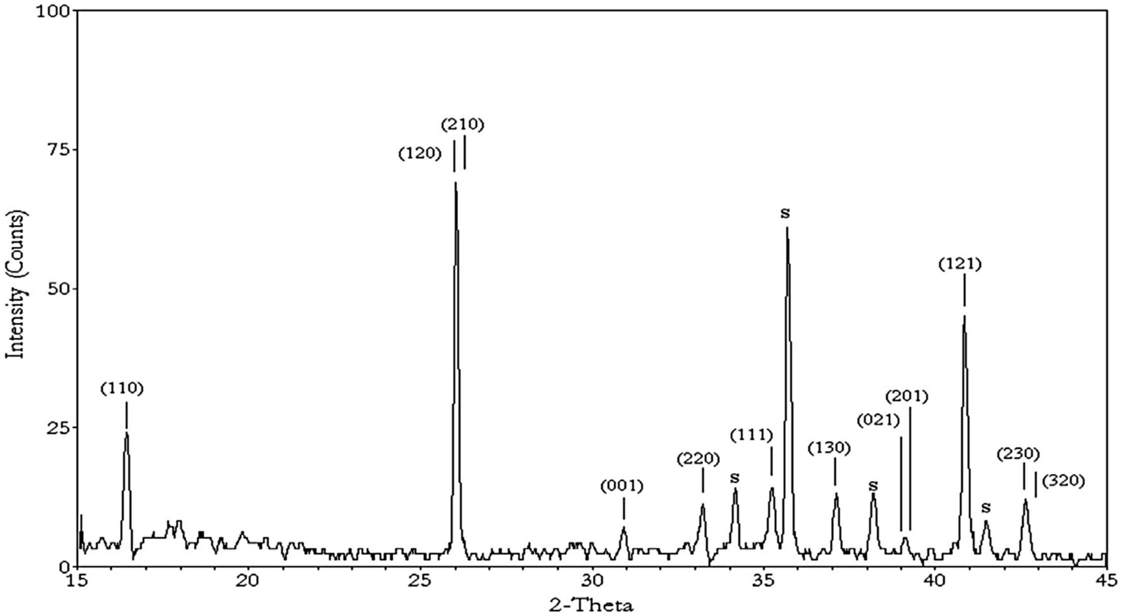

Figure 7 X-ray diffraction scan of a CVD-mullite coating showing that the mullite is phase pure.

Since stoichiometric mullite contains 40 atomic% silica phase, the coating may itself be susceptible to hot corrosion and recession. Hot corrosion of stoichiometric mullite has been reported by Jacobson and Lee (1996), while Haynes et al. (2000) have reported on degradation of stoichiometric mullite in high-pressure, high-temperature air and water vapor mixtures. Reducing the surface-silica content of the mullite coating and reducing the silica activity in the location where the coating is in contact with the aggressive environment will mitigate this problem.

Changing the input gas-phase $AlCl_3/SiCl_4$ ratio into the CVD reactor leads to a change in the composition of the coating. This makes the CVD process ideally suited to functionally grade these mullite coatings from stoichiometric mullite at the substrate/coating interface for CTE match to a low-silica activity coating surface for improved hot corrosion and recession resistance. Figure 8(a) shows such a composition gradation in a coating

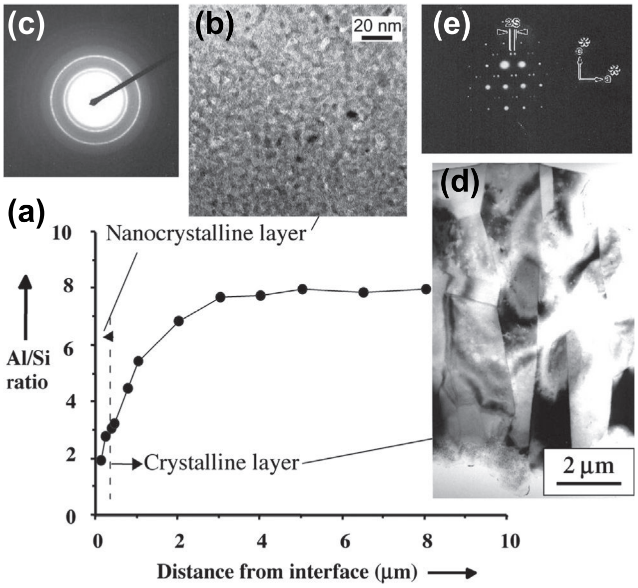

Figure 8 (a) Plot of composition gradation across a functionally graded CVD mullite coating. (b) Cross-sectional TEM micrograph of the nanocrystalline layer showing 5 μm crystallites. (c) SAED pattern of γ-Al_2O_3 in the nanocrystalline layer. (d) Cross-sectional TEM micrograph showing the columnar mullite grains with increasing Al/Si ratio. (e) [010] mullite SAED pattern from a mullite grain.

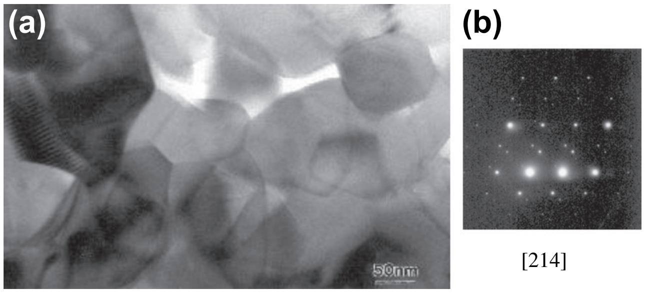

Figure 9 (a) TEM micrograph of the nanocrystalline layer after a 100 h anneal at 1300 °C, with (b) accompanying SAED pattern from a grain, consistent with [214] mullite.

on SiC (Hou, Basu, & Sarin, 2001), where the composition is expressed as the molar ratio of Al/Si. It should be noted that the Al/Si ratio of stoichiometric mullite is 3. The coating is significantly alumina rich at the surface and has an Al/Si ratio of 8.

Hou, Basu, and Sarin (1999) reported that nucleation of the mullite phase does not occur in the coating, unless the composition is in the range Al/Si 3.2 ± 0.3, which is close to the composition of stoichiometric mullite. If the composition of the coating is not close to stoichiometric mullite, the initial growth occurs as an intimate mixture of vitreous SiO_2 and nanocrystalline (~5 nm grain size) γ-Al_2O_3 phases. **Figure 8(b)** shows the transmission electron microscopy (TEM) micrograph of such a "nanocrystalline" layer on an SiC substrate. **Figure 8(c)** shows the selected-area electron diffraction (SAED) pattern from the region, consistent with γ-Al_2O_3.

Annealing mullite coatings for 100 h at temperatures of 1150 °C and above resulted in phase transformations in the nanocrystalline layer. The TEM micrograph in **Figure 9(a)** shows equiaxed mullite grains in the transformed nanocrystalline layer with an accompanying [214] mullite SAED pattern (**Figure 9(b)**) from one such grain formed after a 100 h anneal at 1300 °C (Hou et al., 1999). It is clearly evident from the figure that the transformation occurs with no accompanying microcracking or porosity formation. This phenomenon is consistent with the studies of Wei and Halloran (1988) on mullitization mechanisms in diphasic sol-gels, which transformed into an intimate mixture of γ-Al_2O_3 and vitreous silica. They reported that the nucleation mechanism consisted of three serial steps: dissolution of γ-Al_2O_3 in the vitreous silica matrix, nucleation of mullite after an incubation period, and growth of mullite grains by diffusion in the matrix phase.

The complete mullitization of the nanocrystalline layer is highly desirable in order to avoid the devitrification of silica in the nanocrystalline layer to cristobalite. Devitrification of silica has been known to cause spallation of coatings due to the large stresses that accompany a 3.3% volume reduction that occurs when vitreous silica converts to β-cristobalite, and a further 2.2% volume reduction when β-cristobalite transforms to α-cristobalite (Lynch, 1981). **Figure 10(a)** shows that a CVD mullite coating containing a nanocrystalline layer cracked and spalled when annealed for 100 h at 1400 °C. This is directly attributed to the formation of cristobalite in the

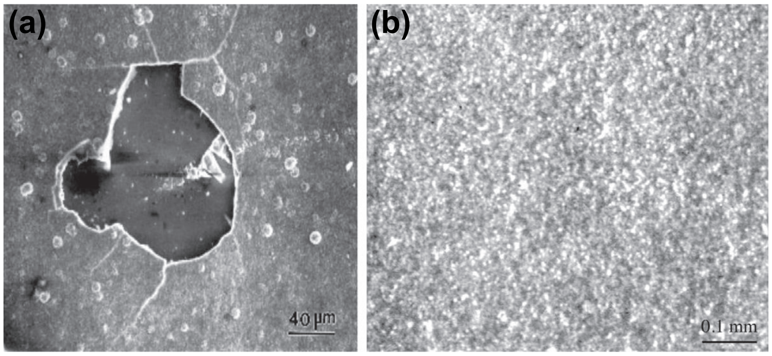

Figure 10 (a) Cracking and spallation in a mullite coating due to devitrification of silica in the nanocrystalline layer when exposed to 1400 °C for 100 h. (b) Mullitization of the nanocrystalline layer led to an intact coating after the same 100 h exposure at 1400 °C.

nanocrystalline layer, as identified by XRD scans (Hou et al., 2001). However, when the same coating was first preannealed for 100 h at 1250 °C, it remained completely adherent and crack free after a subsequent 100 h anneal at 1400 °C, as shown in **Figure 10(b)**. This is attributed to the complete mullitization of the nanocrystalline layer during the 1250 °C preanneal, where the mullitization kinetics are presumably faster than the devitrification kinetics. This is supported by the lack of a cristobalite peak in the XRD scan. Thus, pretreatment of CVD mullite coatings to induce complete mullitization of the nanocrystalline layer is necessary before exposure to temperatures of 1400 °C and higher.

Once the mullite grains nucleate, they can then be made to grow to highly Al-rich nonstoichiometric compositions. Rapid, low-activation energy surface diffusion during the CVD processing allows the ad-atoms to use the coating grain surface as a template for continued growth, even when the ratio of the arrival rates of the Al and Si containing species is far from stoichiometry. The TEM micrograph in **Figure 8(d)** shows some of the columnar mullite grains whose Al/Si ratio was found to increase toward the coating surface. An SAED diffraction pattern from one of the grains is shown in **Figure 8(e)**.

Kulkarni, Wang, Basu, and Sarin (2009) demonstrated that the Al/Si ratio in CVD-deposited functionally graded mullite could be increased to as high as 25 before the mullite structure breaks down. This is the most Al-rich mullite reported in the literature to date. Preliminary XRD and TEM investigations revealed that the structure of this ultrahigh Ai-rich mullite was somewhat similar to γ-Al_2O_3 and δ^*-Al_2O_3 (Argeot, Meercurio, & Dauger, 1990). However, phase transformation studies have clearly indicated that this ultrahigh Ai-rich phase contains Si and therefore is different than either γ-Al_2O_3 or δ^*-Al_2O_3, and falls into the mullite family. Further investigations are necessary to help establish its structure.

One interesting point to consider is that creating Al-rich mullite requires substitution of Al^{+3} cations with Si^{+4} in the mullite structure. Due to charge imbalance, for every two such substitutions, an oxygen vacancy is created. This implies that the concentration of oxygen vacancies should go up significantly in Al-rich mullite. Typically, such an increase in vacancy concentration would correspond to significant increase in oxygen diffusivity in Al-rich mullite, which would make these coatings ineffective as a diffusion barrier. Wang, Kulkarni, Sarin, and Basu (2007) have shown by high-resolution electron microscopy (HREM) that these vacancies order along antiphase boundaries (APB), making them immobile, thus keeping the oxygen diffusivities low and keeping high-Al mullite as an effective diffusion barrier.

2.17.2.1.3 Coating Properties

The mullite coatings are excellent oxidation barriers. **Figure 11** shows the plot of weight gain for mullite-and uncoated Nicalon SiC fibers oxidized in flowing oxygen at 1300 °C (Varadarajan et al., 2001). The uncoated fibers gained weight due to the formation of SiO_2 at the surface, part of which spalled when the samples were cooled. In contrast, the mullite-coated SiC fibers showed practically no weight gain, and exhibited no signs of cracking or spallation after oxidation.

Auger, Sengupta, and Sarin (2000) tested the effectiveness of CVD mullite coatings against corrosion attack by an acidic Fe-based coal slag. As seen in **Figure 12(a)**, after a 300 h exposure at 1260 °C, the uncoated SiC substrates suffered severe material loss and pitting due to coal slag corrosion. Uniform CVD mullite coatings were found to be very effective in protection against the coal slag. The coating did not degrade in the presence of

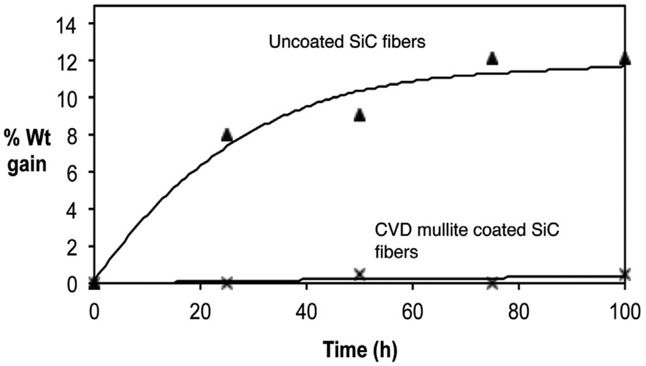

Figure 11 Weight gain versus time plot of mullite coated and uncoated SiC fibers during oxidation at 1300 °C.

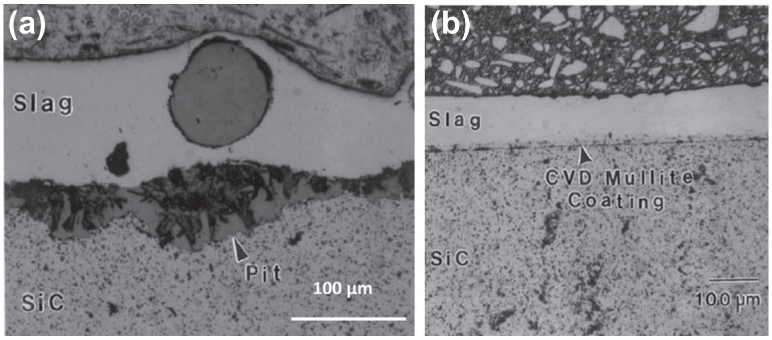

Figure 12 Acidic-slag corrosion of (a) uncoated SiC showing large pit formation, while (b) CVD-mullite-coated SiC was protected (Auger et al., 2000).

the liquid slag and did not allow liquid slag seepage to the SiC substrate, thereby protecting the substrate from pitting, as seen in **Figure 12(b)**. Although some diffusion of Fe to the coating/SiC interface was seen, no cracking or spallation was observed in the uniform mullite coatings.

Kulkarni, Basu, and Sarin (2011) subjected mullite-coated and uncoated SiC substrates to hot-corrosion tests by loading the surface with 5 mg cm^{-2} of Na_2SO_4 and exposing them to 200 sccm of flowing oxygen at 1200 °C for 100 h. **Figure 13(a)** compares the change in weight of coated and uncoated samples, where the composition of the mullite-based EBC surface is given in terms of the Al/Si ratio (i.e. 8:1 corresponds to Al/Si ratio of 8). The figure shows that the degradation rate is roughly linear with silica more fraction (i.e. activity), with pure alumina being completely resistant to hot corrosion. **Figure 13(b)** shows the surface of the uncoated SiC, highlighting severe pit formation. All the coated SiC substrates were completely protected from hot corrosion. However, the surface of the EBC coating shows increasing resistance to hot corrosion with increasing Al/Si ratio, which reflects lowering of the silica activity at the coating surface.

Basu and Sarin (2005a) have reported on the mechanical properties of CVD mullite coatings as a function of composition. A set of nanoindentation scans across polished cross-sections of a functionally graded CVD mullite EBC is shown in **Figure 14(a)**. A typical loading versus displacement curve is shown in **Figure 14(b)**. **Figure 14(c) and (d)** shows that the coating composition (in Al/Si ratio), hardness, and elastic modulus are all proportional, indicating that the properties scale with coating composition, although the absolute values are somewhat lower than in those measured in bulk samples. This is in agreement with measurements reported by Botero et al. (2011).

Botero et al. (2011) also measured the critical load for adhesive failure of the coating/substrate interface, as well as the cohesive failure of the coating by transverse nanoscratch testing. **Figure 15(a)** shows the hardness (and thus the composition) profile across three coatings that can be characterized as uniform stoichiometric mullite, uniform high-Al mullite, and functionally graded mullite. The indenter load was increased incrementally till adhesive failure occurred at the coating/substrate interface on the up stroke

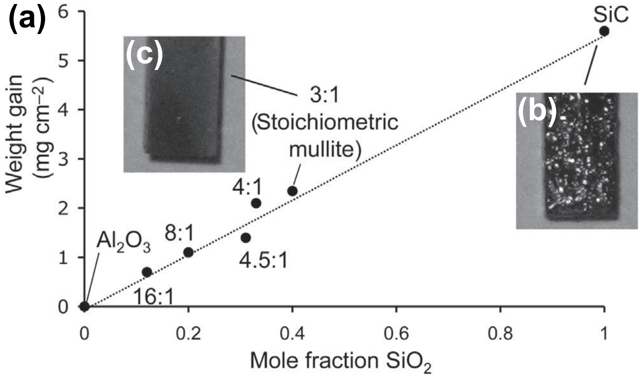

Figure 13 (a) Weight gain due to Na_2SO_4 hot-corrosion for 100 h at 1200 °C in flowing oxygen. (b) Significant pitting occurred on the uncoated SiC, while all coated SiC substrates were protected. (c) The surface of the stoichiometric mullite EBC showed minimal pitting.

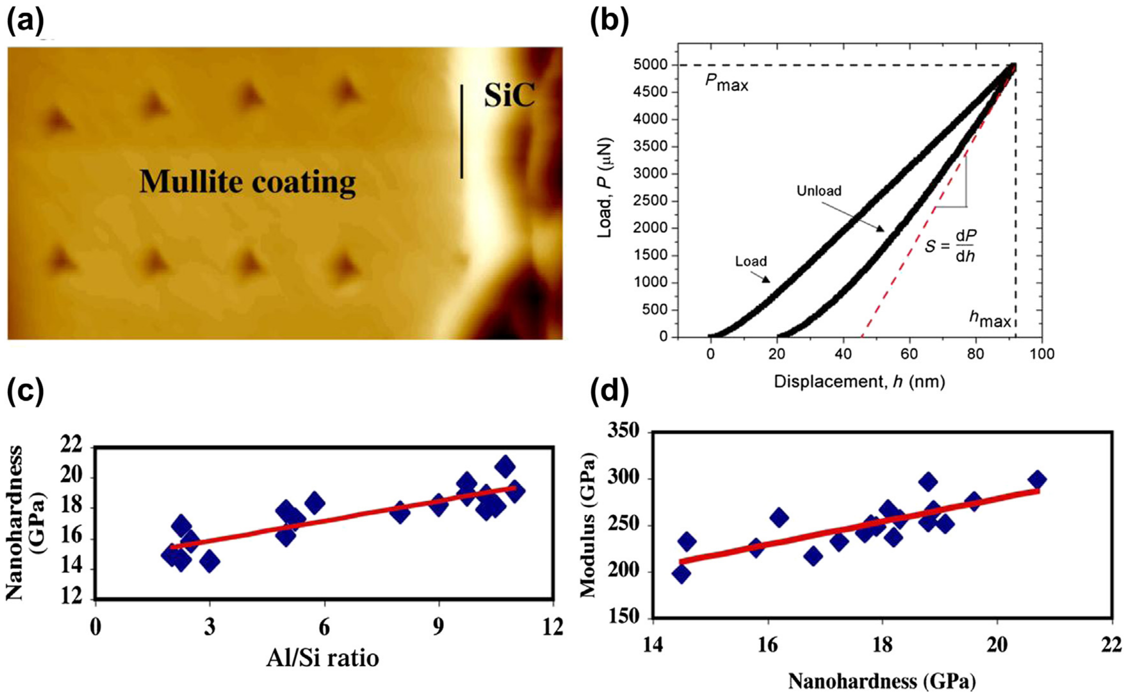

Figure 14 (a) Nanoindents across a functionally graded CVD mullite coating with (b) a typical loading-displacement curve. Plots of (c) hardness versus composition (Al/Si ratio) and (d) elastic modulus versus hardness show that the mechanical properties approximately scale linearly with composition.

(Figure 15(b)), and when cohesive failure occurred with the coating on the down stroke. The authors reported that the stoichiometric mullite coating has the smallest adhesive and cohesive strength, the high-Al mullite had a high cohesive strength but low adhesive strength while the functionally graded coating had the best combination of high adhesive and cohesive strength. This is presumably due to the enhancement in strength with increasing Al content, and the better accommodation of residual stresses by the functionally graded coating.

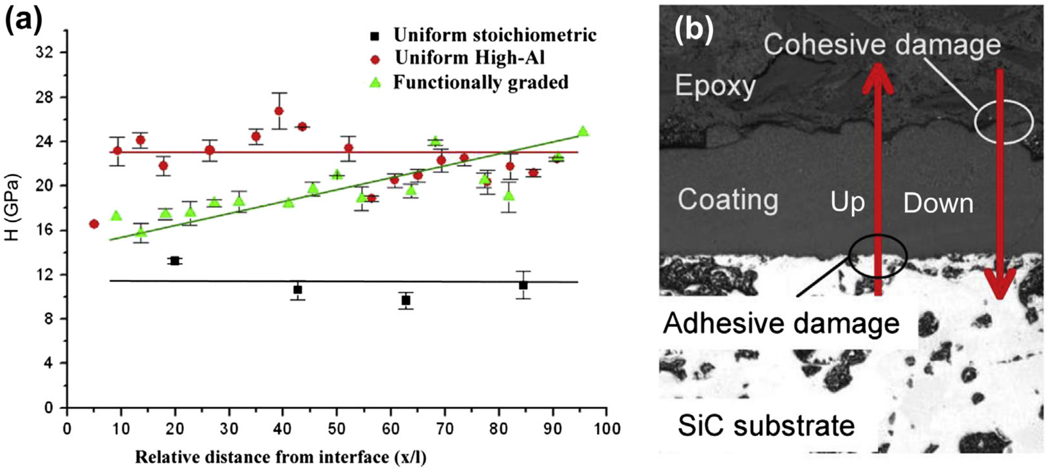

Figure 15 Measurement of adhesive and cohesive strengths of three CVD mullite coatings with different mechanical property distribution. (a) Plot of hardness versus normalized distance across coating thickness showing a uniform stoichiometric coating, a uniform Al-rich mullite coating and a functionally graded mullite coating. (b) The directions of nanoscratch tests, with the UP direction leading to adhesive damage and the down direction leading to cohesive damage (Botero et al., 2011).

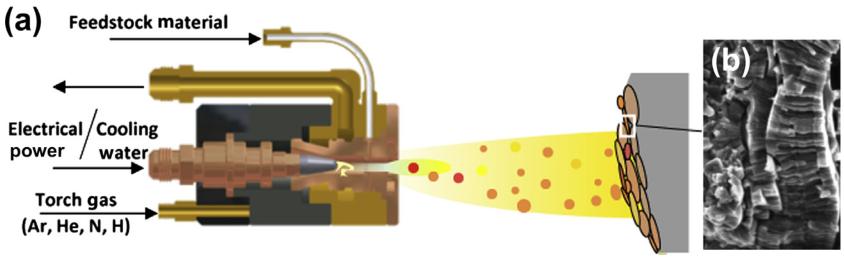

Figure 16 (a) Schematic of the plasma spray deposition process. (b) Fracture cross-section of deposit showing stacking of splats.

2.17.2.2 Plasma-Sprayed EBCs

EBCs have also been deposited by atmospheric plasma spray (APS) deposition processing, shown schematically in Figure 16. The plasma spray process is a line-of-sight process, so it does not have the batch processing capability of the CVD process. On the other hand, almost any material can be deposited at high deposition rates with relatively inexpensive equipment by this process.

2.17.2.2.1 Deposition Process

The plasma spray deposition is one form of thermal spray processing (Davis, 2004), in which powders of coating materials are introduced in a plasma plume (Figure 16(a)). The plasma gas accelerates the particles to high velocities while heating them above their melting temperature. The molten particles impinge on the substrate, and flatten out as splats before rapidly solidifying. The coating is built up by successive deposition of these splats (Figure 16(b)).

2.17.2.2.2 Single-Layer APS Mullite EBCs

Lee, Miller, and Jacobson (1995) first deposited mullite coatings on SiC by air plasma spraying. However, as shown in Figure 17(a), these coatings cracked and debonded after two 24 h thermal cycles between room temperature and 1000 °C. This failure was attributed to the presence of glassy phases in the coatings, formed due to the rapid quenching rates produced when the molten mullite splats solidified on the cold-SiC substrates. Crystallization of these glassy phases to mullite at ~1000 °C, accompanied by a volumetric shrinkage, led to crack formation. In order to eliminate such cracking of the mullite coatings, Lee and coworkers etched the SiC surface with molten Na_2CO_3 to create a rough surface for good mechanical bonding, and then heated the substrate above 1050 °C during deposition. This led to fully crystallized coatings, shown in Figure 17(b) after two 24 h thermal cycles between room temperature and 1000 °C. The reduction in the crack density is obvious from the figure although some through thickness vertical cracks still formed.

Lee and Miller (1996) examined the durability of these fully crystalline plasma-sprayed mullite coatings on SiC and SiC/SiC CMCs under thermal cycling conditions. These coatings exhibited good adherence on the substrates and resistance to cracking. The crack resistance decreased with increasing temperature under higher frequency cycling with an accompanying enhancement in the oxidation rates. These coatings also performed well in hot-corrosion rig tests. The coatings were first subjected to 600 1 h thermal cycles at 1200 °C in air, which

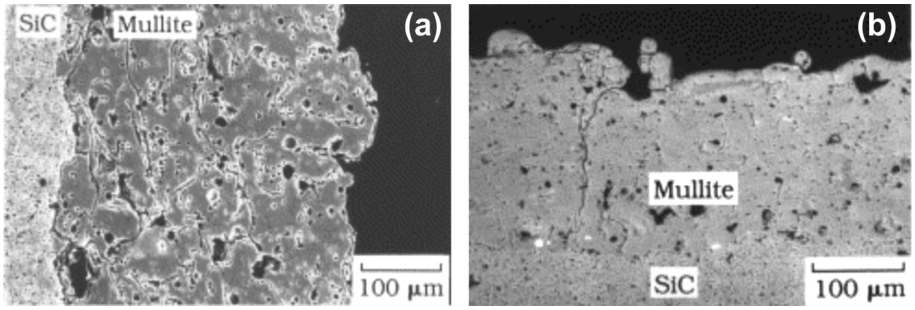

Figure 17 SEM micrographs of plasma-sprayed mullite coating cross-sections on (a) unheated and (b) heated SiC substrates, after two 24 h thermal cycles between room temperature and 1000 °C (Lee et al., 1995).

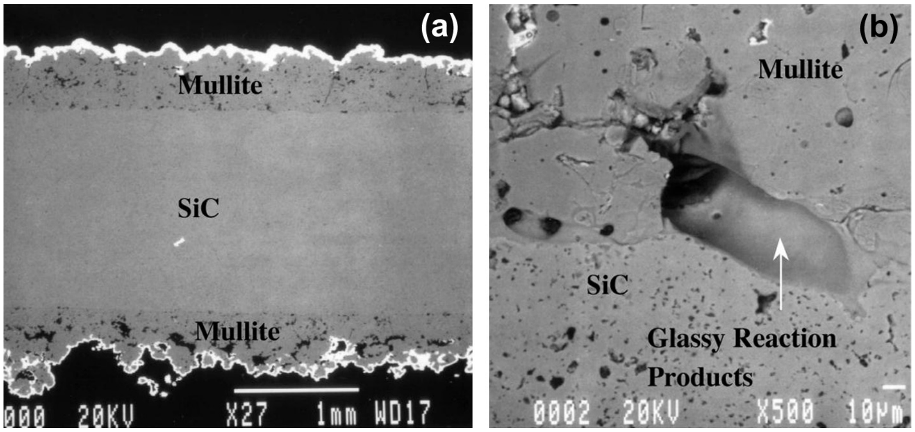

Figure 18 (a) Cross-section of plasma-sprayed mullite coating on SiC after 50 h in a hot corrosion rig at 1000 °C. (b) In areas where through-thickness vertical cracks intersected the interface, glassy sodium silicate phases formed (Lee, 2000b).

led to the formation of some vertical cracks. The samples were then exposed in a hot-corrosion burner rig for 50 h at 1000 °C (Lee, 2000a). The plasma-sprayed mullite coatings protected the substrates for the most part as seen in **Figure 18(a)**, although there was limited attack of the substrate at locations where the vertical cracks intersected the coating/substrate interface, leading to the formation of glassy sodium silicate phases, as seen in **Figure 18(b)**. However, the performance of these coatings were not satisfactory in water vapor-containing atmospheres. As shown in **Figure 19(a)**, plasma-sprayed mullite-coated SiC samples exhibited considerable weight loss in a high-pressure burner rig operating a rich burn condition at 6 atm and 1230 °C (Lee, 2000b). A similar weight loss was also observed after a 2 h cycle exposure in 50% H_2O/O_2 atmosphere at 1300 °C (Lee, 2000a). **Figure 19(b)** shows the cross-section of a mullite-coated SiC sample after the high-pressure burner rig test, where selective volatilization of silica results in the formation of a porous alumina skeleton on the surface.

In order to prevent the selective volatilization of silica from plasma-sprayed mullite, Lee et al. developed a plasma-sprayed yttria-stabilized zirconia (YSZ) overlay coating over the mullite. This reduced silica volatilization considerably in a high-pressure (6 atm) burner rig at 1230 °C, as seen in **Figure 19(a)**. The coating also performed reasonably well when subjected for a total of 100 h to a 2 h cycle exposure in a 90% H_2O/O_2 atmosphere at 1300 °C (Lee, 2000a). Although most interfacial areas exhibited excellent adherence with limited oxidation, some interfacial areas, especially at locations where vertical cracks intersected the interface, exhibited accelerated oxidation leading to the formation of a thick porous silica scale.

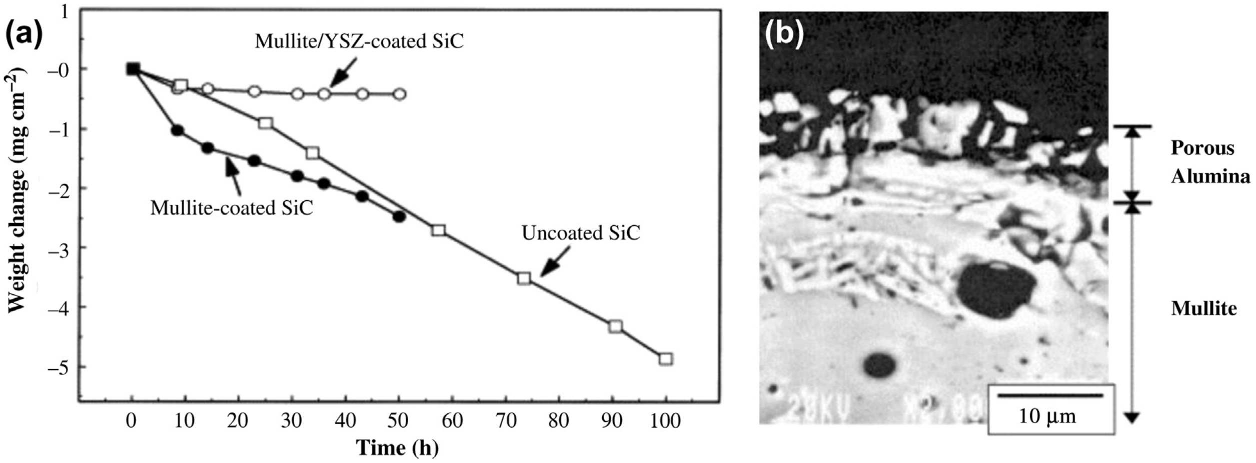

Figure 19 (a) Weight gain versus time plots for uncoated, mullite-coated and mullite/YSZ-coated SiC after exposure at 1230 °C to a high-pressure burner rig at 6 atm for 50 h. (b) Formation of a porous alumina layer on the surface of the plasma-sprayed mullite coating was due to selective volatilization of silica from mullite (Lee, 2000b).

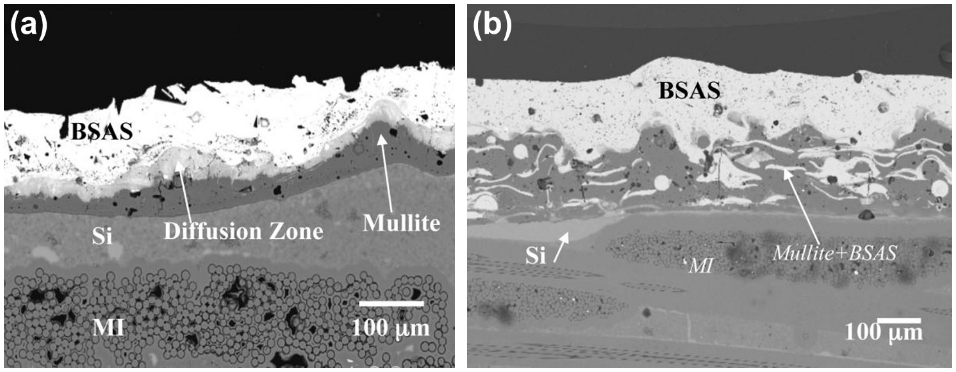

Figure 20 Mullite-based EBC systems consisting of (a) Si/mullite/BSAS and (b) Si/mullite+BSAS/BSAS layers on melt infiltrated (MI) SiC/SiC fiber-reinforced composites, after a 100 h exposure to 1 h cycles at 1300 °C in a 90% H_2O–O_2 atmosphere (Lee et al., 2003).

2.17.2.2.3 Multilayered Plasma-Sprayed EBCs

To improve the crack resistance of the coating, a more crack-resistant overlay coating was developed by Lee et al. (2003). This overlay topcoat, termed as BSAS, is a low-silica activity ceramic of composition $(1-x)$BaO–xSrO–Al_2O_3–SiO_2 $(0 \leq x \leq 1)$, designed to minimize the selective volatilization of silica. The BSAS layer was also more resistant to cracking, presumably due to its low modulus, which enhances the compliance of the coating. Replacing the YSZ topcoat with a BSAS layer delayed the onset of accelerated oxidation in water vapor-containing atmospheres by more than a factor of 2 (Lee et al., 2003). Even further improvement was achieved by adding a Si-bond layer between the mullite and the SiC, as shown in **Figure 22(a)**. This Si layer improved the bond strength between the SiC and mullite, and these coatings exhibited excellent protection of the substrate after a 100 h exposure to 1 h cycles at 1300 °C in a 90% H_2O–O_2 atmosphere. Evidently, the formation of an extensive diffusion zone between the mullite and the BSAS (**Figure 20(a)**) did not appear to affect the durability of the coating system adversely.

Another variant of these multilayered EBCs included an Si bond-coat, a mullite plus BSAS intermediate coat, and a BSAS topcoat, as seen in **Figure 20(b)** (Lee et al., 2003). The coating system exhibited excellent protection of the substrate in water vapor-containing atmospheres at 1300 °C. However, some areas in the mullite/BSAS and Si interface showed the formation of glassy reaction products. This degradation was much more severe at temperatures above 1400 °C. Lee, Eldridge, and Robinson (2005) reported that BSAS exists in two polymorphs, monoclinic celsian, which has a close CTE match with SiC (**Table 1**), and hexagonal celsian with a CTE that is about twice that of the monoclinic phase. In the as-deposited samples, the BSAS phase was mainly a mixture of hexagonal celsian and amorphous phases, with the amorphous phase quickly converting to hexagonal phase at

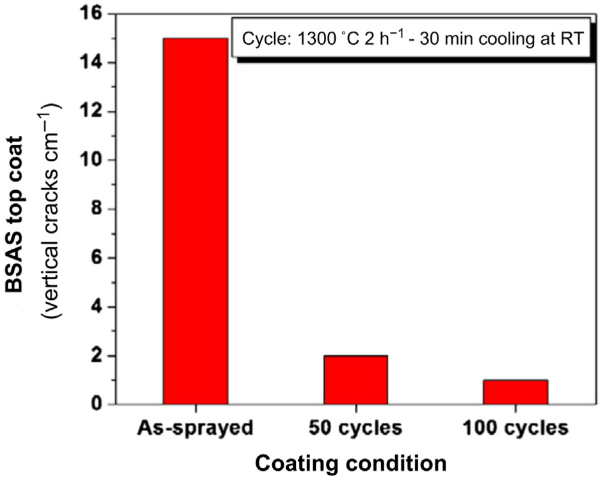

Figure 21 Changes in vertical density in a plasma-sprayed BSAS topcoat after thermal cycling at 1300 °C (Cojocaru et al., 2013).

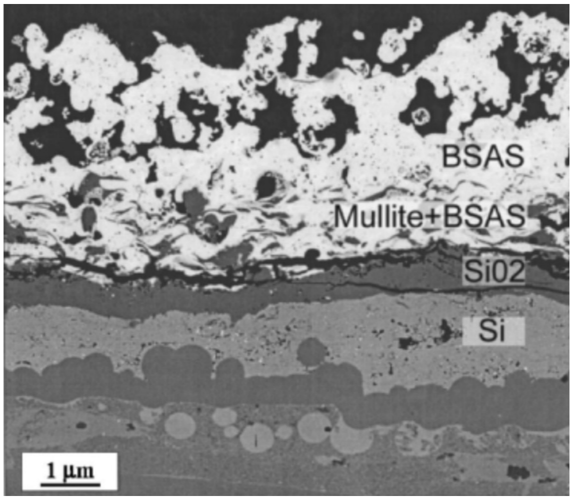

Figure 22 Oxidation of the Si layer to form silica at the Si/(mullite+BSAS) interface of an EBC after a 15,144 h field test with 92 starts (Kimmel et al., 2003).

temperatures above 1200 °C. After exposure to 1400 °C, the hexagonal phase almost completely converted to the monoclinic phase after 24 h.

Lee et al. (2003) concluded that the Si/(mullite+BSAS)/BSAS EBC (**Figure 20(b)**) was more robust than the Si/mullite/BSAS system due to its superior crack resistance, although the former is much more susceptible to formation of glassy phases, especially at higher temperatures. The reduction of cracking in the Si/(mullite+BSAS)/BSAS system was attributed to the reduction of stresses due to the lower elastic modulus [measured to be ~65 GPa (Cojocaru, Kruger, Moreau, & Lima, 2011)] compared to mullite [150 GPa (Lee, Eldridge, et al., 2005)]. Cojocaru, Lévesque, Moreau, and Lima (2013) have reported significant crack-healing characteristics of the BSAS topcoat, with the density of vertical cracks reducing dramatically on cycling the coating at 1300 °C (**Figure 21**). This is related to softening of the celsian phase at temperatures above 1200 °C leading to creep that heals the cracks. Van Roode et al. (2007) have reported results of field tests of these EBCs. They reported that after long-term exposures, a thick silica scale formed due to oxygen diffusion through the microcracks in the topcoat. Such a silica layer with accompanying cracks is shown in **Figure 22** after a 15,144 h field test with 92 starts (Kimmel et al., 2003).

2.17.3 Thermal Barrier/Environmental Barrier Coating Systems

Since EBCs and TBCs both improve the performance and lifetimes of the gas turbines by acting as diffusion barriers and thermal barriers, respectively, a coating system combining both would be better than either individual coating.

2.17.3.1 Mullite/YSZ EBC/TBC Systems

Basu and coworkers (Xu, Dixit, Sarin, & Basu, in preparation) have proposed a coating design for SiC/SiC CMCs, shown schematically in **Figure 23**. The coating system consists of a CVD functionally graded mullite EBC, with the Al/Si ratio increasing toward the EBC surface, with a plasma-sprayed YSZ TBC topcoat, preferably with segmentation cracks for TBC compliance. The advantages of this system include the following:

1. CTE match at the EBC/substrate interface due to the CTE match between SiC and mullite.
2. Improved chemical bonding at the interface between the silica-rich mullite and the Si-based ceramic during CVD growth.
3. CTE gradation across the coating, thereby eliminating abrupt changes in coating composition and phase, resulting in a reduction of growth stresses during deposition and thermal stresses on temperature cycling.
4. CTE match at the EBC/TBC interface due to CTE match between alumina-rich mullite and YSZ.
5. Improved corrosion and recession resistance of the alumina-rich mullite EBC at the EBC/TBC interface in contact with the corrosive atmospheres.

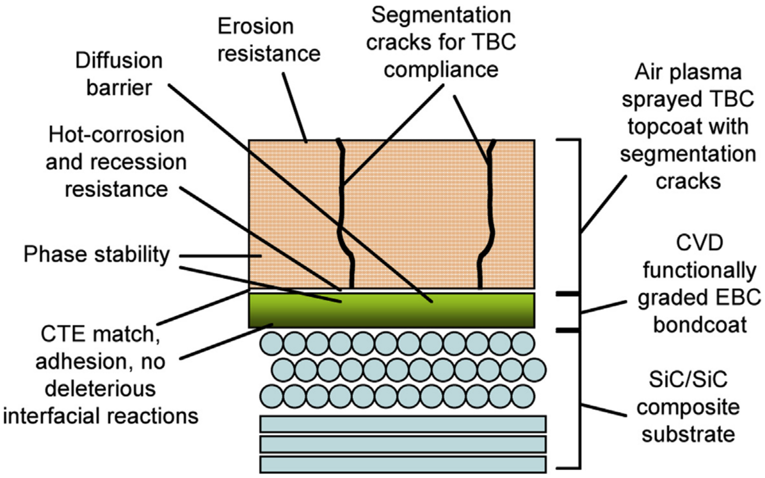

Figure 23 Schematic of TBC/EBC-coating system proposed by Basu et al. (Xu, Dixit, et al., 2013).

6. Uniform, dense, pore and microcrack-free CVD EBC coatings on complex geometries like SiC fibers due to the non-line-of-sight CVD process.
7. Significantly thinner EBC leads to weight savings for aerospace applications.

Figure 24 shows the cross-section of such a coating. The functionally graded CVD coating is about 10 μm thick with a 1 μm nanocrystalline layer, as discussed in Section 2.1.2. The 250 μm-thick APS YSZ coating has microcracks, but no through thickness segmentation cracks. Since the EBC also takes on the role of the bondcoat (Figure 2) and provides a CTE bridge between the SiC and YSZ, it is important that both the TBC/EBC and

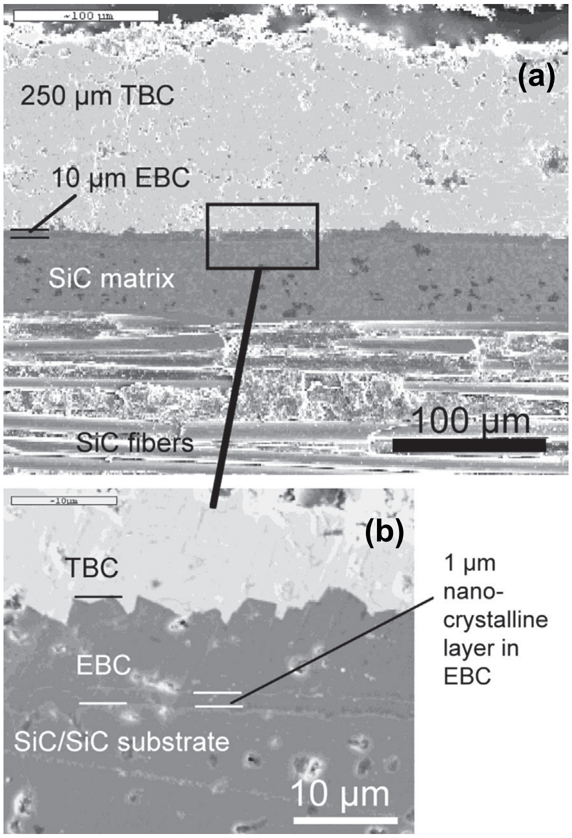

Figure 24 (a) A TBC/EBC coating system, consisting of a plasma-sprayed YSZ TBC, and a functionally graded CVD-mullite EBC on an SiC/SiC CMC. (b) The 10 μm dense EBC coating has a 1-μm-thick nanocrystalline layer.

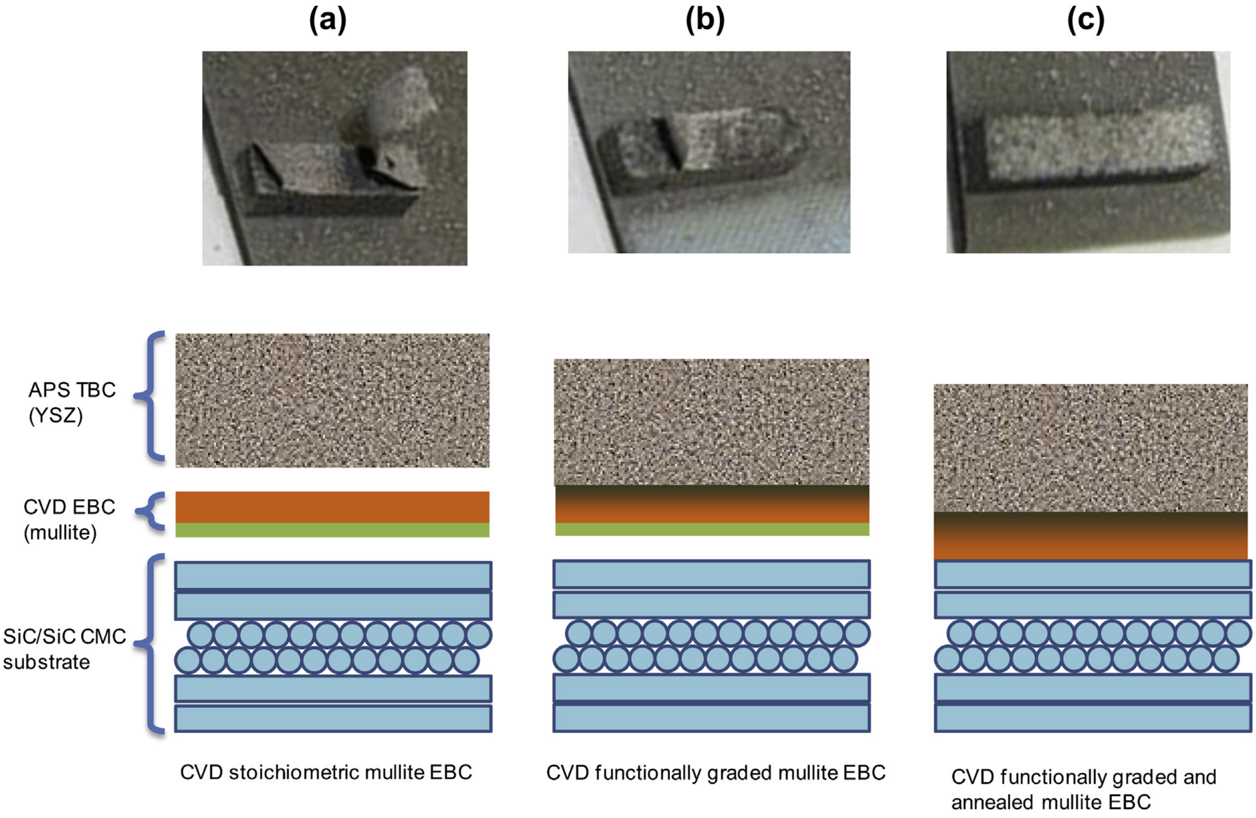

Figure 25 (a) Failure at the stoichiometric mullite EBC/TBC interface due to CTE mismatch, and at the EBC/CMC interface due to silica devitrification. (b) Functionally grading the EBC to alumina-rich mullite keeps the EBC/TBC interface intact, while (c) annealing the EBC to transform the nanocrystalline layer to equiaxed mullite grains keeps the EBC/CMC interface intact.

EBC/CMC interfaces are designed to remain adherent when exposed to thermal shock. Figure 25 shows that the composition gradation and heat treatment of the EBC is critical to achieve this objective. Figure 25(a) shows that an EBC whose composition is close to stoichiometric mullite with a nanocrystalline layer that has not been transformed to equiaxed mullite grains has adhesive failure at both interfaces on thermal shock loading. The TBC/EBC interface fails due to CTE mismatch between mullite and YSZ, while the EBC/CMC interface fails due to devitrification of silica in the nanocrystalline layer. Figure 25(b) shows that functionally grading the mullite to alumina-rich compositions relieves the stresses at the TBC/EBC interface due to CTE match, and keeps that interface intact, while devitrification of the nanocrystalline layer causes adhesive failure if the EBC/CMC interface. Annealing the EBC to transform the nanocrystalline layer to equiaxed mullite allows the EBC/CMC interface to also remain adherent. The functionally graded and annealed EBC/TBC system withstood 50 cycles of rapid 1400 °C plus temperature changes using an oxyacetylene flame, and showed no signs of spallation (Xu, Sarin, & Basu, 2013).

These EBC/TBC coating systems were exposed to molten Na_2SO_4 hot-corrosion tests at 1200 °C for 100 h (Figure 26(a)). Figure 26(b) shows the significant presence of Na in the TBC, which is expected due to the porous nature of APS coatings. However, the sodium migration stopped right above the EBC layer, demonstrating its effectiveness as a diffusion barrier. The EBC itself remained sodium free confirming the resistance of alumina-rich mullite to hot-corrosion. Additionally, no SiC oxidation below the EBC layer was observed (Figure 26(b)) indicating that the EBC also acted as an effective oxygen transport barrier.

2.17.4 Future Directions

Future trends in advanced EBC/TBC coating systems include adding a zirconia or hafnia TBC topcoat that have engineered defect clusters to reduce thermal conductivity over the multilayered BSAS EBCs, and the use of rare-earth silicate to replace BSAS.

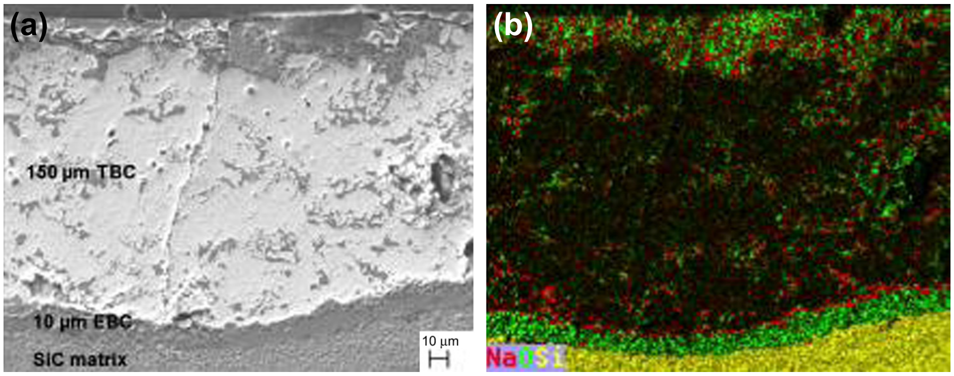

Figure 26 Cross-section of SiC/SiC CMC with a TBC/EBC coating system after exposure to hot-corrosion. (a) SEM of the cross-section (b) EDS mapping overlay of Na, O, and Si.

2.17.4.1 Topcoats with Defect Clusters

Multilayered coating systems containing defect clusters are shown schematically in **Figure 27** (Zhu et al., 2008). The coating consists of a multicomponent zirconia or hafnia-based oxide topcoat that contains the defect clusters. Defect clusters can scatter and attenuate lattice and radiative phonon waves over a wide range of frequencies, thus lowering the intrinsic lattice and the radiative thermal conductivity of the topcoat. These defect clusters, examined by high-resolution transmission electron microscopy (HRTEM), are stable up to 3100 F (1704 °C) (Zhu, Chen, & Miller, 2003). The coating also contains a strain-tolerant interlayer, a mullite/rare-earth silicate environmental barrier layer, and a ceramic oxide/rare-earth silicate-mullite and a silicon bond-coat layer. The thermodynamically stable interfaces also scatter phonons, resulting in a reduction in the thermal radiative thermal conductivity of the coating system.

Figure 28 shows the time evolution of thermal conductivity during exposure at 1316 °C, measured using a laser heat flux technique (Zhu et al., 2008). A coating system containing a defect cluster containing YSZ topcoat has a significant lower thermal conductivity compared to a coating system that has a regular YSZ topcoat. The figure shows that the thermal conductivity increases with time, presumably due to the sintering of the microcracks in the plasma-sprayed coatings. The rate of increase in the thermal conductivity is slightly higher for the coatings with the advanced defect cluster containing topcoats. Moreover, the presence of the strain-tolerant interlayer provides spallation resistance during thermal cycling.

2.17.4.2 Rare-Earth Silicates with Low Volatility

More et al. (2002) reported significant recession of the BSAS topcoat in field tests. **Figure 29** shows the surface of the BSAS topcoat has smoothened considerably after a 40% thickness loss after 13,937 h of service. Rare-earth silicates are being examined to replace BSAS due to their better volatilization resistance as compared to BSAS, making them better for the EBC function. **Figure 30** shows a comparison of the volatilization rate of BSAS compared to some rare-earth silicates in a water vapor/oxygen gas mixture at 1500 °C (Lee, Fox, et al., 2005).

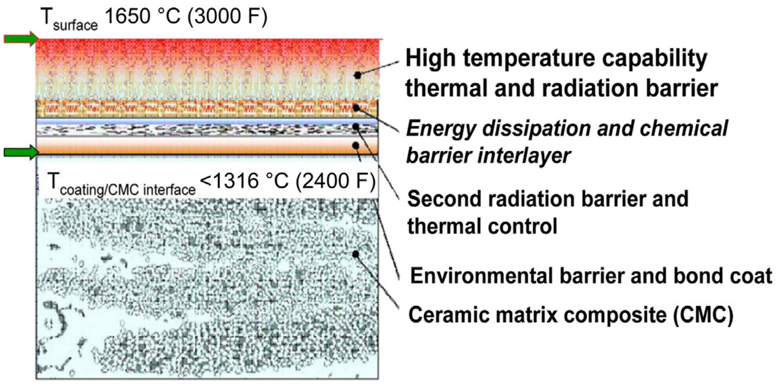

Figure 27 Multilayered TBC/EBC architecture with topcoat containing defect clusters (Zhu et al., 2008).

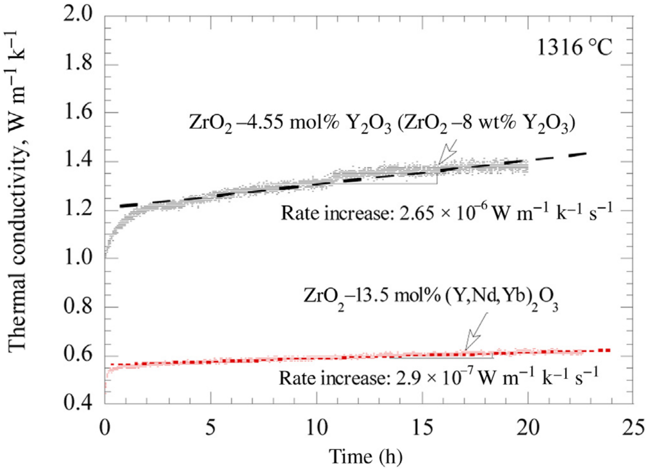

Figure 28 Thermal conductivity of plasma-sprayed oxide cluster thermal barrier coatings, determined by laser heat-flux technique (Zhu et al., 2008).

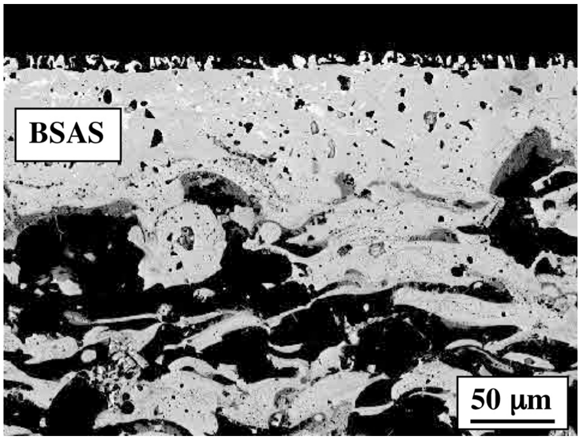

Figure 29 Recession of the BSAS topcoat after 13,937 h of service (More et al., 2002).

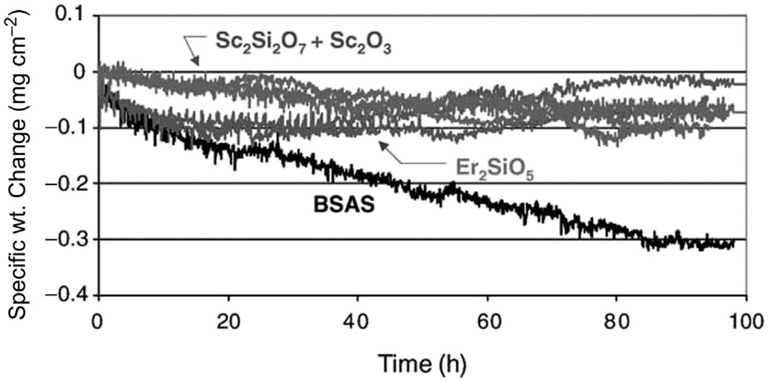

Figure 30 Comparison of volatility of BSAS with some rare-earth silicates exposed to 50% H_2O-balance O_2 at 1 atm total pressure, flowing at 4.4 cm s^{-1} at 1500 °C (Lee, Fox, et al., 2005).

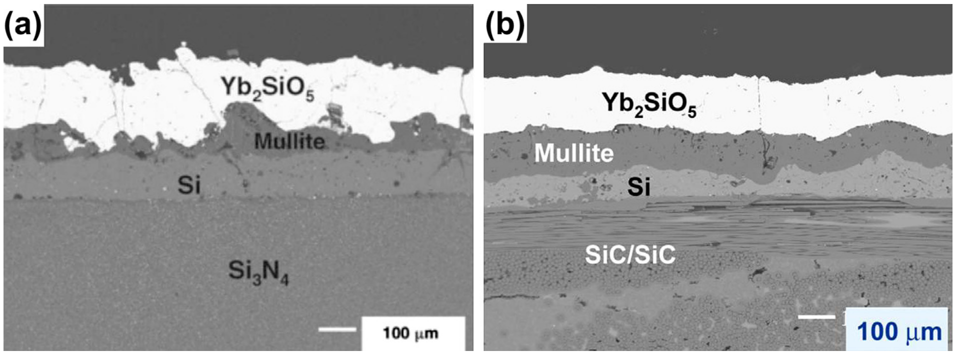

Figure 31 Plasma sprayed Yb_2SiO_5 topcoat with a mullite/silicon interlayer on (a) Si_3N_4, showing extensive cracking, and on (b) SiC/SiC CMC, showing significantly reduced cracking (Jacobson et al., 2005).

These rare-earth silicates tend to have lower thermal conductivities than BSAS making them also attractive for the EBC function (**Table 1**). However, they tend to have higher CTE values compared to BSAS, making them susceptible to crack formation, especially on Si_3N_4 (**Figure 31(a)**) (Lee, Fox, et al., 2005). The propensity of crack formation is significantly lower when deposited on SiC CMCs (**Figure 31(b)**) (Jacobson et al., 2005, pp. 565–578). Ramasamy, Tewari, Lee, Bhatt, and Fox (2011) have reported good oxidation resistance of mullite/Gd_2SiO_2 EBCs on SiC/SiC CMCs.

2.17.5 Conclusions

EBCs and TBCs will continue to play a major role in protecting Si-based ceramics that are increasingly being used in hot sections of gas turbines due to ever-increasing temperature demands. The major requirements for these coating systems are low silica activity for hot-corrosion and recession resistance for environmental protection, and low thermal conductivity for thermal protection from the harsh environments. These coating systems must also have good CTE match at the interfaces to minimize stresses.

Functionally graded CVD mullite and plasma-sprayed BSAS/mullite+BSAS/silicon EBCs have shown considerable promise as EBCs. Current research is focused on replacing BSAS with lower volatility rare-earth silicates, especially on SiC/SiC CMCs, as well as on multilayered EBC/TBC coating systems, where the thermal conductivity of the TBC can be further lowered by forming defect complexes by doping the TBC material.

References

Argeot, D., Meercurio, D., & Dauger, A. (1990). Structural characterization of alumina metastable phase in plasma sprayed deposits. *Materials Chemistry and Physics, 24*, 299–314.

Auger, M. L., & Sarin, V. K. (1997). The development of CVD mullite coatings for high temperature corrosive applications. *Surface and Coatings Technology, 94–95*, 46.

Auger, M. L., & Sarin, V. K. (2001). A kinetic investigation of CVD mullite coatings on Si-based ceramics. *International Journal of Refractory Metals & Hard Materials, 19*(4–6), 479–494.

Auger, M. L., Sengupta, A., & Sarin, V. K. (2000). Coal slag protection of SiC with chemically vapor deposited mullite coatings. *Journal of the American Ceramic Society, 83*(10), 2429–2435.

Basu, S. N., Hou, P., & Sarin, V. K. (1999). Formation of mullite coatings on silicon based ceramics by chemical vapor deposition. *Journal of Refractory Metals and Hard Materials, 16*(4–6), 343–352.

Basu, S. N., Kulkarni, T., Wang, H. Z., & Sarin, V. K. (2008). Functionally graded chemical vapor deposited mullite environmental barrier coatings for Si-based ceramics. *The Journal of the European Ceramic Society, 28*, 437–445.

Basu, S. N., & Sarin, V. K. (2005a). Advanced high temperature coatings in power generation gas turbines. In *Proceedings of the 8th operating pressure equipment conference* (pp. 10–16). Institute of Materials Engineering Australasia Ltd.

Basu, S. N., & Sarin, V. K. (2005b). Mullite coatings. In H. Schneider, & S. Komarneni (Eds.), *Mullite*. Weinheim, Federal Republic of Germany: Wiley-VCH.

Belmonte, M. (2006). Advanced ceramic materials for high temperature applications. *Advanced Engineering Materials*.

Botero, C. A., Jimenez-Piqué, E., Kulkarni, T., Fargas, G., Sarin, V. K., & Llanes, L. (2011). Cross-sectional nanoindentation and nanoscratch of compositionally graded mullite films. *Surface & Coatings Technology, 206*, 1927–1931.

Brindley, W. J., & Miller, R. A. (1989). TBCs for better engine efficiency. *Advanced Materials & Processes, 8*, 29.

Butt, D. P., Mecholsky, J., Roode, M., & Price, J. R. (1990). Effects of plasma-sprayed ceramic coatings on the strength distribution of silicon carbide materials. *Journal of the American Ceramic Society, 73*, 2690–2696.

Clarke, D. R., Oechsner, M., & Padture, N. (Eds.). (2012), *Thermal barrier coatings for more efficient gas turbine engines* (Vol. 37). MRS Bulletin.

Cojocaru, C. V., Kruger, S. E., Moreau, C., & Lima, R. S. (2011). Elastic modulus evolution and behavior of Si/mullite/BSAS-based environmental barrier coatings exposed to high temperature in water vapor environment. *Journal of Thermal Spray Technology, 1–2*, 92–99.

Cojocaru, C. V., Lévesque, D., Moreau, C., & Lima, R. S. (2013). Performance of thermally sprayed Si/mullite/BSAS environmental barrier coatings exposed to thermal cycling in water vapor environment. *Surface & Coatings Technology, 216*, 215–223.

Davis, J. R. (Ed.). (2004). *Handbook of thermal spray technology.* ASM International, No. 06994G.

de Faoite, D., Browne, D. J., Chang-Díaz, F. R., & Stanton, K. T. (2012). A review of the processing, composition, and temperature-dependent mechanical and thermal properties of dielectric technical ceramics. *Journal of Materials Science, 47*(10), 4211–4235.

Doppalapudi, D., & Basu, S. N. (1997). Structure of mullite coatings grown by chemical vapor deposition. *Materials Science and Engineering, A231*, 48–54.

Haynes, J. A., Lance, M. J., Cooley, K. M., Ferber, M. K., Lowden, R. A., & Stinton, D. P. (2000). CVD mullite coatings in high-temperature, high-pressure air-H_2O. *Journal of the American Ceramic Society, 83*(3), 657–659.

Hou, P., Basu, S. N., & Sarin, V. K. (1999). Nucleation mechanisms in chemically vapor-deposited mullite coatings on SiC. *Journal of Materials Research, 14*(7), 2952.

Hou, P., Basu, S. N., & Sarin, V. K. (2001). Structure and high temperature stability of compositionally graded CVD mullite coatings. *International Journal of Refractory Metals and Hard Materials, 19*(4–6), 467–477.

Jacobson, N. S., & Lee, K. N. (1996). Corrosion of mullite by molten salts. *Journal of the American Ceramic Society, 79*(8), 2161–2167.

Jacobson, N. S., Fox, D. S., Smialek, J. L., Opila, E. J., Dellacorte, C., & Lee, K. N. (2005). In S. D. Cramer, & B. S. Covino, Jr. (Eds.), *ASM handbook* (Vol. 13B). Materials Park, OH: ASM International.

Jacobson, N. S. (1993). Corrosion of silicon-based ceramics in combustion environment. *Journal of the American Ceramic Society, 76*(1), 3–28.

Kimmel, J., Sun, E., Linsey, G. D., More, K., Tortorelli, P., & Price, J. (2003). *The evaluation of CFCC liners after field testing in a gas turbine IV.* ASME Paper No. GT20-3-38920.

Kulkarni, T., Wang, H. Z., Basu, S. N., & Sarin, V. K. (2009). Compositionally graded mullite based CVD coatings. *Journal of Materials Research, 24*(2), 470–474.

Kulkarni, T., Basu, S. N., & Sarin, V. K. (2011). Protective Al-rich mullite coatings on Si-based ceramics against hot corrosion at 1200 °C. *Surface & Coatings Technology, 205*, 3313–3318.

Lee, K. N. (2000a). Current status of environmental barrier coatings for Si-based ceramics. *Surface and Coatings Technology, 133–134*, 1–7.

Lee, K. N. (2000b). Key durability issues with mullite-based environmental barrier coatings for Si-based ceramics. *Transactions of the ASME, 122*, 632–636.

Lee, K. N., Eldridge, J. I., & Robinson, R. C. (2005). Residual stresses and their effects on the durability of environmental barrier coatings for SiC ceramics. *Journal of the American Ceramic Society, 88*(12), 3483–3488.

Lee, K. N., Fox, D. S., & Bansal, N. P. (2005). Rare earth silicate environmental barrier coatings for SiC/SiC composites and Si_3N_4 ceramics. *Journal of the European Ceramic Society, 25*, 1705–1715.

Lee, K. N., Fox, D. S., Eldridge, J. I., Zhu, D., Robinson, R. C., Bansal, N. P., et al. (2003). Upper temperature limit of environmental barrier coatings based on mullite and BSAS. *Journal of the American Ceramic Society, 86*(8), 1299–1306.

Lee, K. N., & Miller, R. A. (1996). Oxidation behavior of mullite-coated SiC and SiC/SiC composites under thermal cycling between room temperature and 1200°–1400 °C. *Journal of the American Ceramic Society, 79*(3), 620–626.

Lee, K. N., Miller, R. A., & Jacobson, N. S. (1995). New generation of plasma-sprayed mullite coatings on silicon carbide. *Journal of the American Ceramic Society, 78*(3), 705–710.

Levi, C. G. (2004). Emerging materials and processes for thermal barrier systems. *Current Opinion in Solid State and Materials Science, 8*, 77–91.

Lynch, J. F. (Ed.). (1981), *Single oxides: Vol. III. Engineering property data on selected ceramics*. Columbus, Ohio: Battelle Columbus Laboratories. Metals and Ceramics Information Center Report MCIC-HB-07.

Moore, K. L., Tortorelli, P. F., Ferber, M. K., & Keiser, J. R. (2000). Observation of accelerated silicon carbide recession by oxidation at high water-vapor pressures. *Journal of the American Ceramic Society, 83*, 211–213.

More, K. L., Tortorelli, P. F., Walker, L. R., Kimmel, J. B., Miriyala, N., Price, J. R., et al. (2002). *Evaluating environmental barrier coatings on ceramic matrix composites after engine and laboratory exposures.* Proceedings of ASME TURBO EXPO 2002. GT-2002–30630.

Mulpuri, R. P., & Sarin, V. K. (1996). Synthesis of mullite coatings by chemical vapor deposition. *Journal of Materials Research, 11*(6), 1315.

Nitodas, S. F., & Sotirchos, S. V. (2000). Chemical vapor deposition of aluminosilicates from mixtures of $SiCl_3$, $AlCl_3$, CO_2 and H_2. *Journal of Electrochemical Society, 147*(3), 1050–1058.

Padutre, N. P., Gell, M., & Jordan, E. H. (2002). Thermal barrier coatings for gas-turbine engine applications. *Science, 296*(5566), 280–284.

Price, J. R., van Roode, M., & Stala, C. (1992). Ceramic oxide-coated silicon carbide for high temperature corrosive environments. *Key Engineering Materials, 72–74*, 71–84.

Ramasamy, S., Tewari, S. N., Lee, K. N., Bhatt, R. T., & Fox, D. S. (2011). Mullite–gadolinium silicate environmental barrier coatings for melt infiltrated SiC/SiC composites. *Surface and Coatings Technology, 205*, 3578–3581.

Robinson, R. C., & Smialek, J. L. (1999). SiC recession caused by SiO2 scale volatility under combustion conditions: I, experimental results and empirical model. *Journal of the American Ceramic Society, 82*(7), 1817–1827.

Sarin, V. K., & Mulpuri, R. P. (1998). Chemical vapor deposition of mullite coatings. US Patent No. 576008.

Tingly, G. L. (1966). Kinetics of the water-gas equilibrium reaction. I; the reaction of carbon dioxide with hydrogen. *The Journal of Physical Chemistry, 70*(6), 140–142.

van Roode, M., Price, J., Kimmel, J., Miriyala, N., Leroux, D., Fahme, A., et al. (2007). Ceramic matrix composite combustor liners: a summary of field evaluations. *Journal of Engineering for Gas Turbines and Power, 129*(1), 21–30.

Varadarajan, S., Pattanaik, A. K., & Sarin, V. K. (2001). Mullite interfacial coatings for SiC fibers. *Surface & Coatings Technology, 139*, 153–160.

Wang, H. Z., Kulkarni, T., Sarin, V. K., & Basu, S. N. (2007). Ordered and twinned multi domain structure in highly Al-rich mullite. *Journal of Materials Research, 22*(11), 3210–3217.

Wei, W. C., & Halloran, J. W. (1988). Phase transformation of diphasic aluminosilicate gels. *Journal of the American Ceramic Society, 71*(3), 166–172.

Xu, J. P., Dixit, S., Sarin, V. K., & Basu, S. N. CVD mullite coating as EBC of EBC/TBC dual coating system for SiC/SiC ceramic matrix composite materials, in preparation.

Xu, J. P., Sarin, V. K., & Basu, S. N. (2013). Stability study of EBC/TBC hybrid system on Si-based ceramics in gas turbines. *MRS Proceedings, 1519*. http://dx.doi.org/10.1557/opl.2012.1717.

Zhu, D., Chen, Y. L., & Miller, R. A. (2003). Defect clustering and nano-phase structure characterization of multicomponent rare-earth oxide doped zirconia-yttria thermal barrier coatings. *Ceramic Engineering and Science Proceedings, 24*.

Zhu, D., Miller, R. A., & Fox, D. S. (2008). *Thermal and environmental barrier coating development for advanced propulsion engine systems*. NASA/TM—2008–215040.

This page intentionally left blank

2.18 Ceramic Cutting Tools

Dow Whitney, Retired from Department of Materials Science and Engineering at the University of Florida, Gainesville, Florida, USA

© 2014 Elsevier Ltd. All rights reserved.

Glossary[1]

Cemented carbide A cemented or compacted mixture of powdered binary compounds of carbon and a heavy metal forming a hard material used in metal cutting tools.

Ceramic A product made by the baking or firing of a nonmetallic mineral or man-made material.

Ceramic tool A cutting tool made from a nonmetallic mineral or man-made material.

Cutting tool The part of a machine tool which comes into contact with and removes material from the workpiece by the use of a cutting medium.

Diffusion couple An arrangement for measuring the actual transport of mass, in the form of discrete atoms from the lattice of one crystalline solid to another.

Fracture toughness The resistance of a solid body to the initiation and/or propagation of a crack due to mechanical failure by stress. It is denoted K_{Ic} and has the units of Pa $\mathrm{m}^{1/2}$.

Hot pressing Forming a ceramic powder compact into a particular shape by applying pressure and heat simultaneously at temperatures high enough for sintering (forming a coherent bonded mass by heating powders without melting) to occur.

Isoelectronic Pertaining to atoms having the same number of electrons outside the nucleus of the atom.

Knoop/Vickers hardness values The relative microhardness of a material such as a metal or ceramic determined by the depth to which a diamond-pyramid indenter penetrates.

Machine tool A stationary power-driven machine for shaping, cutting, turning, boring, drilling, grinding or polishing of solid parts, especially metals.

Mohs hardness scale An empirical scale consisting of 10 minerals with reference to which the hardness of all other minerals is measured; it includes, from softest, talc (designated 1), to hardest, diamond (designated 10). On the "modified" Mohs hardness scale, diamond is designated 15.

Phase transformation The change of a solid substance from one crystalline structure to another. Also known as polymorphism, such as diamond and graphite.

Plastic shearing Permanent change in shape or size of a solid body without fracturing resulting from the application of sustained stress beyond the elastic limit.

Surface friction A force which opposes the relative motion of two solid bodies in contact.

Wear mechanism A detailed description of the course of deterioration of a surface due to material removal caused by relative motion between it and another part.

Weibull statistics A distribution that describes lifetime characteristics of parts and components.

Workpiece The solid part in the machine tool system which is being shaped, cut, ground, etc.

---

[1] The definitions/explanations of technical terms (dictionary style) in the glossary, as well as the nomenclature used in the chapter, were taken from: Parker, Sybil P. (Editor in Chief). (1993). Dictionary of scientific and technical terms, 5th edition. New York, NY: McGraw-Hill, Inc. In a few instances, the definitions were modified slightly to put them in compliance with how the term was used in the manuscript.

http://dx.doi.org/10.1016/B978-0-08-096527-7.00037-4

Nomenclature

ASTM American Society for Testing of Materials.

Bar A unit of pressure equal to 10^5 Pa.

GPa Defined as 10^9 Pa.

MPa Defined as 10^6 Pa.

Pascal Pascal is the unit of pressure equal to the pressure resulting from the force of 1 N acting uniformly over an area of 1 m^2.

1 MPa 145 lb $in.^{-2}$

1 GPa 145×10^3 lb $in.^{-2}$

R_C (Rockwell hardness) Arbitrarily defined measure of the hardness of a material by measuring the resistance of the material to indentation (usually via a steel ball) under static load.

Thermal conductivity Defined as the measurement of heat flow across a surface per unit area per unit time per unit temperature difference across the surface.

Thermal expansion The dimensional changes exhibited by a solid for changes in temperature while pressure is held constant.

2.18.1 Introduction and Overview

This chapter deals with a particular type of ceramic product, the ceramic cutting tool, often simply referred to as an "insert" in the metalworking trade. In spite of its small size (almost infinitesimal compared to the size of a typical heavy-duty high-speed machine tool lathe), it is the most important component of the overall cutting tool/machine tool system.

The cutting tool is the critical link between raw materials and the finished product. The rate determining factor in the chip-making process is the cutting tool material itself. Thus, the metalworking operation has always been dependent on the maximum capabilities of new tool materials.

Machine tools and procedures have always been designed around the maximum capabilities of new tool materials. Obviously, to achieve high productivity, a tool must be able to cut at high speed. Since about 1900, there has been an exponential increase in productivity capability as measured by the cutting speeds available.

A tool material must meet several stringent requirements that are dictated by the cutting processes. The deformation energy due to extensive plastic deformation ahead of the tool and the frictional energy due to interactions at the tool-chip and machined surface are converted into heat. Although most of the heat dissipates with the chip, some heat concentrates over an extremely small area near the tool tip, with the tool tip temperature increasing to approximately 1000 °C. Apart from the heating effect, the mechanical stresses at the tool tip are very high. To be effective, cutting tool materials must meet the following basic requirements:

- high hardness for efficient cutting action;
- high mechanical resistance to cutting forces;
- high resistance to wear, fracture and chipping; and
- high hardness and strength at operating temperatures.

The wear resistance of a cutting tool depends on hardness, physical and chemical stability, as well as effective toughness during the actual metal cutting operation. These composite requirements have been met to a certain extent through concentrated research and development activities to develop more refractory and better wear-resistant materials such as ceramics to meet the higher cutting temperatures posed by modern machining.

The ceramic cutting tool represents a different class of cutting tool material with unique chemical and mechanical properties. Thus, there may be a tendency to avoid the use of ceramic tools where they may be applied advantageously. In order to realize the full potential of ceramics, it is essential to have a clear understanding of all the variables which affect the performance of these tools.

In this regard, it may be of interest to note that only three books have ever been published devoted exclusively to the science and technology of ceramic cutting tools. The classic is King and Wheildon's *Ceramics in Machining Processes* (King & Wheildon, 1966). Two and a half decades later, a Russian publication, *Ceramic Tool Materials*, was announced (Gnesin, Osipova, Yaroshenko, & Rontal, 1991). From this author's experience, this book published in the Ukraine is not readily available, translation problems notwithstanding. Finally, in 1994, the book *Ceramic Cutting Tools* was published (Whitney, 1994). Recent updated information is rather limited (Sarin & Buljan, 1984) to some specific sections within book chapters dedicated to advanced cutting tools (e.g. López de la Calle, Lamikiz, Fernández de Larrinoa, & Azkona, 2011).

As discussed below, ceramic cutting tools are generally small in size which vastly diminishes the probability of their mechanical failure during the metal cutting process. Ceramic cutting tools must be hard, or at least harder than the material being cut. In this regard, the concept of hardness, still a poorly understood property, can be examined and an argument presented for expressing Mohs hardness, which is simply a dimensionless number based on the scratching process, in new terms, i.e. Joules per square meter. This unit of "hardness" would seem to be more closely aligned to the complex processes of plastic shearing and surface friction that occur in both surface scratching and metal cutting.

The influence of different wear mechanisms on the overall performance of ceramic cutting tools is of major importance in spite of the fact that there exists no clear theoretical relationship between hardness and wear based on first principles calculations. In reviewing the various cutting tool ceramic materials in use today, it follows that the development and improvement of ceramics for tool application is a further illustration of the fact that where theory fails, engineering must take over.

Probably the first impression one has when inspecting a ceramic cutting tool, whether square, round, etc. is that it is relatively small, about the size of the average man's thumbnail. Indeed, most engineered ceramic products are not large. There are two reasons for this. The first relates to the basic nature of ceramic bodies themselves, whereas the second is related to ceramic fabrication procedures. Thus, with regard to brittle materials, Weibull statistics predicts that the probability that a body will contain a critical flaw which will result in failure under a given load increases with the size of the body (ASTM C1683-10, 2010). With regard to fabrication, most ceramics are formed via the consolidation of crystalline inorganic powders at elevated temperatures and pressures, a procedure commonly known as hot pressing. By its very nature as a fabrication process, enhanced economical forming via hot pressing is best achieved when relatively small ceramic products are being produced.

If one accustomed to handling cemented carbide or even steel cutting tools were to pick up the ceramic insert, the immediate reaction would be surprise at the relative lightness of the latter. Overall, densities of ceramic cutting tools are about 15% that of sintered tungsten carbide inserts.

In many instances, the low density of ceramic materials is of considerable advantage, for example, in the design of lightweight composite armor systems for military personnel, vehicles and aircraft. This author can recall one instance when the inherent low density of a ceramic tool, a hot-pressed alumina insert, proved to be a detriment to its application in a machining operation. It was during a visit to a manufacturing facility many decades ago when an experienced machinist who had always used cemented carbide inserts was asked to try an alumina tool on his metal cutting lathe, whereupon he took the tool, inspected it, and immediately returned it with the comment, "in no way am I going to attempt to cut this metal with something that looks and feels like my wife's chinaware." The world has changed a lot since then.

Of course, a ceramic tool must be hard, or at least harder than the material being machined. Although this statement would appear to be quite obvious, it should be realized that although hardness, as a property of materials, determines many of their technological applications, it still remains a poorly understood property (Oganov & Lyakhov, 2010). Although the concept of hardness has no precise definition and as a result possesses no recognized dimensions, some methods of measurement give it units of pressure, while in others it is dimensionless (McColm, 1990). With ceramics, the Knoop and Vickers tests are most often used to measure hardness. These involve indentation of the surface with a diamond point, the result being reported in gigapascals, the same units as pressure. Mohs hardness, first elaborated by Mohs (1824) in *The Treatise on Mineralogy*, or the *Natural History of the Mineral Kingdom*, scale is dimensionless and involves scratching.

In reality, the physical disturbances involved in a simple scratch test, although not as severe, scale with those forces acting on a cutting tool during the metal cutting process. These include elastic and plastic deformation as the result of shear stresses, forces of friction and the breaking of chemical bonds. For these reasons, it would seem that Mohs hardness would bear a closer relationship, although dimensionless, to ceramic cutting tools than to Knoop and Vickers hardness values.

That Mohs hardness (H_m) could be defined as proportional to the second derivative of lattice (crystal) energy with change in interatomic distance, i.e. $H = \left(\frac{d^2E}{dr^2}\right)_{r_0} \sim H_m$, where H represents "absolute hardness" was first suggested by Goble and Scott (1985). Although these authors did not derive an expression for $\left(\frac{d^2E}{dr^2}\right)_{r_0}$ in their paper, the calculation is straightforward, resulting in the expression, $H = 9V/r_0^2\beta$ where V is the volume occupied in the crystal by a pair of oppositely charged ions, r_0 is the equilibrium interatomic distance and β is the isothermal compressibility. An excellent discussion of the electrostatic model for ionic crystals may be found

Table 1 "Absolute hardness" (H) and Mohs hardness (modified) values (H_m) for selected ceramic cutting tool materials

Material	H *(J m^{-2})*	H$_m$
Diamond	2482	15
Cubic boron nitride	1640	~14.5
Silicon carbide	1291	13
Alumina	1257	12

in Ladd's book on *Structure and Bonding in Solid State Chemistry* (Ladd, 1979, pp. 84–86). The units for the expression $9V/r_0^2\beta$ are Joules per square meter (J m^{-2}).[2]

Table 1 lists the calculated "absolute hardness" values for materials of most importance in a discussion of ceramic cutting tools along with their Mohs (modified) hardness numbers. Note that diamond still maintains its preeminence as the hardest known material.

In addition to the data given in Table 1, "absolute hardness" calculations have been done for some two dozen inorganic solids (mostly carbides, oxides and sulfides) as well as several metallic elements (Whitney, unpublished work). It was found that a plot of log H against H_m gave a straight line of slope log (1.2), the form of the equation being $H = k(1.2)^{H_\mathrm{m}}$. This is exactly the same expression that Tabor (1954) found for the relationship between Mohs hardness number and indentation (Vickers) hardness number of steel strips. Tabor concluded that for a point to scratch a flat surface of a given Vickers hardness, its own hardness must be about 20% greater. Although he stated that, "the reason for this is not clear", he concluded that his results should be of some interest in the abrasion of very hard solids. An abrasive must have a hardness 10–20% greater than that of the solid if abrasion is to be effective. Thus, considering the hardness of cutting tool materials in "absolute" terms, i.e. Joules per square meter, would appear to be reasonable, particularly when one realizes that the scratching process, like the cutting process which it closely resembles, is a complex one involving plastic shearing and surface friction (Tabor, 1954).

2.18.2 Wear Mechanisms of Ceramic Cutting Tools

We should now consider the effects of wear, in both its physical and chemical manifestations, on the performance of ceramic cutting tools. Here again the strong arms of theoretical solid-state physics and chemistry fail to comfort us. There exists no theoretical relationship between hardness and wear. Based on first principles calculations as stated previously, a fundamental understanding of hardness is still elusive and, in addition to this, a rigorous solution of the cutting process has not yet been achieved, due in part to the fact that tool life is an imprecise quantity as it depends on a number of performance characteristics as well as design specifications for the part in question. How then do we attack the problem of wear in the application of ceramic tools?

In general, tool life depends on temperature, pressure compatibility between tool and work materials and the structural inhomogeneity of the tool material, the temperature generated during cutting being the single most important tool life variable (Shaw, 1994). As will be discussed later, this is also true in the machining of refractory hard alloys such as Inconel 718[3] with silicon carbide whisker-reinforced alumina cutting tools (e.g. Aruna, Dhanalakshmi, & Mohan, 2010). Due to improved strength and fracture toughness, these tools can be utilized at much higher cutting speeds resulting in higher temperatures in the tool/chip area resulting in softening of the work metal. Tools can typically fail as a result of combinations of abrasion, which can result in crater and/or flank wear, chemical interaction with the work material, and/or chipping and fracture (e.g. Senthil Kumar, Raja Durai, & Sornakumar, 2006; Zhu, Zhang, & Ding, 2013).

Crater wear is the process of dissolution of the tool material into the freshly formed work metal chip. Being a diffusion process, it becomes more significant as the cutting temperature is increased, which in turn can place a restriction on cutting speeds. A common method for reducing crater wear is the application of coatings on the

---

[2] For isotropic structures $V = k_{r_0}^3$ where k is a structural factor (constant). Thus we may write $H = 9k_{r_0} \sim H_\mathrm{m}$ where K, the bulk modulus, is the reciprocal of β.

[3] "Inconel" is a trade name of Inco Alloys International, Inc. 22.

tool, aluminum oxide being particularly effective. Deformation resistance and toughness are primary functions of the substrate and are not impacted by the presence or absence of a coating.

Flank wear occurs on the bearing surface of the tool. The chip bearing surface wears away slowly by a combination of mechanical abrasion and chemical reaction. As cutting speeds (temperatures) increase, chemical wear becomes more important.

Built-up edge can be a problem particularly at low speeds and is caused when particles of the work material become pressure welded to the tool edge. As speeds are increased, the chip passes the cutting edge too quickly for diffusional bonding to occur and consequently built-up edge decreases. As long as the built-up edge remains on the tip of the cutting tool, it itself acts as the “cutting tool,” usually with a reduction in the quality of the surface finish of the machined part.

Notching occurs at the depth-of-cut line on the cutting tool and is a more complicated failure mechanism because so many factors can contribute to it. Notching is usually caused by mechanical means such as chipping, abrasion from surface scale, or a work-hardened layer, etc. but on occasion, it can be caused by chemical interaction between the work material and the tool in a manner similar to cratering.

In summary, ceramic cutting tools are subjected to an extremely severe rubbing process. There is ceramic to metal contact between the tool and the workpiece under conditions of very high stress at high temperature. With the use of ceramic tools in the machining of nickel-based refractory hard alloys, this situation is further enhanced by tribochemical effects related to the different physical/chemical processes depending on the machining parameters and the metallurgical nature of the material being cut. This helps us to better understand the statement made previously that, “a rigorous solution of the cutting process has not yet been achieved, due in part to the fact that tool life is an imprecise quantity as it depends on a number of performance parameters as well as design specifications for the part in question,” although an attempt has recently been made (Daiic, 2001) to establish modes to determine the reliability of ceramic cutting tools.

2.18.3 Ceramic Cutting Tool Materials

Lacking a theoretical model to work from, modern ceramic cutting tools have been engineered starting with the basic material property requirements necessary to perform the metal cutting operation. Not only must cutting tools be made of a material “harder” than the material which is to be machined, but that material must also have a high hot hardness so that the tool will be able to withstand the heat generated in the metal cutting process since cutting speed is the dominant influence on the cutting temperature of the machining process. Tool materials with higher hot hardness will permit machining at higher productivity rates due to the higher allowable cutting speeds.

As illustrated below in the introduction to the various types of cutting tool materials, the improved performance of these inserts in the machining of more difficult-to-cut refractory metals and alloys has been due to the pronounced advances in ceramic processing and ceramic engineering. Particularly important in this regard has been the control of chemical purity and microstructure developed in materials during the fabrication process. In ceramics, particularly, strength, or fracture toughness, is very much dependent on microstructure.

This is also true in the case of composites where a second hard, nonoxide phase such as titanium carbide, titanium nitride or silicon carbide whiskers on the order of 1 μm in diameter are dispersed in the major (continuous) phase, usually aluminum oxide. There is a sort of “materials synergy” in operation here. One consequence of vastly improved ceramic processing technology has been the development of modern cutting tools operating successfully under the most stringent conditions of temperature and stress. The fact that these tools perform so well under such conditions bears testimony to the progress being made in modern ceramic engineering to develop new and improved high-strength, high-temperature inorganic materials for a variety of applications other than cutting tools themselves. Thus, the cutting tool and the cutting machining operation combined provide a quality control “test”, so to speak, of engineering advancements being made in the development of new and improved high-performance ceramics in general.

2.18.3.1 Aluminum Oxide Cutting Tools

Aluminum oxide (Al_2O_3), with its high melting point (2072 °C), high hardness (15.7 GPa on the Vickers scale and 9 on the Mohs scale), relatively high thermal conductivity ($30\ W\ m^{-1}\ K^{-1}$) for a ceramic, and chemical inertness, is a logical choice as a cutting tool material. The oxide is readily available and relatively inexpensive. Sintered Al_2O_3 cutting tools, developed in the early 1930s, were primarily cold-pressed Al_2O_3. While these tools were chemically inert and had good hot hardness compared to tungsten carbide, they were notoriously low in toughness. This deficiency caused the tools to easily chip and break catastrophically, creating a poor image for early ceramic tools. The development of the hot pressing process (HP) (without excessive grain growth) was a major step forward in producing high-quality ceramic tools. Hot pressing as a densification process is more forgiving than sintering in that full density is virtually assured. Powder properties are still important but not as critical as in sintering. For example, soft agglomerates can be devastating with sintering but are of little or no consequence when the ceramic is hot pressed.

2.18.3.2 Aluminum Oxide/Titanium Carbide Composite Cutting Tools

The first attempts to apply ceramic cutting tools for turning of gray cast irons were made in the early 1930s. The high hot hardness, compressive strength, wear resistance, and chemical inertness of ceramics promised success. However, the difficult manufacturing process of ceramics combined with unsuitable machine tools and lack of experience delayed implementation. Initially, only aluminum oxide ceramics (oxide ceramics) were used, but in the early 1970s, aluminum oxide/titanium carbide composites (carboxide ceramics) were introduced. The HP allowed the addition of TiC to aluminum oxide, producing HP Al_2O_3/TiC, an excellent all-purpose ceramic tool (e.g. Kitagawa, Kuboa, & Maekawa, 1997). Although other ceramic materials may be better for specific applications, HP Al_2O_3/TiC is acceptable for most machining situations where ceramics are applicable (e.g. Barry & Byrne, 2001). They provided improved results in finish turning of ferrous metals and turning tool steels as hard as 60–63 R_C (e.g. Grzesik, 2009; Grzesik & Zalisz, 2008). Optimization of the composition including the introduction of new sintering technologies and composition (Ti[C,N] and even introduction of a metallic phase within the ceramic matrix) as well as of different length-scale reinforcement resulted in further improvements in this group of cutting tool materials (Senthil Kumar, Raja Durai, & Sornakumar, 2003; Yin et al., 2012; Zhu, Luo, Li, & Wu, 2012).

Commercially available cutting tool materials belonging to the group of carboxide ceramics consist of aluminum oxide with additions of 30–40% titanium carbide and/or titanium nitride. The dispersion of these hard particles increases the hardness for temperatures up to 800 °C when compared to oxide ceramics. Simultaneously, the fracture toughness and bending strength is improved through crack impediment, crack deflection, or crack branching caused by the dispersed hard particles. In Al_2O_3/TiC composites, the TiC grains pin the cracks initiated at the tool surface. This is due to the additional expenditure of energy required for the cracks to propagate around the carbide particles. The particulate-dispersed matrix of Al_2O_3/TiC thus exhibits a better fracture toughness. The higher hardness (2200 Vickers) in combination with the higher fracture toughness ($5.4\ \mathrm{mN\ mm^{-2}}$) increases the resistance to abrasive and erosive wear considerably. The lower thermal expansion ($7.0 \times 10^{-6}\ \mathrm{K^{-1}}$) and higher thermal conductivity ($35\ \mathrm{W\ m^{-1}\ K^{-1}}$) of the composite improve the thermal shock resistance and thermal shock cycling capabilities when compared to oxide ceramics. The composite tool is thus capable of cutting dry or with a water base cutting fluid. At temperatures exceeding 800 °C, the titanium carbide and/or titanium nitride particles oxidize and begin to lose their reinforcing properties. The composite weakens and this phenomenon must be taken into consideration when selecting cutting conditions, such as cutting speed, depth of cut, and feed rate.

Powders with a high purity and fine particle size (generally 1 μm or less) are selected for manufacturing aluminum oxide/titanium nitride carbide composites. Uniform blending of these components is achieved through dry or wet milling. Organic binders are added to provide sufficient strength for preforming processes. The heat treatment is very critical. The goal is to minimize porosity while maintaining a fine microstructure.

The titanium carbide and nitride additives impede the densification through heat treatment. Various processes have been developed to overcome this difficulty all based on the simultaneous application of temperature and pressure. Originally, graphite dies at temperatures between 1600 °C and 1750 °C were used to mechanically densify the material at pressures between 200 and 350 bar. Graphite limits the maximum allowable pressure and temperature, and rest porosities of up to 1% may occur in the composite. In recent years, hot isostatic pressing methods were introduced operating at pressures of up to 200 MPa with inert gas (N_2, Ar) as the compacting media. The process requires that the product be hermetically sealed or presintered to 94% minimum density (closed pores only) to prevent penetration by the inert gas. Hot isostatic pressing increases density and reduces porosity, resulting in higher reliability of the composite.

2.18.3.3 Phase Transformation Toughened Cutting Tools

For many years, this author has been interested in and, indeed has undertaken, both theoretical and experimental studies regarding high-temperature, high-pressure phase transformations of zirconium oxide polymorphs (Whitney, 1962, 1965a, 1965b). Thus all aspects in the development of phase transformation toughened ceramic cutting tools have been intriguing to him (Arahori & Whitney, 1988; Whitney & Vaidyanathan, 1985, 1987).

A detailed treatment of phase transformation toughened materials for cutting tool applications was given by Krishnamurthy and Gokularathnam (1994). These authors have scholarly elucidated the fundamental concepts of transformation toughening with its applications in the development of ceramic cutting tools. The phase transformation toughened cutting tool is an outstanding example of what can be achieved utilizing modern ceramic engineering technology (Green, Hannink, & Swain, 1989). Research and development on zirconia ceramics resulted in the development of two distinct classes of ceramics, fully stabilized and partially stabilized zirconia. The basis of these toughening mechanisms is that there is a considerable reduction in the driving force at the propagating crack tip in the matrix of the ceramic material. Crack propagation in a matrix material is due to the crack driving force, which is opposed by the resistance of the microstructure.

The introduction of zirconia into alumina as a sintering and densification aid has been in practice since the early development of Al_2O_3 ceramics. With developments in microstructure, the concept of dispersion strengthening gained momentum. As already mentioned, this led to the development of Al_2O_3/TiC and later, toughening of alumina by dispersion of ZrO_2 in alumina (Claussen, 1976). In zirconia toughened alumina (ZTA), the microstructure contains different phases of alumina and zirconia. The toughening of ZTA is related to volume expansion and shear strain associated with tetragonal crystal structure (t) to monoclinic crystal structure (m) phase transformation in the dispersed zirconia particles.

Application of external stresses on ZTA causes the metastable tetragonal phase to transform to the monoclinic phase. This phase transformation, which is accompanied by a volume expansion of around 4% and a shear strain of about 6%, provides a compressive stress, which can reduce and eventually stop crack propagation. Studies on transformation toughening in ZTA reveal the existence of a critical size of ZrO_2 particles, for the retention of metastable tetragonal phase. Further, it was shown that by altering the free energy associated with transformation, it was possible to toughen and even strengthen the ceramics (Becher, Alexander, Bleier, Waters, & Warmick, 1993; Casellas, Nagl, Llanes, & Anglada, 2005; Casellas, Ràfols, Llanes, & Anglada, 1999; Hori, Yoshimura, & Somiya, 1986; Karihaloo, 1991; Lange, 1982).

Control of microcracks generated due to volume expansion of $t \rightarrow m$ phase transformation during cooling from sintering temperature and due to the stress-induced transformation during fracture process can also facilitate toughening and strengthening of ceramics (Green, 1982; Rühle, Evans, McMeeking, Charambelides, & Hutchinson, 1987).

Overall, stress-induced phase transformation toughened alumina/zirconia composites have excellent properties such as higher order thermal shock resistance and moderate hardness (Brandt, 1986; Mondal, 2005). These qualities provide better machining performance than cold compacted alumina tools, and a large number of studies have been focused on optimizing performance of ZTA cutting tools, on the basis of understanding their wear and failure micromechanisms as well as cutting conditions (Chakraborty, Ray, & Bhaduri, 2000; D'Errico & Calzavarini, 1995; Li & Low, 1994; Mandal, Doloi, & Mondal, 2011; Mandal, Doloi, Mondal, & Das, 2011; Mondal, Chattopadhya, Virkar, & Paul, 1992; Sergo, Lughi, Pezzoti, et al., 1998; Smuk, Szutkowska, & Walter, 2003).

2.18.3.4 Alumina–Silicon Carbide Whisker Composite Tools

For decades, aluminum oxide has been the basic cutting tool material of choice in high-speed machining operations primarily due to its superior hardness and chemical stability at high temperatures. However, the use of essentially pure alumina has been limited because of its low resistance to fracture. Significant research advances in the development of toughening mechanisms for alumina composites has increased the worldwide interest in ceramic tooling, i.e. zirconia toughening via martensitic transformation, as previously discussed, and single-crystal silicon carbide whisker reinforced toughening, the latter being a quite effective approach regarding cutting tool applications. Silicon carbide whiskers are small with dimensions ranging from 0.05 to 1.0 μm in diameter and 5–125 μm in length. Typically, the whiskers contain cubic (β) or a mixture of α (hexagonal) and β polymorphic phases of silicon carbide.

Al_2O_3–$SiC_{(w)}$ composites have been studied by many investigators (e.g. Becher & Wei, 1984; Choll & Smith, 1994; Ko, Kwon, & Kim, 2004). In general, it has been found that the fracture toughness increases as the whisker content increases, while the hardness only increases slightly. This behavior occurs until the whisker loading is so high that full densification is unobtainable. Two toughening mechanisms for SiC whisker-reinforced alumina composites have been theorized: crack deflection and whisker pullout. The crack deflection model describes the effectiveness of second-phase particles (in the form of rods) in increasing fracture toughness. The model is based on an analysis of the tilt and twist of the crack front between particles, which determines the deflection-induced reduction in the crack driving force. Crack deflection can result in significant toughening in composites where there are strong crack/microstructure interactions. The degree of thermal expansion mismatch between the whisker and the matrix determines the extent of the interaction.

The whisker pullout mechanism requires whiskers with high transverse fracture toughness relative to the interfacial fracture toughness so that failure may occur along the whisker/matrix interface. Toughening results from the additional work required to pull the whisker out from the matrix. The stress transferred to the whisker must be less than its fracture strength, and the interfacial shear stress generated must be greater than the shear resistance of the whisker/matrix interface. The shear resistance is controlled by the degree of bonding. For Al_2O_3–$SiC_{(w)}$ composites, interfacial compressive stresses increase the effective shear resistance of the whisker/matrix interface. The factors that result in whisker pullout may lead to whisker bridging. This related mechanism occurs when the whisker remains intact and bridges the crack surfaces in the wake region behind the propagating crack tip. Bridging requires modest interfacial strengths in order to transfer the load to the whisker and high whisker tensile strengths to sustain the applied stress within the wake.

With the advent of whisker-reinforced ceramic materials, the high melting point (in excess of 2000 °C) combined with the toughness and strength at high temperatures has led to the routine application of a cutting tool technology unknown previously. The principle involved is one of maintaining a feed and speed combination which will generate a temperature ahead of the tool high enough to effectively decrease the forces associated with the shear formation, in effect to plasticize the material, to greatly facilitate its displacement.

The most dramatic use of this technology has been in nickel-based alloys which are among the most difficult materials to machine (Altin, Nalbant, & Taskesen, 2007; Bhattacharya, Pashby, & Ezugwu, 1987; Billman, Mehrotra, Shuster, & Beeghy, 1988; Richards & Aspinwall, 1989). These metals work harden rapidly during metal cutting and maintain their strengths to high temperatures. With standard tungsten carbide cutting tools, speeds are limited to the region of 150 surface feet per minute.

It has been shown that most of the heat generated in chip formation occurs in the shear zone immediately ahead of the tool. Some heat comes from the friction of the chip flowing over the top surface of the tool and a small amount from the flank contact with the surface of the part.

Although the concept of setting up a process to purposely generate a high degree of heat can result in the successful fabrication of superalloys, which are very difficult to machine, it simultaneously introduces another mode of tool wear essentially unknown decades ago when ceramic tools were first introduced, i.e. tribochemical wear. With the early ceramic (mostly alumina-based) tools, the major problem was lack of fracture strength of the tool and not chemical interaction between the ceramic and the work metal since at that time cutting speeds and feeds were relatively low. Improvements in the fracture toughness and thermal shock resistance of ceramics over the years (Wayne & Buljan, 1989), and here whiskered ceramics are excelling examples, have led to a pronounced increase in machining feeds and speeds (machining efficiency), together with higher metal cutting temperatures as well, and consequently enhanced chemical interaction between insert and workpiece (Benga & Abrao, 2003; Jun, Jianxin, Jianhua, & Xing, 1997; Wayne & Buljan, 1990).

A case in point is the high-temperature machining of nickel-based alloys with alumina–silicon carbide whisker tools. At high temperatures, alumina is thermodynamically stable in the presence of nickel but silicon carbide is not. Thus a means must be found to chemically protect these whiskers so that they may maintain their toughening function under strenuous metal cutting conditions.

2.18.3.5 Silicon Nitride Cutting Tools

Silicon nitride (Si_3N_4) is a chemical compound of silicon and nitrogen. It is a hard ceramic having high strength over a broad temperature range, moderate thermal conductivity, low coefficient of thermal expansion, moderately high elastic modulus, and unusually high fracture toughness for a ceramic (Dressler & Riedel, 1997; Pasto, 2013; Riley, 2000). Silicon nitride, long in use as a high-temperature and superior bearing material, found its first major application as a cutting tool (Baldoni & Buljan, 1994; Buljan & Sarin, 1982).

The market potential for ceramic cutting tools was greatly expanded with the commercial introduction of silicon nitride, which has been recognized as one of the toughest and most thermally shock-resistant ceramics

(Sarin & Buljan, 1983). Generic references to the material on which these cutting tools are based imply that silicon nitride tools are a single material. This is not the case. In fact, there are three distinct families of ceramic materials based on the compound Si_3N_4. These are (1) silicon nitride containing glass-forming sintering aids, (2) silicon nitride–aluminum–oxygen solid solutions (SiAlONs), and (3) dispersoid–silicon nitride matrix composites. The former two families of materials were initially developed as candidates in vehicular engines, while the latter group was specifically designed for wear-resistant applications (Buljan & Sarin, 1984, 1987).

Single-phase Si_3N_4 is a highly covalent compound that exists in two hexagonal polymorphic crystalline forms, α and the more stable β. Each of these structures is derived from basic Si_3N_4 tetrahedra joined in a three-dimensional network by sharing corners, with each nitrogen corner being common to the three tetrahedral. Actually, the α-Si_3N_4 to β-Si_3N_4 transition is achieved by a solution precipitation reaction of Si_3N_4 and a molten glass (Sarin, 1988). The strongly covalent bonds of Si_3N_4 produce a number of desirable engineering properties in this material: high strength; thermal stability up to approximately 1850 °C, where it decomposes (Whitney & Batha, 1973); good oxidation resistance; low coefficient of thermal expansion (good thermal shock resistance); and a modulus of elasticity greater than that of many metals. However, an adverse effect of this bonding, from the materials processing perspective, is a low self-diffusion coefficient which makes it virtually impossible to fabricate Si_3N_4 into a dense body by classical ceramic processing technology, viz. solid-state sintering, and as such requires sintering additives (densification aids) to achieve full density.

The predominant impurity in Si_3N_4 powder, typically containing a large proportion of the α-phase, is SiO_2, which is present on the surface of the powder particles. The sintering aids, usually added as powders, are mixed by standard comminution procedures, ball or attritor milling, and the resultant mixture is shaped by a variety of techniques. The part is subsequently densified, usually in a nitrogen atmosphere, by firing at high temperatures. Hot pressing, overpressure sintering, or hot isostatic pressing at temperatures in excess of 1600 °C are techniques which have been demonstrated to be amenable to the fabrication of dense silicon nitride parts. In the densification process, the sintering aid admixture reacts with the inherent SiO_2 to form a liquid, i.e. a glass, which facilitates Si_3N_4 particle rearrangement. This step contributes to part densification, and complete densification is achieved through a liquid-phase sintering mechanism. The α-Si_3N_4 particles dissolve in the liquid and precipitate as β-Si_3N_4 via a reconstructive phase transformation. As sintering continues, the β-Si_3N_4 nuclei grow as elongated grains and form an interlocked grain structure. On cooling, additional Si_3N_4 precipitates from the glass and contributes to grain growth.

The sintering aids applied span a wide range of oxides and nitrides, producing a family of materials differing in composition and properties (Becher et al., 2006). A two-phase material consisting of silicon nitride crystals and an intergranular bonding phase represents silicon nitride ceramics. The intergranular phase is a glass or partially devitrified glass based on SiO_2 and other sintering aids such as Al_2O_3, Y_2O_3, MgO, etc. The mechanical properties of a particular Si_3N_4-based ceramic depend on the size distribution of the β-Si_3N_4 grains, assuming complete conversion of the α-phase to the β-phase, which is generally desired, and the quantity and species of the particular sintering aid(s) employed.

The grain size distribution of the Si_3N_4 grains strongly influence the fracture toughness (K_{Ic}) of the material, and hence the strength, since this property is directly proportional to K_{Ic}.

As industrially practiced, the vast majority of densified silicon nitride articles produced by the use of sintering aids can contain intergranular glass phases which may vary in both quantity and composition. Thus, silicon nitride cutting tools produced by this technology comprise a family of materials, and the properties of each individual Si_3N_4 tool material can differ, particularly in the temperature range encountered in high-speed metal cutting (>800 °C), depending on composition, processing route, and means of densification.

In the 1970s, ceramic research showed that aluminum and oxygen could be substituted for silicon and nitrogen, respectively, in the Si_3N_4 crystal structure to form what was termed SiAlON, a silicon–aluminum–oxygen–nitrogen solid solution (Hampshire, Park, Thompson, & Jack, 1978). Since then, α-β-SiAlON ceramics and corresponding composites have positioned as another widely specified and used cutting tool option for machining of aerospace alloys, particularly competing with whisker-reinforced ceramics because of the lower cost of the former, although exhibiting lower performance than the latter too (Altin et al., 2007; Bitterlich, Bitsch, & Friederich, 2008). It is claimed that SiAlONs have physical and mechanical properties similar to silicon nitride due to the similar crystal structure and covalent bonding, and have chemical properties approaching those of Al_2O_3 due to solid solution effects. On this basis, it is of interest to note that both Si_3N_4 and Al_2O_3 are isoelectric substances in that they both contain an average of 10 electrons per atom, the same electronic configuration exhibited by the very stable neon atom. The connection between isoelectronic character and abrasive materials (in the low *Z* elements and compounds) has been discussed by Hall (1965) and Whitney (1972a, 1972b).

Silicon nitride cutting tools have captured application in cast iron machining which had previously been exclusively served by cemented carbide and alumina-based tools (Diniz & Ferrer, 2008; Grzesik, Rech, Zak, & Claudin, 2009; Reddy, Chakraborty, Mahajan, & Prasad, 1990; Souza, Nono, Ribeiro, Machado, & Silva, 2009). While capable of several ceramic applications, Si_3N_4 is possibly the most ideal tool material for machining gray cast iron in turning, boring, and face milling operations. A "good" grade of silicon nitride will machine common grades (used in the automotive industry) of gray iron at cutting speeds of 4000–5000 feet per minute (fpm). Most of the silicon nitride tools are capable of continuous machining at 3000 fpm, which is considerably faster than the productivity obtainable with coated carbides. Laboratory tests in face milling class 30 gray cast iron have been performed at 7000 fpm with tool life values up to 1 h of cutting time.

While silicon nitride-based cutting tools show outstanding wear resistance in cast iron machining, the application of these materials to steel machining has for the most part been unsuccessful. Diffusion couples have shown that the chemical reactivity of Si_3N_4 is higher in contact with steel than with gray cast iron. Crater formation on the tool is the predominant wear feature providing evidence of the increased contribution of chemical wear in steel machining (Kramer & Judd, 1985; Kannatey-Asibu, 1999). Whereas tool wear in gray cast iron machining is observed only on the nose and flank of the tool, with high alloy 4340 steel, massive crater formation is produced at very short cutting times, which dramatically weakens the cutting edge and leads to catastrophic tool failure. Thus, chemical tribology is the culprit. It is evident that the overwhelming contribution of the chemical wear components in steel machining completely obliterates the excellent abrasive wear resistance of typical cast iron-grade Si_3N_4 tool materials (Gomes, Miranda, Silva, & Vieira, 1999; Oliveira, Silva, & Vieira, 2000; Silva, Gomes, Miranda, & Vieira, 1991; Vleugels, Van der Perre, & Van der Biest, 1996). This can be explained in part by the fact that the chemical stability of Si_3N_4 is not as high as that of Al_2O_3, their Gibbs standard free energies of formation being $-1013\ \mathrm{kJ \cdot mol^{-1}}$ and $-1582\ \mathrm{kJ \cdot mol^{-1}}$, respectively. While the mechanical properties of Si_3N_4 ceramics can be enhanced through composite microstructural design, improved performance in this application must be approached by increasing the tribochemical resistance rather than just the mechanical wear one (e.g. Calis Acikbas et al., 2012; Oliveira, Silva, & Vieira, 1998; Oliveira, Silva, & Vieira, 2003). In this regard, the use of chemical vapor-deposited TiC, Ti(C,N), and Al_2O_3/TiN coatings significantly expanded the range of applications for silicon nitride-based tools by including difficult-to-machine materials such as steel, etc. (e.g. Grzesik & Malecka, 2011; Grzesik & Zak, 2009; Sarin & Buljan, 1985).

Finally, the emergence of Si_3N_4/SiC composites as promising materials for wood cutting applications should be highlighted (Eblagon, Ehrle, Graule, & Kuebler, 2007; Strehler et al., 2010; Strehler et al., 2011). Industrial wood cutting is a challenging process, as the wood by nature is inhomogeneous and contains knots, abrasives and acids which attack the cutting material. Further, temperatures up to 800 °C can be reached at the cutting tip during wood machining and no coolant can be used as this would impair the surface quality of the cut wood. As a result, the lifetime of currently used cemented carbide knives is limited by abrasive wear and corrosive attack (e.g. Gauvent, Rocca, Meausoone, & Brenot, 2006). In the above context, on one hand, silicon nitride shows superior wear resistance and chemical inertness, besides high strength and capability for withstanding high structural loads to high temperatures. Furthermore, on the other hand, silicon carbide is even harder and adds its good thermal conductivity. Si_3N_4/SiC composites also exhibit less than one quarter of the density of hardmetals; thus, higher cutting speeds may be achieved because centrifugal forces and clamping forces are reduced. Preliminary feasibility studies have indicated that these composites exhibit three times longer life cycles than commercially available cemented carbides.

2.18.3.6 Polycrystalline Diamond and Cubic Boron Nitride

As is well known, diamond is unique in possessing an unusually high hardness. This can be noted in Table 1 where the "absolute hardness" difference between diamond and the next hardest material, cubic boron nitride (CBN), is $843\ \mathrm{J \cdot m^{-2}}$ followed by the difference in hardness between the next pair in the series, CBN and silicon carbide, i.e. $349\ \mathrm{J \cdot m^{-2}}$ and finally silicon carbide and alumina, i.e. $34\ \mathrm{J \cdot m^{-2}}$. This again illustrates the important role played by highly covalent bonds in determining the hardness of materials. In ceramic materials, ionicity decreases hardness. The approximately 34% decrease in hardness between diamond and CBN corresponds with the approximately 22% ionic character of the boron–nitrogen bond (Pauling, 1967, p. 93). It is logical to examine diamond and CBN (properly described as β-BN) in the same context. Boron nitride is isoelectronic with diamond; like diamond β-BN has an average of six electrons per atom.

Except for the difference in hardness (as has already been discussed, a complex and complicated property less well defined than many other physical properties), there are many crystallographic similarities between the two materials. Diamond exhibits the shortest covalent bond found in a three-dimensional network solid. The length of the C–C bond in diamond is 1.54 Å (sp^3 carbon), whereas the B–N bond length in β-BN is 1.57 Å. Crystallography, both diamond and β-BN are three-dimensional bonded cubic (isotropic) structures with fixed atomic positions in a tetrahedral configuration (topological rigidity). A further comparison of the physical properties of diamond and β-BN important to cutting tools is given by Ratterman and BovenKerk (1994), along with a historical review of the development of sintered polycrystalline diamond (PCD) and sintered polycrystalline CBN materials.

As the above authors point out, diamond is totally inert to metals such as aluminum, copper and zinc, but reacts at high temperatures with metals having high carbon solubility such as iron, nickel and cobalt and carbide-forming element such as titanium, zirconium, tantalum and tungsten. Thus the chemical reactivity between the cutting tool material and the workpiece must always be taken into consideration. In general, diamond tools should not be applied in the machining of ferrous metals or high-temperature alloys.

Diamond is inert to plastic, glass and ceramic. Machining aluminum-, zinc- or copper-based alloy is ideal for diamond as is the cutting of plastic/glass composites. In addition, diamond is widely used in cutting wood and wood composites.

To avoid chemical wear in metal cutting where a chemical reaction is possible, diamond should be used for cutting reactive metals only under conditions where cutting temperatures are below the reaction temperature. This can be done by controlling the tool geometry, cutting speeds and coolants. Threshold temperatures for workpiece chemical reaction vary with the metal in question but can be typically at temperatures in the 400–700 °C range. If a carbon-soluble or carbide-forming metal is totally saturated with carbon, then machining with diamond is less of a problem. Diamond also can wear due to oxidation. Temperatures in excess of 700 °C are needed before this becomes a factor.

Despite limitations, diamond has become a widely used and very cost-effective cutting tool material, especially in the automotive and aerospace industry. The silicon–aluminum alloys, metal matrix composites and fiber-reinforced plastics now used in these industries can only be effectively machined with diamond tools.

CBN is also inert to the same materials as diamond but because of its lower hardness does not generally compete with diamond in cutting these workpieces. However, for iron-, nickel- and cobalt-based alloys, CBN is less reactive than diamond, hence chemical wear is minimized. CBN also has more tolerance to oxidation than diamond. Taking these properties into account, the major cutting tool applications for CBN are ferrous alloys and high-temperature alloys based on nickel, cobalt and iron (Arunachalam, Mannan, & Spowage, 2004; Benga & Abrao, 2003; Chen, 2000; Oliveira, Diniz, & Ursolino, 2009).

In balance, diamond and CBN are very complementary to each other in applications such as cutting tools.

2.18.4 Concluding Comments

Some four decades ago, Professor Milton C. Shaw observed, “As the third ‘law’ of history indicates, new tool materials should be expected to appear in response to new requirements” (Shaw, 1968). This “law” has not been violated. Indeed, since these words were written, advanced aluminum oxide composite, silicon nitride-based CBN and sintered PCD cutting tools are now commonplace. Their introduction into the metalworking field since that time is further proof that the “third law” holds.

This chapter describes the various classes of ceramic cutting tools and their applications. But more than that, it is about manufacturing and productivity. In preparing these pages, a certain type of individual has been kept in mind, i.e. the person who experiences the thrill and joy of making things. And lest we forget the principles on which rest the prosperity of the United States, allow me to restate the following truism: efficiency in manufacturing is fundamental to the growth of America’s economy. To further emphasize this fundamental truth, the following passage is quoted which deals with this cardinal concept (Wilkie & Rimanoczy, 1981).

> “In our intensely competitive world, military wars come and go, but trade wars are never-ending. Every nation wants to take customers away from every other nation. In both wars, tools are a prime factor in determining the outcome. Armaments are the hardware of national security. Machine tools are the hardware of economic security. They are also the hardware of the war on poverty.”

Some three decades later, Barry Ashby has again restated this fundamental concept in a very straightforward and elegant manner in his recent paper, *The De-Industrialization of America* (Ashby, 2011), i.e.

> "A fundamental lesson that U.S. politicians need to learn is that manufacturing is a prized jewel in developing and highly industrialized nations."

Metal cutting, one of man's oldest manufacturing processes (dating back to 1000 BC or earlier) assumes a significant role in today's productivity scenario. This is due to significant advances that have been made in both machine tools and cutting tool materials. In terms of manufacturing efficiency the two are inseparable. Advances in technology in one area require that corresponding technical advances be made in the other. In terms of the cutting tool itself, development of more wear-resistant tool materials for application in high-speed machining will always have a profound impact on productivity.

Today we are in a "going green" environment, not only to make a smaller carbon footprint on our environment but also to conserve our natural resources, particularly fuel supplies. However, as established by Carnot (1824), increasing the efficiency of heat engines requires that they operate at higher and higher temperatures. This in turn requires the development and utilization of advanced refractor metals and alloys which by their very nature (metallurgy) are very difficult to machine. Historically, the overall goal in the development of ceramic cutting tools has been to create through ceramic engineering those materials which can meet the machining and manufacturing challenges of producing more efficient heat engines utilizing high-temperature metals and alloys. Today, the newer, more difficult-to-machine alloys, with impressive high-temperature properties being introduced to meet the increased demands of aircraft engines, include single-crystal alloys, directionally solidified eutectics reinforced with long carbide fibers and new titanium alloys such as the titanium aluminides. Thus the ceramic tool has its unique place in our "going green" environment. In this regard, it should be noted that the color of the aluminum oxide–silicon carbide whisker composite tool, which has been proved to be very successful in the machining of high-temperature superalloys, is green.

References

Altin, A., Nalbant, M., & Taskesen, A. (2007). The effects of cutting speed on tool wear and tool life when machining Inconel 718 with ceramic tools. *Materials Design, 28*, 2518–2522.

Arahori, T., & Whitney, E. D. (1988). Microstructure and mechanical properties of Al_2O_3-Cr_2O_3-ZrO_2 composites. *Journal of Materials Science, 23*, 1605–1609.

Aruna, M., Dhanalakshmi, V., & Mohan, S. (2010). Wear analysis of ceramic cutting tools in finish turning of inconel 718. *International Journal of Engineering Science and Technology, 2*, 4253–4262.

Arunachalam, R. M., Mannan, M. A., & Spowage, A. C. (2004). Residual stress and surface roughness when facing age hardened Inconel 718 with CBN and ceramic cutting tools. *International Journal of Machine Tools and Manufacture, 44*, 879–887.

Ashby, B. (2011). *The de-industrialization of America*. www.industrialheating.com. January 2011 issue (Accessed July 2011).

ASTM C1683–10. (2010). *Standard practice for size scaling of tensile strengths using Weibull statistics for advanced ceramics*. West Conshohocken, PA: American Society for Testing and Materials (ASTM) International.

Baldoni, J. G., & Buljan, S.-T. (1994). Silicon nitride cutting tools. In E. D. Whitney (Ed.), *Ceramic cutting tools* (pp. 191–220). Park Ridge, NJ: Noyes Publications.

Barry, J., & Byrne, G. (2001). Cutting tool wear in the machining of hardened steels: part I – alumina/TiC cutting tool wear. *Wear, 247*, 139–151.

Becher, P. F., & Wei, G. C. (1984). Toughening behavior in SiC-whisker-reinforced alumina. *Journal of the American Ceramic Society, 67*, C267–C269.

Becher, P. F., Alexander, K. B., Bleier, A., Waters, S. B., & Warmick, H. (1993). Influence of ZrO_2 grain size and content on the transformation response in the Al_2O_3-ZrO_2 (12 mol% Ce_2O_3) system. *Journal of the American Ceramic Society, 76*, 612–613.

Becher, P. F., Painter, G. S., Shibata, N., Satet, R. L., Hoffmann, M. J., & Pennycook, S. J. (2006). Influence of additives on anisotropic grain growth in silicon nitride ceramics. *Materials Science and Engineering, A422*, 85–91.

Benga, G. C., & Abrao, A. M. (2003). Turning of hardened 100Cr6 bearing steel with ceramic and PCBN cutting tools. *Journal of Materials Processing Technology, 143–144*, 237–241.

Bhattacharya, S. K., Pashby, I. R., & Ezugwu, E. O. (1987). Machining of INCO 718 and INCO 901 superalloys with SiC-whisker reinforced Al_2O_3 composite ceramic tools. In *Proceedings of the sixth international conference on production engineering* (pp. 176–181). Osaka, Japan.

Billman, E. R., Mehrotra, P. K., Shuster, A., & Beeghy, C. W. (1988). Machining with Al_2O_3-SiC whisker cutting tools. *American Ceramic Society Bulletin, 67*, 1016–1019.

Bitterlich, B., Bitsch, S., & Friederich, K. (2008). SiAlON based ceramic cutting tools. *Journal of the European Ceramic Society, 28*, 989–994.

Brandt, G. (1986). Flank and crater wear mechanisms of alumina-based cutting tools when machining steel. *Wear, 112*, 39–56.

Buljan, S. T., & Sarin, V. K. (1982). Improved productivity through application of silicon nitride cutting tools. *The Carbide and Tool Journal, 14*(3), 40–46.

Buljan, S. T., & Sarin, V. K. (1984). Silicon nitride based composites. In G. S. Upadhyaya (Ed.), *Sintered metal ceramic composites*. Amsterdam, The Netherlands: Elsevier Scientific Publishers, B.V.

Buljan, S. T., & Sarin, V. K. (1987). Silicon nitride-based composites. *Composites, 18*(2).

Calis Acikbas, N., Yurdakul, H., Mandal, H., Kara, F., Turan, S., Kara, A., et al. (2012). Effect of sintering conditions and heat treatment on the properties, microstructure and machining performance of a-b- SiAlON ceramics. *Journal of the European Ceramic Society, 32*, 1321–1327.

Carnot, S. (1824). *Réflexions sur la puissance motrile du fer et sur les machines propres á développer cette puissance.* Paris, France: Bachelier (French).

Casellas, D., Ràfols, I., Llanes, L., & Anglada, M. (1999). Fracture toughness of ZTA. *International Journal of Refractory Metals and Hard Materials, 17*, 11–20.

Casellas, D., Nagl, M. M., Llanes, L., & Anglada, M. (2005). Microstructural coarsening of zirconia-toughened alumina composites. *Journal of the American Ceramic Society, 88*, 1958–1963.

Chakraborty, A., Ray, K. K., & Bhaduri, S. B. (2000). Comparative wear behavior of ceramic and carbide tools during high speed machining of steel. *Materials and Manufacturing Processes, 15*, 269–300.

Chen, W. (2000). Cutting forces and surface finish when machining medium hardness steel using CBN tools. *International Journal of Machine Tools and Manufacture, 40*, 455–466.

Choll, K. J., & Smith, K. H. (1994). Alumina-silicon carbide whisker composite tools. In E. D. Whitney (Ed.), *Ceramic cutting tools* (pp. 86–111). Park Ridge, NJ: Noyes Publications.

Claussen, N. (1976). Fracture toughness of Al_2O_3 with an unstable ZrO_2 dispersed second phase. *Journal of the American Ceramic Society, 59*, 49–51.

D'Errico, G. E., & Calzavarini, J. (1995). Advanced ceramic tools: an experimental assessment in turning tests. *Journal of Materials Processing Technology, 54*, 34–39.

Daiic, P. (2001). Determination of reliability of ceramic cutting tools on the basis of comparative analysis of different functions of distribution. *International Journal of Quality and Reliability Measurement, 18*, 431–443.

Diniz, A. E., & Ferrer, J. A. G. (2008). A comparison between silicon nitride-based ceramic and coated carbide tools in the face milling of irregular surfaces. *Journal of Materials Processing Technology, 206*, 294–304.

Dressler, W., & Riedel, R. (1997). Progress in silicon-based non-oxide structural ceramics. *International Journal of Refractory Metals and Hard Materials, 15*, 13–47.

Eblagon, F., Ehrle, B., Graule, T., & Kuebler, J. (2007). Development of silicon nitride/silicon carbide composites for wood-cutting tools. *Journal of the European Ceramic Society, 27*, 419–428.

Gauvent, M., Rocca, E., Meausoone, P. J., & Brenot, P. (2006). Corrosion of material used as cutting tools of wood. *Wear, 261*, 1051–1055.

Gnesin, G. G., Osipova, I. I., Yaroshenko, V. P., & Rontal, G. D. (1991). *Ceramic tool materials*. Kiev, Ukraine: Tekhnika.

Goble, R. J., & Scott, S. D. (1985). The relationship between mineral hardness and compressibility (or bulk modulus). *Canadian Mineralogist, 23*, 273–285.

Gomes, J. R., Miranda, A. S., Silva, R. F., & Vieira, J. M. (1999). Tribooxidational effects on friction and wear behavior of silicon nitride/tool steel and silicon nitride/grey cast iron contacts. *Journal of the American Ceramic Society, 82*, 953–960.

Green, D. J., Hannink, R. H. J., & Swain, M. V. (1989). *Transformation toughening of ceramics*. Boca Raton, FL: CRC Press.

Green, D. J. (1982). Criticak microstructures for microcracking in Al_2O_3-ZrO_2 composites. *Journal of the American Ceramic Society, 65*, 610–614.

Grzesik, W., & Malecka, J. (2011). Documentation of tool wear progress in the machining of nodular ductile iron with silicon nitride-based ceramic tools. *CIRP Annals – Manufacturing Technology, 60*, 121–124.

Grzesik, W., & Zak, K. (2009). Mechanical, thermal and tribological aspects of the machining process of nodular cast iron with coated carbide and ceramic tools. *Advances in Manufacturing Science and Technology, 33*, 31–43.

Grzesik, W., & Zalisz, Z. (2008). Wear phenomenon in the hard steel machining using ceramic tools. *Tribology International, 41*, 802–812.

Grzesik, W., Rech, J., Zak, K., & Claudin, C. (2009). Machining performance of pearlitic-ferritic nodular cast iron with coated carbide and silicon nitride ceramic tools. *International Journal of Machine Tools and Manufacture, 49*, 125–133.

Grzesik, W. (2009). Wear development on wiper Al_2O_3–TiC mixed ceramic tools in hard machining of high strength steel. *Wear, 266*, 1021–1028.

Hall, H. T. (1965). Period compounds: synthesis at high pressures and temperatures. *Science, 148*, 1331–1333.

Hampshire, S., Park, H. K., Thompson, D. P., & Jack, K. H. (1978). α-SiAlON ceramics. *Nature, 274*, 880–882.

Hori, S., Yoshimura, M., & Somiya, S. (1986). Strength-toughness relations in sintered and isostatically hot-pressed ZrO_2-toughened Al_2O_3. *Journal of the American Ceramic Society, 69*, 169–172.

Jun, Z., Jianxin, D., Jianhua, Z., & Xing, A. (1997). Failure mechanisms of a whisker-reinforced ceramic tool when machining nickel-based alloys. *Wear, 208*, 220–225.

Kannatey-Asibu, E., Jr. (1999). On the performance of silicon nitride cutting tool in machining steel. *Journal of Manufacturing Systems, 9*, 159–168.

Karihaloo, B. L. (1991). Contributions of t-m phase transformation to the toughening of ZTA. *Journal of the American Ceramic Society, 74*, 1703–1706.

King, A. G., & Wheildon, W. M. (1966). *Ceramics in machining processes*. New York, NY: Academic Press.

Kitagawa, T., Kuboa, A., & Maekawa, A. (1997). Temperature and wear of cutting tools in high-speed machining of Inconel 718 and Ti-6Al-6V-2Sn. *Wear, 202*, 142–148.

Ko, M. K., Kwon, W. T., & Kim, Y.-W. (2004). Development of Al_2O_3-SiC composite tool for machining application. *Ceramics International, 30*, 2081--2086.

Kramer, B. M., & Judd, P. K. (1985). Computational design of wear coatings. *Journal of Vacuum Science and Technology A, 3*, 2439–2444.

Krishnamurthy, R., & Gokularathnam, C. V. (1994). Phase transformation toughened materials for cutting tool applications. In E. D. Whitney (Ed.), *Ceramic cutting tools* (pp. 112–190). Park Ridge, NJ: Noyes Publications.

Ladd, M. F. C. (1979). *Structure and bonding in solid state chemistry*, pp. 84–86. New York, NY: John Wiley and Sons.

Lange, F. F. (1982). Transformation toughening. *Journal of Materials Science, 17*, 225–262.

Li, X. S., & Low, I. M. (1994). Evaluation of advanced alumina based ceramic tool inserts when machining high tensile steel. *Journal of Materials Science, 29*, 3121–3127.

López de la Calle, L. N., Lamikiz, A., Fernández de Larrinoa, J., & Azkona, I. (2011). Advanced cutting tools. In J. P. Davim (Ed.), *Machining of hard materials*. London: Springer-Verlag.

Mandal, N., Doloi, B., & Mondal, B. (2011). Development of flank wear prediction model of zirconia toughened alumina (ZTA) cutting tool using response surface methodology. *International Journal of Refractory Metals and Hard Materials, 29*, 273–280.

Mandal, N., Doloi, B., Mondal, B., & Das, R. (2011). Optimization of flank wear using zirconia toughened alumina (ZTA) cutting tool: Taguchi method and regression analysis. *Measurement, 44*, 2149–2155.

McColm, I. J. (1990). *Ceramic hardness*. New York, NY: Plenum Press.

Mohs, F. (1824). *Grundriss der mineralogie*.

Mondal, B., Chattopadhya, A. B., Virkar, A., & Paul, A. (1992). Development and performance of zirconia toughened alumina ceramic tools. *Wear, 156*, 365–383.

Mondal, B. (2005). Zirconia toughened alumina for wear resistance engineering and machinability of steel applications. *Advances in Applied Ceramics, 104*, 256–260.

Oganov, A. R., & Lyakhov, A. O. (2010). Toward the theory of hardness of materials. *Journal of Superhard Materials, 32*, 143–147.

Oliveira, F. J., Silva, R. F., & Vieira, J. M. (1998). Chemical reactivity of silicon nitride with oxide, nitride and carbide dispersoids against carbon steel. *Journal of Materials Synthesis and Processing, 6*, 287–290.

Oliveira, F. J., Silva, R. F., & Vieira, J. M. (2000). Thermochemistry of contacts between silicon nitride ceramics and steel. *Acta Materialia, 18–19*, 4659–4665.

Oliveira, F. J., Silva, R. F., & Vieira, J. M. (2003). Improved wear resistance of Si_3N_4 tool inserts by addition of Al_2O_3 platelets. *Tribology International, 36*, 57–60.

Oliveira, A. J., Diniz, A. E., & Ursolino, D. J. (2009). Hard turning in continuous and interrupted cut with PCBN and whisker-reinforced cutting tools. *Journal of Materials Processing Technology, 209*, 5262–5270.

Pasto, A. (2013). Synthesis/Processing of Silicon Nitride Ceramics. In V. K. Sarin, Luis Llanes, & Daniele Mari (Eds.), *Comprehensive Hard Materials, Vol. 2: Ceramics*. UK: Elsevier Ltd. Oxford.

Pauling, L. (1967). *The nature of the chemical bond*. Ithaca, NY: Cornell University Press, (p. 93).

Ratterman, E., & Bovenkerk, H. P. (1994). Polycrystalline diamond and cubic boron nitride. In E. D. Whitney (Ed.), *Ceramic cutting tools* (pp. 241–304). Park Ridge, NJ: Noyes Publications.

Reddy, J. J., Chakraborty, A., Mahajan, Y. R., & Prasad, N. S. (1990). Performance of ceramic cutting tools in machining cast iron. *Powder Metallurgy International, 22*, 27–31.

Richards, N., & Aspinwall, D. (1989). Use of ceramic tools for machining nickel based alloys. *International Journal of Machine Tools and Manufacture, 29*, 575–588.

Riley, F. L. (2000). Silicon nitride and related materials. *Journal of the American Ceramic Society, 83*, 245–265.

Rühle, M., Evans, A. G., McMeeking, M., Charambelides, P. R., & Hutchinson, J. M. Microcrack toughening in alumina/zirconia. *Acta Metallurgica et Materialia*, 35, 2701–2710.

Sarin, V. K., & Buljan, S. T. (1983). *Advanced silicon nitride based ceramics for cutting tools, SME technical paper no. MR83–189*.

Sarin, V. K., & Buljan, S. T. (1984). Ceramic cutting tools. In *Science and technology yearbook*. McGraw–Hill.

Sarin, V. K., & Buljan, S. T. (1985). Coated ceramic cutting tools. In V. K. Sarin (Ed.), *Proc. high prod. mach., mater. and process.*. ADM.

Sarin, V. K. (1988). On the α to β phase transformation in silicon nitride. *Material Science and Engineering, A, 105/106*, 151–159.

Senthil Kumar, A., Raja Durai, A., & Sornakumar, T. (2003). Machinability of hardened steel using alumina based ceramic cutting tools. *International Journal of Refractory Metals and Hard Materials, 21*, 109–117.

Senthil Kumar, A., Raja Durai, A., & Sornakumar, T. (2006). Wear behavior of alumina based ceramic cutting tools on machining steels. *Tribology International, 39*, 191–197.

Sergo, V., Lughi, V., Pezzotti, G., Lucchini, E., Meriani, S., Muraki, N., et al. (1998). The effect of wear on the tetragonal-to-monoclinic transformation andthe residual-stress distribution in zirconia-toughened alumina cutting tools. *Wear, 214*, 264–270.

Shaw, M. C. (1968). Comments in preface to book. In H. J. Swinehart (Ed.), *Cutting tool material selection* (pp. 1–2). Dearborn, MI: American Society of Tool and Manufacturing Engineers.

Shaw, M. C. (1994). Tool life. In E. D. Whitney (Ed.), *Ceramic cutting tools* (pp. 13–27). Park Ridge, NJ: Noyes Publications.

Silva, R. F., Gomes, J. R., Miranda, A. S., & Vieira, J. M. (1991). Resistance of Si_3N_4 ceramic tools to thermal and mechanical loading in cutting of iron alloys. *Wear, 148*, 69–89.

Smuk, B., Szutkowska, M., & Walter, J. (2003). Alumina ceramics with partially stabilized zirconia for cutting tools. *Journal of Materials Processing Technology, 133*, 195–198.

Souza, J. V. C., Nono, M. C. A., Ribeiro, M. V., Machado, J. P. B., & Silva, O. M. M. (2009). Cutting forces in turning gray cast iron using silicon based cutting tool. *Materials and Design, 30*, 2715–2720.

Strehler, C., Blugan, G., Ehrle, B., Speisser, B., Graule, T., & Kuebler, J. (2010). Influence of sintering and sintering additives on the mechanical and microstructural characteristics of Si_3N_4/SiC wood cutting tools. *Journal of the European Ceramic Society, 30*, 2109–2115.

Strehler, C., Parlinska-Wojtan, M., Blugan, G., Speisser, B., Ehrle, B., Aneziris, C. G., et al. (2011). Influence of intergranular phases on edge integrity of Si_3N_4/SiC wood cutting tools. *Journal of the European Ceramic Society, 31*, 2711–2719.

Tabor, D. (1954). MOHS's hardness scale – a physical interpretation. *Proceedings of the Physics Society B, 67*, 249–257.

Vleugels, J., Van der Perre, I., & Van der Biest, O. (1996). Influence of alloying elements on the chemical reactivity between Si-Al-O-N ceramics and iron-based alloys. *Journal of Materials Research, 11*, 1265–1276.

Wayne, S. F., & Buljan, S.-T. (1989). The role of thermal shock on tool life of selected ceramic cutting tool materials. *Journal of the American Ceramic Society, 72*, 754–760.

Wayne, S. F., & Buljan, S.-T. (1990). Wear of ceramic cutting tools in Ni-based superalloy machining. *Tribology Transactions, 33*, 618–626.

Whitney, E. D., & Batha, H. D. (1973). Kinetics and mechanism of the thermal decomposition of silicon nitride. *Journal of the American Ceramic Society, 56*, 365–369.

Whitney, E. D., & Vaidyanathan, P. N. (1985). Advances in ceramic cutting tools – a researcher's perspective. *Manufacturing Engineering, 94*, 36–37.

Whitney, E. D., & Vaidyanathan, P. N. (1987). Engineered ceramics for high speed machining. In J. A. Swartley-Loush (Ed.), *Tool materials for high speed machining* (pp. 77–82). Metals Park, OH: American Society for Metals International.

Whitney, E. D. (1962). Effect of pressure on monoclinic-tetragonal transition of zirconia. *Journal of the American Ceramic Society, 45*, 612–613.

Whitney, E. D. (1965a). Electrical resistivity and diffusionless phase transformations of zirconia at high temperatures and ultrahigh pressures. *Journal of the Electrochemical Society, 112*, 91–94.

Whitney, E. D. (1965b). Kinetics and mechanism of the transition of metastable tetragonal to monoclinic zirconia. *Transactions of the Faraday Society, 61*, 1991–2000.

Whitney, E. D. (1972a). Thermodynamic properties of abrasive materials. In M. D. Shaw (Ed.), *New developments in grinding* (pp. 53–74). Pittsburg, PA: Carnegie Press, Carnegie-Mellon University.

Whitney, E. D. (1972b). Chemistry of abrasives and the abrasive process. *InterCeram, 21*, 184–188.

Whitney, E. D. (Ed.). (1994). *Ceramic cutting tools*. Park Ridge, NJ: Noyes Publications.

Wilkie, L. A., & Rimanoczy, R. S. (1981). *The principles of American prosperity*. Dallas, TX: The Fisher Institute.

Yin, Z., Huang, C., Zou, B., Liu, H., Zhu, H., & Wang, J. (2012). Preparation and characterization of Al_2O_3/TiC micro–nano-composite ceramic tool materials. *Ceramics International*. http://dx.doi.org/10.1016/j.ceramint.2012.10.277.

Zhu, L., Luo, L., Li, J., & Wu, Y. (2012). The influence of powder characteristics on mechanical properties of Al_2O_3-TiC-Co ceramic materials prepared by Co-coated Al_2O_3/TiC powders. *International Journal of Refractory Metals and Hard Materials, 34*, 61–65.

Zhu, D., Zhang, X., & Ding, H. (2013). Tool wear characteristics in machining of nickel-based superalloys. *International Journal of Machine Tools and Manufacture, 64*, 60–77.

This page intentionally left blank